Transactions of the ASME®

Technical Editor, LEON M. KEER (1992)

The Technological Institute
Northwestern University
Evanston, IL 60201

APPLIED MECHANICS DIVISION

Chairman, WILLIAM S. SARIC
Secretary, THOMAS A. CRUSE
Associate Technical Editors,
R. ABEYARATNE (1994)
T. R. AKYLAS (1994)
S. A. BERGER (1994)
R. M. BOWEN (1993)
S. K. DATTA (1995)
G. J. DVORAK (1995)
M. E. FOURNEY (1993)
R. L. HUSTON (1993)
D. J. INMAN (1995)
S. LICHTER (1995)
X. MARKENSCOFF (1994)
R. M. McMEEKING (1993)
A. K. NOOR (1993)
D. M. PARKS (1995)
J. N. REDDY (1995)
J. W. RUDNICKI (1994)
W. N. SHARPE, JR. (1993)
C. F. SHIH (1995)
P. D. SPANOS (1994)
F. Y. M. WAN (1994)

BOARD ON COMMUNICATIONS
Chairman and Vice-President
R. D. ROCKE
Members-at-Large
T. BARLOW, W. BEGELL, T. F. CONRY,
T. DEAR, J. KITTO, R. MATES,
W. MORGAN, E. M. PATTON,
S. PATULSKI, R. E. REDER,
A. VAN DER SLUYS, F. M. WHITE

OFFICERS OF THE ASME
President, J. A. FALCON
Exec. Director
D. L. BELDEN
Treasurer
ROBERT A. BENNETT

PUBLISHING STAFF
Mng. Dir., Publ.,
CHARLES W. BEARDSLEY
Managing Editor,
CORNELIA MONAHAN
Production Assistant,
MARISOL ANDINO

Transactions of the ASME, Journal of Applied Mechanics (ISSN 0021-8936) is published quarterly (Mar., June, Sept., Dec.) for $165.00 per year by The American Society of Mechanical Engineers, 345 East 47th Street, New York, NY 10017. Second class postage paid at New York, NY and additional mailing office. POSTMASTER: Send address changes to Transactions of the ASME, Journal of Applied Mechanics, c/o THE AMERICAN SOCIETY OF MECHANICAL ENGINEERS, 22 Law Drive, Box 2300, Fairfield, NJ 07007-2300.

CHANGES OF ADDRESS must be received at Society headquarters seven weeks before they are to be effective. Please send old label and new address.

PRICES: To members, $40.00, annually: to nonmembers, $165.00. Add $24.00 for postage to countries outside the United States and Canada.

STATEMENT from By-Laws. The Society shall not be responsible for statements or opinions advanced in papers or ... printed in its publications (B7.1, Par. 3).

COPYRIGHT © 1992 by The American Society of Mechanical Engineers. Authorization to photocopy material for internal or personal use under circumstances not falling within the fair use provisions of the Copyright Act is granted by ASME to libraries and other users registered with the Copyright Clearance Center (CCC) Transactional Reporting Service provided that the base fee of $3.00 per article plus $.30 per page is paid directly to CCC, 27 Congress St., Salem, MA 01970. Request for special permission or bulk copying should be addressed to Reprints/Permission Department.

INDEXED by Applied Mechanics Reviews and Engineering Information, Inc. Canadian Goods & Services Tax Registration #126148048

Journal of Applied Mechanics

Published Quarterly by The American Society of Mechanical Engineers

VOLUME 59 • NUMBER 4 • DECEMBER 1992

705 Editorial

TECHNICAL PAPERS

706 Singular Plastic Fields in Steady Penetration of a Rigid Cone
David Durban and Normal A. Fleck

711 Chaotic Responses of a Two-Degree of Freedom Elastic-Plastic Beam Model to Short Pulse Loading (92-WA/APM-12)
J.-Y Lee, P. S. Symonds, and G. Borino

722 On the Identification of a Harmonic Force on a Viscoelastic Plate From Response Data (92-WA/APM-8)
J. D'Cruz, J. D. C. Crisp, and T. G. Ryall

730 Finite Element Analysis of Multiphase Viscoelastic Solids (92-WA/APM-11)
L. C. Brinson and W. G. Knauss

738 Axial Decay of Self-Equilibrating End Loads in Compressible Solids
David Durban and Boris Karp

744 Saint-Venant End Effects for Materials With Negative Poisson's Ratios
R. S. Lakes

747 Decay Rates for the Hollow Circular Cylinder
N. G. Stephen and M. Z. Wang

754 Finite Deformation Analysis of Pressure-Shear Plate Impact Experiments on an Elastohydrodynamic Lubricant (92-WA/APM-13)
K. T. Ramesh and R. J. Clifton

762 Spectral Decomposition of the Elasticity Tensor
S. Sutcliffe

774 Further Aspects of the Elastic Field for Two Circular Inclusions in Antiplane Elastostatics
E. Honein, T. Honein, and G. Herrman

780 Effects of an Elliptical Inhomogeneous Inclusion With a Slipping Interface on the Elastic Field of a Concentrated Moment
Sriram Vaidyanathan and Demitris Kouris

783 Sliding Inclusions and Inhomogeneities With Frictional Interfaces (92-WA/APM-19)
R. Furuhashi, Jin H. Huang, and T. Mura

789 Stress Distribution in an Edge-Stiffened Semi-infinite Elastic Plate Containing a Circular Hole
Eung J. Lee and Eric C. Klang

796 Interface Blunting of Matrix Cracks in Fiber-Reinforced Ceramics
Anna Dollar and Paul S. Steif

804 Transient Analysis of a Semi-infinite Crack Subjected to Dynamic Concentrated Forces
Chwan-Huei Tsai and Chien-Ching Ma

812 Propagation of Rayleigh Waves in Magneto-Elastic Media (92-WA/APM-9)
Jong S. Lee and Elizabeth N. Its

819 Variational Principles for Hydraulic Fracturing
S. H. Advani, T. S. Lee, and R. H. Dean

827 Boundary Formulations for Three-Dimensional Continuum Structural Shape Sensitivity Analysis
J. H. Kane, G. Zhao, H. Wang, and K. Guru Prasad

835 An Inverse Formulation With Boundary Elements
Xiaogang Zeng and Sunil Saigal

841 Determination of Stress Components From Thermoelastic Data Without Boundary Conditions
T. G. Ryall, M. Heller, and R. Jones

848 Three-Dimensional Solutions for the Thermal Buckling and Sensitivity Derivatives of Temperature-Sensitive Multilayered Angle-Ply Plates (92-WA/APM-2)
A. K. Noor and W. Scott Burton

857 Stress Singularities at the Interface in Bonded Dissimilar Materials Under Mechanical and Thermal Loading
D. Munz and Y. Y. Yang

862 Damping and Resonance Characteristics of Thermal Waves (92-WA/APM-4)
Da Yu Tzou

868 Three-Dimensional Solutions for the Free Vibrations and Buckling of Thermally Stressed Multilayered Angle-Ply Composite Plates
Ahmed K. Noor and W. Scott Burton

878 Elastodynamic Response of a Unidirectional Composite Laminate to Concentrated Surface Loads: Part I (92-WA/APM-6)
Ajit K. Mal and Shyh-Shiuh Lih

887 Elastodynamic Response of a Unidirectional Composite Laminate to Concentrated Surface Loads: Part II (92-WA/APM-15)
Shyh-Shiuh Lih and Ajit K. Mal

893 Nonlinear Dynamics of In-Plane Loaded Imperfect Rectangular Plates
Alvandi Bhirmaraddi

(Contents continued on Inside Back Cover)

Downloaded 04 May 2010 to 171.66.16.49. Redistribution subject to ASME license or copyright; see http://www.asme.org/terms/Terms_Use.cfm

CONTENTS (CONTINUED)

902 **The Effect of Compressibility on the Stress Distributions in Thin Elastomeric Blocks and Annular Bushings**
Yeh-Hung Lai, D. A. Dillard, and J. S. Thornton

909 **The Distributions of Simultaneous Fiber Failures in Fiber Bundles**
Per C. Hemmer and Alex Hansen

915 **On the Proper Boundary Conditions for a Beam**
H. Fan and G. E. O. Widera

923 ***Closed-Form Vibration Analysis of Sagged Cable/Mass Suspensions*** (92-WA/APM-7)
S.-P. Cheng and N. C. Perkins

929 **An Evaluation of Convex Modeling for Multimode Dynamic Buckling**
Herbert E. Lindberg

937 **Convex Models for Uncertain Imperfection Control in Multimode Dynamic Buckling**
Herbert E. Lindberg

946 **Liapunov Stability Analysis of Elastic Shaft-Rigid Disk-Bearing Systems**
H.-Y. Huang and A. L. Schlack, Jr.

955 **On the Transitivity Equations of Rigid-Body Dynamics**
John G. Papastavridis

963 **Coefficients of Restitution** (92-WA/APM-5)
Charles E. Smith and Pao-Pao Liu

970 **A Second-Order Approximate Analytical Solution of a Simple Pendulum by the Process Analysis Method**
S. J. Liao

976 **Dynamic Analysis of Flexible Gear Trains/Transmissions: An Automated Approach**
F. M. L. Amirouche, N. H. Shareef, and M. Xie

983 **Node Control of Uniform Beams Subject to Various Boundary Conditions**
L. Waver, Jr. and L. Silverberg

991 **Dynamics of Flexible Beams and Plates in Large Overall Motions**
Z. E. Boutaghou, Arthur G. Erdman, and Henry K. Stolarski

1000 **Stability of the Vertical Autorotation of a Single-Winged Samara**
D. Seter and A. Rosen

1009 **Transfer Functions of One-Dimensional Distributed Parameter Systems** (92-WA/APM-1)
B. Yang and C. A. Tan

1015 **Robustness of Nonlinear Systems Perturbed by External Random Excitation** (92-WA/APM-3)
G. Leng, N. Sri Namachchivaya, and S. Talwar

1023 **Scattering of Water Waves by a Pair of Semi-infinite Barriers**
P. McIver and A. D. Rawlins

BRIEF NOTES

Alternative Formulation of Elastic Fields Due to Inhomogeneous Isotropic Spherical Inclusions Undergoing Shape-Conserving Volume Change — 1026
S. Schmauder and W. Mader

Equations for the Nonlinear Planar Deformation of Beams — 1028
Avinoam Libai

Some Remarks on a Class of Uniform Fields in Fibrous Composites — 1030
Y. Benveniste and G. J. Dvorak

Another Look at Orthogonal Curvilinear Coordinates in Kinematic and Dynamic Analyses — 1033
C. Q. Liu and R. L. Huston

1036 On Finite Twisting and Bending of Nonhomogeneous Anisotropic Elastic Plates
E. Reissner

1038 Small Vibrations of Rotating Ring Segments and Full Rings Under External or Internal Pressure
Christoph Pelchen and Jörg Wauer

1041 Axisymmetric Vibrations of Layered Tapered Plates
P. V. Navaneethakrishnan, K. Chandrasekaran, and N. Ravisrinivas

DISCUSSIONS

1044 **Circumferential Stresses in Curved Beams, by Robert D. Cook—Discussion by Robert Schmidt**

1045 **Dynamic Crack Propagation Analysis by Moving Singular Boundary Elements, by Rafael Gallego and José Dominguez—Discussion by Robert B. Haber**

1046 **Natural Frequencies and Normal Modes of a Spinning Timoshenko Beam With General Boundary Conditions, by J. W. Z. Zu and R. P. S. Han—Discussion by Charles W. Bert**

ANNOUNCEMENTS AND SPECIAL NOTES

729 12th ASME Freeman Scholar Program in Fluids Engineering—Announcement

922 IABEM 93—Call for Papers

999 Change of Address Form

1048 Books Received by the Office of the Technical Editor

1049 Worldwide Mechanics Meetings List

1051 *1991 Author Index*

1054 Information for Authors

Downloaded 04 May 2010 to 171.66.16.49. Redistribution subject to ASME license or copyright; see http://www.asme.org/terms/Terms_Use.cfm

Lewis T. Wheeler Appointed Technical Editor of the Journal of Applied Mechanics

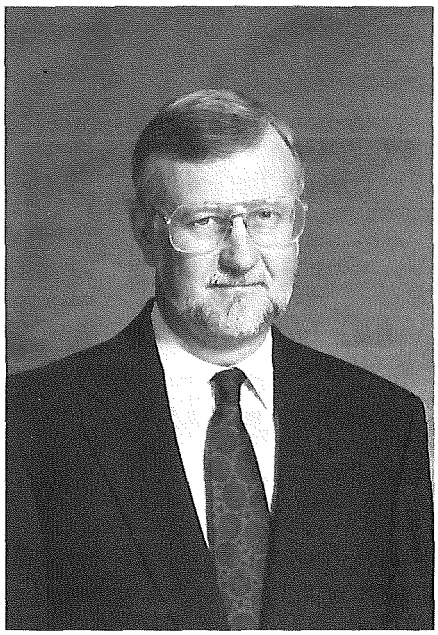
Dr. Lewis T. Wheeler, Professor of Mechanical Engineering at the University of Houston, has been appointed Technical Editor of the *Journal of Applied Mechanics* for a five-year term, beginning Jan. 1, 1993. He succeeds Dr. Leon M. Keer who completes his term of service in this post on Dec. 31, 1992.

Lew Wheeler earned a Bachelor of Science degree in Mechanical Engineering from the University of Houston and a Doctor of Philosophy degree in Applied Mechanics from the California Institute of Technology. He has been on the faculty at the University of Houston since 1968, and has held visiting positions at the University of California, Berkeley, and the University of Pisa. Lew's research interests span solid mechanics and fluid mechanics. He has published research papers on a range of topics, including the theory of elastic waves in solids, stress bounds and spatial decay estimates for stress fields, large strain elasticity, crack mechanics, and viscous flows.

Lew has also been active in ASME through the Applied Mechanics Division. He has served on the Junior Awards Committee, as chair of the AMD Elasticity Committee, and as Associate Editor of the *Journal of Applied Mechanics*. He is a Fellow of ASME.

This appointment represents the final step in a process begun more than 18 months ago, when the AMD Executive Committee formed a selection committee with the charge of nominating a candidate for the post of Technical Editor. The members of the selection committee were David Bogy (chair), Michael Carroll, John Hutchinson, Leon Keer, and myself. After considering a number of possible candidates, the committee conveyed its nomination of Lew Wheeler to the Executive Committee. With the enthusiastic endorsement of the Executive Committee, the nomination was forwarded to the ASME Board on Communications which made the appointment, effective in 1993. The Department of Mechanical Engineering at the University of Houston has generously agreed to make available the space and other institutional resources required to establish and operate the journal editorial office.

This issue of the journal is the last that will bear Leon Keer's name as Technical Editor on the masthead. We wish to express to Leon the deep appreciation of all members of the Applied Mechanics Division, and of the AMD Executive Committee in particular, for his efforts on behalf of the journal over the past five years. Demand for space in the journal has increased steadily, and the corps of talented associate editors has worked



diligently under Leon's leadership to maintain the quality of the *Journal of Applied Mechanics*. This is a complex and demanding job involving technical leadership, organizational skills, a sense of community and, at times, diplomacy. The role of the Editor is invisible when things work well and it is the lightning rod when a problem arises. Leon has handled the role effectively, graciously, and with good cheer.

The vitality of any discipline is most accurately reflected in the quality of its archival literature, and the publication of the *Journal of Applied Mechanics* is the most important single activity of the Applied Mechanics Division. On behalf of the AMD Executive Committee, it is a pleasure to welcome Lewis Wheeler to the post of Technical Editor, and to assure him of the support and cooperation of the Division in his efforts to sustain the health and vigor of the journal.

L. B. Freund
Chair, AMD Publications Committee

Copyright © 1992 by ASME
Downloaded 03 May 2010 to 171.66.16.247. Redistribution subject to ASME license or copyright; see http://www.asme.org/terms/Terms_Use.cfm

Singular Plastic Fields in Steady Penetration of a Rigid Cone

David Durban
Faculty of Aerospace Engineering,
Technion—Israel Institute of Technology,
Haifa 32000, Israel

Norman A. Fleck
Department of Engineering,
Cambridge University,
Cambridge CB2 1PZ, U.K.

The essential features of the active plastic zone at the tip of a penetrating rigid cone are investigated for a rigid/perfectly plastic solid. An exact solution is suggested for the plastic zone. A rigid zone exists ahead of the cone and is separated from the plastic zone by a conical surface of discontinuity. It is assumed that the material yields instantaneously by going through a "shear shock" across the rigid/plastic interface. The orientation of the interface is determined by an ad hoc requirement for minimum shear strain jump at the shear shock. Results are presented for different cone angles and friction factors. The stresses within the plastic zone admit a logarithmic singularity whose level increases with cone angle and wall friction.

Introduction

Local singular fields at the tip of a rigid conical indentor, penetrating an incompressible power-law viscous solid have been studied recently by Fleck and Durban (1990). The limiting case of that analysis for vanishing strain-rate exponent describes possible singular fields of rigid/perfectly plastic materials with logarithmic singularity of the stresses and a power-type strain rate singularity. The plastic zone of this solution extends continuously over the entire near-tip volume of the penetrated solid.

In the present paper we address the problem of rigid/perfectly plastic singular fields, near a tip of a penetrating cone, employing an alternative model. It is thought that the new solution is relevant to surface indentation and to deep penetration by a rigid cone. Following existing studies on discontinuous rigid/plastic conical fields (Lockett, 1963; Shield, 1955; Spencer, 1984) we assume that the material ahead of the cone remains rigid up to a rigid/plastic interface (Fig. 1). At that conically shaped interface, the solid yields instantaneously by passing through a "shear shock." The mathematical model is constructed in the spirit of earlier studies of orthogonal machining, where rigid/perfectly plastic theory gives useful physical insight to the problem. In particular, machining theory suggests a shear shock at an angle which bisects the machining direction and the angle of the tool face. This prediction is borne out by experimental observation (Johnson and Mellor, 1973). The rigid/plastic interface simulates a more diffuse transition zone where the streamlines possess high local curvature.

An exact, almost closed-form solution is suggested for the active plastic zone which extends from the interface to the cone. Surface roughness is accounted for by imposing a friction factor along the wall. The shear stress $\sigma_{r\theta}$ on the wall is given by $|\sigma_{r\theta}| = mk$ where k is the shear yield stress and the friction factor m ranges from zero to unity. The stresses have a logarithmic singularity while the strain rates singularity is r^{-1}. The latter is stronger than the strain rate singularities reported earlier by Fleck and Durban (1990). A similar conclusion holds for the level (amplitude) of the logarithmic stress singularity. More refined boundary value calculations are required in order to assess which of the two solutions is the more frequently encountered in penetration and indentation problems.

At the rigid/plastic interface we impose a pragmatic ad hoc requirement that the finite jump in the shear strain attains its smallest possible value. This condition determines uniquely the shear shock orientation, approximately in a direction bisecting the angle between the cone's wall and the penetrating axis.

Detailed results are presented for the influence of cone angle and wall friction on the interface orientation, the shear strain jump at the interface, level of stress singularity, and shape of streamlines. The paper concludes with a brief discussion of Spencer's (1984) model, which is here recovered as a special case for one particular cone angle and friction condition.

We assume a von Mises yield law and an associated flow rule, while previous studies (Lockett, 1963; Shield, 1955; Spencer, 1984) employ a Tresca yield law. The present analysis

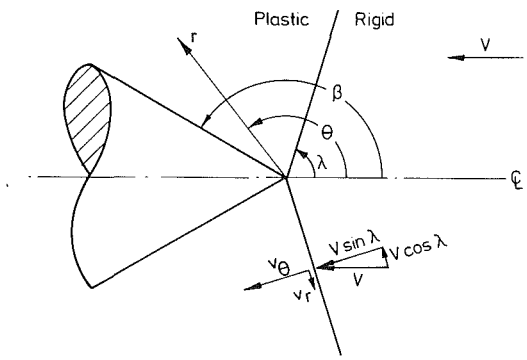


Fig. 1 Convention for steady penetration of a rigid cone. A "shear shock" discontinuity at $\theta = \lambda$ marks the rigid/plastic interface.

Contributed by the Applied Mechanics Division of THE AMERICAN SOCIETY OF MECHANICAL ENGINEERS for publication in the ASME JOURNAL OF APPLIED MECHANICS.

Discussion on this paper should be submitted to the Technical Editor, Prof. Leon M. Keer, The Technological Institute, Northwestern University, Evanston, IL 60208, and will be accepted until four months after final publication of the paper itself in the ASME JOURNAL OF APPLIED MECHANICS.

Manuscript received by the ASME Applied Mechanics Division, Sept. 24, 1990; final revision, July 22, 1991. Associate Technical Editor: J. W. Rudnicki.

Copyright © 1992 by ASME
Downloaded 03 May 2010 to 171.66.16.247. Redistribution subject to ASME license or copyright; see http://www.asme.org/terms/Terms_Use.cfm

provides, apparently for the first time, an analytical solution for the velocities and stresses within the singular plastic zone. This enables us to examine the details of the coupling between wall friction and cone angle.

Field Equations and Solution

We consider a rigid cone that penetrates a rigid/perfectly plastic solid (Fig. 1). Assume low velocity steady-state conditions and concentrate on the near-tip singular field. An Eulerian frame of reference is attached to the apex with spherical coordinates (r, θ, ϕ). Material behavior is modeled as rigid ahead of the cone, up to an instantaneous shear surface at $\theta = \lambda$, and as perfectly plastic within the region bounded by the rigid/plastic interface and the cone's wall at $\theta = \beta$.

The constitutive relation in the plastic sector is given by

$$\mathbf{S} = \sqrt{\frac{2}{3}}\,\sigma_o \frac{\mathbf{D}}{\sqrt{\mathbf{D}\cdot\cdot\mathbf{D}}} \tag{1}$$

where $\mathbf{S}$ is the stress deviator tensor, $\mathbf{D}$ is the Eulerian strain rate tensor, and σ_o is the yield stress in simple tension. Assuming that the velocity field depends only on θ, we find that material incompressibility of (1) is maintained if the velocities are expressed as (Fleck and Durban, 1990)

$$v_r = \phi' + \phi\cot\theta \tag{2}$$

$$v_\theta = -2\phi \tag{3}$$

where (v_r, v_θ) denote the (r, θ) velocity components, ϕ is a velocity potential that depends only on θ, and $(\,)' \equiv d(\,)/d\theta$.

The strain rate components follow from (2)–(3) in the form

$$\epsilon_{rr} = 0 \tag{4}$$

$$\epsilon_{\theta\theta} = -\epsilon_{\phi\phi} = -\frac{1}{r}\,(\phi' - \phi\cot\theta) \tag{5}$$

$$\epsilon_{r\theta} = \frac{1}{2r}\,[(\phi' + \phi\cot\theta)' + 2\phi]. \tag{6}$$

Inserting relations (4)–(6) in (1) we obtain the deviatoric components

$$\sigma_{rr} - \sigma_h = 0 \tag{7}$$

$$\sigma_{\theta\theta} - \sigma_h = -(\sigma_{\phi\phi} - \sigma_h) = -k\,\frac{\phi' - \phi\cot\theta}{\Gamma} \tag{8}$$

$$\sigma_{r\theta} = k\,\frac{Y}{\Gamma} \tag{9}$$

where σ_h is the hydrostatic stress,

$$Y = \frac{1}{2}\,[(\phi' + \phi\cot\theta)' + 2\phi] \tag{10}$$

$$\Gamma^2 = Y^2 + (\phi' - \phi\cot\theta)^2, \tag{11}$$

and $k = \sigma_o/\sqrt{3}$ is the shear yield stress. Notice that $\Gamma(\theta)$ gives the angular dependence of the effective strain rate $\epsilon_{\text{eff}} = (2/3\,\mathbf{D}\cdot\cdot\mathbf{D})^{1/2} \equiv 2\Gamma/\sqrt{3}r$.

Since the state of stress is axially symmetric, there are just two equations of equilibrium, namely

$$r\sigma_{rr,r} + 2\sigma_{rr} - \sigma_{\theta\theta} - \sigma_{\phi\phi} + \sigma_{r\theta,\theta} + \sigma_{r\theta}\cot\theta = 0 \tag{12}$$

$$r\sigma_{r\theta,r} + 3\sigma_{r\theta} + \sigma_{\theta\theta,\theta} + (\sigma_{\theta\theta} - \sigma_{\phi\phi})\cot\theta = 0. \tag{13}$$

On substituting the stresses from (7)–(9) into the radial Eq. (12), we find that the hydrostatic stress must be of the form

$$\sigma_h = k[H(\theta) + D\ln r] \tag{14}$$

where D is a constant and $H(\theta)$ is an unknown function of θ. It follows that radial equilibrium is maintained if

$$Y' - Y\,\frac{\Gamma'}{\Gamma} + Y\cot\theta + D\Gamma = 0 \tag{15}$$

or, after one integration,

$$Y = F(\theta)\Gamma \tag{16}$$

with

$$F = \frac{D\cos\theta + F}{\sin\theta} \tag{17}$$

where E is an integration constant. Combining (16) with (11), and observing that both Γ and $\epsilon_{\phi\phi}$ are positive, gives

$$Y = \frac{F}{\sqrt{1-F^2}}\,(\phi' - \phi\cot\theta). \tag{18}$$

Now eliminate Y between (18) and (10). We arrive at the linear differential equation

$$\phi'' + \left(\cot\theta - \frac{2F}{\sqrt{1-F^2}}\right)\phi' + \left(2 - \frac{1}{\sin^2\theta} + \frac{2F}{\sqrt{1-F^2}}\cot\theta\right)\phi = 0. \tag{19}$$

This equation admits the solution

$$\phi = C_1\sin\theta + C_2 f(\theta)\sin\theta \tag{20}$$

where

$$f(\theta) = \int_\lambda^\theta \frac{g(\theta)}{\sin^3\theta}\,d\theta \tag{21}$$

$$g(\theta) = \exp\int_\lambda^\theta \frac{2F}{\sqrt{1-F^2}}\,d\theta \tag{22}$$

and C_1, C_2 are integration constants.

It still remains to solve the second equation of equilibrium (13); substituting the stresses (7)–(9) and (14) into (13) results in

$$H' = (\sqrt{1-F^2})' + 2\sqrt{1-F^2}\cot\theta - 3F. \tag{23}$$

The integral of (23), obtained with the aid of (17), completes the solution of the equilibrium equations. It is worth noting that the deviatoric components (7)–(9) may be rewritten, by (16) and (18), as

$$\sigma_{rr} - \sigma_h = 0 \tag{24}$$

$$\sigma_{\theta\theta} - \sigma_h = -(\sigma_{\phi\phi} - \sigma_h) = k\sqrt{1-F^2} \tag{25}$$

$$\sigma_{r\theta} = kF. \tag{26}$$

Function F determines the relative contribution of the shear stress to the overall yield stress k.

Boundary Conditions

Turning to the boundary conditions and assuming a maximum shear rigid/plastic interface, we have that $\sigma_{r\theta} = k$ at $\theta = \lambda$ or, from (26),

$$F(\lambda) = 1. \tag{27}$$

Wall friction on the penetrating cone is represented by a shear factor m which controls the level of resisting shear stress at $\theta = \beta$ according to the relation $\sigma_{r\theta} = -mk$. Thus, from (26),

$$F(\beta) = -m. \tag{28}$$

The value of m ranges from $m = 0$ at a smooth wall to $m = 1$ at a perfectly rough wall. Combining conditions (27)–(28) with (17) gives

$$D = \frac{\sin\lambda + m\sin\beta}{\cos\lambda - \cos\beta} \tag{29}$$

$$E = -\frac{\sin\lambda\cos\beta + m\cos\lambda\sin\beta}{\cos\lambda - \cos\beta}. \tag{30}$$

Downloaded 03 May 2010 to 171.66.16.247. Redistribution subject to ASME license or copyright; see http://www.asme.org/terms/Terms_Use.cfm

The "shear-shock" at the rigid/plastic interface is supposed to simulate the narrow elastic-plastic transition zone which is expected to develop near $\theta = \lambda$. This model is constructed in the spirit of early studies on plane-strain machining (Johnson and Mellor, 1973) based on the maximum shear plane hypothesis. In reality, one may expect a relatively large curvature of the streamlines in the vicinity of the idealized shear shock.

The velocity potential (20) contains two constants (C_1, C_2) that can be determined from kinematical conditions. Denoting by V the uniform velocity of the rigid zone, relative to the cone, we have the condition of continuity of velocity normal to the interface (Fig. 1)

$$v_\theta(\lambda) = V\sin\lambda. \tag{31}$$

Along the wall, at $\theta = \beta$, v_θ has to vanish

$$v_\theta(\beta) = 0. \tag{32}$$

Both conditions (31)–(32) involve only the tangential velocity (3) which can be written, by (20), as

$$v_\theta = -2C_1\sin\theta - 2C_2 f(\theta)\sin\theta. \tag{33}$$

Inserting (33) in (31)–(32) we find

$$C_1 = -\frac{V}{2} \quad C_2 = \frac{V}{2f(\beta)}. \tag{34}$$

The interface angle λ is still undetermined. To this end we introduce the ad hoc requirement that the instantaneous shear strain at the interface will be as small as possible. The radial velocity jump at the interface is given by (Fig. 1).

$$\Delta v_r = v_r(\lambda) - (-V\cos\lambda). \tag{35}$$

From (2) and (20) we get the radial velocity component

$$v_r = 2C_1\cos\theta + 2C_2 f(\theta)\cos\theta + C_2\frac{g(\theta)}{\sin^2\theta}. \tag{36}$$

On substituting (36) in (35), observing that $f(\lambda) = 0$ and $g(\lambda) = 1$, and using (34), the velocity jump is

$$\Delta v_r = \frac{V}{2f(\beta)\sin^2\lambda}. \tag{37}$$

A measure of shear strain $\tan\gamma$ at the interface is therefore

$$\tan\gamma = \frac{\Delta v_r}{V\sin\lambda} = \frac{1}{2f(\beta)\sin^3\lambda} \tag{38}$$

where γ is the shear angle. We minimize (38) with respect to λ, for given values of β and m, in order to determine the orientation of the interface.

The strain rate components (4)–(6) may be put in the form

$$\epsilon_{rr} = 0, \quad \epsilon_{\theta\theta} = -\epsilon_{\phi\phi} = -\frac{1}{r}\left(\frac{V}{2f(\beta)}\right)\frac{g(\theta)}{\sin^2\theta}$$

$$\epsilon_{r\theta} = \frac{1}{r}\frac{F}{\sqrt{1-F^2}}\left(\frac{V}{2f(\beta)}\right)\frac{g(\theta)}{\sin^2\theta}.$$

At the rigid/plastic interface the normal components are simplified further, by (37), to

$$\epsilon_{\theta\theta} = -\epsilon_{\phi\phi} = -\frac{\Delta v_r}{r}.$$

Clearly, the shear strain rate component becomes unbounded at the interface where $F = 1$, and also at the wall when the friction factor m attains its highest value. The behavior of $\epsilon_{r\theta}$ near $\theta \approx \lambda$ is governed by

$$\epsilon_{r\theta} \sim \frac{\sqrt{2}\Delta v_r}{2\sqrt{D+\cot\lambda}} \cdot \frac{1}{r\sqrt{\theta-\lambda}}.$$

A similar expansion holds near the wall ($\theta = \beta$) when $m = 1$.

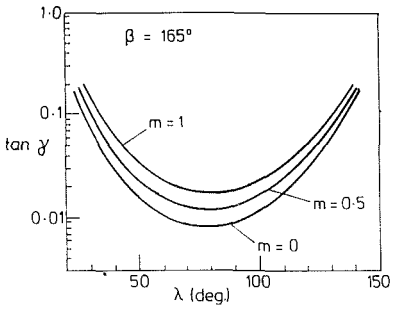


Fig. 2 Variation of shear strain with interface angle for different friction factors m. β = 165 deg.

Numerical Results and Discussion

The variation of the shear strain $\tan\gamma$ with interface angle λ, as evaluated from (38), is illustrated in Fig. 2 for a cone angle of 30 deg and with different values of m. As expected, there exists a clear minimum for the shear strain at a certain value of λ. That value of λ is taken here as the optimal orientation of the rigid/plastic interface within the framework of our model.

The numerical calculation of (38) involves the integrals (21)–(22); at the interface $F = 1$, by (27), and the integrand of (22) becomes unbounded. However, a straightforward expansion shows, with the aid of (17) and (29)–(30), that near $\theta = \lambda$

$$\int_\lambda^{\lambda+\Delta\theta} \frac{2F}{\sqrt{1-F^2}}\,d\theta \sim \frac{2\sqrt{2}}{\sqrt{A}}\sqrt{\Delta\theta} \quad \Delta\theta \ll 1 \tag{39}$$

where

$$A = \frac{1 + m\sin\lambda\sin\beta - \cos\lambda\cos\beta}{(\cos\lambda - \cos\beta)\sin\lambda}. \tag{40}$$

Similarly, when the wall is perfectly rough ($m = 1$) we have, near $\theta = \beta$, the expansion

$$\int_{\beta-\Delta\theta}^{\beta} \frac{2F}{\sqrt{1-F^2}}\,d\theta \sim -\frac{2\sqrt{2}}{\sqrt{B}}\sqrt{\Delta\theta} \quad \Delta\theta \ll 1 \tag{41}$$

with

$$B = \frac{\cos(\beta-\lambda) - \cos 2\beta}{(\cos\lambda - \cos\beta)\sin\beta}. \tag{42}$$

Expansions (39) and (41) have been used to overcome the numerical difficulties near $\theta = \lambda$, and near $\theta = \beta$ when $m = 1$.

The optimal location of the interface varies almost linearly with the angle β but shows little sensitivity to wall friction (Fig. 3). A rough approximation for the interface angle would be $\lambda \approx \beta/2$ provided that the cone is not very sharp. It can be seen from Fig. 3 that λ is smaller for smoother walls. The dependence of the optimal interface angle on β as predicted by the present model resembles the known results for plane-strain orthogonal machining (Johnson and Mellor, 1973). Also, for a smooth flat indentor, with $\beta = \pi/2$ and $m = 0$, we get a shear shock at $\lambda = 46.5$ deg which is slightly above the value of $\lambda = \pi/4$ obtained by Shield (1955) with a slip-line analysis for the flat circular smooth punch.

The criterion $\tan\gamma \rightarrow \min$ is required to compensate for lack of uniqueness in the mathematical model. The fact that the present solution predicts stronger singularities than those obtained by Fleck and Durban (1990) could reflect a better simulation of the actual elastoplastic field. A full elastic, perfectly plastic study may be needed to resolve the issue of competing near-tip singular fields in cone penetration.

The jump in shear strain at the shear shock interface is displayed in Fig. 4. The jump in $\tan\gamma$ across the shear shock

Downloaded 03 May 2010 to 171.66.16.247. Redistribution subject to ASME license or copyright; see http://www.asme.org/terms/Terms_Use.cfm

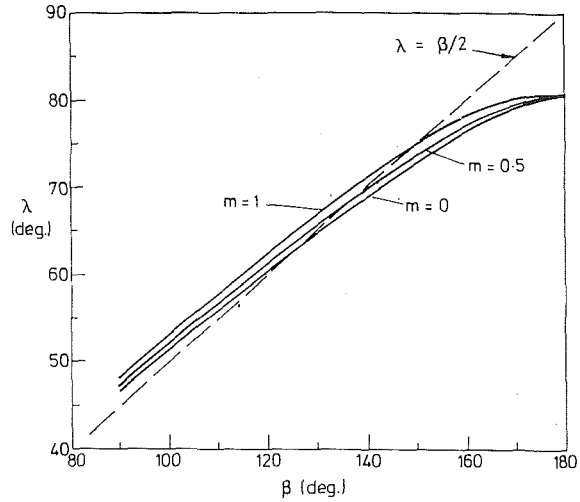


Fig. 3 Variation of optimal interface location λ with wall angle β and friction factor *m*

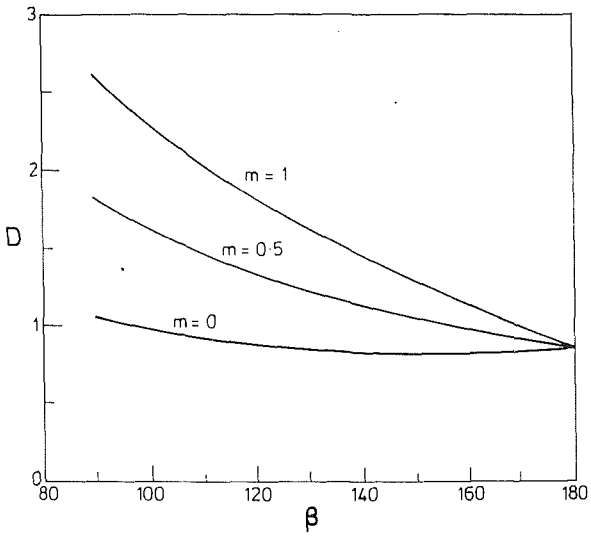


Fig. 5 Levels of stress singularity *D* for different wall angles β and friction factors *m*

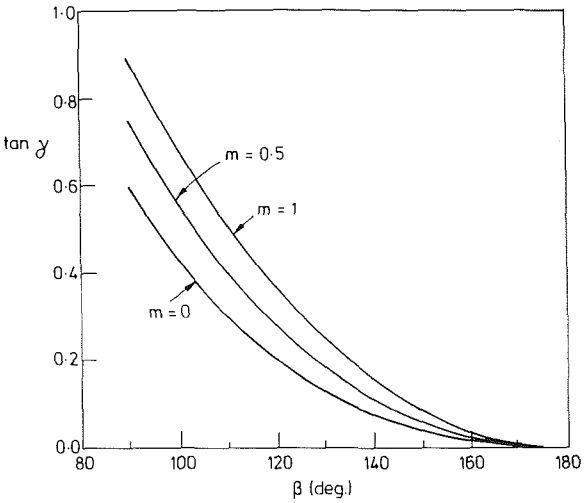


Fig. 4 Variation of shear strain tanγ at the interface with wall angle β and friction factor *m*

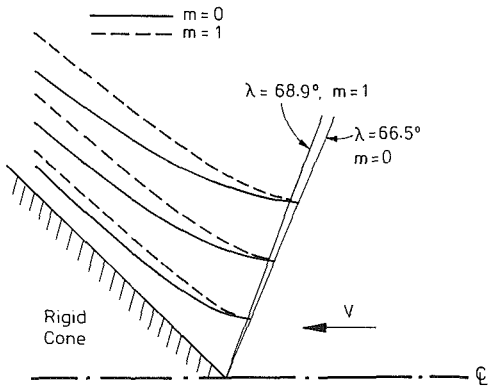


Fig. 6 Streamlines within the plastic zone. β = 135 deg.

increases with wall friction and included cone angle. The influence of m appears to decrease as β increases, though the validity of the model becomes questionable for sharp cones where the elastoplastic transition zone is likely to cover a considerable region of the flow field. This is reflected by vanishingly small values of tanγ as $\beta \to \pi$, which are not compatible with the notion of rigid/plastic discontinuity.

The stress components (24)–(26) are dominated by the logarithmic singularity of the hydrostatic stress (14). The level of that singularity is determined by constant D which is given by (29). The value of D increases with increasing m (Fig. 5) and decreases with increasing β (except for the weak minimum when $m = 0$). This behavior is physically justified since the local drag during penetration is expected to decrease for sharper and smoother cones. The values of D given in Fleck and Durban (1990) are considerably below those obtained here.

Sample calculations were performed for the shape of the streamlines in the plastic zone (Fig. 6). This is done quite easily since along a streamline $dr/r = (v_r/v_\theta)d\theta$ or, from (2)–(3),

$$r^2\phi\sin\theta = \text{constant}, \tag{43}$$

with ϕ expressed by (20).

A Particular Solution

Spencer (1984) has suggested a cone penetration model, based on the rigid/perfectly-plastic Tresca solid, with $\lambda = \pi/2$ and $\sigma_{r\theta} = 0$ everywhere within the plastic field. Thus, there are no radial shear stresses in the plastic zone, and the rigid part occupies a half space. This particular case is easily recovered from our analysis except for the difference in the value of the (Mises) yield stress k. Indeed, with $F \equiv 0$ we have from (22) that $g(\theta) \equiv 1$ and (21) admits the exact integral

$$f(\theta) = \int_{\pi/2}^{\theta} \frac{d\theta}{\sin^3\theta} = \frac{1}{2}\,\text{lntan}\,\frac{\theta}{2} - \frac{1}{2}\,\frac{\cos\theta}{\sin^2\theta}. \tag{44}$$

Equation (23) has now the simple solution $H = 2\text{lnsin}\theta + H_o$, where H_o is an integration constant, resulting in explicit r-independent expressions for the stress components (24)–(25). Likewise, the velocity components of (33) and (36) are given in terms of simple functions.

The interface shear strain (38) follows as

$$\tan\gamma = \frac{1}{\text{lntan}\,\dfrac{\beta}{2} - \dfrac{\cos\beta}{\sin^2\beta}} \tag{45}$$

predicting relatively high values of shear strain. Just to give an example, with $\beta = 135$ deg, Eq. (45) gives $\tan\gamma = 0.436$. By comparison, our model predicts for the same cone angle, with $m = 0$, an interface shear strain of $\tan\gamma = 0.096$ and an interface location of $\lambda = 66.5$ deg.

The solution (44)–(45) is valid only for a smooth cone. The stresses are nonsingular (since $D = 0$) and it is unclear whether

Downloaded 03 May 2010 to 171.66.16.247. Redistribution subject to ASME license or copyright; see http://www.asme.org/terms/Terms_Use.cfm

the jump in the shear strain (45) can exist along the interface in the absence of an active shear stress component.

Case Study: Steady Penetration by a Rod

As an application of the asymptotic analysis we shall estimate the axial force F for deep penetration of an elastic-perfectly plastic solid by a conically tipped circular rod of semi-infinite length. We assume that the rod is reduced slightly in diameter behind its conical head, so that we can neglect the effect on F of friction between the wall of the rod and of the infinite solid. However, we include the effects of friction between the head of the penetrator and the solid.

We take the conical head to be of semi-included angle $\alpha = \pi - \beta$ and of base radius a. The axial force on the penetrator F is

$$F = -\int_o^R (\sigma_{\theta\theta}(\beta)\sin\alpha + \sigma_{r\theta}(\beta)\cos\alpha)2\pi r\sin\alpha dr \qquad (46)$$

where r is the radial coordinate from the apex of the cone, and $R = a/\sin\alpha$ is the flank length of the cone. The average penetration pressure on the conical head $\bar{p} = F/\pi a^2$ is given by evaluation of (46) via (25), (26), and (28),

$$\bar{p} = -k(\sqrt{1-m^2} + H(\beta) + D\ln R) + k\left(\frac{D}{2} + m\cot\alpha\right). \qquad (47)$$

Bishop, Hill, and Mott (1945) have suggested that the penetration pressure may be estimated from the pressure required to expand a circular cylindrical cavity. We follow their suggestion and assume that the hydrostatic pressure (14) at ($r = R$, $\theta = \beta$) equals the limit pressure required to expand a cylindrical cavity in an elastic-perfectly plastic solid (Bishop et al., 1945)

$$\sigma_h(R,\beta) = k(H(\beta) + D\ln R)$$

$$= -k\left(1 + \ln\left(\frac{E}{3k}\right)\right). \qquad (48)$$

Substitution of (48) into (47) gives, using $\alpha_o = k\sqrt{3}$,

$$\frac{\bar{p}}{\sigma_o} = \frac{1}{\sqrt{3}}\left(1 + \ln\left(\frac{E}{\sigma_o\sqrt{3}}\right) + m\cot\alpha + \frac{D}{2} - \sqrt{1-m^2}\right). \qquad (49)$$

The dependence of D upon m and $\alpha = \pi - \beta$ is given in Fig. 5; thus, Eq. (49) gives in an approximate manner the effect of tip singularity, wall friction, and remote elasticity upon the penetration pressure. We note that $\bar{p}/\sigma_o$ increases with increasing E/σ_o, increasing m and decreasing α. At high values of $m \approx 1$ and large $\alpha \gtrsim \pi/4$, we expect that a false cap of nondeforming material sticks to the head of the penetrator; application of Eq. (49) then becomes inappropriate.

Table 1 Comparison of predicted penetration pressure p/σ_o with measured value for work-hardened copper, from Bishop et al. (1945). σ_o = 270 MPA, E = 124 GPA.

	$\alpha = 20^o$		$\alpha = 30^o$	
	Measured $\bar{p}/\sigma_o$	Prediction from (49)	Measured $\bar{p}/\sigma_o$	Prediction from (49)
Unlubricated (m=1)	7.4	5.7	6.8	5.2
Lubricated (m=o)	4.8	3.5	5.5	3.5

The last two terms of Eq. (49) are absent in the estimation of penetration pressure by Bishop et al. (1945). For frictionless penetration ($m = 0$), the sum of the last two terms almost vanishes for $o < \alpha < \pi/2$. For the case of sticking friction ($m = 1$), the last two terms in (49) contribute to $\bar{p}/\sigma_o$ by an amount 0.6 to 1.4, as α ranges from zero to $\pi/2$.

Bishop et al. (1945) measured the penetration pressure in annealed and in work-hardened copper using a penetrator of the type described above. A comparison of their measured penetration pressure for work hardened copper and the predictions of (49) is given in Table 1.

Equation (49) predicts qualitatively the increase in $\bar{p}/\sigma_o$ with increasing m and decreasing α, but consistently underestimates the penetration pressure by approximately 1.7 σ_o. Bishop et al. (1945) improved their estimate of $\bar{p}$ by including the effect of strain hardening in their cavity expansion calculation. The additional pressure due to strain hardening was found to equal $0.2\sigma_o$, which is negligible.

We conclude that a more complete analysis, including the effects of nonproportional loading, is required in order to obtain a more accurate solution to the penetration problem.

Acknowledgment

Part of this research was supported by Technion V.P.R. Fund—Seniel Ostrow Research Fund.

References

Bishop, R. F., Hill, R., and Mott, N. F., 1945, "The Theory of Indentation and Hardness Tests," *Proc. Physical Soc.*, Vol. 57, No. 3, pp. 147–159.

Fleck, N. A., and Durban, D., 1991, "Steady Penetration of a Rigid Cone with a Rough Wall into a Power-Law Viscous Solid," ASME JOURNAL OF APPLIED MECHANICS, Vol. 58, pp. 872–880.

Johnson, W., and Mellor, P. B., 1973, *Engineering Plasticity*, Van Nostrand Reinhold Company, London.

Lockett, F. J., 1963, "Indentation of a Rigid/Plastic Material by a Conical Indenter," *J. Mech. Phys. Solids*, Vol. 11, pp. 345–355.

Shield, R. T., 1955, "On the Plastic Flow of Metals under Conditions of Axial Symmetry," *Proc. Roy. Soc. London*, Vol. A223, pp. 267–287.

Spencer, J. M., 1984, "Plastic Flow Past a Smooth Cone," *Acta Mech.*, Vol. 54, pp. 63–74.

Downloaded 03 May 2010 to 171.66.16.247. Redistribution subject to ASME license or copyright; see http://www.asme.org/terms/Terms_Use.cfm

Chaotic Responses of a Two-Degree-of-Freedom Elastic-Plastic Beam Model to Short Pulse Loading

J.-Y. Lee[1]
Research Assistant,
Mem. ASME.

P. S. Symonds
Professor of Engineering (Research),
Fellow ASME.

G. Borino[2]
Visiting Research Associate.

Division of Engineering,
Brown University,
Providence, RI 02912

The paper discusses chaotic response behavior of a beam model whose ends are fixed, so that shallow arch action prevails after moderate plastic straining has occurred due to a short pulse of transverse loading. Examples of anomalous displacement-time histories of a uniform beam are first shown. These motivated the present study of a two-degree-of-freedom model of Shanley type. Calculations confirm these behaviors as symptoms of chaotic unpredictability. *Evidence of chaos is seen in displacement-time histories, in phase plane and power spectral diagrams, and especially in extreme sensitivity to parameters. The exponential nature of the latter is confirmed by calculations of conventional Lyapunov exponents and also by a direct method. The two-degree-of-freedom model allows use of the energy approach found helpful for the single-degree-of-freedom model (Borino et al., 1989). The strain energy is plotted as a surface over the displacement coordinate plane, which depends on the plastic strains. Contrasting with the single-degree-of-freedom case, the energy diagram illuminates the possibility of chaotic vibrations in an initial phase, and the eventual transition to a smaller amplitude nonchaotic vibration which is finally damped out. Properties of the response are further illustrated by samples of solution trajectories in a fixed total energy plane and by related Poincare section plots.*

1 Introduction

We are treating a problem of structural dynamics: how to determine the response of a fixed-ended beam subjected to a short intense pulse of transverse loading that produces plastic deformation. The constraints against axial displacements mean that membrane forces accompany transverse deflections. Standard numerical methods taking account of geometric as well as material nonlinearity readily furnish the peak deflection (occurring soon after the close of the pulse). However, in certain cases the calculation for the *permanent* displacement runs into surprising difficulties: the predicted final deflection may be in the direction opposite the applied load pulse, and abnormal sensitivity is exhibited to the parameters of the problem and of the numerical treatment. Investigations of these anomalous response behaviors were first given for beams (Symonds and Yu, 1985) and independently for plates (Galiev and Nechitailo, 1985). They have been observed in the laboratory (Li et al., 1991; Kolsky et al., 1991). They must satisfy conditions in rather narrow windows, and their accidental occurrence seems to have been noticed in the literature, to our knowledge, only in two instances (Lavrentiev and Shabat, 1973; Ross et al., 1977).

The plastic elongation of the beam between its fixed-end points effectively converts the beam into a shallow arch, when the plastic strains are small; and snap buckling can occur. Under the short pulse loading, there is an initial "shakedown" period in which the plastic strains are changing, followed by wholly elastic vibrations. What finally happens depends on the total energy available and on the new geometry of the structure. The problem is more difficult than the usual dynamic snap-buckling case because the outcome is sensitive both to the available energy and to the details of the new geometry; these are not given in advance, but determined by the plastic strains.

The paper presents calculated results for a two-degree-of-freedom beam model with lumped parameters. For convenience the load pulse is taken as rectangular in shape with force P applied over a constant time interval, so that P serves as the single load parameter. Since this artificial model is intended to help understand the observed response behavior of uniform beams, a brief review of some results for the latter is first given in Section 2. Some of these are suggestive of *deterministic*

[1]Currently at the Department of Mechanical Engineering, Korea Military Academy, Seoul, Korea 139-799.

[2]Currently at the Division of Structural Engineering and Geotechnics, Palermo University, 90128 Palermo, Italy.

Contributed by the Applied Mechanics Division of THE AMERICAN SOCIETY OF MECHANICAL ENGINEERS for presentation at the 1992 ASME Winter Annual Meeting, Anaheim, CA, Nov. 8-13, 1992.

Discussion on this paper should be addressed to Prof. Leon M. Keer, The Technological Institute, Northwestern University, Evanston, IL 60208, and will be accepted until four months after final publication of the paper itself in the ASME JOURNAL OF APPLIED MECHANICS.

Manuscript received by the ASME Applied Mechanics Division, Mar. 28, 1991; final revision, Jan. 4, 1992. Associate Technical Editor: P. D. Spanos.

Paper No. 92-WA/APM-12.

Copyright © 1992 by ASME
Downloaded 03 May 2010 to 171.66.16.247. Redistribution subject to ASME license or copyright; see http://www.asme.org/terms/Terms_Use.cfm

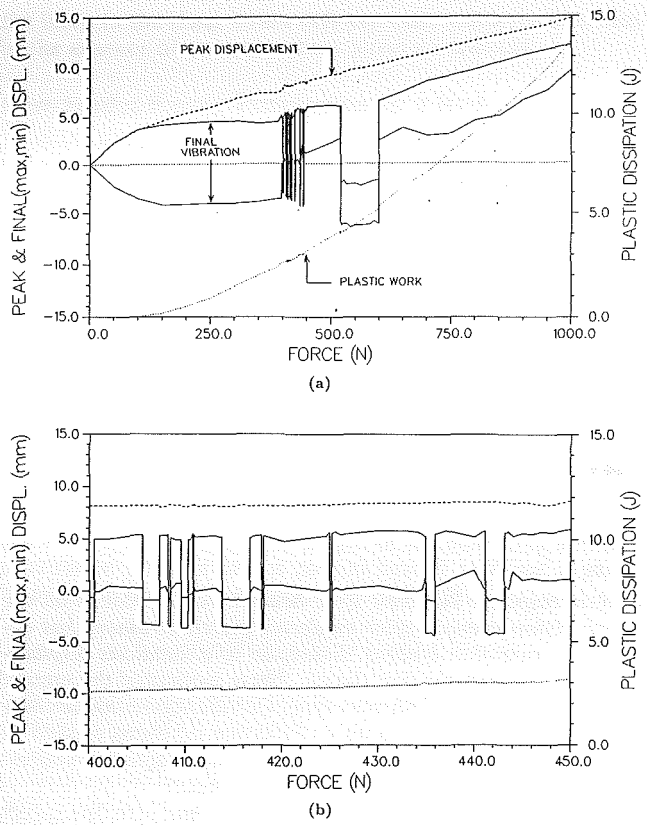


Fig. 1 ***Characteristic diagram*** **of undamped uniform beam showing response to pulse force at midpoint with fixed duration 0.5 × 10^{-3} sec. (*a*) The curves show the envelope of the elastic vibration after completion of plastic deformation (solid lines); the peak displacement (dashed line); and the total plastic work (dotted line). (*b*) Part of diagram to expanded force scale.**

chaos. The two-degree-of-freedom model defined in Section 3 was chosen so as to facilitate the extensive calculations needed to show whether this term is appropriate. The model is an extension of the previously used single-degree-of-freedom model, which provides much information, but cannot exhibit chaos in the present problem. The choice of time step in the numerical integration of the equations listed in Section 3 is treated in Section 4. Sections 5 and 6 illustrate different types of response observed at various pulse force levels. Quasi-periodic motion when the behavior is wholly elastic (but nonlinear) is contrasted with response behaviors seen at certain levels such that the plastic strains are present. These have features characteristic of chaotic vibrations (see Thompson and Stewart, 1986; Moon, 1987), as seen in displacement histories, phase plane portraits, and plots of power spectral densities. The strongest evidence that the observed motions are chaotic is furnished by observations of exponential sensitivity to the load parameter P. This is demonstrated by calculations of conventional Lyapunov exponents over a wide range of P, and also by a direct calculation of a positive "Lyapunov-like" exponent from displacement-time histories, for small variations of a particular pulse force.

The calculations referred to above were made without damping. As illustrated in Fig. 9, when damping is present there is not only a gradual decrease of amplitudes, but eventually an abrupt transition to a smaller amplitude nonchaotic vibration which keeps its sign and is ultimately damped out. The early part of the damped vibration of Fig. 9 is basically similar to the undamped response shown in Figs. 4(*c*) and 8. The responses typified by Fig. 9 may be termed *transitionally chaotic* (Thompson, 1990). The sensitivity to parameters shown in Fig. 9 means that the final displacement is actually unpredictable. To understand why this is so for the new model but not for the single-degree-of-freedom model, energy diagrams provide insight. These consist of plots of the elastic strain energy and the total available energy as functions of the relevant displacement variables, leading to plane and three-dimensional diagrams for the single-degree-of-freedom and two-degree-of-freedom models, respectively. Figure 15 summarizes their use in the latter case by displaying how the qualitative features of the displacement history are controlled by the nearness of the total energy to the energies at the five stationary points of the strain energy surface, as the total energy plane descends.

The energy approach provides a global picture of the whole response process, in terms of the energetic quantities that govern the motion. It is an alternative to the more familiar analytic and geometric methods based on asymptotic properties of trajectories in phase space, and has some advantages in terms of simplicity and directness. Not least of these is the fact that the two-dimensional configuration space of the two-degree-of-freedom model allows the details of the energy surfaces to be visualized (and even physically constructed).

2 Uniform Beam Problem

Consider a beam both of whose ends are fully fixed, and which is subjected to a transverse force pulse at its midpoint. When plastic strains result, in view of the end fixity, it becomes effectively a fixed-ended arch. Assuming a rectangular pulse with the fixed duration 0.5 ms, the pulse force P serves as the load parameter. The general-purpose finite element program ABAQUS version 4.7 (Hibbitt et al., 1987) was used, with the nonlinear geometry and elastic-perfectly plastic material behavior options. The beam was discretized with ten elements in its half-span, and the Timoshenko beam element $B21$ was chosen.

The results of calculations over a wide range of pulse loads, with no damping, are summarized in the *characteristic diagram* Fig. 1(*a*), shown in Fig. 1(*b*) with an expanded scale. This shows the envelope curves of final vibrations at midpoint as a function of magnitude of pulse load, together with the peak displacements and the total plastic dissipations. In Fig. 1, there are irregularly positioned slots, with various widths, where the final vibration lies on the negative side. (Here, "negative" means opposite the pulse force direction.) It is seen that there are irregular transitions of vibration modes from one type to another, as well as between the negative and the positive side.

Note the single wide slot located between approximately 520 N and 600 N. In this range, the major part of the energy is dissipated by the relatively large plastic strains produced during the first swing. Then the beam may snap through to and remain on the negative side because it has insufficient available energy to pass back through its unstable equilibrium state. Thus, the final form of vibration is reached quickly (Fig. 2(*a*)). But, in the range of smaller forces shown in detail in Fig. 1(*b*), the final form of vibration may be reached at a much later time because of the relatively small plastic strains incurred in the first swing and their gradual increases in the subsequent motions (Fig. 2(*b*)). In this region, with small plastic strains, the vibration mode switches from beam type (between positive and negative limits) to a shallow arch type, due to the effect of small increments in plastic strains. Therefore, small changes in plastic strains due to changes in parameters, such as parameters of load, integration method, iteration, time-step control, and discretization, etc., may result in large changes in the transition points or in the vibration modes. Thus, there are irregularly positioned slots with various widths, and more complex time-history behaviors than in the other force regions. The time history given in Fig. 2(*b*) shows the irregular alternation in vibration modes, the unpredictability in the final vibration mode, and a *chaos-like* response behavior.

Downloaded 03 May 2010 to 171.66.16.247. Redistribution subject to ASME license or copyright; see http://www.asme.org/terms/Terms_Use.cfm

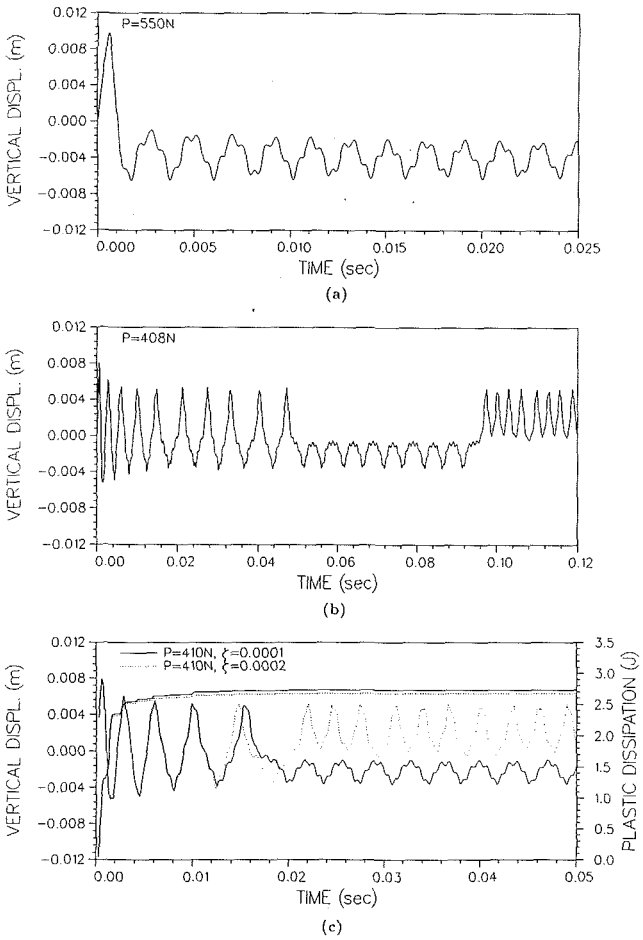


Fig. 2 Time histories of midpoint displacement of uniform beam for pulse force: (*a*) P = 550 N (undamped); (*b*) P = 407 N (undamped); (*c*) Damped displacement-time histories and plastic work for P = 410 N with two damping ratios ζ = 0.0001 and 0.0002.

We briefly mention damping. To study the effects of damping in a uniform beam, we used a Rayleigh damping option available in ABAQUS version 4.7, and somewhat arbitrarily assumed mass proportional damping (Symonds and Lee, 1989). The strong effect of damping, for P = 410 N with damping ratio ζ = 0.0001 and 0.0002, is illustrated in Fig. 2(*c*). As shown, the two vibration modes are initially of beam type, but switch to an arch type vibration after about 0.015 sec. Thereafter they remain small amplitude vibrations, one negative, the other positive. Figure 2(*c*) shows that a small change in the damping parameter may cause a drastic change in the response behavior. Note that there are small differences in plastic work preceding the visible separation of the time histories. Further calculations show that the appearances of anomalous final displacements diminish as damping increases, and disappear for $\zeta \geq 0.05$ (Symonds and Lee, 1989).

3 The Analytical Model

A two-degree-of-freedom Shanley-like beam model is sketched in Fig. 3. Symmetry of the deflected shape is assumed, and the vertical displacements at quarterpoint and midpoint are denoted by w_1 and w_2, respectively. The horizontal displacement at the quarterpoint is u. AB and BC are rigid bars of mass $m/2$ connected to deformable "cells" at B and C, assumed to act as sandwich beam sections. The force acting at the midpoint is a rectangular pulse with constant duration 0.5 msec, as before.

As shown in Fig. 3, the stresses in the four flanges are

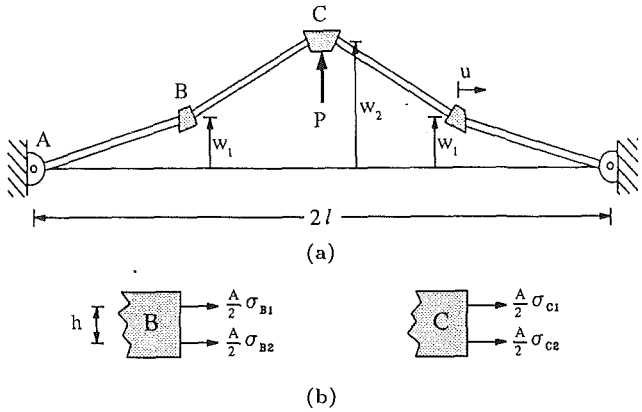


Fig. 3 Two-degree-of-freedom beam model. (*a*) deflected (symmetric) configuration; (*b*) deformable cells at quarterpoints B and midpoint C, treated as sandwich beam sections.

indicated by σ_{B1}, σ_{B2}, σ_{C1}, and σ_{C2}, where the second subscript 1 and 2 refers to the upper and lower flanges, respectively. The yield conditions and flow rules are

$$-\sigma_0 \leq \sigma_{\alpha i} \leq \sigma_0 \tag{1}$$

$$(\sigma_{\alpha i} \pm \sigma_0) d\epsilon^p_{\alpha i} \geq 0 \tag{2}$$

where $\alpha = B, C$, $i = 1, 2$ (no summation over α and i), and σ_0 is the yield stress in each flange. The strain increments at each flange are made up of elastic and plastic components as follows:

$$d\epsilon_{\alpha i} = \frac{1}{E} d\sigma_{\alpha i} + d\epsilon^p_{\alpha i} \tag{3}$$

where E is the Young's modulus.

These may be integrated to obtain stresses

$$\sigma_{\alpha i} = E(\epsilon_{\alpha i} - \epsilon^p_{\alpha i}). \tag{4}$$

The stresses may be expressed as

$$\begin{Bmatrix} \sigma_{B1} \\ \sigma_{B2} \end{Bmatrix} = E\left[\frac{2u}{l} + \frac{2w_1^2}{l^2} \pm \frac{2h}{l^2}(2w_1 - w_2) - \begin{Bmatrix} \epsilon^p_{B1} \\ \epsilon^p_{B2} \end{Bmatrix} \right]$$

$$\begin{Bmatrix} \sigma_{C1} \\ \sigma_{C2} \end{Bmatrix} = E\left[\frac{-2u}{l} + \frac{2(w_2 - w_1)^2}{l^2} \mp \frac{2h}{l^2}(w_1 - w_2) - \begin{Bmatrix} \epsilon^p_{C1} \\ \epsilon^p_{C2} \end{Bmatrix} \right] \tag{5}$$

where

$$\frac{u}{l} = -\frac{w_1^2}{2l^2} + \frac{(w_2 - w_1)^2}{2l^2} + \frac{1}{8}(\epsilon^p_{B1} + \epsilon^p_{B2} - \epsilon^p_{C1} - \epsilon^p_{C2}). \tag{6}$$

This results from our assumption that the axial force is constant over the length of the beam (neglecting axial inertia effects).

The equation of motion for the system may be written as

$$\frac{ml}{24}\begin{bmatrix} 4 & 1 \\ 1 & 2 \end{bmatrix}\begin{Bmatrix} \ddot{w}_1 \\ \ddot{w}_2 \end{Bmatrix} + \frac{cl}{24}\begin{bmatrix} 4 & 1 \\ 1 & 2 \end{bmatrix}\begin{Bmatrix} \dot{w}_1 \\ \dot{w}_2 \end{Bmatrix} + N\begin{bmatrix} 2 & -1 \\ -1 & 1 \end{bmatrix}\begin{Bmatrix} w_1 \\ w_2 \end{Bmatrix} + \begin{bmatrix} 2 & -1 \\ -1 & 1 \end{bmatrix}\begin{Bmatrix} M_1 \\ M_2 \end{Bmatrix} = \begin{Bmatrix} 0 \\ P(t)l/4 \end{Bmatrix} \tag{7}$$

where

$$N = AE\left[\frac{w_1^2}{l^2} + \frac{(w_2 - w_1)^2}{l^2} - \frac{1}{4}(\epsilon^p_{B1} + \epsilon^p_{B2} + \epsilon^p_{C1} + \epsilon^p_{C2}) \right] \tag{8}$$

$$\begin{Bmatrix} M_1 \\ M_2 \end{Bmatrix} = AEh\left(\frac{h}{l^2}\begin{bmatrix} 2 & -1 \\ -1 & 1 \end{bmatrix}\begin{Bmatrix} w_1 \\ w_2 \end{Bmatrix} - \frac{1}{4}\begin{Bmatrix} \epsilon^p_{B1} - \epsilon^p_{B2} \\ \epsilon^p_{C1} - \epsilon^p_{C2} \end{Bmatrix} \right). \tag{9}$$

M_i and N are bending moment and axial force, respectively, exerted by the cells; $A/2$ is the area of each of the four flanges; h is the flange separation; m is the total mass of the half span;

Downloaded 03 May 2010 to 171.66.16.247. Redistribution subject to ASME license or copyright; see http://www.asme.org/terms/Terms_Use.cfm

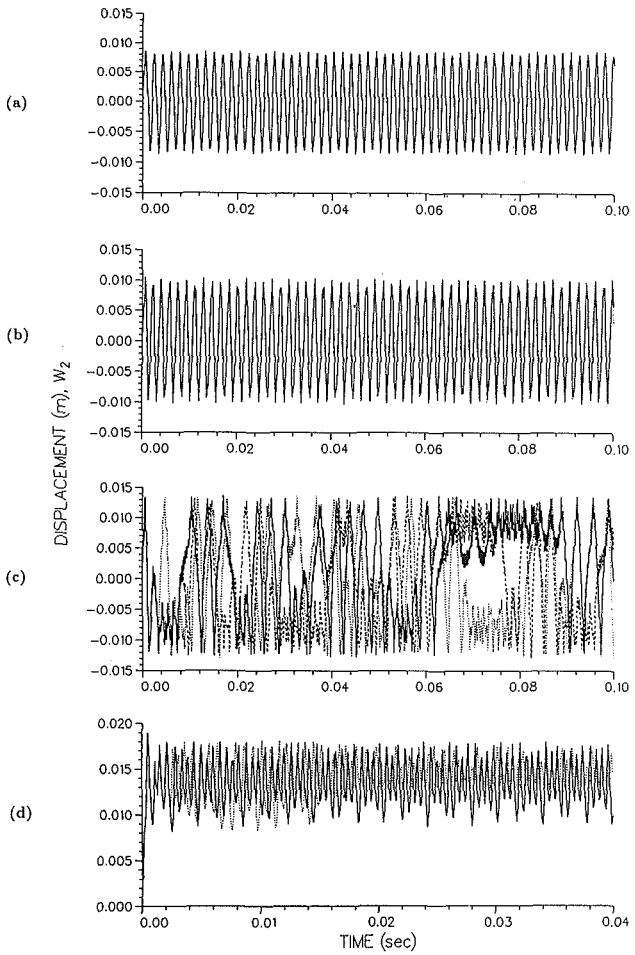


Fig. 4 Displacement histories of two-degree-of-freedom model computed for three time steps: $dt = 1.0 \times 10^{-7}$ sec (solid line); 2.0×10^{-7} sec (dashed line); and 5.0×10^{-7} sec (dotted line) and four pulse forces: (*a*) $P = 1000$ N (elastic); (*b*) $P = 1500$ N (small plastic strains); (*c*) $P = 2500$ N (moderate plastic strains); (*d*) $P = 4000$ N (relatively large plastic strains). Zero damping is assumed.

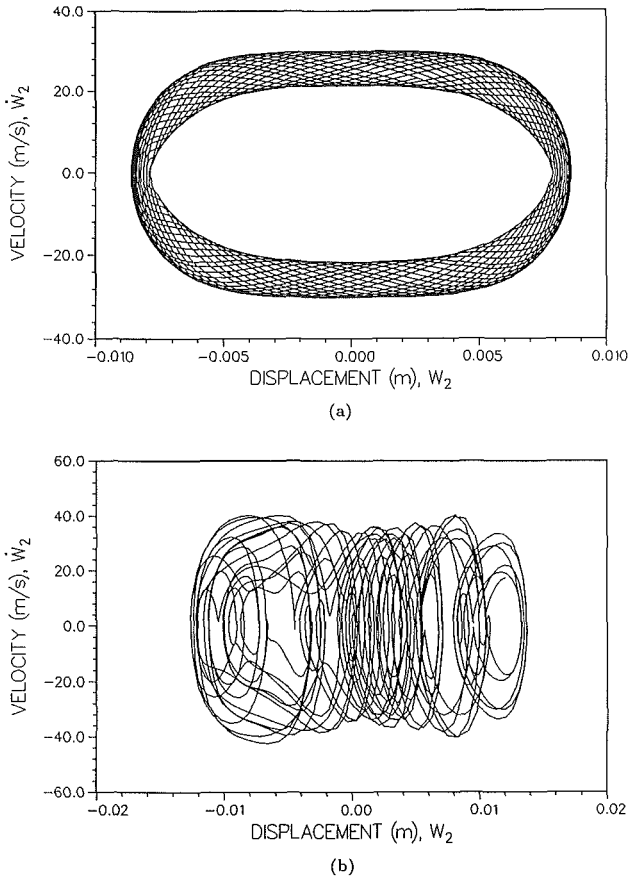


Fig. 5 Phase plane trajectories (midpoint velocity and displacement of two-degree-of-freedom model) for pulse forces: (*a*) $P = 1000$ N (quasi-periodic vibrations); (*b*) $P = 2500$ N (chaotic)

c is the damping coefficient; and an overhead dot denotes the time derivative. Material and structural parameters are taken as $\sigma_0 = 0.3$ GPa, $E = 40$ GPa, $m = 0.0216$ kg, $l = 0.1$ m, $A = 8 \times 10^{-5}$ m^2, and $h/l = 0.0271$.

Note that the coefficients in the governing equations depend on the four plastic strains. Under short pulse loading, the plastic strains are functions of time during an initial period. They reach final constant values, at a time perhaps well after the pulse load becomes zero; the structure can be assumed to "shake down." The governing equations then are coupled autonomous Duffing equations.

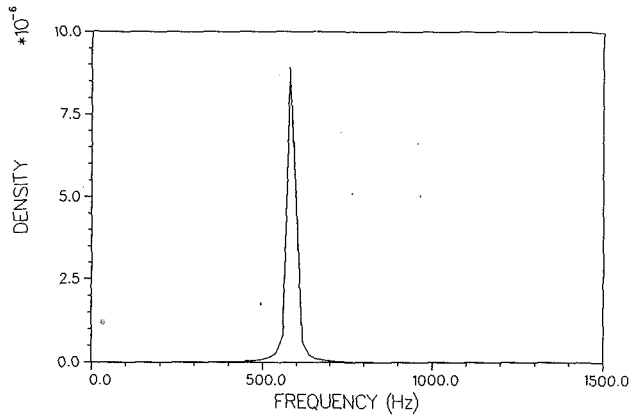
4 Types of Response of the Undamped Model

Equations (7) were integrated numerically using central difference formulas. The standard time step was taken as $dt = 1.0 \times 10^{-7}$ sec. This choice requires justification, since in certain cases the computed responses appear to be chaotic. It is known that too large a time step can give rise to chaotic behavior in a numerical solution by central differences in situations where the differential equation does not exhibit chaos (Reinhall et al., 1989). The standard time step $dt = 1.0 \times 10^{-7}$ sec is at least two orders of magnitude smaller than the magnitude $2/f_{\max}$ suggested by Belytschko et al. (1975) as generally adequate for transient analysis of nonlinear elastic system, where $f_{\max}$ is the highest frequency of the discrete mesh. In a heuristic rather than formal approach we rely on empirical evidence that the appearance of chaotic behavior in our results is not linked to this choice of time step.

In Fig. 4(*a*, *b*, *c*, *d*) are shown time histories of the midpoint displacements for the first 0.1 sec of the response for the four values of the pulse force P: (*a*) 1000 N, (*b*) 1500 N, (*c*) 2500 N, and (*d*) 4000 N. In each case three values of time step are used, namely 1.0×10^{-7}, 2.0×10^{-7}, and 5.0×10^{-7} sec. In case (*a*) the behavior is entirely elastic although geometrically nonlinear, and the three time steps furnish apparently coincident response histories. In case (*b*) small plastic strains are present; at the end of the run, the trace for the largest time step 5.0×10^{-7} sec appears to be very slightly different from those for the two smaller time steps. In case (*c*) moderately large plastic strains are present. The histories for the two larger time steps visibly diverge from that for the standard time step at early times, and the three responses are entirely different from each other, although roughly similar in character. Each consists of an aperiodic mixture of three kinds of vibration, namely large-amplitude "beam" vibrations between positive and negative limits; and smaller amplitude vibrations either wholly positive or wholly negative. Transitions between the three vibration modes occur at irregular, seemingly random, intervals. Finally, in case (*d*) the plastic strains are sufficiently large so that the vibration is wholly on the positive side. The trace for the largest time step diverges from the other two, and appears to be quasi-periodic.

Figure 4(*a*) for $P = 1000$ N demonstrates convergence as the time step decreases to the value of 1.0×10^{-7} sec. Since this case is wholly elastic, the change in time step is the only change in the integration scheme. In the other three cases plastic strains are produced, and change slightly with the time step. These modify the coefficients of the equations of motion. They

Downloaded 03 May 2010 to 171.66.16.247. Redistribution subject to ASME license or copyright; see http://www.asme.org/terms/Terms_Use.cfm



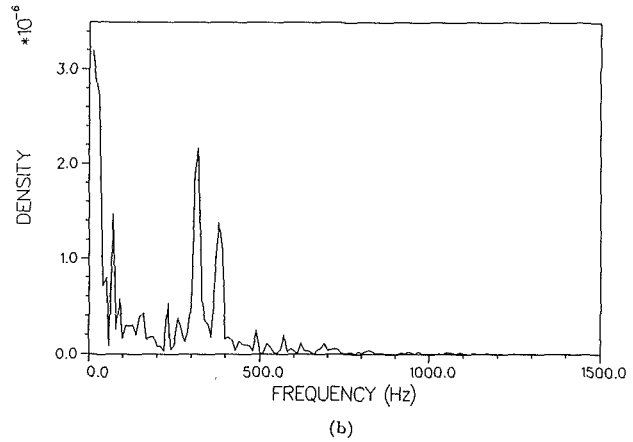


Fig. 6 Power density spectra for pulse forces: (*a*) P = 1000 N; (*b*) P = 2500 N

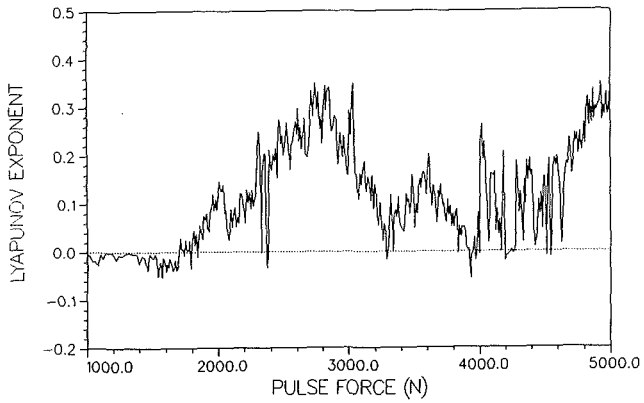


Fig. 7 Largest Lyapunov exponent for full range of pulse force P at intervals of 10 N

define new geometries of the structure, to which the computed response may be highly sensitive. Thus, the divergence of responses in Fig. 4(*c*) for P = 2500 N indicates sensitivity to the plastic strains, regarded as parameters of the structure that are generated during the response.

The two cases: P = 1000 N (nonlinear elastic) and 2500 N (moderate plastic strains) provide examples of quasi-periodic and chaotic responses, respectively. Displacement-time histories are contrasted in Figs. 4(*a*) and 4(*c*); phase plane portraits in Figs. 5(*a*) and 5(*b*); and power spectral densities in Figs. 6(*a*) and 6(*b*). Note that the displacement histories of Figs. 4(*b*) and 4(*d*) involve plastic strains smaller and larger, respectively, than those of Fig. 4(*c*), but they do not exhibit the same sensitivity; they are cases of quasi-periodic and weakly chaotic response, respectively.

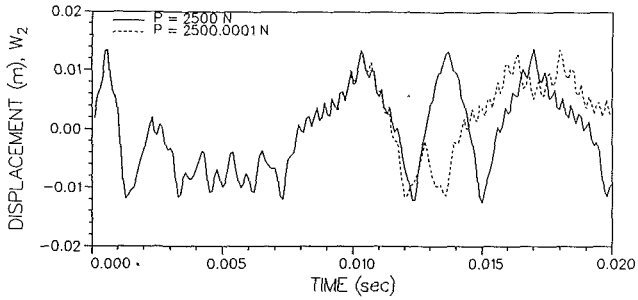


Fig. 8 Displacement histories: fiducial solution for pulse force P = 2500 N (solid line); together with neighboring solution for P = 2500.0001 N (dotted line)

5 Lyapunov Exponent

The Lyapunov characteristic exponent (LCE) provides convincing evidence for deterministic chaos or its absence. Positive values measure the exponential rates of divergence, on the average for a sample time history, of the linearized solution trajectories from that of a fiducial solution. A chaotic system contains at least one positive LCE. Methods for computing LCEs from differential equations as well as from experimental data have been given by Wolf et al. (1985). Our computation is based on their method.

To compute the largest Lyapunov exponent, Eqs. (7) and their linearized variational form were integrated using central difference formulas. The LCE values over a wide range of pulse forces are shown in Fig. 7, computed at pulse force intervals of 10 N. Orthonormalization was repeated at intervals of 2.5×10^{-4} sec. The values are averages over the sample time 0.1 sec. As shown in Fig. 7, there are sharp fluctuations as the pulse force increases. The values are initially negative, but become positive above a pulse force of about 1700 N. This marks the change from quasi-periodic to mainly chaotic vibrations, although nonchaotic vibrations reappear in several narrow force regions. The correlation between the signs of Lyapunov exponents in Fig. 7 and the stationary points (static equilibria) of the strain energy surface is discussed in detail in Lee and Symonds (1992).

A much simpler calculation of a "Lyapunov-like" exponent can be made directly from displacement-time histories. We regard the solution for P = 2500 N as a fiducial solution, shown for a time span of 0.1 sec and our standard time step 1.0×10^{-7} sec by the solid line in Fig. 4(*c*). In Fig. 8 are shown the same displacement history together with that for a slightly varied pulse force, to an expanded time scale. The two curves appear to coincide up to a time t_S, when a chosen visible separation can be identified. This can be estimated roughly but fairly consistently for several values of the force variation δP. Taking these as 0.0001, 0.01, and 1.0 N, the corresponding values of t_S are estimated as 0.0096, 0.0067, and 0.0028 sec. If we assume that the "initial" separation at time t_o = 0.0005 sec (the pulse duration time) is proportional to the relative variation $\delta P/P$, and that it increases exponentially with time thereafter, we can write

$$\Delta_s = A\,(\delta P/P)e^{\mu(t_S - t_o)} \tag{10}$$

where Δ_s is the arbitrarily chosen separation and A is a scale factor. Plotting $\ln(\delta P/P)$ against $t_S - t_o$, we find that the three points fall nearly on a straight line whose slope gives $\mu \approx 1350$ sec^{-1}. This result is not the same as the conventional Lyapunov exponent shown in Fig. 7, but confirms simply that the divergence is exponential and rapid in this part of the response.

Out of interest, the same procedure was applied to the Duffing equation used by Ueda (1979), namely

$$\ddot{x} + k\dot{x} + x^3 = B\cos t. \tag{11}$$

Downloaded 03 May 2010 to 171.66.16.247. Redistribution subject to ASME license or copyright; see http://www.asme.org/terms/Terms_Use.cfm

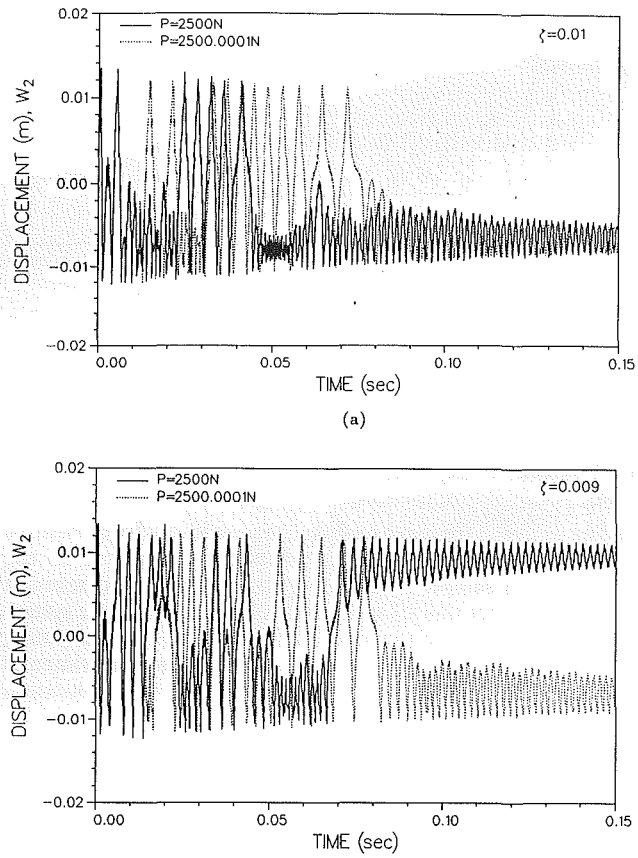


Fig. 9 Displacement histories of the damped two-degree-of-freedom model for pulse forces P = 2500 N and P = 2500.0001 N, with damping ratios: (*a*) ζ = 0.01; (*b*) ζ = 0.009

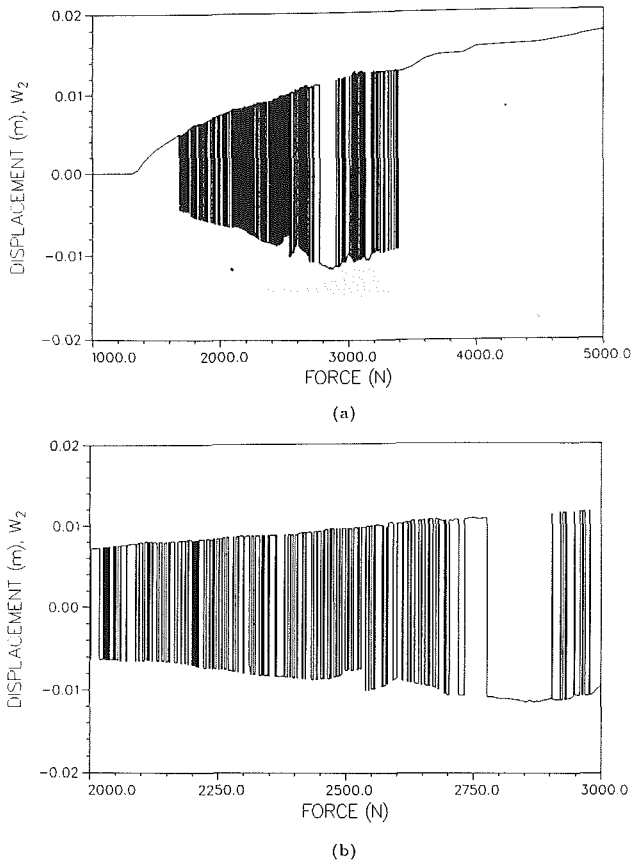


Fig. 10 Final displacements (*characteristic diagram*) of the two-degree-of-freedom model for damping ratio ζ = 0.01, computed at pulse force intervals of 2 N: (*a*) over full range of anomalous responses; (*b*) part of diagram to expanded force scale

Taking k = 0.1, B = 10.0 (one of Ueda's chaotic cases) we obtained $\lambda \approx 0.076\ \text{sec}^{-1}$. This may be compared with the Lyapunov exponent computed by Ueda (1979), λ = 0.102; and by Moon (1987), λ = 0.094. (The difference in order of magnitude between the results for our structural model and those for Ueda's equation stem from the different time scales of the equations, and has no significance.) Ueda's value was computed by a method of his own somewhat similar but more sophisticated than ours, and Moon's by the method described in Moon (1987).

6 Response of Damped Two-Degree-of-Freedom Model

We next consider anomalous responses in the presence of linear viscous damping. We assume small damping ratios. (With large damping, as shown by results for uniform beams (Symonds and Lee, 1989) and for the SDoF model (Genna and Symonds, 1988), anomalous effects may be eliminated.) The case P = 2500 N was shown to lead to a chaotic undamped response (see Figs. 4(*c*) and 8). We use this case to illustrate behaviors of the damped model.

At this load, with sufficiently small damping, Fig. 9 shows that there is first a period of chaotic vibrations similar to those observed in the undamped case: a seemingly random succession of large and small amplitude (positive and negative) oscillations. Eventually, at a time that increases as the damping ratio decreases, there is an abrupt transition to a relatively small amplitude vibration that retains its sign. This is a more regular vibration, becoming still smoother as it is damped out.

The examples of Fig. 9 show these transitions. They also dramatically illustrate the sensitivity of the final state to the two parameters: pulse force P and damping ratio ζ. In both (*a*) and (*b*) of Fig. 9, displacements are plotted for two values of P, 2500 N and 2500.0001 N. In Fig. 9(*a*), for ζ = 0.01, after the transitions have occurred both final vibrations are negative. However, in Fig. 9(*b*), for ζ = 0.009, the two pulse forces lead to vibrations of opposite sign. Note that the force P = 2500 N was chosen merely as a load at which chaos is exhibited. It is instructive to compare the behavior of the *single*-degree-of-freedom model (Genna and Symonds, 1989). The single-degree-of-freedom model shows discontinuous transitions at certain loads, but no such sensitivity as that of Fig. 9.

The final rest displacements for pulse forces over the full range of anomalous responses, calculated at force intervals of 2 N, are shown in Fig. 10 for damping ratio ζ = 0.01. This *characteristic diagram* forms a highly irregular pattern. There are many narrow negative intervals whose widths vary in a seemingly random manner. This should be contrasted with the corresponding pattern for the single-degree-of-freedom model for the same damping ratio, shown in Fig. 11 (Genna and Symonds, 1988). This has a high degree of regularity, with none of the randomness of the diagram for the two-degree-of-freedom model. In the latter case, since chaotic responses occur, further extensive calculations at much smaller intervals may well reveal a fine structure (perhaps fractile), whereas no such structure can occur in the single-degree-of-freedom case.

7 Energy Approach

For the two-degree-of-freedom model the energy diagrams are three-dimensional figures. The plane diagrams of the single-degree-of-freedom model are simpler, and the examples shown in Figs. 11(*b*, *c*) serve both to explain the basic idea, and to

Downloaded 03 May 2010 to 171.66.16.247. Redistribution subject to ASME license or copyright; see http://www.asme.org/terms/Terms_Use.cfm

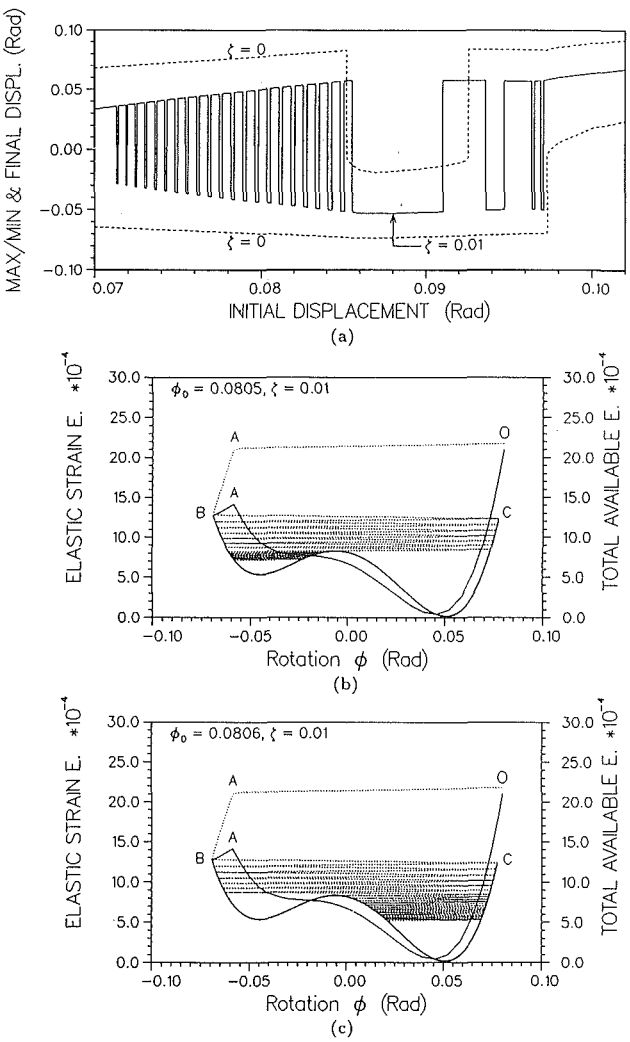


Fig. 11 Response and energy diagrams of the single-degree-of-freedom model for damping ratio $\zeta = 0.01$ (*a*) Anomalous region of *characteristic diagram* showing final displacement as function of load parameter (here taken as initial displacement). Dashed line shows envelope of continuing elastic vibration for zero damping. (*b*) Shows total energy (dotted line) and elastic strain energy (solid line) as functions of displacement angle, for initial value 0.0805; motion starts from rest at point *O*. Plastic deformation is indicated by the change in slope of segments *AB*. No further plastic flow occurs after reaching point *B* (in this single-degree-of-freedom model). (*c*) Shows the same energy quantities for initial value 0.0806; note change in sign of final vibration. This illustrates a transition load for this value of damping, but is not a sign of sensitivity (like that in Fig. 9).

contrast their simplicity with the chaotic complexity of the new model. The energies concerned are the elastic strain energy V and the total available energy U. (Kinetic energy = $U - V$.) For the single-degree-of-freedom model, V and U are plotted as functions of the single displacement variable, while for the two-degree-of-freedom case they are plotted as a surface over the coordinate plane of the two displacements w_1, w_2. In the plane diagrams of Figs. 11(*b*, *c*) the continuous curve for U descends gradually, with many branches, after completion of plastic work at point B. The V curve is also a continuous one with many branches; but after plastic deformation is completed, the solution point moves back and forth on a fixed curve, with changing end points. The final shape of the V curve reflects the presence of plastic strains, with an unstable and two stable equilibrium points. The transition from a wide amplitude vibration takes place when the U curve touches the "potential hill" of the V curve. This happens on the negative side in (*b*) and on the positive side in (*c*), for a slightly larger load parameter. The three-dimensional diagrams of the two-degree-of-freedom model are analogous to the plane diagrams of Fig. 11(*b*, *c*), but as will be seen, the regularity and calculability of the response are no longer present.

We record the definitions of the energies for the two-degree-of-freedom model as follows:

$$V=\frac{Al}{4}\frac{1}{2E}(\sigma_{B1}^2+\sigma_{B2}^2+\sigma_{C1}^2+\sigma_{C2}^2)=V(w_1,w_2;\epsilon_{\alpha i}^p) \tag{12}$$

$$U=V+T \tag{13}$$

$$T=\frac{1}{2}\dot{\mathbf{w}}^T M\dot{\mathbf{w}} \tag{14}$$

where $\alpha = B, C$; $i = 1, 2$.

$$M=\frac{m}{12}\begin{bmatrix}4&1&0\\1&2&0\\0&0&4\end{bmatrix};\quad \dot{\mathbf{w}}=\begin{Bmatrix}\dot{w}_1\\\dot{w}_2\\\dot{u}\end{Bmatrix}$$

As before (Borino et al., 1989), conservation of energy is given by

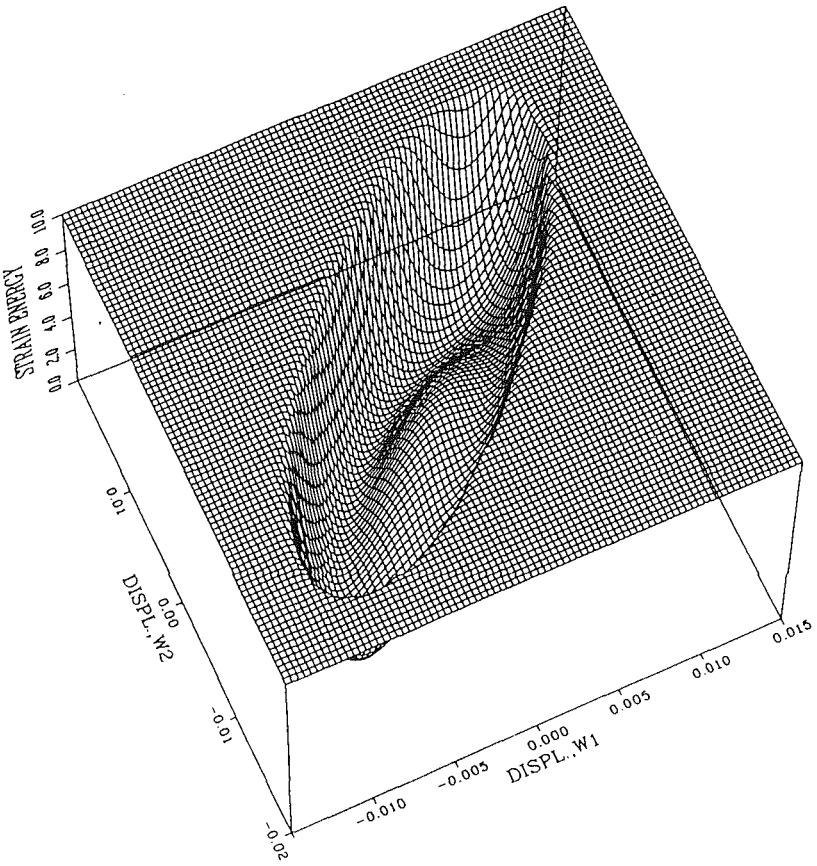
$$V+T=U=U_o-D_p-D_v, \tag{15}$$

where U_o is the total available energy at an arbitrary reference state, D_p is the plastic work done, and D_v is the energy dissipated in damping, in both cases subsequent to reaching the reference state. We take the reference energy as the total energy U_s when all plastic strains have reached constant values, i.e., at the end of the shakedown stage. The strain energy $V_S(w_1, w_2)$ then is a function only of the two displacements (a quartic polynomial with constant coefficients), and can be represented as a fixed surface over the (w_1, w_2) plane. At subsequent times, the state of the system determines the point that moves on this surface as required by the equations of motion, as well as a point that moves in the plane representing the total available energy U. The kinetic energy is given by the distance $U - V_S$ between the two points. The U plane moves downward at a rate determined by the current rate of dissipation by damping. (Plastic work during the shakedown period is indicated by abrupt drops, as can be seen in Fig. 15.) The trace of the state point describes a space curve which arrives asymptotically at one of the two local minima, which are states of static equilibrium.

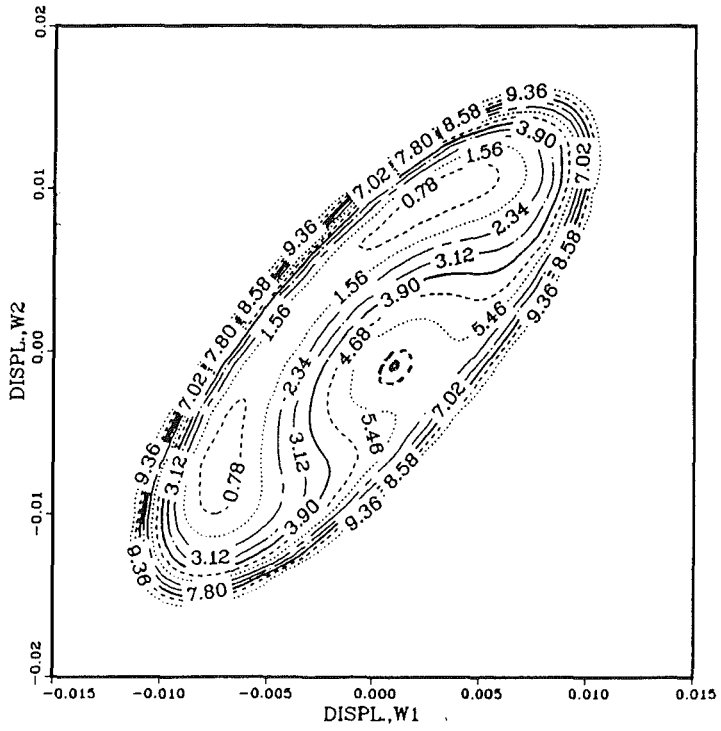
Figure 12(*a*) shows the strain energy surface $V_S(w_1, w_2)$ for $P = 2500$ N, in an isometric view. The top plane here is arbitrarily at energy level 10 J. Part of the elongated central "potential hill" can be seen, and one of the two "potential wells" leading to local minima. There are two saddle points, at the crests of the two valleys at the sides of the hill. The five stationary points (equilibria or fixed points in phase space) in this case are typical of pulse forces P above about 1690 N (Lee and Symonds, 1992). They can be located also in the contour map of Fig. 12(*b*), where the contour curve at the reference energy ($U_s = 3.12$ J for $P = 2500$ N) is labelled. The U_s plane lies between the two saddles, and above the two local minima, and is depicted also in Fig. 13(*a*) as the intersection of the strain energy surface by the plane at 3.12 J. All solution paths subsequent to the instant when plastic deformation is completed must lie inside this contour curve. Figure 13(*b*) illustrates this by showing the solution path for times $t \in [0.006, 0.020$ sec]. Here, to show clearly the role of the contour curve as a bounding curve for the solution, the calculation was made without damping. In Fig. 13(*b*) are seen the irregular mixture of large and small amplitude vibrations seen in Figs. 4(*c*) and 8, and in the first part of Fig. 9.

Poincare section plots are shown in Fig. 14, in (*a*) for $P = 1000$ N (elastic), and in (*b*) for the chaotic case $P = 2500$ N. Here, following Dowell (1984, 1988) we defined the stroboscopic times as instants t_i such that $\dot{w}_1(t_i) = 0$, and plotted $w_2(t_i)$ against $w_1(t_i)$. In Fig. 14(*a*), the quasi-periodic motion

Downloaded 03 May 2010 to 171.66.16.247. Redistribution subject to ASME license or copyright; see http://www.asme.org/terms/Terms_Use.cfm



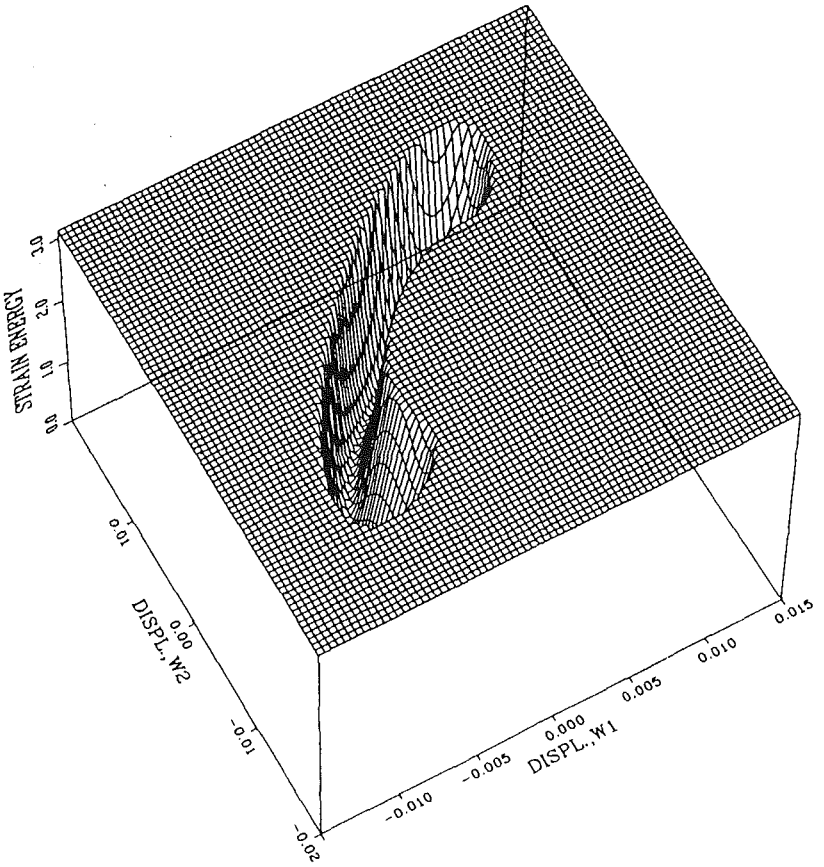
(a)



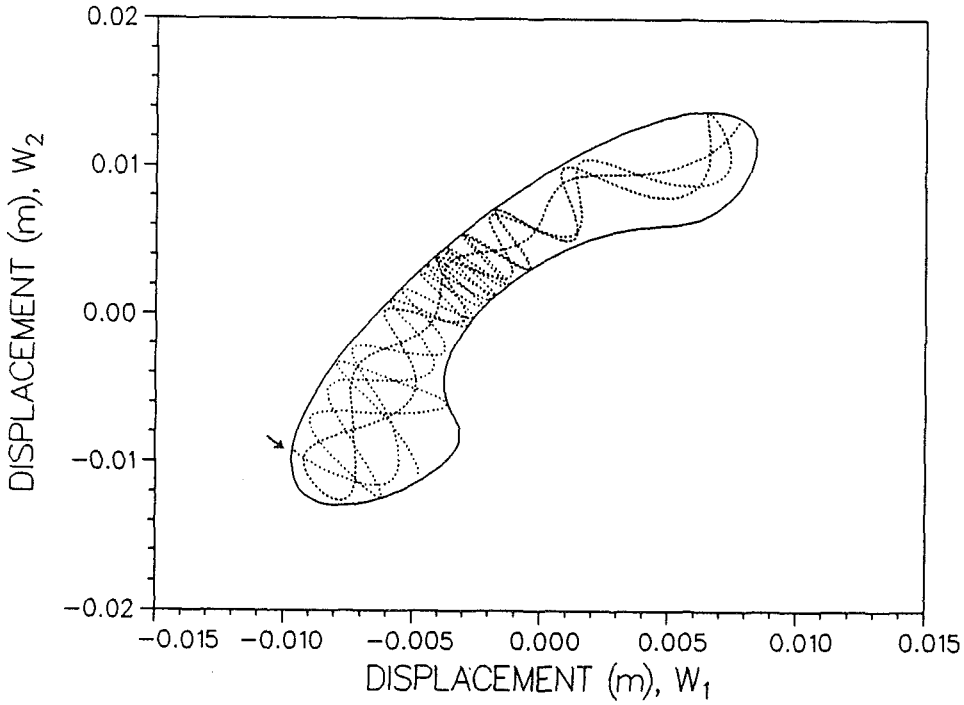
(b)

Fig. 12 Strain energy diagrams for case P = 2500 N, after completion of plastic deformation ("shakedown"). (*a*) Shows strain energy surface $V_s(w_1, w_2)$; note local maximum, two saddles, and two local minima. (*b*) Shows constant energy level curves. Note curve for total energy U_s = 3.12 J at instant when plastic work is completed ("reference" energy).

Downloaded 03 May 2010 to 171.66.16.247. Redistribution subject to ASME license or copyright; see http://www.asme.org/terms/Terms_Use.cfm



(a)



(b)

Fig. 13 (*a*) Strain energy surface V_s for $P = 2500$ N (same as in Fig. 12) cut by reference total energy plane $U_s = 3.12$ J (at completion of plastic deformation). (*b*) Sample of solution trajectory projected into displacement plane (dotted line), for times $0.006 \leq t \leq 0.02$ sec. Solid closed curve shows the contour curve for the reference total energy, as in (*a*) and Fig. 12(*b*).

Downloaded 03 May 2010 to 171.66.16.247. Redistribution subject to ASME license or copyright; see http://www.asme.org/terms/Terms_Use.cfm

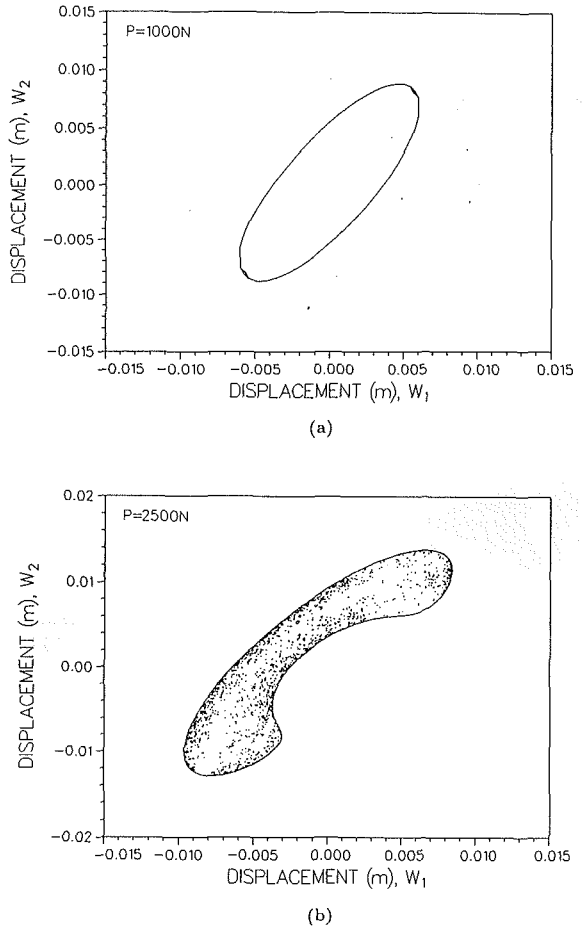


Fig. 14 Poincare section plots and contour curves for corresponding reference total energy: (*a*) P = 1000 N, U_s = 2.92 J (nonlinear elastic; quasi-periodic vibration). (*b*) P = 2500 N, U_s = 3.12 J (chaotic vibration).

is represented by two short curved line segments; the bounding contour curve is also shown. For the chaotic case of Fig. 14(*b*) the points do not form a pattern, but are distributed over the area inside the bounding contour curve. Again, for simplicity, here the calculations were done for the undamped model, so the bounding curve remains fixed.

8 Damped Response: Relation to Energy Magnitudes

Figure 15 shows several features of the response for P = 2500 N with damping ratio ζ = 0.009. The midpoint displacement-time history is shown together with those of the total energy U and of the energies at the five stationary points of the strain energy surface $V_s(w_1, w_2)$. (The surface is changing during the early period (about 0.002 sec) when plastic deformation is occurring; these changes are ignored.) The curve $U(t)$ exhibits rapid decreases during this short stage. Damping causes U to continue to decrease. After the completion of plastic flow, the boundary contour of Fig. 12 shrinks and changes shape as the U plane descends, passing in turn through the stationary points. At any instant the type of vibration depends on the position of the total energy plane relative to the energies at the stationary points. Chaotic vibrations are found to occur when the total energy is near one of the three unstable equilibria. (They depend also on "initial" conditions; see Lee and Symonds, 1992.) In any case, when the total energy falls below the value at the lower saddle, the solution path must lie in one of the potential wells, and remains either positive or negative. The transitions in the time histories of Fig. 9 as well as that in Fig. 15 all demonstrate this rule. In general, no

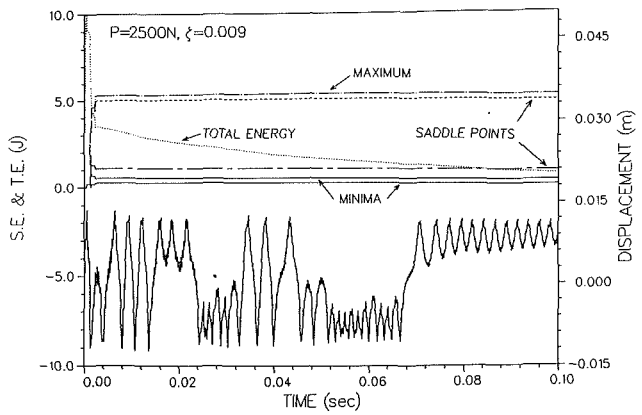


Fig. 15 Damped displacement-time history for P = 2500 N, ζ = 0.009 (solid line), together with curves of total energy $U(t)$ and of strain energies at the five stationary points: local maximum (chain-dotted line); two saddle points (chain-dashed and dashed lines); and two local minima (solid lines)

meaningful prediction can be made as to which sign will be chosen, when the vibration preceding the transition is chaotic, as in these examples.

9 Conclusions

The paper has discussed a seemingly routine problem of inelastic transient response, and shown that in certain circumstances the final rest deflection cannot be determined. This surprising result (due essentially to the nonlinear behavior resulting from the end fixing) is a new case of *chaotic unpredictability*, as demonstrated primarily by studies on a two-degree-of-freedom beam model. The energy approach, in which the total energy and the elastic strain energy are plotted over the coordinate plane of the two displacements, is a useful tool for interpreting responses in this class of problem in which the total energy monotonically decreases. It provides insights on the reasons for the contrasts in behavior between the single-degree-of-freedom model and one with two (or more) degrees-of-freedom, and suggests further promising lines of investigation.

Acknowledgments

The work reported here was supported by the U.S. Army Research Office under coordination of Dr. G. L. Anderson. We acknowledge also many helpful discussions with Prof. U. Lepik of Tartu University, Estonia.

References

Belytschko, T., Holmes, N., and Mullen, R., 1975, "Explicit Integration—Stability, Solution Properties, Cost," *Finite Element Analysis of Transient Nonlinear Structural Behavior*, T. Belytschko, J. R. Osias, and P. V. Marcal, eds., ASME, New York, AMD-Vol. 14, pp. 1-22.

Borino, G., Perego, U., and Symonds, P. S., 1989, "An Energy Approach to Anomalous Damped Elastic-Plastic Response to Short Pulse Loading," ASME Journal of Applied Mechanics, Vol. 56, pp. 430-438.

Dowell, E. H., 1984, "Observation and Evolution of Chaos for an Autonomous System," ASME Journal of Applied Mechanics, Vol. 51, pp. 664-673.

Dowell, E. H., 1988, "Chaotic Oscillations in Mechanical Systems," *Computational Mechanics*, Vol. 3, pp. 199-216.

Galiev, Sh. U., and Nechitailo, N. V., 1985, "The Dynamics of Shape Changes in Thin Plates and Shells of Revolution" (in Russian), preprint of "Institute of Problems of Strength," Academy of Sciences of the Ukrainian SSR, Kiev.

Genna, F., and Symonds, P. S., 1988, "Dynamic Plastic Instabilities in Response to Short Pulse Excitation—Effects of Slenderness Ratio and Damping," *Proc. Royal Society of London*, Vol. A417, pp. 31-44.

Downloaded 03 May 2010 to 171.66.16.247. Redistribution subject to ASME license or copyright; see http://www.asme.org/terms/Terms_Use.cfm

Hibbitt, Karlsson & Sorensen, Inc., 1987, *ABAQUS Version 4.7 Manual*, Hibbitt, Karlsson & Sorensen, Pawtucket, RI.

Kolsky, H., Rush, P., and Symonds, P. S., 1991, "Some Experimental Observations of Anomalous Response of Fully Clamped Beams," *Int. J. Impact Engineering*, Vol. 11, No. 4, pp. 445–456.

Lavrentiev, M. A., and Shabat, V. B., 1973, *Problems of Hydrodynamics and Their Models* (in Russian), Nauka, Moscow.

Lee, J.-Y., and Symonds, P. S., 1992, "Extended Energy Approach to Chaotic Elastic-Plastic Response to Impulsive Loading," *Int. J. Mech. Sci.*, Vol. 34, No. 2, pp. 139–157.

Li, Q. M., Zhao, L. M., and Yan, G. T., 1991, "Experimental Results on the Computer-intuitive Behaviour of Thin Clamped Beams Subjected to Projectile Impact," *Int. J. Impact Engineering*, Vol. 11, No. 3, pp. 341–348.

Moon, F. C., 1987, *Chaotic Vibrations*, John Wiley and Sons, New York.

Reinhall, P. G., Caughey, T. K., and Storti, D. W., 1989, "Order and Chaos in a Discrete Duffing Oscillator: Implications on Numerical Integration," ASME JOURNAL OF APPLIED MECHANICS, Vol. 56, pp. 162–166.

Ross, C. A., Strickland, W. S., and Sierakowski, R. L., 1977, "Response and Failure of Simple Structural Elements Subjected to Blast Loading," *Shock and Vibration Digest*, Vol. 9, No. 12, pp. 15–26.

Symonds, P. S., and Lee, J.-Y., 1989, "Anomalous and Unpredictable Response to Short Pulse Loading," *Recent Advances in Impact Dynamics of Engineering Structures*, D. Hui and N. Jones, eds., ASME, New York, AMD-Vol. 105, pp. 31–38.

Symonds, P. S., and Yu, T. X., 1985, "Counterintuitive Behavior in a Problem of Elastic-Plastic Beam Dynamics," ASME JOURNAL OF APPLIED MECHANICS, Vol. 52, No. 3, pp. 517–522.

Thompson, J. M. T., 1990, personal communication.

Thompson, J. M. T., and Stewart, H. B., 1989, *Nonlinear Dynamics and Chaos*, John Wiley and Sons, New York.

Ueda, Y., 1979, "Randomly Transitional Phenomena in the System Governed by Duffing's Equation," *Journal of Statistical Physics*, Vol. 20, No. 2, pp. 181–196.

Wolf, A., Swift, J. B., Swinney, H. L., and Vastano, J. A., 1985, "Determining Lyapunov Exponents from a Time Series," *Physica D*, Vol. 16, pp. 285–317.

Downloaded 03 May 2010 to 171.66.16.247. Redistribution subject to ASME license or copyright; see http://www.asme.org/terms/Terms_Use.cfm

J. D'Cruz[1]

J. D. C. Crisp

Department of Mechanical Engineering,
Monash University,
Clayton, Victoria 3168,
Australia

T. G. Ryall

Aeronautical Research Laboratory,
Defence Science and
Technology Organisation,
Fishermens Bend, Victoria 3207,
Australia

On the Identification of a Harmonic Force on a Viscoelastic Plate From Response Data

The problem of determining the force acting on a structure from measurements of the response of the structure to the force is an inverse problem. Presented is a method for determining the location, magnitude, and phase of a harmonic point force acting on a simply-supported classical viscoelastic rectangular plate from a number of displacement readings at discrete points on the plate. Presented also is a demonstration of the robustness of the solution technique to the effects of measurement noise as well as a means by which problems involving more general structural and loading configurations may be solved.

1 Introduction

In the study of the response of systems, there are three distinct analytical problems (Baumeister, 1987):

1 given the input and the system parameters, determine the output,
2 given the system parameters and the output, determine the input, and
3 given the input and output, determine the system parameters.

Problems of the first type are described as direct problems. Problems of the second type (the reconstruction problem) and the third type (the identification problem) are together described as inverse problems. de Laine (1975) mentions these problems but deals with the problem of identifying the system parameters from two outputs, the inputs being unknown.

Inverse problems have received much attention. Problems treated include the inverse scattering problem (Colton and Kress, 1983) and the inverse problem of exploration seismology (Bube and Burridge, 1983). It is traditional in structural mechanics to determine the response of a structure to a known force. Treated here is the inverse problem of force identification in which the location, magnitude, and phase of a harmonic point force acting on a simply-supported classical viscoelastic rectangular plate is determined from a number of displacement readings at discrete points on the plate. It is a pertinent problem because it is not always feasible directly to measure the loading applied to a structure—the flow pressures imposed on an aircraft surface, for example.

Among force identification problems already treated is that of Ellis (1973, 1976) who determines the spatial distribution of the fluctuating aerodynamic forces on a flexible building model from strain and acceleration response measurements by dividing the model into a number of individual elements. Blackburn and Melbourne (1989) use a similar technique to determine the aerodynamic forces at a number of points on a vibrating cylinder in turbulent flow. The basis of the technique is that the strains are used to determine the total force acting, with the accelerations being used to remove the inertial force component, thereby leaving the aerodynamic force. Flannelly et al. (1977), Bartlett and Flannelly (1979), Jones et al. (1981), Giansante et al. (1982), and Fabunmi (1986) refer to the technique of "Force Determination" and demonstrate the use of the method in the determination of helicopter loads from acceleration response measurements. Ewins and Hillary (1980) explore the use of the technique in the determination of the forces exerted on turbomachine blading undergoing steady or transient vibration from strain or acceleration response measurements. Richardson (1983) uses inverse finite element modeling techniques to determine the roles of various forces that may drive and resist the tectonic motion of the Earth's 12 major plates. Öry et al. (1985) introduce a method for the reconstruction of external or internal (interface) forces based on measured structural responses. Common to all these techniques is the fact that they deal with forces of known location.

Consider now the identification of loadings on elastic plates. Chang and Sachse (1985) consider the inverse problem of an extended, finite source of elastic waves in a thick plate. Michaels and Pao (1985), Michaels and Pao (1986), and Michaels (1984) describe and demonstrate a method to determine experimentally the oblique force applied to the surface of an elastic plate. Again, these techniques deal with forces of known location. Pao (1978) presents a method by which the location of a source of elastic waves in, for example, a thick plate is determined. The method, known as triangulation, makes use of the arrival time differences of the source signal at a number

[1]Currently at the Structural Dynamics Division, Aeroservoelasticity Branch, NASA Langley Research Center, Mail Stop 243, Hampton VA 23681-0001.

Contributed by the Applied Mechanics Division of The American Society of Mechanical Engineers for presentation at the 1992 ASME Winter Annual Meeting, Anaheim, CA, Nov. 8–13, 1992.

Discussion on this paper should be addressed to Prof. Leon M. Keer, The Technological Institute, Northwestern University, Evanston, IL 60208, and will be accepted until four months after final publication of the paper itself in the ASME Journal of Applied Mechanics.

Manuscript received by the ASME Applied Mechanics Division, Jan. 25, 1991; final revision, Feb. 21, 1992. Associate Technical Editor: C. F. Shih.

Paper No. 92-WA/APM-8.

Copyright © 1992 by ASME

Downloaded 03 May 2010 to 171.66.16.247. Redistribution subject to ASME license or copyright; see http://www.asme.org/terms/Terms_Use.cfm

of transducers at different locations. Doyle (1986) and Daimaruya et al. (1988) present techniques by means of which the time history of the impact force which occurs as a result of a transverse impact with a projectile at a predetermined location on a plate is determined from dynamic strain gauge measurements. Stephens (1987) provides an extensive overview of force identification problems.

The force identification problem treated here evolves essentially as a problem in nonlinear least squares. It is solved by determining a number of initial estimates of the location, magnitude and phase of the force from a simplified set of displacement equations, each of which is then used to initiate an iterative procedure which minimizes a nonlinear least-squares objective function in order to yield the solution to the actual force identification problem. This method of approach is similar in principle to that of the previous work by the same authors (D'Cruz et al., 1991) in which the location and magnitude of a static point force acting on a simply-supported elastic rectangular plate is determined from an array of displacement readings.

In order to demonstrate the practical applicability of the solution technique, the effects of measurement noise were simulated to show that the solution technique is indeed robust to the effect of measurement noise. It is also shown that the technique may be extended to solve problems involving more general structural and loading configurations. In this, the work reported here represents a step taken toward the solution of practical force identification problems.

2 The Force-Displacement Relation

The steady-state displacement response at time t of a point $Q(x, y)$ due to the load $P\cos(\lambda t + \phi)$ acting at the point (ξ, η) on a simply-supported classical viscoelastic rectangular plate (Fig. 1) is given, from Pan (1966), by

$$w(x,y,t)=\frac{4P}{\bar{\rho}ab}\sum_{m=1}^{\infty}\sum_{n=1}^{\infty}\left[\frac{\sin\frac{m\pi\xi}{a}\sin\frac{n\pi\eta}{b}\sin\frac{m\pi x}{a}\sin\frac{n\pi y}{b}}{(\lambda^2-p_{mn}^2)^2+p_{mn}^4\tau_K^2\lambda^2}\right.$$

$$\left.\times[p_{mn}^2\tau_K\lambda\sin(\lambda t+\phi)-(\lambda^2-p_{mn}^2)\cos(\lambda t+\phi)]\right], \quad (1)$$

where $p_{mn}^2 = D\pi^4/\bar{\rho}(m^2/a^2 + n^2/b^2)^2$ represents the square of the undamped natural frequencies, $\bar{\rho}$ is the surface density, τ_K the retardation time, D the flexural rigidity, and ϕ an arbitrary phase angle.

Let $A = 4P/\bar{\rho}ab$. Equation (1) then becomes

$$w=A\sum_{m=1}^{\infty}\sum_{n=1}^{\infty}\left[\frac{\sin\frac{m\pi\xi}{a}\sin\frac{n\pi\eta}{b}\sin\frac{m\pi x}{a}\sin\frac{n\pi y}{b}}{(\lambda^2-p_{mn}^2)^2+p_{mn}^4\tau_K^2\lambda^2}\right.$$

$$\left.\times[p_{mn}^2\tau_K\lambda\sin(\lambda t+\phi)-(\lambda^2-p_{mn}^2)\cos(\lambda t+\phi)]\right], \quad (2)$$

where A may be taken to be the force magnitude. The inverse problem under consideration here is then to determine the magnitude, A, phase angle, ϕ, and location, (ξ, η) of the force from a number of displacement readings at discrete points on the plate. These displacement readings may be determined by the placement of an array of transducers, each transducer assumed to provide a reading for the displacement amplitude and phase.

3 Uniqueness

From Eq. (2), the displacement response may be written as

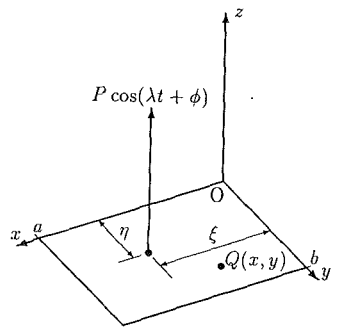


Fig. 1 Problem geometry

$$w = W\cos(\lambda t+\phi+\alpha), \quad (3)$$

where

$$W=\sqrt{\overline{X}^2+\overline{Y}^2}$$

and

$$\tan\alpha=\frac{\overline{Y}}{\overline{X}},$$

with $\overline{X}$ and $\overline{Y}$ being given, respectively, by

$$-A\sum_{m=1}^{\infty}\sum_{n=1}^{\infty}\frac{\sin\frac{m\pi\xi}{a}\sin\frac{n\pi\eta}{b}\sin\frac{m\pi x}{a}\sin\frac{n\pi y}{b}}{(\lambda^2-p_{mn}^2)^2+p_{mn}^4\tau_K^2\lambda^2}(\lambda^2-p_{mn}^2)$$

and

$$-A\sum_{m=1}^{\infty}\sum_{n=1}^{\infty}\frac{\sin\frac{m\pi\xi}{a}\sin\frac{n\pi\eta}{b}\sin\frac{m\pi x}{a}\sin\frac{n\pi y}{b}}{(\lambda^2-p_{mn}^2)^2+p_{mn}^4\tau_K^2\lambda^2}p_{mn}^2\tau_K\lambda.$$

The magnitude and phase of the force may be eliminated from consideration as follows. Now, $|\overline{X} + i\overline{Y}| = W$ and $\arg(\overline{X} + i\overline{Y}) = \alpha$. Hence, with two transducers, one located at (x_k, y_k) and the other at (x_l, y_l), the division of $\overline{X}_l + i\overline{Y}_l$ by $\overline{X}_k + i\overline{Y}_k$ gives, if

$$\theta=\phi+\alpha, \quad (4)$$

$$\frac{\overline{X}_l+i\overline{Y}_l}{\overline{X}_k+i\overline{Y}_k}=\frac{W_l}{W_k}e^{i(\theta_l-\theta_k)}. \quad (5)$$

The quantities on the LHS of Eq. (5) are determined from the estimated location, (ξ_e, η_e), and magnitude, A_e, of the force, while those on the RHS are measured, or observed. Therefore, introduce the following subscript notation:

$$\frac{\overline{X}_{l_e}+i\overline{Y}_{l_e}}{\overline{X}_{k_e}+i\overline{Y}_{k_e}}=\frac{W_{l_o}}{W_{k_o}}e^{i(\theta_{l_o}-\theta_{k_o})}. \quad (6)$$

Cross-multiplying and equating real and imaginary parts gives

$$\overline{X}_{l_e}=\lambda_{kl_o}\overline{X}_{k_e}-\mu_{kl_o}\overline{Y}_{k_e}$$

and

$$\overline{Y}_{l_e}=\lambda_{kl_o}\overline{Y}_{k_e}+\mu_{kl_o}\overline{X}_{k_e} \quad (7)$$

where

$$\frac{W_{l_o}}{W_{k_o}}e^{i(\theta_{l_o}-\theta_{k_o})}=\lambda_{kl_o}+i\mu_{kl_o}.$$

Let

$$\frac{\overline{X}_{k,l_e}}{A_e}=\sum_{m=1}^{\infty}\sum_{n=1}^{\infty}X_{mn_{k,l}}\sin\frac{m\pi\xi_e}{a}\sin\frac{n\pi\eta_e}{b}$$

and

$$\frac{\overline{Y}_{k,l_e}}{A_e}=\sum_{m=1}^{\infty}\sum_{n=1}^{\infty}Y_{mn_{k,l}}\sin\frac{m\pi\xi_e}{a}\sin\frac{n\pi\eta_e}{b}, \quad (8)$$

Downloaded 03 May 2010 to 171.66.16.247. Redistribution subject to ASME license or copyright; see http://www.asme.org/terms/Terms_Use.cfm

where

$$X_{mn_{k,l}} = -\frac{\sin\frac{m\pi x_{k,l}}{a}\sin\frac{n\pi y_{k,l}}{b}(\lambda^2 - p_{mn}^2)}{(\lambda^2 - p_{mn}^2)^2 + p_{mn}^4\tau_K^2\lambda^2}$$

and

$$Y_{mn_{k,l}} = -\frac{\sin\frac{m\pi x_{k,l}}{a}\sin\frac{n\pi y_{k,l}}{b}p_{mn}^2\tau_K\lambda}{(\lambda^2 - p_{mn}^2)^2 + p_{mn}^4\tau_K^2\lambda^2}.$$

Equations (7) then become

$$\sum_{m=1}^{\infty}\sum_{n=1}^{\infty} A_{mn_o}^{(kl)}\sin\frac{m\pi\xi_e}{a}\sin\frac{n\pi\eta_e}{b} = 0$$

and

$$\sum_{m=1}^{\infty}\sum_{n=1}^{\infty} B_{mn_o}^{(kl)}\sin\frac{m\pi\xi_e}{a}\sin\frac{n\pi\eta_e}{b} = 0, \tag{9}$$

where

$$A_{mn_o}^{(kl)} = X_{mn_l} - \lambda_{kl_o}X_{mn_k} + \mu_{kl_o}Y_{mn_k}$$

and

$$B_{mn_o}^{(kl)} = Y_{mn_l} - \lambda_{kl_o}Y_{mn_k} + \mu_{kl_o}X_{mn_k}.$$

Hence, by performing the division of $\overline{X}_l + i\overline{Y}_l$ by $\overline{X}_k + i\overline{Y}_k$, the magnitude and phase of the force have been eliminated from consideration. Making use of the relation

$$\sin z = \frac{e^{iz} - e^{-iz}}{2i} \tag{10}$$

enables Eqs. (9) to be written as

$$\sum_{m=1}^{\infty}\sum_{n=1}^{\infty} A_{mn_o}^{(kl)}\left(z_{1_e}^m - \frac{1}{z_{1_e}^m}\right)\sin\frac{n\pi\eta_e}{b} = 0$$

and

$$\sum_{m=1}^{\infty}\sum_{n=1}^{\infty} B_{mn_o}^{(kl)}\left(z_{1_e}^m - \frac{1}{z_{1_e}^m}\right)\sin\frac{n\pi\eta_e}{b} = 0, \tag{11}$$

where $z_{1_e} = e^{i\pi\xi_e/a}$. For sufficiently large values of m and n, the terms of the infinite series of Eqs. (11) become negligible. This then results, approximately, in the two polynomials

$$a_0 z_1^p + a_1 z_1^{p-1} + \ \ldots\ + a_{p-1}z_1 + a_p = 0$$

and

$$b_0 z_1^q + b_1 z_1^{q-1} + \ \ldots\ + b_{q-1}z_1 + b_q = 0, \tag{12}$$

where p and q are finite, and the coefficients $a_0, a_1, \ldots, a_p$ and $b_0, b_1, \ldots, b_q$ are polynomials of finite degree in $z_{2_e} = e^{i\pi\eta_e/b}$. (Note that z_{1_e} and z_{2_e} must therefore lie on the unit circle.) A solution is obtained if the two polynomials have a root in common. If $q \le p$, $a_0 \ne 0$ and $b_0 \ne 0$, the necessary and sufficient condition for this to occur is (Barnett, 1983)

$$\det \mathbf{S} = 0, \tag{13}$$

where

$$\mathbf{S} = \begin{bmatrix} a_0 & a_1 & a_2 & \ldots & \ldots & a_p & 0 & \ldots & \ldots & \ldots & 0 & 0 \\ 0 & a_0 & a_1 & \ldots & \ldots & a_{p-1} & a_p & \ldots & \ldots & \ldots & 0 & 0 \\ \vdots & \vdots & \vdots & \ddots & \ddots & \vdots & \vdots & \ddots & \ddots & \ddots & \vdots & \vdots \\ 0 & 0 & \ldots & a_0 & \ldots & \ldots & \ldots & \ldots & \ldots & \ldots & a_{p-1} & a_p \\ b_0 & b_1 & b_2 & \ldots & \ldots & \ldots & \ldots & b_q & 0 & \ldots & 0 & 0 \\ 0 & b_0 & b_1 & \ldots & \ldots & \ldots & \ldots & b_{q-1} & b_q & \ldots & 0 & 0 \\ \vdots & \vdots & \vdots & \ddots & \ddots & \ddots & \ddots & \vdots & \vdots & \ddots & \vdots & \vdots \\ 0 & 0 & 0 & \ldots & b_0 & \ldots & \ldots & \ldots & \ldots & \ldots & b_{q-1} & b_q \end{bmatrix} \begin{matrix} \uparrow \\ q \text{ rows} \\ \downarrow \\ \\ \\ \\ \uparrow \\ p \text{ rows} \\ \downarrow \end{matrix}$$

is known as Sylvester's resultant matrix. (The polynomials of Eq. (12) should be deflated to eliminate any trivial roots in common.)

Equation (13) leads to a polynomial of finite degree in z_{2_e}, and therefore yields only a finite number of solutions for η_e. For each of these values of η_e, Eqs. (12) can only have a finite number of roots, and hence values of ξ_e, in common. Thus, with two transducers, there are a finite number of solution pairs (ξ_e, η_e), each pair corresponding to a unique value of the estimated phase, ϕ_e, and amplitude, A_e, of the force (each transducer provides; as mentioned previously, a reading for the displacement phase and amplitude).

A third transducer will lead approximately to another two polynomials like Eqs. (12). Common to the four polynomials will be the root corresponding to the true solution. However, should the polynomials of Eqs. (12) have more than one root in common, there is no a priori reason that the other two polynomials should generically share with them a root other than the one corresponding to the true solution. By this it is meant that if the transducers are configured such that the four polynomials have more than one root in common, an arbitrary perturbation of any one transducer from its position will eliminate all but the root corresponding to the true solution. It is thus asserted that, generically, three transducers are sufficient for a unique solution. It is interesting to note that if the load were a static one (D'Cruz et al., 1991), the number of transducers is four. The reason for this apparent discrepancy is that in the case of the harmonic load, each transducer provides two readings (displacement amplitude and phase) as opposed to one (displacement amplitude) in the case of the static load.

4 An Approximate Solution

4.1 The Force Location. It was shown in the previous section, with two transducer readings, one at the position (x_k, y_k) and the other at (x_l, y_l) (Eqs. (11)), that

$$\sum_{m=1}^{\infty}\sum_{n=1}^{\infty} A_{mn_o}^{(kl)}\left(z_{1_e}^m - \frac{1}{z_{1_e}^m}\right)\sin\frac{n\pi\eta_e}{b} = 0$$

and

$$\sum_{m=1}^{\infty}\sum_{n=1}^{\infty} B_{mn_o}^{(kl)}\left(z_{1_e}^m - \frac{1}{z_{1_e}^m}\right)\sin\frac{n\pi\eta_e}{b} = 0 \tag{14}$$

are obtained. Truncate these infinite series at $m = \overline{m}$ and $n = \overline{n}$ to get

$$\left(z_{1_e} - \frac{1}{z_{1_e}}\right)S_1 + \left(z_{1_e}^2 - \frac{1}{z_{1_e}^2}\right)S_2 + \ \ldots\ + \left(z_{1_e}^{\overline{m}} - \frac{1}{z_{1_e}^{\overline{m}}}\right)S_{\overline{m}} = 0$$

and

$$\left(z_{1_e} - \frac{1}{z_{1_e}}\right)T_1 + \left(z_{1_e}^2 - \frac{1}{z_{1_e}^2}\right)T_2 + \ \ldots\ + \left(z_{1_e}^{\overline{m}} - \frac{1}{z_{1_e}^{\overline{m}}}\right)T_{\overline{m}} = 0, \tag{15}$$

where

Downloaded 03 May 2010 to 171.66.16.247. Redistribution subject to ASME license or copyright; see http://www.asme.org/terms/Terms_Use.cfm

$$S_m = \sum_{n=1}^{\bar{n}} A_{mn_o}^{(kl)} \sin \frac{n\pi\eta_e}{b}$$

and

$$T_m = \sum_{n=1}^{\bar{n}} B_{mn_o}^{(kl)} \sin \frac{n\pi\eta_e}{b}.$$

Rewrite Eqs. (15) as polynomials in $x_{1_e} = z_{1_e} + 1/z_{1_e}$, after removing the trivial roots from consideration, thus:

$$a_0 x_{1_e}^{\bar{m}-1} + a_1 x_{1_e}^{\bar{m}-2} + a_2 x_{1_e}^{\bar{m}-3} + \ \ldots \ + a_{\bar{m}-3} x_{1_e}^2 + a_{\bar{m}-2} x_{1_e} + a_{\bar{m}-1} = 0$$

and

$$b_0 x_{1_e}^{\bar{m}-1} + b_1 x_{1_e}^{\bar{m}-2} + b_2 x_{1_e}^{\bar{m}-3} + \ \ldots \ + b_{\bar{m}-3} x_{1_e}^2 + b_{\bar{m}-2} x_{1_e} + b_{\bar{m}-1} = 0, \quad (16)$$

where

$$a_m = \sum_{\substack{i=0 \\ i=0,2,4,\ldots}}^{m} S_{\bar{m}-i} - \sum_{\substack{i=0 \\ i=0,2,4,\ldots}}^{m-2} a_i^{\bar{m}-i-1} C_{\frac{m-i}{2}}, \quad m = 0,2,4, \ \ldots,$$

$$a_m = \sum_{\substack{i=1 \\ i=1,3,5,\ldots}}^{m} S_{\bar{m}-i} - \sum_{\substack{i=1 \\ i=1,3,5,\ldots}}^{m-2} a_i^{\bar{m}-i-1} C_{\frac{m-i}{2}}, \quad m = 1,3,5, \ \ldots,$$

$$b_m = \sum_{\substack{i=0 \\ i=0,2,4,\ldots}}^{m} T_{\bar{m}-i} - \sum_{\substack{i=0 \\ i=0,2,4,\ldots}}^{m-2} b_i^{\bar{m}-i-1} C_{\frac{m-i}{2}}, \quad m = 0,2,4, \ \ldots,$$

$$b_m = \sum_{\substack{i=1 \\ i=1,3,5,\ldots}}^{m} T_{\bar{m}-i} - \sum_{\substack{i=1 \\ i=1,3,5,\ldots}}^{m-2} b_i^{\bar{m}-i-1} C_{\frac{m-i}{2}}, \quad m = 1,3,5, \ \ldots,$$

and

$$^rC_s = \frac{r(r-1)(r-2)\ldots(r-s+1)}{s!}, \quad s > 0,$$

with

$$^rC_0 = 1.$$

An examination of the two polynomials of Eq. (16) will reveal that the corresponding Sylvester resultant matrix (see Section 3) may be written as

$$\mathbf{S} = \begin{bmatrix} \mathbf{A}_U & \mathbf{A}_L \\ \mathbf{B}_U & \mathbf{B}_L \end{bmatrix}, \quad (17)$$

where

$$\mathbf{A}_U = \begin{pmatrix} a_0 & a_1 & a_2 & \ldots & a_{\bar{m}-2} \\ 0 & a_0 & a_1 & \ldots & a_{\bar{m}-3} \\ \vdots & \vdots & \vdots & \ddots & \vdots \\ 0 & 0 & 0 & \ldots & a_0 \end{pmatrix},$$

$$\mathbf{A}_L = \begin{pmatrix} a_{\bar{m}-1} & 0 & \ldots & 0 & 0 \\ a_{\bar{m}-2} & a_{\bar{m}-1} & \ldots & 0 & 0 \\ \vdots & \vdots & \ddots & \vdots & \vdots \\ a_1 & a_2 & \ldots & a_{\bar{m}-2} & a_{\bar{m}-1} \end{pmatrix},$$

$$\mathbf{B}_U = \begin{pmatrix} b_0 & b_1 & b_2 & \ldots & b_{\bar{m}-2} \\ 0 & b_0 & b_1 & \ldots & b_{\bar{m}-3} \\ \vdots & \vdots & \vdots & \ddots & \vdots \\ 0 & 0 & 0 & \ldots & b_0 \end{pmatrix}$$

and

$$\mathbf{B}_L = \begin{pmatrix} b_{\bar{m}-1} & 0 & \ldots & 0 & 0 \\ b_{\bar{m}-2} & b_{\bar{m}-1} & \ldots & 0 & 0 \\ \vdots & \vdots & \ddots & \vdots & \vdots \\ b_1 & b_2 & \ldots & b_{\bar{m}-2} & b_{\bar{m}-1} \end{pmatrix}.$$

Therefore, the requirement that det $\mathbf{S} = 0$ reduces to

$$\det(\mathbf{A}_U^{-1}\mathbf{A}_L - \mathbf{B}_U^{-1}\mathbf{B}_L) = 0. \quad (18)$$

The points at which this equation is satisfied correspond to possible solutions for the position coordinate η_e of the force. These points may be found, for instance, by conducting a one-dimensional search. The corresponding solutions for the other coordinate ξ_e may be obtained as follows.

The Sylvester resultant matrix of Eq. (17) is obtained by rewriting Eq. (16) as a set of $2\bar{m} - 2$ equations

$$\mathbf{S}\mathbf{x}_{1_e} = 0, \quad (19)$$

where

$$\mathbf{x}_{1_e} = [x_{1_e}^{2\bar{m}-3} x_{1_e}^{2\bar{m}-4} \ \ldots \ x_{1_e} 1]^T.$$

Equation (19) may also be rewritten as

$$\begin{bmatrix} \mathbf{A}_U & \mathbf{A}_L \\ \mathbf{B}_U & \mathbf{B}_L \end{bmatrix} \begin{bmatrix} \mathbf{u}_{1_e} \\ \mathbf{v}_{1_e} \end{bmatrix} = 0, \quad (20)$$

where

$$\mathbf{u}_{1_e} = [x_{1_e}^{2\bar{m}-3} x_{1_e}^{2\bar{m}-4} \ \ldots \ x_{1_e}^{\bar{m}} x_{1_e}^{\bar{m}-1}]^T$$

and

$$\mathbf{v}_{1_e} = [x_{1_e}^{\bar{m}-2} x_{1_e}^{\bar{m}-3} \ \ldots \ x_{1_e} 1]^T.$$

Equation (20) then gives

$$\mathbf{A}_U \mathbf{u}_{1_e} + \mathbf{A}_L \mathbf{v}_{1_e} = 0$$

and

$$\mathbf{B}_U \mathbf{u}_{1_e} + \mathbf{B}_L \mathbf{v}_{1_e} = 0, \quad (21)$$

from which is obtained

$$[\mathbf{A}_U^{-1}\mathbf{A}_L - \mathbf{B}_U^{-1}\mathbf{B}_L]\mathbf{v}_{1_e} = 0, \quad (22)$$

which is an equation of the form $\mathbf{A}\mathbf{x} = 0$, with $\mathbf{A} = [\mathbf{A}_U^{-1}\mathbf{A}_L - \mathbf{B}_U^{-1}\mathbf{B}_L]$ and $\mathbf{x} = \mathbf{v}_{1_e}$. It therefore follows that $\mathbf{A}^T\mathbf{A}\mathbf{x} = 0$. By comparing this to the standard eigenvalue problem, it may be seen that only the zero eigenvalue of $\mathbf{A}^T\mathbf{A}$ and, therefore, the zero singular value of $\mathbf{A}$ is of interest. Only the singular vector of $\mathbf{A}$ (or the eigenvector of $\mathbf{A}^T\mathbf{A}$) corresponding to this is then also of interest. Represent it by

$$K[x_{1_e}^{\bar{m}-2} x_{1_e}^{\bar{m}-3} \ \ldots \ x_{1_e} 1]^T,$$

where K is arbitrary. Let the actual numerical value of the singular vector be

$$[e_1 e_2 \ \ldots \ e_{\bar{m}-2} e_{\bar{m}-1}]^T.$$

Then an estimate of x_{1_e} is

$$x_{1_e} = \frac{\sum_{i=1}^{\bar{m}-2} e_i / e_{i+1}}{\bar{m} - 2}, \quad (23)$$

which is acceptable if it lies in the range $-2 \le x_{1_e} \le 2$. Then the estimate for ξ_e is given by

$$\xi_e = \frac{a}{\pi} \cos^{-1}\left(\frac{x_{1_e}}{2}\right). \quad (24)$$

4.2 Phase and Amplitude. Having determined the estimates, ξ_e and η_e, for the force location, it is possible to obtain estimates for the phase and amplitude, ϕ_e and A_e, of the force in the following manner.

Downloaded 03 May 2010 to 171.66.16.247. Redistribution subject to ASME license or copyright; see http://www.asme.org/terms/Terms_Use.cfm

Define an objective function by

$$S=\frac{1}{N}\sum_{i=1}^{N}[(X_{i_e}-X_{i_o})^2+(Y_{i_e}-Y_{i_o})^2], \tag{25}$$

where $X_i = W_i \cos\theta_i$ and $Y_i = W_i \sin\theta_i$, the subscripts "e" and "o" referring, respectively, to the estimated and observed quantities. Let

$$s_{i_e}=-\sum_{m=1}^{\infty}\sum_{n=1}^{\infty}\frac{\sin\frac{m\pi\xi_e}{a}\sin\frac{n\pi\eta_e}{b}\sin\frac{m\pi x_i}{a}\sin\frac{n\pi y_i}{b}}{(\lambda^2-p_{mn}^2)^2+p_{mn}^4\tau_K^2\lambda^2}(\lambda^2-p_{mn}^2)$$

and

$$t_{i_e}=-\sum_{m=1}^{\infty}\sum_{n=1}^{\infty}\frac{\sin\frac{m\pi\xi_e}{a}\sin\frac{n\pi\eta_e}{b}\sin\frac{m\pi x_i}{a}\sin\frac{n\pi y_i}{b}}{(\lambda^2-p_{mn}^2)^2+p_{mn}^4\tau_K^2\lambda^2}p_{mn}^2\tau_K\lambda. \tag{26}$$

The condition $\partial S/\partial A_e = \partial S/\partial\phi_e = 0$ then leads to the following explicit expressions for the estimated values of the phase and amplitude of the force:

$$\tan\phi_e=\frac{B}{A}, \tag{27}$$

$$A_e=\frac{\sqrt{A^2+B^2}}{\Sigma_{i=1}^{N}(s_{i_e}^2+t_{i_e}^2)}, \tag{28}$$

where $A = \Sigma_{i=1}^{N}(X_{i_o}s_{i_e} + Y_{i_o}t_{i_e})$ and $B = \Sigma_{i=1}^{N}(Y_{i_o}s_{i_e} - X_{i_o}t_{i_e})$.

Hence, with the coordinates of the estimated location, (ξ_e, η_e), of the force, the expressions of Eqs. (27) and (28) may be used to determine the estimates, ϕ_e and A_e, for its phase and amplitude.

5 An Iterative Procedure

The approximate solutions obtained in the previous section may each be used to initiate an iteration with a view to minimizing the objective function of Eq. (25). If $\mathbf{x}^{(k)} = [x_1^{(k)}\ x_2^{(k)}\ x_3^{(k)}\ x_4^{(k)}]^T$ is the kth estimate of the solution vector $[\xi\ \eta\ A\ \phi]^T$ and $\delta^{(k)}$ is the change in the kth estimate after one iteration, then

$$\mathbf{x}^{(k+1)}=\mathbf{x}^{(k)}+\delta^{(k)}, \tag{29}$$

where $\delta^{(k)}$ is determined from the solution of the equation

$$\mathbf{G}^{(k)}\delta^{(k)}=-\mathbf{g}^{(k)}, \tag{30}$$

with

$$G_{jk}=\frac{2}{N}\sum_{i=1}^{N}\left(\frac{\partial X_{i_e}}{\partial x_j}\frac{\partial X_{i_e}}{\partial x_k}+\frac{\partial Y_{i_e}}{\partial x_j}\frac{\partial Y_{i_e}}{\partial x_k}\right), \quad j,k=1,2,3,4,$$

and

$$g_j=\frac{2}{N}\sum_{i=1}^{N}\left[(X_{i_e}-X_{i_o})\frac{\partial X_{i_e}}{\partial x_j}+(Y_{i_e}-Y_{i_o})\frac{\partial Y_{i_e}}{\partial x_j}\right], \quad j=1,2,3,4.$$

This is the Gauss-Newton method (Gill et al., 1981) which is applicable to least-squares problems in general. It is, however, advantageous to make some modifications that make use of the structure of the problem. The first is to update the estimates for the phase and magnitude of the force at each iterative step to the values predicted by Eqs. (27) and (28). The second modification is to make use of the trigonometric identities

$$\sin k\theta=\sin k(\theta+2l\pi)$$

and

$$\sin k\theta=-\sin k(2\pi-\theta+2l\pi), \tag{31}$$

$k = 1, 2, \ldots$ and $l = \ldots, -1, 0, 1, \ldots$ in conjunction with a step-size halving scheme to return the results of an iterative step for ξ_e and η_e to within the plate boundaries, should the iterative scheme predict a value outside.

Therefore, with each of the initial estimates obtained by the method described in the previous section, it is possible to perform an iteration by the method just described. The solution is then taken to be the result of the iteration which produces the smallest value for the objective function.

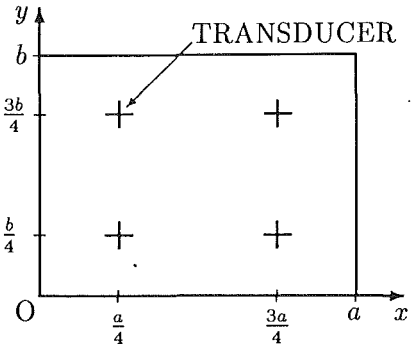


Fig. 2 Transducer configuration

Table 1 Results of least-squares calculation—initial estimate and iterates

Force Co-ordinates ξ_e	η_e	Magnitude A_e	Phase Angle ϕ_e	Objective Function
0.538650	0.0939088	0.574422	4.97091	0.118839×10^{-12}
0.533608	0.135122	0.811345	4.97107	0.883861×10^{-18}
0.533600	0.143563	0.964402	4.97107	0.109271×10^{-19}
0.533600	0.145154	1.00264	4.97107	0.256001×10^{-21}
0.533599	0.145039	0.999744	4.97107	0.161958×10^{-23}
0.533599	0.145050	1.00002	4.97107	0.151986×10^{-25}
0.533599	0.145049	0.999998	4.97107	0.138227×10^{-27}
0.533599	0.145049	1.00000	4.97107	0.126035×10^{-29}
0.533599	0.145049	1.00000	4.97107	0.114894×10^{-31}
0.533599	0.145049	1.00000	4.97107	0.104750×10^{-33}

Dimensions of Plate: $a = 1$, $b = 0.179902$
Actual Force Co-ordinates: $\xi = 0.533599$, $\eta = 0.145049$
Actual Force Magnitude and Phase Angle: $A = 1$, $\phi = 4.97107$
Number of Transducers: 4
Frequency of excitation halfway between frequencies of 2nd and 3rd undamped modes

6 Results of Numerical Simulations

The method described above was implemented on a digital computer. The plate dimensions were denoted by a and b, the force magnitude and phase angle by A and ϕ, and the force coordinates by ξ and η. Without loss of generality, the value of unity was assigned to a and A. Then b, ξ, η, and ϕ were generated randomly. It should be noted that ϕ was allowed to vary between 0 and 2π. A total of 50 test cases was generated.

It was claimed in Section 3 that three transducers were required to ensure a unique solution. However, to ensure an even distribution of transducers over the surface of the plate, four transducers configured as illustrated in Fig. 2 were used. (An even distribution of the transducers over the surface of the plate was considered necessary to avoid the situation in which a large proportion of the transducers is located in a region of the plate with a poor signal to noise ratio.)

Of the 50 test cases generated, five were not considered because the aspect ratios, b/a, of the plates involved (9.5×10^{-4}, 6.3×10^{-2}, 9.7×10^{-5}, 4.9×10^{-2} and 3.4×10^{-3}) were considered too small to be treated as those of a plate. All of the remaining 45 cases were successfully solved. The results of a sample case appear in Table 1. In this instance, only one initial estimate was arrived at by the solution technique and it, together with the resulting iteration, is shown. A degree of confidence may be attached to the results obtained without making use of any a priori knowledge of the true

Downloaded 03 May 2010 to 171.66.16.247. Redistribution subject to ASME license or copyright; see http://www.asme.org/terms/Terms_Use.cfm

Table 2 Results of least-squares calculation with noise—initial estimates and iterates

Force Co-ordinates ξ_e	Force Co-ordinates η_e	Magnitude A_e	Phase Angle ϕ_e	Objective Function
0.499461	0.124132	0.661314	4.96956	0.472242×10^{-11}
0.534390	0.127984	0.723490	4.96942	0.324186×10^{-13}
0.533477	0.151519	1.19508	4.96939	0.411114×10^{-14}
0.533500	0.150341	1.15164	4.96939	0.405192×10^{-14}
0.533500	0.150371	1.15270	4.96939	0.405190×10^{-14}
0.533500	0.150371	1.15268	4.96939	0.405190×10^{-14}
0.533500	0.150371	1.15268	4.96939	0.405190×10^{-14}

Dimensions of Plate: $a = 1$, $b = 0.179902$
Actual Force Co-ordinates: $\xi = 0.533599$, $\eta = 0.145049$
Actual Force Magnitude and Phase Angle: $A = 1$, $\phi = 4.97107$
Number of Transducers: 8
Frequency of excitation halfway between frequencies of 2nd and 3rd undamped modes

values of the estimated parameters. This is done by determining the variance-covariance matrix of the solution vector $[\xi_e \eta_e A_e \phi_e]^T$. If **H** is the inverse of matrix **G** of Eq. (30), then an unbiased estimate of the covariance of the ith and jth parameters is (Wolberg, 1967)

$$\mathrm{Cov}(x_i, x_j) = \frac{2S}{m-n} H_{ij}, \tag{32}$$

where S is the least-squares objective function, m is the number of items of information (i.e., $m = 2N$, N being the number of transducers), and n is the number of parameters estimated. For the sample case of Table 1, this variance-covariance matrix turns out to be

$$0.209576 \times 10^{-27} \begin{bmatrix} 27.6932 & 5325.66 & 133458 & -1 \\ 5325.66 & 4.37058 \times 10^{7} & 1.09512 \times 10^{9} & -1747.18 \\ 133458 & 1.09512 \times 10^{9} & 2.74399 \times 10^{10} & -43778.8 \\ -1 & -1747.18 & -43778.8 & 1321.86 \end{bmatrix}.$$

As may be seen, the magnitude of the entries allows a great deal of certainty to be placed on the solution vector.

7 Effect of Measurement Noise

The technique described above was demonstrated using numerically generated displacement readings. These were obtained from the displacement function without the effect of measurement noise being simulated. However, as the problem is analyzed as a nonlinear least-squares problem, and as least-squares solution procedures are robust to the effects of measurement noise, it is expected that, provided the initial estimates obtained are not severely affected, the addition of measurement noise will not have a significant effect on the results. By this it is meant that the solution vector will still be found, albeit with less accuracy than if the measurement noise were absent.

To demonstrate this point, the 50 test cases were run with Gaussian noise added to the transducer readings. (The noise was directly added to the X_{i_o} and Y_{i_o} values of Eq. (25), the standard deviation in each case being one percent of the r.m.s. of the noiseless X_{i_o} and Y_{i_o} values, i.e., $\sigma = 0.01 \times [1/2N \, \Sigma_{i=1}^{N}(X_{i_o}^2$ and $Y_{i_o}^2)]^{1/2}$. Again, the five cases with aspect ratios considered too small to be those of a plate were not analyzed. The results of the same sample case as that of Table 1 appear in Table 2. Also in this instance, only one initial estimate was found and it, together with the resulting iteration, is shown.

The variance-covariance matrix is now given by

$$0.185745 \times 10^{-8} \begin{bmatrix} 42.1208 & 97.0939 & 3479.25 & -1 \\ 97.0939 & 4990.01 & 176822 & -21.0809 \\ 3479.25 & 176822 & 6268490 & -747.573 \\ -1 & -21.0809 & -747.573 & 2038.76 \end{bmatrix}.$$

It may be seen that the magnitude of the entries still allows a great deal of certainty to be placed on the solution vector.

All of the test cases considered were, again, successfully solved. Some cases, however, required additional transducers for their successful solution. It may therefore be concluded that the solution method is indeed robust to the effects of measurement noise, which would be present in practice. The greater number of transducers required for the successful solution of some cases compared to the number of transducers required in the absence of noise is expected because of the presence of the measurement noise.

8 Generalization of the Solution Technique

The method outlined previously is applicable to a simply-supported rectangular plate acted upon by a single harmonic point force. It may be extended to tackle more general structural configurations and loading conditions in the following manner.

8.1 Structural Configurations. Consider first the extension to more general structural configurations. Let the displacement response at time t of transducer i, located at (x_i, y_i), be given by

$$w_{i_e} = A_e[f(\xi_e, \eta_e, x_i, y_i)\sin(\lambda t + \phi_e) - g(\xi_e, \eta_e, x_i, y_i)\cos(\lambda t + \phi_e)], \tag{33}$$

where (ξ_e, η_e) are the coordinates of the estimated force location, A_e and ϕ_e the estimated force amplitude and phase, and λ the frequency of excitation. This represents the response of a classical viscoelastic structure to harmonic excitation (cf. Eq. (1)). Set $A_e = 1$ and $\phi_e = 0$. Then by exciting, say, a finite element model of the structure with a load of unit magnitude and zero phase, the quantities $f(\xi_e, \eta_e, x_i, y_i)$ and $g(\xi_e, \eta_e, x_i, y_i)$ may be determined.

Define an objective function by

$$S = \frac{1}{N} \sum_{i=1}^{N} [(X_{i_e} - X_{i_o})^2 + (Y_{i_e} - Y_{i_o})^2], \tag{34}$$

where $X_i = W_i \cos\theta_i$ and $Y_i = W_i \sin\theta_i$, W_i and θ_i being the amplitude and phase of the response at (x_i, y_i), the subscripts "e" and "o" referring to the estimated and observed values, respectively (cf. Eq. (25)). Now, the displacement response of transducer i for the simply-supported classical viscoelastic rectangular plate may be written as

$$w_{i_e} = A_e[-t_{i_e}\sin(\lambda t + \phi_e) + s_{i_e}\cos(\lambda t + \phi_e)], \tag{35}$$

where s_{i_e} and t_{i_e} are defined by Eqs. (26). This leads to the analogy

$$s_{i_e} \equiv -g(\xi_e, \eta_e, x_i, y_i)$$

and

$$t_{i_e} \equiv -f(\xi_e, \eta_e, x_i, y_i) \tag{36}$$

between the functions s and t of the simply-supported plate and the functions f and g of the more general structure. Equations (27) and (28) for the estimated phase and amplitude of the force then stand, except that $s_{i_e}^2$ and $t_{i_e}^2$, respectively, are replaced by $g_{i_e}^2$ and $f_{i_e}^2$ where

$$f_{i_e} = f(\xi_e, \eta_e, x_i, y_i)$$

and

$$g_{i_e} = g(\xi_e, \eta_e, x_i, y_i),$$

with

$$A = -\sum_{i=1}^{N} (X_{i_o} g_{i_e} + Y_{i_o} f_{i_e})$$

and

Downloaded 03 May 2010 to 171.66.16.247. Redistribution subject to ASME license or copyright; see http://www.asme.org/terms/Terms_Use.cfm

$$B = -\sum_{i=1}^{N} (Y_{i_o} g_{i_e} - X_{i_o} f_{i_e}).$$

The objective function, S, of Eq. (34) may therefore be evaluated on a coarse grid over the structure to yield, as an initial estimate, the point which results in its smallest value. The iterative scheme outlined in Section 5 may then be used to improve upon the accuracy of the estimate as follows. Equations (29) and (30) show that each iterative step requires the evaluation of first-order derivatives of X_{i_e} and Y_{i_e}. These may be found from the computed values of X_{i_e} and Y_{i_e} at and near the current estimate of the solution vector so that the matrix $\mathbf{G}$ and vector $\mathbf{g}$ may be obtained in order to implement the iterative scheme.

8.2 Loading Conditions. Now consider the extension to more general loadings. If, for instance, the plate is acted upon by a number of harmonic point loads, $P_j \cos(\lambda_j t + \phi_j)$, $j = 1, 2, \ldots, M$, the displacement field, by linear superposition, is given by

$$w(x,y,t) = \sum_{j=1}^{M} \frac{4P_j}{\bar{\rho} ab} \sum_{m=1}^{\infty} \sum_{n=1}^{\infty} \left[\frac{\sin \frac{m\pi\xi_j}{a} \sin \frac{n\pi\eta_j}{b} \sin \frac{m\pi x}{a} \sin \frac{n\pi y}{b}}{(\lambda_j^2 - p_{mn}^2)^2 + p_{mn}^4 \tau_K^2 \lambda_j^2} \times [p_{mn}^2 \tau_K \lambda_j \sin(\lambda_j t + \phi_j) - (\lambda_j^2 - p_{mn}^2) \cos(\lambda_j t + \phi_j)] \right]. \quad (37)$$

Because of the similarity of this displacement function to the corresponding one with the single load, the technique outlined herein may be used as a basis to tackle this more difficult inverse problem.

9 Discussion and Conclusion

Presented above is a method for determining the location, magnitude, and phase of a harmonic point force acting on a simply-supported classical viscoelastic rectangular plate from a number of displacement readings at discrete points on the plate. In practice, these displacement readings would be subject to measurement noise. This is modeled by Gaussian noise and it is shown by numerical experiments that the solution algorithm is robust to its effect. It was seen that the solution vector in the presence of measurement noise was still found, albeit with less accuracy than if the measurement noise was absent. Also, as expected, the presence of the measurement noise produced a requirement for a greater number of transducers in some of the test cases considered.

The method is demonstrated by its application to the problem of a single harmonic point load acting on a rectangular plate. Presented also is a means by which it may be extended to solve a larger class of problems. The extension provides both a means by which structures of a more arbitrary nature and loadings of a more general nature may be treated.

It was claimed that three transducers are sufficient, generically, to ensure a unique solution. However, to ensure an even distribution of the transducers over the surface of the plate, the minimum number of transducers employed was four. This was considered necessary to avoid the situation in which a large proportion of the transducers is located in a region of the plate with a poor signal to noise ratio. It is interesting to note that if the harmonic load were replaced by a static one, the number of transducers claimed to be sufficient generically for a unique solution is four. As previously explained, the reason for this apparent discrepancy is that each transducer in the case of the harmonic load provides two readings, while each transducer in the case of the static load provides only one.

Finally, it may be seen that because of the good results obtained in the test cases considered, the method may be used with some confidence. It may therefore be concluded that the method outlined above for the determination of the location, magnitude, and phase of a harmonic point load acting on a simply-supported classical viscoelastic rectangular plate, apart from being accurate and robust to the effects of measurement noise, may be extended to solve problems of a more general nature. In this, it represents a step taken toward the solution of practical force identification problems.

Acknowledgments

This work was carried out as part of a Ph.D. program in the Department of Mechanical Engineering, Monash University under a Department of Defence Postgraduate Cadetship. The use of the computing facilities at the Aeronautical Research Laboratory is also gratefully acknowledged.

References

Barnett, S., 1983, *Polynomials and Linear Control Systems*, Marcel Dekker, New York, p. 31.

Bartlett, F. D., Jr., and Flannelly, W. G., 1979, "Model Verification of Force Determination for Measuring Vibratory Loads," *Journal of the American Helicopter Society*, Vol. 24, pp. 10–18.

Baumeister, J., 1987, *Stable Solution of Inverse Problems*, Vieweg Advanced Lectures in Mathematics, Friedr. Vieweg and Sohn, Braunschweig/Weisbaden, p. 2.

Blackburn, H. M., and Melbourne, W. H., 1989, "Measurement of Sectional Lift Forces on an Oscillating Cylinder," *Proceedings of the Second Asia-Pacific Symposium on Wind Engineering*, Beijing, China, pp. 332–339.

Bube, K. P., and Burridge, R., 1983, "The One-Dimensional Inverse Problem of Reflection Seismology," *SIAM Review*, Vol. 25, No. 4, pp. 497–559.

Chang, C., and Sachse, W., 1985, "Analysis of Elastic Wave Signals from an Extended Source in a Plate," *Journal of the Acoustical Society of America*, Vol. 77, No. 4, pp. 1335–1341.

Colton, D., and Kress, R., 1983, *Integral Equation Methods in Scattering Theory*, John Wiley and Sons, New York.

Daimaruya, M., Tanimura, S., and Onozaki, S., 1988, "Measurement of Impulsive Force and Duration of Impact in Elastic-Plastic Impact of Bodies," *Proceedings of the VI International Congress on Experimental Mechanics*, Portland, Oregon, pp. 177–182.

D'Cruz, J., Crisp, J. D. C., and Ryall, T. G., 1991, "Determining a Force Acting on a Plate—An Inverse Problem," *AIAA Journal*, Vol. 29, No. 3, pp. 464–470.

de Laine, R. J., 1975, "Identifying a Time-Invariant Linear System from its Outputs," Ph.D. Thesis, Department of Mechanical Engineering, Monash University, Melbourne, Australia.

Doyle, J. F., 1986, "Determining the Contact Force During the Transverse Impact of Plates," *Proceedings of the 1986 SEM Spring Conference on Experimental Mechanics*, New Orleans, pp. 560–567.

Ellis, N., 1973, "A Technique for Evaluating the Fluctuating Aerodynamic Forces on a Flexible Building," *Proceedings of the International Symposium on Vibration Problems in Industry*, Keswick, U.K., Paper 312.

Ellis, N., 1976, "A New Technique for Evaluating the Fluctuating Lift and Drag Force Distributions on Building Structures," Building Research Establishment Current Paper, CP2/76, Watford, U.K.

Ewins, D. J., and Hillary, B., 1980, "A Method for Force Determination from Vibration Response Measurements," *Aeroelasticity in Turbomachines: Proceedings of the Second International Symposium*, Lausanne, pp. 263–283.

Fabunmi, J. A., 1986, "Effects of Structural Modes on Vibratory Force Determination by the Pseudoinverse Technique," *AIAA Journal*, Vol. 24, No. 3, pp. 504–509.

Flannelly, W. G., Bartlett, F. D., Jr., and Fossberg, T. W., 1977, "Laboratory Verification of Force Determination, A Potential Tool for Reliability Testing," USAAMRDL-TR-76-38.

Giansante, N., Jones, R., and Calapodas, N. J., 1982, "Determination of In-Flight Helicopter Loads," *Journal of the American Helicopter Society*, Vol. 27, pp. 58–64.

Gill, P. E., Murray, W., and Wright, M. H., 1981, *Practical Optimization*, Academic Press, London, p. 134.

Jones, R., Flannelly, W. G., Nagy, E. J., and Fabunmi, J. A., 1981, "Experimental Verification of Force Determination and Ground Flying on a Full Scale Helicopter," USAAVRADCOM-TR-81-D-11.

Michaels, J. E., 1984, "An Inverse Source Problem for Elastic Waves," Ph.D. Thesis, Department of Theoretical and Applied Mechanics, Cornell University, Ithaca, New York.

Michaels, J. E., and Pao, Y.-H., 1985, "The Inverse Source Problem for an

Downloaded 03 May 2010 to 171.66.16.247. Redistribution subject to ASME license or copyright; see http://www.asme.org/terms/Terms_Use.cfm

Oblique Force on an Elastic Plate," *Journal of the Acoustical Society of America*, Vol. 77, No. 6, pp. 2005–2011.

Michaels, J. E., and Pao, Y.-H., 1986, "Determination of Dynamic Forces from Wave Motion Measurements," ASME JOURNAL OF APPLIED MECHANICS, Vol. 53, pp. 61–68.

Öry, H., Glaser, H., and Holzdeppe, D., 1985, "Reconstruction of Forcing Functions based on Measured Structural Responses," *International Symposium on Aeroelasticity and Structural Dynamics*, 2nd ed., Aachen, West Germany, pp. 656–668.

Pan, H. H., 1966, "Vibrations of Viscoelastic Plates," *Journal de Mécanique*, Vol. 5, No. 3, pp. 355–374.

Pao, Y.-H., 1978, "Theory of Acoustic Emission," *Elastic Waves and Non-Destructive Testing of Materials*, Y.-H. Pao, ed., AMD-ASME 29, pp. 107–128.

Richardson, R. M., 1983, "Inversion for the Driving Forces of Plate Tectonics," *1983 International Geoscience and Remote Sensing Symposium (IGARSS '83)*, San Francisco, California, pp. 3.1–3.6.

Stephens, K. K., 1987, "Force Identification Problems—An Overview," *Proceedings of the 1987 SEM Spring Conference on Experimental Mechanics*, Houston, Texas, pp. 838–844.

Wolberg, J. R., 1967, *Prediction Analysis*, D. Van Nostrand Company, Princeton, NJ, p. 54.

Downloaded 03 May 2010 to 171.66.16.247. Redistribution subject to ASME license or copyright; see http://www.asme.org/terms/Terms_Use.cfm

Finite Element Analysis of Multiphase Viscoelastic Solids

L. C. Brinson[1]
Mem. ASME

W. G. Knauss
Fellow ASME.

Division of Engineering and Applied Science,
California Institute of Technology,
Pasadena, CA 91125

The properties of composite solids containing multiple, viscoelastic phases are studied numerically. The dynamic correspondence principle of viscoelasticity is utilized in a finite element model to solve boundary value problems for obtaining global complex moduli of the composite. This numerical procedure accounts for the coupled interactive deformation of the phases and thus the resultant accuracy is limited only by that of finite element analyses in general. The example composite considered in this study contains cylindrical viscoelastic inclusions embedded in a viscoelastic matrix. This investigation focuses on the global composite moduli and their relationship to the individual phase properties as a function of volume fraction. A given phase material is shown to have differing effects on the composite properties, depending on whether it is the continuous or the included phase: In general, the composite moduli are dominated by the matrix material. Comparison is made with two simple analytical models for global effective moduli of composites. "Upper Bounds" reproduce the behavior over the whole frequency range when the matrix is the "stiffer" of the two solids while the "lower bond" associates with the converse arrangement, also over the whole frequency range. The nature of time-temperature behavior of multiphase composite materials is examined in a companion paper.

1 Introduction

Multiphase viscoelastic materials usually contain a "stiff" solid and a "softer" viscoelastic material with one phase distributed as inclusions inside of the other phase. Often this type of composite material has advantages over either phase alone. The best known examples of composites are fibrous composites, where the "stiff" phase is usually not viscoelastic, but consists instead of fibers of graphite, glass, or boron. However, there are other structural materials of two or more polymeric phases intended or designed to offer improved performance. Examples include rubber-toughened thermoset adhesives, such as American Cyanamide's FM 73 and 3M's AF153, as well as softer materials, such as Styrene-Butadiene Rubber, used in automotive tires.

Two objectives motivate the following work. It is well known that all polymers possess time-dependent mechanical properties which are sensitive to temperature and solvents. Because engineering applications of these materials may call for very long time scales, it is necessary to resort to a time-acceleration scheme for determining the long-term viscoelastic material characteristics from laboratory measurements. Such a time acceleration scheme is well established for a class of homopolymers called thermorheologically simple (TRS) materials. This scheme enables the calculation of long-time modulus properties for the material based on short-time, multitemperature data (Ferry, 1980; Leaderman, 1943; Tobolsky and Eyring, 1943). (e.g., the Arrhenius, Doolittle, WLF equations).

By contrast, many polymers, and particularly multiphase ones, are thermorheologically complex (TRC). For composites with multiple viscoelastic phases, which are a subclass of TRC materials, there are two or more sets of relaxation mechanisms active in the composite at all times and temperatures. Because their overall time and temperature-dependent mechanical response is determined by the compatible deformation of the individual phases, a *simple* time-temperature response cannot result. In order to provide long-term material properties for engineering design it would seem necessary, therefore, to test these composites over very long time scales at anticipated temperature conditions. A desirable alternative is to devise a computational scheme that draws on the knowledge of the individual phase properties and combines them in an analytically and mechanically correct manner to deduce the complex time-temperature-dependent behavior of the composite. It is this latter idea which provides one objective for this study.

An additional motivation derives from the need to determine the properties of small phase domains in multiphase solids from globally measured properties of the bulk composites. In such an "inverse" situation, it is of interest to examine the properties of one of several phases possessing arbitrary (also viscoelastic) properties if the properties of the other phases and the composite are known. In order to make the best possible statement about the desired phase properties it is then important to provide a computational scheme which maximizes

[1]Department of Mechanical Engineering, Northwestern University, Evanston, IL 60208.

Contributed by the Applied Mechanics Division of THE AMERICAN SOCIETY OF MECHANICAL ENGINEERS for presentation at the 1992 ASME Winter Annual Meeting, Anaheim, Ca, Nov. 8-13, 1992.

Discussion on this paper should be addressed to Prof. Leon M. Keer, The Technological Institute, Northwestern University, Evanston, IL 60208, and will be accepted until four months after final publication of the paper itself in the ASME JOURNAL OF APPLIED MECHANICS.

Manuscript received by the ASME Applied Mechanics Division, June 4, 1990; final revision, Jan. 20, 1992. Associate Technical Editor: L. M. Keer.

Paper No. 92-WA/APM-11.

Copyright © 1992 by ASME
Downloaded 03 May 2010 to 171.66.16.247. Redistribution subject to ASME license or copyright; see http://www.asme.org/terms/Terms_Use.cfm

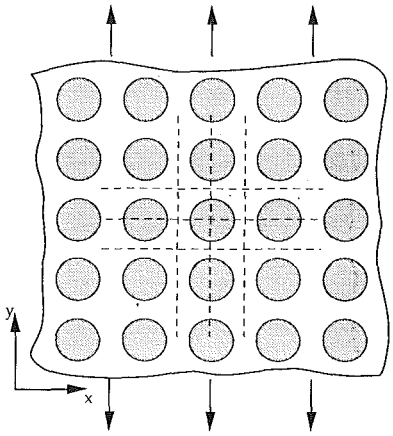


Fig. 1 The global material

precision rather than rely on estimation, especially when the uncertainty in estimation bounds is on the order of contribution from the phase, the properties of which are to be determined. Furthermore, the immediate application of this approach is to address properties of solids with three (or more) phases (Brinson, 1990; Brinson and Knauss, 1991), all of which possess different viscoelastic properties. Bringing the present method to bear on these somewhat more general problems poses no difficulty in principle, only in detail. In fact, whether one deals with two-dimensional problems of fiber-transverse properties or with three-dimensional particulates of well-defined particle arrangements is only a matter of economics in computation.

In this paper we develop a numerical method of viscoelastic stress and deformation analysis and demonstrate it in terms of a two-phase composite. Of particular interest is the effect of volume fraction. The application to the more complex multiphase material behavior (including temperature effects) is considered in companion documents (Brinson, 1990; Brinson and Knauss, 1991).

The problem of determining global composite properties from the properties and geometries of the individual phases (usually two) has been considered by many authors in numerous publications and reports, including references to the viscoelastic behavior of matrix materials. (See review article by Hashin, 1983). Both numerical and "closed-form" analytical results prevail. The use of these methods for the intent described above with respect to multiple phases, each possessing viscoelastic character, has not been examined in application to experimentally determined properties, although there exists an abundance of analytical contributions to composites of elastic properties under small as well as large deformations (Ponte-Castañeda, 1991; Willis, 1991). The extension of previous work to multiple viscoelastic phases suffers from possibly two shortcomings: First, when elastic minimum/maximum principles are involved to derive bounds on the composite material properties, the corresponding viscoelastic problem in the Laplace transform domain does not guarantee similar bounds after inversion to the time domain has been accomplished. Second, formulation of viscoelastic problems by way of the (Laplace) correspondence principle for realistic material descriptions hinges on numerical inversion of the Laplace transform, a topic that still suffers from uncertainties associated with mathematically ill-posed problems.

In this paper we consider composite analysis by way of the dynamic correspondence principle (see also Fung (1965) and Hashin (1974)) applied to a boundary value problem, which is then solved in a finite element procedure.[2] This technique

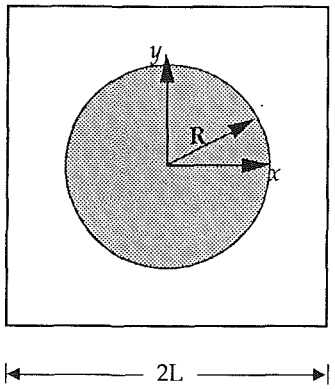


Fig. 2(*a*) The smallest repeating unit

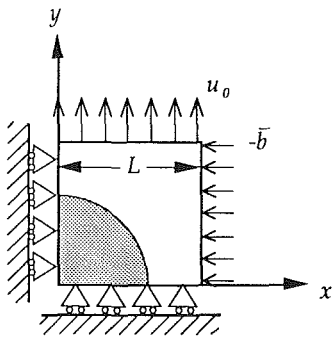


Fig. 2(*b*) Boundary conditions applied to the square unit cell

allows computation of the global complex (real and imaginary) properties of the composite, subject only to the limitations which are part of finite element analysis in general. Once these dynamic properties are determined in the frequency domain, the creep or relaxation functions can be determined by evaluation of well-behaved Fourier integrals. In principle, any phase geometry can be accommodated except that computational-economic constraints limit consideration of random arrangements of one phase within the other. Only regular, two-dimensional arrays will be addressed here: the initial motivation for this choice is derived from the possible regular material structure discussed in other publications (Brinson, 1990; Brinson and Knauss, 1991); beyond that particular reasoning the computations presented here are demonstrative of typical situations, including the limit case of elastic inclusions in a linearly viscoelastic matrix.

2 The Model

The model material examined in this study consists of an array of cylindrical viscoelastic inclusions embedded in a viscoelastic matrix. With largely exemplary purposes in mind, we determine the modulus of the composite in a direction normal to the axes of the cylinders for this microstructure. To this end, a two-dimensional boundary value problem is formulated in plane strain in which the cylinders are represented by circular domains. This situation is depicted by the square array in Fig. 1 in which the unit cells are small in size compared to any other dimensions.[3] One may consider the material array under trac-

[2]In this context the word "dynamic" refers traditionally to sinusoidal deformations with a prescribed frequency, ω, under exclusion of inertia effects.

[3]Note that this material can be considered to be globally homogeneous, but not globally isotropic. The case of a square array of cylinders is presented here. The cylindrical domains in a semihexagonal array has also been studied (Brinson, 1990) in the context of assessing the effect of anisotropy. That study shows that the array structure does not at all change the *character* of the results: the behavior of the global properties with respect to the individual phase properties are nearly unaffected. The differences lacked sufficient incentive to repeat the computation in total for hexagonal arrays. In this work only (plane-strain) simple tension behavior is explored; the corresponding in-plane shear case is considered elsewhere (Brinson, 1990).

Downloaded 03 May 2010 to 171.66.16.247. Redistribution subject to ASME license or copyright; see http://www.asme.org/terms/Terms_Use.cfm

tions averaged over the (many) unit cells and inquire into the average deformation response of the array. Under globally uniform tensile tractions parallel to any axis of array symmetry, the unit cells will deform into rectangles: cell boundaries remain straight. We formulate the following example, mixed boundary value problem on one quadrant of the unit cell shown in Fig. 2(*b*) with u_x, u_y denoting displacement and T_x, T_y traction components in the appropriate directions:

$$\begin{aligned} &x=0, && 0\le y\le L: && u_x=0 && T_y=0\\ &0\le x\le L, && y=0: && u_y=0 && T_x=0\\ &x=L, && 0\le y\le L: && u_x=-b && T_y=0\\ &0\le x\le L, && y=L: && u_y=u_0 && T_x=0 \end{aligned} \tag{1}$$

If b is chosen such that $\int_0^L T_x dy = 0$ for $x = L$, a response results which corresponds to a (plane-strain) uniaxial stress state on the global (average) scale. This quarter unit cell is discretized and studied numerically. From the resulting average deformation and stress state of the unit cell, the effective global moduli of the composite are determined.

3 Finite Element Computations With Complex Variables

The Finite Element Analysis Program (FEAP), developed originally at Berkeley (Taylor, 1982) then modified at Brown University, was chosen for use in this study because of its segmented structure, which allows relatively easy modification of the subroutines without requiring interdependent changes scattered throughout the entire program. In order to address viscoelastic boundary value problems, it was necessary to revise the code's element subroutine. The modifications to FEAP are discussed briefly in two sections: first, the viscoelastic material behavior and the specific relationships which are best suited to the numerical solution of this inclusion problem are described; next, the method by which this material behavior was incorporated into the FEAP code is explained.

3.1 Viscoelastic Material Behavior and the Dynamic Correspondence Principle. Because the constitutive law of viscoelastic materials is expressed through differential equations or convolution integrals, numerical calculations are usually computation-time intensive, requiring iteration over each time-step and retention of the history of the field variables at the previous time-step. Issues dealing explicitly with time dependence can be side-stepped by formulating the problem in the Fourier domain via the dynamic correspondence principle (Read, 1950; Lee, 1955; Fung, 1965); the traditional connotation in viscoelastic material characterization for this formulation relates to a dynamic or complex material description. Because these principles have been recorded a considerable time ago and are not necessarily common repertoire, we outline them briefly for reference. For an isotropic, linearly viscoelastic material, the constitutive law may be written as

$$\begin{aligned} s_{nj}(\mathbf{x}, t) &= \int_{-\infty}^{t} 2G(t-\tau)\frac{de_{nj}(\mathbf{x}, t)}{d\tau}\,d\tau\\ \sigma_{kk}(\mathbf{x}, t) &= \int_{-\infty}^{t} 3K(t-\tau)\frac{d\epsilon_{kk}(\mathbf{x}, t)}{d\tau}\,d\tau \end{aligned} \tag{2}$$

where s_{nj} and σ_{kk} are the deviatoric and dilatational components of the stress tensor, e_{nj} and ϵ_{kk} are the corresponding strain components, and $G(t)$ and $K(t)$ are, respectively, the time-dependent shear and bulk moduli of the material. For time-harmonic deformation histories.

$$\epsilon_{nj}(\mathbf{x}, t) = \bar{\epsilon}_{nj}(\mathbf{x}, \omega)e^{i\omega t}, \tag{3}$$

under steady-state conditions (2) reduces to

$$\begin{aligned} \bar{s}_{nj}(\mathbf{x}, \omega) &= 2i\omega\bar{G}(\omega)\bar{e}_{nj}(\mathbf{x}, \omega)\\ \bar{\sigma}_{kk}(\mathbf{x}, \omega) &= 3i\omega\bar{K}(\omega)\bar{\epsilon}_{kk}(\mathbf{x}, \omega) \end{aligned} \tag{4}$$

where $\bar{\cdot}(\cdot)$ denotes the complex quantities and $\bar{G}(\omega)$ and $\bar{K}(\omega)$ which are the half-sided Fourier transforms of the shear and bulk moduli, respectively, defined by[4]

$$\begin{aligned} \bar{G}(\omega) &= \int_0^\infty G(t)e^{-i\omega t}dt\\ \bar{K}(\omega) &= \int_0^\infty K(t)e^{-i\omega t}dt. \end{aligned} \tag{5}$$

The functions $i\omega\bar{G}(\omega)$ and $i\omega\bar{K}(\omega)$ are referred to as the complex moduli of the viscoelastic material and are described in terms of their real and imaginary parts, the storage moduli, and loss moduli, respectively.

$$\begin{aligned} i\omega\bar{G}(\omega) &\equiv G^*(\omega) = G'(\omega) + iG''(\omega)\\ i\omega\bar{K}(\omega) &\equiv K^*(\omega) = K'(\omega) + iK''(\omega). \end{aligned} \tag{6}$$

"Dynamic testing," which determines the storage and loss moduli, is a common means of assessing viscoeleastic material behavior in the laboratory.

Based on the preceding relations, the dynamic correspondence principle is applicable when the boundary conditions vary in a time harmonic fashion and conditions of proportional loading apply. In this case, Eqs. (2), reduce to the form (4). Explicit time dependence has vanished from the constitutive equations in favor of the frequency, ω, resulting in equations in the Fourier (frequency) domain which are analogous to the equations of elasticity. Equations (4) are valid for any value of ω, analogous to the corresponding elasticity problem, but now each field quantity possesses, in general, both real and imaginary parts. In applying this principle to an inhomogeneous domain we assume that the deformations throughout all phases are synchronous, as they must be on the interface boundaries; moreover, inertial effects are excluded in the sequel.

3.2 Finite Element Modifications. Only a few crucial changes to the basic finite element code that are essential to the analysis are mentioned here. It should be noted that the present study employs exclusively infinitesimal deformation analysis with strains and displacements such that the linear theory of viscoelasticity holds.

Since the field quantities become complex variables in Eq. (4), the finite element procedure must be modified to allow for complex field quantities and stiffness matrices. In light of the segmented substructure of the finite element program, this change was implemented by doubling the degrees-of-freedom at each node to allow for real and imaginary displacements in each direction. This method required considerable modification of the element subroutine of the code, but left all other portions of the elasticity numerical procedure untouched.

The separated dilatational and deviatoric parts of both stress and strain in Eqs. (4) are recombined into $\bar{\sigma}_{nj}$ and $\bar{\epsilon}_{nj}$, respectively,

$$\bar{\sigma}_{nj} = 2i\omega\bar{G}(\omega)\bar{\epsilon}_{nj} + i\omega(\bar{K}(\omega) - \frac{2}{3}\bar{G}(\omega))\bar{\epsilon}_{kk}\delta_{nj}, \tag{7}$$

where for simplicity of writing the arguments of $\bar{\sigma}_{nj}$ and $\bar{\epsilon}_{nj}$ have been omitted. In matrix form the complex constitutive relation (7) becomes

[4]The usual factor $1/2\pi$ appearing in the Fourier transform is contained in the inverse transform.

Downloaded 03 May 2010 to 171.66.16.247. Redistribution subject to ASME license or copyright; see http://www.asme.org/terms/Terms_Use.cfm

$$\begin{Bmatrix} \bar{\sigma}_{11} \\ \bar{\sigma}_{22} \\ \bar{\sigma}_{33} \\ \bar{\sigma}_{12} \end{Bmatrix} = \begin{bmatrix} i\omega\left(\frac{4}{3}\bar{G}+\bar{K}\right) & i\omega\left(-\frac{2}{3}\bar{G}+\bar{K}\right) & i\omega\left(-\frac{2}{3}\bar{G}+\bar{K}\right) & 0 \\ i\omega\left(\frac{2}{3}\bar{G}+\bar{K}\right) & i\omega\left(-\frac{4}{3}\bar{G}+\bar{K}\right) & i\omega\left(-\frac{2}{3}\bar{G}+\bar{K}\right) & 0 \\ i\omega\left(\frac{2}{3}\bar{G}+\bar{K}\right) & i\omega\left(-\frac{2}{3}\bar{G}+\bar{K}\right) & i\omega\left(-\frac{4}{3}\bar{G}+\bar{K}\right) & 0 \\ 0 & 0 & 0 & 2i\omega\bar{G} \end{bmatrix} \begin{Bmatrix} \bar{\epsilon}_{11} \\ \bar{\epsilon}_{22} \\ \bar{\epsilon}_{33} \\ \bar{\epsilon}_{12} \end{Bmatrix}, \quad (8)$$

where the 4×4 matrix will be referred to as $[\bar{D}]$ i.e.,

$$[\bar{D}] = [D]_{\mathrm{Re}} + i[D]_{Im}. \quad (9)$$

The element stiffness matrix $[\bar{K}]^e$ is a function of $[\bar{D}]$, and is also complex

$$\begin{aligned}[\bar{K}]^e &= \int_{V^e} [B]^T[\bar{D}][B]dV^e \\ &= \int_{V^e} [B]^T\{[D]_{\mathrm{Re}} + i[D]_{\mathrm{Im}}\}[B]dV^e \\ &= [K^e]_{\mathrm{Re}} + i[K^e]_{\mathrm{Im}}.\end{aligned} \quad (10)$$

Here, $[B]$ is the matrix which relates the nodal displacements to the strains in the element, and which contains the derivatives of the shape functions. The B-matrix does not contain complex quantities; however, it must be reformed to properly accommodate the extra degrees-of-freedom. Considering the usual equilibrium equation for finite elements, $[K]^E\mathbf{u} + \mathbf{f} = 0$, one obtains, upon substitution of complex quantities and separation into real and imaginary parts,

$$[[K^e]_{\mathrm{Re}} + i[K^e]_{\mathrm{Im}}]\{\mathbf{u}_{\mathrm{Re}} + i\mathbf{u}_{Im}\} + [\mathbf{f}_{\mathrm{Re}} + i\mathbf{f}_{\mathrm{Im}}\} = 0, \quad (11)$$

which may be rewritten, with a change of sign through one row to obtain a symmetric stiffness matrix, as

$$\begin{bmatrix} [K^e]_{\mathrm{Re}} & -[K^e]_{\mathrm{Im}} \\ -[K^e]_{\mathrm{Im}} & -[K^e]_{\mathrm{Re}} \end{bmatrix} \begin{Bmatrix} \mathbf{u}_{\mathrm{Re}} \\ \mathbf{u}_{\mathrm{Im}} \end{Bmatrix} + \begin{Bmatrix} \mathbf{f}_{\mathrm{Re}} \\ -\mathbf{f}_{\mathrm{Im}} \end{Bmatrix} = \{\mathbf{0}\}. \quad (12)$$

Equation (12) is again analogous to the elasticity form without explicitly complex quantities, but with double the degrees-of-freedom.

The input section to the code was also modified to allow input of viscoelastic (dynamic) properties and related parameters. The modified code can thus solve viscoelastic problems which are addressed through the same finite element analyses as for elastic solids. In general, both the real and imaginary parts of the boundary conditions are required explicitly as input.

3.3 Application to the Viscoelastic Inclusion Problem. Consider next the boundary value problem represented by Eqs. (1): Replacing the displacement boundary conditions $u_y = u_0$ and $u_x = -b$ in Fig. 2(*b*) with $u_y = u_0e^{i\omega t}$ and $u_x = -\bar{b}e^{i\omega t}$, the problem can be solved numerically in the Fourier domain for each value of ω as a complex elasticity-type problem. The corresponding complex boundary values are

$$\begin{aligned} &x=0, && 0\le y\le L: && \bar{u}_x = 0+i0 && \bar{T}_y = 0+i0 \\ &0\le x\le L, && y=0: && \bar{u}_y = 0+i0 && \bar{T}_x = 0+i0 \\ &x=L, && 0\le y\le L: && \bar{u}_x = -\bar{b} && \bar{T}_y = 0+i0 \\ &0\le x\le L, && y=L: && \bar{u}_y = u_0+i0 && \bar{T}_x = 0+i0.^5 \end{aligned} \quad (13)$$

The solution to the (complex) boundary value problem subject to (13) yields the complex plane-strain Young's Modulus of the global composite material. By combining the "average" resulting normal stress, $\bar{\sigma}_y|_{\mathrm{avg}}$ obtained by a nodal average on $y = L$, along with the applied average normal strain, $\bar{\epsilon}_y = u_0/L$, the complex modulus, $E^*(\omega) = E'(\omega) + iE''(\omega)$, is computed for the two-phase composite through

$$\frac{\bar{\sigma}_y|_{\mathrm{avg}}(\omega)}{\bar{\epsilon}_y(\omega)} \equiv i\omega\bar{E}(\omega) = E^*(\omega). \quad (14)$$

3.4 Low-Frequency/High-Temperature Limits. A special consideration for the numerical analysis arises when one of the materials possesses a shear modulus which vanishes at $t\to\infty$ (uncrosslinked polymer). In this case, the (near) incompressibility resulting from the vanishing shear modulus places excessive constraints on the elements such that the individual components of the dilatational strain are forced to be constant, giving the illusion of excessive "stiffness." Procedures to correctly address the limit cases of incompressibility in finite element analyses have been thoroughly addressed by Herman (1965), Nagtegaal et al. (1974), and Rice et al. (1979).

To cope with this problem, the B-Bar method (Nagtegaal et al., 1974; Rice et al., 1979) was employed throughout the analysis. While in the examples presented in this paper all material components possess nonzero asymptotic moduli, the modeling of a real block co-polymer (Brinson and Knauss, 1991) invokes the situation of an asymptotically vanishing shear modulus in one of the individual phase materials and the B-Bar method of accommodating the accompanying numerical difficulties is necessary.

4 Circular Inclusion Problem

To examine the model composite of Fig. 1, the individual phase properties are chosen as (idealized) viscoelastic properties such that the functions for each phase have distinct long-term and glassy asymptotic values and one phase is "stiffer" for all frequencies than the other, "softer" phase. Figure 3

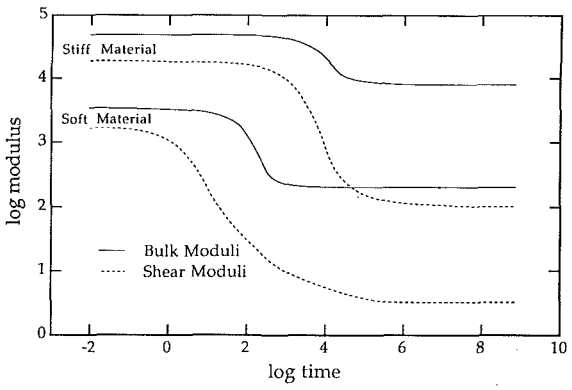


Fig. 3 Relaxation modulus data for individual phases used in analysis

[5]The displacement $\bar{b}$ necessary to satisfy $\int_0^L \bar{T}_x dy \equiv 0$ can be achieved in either one of three different ways. One may employ an interpolation procedure: apply an arbitrary b, solve the boundary value problem, and use the average resulting (nonzero) $\bar{T}_x$ to determine the value of b such that $\int_0^L \bar{T}_x dy \equiv 0$; the boundary value problem can then be solved again with this b to determine the global material response. Two other methods involving specialized finite element techniques may be employed to save computation time by avoiding the extra solution needed for interpolation. The simplest of these two methods assigns the same equation number to the x degrees-of-freedom for all the nodes along the boundary $x = L$ in the assembly process. This method then ensures that the boundary displaces as a unit and leads to the resultant average x-forces along that boundary being zero.

Downloaded 03 May 2010 to 171.66.16.247. Redistribution subject to ASME license or copyright; see http://www.asme.org/terms/Terms_Use.cfm

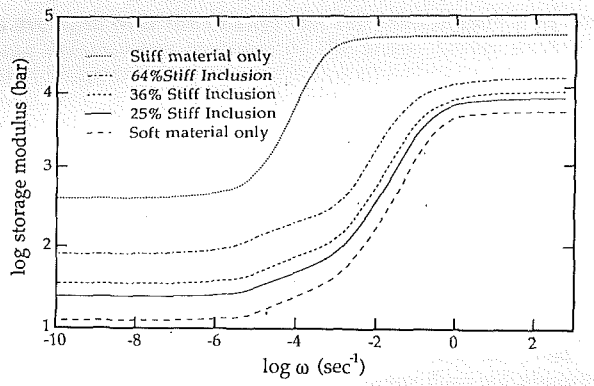


Fig. 4(*a*) Storage modulus of composite with soft (low modulus) matrix and stiff modulus inclusions, at varying volume fractions

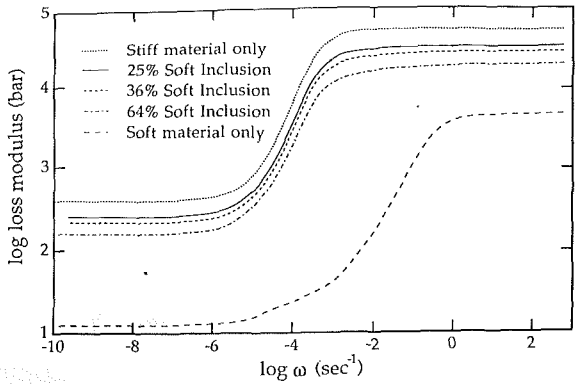


Fig. 5(*a*) Storage modulus of composite with stiff (high modulus) matrix and soft (low modulus) inclusions, at varying volume fractions

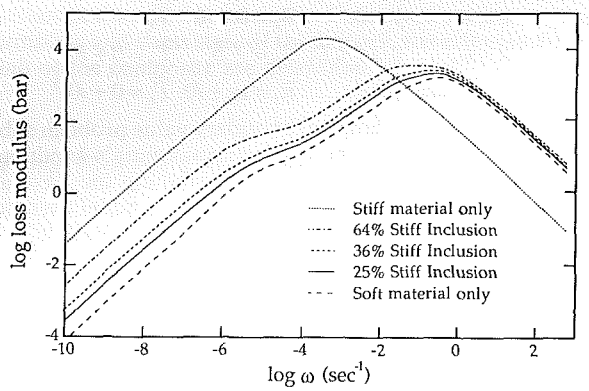


Fig. 4(*b*) Loss modulus of composite with soft (low modulus) matrix and stiff (high modulus) inclusions, at varying volume fractions

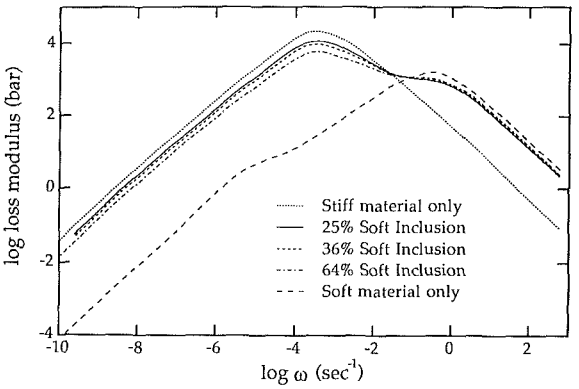


Fig. 5(*b*) Low modulus of composite with stiff (high modulus) matrix and soft (low modulus) inclusions, at varying volume fractions

shows the bulk and shear relaxation functions for these model phases. We include these computations with idealized phase properties rather than the properties of a real system (as are studied in Brinson and Knauss (1991)) in order to emphasize the understanding of viscoelastic composite behavior, before addressing the more complicated behavior of a real composite.

4.1 Variation of Composite Properties as a Function of Volume Fraction. A total of six cases are presented here, three of which contain 25, 36, or 64 percent of the stiff phase embedded in the soft matrix, and three of which locate the same volume fractions of soft material inclusions in a stiff matrix. The results are presented as separate storage and loss moduli. For comparison purposes, the complex Young's moduli for each homogeneous phase are also included.

Figure 4 shows the complex Young's modulus for a composite with a soft matrix and stiff inclusions. It is clear from these figures that the behavior of the composite is dominated by the behavior of the continuous matrix material, even when the volume fraction of the inclusions exceeds 50 percent. The magnitude of the storage modulus increases with increasing volume fraction of the stiff inclusion, but the character of the glass-to-rubber transition (shape, length, location) remains dominated by the (soft) matrix material. Except in response at high frequencies, the values of the composite moduli (storage and loss) lie between the values of the moduli of the soft material and the stiff material, as one would expect intuitively. At high frequencies where the loss modulus of the stiff material is lower than the loss modulus of the soft material, the composite's loss modulus is completely dominated by the soft material and is nearly independent of the volume fraction. Before discussing this phenomenon, it is instructive to examine also the inverse composite for which the stiff material comprises the matrix which contains soft inclusions.

Figure 5 shows the complex modulus for increasing volume fractions of soft inclusions. The results here are quite similar to the complementary situation in Fig. 4. Once again, the composite properties are governed primarily by the matrix properties and the magnitudes of the composite moduli are intermediate to stiffnesses of the two phases except for the loss modulus at high frequencies. Again, the high-frequency loss modulus for the composite is almost equal in magnitude to the loss modulus of the soft material and nearly independent of volume fraction.

The universal domination of the high-frequency loss modulus by the soft phase can be most easily understood by the following physical argument: If one considers the frequency increasing (or time decreasing), Fig. 4 and 5 indicate that the stiff material reaches "elastic" behavior (low losses) before the soft material reacts as a nearly "elastic" material (with reduced dissipation). Accordingly, one expects that the dissipative characteristics of the soft phase control the dissipation of the composite as frequency sweeps to high values. The low losses of the stiff material at the high frequencies cannot *prohibit* dissipation in the composite.

Also worth noting in comparing the results in Figs. 4 and 5 is the relative influence of the included phase on the composite properties. Consider, for example, Figs. 4(*a*) and 5(*a*). For a given volume fraction of inclusions, the magnitude of its effect on the properties of the composite depends greatly on whether the inclusions are "stiffer" or "softer" than the matrix. The magnitude of the effect of a 64 percent volume fraction of inclusions, measured by the percent change of the composite modulus from the matrix material modulus, is much greater in the case of stiff inclusions. Except for the loss modulus at high frequency, a stiff material in the matrix "shields" or blocks the influence of a softer inclusion material more than a soft material is able to block the influence of a stiff material.

Downloaded 03 May 2010 to 171.66.16.247. Redistribution subject to ASME license or copyright; see http://www.asme.org/terms/Terms_Use.cfm

Likewise, stiff material inclusions constrain the deformation of a softer matrix more than soft inclusions are able to constrain a stiffer matrix.

It is noted that the loss modulus of the composite with the stiff (continuous) matrix phase shown in Fig. 5 (*b*) shows clearly two distinct loss peaks, a main one due to the stiff matrix itself and a smaller one as the contribution from the soft inclusion. The loss modulus of the composite with the soft continuous phase (Fig. 4*b*) also shows two loss peaks; however, while the loss peak due to the soft matrix is distinct, the contribution from the stiff inclusion is partially obscured by the fact that the loss modulus of the soft material itself has a slight second rise at approximately the same frequency as the stiff material.[6] It turns out that for the case of stiff inclusions in a soft matrix, the secondary loss peak in the composite does not necessarily coincide exactly with the loss peak of the stiff phase alone. The precise frequency of the secondary loss peak in the composite depends on many factors, including the relative magnitudes of the stiff and soft phase moduli.

4.2 Comparison With Analytical Estimation. For multiphased composites, certain rules for estimating their properties from constituent properties have been proposed. We choose two of these for comparison with the results of this initial study. Also, since the two methods considered here are derived explicitly for elastic phases, in light of the dynamic correspondence principle, we replace the elastic phase properties in each procedure by the complex, dynamic properties of the viscoelastic phases.

The Rule of Mixtures. The Rule of Mixtures is a simple, "quick" procedure which is commonly used to estimate the mechanical properties of composite materials. For example, the Rule of Mixtures yields the transverse modulus for unidirectional cylindrical inclusions in a matrix (cf. Fig. 1)

$$\frac{1}{E_{\text{comp}}}=\frac{V_I}{E_I}+\frac{V_{II}}{E_{II}} \tag{15}$$

where V_j and E_j are the volume fraction and modulus of phase j, and E_{comp} is the estimated modulus of the composite. Applying the dynamic correspondence principle, this result is equivalent to

$$\frac{1}{E^*}=\frac{V_I}{E_I^*}+\frac{V_{II}}{E_{II}^*} \text{ or } \frac{1}{E'+iE''}=\frac{V_I}{E_I'+iE_I''}+\frac{V_{II}}{E_{II}''+iE_{II}''} \tag{16}$$

which then renders explicit expressions for estimating E' and E'' of the composite. The formula for E' is shown here as an example:

$$E'=\frac{(E_I'E_{II}'-E_I''E_{II}'')(V_1E_{II}'+V_2E_I')+(E_I'E_{II}''+E_I''E_{II}')(V_1E_{II}''+V_{2I}'')}{(V_1E_{II}'+V_2E_I')^2+(V_1E_{II}''+V_2E_I'')^2}$$

The Rule of Mixtures does not distinguish between which phase is contained in the inclusions or in the matrix for the same volume fraction of materials. Thus, the Rule of Mixtures predicts the same composite moduli for stiff matrix/soft inclusions as for soft matrix/stiff inclusions as long as the volume fractions remain fixed.

While it is not usually acceptable to apply the Rule of Mixtures to nearly equal volume fraction composites, it is instructive, as an example, to consider two cases of 36 percent stiff material and 64 percent soft material in the composite. The calculated complex Young's moduli for both the composite with the 36 percent stiff material in the inclusion (Fig. 4) and the composite with the 36 percent stiff material in the matrix

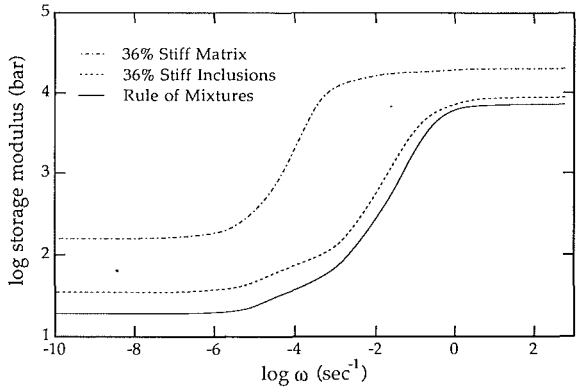


Fig. 6(*a*) Comparison of storage moduli of composite with 36 percent stiff material in (a) matrix and (b) inclusion with rule of mixtures

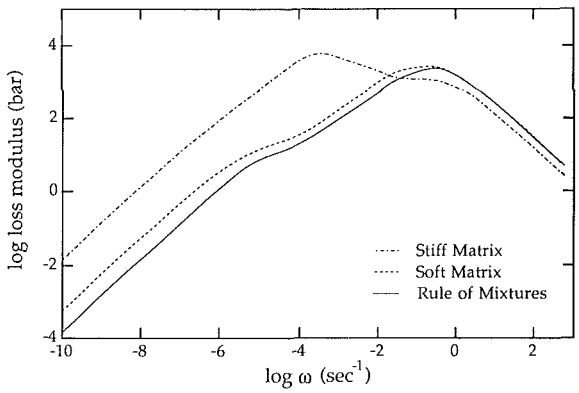


Fig. 6(*b*) Comparison of loss moduli of composite with 36 percent stiff material in (a) matrix and (b) inclusion with rule of mixtures

(Fig. 5) are plotted again in Fig. 6. Note the significant difference between the moduli of these two cases, greater than 50 percent (of the stiff inclusion case) at some frequencies on the log scale of the plots. As illustrated earlier, the composite with the 36 percent stiff material in the matrix possesses moduli dominated in magnitude and functional form by the stiff material, whereas the composite with the 36 percent stiff material in the inclusion exhibits moduli dominated in magnitude and form by the soft matrix material. Figure 6 also shows the Rule of Mixtures prediction, which is the same for these two cases. The Rule of Mixtures best approximates the modulus for the stiff inclusions in a soft matrix (both in magnitude and shape), for the particular properties used here, although the magnitude of the modulus is underestimated in either case.

Comparison with Hashin and Hashin-Shtrikman Bounds. Hashin and Shrikman have formulated upper and lower bounds for the moduli of multiphase composite materials of arbitrary phase geometry by use of variational principles (Hashin and Shtrikman, 1963) and Hashin provided the corresponding bounds for cylindrical inclusions (Hashin, 1965). That development is based upon multiphase materials composed of homogeneous, isotropic elastic phases arranged in such a manner that the composite can be viewed as quasi-homogeneous and quasi-isotropic. The composite under consideration in this work is indeed globally homogeneous, but as noted previously, not really globally isotropic. Thus one would not necessarily expect the Hashin-Shtrikman bounds to be totally consistent with this material; however, inasmuch as one would expect differences between a square array and the quoted bounds to be rather limited, a comparison of the com-

[6]In companion papers it is shown that when the loss peaks of the stiff material and the soft material are separated farther in frequency than in this example, the second loss peak from the stiff inclusion is quite clear (Brinson and Knauss, 1990; Brinson, 1990). The location in frequency of the secondary loss peak of the composite is also discussed in these other papers.

Downloaded 03 May 2010 to 171.66.16.247. Redistribution subject to ASME license or copyright; see http://www.asme.org/terms/Terms_Use.cfm

posite properties derived from the computational analysis with these bounds is still instructive.

The expressions for the bounds on the effective bulk and shear moduli of a two-phase elastic material are

$$K_1^* = K_1 + \frac{v_2}{\dfrac{1}{K_2 - K_1} + \dfrac{(2n+1)v_1}{(2n+1)K_1 + (3n+1)G_1}}$$

$$K_2^* = K_2 + \frac{v_1}{\dfrac{1}{K_1 - K_2} + \dfrac{(2n+1)v_2}{(2n+1)K_2 + (3n+1)G_2}}$$

$$G_1^* = G_1 + \frac{v_2}{\dfrac{1}{G_2 - G_1} + \dfrac{(5n+1)v_1(K_1 + 2G_1)}{(4n+1)G_1(2n+1)K_1 + (3n+1)G_1)}}$$

$$G_2^* = G_2 + \frac{v_1}{\dfrac{1}{G_1 - G_2} + \dfrac{(5n+1)v_2(K_2 + 2G_2)}{(4n+1)G_2((2n+1)K_2 + (3n+1)G_2)}}$$

where K_1 and G_1 are the bulk and shear moduli of one phase, K_2 and G_2 are the bulk and shear moduli of the other phase, v_1 and v_2 are the volume fractions of the two phases, (respectively), K_1^* and G_1^* are the lower bounds on the bulk and shear moduli for the composite, and K_2^* and G_2^* are the upper bounds for the bulk and shear moduli for the composite. It is assumed here that $K_2 > K_1$ and $G_2 > G_1$. If $n = 1$, Eqs. (18) are those derived by Hashin and Shtrikman (1963) for spherical included domains, while $n = 0$ corresponds to the Hashin bounds (1965) for cylindrical inclusions.

One must exercise caution in extending these bounds with the dynamic correspondence principle to encompass viscoelastic composite behavior. The correspondence principle may be applied such that bounds on effective elastic moduli convert to give bounds on transformed properties (in the frequency domain). However, bounds on the transformed properties will not necessarily convert for every instant in time to bounds on the functions inverted to the time domain (Hashin, 1983). Since viscoelastic materials are frequently characterized in terms of the dynamic properties (in the frequency domain), it is acceptable in this presentation to use the transformed bounds on the modulus functions, without attempting the conversion to the time domain.

The correspondence principle described in Section 2 was applied to Eqs. (18) for both $n = 0$ and $n = 1$ by replacing the elastic moduli with complex viscoelastic moduli. The expressions for the upper and lower bounds on the complex Young's moduli were obtained by the usual relation $\bar{E} = 9\bar{K}\,\bar{G}/(3\bar{K} + \bar{G})$. The plane-strain value of these bounds were attained through $\bar{E}_{pl-\epsilon} = \bar{E}/(1 - \bar{\nu}^2)$, where $\bar{\nu}$ is Poisson's ratio and $\bar{E}_{pl-\epsilon}$ is the plane-strain value of Young's modulus.

The numerical results for two cases of a 36 percent volume fraction of stiff material in the composite are compared to the complex Hashin-Shtrikman and the Hashin bounds in Figs. 7(*a*) and 7(*b*). From these figures one determines first that the differences between the particulate composite (Hashin-Shtrikman) and the fiber composite (Hashin) is rather small. One notes further that the lower bounds are similar in magnitude and shape to the composite modulus for the case of the soft material in the matrix, while the upper bounds are very similar to the composite modulus for the case with the stiff material in the matrix.

The case of the composite with the stiff matrix actually lies outside of the upper bound. This small discrepancy is probably a consequence of the fact that the composite is not globally isotropic, a precondition for the Hashin-Shtrikman and Hashin considerations. In fact, the magnitude of the discrepancy is on the same order of the difference between the effective moduli of a square array of inclusions and the moduli of an array of inclusions taking *x-y* axes of Fig. 1 to be rotated by 45 deg (Brinson, 1990). Another point of interest is that at high frequencies, the "switch" for the loss modulus in the two cases is reproduced faithfully by the upper and lower bounds.

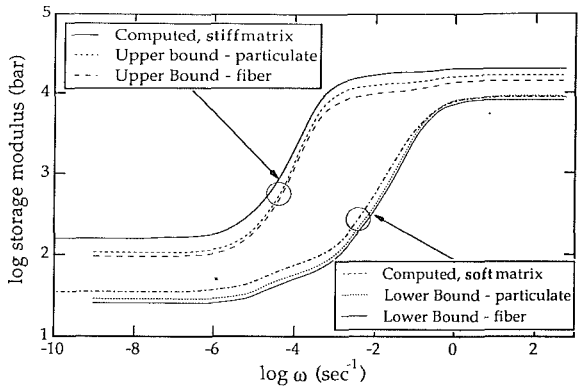


Fig. 7(*a*) Comparison of storage moduli of composite with 36 percent stiff material with Hashin-Shtrikman bounds

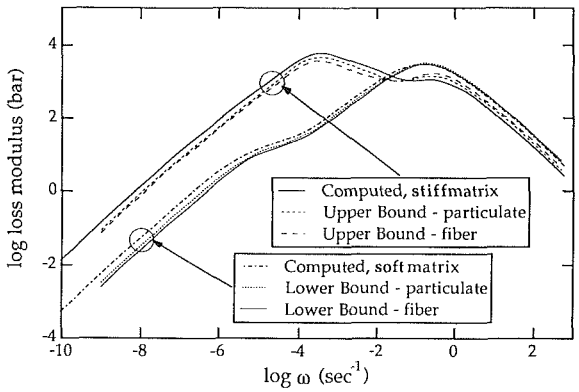


Fig. 7(*b*) Comparison of loss moduli of composite with 36 percent stiff material with Hashin-Shtrikman bounds

As a final note on this subject, Roscoe (1972) has also derived bounds for viscoelastic composites. However, these bounds do not appear to be as concise as the Hashin-Shtrikman and Hashin bounds, especially with regard to the loss modulus (Brinson and Knauss, 1990). The results are not as physically reasonable in that (for this example) the loss modulus of the soft material alone lies well outside the Roscoe bounds, implying that the soft material cannot control, or even significantly affect, energy dissipation at high frequencies.

5 Conclusion

A theoretical and numerical model for examining the properties of multiphase viscoelastic composites has been presented utilizing the dynamic correspondence principle of viscoelasticity to create an elasticity-like finite element analysis involving complex variables. With this procedure one can obtain the modulus properties of certain classes of multiphase materials from a knowledge of their microstructure and individual phase properties. In addition, the numerical method is capable of supporting any number of physical phase arrangements other than the square array of cylindrical inclusions considered here. One need only to be able to define the appropriate boundary value problem on a representative unit cell. It is this flexibility of the tool to adapt to known aspects of material structure that makes it attractive. The presentation of results in this work is limited to the plane-strain Young's modulus; the in-plane shear modulus, presented in another summary (Brinson, 1990), follows similar behavior.

The effect of different inclusion sizes and the difference in behavior between soft matrix/stiff inclusions and stiff matrix/

Downloaded 03 May 2010 to 171.66.16.247. Redistribution subject to ASME license or copyright; see http://www.asme.org/terms/Terms_Use.cfm

soft inclusions has been studied. The composite moduli are typically dominated by the matrix phase except for the loss modulus at high frequencies, for which the soft material (or the material with the larger loss modulus) controls dissipation nearly independently of volume fraction and phase orientation. Also, the composite properties are affected more by stiff inclusions in a soft matrix than by soft inclusions in a stiff matrix. Comparison with results obtained by way of the Rule of Mixtures clearly shows the inadequacy of that approach to determine multiphase viscoelastic properties reliably, except in the case of the softer matrix. The Hashin-Shtrikman and Hashin bounds agree well with the results from the numerical procedure (within the limitations placed by anisotropy): for the given composite geometry, the stiff inclusion/soft matrix case is close to the Hashin-(Shtrikman) lower bounds and the soft inclusion/stiff matrix is close to the upper bounds.

The current model is embedded in a two-dimensional finite element code; however, it is feasible to formulate this type of analysis for three-dimensional finite element procedures (spherical domains, for example). It should then also be possible to use stochastic (Montecarlo) methods to compute the properties of materials with random size and spatial distributions of inclusions.

Throughout the analysis it has been assumed that the boundary between phases is distinct and the phases are rigidly bonded together (no slipping or separation at the interface). The current numerical procedure is capable of accounting for imperfect bonding at an interface within finite element analysis, although the solution of that problem may require special consideration because the problem is likely to involve time-dependent contact. Situations involving more than two viscoelastic phases are addressed without complication (see Brinson and Knauss (1991)) and the time-temperature behavior of the composite properties are examined in detail in that same publication.

Acknowledgments

The authors would like to acknowledge support by the Office of Naval Research under grant number N00014-H4-K-0424, in particular Drs. L. Peebles and P. Schmidt for technical interaction and guidance.

References

Brinson, L. C., 1990, "Time-temperature Response of Multi-Phase Viscoelastic Solids Through Numerical Analysis," Ph.D. Thesis, California Institute of Technology.

Brinson, L. C., and Knauss, W. G., 1990, "A Note on Comparison of Variational Bounds to Numerically Predicted Properties of Multi-Phase Viscoelastic Materials," California Institute of Technology, GALCIT SM #90-4, (1990).

Brinson, L. C., and Knauss, W. G., 1991, "Thermorheologically Complex Behavior of Multi-Phase Viscoelastic Composites," *J. Mech. Phys. Solids*, Vol. 39, pp. 859-880.

Ferry, J. D., 1980, *Viscoelastic Properties of Polymers*, 3rd ed., John Wiley and Sons, New York.

Fung, Y. C., 1965, *Foundations of Solid Mechanics*, Prentice-Hall, Englewood Cliffs, NJ.

Hashin, Z., 1965, "On Elastic Behavior of Fibre Reinforced Materials of Arbitrary Transverse Phase Geometry," *J. Mech. Phys. Solids*, Vol. 13, pp. 119-134.

Hashin, Z., 1974, "Theory of Fiber Reinforced Materials," University of Pennsylvania (March 1972), NASA Contractor Report #NASA Cr-1974.

Hashin, Z., 1983, "Analysis of Composite Materials—A Survey," ASME JOURNAL OF APPLIED MECHANICS, Vol. 50, pp. 481-505.

Hashin, Z., and Shtrikman, S., 1963, "A Variational Approach to the Theory of the Elastic Behavior of Multiphase Materials," *J. Mech. Phys. Solids*, Vol. 11, pp. 127-140.

Herman, L. R., 1965, "Elasticity Equations for Incompressible and Nearly Incompressible Materials by a Variational Theorem," *AIAA*, Vol. 3:10, pp. 1896-1900.

Leaderman, H., 1943, *Elastic and Creep Properties of Filamentous Materials and Other High Polymers*, The Textile Foundation, Washington, D.C.

Lee, E. H., 1955, "Stress Analysis in Visco-Elastic Bodies," *Quart. Appl. Math.*, Vol. 13, pp. 183-190.

Nagtegaal, J. C., Parks, D. M., and Rice, J. R., 1974, "On Numerically Accurate Finite Element Solutions in the Fully Plastic Range," *Comp. Meths. Appl. Mech. Eng.*, Vol. 4, pp. 153-177.

Ponte-Castañeda, P., 1991, "The Effective Mechanical Properties of Nonlinear Isotropic Composites," *J. Mech. Phys. Solids*, Vol. 39, pp. 45-71.

Read, W. T., 1950, "Stress Analysis for Compressible Visco-Elastic Materials," *J. Appl. Phys.*, Vol. 21, pp. 671-674.

Rice, J. R., McMeeking, R. M., Parks, D. M., and Sorensen, E. P., 1979, "Recent Finite Element Studies in Plasticity and Fracture Mechanics," *Comp. Meths. Appl. Mech. Eng.*, Vol. 17/18, pp. 411-442.

Roscoe, R., 1972, "Improved Bounds for Real and Imaginary Parts of Complex Moduli of Isotropic Viscoelastic Composites," *J. Mech. Phys. Solids*, Vol. 20, pp. 91-99.

Taylor, 1982, "FEAP—Finite Element Analysis Program," University of California, Berkeley, CA.

Tobolsky, A. V., and Eyring, R., 1943, "Mechanical Properties of Polymeric Materials," *J. Chem. Phys.*, Vol. 11, pp. 125-134.

Willis, J. R., 1991, "On Methods for Bounding the Overall Properties of Nonlinear Composites," *J. Mech. Phys. Solids*, Vol. 39, pp. 73-86.

Downloaded 03 May 2010 to 171.66.16.247. Redistribution subject to ASME license or copyright; see http://www.asme.org/terms/Terms_Use.cfm

Axial Decay of Self-Equilibrating End Loads in Compressible Solids[1]

David Durban

Boris Karp

Faculty of Aerospace Engineering,
Technion—Israel Institute of Technology,
Haifa 32000 Israel

The axial diffusion rate of self-equilibrating surface loads is investigated for axially prestretched solids under plane-strain conditions. The perturbed field within the body, induced by an instantaneous end disturbance, is examined by using the eigenfunction spectral analysis. A general solution is given for a wide range of compressible materials. Particular examples are presented for a few hyperelastic solids. Very slow rate of decay, of the first antisymmetric eigencomponent, has been found near the stress-free configuration. Also, there is almost no decay of the first symmetric eigencomponent near the ultimate tension load. The diffusion length is greater for less compressible solids. Axial decay is exponential and depends quite strongly on material moduli and prestrain.

1 Introduction

Axial diffusion of self-equilibrating end loads, applied instantaneously over the edge of long and initially strained prisms, has been studied recently by Durban and Stronge (1988a, 1988b, 1988c, 1988d, 1990). The main findings reported in these papers are the very low rates of decay near the stress-free configuration and near the ultimate tension stress. There is also an appreciable constitutive sensitivity of the characteristic diffusion length as well as considerable dependence on initial stretch. These results provide an estimation of the validity of Saint-Venant's principle within the context of an instantaneous response of a finitely deformed continuum. Material behavior was assumed to be elastoplastic or hyperelastic along with the incompressibility constraint. An earlier study of this nature for incompressible hyperelastic solids has been given by Abeyaratne, Horgan, and Chung (1985). Detailed reviews on Saint Venant's principle can be found in the articles by Horgan and Knowles (1983) and Horgan (1989).

The constraint of incompressibility is relaxed in the present paper where we enhance the plane-strain analysis by Durban and Stronge (1988b, 1988c) to include material compressibility. A broad class of solids is considered by adopting Hill's (1979) general analysis for perturbed fields of initially stressed solids under plane-strain conditions.

The basic setting is that of a long rectangular prism uniformly deformed, in a plane-strain pattern, under axial tension. A self-equilibrating disturbance is then suddenly imposed over the end, thus inducing a perturbed field within the body. The instantaneous response of the material is examined, in the classical spirit of linear elasticity (Timoshenko and Goodier, 1970), by applying the eigenfunction expansion method to the field equations. The axial decay of each eigencomponent is exponential—predicting diffusion of the end effects away from the edge. Here we concentrate on the eigenfunctions with the slowest rate of decay since they provide a bound on the axial decay rate of the surface disturbance. The governing equations are solved exactly and both symmetric and antisymmetric eigenfields are considered.

Specific examples are presented for two foam rubbers, one is highly compressible and the second is nearly incompressible. The slowest decay rate for both materials is governed by antisymmetric eigenfunctions, and the rate of diffusion is higher for the more compressible material. The characteristic diffusion length increases considerably as the initial stretch becomes very small near the stress-free configuration.

A further example is given for the Blatz-Ko foam rubber. Here, the slowest decay rate is associated with an antisymmetric eigenfunction as long as the initial stretch remains below a certain value. For high prestrain levels, the slowest diffusion rate is associated with a symmetric eigenfunction. The diffusion length becomes very large near the ultimate load as well as near the unstrained state. The smallest decay rate for this material is very sensitive to initial stretch.

The paper contains also a discussion on axial decay of self-equilibrating end loads near unstable points. We show that the diffusion length increases indefinitely in the vicinity of the stress-free state for a broad class of solids characterized by instantaneously linear response. A similar result can be obtained from elementary beam theory. It is also shown that, for the same class of solids, the rate of diffusion vanishes at strains which correspond to points of ultimate axial stress.

2 Field Equations

A semi-infinite strip of a rectangular cross-section is subjected to uniform tension stress σ. The deformation pattern is

[1]This work is based on part of a thesis submitted by Boris Karp to the Technion—Israel Institute of Technology in partial fulfillment of the requirements for the degree of Master of Science.

Contributed by the Applied Mechanics Division of THE AMERICAN SOCIETY OF MECHANICAL ENGINEERS for publication in the ASME JOURNAL OF APPLIED MECHANICS.

Discussion on this paper should be addressed to the Technical Editor, Prof. Leon M. Keer, The Technological Institute, Northwestern University, Evanston, IL 60208, and will be accepted until four months after final publication of the paper itself in the ASME JOURNAL OF APPLIED MECHANICS. Manuscript received by the ASME Applied Mechanics Division, July 11, 1990; final revision, May 15, 1991. Associate Technical Editor: C. Horgan.

Copyright © 1992 by ASME
Downloaded 03 May 2010 to 171.66.16.247. Redistribution subject to ASME license or copyright; see http://www.asme.org/terms/Terms_Use.cfm

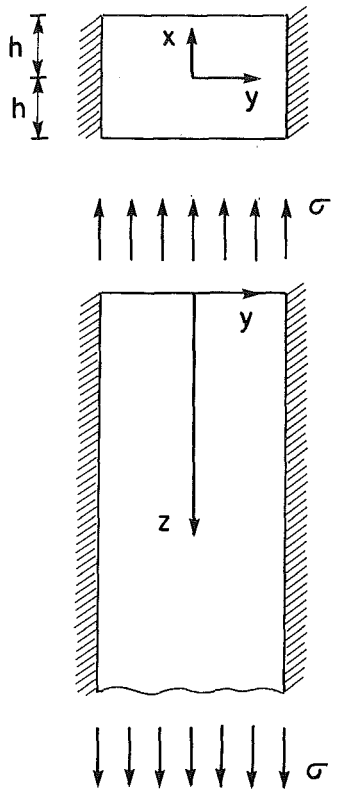


Fig. 1 Semi-infinite strip in uniform tension stress σ under plane-strain conditions. Current thickness is $2h$.

restricted by the plane-strain constraint (Fig. 1) with principal stretches (λ_x, $\lambda_y = 1$, $\lambda_z = \lambda$) and associated Cauchy stresses ($\sigma_x = 0$, σ_y, $\sigma_z = \sigma$). The current thickness is $2h = 2H\lambda_x$, where H is the original undeformed thickness.

Consider now an instantaneous self-equilibrating surface disturbance imposed over the end $z = 0$. Let (u, w) denote the velocity components within the body in the (x, z) directions, respectively. The Eulerian strain-rate tensor follows as:

$$\mathbf{D} = \epsilon_x \mathbf{ii} + \gamma_{xz}(\mathbf{ik} + \mathbf{ki}) + \epsilon_z \mathbf{kk} \tag{1}$$

where $(\mathbf{i}, \mathbf{j}, \mathbf{k})$ is an orthonormal triad associated with the spatial (x, y, z) system, and the strain-rate components are given by the usual relations

$$\epsilon_x = u_{,x} \quad \gamma_{xz} = \frac{1}{2}(u_{,z} + w_{,x}) \quad \epsilon_z = w_{,z}. \tag{2}$$

Similarly, the spin tensor is expressed by

$$\mathbf{W} = \omega_{xz}(\mathbf{ik} - \mathbf{ki}) \quad \text{with} \quad \omega_{xz} = -\frac{1}{2}(u_{,z} - w_{,x}). \tag{3}$$

The constitutive relations that govern the in-plane perturbed field within the material are (Hill, 1979)

$$\overset{\nabla}{\sigma}_x = a\epsilon_x + c\epsilon_z \tag{4a}$$

$$\overset{\nabla}{\sigma}_z = (c - \sigma)\epsilon_x + b\epsilon_z \tag{4b}$$

$$\overset{\nabla}{\tau}_{xz} = 2\mu\gamma_{xz}, \tag{4c}$$

where the instantaneous moduli (a, b, c, μ) are determined by the uniform strain history and will be specified later, and the objective Jaumann stress rate $\overset{\nabla}{\sigma}$ is related to the usual time derivative of the Cauchy stress tensor $\dot{\sigma}$ by

$$\overset{\nabla}{\sigma} = \dot{\sigma} + \mathbf{W}\cdot\sigma - \sigma\cdot\mathbf{W}. \tag{5}$$

The rate form of the equilibrium equation is

$$\nabla\cdot\left(\overset{\nabla}{\sigma} - \mathbf{D}\cdot\sigma + \sigma\cdot\mathbf{W} + \mathbf{I}\cdot\cdot\mathbf{D}\sigma\right) = \mathbf{0}, \tag{6}$$

where ∇ is the gradient operator and $\mathbf{I}$ is the second-order unit tensor. Inserting Eq. (1) and the first of (3) in (6), and observing that here

$$\sigma = \sigma_y \mathbf{jj} + \sigma \mathbf{kk}, \tag{7}$$

we get the two scalar equations

$$\overset{\nabla}{\sigma}_{x,x} + \left(\overset{\nabla}{\tau}_{xz} - \sigma\omega_{xz}\right)_{,z} = 0 \tag{8a}$$

$$\left(\overset{\nabla}{\tau}_{xz} - \sigma\gamma_{xz}\right)_{,x} + \left(\overset{\nabla}{\sigma}_z + \sigma\epsilon_x\right)_{,z} = 0. \tag{8b}$$

A further substitution of the constitutive relations (4) in (8), and use of (2) and the second of (3), results in the two differential equations (Hill, 1979)

$$a u_{,xx} + \beta u_{,zz} + (c + \alpha) w_{,xz} = 0 \tag{9a}$$

$$(c + \alpha) u_{,xz} + \alpha w_{,xx} + b w_{,zz} = 0 \tag{9b}$$

where

$$\alpha = \mu - \frac{1}{2}\sigma \quad \beta = \mu + \frac{1}{2}\sigma. \tag{10}$$

Equations (9) are supplemented by the stress-free boundary conditions at $x = \pm h$. The vectorial rate form of that boundary data reads

$$\mathbf{i}\cdot\left(\overset{\nabla}{\sigma} - \mathbf{D}\cdot\sigma + \sigma\cdot\mathbf{W} + \epsilon_x\sigma\right) = \mathbf{0} \quad \text{at} \quad x = \pm h \tag{11}$$

or, in the equivalent scalar form,

$$\overset{\nabla}{\sigma}_x = 0 \quad \overset{\nabla}{\tau}_{xz} - \sigma\gamma_{xz} = 0 \quad \text{at} \quad x = \pm h. \tag{12}$$

Conditions (12) are now expressed, with the aid of the constitutive Eqs. (4) and the kinematical relations (2), directly in terms of the velocities as

$$a u_{,x} + c w_{,z} = 0 \tag{13a}$$

$$\text{at } x = \pm h$$

$$u_{,z} + w_{,x} = 0. \tag{13b}$$

Thus, the instantaneous response of the body to the surface disturbance at $z = 0$ is described by two differential Eqs. (9) along with the boundary data (13). That homogeneous system generates a set of eigenfunctions which in turn may be used to comply with specific boundary data at $z = 0$. Here, however, we do not specify the exact details of the end disturbance except for the requirement of being self-equilibrated. Attention is focused on the eigenfunctions themselves with emphasis on the axial decay rate of the perturbed field. This eigenfunction expansion method has been used extensively in linear elasticity for investigating problems of edge loads applied to long beams, and for assessing the validity of Saint-Venant's principle (Timoshenko and Goodier, 1970; Horgan and Knowles, 1983).

3 Eigenfunction Analysis

Expecting exponential diffusion of the surface disturbance along the z-axis we seek a representative solution of (9) in the form

$$u = U(x)\exp\left(-k\frac{z}{h}\right) \quad w = W(x)\exp\left(-k\frac{z}{h}\right) \tag{14}$$

where the transverse profiles $U(x)$, $W(x)$ and the associated eigenvalue k remain to be determined. We examine solutions of the form (14) with $\mathrm{Re}\{k\} > 0$ to ensure axial decay. Of particular interest is the first eigenvalue—the one with the smallest real part—since it provides a lower bound on the axial decay rate. It is understood that only the real parts of solutions (14) are considered in this analysis.

Inserting (14) in Eqs. (9) results in the two ordinary differential equations

Downloaded 03 May 2010 to 171.66.16.247. Redistribution subject to ASME license or copyright; see http://www.asme.org/terms/Terms_Use.cfm

$$aU'' + \left(\frac{k}{h}\right)^2 \beta U - \left(\frac{k}{h}\right)(c+\alpha)W' = 0 \tag{15a}$$

$$-\left(\frac{k}{h}\right)(c+\alpha)U' + \alpha W'' + \left(\frac{k}{h}\right)^2 bW = 0 \tag{15b}$$

where the prime denotes differentiation with respect to x. The solutions of (15) are given by (A_1, A_2, A_3, A_4 are integration constants)

$$U = A_1 \sin\Gamma_1 k\frac{x}{h} + A_2 \sin\Gamma_2 k\frac{x}{h} \tag{16}$$

$$W = A_1\eta_1 \cos\Gamma_1 k\frac{x}{h} + A_2\eta_2 \cos\Gamma_2 k\frac{x}{h} \tag{17}$$

for symmetric eigenfunctions, and by

$$U = A_3 \cos\Gamma_1 k\frac{x}{h} + A_4 \cos\Gamma_2 k\frac{x}{h} \tag{18}$$

$$W = -A_3\eta_1 \sin\Gamma_1 k\frac{x}{h} - A_4\eta_2 \sin\Gamma_2 k\frac{x}{h} \tag{19}$$

for antisymmetric eigenfunction. Here,

$$\Gamma_1 = \sqrt{\frac{d - \sqrt{d^2 - 4ab\alpha\beta}}{2a\alpha}} \quad \Gamma_2 = \sqrt{\frac{d + \sqrt{d^2 - 4ab\alpha\beta}}{2a\alpha}} \tag{20}$$

where

$$d = ab + \alpha\beta - (c+\alpha)^2 \tag{21}$$

and

$$\eta_1 = \frac{a\Gamma_1^2 - \beta}{(c+\alpha)\Gamma_1} \quad \eta_2 = \frac{a\Gamma_2^2 - \beta}{(c+\alpha)\Gamma_2}. \tag{22}$$

The stress-free boundary conditions (13) can be written, with the aid of (14), in the form

$$aU' - \left(\frac{k}{h}\right)cW = 0 \tag{23a}$$

at $x = \pm h$

$$-\left(\frac{k}{h}\right)U + W' = 0. \tag{23b}$$

Substituting solutions (16)–(17) and (18)–(19) in (23) and requiring a nontrivial solution for the integration constants leads to the following transcendental equations:

$$(a\Gamma_1 - c\eta_1)(1 + \eta_2\Gamma_2)\cos\Gamma_1 k \sin\Gamma_2 k$$

(symmetric eigenfunctions)

$$-(a\Gamma_2 - c\eta_2)(1 + \eta_1\Gamma_1)\sin\Gamma_1 k \cos\Gamma_2 k = 0 \tag{24}$$

$$(a\Gamma_1 - c\eta_1)(1 + \eta_2\Gamma_2)\sin\Gamma_1 k \cos\Gamma_2 k$$

(antisymmetric eigenfunctions)

$$-(a\Gamma_2 - c\eta_2)(1 + \eta_1\Gamma_1)\cos\Gamma_1 k \sin\Gamma_2 k = 0. \tag{25}$$

Equations (24)–(25) can be solved numerically, for given stretch history and material moduli, to obtain the entire spectrum of eigenvalues k.

It remains to be proved that the eigenfunctions space contains a complete set. Nevertheless, it is conceivable that an arbitrary instantaneous surface disturbance will contain eigencomponents given by the first symmetric and antisymmetric eigenfunctions. In that sense we may argue that the eigenvalues with smallest $\mathrm{Re}\{k\}$ provide a lower bound on the axial decay rate of surface disturbances at any given initial stretch.

4 Constitutive Specifications

Eigenvalues have been calculated for hyperelastic solids with the strain energy function (Hill, 1978)

$$W = \Sigma \frac{c^{(m)}}{m}\left[\lambda_1^m + \lambda_2^m + \lambda_3^m - 3 + \frac{1}{n}(J^{-nm} - 1)\right] \tag{26}$$

where $J = \lambda_1\lambda_2\lambda_3$, λ_i ($i = 1, 2, 3$) are the principal stretches, the summation is carried over the pairs ($c^{(m)}$, m)—parameters m are not necessarily integers—and n is an additional material parameter. The specific values of the material constants used in the computations were determined experimentally by Storåkers (1986) for two vulcanized foam rubbers. The first material (I), a highly compressible natural rubber, has the parameters (constants $c^{(m)}$ have dimensions of 10^{-2} Nmm^{-2}).

$$\text{(I)} \quad m_1 = -m_2 = 4.5 \quad c^{(1)} = 1.85 \quad c^{(2)} = -9.20 \quad n = 0.92, \tag{27}$$

while for the second material (II), a nearly incompressible synthetic rubber,

$$\text{(II)} \quad m_1 = -m_2 = 3.6 \quad c^{(1)} = 2.04 \quad c^{(2)} = -0.51 \quad n = 25. \tag{28}$$

A third material model examined in this study is the Blatz-Ko (1962) solid with the single-term representation

$$\text{BK:} \quad m_1 = -2 \quad c^{(1)} = -22 \quad n = 0.5. \tag{29}$$

The principal Cauchy stresses σ_i are derived from (26) by the relations

$$J\sigma_i = \Sigma c^{(m)}(\lambda_i^m - J^{-nm}) \quad i = 1, 2, 3. \tag{30}$$

Recalling that under plane-strain conditions $\lambda_y = 1$ and $\sigma_x = 0$, we find from (30)

$$\lambda_x = \lambda^{-\frac{n}{n+1}} \tag{31}$$

$$J = \lambda^{\frac{1}{n+1}} \tag{32}$$

and the in-plane stress-stretch relations become

$$\sigma_y = \lambda^{-\frac{1}{n+1}}\Sigma c^{(m)}\left(1 - \lambda^{-\frac{nm}{n+1}}\right) \tag{33}$$

$$\sigma = \lambda^{-\frac{1}{n+1}}\Sigma c^{(m)}\left(\lambda^m - \lambda^{-\frac{nm}{n+1}}\right) \tag{34}$$

Equation (33) determines the reaction at the smooth walls which is required to maintain the plane-strain deformation pattern. The axial force-stretch path follows from (34) as

$$F = \lambda^{-1}\Sigma c^{(m)}\left(\lambda^m - \lambda^{-\frac{nm}{n+1}}\right) \tag{35}$$

where $F = \lambda_x\sigma$ is the axial force per unit of undeformed area (nominal stress). Curves evaluated from (35) are shown in Fig. 2 for the three materials (27)–(29). The axial force in this figure has been normalized with respect to the ground state shear modulus

$$2\mu_o = 2\mu(\lambda = 1) = \Sigma m c^{(m)}. \tag{36}$$

Figure 2 illustrates a striking difference, in the $F - \lambda$ curves, between materials (27)–(28) and the Blatz-Ko material. The latter has an ultimate load where the force F attains its maximum value. This happens when $dF/d\lambda = 0$ and the corresponding stretch is readily found to be

$$\lambda_u = \sqrt[3]{3} \approx 2.28. \tag{37}$$

By contrast, materials (27)–(28) do not admit an ultimate load and exhibit a monotonous load-elongation behavior.

Turning to the instantaneous moduli of the hyperelastic solids (26) and employing an available recipe derived by Hill (1979), we get

Downloaded 03 May 2010 to 171.66.16.247. Redistribution subject to ASME license or copyright; see http://www.asme.org/terms/Terms_Use.cfm

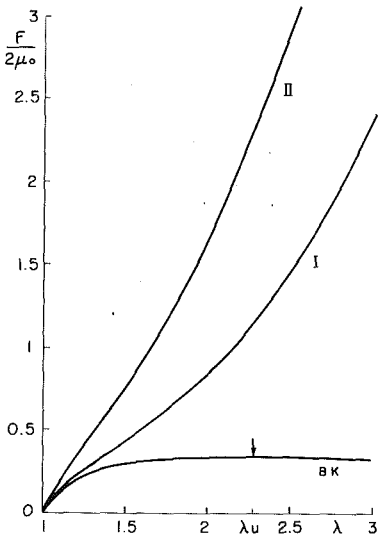


Fig. 2 Force-stretch relations in uniform tension under plane-strain conditions. I = highly compressible natural rubber, II = nearly incompressible synthetic rubber, BK = Blatz-Ko foam rubber. The ultimate load for the BK material is indicated by an arrow.

$$a=\frac{\lambda_x}{\lambda_z}\frac{\partial^2 W}{\partial\lambda_x^2}=(n+1)\Sigma mc^{(m)}\lambda^{-\frac{nm+1}{n+1}} \tag{38}$$

$$b=\frac{\lambda_z}{\lambda_x}\frac{\partial^2 W}{\partial\lambda_z^2}=\Sigma c^{(m)}\left[(m-1)\lambda^{\frac{(n+1)m-1}{n+1}}+(nm+1)\lambda^{-\frac{nm+1}{n+1}}\right] \tag{39}$$

$$c=\frac{\partial^2 W}{\partial\lambda_x\partial\lambda_z}=n\Sigma mc^{(m)}\lambda^{-\frac{nm+1}{n+1}} \tag{40}$$

$$2\mu=\frac{\lambda_x^2+\lambda_z^2}{\lambda_x^2-\lambda_z^2}(\sigma_x-\sigma_z)=\frac{\lambda^{\frac{2(2n+1)}{n+1}}+1}{\lambda^{\frac{2(2n+1)}{n+1}}-1}\sigma \quad \lambda_x\neq\lambda_z \tag{41}$$

where the tension stress σ is given by (34). As a quick check it can easily be verified that the shear modulus (41) approaches (36) as $\lambda \to 1$.

For given material constants, the instantaneous moduli depend only on the initial stretch λ. It becomes therefore possible to trace the variation of the eigenvalues k with λ by solving the transcendental Eqs. (24)–(25).

Ellipticity of the field equations has been found to hold for materials (27)–(28) over the entire stretch range considered here. For the Blatz-Ko material (29), ellipticity is maintained beyond the ultimate load level (37), but will fail when (Hill, 1979)

$$d^2=4ab\alpha\beta \tag{42}$$

with d defined in (21). The instantaneous moduli (38)–(41) for that material take the simple form

$$a=3\mu_o \quad b=3\mu_o\lambda^{-\frac{8}{3}} \quad c=\mu_o \quad 2\mu=\mu_o\left(1+\lambda^{-\frac{8}{3}}\right). \tag{43}$$

The stress-stretch relation (34) is

$$\sigma=\mu_o\left(1-\lambda^{-\frac{8}{3}}\right) \tag{44a}$$

and, from (10),

$$\alpha=\mu_o\lambda^{-\frac{8}{3}} \quad \beta=\mu_o. \tag{44b}$$

Inserting these expression in (42) we find that failure of ellipticity will occur when

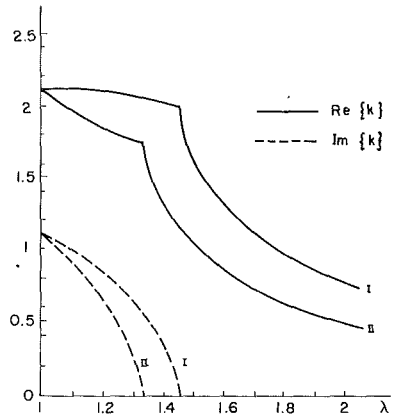


Fig. 3 First eigenvalues associated with symmetric eigenfunctions for vulcanized foam rubbers. I = highly compressible natural rubber; II = nearly incompressible synthetic rubber.

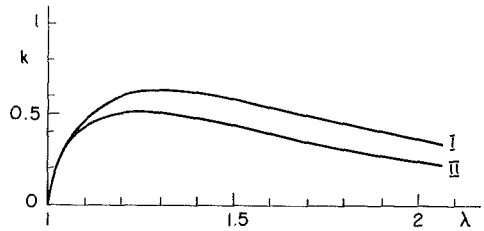


Fig. 4 First eigenvalues associated with antisymmetric eigenfunctions for vulcanized foam rubbers. I = highly compressible natural rubber, II = nearly incompressible synthetic rubber. The eigenvalues are purely real and vanish as $\lambda \to 1$.

$$\lambda=(7-4\sqrt{3})^{-\frac{3}{8}}\approx 2.685 \tag{45}$$

which is beyond the instability stretch (37). A similar result has been found by Knowles and Sterenberg (1989).

It is worth mentioning that compressibility of materials (26) is governed solely by parameter n, as is evident from (32). As n increases the material becomes less compressible, attaining the incompressibility limit when $n \to \infty$.

5 Numerical Results and Discussion

Equations (24)–(25) were solved numerically with the aid of a standard technique to obtain the first eigenvalues (those with the smallest real part). Results for the real and imaginary parts of the first eigenvalues associated with symmetric eigenfunctions for materials (27)–(28) are shown in Fig. 3. Near the stretch-free configuration ($\lambda = 1$) we recover the Papkovich-Fadle result

$$k=2.1061+i\ 1.1254. \tag{46}$$

Both real and imaginary parts of k decrease with increasing stretch. The imaginary part vanishes at a certain stretch (which corresponds to the corner on the real branch in Fig. 3) beyond which the decay rate k is a purely real number. By comparison, the decay length is shorter for the more compressible foam rubber (27).

Much lower decay rates are associated with the first antisymmetric eigenfunction. Numerical results evaluated from (25) and shown in Fig. 4 indicate a purely exponential decay with increasing decay length as $\lambda \to 1$. A straightforward asymptotic solution of (25) for small values of k gives

$$k^2\approx\frac{3a\sigma}{ab-(c-\sigma)^2}. \tag{47}$$

Downloaded 03 May 2010 to 171.66.16.247. Redistribution subject to ASME license or copyright; see http://www.asme.org/terms/Terms_Use.cfm

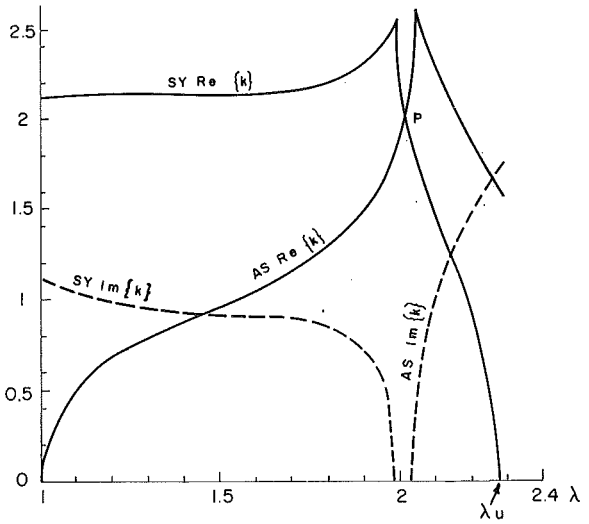


Fig. 5 First eigenvalues for the Blatz-Ko material. SY = symmetric eigenfunctions; AS = antisymmetric eigenfunctions. Very low decay rates exist near $\lambda = 1$ and $\lambda = \lambda_u$.

At low levels of stretch, with $\lambda = 1 + \Delta$ and $\Delta \ll 1$, relation (47) is further reduced to

$$k \approx \sqrt{3\Delta}, \tag{48}$$

with the aid of the small strain expansions of (34) and (38)–(40) for the entire family of solids represented by (26). This asymptotic behavior is in agreement with earlier studies on decay rates in elastoplastic and elastic materials (Durban and Stronge, 1988b, 1988c). The variation of the first eigenvalues with stretch, as displayed in Figs. 3–4, resembles the results for the incompressible Mooney-Rivlin material (Durban and Stronge, 1988c).

We may conclude that for materials (27)–(28) the slowest decay rate is associated with the first antisymmetric eigenfunction, is purely exponential, and vanishes as $\lambda \to 1$. The value of k reaches a maximum at a certain stretch (Fig. 4) and then decreases as λ increases. The rate of diffusion is higher for the more compressible solid. Further results of this kind have been obtained by Karp (1989) for other materials represented by (26).

Turning to the Blatz-Ko material (29) we find a more complicated picture (Fig. 5). The first eigenvalue associated with symmetric eigenfunctions begins at the linear elastic result (46). The real part increases with the stretch until it reaches a sharp peak, while the imaginary part decreases with λ until it vanishes at the same stretch where the real part attains its peak value. For higher levels of stretch, k is purely real and decreases sharply towards zero at the ultimate stress. This behavior is similar to the findings reported by Durban and Stronge (1988b, 1988c) for elastoplastic and elastic power-law solids. Near the necking load, where k is small, we get from (24) the asymptotic expansion

$$k^2 \approx \frac{3(ab-c^2)a\alpha}{ab\alpha\sigma - (ab-c^2)d}. \tag{49}$$

Using the asymptotic expansions of relations (43)–(44) near $\lambda = \lambda_u$, where λ_u is given by (37), we obtain from (49) in the vicinity of λ_u

$$k \approx 3\sqrt{3\left(1-\frac{\lambda}{\lambda_u}\right)}. \tag{50}$$

A lower bound on the diffusion rate for the Blatz-Ko solid is provided by the combined real branches of the first eigenvalues associated with symmetric and antisymmetric eigenfunctions. On Fig. 5 this takes a shape which starts at the origin ($\lambda = 1$), increases along the first eigenvalue of the antisymmetric solution up to the sharp point P, and then decreases, along the first eigenvalue of the symmetric solution, to zero at the necking stretch λ_u.

It is remarkable that the smallest decay rate vanishes near unstable points, namely the zero buckling load of an infinite strip and the ultimate tension stress. A similar observation has been made by Durban and Stronge (1990) for the analogous circular cylinder problem. The connection between low rates of diffusion and loss of stability is not restricted just to the hyperelastic materials (26), but remains true for the whole class of material response characterized by the instantaneous linear relations (4). Consider first a small increment along the uniform tension loading path near the stress-free state. Relations (4*a*)–(4*b*) can then be integrated to give

$$a_o\delta + c_o\Delta = 0 \tag{51a}$$

$$\sigma = c_o\delta + b_o\Delta \tag{51b}$$

where (δ, Δ) are the small strain components in the (x, z) directions, respectively, and (a_o, b_o, c_o) are the nonvanishing stress-free values of the instantaneous moduli. Thus, near $\lambda = 1$ we have

$$\sigma = \frac{a_o b_o - c_o^2}{a_o}\Delta. \tag{52}$$

Now, the asymptotic expansion (47) is reduced, in the neighborhood of $\sigma = 0$, to

$$k^2 \approx \frac{3a_o\sigma}{a_o b_o - c_o^2}. \tag{53}$$

Combining (52) with (53) we find that

$$k \approx \sqrt{3\Delta} \tag{54}$$

as $\Delta \to 0$, universally for the whole class (4) with nonvanishing values of (a_o, b_o, c_o).

Similarly, if a point of necking-type instability exists along the axial force-stretch curve, then it is given by the condition $\dot{\lambda}_x\sigma + \lambda_x\dot{\sigma} = 0$ or, put differently, by

$$\epsilon_x\sigma + \dot{\sigma} = 0. \tag{55}$$

However, in uniform tension $\dot{\sigma} \equiv \overset{\nabla}{\sigma}_z$ and $\overset{\nabla}{\sigma}_x \equiv 0$ so that, by (4*a*)–(4*b*),

$$\dot{\sigma} = \left(c - \sigma - \frac{ab}{c}\right)\epsilon_x. \tag{56}$$

Inserting (56) back in (55) gives the instability condition

$$c^2 = ab. \tag{57}$$

It follows that the first eigenvalue associated with symmetric eigenfunctions (49) vanishes at the ultimate load. Unlike (54), however, the asymptotic behavior near λ_u is constitutive dependent. For example, with a pure power-law incompressible hyperelastic solid we have near necking (Durban and Stronge, 1988c)

$$k \approx \sqrt{3n\left(1-\frac{\lambda}{\lambda_u}\right)} \quad (\lambda_u = e^{1/n}), \tag{58}$$

where $n \geq 1$ is the hardening exponent. The tension response of that material, under plane-strain conditions, is described by $\sigma = \sigma_o(\ln\lambda)^{1/n}$ where σ_o is a material parameter.

An illuminating observation that connects the universal relation (54) with elementary beam theory has been suggested to us by Professor Libai (1990). Consider a long cantilever under axial tension force F and edge moment M_o (Fig. 6). The lateral deflection is given by (Timoshenko, 1956)

$$Y = \left(\frac{M_o}{F}\right)\frac{\cosh(pL-pz)-1}{\cosh pL} \tag{59}$$

where

Downloaded 03 May 2010 to 171.66.16.247. Redistribution subject to ASME license or copyright; see http://www.asme.org/terms/Terms_Use.cfm

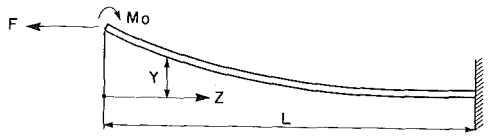


Fig. 6 Long cantilever under axial tension force F and edge moment M_o

$$p=\sqrt{\frac{F}{EI}}. \tag{60}$$

E being the elastic modulus and I is the moment of inertia. Assume now that the beam is sufficiently long so that $pL \gg 1$. Then, in the range $z \ll L$, we have from (59)

$$Y\approx\frac{M_o}{F}\exp(-pz), \tag{61}$$

and the end loads are self-equilibrating since $M_o = FY(z = 0)$. For a rectangular cross-section of thickness $2h$, we find that

$$ph=\sqrt{\frac{3F}{EA}}, \tag{62}$$

where A is the area of the cross-section. But F/EA is just the axial strain Δ and (61) becomes

$$Y\approx\frac{M_o}{F}\exp\left(-\sqrt{3\Delta}\,\frac{z}{h}\right), \tag{63}$$

implying the same decay rate as (54).

It should be noted that the plane-strain constraint has not been implemented in (63), and area changes are not accounted for. However, the remarkable fact that elementary beam theory can produce the decay rate (54) poses the challenging question whether relation (54) is inherent in the geometrical nature of a long rectangular strip under edge loads. It is hoped that future work will clarify this problem via a more refined analysis.

The surface disturbance produced by each eigenfunction (14) is described by the force rate

$$-\left(\overset{\nabla}{\tau}_{xz}-\sigma\omega_{xz}\right)\mathbf{i}-\left(\overset{\nabla}{\sigma}_z+\sigma\epsilon_x\right)\mathbf{k} \quad \text{at } z=0 \tag{64}$$

and moment rate

$$-y\left(\overset{\nabla}{\sigma}_z+\sigma\epsilon_z\right)\mathbf{i}+\left[x\left(\overset{\nabla}{\sigma}_z+\sigma\epsilon_x\right)+\sigma u\right]\mathbf{j} +y\left(\overset{\nabla}{\tau}_{xz}-\sigma\omega_{xz}\right)\mathbf{k} \quad \text{at } z=0 \tag{65}$$

both per unit area $dxdy$. Expressions (64)-(65) follow from the standard relations of a deforming continuum. As expected, the surface integral of vectors (64) and (65) vanishes for each eigenfield. This can be proved along the lines of the analysis in (Durban and Stronge, 1988b).

Of particular interest is the end moment about the y-axis, given by the $\mathbf{j}$ term in (65), for the first antisymmetric eigenfunction near the initial load-free configuration. The second part of this term, $\sigma u(z = 0)$, represents the local contribution of the axial stress due to the transverse velocity of the perturbed field. Its surface integral cancels the part contributed by the axial traction rate $x(\overset{\nabla}{\sigma}_z + \sigma\epsilon_x)_{z=0}$, but both parts remain, near $\sigma = 0$, a second-order effect not given by linear elasticity theory. It is likely that a higher-order perturbation analysis will be required for further investigation of the nature of this eigensolution near the stress-free state.

Acknowledgment

We wish to express our thanks to Professor Libai for helpful discussions during the course of this work. Part of the research was supported by Technion V.P.R. Fund—J. Gringorten Research Fund.

References

Abeyaratne, R., Horgan, C. O., and Chung, D.-T., 1985, "Saint Venant End Effects for Incremental Plane Deformations of Incompressible Nonlinearly Elastic Materials," ASME JOURNAL OF APPLIED MECHANICS, Vol. 52, pp. 847-852.

Blatz, P. J., and Ko, W. L., 1962, "Application of Finite Elastic Theory to the Deformation of Rubbery Materials," *Trans. Soc. Rheo.*, Vol. 6, pp. 223-251.

Durban, D., and Stronge, W. J., 1988a, "On the Validity of Saint-Venant's Principle in Finite Strain Plasticity," ASME JOURNAL OF APPLIED MECHANICS, Vol. 110, pp. 11-16.

Durban, D., and Stronge, W. J., 1988b, "Diffusion of Self-Equilibrating End Loads in Plane Strain Plasticity," *J. Mech. Phys. Solids*, Vol. 36, pp. 459-476.

Durban, D., and Stronge, W. J., 1988c, "Diffusion of Self-Equilibrating End Loads in Elastic Solids," ASME JOURNAL OF APPLIED MECHANICS, Vol. 110, pp. 492-495.

Durban, D., and Stronge, W. J., 1988d, "End Effects in Instantaneous Torsion of Initially Stretched Elastoplastic Cylinders," *Quart. Appl. Math.*, Vol. 46, pp. 499-504.

Durban, D., and Stronge, W. J., 1990, "Diffusion of Self-Equilibrating End Loads in a Stretched Elastoplastic Circular Cylinder," ASME JOURNAL OF APPLIED MECHANICS, Vol. 57, pp. 805-809.

Hill, R., 1978, "Aspects of Invariance in Solid Mechanics," *Adv. Appl. Mech.*, Vol. 18, pp. 1-75.

Hill, R., 1979, "On the Theory of Plane Strain in Finitely Deformed Compressible Materials," *Math. Proc. Camb. Phil. Soc.*, Vol. 86, pp. 161-178.

Horgan, C. O., and Knowles, J. K., 1983, "Recent Developments Concerning Saint-Venant's Principle," *Adv. Appl. Mech.*, Vol. 23, pp. 179-269.

Horgan, C. O., 1989, "Recent Developments Concerning Saint-Venant's Principle: An Update," *Appl. Mech. Rev.*, Vol. 42, pp. 295-303.

Karp, B., 1989, "Diffusion of End Effects in Compressible Hyperelastic Solids," M.Sc. Research Thesis, Technion, Haifa, Israel.

Knowles, T. K., and Sterenberg, E., 1975, "On the Ellipticity of the Equations of Nonlinear Elastostatics for a Special Material," *J. Elasticity*, Vol. 5, pp. 341-361.

Libai, A., 1990, private communication.

Storåkers, B., 1986, "On Material Representation and Constitutive Branching in Finite Compressible Elasticity," *J. Mech. Phys. Solids*, Vol. 34, pp. 125-145.

Timoshenko, S. P., 1956, *Strength of Materials, Part II*, Van Nostrand, Reinhold, Chapter 2.

Timoshenko, S. P., and Goodier, J. N., 1970, *Theory of Elasticity*, McGraw-Hill, New York.

Downloaded 03 May 2010 to 171.66.16.247. Redistribution subject to ASME license or copyright; see http://www.asme.org/terms/Terms_Use.cfm

Saint-Venant End Effects for Materials With Negative Poisson's Ratios

R. S. Lakes[1]
Professor,
Department of Engineering Mechanics,
University of Wisconsin,
Madison, WI 53706

In this paper we analyze Saint-Venant end effects for materials with negative Poisson's ratios. We present an example of slow decay of stress arising from self-equilibrated stress at the end of a circular cylinder of elastic material with a negative Poisson's ratio. By contrast, a sandwich panel containing rigid face sheets and a compliant core exhibits no anomalous effects for negative Poisson's ratio, but exhibits slow stress decay for core Poisson's ratio approaching 0.5. In sandwich panels with stiff but not perfectly rigid face sheets, slow decay of stress is known to occur; a negative Poisson's ratio results in end stress decay, which is faster than it would be otherwise.

1 Introduction

Recently, the invention of negative Poisson's ratio foams was reported by Lakes (1987a,b) and further developments were reported by Friis et al. (1988) and Lakes (1991). Poisson's ratios as small as -0.7 were observed in polymer foams and values to -0.8 have been observed in metal foams. It is therefore of interest to re-examine some of those three-dimensional stress distributions which depend on Poisson's ratio. In this article we consider stress fields which are relevant to Saint-Venant's principle. Saint-Venant's principle is important in the application of elasticity solutions in many situations in which boundary conditions are satisfied in the sense of resultants rather than pointwise. Research in the area of Saint-Venant's principle is reviewed by Horgan and Knowles (1983), and Horgan (1989). It is now known that self-equilibrated end stresses can decay slowly in highly anisotropic solids (Horgan, 1974, 1982, 1989; Choi and Horgan, 1977). We remark that considerations of positive definite internal energy (hence stability) restrict the range of Poisson's ratio in linear isotropic elastic solids to $-1 < \nu < 1/2$. Peculiarities are known to arise for Poisson's ratios approaching the upper limit 1/2, as in rubbery solids. In this paper we explore a case of slow stress decay in isotropic solids with negative Poisson's ratios ν, particularly for values approaching the lower limit -1.

2 The Axisymmetric End Problem for Circular Cylinders. Self-equilibrated axisymmetric shear and normal tractions acting on the end surface of a right circular isotropic elastic cylinder give rise to stresses which decay exponentially along the length of the cylinder. An exact solution for the problem of end stress upon a circular cylinder with stress-free lateral surfaces is given (Horvay and Mirabal, 1958) by the Love function (Little, 1973)

$$\mathcal{L} = e^{-\gamma z} J_0(\gamma r) + \frac{\gamma r e^{-\gamma z} J_1(\gamma r)}{2(1-\nu) + \gamma J_0(\gamma r)/J_1(\gamma r)} \tag{1}$$

in which r is a radial coordinate in units of the cylinder radius, z is a similarly normalized axial coordinate along the cylinder axis, and J_0 and J_1 are Bessel functions of order zero and one, respectively. The construction of $\mathcal{L}$ in terms of spatial derivatives of the stresses results in satisfaction of the compatibility conditions and of one equilibrium equation; the second equilibrium equation is satisfied if $\mathcal{L}$ is required to be biharmonic (Little, 1973). An exact solution which satisfies the boundary conditions is obtained if γ satisfies the eigenvalue equation

$$\frac{J_0^2(\gamma r)}{J_1^2(\gamma r)} - \frac{2(1-\nu)}{\gamma^2} + 1 = f(\gamma, \nu) = 0. \tag{2}$$

Since the shear and normal stresses associated with these eigenvalues occur together, various orthogonalization and approximation schemes have been developed to obtain solutions for prescribed tractions on the end. For the purposes of this study it suffices to consider the real part of the lowest eigenvalue γ_2 since that determines the longest decay length $L = 1/\gamma_2$. We determined the eigenvalue by using a computer to generate contour plots of the real and imaginary parts of $f(\gamma, \nu)$ versus the real and imaginary parts of γ. An approximate value of γ_2 was extracted from the intersection of the zero contours of $\mathrm{Re}(f(\gamma, \nu))$ and $\mathrm{Im}(f(\gamma, \nu))$, and a steepest descent approach was used to converge from this approximate value to γ_2. Results are shown in Figs. 1 and 2. Figure 1 also shows the next eigenvalue γ_4. The asymptotic behavior of γ_2 for $\nu \approx -1$ is $\gamma_2 \propto (1 + \nu)^{1/4}$ which is consistent with the slope of the curve in Fig. 2. Observe that as ν tends to its lower limit -1,

[1]On leave from the Department of Mechanical Engineering, Department of Biomedical Engineering, Center for Laser Science and Engineering, University of Iowa, Iowa City, IA 52242.

Contributed by the Applied Mechanics Division of THE AMERICAN SOCIETY OF MECHANICAL ENGINEERS for publication in the ASME JOURNAL OF APPLIED MECHANICS.

Discussion on this paper should be addressed to the Technical Editor, Prof. Leon M. Keer, The Technological Institute, Northwestern University, Evanston, IL 60208, and will be accepted until four months after final publication of the paper itself in the ASME JOURNAL OF APPLIED MECHANICS.

Manuscript received by the ASME Applied Mechanics Division, Jan. 16, 1991; final revision, June 3, 1991. Associate Technical Editor: C. Horgan.

Copyright © 1992 by ASME
Downloaded 03 May 2010 to 171.66.16.247. Redistribution subject to ASME license or copyright; see http://www.asme.org/terms/Terms_Use.cfm

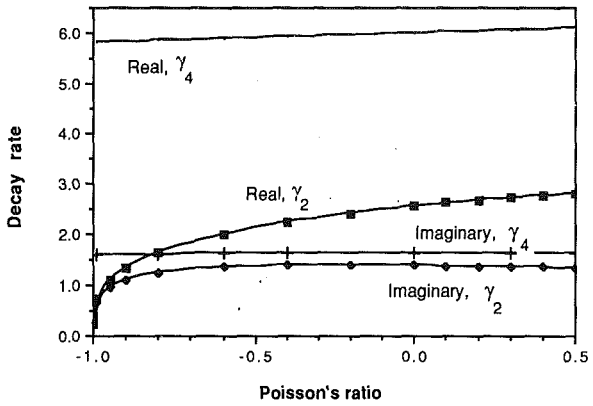


Fig. 1 Decay constant γ_2 and γ_4 versus Poisson's ratio for end stress on a circular cylinder

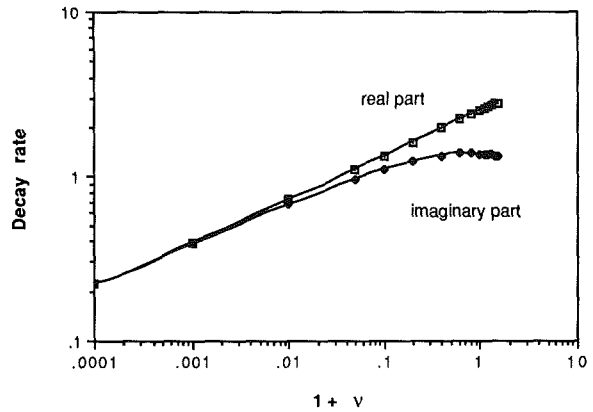


Fig. 2 Decay constant γ_2 versus $1 + \nu$ for end stress on a circular cylinder

γ_2 approaches zero; hence the decay length for the stresses goes to infinity. This result is physically reasonable since for $\nu \approx -1$, the shear modulus $G = 3B(1 - 2\nu)/2(1 + \nu)$ greatly exceeds the bulk modulus B; consequently, a volume change over a large region of the cylinder is more energetically favorable than a large shear deformation localized near the end. In contrast, γ_4 did not exhibit much dependence on Poisson's ratio as shown in Fig. 1. γ_4 corresponds to a shear stress distribution which changes sign once versus r, in contrast to γ_2 in which the stress does not change sign. The result for $\nu \approx -1$ was checked by performing a Taylor expansion approximation for the Bessel functions in Eq. (2), resulting in

$$\gamma_2 \approx (1+i)(8.7(1+\nu))^{1/4}, \tag{3}$$

which is consistent with the limiting behavior found above and shown in Fig. 2. In comparing the present results for γ_2 with those of Horvay and Mirabal (1958) we find excellent agreement (within the most significant figure quoted for the "exact" value) for $\nu = 0.3$, for which both an exact and an approximate value were presented in Horvay and Mirabal (1958), and good agreement with graphical values was presented for $\nu > 0$. However, the approximate analysis in Horvay and Mirabal (1958) gives $\mathrm{Re}(\gamma_2) = 2.2$ for $\nu = -1$, in contrast to a limiting value of zero in the present study. Moreover, inequalities based on energy considerations Knowles and Horgan (1969) yield a decay constant about a factor of two smaller than that given in Horvay and Mirabal (1958), at least for $0 \le \nu \le 0.5$. We conclude that the error in the variational approach in Horvay and Mirabal (1958) is not uniform in Poisson's ratio. The implications for other similar approximate analyses intended to cover the full range of elastic constants are obvious. Exact

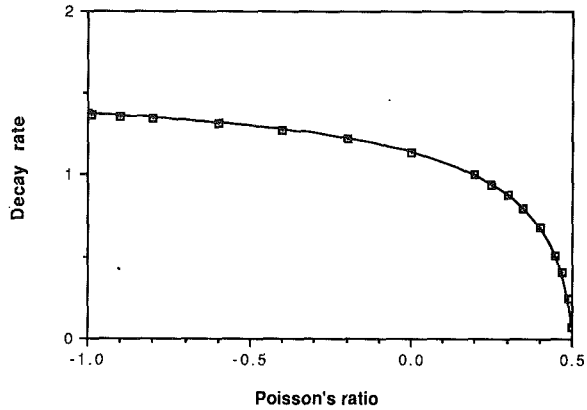


Fig. 3 Decay constant γ versus Poisson's ratio for end stress on a sandwich strip with perfectly rigid face sheets in plane strain

treatments of the cylinder end problem for prescribed end tractions have been presented in many articles. In some cases a restricted range of positive Poisson's ratio is assumed, but the main difficulty in the exact solutions is their complexity: the dependence of decay rate on Poisson's ratio is not at all obvious and can only be extracted with much labor.

2 The End Problem for a Sandwich Panel. Sandwich panels consisting of stiff face sheets bonded to a low-density core material are very useful in the aircraft industry and in other applications requiring high stiffness per unit weight. End effects in sandwich structures have been examined by Choi and Horgan (1978) and results have been displayed for $\nu \ge 0$. We consider here some of the implications of $\nu < 0$.

Limiting Case: Rigid Face Layers. The eigenvalue equation for the case of face sheets much stiffer than the core, for plane strain, is (Choi and Horgan, 1978),

$$4 - \frac{2(1+\nu)}{(1-\nu^2)}\sin(2\gamma) + 2\gamma\frac{2(1+\nu)}{(1-\nu^2)} = 0 \tag{4}$$

in which ν is the core Poisson's ratio. We compute the decay rate for the full range of Poisson's ratio and display the results in Fig. 3. In this case there is nothing unusual for $\nu \to -1$; however (Choi and Horgan, 1978), for $\nu \to 0.5$, the decay rate ν goes to zero (as $[3(1 - 2\nu)/(3 - 4\nu)]^{1/2}$), and consequently the decay length diverges. Practical sandwich panels incorporate as core anisotropic honeycombs or relatively stiff foam (with a Poisson's ratio of about 0.3). Use of a negative Poisson's ratio foam as core is possible; no dramatic effect on Saint Venant's principle is anticipated for the sandwich geometry for perfectly rigid face sheets.

Stiff Face Layers. If the face layers are much stiffer than the core, but not perfectly rigid, new roots appear for the eigenvalue equation which were not anticipated in the above case (Choi and Horgan, 1978); for $\gamma \ll 1$,

$$\gamma \approx \sqrt{\left(\frac{2(f^2-3f+3)(1-\nu_1^2)E_2}{f^3(1-f)(1+\nu_2)E_1}\right)} \tag{5}$$

in which the subscripts 1 and 2 refer to the face and core materials, respectively, and f is the volume fraction of the face material. Here, γ becomes smaller and the decay length becomes larger as the face material becomes stiffer than the core material (Choi and Horgan, 1978): $E_1 \gg E_2$. This slow stress decay can, however, be mitigated by using a negative Poisson's ratio material for the core.

3 Discussion

Slow decay of end stress with respect to distance can arise from extreme values of the Poisson's ratio as well as from the

Downloaded 03 May 2010 to 171.66.16.247. Redistribution subject to ASME license or copyright; see http://www.asme.org/terms/Terms_Use.cfm

geometry or anisotropy of the solid which had been previously known. In some situations, a negative Poisson's ratio results in slow stress decay; in other situations, more rapid stress decay can result. As for a general rule, to discriminate in these situations, we can only offer at this point the heuristic view that if a material can undergo either rapid stress decay via shear or slow stress decay via a volume change, the latter will be favored for negative Poisson's ratios approaching the lower limit.

The effect of a negative Poisson's ratio differs from the effect of anisotropy in the following ways: Anisotropy alters the rate of stress decay in a two-dimensional strip (Choi and Horgan, 1977). In contrast, in an isotropic two-dimensional strip, the Poisson's ratio has no effect on stress decay (Choi and Horgan, 1978). In an anisotropic strip $\gamma \approx \pi\sqrt{G_{LT}/E_L} \ll 1$, with L referring to the longitudinal direction and T to the transverse direction. In three dimensions, anisotropy can also give rise to slow stress decay. In the isotropic three-dimensional case, $G/E = 1/(2(1 + \nu)) > > 1$ for $\nu \to -1$; however, for the circular cylinder considered previously, $\gamma \to 0$. There is no contradiction since the anisotropic relation was based on the assumptions $E_T/E_L \ll 1$, $G_{LT}/E_L \ll 1$, $E_T/G_{LT} \approx 1$ which are certainly sensible for unidirectional fibrous composites but which do not permit passage to the isotropic limit.

As for physically realizable materials, we have achieved $\nu \approx -0.8$ in cellular solids thus far and lower values are certainly possible. As for the use of linear elasticity to describe materials with microstructure such as foams, foams can certainly be given large deformations which would require a nonlinear theory; however, for sufficiently small strain, they behave linearly as do other materials. Some foams are better described by Cosserat elasticity (Lakes, 1986) rather than classical elasticity—however, such effects depend on the cell size. Negative Poisson's ratio materials can be prepared with arbitrarily small cell size (Lakes, 1987a,b), and these materials would be classically elastic.

4 Conclusions

1 Slow decay of end stress occurs in circular cylinders of negative Poisson's ratio material.

2 In comparison, a variational determination of the decay rate had an error which was highly nonuniform in Poisson's ratio. Caution is recommended in the interpretation of such approximate analyses over a range in elastic constants.

3 The slow stress decay previously predicted for sandwich strips in plane deformation as a result of the geometry can be mitigated by use of a negative Poisson's ratio material for the core.

5 Acknowledgments

Support of this research by the NASA/Boeing ATCAS program under contract #NAS1-18889, and by a University Faculty Scholar Award to RSL, is gratefully acknowledged. Partial support by the NSF is also gratefully acknowledged. I thank W. Drugan and M. Johnson of the University of Wisconsin for their encouragement and discussions.

6 References

Choi, I., and Horgan, C. O., 1977, "Saint-Venant's Principle and End Effects in Anisotropic Elasticity," ASME JOURNAL OF APPLIED MECHANICS, Vol. 44, pp. 424–430.

Choi, I., and Horgan, C. O., 1978, "Saint-Venant End Effects for Plane Deformation of Sandwich Strips," *Int. J. Solids, Structures*, Vol. 14, pp. 187–195.

Friis, E. A., Lakes, R. S., and Park, J. B., 1988, "Negative Poisson's Ratio Polymeric and Metallic Foams," *J. Materials Sci.*, Vol. 23, pp. 4406–4414.

Horgan, C. O., 1974, "The Axisymmetric End Problem for Transversely Isotropic Circular Cylinders," *Int. J. Solids, Structures*, Vol. 10, pp. 837–852.

Horgan, C. O., 1982, "Saint-Venant End Effects in Composites," *J. Composite Materials*, Vol. 16, pp. 411–422.

Horgan, C. O., 1989, "Recent Developments Concerning Saint-Venant's Principle: An Update," *Applied Mechanics Reviews*, Vol. 42, ASME, New York, pp. 295–303.

Horgan, C. O., and Knowles, J. K., 1983, "Recent Developments Concerning Saint-Venant's Principle," *Adv. Appl. Mech.*, T. Y. Wu and J. W. Hutchinson, eds., Academic, New York, pp. 179–269.

Horvay, G., and Mirabal, J. A., 1958, "The End Problem of Cylinders," ASME JOURNAL OF APPLIED MECHANICS, Vol. 25, pp. 561–570.

Knowles, J. K., and Horgan, C. O., 1969, "On the Exponential Decay of Stresses in Circular Elastic Cylinders Subject to Self Equilibrated Loads," *Int. J. Solids Structures*, Vol. 5, pp. 33–50.

Lakes, R. S., 1986, "Experimental Microelasticity of Two Porous Solids," *International Journal of Solids and Structures*, Vol. 22, pp. 55–63.

Lakes, R. S., 1987a, "Foam Structures with a Negative Poisson's Ratio," *Science*, Vol. 235, pp. 1038–1040.

Lakes, R. S., 1987b, "Negative Poisson's Ratio Materials," *Science*, Vol. 238, p. 551.

Lakes, R. S., 1991, "Deformation Mechanisms in Negative Poisson's Ratio Materials: Structural Aspects," *J. Materials Science*, Vol. 26, pp. 2287–2292.

Little, R., 1973, *Elasticity*, Prentice-Hall, Englewood Cliffs, NJ.

Downloaded 03 May 2010 to 171.66.16.247. Redistribution subject to ASME license or copyright; see http://www.asme.org/terms/Terms_Use.cfm

Decay Rates for the Hollow Circular Cylinder

N. G. Stephen

M. Z. Wang[1]

Department of Mechanical Engineering,
The University,
Southampton, SO9 5NH, U.K.

The self-equilibrated end load problem for a hollow circular cylinder is considered using the Papkovitch-Neuber solution to the elastostatic displacement equations of equilibrium; both axi- and nonaxisymmetric solutions are derived. The requirement of zero traction on the surface generators of the cylinder leads to an eigenequation whose roots determine the rate of decay with axial coordinate. The locus of the smaller roots is plotted for circumferential harmonic loadings n = *0, 1, 2, and 3, for different wall thicknesses, and supplement previously known decay rates for the solid section and the circular cylindrical shell which are the extremes of diameter ratio. The loci are of considerable intricacy, and for small wall thickness, simple shell theory and two modes of decay for the semi-infinite plate are employed to identify the various modes of decay. Whereas for the solid cylinder the characteristic decay length of Saint-Venant's principle is the radius (or diameter), for the hollow cylinder it becomes possible to discriminate between "wall thickness" and "*$\sqrt{r_m t}$*" modes of decay according to the limiting behavior as the cylinder assumes shell-like proportions; the one exception is "membrane bending" for which self-equilibrating end loading does not decay as thickness tends to zero.*

1 Introduction

Saint-Venant's Principle (SVP) underpins much of solid mechanics by allowing the replacement of an actual load system on a structural member by a statically equivalent load distributed in a particular way demanded by the elastostatic solution; the difference between the two load distributions is termed "self-equilibrating," and since it has no stress resultant or couple which requires reaction at some other location on the structure, there seems no reason why the associated stress field should penetrate any great distance into the structure; according to SVP this depth of penetration should be small.

Southwell (1941) expressed the principle in two ways: "forces applied at one part of an elastic body will involve stresses which, except in a region close to that part, will depend almost entirely upon their resultant action, and very little upon their distribution" and "the effect of a system of forces statically equivalent to zero force and zero couple has negligible magnitude at distances which are large compared with the linear dimensions of that part."

The second statement implies a characteristic linear dimension of the body—the thickness or diameter—and the effects of self-equilibrating loads are negligible at distance several times this dimension; thus, according to Sokolnikoff (1956), "in problems of beams it is commonly assumed that the local eccentricities are not felt at distances that are about five times the greatest linear dimension of the area over which the forces are distributed."

However, there are well-known loading distributions, particularly for thin-walled structural members, where SVP does not really apply: for example, the effect of (self-equilibrating) warping restraint during torsion does not decay at all rapidly and it is necessary to introduce the *bimoment* (Vlasov, 1961), which is not a stress resultant in the conventional sense, to give a plausible engineering theory. Similarly, the effects of self-equilibrating edge loads on shell structures, as in the periodic support of a cooling tower (Flugge, 1973), decay so slowly that SVP can hardly be said to apply. Finally, it was reported by Horgan (1982) that decay rates for composite structures can be so small that the routine invocation of SVP is, in general, not justified.

To determine minimum rates of decay, researchers have taken two main directions: in one, bounds for the decay rate of strain energy, and hence stress, are determined from various energy inequalities; an overview of this approach has been provided by Horgan and Knowles (1983), and recently updated by Horgan (1989). In the second, exact solutions (within the spirit of the linear mathematical theory of elasticity) for the self-equilibrating or "end" problem are sought, in semi-inverse fashion, by assuming exponential or power-law decay.

Such solutions have been found only for a few cases where the bounding geometry is of amenable mathematical form; for example, the cylinder of solid circular section has been considered by many authors—two of the most complete analyses being provided by Klemm and Little (1970) who employed the Love displacement solution, and Robert and Keer (1988) who considered the practical effect on stiffness for a short rod "rigidly" clamped at one end. The semi-infinite (plane-strain)

[1]Visiting Professor from the Department of Mechanics, Peking University, Beijing 100871, P.R. China.

Contributed by the Applied Mechanics Division of THE AMERICAN SOCIETY OF MECHANICAL ENGINEERS for publication in the ASME JOURNAL OF APPLIED MECHANICS.

Discussion on this paper should be addressed to the Technical Editor, Prof. Leon M. Keer, The Technological Institute, Northwestern University, Evanston, IL 60208, and will be accepted until four months after final publication of the paper itself in the ASME JOURNAL OF APPLIED MECHANICS.

Manuscript received by the ASME Applied Mechanics Division, Aug. 23, 1990; final revision, June 25, 1991. Associate Technical Editor: J. G. Simmonds.

Copyright © 1992 by ASME
Downloaded 03 May 2010 to 171.66.16.247. Redistribution subject to ASME license or copyright; see http://www.asme.org/terms/Terms_Use.cfm

strip or plate (see, for example, Timoshenko and Goodier, 1970) may be solved using the Airy stress function, the solution being attributed to Papkovitch and Fadle. Both of the above admit exponential decay, whereas the (plane-strain) truncated wedge (Horvay, 1957) admits power-law decay.

A third approach, which has received comparatively little research attention but should eventually prove the most flexible for "engineering" cross-sections, is the use of finite element methods: see, for example, Dong et al. (1982), and Goetschel et al. (1985).

In the present paper, the authors follow the second approach to determine the exact decay rates for the hollow circular cylinder; displacements and thence stresses are determined from the Papkovitch-Neuber solution to the (Navier) displacement equilibrium equations and the requirement of traction-free surface generators leads to an eigenequation whose roots give the possible decay rates.

The locus of these roots is plotted for circumferential harmonic loading $n = 0$ (axisymmetric), 1, 2, and 3 (nonaxisymmetric), for different wall thicknesses. The resulting loci are of considerable complexity and in order to explain the predictions, two modes of decay for the semi-infinite plate together with shell and membrane predictions (to which the hollow cylinder can degenerate as the ratio of wall thickness to mean radius becomes small) are considered.

The two plate modes of decay are both static counterparts to known dynamic stress wave propagation solutions; we observe that the static decay of a self-equilibrating end load, when stresses vary as $\sigma_{ij} = \sigma_{ij}(x, y)e^{-kz}$, is the limiting zero frequency condition of dynamic stress wave propagation, when stresses vary as $\sigma_{ij} = \sigma_{ij}(x, y)e^{i(\gamma z - \omega t)}$ where γ is wave number and ω is circular frequency (thus the well-known Papkovitch-Fadle result for the semi-infinite plate can be derived from the Rayleigh-Lamb frequency equation for the infinite plate, by setting frequency to zero, see Miklowitz (1981)). One of these decay modes, Stephen (1992), is an extension of the plane-strain Papkovitch-Fadle solution for the semi-infinite plate to allow for harmonic edge loading, and is the static counterpart to an exact simply-supported dynamic plate theory due to Levinson (1985); the second decay mode is the static counterpart to symmetric and asymmetric SH waves, and has been previously considered by Shun Cheng (1979). The shell theory employed is due to Morley (1959).

2 Theory

2.1 Papkovitch-Neuber Solution. For the semi-infinite hollow circular cylinder (Fig. 1), we must satisfy the displacement equilibrium equation, for zero-body force,

$$\nabla^2\mathbf{u} + \nabla(\nabla\cdot\mathbf{u})/(1-2\nu) + \mathbf{F}/\mu = 0, \tag{1}$$

subject to the traction-free boundary conditions on the surface generators,

$$\sigma_r = \tau_{rz} = \tau_{r\theta} = 0 \quad \text{on} \quad r = a,\ r = b, \tag{2}$$

with stresses and displacements related by the Hooke's Law, in cylindrical coordinates, as

$$\sigma_r = \frac{E}{(1+\nu)(1-2\nu)}\left[(1-\nu)\partial u_r/\partial r + \nu(\partial u_\theta/r\partial\theta + u_r/r + \partial u_z/\partial z)\right]$$

$$\sigma_\theta = \frac{E}{(1+\nu)(1-2\nu)}\left[(1-\nu)(u_r/r + \partial u_\theta/r\partial\theta) + \nu(\partial u_r/\partial r + \partial u_z/\partial z)\right]$$

$$\sigma_z = \frac{E}{(1+\nu)(1-2\nu)}\left[(1-\nu)\partial u_z/\partial z + \nu(\partial u_r/\partial r + u_r/r + \partial u_\theta/r\partial\theta)\right]$$

$$\tau_{r\theta} = \mu[\partial u_\theta/\partial r - u_\theta/r + \partial u_r/r\partial\theta]$$

$$\tau_{rz} = \mu[\partial u_z/\partial r + \partial u_r/\partial z]$$

$$\tau_{\theta z} = \mu[\partial u_z/r\partial\theta + \partial u_\theta/\partial z], \tag{3}$$

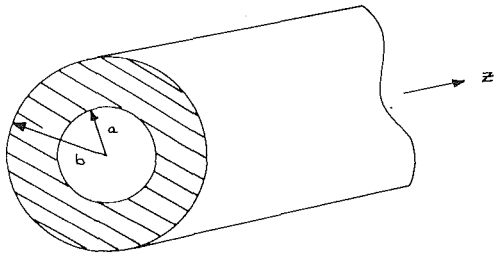


Fig. 1 Semi-infinite hollow circular cylinder

where μ and E are, respectively, the shear and Young's modulus and ν is Poisson's ratio; vector quantities are shown in boldface type.

The Papkovitch-Neuber solution to the displacement equation is

$$\mathbf{u} = \mathbf{B} - \frac{1}{4(1-\nu)}\nabla(\mathbf{r}\cdot\mathbf{B} + B_0) \tag{4}$$

where $\mathbf{r} = r\mathbf{i}_r + z\mathbf{i}_z$ is the position vector, $\mathbf{B} = B_r\mathbf{i}_r + B_\theta\mathbf{i}_\theta + B_z\mathbf{i}_z$, and B_0 is a scalar function. For zero-body force, $\nabla^2 B_0 = \nabla^2\mathbf{B} = 0$.

Although not strictly the case (see Sokolnikoff, Article 90), it is often assumed that one of the functions B_0, B_r, B_θ, or B_z may be set equal to zero without affecting the generality of the solution; now, $\mathbf{r}\cdot\mathbf{B} = rB_r + zB_z$, and by choosing $B_z = 0$, which is justifiable as the cylinder is z-convex, the displacement components reduce to

$$u_r = B_r - \partial/\partial r\{(rB_r + B_0)/4(1-\nu)\}$$

$$u_\theta = B_\theta - \partial/r\partial\theta\{(rB_r + B_0)/4(1-\nu)\}$$

$$u_z = -\partial/\partial z\{(rB_r + B_0)/4(1-\nu)\}. \tag{5}$$

In accordance with the expectation of exponential decay and the periodicity of the displacements, we write

$$(u_r, u_\theta, u_z) = (U(r), iV(r), W(r))e^{in\theta}e^{-kz}$$

$$(B_0, B_r, B_\theta) = (G_0(r), G_r(r), iG_\theta(r))e^{in\theta}e^{-kz} \tag{6}$$

where n is an integer and $i = \sqrt{-1}$, from which

$$U(r) = G_r - \frac{1}{4(1-\nu)}\frac{d}{dr}(rG_r + G_0)$$

$$V(r) = G_\theta - \frac{1}{4(1-\nu)}\frac{n}{r}(rG_r + G_0)$$

$$W(r) = \frac{k}{4(1-\nu)}(rG_r + G_0). \tag{7}$$

We now obtain general solutions for the functions G_0, G_r, G_θ.

The Laplacian $\nabla^2 = \partial^2/\partial r^2 + \partial/r\partial r + \partial^2/r^2\partial\theta^2 + \partial^2/\partial z^2$, and the requirement $\nabla^2 B_0 = 0$ gives

$$(d^2/dr^2 + d/rdr + k^2 - n^2/r^2)G_0 = 0 \tag{8}$$

whence $G_0 = C_1 J_n(kr) + C_2 Y_n(kr)$, where J_n and Y_n are the Bessel and Neumann functions of order n, and C_1 and C_2 are constants.

We next require $\nabla^2\mathbf{B} = 0$ or $(\partial^2/\partial r^2 + \partial/r\partial r + \partial^2/r^2\partial\theta^2 + \partial^2/\partial z^2)(B_r\mathbf{i}_r + B_\theta\mathbf{i}_\theta) = 0$, and noting the results $\partial\mathbf{i}_r/\partial\theta = \mathbf{i}_\theta$, $\partial^2\mathbf{i}_r/\partial\theta^2 = -\mathbf{i}_n$, $\partial\mathbf{i}_\theta/\partial\theta = -\mathbf{i}_r$, $\partial^2\mathbf{i}_\theta/\partial\theta^2 = -\mathbf{i}_\theta$, we find

$$\nabla^2\mathbf{B} = (\partial^2 B_r/\partial r^2 + \partial B_r/r\partial r + \partial^2 B_r/r^2\partial\theta^2 + \partial^2 B_r/\partial z^2 - B_r/r^2 - 2\partial B_\theta/r^2\partial\theta)\mathbf{i}_r + (\partial^2 B_\theta/\partial r^2 + \partial B_\theta/r\partial r + \partial^2 B_\theta/r^2\partial\theta^2 + \partial^2 B_\theta/\partial z^2 - B_\theta/r^2 + 2\partial B_r/r^2\partial\theta)\mathbf{i}_\theta = 0. \tag{9}$$

Taking the two components separately and noting

$$(B_r, B_\theta) = (G_r(r), iG_\theta(r))e^{in\theta}e^{-kz}$$

gives

$$(d^2/dr^2 + d/rdr + k^2 - (n^2+1)/r^2)G_r + 2nG_\theta/r^2 = 0$$

and

Downloaded 03 May 2010 to 171.66.16.247. Redistribution subject to ASME license or copyright; see http://www.asme.org/terms/Terms_Use.cfm

$$(d^2/dr^2 + d/rdr + k^2 - (n^2+1)/r^2)G_\theta + 2nG_r/r^2 = 0 \quad (10)$$

whence

$$G_r = C_3J_{n+1}(kr) + C_4J_{n-1}(kr) + C_5Y_{n+1}(kr) + C_6Y_{n-1}(kr)$$
$$G_\theta = -C_3J_{n+1}(kr) + C_4J_{n-1}(kr) - C_5Y_{n+1}(kr) + C_6Y_{n-1}(kr) \quad (11)$$

where $C_{3,4,5,6}$ are constants.

Note that for the axisymmetric case, $n = 0$, Eqs. (10) have solutions

$$G_r = C_3J_1(kr) + C_5Y_1(kr)$$
$$G_\theta = C_4J_1(kr) + C_6Y_1(kr). \quad (12)$$

2.2 Displacement and Stress Components. The displacement components may now be written as

$$u_r = \Big[C_3J_{n+1} + C_4J_{n-1} + C_5Y_{n+1} + C_6Y_{n-1} - \frac{1}{4(1-\nu)}\frac{d}{dr}(C_3rJ_{n+1} + C_4rJ_{n-1} + C_1J_n + C_5rY_{n+1} + C_6rY_{n-1} + C_2Y_n)\Big]e^{in\theta}e^{-kz}$$

$$u_\theta = i\Big[-C_3J_{n+1} + C_4J_{n-1} - C_5Y_{n+1} + C_6Y_{n-1} - \frac{n}{4(1-\nu)r}(C_3rJ_{n+1} + C_4rJ_{n-1} + C_1J_n + C_5rY_{n+1} + C_6rY_{n-1} + C_2Y_n)\Big]e^{in\theta}e^{-kz}$$

$$u_z = \frac{k}{4(1-\nu)}(C_3rJ_{n+1} + C_4rJ_{n-1} + C_1J_n + C_5rY_{n+1} + C_6rY_{n-1} + C_2Y_n]e^{in\theta}e^{-kz},$$

where the Bessel and Neumann function argument (kr) has been omitted for brevity.

The six stress components are

$$\tau_{rz} = \mu k[C_1\{kJ_{n-1} - nJ_n/r\} + C_3\{krJ_n - (n+2-2\nu)J_{n+1}\} + C_4\{(n-2+2\nu)J_{n-1} - krJ_n\} + C_2\{kY_{n-1} - nY_n/r\} + C_5\{krY_n - (n+2-2\nu)Y_{n+1}\} + C_6\{(n-2+2\nu)Y_{n-1} - krY_n\}]e^{in\theta}e^{-kz}/(2-2\nu),$$

$$\tau_{r\theta} = i\mu[C_1\{-nkJ_{n-1}/r + n(n+1)J_n/r^2\} + C_3\{(n+1)(4-4\nu+n)J_{n+1}/r - (2-2\nu+n)kJ_n\} + C_4\{(n-1)(4-4\nu-n)J_{n-1}/r - (2-2\nu-n)kJ_n\} + C_2\{n(n+1)Y_n/r^2 - nkY_{n-1}/r\} + C_5\{(n+1)(4-4\nu+n)Y_{n+1}/r - (2-2\nu+n)kY_n\} + C_6\{(n-1)(4-4\nu-n)Y_{n-1}/r - (2-2\nu-n)kY_n] \times e^{in\theta}e^{-kz}/(2-2\nu),$$

$$\tau_{\theta z} = i\mu k[C_1nJ_n/r + C_3(2-2\nu+n)J_{n+1} + C_4(-2+2\nu+n)J_{n-1} + C_2nY_n/r + C_5(2-2\nu+n)Y_{n+1} + C_6(-2+2\nu+n)Y_{n-1}]e^{in\theta}e^{-kz}/(2-2\nu),$$

$$\sigma_r = E[C_1\{(k^2r^2 - n(n+1))J_n/r^2 + kJ_{n-1}/r\} + C_3\{(3-2\nu)kJ_n + (k^2r^2 - (n+1)^2 - (3-4\nu)(n+1))J_{n+1}/r\} + C_4\{(k^2r^2 - (n-1)^2 + (3-4\nu)(n-1))J_{n-1}/r - (3-2\nu)kJ_n\} + C_2\{(k^2r^2 - n(n+1))Y_n/r^2 + kY_{n-1}/r\} + C_5\{(3-2\nu)kY_n + (k^2r^2 - (n+1)^2 - (3-4\nu)(n+1))Y_{n+1}/r\} + C_6\{(k^2r^2 - (n-1)^2 + (3-4\nu)(n-1))Y_{n-1}/r - (3-2\nu)kY_n\}]e^{in\theta}e^{-kz}/(4-4\nu^2),$$

$$\sigma_\theta = E[C_1\{kJ_{n+1}/r + n(n-1)J_n/r^2\} + C_3\{-k(1-2\nu)J_n + (n(n+1) + 4(1-\nu)(n+1))J_{n+1}/r\} + C_4\{k(1-2\nu)J_n + (n(n-1) - 4(1-\nu)(n-1))J_{n-1}/r\} + C_2\{kY_{n+1}/r + n(n-1)Y_n/r^2\} + C_5\{-k(1-2\nu)Y_n + (n(n+1) + 4(1-\nu)(n+1))Y_{n+1}/r\} + C_6\{k(1-2\nu)Y_n + (n(n-1) - 4(1-\nu)(n-1))Y_{n-1}/r\}]e^{in\theta}e^{-kz}/(4-4\nu^2),$$

$$\sigma_z = Ek[-C_1kJ_n + C_3\{2\nu J_n - krJ_{n+1}\} - C_4\{2\nu J_n + krJ_{n-1}\} - C_2kY_n + C_5\{2\nu Y_n - krY_{n+1}\} - C_6\{2\nu Y_n + krY_{n-1}\}]e^{in\theta}e^{-kz}/(4-4\nu^2). \quad (13)$$

The requirement of zero traction on the surface generators $r = a$, $r = b$ leads to the matrix equation

$$[A_{ij}][C_1\ C_3\ C_4\ C_2\ C_5\ C_6]^T = 0 \quad (14)$$

where

$$A_{11} = kJ_{n-1}(kb) - \frac{nJ_n}{b}(kb),$$
$$A_{12} = kbJ_n(kb) - (2-2\nu+n)J_{n+1}(kb),$$
$$A_{13} = -kbJ_n(kb) + (n-2+2\nu)J_{n-1}(kb),$$
$$A_{21} = n(n+1)\frac{J_n}{b^2}(kb) - \frac{nkJ_{n-1}}{b}(kb),$$
$$A_{22} = (n+1)(4-4\nu+n)\frac{J_{n+1}}{b}(kb) - (2-2\nu+n)kJ_n(kb),$$
$$A_{23} = (n-1)(4-4\nu-n)\frac{J_{n-1}}{b}(kb) - (2-2\nu-n)kJ_n(kb),$$
$$A_{31} = (k^2b^2 - n^2 - n)\frac{J_n}{b^2}(kb) + \frac{kJ_{n-1}}{b}(kb),$$
$$A_{32} = (3-2\nu)kJ_n(kb) + (k^2b^2 - (n+1)^2 - (3-4\nu)(n+1))\frac{J_{n+1}}{b}(kb),$$
$$A_{33} = -(3-2\nu)kJ_n(kb) + (k^2b^2 - (n-1)^2 - (3-4\nu)(n-1))\frac{J_{n-1}}{b}(kb). \quad (15)$$

The remaining elements of the matrix $[A_{ij}]$ are of the same form as the foregoing equations but with either the Bessel function replaced by the corresponding Neumann function, and/or the external radius b replaced with the internal radius a throughout, and may be written as

$$[A_{ij}] = \left[\begin{array}{ccc|c} A_{11} & A_{12} & A_{13} & \text{Neumann Function,} \\ A_{21} & A_{22} & A_{23} & \text{external radius } b \\ A_{31} & A_{32} & A_{33} & \\ \hline \multicolumn{3}{c|}{\text{Bessel Function,}} & \text{Neumann Function,} \\ \multicolumn{3}{c|}{\text{internal radius } a} & \text{internal radius } a \end{array}\right]$$

and a zero value of the determinant A_{ij} is required.

For the axisymmetric case, $n = 0$, the determinant factors as

Downloaded 03 May 2010 to 171.66.16.247. Redistribution subject to ASME license or copyright; see http://www.asme.org/terms/Terms_Use.cfm

$$\begin{vmatrix} J_2(kb) & Y_2(kb) \\ J_2(ka) & Y_2(ka) \end{vmatrix}$$

$$\times \left| \begin{array}{cc|c} A_{11} & A_{12} & \text{Neumann Function,} \\ A_{21} & A_{22} & \text{external radius } b \\ \hline \multicolumn{2}{c|}{\text{Bessel Function,}} & \text{Neumann Function,} \\ \multicolumn{2}{c|}{\text{internal radius } a} & \text{internal radius } a \end{array} \right|$$

where now

$$A_{11} = J_0(kb) - \frac{J_1}{kb}(kb),$$

$$A_{12} = (3-2\nu)J_0(kb) + (k^2b^2 - 4(1-\nu))\frac{J_1}{kb}(kb),$$

$$A_{21} = -J_1(kb),$$

$$A_{22} = kbJ_0(kb) - 2(1-\nu)J_1(kb), \tag{16}$$

and again, the remaining elements are of the same form but with Neumann functions replacing the corresponding Bessel function and/or internal radius replacing external radius.

A zero value of the first (2×2) determinant gives the decay rates for the axisymmetric "torsional" displacements, which are independent of Poisson's ratio, and the second (4×4) gives the decay rates for the "torsionless" axisymmetric case; factorization indicates that the decay modes are uncoupled.

The displacement components degenerate to

$$u_r = \left[(C_3 - C_4)J_1 + (C_5 - C_6)Y_1 - \frac{1}{4(1-\nu)}\frac{d}{dr}\left((C_3 - C_4)rJ_1 + C_1J_0 + (C_5 - C_6)rY_1 + C_2Y_0\right)\right] e^{-kz}$$

$$u_\theta = -i[(C_3 + C_4)J_1 + (C_5 + C_6)Y_1]e^{-kz}$$

$$u_z = \frac{k}{4(1-\nu)}[(C_3 - C_4)rJ_1 + C_1J_0 + (C_5 - C_6)rY_1 + C_2Y_0]e^{-kz}. \tag{17}$$

For the solid circular section the Neumann functions are omitted when the present determinants reduce to the eigenequations derived by Klemm and Little (1970).

Values of decay rate with respect to external radius, i.e., kb, to give a zero value of the determinants for Poisson's ratio $\nu = 0.25$ have been determined using a secant algorithm written in MATLAB software and run on a PC computer. Each evaluated root was used as the starting point for the incremented (a/b) value, with some manual searching necessary close to the "bifurcation" points.

3 Discussion of Results

First we note that for the solid circular cross-section $(a/b = 0)$, the calculated decay rates agree with those found by Klemm and Little. The minimum decay, $e^{-2.1044z/b}$, occurs for the nonaxisymmetric distribution $n = 2$ (similar to the bimoment) when stress level will decay to less than 1.5 percent of its initial value at a penetration $z = 2b$, i.e., at one diameter; the characteristic dimension of SVP for the solid cylinder is clearly the diameter or radius.

Next we consider the new results for the hollow cylinder; for the axisymmetric case, $n = 0$, torsional and torsionless displacements are uncoupled and may be considered separately. For the torsional case, Fig. 2, there are only real roots which increase as (a/b) increases, implying a more rapid axial decay. As indicated, the root loci are bounded from below by the plate shear decay rates (static counterparts to SH waves, see Shun Cheng, 1979), i.e., $kt = m\pi$ or $kb = m\pi/(1 - a/b)$ where $t = b - a$, is the wall or plate thickness, $m = 1$, 2, 3, etc. For such a loading, as sketched in Fig. 7(*a*), the characteristic dimension is now the wall thickness; such a distinction is not possible with the solid cylinder as the radius and "wall thickness" are obviously identical.

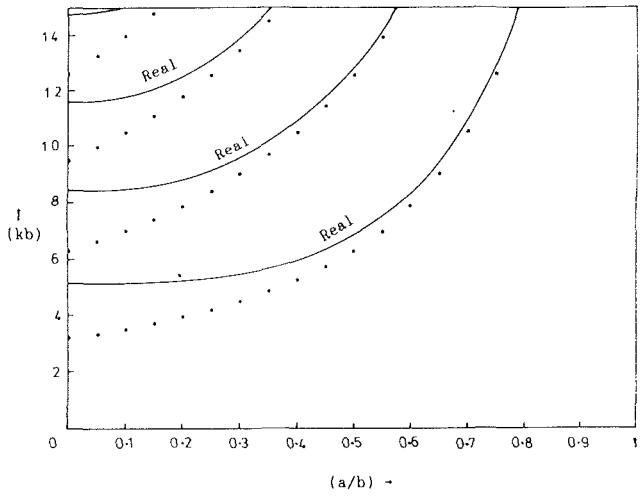


Fig. 2 Real decay roots (kb) for axisymmetric, $n = 0$, torsional displacements; . denotes the decay rate, $kt = m\pi$, for plate shear decay

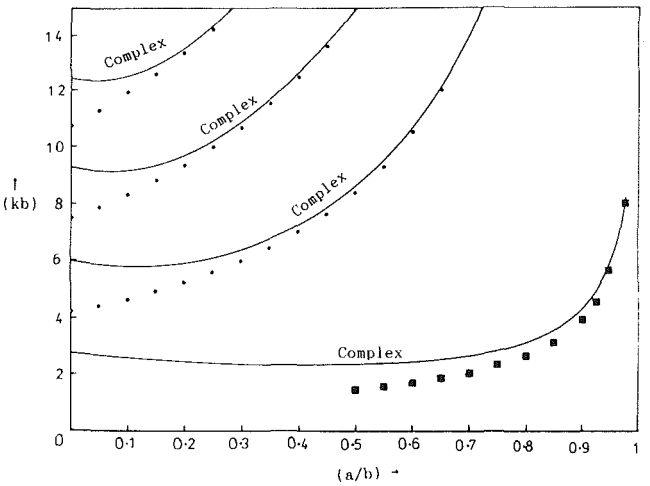


Fig. 3 Complex decay roots (kb) for axisymmetric, $n = 0$, torsionless displacements; . denotes the decay rates from the Papkovitch-Fadle plane-strain results for the plate. ■ denotes the Morley shell theory prediction. Poisson's ratio $\nu = 0.25$. Only real parts of the root are shown.

For the torsionless axisymmetric case there are only complex roots, of which only the real parts are plotted in Fig. 3; with the exception of the lowest root locus, as a/b increases from zero, the loci show an initial decrease followed by a substantial rise. Again, these root loci are bounded from below by a known decay rate for the semi-infinite plate, now the plane-strain Papkovitch-Fadle result, determined by the eigenequation $\sin 2kc \pm 2kc = 0$, where c is plate semi-thickness; the smallest decay is given by $e^{-2.1062z/c}$ or $e^{-4.2124z/t}$ where $t = b - a$ is plate thickness, which corresponds to $kb = 4.2124/(1 - a/b)$. Again, for these decay modes, the characteristic dimension is the wall thickness, and they are associated with loadings as sketched in Fig. 7(*b*).

For the smallest decay mode locus in Fig. 3 the decay rates again show a small decrease as a/b increases from zero, but then remain essentially constant before increasing rapidly in value as the cylinder assumes "shell-like" proportions. For large a/b, the locus is bounded from below by the decay prediction from closed cylinder shell theory; here comparison is made with the simplest "accurate" theory due to Morley (1959)

Downloaded 03 May 2010 to 171.66.16.247. Redistribution subject to ASME license or copyright; see http://www.asme.org/terms/Terms_Use.cfm

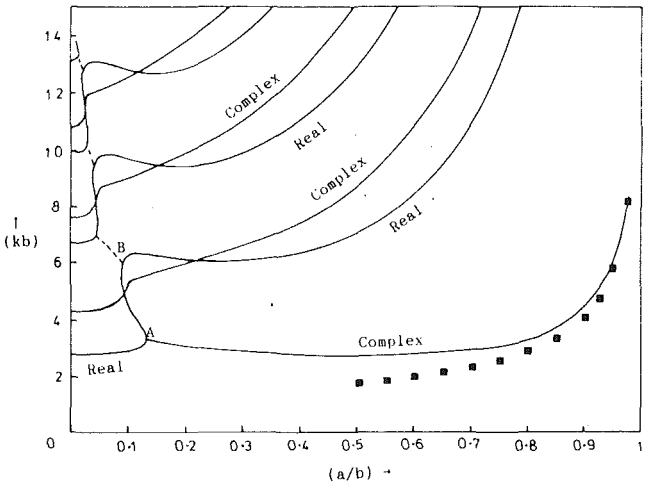


Fig. 4 Real and complex decay roots (kb) for nonaxisymmetric, $n = 1$, displacements; ■ denotes the Morley shell theory prediction. - - - - denotes additional complex branches joining real branches at the turning points. Poisson's ratio $\nu = 0.25$. Only real parts of the root are shown.

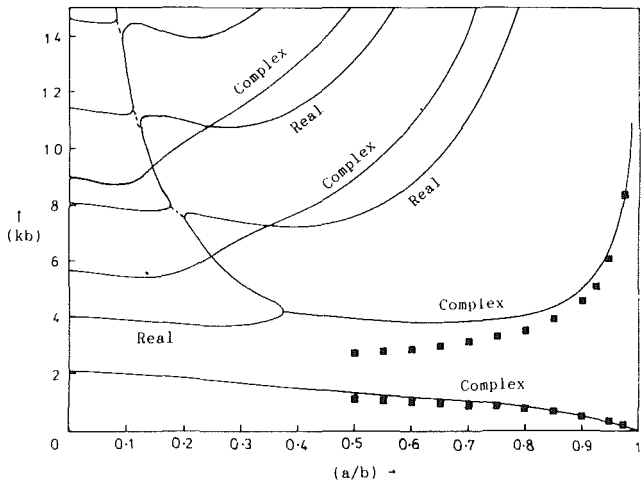


Fig. 5 Real and complex decay rates (kb) for nonaxisymmetric, $n = 2$, displacements: ■ denotes the Morley shell theory prediction. - - - - denotes additional complex branches joining real branches at the turning points. Poisson's ratio $\nu = 0.25$. Only real parts of the root are shown.

(see the Appendix) which has just one mode of decay for $n = 0$. A knowledge of that theory suggests possible loadings as sketched in Fig. 7(c); as was first shown by Simmonds (1977), the characteristic decay length is now the geometric mean of the mean radius and the wall thickness, i.e., $\sqrt{r_m t}$, where $r_m = (a + b)/2$ is the mean radius and t is the wall thickness.

For the nonaxisymmetric cases, $n \neq 0$, there exists coupling between torsional (circumferential) and torsionless (radial and axial) displacements which results in an intriguing interaction of real and complex root loci particularly for the smaller range of a/b values, although the coupling range increases with the circumferential harmonic number n. For $n = 1$, Fig. 4, this root interaction is restricted to $a/b < 0.13$, beyond which the decay modes can be clearly designated as "wall thickness" or "$\sqrt{r_m t}$" effects; here the real roots are again asymptotic to $kt = m\pi$, while the complex "thickness" roots are, for given a/b, slightly larger than the corresponding value for $n = 0$. This increase is as expected from the corresponding plate problem (see Stephen, 1992)—the extension to the Papkovitch-Fadle result for harmonic edge loading—which is, remarkably, still governed by the eigenequation $\sin 2\Lambda c \pm 2\Lambda c = 0$, which again has the smallest root $\Lambda c = 2.1062 + 1.1254i$ but where the decay rate is now given by $k = (\Lambda^2 + (\pi/\lambda)^2)^{1/2}$ where λ is harmonic loading semi-wavelength. This lower bounding by the corresponding plate problem is also evident for $n = 2$ and $n = 3$, Figs. 5 and 6, respectively, where mode coupling occurs at much larger a/b.

Returning to Fig. 4, we note the peculiar "terraced" behavior of the real root loci, and the issuance and termination of complex root branches from the real root locus "turning points;" thus the smallest real locus has a complex root issuing at point A and the termination of a second complex branch at point B. Additionally, the complex root loci show a perturbation in the region of these real root "turning points." The reason for this behavior, which occurs also for the higher roots and higher harmonic loading (n), is not yet clear to the authors and further work in this area is required.

The smallest complex locus, having issued from the real root at point A, remains essentially constant before increasing rapidly as the cylinder assumes "shell-like" proportions; again, the real part is lower bounded by the Morley shell edge effect prediction, and the characteristic decay length of SVP is $\sqrt{r_m t}$. Self-equilibrated loading with $n = 1$ might be as sketched in Fig. 7(d).

For the cases $n = 0$, $n = 1$ consider thus far, there is no

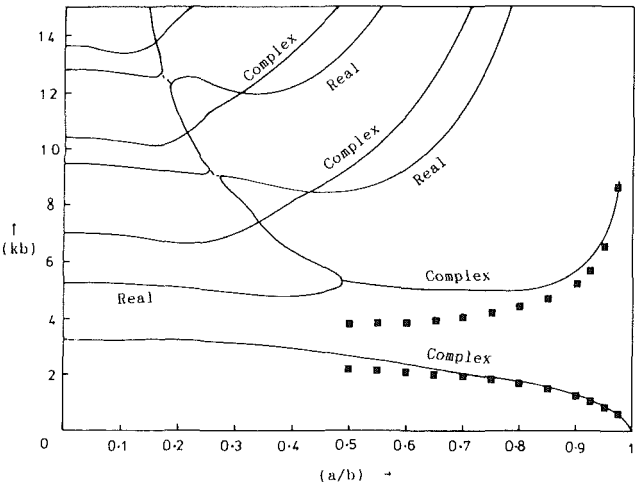


Fig. 6 Real and complex decay rates (kb) for nonaxisymmetric, $n = 3$, displacements; ■ denotes the Morley shell theory prediction. - - - - denotes additional complex branches joining real branches at the turning points. Poisson's ratio $\nu = 0.25$. Only real parts of the root are shown.

doubt as to the validity of Saint-Venant's principle; rather the only question concerns the characteristic cross-sectional dimension.

However, for the higher harmonic displacements, $n = 2, 3$, Figs. 5 and 6, respectively, while the essential features of $n = 1$ are retained, the addition of a new, uncoupled, complex root provides a much slower decay rate which tends to zero as a/b approaches unity. In the context of shell theory, such nondecaying solutions for self-equilibrating edge loading correspond to *membrane-bending*, which is obtained by setting bending stiffness and stretching compliance to zero.

The loading associated with this decay mode, for $n = 2$, is sketched in Fig. 7(e), and the term *bimoment* is often used—more often in the context of restrained warping of thin-walled prismatic structures under torsion. Interestingly, theories on restrained warping (see, for example, Reissner, 1952), while not exact within the spirit of the linear theory of elasticity, are normally based upon a relaxation of the displacement assumptions of Saint-Venant torsion (where warping is not restrained), with axial direct stress σ_z distributed over the cross-section according to the axial warping (torsion) function; such

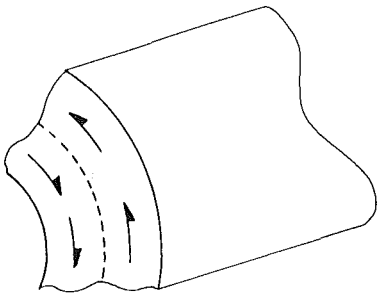
Downloaded 03 May 2010 to 171.66.16.247. Redistribution subject to ASME license or copyright; see http://www.asme.org/terms/Terms_Use.cfm

a distribution is, of course, self-equilibrating. Again shell theory decay predictions for the simple Morley theory are shown.

Figure 6 shows decay rates for $n = 3$; for the lowest decay mode—when decay is faster than the corresponding mode for $n = 2$—loading would be as sketched in Fig. 7(*f*) and the term *trimoment* or *multi-moment* might be applied. Again, the Morley shell theory decay predictions provide good agreement for large a/b when the cylinder is of shell-like proportions.

Acknowledgments

The second author gratefully acknowledges financial support from the Royal Society Sino-British Fellowship Trust



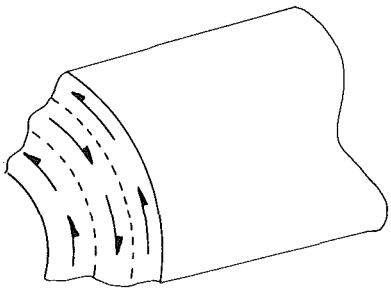
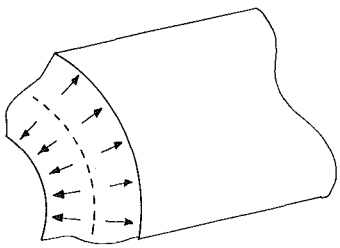


Fig. 7(*a*) Self-equilibrating axisymmetric, $n = 0$, torsional end loading; characteristic decay length is wall thickness



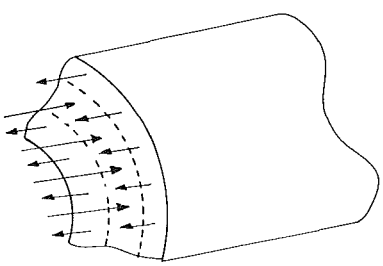
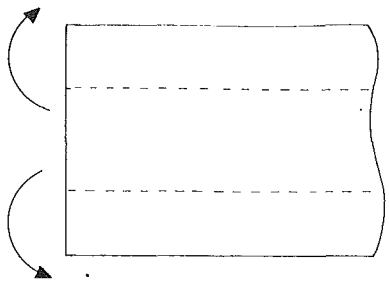


Fig. 7(*b*) Self-equilibrating axisymmetric, $n = 0$, torsionless end loading; decay length is wall thickness



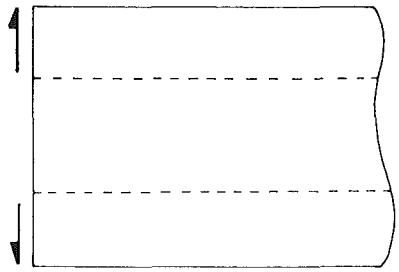


Fig. 7(*c*) Self-equilibrating axisymmetric, $n = 0$, torsionless end loading; decay length is $\sqrt{r_m t}$

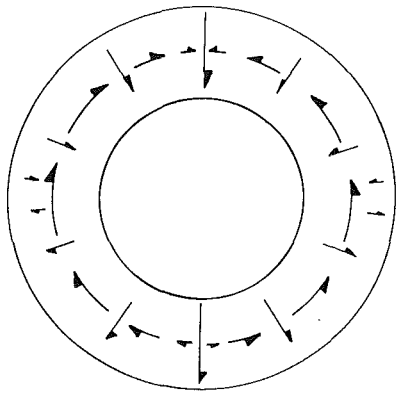


Fig. 7(*d*) Self-equilibrating nonaxisymmetric, $n = 1$, end loading; decay length is $\sqrt{r_m t}$

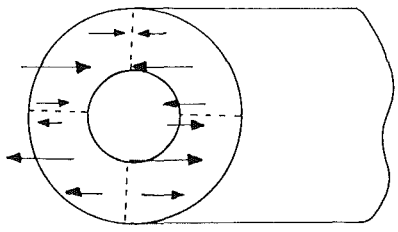


Fig. 7(*e*) Self-equilibrating nonaxisymmetric, $n = 2$, end loading

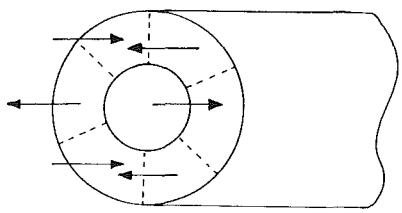


Fig. 7(*f*) Self-equilibrating nonaxisymmetric, $n = 3$, end loading

Downloaded 03 May 2010 to 171.66.16.247. Redistribution subject to ASME license or copyright; see http://www.asme.org/terms/Terms_Use.cfm

Award. Both authors are grateful to the referees for their helpful remarks regarding shell theories.

References

Dong, S. B., and Goetschel, D. B., 1982, "Edge Effects in Laminated Composite Plates," ASME JOURNAL OF APPLIED MECHANICS, Vol. 49, pp. 129–135.

Flugge, W., 1973, *Stresses in Shells*, 2nd ed., Springer-Verlag, Berlin, Section 5.3.

Goetschel, D. B., and Hu, T. H., 1985, "Quantification of Saint-Venant's Principle for a General Prismatic Member," *Computers and Structures*, Vol. 21, pp. 869–874.

Horgan, C. O., 1982, "Saint-Venant End Effects in Composites," *Journal of Composite Materials*, Vol. 16, pp. 411–422.

Horgan, C. O., and Knowles, J. K., 1983, "Recent Developments Concerning Saint-Venant's Principle," *Advances in Applied Mechanics*, Vol. 23, J. W. Hutchinson, ed., Academic Press, New York, pp. 179–269.

Horgan, C. O., 1989, "Recent Developments Concerning Saint-Venant's Principle: An Update," *Applied Mechanics Review*, Vol. 42, No. 11, pp. 295–303.

Horvay, G., 1957, "Saint-Venant's Principle: A Biharmonic Eigenvalue Problem," ASME JOURNAL OF APPLIED MECHANICS, Vol. 24, pp. 381–386.

Klemm, J. L., and Little, R. W., 1970, "The Semi-Infinite Elastic Cylinder Under Self-Equilibrated End Loading," *SIAM Journal of Applied Mechanics*, Vol. 19, pp. 712–729.

Levinson, M., 1985, "Free-Vibration of a Simply-Supported Rectangular Plate: An Exact Elasticity Solution," *Journal of Sound and Vibration*, Vol. 98, pp. 289–298.

Miklowitz, J., 1981, *The Theory of Elastic Waves and Wave Guides*, North Holland, Amsterdam.

Morley, L. S. D., 1959, "An Improvement on Donnell's Approximation for Thin-Walled Circular Cylinders," *Q. J. Mech. Appl. Math.*, Vol. 12, pp. 89–99.

Reissner, E., 1952, "On Non-Uniform Torsion of Cylindrical Rods," *Journal of Mathematics and Physics*, Vol. 31, pp. 214–221.

Robert, M., and Keer, L. M., 1988, "Stiffness of an Elastic Circular Cylinder of Finite Length," ASME JOURNAL OF APPLIED MECHANICS, Vol. 55, pp. 560–565.

Shun Cheng, 1979, "Elasticity Theory of Plates and a Refined Theory," ASME JOURNAL OF APPLIED MECHANICS, Vol. 46, pp. 644–650.

Simmonds, J. G., 1977, "Saint-Venant's Principle for Semi-Infinite Shells of Revolution," *Recent Advances in Engineering Science*, Vol. 8, A. C. Eringen, ed., Proceedings of the 10th Anniversary Meeting, Society of Engineering Science, Rayleigh, NC, 1973, Science Publishers, Boston, pp. 367–374.

Sokolnikoff, I. S., 1956, *Mathematical Theory of Elasticity*, 2nd ed., McGraw-Hill, New York.

Southwell, R. V., 1941, *An Introduction to the Theory of Elasticity*, Oxford University Press, Oxford, U.K.

Stephen, N. G., 1992, "On Edge Effects for the Semi-Infinite Plate," *Journal of Elasticity*, to be published.

Timoshenko, S. P., and Goodier, J. N., 1970, *Theory of Elasticity*, 3rd ed., McGraw-Hill, New York, Article 26.

Vlasov, V. V., 1961, *Thin Walled Elastic Beams*, 2nd ed., The Israel Program For Scientific Translation.

APPENDIX

Morley Shell Theory The characteristic equation governing the decay of edge effects according to Morley shell theory is, in the present notation,

$$(k^2-n^2)^2(k^2-n^2+1)^2+4K^4k^4=0,$$

where $K^4 = 3(1-\nu^2)(r_m/t)^2$, r_m is mean radius, and t is wall thickness.

Downloaded 03 May 2010 to 171.66.16.247. Redistribution subject to ASME license or copyright; see http://www.asme.org/terms/Terms_Use.cfm

Finite Deformation Analysis of Pressure-Shear Plate Impact Experiments on an Elastohydrodynamic Lubricant

K. T. Ramesh
Department of Mechanical Engineering,
The Johns Hopkins University,
Baltimore, MD 21218
Assoc. Mem. ASME

R. J. Clifton
Division of Engineering,
Brown University,
Providence, RI 02912
Mem. ASME

Pressure-shear plate impact experiments on an elastohydrodynamic lubricant (5P4E) are interpreted by means of a full finite deformation analysis of stress wave propagation in an elastic/viscoplastic material. The elastic response is modeled as that of a neo-Hookean solid, modified to include compressibility in such a way that the shock velocity increases linearly with increasing particle velocity; the viscoplastic response is modeled by means of a thermal activation model in which the activation energy is taken to be pressure dependent. The parameters in the elasticity relation are determined from the rising part of the transmitted stress profiles, which are related to transit times for multiple reverberations through the thickness of the lubricant layer. The parameters in the viscoplastic model are determined from the shear stress transmitted after nominally homogeneous states of stress are established through the thickness of the lubricant. Good agreement between measured and computed wave profiles is obtained over the entire range of pressures used in the experiments.

1 Introduction

Pressures of several GPa and shear rates of 10^5 sec^{-1} may be encountered during elastohydrodynamic (EHD) lubrication (Johnson and Cameron, 1968); under these conditions, the lubricant is likely to be in the glassy state (Bair and Winer, 1980). At small stresses and small strains, glassy lubricants exhibit a high-frequency elastic shear modulus in shear wave experiments using ultrasonics (Barlow et al., 1972). At high shear stresses, the glassy lubricant is believed to behave like a plastic solid, with a "limiting shear stress" which depends on the pressure and the temperature but which is essentially independent of the strain and strain rate (Johnson, 1978). This limiting shear stress is a material characteristic which together with the low shear stress viscosity and the shear modulus can be used to predict EHD behavior (Bair and Winer, 1979b).

An experimental technique (pressure-shear plate impact) has been developed to investigate the viscoplastic response of elastohydrodynamic lubricants subjected to very high pressures and deformed at very high shear rates (Ramesh and Clifton, 1987). Pressures up to 5 GPa and shear rates up to 1.5×10^6 sec^{-1} are obtained for durations of approximately one microsecond. During this time the lubricant is subjected to simple shearing while under hydrostatic compressions.

The analysis presented by Ramesh and Clifton (1987) was based solely on the values of the flow stress at late times, when the deformation becomes essentially the homogeneous simple shearing of a compressed material. No interpretation of the experimental information at times during which wave propagation effects are still significant was included. The present paper contains analysis and computational results designed to provide a complete description of the plane wave propagation through the specimen, including the effects of the boundaries. In this way, the experimental observations at all times of interest can be used to examine the validity of trial models for the constitutive description of the material. In particular, the rising segments of the velocity-time profiles can be used to determine the elastic response of the lubricant.

This paper begins with a presentation of results obtained from pressure-shear plate impact experiments. These results are then compared with a full finite deformation analysis of the wave propagation in the specimen (modeled as an elastic/viscoplastic solid). Finally, some implications of the lubricant response for understanding elastohydrodynamic lubrication are discussed.

2 Experimental Results

The pressure-shear plate impact experiment involves the impact of plates that are parallel but inclined relative to their direction of approach, as shown in Fig. 1. A hard metallic plate moving at a velocity V_0 and inclined at an angle θ relative

Contributed by the Applied Mechanics Division of THE AMERICAN SOCIETY OF MECHANICAL ENGINEERS for presentation at the 1992 ASME Winter Annual Meeting, Anaheim, CA, Nov. 8–13, 1992.

Discussion on this paper should be addressed to the Technical Editor, Prof. Leon M. Keer, The Technological Institute, Northwestern University, Evanston, IL 60208, and will be accepted until four months after final publication of the paper itself in the JOURNAL OF APPLIED MECHANICS.

Manuscript received by the ASME Applied Mechanics Division, Feb. 5, 1991; final revision, Jan. 27, 1992. Associate Technical Editor: R. M. Bowen.

Paper No. 92-WA/APM-13.

Copyright © 1992 by ASME
Downloaded 03 May 2010 to 171.66.16.247. Redistribution subject to ASME license or copyright; see http://www.asme.org/terms/Terms_Use.cfm

to its direction of motion impacts a parallel, stationary target. The target is a sandwich, in which a thin layer of lubricant is confined between two hard metal plates that remain elastic under the impact. Impact occurs on the front plate; the waves transmitted through the lubricant are monitored (using laser interferometry) at the rear surface of the rear plate. Because the metal plates remain elastic throughout the experiment, stresses at the interface between the lubricant and the rear plate can be computed from measured particle velocities at the rear surface of the sandwich. Within the observation time of the experiment (i.e., before any release waves from the periphery of the target arrive at the point of observation), the waves of interest are plane waves that depend on only the spatial coordinate normal to the impact plane.

When impact occurs, normal and transverse components of the projectile velocity are imposed on the impact face of the front target plate. The impact generates two elastic stress waves: a compression wave that propagates at a velocity c_1 and a shear wave that propagates at a velocity c_2. The propagation of these waves is shown on the time-distance (t—X) diagram in Fig. 2.

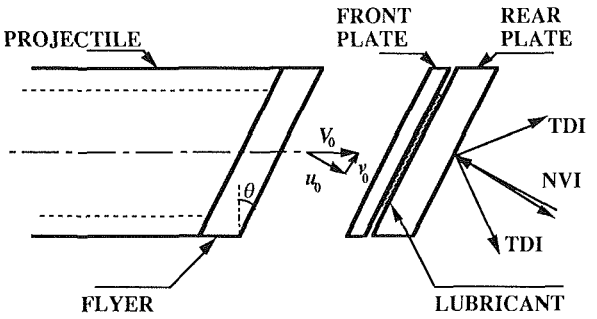


Fig. 1 Experimental configuration for pressure-shear studies on lubricants

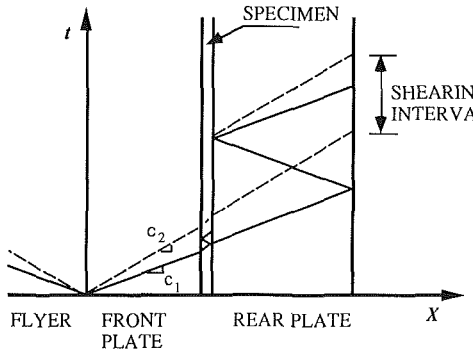


Fig. 2 Time-distance (t—X) diagram

The longitudinal wave arrives at the lubricant layer first, passes through it, and then arrives at the interface between the lubricant and the metallic rear target plate. Because the metal has a higher impedance than the lubricant, the part of the wave that is reflected from this interface is again a loading wave. This loading wave reverberates several times through the thickness of the lubricant until the stress state in the lubricant becomes one of nominally homogeneous stress under conditions of uniaxial strain. The difference in the principal stresses decreases due to viscoplastic flow so that by the time the shear wave arrives at the lubricant, a state of essentially uniform pressure has been attained. The shear wave also reverberates within the specimen, and a nominally homogeneous state is achieved at a shear stress σ_{21} and a constant shear rate $\dot{\gamma}$ (corresponding to a difference in transverse velocity being maintained across the thickness of the lubricant). The shear γ in the lubricant is obtained by integrating the shear rate over the time of observation. Thus, the stress-strain behavior of the lubricant in shear (under a given hydrostatic pressure and at a high shear rate) can be obtained directly from the known projectile velocity and skew angle and the recorded time histories of the normal and transverse motion at the rear surface of the target. A more detailed description of the experiment has been given previously (Ramesh and Clifton, 1987).

The experiments discussed in this paper were performed on a synthetic lubricant known as 5P4E. Albeit liquid at room temperature and atmospheric pressure, this material undergoes a glass transition at a temperature T_g that is a function of pressure, and presumably of cooling rate (Bair and Winer, 1980). The shear stress sustained by this lubricant saturates with increasing shear rate (Bair and Winer, 1979a; Evans and Johnson, 1986); this saturation shear stress is known as the "limiting shear stress" and appears to be a function of the imposed pressure.

A summary of the plate impact experiments is presented in Table 1 for 5P4E. The intent of the experimental program was twofold: (i) to determine the shear behavior of the lubricant over a range of pressures while holding the shear rate approximately constant, and (ii) to investigate the lubricant response over a small range of shear rates at approximately constant pressure. All tests were conducted at room temper-

Table 1 Summary of experiments on 5P4E

Shot No.	Proj. Velocity V_0 mm/μs	Skew Angle θ	Pressure p MPa	Shear Stress MPa	Shear Rate 10^5 sec^{-1}	Maximum Shear
02-84-L1	0.174	18.5	2085	93	10.3	0.27
17-85-L1	0.146	18.0	3152	170	8.1	0.76
18-85-L1	0.171	18.0	3709	218	9.7	0.81
20-86-L1	0.126	20.0	1493	81	7.2	0.26
21-86-L1	0.117	20.0	2499	164	7.2	0.58
23-86-L1	0.198	18.0	4280	230	15.1	1.25
24-86-L1	0.222	15.0	4878	242	15.0	1.38
25-86-L1	0.101	20.0	1197	92	4.7	0.32
26-86-L1	0.105	22.0	2204	159	6.7	0.59
27-86-L1	0.144	17.0	1741	125	5.5	0.46
28-86-L1	0.149	20.0	3185	171	11.0	0.82
38-87-L1	0.169	22.0	3563	180	13.1	0.80
39-87-L1	0.165	8.0	3706	170	2.4	0.35
40-87-L1	0.167	16.0	3648	190	5.5	0.49

Downloaded 03 May 2010 to 171.66.16.247. Redistribution subject to ASME license or copyright; see http://www.asme.org/terms/Terms_Use.cfm

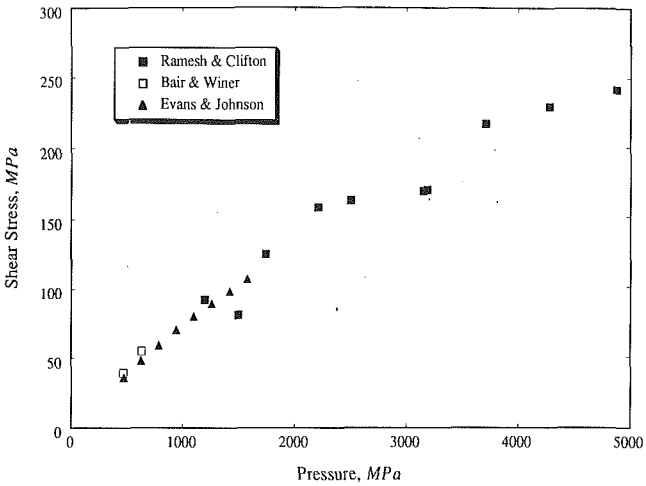


Fig. 3 Comparison of results of pressure-shear plate impact tests with results of high-pressure chamber (Bair and Winer, 1979a) and disk machine (Evans and Johnson, 1986) tests

ature, for which the glass transition pressure is about 400 MPa for 5P4E (Alsaad et al., 1978). All of the plate impact experiments were performed in the glassy regime.

In Fig. 3 the plate impact results on the dependence of the limiting shear stress on pressure for 5P4E are compared with those obtained by Bair and Winer (1979a) using a high-pressure chamber, and with those obtained by Evans and Johnson (1986) using a disk machine. In general, the plate impact results show good agreement with the results obtained using these completely different experimental techniques. The limiting shear stress sustained by 5P4E appears to vary almost linearly with pressure at the lower pressures; the pressure-shear experiments show some deviation from linearity at the higher pressures. Similar behavior at high pressures has been observed for some polymeric materials (Silano, 1982).

3 Finite Deformation Analysis

Large compressive and shearing deformations occur during these pressure-shear experiments on lubricants. For example, Fig. 5 shows the measured rise of the target rear-surface normal particle velocity with time during a typical experiment ("shot"). The velocity reaches its final level after approximately 400 nanoseconds. This is a slow rise, in comparison with that observed for metal specimens, for instance, and indicates that the material is highly compressible. Further, shear rates of 10^6 $\sec^{-1}$ are sustained for times on the order of a microsecond; thus the total shears obtained in these experiments are of the order of unity (see Table 1).

Thus, a formulation is required that accounts for large elastic compressibility, as well as large shear. The formulation presented involves large elastic compressibility through a hyperelastic relation, and incompressible viscoplastic flow extended to large deformations. The experiment is modeled in terms of the propagation of longitudinal and transverse waves in an infinite plate bounded by linear elastic half-spaces. In this section the model is described and the associated wave analysis is presented.

3.1 Finite Deformation Kinematics of Pressure Shear. Pressure-shear deformation may be represented locally by the homogeneous deformation

$$x_1=\lambda(t)X_1,\ x_2=X_2-\kappa(t)X_1,\ x_3=X_3 \tag{1}$$

where x_1, x_2, x_3 denote the position at time t of the particle that was initially at X_1, X_2, X_3. For the deformation (1), the total deformation gradient is

$$\mathbf{F}=\begin{bmatrix}\lambda(t) & 0 & 0\\ -\kappa(t) & 1 & 0\\ 0 & 0 & 1\end{bmatrix}. \tag{2}$$

A multiplicative decomposition of the deformation gradient gives

$$\mathbf{F}=\mathbf{F}^e\mathbf{F}^p, \tag{3}$$

where $\mathbf{F}^e$ represents the elastic part and F^p represents the inelastic part. The stresses are assumed to be derivable solely from the elastic part of the deformation $\mathbf{F}^e=\mathbf{F}\mathbf{F}^{p^{-1}}$ (specifically, from a hyperelastic potential W, to be described et seq.). From the multiplicative decomposition (3), one obtains an additive decomposition of the total rate of deformation $\mathbf{D}$:

$$\mathbf{D}=\mathbf{D}^e+\mathbf{D}^p \tag{4}$$

where $\mathbf{D}^e$ and $\mathbf{D}^p$ denote elastic and inelastic rates of deformation. Now, $\mathbf{D}$ is the symmetric part of the total velocity gradient $\dot{\mathbf{F}}\mathbf{F}^{-1}$, and $\mathbf{D}^p$ can be expressed in terms of the stresses by means of an assumed flow law. Then if $\mathbf{D}^e = \mathbf{D} - \mathbf{D}^p$ is related to the stress rates by an elastic rate equation, one obtains equations relating the stresses and particle velocities.

The ratio of the current volume to the reference volume is given by $J = \det(\mathbf{F})$. Assuming plastic incompressibility, in agreement with the experimental observation that most amorphous solids have little or no plastic volumetric change after deformation (Argon, 1973), one obtains $J = \lambda = \det(\mathbf{F}^e)$. Without loss of generality, one can choose the intermediate configuration to be obtained without rotation so that $\mathbf{F}^p$ becomes a symmetric, positive definite tensor

$$\mathbf{F}^p=\begin{bmatrix}\lambda_1^p & -\kappa^p & 0\\ -\kappa^p & \lambda_2^p & 0\\ 0 & 0 & \lambda_3^p\end{bmatrix} \tag{5}$$

where the zero entries follow from symmetry arguments. Using the plastic incompressibility condition, only three independent components are required to completely define $\mathbf{F}^p$.

3.2 Momentum Balance Relations. The balance of linear momentum for this one-dimensional problem is given by the relations

$$\frac{\partial T_{11}}{\partial X_1}=\rho_0\frac{\partial u}{\partial t} \tag{6a}$$

$$\frac{\partial T_{21}}{\partial X_1}=\rho_0\frac{\partial v}{\partial t} \tag{6b}$$

where u and v are, respectively, the longitudinal and transverse components of particle velocity and T_{ij} are the components of the first Piola-Kirchhoff stress tensor $\mathbf{T}$, related to the Cauchy stress tensor $\boldsymbol{\sigma}$ by

$$\boldsymbol{\sigma}=\frac{1}{J}\mathbf{F}\mathbf{T}^T. \tag{7}$$

For isotropic materials undergoing the deformations (1), and using the symmetry of the Cauchy stress, it follows that $T_{i3} = T_{3i} = 0$ for $i = 1, 2$. Hence, for pressure-shear deformations the stress tensor $\mathbf{T}$ is determined completely by the four independent components T_{11}, T_{21}, T_{22}, and T_{33}.

3.3 Constitutive Behavior. The material is modeled as an elastic/viscoplastic solid undergoing both finite elastic strains and finite viscoplastic deformations. In broad terms, the objective is to account for large elastic compressibility as well as large viscoplastic shearing. It is assumed that the material remains isotropic throughout the deformation.

Consider first the hyperelastic response. The constitutive

Downloaded 03 May 2010 to 171.66.16.247. Redistribution subject to ASME license or copyright; see http://www.asme.org/terms/Terms_Use.cfm

relation for the general isotropic compressible hyperelastic solid has the form (e.g., Gurtin, 1981)

$$\sigma = \alpha_0 \mathbf{I} + \alpha_1 \mathbf{B}^e + \alpha_2 \mathbf{B}^{e^2} \tag{8}$$

where α_0, α_1, α_2 are scalar functions of the invariants I_1, I_2, I_3 of the elastic left Cauchy-Green deformation tensor $\mathbf{B}^e = \mathbf{F}^e \mathbf{F}^{e^T}$. The scalar functions α_0, α_1, α_2 are obtained from the relations

$$\alpha_0 = 2J^e \frac{\partial W}{\partial I_3}, \quad \alpha_1 = \frac{2}{J^e}\left(\frac{\partial W}{\partial I_1} + I_1 \frac{\partial W}{\partial I_2}\right), \text{ and } \alpha_2 = -\frac{2}{J^e}\frac{\partial W}{\partial I_2} \tag{9}$$

where W is a hyperelastic potential. The hyperelastic potential is chosen to correspond to a neo-Hookean solid with an additive term to account for compressibility:

$$W = C_1(I_1 - 3) + f(I_3) \tag{10}$$

where C_1 is a positive constant; I_1 and I_3 are the first and third invariants of $\mathbf{B}^e$. For the case of uniaxial strain, the material is assumed to have the behavior commonly observed in shock wave experiments (Davison and Graham, 1979) that the shock wave speed increases linearly with increasing particle velocity. This behavior leads to the requirement that the Hugoniot stress-strain relation for uniaxial strain has the form

$$\sigma_{11} = \frac{K\epsilon}{(1 + a\epsilon)^2} \tag{11}$$

where K and a are positive constants; σ_{11} and ϵ are, respectively, the normal stress and normal strain in the direction of wave propagation. The constant a in (11) is the slope of a plot of shock velocity versus particle velocity (Hugoniot). Using Eq. (9) and the hyperelastic potential (10) together with the requirement that the response in uniaxial strain satisfy (11) results in the relations:

$$\alpha_0 = 2\lambda f'(I_3), \ \alpha_1 = 2C_1/\lambda, \ \alpha_2 = 0 \tag{12}$$

where

$$f'(I_3) = \frac{K(\lambda - 1)}{2\lambda\{1 + a(\lambda - 1)\}^2} - C_1. \tag{13}$$

For infinitesimal deformations $C_1 = \mu/2$ and $K = (\bar{\lambda} + 2\mu)$, where μ and $\bar{\lambda}$ are the Lamé constants of linear isotropic elasticity. The hyperelastic potential (10) is chosen as the simplest potential which incorporates the well-known qualities of the neo-Hookean model for incompressible deformations and the commonly observed form of the Hugoniot.

The inelastic deformation gradient $\mathbf{F}^p$ (required for the computation of $\mathbf{F}^e$ and hence of $\mathbf{B}^e$) is obtained by integration of the viscoplastic flow law

$$\mathbf{D}^p = \langle \Phi \rangle \frac{\mathbf{S}}{2\sigma_e} \tag{14}$$

where $\mathbf{S}$ is the deviatoric part of the Cauchy stress tensor and $\sigma_e^2 = J_2$ is the second invariant of $\mathbf{S}$. Φ is a viscoplastic strain rate function, the form of which is chosen as follows.

The flow stress of 5P4E is observed to be very weakly rate-dependent (Bair and Winer, 1979a; Evans and Johnson, 1986). This weak rate dependence can be modeled within a framework of thermally activated processes. In view of the observed pressure dependence of the flow stress (Fig. 3) the activation energy may be expected to vary with the pressure p. This suggests that the inelastic strain rate $\dot{\gamma}$ be described by (e.g., Ward, 1971):

$$\dot{\gamma} = \dot{\gamma}_0 \exp\left(\frac{-\Delta U - p\Omega(p)}{kT}\right) \sinh\left(\frac{\tau v}{kT}\right) \tag{15}$$

where $\dot{\gamma}_0$ is a constant, ΔU represents the activation energy (at $p = 0$) for the flow process, k is the Boltzmann constant, T is the absolute temperature, τ is the applied shear stress, v represents the activation volume, and the function $\Omega(p)$ can be interpreted as a "pressure activation volume." In essence, $\Omega(p)$ and v are quantities such that the increase in the activation energy under the confining pressure is $p\Omega(p)$ and the work done by the shear stress during the motion of a flow unit from one potential well to the next is τv. Equation (15) leads to the Barus law for viscosity (Johnson and Cameron, 1968; Evans and Johnson, 1986).

In the high flow stress regime, the hyperbolic sine in (15) can be replaced by the exponential to obtain

$$\dot{\gamma} = \dot{\gamma}_0 \exp\left(\frac{-\Delta U - p\Omega(p)}{kT}\right) \exp\left(\frac{\tau v}{kT}\right), \tag{16}$$

where a factor of two has been absorbed in the pre-exponential factor $\dot{\gamma}_0$. Solving Eq. (16) for the shear stress τ and rearranging the terms one obtains

$$\tau = \tau_0 + \alpha p + \beta \ln\left(\frac{\dot{\gamma}}{\dot{\gamma}_0}\right) \tag{17}$$

where

$$\tau_0 = \frac{\Delta U}{v}, \ \alpha = \frac{\Omega(p)}{v}, \ \beta = \frac{kT}{v}. \tag{18}$$

Equation (17) provides for the observed approximately linear dependence of the flow stress on pressure (linearity results when $\Omega(p)$ is constant) and the observed weak dependence of the flow stress on flow rate. Measurement of the pressure sensitivity of the flow stress (e.g., from Fig. 3) at constant strain rate determines α; measurement of the rate sensitivity (at constant pressure) provides an estimate of β. Assuming that the temperature remains constant and is known, one can use Eq. (18) to estimate v from β; once v is known $\Omega(p)$ can be obtained from α. The reference strain rate $\dot{\gamma}_0$ and the activation energy ΔU at zero pressure cannot be obtained individually from the pressure-shear experiments, which determine only the combination $\tau_0 - \beta \ln \dot{\gamma}_0$. However, because only this combination is required to determine the flow law, the independent determination of ΔU and $\dot{\gamma}_0$ is not required.

Equation (15) is extended to general states of stress by replacing the driving shear stress τ by the effective stress σ_e, and identifying $\dot{\gamma}$ as the effective viscoplastic strain rate, Φ. This is the viscoplastic strain rate function used in Eq. (14). No strain hardening is introduced in this constitutive model, since no evidence of hardening has been observed (e.g., Bair and Winer, 1979a).

For use with the additive decomposition of elastic and inelastic rates of deformation (4), the elasticity relation needs to be expressed in rate form. For this purpose the objective stress rate is chosen to be the Jaumann rate with the spin identified as the elastic spin $\mathbf{W}^e$:

$$\overset{\nabla}{\sigma} = \dot{\sigma} - \mathbf{W}^e \sigma + \sigma \mathbf{W}^e. \tag{19}$$

Taking this Jaumann rate of Eq. (8), noting that $\alpha_2 = 0$ for this hyperelastic potential, and using Eq. (8) again to eliminate σ, one obtains $\dot{\sigma}$ in terms of deformation rates. Then, from Eq. (7), one obtains the rate equation for $\mathbf{T}$ as

$$\dot{\mathbf{T}} = \lambda \dot{\sigma} \mathbf{F}^{-T} + (\dot{\lambda}/\lambda)\mathbf{T} - \mathbf{T}\dot{\mathbf{F}}^T \mathbf{F}^{-T} \tag{20}$$

where $\mathbf{F}^{-T} = (\mathbf{F}^{-1})^T$. For the special case of pressure-shear deformations with the deformation gradient tensor of Eq. (2), the rate equations for the required components of the Piola-Kirchhoff stress tensor $\mathbf{T}$ may be written in the form

$$\dot{T}_{11} = \tilde{A}_{11}\dot{\lambda} + \tilde{B}_{11}\dot{\kappa} + \tilde{C}_{11} \tag{21a}$$

$$\dot{T}_{21} = \tilde{A}_{21}\dot{\lambda} + \tilde{B}_{21}\dot{\kappa} + \tilde{C}_{21} \tag{21b}$$

$$\dot{T}_{22} = \tilde{A}_{22}\dot{\lambda} + \tilde{B}_{22}\dot{\kappa} + \tilde{C}_{22} \tag{21c}$$

$$\dot{T}_{33} = \tilde{A}_{33}\dot{\lambda} + \tilde{B}_{33}\dot{\kappa} + \tilde{C}_{33} \tag{21d}$$

where $\tilde{A}_{ij}$ and $\tilde{B}_{ij}$ are collections of terms representing, respectively, the coefficients of the $\dot{\lambda}$ and $\dot{\kappa}$ terms in Eq. (20).

Downloaded 03 May 2010 to 171.66.16.247. Redistribution subject to ASME license or copyright; see http://www.asme.org/terms/Terms_Use.cfm

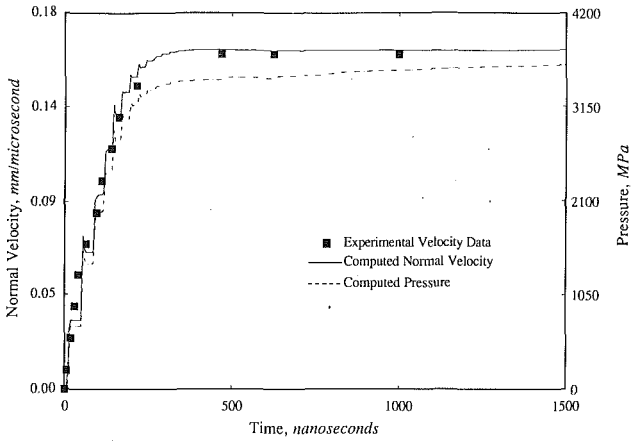


Fig. 4 Comparison of experimental normal velocity-time record with computed time histories of normal velocity and pressure (Shot 18-85-L1)

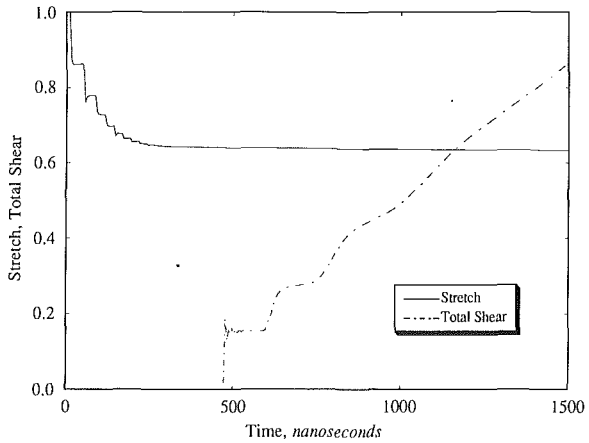


Fig. 5 Computed time histories of the total stretch and the total shear (Shot 18-85-L1)

The terms $\tilde{C}_{ij}$ result from the viscoplasticity. The relations for $\tilde{A}_{ij}$, $\tilde{B}_{ij}$, $\tilde{C}_{ij}$, obtained from Eq. (20) after extensive algebraic manipulations, are quite complex; they are presented in the Appendix.

3.4 Wave Analysis. The governing equations for dynamic pressure-shear loading consist of the momentum balance relations (6) and the four rate Eqs. (21). In the latter equations the rates of deformation $\dot{\lambda}$ and $\dot{\kappa}$ can be replaced by the velocity gradients using the compatibility conditions

$$\frac{\partial u}{\partial X_1} = \frac{\partial \lambda}{\partial t} \tag{22a}$$

$$\frac{\partial v}{\partial X_1} = -\frac{\partial \kappa}{\partial t} \tag{22b}$$

Then the governing relations provide six equations in the six unknowns u, v, T_{11}, T_{21}, T_{22}, and T_{33}. However, because there is no dependence of T_{22} and T_{33} on X_1, the problem can be reduced to the solution of four partial differential equations:

$$\rho_0 \frac{\partial u}{\partial t} = \frac{\partial T_{11}}{\partial X_1} \tag{23a}$$

$$\rho_0 \frac{\partial v}{\partial t} = \frac{\partial T_{21}}{\partial X_1} \tag{23b}$$

$$\frac{\partial T_{11}}{\partial t} = \tilde{A}_{11} \frac{\partial u}{\partial X_1} - \tilde{B}_{11} \frac{\partial v}{\partial X_1} + \tilde{C}_{11} \tag{23c}$$

$$\frac{\partial T_{21}}{\partial t} = \tilde{A}_{21} \frac{\partial u}{\partial X_1} - \tilde{B}_{21} \frac{\partial v}{\partial X_1} + \tilde{C}_{21}. \tag{23d}$$

T_{22} and T_{33} are obtained by direct integration of the rate Eqs. (21c) and (21d).

Equations (23) comprise a strongly hyperbolic, quasi-linear system of partial differential equations that are to be solved subject to the boundary conditions on the two faces of the specimen. Initially all stresses, velocities, and deformations are zero. This system is solved using a second-order accurate difference scheme based on integration along characteristics (Ranganath and Clifton, 1972).

4 Computational Results

The values of the constants used in the computations were obtained as follows. The values of a and K were chosen to provide the best match to the rising portions of the plots of normal particle velocity versus time over the entire range of pressures. Similarly, the shear modulus μ was chosen to provide the best match of the rising portions of the experimental curve of transverse velocity versus time over the full range of impact conditions.

The values for the viscoplastic parameters were obtained by matching the experimental curves of transverse velocity versus time at late times, over the range of pressures. Since there is some influence of the viscoplastic flow even during the early shearing, the value of μ cannot be estimated entirely independently of the values chosen for the viscoplastic parameters. However, the calculations indicate that the risetime is determined *primarily* by the shear modulus.

Figure 4 shows a plot of the history of the normal velocity at the free surface, as computed from the finite deformation analysis and from the experimental data for one shot, 18-85-L1. The agreement is excellent, being within the accuracy with which normal velocities can be computed from the interferometer data. The step structure in the early part of the computed curves corresponds to the successive arrival of longitudinal wave fronts at the rear surface. Figure 4 also shows the computed hydrostatic pressure at the rear surface as a function of time. The rise in the pressure follows the rise in the normal velocity (and therefore normal stress), though more slowly; at late times the pressure tends towards σ_{11}. For this reason the experiments were characterized as simple shear of a hydrostatically pressurized lubricant. The degree to which the pressure has approached the normal stress at the time of arrival of the shear wave varies from test to test, according to these simulations; however, the difference is never greater than ten percent.

It is important to note that the effective stress, which drives the viscoplastic response, is not zero during the time after the arrival of the longitudinal wave and before the arrival of the shear wave. Although σ_{21} remains zero until the shear wave arrives, there is a sufficient difference between σ_{22} and σ_{11} during the reverberation of the longitudinal wave to cause significant viscoplastic flow. Indeed, this viscoplastic flow is responsible for significant reduction in the difference $|\sigma_{11}-\sigma_{22}|$ before the arrival of the shear wave (Ramesh and Clifton, 1989).

The history of the computed total stretch λ is shown in Fig. 5. The stretch decreases until it levels off at a value corresponding to the thickness reduction. The computed history of the total shear κ is also shown in Fig. 5. The total shear is zero during the uniaxial strain part of the deformation. Steady shearing is observed at late times.

Computational results are presented for three tests covering the range of pressures in Figs. 6 and 7. The overall agreement between computed and measured velocity-time profiles suggests that the principal features of the lubricant response are being modeled quite well.

Downloaded 03 May 2010 to 171.66.16.247. Redistribution subject to ASME license or copyright; see http://www.asme.org/terms/Terms_Use.cfm

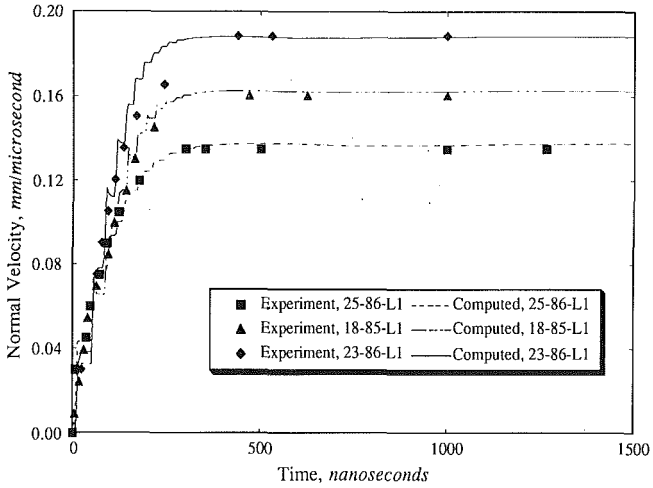


Fig. 6 Comparison of computed and experimental normal velocity-time records

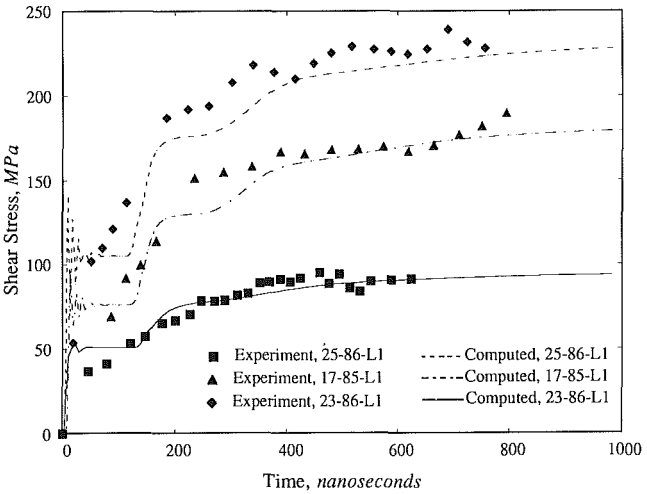


Fig. 7 Comparison of computed and experimental shear stress-time records

5 Discusssion

The computational results using the Hugoniot relation (11) indicate that the experimental data can be matched (Fig. 6) over the full range of pressures by using $K = 4.3$ GPa and $a = 1$. In comparison, Schuler (1970) found a to be 3.6 from his experiments on PMMA. A similar value for a has been obtained for a phenolic resin (Dandekar, 1983). The slope of the shock speed versus particle velocity curve (i.e., a) is similar for materials of given type, e.g., the slope for several pure metals ranges from 1.1 to 1.8 (Nellis, 1982).

The computed pressure continues to rise, although slowly, during shearing (Fig. 4). This rise in pressure is believed to be responsible for the slow increase in the experimentally obtained shear stress values with time since there appears to be no strain hardening in these materials (Bair and Winer, 1979a).

The value for the activation volume v obtained from these simulations is 2.8×10^{-27} m^3. This is approximately 25 times the molecular volume, and is comparable to the activation volume obtained by Johnson and Tevaarwerk (1977) of 3.4×10^{-27} m^3. While this is a rather large activation volume for a thermally activated process, the value does not seem to be unreasonable in view of the evidence of cooperative flow in polymers (Argon, 1973). Since the experiments have yielded insufficient data to fully characterize the rate sensitivity at these pressures, the value for v should be regarded only as an approximate lower bound. The computational results on the low shear rate shot 39-87-L1 (Ramesh and Clifton, 1989) support the weak rate sensitivity that is represented by the model.

The finite deformation computations appear to provide a good fit (Fig. 7) to the risetimes of the experimental shear stress-time curves over the entire range of pressures using a value for μ of approximately 0.6 GPa. It should be noted that the pressure-shear experiments were not designed for determining the shear modulus; thus, there are not sufficient data points available during the risetime of the experimental shear stress-time curves to provide a very accurate measure of μ. Comparison of the experimental and computational results for the entire range of plate impact experiments would allow μ to vary in the range of 0.5 to 0.8 GPa, with a value of 0.6 GPa providing the best overall agreement. It is interesting to note that Bair and Winer (1979a), using a completely different experiment, obtained a value for the shear modulus of 1.2 GPa at a pressure of 0.275 GPa and at temperatures well below the glass transition. Since the modulus is expected to increase with pressure, and since the pressures reported here are so much higher, the value for μ that is obtained here is surprisingly low. However, values of μ larger than 0.8 GPa in the simulations would certainly predict risetimes that are not in accord with the experiments.

From the Bair and Winer data, the rate of decrease of the shear modulus with temperature is very small at pressures and temperatures that are well within the glassy regime. The plate impact experiments are always at pressures and temperatures in the glassy regime, even accounting for shear heating (see Ramesh and Clifton, 1987; adiabatic estimates of the temperature rise in the specimen as a result of shear heating range from 6°C for Shot 25-86-L1 up to 78°C for Shot 24-86-L1). Further, the temperature rise due to shear heating increases as the tangential component v_0 of the projectile impact velocity increases; yet, the value of μ necessary to match the experimental results does not increase with v_0. Thus, the softening effect of temperature does not appear to be sufficient to lower the modulus significantly.

In these simulations, the parameters describing the elastic response are obtained from the observed risetimes, while the modeling of the viscoplasticity is determined entirely by the high shear stress behavior. However, the simulated risetimes are also affected by the viscoplastic response. If the viscoplastic model were seriously in error at low stresses, then the contribution to the risetime of the viscoplasticity could be substantially different, resulting in changes in the estimate of the shear modulus.

The step-like feature in the computed profile at early times arises from reverberations of elastic wavefronts through the thickness of the specimen. There is insufficient plastic disipation in the model at these times to smooth the fronts. While the data reduction process used in the analysis of the experimental traces eliminates such details through averaging, it is also possible that the discrepancies between predicted and measured profiles are due in part to deficiencies in the model. For example, the temperature increase due to viscoplastic dissipation could enhance plastic flow significantly and smooth the step-like features. It should be remembered in this regard that significant viscoplastic flow occurs even before the shear wave arrives; hence, the temperature will have increased even during the early stages of the shearing. The inclusion of temperature effects should be considered in the further development of the simulation.

It is possible that the times involved in the pressure-shear experiments are so short that there is insufficient time for molecular rearrangement to the equilibrium state at the high pressure. If so, the response of the material could be comparable to that at a lower effective pressure, applied sufficiently slowly. This could account for the low value of the shear

Downloaded 03 May 2010 to 171.66.16.247. Redistribution subject to ASME license or copyright; see http://www.asme.org/terms/Terms_Use.cfm

modulus obtained from the simulations. However, it would be expected that such a "structural relaxation" would also have a strong influence on the flow stress sustained by the material under the applied pressure. The measured values of the shear stress, however, correlate very well with those of Bair and Winer (1979a), and Evans and Johnson (1986), obtained at lower pressures and longer time scales. Some of the plate impact experiments, e.g., 25-86-L1, are in the same pressure range as those of Evans and Johnson (1986), and very similar flow stresses are obtained. Thus, it appears that if a structural relaxation phenomenon is important here, then the influence of the structural relaxation on the modulus must be much stronger than its influence on the flow stress under pressure.

Feng and Ramesh (1990) and Ramesh (1991) have recently obtained experimental results on the short-time (10^{-4} s) compressibility of the same lubricant for pressures up to 1 GPa using a modified compression Kolsky bar. The relation (11), with constants obtained *solely* from simulation of the plate impact experiments, provides an excellent representation also of the (lower pressure) Kolsky bar data. This agreement provides corroborating evidence that the procedure used here to simulate the plate impact experiments is capable of providing information on the elastic response of the lubricant. The agreement with the Kolsky bar data also suggests that structural relaxation in compression is not very significant in the elastic response of this lubricant over the time scales of the Kolsky bar and pressure-shear plate impact experiments.

Finally, by not including thermal softening, the analysis has resulted in shearing deformations that remain homogeneous during the experiment. While it is possible to develop inhomogeneous velocity fields (and perhaps even localized shearing) with these boundary conditions, recent work by Feng (1992) indicates that for the time scales of these experiments the flow field remains homogeneous. However, localized shearing deformations may be associated with the limiting shear stress phenomenon (Feng and Ramesh, 1991; (Feng, 1992) at lower shear rates.

6 Conclusions

The rheological behavior of an EHD lubricant (5P4E) under high pressures and high shear rates has been investigated using pressure-shear plate impact experiments. The experiment allows the direct measurement of the rheology of the lubricant at pressures up to 5 GPa and shear rates of 10^5–10^6 per second. The limiting shear stress sustained by 5P4E increases with increasing pressure, although apparently less than proportionately at pressures above approximately 3.5 GPa. The shear stress appears to be independent of the total shear. Even though the lubricant was only sheared for approximately one microsecond, the results agree reasonably well with those obtained by other investigators in isothermal, quasi-static experiments involving shearing for much longer periods.

Mathematical modeling of the pressure-shear experiments was carried out for the finite deformation problem. The material model used is that of an elastic/viscoplastic solid, in which a hyperelastic potential is used for the elastic behavior, and the viscoplasticity is obtained from a pressure-dependent thermal activation model. The experiment is modeled in terms of the propagation of longitudinal and shear waves in an infinite plate bounded by linear elastic half-spaces. The numerical scheme used is a finite difference scheme based on integration along characteristics.

The finite deformation computations are able to match the experimental velocity-time profiles over the entire range of pressures. The value of the constant μ required to match the risetimes of the shear-stress time profiles ranges from 0.5 GPa to 0.8 GPa with the best overall agreement obtained for μ = 0.6 GPa. This value is below that obtained by other investigators at much lower pressures in experiments carried out over much longer times. No satisfactory explanation of this discrepancy is known. Values for the parameters K and a which characterize the compressibility of the material under conditions of uniaxial strain (i.e., K = 4.3 GPa; a = 1) are in good agreement with values required to describe the compressibility measured in Kolsky bar experiments by Feng and Ramesh (1990) at lower pressures and lower rates of loading. The activation volume is obtained as 2.8×10^{-27} m^3, which is 25 times the molecular volume, indicating that several molecules must move in concert.

Acknowledgments

This research was supported by the National Science Foundation through the Program in Tribology and through the Program in Solid Mechanics. Computations were performed on an Alliant FX/8 in the Computational Mechanics Facility at Brown University, on the CYBER-205 at the John von Neumann Supercomputer Center at Princeton, and on a Sun SparcStation (funded by a DURIP grant) at The Johns Hopkins University.

References

Alsaad, M. A., et al., 1978, "Light-Scattering Study of the Glass Transition in Lubricants," ASME *Journal of Lubrication Technology*, Vol. 100, pp. 418–422.

Argon, A. S., 1973, "A Theory for the Low-temperature Plastic Deformation of Glassy Polymers," *Philosophical Magazine*, Vol. 28, No. 4, pp. 839–865.

Bair, S., and Winer, W. O., 1979a, "Shear Strength Measurements of Lubricants at High Pressure," ASME *Journal of Lubrication Technology*, Vol. 101, pp. 251–257.

Bair, S., and Winer, W. O., 1979b, "A Rheological Model for Elastohydrodynamic Contacts Based on Primary Laboratory Data," ASME *Journal of Lubrication Technology*, Vol. 101, pp. 258–265.

Bair, S., and Winer, W. O., 1980, "Some Observations on the Relationship between Lubricant Mechanical and Dielectric Transitions Under Pressure," ASME *Journal of Lubrication Technology*, Vol. 102, pp. 229–235.

Barlow, A. J., et al., 1972, "The Effect of Pressure on the Viscoelastic Properties of Liquids," *Proc. R. Soc. Lond.*, Vol. A327, pp. 403–412.

Dandekar, D. P., and Lamothe, R. M., 1983, "Shock, Re-shock, and Release Behavior of a Phenolic Resin FF-17," *Shock Waves in Condensed Matter*, J. R. Asay, et al., eds., pp. 125–128.

Davison, L., and Graham, R. A., 1979, "Shock Compression of Solids," *Physics Reports*, Vol. 55, No. 4.

Evans, C. R., and Johnson, K. L., 1986, "The Rheological Properties of Elastohydrodynamic Lubricants," *Proc. Inst. Mech. Engrs., Part C*, London, Vol. 200, C5, pp. 301–309.

Feng, R., 1992, Ph.D. Dissertation, The Johns Hopkins University, Baltimore, MD.

Feng, R., and Ramesh, K. T., 1990, "The Dynamic Compressibility of an Elastohydrodynamic Lubricant," Johns Hopkins University Technical Report No. DIL-9003.

Feng, R., and Ramesh, K. T., 1991, "The Dynamic Shearing of an Elastohydrodynamic Lubricant," Johns Hopkins University Technical Report No. DIL-9101.

Gurtin, M. E., 1981, *An Introduction to Continuum Mechanics*, Academic Press, New York.

Johnson, K. L., 1978, "Introductory Review of Lubricant Rheology and Traction," *Proc. of the 5th Leeds-Lyon Symposium on Tribology*, Leeds, pp. 1–11.

Johnson, K. L., and Cameron, R., 1968, "Shear Behavior of Elastohydrodynamic Oil Films at High Rolling Contact Pressures," *Proc. Instn. Mech. Engrs.*, Vol. 182, pp. 307–319.

Johnson, K. L., and Tevaarwerk, J. L., 1977, "Shear Behavior of Elastohydrodynamic Oil Films," *Proc. Roy. Soc. Lond.*, Vol. A356, pp. 215–236.

Nellis, W. J., et al., eds., 1982, *Shock Waves in Condensed Matter—1981*, American Institute of Physics, New York.

Ramesh, K. T., 1991, "The Short-Time Compressibility of Elastohydrodynamic Lubricants," ASME *Journal of Tribology*, Vol. 113, pp. 361–371.

Ramesh, K. T., and Clifton, R. J., 1987, "A Pressure-Shear Impact Experiment for Studying the Rheology of Lubricants at High Pressures and High Shearing Rates," ASME *Journal of Tribology*, Vol. 109, pp. 215–222.

Ramesh, K. T., and Clifton, R. J., 1989, "Finite Deformation Analysis of Pressure-Shear Plate Impact Experiments on Elastohydrodynamic Lubricants," Brown University Technical Report SMMS-89/25.

Ranganath, S., and Clifton, R. J., 1972, "A Second-Order Accurate Differ-

Downloaded 03 May 2010 to 171.66.16.247. Redistribution subject to ASME license or copyright; see http://www.asme.org/terms/Terms_Use.cfm

ence Method for Systems of Hyperbolic Partial Difference Equations," *Computer Methods in Applied Mechanics and Engineering*, Vol. 1, pp. 173–188.

Schuler, K. W., 1970, "Propagation of Steady Shock Waves in Polymethyl Methacrylate," *Journal of the Mechanics and Physics of Solids*, Vol. 18, pp. 277–293.

Silano, A. A., 1982, "Pressure-Dependent Shear Deformation of Polymers," *Reviews on the Deformation Behavior of Materials*, Vol. 4, No. 4, Freund, London.

Ward, I. M., 1971, "Review: The Yield Behavior of Polymers," *Journal of Materials Science*, Vol. 6, pp. 1397–1403.

APPENDIX

We provide here the expressions for the terms $\tilde{A}_{ij}$, $\tilde{B}_{ij}$, and $\tilde{C}_{ij}$ in Eq. (21).

$$\tilde{A}_{11}=\frac{(\lambda_2^{p2}+\kappa^{p2}-\Delta)\,(1-a(1-\lambda))^3\mu+aK\Delta\,(1-\lambda)+K\Delta}{\Delta\,(1-a(1-\lambda))^3}$$

$$\tilde{B}_{11}=0$$

$$\tilde{C}_{11}=(\mu\lambda/\Delta^2)\,(2\Delta(\lambda_2^p\dot{\lambda}_2^p+\kappa^p\dot{\kappa}^p)-\dot{\Delta}(\lambda_2^{p2}+\kappa^{p2}))$$

$$\tilde{A}_{21}=0$$

$$\tilde{B}_{21}=-\mu\,\frac{\lambda_2^{p2}+\kappa^{p2}}{\Delta}$$

$$\tilde{C}_{21}=(-\mu/\Delta^2)\,\{2\Delta\kappa(\lambda_2^p\dot{\lambda}_2^p+\kappa^p\dot{\kappa}^p)-\dot{\Delta}\kappa(\lambda_2^{p2}+\kappa^{p2})-\Delta\kappa^p(\dot{\lambda}_1^p+\dot{\lambda}_2^p)+(\dot{\Delta}\kappa^p-\Delta\dot{\kappa}^p)(\lambda_1^p+\lambda_2^p)\}$$

$$\tilde{A}_{22}=-\frac{2\mu\lambda(1-a(1-\lambda))^3+(a-2)K\lambda+(1-a)K}{(1-a(1-\lambda))^3}$$

$$\tilde{B}_{22}=-\mu\kappa^p(\lambda_1^p+\lambda_2^p)/\Delta$$

$$\tilde{C}_{22}=(-\mu/\Delta^2)\,\{\Delta\kappa\kappa^p(\dot{\lambda}_1^p+\dot{\lambda}_2^p)+(\Delta\dot{\kappa}^p-\dot{\Delta}\kappa^p)\kappa(\lambda_1^p+\lambda_2^p)+\dot{\Delta}(\lambda_1^{p2}+\kappa^{p2})-2\Delta(\lambda_1^p\dot{\lambda}_1^p+\kappa^p\dot{\kappa}^p)\}$$

$$\tilde{A}_{33}=-\frac{2\mu\lambda(1-a(1-\lambda))^3+(a-2)K\lambda+(1-a)K}{(1-a(1-\lambda))^3}$$

$$\tilde{B}_{33}=0$$

$$\tilde{C}_{33}=\mu\dot{\Delta}$$

where

$$\Delta=(\lambda_1^p\lambda_2^p-\kappa^{p2})^2.$$

Downloaded 03 May 2010 to 171.66.16.247. Redistribution subject to ASME license or copyright; see http://www.asme.org/terms/Terms_Use.cfm

Spectral Decomposition of the Elasticity Tensor

S. Sutcliffe
Department of Civil Engineering,
Tufts University,
Medford, MA 02155

The elasticity tensor in anisotropic elasticity can be regarded as a symmetric linear transformation on the nine-dimensional space of second-order tensors. This allows the elasticity tensor to be expressed in terms of its spectral decomposition. The structures of the spectral decompositions are determined by the sets of invariant subspaces that are consistent with material symmetry. Eigenvalues always depend on the values of the elastic constants, but the eigenvectors are, in part, independent of these values. The structures of the spectral decompositions are presented for the classical symmetry groups of crystallography, and numerical results are presented for representative materials in each group. Spectral forms for the equilibrium equations, the acoustic tensor, and the stored energy function are also derived.

Introduction

If the stress tensor and strain tensor are regarded as vectors in an inner product space of suitable dimension, the elasticity tensor can be viewed as a linear transformation on that space. This allows a natural representation of the elasticity tensor in its spectral form, which permits a simple geometrical interpretation of the relationship between stress and strain regardless of the degree of anisotropy.

The restrictions placed on the form of the elasticity tensor by the symmetry theory of classical crystallography are reflected in the invariant structures of the spectral decompositions. The spectral forms are determined by the symmetry groups, and are independent of the values of the elastic constants in the sense that for every material in a particular symmetry group, the eigenspaces have the same pattern of dimension and basis.

Reduction to the spectral form enhances the process of comparison of different materials within the same symmetry group, and in some cases reveals similarities among materials in different symmetry groups. In particular there are striking similarities among the metals with cubic, hexagonal, and tetragonal symmetry. Other applications include alternative forms for the equations of equilibrium and motion, and the acoustic tensor.

The eigenvalues and eigenvectors of the elasticity tensor were first discussed by Kelvin (1856), and his results are summarized in the Encyclopedia Britanica (1878). More recently, Cowin and Mehrabadi (1987) and Mehrabadi and Cowin (1990) have determined the eigenvalues and eigenvectors for anisotropic elasticity. Ting (1987) has discussed the eigenvalue problem in connection with his study of the invariants of the elasticity tensor.

Contributed by the Applied Mechanics Division of THE AMERICAN SOCIETY OF MECHANICAL ENGINEERS for publication in the ASME JOURNAL OF APPLIED MECHANICS.

Discussion on this paper should be addressed to the Technical Editor, Professor Leon M. Keer, The Technological Institute, Northwestern University, Evanston, IL 60208, and will be accepted until four months after final publication of the paper itself in the ASME JOURNAL OF APPLIED MECHANICS.

Manuscript received by the ASME Applied Mechanics Division, July 5, 1991; final revision, Nov. 18, 1991. Associate Technical Editor: R. Abeyaratne.

In these previous works, the elasticity tensor has been reduced from a fourth-order symmetric linear transformation on the space of all 3 × 3 second-order tensors to a 6 × 6 second-order tensor. While this reduction is convenient for much of the theory, the 6 × 6 rotation tensor derived from a rotation of coordinates in the underlying three-dimensional space is somewhat awkward, and the explicit representation of the eigenvectors quite complicated. In this paper the elasticity tensor is treated as a fourth-order tensor, and the eigenspaces described on the basis of the applicable material symmetries. Numerical results are presented for a selection of materials with measured elastic constants, with representatives from each symmetry group included.

Classical Anisotropic Elasticity

The Elasticity Tensor. Let $\mathbf{S}$ and $\mathbf{E}$ represent the stress and strain tensors, respectively. The elasticity tensor $\mathbf{C}$ is a fourth-order tensor such that $\mathbf{S} = \mathbf{C}[\mathbf{E}]$. In component form, $S_{ij} = C_{ijkl}E_{kl}$, with the usual summation convention for cartesian tensors. From the symmetries of the stress and strain tensors, and the existence of a stored energy function, the symmetries of the elasticity tensor are $C_{ijkl} = C_{jikl} = C_{ijlk} = C_{klij}$.

Classical anisotropic elasticity is based on the point group morphology of crystalline materials, which can be described in terms of subgroups of the proper orthogonal group (Smith and Rivlin, 1958). Eleven such subgroups correspond to the 32 crystal classes, and a twelfth corresponds to transverse isotropy, (the symmetry of orthotropic materials is contained in the subgroups for the crystal classes). A symmetry group G of a material is defined as the set of all orthogonal tensors $\mathbf{Q}$ such that $\mathbf{Q}C[\mathbf{Q}^T\mathbf{E}\mathbf{Q}]\mathbf{Q}^T = C[\mathbf{E}]$ for every symmetric tensor $\mathbf{E}$. The twelve subgroups of the proper orthogonal group form seven symmetry groups that correspond to the crystal classes. In many references, the trigonal and tetragonal systems are each divided into two symmetry groups, but as has been shown (Federov, 1968), the distinctions are easily eliminated by an appropriate choice of coordinate axes. In order of increasing symmetry, the triclinic, monoclinic, orthorhombic, trigonal,

Copyright © 1992 by ASME
Downloaded 03 May 2010 to 171.66.16.247. Redistribution subject to ASME license or copyright; see http://www.asme.org/terms/Terms_Use.cfm

tetragonal, hexagonal, and isometric systems furnish seven distinct arrangements of the elastic constants for crystalline solids.

For ease of display of the components of the elasticity tensor, the indices in the stress and strain tensors can be taken in pairs and without regard for the order of the indices. In this case there are only six distinct stresses and strains, and the components of the elasticity tensor can be written as a 6×6 array. The components of the elasticity tensor are written below in this form, together with the point group designations for each system.

Triclinic 1, $\bar{1}$

$$\begin{matrix} C_{1111} & C_{1122} & C_{1133} & C_{1123} & C_{1113} & C_{1112} \\ & C_{2222} & C_{2233} & C_{2223} & C_{2213} & C_{2212} \\ & & C_{3333} & C_{3323} & C_{3313} & C_{3312} \\ & & & C_{2323} & C_{2313} & C_{2312} \\ & & & & C_{1313} & C_{1312} \\ & & & & & C_{1212} \end{matrix}$$

Monoclinic 2, m, $\frac{2}{m}$

$$\begin{matrix} C_{1111} & C_{1122} & C_{1133} & 0 & 0 & C_{1112} \\ & C_{2222} & C_{2233} & 0 & 0 & C_{2212} \\ & & C_{3333} & 0 & 0 & C_{3312} \\ & & & C_{2323} & C_{2313} & 0 \\ & & & & C_{1313} & 0 \\ & & & & & C_{1212} \end{matrix}$$

Orthorhombic 222, $mm2$, $\frac{222}{mmm}$

$$\begin{matrix} C_{1111} & C_{1122} & C_{1133} & 0 & 0 & 0 \\ & C_{2222} & C_{2233} & 0 & 0 & 0 \\ & & C_{3333} & 0 & 0 & 0 \\ & & & C_{2323} & 0 & 0 \\ & & & & C_{1313} & 0 \\ & & & & & C_{1212} \end{matrix}$$

Trigonal 3, $\bar{3}$, 32, $3m$, $\bar{3}\frac{2}{m}$

$$\begin{matrix} C_{1111} & C_{1122} & C_{1133} & 0 & -C_{1113} & 0 \\ & C_{1111} & C_{1133} & 0 & C_{1113} & 0 \\ & & C_{3333} & 0 & 0 & 0 \\ & & & C_{2323} & 0 & C_{1113} \\ & & & & C_{2323} & 0 \\ & & & & & 1/2(C_{1111} - C_{1122}) \end{matrix}$$

Tetragonal 4, $\bar{4}$, $\frac{4}{m}$, 422, $4mm$, $\bar{4}2m$, $\frac{422}{mmm}$

$$\begin{matrix} C_{1111} & C_{1122} & C_{1133} & 0 & 0 & 0 \\ & C_{1111} & C_{1133} & 0 & 0 & 0 \\ & & C_{3333} & 0 & 0 & 0 \\ & & & C_{2323} & 0 & 0 \\ & & & & C_{2323} & 0 \\ & & & & & C_{1212} \end{matrix}$$

Hexagonal 6, $\bar{6}$, $\frac{6}{m}$, 622, $\bar{6}m2$, $6mm$, $\frac{622}{mmm}$

$$\begin{matrix} C_{1111} & C_{1122} & C_{1133} & 0 & 0 & 0 \\ & C_{1111} & C_{1133} & 0 & 0 & 0 \\ & & C_{3333} & 0 & 0 & 0 \\ & & & C_{2323} & 0 & 0 \\ & & & & C_{2323} & 0 \\ & & & & & 1/2(C_{1111} - C_{1122}) \end{matrix}$$

Cubic 23, 432, $\frac{2}{m}\bar{3}$, $\bar{4}3m$, $\frac{4}{m}\bar{3}\frac{2}{m}$

$$\begin{matrix} C_{1111} & C_{1122} & C_{1122} & 0 & 0 & 0 \\ & C_{1111} & C_{1122} & 0 & 0 & 0 \\ & & C_{1111} & 0 & 0 & 0 \\ & & & C_{2323} & 0 & 0 \\ & & & & C_{2323} & 0 \\ & & & & & C_{2323} \end{matrix}$$

Spectral Decomposition

Geometrical Preliminaries. The space of all real 3×3 second-order tensors in a nine-dimensional inner product space with the product basis $\mathbf{e}_i \otimes \mathbf{e}_j$, where $\mathbf{e}_i$ form the basis of the underlying euclidean space R^3. In the product basis a tensor $\mathbf{S}$ takes the form $\mathbf{S} = S_{ij}\mathbf{e}_i \otimes \mathbf{e}_j$. The space of second-order tensors has a natural direct sum decomposition into the six-dimensional space of symmetric tensors, and the three-dimensional space of skew tensors. Orthonormal bases for these subspaces are as follows:

SPACE	BASIS
All second-order tensors (nine-dimensions)	$e_i \otimes e_j$
Symmetric second-order tensors (six-dimensions)	$e_i \otimes e_j$, $i = j$ $\sqrt{2}$ sym $e_i \otimes e_j$, $i \neq j$
Skew second-order tensors (three-dimensions)	$\sqrt{2}$ skw $e_i \otimes e_j$, $i \neq j$

The fourth-order elasticity tensor is a symmetric linear transformation on the space of second-order tensors, and has the space of skew tensors as its null space, thus the elasticity tensor maps the space of symmetric tensors onto itself.

Spectral Decompositions. The spectral decomposition of linear transformations has important applications in many physical theories. In its applications to linear transformations on finite-dimensional vector spaces, the spectral theorem allows the decomposition of a linear transformation into components acting on lower dimensional spaces, often permitting interpretation of the behavior of complicated systems in terms of the results for simpler systems. (For a more complete treatment of spectral decompositions see Halmos (1974).)

Eigenvalues and Eigenspaces. Let $\mathbf{A}$ be a real, symmetric linear transformation on a finite-dimensional inner product space V, and let λ_k be the distinct eigenvalues of $\mathbf{A}$, that is, $\mathbf{A}\mathbf{n}_k = \lambda_k\mathbf{n}_k$. The mutually orthogonal subspaces $V(\lambda_k)$ of V defined by $V(\lambda_k) = \{\mathbf{x} \in V | \mathbf{A}\mathbf{x} = \lambda_k\mathbf{x}\}$, and called the eigenspaces corresponding to λ_k, allow a direct sum representation of V as: $V = V(\lambda_1) \oplus V(\lambda_2) \oplus \ldots \oplus V(\lambda_n)$.

If $\mathbf{n}_i$ is the eigenvector corresponding to an isolated eigenvalue λ_i, then $V(\lambda_i)$ is a one-dimensional vector space spanned by $\mathbf{n}_i$. If $\mathbf{n}_{j1}, \mathbf{n}_{j2}, \ldots, \mathbf{n}_{jr}$ are mutually orthogonal eigenvectors corresponding to a repeated eigenvalue of multiplicity r, then $V(\lambda_j)$ is an r-dimensional vector space spanned by $\mathbf{n}_{j1}, \mathbf{n}_{j2}, \ldots, \mathbf{n}_{jr}$.

Downloaded 03 May 2010 to 171.66.16.247. Redistribution subject to ASME license or copyright; see http://www.asme.org/terms/Terms_Use.cfm

Spectral Decomposition Theorem. Let $\mathbf{u} = \sum_{k=1}^{N} \alpha_k \mathbf{n}_k$ be an arbitrary vector, where $\mathbf{n}_k$ are the N mutually orthogonal eigenvectors of the symmetric linear transformation $\mathbf{A}$ on an N-dimensional space, then

$$\mathbf{Au} = \sum_{k=1}^{N} \alpha_k \mathbf{A}\mathbf{n}_k = \sum_{k=1}^{N} \alpha_k \lambda_k \mathbf{n}_k.$$

The projection $\mathbf{n}_k \otimes \mathbf{n}_k$ takes $\mathbf{u}$ into $\alpha_k \mathbf{n}_k$, i.e., $\mathbf{n}_k \otimes \mathbf{n}_k \mathbf{u} = (\mathbf{u} \cdot \mathbf{n}_k)\mathbf{n}_k = \alpha_k \mathbf{n}_k$, thus $\mathbf{Au} = \sum_{k=1}^{N} \alpha_k \lambda_k \mathbf{n}_k = \sum_{k=1}^{N} \lambda_k \mathbf{n}_k \otimes \mathbf{n}_k \mathbf{u}$, which implies the spectral decomposition:

$$\mathbf{A} = \sum_{k=1}^{N} \lambda_k \mathbf{n}_k \otimes \mathbf{n}_k. \tag{1}$$

Application to the Elasticity Tensor. Although the stress and strain tensors of elasticity are normally written as square arrays, they may also be considered nine-dimensional vectors, and written as a string, e.g., $\epsilon = \{\epsilon_{11}, \epsilon_{22}, \epsilon_{33}, \epsilon_{23}, \epsilon_{13}, \epsilon_{12}, \epsilon_{32}, \epsilon_{31}, \epsilon_{21}\}$ for the strain tensor. In this notation, C can be regarded as a 9×9 matrix. Numerical extraction of the eigenvalues and eigenvectors is a straightforward process, and the eigenvectors are easily rewritten as standard 3×3 arrays. Since the elasticity tensor is symmetric, its nullity is three, so that there are three zero eigenvalues, each corresponding to a skew eigenvector. When restricted to the space of symmetric tensors, the elasticity tensor is positive definite, so that the remaining eigenvalues are real and positive.

Let $\mathbf{N}_k$ designate the symmetric eigenvectors of $\mathbf{C}$, defined by $\mathbf{C}[\mathbf{N}_k] = \lambda_k \mathbf{N}_k$, then the spectral form of the elasticity tensor becomes

$$\mathbf{C} = \sum_{k=1}^{6} \lambda_k \mathbf{N}_k \otimes \mathbf{N}_k. \tag{2}$$

This expression holds even if the eigenvalues are not all distinct, since an orthonormal basis can always be found for higher dimensional eigenspaces.

Since $\mathbf{C}$ is real symmetric, the eigenspaces are orthogonal, and since an orthonormal basis can always be selected for each eigenspace (Bowen and Wang, 1976), it follows that an orthonormal set of six eigenvectors can be constructed even when there are eigenvalues with multiplicity greater than one. For example, the eigenspace associated with an eigenvalue of multiplicity p is a p-dimensional space that is spanned by p linearly independent vectors. These vectors can be selected to form an orthonormal basis and designated as eigenvectors. Since the eigenspace defined by this basis is orthogonal to all other eigenspaces, these eigenvectors are orthogonal to every vector in any other eigenspace.

Invariant Subspaces

An important property of spectral decompositions is the invariance of the eigenspaces under symmetry operations. If $\mathbf{Q}$ is a member of the symmetry group of $\mathbf{C}$, then for the eigenvalue λ_k both $\mathbf{N}_k$ and $Q\mathbf{N}_k\mathbf{Q}^T$ are eigenvectors. If λ_k is an isolated eigenvalue, then the eigenspace is a one-dimensional vector space. Since they are both unit vectors that span the same one-dimensional space, it follows that $\mathbf{N}_k = \pm Q\mathbf{N}_k\mathbf{Q}^T$. If λ_k is a repeated eigenvalue of multiplicity p, then the associated p-dimensional eigenspace is spanned by both $\mathbf{N}_1, \mathbf{N}_2, \ldots, \mathbf{N}_p$ and $\mathbf{QN}_1\mathbf{Q}^T, \mathbf{QN}_2\mathbf{Q}^T, \ldots, \mathbf{QN}_p\mathbf{Q}^T$. Both sets of eigenvectors span the same vector space, thus $\mathbf{QN}_k\mathbf{Q}^T = \alpha_{kl}\mathbf{N}_l$. From the preservation of the inner product, i.e., $\mathbf{QMQ}^T \cdot \mathbf{QNQ}^T = \mathbf{M} \cdot \mathbf{N}$, it follows that $\alpha_{kl}\alpha_{ml} = \delta_{km}$. The coefficients α_{kl} can be regarded as the elements of a $p \times p$ orthogonal matrix, so that $\alpha_{kl}\alpha_{km} = \delta_{lm}$.

Invariants of the Space of Second-Order Tensors. The eigenspaces of the elasticity tensor must have the same symmetries as the elasticity tensor, thus the structure of the spectral decomposition is determined by the subspaces of the space of second-order tensors that are invariant under rotational symmetry operations. A subspace of the space of second-order tensors is a p-invariant subspace if it is spanned by the tensors $\mathbf{A}_1, \mathbf{A}_2, \ldots, \mathbf{A}_p$ with the property $\mathbf{QAQ}^T = \pm\alpha_{kl}\mathbf{A}_l$. As before, the coefficients α_{kl} can be regarded as the elements of a $p \times p$ orthogonal matrix. An invariant subspace is proper when the plus sign holds, and improper for the minus sign. Improper invariants alternate sign through the cycle of $\mathbf{Q}$, so that they are possible only for even rotation axes.

For a single symmetry axis, the most important invariant subspaces in the spectral decomposition of the elasticity tensor are one-dimensional and two-dimensional subspaces. For a one-dimensional invariant subspace spanned by $\mathbf{N}$, $\mathbf{QNQ}^T = \pm\mathbf{N}$. For two-dimensional invariants, the matrix of the α_{kl} takes the form

$$\begin{bmatrix} \cos\theta & \sin\theta \\ -\sin\theta & \cos\theta \end{bmatrix},$$

and since $[\alpha]^n = \mathbf{I}$, $\theta = 2r\pi/n$, where $r = 1, 2, \ldots$ is the order of the invariant subspace. All of the invariant subspaces corresponding to symmetry about a single axis, except for transverse isotropy, are first-order invariant subspaces determined by $r = 1$. For transverse isotropy, there is a two-dimensional second-order invariant subspace determined by $r = 2$.

Induced Axis of Rotation. A rotation about an axis in the underlying euclidean space induces a rotation in the space of all symmetric tensors. The one-dimensional subspaces of the space of symmetric tensors that remain invariant for all rotations about some fixed axis in R^3 span a subspace that is defined to be the induced axis of rotation.

For every rotation about an axis $\mathbf{e}$, the tensors $\mathbf{I}$ and $\mathbf{e} \otimes \mathbf{e}$ remain invariant. Every linear combination of these tensors is also invariant, so that $\mathbf{I}$ and $\mathbf{e} \otimes \mathbf{e}$ span a two-dimensional subspace that is the induced axis of rotation. For further work an orthonormal basis is preferable, and $\mathbf{e} \otimes \mathbf{e}$ and $1/\sqrt{2}(\mathbf{I} - \mathbf{e} \otimes \mathbf{e})$ will be used for this purpose. Tensors in the induced axis of rotation are proper one-dimensional invariants.

Every tensor can be decomposed into a component in the direction of the induced axis of rotation and a component normal to the induced axis. Let $\mathbf{A}_E$ be the component of $\mathbf{A}$ in the direction of the induced axis of rotation, and $\mathbf{A}_N$ its orthogonal compliment, then $\mathbf{A} = \mathbf{A}_E + \mathbf{A}_N$, with $\mathbf{A}_E = (\mathbf{A} \cdot \mathbf{I})\mathbf{I} + 1/2[\mathbf{A} \cdot (\mathbf{I} - \mathbf{e} \otimes \mathbf{e})](\mathbf{I} - \mathbf{e} \otimes \mathbf{e})$. For x_3, the axis of rotation, and with $A' = 1/2(A_{11} - A_{22})$, $\mathbf{A}_N$ becomes

$$\mathbf{A}_N = \begin{bmatrix} A' & A_{12} & A_{13} \\ A_{12} & -A' & A_{23} \\ A_{13} & A_{23} & 0 \end{bmatrix}. \tag{3}$$

All invariant subspaces, other than the induced axis of rotation, are spanned by tensors of the form of $\mathbf{A}_N$, except in the case of a single 2-axis in which the proper one-dimensional invariants are linear combinations of tensors of the form of $\mathbf{A}_N$ and tensors in the induced axis of rotation.

One-Dimensional Invariant Subspaces. For a proper one-dimensional invariant subspace normal to the induced axis of rotation, $\mathbf{QA}_N\mathbf{Q}^T = \mathbf{A}_N$, $\mathbf{Q}(\mathbf{QA}_N\mathbf{Q}^T)\mathbf{Q}^T = \mathbf{A}_N$ and so forth throughout the cycle of $\mathbf{Q}$. For an improper invariant, $\mathbf{QA}_N\mathbf{Q}^T = -\mathbf{A}_N$, $\mathbf{Q}(\mathbf{QA}_N\mathbf{Q}^T)\mathbf{Q}^T = +\mathbf{A}_N$, with the signs alternating throughout the cycle of $\mathbf{Q}$.

Proper Invariant Subspaces. The condition $\mathbf{QA}_N\mathbf{Q}^T = \mathbf{A}_N$ leads to two pairs of homogeneous equations:

Downloaded 03 May 2010 to 171.66.16.247. Redistribution subject to ASME license or copyright; see http://www.asme.org/terms/Terms_Use.cfm

$$(\cos^2\theta - \sin^2\theta - 1)A' + 2\sin\theta\cos\theta A_{12} = 0 \quad (4a)$$
$$-2\sin\theta\cos\theta A' + (\cos^2\theta - \sin^2\theta - 1)A_{12} = 0$$
$$(\cos\theta - 1)A_{13} + \sin\theta A_{23} = 0 \quad (4b)$$
$$-\sin\theta A_{13} + (\cos\theta - 1)A_{23} = 0.$$

For (4a), the determinant reduces to $\sin^2\theta = 0$, so that $\theta = 0, \pi, 2\pi$. With this condition, A' and A_{12} can be specified arbitrarily, thus there are two proper one-dimensional invariant subspaces, consistent with a 2-axis, and spanned by the orthogonal tensors:

$$\begin{bmatrix} A' & A_{12} & 0 \\ A_{12} & -A' & 0 \\ 0 & 0 & 0 \end{bmatrix} \begin{bmatrix} -A_{12} & A' & 0 \\ A' & A_{12} & 0 \\ 0 & 0 & 0 \end{bmatrix}. \quad (5)$$

Every linear combination of (5) and a tensor in the induced axis of rotation also spans a proper one-dimensional invariant subspace, so that the most general form for the basis of a proper one-dimensional invariant subspace consistent with a 2-axis is

$$\begin{bmatrix} A_{11} & A_{12} & 0 \\ A_{12} & A_{22} & 0 \\ 0 & 0 & A_{33} \end{bmatrix}. \quad (6)$$

There are four proper one-dimensional invariant subspaces for a single 2-axis, each spanned by a tensor of the form of Eq. (6).

From (4b), the determinant reduces to $\cos\theta = 1$, so that there are no proper invariant subspaces consistent with this condition.

Improper Invariant Subspaces. Following the same procedure, but with $\mathbf{Q}\mathbf{A}_N\mathbf{Q}^T = -\mathbf{A}_N$, the following equations result:

$$(\cos^2\theta - \sin^2\theta + 1)A' + 2\sin\theta\cos\theta A_{12} = 0 \quad (7a)$$
$$-2\sin\theta\cos\theta A' + (\cos^2\theta - \sin^2\theta + 1)A_{12} = 0$$
$$(\cos\theta + 1)A_{13} + \sin\theta A_{23} = 0 \quad (7b)$$
$$-\sin\theta A_{13} + (\cos\theta + 1)A_{23} = 0.$$

From (7a), $\cos^2\theta = 0$, so that $\theta = \pi/2, 3\pi/2$ are solutions. Again, A' and A_{12} can be specified arbitrarily. Combining this with the results for proper invariants, two improper one-dimensional invariant subspaces, consistent with a 4-axis, are determined. Bases for these subspaces are as given in Eq. (5).

From (7b), $\cos\theta = -1$. Here, A_{13} and A_{23} can be specified arbitrarily so that there are two improper invariant subspaces, consistent with a 2-axis, which are spanned by

$$\begin{bmatrix} 0 & 0 & A_{13} \\ 0 & 0 & A_{23} \\ A_{13} & A_{23} & 0 \end{bmatrix} \begin{bmatrix} 0 & 0 & A_{23} \\ 0 & 0 & -A_{13} \\ A_{23} & -A_{13} & 0 \end{bmatrix}. \quad (8)$$

Two-Dimensional Invariant Subspaces. Let $\mathbf{A}$ and $\mathbf{B}$ form an orthonormal basis for a first-order two-dimensional invariant subspace with $\theta = 2\pi/n$ for an n-axis, then

$$\mathbf{Q}\mathbf{A}\mathbf{Q}^T = \cos\theta\mathbf{A} + \sin\theta\mathbf{B} \quad (9a)$$
$$\mathbf{Q}\mathbf{B}\mathbf{Q}^T = -\sin\theta\mathbf{A} + \cos\theta\mathbf{B}$$

for a proper invariant subspace, and

$$\mathbf{Q}\mathbf{A}\mathbf{Q}^T = -\cos\theta\mathbf{A} - \sin\theta\mathbf{B} \quad (9b)$$
$$\mathbf{Q}\mathbf{B}\mathbf{Q}^T = \sin\theta\mathbf{A} - \cos\theta\mathbf{B}$$

for an improper invariant subspace.

Since $\mathbf{A}$ and $\mathbf{B}$ are orthogonal to the induced axis of rotation, they take the form of (3).

Proper Two-Dimensional Invariant Subspaces. Upon expansion, (9a) can be separated into two sets of equations, one set involving the elements of $\mathbf{A}$ and $\mathbf{B}$ in the 11, 12, and 22 positions, and the other involving the elements in the 13 and 23 positions. These equations take the form

$$\begin{bmatrix} \cos^2\theta - \sin^2\theta - \cos\theta & 2\sin\theta\cos\theta & -\sin\theta & 0 \\ -2\sin\theta\cos\theta & \cos^2\theta - \sin^2\theta - \cos\theta & 0 & -\sin\theta \\ \sin\theta & 0 & \cos^2\theta - \sin^2\theta - \cos\theta & 2\sin\theta\cos\theta \\ 0 & \sin\theta & -2\sin\theta\cos\theta & \cos^2\theta - \sin^2\theta - \cos\theta \end{bmatrix} \times \begin{Bmatrix} A' \\ A_{12} \\ B' \\ B_{12} \end{Bmatrix} = 0 \quad (10a)$$

$$\begin{bmatrix} 0 & \sin\theta & -\sin\theta & 0 \\ -\sin\theta & 0 & 0 & -\sin\theta \\ \sin\theta & 0 & 0 & \sin\theta \\ 0 & \sin\theta & \sin\theta & 0 \end{bmatrix} \begin{Bmatrix} A_{13} \\ A_{23} \\ B_{13} \\ B_{23} \end{Bmatrix} = 0. \quad (10b)$$

The second of these equations reduces to

$$(A_{13} + B_{23})\sin\theta = 0$$
$$(A_{23} - B_{13})\sin\theta = 0$$

so that either $\theta = 0, \pi, 2\pi$, with $A_{13} + B_{23}$ and $A_{23} - B_{13}$ arbitrary, or $A_{13} = -B_{23}$ and $A_{23} = B_{13}$ for every value of θ. The first solution does not by itself correspond to a two-dimensional invariant subspace, since $\mathbf{A}$ and $\mathbf{B}$ are simply mapped into their negatives (the conditions for two improper one-dimensional invariants); however, this solution is important in the determination of improper two-dimensional invariants. The second solution produces a proper two-dimensional invariant subspace consistent with an n-axis spanned by

$$\begin{bmatrix} 0 & 0 & A_{13} \\ 0 & 0 & A_{23} \\ A_{13} & A_{23} & 0 \end{bmatrix} \begin{bmatrix} 0 & 0 & A_{23} \\ 0 & 0 & -A_{13} \\ A_{23} & -A_{13} & 0 \end{bmatrix}. \quad (11)$$

The determinant of the first set of equations can be factored into $(\cos\theta - 1)^2(2\cos\theta + 1)^2 = 0$, which produces the solutions $\theta = 0, 2\pi/3, 4\pi/3, 2\pi$. Substitution then produces the conditions $A_{12} = -B'$ and $B_{12} = A'$, giving a proper invariant subspace spanned by

$$\begin{bmatrix} A' & A_{12} & 0 \\ A_{12} & -A' & 0 \\ 0 & 0 & 0 \end{bmatrix} \begin{bmatrix} -A_{12} & A' & 0 \\ A' & A_{12} & 0 \\ 0 & 0 & 0 \end{bmatrix}. \quad (12)$$

Since (11) defines a proper two-dimensional invariant subspace for all θ, it can be combined with (12) to produce the most general basis for a proper two-dimensional invariant subspace consistent with a 3-axis, as given here:

$$\begin{bmatrix} A' & A_{12} & A_{13} \\ A_{12} & -A' & A_{23} \\ A_{13} & A_{23} & 0 \end{bmatrix} \begin{bmatrix} -A_{12} & A' & A_{23} \\ A' & A_{12} & -A_{13} \\ A_{23} & -A_{13} & 0 \end{bmatrix}. \quad (13)$$

Improper Two-Dimensional Invariant Subspaces. The procedure outlined above can be applied to the improper two-

Downloaded 03 May 2010 to 171.66.16.247. Redistribution subject to ASME license or copyright; see http://www.asme.org/terms/Terms_Use.cfm

dimensional invariant subspaces. In (10a), the $-\cos\theta$ term in the diagonal terms changes sign, and in (10b), the diagonal terms change from 0 to $-\cos\theta$. The second set of equations is satisfied for $\cos^2\theta = 0$, so that for $\theta = \pi/2, 3\pi/2$ the following equations hold:

$$(A_{13}-B_{23})\sin\theta=0$$
$$(A_{23}+B_{13})\sin\theta=0$$

Since $\sin\theta \neq 0$, $B_{13} = -A_{23}$ and $B_{23} = A_{13}$. This can be combined with the result for $\theta = \pi$ for proper invariants to produce a two-dimensional improper invariant subspace consistent with a 4-axis that is spanned by

$$\begin{bmatrix} 0 & 0 & A_{13} \\ 0 & 0 & A_{23} \\ A_{13} & A_{23} & 0 \end{bmatrix} \begin{bmatrix} 0 & 0 & -A_{23} \\ 0 & 0 & A_{13} \\ -A_{23} & A_{13} & 0 \end{bmatrix}. \tag{14}$$

In the first set of equations, the determinant can be factored into $(\cos\theta + 1)^2(2\cos\theta - 1)^2 = 0$, so that $\theta = \pi/3, \pi, 5\pi/3$. This solution requires that $A_{12} = -B'$ and $B_{12} = A'$. This result can be combined with the preceding result for proper invariants to produce a two-dimensional improper invariant consistent with a 6-axis, and spanned by

$$\begin{bmatrix} A' & A_{12} & 0 \\ A_{12} & -A' & 0 \\ 0 & 0 & 0 \end{bmatrix} \begin{bmatrix} -A_{12} & A' & 0 \\ A' & A_{12} & 0 \\ 0 & 0 & 0 \end{bmatrix}. \tag{15}$$

Higher Dimensional Invariant Subspaces. For a rotation about x_3, there is no interaction between the elements in the 11, 12, 22 positions and the elements in the 13, 23 positions so that for computational purposes, $\mathbf{A}_N$ can be separated into a two-dimensional tensor and a two-dimensional vector, and $\mathbf{Q}$ is reduced to a two-dimensional orthogonal tensor:

$$\mathbf{A}_N' = \begin{bmatrix} 1/2(A_{11}-A_{22}) & A_{12} \\ A_{12} & -1/2(A_{11}-A_{22}) \end{bmatrix} \quad \mathbf{A}_N'' = \begin{Bmatrix} A_{12} \\ A_{23} \end{Bmatrix}$$

$$\mathbf{Q} = \begin{bmatrix} \cos\theta & \sin\theta \\ -\sin\theta & \cos\theta \end{bmatrix}. \tag{16}$$

The conditions for a p-dimensional invariant subspace become $\mathbf{QA}_k'\mathbf{Q}^T = \alpha_{kl}\mathbf{A}_l'$, $\mathbf{QA}_k'' = \beta_{kl}\mathbf{A}_l''$. Since both $\mathbf{A}_l'$ and $\mathbf{A}_l''$ are two-dimensional vectors, there are no invariant subspaces of dimension higher than two when the structure of the elasticity tensor is determined by a single axis of symmetry.

Higher Order Invariant Subspaces. The only higher order invariant subspace of interest is a second-order two-dimensional proper invariant subspace characterized by

$$\mathbf{QAQ}^T = \cos2\theta\mathbf{A} + \sin2\theta\mathbf{B}$$
$$\mathbf{QBQ}^T = -\sin2\theta\mathbf{A} + \cos2\theta\mathbf{B}.$$

Under this condition, (10a) becomes

$$\begin{bmatrix} 0 & \sin2\theta & -\sin2\theta & 0 \\ -\sin2\theta & 0 & 0 & -\sin2\theta \\ \sin2\theta & 0 & 0 & \sin2\theta \\ 0 & \sin2\theta & -\sin2\theta & 0 \end{bmatrix} \begin{Bmatrix} A' \\ A_{12} \\ B' \\ B_{12} \end{Bmatrix} = 0. \tag{17}$$

Thus, $[A_{12} - B']\sin2\theta = 0$ and $[A' + B_{12}]\sin2\theta = 0$, which define a proper invariant subspace spanned by (11) that is valid for every θ and is appropriate to a transversely isotropic material.

Structure of the Spectral Decompositions

Just as the various symmetry groups give distinctive structures to the elasticity tensor, the invariance of the eigenspaces gives distinctive structures to the spectral decompositions. A single rotation axis is sufficient to determine the structure of the elasticity tensors for triclinic, monoclinic, trigonal, tetragonal, and hexagonal systems and transverse isotropy.[1] Thus, the eigenspaces for these cases correspond to the invariant subspaces determined for a single rotation axis.

Triclinic. The symmetry of the triclinic system imposes no restrictions on the spectral decomposition. Any one-dimensional subspace of the space of symmetric tensors is invariant under this symmetry, so that the spectral decomposition for the triclinic system consists of six one-dimensional eigenspaces and six isolated eigenvalues, all determined by the relative values of the elastic constants.

Monoclinic. The invariant subspaces consistent with a 2-axis in the x_3-direction are four proper one-dimensional invariants of the form given in (6) and the two improper one-dimensional invariants given in (8). Thus, these constitute the eigenspaces for the monoclinic system.

In the determination of the orientation of the coordinate axes for the monoclinic system, the x_3-axis is chosen to correspond to the 2-axis. Symmetry alone does not indicate a preferred orientation for the x_1 and x_2-axes.

Trigonal. Invariant subspaces consistent with a 3-axis in the x_3-direction are two one-dimensional invariant subspaces in the induced axis of rotation and two two-dimensional proper invariant subspaces spanned by tensors of the form of (13). Since all the subspaces are orthogonal, their bases take the form

$$k_1 \begin{bmatrix} 0 & 0 & 0 \\ 0 & 0 & 0 \\ 0 & 0 & 1 \end{bmatrix} + k_2/\sqrt{2} \begin{bmatrix} 1 & 0 & 0 \\ 0 & 1 & 0 \\ 0 & 0 & 0 \end{bmatrix} \tag{18a}$$

$$k_2 \begin{bmatrix} 0 & 0 & 0 \\ 0 & 0 & 0 \\ 0 & 0 & 1 \end{bmatrix} - k_1/\sqrt{2} \begin{bmatrix} 1 & 0 & 0 \\ 0 & 1 & 0 \\ 0 & 0 & 0 \end{bmatrix} \tag{18b}$$

$$\begin{bmatrix} A' & A_{12} & A_{13} \\ A_{12} & -A' & A_{23} \\ A_{13} & A_{23} & 0 \end{bmatrix} \begin{bmatrix} -A_{12} & A' & A_{23} \\ A' & A_{12} & -A_{13} \\ A_{23} & -A_{13} & 0 \end{bmatrix} \tag{18c}$$

$$\begin{bmatrix} A_{13} & A_{23} & -A' \\ A_{23} & -A_{13} & -A_{12} \\ -A' & -A_{12} & 0 \end{bmatrix} \begin{bmatrix} -A_{23} & A_{13} & A_{12} \\ A_{13} & A_{23} & A' \\ A_{12} & A' & 0 \end{bmatrix}. \tag{18d}$$

The bases of the two two-dimensional invariant subspaces can be simplified if coordinates are chosen such that $C_{1123} = 0$. Let λ_1 and λ_2 be the eigenvalues for the two-dimensional invariant subspaces. Then for $C_{1123} = 0$,

$$(\lambda_1-\lambda_2)[1/2(A_{11}-A_{22})A_{23}+A_{12}A_{13}]=0.$$

In this case C_{1113} is negative so that

$$(\lambda_1-\lambda_2)[1/2(A_{11}-A_{22})A_{13}-A_{12}A_{23}]<0.$$

For $\lambda_2 > \lambda_1$, $1/2(A_{11} - A_{22})A_{13} - A_{12}A_{23} > 0$.

Let $1/2(A_{11} - A_{22}) = x$, $A_{13} = y$, $A_{23} = a$, $A_{12} = b$. Then the two conditions take the form

$$ax+by=0$$
$$xy-ab>0,$$

[1] Even though the symmetry groups for the trigonal, tetragonal, and hexagonal systems contain elements involving additional symmetry axes, these do not impose additional restrictions on the elasticity tensor above those obtained from a single 3, 4, or 6-axis.

Downloaded 03 May 2010 to 171.66.16.247. Redistribution subject to ASME license or copyright; see http://www.asme.org/terms/Terms_Use.cfm

which only have a solution if $a = b = 0$. Thus $A_{12} = A_{23} = 0$, and the bases for the two-dimensional invariant subspaces become

$$\begin{bmatrix} A' & 0 & A_{13} \\ 0 & -A' & 0 \\ A_{13} & 0 & 0 \end{bmatrix} \begin{bmatrix} 0 & A' & 0 \\ A' & 0 & -A_{13} \\ 0 & -A_{13} & 0 \end{bmatrix} \tag{19a}$$

$$\begin{bmatrix} A_{13} & 0 & -A' \\ 0 & -A_{13} & 0 \\ -A' & 0 & 0 \end{bmatrix} \begin{bmatrix} 0 & A_{13} & 0 \\ A_{13} & 0 & A' \\ 0 & A' & 0 \end{bmatrix}. \tag{19b}$$

The invariant subspaces (18*a*), (18*b*), (19*a*), (19*b*) constitute the eigenspaces for trigonal system when coordinates have been chosen such that $C_{1123} = 0$.

Tetragonal. Invariant subspaces consistent with a 4-axis in the x_3-direction are two one-dimensional invariant subspaces in the induced axis of rotation, two improper one-dimensional subspaces of the form of (5), and a proper two-dimensional subspace of the form of (11). If coordinates are chosen such that $C_{1112} = 0$, $A'A_{12} = 0$, and since $C_{1323} = 0$, $A_{13}A_{23} = 0$.

Selecting $A_{12} = A_{23} = 0$, the bases for the eigenspaces for the tetragonal system become

$$k_1 \begin{bmatrix} 0 & 0 & 0 \\ 0 & 0 & 0 \\ 0 & 0 & 1 \end{bmatrix} + k_2/\sqrt{2} \begin{bmatrix} 1 & 0 & 0 \\ 0 & 1 & 0 \\ 0 & 0 & 0 \end{bmatrix} \tag{20a}$$

$$k_2 \begin{bmatrix} 0 & 0 & 0 \\ 0 & 0 & 0 \\ 0 & 0 & 1 \end{bmatrix} - k_1/\sqrt{2} \begin{bmatrix} 1 & 0 & 0 \\ 0 & 1 & 0 \\ 0 & 0 & 0 \end{bmatrix} \tag{20b}$$

$$1/\sqrt{2} \begin{bmatrix} -1 & 0 & 0 \\ 0 & 1 & 0 \\ 0 & 0 & 0 \end{bmatrix} \tag{20c}$$

$$1/\sqrt{2} \begin{bmatrix} 0 & 1 & 0 \\ 1 & 0 & 0 \\ 0 & 0 & 0 \end{bmatrix} \tag{20d}$$

$$1/\sqrt{2} \begin{bmatrix} 0 & 0 & 1 \\ 0 & 0 & 0 \\ 1 & 0 & 0 \end{bmatrix} \quad -1/\sqrt{2} \begin{bmatrix} 0 & 0 & 0 \\ 0 & 0 & 1 \\ 0 & 1 & 0 \end{bmatrix}. \tag{20e}$$

Hexagonal. Invariant subspaces consistent with a 6-axis in the x_3-direction are two one-dimensional invariant subspaces in the induced axis of rotation, a proper two-dimensional invariant subspace of the form of (11), and an improper two-dimensional subspace of the form of (15). Since $C_{1323} = 0$, $A_{13}A_{23} = 0$. The bases of the two-dimensional improper invariant subspace are eigenvectors of the elasticity tensor only if either $A' = 0$, or $A_{12} = 0$. Selecting $A_{12} = A_{13} = 0$, the bases of the eigenspaces for the hexagonal system become

$$k_1 \begin{bmatrix} 0 & 0 & 0 \\ 0 & 0 & 0 \\ 0 & 0 & 1 \end{bmatrix} + k_2/\sqrt{2} \begin{bmatrix} 1 & 0 & 0 \\ 0 & 1 & 0 \\ 0 & 0 & 0 \end{bmatrix} \tag{21a}$$

$$k_2 \begin{bmatrix} 0 & 0 & 0 \\ 0 & 0 & 0 \\ 0 & 0 & 1 \end{bmatrix} - k_1/\sqrt{2} \begin{bmatrix} 1 & 0 & 0 \\ 0 & 1 & 0 \\ 0 & 0 & 0 \end{bmatrix} \tag{21b}$$

$$1/\sqrt{2} \begin{bmatrix} -1 & 0 & 0 \\ 0 & 1 & 0 \\ 0 & 0 & 0 \end{bmatrix} \quad 1/\sqrt{2} \begin{bmatrix} 0 & 1 & 0 \\ 1 & 0 & 0 \\ 0 & 0 & 0 \end{bmatrix} \tag{21c}$$

$$1/\sqrt{2} \begin{bmatrix} 0 & 0 & 1 \\ 0 & 0 & 0 \\ 1 & 0 & 0 \end{bmatrix} \quad 1/\sqrt{2} \begin{bmatrix} 0 & 0 & 0 \\ 0 & 0 & 1 \\ 0 & 1 & 0 \end{bmatrix}. \tag{21d}$$

Transverse Isotropy. The elasticity tensor for transverse isotropy is identical to that for hexagonal symmetry, and the spectral decomposition has the same form; however, the two-dimensional improper invariant subspace of hexagonal symmetry becomes a second-order invariant subspace in transverse isotropy, although the basis is unchanged. Thus, the spectral decompositions are in fact different, despite the appearance to the contrary.

Combined Symmetry Operations. The symmetries of the orthorhombic and cubic systems require the consideration of combined symmetry operations. In either case, any of the symmetry classes is satisfactory for the determination of the structure of the spectral decomposition. For simplicity, class 222 has been selected for the orthorhombic system and class 23 was selected for the cubic system. Isotropy, in which every direction is an axis of full rotational symmetry, is also included under combined symmetry operations. It should be noted that the invariant subspaces for combined symmetry operations must be invariant for each symmetry operation.

Orthorhombic. For class 222 the coordinate axes are all equivalent, and the three associated induced axes of rotation are not the same; however, the three tensors $\mathbf{e}_1 \otimes \mathbf{e}_1$, $\mathbf{e}_2 \otimes \mathbf{e}_2$, $\mathbf{e}_3 \otimes \mathbf{e}_3$ remain as proper one-dimensional invariants. Any linear combination of these three tensors also spans a proper one-dimensional invariant subspace.

The remaining invariant subspaces are easily determined by a direct approach. The three tensors $\text{sym}\mathbf{e}_1 \otimes \mathbf{e}_2$, $\text{sym}\mathbf{e}_1 \otimes \mathbf{e}_3$, $\text{sym}\mathbf{e}_2 \otimes \mathbf{e}_3$ are each proper one-dimensional invariants with respect to a rotation of π about one of the coordinate axes, and improper one-dimensional invariants with respect to a rotation of π about the other two coordinate axes; thus, each is a proper one-dimensional invariant when all three symmetry operations are considered. As before, any linear combination of these three tensors also spans a one-dimensional invariant subspace; however, when the standard coordinate orientation is chosen for orthorhombic symmetry, the three tensors given above each span a one-dimensional invariant subspace. The resulting structure of the spectral decomposition for the orthorhombic system consists of six proper one-dimensional eigenspaces given as follows:

$$k_{j1} \begin{bmatrix} 1 & 0 & 0 \\ 0 & 0 & 0 \\ 0 & 0 & 0 \end{bmatrix} + k_{j2} \begin{bmatrix} 0 & 0 & 0 \\ 0 & 1 & 0 \\ 0 & 0 & 0 \end{bmatrix} + k_{j3} \begin{bmatrix} 0 & 0 & 0 \\ 0 & 0 & 0 \\ 0 & 0 & 1 \end{bmatrix} \quad j = 1,2,3$$

$$1/\sqrt{2} \begin{bmatrix} 0 & 0 & 1 \\ 0 & 0 & 0 \\ 1 & 0 & 0 \end{bmatrix} \quad 1/\sqrt{2} \begin{bmatrix} 0 & 0 & 0 \\ 0 & 0 & 1 \\ 0 & 1 & 0 \end{bmatrix} \quad 1/\sqrt{2} \begin{bmatrix} 0 & 1 & 0 \\ 1 & 0 & 0 \\ 0 & 0 & 0 \end{bmatrix}. \tag{22}$$

Cubic. For cubic symmetry, the bases of the induced axes of rotation are conveniently taken in the form $1/\sqrt{3}\ \mathbf{I}$, $1/\sqrt{2}\ (\mathbf{I} - \mathbf{e} \otimes \mathbf{e})$ where $\mathbf{e}$ is in the direction of an axis of symmetry in the underlying space. It is clear that the only one-dimensional invariant subspace consistent with all the symmetry axes is $1/\sqrt{3}\ \mathbf{I}$. All other invariant subspaces are orthogonal to $\mathbf{I}$, so their bases take the form

Downloaded 03 May 2010 to 171.66.16.247. Redistribution subject to ASME license or copyright; see http://www.asme.org/terms/Terms_Use.cfm

$$\mathbf{A}_N = \begin{bmatrix} A_{11}-A' & A_{12} & A_{13} \\ A_{12} & A_{22}-A' & A_{23} \\ A_{13} & A_{23} & A_{33}-A' \end{bmatrix}, \tag{23}$$

where $A' = 1/3(A_{11} + A_{22} + A_{33})$.

Taking the rotation about (1,1,1) as typical,

$$\mathbf{Q} = \begin{bmatrix} 0 & 0 & 1 \\ 1 & 0 & 0 \\ 0 & 1 & 0 \end{bmatrix}.$$

Under this rotation, $\mathbf{Q}\mathbf{A}_N\mathbf{Q}^T$ becomes

$$\mathbf{Q}\mathbf{A}_N\mathbf{Q}^T = \begin{bmatrix} A_{22}-A' & A_{12} & A_{13} \\ A_{12} & A_{33}-A' & A_{23} \\ A_{13} & A_{23} & A_{11}-A' \end{bmatrix}.$$

Clearly, this can be split into two parts:

$$\mathbf{A}'_N = \begin{bmatrix} A_{22}-A' & 0 & 0 \\ 0 & A_{33}-A' & 0 \\ 0 & 0 & A_{11}-A' \end{bmatrix}$$

$$\mathbf{A}''_N = \begin{bmatrix} 0 & A_{23} & A_{12} \\ A_{23} & 0 & A_{13} \\ A_{12} & A_{13} & 0 \end{bmatrix}.$$

The tensor $\mathbf{A}'_N$ is two-dimensional, since the specification of any two of its nonzero elements allows the determination of the third, while $\mathbf{A}''_N$ is clearly a three-dimensional tensor. Thus, it can be expected that cubic symmetry has a two-dimensional subspace and a three-dimensional invariant subspace.

Two-Dimensional Invariant Subspace. The two-dimensional invariant subspace is spanned by two orthogonal tensors of the form

$$\begin{bmatrix} A_{11}-A' & 0 & 0 \\ 0 & A_{22}-A' & 0 \\ 0 & 0 & A_{33}-A' \end{bmatrix}.$$

These tensors are subject to the conditions of (9*a*). Expansion of these equations is simplified by taking $A_{11} - A' = -(A_{22} - A') - (A_{33} - A')$ and $B_{11} - B' = -(B_{22} - B') - (B_{33} - B')$, and also by noting that only four of the resulting equations are independent. With this reduction, the conditions for $\theta = 2\pi/3$ become

$$\begin{bmatrix} 0.5 & 1.0 & -0.866 & 0 \\ -1.0 & -0.5 & 0 & -0.866 \\ 0.866 & 0 & 0.5 & 1.0 \\ 0 & 0.866 & -1.0 & -0.5 \end{bmatrix} \begin{Bmatrix} A_{22}-A' \\ A_{33}-A' \\ B_{22}-B' \\ B_{33}-B' \end{Bmatrix} = 0,$$

which has the solution $A_{33} - A' = -2(A_{22} - A')$, $B_{22} - B' = -\sqrt{3}(A_{22} - A')$, $B_{33} - B' = 0$, so that $A_{11} - A' = A_{33} - A'$, and $B_{11} - B' = -(B_{22} - B')$. Normalization produces the following basis for a two-dimensional invariant subspace:

$$1/\sqrt{6}\begin{bmatrix} -1 & 0 & 0 \\ 0 & -1 & 0 \\ 0 & 0 & 2 \end{bmatrix} \quad 1/\sqrt{2}\begin{bmatrix} -1 & 0 & 0 \\ 0 & 1 & 0 \\ 0 & 0 & 0 \end{bmatrix}. \tag{24}$$

Three-Dimensional Invariant Subspace. Let $\mathbf{A}^{(1)}$, $\mathbf{A}^{(2)}$, $\mathbf{A}^{(3)}$ be the basis of a three-dimensional invariant subspace, then $\mathbf{Q}\mathbf{A}^{(k)} = [\alpha_{kl}]\mathbf{A}^{(l)}$, where $[\alpha_{kl}]$ is an orthogonal tensor of period $2\pi/3$. Clearly $[\alpha_{kl}] = \mathbf{Q}$ satisfies these conditions, which produces the solution: $A_{12} = A_{13} = A_{23}$ for each of the three tensors. Taking the preceding equation and applying it to $\mathbf{A}^{(1)}$ and setting $\mathbf{A}^{(2)} = \mathbf{A}^{(3)}$ (any similar combination does not alter the results) yields the following basis for a three-dimensional invariant subspace:

$$1/\sqrt{2}\begin{bmatrix} 0 & 1 & 0 \\ 1 & 0 & 0 \\ 0 & 0 & 0 \end{bmatrix} \quad 1/\sqrt{2}\begin{bmatrix} 0 & 0 & 1 \\ 0 & 0 & 0 \\ 1 & 0 & 0 \end{bmatrix} \quad 1/\sqrt{2}\begin{bmatrix} 0 & 0 & 0 \\ 0 & 0 & 1 \\ 0 & 1 & 0 \end{bmatrix}. \tag{25}$$

Thus, the spectral decomposition for cubic symmetry consists of a dilitation, a two-dimensional eigenspace (24), and a three-dimensional eigenspace (25).

Isotropic. For an isotropic material, every direction is an axis of full rotational symmetry. The unit tensor is the only tensor that is invariant under all rotations and provides a one-dimensional invariant subspace for isotropic symmetry. The only other invariant subspace under isotropic symmetry is the five-dimensional subspace of all symmetric tensors with zero trace (the orthogonal compliment of the unit tensor). A suitable basis for the five-dimensional subspace of tensors of zero trace is given as follows:

$$1/\sqrt{6}\begin{bmatrix} -1 & 0 & 0 \\ 0 & -1 & 0 \\ 0 & 0 & 2 \end{bmatrix} \quad 1/\sqrt{2}\begin{bmatrix} -1 & 0 & 0 \\ 0 & 1 & 0 \\ 0 & 0 & 0 \end{bmatrix}$$

$$1/\sqrt{2}\begin{bmatrix} 0 & 1 & 0 \\ 1 & 0 & 0 \\ 0 & 0 & 0 \end{bmatrix} \quad 1/\sqrt{2}\begin{bmatrix} 0 & 0 & 1 \\ 0 & 0 & 0 \\ 1 & 0 & 0 \end{bmatrix} \quad 1/\sqrt{2}\begin{bmatrix} 0 & 0 & 0 \\ 0 & 0 & 1 \\ 0 & 1 & 0 \end{bmatrix}. \tag{26}$$

The spectral decomposition for isotropy consists of a one-dimensional eigenspace spanned by the unit tensor and a five-dimensional eigenspace (26).

Numerical Examples

Since the pioneering work of Voight, numerous researchers have measured the elastic constants for a variety of anisotropic materials. Only for materials of low symmetry, particularly materials with triclinic or monoclinic symmetry, is there a scarcity of measured values. Except as noted, the numerical values of the elastic constants used in the following examples are from Federov (1968), Landolt and Bornestein (1969), and some of Voight's values (Love, 1944). Units are 10^{11} dynes/cm^2. The numerical values for the elasticity tensors have been presented in a condensed 6 × 6 form for simplicity; however, the full 9 × 9 form has been used in the calculation of the eigenvalues and eigenvectors.

Isotropic. The eigenvectors for isotropic symmetry are fixed, and not functions of the values of the elastic constants. They consist of a dilatation, $1/\sqrt{3}$ 1, and the eigenvectors (26). The eigenvalues are determined explicitly in terms of the Lamé constants as $3\lambda + 2\mu$ (three times the bulk modulus), for the isolated eigenvalue associated with the dilitation, and 2μ for the eigenvalue with multiplicity of five.

Cubic. As in the isotropic case, the eigenvectors for cubic symmetry are independent of the values of the elastic constants. In this case they consist of a dilitation, the basis of the two-dimensional eigenspace (24), and the basis of the three-dimensional eigenspace (25). Once again, the eigenvalues can be written explicitly in terms of the elastic constants, with λ_1 =

Downloaded 03 May 2010 to 171.66.16.247. Redistribution subject to ASME license or copyright; see http://www.asme.org/terms/Terms_Use.cfm

$C_{1111} + 2C_{1122}$, $\lambda_2 = \lambda_3 = C_{1111} - C_{1122}$, $\lambda_4 = \lambda_5 = \lambda_6 = 2C_{2323}$. The spectrum of copper given as follows is typical of materials with cubic symmetry.

Copper

$$\begin{bmatrix} 17.0 & 12.3 & 12.3 & 0 & 0 & 0 \\ & 17.0 & 12.3 & 0 & 0 & 0 \\ & & 17.0 & 0 & 0 & 0 \\ & & & 7.5 & 0 & 0 \\ & & & & 7.5 & 0 \\ & & & & & 7.5 \end{bmatrix}$$

$$\lambda_1 = 41.6 \quad \mathbf{N}_1 = 1/\sqrt{3} \begin{bmatrix} 1 & 0 & 0 \\ 0 & 1 & 0 \\ 0 & 0 & 1 \end{bmatrix}$$

$$\lambda_2 = \lambda_3 = \lambda_4 = 15 \quad \mathbf{N}_2 = 1/\sqrt{2} \begin{bmatrix} 0 & 1 & 0 \\ 1 & 0 & 0 \\ 0 & 0 & 0 \end{bmatrix}$$

$$\mathbf{N}_3 = 1/\sqrt{2} \begin{bmatrix} 0 & 0 & 1 \\ 0 & 0 & 0 \\ 1 & 0 & 0 \end{bmatrix} \quad \mathbf{N}_4 = 1/\sqrt{2} \begin{bmatrix} 0 & 0 & 0 \\ 0 & 0 & 1 \\ 0 & 1 & 0 \end{bmatrix}$$

$$\lambda_5 = \lambda_6 = 4.7 \quad \mathbf{N}_5 = 1/\sqrt{6} \begin{bmatrix} -1 & 0 & 0 \\ 0 & -1 & 0 \\ 0 & 0 & 2 \end{bmatrix}$$

$$\mathbf{N}_6 = 1/\sqrt{2} \begin{bmatrix} 1 & 0 & 0 \\ 0 & -1 & 0 \\ 0 & 0 & 0 \end{bmatrix}$$

The succession of eigenvalues for copper is typical of most cubic metals with the lowest eigenvalue associated with the two-dimensional eigenspace. Two exceptions are molybdenum and vanadium, in which the eigenvalue associated with the three-dimensional eigenspace is the lowest.

Hexagonal. For hexagonal symmetry, four of the eigenvectors are independent of the values of the elastic constants, and consist of the bases of the two two-dimensional eigenspaces (21*c*) and (21*d*). The other two eigenvectors are linear combinations of the basis of the induced axis of rotation and are dependent upon the values of the elastic constants. Three examples will be presented for hexagonal symmetry, beryl, a complex framework silicate, and two hexagonally closest-packed metals: cobalt and magnesium.

Beryl

$$\begin{bmatrix} 26.91 & 9.60 & 6.61 & 0 & 0 & 0 \\ & 26.91 & 6.61 & 0 & 0 & 0 \\ & & 23.61 & 0 & 0 & 0 \\ & & & 6.53 & 0 & 0 \\ & & & & 6.53 & 0 \\ & & & & & 8.65 \end{bmatrix}$$

$$\lambda_1 = 41.42 \quad \mathbf{N}_1 = \begin{bmatrix} .6262 & 0 & 0 \\ 0 & .6262 & 0 \\ 0 & 0 & .4645 \end{bmatrix}$$

$$\lambda_2 = 18.71 \quad \mathbf{N}_2 = \begin{bmatrix} -.3285 & 0 & 0 \\ 0 & -.3285 & 0 \\ 0 & 0 & .8856 \end{bmatrix}$$

$$\lambda_3 = \lambda_4 = 17.31 \quad \mathbf{N}_3 = \begin{bmatrix} -.7071 & 0 & 0 \\ 0 & .7071 & 0 \\ 0 & 0 & 0 \end{bmatrix}$$

$$\mathbf{N}_4 = \begin{bmatrix} 0 & .7071 & 0 \\ .7071 & 0 & 0 \\ 0 & 0 & 0 \end{bmatrix}$$

$$\lambda_5 = \lambda_6 = 13.05 \quad \mathbf{N}_5 = \begin{bmatrix} 0 & 0 & 0 \\ 0 & 0 & .7071 \\ 0 & .7071 & 0 \end{bmatrix}$$

$$\mathbf{N}_6 = \begin{bmatrix} 0 & 0 & .7071 \\ 0 & 0 & 0 \\ .7071 & 0 & 0 \end{bmatrix}$$

Cobalt

$$\begin{bmatrix} 30.7 & 16.5 & 10.27 & 0 & 0 & 0 \\ & 30.7 & 10.27 & 0 & 0 & 0 \\ & & 35.81 & 0 & 0 & 0 \\ & & & 7.55 & 0 & 0 \\ & & & & 7.55 & 0 \\ & & & & & 7.10 \end{bmatrix}$$

$$\lambda_1 = 57.11 \quad \mathbf{N}_1 = \begin{bmatrix} .5842 & 0 & 0 \\ 0 & .5842 & 0 \\ 0 & 0 & .5634 \end{bmatrix}$$

$$\lambda_2 = 25.90 \quad \mathbf{N}_2 = \begin{bmatrix} -.3984 & 0 & 0 \\ 0 & -.3984 & 0 \\ 0 & 0 & .8262 \end{bmatrix}$$

$$\lambda_3 = \lambda_4 = 15.10 \quad \mathbf{N}_3 = \begin{bmatrix} 0 & 0 & 0 \\ 0 & 0 & .7071 \\ 0 & .7071 & 0 \end{bmatrix}$$

$$\mathbf{N}_4 = \begin{bmatrix} 0 & 0 & .7071 \\ 0 & 0 & 0 \\ .7071 & 0 & 0 \end{bmatrix}$$

$$\lambda_5 = \lambda_6 = 14.20 \quad \mathbf{N}_5 = \begin{bmatrix} -.7071 & 0 & 0 \\ 0 & .7071 & 0 \\ 0 & 0 & 0 \end{bmatrix}$$

$$\mathbf{N}_6 = \begin{bmatrix} 0 & .7071 & 0 \\ .7071 & 0 & 0 \\ 0 & 0 & 0 \end{bmatrix}$$

Magnesium

$$\begin{bmatrix} 5.97 & 2.62 & 2.17 & 0 & 0 & 0 \\ & 5.97 & 2.17 & 0 & 0 & 0 \\ & & 6.17 & 0 & 0 & 0 \\ & & & 1.64 & 0 & 0 \\ & & & & 1.64 & 0 \\ & & & & & 1.675 \end{bmatrix}$$

Downloaded 03 May 2010 to 171.66.16.247. Redistribution subject to ASME license or copyright; see http://www.asme.org/terms/Terms_Use.cfm

$$\lambda_1 = 10.68 \quad \mathbf{N}_1 = \begin{bmatrix} .5846 & 0 & 0 \\ 0 & .5846 & 0 \\ 0 & 0 & .5627 \end{bmatrix}$$

$$\lambda_2 = 4.08 \quad \mathbf{N}_2 = \begin{bmatrix} -.3979 & 0 & 0 \\ 0 & -.3979 & 0 \\ 0 & 0 & .8267 \end{bmatrix}$$

$$\lambda_3 = \lambda_4 = 3.28 \quad \mathbf{N}_3 = \begin{bmatrix} -.7071 & 0 & 0 \\ 0 & .7071 & 0 \\ 0 & 0 & 0 \end{bmatrix}$$

$$\mathbf{N}_4 = \begin{bmatrix} 0 & .7071 & 0 \\ .7071 & 0 & 0 \\ 0 & 0 & 0 \end{bmatrix}$$

$$\lambda_5 = \lambda_6 = 3.35 \quad \mathbf{N}_5 = \begin{bmatrix} 0 & 0 & 0 \\ 0 & 0 & .7071 \\ 0 & .7071 & 0 \end{bmatrix}$$

$$\mathbf{N}_6 = \begin{bmatrix} 0 & 0 & .7071 \\ 0 & 0 & 0 \\ .7071 & 0 & 0 \end{bmatrix}$$

In both metals, the eigenvector corresponding to the highest eigenvalue is very nearly a dilitation. The condition for a dilitation as an eigenvector for hexagonal symmetry is $C_{1111} + C_{1122} + C_{1133} = 2C_{1133} + C_{3333}$. The reported values of the elastic constants differ from this condition by 2.3 percent for magnesium and 1.9 percent for cobalt.

Tetragonal. For tetragonal symmetry, four eigenvectors are independent of the values of the elastic constants and consist of the bases of two one-dimensional eigenspaces ($20c$) and ($20d$) and the two-dimensional eigenspace ($20e$). Three examples will be presented for tetragonal symmetry. In the first, pentaerythritol (class $\bar{4}$), the number of elastic constants has been reduced to six following Fedorov's method. The second example is the body-centered tetragonal metal (white) tin and the third example is indium, for which the unit cell structure is usually regarded as face-centered tetragonal, since its axial ratio is 1.08.

Pentaerythritol

$$\begin{bmatrix} 0.6667 & -0.3068 & 0.050 & 0 & 0 & 0 \\ & 0.6667 & 0.050 & 0 & 0 & 0 \\ & & 0.80 & 0 & 0 & 0 \\ & & & 0.35 & 0 & 0 \\ & & & & 0.35 & 0 \\ & & & & & 0.4032 \end{bmatrix}$$

$$\lambda_1 = 0.9735 \quad \mathbf{N}_1 = \begin{bmatrix} -.7071 & 0 & 0 \\ 0 & .7071 & 0 \\ 0 & 0 & 0 \end{bmatrix}$$

$$\lambda_2 = 0.8111 \quad \mathbf{N}_2 = \begin{bmatrix} .1094 & 0 & 0 \\ 0 & .1094 & 0 \\ 0 & 0 & .9879 \end{bmatrix}$$

$$\lambda_3 = 0.8064 \quad \mathbf{N}_3 = \begin{bmatrix} 0 & .7071 & 0 \\ .7071 & 0 & 0 \\ 0 & 0 & 0 \end{bmatrix}$$

$$\lambda_4 = \lambda_5 = 0.7000 \quad \mathbf{N}_4 = \begin{bmatrix} 0 & 0 & .7071 \\ 0 & 0 & 0 \\ .7071 & 0 & 0 \end{bmatrix}$$

$$\mathbf{N}_5 = \begin{bmatrix} 0 & 0 & 0 \\ 0 & 0 & .7071 \\ .7071 & 0 & 0 \end{bmatrix}$$

$$\lambda_6 = 0.3488 \quad \mathbf{N}_6 = \begin{bmatrix} -.6986 & 0 & 0 \\ 0 & -.6986 & 0 \\ 0 & 0 & .1548 \end{bmatrix}$$

Tin

$$\begin{bmatrix} 8.391 & 4.870 & 2.810 & 0 & 0 & 0 \\ & 8.391 & 2.810 & 0 & 0 & 0 \\ & & 9.665 & 0 & 0 & 0 \\ & & & 1.754 & 0 & 0 \\ & & & & 1.754 & 0 \\ & & & & & 0.7407 \end{bmatrix}$$

$$\lambda_1 = 15.83 \quad \mathbf{N}_1 = \begin{bmatrix} .5942 & 0 & 0 \\ 0 & .5942 & 0 \\ 0 & 0 & .5421 \end{bmatrix}$$

$$\lambda_2 = 7.101 \quad \mathbf{N}_2 = \begin{bmatrix} -.3834 & 0 & 0 \\ 0 & -.3834 & 0 \\ 0 & 0 & .8403 \end{bmatrix}$$

$$\lambda_3 = 3.521 \quad \mathbf{N}_3 = \begin{bmatrix} -.7071 & 0 & 0 \\ 0 & .7071 & 0 \\ 0 & 0 & 0 \end{bmatrix}$$

$$\lambda_4 = \lambda_5 = 3.508 \quad \mathbf{N}_4 = \begin{bmatrix} 0 & 0 & .7071 \\ 0 & 0 & 0 \\ .7071 & 0 & 0 \end{bmatrix}$$

$$\mathbf{N}_5 = \begin{bmatrix} 0 & 0 & 0 \\ 0 & 0 & .7071 \\ 0 & .7071 & 0 \end{bmatrix}$$

$$\lambda_6 = 1.481 \quad \mathbf{N}_6 = \begin{bmatrix} 0 & .7071 & 0 \\ .7071 & 0 & 0 \\ 0 & 0 & 0 \end{bmatrix}$$

Indium

$$\begin{bmatrix} 4.45 & 3.944 & 4.051 & 0 & 0 & 0 \\ & 4.45 & 4.051 & 0 & 0 & 0 \\ & & 4.44 & 0 & 0 & 0 \\ & & & 0.655 & 0 & 0 \\ & & & & 0.655 & 0 \\ & & & & & 1.22 \end{bmatrix}$$

$$\lambda_1 = 12.48 \quad \mathbf{N}_1 = \begin{bmatrix} .5758 & 0 & 0 \\ 0 & .5758 & 0 \\ 0 & 0 & .5804 \end{bmatrix}$$

Downloaded 03 May 2010 to 171.66.16.247. Redistribution subject to ASME license or copyright; see http://www.asme.org/terms/Terms_Use.cfm

$$\lambda_2 = 2.44 \quad \mathbf{N}_2 = \begin{bmatrix} 0 & .7071 & 0 \\ .7071 & 0 & 0 \\ 0 & 0 & 0 \end{bmatrix}$$

$$\lambda_3 = \lambda_4 = 1.31 \quad \mathbf{N}_3 = \begin{bmatrix} 0 & 0 & .7071 \\ 0 & 0 & 0 \\ .7071 & 0 & 0 \end{bmatrix}$$

$$\mathbf{N}_4 = \begin{bmatrix} 0 & 0 & 0 \\ 0 & 0 & .7071 \\ 0 & .7071 & 0 \end{bmatrix}$$

$$\lambda_5 = 0.506 \quad \mathbf{N}_5 = \begin{bmatrix} -.7071 & 0 & 0 \\ 0 & .7071 & 0 \\ 0 & 0 & 0 \end{bmatrix}$$

$$\lambda_6 = 0.356 \quad \mathbf{N}_6 = \begin{bmatrix} -.4104 & 0 & 0 \\ 0 & -.4104 & 0 \\ 0 & 0 & .8143 \end{bmatrix}$$

As observed in the examples of the *hcp* metals, the eigenvector corresponding to the largest eigenvalue for the tetragonal metals tin and indium is very nearly a dilitation. The condition for a dilitation as an eigenvector for tetragonal symmetry is the same as that for hexagonal symmetry, i.e., $C_{1111} + C_{1122} + C_{1133} = 2C_{1133} + C_{3333}$. The reported values of the elastic constants differ from this condition by 5.1 percent for tin and -0.78 percent for indium.

Trigonal. As in the case of hexagonal symmetry, the eigenvectors for trigonal symmetry consist of two one-dimensional eigenvectors in the induced axis of rotation, and the bases of two two-dimensional invariant subspaces, (19*a*) and (19*b*). In this case, however, all of the eigenvectors depend on the values of the elastic constants. Two examples will be presented for trigonal symmetry: α-quartz and tourmaline.

α-Quartz

$$\begin{bmatrix} 8.76 & 0.60 & 1.33 & 0 & -1.73 & 0 \\ & 8.76 & 1.33 & 0 & 1.73 & 0 \\ & & 10.68 & 0 & 0 & 0 \\ & & & 5.72 & 0 & 1.73 \\ & & & & 5.72 & 0 \\ & & & & & 4.08 \end{bmatrix}$$

$$\lambda_1 = \lambda_2 = 13.63 \quad \mathbf{N}_1 = \begin{bmatrix} .3781 & 0 & -.5976 \\ 0 & -.3781 & 0 \\ -.5976 & 0 & 0 \end{bmatrix}$$

$$\mathbf{N}_2 = \begin{bmatrix} 0 & .3781 & 0 \\ .3781 & 0 & .5976 \\ 0 & .5976 & 0 \end{bmatrix}$$

$$\lambda_3 = 12.01 \quad \mathbf{N}_3 = \begin{bmatrix} .4089 & 0 & 0 \\ 0 & .4089 & 0 \\ 0 & 0 & .8158 \end{bmatrix}$$

$$\lambda_4 = 8.027 \quad \mathbf{N}_4 = \begin{bmatrix} -.5769 & 0 & 0 \\ 0 & -.5769 & 0 \\ 0 & 0 & .5783 \end{bmatrix}$$

$$\lambda_5 = \lambda_6 = 5.971 \quad \mathbf{N}_5 = \begin{bmatrix} .5976 & 0 & .3781 \\ 0 & -.5976 & 0 \\ .3781 & 0 & 0 \end{bmatrix}$$

$$\mathbf{N}_6 = \begin{bmatrix} 0 & -.5976 & 0 \\ -.5976 & 0 & .3781 \\ 0 & .3781 & 0 \end{bmatrix}$$

Tourmaline

$$\begin{bmatrix} 27.2 & 4.0 & 3.5 & 0 & -0.68 & 0 \\ & 27.2 & 3.5 & 0 & 0.68 & 0 \\ & & 16.5 & 0 & 0 & 0 \\ & & & 6.5 & 0 & 0.68 \\ & & & & 6.5 & 0 \\ & & & & & 11.6 \end{bmatrix}$$

$$\lambda_1 = 32.71 \quad \mathbf{N}_1 = \begin{bmatrix} .6763 & 0 & 0 \\ 0 & .6763 & 0 \\ 0 & 0 & .2920 \end{bmatrix}$$

$$\lambda_2 = \lambda_3 = 23.39 \quad \mathbf{N}_2 = \begin{bmatrix} -.7011 & 0 & .0919 \\ 0 & .7011 & 0 \\ .0919 & 0 & 0 \end{bmatrix}$$

$$\mathbf{N}_3 = \begin{bmatrix} 0 & .7011 & 0 \\ .7011 & 0 & .0919 \\ 0 & .0919 & 0 \end{bmatrix}$$

$$\lambda_4 = 14.99 \quad \mathbf{N}_4 = \begin{bmatrix} -.2065 & 0 & 0 \\ 0 & -.2062 & 0 \\ 0 & 0 & .9564 \end{bmatrix}$$

$$\lambda_5 = \lambda_6 = 12.82 \quad \mathbf{N}_5 = \begin{bmatrix} .0919 & 0 & .7011 \\ 0 & -.0919 & 0 \\ .7011 & 0 & 0 \end{bmatrix}$$

$$\mathbf{N}_6 = \begin{bmatrix} 0 & -.0919 & 0 \\ -.0919 & 0 & .7011 \\ 0 & .7011 & 0 \end{bmatrix}$$

Orthorhombic. The eigenvectors for orthorhombic materials are of the form given by (22). Three of the eigenvectors are independent of the elastic constants, and three are determined by the elastic constants but are of a specified form. Two examples are presented: the mineral topaz and the orthorhombic metal gallium. It can be seen from the results for gallium that the relationship among the cubic, hexagonal, and tetragonal metals does not extend to this orthorhombic metal.

Topaz

$$\begin{bmatrix} 28.12 & 12.54 & 8.43 & 0 & 0 & 0 \\ & 34.89 & 8.82 & 0 & 0 & 0 \\ & & 29.40 & 0 & 0 & 0 \\ & & & 10.78 & 0 & 0 \\ & & & & 13.23 & 0 \\ & & & & & 13.03 \end{bmatrix}$$

Downloaded 03 May 2010 to 171.66.16.247. Redistribution subject to ASME license or copyright; see http://www.asme.org/terms/Terms_Use.cfm

$$\lambda_1 = 51.25 \quad \mathbf{N}_1 = \begin{bmatrix} .5470 & 0 & 0 \\ 0 & .6815 & 0 \\ 0 & 0 & .4862 \end{bmatrix}$$

$$\lambda_2 = 26.46 \quad \mathbf{N}_2 = \begin{bmatrix} 0 & 0 & .7071 \\ 0 & 0 & 0 \\ .7071 & 0 & 0 \end{bmatrix}$$

$$\lambda_3 = 26.07 \quad \mathbf{N}_3 = \begin{bmatrix} 0 & .7071 & 0 \\ .7071 & 0 & 0 \\ 0 & 0 & 0 \end{bmatrix}$$

$$\lambda_4 = 22.97 \quad \mathbf{N}_4 = \begin{bmatrix} .0894 & 0 & 0 \\ 0 & .5299 & 0 \\ 0 & 0 & -.8434 \end{bmatrix}$$

$$\lambda_5 = 21.56 \quad \mathbf{N}_5 = \begin{bmatrix} 0 & 0 & 0 \\ 0 & 0 & .7071 \\ 0 & .7071 & 0 \end{bmatrix}$$

$$\lambda_6 = 18.20 \quad \mathbf{N}_6 = \begin{bmatrix} -.8324 & 0 & 0 \\ 0 & .5047 & 0 \\ 0 & 0 & .2289 \end{bmatrix}$$

Gallium

$$\begin{bmatrix} 9.8 & 3.3 & 2.8 & 0 & 0 & 0 \\ & 8.76 & 4.2 & 0 & 0 & 0 \\ & & 13.3 & 0 & 0 & 0 \\ & & & 3.42 & 0 & 0 \\ & & & & 3.92 & 0 \\ & & & & & 4.2 \end{bmatrix}$$

$$\lambda_1 = 17.9 \quad \mathbf{N}_1 = \begin{bmatrix} .4574 & 0 & 0 \\ 0 & .5017 & 0 \\ 0 & 0 & .7342 \end{bmatrix}$$

$$\lambda_2 = 8.43 \quad \mathbf{N}_2 = \begin{bmatrix} -.7617 & 0 & 0 \\ 0 & -.2050 & 0 \\ 0 & 0 & .6196 \end{bmatrix}$$

$$\lambda_3 = 8.40 \quad \mathbf{N}_3 = \begin{bmatrix} 0 & .7071 & 0 \\ .7071 & 0 & 0 \\ 0 & 0 & 0 \end{bmatrix}$$

$$\lambda_4 = 7.84 \quad \mathbf{N}_4 = \begin{bmatrix} 0 & 0 & .7071 \\ 0 & 0 & 0 \\ .7071 & 0 & 0 \end{bmatrix}$$

$$\lambda_5 = 6.84 \quad \mathbf{N}_5 = \begin{bmatrix} 0 & 0 & 0 \\ 0 & 0 & .7071 \\ 0 & .7071 & 0 \end{bmatrix}$$

$$\lambda_6 = 5.52 \quad \mathbf{N}_6 = \begin{bmatrix} .4589 & 0 & 0 \\ 0 & -.8404 & 0 \\ 0 & 0 & .2884 \end{bmatrix}$$

Monoclinic. The eigenvectors for the monoclinic system consist of four proper one-dimensional invariants given in (6) and two improper one-dimensional invariants given in (8). If the number of elastic constants is reduced from 13 to 12 following Fedorov's method, the improper invariants take the standard form

$$1/\sqrt{2}\begin{bmatrix} 0 & 0 & 1 \\ 0 & 0 & 0 \\ 1 & 0 & 0 \end{bmatrix} \quad 1/\sqrt{2}\begin{bmatrix} 0 & 0 & 0 \\ 0 & 0 & 1 \\ 0 & 1 & 0 \end{bmatrix}.$$

The only example presented for the monoclinic system is for the monoclinic mineral gypsum. Here Fedorov's reduction has not been employed; however, a coordinate rotation of 33.63925 degrees eliminates C_{2313} and reduces the two improper invariants ($\mathbf{N}_4$, $\mathbf{N}_6$) to standard form.

Gypsum

$$\begin{bmatrix} 7.86 & 4.1 & 2.68 & 0 & 0 & -0.7 \\ & 6.27 & 2.42 & 0 & 0 & 0.31 \\ & & 7.26 & 0 & 0 & -1.74 \\ & & & 0.910 & -0.16 & 0 \\ & & & & 1.044 & 0 \\ & & & & & 2.64 \end{bmatrix}$$

$$\lambda_1 = 13.72 \quad \mathbf{N}_1 = \begin{bmatrix} .6388 & -.1445 & 0 \\ -.1445 & .5135 & 0 \\ 0 & 0 & .5353 \end{bmatrix}$$

$$\lambda_2 = 6.95 \quad \mathbf{N}_2 = \begin{bmatrix} .2979 & .4838 & 0 \\ .4838 & .4308 & 0 \\ 0 & 0 & -.5075 \end{bmatrix}$$

$$\lambda_3 = 3.81 \quad \mathbf{N}_3 = \begin{bmatrix} -.5791 & .3424 & 0 \\ .3424 & .3113 & 0 \\ 0 & 0 & .5773 \end{bmatrix}$$

$$\lambda_4 = 2.30 \quad \mathbf{N}_4 = \begin{bmatrix} 0 & 0 & -.5889 \\ 0 & 0 & .3917 \\ -.5889 & .3917 & 0 \end{bmatrix}$$

$$\lambda_5 = 2.19 \quad \mathbf{N}_5 = \begin{bmatrix} .4097 & .3537 & 0 \\ .3537 & -.6736 & 0 \\ 0 & 0 & .3503 \end{bmatrix}$$

$$\lambda_6 = 1.61 \quad \mathbf{N}_6 = \begin{bmatrix} 0 & 0 & .3917 \\ 0 & 0 & .5887 \\ .3917 & .5887 & 0 \end{bmatrix}$$

Triclinic. For the triclinic system there are no restrictions on the eigenvectors. All the eigenvalues are isolated, and the eigenspaces are one-dimensional. Only one example is presented, that for copper sulfate (von Haussuhl and Siegert, 1969).

$CuSO_4 \cdot 5H_2O$

$$\begin{bmatrix} 5.709 & 2.062 & 3.164 & -0.426 & -0.042 & -0.221 \\ & 3.577 & 2.34 & -0.281 & -0.012 & -0.058 \\ & & 5.841 & -0.084 & -0.284 & -0.075 \\ & & & 1.65 & -0.185 & 0.119 \\ & & & & 1.515 & -0.353 \\ & & & & & 1.205 \end{bmatrix}$$

Downloaded 03 May 2010 to 171.66.16.247. Redistribution subject to ASME license or copyright; see http://www.asme.org/terms/Terms_Use.cfm

$$\lambda_1 = 10.44 \quad \mathbf{N}_1 = \begin{bmatrix} .6288 & -.0261 & -.0236 \\ -.0261 & .4157 & -.0611 \\ -.0236 & -.0611 & .6495 \end{bmatrix}$$

$$\lambda_2 = 3.978 \quad \mathbf{N}_2 = \begin{bmatrix} -.1701 & .2762 & -.4408 \\ .2762 & -.0324 & .4263 \\ -.4408 & .4263 & .2559 \end{bmatrix}$$

$$\lambda_3 = 2.930 \quad \mathbf{N}_3 = \begin{bmatrix} .0772 & .2797 & -.3823 \\ .2797 & .0119 & -.5058 \\ -.3823 & -.5058 & -.1828 \end{bmatrix}$$

$$\lambda_4 = 2.549 \quad \mathbf{N}_4 = \begin{bmatrix} -.7477 & .0189 & .0875 \\ .0189 & .4026 & -.1873 \\ .0875 & -.1873 & .4389 \end{bmatrix}$$

$$\lambda_5 = 2.091 \quad \mathbf{N}_5 = \begin{bmatrix} .0814 & .2931 & .1490 \\ .2931 & .7134 & .1495 \\ .1490 & .1495 & -.4728 \end{bmatrix}$$

$$\lambda_6 = 1.875 \quad \mathbf{N}_6 = \begin{bmatrix} .0630 & .5085 & .3593 \\ .5085 & -.3938 & -.0356 \\ .3593 & -.0356 & .2512 \end{bmatrix}$$

The numerical examples presented clearly support the spectral decomposition structures previously derived. The most remarkable result of the numerical work is the relationship among the cubic, hexagonal, and tetragonal metals where (within the limits of experimental values) the eigenvectors are the same, although arranged in eigenspaces of differing dimension.

Other Applications

The spectral decomposition of the elasticity tensor can be used to present alternative forms of more general results in the theory of anisotropic elasticity. For example, the equations of equilibrium (and motion), and the acoustic tensor are easily written in spectral form. While a detailed interpretation of these results is yet to be worked out, the forms offer some intriguing glimpses.

Equilibrium Equations. The basic equilibrium equation of elasticity in terms of the stress tensor $\mathbf{S}$ can be written $\mathrm{div}\mathbf{S} + \mathbf{b} = 0$, where $\mathbf{b}$ is the body force, and $(\mathrm{div}\mathbf{S})_i = \mathbf{S}_{ij,j}$. In terms of the displacement gradient $\nabla\mathbf{u}$, the strain tensor $\mathbf{E}$ is given by $\mathbf{E} = \mathrm{sym}\nabla\mathbf{u}$. Combining this with the stress strain relation $\mathbf{S} = C[\mathbf{E}]$ yields $\mathrm{div}C[\nabla\mathbf{u}] + \mathbf{b} = 0$, where $C[\mathrm{sym}\nabla\mathbf{u}] = C[\nabla\mathbf{u}]$ from the symmetry of the elasticity tensor. Substitution of the spectral form of the elasticity tensor (2) yields

$$\mathrm{div}\sum_{k=1}^{6}\lambda_k(\mathbf{N}_k\cdot\nabla\mathbf{u})\mathbf{N}_k + \mathbf{b} = 0 \tag{27}$$

which may be rewritten

$$\sum_{k=1}^{6}\lambda_k\mathbf{N}_k[\nabla(\mathbf{n}_k\cdot\nabla\mathbf{u})] + \mathbf{b} = 0. \tag{28}$$

In the first form the displacement gradient tensor is resolved into components in the principal directions of the elasticity tensor before the divergence operator is applied, while in the second form, the gradients of the principal magnitudes of the displacement gradient tensor are mapped by the eigenvectors into vectors in 3-space.

Acoustic Tensor. The acoustic tensor $\mathbf{A}(\mathbf{m})$ is defined as $\mathbf{A}(\mathbf{m}) = 1/\rho C_{ijkl}\mathbf{m}_j\mathbf{m}_l$, Gurtin (1972) where ρ is the mass density and $\mathbf{m}$ is a unit vector. In terms of the spectral decomposition, $\mathbf{A}(\mathbf{m})$ becomes

$$\mathbf{A}(\mathbf{m}) = 1/\rho\sum_{k=1}^{6}\lambda_k(\mathbf{N}_k\mathbf{m})\otimes(\mathbf{N}_k\mathbf{m}) \tag{29}$$

Stored Energy Function. The stored energy function $\epsilon(\mathbf{E})$ is defined as $\epsilon(\mathbf{E}) = 1/2\mathbf{E}\cdot\mathbf{C}[\mathbf{E}]$. In terms of the spectral decomposition, $\epsilon(\mathbf{E})$ becomes

$$\epsilon(\mathbf{E}) = 1/2\sum_{k=1}^{6}\lambda_k(\mathbf{E}\cdot\mathbf{N}_k)^2.$$

This form of the stored energy function offers the tantalizing prospect of the extension of the von Mises yield criterion for isotropic materials to anisotropy, especially for the cubic, hexagonal, and tetragonal metals. As pointed out earlier, each of these classes of metals have a dilatational eigenvector, either by necessity (cubic), or as indicated from experimental values (hexagonal and tetragonal). Thus, the effect of volume change is easily eliminated. For cubic metals a yield criterion fashioned on this basis would be a function of two variables, while for hexagonal metals it would be a function of three variables, and for tetragonal metals, four variables.

Conclusion

When the elasticity tensor is regarded as a linear transformation on the space of second-order tensors, it can be reduced to its spectral form. Since the eigenspaces must conform to material symmetry, the structure of the spectral form is determined by material symmetry. Each of the symmetry groups provides a distinctive structure to the spectral decomposition. Numerical examples, for representative materials within each symmetry group, correspond to the predicted structures, and substantiate the theoretical derivation.

Utilization of the spectral form in the equilibrium Eqs. (25), allows a general geometric interpretation of the processes involved. These equations can be regarded as a generalization of Navier's equation to the general anisotropic case.

References

Bowen, R. M., and Wang, C.-C., 1974, *Introduction to Vectors and Tensors*, Plenum Press, New York, pp. 133–138.

Cowin, S. C., and Mehrabadi, M. M., 1987, "On the Identification of Material Symmetry for Anisotropic Elastic Materials," *Quarterly Journal of Mechanics and Applied Mathematics*, Vol. 40, Part 4, pp. 451–476.

Federov, F. I., 1968, *Theory of Elastic Waves in Crystals*, Plenum Press, New York, pp. 27–31.

Gurtin, M. E., 1972, "The Linear Theory of Elasticity," *Encyclopedia of Physics*, Vol. 6, Springer-Verlag, Berlin, pp. 243–244.

Halmos, P. R., 1974, *Finite Dimensional Vector Spaces*, Springer-Verlag, Berlin, pp. 155–158.

von Haussuhl, S., and Siegert, H., 1969, *Zeitschrift fur Kristallographie*, Vol. 129, p. 142.

Landolt-Bornstein, 1969, *Numerical Data and Fundamental Relationships in Science and Technology, New Series, Group III*, (Crystals and Solid State Physics), Vol. 2, Springer-Verlag, Berlin.

Lord Kelvin (W. Thompson), (1856), *Phil. Trans. R. Soc.*, Vol. 166, p. 481.

Lord Kelvin (W. Thompson), (1878), *Encyclopedia Britanica*, 9th ed., London and Edinburgh, pp. 796–825.

Love, A. E. H., 1944, *Mathematical Theory of Elasticity*, Dover Publications, New York, pp. 163–164.

Mehrabadi, M. M., and Cowin, S. C., 1990, "Eigentensors of Linear Anisotropic Elastic Materials," *Quarterly Journal of Mechanics and Applied Mathematics*, Vol. 43, Part 1, pp. 15–41.

Smith, G. F., and Rivlin, R. S., 1958, "The Strain Energy Function for Anisotropic Elastic Materials," *Transactions of the American Mathematical Society*, Vol. 88, pp. 175–193.

Ting, T. C. T., 1987, "Invariants of Anisotropic Elastic Constants," *Quarterly Journal of Mechanics and Applied Mathematics*, Vol. 40, Part 3, pp. 431–448.

Downloaded 03 May 2010 to 171.66.16.247. Redistribution subject to ASME license or copyright; see http://www.asme.org/terms/Terms_Use.cfm

Further Aspects of the Elastic Field for Two Circular Inclusions in Antiplane Elastostatics

E. Honein
Postdoctoral Research Affiliate.

T. Honein
Postdoctoral Research Affiliate.

G. Herrmann
Professor of Applied Mechanics,
Honorary Mem. ASME.

Division of Applied Mechanics,
Stanford University,
Stanford, CA 94305-4040

The heterogenization technique, recently developed by the authors, is applied to the problem, in antiplane elastostatics, of two circular inclusions of arbitrary radii and of different shear moduli, and perfectly bonded to a matrix, of infinite extent, subjected to arbitrary loading. The solution is formulated in a manner which leads to some exact results. Universal formulae are derived for the stress field at the point of contact between two elastic inclusions. It is also discovered that the difference in the displacement field, at the limit points of the Apollonius family of circles to which the boundaries of the inclusions belong, is the same for the heterogeneous problem as for the corresponding homogeneous one. This discovery leads to a universal formula for the average stress between two circular holes or rigid inclusions. Moreover, the asymptotic behavior of the stress field at the closest points of two circular holes or rigid inclusions approaching each other is also studied and given by universal formulae, i.e., formulae which are independent of the loading being considered.

Introduction

In a recent paper (E. Honein et al., 1992), the present authors have considered the problem, in antiplane elastostatics, of two circular inclusions, of arbitrary radii and of different shear moduli, and perfectly bonded to a matrix, of infinite extent, subjected to *arbitrary* loading (singularities).

They expressed the solution to this heterogeneous problem in terms of the solution to the corresponding homogeneous problem, i.e., the problem when the matrix material occupies the whole space and is subjected to the same loading (singularities), a methodology which was termed "*heterogenization*." To this end, they exploited, for the first time in elasticity, the structure of the Möbius transformations which arise by composition of the inversion transformations relative to the two circles bounding the two inclusions. In their derivation, a crucial role was played by the fixed points of the Möbius transformations.

From the results achieved in their paper, it can be shown that, under arbitrary loading, the "tangential" shear stress $\sigma_{3\theta}$, at the closest points of two neighboring circles bounding traction-free holes, tends, in the general case, to infinity as the two holes become infinitely close to each other. Similar results hold for the "radial" shear stress σ_{3r} at the closest points of two rigid circular inclusions approaching each other. Indeed, these stress components are infinite at the point of contact of two holes or rigid inclusions, respectively.

A challenging problem is to find the asymptotic behavior of these quantities. This question has attracted much attention recently, since, for example, the high-stress concentration has been used to explain the unexpected low strength of fiber-reinforced composites under longitudinal shear.

The particular problem, of two circular inclusions under remote, uniform, longitudinal shear, has been solved by Goree and Wilson (1967) who surmised that, by numerical calculation, the stress concentration factor would become infinite as two holes approach each other. This observation has prompted Budiansky and Carrier (1984) to revisit Goree-Wilson solution and rederive it in a way which led to some exact results. It is to be noted, however, that Budiansky and Carrier considered two identical rigid fibers in a special orientation relative to the uniform remote loading and gave the average stress between the fibers. They also provided the radial shear stress at the point of contact of two identical elastic fibers. The corresponding problem of two traction-free holes has been considered recently by Steif (1989) using Budiansky-Carrier results and a general analogy between solutions for traction-free holes and those for rigid inclusions. These authors did not, however, provide the asymptotic behavior of the stress concentration which, it seems, is hard to come by, even when the series solution is given explicitly. This is perhaps due to the fact that the series solution is not uniformly convergent as the holes (or rigid inclusions) become infinitely close. For example, in plane elastostatics, to extract the asymptotic behavior from the Jeffrey-Mindlin solution (Jeffrey, 1920; Mindlin, 1948) of a circular hole interacting with a free straight boundary, and subjected to uniform remote tension, Duan, Kienzler, and Herrmann (1986) had to make some intuitive assumptions to arrive at the result which was rigorously confirmed later by Callias and Markenscoff (1989), but after using some heavy

Contributed by the Applied Mechanics Division of THE AMERICAN SOCIETY OF MECHANICAL ENGINEERS for publication in the ASME JOURNAL OF APPLIED MECHANICS.

Discussion on this paper should be addressed to the Technical Editor, Prof. Leon M. Keer, The Technological Institute, Northwestern University, Evanston, IL 60208, and will be accepted until four months after final publication of the paper itself in the ASME JOURNAL OF APPLIED MECHANICS.

Manuscript received by the ASME Applied Mechanics Division, Mar. 7, 1991; final revision, Nov. 12, 1991. Associate Technical Editor: J. W. Rudnicki.

Copyright © 1992 by ASME
Downloaded 03 May 2010 to 171.66.16.247. Redistribution subject to ASME license or copyright; see http://www.asme.org/terms/Terms_Use.cfm

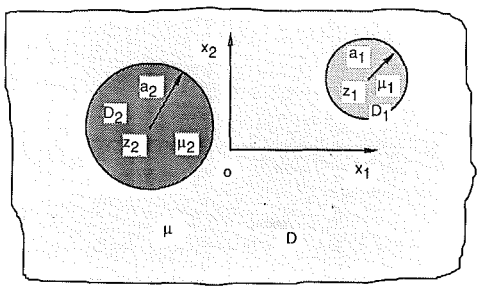


Fig. 1 Two circular inclusions in a domain of infinite extent. The inclusions are of arbitrary radii and occupied by different materials.

analysis. Zimmerman (1988) also considered the corresponding plane problem of two circular traction-free holes in an infinite plate subjected to uniform all-around remote tension. To extract the asymptotic behavior from Ling's solution (1948), he had to use a semi-rigorous step by applying Euler's summation procedure for a divergent series. The result he obtained does not agree with the numerical result obtained by Duan, Kienzler, and Herrmann (1986). Recent rigorous studies by Callias and Markenscoff and the present authors show that the result achieved by Zimmerman is the correct one.

However, in this paper we will concentrate on the antiplane problem, and show that, by applying the heterogenization technique, the results achieved by Budiansky and Carrier (1984) and Steif (1989) can be extended considerably and can be obtained with little calculation. The stress components, at the point of contact between two circular inclusions of different radii and shear moduli and subjected to arbitrary loading, are given by universal formulae in terms of the stress field of the corresponding homogeneous problem evaluated at the same point. The average stress, between two circular traction-free holes or rigid inclusions of different radii and inserted into a matrix of infinite extent subjected to *arbitrary* loading, is obtained in closed form. The derivation hinges on the discovery that the difference in the displacement field, at the limit points of the Apollonius family of circles to which the boundaries of the inclusions belong, is the same for the heterogeneous problem as for the corresponding homogeneous one. Moreover, the solution presented in (E. Honein et al., 1992) is rederived here in a way which allows the evaluation of the asymptotic behavior on one hand and an extension to plane and even three-dimensional elastostatics, on the other hand. This new formulation draws on ideas presented by the authors in (T. Honein et al., 1991) and is presented in Section 1. The universal formulae which are valid under arbitrary loading are given in Section 2, and the asymptotic behavior is derived in Section 3. The results of this paper are summarized in Section 4. In this new formulation, a key role will again be played by the fixed points of Möbius transformations which are also the limit points of the Apollonius family mentioned above.

1 Two Circular Inclusions in Anti-Plane Elastostatics

Under antiplane deformations, the displacement field satisfies

$$u_1 = u_2 = 0, \quad u = u_3 = u_3(x_1, x_2), \tag{1}$$

i.e., the only nonvanishing component of displacement, with respect to a Cartesian coordinate system $Ox_1x_2x_3$, is $u = u_3$ which is a function of the coordinates x_1 and x_2 only.

As is well known, the displacement field u can be given, in the case of antiplane elastostatics, in terms of an analytic complex function ϕ of a complex variable $z = x_1 + ix_2$, namely

$$u = \frac{1}{\mu}\,\mathfrak{I}\{\phi(z)\}, \tag{2}$$

where μ is the shear modulus and $\mathfrak{I}$ stands for the imaginary part of the argument. Then the stress field, in Cartesian coordinates, is related to ϕ by

$$\sigma_{23} + i\sigma_{13} = \phi', \tag{3}$$

and, in polar coordinates, by

$$\sigma_{3\theta} + i\sigma_{3r} = e^{i\theta}\phi', \tag{4}$$

where, throughout the paper, a prime indicates differentiation with respect to the complex variable z.

Consider now the system shown in Fig. 1, consisting of three domains D, D_1, and D_2, where D is of infinite extent and is occupied by a material, of shear modulus μ, subjected to arbitrary loading (singularities). The regions D_1 and D_2 are circular domains centered at z_1 and z_2, of radii a_1 and a_2, and occupied by materials of shear moduli μ_1 and μ_2, respectively.

We assume that the arbitrary singularities would produce the complex potential ϕ in antiplane elastostatics if D occupied the whole space. We seek the solution of the heterogeneous problem in terms of complex potentials in the form

$$\text{in } D\text{: } \Phi = \phi + \mathcal{H}_1(f_1) + \mathcal{H}_2(f_2), \tag{5}$$

$$\text{in } D_1\text{: } \Phi_1 = \phi + \phi_1, \tag{6}$$

$$\text{in } D_2\text{: } \Phi_2 = \phi + \phi_2, \tag{7}$$

where ϕ_1 and f_1 are analytic in D_1, while ϕ_2 and f_2 are analytic in D_2.

Here, $\mathcal{H}_i$ ($i = 1, 2$) designates the "hat" transformation with respect to the circle $C_i = \partial D_i$ bounding D_i, i.e., $\mathcal{H}_i$ is defined by

$$\mathcal{H}_i(f_i)(z) = \overline{f_i(A_i z)}, \tag{8}$$

where the overbar indicates complex conjugation and A_i is the inversion with respect to C_i. We recall that A_i is given by

$$A_i z = \frac{a_i^2}{\bar{z} - \bar{z}_i} + z_i. \tag{9}$$

In the present formulation, the problem reduces to the determination of the four unknown analytic functions ϕ_1, ϕ_2, f_1, and f_2. Four equations can be supplied by writing down the continuity of tractions and displacements across ∂D_1 and ∂D_2. These will lead to the result that ϕ_1 and ϕ_2 are simply expressible in terms of f_1 and f_2 and ϕ and that the governing equation for f_1 is a functional equation relating the values of f_1 at two distinct points, namely z and $Mz = A_1A_2z$, where M is the Möbius transformation introduced earlier by the authors (E. Honein et al., 1992). Similar result holds for f_2.

The governing equations for f_1 and f_2, if solved by iterations, yield the same results as in (E. Honein et al., 1992). However, an important amount of information can be extracted from these equations with very little calculation. On the other hand, they open the door for alternate methods of solution. One such method, which appears most amenable for studying the asymptotic behavior of the stress at the closest points as the two circular holes or rigid inclusions approach each other, will be herein explored and exploited for this purpose.

1.1 Continuity of Displacement Across ∂D_1 and ∂D_2.

It follows from Eq. (2) that the displacement field will be continuous across ∂D_1 provided the following relation holds:

$$\frac{1}{\mu}\,\mathfrak{I}\Phi = \frac{1}{\mu_1}\,\mathfrak{I}\Phi_1. \tag{10}$$

On substituting in (10) Φ and Φ_1 by their expressions given by (5) and (6) and noting that $\mathcal{H}_1(f_1) = \overline{f_1}$ along ∂D_1, we obtain, along ∂D_1,

$$\mathfrak{I}\{\phi - f_1 + \mathcal{H}_2(f_2)\} = \frac{\mu}{\mu_1}\,\mathfrak{I}\{\phi + \phi_1\}, \tag{11}$$

which would be satisfied if the following relation holds:

$$\phi + \phi_1 = m_1\{\phi - f_1 + \mathcal{H}_2(f_2)\}. \tag{12}$$

Downloaded 03 May 2010 to 171.66.16.247. Redistribution subject to ASME license or copyright; see http://www.asme.org/terms/Terms_Use.cfm

A similar argument leads to the result that the displacement field will be continuous across ∂D_2 provided

$$\phi + \phi_2 = m_2\{\phi - f_2 + \mathcal{K}_1(f_1)\}. \tag{13}$$

In (12) and (13), the relative shear modulus m_i ($i = 1, 2$) is defined by $m_i = \mu_i/\mu$.

1.2 Continuity of Traction Across ∂D_1 and ∂D_2. The σ_{3r} component of the stress field will be continuous across ∂D_1 if

$$\mathcal{G}\left\{\frac{z-z_1}{a_1}\,\Phi'\right\} = \mathcal{G}\left\{\frac{z-z_1}{a_1}\,\Phi_1'\right\}. \tag{14}$$

On substituting in (14) Φ and Φ_1 by their values given by (5) and (6), we obtain the following relation:

$$\phi_1 = f_1 + \mathcal{K}_2(f_2) + \text{constant}. \tag{15}$$

A similar argument leads to the result that the traction will be continuous across ∂D_2 provided

$$\phi_2 = f_2 + \mathcal{K}_1(f_1) + \text{constant}. \tag{16}$$

Throughout this paper, *constant* refers to complex numbers which do not contribute to the stress field.

The elimination of ϕ_1 from (12) and (15) and ϕ_2 from (13) and (16), gives the following two relations:

$$f_1 - \alpha_1\mathcal{K}_2(f_2) = \alpha_1\phi + \text{constant}, \tag{17}$$

and

$$f_2 - \alpha_2\mathcal{K}_1(f_1) = \alpha_2\phi + \text{constant}, \tag{18}$$

where α_i ($i = 1, 2$) is defined by $\alpha_i = (m_i - 1)(m_i + 1)^{-1} = (\mu_i - \mu)(\mu_i + \mu)^{-1}$.

These last two equations can be combined to yield the governing equations for f_1 and f_2 as

$$f_1(z) - \alpha_1\alpha_2 f_1(Mz) = \alpha_1\phi + \alpha_1\alpha_2\overline{\phi(A_2z)} + \text{constant}, \tag{19}$$

and

$$f_2(z) - \alpha_1\alpha_2 f_2(Nz) = \alpha_2\phi + \alpha_1\alpha_2\overline{\phi(A_1z)} + \text{constant}, \tag{20}$$

where we recall that $Mz = A_1A_2z$ is a Möbius transformation and $Nz = A_2A_1z$ is its inverse.

The solution when $\alpha_1\alpha_2 \neq 1$ can be obtained, for example, by setting conveniently the constants equal to zero in Eqs. (19) and (20) and then using iteration. This leads to the solution as

$$f_1(z) = \alpha_1\sum_{n=0}^{\infty}(\alpha_1\alpha_2)^n\phi(M^nz) + \sum_{n=1}^{\infty}(\alpha_1\alpha_2)^n\overline{\phi(A_2M^{n-1}z)}, \tag{21}$$

and

$$f_2(z) = \alpha_2\sum_{n=0}^{\infty}(\alpha_1\alpha_2)^n\phi(N^nz) + \sum_{n=1}^{\infty}(\alpha_1\alpha_2)^n\overline{\phi(A_1N^{n-1}z)}. \tag{22}$$

Then, ϕ_1 and ϕ_2 are obtained from (15) and (16).

The foregoing solution is identical with the one obtained earlier by the authors (E. Honein et al., 1992).

2 Some Universal Formulae

In this section, we show that useful information can be extracted from the governing equations for f_1 and f_2 with little calculation.

For this purpose, a crucial role will be played by the fixed points of the Möbius transformation M: γ_1 and γ_2 defined by $M\gamma_i = \gamma_i$, $i = 1, 2$. These fixed points are the limit points of the Apollonius family of circles (see Ahlfors, 1979) to which ∂D_1 and ∂D_2 belong. We choose γ_1 and γ_2 inside ∂D_1 and ∂D_2, respectively. It can be shown that γ_1 and γ_2 are given by

$$\gamma_1 = \frac{L - \sqrt{\Delta}}{2(\bar{z}_2 - \bar{z}_1)},\quad \gamma_2 = \frac{L + \sqrt{\Delta}}{2(\bar{z}_2 - \bar{z}_1)}, \tag{23}$$

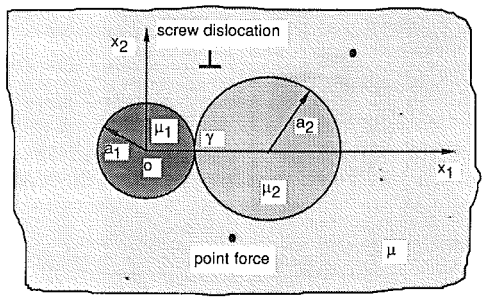


Fig. 2 Two circular inclusions touching each other. The point of contact γ is the fixed point of the Möbius transformations.

where

$$L = a_1^2 - a_2^2 + (z_2 + z_1)(\bar{z}_2 - \bar{z}_1), \tag{24}$$

and

$$\Delta = (a_1^2 + a_2^2 - |z_2 - z_1|^2)^2 - 4a_1^2a_2^2. \tag{25}$$

Here, a_1 and a_2 designate the radii of C_1 and C_2 while z_1 and z_2 are their centers, respectively.

In the remainder of this paper, we take, without loss of generality, the x_1-axis along the line joining the centers of the two inclusions.

Let us consider first the case where the two circular inclusions touch each other (see Fig. 2). In this instance, the two fixed points γ_1 and γ_2 collapse to a single fixed point γ which is the point of contact. We wish to find the stress field at the point of contact between the two inclusions.

It follows from Eqs. (5), (6), and (15) that

$$\Phi' = \phi' + (\overline{A_1z})'\overline{f_1'(A_1z)} + (\overline{A_2z})'\overline{f_2'(A_2z)}, \tag{26}$$

and

$$\Phi_1' = \phi' + \phi_1' = \phi' + f_1' + (\overline{A_2z})'\overline{f_2'(A_2z)}. \tag{27}$$

At the point of contact, and since the x_1-axis is along the line joining the centers of the two inclusions, we obtain

$$\Phi'(\gamma) = \phi'(\gamma) - \overline{f_1'(\gamma)} - \overline{f_2'(\gamma)}, \tag{28}$$

and

$$\Phi_1'(\gamma) = \phi'(\gamma) + f_1'(\gamma) - \overline{f_2'(\gamma)}. \tag{29}$$

On the other hand, by differentiating Eqs. (19) and (20) and setting $z = \gamma$, we obtain

$$f_1'(\gamma) = \frac{\alpha_1\phi'(\gamma) - \alpha_1\alpha_2\overline{\phi'(\gamma)}}{1 - \alpha_1\alpha_2}, \tag{30}$$

and

$$f_2'(\gamma) = \frac{\alpha_2\phi'(\gamma) - \alpha_1\alpha_2\overline{\phi'(\gamma)}}{1 - \alpha_1\alpha_2}, \tag{31}$$

yielding the following expressions for $\Phi'(\gamma)$ and $\Phi_1'(\gamma)$,

$$\Phi'(\gamma) = (1 - \alpha_1\alpha_2)^{-1}((1 + \alpha_1\alpha_2)\phi'(\gamma) - (\alpha_1 + \alpha_2)\overline{\phi'(\gamma)}), \tag{32}$$

and

$$\Phi_1'(\gamma) = (1 - \alpha_1\alpha_2)^{-1}((1 + \alpha_1)\phi'(\gamma) - \alpha_2(1 + \alpha_1)\overline{\phi'(\gamma)}). \tag{33}$$

Finally, we obtain, after some simple manipulations for the stress components at the point of contact:

$$\sigma_{13}^D = \sigma_{13}^{D_1} = \sigma_{13}^{D_2} = m_H\sigma_{13}, \tag{34}$$

$$\sigma_{23}^D = m_A^{-1}\sigma_{23}, \tag{35}$$

$$\sigma_{23}^{D_1} = m_1m_A^{-1}\sigma_{23}, \tag{36}$$

and by similar consideration,

$$\sigma_{23}^{D_2} = m_2m_A^{-1}\sigma_{23}, \tag{37}$$

Downloaded 03 May 2010 to 171.66.16.247. Redistribution subject to ASME license or copyright; see http://www.asme.org/terms/Terms_Use.cfm

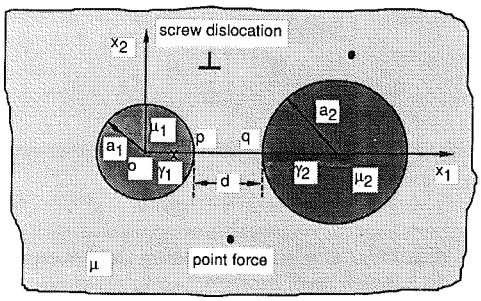


Fig. 3 Two circular inclusions in a domain of infinite extent and subjected to arbitrary antiplane deformation. The closest points of the two inclusions, *p* and *q*, are separated by a distance *d*.

where m_A and m_H are the arithmetic and harmonic average of m_1 and m_2 and are defined by

$$2m_A = m_1 + m_2, \tag{38}$$

and

$$2m_H^{-1} = m_1^{-1} + m_2^{-1}. \tag{39}$$

The stress without superscript refers to the stress field in the corresponding homogeneous problem.

Now we return to the general case and we wish to evaluate the difference in the displacement field evaluated at γ_1 and γ_2 in the heterogeneous problem. We obtain from Eqs. (2), (6), and (7),

$$u^{D_2}(\gamma_2) - u^{D_1}(\gamma_1) = \mathcal{I}\left\{\frac{\Phi_2(\gamma_2)}{\mu_2} - \frac{\Phi_1(\gamma_1)}{\mu_1}\right\}, \tag{40}$$

but using Eqs. (12) and (13), we obtain the following important formula:

$$u^{D_2}(\gamma_2) - u^{D_1}(\gamma_1) = \frac{1}{\mu}\,\mathcal{I}\{\phi(\gamma_2) - \phi(\gamma_1)\} = u(\gamma_2) - u(\gamma_1). \tag{41}$$

This universal formula states that the difference in the displacement field evaluated at the two fixed points is preserved when the two inclusions are introduced. As an important application of (41), consider the case of two rigid inclusions (see Fig. 3). The average stress $\langle \sigma_{31}^D \rangle$ between the two rigid inclusions (when σ_{31} is integrable) is given by

$$\langle \sigma_{31}^D \rangle d = \int_p^q \sigma_{31}^D dx_1 = \int_p^q \mu \frac{\partial u^D}{\partial x_1}\, dx_1 = \mu(u^D(q) - u^D(p)), \tag{42}$$

but

$$u^D(q) - u^D(p) = u^{D_2}(\gamma_2) - u^{D_1}(\gamma_1) = u(\gamma_2) - u(\gamma_1). \tag{43}$$

Hence,

$$\langle \sigma_{31}^D \rangle = \frac{\mu}{d}\,(u(\gamma_2) - u(\gamma_1)), \tag{44}$$

which is a closed-form formula giving the average stress between the rigid inclusions. When these inclusions approach each other we conclude that

$$\langle \sigma_{31}^D \rangle = \frac{\mu}{d}\left((\gamma_2 - \gamma_1)\frac{\partial u}{\partial x_1}(\gamma_1)\right) + O((\gamma_2 - \gamma_1)^2)$$

$$= \frac{2\mu}{d}\left(\frac{2da_1a_2}{a_1 + a_2}\right)^{1/2} \frac{\partial u}{\partial x_1}(\gamma_1) + O(1)$$

$$= \frac{2}{\sqrt{\epsilon}}\,\sigma_{31}(\gamma_1) + O(1), \tag{45}$$

where we have defined ϵ by $\epsilon = d/a_H$, a_H being the harmonic average of a_1 and a_2.

Using the analogy of Steif, we obtain the corresponding results for circular holes as

$$\langle \sigma_{32}^D \rangle = \frac{1}{d}\,\Re\{\phi(\gamma_2) - \phi(\gamma_1)\}, \tag{46}$$

which yields

$$\langle \sigma_{32}^D \rangle = \frac{2}{\sqrt{\epsilon}}\,\sigma_{32}(\gamma_1) + O(1). \tag{47}$$

These results constitute a considerable generalization of the ones achieved by Budiansky and Carrier (1984) (and Steif, 1989). Their analysis was carried out only for two identical rigid inclusions (and holes) in a particular position with respect to a uniform remote shear.

3 Asymptotic Behavior of the Stress Concentration

In the remainder of this paper we consider, without loss of generality, the situation depicted in Fig. 3. Our purpose is to find the asymptotic behavior of $\sigma_{32}(p)$ and $\sigma_{31}(p)$ as d tends to zero, for the case of two holes or rigid inclusions, respectively. To this end, we consider Eqs. (19) and (20), and transform them into two equations which can simply be solved using power series expansions. The crucial step in the following development hinges on transforming the Möbius transformations into their normal forms (see Schwerdtfeger, 1979). For this purpose we consider the Möbius transformation defined by

$$z_1^* = T_1 z = \frac{z - \gamma_1}{z - \gamma_2}. \tag{48}$$

The inverse of T_1 will then be given by

$$T_1^{-1} z = \frac{\gamma_2 z - \gamma_1}{z - 1}. \tag{49}$$

Now, it can be easily verified, since

$$Mz = \frac{(\gamma_2 k - \gamma_1)z + \gamma_1\gamma_2(1 - k)}{(k - 1)z + \gamma_2 - k\gamma_1}, \tag{50}$$

that

$$T_1 M T_1^{-1} z = kz, \tag{51}$$

where

$$k = \frac{a_1^2 + a_2^2 - |z_1 - z_2|^2 + \sqrt{\Delta}}{a_1^2 + a_2^2 - |z_1 - z_2|^2 - \sqrt{\Delta}}.$$

By using similar considerations, we can verify that

$$T_2 N T_2^{-1} z = kz \tag{52}$$

where T_2 is defined by

$$z_2^* = T_2 z = \frac{z - \gamma_2}{z - \gamma_1}, \tag{53}$$

and

$$T_2^{-1} z = \frac{\gamma_1 z - \gamma_2}{z - 1}. \tag{54}$$

These considerations lead us to define new unknown functions g_1 and g_2 by

$$g_1 = f_1 \circ T_1^{-1}, \tag{55}$$

and

$$g_2 = f_2 \circ T_2^{-1}, \tag{56}$$

where $\circ$ denotes composition of functions defined by $(f \circ h)x = f(h(x))$. Then,

$$g_1(z_1^*) = f_1(T_1^{-1} z_1^*) = f_1(z), \tag{57}$$

$$g_2(z_2^*) = f_2(T_2^{-1} z_2^*) = f_2(z). \tag{58}$$

Downloaded 03 May 2010 to 171.66.16.247. Redistribution subject to ASME license or copyright; see http://www.asme.org/terms/Terms_Use.cfm

Equations (19) and (20) will be transformed into

$$g_1(z_1^*) - \alpha_1\alpha_2 g_1(kz_1^*) = \alpha_1\phi(z) + \alpha_1\alpha_2\overline{\phi(A_2z)} + \text{const} = R_1(z_1^*), \quad (59)$$

and

$$g_2(z_2^*) - \alpha_1\alpha_2 g_2(kz_2^*) = \alpha_2\phi(z) + \alpha_1\alpha_2\overline{\phi(A_1z)} + \text{const} = R_2(z_2^*). \quad (60)$$

These equations can be simply solved using power series expansions.

We turn our attention to the case of two holes ($\alpha_1 = \alpha_2 = -1$).

The "const" in (59) may be determined by setting $z_1^* = 0$, leading to

$$R_1(z_1^*) = \phi(\gamma_1) - \overline{\phi(\gamma_2)} - \phi(z) + \overline{\phi(A_2z)}. \quad (61)$$

If we expand $R_1(z_1^*)$ in the form

$$R_1(z_1^*) = \sum_{n=1}^{\infty} c_n z_1^{*n}, \quad (62)$$

then the solution of Eq. (59) is given by

$$g_1(z_1^*) = \sum_{n=1}^{\infty} \frac{c_n z_1^{*n}}{1-k^n}, \quad (63)$$

which also can be written as

$$g_1(z_1^*) = \frac{1}{1-k}\sum_{n=1}^{\infty} \frac{c_n z_1^{*n}}{1+k+\ldots+k^{n-1}}, \quad (64)$$

and by similar considerations we find that

$$R_2(z_2^*) = \phi(\gamma_2) - \overline{\phi(\gamma_1)} - \phi(z) + \overline{\phi(A_1z)}, \quad (65)$$

and if expanded in the form

$$R_2(z_2^*) = \sum_{n=1}^{\infty} d_n z_2^{*n}, \quad (66)$$

then the solution of Eq. (60) can be written as

$$g_2(z_2^*) = \frac{1}{1-k}\sum_{n=1}^{\infty} \frac{d_n z_2^{*n}}{1+k+\ldots+k^{n-1}}. \quad (67)$$

By differentiating Eq. (5), we obtain

$$\Phi'(z) = \phi'(z) + (\overline{A_1z})'\overline{f_1'(A_1z)} + (\overline{A_2z})'\overline{f_2'(A_2z)}, \quad (68)$$

and noting that

$$(\overline{A_iz})' = \frac{-a_i^2}{(z-z_i)^2} \quad i=1, 2, \quad (69)$$

we obtain

$$\Phi'(z) = \phi'(z) - \frac{a_1^2}{(z-z_1)^2}\overline{f_1'(A_1z)} - \frac{a_2^2}{(z-z_2)^2}\overline{f_2'(A_2z)}. \quad (70)$$

Hence the stress field at the point p will be given by

$$\sigma_{23}^D + i\sigma_{13}^D = \Phi'(p) = \phi'(p) - \overline{f_1'(p)} - \frac{a_2^2}{(a_2+d)^2}\overline{f_2'(A_2p)}. \quad (71)$$

By using the chain rule and the fact that

$$\frac{dg_1}{dz_1^*} \sim \frac{R_1(z_1^*)}{(1-k)z_1^*}, \quad (72)$$

and

$$\frac{dg_2}{dz_2^*} \sim \frac{R_2(z_2^*)}{(1-k)z_2^*}, \quad (73)$$

we obtain

$$f_1'(p) \sim -\frac{1}{\sqrt{d}}\sqrt{\frac{2a_1a_2}{a_1+a_2}}\,\Re\phi'(p) \sim f_2'(A_2p), \quad (74)$$

which leads to

$$\sigma_{23}^D + i\sigma_{13}^D \sim \frac{2}{\sqrt{d}}\sqrt{\frac{2a_1a_2}{a_1+a_2}}\,\Re\phi'(p). \quad (75)$$

Hence, we obtain the result that

$$\sigma_{23}^D(p) \sim \frac{2}{\sqrt{\epsilon}}\,\sigma_{23}(p), \quad (76)$$

where we recall that $\epsilon = d/a_H$, a_H being the harmonic average of a_1 and a_2. The corresponding result for two rigid inclusions reads

$$\sigma_{13}^D(p) \sim \frac{2}{\sqrt{\epsilon}}\,\sigma_{13}(p). \quad (77)$$

It is to be noted that

$$\langle\sigma_{23}^D\rangle \sim \sigma_{23}^D(p) \quad \text{(holes)}, \quad (78)$$

and

$$\langle\sigma_{13}^D\rangle \sim \sigma_{13}^D(p) \quad \text{(rigid inclusions)}, \quad (79)$$

since

$$\gamma_1 = p + O(\epsilon^{1/2}). \quad (80)$$

4 Summary and Concluding Remarks

In this paper we considered the problem, in antiplane elastostatics, of two circular inclusions of arbitrary radii and of different shear moduli, perfectly bonded to a matrix of infinite extent which is subjected to arbitrary loading. Using the heterogenization technique developed by the authors, we casted the problem into a governing functional equation and we established the following universal results.

(1) The stress field at the point of contact of two circular inclusions satisfies:

(i)
$$\sigma_{13}^D = \sigma_{13}^{D1} = \sigma_{13}^{D2} = m_H\sigma_{13}, \quad (81)$$

(ii)
$$\sigma_{23}^D = m_A^{-1}\sigma_{23}, \quad (82)$$

(iii)
$$\sigma_{23}^{D1} = m_1m_A^{-1}\sigma_{23}, \quad (83)$$

(iv)
$$\sigma_{23}^{D2} = m_2m_A^{-1}\sigma_{23}, \quad (84)$$

where the x_1-axis is taken along the line joining the two centers. m_1 and m_2 are the relative shear moduli of the two inclusions with respect to the matrix, and m_A and m_H are the arithmetic and harmonic means of m_1 and m_2, respectively. The stress without superscript refers to the stress field in the corresponding homogeneous problem.

(2) The difference in the displacement field between the two fixed points is preserved, i.e., its value for the heterogeneous problem is the same as for the homogeneous one. As a consequence, we showed that the average stress between two rigid inclusions is given by the exact formula

$$\langle\sigma_{31}^D\rangle = \frac{\mu}{d}\,(u(\gamma_2) - u(\gamma_1)), \quad (85)$$

where μ is the shear modulus and d is the distance between the rigid inclusions and u designates the displacement field in the homogeneous problem. The corresponding result for circular holes is

$$\langle\sigma_{32}^D\rangle = \frac{1}{d}\,\Re\{\phi(\gamma_2) - \phi(\gamma_1)\}, \quad (86)$$

where ϕ is the complex potential of the homogeneous problem.

(3) For two circular holes the stress field at one of the closest point has the asymptotic expansion

Downloaded 03 May 2010 to 171.66.16.247. Redistribution subject to ASME license or copyright; see http://www.asme.org/terms/Terms_Use.cfm

$$\sigma_{23}^{D}(p) \sim \frac{2}{\sqrt{\epsilon}}\,\sigma_{23}(p), \tag{87}$$

where $\epsilon = d/a_H$, a_H being the harmonic mean of the radii of the two circles.

The corresponding result for two rigid inclusions reads

$$\sigma_{13}^{D}(p) \sim \frac{2}{\sqrt{\epsilon}}\,\sigma_{13}(p). \tag{88}$$

The average stress between the circles has the same asymptotic expansion.

These results are universal in the sense of being independent of the loading considered.

The case when one or both the boundaries of the inclusions are straight lines can be treated using the same method.

The technique used here can be applied to other problems governed by Laplace's equation. The case of biharmonic problem will be treated in a forthcoming paper.

Acknowledgment

This work was performed with the support of the U.S. Department of Energy and the National Science Foundation. This support is gratefully acknowledged.

References

Ahlfors, L. V., 1979, *Complex Analysis*, 3rd ed., McGraw-Hill, New York.

Budiansky, B., and Carrier, G. F., 1984, "High Shear Stress in Stiff-Fiber Composites," ASME JOURNAL OF APPLIED MECHANICS, Vol. 51, pp. 733–735.

Callias, C. B., and Markenscoff, X., 1989, "Singular Asymptotics Analysis for the Singularity at a Hole near a Boundary," *Quarterly of Applied Mathematics*, Vol. 47, No. 2, p. 233–245.

Duan, Z.-P., Kienzler, R., and Herrmann, G., 1986, "An Integral Equation Method and its Application to Defect Mechanics," *J. Mech. Phys. Solids*, Vol. 36, pp. 539–562.

Goree, J. G., and Wilson, Jr., H. B., 1967, "Transverse Shear Loading in an Elastic Matrix Containing Two Circular Cylindrical Inclusions," ASME JOURNAL OF APPLIED MECHANICS, June 1967, pp. 511–513.

Honein, E., Honein, T., and Herrmann, G., 1991, "On Two Circular Inclusions in Harmonic Problems," *Quarterly of Applied Mathematics*, Vol. L, No. 3, Sept., pp. 479–499.

Honein, T., Honein, E., and Herrmann, G., 1991, "On Cylindrical and Plane Layered Media in Anti-Plane Elastostatics," ASME JOURNAL OF APPLIED MECHANICS, to appear.

Jeffrey, G. B., 1920, "Plane Stress and Plane Strain in Bipolar Coordinates," *Trans. Roy. Soc. London*, Vol. A221, pp. 265–293.

Ling, C. B., 1948, "On the Stresses in a Plate Containing Two Circular Holes," *J. Appl. Phys.*, Vol. 19, pp. 77–82.

Mindlin, R. D., 1948, "Stress Distribution around a Hole near the Edge of a Plate under Tension," *Proc. Soc. Exptl. Stress Anal.*, Vol. 5, pp. 56–67.

Schwerdtfeger, H., 1979, *The Geometry of Complex Numbers*, Dover, New York.

Steif, Paul S., 1989, "Shear Stress Concentration Between Holes," ASME JOURNAL OF APPLIED MECHANICS, Vol. 56, pp. 719–721.

Zimmerman, R. B., 1988, "Stress Singularity Around Two Nearby Holes," *Mechanics Research Communications*, Vol. 15, No. 2, pp. 87–90.

Downloaded 03 May 2010 to 171.66.16.247. Redistribution subject to ASME license or copyright; see http://www.asme.org/terms/Terms_Use.cfm

Sriram Vaidyanathan
Graduate Student.

Demitris Kouris
Assoc. Mem. ASME

Department of Mechanial and Aerospace Engineering, Arizona State University, Tempe, AZ 85287-6106

Effects of an Elliptical Inhomogeneous Inclusion With a Slipping Interface on the Elastic Field of a Concentrated Moment

Introduction

The plane problem associated with the interaction of point defects with inhomogeneities has been the subject of a number of studies in the past. The majority of those analyses involve circular inclusions in the vicinity of a dislocation. A comprehensive review of the subject has been presented by Dundurs (1969).

Warren (1983) solved the dislocation/elliptical inclusion case utilizing a formulation in terms of complex potentials.

The related problem of a concentrated couple in the vicinity of an elliptical elastic inhomogeneity has been solved by Kouris and Tsuchida (1990), for the case of a perfectly bonded inclusion/matrix interface. However, the condition of a perfect bonding is often inadequate in describing the mechanical behavior of inclusions. Common examples of incoherent interfaces include debonded inclusions in high-strength steel, grain boundary sliding in polycrystals, and fibers in composite materials (Mura, 1987). It is therefore important to evaluate the effects of local defects on the elastic field of sliding inclusions.

In the present investigation, the analysis involves a concentrated couple in the vicinity of an inclusion with a slipping interface. Such an interface cannot sustain any shear tractions. In order to evaluate the effects of the interfacial integrity, a number of examples are presented illustrating the differences between perfect bonding (PB) and sliding (SL).

Mathematical Formulation and Solution Technique

Let us consider a concentrated moment at 0_1 (x_1, y_1) which is at a distance d from the center 0 (x, y) of an elliptical inhomogeneity, as illustrated in Fig. 1. Both the inhomogeneity and the surrounding matrix are assumed to be linearly elastic and isotropic.

The total elastic field can be formulated by superimposing the effect of the moment on the disturbance field due to the presence of the inhomogeneity. According to the Papkovich-Neuber displacement formulation (Papkovich, 1932; Neuber, 1934), the elastic field can be expressed by

$$2Gu = \text{grad}(\Phi_0 + x\Phi_1 + y\Phi_2) - (\kappa+1)[\Phi_1, \Phi_2] \tag{1}$$

and

$$2Gu_1 = \text{grad}(\Phi_{01} + x_1\Phi_{11} + y_1\Phi_{21}) - (\kappa+1)[\Phi_{11}, \Phi_{21}] \tag{2}$$

where the Φ's denote arbitrary harmonic functions and $\kappa = 3\text{–}4\nu$ for plane strain, or $\kappa = (3\text{–}\nu)/(1 + \nu)$ for plane stress. The potentials in the angular brackets correspond to the x and y components of the displacement vector, respectively.

Based upon the given geometry,

$$x_1 = x - d \text{ and } y_1 = y. \tag{3}$$

Therefore, according to the above transformation, (2) becomes

$$2Gu_1 = \text{grad}((\Phi_{01} - d\,\Phi_{11}) + x\Phi_{11} + y\Phi_{21}) - (\kappa+1)[\Phi_{11}, \Phi_{21}]. \tag{4}$$

The couple M can be expressed by a single potential function Φ_{01} $\Phi_{01} = M/2\pi\,\theta_1$, which in elliptical coordinates becomes

$$\Phi_{01} = p_0\left\{\pi - 2\sum_{n=1}^{\infty}\frac{1}{n}e^{-n\alpha d}\sinh(n\alpha)\sin(n\beta)\right\}, \qquad \text{[I]}$$

where $p_0 = M/2\pi$ and (α, β) are defined by the transformation

$$x = c\cosh\alpha\cos\beta$$
$$y = c\sinh\alpha\sin\beta.$$

The disturbance due to the elastic inhomogeneity is expressed by

$$\Phi_0 = p_0\left[F_0\beta + \sum_{n=1}^{\infty}A_n e^{-n\alpha}\sin(n\beta)\right]$$
$$\Phi_1 = p_0\sum_{n=1}^{\infty}B_n e^{-n\alpha}\sin(n\beta) \qquad \text{[II]}$$

for the matrix $(\alpha > \alpha_0)$, and

Contributed by the Applied Mechanics Division of The American Society of Mechanical Engineers for publication in the ASME Journal of Applied Mechanics.

Discussion on this paper should be addressed to the Technical Editor, Professor Leon M. Keer, The Technological Institute, Northwestern University, Evanston, IL 60208, and will be accepted until four months after final publication of the paper itself in the ASME Journal of Applied Mechanics.

Manuscript received by the ASME Applied Mechanics Division, Mar. 28, 1991; final revision, Aug. 13, 1991. Associate Technical Editor: J. W. Rudnicki.

Copyright © 1992 by ASME
Downloaded 03 May 2010 to 171.66.16.247. Redistribution subject to ASME license or copyright; see http://www.asme.org/terms/Terms_Use.cfm

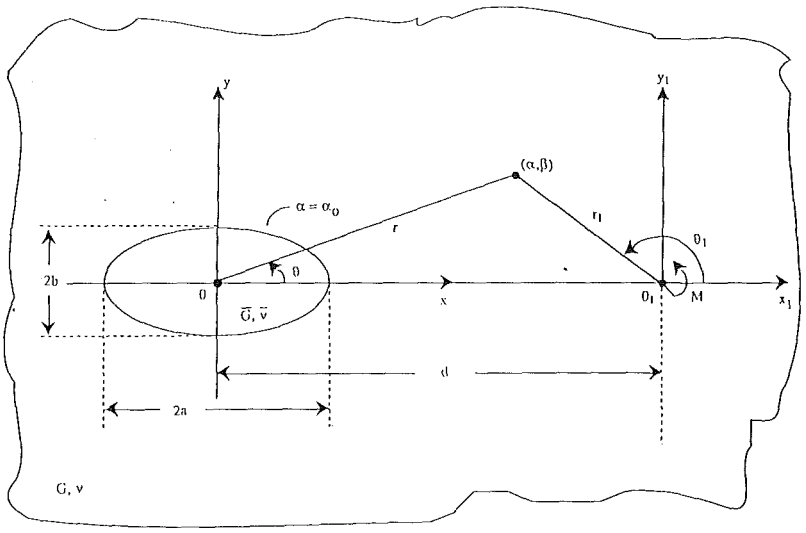


Fig. 1 Geometry of the problem

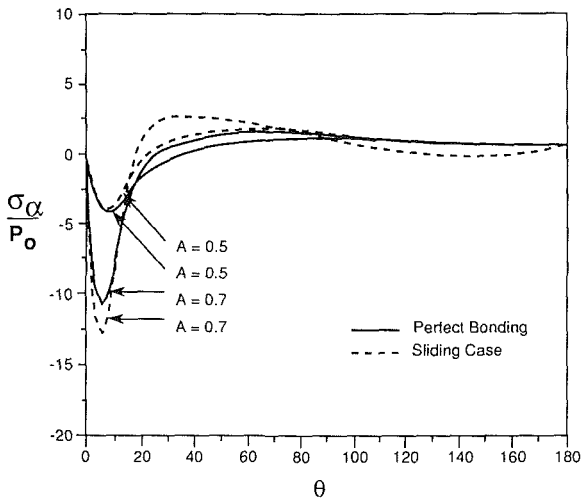


Fig. 2 Normal stress along the interace

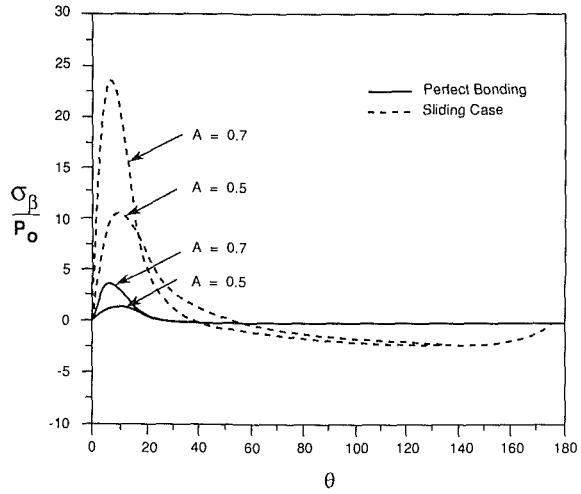


Fig. 3 Variation of the hoop stress along the interface

$$\Phi_0 = p_0 \sum_{n=1}^{\infty} \overline{A}_n \sinh(n\alpha)\sin(n\beta)$$

$$\Phi_1 = p_0 \sum_{n=1}^{\infty} \overline{B}_n \sinh(n\alpha)\sin(n\beta) \qquad \text{[III]}$$

for the inclusion ($\alpha < \alpha_0$).

Utilizing the displacement potentials [I], [II], and [III], stresses and displacements in the matrix and the inhomogeneity can be evaluated in terms of the unknown coefficients F_0, A_n, B_n, $\overline{A}_n$ and $\overline{B}_n$.

Based on the assumption that the interface cannot sustain any shear tractions, the boundary conditions along the interface are

$$(u_\alpha)_{\alpha=\alpha_0} = (\overline{u}_\alpha)_{\alpha=\alpha_0}, \quad (\sigma_\alpha)_{\alpha=\alpha_0} = (\overline{\sigma}_\alpha)_{\alpha=\alpha_0},$$
$$(\tau_{\alpha\beta})_{\alpha=\alpha_0} = 0 \quad \text{and} \quad (\overline{\tau}_{\alpha\beta})_{\alpha=\alpha_0} = 0. \qquad (5)$$

The solution is obtained by enforcing the boundary conditions (5) and utilizing the stresses and displacements obtained from the potentials (I)–(III). This approach is similar to the one used by Kouris and Mura (1989) and yields a linear system of algebraic equations for the series coefficients.

Comparison of the Results Between Perfect Bonding and Sliding

The stresses along the slipping interface of the inhomogeneous inclusion, were compared with those obtained for the case of perfect bonding.

Calculations were performed under conditions of plane stress, with $\nu = \bar{\nu} = 0.3$. Initially, the effect of the relative distance between the couple and the inhomogeneity ($A = a/d$) was considered, while the shear moduli ($\Gamma = \overline{G}/G$) and the inclusion aspect ratio ($S = a/b$) were kept fixed and equal to 2 and 1/2, respectively.

As shown in Fig. 2, the distribution of the normal stress σ_α along the interface, for various values of A, does not indicate appreciable deviation between PB and SL, whereas the hoop stress σ_β shows a significant increase in its maximum tensile value for the sliding case, when compared to that of PB (Fig. 3).

Consequently, stresses and displacements were evaluated by varying the shear moduli ratio Γ, while the values of S and A were each taken equal to 1/2. It can be observed that the normal stress σ_α does not exhibit any significant deviation between the two cases of PB and SL.

Downloaded 03 May 2010 to 171.66.16.247. Redistribution subject to ASME license or copyright; see http://www.asme.org/terms/Terms_Use.cfm

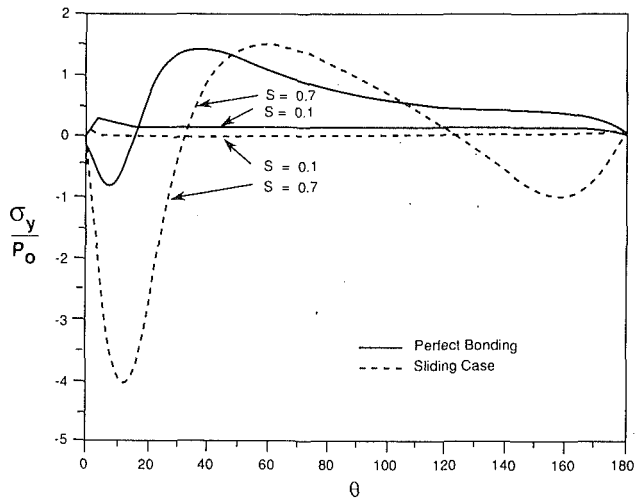


Fig. 4 Distribution of σ_y along the interface

Finally, the effects of changing the aspect ratio S were studied, while the shear moduli ratio Γ and the relative distance A were taken equal to 2 and 1/2, respectively. The matrix stress σ_y shows a considerable increase in its maximum compressive value, in the case of SL, for θ between 0 and 20 (Fig. 4).

References

Dundurs, J., 1969, "Elastic Interaction of Dislocations with Inhomogeneities," *Mathematical Theory of Dislocations*, T. Mura ed., ASME, New York, pp. 70–115.

Kouris, D., and Mura, T., 1989, "The Elastic Field of a Hemispherical Inhomogeneity at the Free Surface of an Elastic Half Space," *J. Mech. Phys. Solids*, Vol. 37, pp. 365–379.

Kouris, D., and Tsuchida, E., 1990, "The Concentrated Couple in the Vicinity of an Elastic Elliptical Inhomogeneity," submitted for publication.

Mura, T., 1987, *Micromechanics of Defects in Solids*, Martinus Nijhoff, Dordrecht.

Neuber, H., 1934, "Ein Neuer Ansatz zur Losung Raumlicher Probleme der Elastizitatstheorie," *Z. Angew. Math. Mech.*, Vol. 14, pp. 203–212.

Papkovich, P. F., 1932, "Solution Generale des Equations Differntielles Fondamentales d'elasticite, Exprimee par Trois Fonctions Harmoniques," *C. R. Acad. Sci.*, Vol. 195, pp. 513–515.

Warren, W., 1983, "The Edge Dislocation Inside an Elliptical Inclusion," *Mech. Mat.*, Vol. 2, pp. 319–330.

Downloaded 03 May 2010 to 171.66.16.247. Redistribution subject to ASME license or copyright; see http://www.asme.org/terms/Terms_Use.cfm

R. Furuhashi
Professor,
Department of Mathematics,
Meiji University
Higashi-mita,
Kawasaki 214, Japan

Jin H. Huang
Graduate Student,
Department of Mechanical Engineering.

T. Mura
ASME Fellow,
Department of Civil Engineering.

Northwestern University,
Evanston, IL 60208-3109

Sliding Inclusions and Inhomogeneities With Frictional Interfaces

Elastic fields due to a sliding inclusion and inhomogeneity with the frictional interface are investigated. The exact solution in closed form is presented for three cases: (i) a spherical inclusion which undergoes constant eigenstrains, (ii) a nondegenerate ellipsoidal inclusion with uniform shear eigenstrains and (iii) a nondegenerate ellipsoidal inhomogeneity subjected to an applied shear stress at infinity. Moreover, the existence of solution for a sliding inclusion and inhomogeneity with frictional interface is also demonstrated.

1 Introduction

Most of the inclusion problems solved by many researchers (Dvorak, 1983; Dvorak et al., 1988; Weng, 1988; among others) are based on the assumption that the displacement and the interfacial traction across the boundary must be continuous. This perfect bonding condition is sometimes inadequate in describing mechanical behavior of inclusion. Inclusions in high-strength steel, for instance, are easily debonded by a few cycle loadings. Grain boundary sliding in polycrystals and granular media even at room temperature (Mori et al., 1983), debonding of fibers in composite material, are also common phenomena.

In the previous papers (Mura and Furuhashi, 1984; Mura et al., 1987), we solved the inclusion and inhomogeneity problems with nonfrictional interface by adding a distribution of Somigliana dislocation to simulate sliding and we found the following results:

(i) When a nondegenerate ellipsoidal inclusion is subjected to uniform shear eigenstrains, the inclusion preserves its shape and the stress field vanishes everywhere in the inclusion and surrounding matrix.

(ii) When an isotropic spherical inclusion is subjected to uniform eigenstrains, the stress field in the inclusion is given by a quadratic polynomial of coordinates.

(iii) When a nondegenerate ellipsoidal inhomogeneity is subjected to an applied shear stress at infinity, the inhomogeneity behaves like a void.

The main objective of this paper is to extend the above results to the case when the interface has a frictional resistance and we intend to establish the following:

(1) When a nondegenerate ellipsoidal inclusion with shear eigenstrains begins to slide, the stress field vanishes everywhere in the inclusion and surrounding matrix.

(2) When an isotropic spherical inclusion with uniform eigenstrains starts to slide along the interface, the stress field in the inclusion is given by a quadratic polynomial of coordinates.

(3) When an ellipsoidal inhomogeneity begins to slide due to an applied shear stress at infinity, the inhomogeneity behaves like a void.

2 Some Preliminaries

Consider an infinitely extended elastic body and let Ω be a subset of this whole space. If elastic constants of the subset Ω and the remainder are identical and Ω has eigenstrains ϵ^*_{ij} within it, the subset is called an inclusion. If the inclusion Ω is perfectly bounded, the well-known Eshelby's displacement solution is given by (Mura, 1987)

$$u_i^E(\mathbf{x}) = -\frac{\partial}{\partial x_k}\int_\Omega G_{ij}(\mathbf{x}-\mathbf{x}')C_{jklm}\epsilon^*_{lm}(\mathbf{x}')d\mathbf{x}'. \tag{1}$$

Here, $G_{ij}(\mathbf{x})$ is the Green's function of elasticity and C_{jklm} elastic constants of material. All indices range from 1 to 3 with the usual convention of summation over repeated Latin indices implied throughout the paper. The corresponding strain and stress components are

$$\gamma_{ij}^E = \frac{1}{2}(u_{i,j}^E + u_{j,i}^E),$$
$$\sigma_{ij}^E(\epsilon^*) = C_{ijkl}(\gamma_{kl}^E - \epsilon^*_{kl}) = -C_{ijkl}\left[\int_\Omega G_{kp,ql}(\mathbf{x}-\mathbf{x}')C_{pqmn}\epsilon^*_{mn}(\mathbf{x}')d\mathbf{x}' + \epsilon^*_{kl}(\mathbf{x})\right]. \tag{2}$$

The displacement field caused by a Somigliana dislocation

Contributed by the Applied Mechanics Division of THE AMERICAN SOCIETY OF MECHANICAL ENGINEERS for presentation at the 1992 ASME Winter Annual Meeting, Anaheim, CA, Nov. 8-13, 1992.

Discussion on this paper should be addressed to Prof. Leon M. Keer, The Technological Institute, Northwestern University, Evanston, IL 60208, and will be accepted until four months after final publication of the paper itself in the ASME JOURNAL OF APPLIED MECHANICS.

Manuscript received by the ASME Applied Mechanics Division, May 14, 1991; final revision, Dec. 12, 1991. Associate Technical Editor: R. M. McMeeking.

Paper No. 92-WA/APM-10.

Copyright © 1992 by ASME
Downloaded 03 May 2010 to 171.66.16.247. Redistribution subject to ASME license or copyright; see http://www.asme.org/terms/Terms_Use.cfm

$\hat{b}_i$ on the frictional interface S is given by Volterra's integral formula (Mura, 1987) as

$$u_i^V(\mathbf{x}) = \frac{\partial}{\partial x_k} \int_S G_{ij}(\mathbf{x}-\mathbf{x}')C_{jkmn}\hat{b}_m(\mathbf{x}')n_n(\mathbf{x}')dS(\mathbf{x}'), \quad (3a)$$

where n_i is the unit outward normal on S. If the vector $\hat{b}_i$ is extended to inside Ω and if impotent components are excluded, the expression u_i^V can be rewritten (Mura and Furuhashi, 1984) as

$$u_i^V(\mathbf{x}) = \frac{\partial}{\partial x_k} \int_\Omega G_{ij}(\mathbf{x}-\mathbf{x}')C_{jklm} \frac{\partial \hat{b}_l(\mathbf{x}')}{\partial x_m'} d\mathbf{x}' + \hat{b}_i(\mathbf{x}). \quad (3b)$$

The corresponding strain and stress components are

$$\gamma_{ij}^V(\hat{\mathbf{b}}) = \frac{1}{2}(u_{i,j}^V + u_{j,i}^V),$$

$$\sigma_{ij}^V(\hat{\mathbf{b}}) = C_{ijkl}\gamma_{kl}^V(\hat{\mathbf{b}})$$

$$= \frac{1}{2} C_{ijkl}\left[\int_\Omega G_{kp,ql}(\mathbf{x}-\mathbf{x}')C_{pqmn}\left(\frac{\partial \hat{b}_m}{\partial x_n'} + \frac{\partial \hat{b}_n}{\partial x_m'}\right) d\mathbf{x}' + (\hat{b}_{k,l}(\mathbf{x}) + \hat{b}_{l,k}(\mathbf{x}))\right]. \quad (4)$$

It is observed that $\sigma_{ij}^V(\hat{\mathbf{b}})$ is linear respect to $\hat{b}_i$.

3 Statement of Sliding Inclusion Problems

The surface traction $\sigma_{ij}^E n_j$ on S can be decomposed to the shear and normal components, $(\sigma_T^E)_i$ and $\sigma_N^E n_i$, respectively, which are defined by

$$\sigma_T^E = (\sigma_T^E)_i = \sigma_{ij}^E n_j - \sigma_N^E n_i, \quad \sigma_N^E = \sigma_{ij}^E n_i n_j, \quad (5)$$

as shown in Fig. 1. To evaluate the magnitudes of vector σ_T^E and scalar σ_N^E, the following norms averaged over the interface are defined:

$$\|\sigma_T^E\| = \sqrt{\int_S (\sigma_T^E)_i(\sigma_T^E)_i dS}, \quad \|\sigma_N^E\| = \sqrt{\int_S \sigma_N^E \sigma_N^E dS}. \quad (6)$$

Next, the following sliding inclusion problems with frictional interface will be set up:

(A) If the condition $\|\sigma_T^E\| \le \alpha\|\sigma_N^E\|$ is satisfied for some constant $\alpha \ge 0$, the solution τ_{ij} is defined to be σ_{ij}^E.

(B) If the condition $\|\sigma_T^E\| > \alpha\|\sigma_N^E\|$ is satisfied for some constant $\alpha > 0$, a sliding on S occurs, and the stress field τ_{ij} which satisfies the Coulomb's condition $\|\tau_T\| = \alpha\|\tau_N\|$ will be determined. The parameter α is a frictional constant of the material.

4 Method of Solution

Case (A) is not of interest, since no sliding occurs. Suppose the condition in case (B) is satisfied. Then the frictional constant α must in the interval

$$0 \le \alpha < \frac{\|\sigma_T^E\|}{\|\sigma_N^E\|}. \quad (7)$$

As in the previous paper (Mura and Furuhashi, 1984), the stress field τ_{ij} is written in the form

$$\tau_{ij} = \sigma_{ij}^E(\epsilon^*) + \sigma_{ij}^V(\hat{\mathbf{b}}). \quad (8)$$

The Somigliana dislocation $\hat{b}_i$ on the frictional interface must satisfy the interfacial condition

$$\hat{b}_i n_i = 0 \text{ on } S. \quad (9)$$

In view of the statement (B), it is sufficient to determine the slip vector $\hat{b}_i$ which satisfies the condition

$$\|\sigma_T^E + \sigma_T^V(\hat{\mathbf{b}})\| = \alpha\|\sigma_N^E + \sigma_N^V(\hat{\mathbf{b}})\|. \quad (10)$$

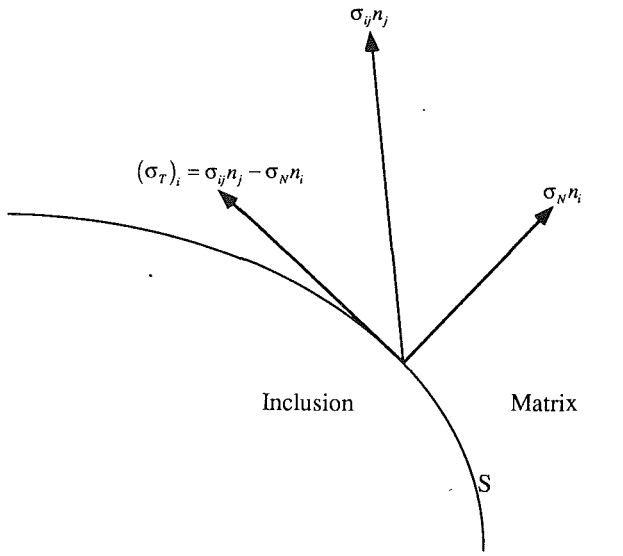


Fig. 1 Schematic representation of the tractions along the interface between matrix and inclusion

Assume that the Somigliana dislocation b_i on the nonfrictional interface is known. This means that the Somigliana dislocation b_i, which leads the shear traction σ_T to vanish on S, can be solved. Because b_i and $\hat{b}_i$ have the same direction, one can expect that there exists a scalar function $s(x)$ relating b_i to $\hat{b}_i$ in the form

$$\hat{b}_i = s(x)b_i. \quad (11)$$

Since the norm used in this paper involves the norm averaged over the interface S, we further assume that $s(x)$ is constant, denoted as $s(x) = s$. As noted before that $\sigma_{ij}^V(\hat{\mathbf{b}})$ is linear with respect to $\hat{b}_i$, the above assumption leads to the following relation

$$\sigma_{ij}^V(s\mathbf{b}) = s\sigma_{ij}^V(\mathbf{b}). \quad (12)$$

Then Eq. (10) turns out to be

$$\|\sigma_T^E + s\sigma_T^V(\mathbf{b})\| = \alpha\|\sigma_N^E + s\sigma_N^V(\mathbf{b})\|. \quad (13)$$

By taking square of this equality, we have the following quadratic equation about the unknown s.

$$\{\langle\sigma_T^E, \sigma_T^E\rangle - \alpha^2\langle\sigma_N^V(\mathbf{b}), \sigma_N^V(\mathbf{b})\rangle\}s^2 - 2\{\langle\sigma_T^E, \sigma_T^E\rangle + \alpha^2\langle\sigma_N^E, \sigma_N^V(\mathbf{b})\rangle\}s + \{\langle\sigma_T^E, \sigma_T^E\rangle - \alpha^2\langle\sigma_N^E, \sigma_N^E\rangle\} = 0, \quad (14)$$

where the notations of norms are defined as

$$\langle\sigma_T^E, \sigma_T^E\rangle = \|\sigma_T^E\|^2, \ \langle\sigma_N^E, \sigma_N^E\rangle = \|\sigma_N^E\|^2, \ \langle\sigma_N^V(\mathbf{b}), \sigma_N^V(\mathbf{b})\rangle = \int_S \sigma_N^V(\mathbf{b})\sigma_N^V(\mathbf{b})dS, \ \langle\sigma_N^E, \sigma_N^V(\mathbf{b})\rangle = \int_S \sigma_N^E\sigma_N^V(\mathbf{b})dS. \quad (15)$$

Here the condition $\sigma_T = \sigma_T^E + \sigma_T^V(\mathbf{b}) = 0$, that the nonfrictional interface cannot sustain any shear traction, is employed in Eq. (14).

If there exists a root for the Eq. (14) within the interval $0 \le s \le 1$, we claim that the present problem can be solved.

5 Ellipsoidal Inclusion With Shear Eigenstrains

Let Ω be a nondegenerate ($a_1 \ne a_2 \ne a_3$) ellipsoidal inclusion which is defined by

$$\frac{x_1^2}{a_1^2} + \frac{x_2^2}{a_2^2} + \frac{x_3^2}{a_3^2} \le 1. \quad (16)$$

If eigenstrains are uniform shear inside Ω and the inclusion interface cannot sustain any shear traction (nonfrictional in-

Downloaded 03 May 2010 to 171.66.16.247. Redistribution subject to ASME license or copyright; see http://www.asme.org/terms/Terms_Use.cfm

terface), according to the work of Mura and Furuhashi (1984), all stresses vanish everywhere, i.e.,

$$\sigma_{ij} = \sigma_{ij}^E + \sigma_{ij}^V(\mathbf{b}) = 0 \tag{17}$$

holds throughout the domain. The Somigliana dislocation for this problem is given by

$$b_i = \overset{*}{\epsilon}_{ij} x_j - \omega_{ij} x_j, \tag{18}$$

where ω_{ij} is the rotation tensor

$$\omega_{12} = \overset{*}{\epsilon}_{12} \left(\frac{1}{a_1^2} + \frac{1}{a_2^2}\right) \Big/ \left(\frac{1}{a_1^2} - \frac{1}{a_2^2}\right), \text{ etc.} \tag{19}$$

Then, from Eq. (17), it is easy to obtain the relations

$$\sigma_T^E = -\sigma_T^V(\mathbf{b}),\ \sigma_N^E = -\sigma_N^V(\mathbf{b}). \tag{20}$$

Substituting Eq. (20) into Eq. (14), it turns out that

$$s^2 - 2s + 1 = 0. \tag{21}$$

Hence the solution of Eq. (21) is $s = 1$ if $\langle \sigma_T^E, \sigma_T^E \rangle - \alpha^2 \langle \sigma_N^V(\mathbf{b}), \sigma_N^V(\mathbf{b}) \rangle \neq 0$ which is satisfied by Eq. (7). This result means that, for all frictional constants within the interval of (7), once the nondegenerate ellipsoidal inclusion with shear eigenstrains starts to slide, the inclusion will not stop until all stress fields vanish everywhere throughout the space. This result is identical with (Mura and Furuhashi, 1984; Mura et al., 1987).

6 Isotropic Spherical Inclusion

The material considered here is isotropic and Ω is a sphere with radius a defined by

$$x_i x_i \leq a^2 \tag{22}$$

with uniform eigenstrains $\overset{*}{\epsilon}_{ij}$. The stress inside Ω for Eshelby's inclusion (perfect bonding) is given by (Mura, 1987)

$$\sigma_{ij}^E(\epsilon^*) = \frac{-2\mu}{15(1-\nu)} [(1+5\nu)\overset{*}{\epsilon}_{ll}\delta_{ij} + (7-5\nu)\overset{*}{\epsilon}_{ij}], \tag{23}$$

where μ denotes the shear modulus, ν is Poisson's ratio, and δ_{ij} stands for Kronecker's delta.

First, we consider the case when $\overset{*}{\epsilon}_{ij}$ is dilatational, which means that $\overset{*}{\epsilon}_{ij} = \epsilon\delta_{ij}$ for some constant ϵ. Since $n_i = x_i/a$, we have

$$\sigma_N^E = -\frac{4\mu(1+\nu)}{3(1-\nu)}\epsilon,\ \sigma_T^E = 0. \tag{24}$$

Accordingly,

$$\|\sigma_N^E\| = \sqrt{\pi}\,\frac{8\mu(1+\nu)a}{3(1-\nu)}\epsilon,\ \|\sigma_T^E\| = 0. \tag{25}$$

Then the inequality

$$\|\sigma_T^E\| \leq \alpha \|\sigma_N^E\| \text{ for all } \alpha \geq 0 \tag{26}$$

is valid. Therefore, sliding does not arise in this case and the stress field is nothing but a Eshelby's solution, i.e., $\tau_{ij} = \sigma_{ij}^E$.

Furthermore, if $\overset{*}{\epsilon}_{ij}$ is not dilatational, then the sliding Somigliana dislocation for the nonfrictional case is given by (Mura and Furuhashi, 1984)

$$b_i = \frac{7(7-5\nu)}{3(21+\nu)a^2}(\overset{*}{\epsilon}_{ij}x_j a^2 - \overset{*}{\epsilon}_{jk}x_j x_k x_i). \tag{27}$$

The stress field $\sigma_{ij}^V(\mathbf{b})$ inside Ω can be derived as follows:

$$\sigma_{ij}^V(\mathbf{b}) = \frac{14\mu(7-5\nu)}{45(1-\nu)(21+\nu)}[(1+5\nu)\overset{*}{\epsilon}_{ll}\delta_{ij} + (7-5\nu)\overset{*}{\epsilon}_{ij}]$$
$$+ \frac{28\nu\mu(7-5\nu)}{15(1-\nu)(21+\nu)a^2}\delta_{ij}\left(2\overset{*}{\epsilon}_{ll}|x|^2 - 6\overset{*}{\epsilon}_{kl}x_k x_l - \frac{5}{3}a^2\overset{*}{\epsilon}_{ll}\right)$$
$$+ \frac{4\mu(7-5\nu)}{15(1-\nu)(21+\nu)a^2}\Big[-4\nu\overset{*}{\epsilon}_{ll}|x|^2\delta_{ij} - 8\nu\overset{*}{\epsilon}_{ll}x_i x_j$$
$$+ 2(7-4\nu)\overset{*}{\epsilon}_{ij}|x|^2 + 12\nu\overset{*}{\epsilon}_{il}x_l x_j + 12\nu\overset{*}{\epsilon}_{jl}x_l x_i + 2(10\nu-7)\overset{*}{\epsilon}_{kl}x_k x_l\delta_{ij}$$
$$+ 7\nu a^2\overset{*}{\epsilon}_{ll}\delta_{ij} + \frac{7}{3}(\nu-5)a^2\overset{*}{\epsilon}_{ij}\Big]. \tag{28}$$

By virtue of definition of Eq. (15), the following norms are determined:

$$\langle \sigma_T^E, \sigma_T^E \rangle = \frac{4\pi a^2}{15}\left[\frac{2(7-5\nu)\mu}{15(1-\nu)}\right]^2 (3\overset{*}{\epsilon}_{kl}\overset{*}{\epsilon}_{kl} - \overset{*}{\epsilon}_{kk}\overset{*}{\epsilon}_{ll}),$$
$$\langle \sigma_N^E, \sigma_N^E \rangle = \frac{4\pi a^2}{15}\left[\frac{2\mu}{15(1-\nu)}\right]^2 (2(7-5\nu)^2\overset{*}{\epsilon}_{kl}\overset{*}{\epsilon}_{kl} + (375\nu^2 + 155\nu + 134)\overset{*}{\epsilon}_{kk}\overset{*}{\epsilon}_{ll}),$$
$$\langle \sigma_N^V(\mathbf{b}), \sigma_N^V(\mathbf{b}) \rangle = \frac{8\pi a^2}{45}\left(\frac{7+19\nu}{21+\nu}\right)^2\left[\frac{2(7-5\nu)\mu}{15(1-\nu)}\right]^2 \times (3\overset{*}{\epsilon}_{kl}\overset{*}{\epsilon}_{kl} - \overset{*}{\epsilon}_{kk}\overset{*}{\epsilon}_{ll}),$$
$$\langle \sigma_N^E, \sigma_N^V(\mathbf{b}) \rangle = \frac{8\pi a^2}{45}\frac{7+19\nu}{21+\nu}\left[\frac{2(7-5\nu)\mu}{15(1-\nu)}\right]^2 (3\overset{*}{\epsilon}_{kl}\overset{*}{\epsilon}_{kl} - \overset{*}{\epsilon}_{kk}\overset{*}{\epsilon}_{ll}). \tag{29}$$

Let $\tilde{\alpha}$ be the ratio of the shear and normal tractions of Eshelby's solution, i.e.,

$$\tilde{\alpha} = \frac{\|\sigma_T^E\|}{\|\sigma_N^E\|}. \tag{30}$$

Substituting the first two expressions of Eq. (29) into Eq. (30), $\tilde{\alpha}$ has the value

$$\tilde{\alpha} = \frac{(7-5\nu)\sqrt{3\overset{*}{\epsilon}_{kl}\overset{*}{\epsilon}_{kl} - \overset{*}{\epsilon}_{kk}\overset{*}{\epsilon}_{ll}}}{\sqrt{2(7-5\nu)^2\overset{*}{\epsilon}_{kl}\overset{*}{\epsilon}_{kl} + (375\nu^2 + 155\nu + 134)\overset{*}{\epsilon}_{ll}^2}}. \tag{31}$$

Since

$$3\overset{*}{\epsilon}_{kl}\overset{*}{\epsilon}_{kl} - \overset{*}{\epsilon}_{kk}\overset{*}{\epsilon}_{ll} = 6(\overset{*}{\epsilon}_{12}^2 + \overset{*}{\epsilon}_{23}^2 + \overset{*}{\epsilon}_{31}^2) + (\overset{*}{\epsilon}_{11} - \overset{*}{\epsilon}_{22})^2 + (\overset{*}{\epsilon}_{22} - \overset{*}{\epsilon}_{33})^2 + (\overset{*}{\epsilon}_{33} - \overset{*}{\epsilon}_{11})^2, \tag{32}$$

the following lemmas are proposed.

Lemma 1. *$\tilde{\alpha} = 0$ if and only if $\overset{*}{\epsilon}_{ij}$ is dilatational.*

Suppose that eigenstrains are not dilatational, then $\tilde{\alpha} > 0$ from Eq. (32). The value $\tilde{\alpha}$ represents the upper limit of the frictional constant which allows sliding to occur on the interface. From Eqs. (7) and (30), the frictional constant must be within the interval

$$0 \leq \alpha < \tilde{\alpha}. \tag{33}$$

Moreover, Eq. (31) implicitly reveals that

$$0 < \tilde{\alpha} \leq \sqrt{\frac{3}{2}}. \tag{34}$$

Substituting the norms in Eq. (29) into Eq. (14), the quadratic equation turns out to be

$$\left(1 - \frac{2}{3}\alpha^2\left(\frac{7+19\nu}{21+\nu}\right)^2\right)s^2 - 2\left(1 + \frac{2}{3}\alpha^2\frac{7+19\nu}{21+\nu}\right)s + \left(1 - \left(\frac{\alpha}{\tilde{\alpha}}\right)^2\right) = 0. \tag{35}$$

The discriminant for this equation is defined by

$$\mathfrak{D} = \left(1 + \frac{2}{3}\alpha^2\frac{7+19\nu}{21+\nu}\right)^2 - \left(1 - \frac{2}{3}\alpha^2\left(\frac{7+19\nu}{21+\nu}\right)^2\right)\left(1 - \left(\frac{\alpha}{\tilde{\alpha}}\right)^2\right). \tag{36}$$

Lemma 2. *The quadratic Eq. (35) has real roots.*

Proof. Equation (36) can be rewritten as

Downloaded 03 May 2010 to 171.66.16.247. Redistribution subject to ASME license or copyright; see http://www.asme.org/terms/Terms_Use.cfm

$$\mathfrak{D}=\frac{2}{3}\alpha^2\left(\frac{7+19\nu}{21+\nu}\right)^2\left(2\,\frac{21+\nu}{7+19\nu}+\frac{2}{3}\alpha^2+1-\left(\frac{\alpha}{\tilde{\alpha}}\right)^2\right)+\left(\frac{\alpha}{\tilde{\alpha}}\right)^2, \tag{37}$$

then the inequality (33) gives $\mathfrak{D} \geq 0$. Q.E.D.

The roots for Eq. (35) are

$$s_1=\frac{1+\frac{2}{3}\alpha^2\frac{7+19\nu}{21+\nu}-\sqrt{\mathfrak{D}}}{1-\frac{2}{3}\alpha^2\left(\frac{7+19\nu}{21+\nu}\right)^2},$$

$$s_2=\frac{1+\frac{2}{3}\alpha^2\frac{7+19\nu}{21+\nu}+\sqrt{\mathfrak{D}}}{1-\frac{2}{3}\alpha^2\left(\frac{7+19\nu}{21+\nu}\right)^2}. \tag{38}$$

Lemma 3. $s_2 \geq 1$.

Proof. From Eqs. (33) and (34), we have

$$0\leq\alpha<\sqrt{\frac{3}{2}}. \tag{39}$$

Then the denominator of Eq. (38) must satisfy

$$0<\left(1-\frac{2}{3}\alpha^2\left(\frac{7+19\nu}{21+\nu}\right)^2\right)\leq 1. \tag{40}$$

Therefore, $s_2 \geq 1$. Q.E.D.

Lemma 4. $s_1 \geq 0$.

Proof. Using the well-known relationship[1] between the roots and the coefficients of quadratic Eq. (35), we obtain

$$s_1 \cdot s_2=\frac{1-\left(\frac{\alpha}{\tilde{\alpha}}\right)^2}{1-\alpha^2\frac{2}{3}\left(\frac{7+19\nu}{21+\nu}\right)^2}. \tag{41}$$

The inequalities $0 \leq \alpha < \tilde{\alpha}$ and $0 < \tilde{\alpha} \leq \sqrt{3/2}$ give

$$1-\left(\frac{\alpha}{\tilde{\alpha}}\right)^2>0,\ 1-\alpha^2\frac{2}{3}\left(\frac{7+19\nu}{21+\nu}\right)^2\geq 0. \tag{42}$$

Hence, $s_1 \cdot s_2 \geq 0$. Therefore, from lemma 3, we get $s_1 \geq 0$. Q.E.D.

Lemma 5. $0 \leq s_1 \leq 1$.

Proof. Equation (41) can be written as

$$s_1 \cdot s_2=\frac{1-\left(\frac{\alpha}{\tilde{\alpha}}\right)^2}{1-\left(\frac{\alpha}{\tilde{\alpha}}\right)^2+\frac{2}{3}\left(\frac{\alpha}{\tilde{\alpha}}\right)^2\left(\frac{3}{2}-\tilde{\alpha}^2\left(\frac{7+19\nu}{21+\nu}\right)^2\right)}. \tag{43}$$

Since the inequality

$$\frac{3}{2}-\tilde{\alpha}^2\left(\frac{7+19\nu}{21+\nu}\right)^2\geq 0 \tag{44}$$

is obviously valid from the inequality $0 < \tilde{\alpha} \leq \sqrt{3/2}$, then the first inequality of (42) gives

$$s_1 \cdot s_2 \leq 1. \tag{45}$$

From lemmas 3 and 4, the desired result is proved. Q.E.D.

In view of lemma 5, it can be concluded that the quadratic Eq. (35) always has a root within the interval $0 \leq s \leq 1$, and this root is determined from the following expression:

$$s=\frac{1+\frac{2}{3}\alpha^2\frac{7+19\nu}{21+\nu}-\sqrt{\mathfrak{D}}}{1-\frac{2}{3}\alpha^2\left(\frac{7+19\nu}{21+\nu}\right)^2}. \tag{46}$$

Example. As a simple example, a pure shear eigenstrain prescribed inside the inclusions is considered. From Eqs. (31) and (32) we have

$$\tilde{\alpha}=\sqrt{\frac{3}{2}}. \tag{47}$$

Then the frictional constant must be in the interval

$$0\leq\alpha<\sqrt{\frac{3}{2}}. \tag{48}$$

By Eqs. (36) and (46), the sliding parameter s is determined as follows:

$$s=\frac{1+\alpha^2\frac{2}{3}\frac{7+19\nu}{21+\nu}-\sqrt{\frac{2}{3}}\alpha\left(1+\frac{7+19\nu}{21+\nu}\right)}{1-\alpha^2\frac{2}{3}\left(\frac{7+19\nu}{21+\nu}\right)^2}. \tag{49}$$

By keeping $\nu = 0.2$, the plot of s versus α is shown in Fig. 2. It is interesting to note that when s is equal to zero, this would imply that the interface is perfectly bonded, which means that the predicted stress field is nothing but Eshelby's solution $\sigma_{ij}^{E}(\epsilon^*)$ as shown by Eq. (23). In contrast with perfect bonding, when s is equal to unity, this is a case of free sliding.

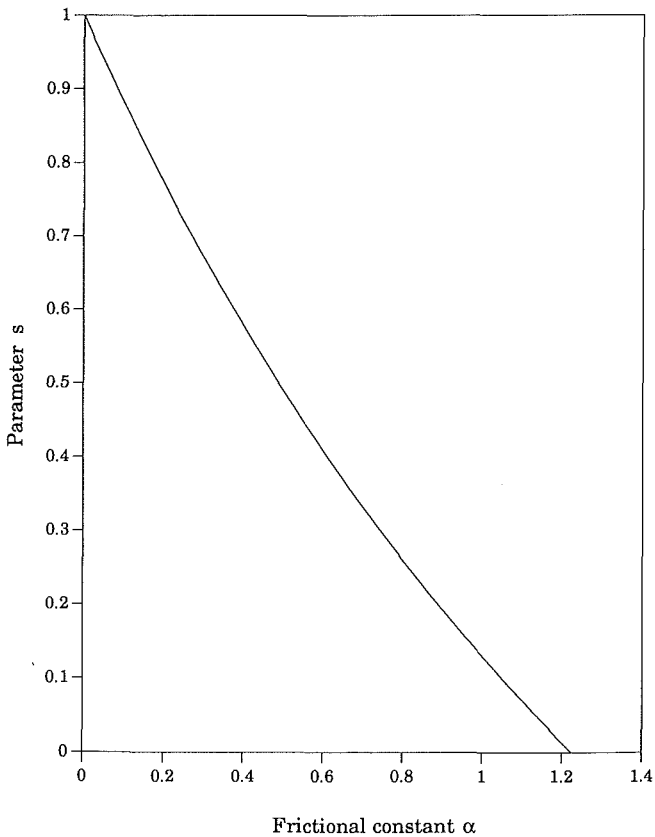


Fig. 2 The variation of frictional constant α with parameter s when $\nu = 0.2$

[1] For any quadratic equation $as^2 + bs + c = 0$, the relation $s_1 \cdot s_2 = c/a$ holds.

Downloaded 03 May 2010 to 171.66.16.247. Redistribution subject to ASME license or copyright; see http://www.asme.org/terms/Terms_Use.cfm

7 Existence of Solution for Sliding at the Frictional Interface of the Inclusion

In this section, a proof of the existence of solution for the Somigliana dislocation $\hat{b}_i$ for sliding at the frictional interface of the inclusion is given here.

Proposition 1. *If the Somigliana dislocation* b_i *for the nonfrictional interface of the inclusion exists, then the Somigliana dislocation* $\hat{b}_i$ *for the frictional case also exists.*

To prove this proposition, it is sufficient to show that Eq. (13) has a root s in the closed interval [0, 1]. Consider the function

$$F(s) = \|\sigma_T^E + s\sigma_T^V(\mathbf{b})\| - \alpha\|\sigma_N^E + s\sigma_N^V(\mathbf{b})\|. \tag{50}$$

By means of the condition (B) in Section 3, we have

$$F(0) = \|\sigma_T^E\| - \alpha\|\sigma_N^E\| > 0, \tag{51}$$

and substituting

$$\sigma_T^E + \sigma_T^V(\mathbf{b}) = 0 \tag{52}$$

into Eq. (50) and taking $s = 1$, $F(s)$ becomes

$$F(1) = -\alpha\|\sigma_N^E + s\sigma_N^V(\mathbf{b})\| \le 0. \tag{53}$$

Since $F(s)$ is a continuous function defined on the closed interval [0, 1], the inequalities (51) and (53) show that the function $F(s)$ has at least one zero point in [0, 1]. Because of $\hat{b}_i = sb_i$, the proposition is thus proved.

8 Sliding Inhomogeneity and the Equivalent Inclusion Method

In contrast to the definition of inclusion defined in Section 2, if a subset Ω has elastic constants differing from those of the remainder, this subset Ω is called an inhomogeneity. Eshelby (1957) first pointed out that the presence of an inhomogeneity can be equivalent to the stress field due to an inclusion if the eigenstrains ϵ_{ij}^* are chosen properly. This equivalency is called the *equivalent inclusion method.*

If the sliding is allowed on the nonfrictional interface which cannot sustain any shear traction on it, the equivalent equation and interfacial conditions are represented, respectively, as

(a) $C_{ijkl}^*(\epsilon_{kl}^0 + \gamma_{kl}^E(\epsilon^*) + \gamma_{kl}^V(\mathbf{b})) = C_{ijkl}(\epsilon_{kl}^0 + \gamma_{kl}^E(\epsilon^*) + \gamma_{kl}^V(\mathbf{b}) - \epsilon_{kl}^*)$ in Ω,

(b) $\sigma_T(\sigma^0) = \sigma_{ij}(\sigma^0)n_j = 0$ on S.

(c) $b_i n_i = 0$ on S.

Here, C_{ijkl}^* stands for the elastic constant of inhomogeneity and ϵ_{ij}^0 is the strain field corresponding to the applied stress σ_{ij}^0 at infinity. The sliding stress $\sigma_{ij}(\sigma^0)$ for the nonfrictional interface is written as

$$\sigma_{ij}(\sigma^0) = \sigma_{ij}^0 + \sigma_{ij}^E(\epsilon^*) + \sigma_{ij}^V(\mathbf{b}) \text{ in } \Omega. \tag{54}$$

Since n_j is a function of positions, the condition (b) is satisfied only when $\sigma_{ij}(\sigma^0) = 0$, i.e., the stress is identically zero in Ω. The slip vector b_i and equivalent eigenstrain ϵ_{ij}^* can be determined through Eqs. (a) to (c). In a previous paper (Mura et al., 1987), we showed that if an applied stress σ_{ij}^0 is shear type and the inhomogeneity is a nondegenerate ellipsoid defined by Eq. (16), Eqs. (a) to (c) have the following solutions:

$$\epsilon_{ij}^* = 0, \text{ and } b_i = B_{ij}x_j - \omega_{ij}x_j, \tag{55}$$

where

$$\omega_{12} = B_{12}\frac{\frac{1}{a_1^2} + \frac{1}{a_2^2}}{\frac{1}{a_1^2} - \frac{1}{a_2^2}}, \text{ etc.,} \tag{56}$$

and B_{ij} is obtained by the following linear system equations

$$\epsilon_{ij}^0 = -B_{ij} + S_{ijkl}B_{kl}, \tag{57}$$

where S_{ijkl} is the Eshelby tensor (Mura, 1987) for the ellipsoid of Eq. (16). For instance, B_{12} is given by

$$B_{12} = \frac{1}{\Delta}\begin{vmatrix} \epsilon_{12}^0 & 2S_{1223} & 2S_{1231} \\ \epsilon_{23}^0 & 2S_{2323} - 1 & 2S_{2331} \\ \epsilon_{31}^0 & 2S_{3123} & 2S_{3131} - 1 \end{vmatrix}, \tag{58}$$

where

$$\Delta = \begin{vmatrix} 2S_{1212} - 1 & 2S_{1223} & 2S_{1231} \\ 2S_{2312} & 2S_{2323} - 1 & 2S_{2331} \\ 2S_{3112} & 2S_{3123} & 2S_{3131} - 1 \end{vmatrix}. \tag{59}$$

From Eqs. (1) to (4), the solution (55) gives

$$\gamma_{ij}^E(\epsilon^*) = 0, \text{ and } \gamma_{ij}^V(\mathbf{b}) = -S_{ijkl}B_{kl} + B_{ij} \text{ in } \Omega. \tag{60}$$

Using Eq. (57) and Hooke's law (2) and (3), we have

$$\sigma_{ij}^E(\epsilon^*) = 0, \text{ and } \sigma_{ij}^V(\mathbf{b}) = -\sigma_{ij}^0 \text{ in } \Omega. \tag{61}$$

Therefore, Eq. (54),

$$\sigma_{ij}(\sigma^0) = 0 \text{ in } \Omega, \tag{62}$$

holds. The foregoing equation depicts that when the nondegenerate ellipsoidal inhomogeneity defined by Eq. (16) is subjected to an applied shear stress at infinity and its interface cannot sustain any shear traction, the inhomogeneity behaves like a void.

9 Frictional Sliding Ellipsoidal Inhomogeneity Under Shear

Let Ω be a bounded inhomogeneity and σ_{ij}^0 a remote applied stress. Suppose that Ω is a perfectly bonded inhomogeneity and the stress field $\sigma_{ij}^E(\sigma^0)$ is given under an applied stress σ_{ij}^0. The following sliding inhomogeneity problem with a frictional interface is set up.

(C) If the condition $\|\sigma_T^E(\sigma^0)\| \le \alpha\|\sigma_N^E(\sigma^0)\|$ is satisfied for some constant $\alpha \ge 0$, the solution τ_{ij} is defined to be $\sigma_{ij}^E(\sigma^0)$.

(D) If the condition $\|\sigma_T^E(\sigma^0)\| > \alpha\|\sigma_N^E(\sigma^0)\|$ is satisfied for some constant $\alpha > 0$, sliding on S occurs, and the stress field τ_{ij} which satisfies the condition $\|\tau_T\| = \alpha\|\tau_N\|$ will be determined.

The equivalent equation and interfacial conditions for this problem are represented, respectively, as:

(d) $C_{ijkl}^*(\epsilon_{kl}^0 + \gamma_{kl}^E(\hat{\epsilon}^*) + \gamma_{kl}^V(\hat{\mathbf{b}})) = C_{ijkl}(\epsilon_{kl}^0 + \gamma_{kl}^E(\hat{\epsilon}^*) + \gamma_{kl}^V(\hat{\mathbf{b}}) - \hat{\epsilon}_{kl}^*)$ in Ω.

(e) $\|\sigma_T^0 + \sigma_T^E(\hat{\epsilon}^*) + \sigma_T^V(\hat{\mathbf{b}})\| = \alpha\|\sigma_N^0 + \sigma_N^E(\hat{\epsilon}^*) + \sigma_N^V(\hat{\mathbf{b}})\|$ on S.

(f) $\hat{b}_i n_i = 0$ on S.

Denote the sliding stress as

$$\tau_{ij} = \sigma_{ij}^0 + \sigma_{ij}^E(\hat{\epsilon}^*) + \sigma_{ij}^V(\hat{\mathbf{b}}) \text{ in } \Omega. \tag{63}$$

Let the applied stress σ_{ij}^0 be shear type and the inhomogeneity Ω be a nondegenerate ellipsoid defined by Eq. (16). Then, according to the inclusion problem which was explained in Section 4, we have assumed that the desired Somigliana dislocation $\hat{b}_i$ for the frictional case is represented in the form

$$\hat{b}_i = sb_i \tag{64}$$

for some constant s which is within the interval $0 \le s \le 1$. The Somigliana dislocation b_i for the nonfrictional case is determined in the previous section. By assuming $\hat{\epsilon}_{ij}^*$ is constant and using the second part of Eqs. (60) and (61), we can rewrite the equivalent Eq. (d) and the interfacial condition (e) as follows:

$$(d')\ (s-1)(C_{ijkl}^* - C_{ijkl})(S_{klmn}B_{mn} - B_{kl}) = (C_{ijkl}^* - C_{ijkl})S_{klmn}\hat{\epsilon}_{mn}^* + C_{ijkl}\hat{\epsilon}_{kl}^*.$$

$$(e')\ \|(s-1)\sigma_T^V(\mathbf{b}) + \sigma_T^E(\hat{\epsilon}^*)\| = \alpha\|(s-1)\sigma_N^V(\mathbf{b}) + \sigma_N^E(\hat{\epsilon}^*)\|.$$

Then the solutions for the equations above are

$$s = 1, \text{ and } \hat{\epsilon}_{ij}^* = 0. \tag{65}$$

Downloaded 03 May 2010 to 171.66.16.247. Redistribution subject to ASME license or copyright; see http://www.asme.org/terms/Terms_Use.cfm

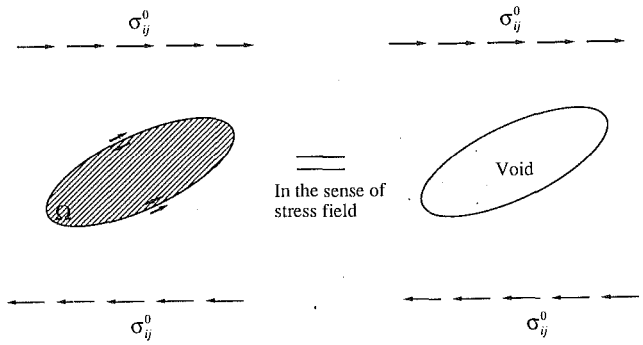


Fig. 3 When the ellipsoidal inhomogeneity of Eq. (16) under the remotely applied shear stress begins to slide, this inhomogeneity behaves like a void

Hence, from Eqs. (63) and (61), these solutions give

$$\tau_{ij} = 0 \tag{66}$$

for every point in Ω. This result means that, for all frictional constants which are within the interval

$$0 \le \alpha < \frac{\|\sigma^E_T(\sigma^0)\|}{\|\sigma^E_N(\sigma^0)\|}, \tag{67}$$

once the ellipsoidal inhomogeneity defined by Eq. (16) begins to slide due to the applied shear stress at the infinity, this inhomogeneity behaves like a void. It should be especially emphasized that this salient property does not depend on the material. This is shown schematically in Fig. 3.

10 Existence of Solution for Sliding at the Frictional Interface of the Inhomogeneity

In this section, we will prove that the existence of solution for the Somigliana dislocation $\hat{b}_i$ for sliding at the frictional interface of the inhomogeneity exists.

Proposition 2. *If the Somigliana dislocation* b_i *for the nonfrictional interface of the inhomogeneity exists, then the Somigliana dislocation* $\hat{b}_i$ *for the frictional case also exists.*

To prove this proposition, we will use the equivalent inclusion method for sliding inhomogeneities. The conditions (d) to (f) and Eq. (63) must be explored.

Suppose that there exist the solutions ϵ^*_{ij} and b_i for the nonfrictional interface. These solutions satisfy conditions (a) to (c) and Eq. (54) in Section 8. Assume that the unknown slip vector $\hat{b}_i$ and the tensor $\hat{\epsilon}^*_{ij}$ can be expressed as

$$\begin{aligned} \hat{b}_i &= s b_i, \\ \hat{\epsilon}^*_{ij} &= s\epsilon^*_{ij} + (1-s)\hat{\epsilon}^{**}_{ij}, \end{aligned} \tag{68}$$

for some constant s, where $\hat{\epsilon}^{**}_{ij}$ is a new symmetric tensor. The condition (f) then obviously results from condition (c).

If we substitute Eq. (68) into the equivalent Eq. (d) and make use of the condition (a), we have

$$C^*_{ijkl}(\epsilon^0_{kl} + \gamma^E_{kl}(\hat{\epsilon}^{**})) = C_{ijkl}(\epsilon^0_{kl} + \gamma^E_{kl}(\hat{\epsilon}^{**}) - \hat{\epsilon}^{**}_{kl}). \tag{69}$$

This equation means that the solution $\hat{\epsilon}^{**}_{kl}$ is nothing but the equivalent eigenstrain for perfect bonding case. Then, we obtain the expression

$$\sigma^E_{ij}(\sigma^0) = \sigma^0_{ij} + \sigma^E_{ij}(\hat{\epsilon}^{**}). \tag{70}$$

On the other hand, the condition (e) and Eq. (68) give

$$\begin{aligned} &\|s[\sigma^0_T + \sigma^E_T(\epsilon^*) + \sigma^V_T(\mathbf{b})] + (1-s)[(\sigma^0_T + \sigma^E_T(\hat{\epsilon}^{**})]\| \\ &= \alpha\|s[(\sigma^0_N + \sigma^E_N(\epsilon^*) + \sigma^V_N(\mathbf{b})] + (1+s)[\sigma^0_N + \sigma^E_N(\hat{\epsilon}^{**})]\|. \end{aligned} \tag{71}$$

According to condition (b) in Section 8 and Eqs. (54) and (70), we have

$$(1-s)\|\sigma^E_T(\sigma^0)\| = \alpha\|s\sigma_N(\sigma^0) + (1-s)\sigma^E_N(\sigma^0)\|. \tag{72}$$

Therefore, to prove this proposition, it is sufficient to show that Eq. (72) has a solution s within the closed interval [0, 1].

Let us consider the function

$$F(s) = (1-s)\|\sigma^E_T(\sigma^0)\| - \alpha\|s\sigma_N(\sigma^0) + (1-s)\sigma^E_N(\sigma^0)\| \tag{73}$$

which is defined on the closed interval [0, 1]. Using the condition (D) in Section 9, the function $F(s)$ becomes

$$F(0) = \|\sigma^E_T(\sigma^0)\| - \alpha\|\sigma^E_N(\sigma^0)\| > 0, \tag{74}$$

and

$$F(1) = -\alpha\|\sigma_N(\sigma^0)\| \le 0. \tag{75}$$

Since $F(s)$ is a continuous function defined on the interval [0, 1], the inequalities (74) and (75) show that the function $F(s)$ has at least one zero point in [0, 1]. Because of $\hat{b}_i = sb_i$, the proposition is thus proved.

11 Conclusions

The sliding solution of the elastic field in closed form is presented for three cases: (i) a spherical inclusion which undergoes constant eigenstrains, (ii) a nondegenerate ellipsoidal inclusion with uniform shear eigenstrains, and (iii) a nondegenerate ellipsoidal inhomogeneity subjected to an applied shear stress at infinity. The exact solutions, Eqs. (18) and (27), exhibit the amount of slip of a sliding ellipsoidal and spherical inclusion, respectively.

When the parameter s is equal to zero, this would imply that the interface is perfectly bonded, which means that the predicted stress field is nothing but Eshelby's solution $\sigma^E_{ij}(\epsilon^*)$ as shown by Eq. (23). In contrast with perfect bonding, when s is equal to unity, this is the case of free sliding (nonfrictional interface).

It was shown that once a nondegenerate ellipsoidal inclusion with shear eigenstrains begins to slide, the inclusion never stops until the stress field vanishes everywhere. An isotropic spherical inclusion with uniform eigenstrains starts to slide along the interface, then the stress field in the inclusion is expressed by a quadratic polynomial of coordinates. Moreover, when a nondegenerate ellipsoidal inhomogeneity begins to slide due to an applied shear stress at infinity, the inhomogeneity behaves like a void.

Finally, the existence of solution for sliding at the frictional interface of the inclusion is demonstrated. By using the equivalent inclusion method, we have proven that the solution for a sliding inhomogeneity with the frictional interface also exists.

Acknowledgment

This work was supported by U.S. Army Research Office under Grant No. DAAL03-89-k-0019.

References

Dvorak, G. J., 1983, "Metal Matrix Composites: Plasticity and Fatigue," *Mechanics of Composite Materials—Recent Advance*, Z. Hashin and C. T. Herakovich, eds., Pergamon Press, New York, pp. 73–92.

Dvorak, G. J., Bahei-El-Din, Y. A., Macheret, Y., and Liu, C. H., 1988, "An Experimental Study of Elastic-Plastic Behavior of a Fibrous Boron-Aluminum Composite," *Journal of the Mechanics and Physics of Solids*, Vol. 36, pp. 655–687.

Eshelby, J. D., 1957, "The Determination of the Elastic Field of an Ellipsoidal Inclusion and Related Problems," *Proceedings of the Royal Society, London*, Vol. A241, pp. 376–396.

Mori, T., Koda, M., Monzen, R., and Mura, T., 1983, "Particle Blocking in Grain Boundary Sliding and Associated Internal Friction," *Acta Metallurgica*, Vol. 31, pp. 275–283.

Mura, T., and Furuhashi, R., 1984, "The Elastic Inclusion with a Sliding Interface," ASME JOURNAL OF APPLIED MECHANICS, Vol. 51, pp. 308–310.

Mura, T., Furuhashi, R., and Mori, T., 1987, "Sliding Ellipsoidal Inhomogeneities under Shear," *Advanced Composite Materials and Structures*, G. C. Sih and S. E. Hsu, eds., VNU Science Press, pp. 113–122.

Mura, T., 1987, *Micromechanics of Defects in Solids*, 2nd rev. ed., Martinus Nijhoff Publishers.

Weng, G. J., 1988, "Theoretical Principles for the Determination of Two Kinds of Composite Plasticity," *Mechanics of Composite Materials*, G. J. Dvorak and N. Laws, eds., AMD-Vol. 92, ASME, New York, pp. 193–208.

Downloaded 03 May 2010 to 171.66.16.247. Redistribution subject to ASME license or copyright; see http://www.asme.org/terms/Terms_Use.cfm

Eung J. Lee
Graduate Student.

Eric C. Klang
Assist. Professor.

Department of Mechanical and Aerospace Engineering,
North Carolina State University,
Raleigh, NC 27695-7910

Stress Distribution in an Edge-Stiffened Semi-infinite Elastic Plate Containing a Circular Hole

An edge-stiffened semi-infinite elastic plate containing a circular hole under tension at infinity has been studied using a conformal mapping technique. Melan's stiffener condition in Cartesian coordinates has been newly formulated as a resultant shear stress condition in bipolar coordinates. The solution is sought in series form, and by truncating the system of equations, it is numerically solved. Pertinent stress distributions are examined to illustrate the roll of the stiffener under the presence of a circular hole near the straight edge. It has been concluded that the stiffener contributes to indirectly suppressing the stress concentration around the hole.

1 Introduction

Plates stiffened with stringers are recognized as important aircraft components. As a result, many analyses have been reported to illustrate the role of stringers in the load transfer to an elastic plate. The earliest classical studies on this subject appear to be initiated by Melan (1932a, b) who analyzed a stiffened elastic sheet acted on by a concentrated force in the direction of the stiffener in whole and half planes. Additionally, Gladwell (1980) reviewed several studies with various stiffener models such as a stiffener whose length was finite or semi-infinite and one periodically configured in a semi-infinite plate.

In Melan's problem, the stiffener was considered as an uniaxial bar, and the thin sheet as a two-dimensional plate in generalized plane stress. But, because of its simplicity, the validity as a general stiffener model was questioned in connection with the rigorous elasticity theory of Muki and Sternberg (1967). As a means of comparison with Melan's problem, two, more exact stiffener models were introduced by Muki and Sternberg. One stiffener model was regarded as an infinite elastic strip of finite width and the other one as a generalization of Melan's first problem based on elementary beam theory which introduced the bending stiffness effect. Through their refinements, it was verified that Melan's stiffener model, regardless of its simplicity, agreed well with the two alternative models in various aspects such as interface stresses and axial stiffener force distribution.

A separate problem involving a semi-infinite plate containing a circular hole was considered by Jeffery (1921) and later, more extensively, by Mindlin (1948). It was shown that the presence of such a circular hole near the straight edge of the plate can generate high stress concentrations around the hole boundary.

The goal of this work was to solve the problem of an edge-stiffened semi-infinite plate containing a circular hole by combining and extending the concepts developed by Melan and Mindlin.

In the next section, a conformal mapping technique is employed to describe all stresses in terms of bipolar coordinates. In the third section, the stress potential function and the pertinent formulae are expressed in bipolar coordinates. By considering the symmetric properties of the problem, the stress potential is simplified, and three of the four boundary conditions are applied. The fourth section is devoted to establishing the stiffener boundary condition described in Cartesian coordinates which is modified to an appropriate form manageable in bipolar coordinates. Using conformal mapping, the boundary condition is converted to a shear resultant condition. In the fifth section, the system of equations is organized in series form having infinitely many coefficients, and solved by truncating higher-order terms. Finally, several stress distributions along the boundary are presented to illustrate the role of the stiffener.

2 Bipolar Coordinates

The problem of an edge-stiffened semi-infinite body weakened by a circular hole under uniform tension is considered using bipolar coordinates. The stiffener boundary conditions are usually described in Cartesian coordinates and, accordingly, an appropriate conformal mapping will be introduced to transform them to bipolar coordinates. Additionally, the pertinent symmetry conditions for the stresses depend not only on the geometry of the problem but also on the loading condition.

Let a conformal mapping function from Cartesian coordinates to bipolar coordinates be taken as

$$z = x + iy = \omega(\zeta) = ia \coth\left(\frac{\zeta}{2}\right), \quad \zeta = \alpha + i\beta, \tag{1}$$

Contributed by the Applied Mechanics Division of THE AMERICAN SOCIETY OF MECHANICAL ENGINEERS for publication in the ASME JOURNAL OF APPLIED MECHANICS.

Discussion on this paper should be addressed to the Technical Editor Prof. Leon M. Keer, The Technological Institute, Northwestern University, Evanston, IL 60208, and will be accepted until four months after final publication of the paper itself in the JOURNAL OF APPLIED MECHANICS.

Manuscript received by the ASME Applied Mechanics Division, Jan. 3, 1991; final revision, Sept. 30, 1991. Associate Technical Editor: C. F. Shih.

Copyright © 1992 by ASME
Downloaded 03 May 2010 to 171.66.16.247. Redistribution subject to ASME license or copyright; see http://www.asme.org/terms/Terms_Use.cfm

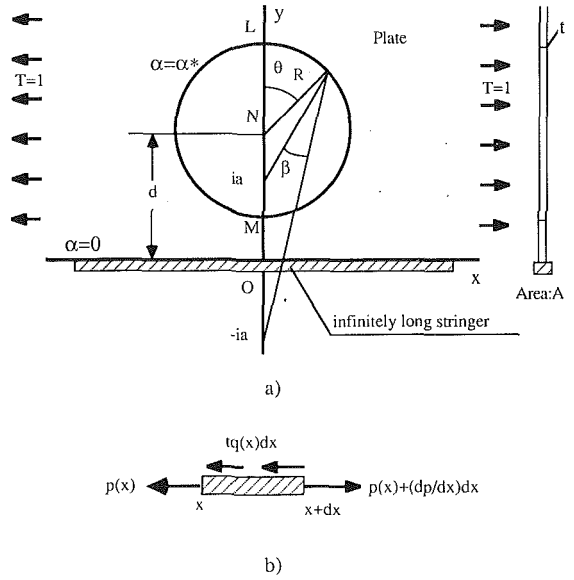


Fig. 1(*a*) Edge-stiffened semi-infinite plate containing a circular hole under tension $T = 1$ parallel to the straight edge; (*b*) free-body diagram of the stiffener element

where "a" is a positive real measure of length and $i = \sqrt{-1}$.

Thus, each Cartesian coordinate x and y are described in terms of bipolar coordinates as follows:

$$x = \frac{\sin \beta}{h}, \quad y = \frac{\sinh \alpha}{h} \tag{2}$$

where h is defined as

$$h = \frac{\cosh \alpha - \cos \beta}{a}. \tag{3}$$

The circular boundary and the straight edge are defined by $\alpha = \alpha^* > 0$ and $\alpha = 0$, respectively, so that the circle radius R and the distance of its center from the stiffener edge d are given by

$$R = a \operatorname{cosech} \alpha^*, \quad d = a \coth \alpha^*, \quad d/R = \cosh \alpha^*, \tag{4}$$

and the curves $\beta =$ constant are all those circles passing through both poles $(0, +a)$ and $(0, -a)$. A measure of angle θ around the hole in Fig. 1(*a*) is introduced as follows:

$$\sin \theta = \frac{\sinh \alpha^* \sin \beta}{\cosh \alpha^* - \cos \beta}. \tag{5}$$

Conversely, we may take an inverse mapping function from bipolar coordinates to Cartesian such that

$$\zeta = \omega^{-1}(z) = \log \frac{(z + ia)}{(z - ia)}. \tag{4}$$

Provided that such a conformal mapping function exists between the two coordinate systems, by Muskhelishvili (1954) the stresses in plane elasticity in both systems are written as

$$\sigma_{\alpha\alpha} + \sigma_{\beta\beta} = \sigma_{xx} + \sigma_{yy}. \tag{7a}$$

$$\sigma_{\beta\beta} - \sigma_{\alpha\alpha} + 2i\sigma_{\alpha\beta} = \exp(2i\eta)(\sigma_{yy} - \sigma_{xx} + 2i\sigma_{xy}) \tag{7b}$$

where

$$\exp(2i\eta) = -\frac{\sinh^2 \bar{\zeta}}{\sinh^2 \zeta}.$$

From these relations, some basic characteristics of boundary conditions along the stiffener can be deduced for future use. The fact that the normal stress along the edge may be neglected in the stiffener model requires that $\sigma_{\alpha\alpha}(0, \beta) = \sigma_{yy}(x, 0) = 0$ on the x-axis, so that the formula (7*a*) becomes

$$\sigma_{xx}(x, 0) = \sigma_{\beta\beta}(0, \beta). \tag{8}$$

For the second relation (7*b*), since $\exp(2i\eta) = -1$ on the x-axis, with the use of condition (8) the following expression is immediately obtained:

$$\sigma_{xy}(x, 0) = -\sigma_{\alpha\beta}(0, \beta). \tag{9}$$

Along section OM, it can be seen that the relation $\exp(2i\eta) = -1$ still holds for $\beta = \pm\pi$, and we may obtain the following relations:

$$\sigma_{xx}(0, y) = \sigma_{\beta\beta}(\alpha, \pm\pi), \quad \sigma_{yy}(0, y) = \sigma_{\alpha\alpha}(\alpha, \pm\pi). \tag{10}$$

These stress distributions will be examined to illustrate the role of the stiffener.

3 Formulation

3.1 Stress Potential. The problem is formulated using a stress potential, χ, in bipolar coordinates corresponding to that of Airy's in a Cartesian system. However, since the mathematical formulation has already been established by Jeffery (1921), it will be taken here with only one correction. Jeffery omitted one term in the series of the stress potential function in his analysis, as was indicated by Mindlin (1948), therefore its corrected form is taken as

$$\frac{h\chi}{a} = \frac{\sinh^2 \alpha}{2(\cosh \alpha - \cos \beta)} + B_0\alpha(\cosh \alpha - \cos \beta) + \sum_{n=1}^{\infty} \{\phi_n(\alpha)\cos n\beta + \psi_n(\alpha)\sin n\beta\}. \tag{11}$$

The first term due to uniform tension can be expanded for $\alpha > 0$ in a series form:

$$\frac{h\chi}{a} = \frac{\sinh \alpha}{2}\left(1 + 2\sum_{n=1}^{\infty} e^{-n\alpha}\cos n\beta\right) + B_0\alpha(\cosh \alpha - \cos \beta) + \sum_{n=1}^{\infty} \{\phi_n(\alpha)\cos n\beta + \psi_n(\alpha)\sin n\beta\}. \tag{12}$$

It is noted that two functions $\phi_n(\alpha)$ and $\psi_n(\alpha)$ are chosen to satisfy the governing equation in bipolar coordinates corresponding to the biharmonic equation in Cartesian coordinates. More specifically, they are written for $n = 1$ as

$$\phi_1(\alpha) = A_1\cosh 2\alpha + B_1 + C_1\sinh 2\alpha$$
$$\psi_1(\alpha) = P_1\cosh 2\alpha + Q_1\sinh 2\alpha, \tag{13a}$$

and for $n \geq 2$,

$$\phi_n(\alpha) = A_n\cosh(n+1)\alpha + B_n\cosh(n-1)\alpha + C_n\sinh(n+1)\alpha + D_n\sinh(n-1)\alpha$$
$$\psi_n(\alpha) = P_n\cosh(n+1)\alpha + Q_n\cosh(n-1)\alpha + S_n\sinh(n+1)\alpha + T_n\sinh(n-1)\alpha. \tag{13b}$$

The stresses in the bipolar coordinates are defined as

$$a\sigma_{\alpha\alpha} = \left\{(\cosh \alpha - \cos\beta)\frac{\partial^2}{\partial\beta^2} - \sinh \alpha \frac{\partial}{\partial\alpha} - \sin \beta \frac{\partial}{\partial\beta} + \cosh \alpha\right\}(h\chi) \tag{14a}$$

$$a\sigma_{\beta\beta} = \left\{(\cosh \alpha - \cos \beta)\frac{\partial^2}{\partial\alpha^2} - \sinh \alpha \frac{\partial}{\partial\alpha} - \sin \beta \frac{\partial}{\partial\beta} + \cosh \beta\right\}(h\chi) \tag{14b}$$

$$a\sigma_{\alpha\beta} = -\left\{(\cosh \alpha - \cos \beta)\frac{\partial^2}{\partial\alpha\partial\beta}\right\}(h\chi). \tag{14c}$$

Downloaded 03 May 2010 to 171.66.16.247. Redistribution subject to ASME license or copyright; see http://www.asme.org/terms/Terms_Use.cfm

Upon substitution of (12) into (14a, b, c), the stresses are

$$2\sigma_{\alpha\alpha}=\sum_{n=1}^{\infty}[(-n^2\sinh 2\alpha+2n\sinh^2\alpha)e^{-n\alpha}\cos n\beta$$
$$+n^2\sinh\alpha e^{-n\alpha}\{\cos(n-1)\beta+\cos(n+1)\beta\}$$
$$+n\sinh 2\alpha e^{-n\alpha}\{\cos(n-1)\beta-\cos(n+1)\beta\}]$$
$$-2B_0\sinh\alpha\cosh\alpha+2\phi_1(\alpha)+2B_0\sinh\alpha\cos\beta$$
$$+\sum_{n=1}^{\infty}[\{(n+1)(n+2)\phi_{n+1}(\alpha)-2(n^2-1)\cosh\alpha\phi_n(\alpha)$$
$$+(n-1)(n-2)\phi_{n-1}(\alpha)\}\cos n\beta$$
$$+\{(n+1)(n+2)\psi_{n+1}(\alpha)-2(n^2-1)\cosh\alpha\psi_n(\alpha)$$
$$+(n-1)(n-2)\psi_{n-1}(\alpha)\}\sin n\beta$$
$$-2\sinh\alpha\{\phi'_n(\alpha)\cos n\beta+\psi'_n(\alpha)\sin n\beta\}], \quad (15)$$

$$\sigma_{\beta\beta}=\sigma_{\alpha\alpha}+2(\cosh\alpha-\cos\beta)\sum_{n=1}^{\infty}(n^2\sinh\alpha-n\cosh\alpha)$$
$$\times e^{-n\alpha}\cos n\beta+2(\cosh\alpha-\cos\beta)\{B_0\sinh\alpha$$
$$+(2A_1\cosh 2\alpha+2C_1\sinh 2\alpha)\cos\beta\}$$
$$+(\cosh\alpha-\cos\beta)\sum_{n=2}^{\infty}\{\phi''_n(\alpha)$$
$$+(n^2-1)\phi_n(\alpha)\}\cos n\beta \quad (16a)$$

or

$$\sigma_{\beta\beta}=\sigma_{\alpha\alpha}+1-\frac{2\sinh^2\alpha\sin^2\beta}{(\cosh\alpha-\cos\beta)^2}$$
$$+2(\cosh\alpha-\cos\beta)\{B_0\sinh\alpha$$
$$+(2A_1\cosh 2\alpha+2C_1\sinh 2\alpha)\cos\beta\}$$
$$+(\cosh\alpha-\cos\beta)\sum_{n=2}^{\infty}\{\phi''_n(\alpha)+(n^2-1)\phi_n(\alpha)\cos n\beta \quad (16b)$$

and

$$2\sigma_{\alpha\beta}=\sum_{n=1}^{\infty}2\{(n\cosh^2\alpha e^{-n\alpha}-n^2\cosh\alpha\sinh\alpha e^{-n\alpha})\sin n\beta$$
$$-2(n\cosh\alpha e^{-n\alpha}-n^2\sinh\alpha e^{-n\alpha})\sin(n-1)\beta$$
$$-2(n\cosh\alpha e^{-n\alpha}-n^2\sinh\alpha e^{-n\alpha})\sin(n+1)\beta\}$$
$$+\psi'_1(\alpha)-2B_0\cosh\alpha\sin\beta+B_0\sin 2\beta$$
$$+\sum_{n=1}^{\infty}[\{(n+1)\psi'_{n+1}(\alpha)-2n\cosh\alpha\psi'_n(\alpha)$$
$$+(n-1)\psi'_{n-1}(\alpha)\}\cos n\beta-\{(n+1)\phi'_{n+1}(\alpha)$$
$$-2n\cosh\alpha\phi'_n(\alpha)+(n-1)\phi'_{n-1}(\alpha)\sin n\beta]. \quad (17)$$

3.2 Symmetry Conditions. By considering the symmetric property of the loading condition at infinity and the geometric configuration it is easily found that the stress distribution has the following symmetry properties:

$$\sigma_{\alpha\alpha}(\alpha,-\beta)=\sigma_{\alpha\alpha}(\alpha,\beta),$$
$$\sigma_{\beta\beta}(\alpha,-\beta)=\sigma_{\beta\beta}(\alpha,\beta),$$
$$\sigma_{\alpha\beta}(\alpha,-\beta)=-\sigma_{\alpha\beta}(\alpha,\beta). \quad (18a,b,c)$$

The application of the last symmetric condition (18c) to the formula (17) yields

$$\psi'_1(\alpha)=0$$
$$(n+1)\psi'_{n+1}(\alpha)-2n\cosh\alpha\psi'_n(\alpha)$$
$$+(n-1)\psi'_{n-1}(\alpha)=0 \quad \text{for } n\geq 2. \quad (19)$$

This recurrence relation shows that all $\psi'_n(\alpha)=0$, so that $\psi_n(\alpha)$ becomes constant. Unfortunately, it seems that there is no condition to determine the constant. But since real values of these constants do not matter in considering stress quantities, they are not sought in this analysis.

3.3 Boundary Conditions. First, two boundary conditions along the straight edge at $\alpha=0$ are required. One of them is the normal traction condition along the straight edge, which is

$$\sigma_{\alpha\alpha}(0,\beta)=0. \quad (20a)$$

The remaining boundary condition at $\alpha=0$ is the stiffener condition, which is separately described in next section. Two remaining stress-free conditions around the hole are specified as

$$\sigma_{\alpha\alpha}(\alpha^*,\beta)=0,\ \sigma_{\alpha\beta}(\alpha^*,\beta)=0. \quad (20b,c)$$

From the application of (20a), we have

$$\phi_1(0)=0$$
$$(n+1)(n+2)\phi_{n+1}(0)-2(n^2-1)\phi_n(0)$$
$$+(n-1)(n-2)\phi_{n-1}(0)=0. \quad (21a,b)$$

This recurrence relation follows that $\phi_n(0)=0$ for $n=2, 3, 4, \ldots$. Around the hole, the normal traction condition (20b) yields

$$\sum_{n=1}^{\infty}[(-n^2\sinh 2\alpha^*+2n\sinh^2\alpha^*)e^{-n\alpha^*}\cos n\beta$$
$$+n^2\sinh\alpha^*e^{-n\alpha^*}\{\cos(n-1)\beta+\cos(n+1)\beta\}$$
$$+n\sinh 2\alpha^*e^{-n\alpha^*}\{\cos(n-1)\beta-\cos(n+1)\beta\}]$$
$$-2B_0\sinh\alpha^*\cosh\alpha^*+2\phi_1(\alpha^*)+2B_0\sinh\alpha^*\cos\beta$$
$$+\sum_{n=1}^{\infty}[\{(n+1)(n+2)\phi_{n+1}(\alpha^*)-2(n^2-1)\cosh\alpha^*\phi_n(\alpha^*)$$
$$+(n-1)(n-2)\phi_{n-1}(\alpha^*)\cos n\beta]=0 \quad (22)$$

where the odd symmetric terms, such as $\sin n\beta$ for $n=1, 2, 3, \ldots$, were already eliminated from symmetry considerations (18a, b, c). Upon gathering the coefficients of like terms of the type $\cos n\beta$ for $n=0, 1, 2, 3, \ldots$, it follows that the constant term becomes

$$-2B_0\sinh\alpha^*\cosh\alpha^*+2\phi_1(\alpha^*)+2e^{-\alpha^*}\sinh\alpha^*=0, \quad (23a)$$

the $\cos\beta$ term becomes

$$2e^{-\alpha^*}(1-e^{-2\alpha^*})+2B_0\sinh\alpha^*+6\phi_2(\alpha^*)$$
$$-2\sinh\alpha^*\phi'_1(\alpha^*)=0, \text{ and} \quad (23b)$$

the $\cos 2\beta$ term becomes

$$12\phi_3(\alpha^*)-6\cosh\alpha^*\phi_2(\alpha^*)-2\sinh\alpha^*\phi'_2(\alpha^*)$$
$$+(-1+4e^{-2\alpha^*}-3e^{-4\alpha^*})=0. \quad (23c)$$

The final boundary condition around the hole is a tangential traction condition (20c). For the purpose of simplicity in dealing with this condition, it must be understood that we do not need to use the full expression of $\sigma_{\alpha\beta}(\alpha,\beta)$. Instead, since it is always true that $\cosh\alpha^*-\cos\beta\neq 0$, the condition $\{\partial(h\chi/a)/\partial\alpha\partial\beta\}_{\alpha=\alpha^*}=0$ may be utilized to obtain the following result:

$$\left\{\frac{\partial^2(h\chi/a)}{\partial\alpha\partial\beta}\right\}_{\alpha=\alpha^*}=\sum_{n=1}^{\infty}(n\sinh\alpha^*-\cosh\alpha^*)ne^{-n\alpha^*}\sin n\beta$$
$$+B_0\sin\beta-\sum_{n=1}^{\infty}n\phi'_n(\alpha^*)\sin n\beta=0. \quad (24)$$

The coefficients of like terms of the type $\sin n\beta$ for $n=1, 2, 3, \ldots$, are

Downloaded 03 May 2010 to 171.66.16.247. Redistribution subject to ASME license or copyright; see http://www.asme.org/terms/Terms_Use.cfm

sin β term:

$$e^{-2\alpha^*} - B_0 + \phi'_1(\alpha^*) = 0, \tag{25a}$$

sin 2β term:

$$(2 \sinh \alpha^* - \cosh \alpha^*)e^{-2\alpha^*} - \phi'_2(\alpha^*) = 0, \tag{25b}$$

sin 3β term:

$$(3 \sinh \alpha^* - \cosh \alpha^*)e^{-3\alpha^*} - \phi'_3(\alpha^*) = 0. \tag{25c}$$

4 Stiffener Condition

Referring to Fig. 1(b), the stiffener condition as in Melan's problem in a Cartesian system is described by the following relation:

$$\frac{dp(x)}{dx} = tq(x) \tag{26}$$

where $p(x)$ is the axial force in the stiffener, t the thickness of the plate, and $q(x)$ the shearing stress between the plate and the stiffener.

The longitudinal condition along the stiffener is represented as

$$\epsilon_s(x) = \frac{p(x)}{AE_s} \tag{27}$$

where the subscript s refers to the stiffener and A is its area of cross-section.

On the interface between the plate and stiffener, it is required that the displacement of the plate and that of the stiffener must be the same and joined together to transmit the shear stress $\sigma_{\alpha\beta}(0, \beta)$ along the straight edge. The displacement condition can be replaced by strain terms such that

$$\epsilon_s(x) = \epsilon_{xx}(x, 0). \tag{28}$$

Since along the straight edge the normal stress component $\sigma_{yy}(x, 0)$ or $\sigma_{\alpha\alpha}(0, \beta)$ is assumed to be negligible, the elasticity equation is simply given by the expression

$$\epsilon_{xx}(x, 0) = \frac{1}{E}\sigma_{xx}(x, 0) \tag{29}$$

where E is the modulus of the plate.

Then, the axial force distribution $p(x)$ may be expressed in terms of $\sigma_{\beta\beta}(0, \beta)$ using condition (8) as given by

$$p(x) = AE_s\epsilon_s(x) = AE_s\epsilon_{xx}(x, 0) = \frac{AE_s}{E}\sigma_{xx}(x, 0) = \frac{AE_s}{E}\sigma_{\beta\beta}(0, \beta) \tag{30}$$

where E_s is the modulus of the stiffener. Then, using (9) and (30), the stiffener Eq. (26) becomes

$$-\frac{AE_s}{E}\left(\frac{\partial\beta}{\partial x}\right)_{\alpha=0} 2a\frac{d\sigma_{\beta\beta}(0, \beta)}{d\beta} + 2t\,a\,\sigma_{\alpha\beta}(0, \beta) = 0 \tag{31}$$

or

$$-\kappa\frac{d\sigma_{\beta\beta}(0, \beta)}{d\beta} + \frac{1}{a}\left(\frac{\partial x}{\partial\beta}\right)_{\alpha=0}\sigma_{\alpha\beta}(0, \beta) = 0, \tag{31b}$$

where we have introduced a nondimensional stiffener parameter

$$\kappa = \frac{AE_s}{atE}. \tag{32}$$

It should be noted that the above expressions (31a) and (31b) are not convenient for extracting the complete recurrence relation as was done with previous boundary conditions. It is clearly seen that the three conditions (21a), (23a), and (25a) contain four unknowns B_0, A_1, B_1, C_1. That is to say, such relations consist of B_0, the boundary values of $\phi_1(\alpha)$ and its derivative $\phi'_1(\alpha)$ for $\alpha = 0$ or $\alpha = \alpha^*$. Thus, to determine the four coefficients successfully, it is desirable that the remaining condition at $\alpha = 0$ does not involve terms such as $\phi'_n(0)$ or $\phi''_n(0)$ for $n \geq 2$. The significance of this point will be stated again in the next section in connection with the unstiffened case. The first recurrence relation (31b) contains terms such as $\phi'_1(0)$, $\phi''_1(0)$, and $\phi''_2(0)$. In a manner similar to the first relation, the nth recurrence relation consists of $\phi'_n(0)$, $\phi''_n(0)$ and $\phi''_{n+1}(0)$ (see Appendix A). From this, it is clearly seen that the first set of the 4 recurrence relations including (21a), (23a), and (25a) provides six unknowns B_0, A_1, B_1, C_1, A_2, and B_2. These are also inductively true for the nth set. It seems that the direct application of (31b) may not produce a desirable result. Thus, its integral form is chosen rather than the differential form. Through integrating (31a) with respect to x from $x = -\infty$ to a certain arbitrary position, it is given as

$$-\int_{-\infty}^{x}\frac{AE_s}{E}2a\frac{d\sigma_{\beta\beta}(0, \beta)}{d\beta}\left(\frac{\partial\beta}{\partial x}\right)_{\alpha=0}dx + \int_{-\infty}^{x} 2t\,a\,\sigma_{\alpha\beta}(0, \beta)dx = 0. \tag{33}$$

The chain rule is applied to change the integration variable from x to β for the integrands. Finally, condition (33) can be expressed only in terms of bipolar coordinates β as follows:

$$-\int_0^{\beta}\left(\frac{AE_s}{Et}\right)\frac{d\sigma_{\beta\beta}(0, \beta)}{d\beta}d\beta + \int_0^{\beta}\sigma_{\alpha\beta}(0, \beta)\left(\frac{\partial x}{\partial\beta}\right)_{\alpha=0}d\beta = 0. \tag{34}$$

It is noted that $\beta = 0$ corresponds to $x = -\infty$. Finally, this is set as the fourth boundary condition to close the given elasticity problem. To perform the above integration, it is necessary to specify the value of $\sigma_{\beta\beta}(0, \beta)$ and $\sigma_{\alpha\beta}(0, \beta)$ at $\beta = 0$ to make sure the uniqueness of the solution. The definite integration of the second part of (34) is given by

$$Q = -\int_0^{\pi}\sigma_{\alpha\beta}(0, \beta)\left(\frac{\partial x}{\partial\beta}\right)_{\alpha=0}d\beta = -[a\{B_o(1 - \cos\beta) - \sum_{n=1}^{\infty}\phi'_n(0) + \sum_{n=1}^{\infty}\phi'_n(0)\cos n\beta\}]_0^{\pi} \tag{35}$$

where we define Q as the shear resultant acting on the edge of the plate from $\beta = 0$ ($x = -\infty$) to $\beta = -\pi$ ($x = 0$). Additionally, a normal resultant force H acting on section OM given by Mindlin (1948) is

$$H = \left\{\left[\frac{\partial\alpha}{\partial y}\left(\frac{\partial}{h\partial\alpha} + \frac{\partial(1/h)}{\partial\alpha}\right)(h\chi) + \frac{\partial\beta}{\partial y}\left(\frac{\partial}{h\partial\beta} + \frac{\partial(1/h)}{\partial\beta}\right)(h\chi)\right]_0^{\alpha^*}\right\}_{\beta=\pi}. \tag{36}$$

At infinity $\alpha = 0$, $\beta = 0$ ($r = \sqrt{x^2 + y^2} \to \infty$), the first series expression of (12) diverges, so it must be replaced by its original expression (11) to evaluate (34). Then, it follows that the limiting value of $[\{\partial/\partial\alpha\}(h\chi)]_{\alpha=0}$ approaches zero as x goes to $-\infty$ and, in the same way, $\sigma_{\beta\beta}(0, \beta)$ to 1.

These relations are submitted into (34) to yield the following conditions with respect to the coefficients of like terms of the type cos $n\beta$ for $n = 0, 1, 2, 3, \ldots$:

constant term:

$$\kappa\phi''_1(0) + 2B_o - \sum_{n=1}^{\infty} 2\phi'_n(0) = 0, \tag{37a}$$

Downloaded 03 May 2010 to 171.66.16.247. Redistribution subject to ASME license or copyright; see http://www.asme.org/terms/Terms_Use.cfm

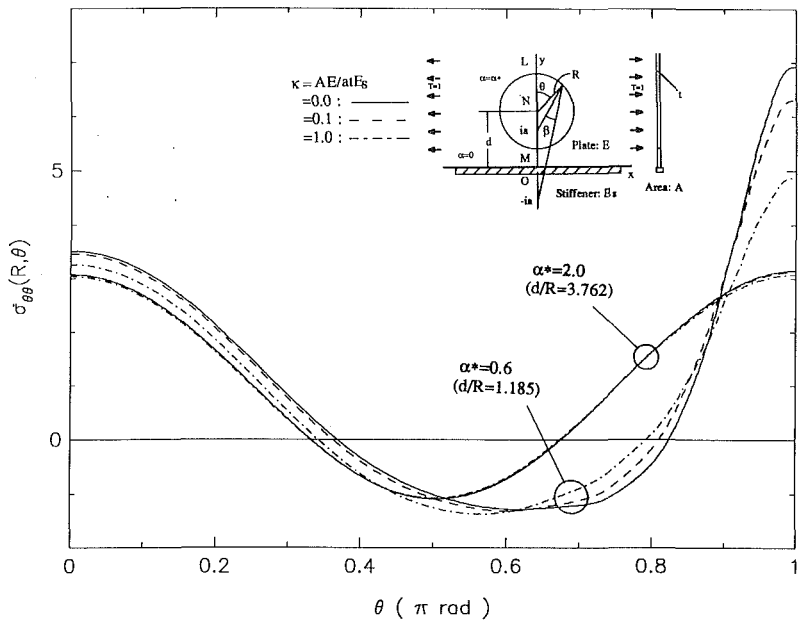


Fig. 2 Hoop stress variations along θ

cos β term:

$$\kappa\{-2\phi''_1(0)+\phi''_2(0)\}-2B_o+2\phi'_1(0)=0 \qquad (37b)$$

cos $n\beta$ term for $n = 2, 3, 4, \ldots$:

$$\kappa\{\phi''_{n-1}(0)-2\phi''_n(0)+\phi''_{n+1}(0)\}+2\phi'_n(0)=0. \qquad (37c)$$

5 Solution

To determine the function $\phi_n(\alpha)$ for $n = 1, 2, 3, \ldots$ and the unknown coefficient B_0, the results obtained from the application of the boundary conditions are rearranged in the following order:

First set:

$\sigma_{\alpha\alpha}(0, \beta)=0 \quad : \phi_1(0)=0$

stiffner $\quad : \kappa\phi''_1(0)+2B_0-\sum_{n=1}^{\infty} 2\phi'_n(0)=0$

$\sigma_{\alpha\beta}(\alpha^*, \beta)=0 : e^{-2\alpha^*}-B_0+\phi'_1(\alpha^*)=0$

$\sigma_{\alpha\alpha}(\alpha^*, \beta)=0 : -2B_0 \sinh \alpha^* \cosh \alpha^*+2\phi_1(\alpha^*)$
$+2e^{-\alpha^*} \sinh \alpha^*=0. \qquad (38a,b,c,d)$

These yield a set of linear equations with infinite number of unknown coefficients:

$B_1+A_1=0$

$4A_1\kappa+B_0-4C_1-4C_2-4D_2-4C_3-4D_3-\ldots=0$

$2A_1 \sinh 2\alpha^*-B_0+2C_1 \cosh 2\alpha^*+e^{-2\alpha^*}=0$

$2A_1 \cosh 2\alpha^*+2B_1+2C_1 \sinh 2\alpha-B_0 \sinh 2\alpha^*$
$+(1-e^{-2\alpha^*})=0. \qquad (39a,b,c,d)$

Second set:

$\sigma_{\alpha\alpha}(0, \beta)=0 \quad : \phi_2(0)=0$

stiffner $\quad : \kappa\{-2\phi''_1(0)+\phi''_2(0)\}-2B_0+2\phi'_1(0)=0$

$\sigma_{\alpha\beta}(\alpha^*, \beta)=0 : (2\sinh \alpha^*-\cosh \alpha^*)e^{-2\alpha^*}-\phi'_2(\alpha^*)=0$

$\sigma_{\alpha\alpha}(\alpha^*, \beta)=0 : 2e^{-\alpha^*}(1-e^{-2\alpha^*})+2B_0 \sinh \alpha^*+6\phi_2(\alpha^*)$
$-2\sinh \alpha^*\phi'_1(\alpha^*)=0. \qquad (40a,b,c,d)$

Equation (39b) shows a fundamental difference between Jeffery's work and this analysis. The system of the equations is coupled with respect to every coefficient of all the other sets, and it is required that they should be solved simultaneously. However, if the parameter κ approaches zero, the present formulation can be reduced to the shear-free stress condition of Jeffery's solution. For this limiting case, the coefficients are not coupled with each other, and they are simply expressed in the analytical form given by Mindlin (1948) (see Appendix B).

Table 1 Stress concentration at the point M and L

α^*	d/R	$\sigma_{\beta\beta}$: κ=0.0		$\sigma_{\beta\beta}$: κ=1.0	
		At point M	At point L	At point M	At point L
0.6	1.185	6.926	3.514	4.868	3.261
0.8	1.337	5.385	3.413	4.189	3.206
1.0	1.543	4.494	3.323	3.755	3.159
1.2	1.811	3.944	3.249	3.476	3.121
1.4	2.151	3.597	3.189	3.299	3.092
1.6	2.577	3.376	3.142	3.187	3.069
1.8	3.107	3.238	3.104	3.117	3.051
2.0	3.762	3.151	3.076	3.074	3.037
2.2	4.507	3.096	3.054	3.048	3.026
∞	∞	3.000	3.000	3.000	3.000

6 Numerical Results

The coupled system of equations were solved using a Gaussian elimination method. The results presented here correspond to a series with 15 terms. Referring to Fig. 2, it is apparent that for relatively large values of α^*, for instance $\alpha^* = 2.0$ ($d/R = 3.762$), the stress concentration factor of the stiffened plate approaches 3.0. This is because the hoop stress expressions (16b) are nearly the same for both the stiffened and unstiffened plate and their dominant terms may be commonly reduced to $\sigma_{\beta\beta}(\alpha, \beta) = (1+2 \cos 2\theta)$, as was done by Jeffery (1921). That is, the presence of the stiffener does not seriously influence to the hoop stress distribution around the circular hole. Conversely, as the hole is located near the straight bound-

Downloaded 03 May 2010 to 171.66.16.247. Redistribution subject to ASME license or copyright; see http://www.asme.org/terms/Terms_Use.cfm

Table 2 Normal resultant force H on section OM and shear resultant force Q on the half of the straight edge

α^*	d/R	κ=0.0		κ=0.1		κ=1.0	
		H/a	Q/a	H/a	Q/a	H/a	Q/a
0.6	1.185	0.996	0.0	1.038	0.028	0.869	0.487
0.8	1.337	0.997	0.0	1.036	0.003	0.931	0.281
1.0	1.543	0.991	0.0	1.023	-0.007	1.033	0.165
1.2	1.811	0.993	0.0	1.019	-0.010	0.981	0.097
1.4	2.151	0.994	0.0	1.014	-0.010	0.991	0.058
1.6	2.577	0.990	0.0	1.005	-0.008	1.121	0.035
1.8	3.107	0.991	0.0	1.002	-0.006	0.993	0.021
2.0	3.762	0.991	0.0	0.999	-0.005	0.994	0.013
2.2	4.507	1.000	0.0	1.006	-0.003	1.002	0.009

ary, the highest stress concentration occurs at the point M ($\theta = \pi$). These facts are identified in Fig. 2 where the influence of the parameter κ on the hoop stress distribution is represented by the curves for $\alpha^* = 0.6$ ($d/R = 1.185$).

It is easily seen that as κ increases with a fixed α^*, the stress concentration at point M decreases. Numerical values are given in Table 1. It was also found that, depending on range of κ and α^*, the behavior of the present series solution may become oscillatory. But, if $\alpha^* > 0.6$ ($d/R > 1.185$), the parameter κ may be raised above 2.5.

The role of the edge stiffener was also investigated with respect to how the stress profile σ_{xx} (0, y) along section OM may be changed from that of the unstiffened plate. Figure 3 shows not only the decrease of stress concentration at the point M, its effect being appreciable as κ increases, but also the change in shape of the stress profile σ_{xx} (0, y). It should be noted that in the neighborhood of the straight boundary (i.e., for small α), $\sigma_{xx}(0, y)$ cannot be accurately evaluated because

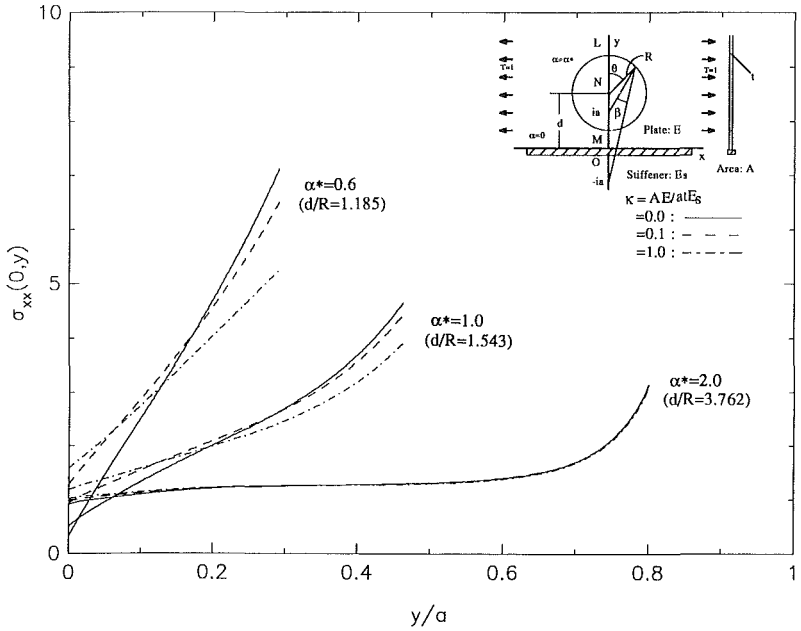


Fig. 3 Normal stress distributions on section OM

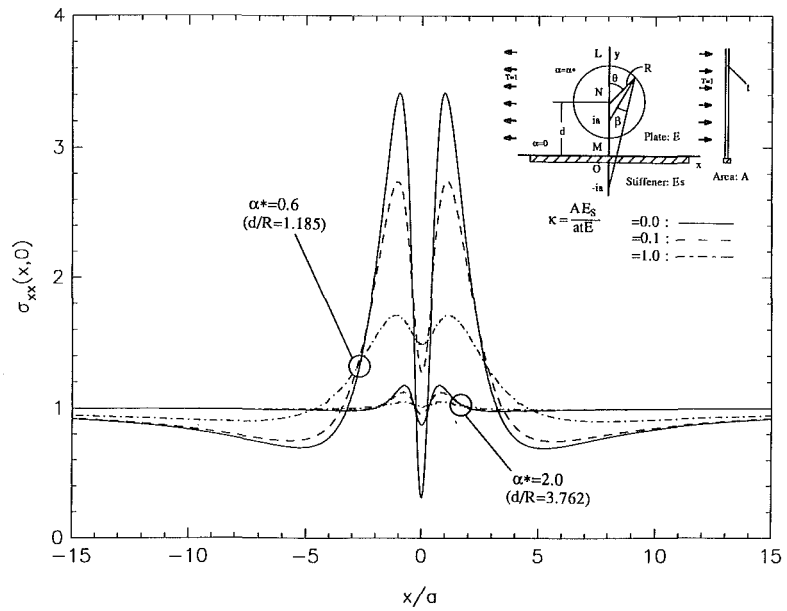


Fig. 4 Stress variations along the edge stiffener

Downloaded 03 May 2010 to 171.66.16.247. Redistribution subject to ASME license or copyright; see http://www.asme.org/terms/Terms_Use.cfm

of the slow convergence of the series solution as was also mentioned by Jeffery (1921).

The resultant force, H, on section OM may involve error caused by summing the serial part of $\sigma_{xx}(0, y)$ near origin. Using formula (36), a closed-form expression for (H/a) was found for the unstiffened case of Mindlin (1948). Numerical estimation by series summation shows one percent error for the unstiffened case (see Table 2). In contrast, the shear stress resultant Q can be easily evaluated with formula (35) without any convergence problems. Table 2 shows the dependence of Q on the parameter κ and the coordinate α^*. As κ approaches unity and α^* becomes smaller, the quantity H rapidly decreases but Q approaches a magnitude comparable to that of H.

Typical stress distributions for $\sigma_{xx}(x, 0)$ are plotted in Fig. 4 for two different choices of the parameter κ. It is seen that the stress $\sigma_{xx}(x, 0)$ of the stiffened case with small α^* shows weaker variations than those of the unstiffened plate.

7 Concluding Remark

Through an analytical formulation based on bipolar series expansion, the stress distribution around a circular hole under the influence of an edge stiffener was examined for a variety of dimensionless parameters. Consequently, it leads to the conclusion that an edge stiffener indirectly suppresses the stress concentration around a hole when the hole is near the edge and that appreciable interaction between the hole and stiffener occurs.

References

Gladwell, G. M. L., 1980, *Contact Problems in the Classical Theory of Elasticity*, Sijthoff and Noordhoff International Publishers, pp. 318–322.

Jeffery, G. B., 1921, "Plane Stress and Plane Strain in Bipolar Coordinates," *Trans. Roy. Soc., London*, Vol. A221, pp. 265–293.

Melan, E., 1932a, "Der Spannungszustand der durch eine Einzelkraft im Innern beanspurchten Halscheibe," *Zeitschrift fuer angewandte Mathematik und Mechanik*, Vol. 12, pp. 343–346.

Melan, E., 1932b, "Ein Beitrag zur Theori geschweisster Verbindungen," *Ingenier-Archiv*, Vol. 3, pp. 123–129.

Mindlin, R. L., 1948, "Stress Distribution Around a Hole Near the Edge of a Plate Under Tension," *Proc. Soc. for Exptl. Stress Anal.*, Vol. 5, pp. 56–68.

Muki, R., and Sternberg, E., 1967, "Transfer of Load From an Edge Stiffener to a Sheet—A Reconsideration of Melan's Problem," ASME JOURNAL OF APPLIED MECHANICS, Vol. 34, pp. 679–686.

Muskhelishvili, N. I., 1954, *Some Basic Problems of the Mathematical Theory of Elasticity*, 4th ed., Moscow (translated into English by J. R. M. Radok, P. Noordhoff Ltd., Groningen).

Savin, G. N., 1970, *Stress Distribution Around Holes*, NASA Technical Translation, NASA TT F-607, National Aeronautics and Space Administration, Washington, D.C., pp. 128–137.

Timoshenko, S. P., and Goodier, J. N., 1970, *Theory of Elasticity*, 3rd ed., McGraw-Hill, New York, pp. 196–202.

APPENDIX A

From formula (16b), the stress $\sigma_{\beta\beta}(\alpha, \beta)$ on $\alpha = 0$ is of the form

$$\sigma_{\beta\beta}(0, \beta) = 1 + (1 - \cos\beta)\sum_{n=1}^{\infty} \phi''_n(o)\cos n\beta. \qquad \text{(A1)}$$

Its first derivative with respect to β is

$$\begin{aligned}\frac{d\sigma_{\beta\beta}(0, \beta)}{d\beta} &= \sin\beta \sum_{n=1}^{\infty} \phi''_n(o)\cos n\beta \\ &\quad - (1-\cos\beta)\sum_{n=1}^{\infty} n\phi''_n(o)\sin n\beta = \phi''_1(0)\sin\beta\cos\beta \\ &\quad + \phi''_2(0)\sin\beta\cos 2\beta + \phi''_3(0)\sin\beta\cos 3\beta + \dots \\ &\quad - \phi'_1(0)\sin\beta - 2\phi'_2(0)\sin 2\beta - \dots + \phi'_1(0)\cos\beta\sin\beta \\ &\quad + 2\phi''_2(0)\cos\beta\sin 2\beta + 3\phi''_3(0)\cos\beta\sin 3\beta + \dots \\ &= \left\{\frac{1}{2}\phi''_2(0) - \phi''_1(0)\right\}\sin\beta + \{\phi''_1(0) \\ &\quad - 2\phi''_2(0 + \phi''_3(0)\}\sin 2\beta + \dots \qquad \text{(A2)}\end{aligned}$$

The second term in (31b) is:

$$\begin{aligned}\frac{1}{a}\left(\frac{\partial x}{\partial\beta}\right)_{\alpha=0}\sigma_{\alpha\beta}(0, \beta) &= \left\{\frac{\partial^2(h\chi/a)}{\partial\alpha\partial\beta}\right\}_{\alpha=0} = \sum_{n=1}^{\infty} n\phi'_n(o)\sin n\beta \\ &= \phi'_1(0)\sin\beta + 2\phi'_2(0)\sin 2\beta + \dots . \qquad \text{(A3)}\end{aligned}$$

By taking a linear combination of (A2) and (A3), one easily finds that the first recurrence relation with respect to $\sin\beta$ of (31b) may contain $\phi'_1(0)$, $\phi''_1(0)$ and $\phi''_2(0)$ and that for the nth step those inductively hold.

APPENDIX B

In the case of $\kappa = 0$, we can take the more simplified expression of the stiffener condition for each step as follows:

$$\begin{aligned}&\text{1st set}: B_0 - \sum_{n=1}^{\infty}\phi'_n(0) = 0 \\ &\text{2nd set}: B_0 - \phi'_1(0) = 0 \qquad \text{(B1)} \\ &n\text{th set}: \phi'_{n-1}(0) = 0 \text{ for } n \geq 3.\end{aligned}$$

The summation term appearing in the first set can be eliminated except for the term $n = 1$ by substituting all conditions starting from $n = 3$ into the first set. As a result, one can obtain the same expression with the second set. The conditions that $B_0 = \phi'_1(0)$ and $\phi'_n(0) = 0$ for $n > 2$ are identically the same as the shear-free stress condition along the straight edge.

Downloaded 03 May 2010 to 171.66.16.247. Redistribution subject to ASME license or copyright; see http://www.asme.org/terms/Terms_Use.cfm

Interface Blunting of Matrix Cracks in Fiber-Reinforced Ceramics

Anna Dollar

Paul S. Steif
Assoc. Mem. ASME.

Department of Mechanical Engineering,
Carnegie-Mellon University,
Pittsburgh, PA 15213

A crack impinging upon an interface that can debond and then offer frictional resistance is studied theoretically. The central question at issue is the level of the remote load at which the crack penetrates the interface, whether or not some debonding of the interface occurs first. To answer this question, we compute the stress enhancement experienced by the impinged material—averaged over a microstructural length such as the fiber diameter—as a function of interface parameters. The solution to this elasticity problem is arrived at by means of distributed dislocations to represent relative motion at the interface. Special care needs to be taken to account properly for the contact problem at the interface. Not unexpectedly, it is found that higher debond energies and greater frictional resistances lead to higher stress concentrations and, hence, to lower remote failure loads.

1 Introduction

It is increasingly accepted that the fiber-matrix interface plays a significant role in the fracture resistance of fiber-reinforced composites. For ceramic-matrix composites, in particular, a relatively weak interface generally promotes composite toughness, although sometimes at the expense of other properties such as transverse strength and shear strength. Under longitudinal tension, cracks growing in the matrix are diverted to a weak interface, thereby sparing the fiber, at least until higher levels of load are achieved. A quantitative understanding of this phenomenon is still rather primitive, however.

Various studies of cracks lying perpendicular to, penetrating, and branching at interfaces have been carried out, including Cook and Erdogan (1972), Erdogan and Biricikoglu (1973), Goree and Venezia (1977), and Lu and Erdogan (1983). A recent treatment of this problem by He and Hutchinson (1989) is typical of the approach commonly taken to the crack diversion phenomenon. Whether the crack is diverted to the interface depends on the relative values of the interfacial fracture toughness and the fiber fracture toughness. He and Hutchinson (1989) considered a set of problems in which the elastic energy release rate associated with the crack extending into the fiber is compared with the elastic energy release rate associated with the crack diverting to the interface. It is the ratio of these energy release rates which must be compared with the toughness ratio to determine whether diversion occurs.

The present paper is devoted to elaborating upon an alternative view of the problem of crack diversion. To appreciate this alternative approach, it is first necessary to pose the central questions at issue in the following different way: Given that there are matrix cracks which impinge upon fibers, what is the level of load at which the impinged fibers will break? Is that load greater than or less than the load necessary to propagate the matrix crack around the fiber? And, how is this process influenced by microstructural material parameters such as interface strength? Now, say it is determined, via the relative toughness analysis, that the matrix crack penetrates the fiber rather than diverts to the interface. Then, with the same analysis, one can predict the load at which the fiber would fail. On the other hand, say the relative toughness, analysis predicts that the crack is diverted to the interface. Surely the fiber will fail at some higher level of remote load, whether or not the matrix crack first manages to propagate around the fiber. Furthermore, the increment in remote load which is needed to cause fiber failure is critical to determining the composite strength. Yet, current methods of analysis, including relative toughness arguments, are incapable of resolving this question.

In other words, the relative toughness analysis distinguishes only between those interfaces that divert matrix cracks and those that do not. The far more important requirement (from a practical point of view) of distinguishing between different interfaces *all of which allow some diversion* cannot be met with the relative toughness analysis. As evidence of the necessity of making such a distinction, consider fracture surfaces of ceramic-matrix composites: there are very fibrous (broom-like) fracture surfaces, and there are surfaces with very short pullout lengths. Only occasionally will the surface appear to be almost perfectly flat, with virtually no pullout. While the variety of pullout lengths is a consequence of the random distribution of flaws in the fibers, it undoubtedly necessitates

Contributed by the Applied Mechanical Division of THE AMERICAN SOCIETY OF MECHANICAL ENGINEERS for publication in the ASME JOURNAL OF APPLIED MECHANICS.

Discussion on this paper should be addressed to the Technical Editor, Professor Leon M. Keer, The Technological Institute, Northwestern University, Evanston, IL 60208, and will be accepted until four months after final publication of the paper itself in the JOURNAL OF APPLIED MECHANICS.

Manuscript received by the ASME Applied Mechanics Division, Apr. 23, 1990; final revision, Sept. 25, 1991. Associate Technical Editor: G. J. Dvorak.

Copyright © 1992 by ASME
Downloaded 03 May 2010 to 171.66.16.247. Redistribution subject to ASME license or copyright; see http://www.asme.org/terms/Terms_Use.cfm

prior debonding of the interface as well. Therefore, it would clearly be valuable to have a model which distinguishes among the vast majority of cases in which matrix cracks cause some debonding of the interface prior to failure of the fibers. A more comprehensive model involves an evaluation of stresses acting on the fiber *after* the matrix crack has been diverted to the interface.

An initial attempt at such an approach was recently presented by the authors (Dollar and Steif, 1989). We were contemplating an infinite, two-dimensional solid subjected to remote tension, which contains a crack impinging upon an interface that is characterized by a Coulomb friction law. The choice for the interface law was motivated by experimental observations that the interface in ceramic-matrix composites can be extremely weak, with perhaps only sliding friction to provide shear coupling between the fiber and the matrix. For this problem, Dollar and Steif (1989) found that the tensile stress ahead of the crack tip is *finite*, and that it depends on material parameters such as the residual compressive stress and the friction coefficient, as well as on the applied stress.

The purpose of the present paper is twofold. First, we will extend the analysis of Dollar and Steif (1989) so as to include debonding at the interface, as well as Coulomb friction. This reflects observations that some, albeit small, degree of chemical bonding is often present at the fiber-matrix interface. In particular, the evolution of the relevant stresses and the interface motion under a monotonically increasing remote loading will be investigated. Secondly, we will impose upon the solution a simple, unified fiber breakage criterion. This criterion, which differs from the usual fracture mechanics energy release criterion, is unified in the sense that it can be applied whether or not diversion to the interface has taken place.

By comparison with most other analyses of cracks near interfaces, the present analysis of the effect of crack diversion to the interface has been simplified in one important respect: we neglect differences in fiber and matrix elastic moduli. Insofar as the calculation of interfacial debonding is concerned, this assumption would appear to be acceptable. For example, in an experimental study of bimaterial interfacial fracture, Cao and Evans (1989) found the fracture resistance to depend on the combination of mode I and mode II, as measured by the phase angle Ψ; the phase angle depends, in turn, on the specimen geometry, but is relatively insensitive to the modulus ratio (see their Figs. 2 and 3). With regard to the stress concentration ahead of the impinging crack, some recent investigations into cracks impinging upon bimaterial frictional interfaces (Schwietert and Steif, 1989; Wang et al., 1989) have suggested that the influence of relative modulus is slight. Therefore, besides simplifying the analysis substantially, neglecting modulus differences does seem reasonable for ceramic-matrix composites in which the modulus ratio is not far from one anyway. Furthermore, it is our contention that the effects of interface parameters are of paramount concern and deserve to be investigated in the absence of less critical variables.

2 Problem Statement and Analysis

Consider an infinite elastic plane deforming in plane strain, subjected to a remote tension $\sigma_{yy}=\sigma_\infty$, which contains a single crack lying along $-2a<x<0$. The crack faces are free of tractions, and both crack tips impinge upon an interface which can debond and slide with frictional resistance (see Fig. 1). There is also a remote stress $\sigma_{xx}=\sigma_o$, which mimics the residual normal stress acting on the interface. Note that the residual stress can be either tensile ($\sigma_o>0$) or compressive ($\sigma_o<0$). Once debonding has begun, this configuration resembles the so-called H crack; that is, a main crack with two symmetric branches emanating normally from each tip. Branched cracks of this type have been studied by a number of investigators

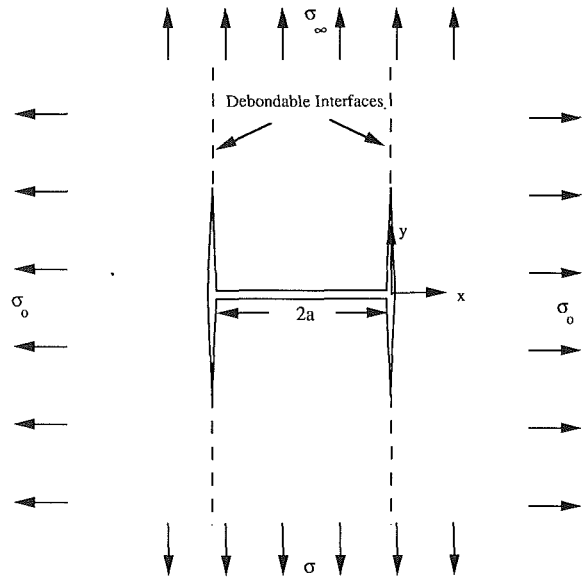


Fig. 1 Schematic of crack impinging upon a debondable slipping interface

(Vitek, 1977; Kitagawa and Yuuki, 1977; Lo, 1978; and Benveniste et al., 1989). An important difference between the present analysis and most treatments of branch crack problems consists in the boundary conditions along the branch crack. Typically, it is assumed that the tractions along the branch cracks are zero. By contrast, the purpose here is to capture some features of a real composite interface. Accordingly, we model the interface in the following manner.

Each point along the interfaces $x=-2a$ and $x=0$ is in one of two states: bonded or debonded. Debonding of the interface is handled with a typical fracture mechanics approach: a crack along the interface can extend if the elastic energy release rate is equal to the critical energy release rate for debonding, G_d. Once a point of the interface has debonded, from then on it remains debonded (there is no healing), and it obeys a Coulomb friction interface law. That is, at each instant subsequent to debonding, a point along the interface is either opening, sticking, or slipping; these conditions are expressed mathematically (for the interface $x=0$) by

stick condition

$$\sigma<0,\ |\tau|<\mu|\sigma|,\ \frac{dg}{dt}=0,\ h=\frac{dh}{dt}=0, \tag{1a}$$

slip condition

$$\sigma<0,\ |\tau|=\mu|\sigma|,\ \operatorname{sgn}\left(\frac{dg}{dt}\right)=\operatorname{sgn}(\tau),\ h=\frac{dh}{dt}=0, \tag{1b}$$

open condition

$$\sigma=\tau=0,\ h>0, \tag{1c}$$

with

$$\sigma=\sigma_{xx}\quad \tau=\sigma_{xy}$$

$$g=\lim_{\epsilon\to 0^+}\ [v(\epsilon,y)-v(-\epsilon,y)]$$

$$h=\lim_{\epsilon\to 0^+}\ [u(\epsilon,y)-u(-\epsilon,y)].$$

In these equations, u and v denote the x- and y-components of displacement, respectively, μ is the friction coefficient, and $d(\ )/dt$ denotes the derivative with respect to a timelike parameter that increases as the loading proceeds. The condition $\operatorname{sgn}(dg/dt)=\operatorname{sgn}(\tau)$ corresponds to positive energy dissipation, which requires the slippage to be in the same direction as the shear stress. In applying Eqs. (1), one must be careful to use

Downloaded 03 May 2010 to 171.66.16.247. Redistribution subject to ASME license or copyright; see http://www.asme.org/terms/Terms_Use.cfm

the total stresses, including any residual stresses. Thus, two parameters characterize each point on the debonded portion of the interface: the residual stress σ_o and the coefficient of friction μ.

Thus, the present work involves a careful accounting for the possible contact that can occur between the faces of the branch cracks. Proper accounting for crack face contact (even in the absence of friction) appears to be lacking in all previous analyses of branch cracks. As was pointed out recently by Dollar and Steif (1991), all existing branch crack solutions (of this configuration) involve a *negative* mode I stress intensity factor at the branch crack tips, provided the branch cracks are at least one quarter as long as the main crack. Since it is impossible for the branch crack faces to overlap, a more careful treatment that accounts for contact would lead to a mode I stress intensity factor which is non-negative.

Our method of analysis, which follows closely that of Lo (1978), begins with the solution to a traction-free crack in an infinite plane under remote tension. To simulte the debonds along the interface (the branch cracks), we superpose distributions of dislocations. In order to keep the main crack free of tractions, the kernel dislocation solution is that of a dislocation in the presence of a traction-free crack. The dislocation solution is most conveniently expressed in terms of the Muskhelishvili (1953) complex analytic functions $\phi(z)$ and $\psi(z)$, which are related to the stress and displacements according to

$$\sigma_{xx}+\sigma_{yy}=2(\phi'+\overline{\phi'}) \tag{2a}$$

$$\sigma_{yy}-\sigma_{xx}+2i\sigma_{xy}=2(\bar{z}\phi''+\psi') \tag{2b}$$

$$2G(u+iv)=\kappa\phi-z\overline{\phi'}-\overline{\psi} \tag{2c}$$

where $z=x+iy$, $()'$ denotes differentiation with respect to z, an overbar denotes complex conjugation, G is the shear modulus, $\kappa=3-4\nu$ in plane strain, and ν is Poisson's ratio.

For a dislocation with Burgers vector $\mathbf{b}=b_x\mathbf{i}+b_y\mathbf{j}$, one finds this kernel solution to be given by

$$\phi'=\phi'_\infty+\phi'_R \tag{3a}$$

$$\psi'=\psi'_\infty+\psi'_R \tag{3b}$$

where

$$\phi'_\infty(z,z_0)=\frac{\alpha}{z-z_0}\qquad \psi'_\infty=\frac{\overline{\alpha}}{z-z_0}+\frac{\alpha\bar{z}_0}{(z-z_0)^2} \tag{4a,b}$$

$$\phi'_R(z,z_0)=-[\alpha F(z,z_0)+\alpha F(z,\bar{z}_0)+\overline{\alpha}(z_0-\bar{z}_0)H(z,\bar{z}_0)] \tag{5}$$

$$\psi'_R(z,z_0)=\overline{\phi'_R}(z,z_0)-\phi'_R(z,z_0)-z\phi''_R(z,z_0) \tag{6}$$

$$F(z,z_0)=\frac{1-\dfrac{X(z_0)}{X(z)}}{2(z-z_0)} \tag{7}$$

$$H(z,z_0)=\frac{\partial F(z,z_0)}{\partial z_0} \tag{8}$$

$$X(z)=\sqrt{z(z+2a)} \tag{9}$$

$$\alpha=\frac{G(b_y-ib_x)}{\pi(\kappa+1)}. \tag{10}$$

Note that the solution for a dislocation in the presence of a traction-free crack has stresses that are square root singular at the crack tips.

Although the interpretation of the results presented below will be for a monotonically increasing remote stress, solutions can be obtained with the following procedure. We assume that under some value of the remote load, the branch cracks at both ends of the main crack extend over the region $-L_s<y<L_s$; this portion of the interface is debonded and, therefore, satisfies the interface law (1). It turns out that some portions of the debonded interface satisfy (1b), while others satisfy (1c). In the region $|y|>L_s$, the interface is perfectly bonded with continuity of traction and displacement. More specifically, we have found, after extensive experience with this class of problems, that the interface opens over one portion of the interface, $0<|y|<L_g$, and merely slides in contact over the remainder $L_g<|y|<L_s$. (Exceptions to this will be noted explicitly as follows.) Depending on the material parameters and on the load, L_g can be zero (no opening), between 0 and L_s (partial opening), or equal to L_s (complete opening). The relative motion of the interface can be represented by a distribution of "opening" dislocations, of intensity $b_x(y)$, along $0<|y|<L_g$, and "sliding" dislocations, of intensity $b_y(y)$, along $0<|y|<L_s$. Imposing the traction-free conditions (1c) over the opening zone $0<|y|<L_g$ and the frictional sliding condition (1b) over the slipping zone $L_g<|y|<L_s$ leads to a set of integral equations of the form

$$\int_0^{L_s} b_y(y')\left[\frac{2}{y'-y}+A(y',y)\right]dy' + \int_0^{L_g} b_x(y')B(y',y)dy'+f_1(y)=0 \quad (0<y<L_g) \tag{11a}$$

$$\int_0^{L_s} b_y(y')C(y',y)dy' + \int_0^{L_g} b_x(y')\left[\frac{-2}{y'-y}+D(y',y)\right]d_y' + f_2(y)=0 \quad (0<y<L_g) \tag{11b}$$

$$\int_0^{L_s} b_y(y')\left[\frac{2}{y'-y}+E(y',y)\right]dy' + \int_0^{L_g} b_x(y')\left[\frac{-2}{y'-y}+F(y',y)\right]dy' + f_3(y)=0 \quad (L_g<y<L_s). \tag{11c}$$

Equations (11a) and (11b) represent imposition of zero traction σ_{xy} and σ_{xx}, respectively, along the opening zone; Eq. (11c) represents imposition of the Coulomb friction law along the slip zone. The kernels $A(y',y)$, $B(y',y)$, $C(y',y)$, $D(y',y)$, $E(y',y)$, and $F(y',y)$, as well as the functions $f_1(y)$, $f_2(y)$, and $f_3(y)$, are given in the Appendix. In deriving these equations, advantage has been taken of the symmetry with respect to the x-axis. It is also possible to handle the case of a vanishingly small debond explicitly. This was done using an approach which is identical to that leding to (11), except that the kernel solution is that of a dislocation in the presence of a traction-free, semi-infinite crack (see Lo (1978) or Dollar and Steif (1989)).

Crucial to solving Eqs. (11) is knowing the behavior of the dislocation intensities at the ends of the intervals. For example, at the end of the debond, $y = L_s$, the stress is square root singular. In general, the mode II stress intensity factor is nonzero, while the mode I stress intensity factor is nonzero only when $L_g=L_s$; i.e., when the debond is fully open. Accordingly, $b_y(y)$ is square root singular as $y\to L_s$. $b_x(y)$ is square root singular as $y\to L_g$ only when $L_g=L_s$; otherwise, the necessary smooth transition from opening to slipping requires $b_x(L_g)=0$ (Dundurs and Comninou, 1979). The energy release at the tip of the debond is computed from the stress intensity factors, as will be described in the results section.

Since the stresses *ahead* of the main crack *after* diversion to the interface are an essential element of the present work, it is of interest to consider the nature of these stresses. There are three possibilities to consider: (i) no diversion has occurred; (ii) diversion has occurred, and there is frictional slippage along the interface near the main crack tip with (1b) being satisfied there; (iii) diversion has occurred, and the interface is open near the main crack tip with (1c) being satisfied there. For case (i), the usual square root stress singularity prevails (since fiber and matrix have identical moduli). Case (ii) corresponds to the main crack impining upon a frictional interface; as shown by Dollar and Steif (1989), the near-tip stresses in this case are

Downloaded 03 May 2010 to 171.66.16.247. Redistribution subject to ASME license or copyright; see http://www.asme.org/terms/Terms_Use.cfm

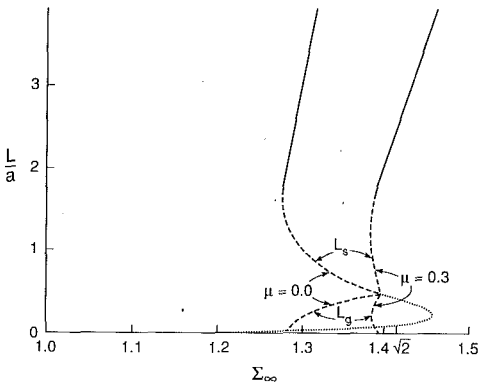


Fig. 2 Extent of debonding L_s and extent of opening zone L_g as a function of applied stress Σ_∞, (..... ~ fully open debond; ----- ~ partially open debond; —— fully closed debond).

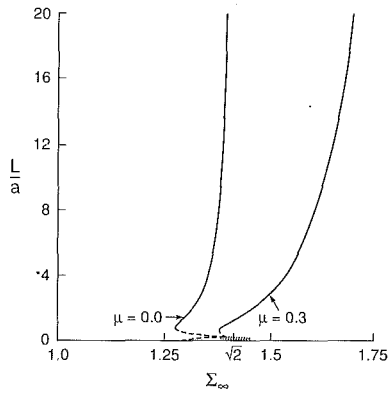


Fig. 3 Extent of debonding as a function of applied stress Σ_∞. (..... ~ fully open debond; ----- ~ partially open debond; — fully closed debond.)

finite. For case (iii), the material in the vicinity of the main crack and to the right of the interface is like a traction-free half-plane. The only admissible singular stress field would be that due to a point force, which is not present; hence, the stresses near the main crack tip are also nonsingular when the crack diverts and the interface is open. Therefore, provided some diversion to the interface has occurred, the stresses immediately ahead of the crack are finite. In particular, the tensile stress, denoted by $(\sigma_{yy})_{\text{tip}}$, is presented below as one measure of the blunting effect of the interface on a matrix crack.

These near-tip stresses provide additional information regarding the behavior of the dislocation intensities. As indicated above, the stresses near the main crack tip are finite, provided there is some debonding. Recall that our method of solution involves a superposition of the solution of the Griffith crack which is singular at the crack tip and a distribution of dislocations each of which induces a singularity at the crack tip. Enforcing the condition of *zero* net singularity at the crack tip yields the following equation:

$$\int_0^{L_s} b_y(y_o)\left[\frac{3a+2\,z_o}{X(z_o)(z_o+2a)}+\frac{3a+2\,\bar{z}_o}{X(\bar{z}_o)(\bar{z}_o+2a)}\right]dy_o + i\int_0^{L_g} b_x(y_o)\left[\frac{z_o+a}{X(z_o)\,(z_o+2a)}-\frac{\bar{z}+a}{X(\bar{z}_o)\,(\bar{z}_o+2a)}\right]dy_o=\frac{1}{4}. \tag{12}$$

Consider now the values of $b_x(y)$ and $b_y(y)$ as $y\to 0$. First, it can be shown (Dollar and Steif, 1989) that the finite stress at the crack tip is related to the dislocation intensity there by

$$(\sigma_{yy})_{\text{tip}}=\frac{E\,b_y(0)}{1-\nu^2}.$$

Next, using the equations of equilibrium, the isotropic linear elastic constitutive law, and symmetry, one can show that

$$\left.\frac{\partial b_y}{\partial y}\right|_{y=0}=0.$$

The symmetry about the x-axis dictates that $b_x(y)$ must be odd in y, though not necessarily zero at $y = 0$. Of course, this presumes that there is some opening near $y = 0$; if not, then $b_x(y)$ is identically zero.

We turn now to consider a criterion for determining whether an impinging matrix crack, which may have diverted to the interface, causes fiber failure. Since it does not seem fruitful to compare singular stresses (which are predicted when there is no debonding) with finite stresses (which are predicted after debonding), the following unified fiber failure criterion is adopted. Fiber failure ahead of the matrix crack occurs when the tensile stress there, *averaged over a distance equal to the fiber diameter*, is equal to the fiber strength. Since the square root singularity is integrable, this averaged stress is obviously finite even if no diversion has occurred. Note that the concept of a failure criterion that involves the stress over some finite distance ahead of a stress concentrator is not new, having been applied to the fracture of metals and composites.

3 Results and Discussion

Since the response of a crack impinging upon a debondable and slipping interface is rather complex, we first explain in some detail the results for the case of zero residual stress ($\sigma_o = 0$), with $\mu = 0.0$ and with $\mu = 0.3$. These results are illustrated in two separate figures (2 and 3), which differ only in the scale of the axes. In these plots are shown the slip length and the opening length as functions of a normalized stress Σ_∞, which is defined by

$$\Sigma_\infty=\frac{\sigma_\infty\sqrt{a}}{\sqrt{G_dE/(1-\nu^2)}}$$

where G_d, the energy necessary to extend the debond a unit distance, is considered to be a fixed material parameter, and E is Young's modulus. Since the debond is assumed to be constantly in equilibrium with the increasing applied load, G_d is related to the mode I and mode II branch crack-tip stress intensity factors according to the usual Irwin relation

$$G_d=\frac{K_I^2+K_{II}^2}{E/(1-\nu^2)}.$$

This criterion implies that the critical stress intensity factor is the same under pure model I or mode II conditions. Since this may not be true (see Cao and Evans (1989)), a modified criterion of the form

$$G_d=\frac{\beta K_I^2+K_{II}^2}{E/(1-\nu^2)}$$

will also be employed. The constant β is given by

$$\beta=\frac{G_{d_{II}}}{G_{d_I}}$$

where G_{d_I} is the critical energy release in pure mode I, and $G_{d_{II}}$ is the critical energy release in pure mode II. To avoid any confusion as to our procedure, we emphasize: although the results will be interpreted as if G_d were a material parameter, operationally, we have assumed values for L_s and σ_∞; the solution of the integral equations provides L_g, K_{I}, and K_{II}, and, hence, G_d.

For relatively short debonds, the extent of the opening zone is coincident with the extent of the slip zone ($L_g = L_s$); that is, the branch crack is fully open. This is indicated by the dotted curves in Figs. 2 and 3. (Unless explicitly noted, the results that are presented will be for $\beta = 1$.) The energy release rate

Downloaded 03 May 2010 to 171.66.16.247. Redistribution subject to ASME license or copyright; see http://www.asme.org/terms/Terms_Use.cfm

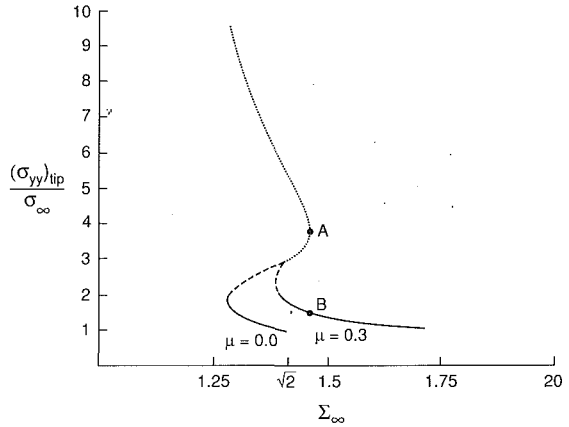


Fig. 4 Stress concentration at the crack tip as a function of applied stress Σ_∞. (..... ~ fully open debond; ····· ~ partially open debond;—fully closed debond.)

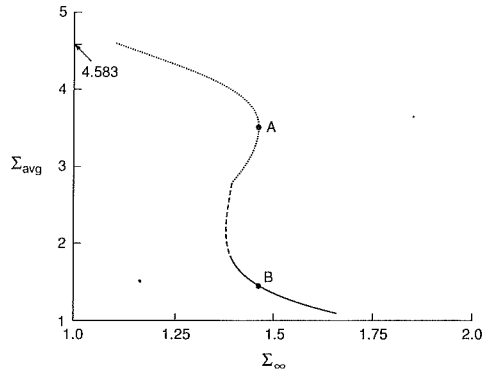


Fig. 5 Stress concentration averaged over a distance $d_f = 0.1a$ ahead of the crack tip. (..... ~ fully open debond; ---- ~ partially open debond; — fully closed debond.)

normalized by the applied stress decreases upon initial extension of the branch crack; this means that branch crack extension is initially stable as Σ_∞ to drive the crack must increase. After Σ_∞ reaches a critical value $(\Sigma_\infty)_o$, however, the load to continue branch crack extension decreases. This critical value depends on β: when $\beta = 1$, $(\Sigma_\infty)_c = 1.46$; when $\beta = 10$, $(\Sigma_\infty)_c = 1.40$. (There is an instability here which will be discussed further.) When the slip zone reaches a length $0.24a$, the mode I stress intensity factor K_I at the branch crack tip goes to zero. For slip zones longer than $0.24a$, a portion of the branch crack near the branch crack tip is *closed*, and, hence, the opening length is less than the slip length. In this regime Σ_∞, indicated by the dashed curves, first decreases and then increases, and the opening length decreases steadily to zero. Once the slip length is greater than some critical value ($0.71a$, when $\mu = 0.0$; $0.88a$ when $\mu = 0.3$), the branch crack is completely closed (solid curves).

There is a crucial difference, however, between the cases of $\mu = 0$ and $\mu > 0$. When there is zero frictional resistance at the interface, the mode II stress intensity factor at the branch crack tip reaches the asymptotic value $\sigma_\infty\sqrt{a/2}$ as $L_s/a \to \infty$. This was demonstrated using a simple energy argument (Dollar and Steif, 1991) and was found to be consistent with numerical calculations of the stress intensity factors. On the other hand, when there is frictional resistance as indicated above, the stress intensity factor normalized by the applied stress decreases continually as $L_s/a \to \infty$; hence, Σ_∞ increases continually.

Turning now to the instability mentioned above, we consider first the case of $\mu = 0.3$. Though solutions were arrived at by considering a monotonically increasing slip length, they are now *interpreted* as if Σ_∞ were increased monotonically (say G_d is held fixed and σ_∞ is increased). Initially, the branch crack is fully open ($L_s = L_g$). When Σ_∞ reaches the value 1.46 (for $\beta = 1$), the only solution for increasing Σ_∞ corresponds to a slip length of $1.88a$. We interpret these results to mean that the interface "unzips" suddenly to a length which is consistent with the applied load. Any further extension of the slip zone requires an increase in the load. When there is no frictional resistance ($\mu = 0$), however, there is *no solution at all* corresponding to $\Sigma_\infty > 1.46$. This implies that a frictionless interface completely unzips when the remote stress reaches the value $\Sigma_\infty = 1.46$. As will be seen subsequently, complete unzipping of the interface is also a feature of solutions when there is residual tension at the interface. Note that the complete unzipping observed here is perfectly analogous to the unstable growth of a Griffith crack under remote tension.

Consider now the stress at the main crack tip as a function of the remotely applied stress (Fig. 4). For $\Sigma_\infty < 1.1$, there is no branch crack; that is, the energy release associated with any branch crack (even one that is infinitesimally small compared with the main crack) is less than the critical energy release of the interface. In this case, the crack along $-2a < x < 0$ is the usual Griffith crack with the stress being square root singular as the tip is approached. As soon as there is any branch crack, the tensile stress at the crack tip is finite, as discussed in Section 2. In the small-scale branching limit of $a/L_z \to \infty$, one can see, by dimensional considerations, that the stress at the crack tip $(\sigma_{yy})_{tip}$ is proportional to $\sigma_\infty\sqrt{a/L_s}$. As the branch crack extends, the stress concentration drops steadily with Σ_∞. Accepting the argument given above regarding the sudden unzipping to a longer slip length, one would say that the stress concentration associated with the point A drops to that of point B, as the Σ_∞ passes the value 1.46 (for $\beta = 1$ and $\mu = 0.3$). For zero frictional resistance, the interface completely unzips.

Next, the unified fiber failure criterion is imposed on the results discussed so far; the outcome is depicted in Fig. 5. The average stress concentration, Σ_{avg}, which is the tensile stress σ_{yy} (normalized by σ_∞) averaged, in this instance, over a fiber diameter equal to one-tenth of the crack half-length, is plotted as a function of Σ_∞. Clearly, the average stress concentration is maximum when the singular solution prevails and decreases whenever there is debonding. From the Griffith crack solution, one finds this maximum average stress concentration $(\Sigma_{avg})_{max}$ to be

$$(\Sigma_{avg})_{max} = \sqrt{1 + \frac{2a}{d_f}}$$

where d_f is the fiber diameter. In the case of $\mu = 0.3$, and under a monotonically increasing load, the average stress concentration jumps from point A to point B. In the case of $\mu = 0.0$, the stress concentration goes from A directly to one, since complete unzipping of the interface occurs. It is interesting to note that the stress concentrating power of a matrix crack diminishes substantially by the time the remote stress is increased to a value that is, say, 50 percent above that required to cause first debonding. From a plot such as Fig. 5, one can estimate the value of the load at which the fiber would fail, given the necessary material parameters.

So far we have taken the residual stress at the interface to be zero; the effect of a nonzero residual normal stress σ_o at the interface is now considered. From the point of view of interpreting the results, it is convenient to introduce a dimensionless residual stress, Σ_o, which is defined by

$$\Sigma_o = \frac{\sigma_o\sqrt{a}}{\sqrt{G_d E/(1-\nu^2)}}.$$

Since shear resistance at the interface has two sources, bonding

Downloaded 03 May 2010 to 171.66.16.247. Redistribution subject to ASME license or copyright; see http://www.asme.org/terms/Terms_Use.cfm

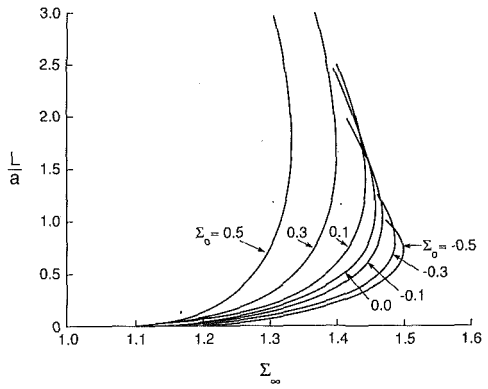


Fig. 6 Extent of debonding for various levels of residual stress Σ_o (fully open debond, $L_s = L_g$)

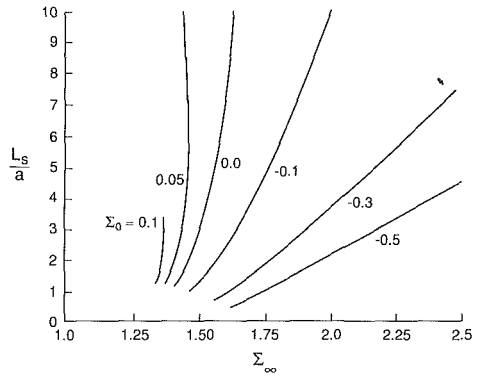


Fig. 7 Extent of debonding for various levels of residual stress Σ_o (fully closed debond, $L_g = 0$; $\mu = 0.3$)

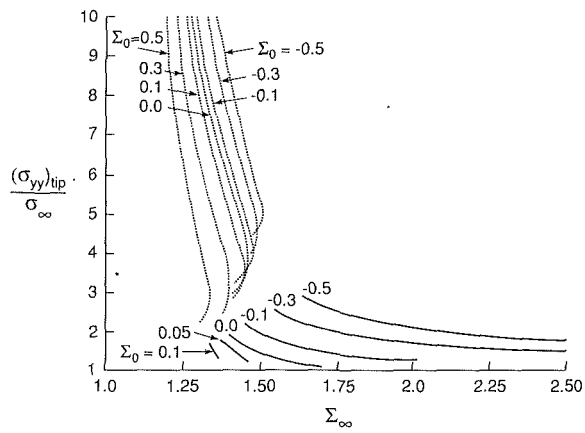


Fig. 8 Stress concentration at the crack tip for various levels of residual stress Σ_0. (..... ~ fully open debond; —— fully closed debond; $\mu = 0.3$.)

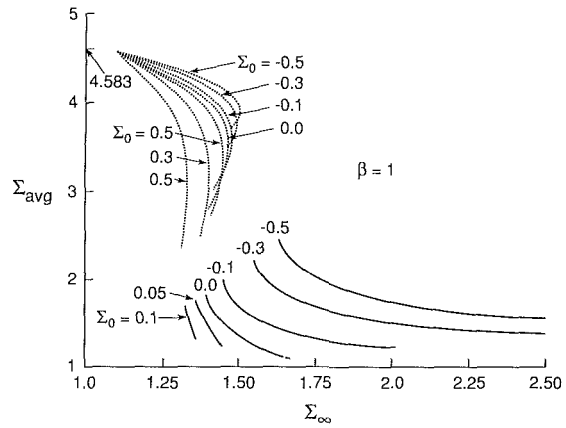


Fig. 9 Averaged stress concentration ahead of crack tip for various levels of residual stress Σ_0. (..... ~ fully open debond; —— fully closed debond.)

and friction, and since the degree of friction is at least partially tied to σ_o (μ also matters, obviously), the parameter Σ_o gives the relative contribution of these two sources of shear resistance. Just as with the results presented in Figs. 2 and 3, there are three regimes: (i) fully open debond, (ii) partially open debond, and (iii) fully closed debond. The extent of debonding as a function of Σ_∞ for various $\Sigma_o(\mu = 0.3)$ is shown in Fig. 6 for fully open debonds and in Fig. 7 for fully closed debonds.

Given a monotonically increasing remote stress, the results indicate that there is, again, a sudden unzipping of the interface from the fully open regime; the extent to which the interface unzips depends strongly on σ_o (and on the frictional resistance). When residual stress is strongly tensile there is complete unzipping of the interface; for small residual stresses (Σ_o near zero), the interface unzips directly to the fully closed regime; for strongly compressive residual stresses the interface unzips to the partially open regime. As expected, the trend, in general, is for residual compression to inhibit debonding and slippage, and for residual tension to promote them. Also, as seen in Fig. 6, the remote stress at which unzipping occurs is higher when $\sigma_o < 0$ than when $\sigma_o > 0$, assuming the energy of debonding is held fixed. The curve for $\Sigma_o = 0.10$ in Fig. 7 ends abruptly at the point at which *reopening* of the interface occurs; reopening typically occurs away from the main crack tip. Since complete unzipping of the interface would have already occurred, however, reopening was not explored in any detail.

In Fig. 8 we plot the normalized stress at the tip versus Σ_∞ for a range of values of Σ_o. The dotted lines correspond to complete opening of the interface; solid lines correspond to complete closing of the interface. In the course of a monotonically increasing applied loading, the crack-tip stress concentration decreases from the infinite value associated with no debond. When the interface unzips, the stress concentration drops suddenly and thereafter continues to decrease for $\Sigma_o < 0$; for $\Sigma_o > 0$, there eventually is no solution, as discussed above. Though results for partially open debonds can be obtained for $\Sigma_o = 0$ (they were exhibited above), they are extremely inconvenient to obtain when $\Sigma_o \neq 0$. Because these results were not obtained, there are gaps in the curves shown in Fig. 8. For a monotonically increasing Σ_∞, this gap is only significant in instances of high residual compressive stresses ($\Sigma_o = 0.3$ and 0.5 in Fig. 8). where the unzipping would *not* bypass the regime of partial opening. Given the results presented in Fig. 4, however, one can reasonably surmise that the missing portions appear somewhat like the dashed portions in Fig. 4.

To this set of results we applied the unified fiber failure criterion to obtain the plot in Fig. 9. Under a monotonically increasing Σ_∞, there is first the perfectly bonded regime in which the stress average stress concentration Σ_{avg} is maximum (equal to 4.583 in this case of the fiber diameter being 1/20 of the crack length). When Σ_∞ reaches a value which is independent of the residual stress, debonding of the interface beings, and the average stress concentration begins to drop off. (Debond initiation is independent of Σ_o because the stress intensity factor due to σ_o is proportional to $\sqrt{L_s}$; that due to σ_∞ is proportional to $\sqrt{a}$.) As the debond extends, the average stress concentration continues to diminish up to the unzipping point; at that point the stress concentration drops suddenly either to one (when there is sufficient residual tension) or to a nonzero value which depends on the residual stress and on the friction coefficient. Though computations were only carried out for one friction coefficient ($\mu = 0.3$), the results of Dollar and Steif (1989) which neglect the debonding energy and consider only friction at the interface suggest a substantial dependence on μ.

Downloaded 03 May 2010 to 171.66.16.247. Redistribution subject to ASME license or copyright; see http://www.asme.org/terms/Terms_Use.cfm

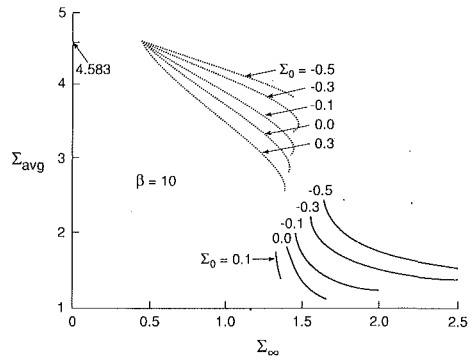


Fig. 10 Average stress concentration ahead of crack tip for unequal mode I and mode II debond emergies, $\beta = 10$. (.....~ fully open debond; —— fully closed debond.)

In order to see the dependence on the parameter β, which captures the tendency for debonding to occur more easily in mode I than in mode II, the calculations were repeated for $\beta = 10$. The results for the average stress concentration in the fiber are shown in Fig. 10. As can be seen, initial debonding can occur at lower remote loads than when $\beta = 1$ due to the substantial mode I contribution when the debond is short. Recall, though, that the mode I contribution diminishes rapidly as the debond extends (and eventually goes to zero at $L_s = 0.24a$). Hence, the level of the applied stress at which the interface unzips (and the solution jumps to the fully closed regime) is not strongly affected by β; the fully closed regime is completely independent of β, since K_I is precisely zero.

4 Conclusions

The fibers in a brittle-matrix composite can be sensitive to the presence of matrix cracks, with the degree of sensitivity most dependent on the properties of the fiber-matrix interface. Accordingly, a model problem has been studied which reveals, at least qualitatively, the influence of interface debonding and friction on the stress fields of impinging matrix cracks. In particular, we find that the stress concentrating effect of a matrix crack is quite sensitive to the energy to debond the interface, and to the residual stress at the interface. The results clearly point out that a fiber is more likely to fail at a given load when the energy to debond the interface is high, assuming all other parameters are held fixed. This is in agreement with widespread intuition regarding the effect of the interface. Also of possible interest is the fact that a compressive stress at the interface—and some interfacial friction—can maintain the stress concentration at a reasonable level even if substantial debonding occurs.

The results here are most helpful in assessing the *relative* effect of changing the debonding energy and the residual stress. Absolute values for the average stress concentration in the fiber should be viewed with skepticism, as some important effects have been left out, in particular, the bridging effect of fibers which may be spanning the matrix crack. (Recall that the results presented in Figs. 5, 9, and 10 were based on a fiber diameter which is 1/20 of the crack length.) Furthermore, the fiber failure criterion is still quite tentative. Should this criterion turn out to be reasonable, however, its application to real composites would be quite simple. One needs only the fiber strength and diameter, which are readily found and rather reliable. By contrast, the relative toughness approach requires the fiber fracture energy, which is difficult to measure, and still more difficult to believe. Of course, either approach requires the interface energy, which is also challenging to measure. In any event, future efforts in this area should attempt to relate composite properties to microstructural parameters which are reliably measured.

Acknowledgments

A. D. is grateful for the support provided by the National Science Foundation under grant MSM-8451080, and P.S.S. is grateful for the support provided by the Air Force Office of Scientific Research under grant AFOSR 890548. Additional funding was provided by the General Electric Engine Business Group, and by the Department of Mechanical Engineering, Carnegie Mellon University.

References

Benveniste, Y., Dvorak, G. J., Zarzour, J., and Wang, E. C. J., 1989, "On Interacting Cracks and Complex Crack Configurations in Linear Elastic Media," *Internationc! Journal of Solids and Structures*, Vol. 25, pp. 1279-1293.

Cao, H. C., and Evans, A. G., 1989, "An Experimental Study of the Fracture Resistancer of Bimaterial Interfaces," *Mechanics of Materials*, Vol. 7, pp. 295-304.

Cook, T. S., and Erdogan, F., 1972, "Stresses in Bonded Materials With a Crack Perpendicular to the Interface," *International Journal of Engineering Sciences*, Vol. 10, pp. 677-697.

Dollar, A., and Steif, P. S., 1989, "A Tension Crack Impinging Upon Frictional Interfaces," ASME JOURNAL OF APPLIED MECHANICS, Vol. 56, pp. 291-298.

Dollar, A., and Steif, P. S., 1991, "The Branched Problem Revisited," ASME JOURNAL OF APPLIED MECHANICS, Vol. 58, pp. 584-586.

Dundurs, J., and Comninou, M., 1979, "Some Consequences of the Inequality Conditions in Contact and Crack Problems," *Journal of Elasticity*, Vol. 9, pp. 71-82.

Erdogan, F., and Biricikoglu, V., 1973, "Two Bonded Half Planes with an Crack Going Through the Interface," *International Journal of Engineering Sciences*, Vol. 11, pp. 745-766.

Goree, J. G., and Venezia, W. A., 1977, "Bonded Elastic Half-Planes with an Interface Crack and a Perpendicular Intersection Crack that Extends into the Adjacent Material," *International Journal of Engineering Sciences*, Vol. 15, Part I, pp. 1-17; Part II, pp. 19-27.

He, M.-Y., and Hutchinson, J. W., 1989, "Crack Deflection at an Interface Between Dissimilar Elastic Materials," *International Journal of Solids and Structures*, Vol. 25, pp. 1053-1067.

Kitagawa, H., and Yuuki, R., 1977, "Analysis of Branched Cracks Under Biaxial Stresses," *Fracture 1977*, Vol. 3, D. M. R. Taplin, ed., University of Waterloo, Waterloo, Canada, pp. 201-211.

Lo, K. K., 1978, "Analysis of Branched Cracks," ASME JOURNAL OF APPLIED MECHANICS, Vol. 45, pp. 797-802.

Lu, M.-C., and Erdogan, F., 1983, "Stress Intensity Factors in Two Bonded Elastic Layers Containing Cracks Perpendicular to and on the Interface," *Engineering Fracture Mechanics*, Vol. 18, Part I, pp. 491-506; Part II, pp. 507-528.

Muskhelishvili, N. E., 1963, *Some Basic Problems of the Mathematical Theory of Elastcity*, Noordhoff, Amsterdam.

Schwietert, H. R., and Steif, P. S., 1991, "An Interface Integral Equation Method Applied to a Crack Impinging Upon a Bimaterial, Frictional Interface," *Int. J. Fracture*, Vol. 49, pp. 257-272.

Vitek, V., 1977, "Plane Strain Stress-Intensity Factors for Branched Cracks," *International Journal of Fracture*, Vol. 13, pp. 481-501.

Wang, Y. C., Hui, C. Y., and Lagoudas, D., 1991, "Small-Scale Crack Blunting at a Bimaterial Interface With Coulomb Friction," *International Journal of Fracture*, Vol. 52, pp. 293-306.

APPENDIX

In this Appendix we give expressions for the terms in the dimensionless version of Eqs. (11). Stresses have been nondimensionalized by σ_∞, spatial variables (and a) by L_s, and the dislocation intensity $b(y_o)$ by $\sigma_\infty \pi(\kappa+1)/(2G)$.

$$A(y_o,y) = \frac{-2}{y+y_o} + \mathrm{Im}\left[\frac{\bar{h}_3}{h_3^2} + \frac{\bar{h}_4}{h_4^2} + \frac{1}{\bar{h}_3} + \frac{1}{\bar{h}_4}\right] - 2y\mathrm{Re}[G_1'(y_o,y)]$$

$$B(y_o,y) = \mathrm{Re}\left[\frac{2}{h_3} - \frac{2}{h_4} + \frac{\bar{h}_3}{h_3^2} - \frac{\bar{h}_4}{h_4^2} + \frac{1}{\bar{h}_4} - \frac{1}{\bar{h}_3}\right] + 2y\mathrm{Im}[G_2'(y_o,y)]$$

$$C(y_o,y) = -\mathrm{Re}\left[\frac{\bar{h}_3}{h_3^2} + \frac{\bar{h}_4}{h_4^2} + \frac{1}{\bar{h}_3} + \frac{1}{\bar{h}_4}\right] + 2\mathrm{Re}[G_1(y_o,y)] - 2y\mathrm{Im}[G_1'(y_o,y)]$$

Downloaded 03 May 2010 to 171.66.16.247. Redistribution subject to ASME license or copyright; see http://www.asme.org/terms/Terms_Use.cfm

$$D(y_o,y) = -\frac{2}{y+y_o}\,\mathrm{Im}\left[\frac{2}{h_3}-\frac{2}{h_4}+\frac{\bar{h}_3}{h_3^2}-\frac{\bar{h}_4}{h_4^2}+\frac{1}{\bar{h}_4}-\frac{1}{\bar{h}_3}\right] - 2\mathrm{Im}[G_2(y_o,y)] - 2y\mathrm{Re}[G_2'(y_o,y)]$$

$$E(y_o,y) = A(y_o,y) - \mu\, C(y_o,y)$$

$$F(y_o,y) = B(y_o,y) - \mu D(y_o,y)$$

$$h_3 = z + z_o + 2a$$

$$h_4 = z + \bar{z}_o + 2a$$

$$G_1(y_o,y) = g_1(z,z_o) - g_1(z,-z_o-2a) + g_1(z,\bar{z}_o) - g_1(z,-\bar{z}_o-2a)$$

$$G_2(y_o,y) = g_2(z,z_o) - g_2(z,-z_o-2a) - g_2(z,\bar{z}_o) + g_2(z,-\bar{z}_o-2a)$$

$$G_1'(y_o,y) = \frac{\partial G_1(y_o,y)}{\partial y}$$

$$G_2'(y_o,y) = \frac{\partial G_2(y_o,y)}{\partial y}$$

$$g_1(z,z_o) = \frac{1}{z-z_o}\left\{\left[1-\frac{X(z_o)}{X(z)}\right]\left[\frac{z_o-\bar{z}_o}{2(z-z_o)}-1\right] + \frac{(\bar{z}_o-z_o)(z_o+a)}{2X(z_o)X(z)}\right\}$$

$$g_2(z,z_o) = g_1(z,z_o) + \frac{1}{z-z_o}\left[1-\frac{X(z_o)}{X(z)}\right]$$

$$f_1(y) = \frac{-a^2}{2}\,\mathrm{Im}\left[\frac{\bar{z}-z}{[X(z)]^3}\right]$$

$$f_2(y) = -1 + \mathrm{Re}\left[\frac{z+a}{X(z)}\right] + \frac{a^2}{2}\,\mathrm{Re}\left[\frac{\bar{z}-z}{[X(z)]^3}\right] - \frac{\sigma_o}{\sigma_\infty}$$

$$f_3(y) = f_1(y) - \mu f_2(y)$$

Downloaded 03 May 2010 to 171.66.16.247. Redistribution subject to ASME license or copyright; see http://www.asme.org/terms/Terms_Use.cfm

Transient Analysis of a Semi-infinite Crack Subjected to Dynamic Concentrated Forces

Chwan-Huei Tsai[1]
Graduate Student.

Chien-Ching Ma[2]
Professor.

Department of Mechanical Engineering,
National Taiwan University,
Taipei, Taiwan, 10764,
Republic of China

An exact transient closed-form solution for a semi-infinite crack subjected to a time-dependent concentrated force is obtained in this study. The total wave field is due to the effect of this point source and the scattering of the incident waves by the crack tip. An alternative methodology for constructing the reflected and diffracted field is proposed, which proves both powerful and efficient in solving complicated dynamic crack problems. An exponentially distributed loading at the crack surfaces in the Laplace transform domain is used as the fundamental problem. The waves reflected by the traction-free crack surface and diffracted from the crack tip can be constructed by superimposing this fundamental solution. The superposition is performed in the Laplace transform domain. Numerical results for the time history of stresses and stress intensity factors during the transient process are obtained and compared with the corresponding static values. It is shown that the field solution will approach the static value after the last diffracted wave has passed.

1 Introduction

The interaction of a stress wave with a crack in an unbounded medium is a complicated problem. The incident wave will be reflected by the crack surface and diffracted from the crack tip. The analytical study of this problem is restricted to relatively simple cases. The investigation of transient elastodynamic crack problem was studied by de Hoop (1958) who analyzed the response of applying uniform normal pressure on the surfaces of a semi-infinite crack. Handelman and Rubenfeld (1969) investigated the reflection and diffraction of a horizontally polarized plane shear wave by a semi-infinite crack. Thau and Lu (1971) studied the diffraction of an incident longitudinal plane wave disturbed by a crack of finite length. They did not solve this problem completely. They used a solution to a semi-infinite crack to track the waves from one crack tip to the other, and stopped after one interaction. These problems were solved using the method of integral transforms together with the application of Wiener-Hopf technique (Noble, 1958) and Cagniard-de Hoop method (de Hoop, 1958) of Laplace inversion. Because there is no characteristic length involved, the integral transform can be applied directly and the standard Wiener-Hopf equation can be obtained. In a series of papers, Freund (1972a, 1972b, 1973, 1974a) developed important analytical methods for evaluating the transient field of a propagating crack. In Freund's papers, a fundamental solution is obtained and is used to develop by superposition the solution for the negation of the stress distribution on the prospective fracture plane. A generalization of this idea also led to solutions to problems in crack kinking under dynamic loading analyzed by Ma and Burgers (1987, 1988) and Ma (1988, 1990).

The problem of applied dynamic point loading on the crack surfaces was solved by Freund (1974b). Since this problem possesses a characteristic length, the distance from loading to crack tip, the Wiener-Hopf technique cannot be applied directly. Freund proposed a fundamental solution arising from a climbing edge dislocation with a constant speed. The transient response can be constructed by taking an integration over a climbing dislocation of different velocity. This methodology was also used by Brock (1982, 1984, 1985b, 1986, 1989), Brock et al. (1985a), Brock and Jolles (1987), and Ma and Hou (1991a, 1991b) to analyze other problems. Lee and Freund (1990) also applied this method to analyze fracture initiation of an edge crack due to impact loading.

In this paper, the two-dimensional problem of concentrated in-plane body force imposed suddenly near a semi-infinite crack is investigated. Brock (1985b) solved similar problems by superimposing Freund's solution (1974b) and obtained dynamic stress intensity factors only. But Brock's solution seems to be difficult in further application, since the multiple integrations are involved in his formulations. A similar but simpler problem was studied by Harris (1980), who solved the problem of diffraction by a stationary semi-infinite crack of a cylindrical longitudinal wave. In this study, we obtained not only the dynamic stress intensity factor but also the transient response of stresses. This problem can be treated as the superposition of two problems. The first problem is the disturbance by a concentrated force in the crack-free, unbounded medium. The second problem considers the crack surfaces subjected to the

[1]Currently at the Huafan Institute of Technology.
[2]To whom all correspondence should be addressed.

Contributed by the Applied Mechanics Division of THE AMERICAN SOCIETY OF MECHANICAL ENGINEERS for publication in the ASME JOURNAL OF APPLIED MECHANICS.

Discussion on this paper should be addressed to the Technical Editor, Prof. Leon M. Keer, The Technological Institute, Northwestern University, Evanston, IL 60208, and will be accepted until four months after final publication of the paper itself in the JOURNAL OF APPLIED MECHANICS.

Manuscript received by the ASME Applied Mechanics Division, Dec. 18, 1990; final revision, July 16, 1991. Associate Technical Editor: S. K. Datta.

Copyright © 1992 by ASME
Downloaded 03 May 2010 to 171.66.16.247. Redistribution subject to ASME license or copyright; see http://www.asme.org/terms/Terms_Use.cfm

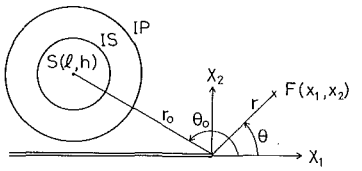


Fig. 1 Configuration and coordinate systems of a semi-infinite crack in an infinite medium

negatives of the tractions induced by the first problem. To solve this problem we propose an alternative fundamental solution of an applied exponentially distributed traction on crack surfaces in the Laplace transform domain. This methodology was first addressed by Tsai and Ma (1991) in solving the problem of an applied buried point loading in a half space. From the physical considerations, the reflected fields are generated in order to eliminate the stress induced by incident waves on the traction-free boundary. In a great number of dynamic problems, the incident waves can be represented by multiple Laplace transforms, so that the stress field in the Laplace transform domain (with respect to time) can be represented in a integral form for Laplace inversion (with respect to geometric coordinate) of which the kernel is usually an exponential function. Hence, if the responses to an applied exponentially distributed traction in Laplace transform domain can be obtained preliminarily, then the reflected and diffracted field can be constructed by the superposition method.

The analysis of the transient effect on the crack subjected to dynamic point loading is also investigated by numerical calculations using the available results. The characteristic time after which the transient effect can be neglected is investigated in detail. It is found in this study that the full-field solutions will approach the static value after the last diffracted wave has passed.

2 Required Fundamental Solutions

In this paper, an alternative fundamental solution is proposed and the superposition is made in the Laplace transform domain. The advantage is that the fundamental solution is easy to obtain and the solution is easy to construct. The wave motion generated by the diffraction of incident waves consists of the superposition of incident waves and the solutions of two fundamental problems, which are symmetric and antisymmetric with respect to the plane $x_2 = 0$.

Consider a stationary semi-infinite crack in an unbounded medium initially at rest. At time $t = 0$, an exponentially distributed traction is applied on the crack faces. The traction force can be divided into normal force (mode I) and tangential force (mode II). The geometry and coordinate system is shown in Fig. 1. Since it is a symmetrical problem with repect to the x_1-axis, it can be viewed as a half-plane problem with the material occupying the region $x_2 \geq 0$.

2.1 Fundamental Solution of Mode I. Consider the upper and lower crack faces to which are applied opposite normal traction with the following form:

$$\sigma_{22}(x_1,0,t) = \frac{1}{2\pi i}\int_{-\infty}^{\infty} \exp((p_1\eta_1 - p_2\eta_2)x_1 + p_1 t)\exp(i(p_2\eta_1 + p_1\eta_2)x_1 + p_2 t)dp_2 \quad \text{for} \quad -\infty < x_1 < 0. \tag{1}$$

Letting $p' = p_1 + ip_2$ and $\eta = \eta_1 + i\eta_2$, the special distribution of stress on the crack faces represented in Eq. (1) becomes

$$\sigma_{22}(x_1,0,t) = \frac{1}{2\pi i}\int_{p_1 - i\infty}^{p_1 + i\infty} e^{p'\eta x_1 + p't}dp' \text{ for } \quad -\infty < x_1 < 0, \tag{2}$$

with the other two boundary conditions

$$\sigma_{12}(x_1,0,t) = 0 \quad \text{for} \quad -\infty < x_1 < \infty, \tag{3}$$

$$u_2(x_1,0,t) \quad \text{for} \quad 0 < x_1 < \infty. \tag{4}$$

Applying of the Laplace transform over time t by parameter p to the boundary conditions (2)–(4) yields

$$\bar{\sigma}_{22}(x_1,0,p) = e^{p\eta x_1} \quad \text{for} \quad -\infty < x_1 < 0, \tag{5}$$

$$\bar{\sigma}_{12}(x_1,0,p) = 0 \quad \text{for} \quad -\infty < x_1 < \infty, \tag{6}$$

$$\bar{u}_2(x_1,0,p) = 0 \quad \text{for} \quad 0 < x_1 < \infty. \tag{7}$$

Equation (5) indicates the exponentially distributed loading in the Laplace transform domain. Applying the two-sided Laplace transform with respect to x_1 under the restriction of $\mathrm{Re}(\eta) > \mathrm{Re}(\lambda)$ and using the Wiener-Hopf technique, the final result of stress σ_{22} in the Laplace transform domain is

$$\bar{\sigma}_{22}(x_1,x_2,p) = \frac{1}{2\pi i}\int [B_1(\eta,\lambda)e^{-p\alpha x_2 + p\lambda x_1} + B_2(\eta,\lambda)e^{-p\beta x_2 + p\lambda x_1}]d\lambda, \tag{8}$$

where

$$B_1(\eta,\lambda) = \frac{(b^2 - 2\lambda^2)^2(a+\eta)^{1/2}}{2(b^2 - a^2)(a+\lambda)^{1/2}(\eta - \lambda)(c - \lambda)(c + \eta)S_-(\lambda)S_+(\eta)},$$

$$B_2(\eta,\lambda) = \frac{2\beta\lambda^2(a-\lambda)^{1/2}(a+\eta)^{1/2}}{(b^2 - a^2)(\eta - \lambda)(c - \lambda)(c + \eta)S_-(\lambda)S_+(\eta)}, \tag{9}$$

$$\alpha = (a^2 - \lambda^2)^{1/2},\ \beta = (b^2 - \lambda^2)^{1/2},$$

$$S_\pm(\lambda) = \exp\left(-\frac{1}{\pi}\int_a^b \tan^{-1}\left[\frac{4\xi^2(\xi^2 - a^2)^{1/2}(b^2 - \xi^2)^{1/2}}{(b^2 - 2\xi^2)^2}\right]\frac{d\xi}{\xi \pm \lambda}\right). \tag{10}$$

$a = \sqrt{\rho/(\gamma + 2\mu)}$, $b = \sqrt{\rho/\mu}$, a, b and c are the slownesses of the longitudinal wave, shear wave and Rayleigh wave, μ and ρ are the shear modulus and mass density, respectively, and γ is the Lame elastic constant. To ensure $\mathrm{Re}(\alpha)$ (or β) ≥ 0 everywhere in the λ-plane, branch cuts are introduced from a (or b) to ∞, and from $-a$(or $-b$) to $-\infty$. The stress intensity factor of this problem in the Laplace transform domain can be expressed as

$$\bar{K}_I(p) = \lim_{x_1 \to 0^+} \sqrt{2\pi x_1}\,\bar{\sigma}_{22}(x_1,0,p) = -\sqrt{\frac{2}{p}}\,K_I^F(\eta), \tag{11}$$

where

$$K_I^F(\eta) = \frac{(a+\eta)^{1/2}}{(c+\eta)S_+(\eta)}. \tag{12}$$

2.2 Fundamental Solution of Mode II. Consider the same stationary semi-infinite crack as shown in Fig. 1. The tangential traction is applied on the upper and lower crack surfaces. The boundary conditions in the Laplace transform domain have the following forms:

$$\bar{\sigma}_{22}(x_1,0,p) = 0 \quad \text{for} \quad -\infty < x_1 < \infty, \tag{13}$$

$$\bar{\sigma}_{12}(x_1,0,p) = e^{p\eta x_1} \quad \text{for} \quad -\infty < x_1 < 0, \tag{14}$$

$$\bar{u}_1(x_1,0,p) = 0 \quad \text{for} \quad 0 < x_1 < \infty. \tag{15}$$

The stress field $\bar{\sigma}_{22}$ and stress intensity factor $\bar{K}_{II}$ expressed in the Laplace transform domain are

$$\bar{\sigma}_{22}(x_1,x_2,p) = \frac{1}{2\pi i}\int [B_3(\eta,\lambda)e^{-p\alpha x_2 + p\lambda x_1} + B_4(\eta,\lambda)e^{-p\beta x_2 + p\lambda x_1}]d\lambda, \tag{16}$$

Downloaded 03 May 2010 to 171.66.16.247. Redistribution subject to ASME license or copyright; see http://www.asme.org/terms/Terms_Use.cfm

$$\bar{K}_{II}(p) = -\sqrt{\frac{2}{p}}\, K^F_{II}(\eta), \tag{17}$$

where

$$B_3(\eta,\lambda) = \frac{-\lambda(b-\lambda)^{1/2}(b^2-2\lambda^2)(b+\eta)^{1/2}}{(b^2-a^2)(\eta-\lambda)(c-\lambda)(c+\eta)S_-(\lambda)S_+(\eta)}, B_4 = -B_3, \tag{18}$$

$$K^F_{II}(\eta) = \frac{(b+\eta)^{1/2}}{(c+\eta)S_+(\eta)}. \tag{19}$$

3 Green Functions of Semi-infinite Crack

In this paper, a semi-infinite crack subjected to a singular source of concentrated dynamic force is considered. The applied concentrated loading can be divided into the components which are perpendicular and parallel to the crack faces. The solution for an arbitrary applied loading direction can be constructed from the combination of the solutions for these two directions. Given that the problem considered in this study has two characteristic lengths, a direct attempt to solve this problem by transform and Wiener-Hopf techniques is apparently not applicable. The transient elastodynamic crack problem is solved by the superposition method in the Laplace transform domain. The exact expressions for the full-field solutions and mixed-mode stress intensity factors are obtained in this study. The solutions are composed of incident field, reflected field, and diffracted field denoted by superscripts of *I*, *R*, and *D*, respectively. The incident fields are the responses to loading applied to an unbounded medium. The reflected and diffracted waves are generated by applying opposite traction at the crack surface to eliminate the stress induced by incident wave.

3.1 Vertical Concentrated Force. We have a stationary semi-infinite crack extending over $-\infty < x_1 \le 0$. Initially, the body is stress-free and at rest. At time $t=0$, a vertical concentrated force is produced at position (l,h). The two-dimensional geometry of the problem is shown in Fig. 1. The time dependence of the loading is represented by the Heaviside step function $H(t)$. As shown in Achenbach (1973), the incident fields at $x_2 = 0$ expressed in the Laplace transform domain are

$$\bar{\sigma}^I_{22} = \frac{1}{2\pi i}\int [A_{11}(\lambda)e^{-p\alpha h + p\lambda(x_1-l)} + A_{12}(\lambda)e^{-p\beta h + p\lambda(x_1-l)}]d\lambda, \tag{20}$$

$$\bar{\sigma}^I_{12} = \frac{1}{2\pi i}\int [A_{13}(\lambda)e^{-p\alpha h + p\lambda(x_1-l)} + A_{14}(\lambda)e^{-p\beta h + p\lambda(x_1-l)}]d\lambda, \tag{21}$$

where

$$A_{11}(\lambda) = \frac{b^2-2\lambda^2}{2b^2},\ A_{12}(\lambda) = \frac{\lambda^2}{b^2},$$
$$A_{13}(\lambda) = \frac{\alpha\lambda}{b^2},\ A_{14}(\lambda) = \frac{-\lambda(b^2-2\lambda^2)}{2b^2\beta}. \tag{22}$$

The applied tractions on the crack face, in order to eliminate the incident wave as indicated in (20) and (21), have the functional form $e^{p\lambda x_1}$. The fundamental solutions for normal traction $e^{p\eta x_1}$ and tangential traction $e^{p\eta x_1}$ applied at crack faces have been solved in Section 2. The reflected and diffracted fields can be obtained by superimposing the incident wave tractions that are equal and opposite to (20) and (21). The result of the normal stress is

$$\bar{\sigma}_{22}(x_1,x_2,p) = \frac{1}{4\pi^2}\int_{\Gamma^\eta}\int_{\Gamma^\lambda} [(A_{11}(\eta)B_1(\eta,\lambda) + A_{13}(\eta)B_3(\eta,\lambda))e^{-p(\alpha^* h + \eta l)}e^{-p(\alpha x_2 - \lambda x_1)}d\lambda + (A_{11}(\eta)B_2(\eta,\lambda) + A_{13}(\eta)B_4(\eta,\lambda))e^{-p(\alpha^* h + \eta l)}e^{-p(\beta x_2 - \lambda x_1)}d\lambda + (A_{12}(\eta)B_1(\eta,\lambda) + A_{14}(\eta)B_3(\eta,\lambda))e^{-p(\beta^* h + \eta l)}e^{-p(\alpha x_2 - \lambda x_1)}d\lambda + (A_{12}(\eta)B_2(\eta,\lambda) + A_{14}(\eta)B_4(\eta,\lambda))e^{-p(\beta^* h + \eta l)}e^{-p(\beta x_2 - \lambda x_1)}d\lambda]d\eta, \tag{23}$$

where $\alpha^* = (a^2-\eta^2)^{1/2}$, $\beta^* = (b^2-\eta^2)^{1/2}$. Equation (23) constitutes a double inversion integral where the paths Γ^λ and Γ^η refer to Laplace inversion contours in the λ-plane and the η-plane, respectively. Here we shall carry out the inverse transformation using an extension of the Cagniard-de Hoop technique. In the usual case this technique enables two successive inversions to be performed in one step. In this particular problem we use the technique proposed by Harris (1980) to perform the three successive inversions. Let us start by inverting the first term of (23). We introduce Cagniard contours in both the η and λ-plane by setting

$$\tau = \eta l + \alpha^* h, \tag{24}$$

$$t = -\lambda x_1 + \alpha x_2. \tag{25}$$

Equations (24) and (25) can be solved for η and λ to yield

$$\eta^\pm(\tau) = \frac{\tau}{r_0}\cos\theta_0 \pm i\sqrt{\frac{\tau^2}{r_0^2} - a^2}\,\sin\theta_0, \tag{26}$$

$$\lambda^\pm(t) = -\frac{t}{r}\cos\theta \pm i\sqrt{\frac{t^2}{r^2} - a^2}\,\sin\theta, \tag{27}$$

where (r_0, θ_0) and (r, θ) are the polar coordinates of the source point and field point, respectively, and

$$r_0 = \sqrt{h^2+l^2},\ \cos\theta_0 = \frac{l}{r_0},\ \sin\theta_0 = \frac{h}{r_0}, \tag{28}$$

$$r = \sqrt{x_1^2+x_2^2},\ \cos\theta = \frac{x_1}{r},\ \sin\theta = \frac{x_2}{r}. \tag{29}$$

In the η-plane (or λ-plane), (26) (or (27)) describes a hyperbola which is denoted as the Cagniard contour. We shift the η and λ-integrations onto Cagniard contours along which τ and t are both real and positive. In this technique, the two Cagniard contours must be superimposed in order to determine how and when they overlap for different locations of source and field points. Depending on this, the reflected and diffracted waves can be constructed automatically. Because $B_i(\eta,\lambda)$ possesses a pole at $\eta = \lambda$, the contribution of the pole at $\eta = \lambda$ and $\lambda = \eta$ has to be taken into account in the change of integral paths from η to τ and λ to t. Consider the deformed integral contour shown in Fig. 2(*a*). The requirement of $\mathrm{Re}(\eta) > \mathrm{Re}(\lambda)$ dictates that the integral path Γ^η is always located at the right-hand side of Γ^λ. Recall from (23) that a pole term arises, representing the reflected waves. A source point denoted by $S_2(\theta_0 = 150$ deg) and two field points denoted by $F_1(\theta = 45$ deg) and $F_2(\theta = 15$ deg) are chosen to explain the generation of a reflected wave. At the field point F_1, where the integral path changes from η to τ, the pole at $\eta = \lambda$ will be embraced. The contribution of this pole represents the reflected RPP wave generated from the crack-free surface. But no pole should be taken into account for the field point F_2, meaning that the reflected RPP wave will not pass through F_2. It is concluded that the reflected RPP waves will pass the region for $\theta > \theta_2$, where $\theta_2 = \cos^{-1}((x_1-l)/r_2)$, $r_2^2 = (x_1-l)^2 + (x_2+h)^2$. The con-

Downloaded 03 May 2010 to 171.66.16.247. Redistribution subject to ASME license or copyright; see http://www.asme.org/terms/Terms_Use.cfm

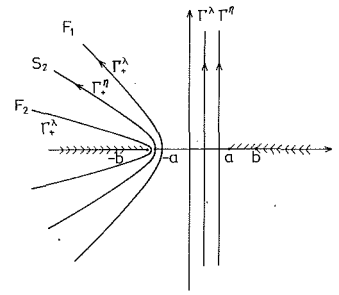


Fig. 2(*a*) Deformed integral contour for the first term of Eq. (23)

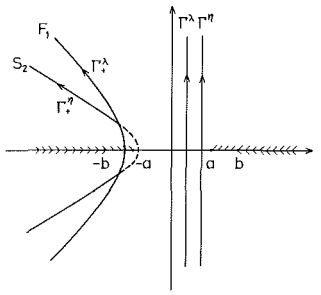


Fig. 2(*b*) Deformed integral contour for the second term of Eq. (23)

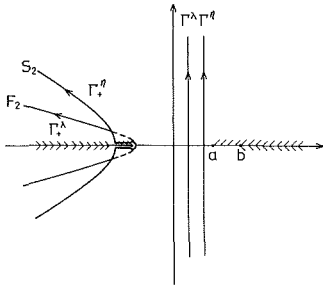


Fig. 2(*c*) Deformed integral contour for the third term of Eq. (23)

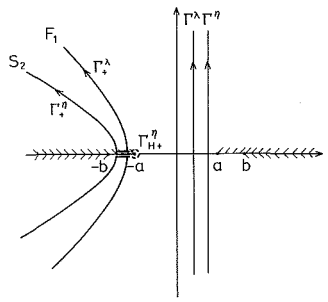


Fig. 2(*d*) Deformed integral contour for the fourth term of Eq. (23)

tribution of the pole in (23) can be obtained by the Cauchy theorem as follows:

$$\bar{\sigma}_{22}^{R}(x_1,x_2,p) = -\frac{1}{2\pi i}\int\left[\frac{(b^2-2\lambda^2)^3-4\alpha\beta\lambda^2(b^2-2\lambda^2)}{2b^2R}e^{-p\alpha(x_2+h)+p\lambda(x_1-l)} + \frac{4\alpha\beta\lambda^2(b^2-2\lambda^2)}{b^2R}e^{-p\beta x_2-p\alpha h+p\lambda(x_1-l)} + \frac{2\lambda^2(b^2-2\lambda^2)^2}{b^2R}e^{-p\alpha x_2-p\beta h+p\lambda(x_1-l)}\right]$$

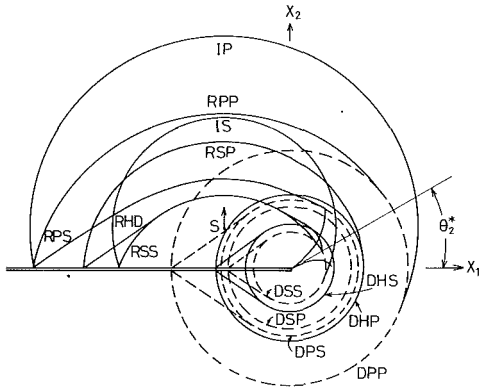


Fig. 3 Wave fronts of the incident, reflected, and diffracted waves with loading applied at $\theta_0 = 150$ deg

$$+\frac{4\alpha\beta\lambda^4-\lambda^2(b^2-2\lambda^2)^2}{b^2R}e^{-p\beta(x_2+h)+p\lambda(x_1-l)}\Bigg]d\lambda, \tag{30}$$

where $R(\lambda)$ is the Rayleigh wave function defined by

$$R(\lambda)=(b^2-2\lambda^2)^2+4\alpha\beta\lambda^2.$$

The superscript R indicates that the reflected field is being considered. The first term of (30) represents the reflected RPP wave—the reflected primary wave from the incident primary wave. The other three terms in (30) are RPS, RSP, and RSS reflected waves, respectively. The reflected head wave RHD is contained in the last term of (30). A somewhat similar problem which has the same functional form as (30) arises from the reflection of a buried concentrated force from a traction-free half-space. For more details on the evaluation of (30), the reader is referred to Tsai and Ma (1991), which deals with the above problem. Some interesting phenomena of the reflected waves can be explained by the deformed integral contours shown in Figs. 2(*b*)–2(*d*). For the second term of (23), two Cagniard contours overlap for $\theta_2^* (=\pi-\theta_0)<\theta<\cos^{-1}(-a\cos\theta_0/b)$; see Fig. 2(*b*). This overlap would cause the RPS wave to distort in that region as shown in Fig. 3. Consider the third term of (23) and the deformed contours shown in Fig. 2(*c*). The overlap of these two Cagniard contours occurs in the region $0<\theta<\theta_2^*$. The integration path represented by the dash line will terminate at the intersection point of these two contours. This illustrates that the RSP wave is not complete in the region $0<\theta<\theta_2^*$ and only exists before the extended RSP wave from the crack tip arrives. Finally, consider the fourth term of (23) and the corresponding deformed contours shown in Fig. 2(*d*). The most important phenomenon is the distortion of the straight reflected head wave RHD at the right-hand side in the region, $\theta_2^*<\theta<\cos^{-1}(a/b)$. The threshold is determined from the intersection of $\Gamma_{H\pm}^{\eta}$ and $\Gamma_{\pm}^{\lambda}$, indicating that the straight wave front of the head wave will be deformed and terminated at the wave front of the DSS wave. The arrival time of these distorted wave fronts is presented in Eq. (A2) of the Appendix. By using the Cagniard-de Hoop method of the Laplace inversion, reflected fields in the time domain are represented in simple closed form and are shown in the Appendix.

Next we consider the diffracted waves generated from the crack tip. Here we shall carry out the inverse transformation for diffracted waves using an extension of the Cagniard-de Hoop technique. The deduction is explained in detail from the first term of (23). Recalling that p is real and positive, we shift the η and λ-integrations onto Cagniard contours. It can be written as

Downloaded 03 May 2010 to 171.66.16.247. Redistribution subject to ASME license or copyright; see http://www.asme.org/terms/Terms_Use.cfm

$$\bar{\sigma}_{22}^{\mathrm{DPP}}(x_1,x_2,p) = \frac{1}{2\pi^2}\int_{ar_0}^{\infty}\int_{ar}^{\infty} C^1_{1133}(\eta^{\pm}(\tau),\lambda(t))e^{-p(t+\tau)}dtd\tau, \quad (31)$$

where

$$C^m_{ijkl}(\eta^{\pm}(\tau),\lambda(t)) = \mathrm{Re}\left[(A_{mi}(\eta^{+}(\tau))B_j(\eta^{+}(\tau),\lambda(t))\right.$$
$$+ A_{mk}(\eta^{+}(\tau))B_l(\eta^{+}(\tau),\lambda(t)))\frac{\partial\eta^{+}(\tau)}{\partial\tau}\frac{\partial\lambda(t)}{\partial t}$$
$$-(A_{mi}(\eta^{-}(\tau))B_j(\eta^{-}(\tau),\lambda(t))$$
$$\left.+A_{mk}(\eta^{-}(\tau))B_l(\eta^{-}(\tau),\lambda(t)))\frac{\partial\eta^{-}(\tau)}{\partial\tau}\frac{\partial\lambda(t)}{\partial t}\right]. \quad (32)$$

From the Cagniard-de Hoop method, the inverse transform can be obtained by inspection and the DPP wave in the time domain can be expressed as

$$\sigma_{22}(x_1,x_2,t) = \frac{1}{2\pi^2}\int_{ar_0}^{t-ar} C^1_{1133}(\eta^{\pm}(\tau),\lambda(t'))d\tau, \quad (33)$$

where $t' = t-\tau$. The physical meaning of the DPP wave is the diffracted longitudinal wave induced by the incident IP wave and reflected RPP and RPS waves. The second term of (23) represents the DPS wave, the diffracted shear wave induced by the same waves that generate the DPP wave. There is a head wave DPH generated in the left-hand side of the crack tip by the additional branch cut at $\lambda = a$. The integral path Γ^{η} of the third and fourth terms in (23) can be divided into two intervals $\Gamma^{\eta}_{H\pm}$ and $\Gamma^{\eta}_{\pm}$ as shown in Figs. 2(*c*) and 2(*d*). $\Gamma^{\eta}_{H\pm}$ represents the diffracted waves DHP, DHH, and DHS generated by RSP and RHD waves from the crack tip, while $\Gamma^{\eta}_{\pm}$ represents the diffracted waves DSP, DSH, and DSS induced by IS and RSS waves. Omitting the detailed deductions here, the stress caused by diffracted waves are found to be

$$2\pi^2\sigma^D_{22}(x_1,x_2,t) = \int_{ar_0}^{t-ar} C^1_{1133}(\eta_1^{\pm}(\tau),\lambda_1(t'))d\tau$$
$$+\int_{ar_0}^{t-t_H} C^1_{1234}(\eta_1^{\pm}(\tau),\lambda_2(t'))H(br-t')d\tau$$
$$+\int_{ar_0}^{t-br} C^1_{1234}(\eta_1^{\pm}(\tau),\lambda_3(t'))d\tau$$
$$+\int_{t_{H_0}}^{t-ar} C^1_{2143}(\eta_2^{\pm}(\tau),\lambda_1(t'))H(br_0-\tau)d\tau$$
$$+\int_{t_{H_0}}^{t-t_H} C^1_{2244}(\eta_2^{\pm}(\tau),\lambda_2(t'))H(br_0-\tau)H(br-t')d\tau$$
$$+\int_{t_{H_0}}^{t-br} C^1_{2244}(\eta_2^{\pm}(\tau),\lambda_3(t'))H(br_0-\tau)d\tau$$
$$+\int_{br_0}^{t-ar} C^1_{2143}(\eta_3^{\pm}(\tau),\lambda_1(t'))d\tau$$
$$+\int_{br_0}^{t-t_H} C^1_{2244}(\eta_3^{\pm}(\tau),\lambda_2(t'))H(br-t')d\tau$$
$$+\int_{br_0}^{t-br} C^1_{2244}(\eta_3^{\pm}(\tau),\lambda_3(t'))d\tau, \quad (34)$$

where

$$\eta_1^{\pm}(\tau) = \frac{\tau}{r_0}\cos\theta_0 \pm i\sqrt{\frac{\tau^2}{r_0^2}-a^2}\sin\theta_0,$$

$$\lambda_1(t') = -\frac{t'}{r}\cos\theta + i\sqrt{\frac{t'^2}{r^2}-a^2}\sin\theta,$$

$$\eta_2^{\pm}(\tau) = \frac{\tau}{r_0}\cos\theta_0 + \sqrt{b^2-\frac{\tau^2}{r_0^2}}\sin\theta_0,$$

$$\lambda_2(t') = -\frac{t'}{r}\cos\theta - \sqrt{b^2-\frac{t'^2}{r^2}}\sin\theta,$$

$$\eta_3^{\pm}(\tau) = \frac{\tau}{r_0}\cos\theta_0 \pm i\sqrt{\frac{\tau^2}{r_0^2}-b^2}\sin\theta_0,$$

$$\lambda_3(t') = -\frac{t'}{r}\cos\theta + i\sqrt{\frac{t'^2}{r^2}-b^2}\sin\theta,$$

$$t_{H_0} = r_0|\cos\theta_0| + r_0\sqrt{b^2-a^2}\sin\theta_0,$$

$$t_H = r|\cos\theta| + r\sqrt{b^2-a^2}\sin\theta. \quad (35)$$

The superscript D is used to indicate diffracted waves. Equation (34) contains nine terms which represent diffracted waves DPP, DPH, DPS, DHP, DHH, DHS, DSP, DSH, and DSS, respectively. The arrival time for each diffracted wave front is

$$T_{\mathrm{DPP}} = ar_0 + ar,\ T_{\mathrm{DPH}} = ar_0 + t_H,\ T_{\mathrm{DPS}} = ar_0 + br,$$
$$T_{\mathrm{DHP}} = t_{H_0} + ar,\ T_{\mathrm{DHH}} = t_{H_0} + t_H,\ T_{\mathrm{DHS}} = t_{H_0} + br,$$
$$T_{\mathrm{DSP}} = br_0 + ar,\ T_{\mathrm{DSH}} = br_0 + t_H,\ T_{\mathrm{DSS}} = br_0 + br. \quad (36)$$

The complete structures for the incident, reflected, and diffracted waves are represented in Fig. 3. Mixed-mode stress intensity factors in the Laplace transform domain can be represented as

$$\bar{K}_I(p) = \frac{\sqrt{2}}{2\pi i\sqrt{p}}\int [A_{11}(\eta)K^F_I(\eta)e^{-p\alpha^* h-p\eta l}$$
$$+A_{12}(\eta)K^F_I(\eta)e^{-p\beta^* h-p\eta l}]dd, \quad (37)$$

$$\bar{K}_{II}(p) = \frac{\sqrt{2}}{2\pi i\sqrt{p}}\int [A_{13}(\eta)K^F_{II}(\eta)e^{-p\alpha^* h-p\eta l}$$
$$+A_{14}(\eta)K^F_{II}(\eta)e^{-p\beta^* h-p\eta l}]dd. \quad (38)$$

Appling the Cagniard-de Hoop method for Laplace inversion, the stress intensity factors in the time domain can be obtained as follows:

$$\frac{\pi^{3/2}}{\sqrt{2}}K_I(t) = \int_{ar_0}^{t}\frac{1}{t-\tau}\mathrm{Im}\left[A_{11}(\eta_1^{+})K^F_I(\eta_1^{+})\frac{\partial\eta_1^{+}}{\partial\tau}\right]d\tau$$
$$+\int_{t_{H_0}}^{t}\frac{1}{\sqrt{t-\tau}}\mathrm{Im}\left[A_{12}(\eta_2^{+})K^F_I(\eta_2^{+})\frac{\partial\eta_2^{+}}{\partial\tau}\right]H(br_0-\tau)d\tau$$
$$+\int_{br_0}^{t}\frac{1}{\sqrt{t-\tau}}\mathrm{Im}\left[A_{12}(\eta_3^{+})K^F_I(\eta_3^{+})\frac{\partial\eta_3^{+}}{\partial\tau}\right]d\tau, \quad (39)$$

$$\frac{\pi^{3/2}}{\sqrt{2}}K_{II}(t) = \int_{ar_0}^{t}\frac{1}{\sqrt{t-\tau}}\mathrm{Im}\left[A_{13}(\eta_1^{+})K^F_{II}(\eta_1^{+})\frac{\partial\eta_1^{+}}{\partial\tau}\right]d\tau$$
$$+\int_{t_{H_0}}^{t}\frac{1}{\sqrt{t-\tau}}\mathrm{Im}\left[A_{14}(\eta_2^{+})K^F_{II}(\eta_2^{+})\frac{\partial\eta_2^{+}}{\partial\tau}\right]H(br_0-\tau)d\tau$$
$$+\int_{br_0}^{t}\frac{1}{\sqrt{t-\tau}}\mathrm{Im}\left[A_{14}(\eta_3^{+})K^F_{II}(\eta_3^{+})\frac{\partial\eta_3^{+}}{\partial\tau}\right]d\tau. \quad (40)$$

Downloaded 03 May 2010 to 171.66.16.247. Redistribution subject to ASME license or copyright; see http://www.asme.org/terms/Terms_Use.cfm

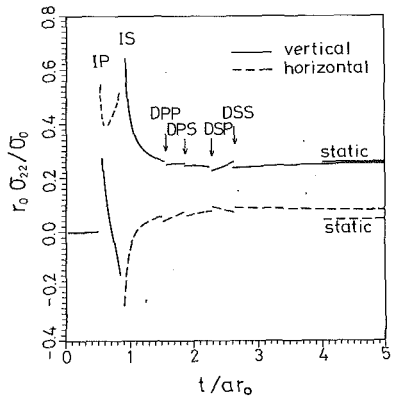


Fig. 4 Normal stress σ_{22} at field point F_1 subjected to concentrated force applied at source point S_1

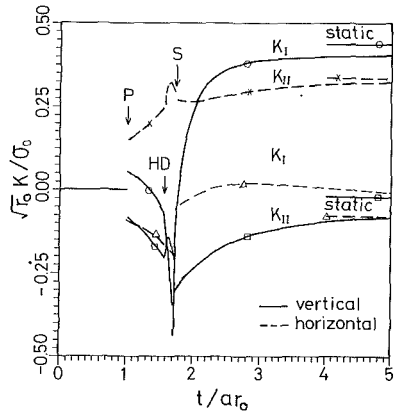


Fig. 6 Stress intensity factors K_I and K_{II} subjected to concentrated force applied at source point S_2

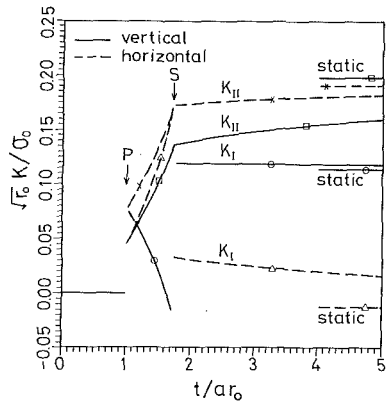


Fig. 5 Stress intensity factors K_I and K_{II} subjected to concentrated force applied at source point S_1

3.2 Horizontal Concentrated Force. Consider the same cracked body as shown in Fig. 1. Now the direction of the concentrated force is applied along the positive x_1 direction at the position (l, h). Following the similar procedure of case (1) for the vertical direction, the diffracted waves and stress intensity factors can be represented in the same form as (34), (39), and (40) by replacing C^1_{ijkl} by C^2_{ijkl}, and using the corresponding unknown functions A_{2i}

$$A_{21}(\eta)=\frac{\eta(b^2-2\eta^2)}{2b^2\alpha^*},\ A_{22}(\eta)=-\frac{\eta\beta^*}{b^2},$$
$$A_{23}(\eta)=\frac{\eta^2}{b^2},\ A_{24}(\eta)=\frac{(b^2-2\eta^2)}{2b^2}. \quad (41)$$

The procedure of finding incident and reflected waves can be obtained in the paper of Tsai and Ma (1991), and only the brief results are shown in the Appendix.

4 Numerical Results

The explicit analytical results for the stress σ_{22} and the stress intensity factors have been given in the previous sections. For simplicity of the numerical calculation of the full-field solution, the source and field points are situated in such a manner that no reflected waves need be accounted for. A Poisson's ratio $\nu=0.25$ is used which gives ratios of wave speeds $b = \sqrt{3}a$ and $c = 1.88a$. The transient response of stress σ_{22} for applied singular sources with Heaviside function dependence of concentrated force is shown in Fig. 4. The singular source is applied suddenly at the position $S_1(r_0, 45\text{ deg})$ and the transient stress σ_{22} is evaluated at the field point $F(r_0/2, 45\text{ deg})$. There will be no reflected waves, only the incident waves (IP and IS) and diffracted waves (DPP, DPS, DSP, and DSS) will be generated. The time has been normalized by dividing by ar_0 and the arrival time for each wave front is indicated in the figures. The solid lines are valid for applying the singular source in the vertical x_2-direction while the dash lines are valid in the horizontal x_1-direction. The incident waves for the applied concentrated force have a singularity at their wave fronts while the diffracted waves have finite jumps at their wave fronts. The corresponding stress intensity factor is shown in Fig. 5. Next, a more complicated situation is considered in which the singular sources are applied at the position $S_2(r_0, 150\text{ deg})$. For this case, we evaluate only the time histories of dynamic stress intensity factors whose results are shown in Fig. 6.

In some classes of dynamic problems, the ability to find a static field may hinge on waiting for the wave fronts to pass and the transient effect to die away. The static solution obtained by Tada et al. (1973) for an applied static point force on a semi-infinite crack is used to construct the static solution and to compare with the transient result. It is found in this study that the transient full-field solutions for stress σ_{22} will approach the corresponding static value after the last diffracted DSS wave has passed. The dynamic stress intensity factors will tend to the corresponding static values after the incident IS wave has arrived at the crack tip. The time needed for the transient field quantities to approach the static values depends on the direction of applied loading. If the loading is applied along the x_2-direction, then the time needed for σ_{22} and K_I to approach the static values will be less than that for $\sigma_{12}$and K_{II}.

In order to investigate the possibility of the crack surface interpenetration based on the transient solution obtained in this analysis, the vertical crack surface opening displacement is calculated for a vertical point loading in front of the crack tip (θ_0 = 45 deg) and behind the crack tip (θ_0 = 150 deg), respectively. In Fig. 7, the transient solution of opening displacement at different positions at the crack surface is evaluated for the vertical point loading in front of the crack tip. Where u_2 represents the difference of the displacement for the upper and lower crack surface, the contact of the crack surface will occur if u_2 is less than zero. It shows in this figure that the transient solution obtained in this study does predict contact of the crack surface, but the contact time is quite small. The general feature is that after the RSS wave has passed, the displacement at the upper and lower crack surface will move outward and the crack surface will be opened again. The contact time will be small if the material point is closed to the applied load. If the point loading is applied behind the crack tip, the transient displacement responses for five material points are plotted in Fig. 8. If the material points at the crack surface are directly below the applied loading (i.e., r/r_0= 1, 0.5), then

Downloaded 03 May 2010 to 171.66.16.247. Redistribution subject to ASME license or copyright; see http://www.asme.org/terms/Terms_Use.cfm

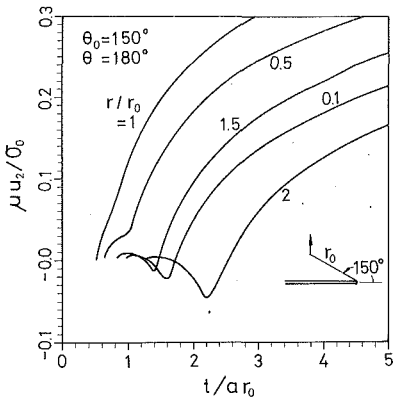


Fig. 7 Vertical opening displacements of crack surfaces for applied concentrated load in front of the crack tip (θ_0 = 45 deg)

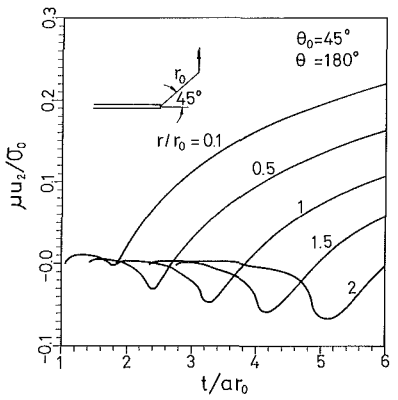


Fig. 8 Vertical opening displacements of crack surfaces for applied concentrated load behind the crack tip (θ_0 = 150 deg)

there will be no contact for the whole time history. For the material points far from the applied load, the contact will occur but the contact time will be smaller than that for the loading applied in front of the crack tip. If the contact does occur at some material points, then the crack surface will be opened again after the RSS wave has passed.

5 Conclusions

The difficulty in determining the transient stress field in a cracked body subjected to dynamic loading is well known. It will become more complicated and difficult to solve if a characteristic length is involved in the analysis. The transient stress generated by the application of a concentrated force to a semi-infinite crack is obtained in an exact, closed form. A new fundamental solution is proposed for constructing the complicated reflected and diffracted waves generated by the crack. The fundamental problem is the application of exponentially distributed traction on the crack faces in the Laplace transform domain. Unlike the usual superposition method which is performed in the time domain, the transient solutions are determined by superposition of the fundamental solution in the Laplace transform domain. The extension of the Cagniard-de Hoop inverse method is used to investigate in detail the structure of the wave pattern.

In this paper we have obtained the transient response, at an arbitrary point in space and an arbitrary time, to waves reflected and diffracted in a semi-infinite crack which is struck by cylindrical incident waves generated by a concentrated force. The purpose was to investigate the characteristic time during which the transient effect is important. Numerical results for the analysis of transient effects are presented and compared to the corresponding static values. It is found that the dynamic transient solution will approach the static value after the last diffracted DSS wave has passed the field point.

Acknowledgment

The authors gratefully acknowledge the financial support of this research by the National Science Council (Republic of China) under Grant NSC 79-0401-E002-36 and to the National Tawian University.

References

Achenbach, J. D., 1973, *Wave Propagation in Elastic Solids*, Elsevier, New York.

Brock, L. M., 1982, "Shear and Normal Impact Loadings on One Face of a Narrow Slit," *International Journal of Solids and Structures*, Vol. 18, pp. 467-477.

Brock, L. M., 1984, "Stresses in a Surface Obstacle Undercut Due to Rapid Indentation," *Journal of Elasticity*, Vol. 14, pp. 415-424.

Brock, L. M., Jolles, M., and Schroedl, M., 1985a, "Dynamic Impact Over a Subsurface Crack: Applications to the Dynamic Tear Test," ASME JOURNAL OF APPLIED MECHANICS, Vol. 52, pp. 287-290.

Brock, L. M., 1985b, "The Dynamic 2D Analysis of a Concentrated Force Near a Semi-infinite Crack," *Quarterly of Applied Mathematics*, Vol. 43, pp. 201-210.

Brock, L. M., 1986, "Transient Dynamic Green's Functions for a Cracked Plane," *Quarterly of Applied Mathematics*, Vol. 44, pp. 265-275.

Brock, L. M., and Jolles, M., 1987, "Dislocation-Crack Edge Interaction in Dynamic Brittle Fracture and Crack Propagation," *International Journal of Solids and Structures*, Vol. 23, pp. 607-619.

Brock, L. M., 1989, "An Exact Transient Analysis of Dislocation Emission and Fracture," *Journal of the Mechanics and Physics of Solids*, Vol. 37, pp. 47-69.

de Hoop, A. T., 1958, "Representation Theorems for the Displacement in an Elastic Solid and Their Application to Elastodynamic Diffraction Theory," Doctoral Dissertation, Technische Hoegschool, Delft, The Netherlands.

Freund, L. B., 1972a, "Crack Propagation in an Elastic Solid Subjected to General Loading—I. Constant Rate of Extension," *Journal of the Mechanics and Physics of Solids*, Vol. 20, pp. 129-140.

Freund, L. B., 1972b, "Crack Propagation in an Elastic Solid Subjected to General Loading—II. Non-uniform Rate of Extension," *Journal of the Mechanics and Physics of Solids*, Vol. 20, pp. 141-152.

Freund, L. B., 1973, "Crack Propagation in an Elastic Solid Subjected to General Loading-III. Stress Wave Loading," *Journal of the Mechanics and Physics of Solids*, Vol. 21, pp. 47-61.

Freund, L. B., 1974a, "Crack Propagation in an Elastic Solid Subjected to General Loading—IV. Obliquely Incident Stress Pulse," *Journal of the Mechanics and Physics of Solids*, Vol. 22, pp. 137-146.

Freund, L. B., 1974b, "The Stress Intensity Factor Due to Normal Impact Loading of the Faces of a Crack," *International Journal of Engineering Science*, Vol. 12, pp. 179-189.

Handelman, G. H., and Rubenfeld, L. A., 1969, "Diffraction Of Horizontal Shear Waves by a Half Plane," ASME JOURNAL OF APPLIED MECHANICS, Vol. 36, pp. 873-874.

Harris, J. G., 1980, "Diffraction by a Crack of a Cylindrical Longitudinal Pulse," *Journal of Applied Mathematics and Physics*, Vol. 31, pp. 367-383.

Lee, Y. J., and Freund, L. B., 1990, "Fracture Initiation Due to Asymmetric Impact Loading of an Edge Cracked Plate," ASME JOURNAL OF APPLIED MECHANICS, Vol. 57, pp. 104-111.

Ma, C. C., and Burgers, P., 1987, "Dynamic Mode I and Mode II Crack Kinking Including Delay Time Effects," *International Journal of Solids and Structures*, Vol. 23, pp. 897-918.

Ma, C. C., and Burgers, P., 1988, "Initiation, Propagation, and Kinking of an Antiplane Crack," ASME JOURNAL OF APPLIED MECHANICS, Vol. 55, pp. 111-119.

Ma, C. C., 1988, "Initiation, Propagation, and Kinking of an In-plane Crack," ASME JOURNAL OF APPLIED MECHANICS, Vol. 55, pp. 587-595.

Ma, C. C., 1990, "Dynamic Mixed Mode I-II Crack Kinking under Oblique Stress Wave Loading in Brittle Solids," ASME JOURNAL OF APPLIED MECHANICS, Vol. 57, pp. 117-127.

Ma, C. C., and Hou, Y. C., 1991a, "Transient Analysis for Antiplane Crack Subjected to Dynamic Loadings," ASME JOURNAL OF APPLIED MECHANICS, Vol. 58, pp. 703-709.

Ma, C. C., and Hou, Y. C., 1991b, "Theoretical Analysis of the Transient Response for a Stationary Inplane Crack Subjected to Dynamic Impact Loading," *International Journal of Engineering Science*, in press.

Noble, B., 1958, *The Wiener-Hopf Technique*, Pergamon Press.

Thau, S. A., and Lu, T. H., 1971, "Transient Stress Intensity Factors for a Finite Crack in an Elastic Solid Caused by a Dilatational Wave," *International Journal of Solids and Structures*, Vol. 7, pp. 731-750.

Tada, H., Paris, P. C., and Irwin, G. R., 1973, *The Stress Analysis of Cracks Handbook*, Del Research Corporation, Hellertown, PA.

Downloaded 03 May 2010 to 171.66.16.247. Redistribution subject to ASME license or copyright; see http://www.asme.org/terms/Terms_Use.cfm

Tsai, C. H., and Ma, C. C., 1991, "Exact Transient Solutions of Buried Dynamic Point Forces and Displacement Jumps for an Elastic Half Space," *International Journal of Solids and Structures*, Vol. 28, pp. 955-974.

APPENDIX

The Laplace transform of incident and reflected waves can be inverted immediately by the Cagniard-de Hoop scheme to give

$$\sigma_{22}(x_1,x_2,t)=\frac{1}{\pi}\sum_{j=1}^{6}\text{Im}\left[D_{ij}(\xi_j)\frac{\partial\xi_j}{\partial t}\right]H(t-T_j)+\frac{1}{\pi}\text{Im}\left[D_{i7}(\xi_7)\frac{\partial\xi_7}{\partial t}\right](H(t-T_7)-H(t-T_6)) \quad \text{(A1)}$$

where $i = 1,2$, representing the case of vertical and horizontal concentrated force, respectively. In which j represents the IP, IS, RPP, RPS, RSP, RSS, and RHD waves, j equals to 1 to 7, respectively. The reflected waves only exist in the region $\theta>\theta_2$, except the RSP wave. The distorted wave fronts of RPS, RSP, and RHD are shown in Fig. 3. The arrival times of the distorted wave front for the given regions are

$$T_{\text{RPS}}=\sqrt{\frac{b^2\sin^2\theta-a^2\sin^2\theta_0}{\cos^2\theta_0-\cos^2\theta}}\,(r_0\cos\theta-r\cos\theta_0) \quad \text{for } \theta_2^*<\theta<\cos^{-1}\left(-\frac{a}{b}\cos\theta_0\right),$$

$$T_{\text{RSP}}=\sqrt{\frac{b^2\sin^2\theta_0-a^2\sin^2\theta}{\cos^2\theta-\cos^2\theta_0}}\,(r_0\cos\theta-r\cos\theta_0) \text{ for } 0<\theta<\theta_2^*,$$

$$T_{\text{RHD}}=br-br_0\cos(\theta+\theta_0) \quad \text{for } \theta_2^*<\theta<\cos^{-1}\frac{a}{b}. \quad \text{(A2)}$$

The RSP wave in the distorted region ($0<\theta<\theta_2^*$) is valid in the time interval between arrival of the first RSP wave and T_{RSP}. The last term of (A1) represents the head wave which only exists in the region $b|\cos\theta_2|>a$. The unknown functions ξ_j, D_{ij}, and T_j shown in (A1) can be found in Tsai and Ma (1991).

Downloaded 03 May 2010 to 171.66.16.247. Redistribution subject to ASME license or copyright; see http://www.asme.org/terms/Terms_Use.cfm

Jong S. Lee
Asst. Professor,
Mem. ASME

Elizabeth N. Its
Research Associate.

Department of Civil and
Environmental Engineering,
Clarkson University,
Potsdam, NY 13676

Propagation of Rayleigh Waves in Magneto-Elastic Media

Propagation of Rayleigh waves in a perfectly conducting elastic half-space in the presence of magnetic fields is considered for a possible application in nondestructive measurements of mechanical and/or electromagnetic parameters in electromagnetic materials. In particular, the dependence of Rayleigh wave velocity on magnetic and elastic parameters of the conducting medium in tangentially and normally oriented primary magnetic fields is investigated. Numerical results for three elastic materials with different elastic parameters are presented for a range of magnetic permeability. It is shown that the effect of magnetic fields render the medium essentially anisotropic and that the magnetic permeability of the medium and the orientation of the primary magnetic field strongly affect the Rayleigh wave velocity field.

1 Introduction

Since Knopoff (1955) studied the effect of the earth's magnetic field on the propagation of seismic waves in the conducting core of the earth, the propagation of mechanical waves through a magnetic field has been a topic for many investigations. Dunkin and Eringen (1963) studied the problem of plane waves traveling through an infinite medium and an infinite plate in the presence of large magnetostatic and electrostatic fields. In a series of articles, Kaliski (e.g., 1965) considered various mechanical problems coupled to electromagnetic effects through a large magnetic field. Other publications on the topic include works by Paria (1962), Wilson (1963), Baser and Karal (1971), Maugin (1979), Verma (1986), and Lee et al. (1990). The problem of coupled electromagnetic and elastic waves in a random medium was considered by Dhar (1979). More recently, Massalas and Tsolakidis (1990) studied plane magneto-thermoelastic wave propagation in a prestressed body. Detailed consideration of both linear and nonlinear coupled magneto-elastic problems such as magnon-phonon coupling and magneto-acoustic resonance is reviewed by Maugin (1981). General discussions and many references on the subject matter can be found in recently published monographs of Maugin (1988) and Eringen and Maugin (1990).

Most of the aforementioned studies, however, are concerned with propagation of body waves. Propagation of surface waves in magneto-elastic media has also received some scattered attention. Bleustein (1968) and Gulyaev (1969) showed that in a piezoelectric material not only pure Rayleigh but also shear surface elastic waves coupled to electrostatic potential can exist. Viktorov (1975) showed that shear waves can become inhomogeneous also in a metal under the action of a strong magnetic field directed along the free surface of the metal at an angle relative to the direction of wave propagation. Pouget and Maugin (1981a,b) studied Rayleigh waves coupled with the electric polarization and a Gulyaev-Bleustein-type wave in ferroelectric crystals. A similar problem for elastic ferromagnets was treated by Maugin and Hakmi (1985).

It has been recognized that surface waves may be used for material characterization (see, e.g., Rose et al., 1990). Despite its practical implication, propagation of surface waves in elastic conductors has not received much attention except Kaliski and Rogula (1960, 1961) and Tomita and Shindo (1979). Surface waves in a solid body propagating under the influence of a superimposed magnetic field can differ significantly from the ones propagating in the absence of a magnetic field. Surface waves can convey information on electromagnetic properties of the material as well as on its elastic parameters. Moreover, the very existence of normal surface waves can also be affected by the intensity of electromagnetic fields and elastic or electromagnetic parameters of the material. Kaliski and Rogula (1960) considered the question of existence of Rayleigh waves for a perfectly conducting half-space in a magnetic field. In a subsequent paper (1961), they treated a similar problem for the case of a curved surface. Tomita and Shindo (1979) considered the propagation of Rayleigh waves in an electrically and thermally conducting half-space and obtained an approximate solution for small thermoelastic and magnetoelastic coupling. It is noted, however, that in the above studies they assumed that the magnetic permeability of the medium is the same as the magnetic permeability of the vacuum. Thus, some interesting problems such as the influence of magnetic permeability of conductors on the Rayleigh wave velocity, for instance, could not be adequately investigated. A careful study of the influence of the magnetic field on the propagation of Rayleigh waves may reveal certain possibilities of nondestructive measurement of the electromagnetic and/or mechanical parameters. Moreover, the solution of this problem may be used as a preliminary analysis for more complicated problems

Contributed by the Applied Mechanics Division of THE AMERICAN SOCIETY OF MECHANICAL ENGINEERS for presentation at the 1992 ASME Winter Annual Meeting, Anaheim, CA, Nov. 8-13, 1992.

Discussion on this paper should be addressed to Prof. Leon M. Keer, The Technological Institute, Northwestern University, Evanston, IL 60208, and will be accepted until four months after final publication of the paper itself in the ASME JOURNAL OF APPLIED MECHANICS.

Manuscript received by the ASME Applied Mechanics Division, Mar. 14, 1991; final revision, Sept. 21, 1991. Associate Technical Editor: S. K. Datta.

Paper No. 92-WA/APM-9.

Copyright © 1992 by ASME
Downloaded 03 May 2010 to 171.66.16.247. Redistribution subject to ASME license or copyright; see http://www.asme.org/terms/Terms_Use.cfm

which manifests nonlinear magneto-mechanical surface waves due to, for instance, under-surface bursts, etc.

In this paper the propagation of Rayleigh waves in a conducting half-space immersed in a magnetic field is considered for possible applications in nondestructive testing of electromagnetic materials. In particular, the dependence of the Rayleigh wave velocity on elastic and electromagnetic properties of the medium as well as on the magnetic field intensity is discussed in some detail with numerical examples.

2 Fundamental Equations

Here we restrict ourselves to an a priori linear theory of magneto-elasticity (for infinitesimal deformations) in which only the ponderomotive force remains nonlinear in the presence of a magnetic field. A formal exposition of general theory of nonlinear magneto-elasticity can be found in Maugin (1988) and Eringen and Maugin (1990). It is assumed that the elastic medium under consideration is a homogeneous, isotropic, and electrically conducting one. Equations governing the propagation of small elastic disturbances including the interaction of the mechanical field and electromagnetic fields are (e.g., Dunkin and Eringen, 1963)

$$\rho\ddot{\mathbf{u}} = \nabla\cdot\mathbf{T} + \mathbf{f} + \mathbf{J}\times\mathbf{B} \tag{1}$$

where $\mathbf{u}$ is the mechanical displacement, $\mathbf{T}$ Cauchy's stress tensor, ρ the mass density, $\mathbf{f}$ the mechanical volume force (in the following we assume $\mathbf{f} = 0$), and $\mathbf{J}\times\mathbf{B}$ the Lorentz force exerted on a unit volume element of current density $\mathbf{J}$ in the magnetic induction field $\mathbf{B}$. The electromagnetic field is governed by Maxwell's equations

$$\nabla\times\mathbf{E} = -\dot{\mathbf{B}}, \quad \nabla\cdot\mathbf{B} = 0, \quad \nabla\times\mathbf{H} = \mathbf{J} \tag{2}$$

where $\mathbf{H}$ is the magnetic field, $\mathbf{B}$ the magnetic induction, $\mathbf{E}$ the electric field, and $\mathbf{J}$ is the current density. In the above Maxwell's equations, we have neglected the displacement current $\mathbf{D}$. Equations (1) and (2) are supplemented by the following constitutive equations:

$$\mathbf{B} = \mu\mathbf{H}, \quad \mathbf{J} = \sigma(\mathbf{E} + \dot{\mathbf{u}}\times\mathbf{B}) \tag{3}$$

$$\mathbf{T} = \lambda(tr\mathbf{e})\mathbf{I} + 2G\mathbf{e}, \tag{4}$$

where $\mathbf{e} = (\nabla\mathbf{u} + \mathbf{u}\nabla)/2$, μ is the magnetic permeability, σ the electric conductivity, $\mathbf{e}$ the elastic strain tensor, λ and G Lame's constants for a linear, isotropic elastic material, and $\mathbf{I}$ is the identity tensor. Super dots $\dot{}$ and $\ddot{}$ denote the first and second differentiations with respect to time, respectively. $\mathbf{u}\nabla$ denotes the transpose of the displacement gradient $\nabla\mathbf{u}$. The boundary conditions are

$$\mathbf{n}\times\|\mathbf{E} + \dot{\mathbf{u}}\times\mathbf{B}\| = 0, \quad \mathbf{n}\cdot\|\mathbf{B}\| = 0, \quad \mathbf{n}\times\|\mathbf{H}\| = 0 \tag{5}$$

$$\mathbf{n}\cdot\|\mathbf{T} + \mathbf{T}^E\| = 0 \tag{6}$$

where $\mathbf{n}$ is the unit outward normal vector, $\|\ \|$ denotes the jump between the values from the positive and negative sides of the discontinuity surface, and Maxwell's stress tensor $\mathbf{T}^E$ in (6) is given by

$$\mathbf{T}^E = \mu\mathbf{H}\otimes\mathbf{H} + \epsilon\mathbf{E}\otimes\mathbf{E} - \frac{1}{2}(\mu\mathbf{H}\cdot\mathbf{H} + \epsilon\mathbf{E}\cdot\mathbf{E})\mathbf{I} \tag{7}$$

where ϵ is the electric permittivity.

Another set of governing equations is needed for vacuum and may be obtained by setting $\mu = \mu_o$ and $\sigma = 0$ in Eqs. (3). All field variables in vacuum will be denoted by a bar on the corresponding variables in the magneto-elastic medium. Linearization is carried out on a small perturbation of a primary bias field due to the electromagneto-mechanical interaction:

$$\mathbf{H}(\mathbf{x},t) = \mathbf{H}^o + \mathbf{h}(\mathbf{x},t), \quad \mathbf{E}(\mathbf{x},t) = 0 + \mathbf{e}(\mathbf{x},t), \quad \mathbf{J}(\mathbf{x},t), = 0 + \mathbf{j}(\mathbf{x},t) \tag{8}$$

where the field quantities in lower case letters are assumed small such that their products can be neglected.

3 Formulation of the Problem

We consider Rayleigh waves propagating in the x-direction in a conducting elastic half-space ($z \geq 0$) in contact with vacuum which is permeated by a magnetic field $\overline{\mathbf{B}} = (\overline{B}_1, 0, \overline{B}_3)$. Equations of motion (1) in the half-space take the form upon linearization,

$$G\nabla^2\mathbf{u} + (\lambda + G)\nabla\nabla\cdot\mathbf{u} + \mathbf{j}\times\mathbf{B}^o = \rho\ddot{\mathbf{u}}. \tag{9}$$

Perturbed electromagnetic fields in the half-space under consideration are described by

$$\nabla\times\mathbf{h} = \mathbf{j}, \quad \nabla\times\mathbf{e} = -\mu\dot{\mathbf{h}}, \quad \nabla\cdot\mathbf{h} = 0 \tag{10}$$

with

$$\mathbf{j} = \sigma(\mathbf{e} + \mu\dot{\mathbf{u}}\times\mathbf{H}^o) \tag{11}$$

where $\mathbf{h}$ and $\mathbf{e}$ are the perturbed magnetic and electric fields under the action of Rayleigh wave propagation, respectively. We shall drop the superscript o from the primary field (e.g., $\mathbf{H}^o$) for simplicity since there is no danger of confusion. By assuming perfect conductivity of the medium ($\sigma \to \infty$), perturbed electromagnetic fields can be expressed in terms of the displacement from Eqs. (11) and (10) as

$$\mathbf{e} = -\mu\dot{\mathbf{u}}\times\mathbf{H}, \quad \mathbf{h} = \nabla\times(\mathbf{u}\times\mathbf{H}). \tag{12}$$

By using Eqs. (10) and (12), equations of motion (9) can be rewritten as

$$G\nabla^2\mathbf{u} + (\lambda + G)\nabla\nabla\cdot\mathbf{u} + \mu[\nabla\times\nabla\times(\mathbf{u}\times\mathbf{H})]\times\mathbf{H} = \rho\ddot{\mathbf{u}}. \tag{13}$$

Equation (13) in scalar form constitutes a system of two equations for u_1 and u_3:

$$(\lambda + 2G)\frac{\partial^2 u_1}{\partial x^2} + (\lambda + G)\frac{\partial^2 u_3}{\partial x\partial z} + G\frac{\partial^2 u_1}{\partial z^2} + \mu[H_3^2\nabla^2 u_1 - H_3H_1\nabla^2 u_3] = \rho\frac{\partial^2 u_1}{\partial t^2}$$

$$(\lambda + 2G)\frac{\partial^2 u_3}{\partial z^2} + (\lambda + G)\frac{\partial^2 u_1}{\partial x\partial z} + G\frac{\partial^2 u_3}{\partial x^2} + \mu[H_1^2\nabla^2 u_3 - H_3H_1\nabla^2 u_1] = \rho\frac{\partial^2 u_3}{\partial t^2} \tag{14}$$

where $H_1 = \overline{H}_1 = \overline{B}_1/\mu_o$ and $H_3 = (\mu_0/\mu)\overline{H}_3 = \overline{B}_3/\mu$.

The boundary conditions on the surface of the half-space in the primary magnetic field are

$$T_{3i} + T_{3i}^E - \overline{T}_{3i}^E = 0 \quad i = 1, 2, 3 \tag{15}$$

$$h_1 = \overline{h}_1, \quad \mu h_3 = \mu_o\overline{h}_3. \tag{16}$$

For the problem under consideration boundary conditions (15) and (16) can be recast in terms of displacements as follows:

$$(\lambda + 2G)\frac{\partial u_3}{\partial z} + \lambda\frac{\partial u_1}{\partial x} + (\mu - \mu_o)\left[H_1^2\frac{\partial u_3}{\partial z} - H_1H_3\frac{\partial u_1}{\partial z}\right] + \mu\left(\frac{\mu}{\mu_o} - 1\right)\left[H_3^2\frac{\partial u_1}{\partial x} - H_1H_3\frac{\partial u_3}{\partial x}\right] = 0$$

$$\frac{\partial u_1}{\partial z} + \frac{\partial u_3}{\partial x} = 0. \tag{17}$$

The propagation of Rayleigh waves in a magneto-elastic half-space under the action of external magnetic fields $\overline{\mathbf{B}}$ is now described by the field Eqs. (14) and boundary conditions (17).

We seek a solution to Eqs. (14) in the form

$$u_j(x,z) = U_j(z)\exp\left[i\omega\left(t - \frac{x}{v_R}\right)\right] \quad j = 1, 3 \tag{18}$$

where functions U_j describe the Rayleigh wave amplitudes decaying with depth z and v_R is the velocity of the Rayleigh wave.

For clarity we consider the influence of tangential and nor-

Downloaded 03 May 2010 to 171.66.16.247. Redistribution subject to ASME license or copyright; see http://www.asme.org/terms/Terms_Use.cfm

mal external magnetic fields on Rayleigh wave propagation separately, i.e., we consider the following two cases:

(1) Case I: $\bar{\mathbf{B}} = (\bar{B}_1, 0, 0)$

(2) Case II: $\bar{\mathbf{B}} = (0, 0, \bar{B}_3)$.

Equations (14) can be recast by the use of (18) to a set of fourth-order differential equations with constant coefficients as

$$a_i \frac{d^4U_i}{dz^4} + b_i \frac{d^2U_i}{dz^2} + c_iU_i = 0, \quad i = 1 \text{ or } 3 \tag{19}$$

where coefficients a_i, b_i, and c_i are given in the following:

(1) Case I:

$$a_1 = (\lambda + 2G + \mu H^2)G$$

$$b_1 = \omega^2\left[\frac{(\lambda+G)^2 - (\lambda+2G)(\lambda+2G+\mu H^2) - G(G+\mu H^2)}{v_R^2} + \rho(G+\mu H^2+\lambda+2G)\right]$$

$$c_1 = \omega^4\left[\rho - \frac{G+\mu H^2}{v_R^2}\right]\left[\rho - \frac{\lambda+2G}{v_R^2}\right] \tag{20}$$

(2) Case II:

$$a_3 = (\lambda+2G)(G+\mu H^2)$$

$$b_3 = \omega^2\left[\frac{(\lambda+G)^2 - (\lambda+2G)(\lambda+2G+\mu H^2) - G(G+\mu H^2)}{v_R^2} + \rho(G+\mu H^2+\lambda+2G)\right]$$

$$c_3 = \omega^4\left[\rho - \frac{G}{v_R^2}\right]\left[\rho - \frac{\mu H^2+\lambda+2G}{v_R^2}\right] \tag{21}$$

where H is the magnetic field intensity in the medium either in the longitudinal or transverse direction depending on the case considered.

The functions U_i (i = 1 or 3) are assumed to have the form

$$U_i = A_ie^{-\alpha\omega z} + B_ie^{-\beta\omega z} \tag{22}$$

where α and β are roots of the bi-quadratic characteristic equation corresponding to (19). The condition of existence of the surface waves is

$$\text{Re}(\alpha) > 0 \text{ and } \text{Re}(\beta) > 0. \tag{23}$$

If the roots are complex, they are necessarily conjugate. Therefore the product $\alpha\beta$, and consequently $\alpha^2\beta^2$, are real and positive. Since $\alpha^2\beta^2$ has the following form

$$\alpha^2\beta^2 = \frac{\omega^4}{G(\lambda+2G+\mu H^2)}\left[\rho - \frac{G+\mu H^2}{v_R^2}\right]\left[\rho - \frac{\lambda+2G}{v_R^2}\right] \quad \text{Case I}$$

$$\alpha^2\beta^2 = \frac{\omega^4}{(G+\mu H^2)(\lambda+2G)}\left[\rho - \frac{G}{v_R^2}\right] \times \left[\rho - \frac{\lambda+2G+\mu H^2}{v_R^2}\right] \quad \text{Case II,} \tag{24}$$

it follows that v_R must not be in the following intervals:

$$\begin{aligned} &v_R \notin [v_A^2 + v_S^2,\ v_P^2] \quad \text{Case I} \\ &v_R \notin [v_S^2,\ v_A^2 + v_P^2] \quad \text{Case II} \end{aligned} \tag{25}$$

where v_P, v_S, and v_A are the velocity of compression, shear and Alfven wave (see, e.g., Maugin, 1981), respectively, and defined as

$$v_P^2 = \frac{\lambda+2G}{\rho},\ v_S^2 = \frac{G}{\rho},\ v_A^2 = \frac{\mu H^2}{\rho}. \tag{26}$$

Finally, by substituting the solution (22) into (17), one can get the characteristic equation for the determination of Rayleigh wave velocity v_R:

$$F(v_R,\ \alpha(v_R),\ \beta(v_R),\ \lambda,\ G,\ \mu,\ H) = 0 \tag{27}$$

or

$$F = \begin{vmatrix} K_{11} & K_{12} \\ K_{21} & K_{22} \end{vmatrix} = 0 \tag{28}$$

where the components of the characteristic matrix have the following form:

(1) Case I:

$$K_{11} = (\lambda+2G)\alpha a + \frac{\lambda}{v_R^2} + (\mu-\mu_o)H^2\alpha a$$

$$K_{12} = (\lambda+2G)\beta b + \frac{\lambda}{v_R^2} + (\mu-\mu_o)H^2\beta b$$

$$K_{21} = -\alpha + a$$

$$K_{22} = -\beta + b \tag{29}$$

where

$$a = \frac{G\alpha^2 + \rho - (\lambda+2G)v_R^{-2}}{\alpha(\lambda+G)},\ b = \frac{G\beta^2 + \rho - (\lambda+2G)v_R^{-2}}{\beta(\lambda+G)} \tag{30}$$

(2) Case II:

$$K_{11} = (\lambda+2G)\alpha + \lambda a + \mu\left(\frac{\mu}{\mu_o} - 1\right)H^2a$$

$$K_{12} = (\lambda+2G)\beta + \lambda b + \mu\left(\frac{\mu}{\mu_o} - 1\right)H^2b$$

$$K_{21} = -\alpha a + \frac{1}{v_R^2}$$

$$K_{22} = -\beta b + \frac{1}{v_R^2} \tag{31}$$

where

$$a = \frac{Gv_R^{-2} - \rho - (\lambda+2G)\alpha^2}{\alpha(\lambda+G)},\ b = \frac{Gv_R^{-2} - \rho - (\lambda+2G)\beta^2}{\beta(\lambda+G)} \tag{32}$$

Equations (27)–(32) will be used for the calculation of Rayleigh wave velocity for materials with different elastic parameters in tangential and normal magnetic fields for a wide range of magnetic permeability.

4 Numerical Results and Discussions

We wish to investigate the variation of Rayleigh wave velocity in a perfectly conducting medium in an external magnetic field as a function of elastic parameters and the magnetic permeability of the medium. The range of the magnetic permeability of the conducting medium used in the calculation is from $\mu = \mu_o$ to $\mu = 1000\mu_o$. For the two cases under consideration, we can rewrite Rayleigh function (27) in the following form:

$$F_i = R_i(v_p,\ v_S,\ \rho,\ v_R,\ v_A) + \left(\rho v_A^2 - \frac{\bar{B}_i^2}{\mu_o}\right)S_i(v_P,\ v_S,\ \rho,\ v_R,\ v_A) \quad i = 1, 3 \tag{33}$$

where R_i describes the magneto-elastic interaction arising through the field equations, and the second term, which contains a slowly varying function S_i, describes the interaction due to the boundary conditions (17). It is noted from (14) that R_i and S_i are functions of Alfven velocity $v_A^2 = \mu H^2/\rho$ which can be rewritten in terms of the external magnetic field as v_A^2

Downloaded 03 May 2010 to 171.66.16.247. Redistribution subject to ASME license or copyright; see http://www.asme.org/terms/Terms_Use.cfm

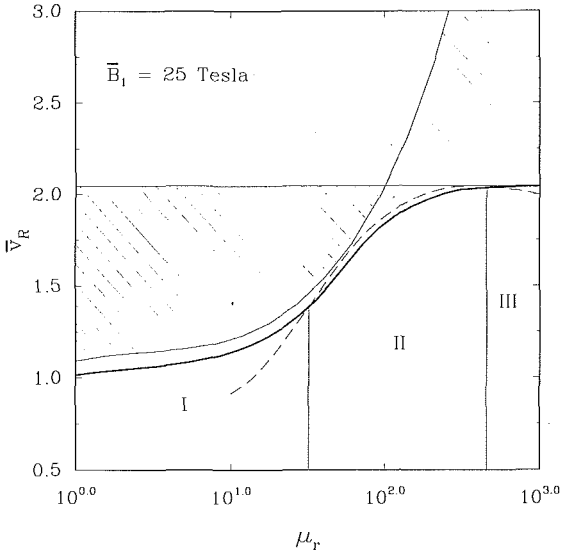


Fig. 1 Variation of dimensionless Rayleigh wave velocity with relative magnetic permeability ($\bar{B}_1$ = 25 Tesla)

$= \mu\bar{B}_1^2/\mu_o^2\rho$ for the tangential field (Case I) and $v_A^2 = \bar{B}_3^2/\mu\rho$ for the normal field (Case II).

In the case of tangential magnetic fields (Case I) when μ is close to μ_o, the second term in (33) can be dropped since the coefficient of the second term $\rho v_A^2 - \bar{B}_1^2/\mu_o \to 0$. But when μ is considerably larger than μ_o, an increase of magnetic permeability is accompanied by an increase in ρv_A^2 but not in $\bar{B}_1^2/\mu_o$, so the latter can be neglected, i.e., (33) becomes

$$F_1 = R_1(v_P, v_S, \rho, v_R, v_A) + \rho v_A^2 S_1(v_P, v_S, \rho, v_R, v_A). \quad (34)$$

Therefore, for a wide range of μ, F_1 (and consequently v_R) becomes essentially a function of Alfven velocity but not an explicit function of intensity of the external field. In the case of a normal magnetic field (Case II), however, the Alfven velocity decreases as the magnetic permeability increases. Therefore, for a material with large μ, ρv_A^2 is negligible compared to $\bar{B}_3^2/\mu_o$, i.e.,

$$F_3 = R_3(v_P, v_S, \rho, v_R, v_A) - \frac{\bar{B}_i^2}{\mu_o} S_3(v_P, v_S, \rho, v_R, v_A). \quad (35)$$

In this case, F_3 is a function of both the Alfven velocity and the intensity of external magnetic field (via the coefficient of the second term). In order to present numerical results in a consistent manner for both cases, effects of the magnetic permeability and the field intensity were treated separately, and the relative magnetic permeability $\mu_r = \mu/\mu_o$ was chosen as the primary variable instead of the Alfven velocity or Alfven parameter. Taking the different dependences of Rayleigh velocity on v_A and $\bar{B}$ into account, only one value of magnetic field intensity (25 Tesla) was used in Case I, while three different values were used in Case II. Moreover, in Case II, where v_A decreases as μ increases, very strong field intensities were selected to show the variation of Rayleigh velocity. A dimensionless Rayleigh wave velocity $\bar{v}_R$, which is the Rayleigh velocity in the presence of the magnetic field normalized with respect to the Rayleigh velocity in the absence of the field, is used throughout.

Figure 1 shows the variation of dimensionless Rayleigh wave velocity (solid line) for a medium with elastic parameters v_P = 8298 m/s, v_S = 5532 m/s, ρ = 3000 kg/m^3 in a tangential field of $\bar{B}_3$ = 25 Tesla. Hatched zones are the area where no solutions can exist according to (23). A line representing $\alpha = \beta$ (dashed line in the figure) further divides the valid region into two regions: α and β are real above the line and complex below the line. The dimensionless Rayleigh velocity crosses the dotted line twice in the range of magnetic permeability con-

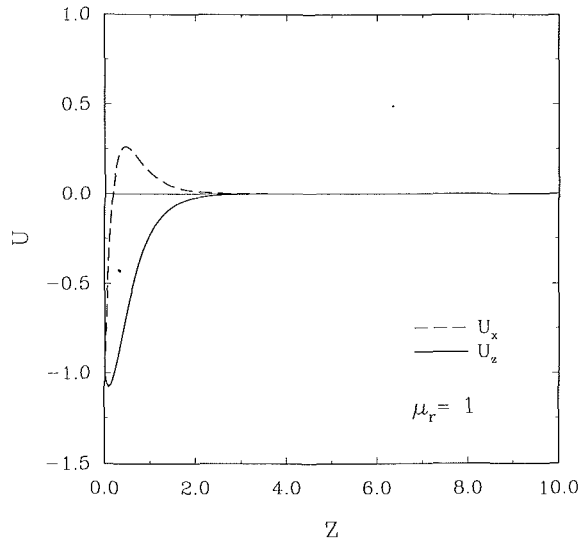


Fig. 2(a) μ_r = 1 (Zone I)

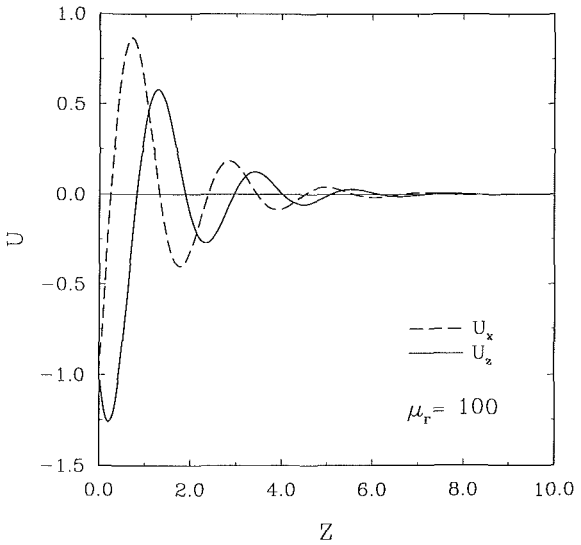


Fig. 2(b) μ_r = 100 (Zone II)

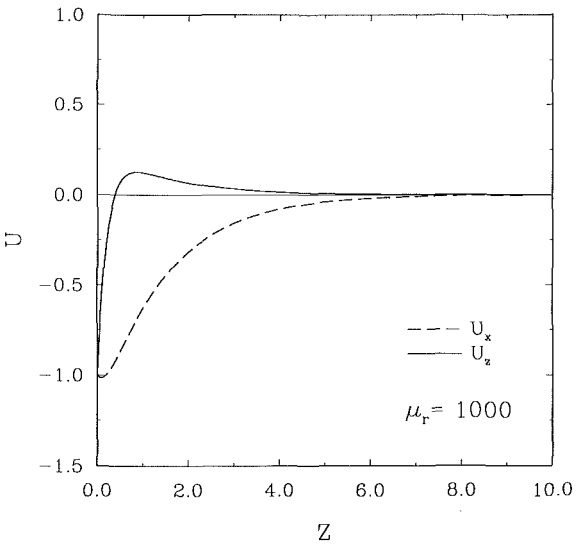


Fig. 2(c) μ_r = 1000 (Zone III)

Fig. 2 Amplitude as a function of depth for $\bar{B}_1$ = 25 Tesla

Downloaded 03 May 2010 to 171.66.16.247. Redistribution subject to ASME license or copyright; see http://www.asme.org/terms/Terms_Use.cfm

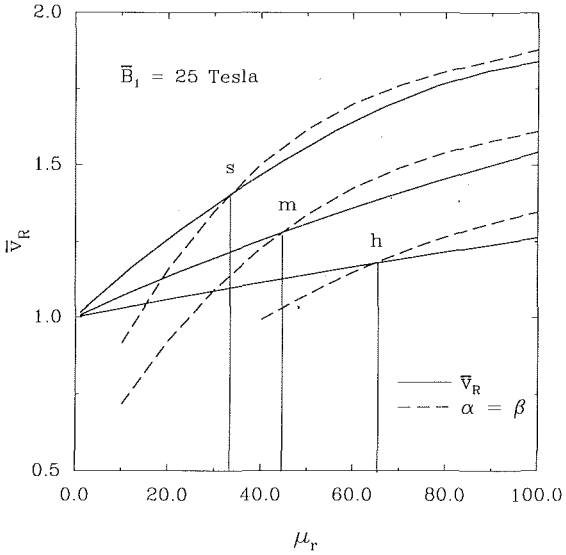


Fig. 3 $\bar{v}_R$ versus μ_R for three different elastic materials ($\bar{B}_1$ = 25 Tesla)

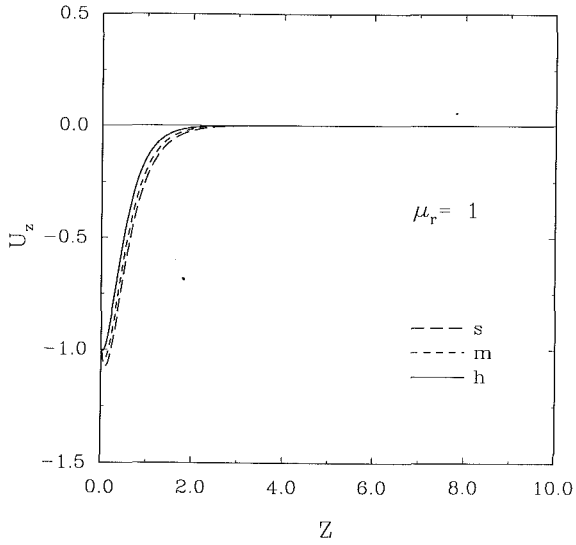


Fig. 4(*a*) μ_r = 1

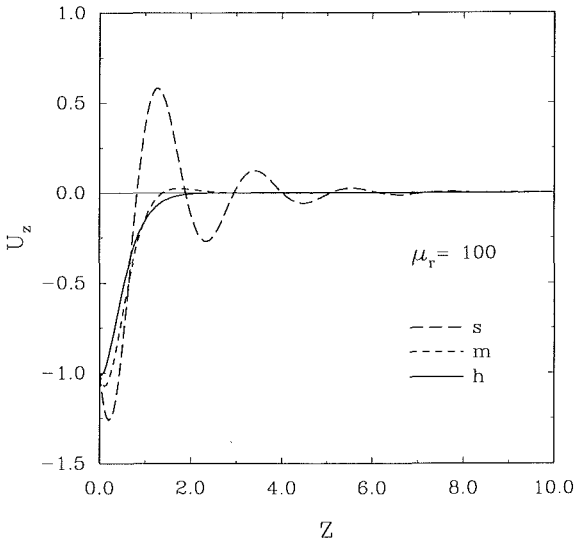


Fig. 4(*b*) μ_r = 100

Fig. 4 Comparison of amplitude profiles for three different elastic materials

sidered. The range of μ_r is thus divided into three zones (Zone I, II, and III) depending on the values of the exponents α and β. In the first zone (Zone I), α and β are real and positive and the Rayleigh velocities are close to those of purely elastic Rayleigh waves. Figure 2(*a*) shows profiles of the x and z components of amplitude as function of depth $Z = z/L$ (L = wave length) for $\mu_r = 1$ which falls into Zone I. As is shown in the figure, the variation of amplitude with depth is nonoscillatory and the depth of penetration is approximately one wave length. In Zone II, amplitudes exhibit oscillations and the penetration depth is increased as α and β become complex (Fig. 2(*b*)). This is a characteristic behavior of surface waves in anisotropic elastic materials with the role of anisotropic parameter played by Alfven parameter in our case. Unlike the case of purely elastic anisotropic materials, where the intensity of oscillation and the depth of penetration increase as the anisotropic parameter increases (Royer and Dieulesaint, 1984), in our case, however, the oscillation disappears as μ_r (or Alfven parameter in that regard) is further increased, since α and β become real again. In this zone (Zone III), where $v_R > v_P$, the amplitudes decay more slowly than in Case I but do not oscillate (Fig. 2(*c*)). This implies that in Zone III there exists a degenerating wave with its amplitude becoming asymptotically independent of z. The Rayleigh wave in this case is essentially losing the characteristics of a surface wave.

From the point of view of studying surface waves and its possible application for evaluation of near-surface properties of materials, the behavior of Rayleigh waves in the vicinity of μ_r corresponding to the transition between Zones I and II is the most interesting. Therefore, we studied the variation of $\bar{v}_R$ for elastic conductors with three different sets of elastic parameters in the vicinity of such points. The material with v_P/v_S = 1.9 and v_S = 2527 m/s will be referred as the "soft" elastic material, one with v_P/v_S = 1.7 and v_S = 3442 m/s as the "medium," and one with v_P/v_S = 1.5 and v_S = 5327 m/s as the "hard" elastic material for convenience. The variation of dimensionless Rayleigh wave velocity in these three materials in an external field of $\bar{B}_1$ = 25 Tesla is shown in Fig. 3 in which the dashed line represents $\alpha = \beta$ as before. It is interesting to note that in the soft material the transition between Zones I and II takes place at a lower μ_r than in the medium or hard material despite a larger interval of possible variation of $\bar{v}_R$. Figures 4(*a*)-(*b*) show the comparison of the z component of amplitude for the three materials. When μ_r = 1 (Fig. 4(*a*)) the decay characteristics are very similar for all three materials. But when μ_r = 100 (Fig. 4(*b*)) which falls into Zone II (Fig. 4(*b*)), the amplitude profiles are quite different for these three materials. In the case of the soft elastic material, the decay of amplitudes with depth is slow and exhibits an intensive oscillation as the imaginary part of α and β become more significant (due to greater distance to the transition between Zones I and II) compared to that of the other materials. For the medium and hard materials we can observe relatively mild and insignificant oscillations. This suggests that, in the vicinity of μ_r corresponding to the transition between Zones I and II, the intensity of oscillation and the penetration depth increase with elastic "softness" of a material.

Numerical results for the variation of dimensionless Rayleigh velocity for the three elastic materials in a normal magnetic field $\bar{B}_3$ are given in Figs. 5(*a*)-(*c*). As it was mentioned earlier, the effect of boundary conditions exhibits an asymptotic behavior of $\bar{v}_R$ with μ_r. As in Case I, $\bar{v}_R$ increases as μ_r increases for all materials under consideration, and the increase of v_R is more significant in the soft elastic material (Fig. 5(*c*)) than in the medium (Fig. 5(*b*)) or hard (Fig. 5(*a*)) material. Nevertheless, the characteristic of dependence is quite different from Case I. In the case when $\bar{B}_3$ = 100 Tesla, for example, the Rayleigh velocity approaches an asymptotic value which is

Downloaded 03 May 2010 to 171.66.16.247. Redistribution subject to ASME license or copyright; see http://www.asme.org/terms/Terms_Use.cfm

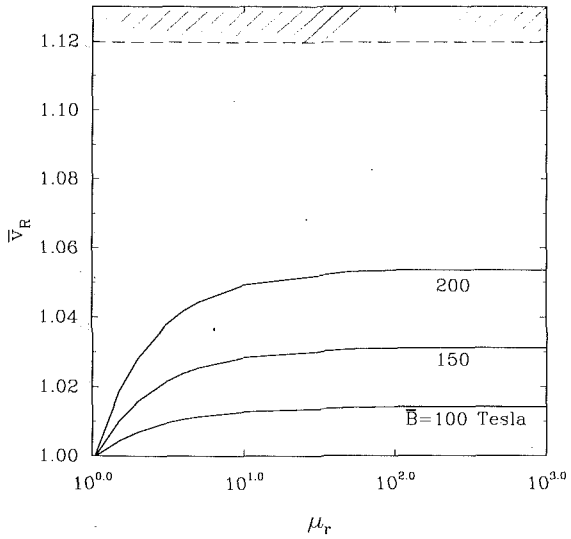


Fig. 5(*a*) "hard" material

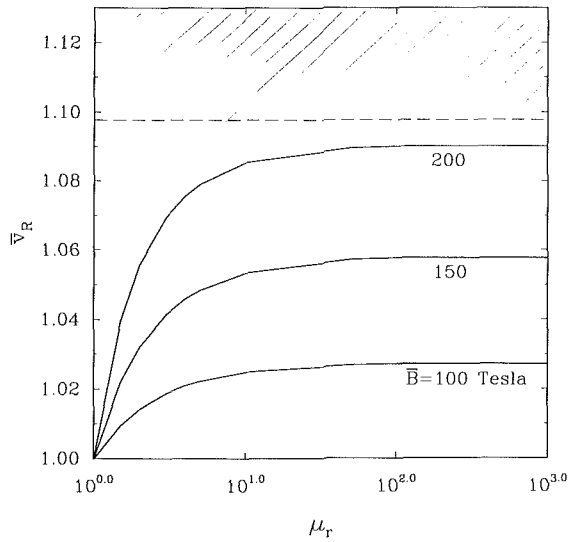


Fig. 5(*b*) "medium" material

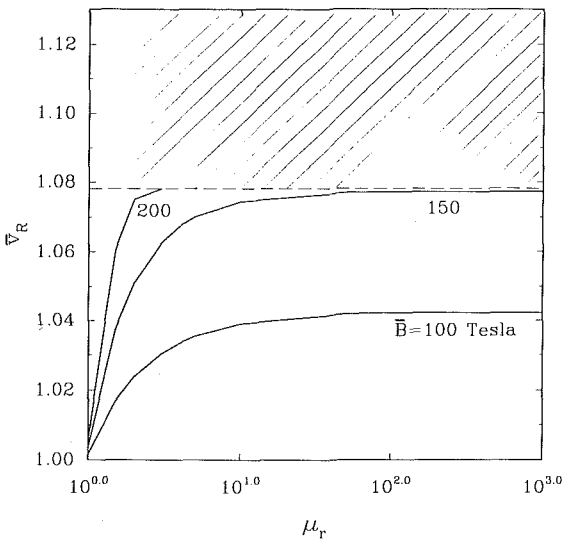


Fig. 5(*c*) "soft" material

Fig. 5 Variation of $\bar{v}_R$ in a normal magnetic field

considerably smaller than the limiting value ($v_R = v_S$) in all three materials and surface waves can exist for all values of magnetic permeability. The characteristic behavior of amplitude decay with depth changes very little for all values of $\bar{v}_R$ and is close to the one shown in Fig. 4(*a*). The asymptotic value of $\bar{v}_R$ grows larger as the velocity ratio v_P/v_S increases. In order to investigate the behavior of Rayleigh wave velocity near the limiting value $v_R = v_S$ we considered a very strong field $\bar{B}_3 = 200$ Tesla. For the hard and medium material the asymptotic values still remain under the limiting value of v_S (Figs. 5(*a*) and 5(*b*)). For the soft material, however, the asymptotic value ceases to exist resulting in a critical relative permeability beyond which surface waves do not exist (Fig. 5(*c*)). It is obvious that the critical values for the medium and hard materials can also be reached, but in an extremely strong magnetic field.

Numerical results presented in this section have demonstrated a strong variation of Rayleigh wave velocity in a tangential magnetic field for materials with different elastic and magnetic parameters. It has been shown that not only the Rayleigh wave velocity but also the decay characteristic of amplitudes with depth can vary dramatically with different elastic parameters. In the case of normal magnetic fields, the variation of Rayleigh velocity is limited to a small interval (below the value of shear wave velocity) and the wave amplitudes exhibit nonoscillatory decay with depth since exponents α and β are real. It has been shown that, in an extremely large normal field, Rayleigh waves can not exist beyond a critical value of μ_r, and the intensity of magnetic field for this critical behavior depends on elastic properties of the medium. Different characteristic dependences of Rayleigh velocity on the magnetic permeability under the action of magnetic fields reveal that the propagation of Rayleigh waves is rather sensitive to the direction of the magnetic field for all materials considered. This suggests that the stationarity of Rayleigh wave velocity with respect to an arbitrary magnetic field orientation may require a further investigation.

5 Conclusions

The propagation of Rayleigh waves in a conducting elastic half-space in contact with vacuum permeated by magnetic fields was considered for a possible application in nondestructive measurements of electromagnetic and elastic parameters in advanced electromagnetic materials. Assuming perfect conductivity, the dependence of Rayleigh wave velocity on magnetic and elastic parameters of the conductor for normal and tangential orientation of original field was investigated. This dependence was given in the form of simple expressions for the estimation of Rayleigh wave velocity in conducting media. Numerical results for the variation of Rayleigh wave velocity in three different elastic materials are presented for a wide range of magnetic permeability. It was shown that the variation of magnetic permeability (or Alfven velocity) of the conducting medium results in a dramatic change in Rayleigh wave velocity in the case of a tangential magnetic field. It was also shown that not only the Rayleigh velocity but also the decay characteristics of amplitude with depth strongly depend on both elastic and electromagnetic parameters of the medium. This suggests that by introducing a tangential magnetic field it is possible to use Rayleigh waves for studying properties of conducting materials beyond the typical depth of penetration (e.g., depth of one wavelength). It was shown in the case of a normal magnetic field that the variation of Rayleigh wave velocity is rather small even under the action of very strong magnetic fields and exhibits an asymptotic behavior. It was also shown that for an extremely strong magnetic field there exists a critical permeability beyond which Rayleigh waves cease to exist for a certain combination of elastic parameters.

Downloaded 03 May 2010 to 171.66.16.247. Redistribution subject to ASME license or copyright; see http://www.asme.org/terms/Terms_Use.cfm

6 Acknowledgments

This research was supported in part by a grant from the National Science Foundation (MSS-9009490). The authors gratefully acknowledge the support. The authors are also grateful to two anonymous reviewers for their valuable comments.

References

Basar, J., and Karal, F., 1971, "Simple Wave Motion in Magnetoelasticity," *Geophysical Journal of the Royal Astronomical Society*, Vol. 25, pp. 127–156.

Bleustein, J. L., 1968, "A New Surface Wave in Piezoelectric Materials," *Applied Physical Letters*, Vol. 13, pp. 412–414.

Dhar, P. K., 1979, "Coupled Electromagnetic and Elastic Waves in Random Media," *International Journal of Engineering Science*, Vol. 17, pp. 145–150.

Dunkin, J. W., and Eringen, A. C., 1963, "On the Propagation of Waves in an Electromagnetic Elastic Solid," *International Journal of Engineering Science*, Vol. 1, pp. 461–495.

Eringen, A. C., and Maugin, G. A., 1990, *Electrodynamics of Continua*, Vol. I, Springer-Verlag, New York.

Gulyaev, Y. V., 1969, "Electroacoustic Surface Waves in Solids," *Soviet Physics JETP*, Vol. 9, pp. 37–38.

Kaliski, S., and Rogula, D., 1960, "Rayleigh's Waves in a Magnetic Field in the case of Perfect Conductor," *Proceedings of Vibration Problems*, Vol. 1, pp. 63–80.

Kaliski, S., and Rogula, D., 1961, "Rayleigh Elastic Waves on Cylindrical Surfaces in Magnetic Fields," *Proceedings of Vibration Problems*, Vol. 2, pp. 29–39.

Kaliski, S., 1965, "Wave Equations of Thermo-Electro-Magnetoelasticity," *Proceedings of Vibration Problems*, Vol. 6, pp. 231–265.

Knopoff, L., 1955, "The Interaction between Elastic Wave Motion and a Magnetic Field in Electrical Conductors," *Journal of Geophysical Research*, Vol. 60, pp. 441–456.

Lee, J. S., Lee, P. C. Y., and Prevost, J. H., 1990, "Coupled Thickness Vibrations of Conductor Plates in Strong Magnetic Fields," *Computational Acoustics: Scattering, Gaussian Beams, and Aeroacoustics*, D. Lee, A. Cakmak, and R. Vichnevetsky, eds., North-Holland, Amsterdam, pp. 253–267.

Massalas, C. V., and Tsolakidis, I., 1990, "On Magneto-Thermo-Elastic Waves in Initially Stressed Conductors," *Ingenieur-Archiv*, Vol. 60, pp. 323–334.

Maugin, G. A., 1979, "A Continuum Approach to Magnon-Phonon Couplings: I and II," *International Journal of Engineering Science*, Vol. 17, pp. 1073–1108.

Maugin, G. A., 1981, "Wave Motion in Magnetizable Deformable Solids," *International Journal of Engineering Science*, Vol. 19, pp. 321–388.

Maugin, G. A., 1990, *Continuum Mechanics of Electromagnetic Solids*, North-Holland, Amsterdam.

Maugin, G. A., and Hakmi, A., 1985, "Magnetoelastic Surface Waves in Elastic Ferromagnets," *Journal of Acoustical Society of America*, Vol. 77, pp. 1010–1026.

Paria, G., 1962, "On Magneto-Thermo-Elastic Plane Waves," *Proceedings of Cambridge Philosophical Society*, Vol. 58, pp. 527–553.

Pouget, J., and Maugin, G. A., 1981a, "Surface Modes in Elastic Ferroelectrics," *Journal of Acoustical Society of America*, Vol. 69, pp. 1304–1318.

Pouget, J., and Maugin, G. A., 1981b, "Piezoelectric Rayleigh waves in Elastic Ferroelectrics," *Journal of Acoustical Society of America*, Vol. 69, pp. 1319–1325.

Rose, J. L., Nayfeh, A., and Pilarski, A., 1990, "Surface Waves for Material Characterization," ASME JOURNAL OF APPLIED MECHANCIS, Vol. 57, pp. 7–11.

Royer, D., and Dieulesaint, E., 1984, "Rayleigh Wave Velocity and Displacement in Orthorhombic, Tetragonal, Hexagonal and Cubic Crystals," *Journal of the Acoustical Society of America*, Vol. 76, pp. 1438–1444.

Tomita, S., and Shindo, Y., 1979, "Rayleigh Waves in Magneto-Thermoelastic Solid with Thermal Relaxation," *International Journal of Engineering Science*, Vol. 17, pp. 227–232.

Verma, P. D. S., 1986, "Magnetoelastic Shear Waves in Self-Reinforced Bodies," *International Journal of Engineering Science*, Vol. 24, pp. 1067–1073.

Viktorov, I. A., 1975, "Elastic Waves in a Solid Half-Space with a Magnetic Field," *Soviet Physics Proceedings*, Vol. 20, p. 273.

Willson, A. J., 1963, "The Propagation of Magneto-thermo-elastic Plane Waves," *Proceedings of Cambridge Philosophical Society*, Vol. 59, pp. 483–488.

Downloaded 03 May 2010 to 171.66.16.247. Redistribution subject to ASME license or copyright; see http://www.asme.org/terms/Terms_Use.cfm

S. H. Advani
Fellow ASME.

T. S. Lee
Assoc. Mem. ASME.

Department of Mechanical Engineering
and Mechanics,
Lehigh University,
Bethlehem, PA 18015

R. H. Dean
ARCO Oil and Gas Co.,
Plano, TX 75075

Variational Principles for Hydraulic Fracturing

A new application of an energy rate variational principle for hydraulic fracturing processes is introduced. The formation structural, fracture mechanics, and fracture fluid flow responses are integrally coupled in this treatment. This unified principle, with various specialized forms, provides a formal framework for the study of continuum as well as discrete models. The applicability of the developed formulations is demonstrated by deriving time-explicit solutions for a penny-shaped model and comparing numerical results with corresponding responses from Lagrangian and finite element methods.

Introduction

Hydraulic fracture processes involve the initiation and extension of cracks in target formations through the pressurized injection of proppant-laden viscous fluids at controlled rates (Veatch et al., 1989). Various methodologies have been employed for the evaluation of hydraulically-induced fracture responses, including both energy as well as variational approaches. Perkins and Krech (1968), based on the pioneering work of Sack (1946) and Barenblatt (1956), introduced the concept of a damage zone using a modified energy balance equation for the case of a nonpenetrating fracture fluid. The computed fracture extension pressures employing laboratory-determined Griffith surface energies are consistent with corresponding pressures measured in experimental models.

A variational formulation coupling the formation structural stiffness and fracturing fluid response via the crack fluid pressure was first advanced by Clifton and Abou-Sayed (1982). They employed separate variational principles for the formation structural responses and viscous fracture fluid flow, with the linear elastic fracture mechanics (LEFM) criterion expressed as an auxiliary equation. The subsequent discretizations for the crack width and pressure provide the underpinnings for the numerical solutions (Abou-Sayed et al., 1984; Clifton, 1989). A related variational technique for simulating fracture propagation has also been reported by Toubul et al. (1986).

The use of generalized coordinates, in a Lagrangian formulation, for deriving solutions associated with constant height hydraulic fracture models was motivated by Biot et al. (1986). The time-dependent generalized coordinates for this discrete model are defined from the admissible functions for the assumed crack dimensions and pressure profile. This technique is similar to the Rayleigh-Ritz type solution procedures which have traditionally served as precursors to advanced numerical techniques. Its applicability to elliptical (Advani et al., 1986) and penny-shaped (Advani et al., 1987) fractures has also been demonstrated. In the latter context, fundamental studies on the propagation of a penny-shaped crack have been conducted by Abe et al. (1976).

The significance of different energy contributions for examining fracture response phenomena has received considerable attention. Thiercelin et al. (1987) studied the influence of fracture toughness for penny-shaped cracks. They contrasted their results with those of Wong and Cleary (1985) who studied the limiting case of zero fracture toughness value in their previously developed model. Conversely, substantially enhanced fracture toughness scaling laws have been hypothesized by Shlyapobersky et al. (1988). The relative contributions of Griffith surface and viscous dissipation energy components have been systematically investigated by Lee et al. (1989). The ensuing characteristic time measures developed in these studies serve as diagnostic indicators for parametric sensitivity evaluation, fracture fluid selection, bottom-hole treatment pressure-flow analysis, and eventual fracture configuration control in multilayered reservoirs.

In this paper, application of a rigorous and integrated energy rate variational formulation governing the coupled structural, fluid flow, and fracture mechanics responses is detailed. This unified treatment not only provides a formal framework for investigating discrete Lagrangian models (Biot et al., 1986) with preselected configurations and lumped generalized forces but it also facilitates the formulation and computational work associated with advanced finite element hydraulic fracture simulators. Applications stemming from the theoretical development are detailed for a penny-shaped fracture.

Formulation of a General Energy Rate Functional

Consider a hydraulically-induced fracture represented by a planar vertical crack in a multilayered formation, as shown in Fig. 1. We denote the volumes of the reservoir (excluding the fracture) and the fluid (occupying the entire fracture) by $\Omega_s(t)$ and $\Omega_f(t)$, respectively. The fracture surface area and the crack front are designated by $A(t)$ and ∂A, respectively.

Contributed by the Applied Mechanics Division of THE AMERICAN SOCIETY OF MECHANICAL ENGINEERS for publication in the ASME JOURNAL OF APPLIED MECHANICS.

Discussion on this paper should be addressed to the Technical Editor, Professor Leon M. Keer, The Technological Institute, Northwestern University, Evanston, IL 60208, and will be accepted until four months after final publication of the paper itself in the ASME JOURNAL OF APPLIED MECHANICS.

Manuscript received by the ASME Applied Mechanics Division, Mar. 14, 1991; final revision, Nov. 12, 1991. Associate Technical Editor: J. W. Rudnicki.

Copyright © 1992 by ASME
Downloaded 03 May 2010 to 171.66.16.247. Redistribution subject to ASME license or copyright; see http://www.asme.org/terms/Terms_Use.cfm

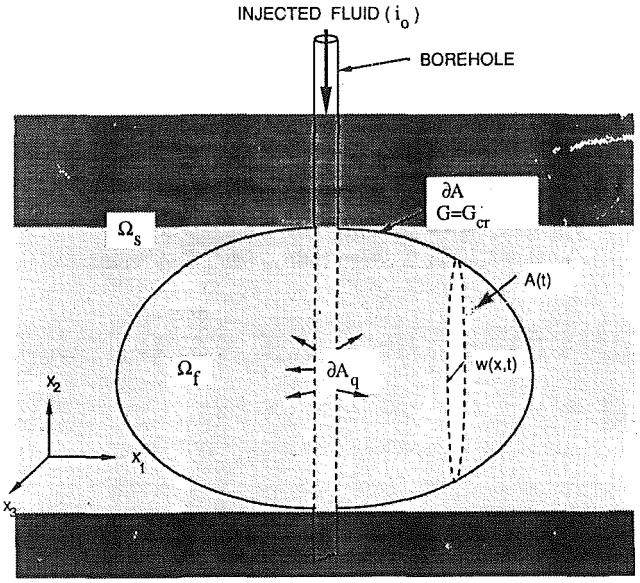


Fig. 1 Hydraulically-induced planar crack with arbitrary shape

A general form of an energy rate functional, coupling the elastic reservoir structural, linear elastic fracture mechanics, and viscous incompressible fracturing fluid, is motivated from Appendix A. This functional, obtained from the principle of virtual work, is

$$F(\mathbf{v}_s, \mathbf{v}_f, p, \dot{a}_n) = \frac{d}{dt}\int_{\Omega_s} e dv + \int_{\Omega_f} \psi dV + \int_{\Omega_f} v_{fi}(p_{,i} - f_{gi}) dV - 2\int_A p v_L dA - 2\int_A p v_{si} n_i dA + \frac{d}{dt}\int_A G_{cr} dA - \int_{\partial A_q} p v_{fn} dA \tag{1}$$

where e is the specific strain energy for the reservoir and ψ is the fracture fluid dissipation energy rate. For the crack, we note that the boundary areas for the crack surfaces are represented by $|\partial\Omega_s| = |\partial\Omega_f| = 2|A|$. These integrals over the area A in Eq. (1) are calculated for one face of the fracture only; the factor of two accounts for the opposite face. Also, the energy release rate $G_{cr} = 2\Gamma$ with Γ defined as the surface energy. In Eq. (1), $\mathbf{v}_s$, $\mathbf{v}_f$, and v_L denote the solid, fluid, and leakoff velocities, respectively, p designates the fracture fluid pressure, $\mathbf{n}$ is the unit vector normal to A and pointing outward from Ω_f, $\mathbf{f}_g$ is the fluid gravitational body force, and v_{fn} is the fracture fluid injection velocity at the boundary ∂A_q.

One can readily identify the origin of the various terms in Eq. (1) and pertinent mechanisms. The first term in Eq. (1) represents the rate of increase in strain energy in the solid and the second term is directly related to the rate of energy loss through fluid dissipation. The $v_{fi}p_{,i}$ term includes the rate at which the fracture fluid does work at the boundaries A and ∂A_q, and enforces the incompressibility constraint. The $-v_{fi}f_{gi}$ term represents the rate of increase in the gravitational potential. The terms $2pv_L$ and $2pv_{si}n_i$ account for the rate at which energy is lost through fluid leakoff, and the rate at which work is done on the solid. The term containing G_{cr} in Eq. (1) represents the rate at which energy goes into creating new surface area. Since v_{fn} is defined to be negative for injection, $-pv_{fn}$ represents the rate at which energy is supplied to the fracture at the injection boundary ∂A_q.

We introduce, in Eq. (1), the expressions

$$e = \frac{1}{2}\epsilon_{ij}C_{ijkl}\epsilon_{kl} + \sigma^o_{ij}\epsilon_{ij} \tag{2}$$

for the linear elastic formation subjected to initial stresses σ^o_{ij}, and

$$\psi = \frac{\eta_o}{1+m}(L_{ij}L_{ij})^{(1+m)/2} \tag{3}$$

for the power-law type non-Newtonian fracturing fluid ($\tau_{ij} = \eta_o|L|^{m-1}L_{ij}$), with η_o and m denoting the fluid consistency and behavior indices, respectively, and L_{ij} designating the components of the fluid velocity gradient tensor (defined in Appendix A). Also, we note that the fracture energy rate term in Eq. (1) can be equivalently written as

$$\frac{d}{dt}\int_{A(t)} G dA = \int_{\partial A} G_{cr}\dot{a}_n dS \tag{4}$$

with $\dot{a}_n$ representing the normal crack propagation velocity on ∂A. Equation (1) can now be rewritten in the form

$$F(\mathbf{v}_s, \mathbf{v}_f, p, \dot{a}_n) = \frac{d}{dt}\int_{\Omega_s}\left\{\frac{1}{2}\epsilon_{ij}C_{ijkl}\epsilon_{kl} + \sigma^o_{ij}\epsilon_{ij}\right\}dV + \frac{\eta_o}{1+m}\int_{\Omega_f}(L_{ij}L_{ij})^{(1+m)/2}dV + \int_{\Omega_f} v_{fi}(p_{,i} - f_{gi})dV - 2\int_A p v_{si} n_i dA - 2\int_A p v_L dA + \int_{\partial A} G_{cr}\dot{a}_n dS - \int_{\partial A_q} p v_{fn} dA. \tag{5}$$

We take variations with respect to the variables $\mathbf{v}_s$, $\mathbf{v}_f$, p, and $\dot{a}_n$ only. The solid displacement $\mathbf{u}_s$ and all spatial regions (Ω_s, Ω_f, A, ∂A, and ∂A_q) are not varied, and the first integral (strain energy term) in Eq. (5) must be expressed in terms of $\mathbf{v}_s$ and $\mathbf{u}_s$ only. We also assume that v_{fn} and v_L are prescribed with v_{fn} defined to be negative for injection.

The resulting Euler equations, obtained from setting the first variation of Eq. (5) to zero, are:
equilibrium equations for the reservoir,

$$(\sigma_{ij} + \sigma^o_{ij})_{,j} = 0 \text{ in } \Omega_s; \tag{6}$$

traction boundary conditions for the reservoir,

$$(\sigma_{ij} + \sigma^o_{ij})n_j + pn_i = 0 \text{ on } A; \tag{7}$$

fluid linear momentum equations for the fracturing fluid,

$$-p_{,j} + \tau_{ij,j} + f_{gi} = 0 \text{ in } \Omega_f; \tag{8}$$

fracturing fluid incompressibility equation,

$$v_{fi,i} = 0 \text{ in } \Omega_f; \tag{9}$$

fracturing fluid and reservoir velocity relations on the crack surface,

$$v_{fi}n_i = v_{si}n_i + v_L \text{ on } A; \tag{10}$$

injection flow condition for the fracturing fluid,

$$v_{fi}n_i = v_{fn} \text{ on } \partial A_q; \text{ and} \tag{11}$$

reservoir fracture propagation criterion,

$$G = G_{cr} \text{ on } \partial A. \tag{12}$$

We assume that the values of $\tau_{ij}n_j$ are negligible along the surface A and at the injection boundary, ∂A_q. For hydraulic fracturing studies, one can show that the deviatoric stress τ_{ij} are much smaller than the pressure p. The stationary value of the functional given by Eq. (5) yields the necessary field equations and boundary conditions for investigating the overall hydraulic fracture responses.

Simplified Energy-Rate Functionals

We simplify the general functional (5), for application to hydraulic fracturing, by using the boundary integral form for the crack-opening mode and invoking the lubrication flow approximation. Although the functional and associated anal-

Downloaded 03 May 2010 to 171.66.16.247. Redistribution subject to ASME license or copyright; see http://www.asme.org/terms/Terms_Use.cfm

ysis are applicable to a general state of in-situ stress σ_{ij}^o, we assume in the sequel that the crack is planar and that it propagates perpendicular to the minimum in-situ stress, $\sigma_o = -\sigma_{33}^o$, in the $x_3 = 0$ plane (Fig. 1).

First, the boundary integral representation of the strain energy term for the crack opening mode ($u_{s1} = u_{s2} = 0$, $u_{s3} = w/2$) can be written as (Bui, 1977)

$$\int_{\Omega_s} \frac{1}{2}\epsilon_{ij}C_{ijkl}\epsilon_{kl}dV = \frac{1}{2}B(w, w)_A \tag{13}$$

with the symmetric bilinear term $B(w, w)_A$ defined in terms of the crack opening width, w, by

$$B(w, w)_A = \int_A wK_A[w]dA$$
$$= \int_A w(x, t)\left\{\frac{\mu}{4\pi(1-\nu)}\int_A \frac{\partial}{\partial x_i}\left(\frac{1}{|x-\xi|}\right)\frac{\partial w(\xi, t)}{\partial \xi_i}dA\right\}dA \tag{14}$$

where $K_A[w]$ represents the boundary integral for the crack surface A and μ and ν, respectively, are the reservoir shear modulus and Poisson's ratio. The appropriate forms for a planar fracture in a multilayered formation, reported by Lee et al. (1988), have been obtained by extending the basic work by Lee and Keer (1986). We note that the integral expression (14) is defined in terms of the fracture opening width, w, and the fracture area, A, instead of the displacement, $\mathbf{u}_s$, and volume, Ω_s. This representation, therefore, significantly reduces the computational effort. The corresponding terms in Eq. (5), obtained by using Eqs. (13), (14), and Appendix B, for an opening mode planar crack, can be derived as

$$\frac{d}{dt}\int_{\Omega_s}\left\{\frac{1}{2}\epsilon_{ij}C_{ijkl}\epsilon_{kl} + \sigma_{ij}^o\epsilon_{ij}\right\}dV$$
$$= \int_A \dot{w}\{K_A[w] + \sigma_o\}dA + \int_{\partial A}\dot{a}_n\frac{\pi\mu}{8(1-\nu)}w\nabla w\cdot\mathbf{n}dS \tag{15}$$

where the gradient, ∇w, is defined with respect to the coordinates x_1 and x_2.

Next, from the lubrication flow approximation, we express the dissipation energy integral in the form

$$\frac{\eta_o}{1+m}\int_{\Omega_f}(L_{ij}L_{ij})^{(1+m)/2}dV$$
$$= \frac{\eta_o}{1+m}\int_A\int_{-w/2}^{w/2}(L_{ij}L_{ij})^{(1+m)/2}dx_3dA. \tag{16}$$

We now evaluate the volume integral for laminar Hele-Shaw flow behavior in a channel with width $w(x_1, x_2, t)$ and fluid pressure $p(x_1, x_2, t)$ using the relations (Clifton and Abou-Sayed, 1982)

$$v_{f1} = \frac{2m+1}{m+1}\left[1 - \left(\frac{|x_3|}{w/2}\right)^{(1+m)/m}\right]q_1/w \tag{17}$$

$$v_{f2} = \frac{2m+1}{m+1}\left[1 - \left(\frac{|x_3|}{w/2}\right)^{(1+m)/m}\right]q_2/w \tag{18}$$

$$\int_{-w/2}^{w/2} v_{f3}\,dx_3 = 0 \tag{19}$$

where q_i/w is the average velocity defined by

$$q_i = \int_{-w/2}^{w/2} v_{fi}\,dx_3. \tag{20}$$

The dissipation term can now be shown to have the form

$$\frac{\eta_o}{1+m}\int_{\Omega_f}(L_{ij}L_{ij})^{(1+m)/2}dV = \frac{\bar{\eta}}{1+m}\int_A\frac{|\mathbf{q}|^{1+m}}{w^{2m+1}}dA, \tag{21}$$

where $\bar{\eta} = \eta_o(2+1/m)^m 2^{1+m}$. Also, for a vertical planar crack we have

$$\int_{\Omega_f} v_{fi}(p_{,i} - f_{gi})dV = \int_A \mathbf{q}\cdot(\nabla p - \mathbf{f}_g)dA \tag{22}$$

and

$$\int_{-w/2}^{w/2} v_{fn}\,dx_3 = Q_n \text{ on } \partial A_q. \tag{23}$$

On the crack surface, A, the velocities are represented by

$$\dot{w}/2 = \mathbf{v}_s\cdot\mathbf{n} \text{ and } q_L = 2v_L. \tag{24}$$

Using Eqs. (15), (21), (22), (23), and (24), the functional (5) can be rewritten in the following simplified form:

$$F(\dot{w}, \mathbf{q}, p, \dot{a}_n) = \int_A \dot{w}\{K_A[w] - p + \sigma_o\}dA$$
$$+\frac{\bar{\eta}}{1+m}\int_A\frac{|\mathbf{q}|}{w^{2m+1}}dA + \int_A \mathbf{q}\cdot(\nabla p - \mathbf{f}_g)dA - \int_A pq_L dA$$
$$+\int_{\partial A}\dot{a}_n\left\{\frac{\pi\mu}{8(1-\nu)}w\nabla w\cdot\mathbf{n} + G_{cr}\right\}dS - \int_{\partial A_q} pQ_n dS. \tag{25}$$

The resulting Euler equations, obtained from the first variation of only the velocity-dependent and pressure terms in (25), are

$$\delta\dot{w}\text{: } K_A[w] = p - \sigma_o \text{ in } A \tag{26}$$

$$\delta p\text{: } \nabla\cdot\mathbf{q} + \dot{w} + q_L = 0 \text{ in } A \tag{27}$$

$$\mathbf{q}\cdot\mathbf{n} = Q_n \text{ along } \partial A_q \tag{28}$$

$$\delta\mathbf{q}\text{: } \bar{\eta}\frac{|\mathbf{q}|^{m-1}}{w^{2m+1}}\mathbf{q} + \nabla p - \mathbf{f}_g = \mathbf{0} \text{ in } A \tag{29}$$

$$\partial\dot{a}_n\text{: } -\frac{\pi\mu}{8(1-\nu)}w\nabla w\cdot\mathbf{n} = G_{cr} \text{ along } \partial A. \tag{30}$$

Another simplified form of the functional, using relation (29) and eliminating the flux, $\mathbf{q}$, from the generalized coordinates, can be derived as

$$F(\dot{w}, p, \dot{a}_n) = \int_A \dot{w}\{K_A[w] - p + \sigma_o\}dA - \int_A pq_L dA$$
$$-\frac{m}{1+m}(\bar{\eta})^{-1/m}\int_A w^{(2+1/m)}\{(\nabla p - \mathbf{f}_g)$$
$$\cdot(\nabla p - \mathbf{f}_g)\}^{(1+m)/(2m)}dA$$
$$+\int_{\partial A}\dot{a}_n\left\{\frac{\pi\mu}{8(1-\nu)}w\nabla w\cdot\mathbf{n} + G_{cr}\right\}dS - \int_{\partial A_q} pQ_n dS. \tag{31}$$

The Euler equations, resulting from (31) after applying the variational procedure and divergence theorem, are

$$\delta\dot{w}\text{: } K_A[w] = p - \sigma_o \text{ in } A \tag{32}$$

$$\delta p\text{: } -(\bar{\eta})^{-1/m}\nabla\cdot\{w^{(2+1/m)}|\nabla p - \mathbf{f}_g|^{(1-m)/m}(\nabla p - \mathbf{f}_f)\}$$
$$+\dot{w} + q_L = 0 \text{ in } A \tag{33}$$

$$Q_n = -(\bar{\eta})^{-1/m}\{w^{(2+1/m)}|\nabla p - \mathbf{f}_f|^{(1-m)/m}(\nabla p - \mathbf{f}_g)\}\cdot\mathbf{n}$$
$$\text{along } \delta A_q \tag{34}$$

$$\delta\dot{a}_n\text{: } -\frac{\pi\mu}{8(1-\nu)}w\nabla w\cdot\mathbf{n} = G_{cr} \text{ along } \partial A. \tag{35}$$

In summary, the functionals representing the mechanics of hydraulic fracturing are given by Eqs. (5), (25), or (31), depending on the inherent assumptions. Theoretically, the functional given by Eq. (31) can be expressed in terms of two variables, by eliminating the pressure variable using Eq. (32).

Downloaded 03 May 2010 to 171.66.16.247. Redistribution subject to ASME license or copyright; see http://www.asme.org/terms/Terms_Use.cfm

However, this additional reduction requires the derivation of a computationally tractable expression for $K_A[w]$, associated with preselected fracture geometries.

Applications: Discrete Penny-Shaped Model

We consider the hydraulically induced growth of a penny-shaped fracture in an isotropic formation. The fracture geometry at any time instant is approximated by the fracture radius ($R(t)$) and fracture opening width profile assumed as

$$w(r, t) = W_1(t)(1-\rho^2)^{1/2} + W_2(t)(1-\rho^2)^{3/2} \quad (36)$$

where $\rho = r/R$ is the normalized radial coordinate. The first term in Eq. (36) represents the crack singular behavior while the second term corresponds to the equilibrium crack growth condition (Barenblatt, 1956), satisfying a zero slope at the crack front ($\rho = 1$). The compatible polynomial expression for the effective pressure profile derived from the crack opening width profile (36) is

$$p(r, t) - \sigma_o = P(t)\{1 - \alpha(t)\rho^2\} \quad (37)$$

where σ_o is the reservoir minimum in-situ stress. The approximate distribution in Eq. (37) assumes that the fracturing fluid occupies the tip of the advancing fracture and ignores the pressure singularity at the front, arising from the lubrication approximation (Bui and Parnes, 1982).

The energy rate components and governing equations of motion corresponding to the five generalized coordinates, $\dot{W}_1$, $\dot{W}_2$, $\dot{R}$, P, and α, are derived in Appendix C. The governing elasticity Eqs. (C11) and (C12) can be re-expressed as

$$W_1 = \frac{4(1-\nu)}{\pi\mu} PR\left(1 - \frac{2}{3}\alpha\right) \quad (38)$$

$$W_2 = \frac{4(1-\nu)}{\pi\mu} PR\frac{4}{9}\alpha \quad (39)$$

along with the crack propagation condition from Eqs. (38), (39), and (C13)

$$\frac{\pi\mu}{8(1-\nu)R} W_1^2 = G_{cr}. \quad (40)$$

The mass conservation equation, deduced from Eqs. (C14) and (C15), is

$$i_o = \frac{d}{dt}\left(\frac{2\pi}{3} W_1R^2 + \frac{2\pi}{5} W_2R^2\right) + 4\pi C_L R^2 \int_0^1 \{t - \tau(\rho)\}^{-l}\rho d\rho \quad (41)$$

where the last term represents the fluid leakoff volume rate. The additional equation reflecting the variation in α (Eq. (C15)) is

$$2\pi R^2\left(\frac{2}{15}\dot{W}_1 + \frac{2}{35}\dot{W}_2\right) + 2\pi R\dot{R}\left(\frac{8}{15}W_1 + \frac{8}{35}W_2\right) - \frac{2\pi m}{2m+1}(\eta_o)^{-1/m}R^{(m-1)/m}\alpha^{1/m}P^{1/m}I(W_1, W_2, m) + 4\pi C_L R^2 J_l = 0 \quad (42)$$

where

$$J_l = \int_0^1 \frac{\rho^3}{\{t - \tau(\rho)\}^l} d\rho \quad (43)$$

and

$$I(W_1, W_2, m) = \int_0^1 [\rho(1-\rho^2)^{1/2}\{W_1 + W_2(1-\rho^2)\}]^{(2m+1)/m} d\rho. \quad (44)$$

The procedures for solving Eqs. (38) through (42), utilizing an incremental time marching scheme, are detailed in Appendix C.

Table 1 Constants for dissipation dominant solutions

m	$C_1(m)$	$C_2(m)$	$C_3(m)$
0.1	0.797	1.252	1.851
0.2	0.774	1.327	2.020
0.3	0.758	1.385	2.153
0.4	0.745	1.434	2.267
0.5	0.734	1.476	2.369
0.6	0.725	1.515	2.461
0.7	0.717	1.550	2.548
0.8	0.709	1.582	2.628
0.9	0.702	1.613	2.705
1.0	0.696	1.641	2.777

Table 2 Selected input parameters and characteristic values (Lee et al., 1989)

	Unit	Value
INPUT PARAMETERS		
Shear modulus (μ)	GPa	2.0
Poisson's ratio (ν)	–	0.2
Consistency index(η_o)	Pa–min^m	1.6E–4
Behavior index(m)	–	1.0
Injection rate(i_o)	m^3/min	5.0
Critical Energy Release Rate (G_{cr})	Pa–m	200
CHARACTERISTIC VALUES		
Time (τ)	min	1.0
Opening Width (W_o)	m	2.0E–3
Radius (R_o)	m	50
Pressure (P_o)	MPa	0.1

Asymptotic Solutions. In the absence of leakoff ($C_L = 0$), the solutions to Eqs. (38)–(42) are identical to the time-explicit forms derived from Lagrange's method (Lee et al., 1989). For the limiting case of negligible fracture energy ($G_{cr} = 0$), we obtain the following relations from Eqs. (38) through (41):

$$W_1 = 0,\ \alpha = 3/2,\ W_2 = \frac{8(1-\nu)}{3\pi\mu} PR,\ i_o = \frac{d}{dt}\left(\frac{2\pi}{5} W_2R^2\right). \quad (45)$$

Substituting these values into Eqs. (42), we have

$$R(t) = C_1(m)\left[\frac{i_o^{m+2}\mu}{\eta_o(1-\nu)}\right]^{\frac{1}{3(m+2)}} t^{\frac{2(m+1)}{3(m+2)}} \quad (46a)$$

$$W(t) = W_2(t) = C_2(m)\left[\frac{(1-\nu)^2 i_o^{m+2}\eta_o^2}{\mu^2}\right]^{\frac{1}{3(m+2)}} t^{\frac{2-m}{3(m+2)}} \quad (46b)$$

$$P(t) = C_3(m)\left[\frac{\mu^{m+1}\eta_o}{(1-\nu)^{m+1}}\right]^{\frac{1}{m+2}} t^{\frac{-m}{m+2}}. \quad (46c)$$

The numerical constants $C_i(m)$ are detailed in Table 1. The difference in the constant values using a previous Lagrangian formulation (Lee et al., 1989) can be attributed to the assumed

Downloaded 03 May 2010 to 171.66.16.247. Redistribution subject to ASME license or copyright; see http://www.asme.org/terms/Terms_Use.cfm

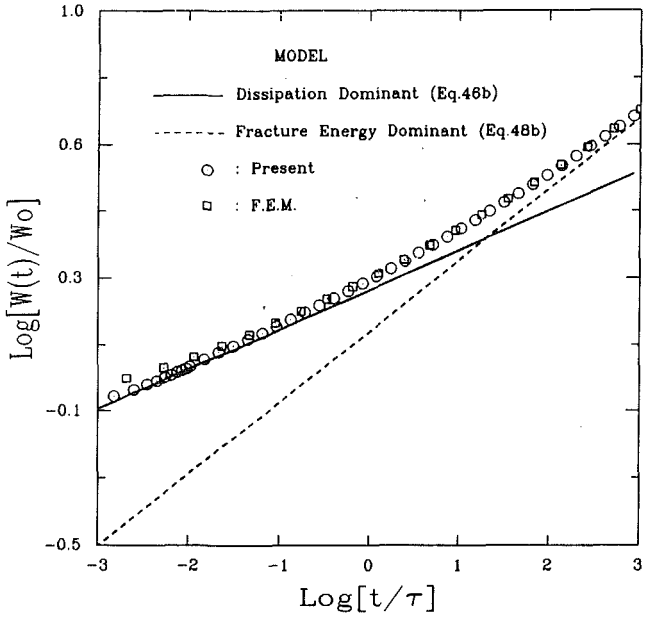


Fig. 2 Fracture opening width versus time comparisons for penny-shaped model

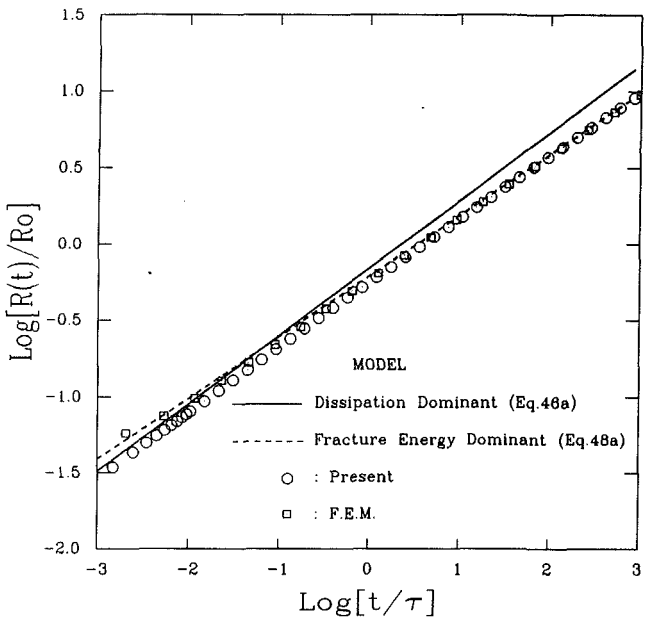


Fig. 3 Fracture radius versus time comparisons for penny-shaped model

constant crack pressure and corresponding elliptical crack opening width profile.

The other limiting threshold is characterized by zero dissipation energy rate ($\eta_o = 0$). This case correctly yields a constant pressure profile, and from Eqs. (38) through (42) we obtain

$$\alpha = 0,\ W_2 = 0,\ W_1 = \frac{4(1-\nu)}{\pi\mu} RP,\ i_o = \frac{d}{dt}\left(\frac{2\pi}{3} W_1 R^2\right) \tag{47}$$

$$R(t) = 0.617 \left[\frac{\mu i_o^2}{(1-\nu)G_{cr}}\right]^{1/5} t^{2/5} \tag{48a}$$

$$W(t) = W_1(t) = 1.254 \left[\frac{G_{cro}^{2\,i}(1-\nu)^2}{\mu^2}\right]^{1/5} t^{1/5} \tag{48b}$$

$$P(t) = 1.595 \left[\frac{\mu^2 G_{cr}^3}{(1-\nu)i_o^2}\right]^{1/5} t^{-1/5}. \tag{48c}$$

Numerical Results. For the cases wherein the effects of dissipation and fracture energy rate are both prevalent, the governing Eqs. (38) through (42) do not yield closed-form time-explicit solutions. Therefore, the nonlinear coupled differential equations are solved using a numerical procedure (Appendix C). To illustrate the transition of the solution behavior from the dissipation dominant regime to the fracture surface energy dominant regime, we select an example (Table 2) wherein the effects of dissipation and fracture energy are clearly evident. Figure 2 illustrates the numerical results and the transition of the bore-hole crack-opening width response from the dissipation dominant regime solution (Eq. (46*b*)) to the fracture energy dominant regime solution (Eq. (48*b*)). The results from a previously developed three-dimensional finite element simulator (Advani et al., 1990) are also included for comparison. The corresponding fracture radius and bottom-hole effective pressure responses are also presented in Figs. 3 and 4, respectively. The domain transition, for the fracture radius growth, is not discerned readily in Fig. 3 since the slope changes from a value of 0.44 (Eq. (46*a*) with $m = 1$) to 0.40 (Eq. (48*a*)). Another interpretation of this transition behavior can be found by examining the value of the pressure-width response variable $\alpha(t)$. The extreme values of α are 1.50 and 0 associated with the dissipation (Eq. (46)) and fracture energy dominant (Eq. (48)) regimes, respectively. The computed values of α, for this numerical example, decrease monotonically from 1.22 ($t = 5 \times 10^{-3}$ min) to 0.10 ($t = 1000$ min).

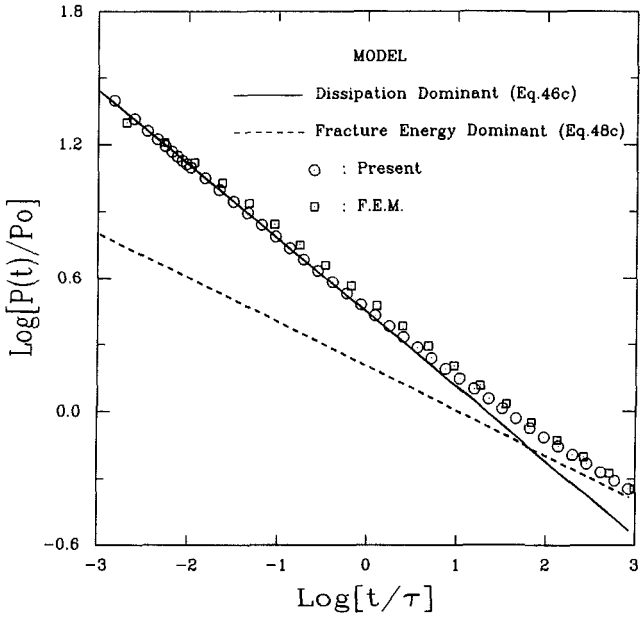


Fig. 4 Bottom-hole pressure versus time comparisons for penny-shaped model

Concluding Remarks

An application of variational principles integrating the elastic reservoir structural and fracture mechanics as well as fracture fluid flow behavior are presented. The formulations yield a comprehensive set of field equations for characterizing the overall hydraulic fracture responses. They also facilitate the computation of pertinent energy rates during fracture evolution. Application of the developed methodology for a penny-shaped fracture is readily demonstrated by using a Rayleigh-Ritz type solution technique. This procedure can also be implemented for the case wherein the lag in the fracturing fluid front relative to the crack-tip front is represented by an ad-

Downloaded 03 May 2010 to 171.66.16.247. Redistribution subject to ASME license or copyright; see http://www.asme.org/terms/Terms_Use.cfm

ditional generalized coordinate. It is believed, however, that in-situ stress effects in the presence of the fluid lag are less significant for penny-shaped rather than rectangular fractures. Investigations on the evolution of an elliptical fracture in a three-layered formation with stress contrasts and leakoff effects, using the presented variational formalism, are in progress.

Acknowledgment

This research is partially supported by Chevron Oil Field Research Inc., Conoco Inc., Mobil R&D Corp., U.S. Department of Energy, Amoco Foundation, and Cray Research Inc. The authors also acknowledge the generous support of the Ohio Supercomputer Center for use of its computational facilities.

References

Abe, H., Mura, T., and Keer, L. M., 1976, "Growth Rate of a Penny-Shaped Crack in Hydraulic Fracture of Rocks," *J. Geophysical Research*, Vol. 81, pp. 5335-5340.

Abou-Sayed, A. S., Clifton, R. J., Dougherty, R. L., and Morales, R. H., 1984, "Evaluation of the Influence of In-situ Reservoir Conditions on the Geometry of Hydraulic Fracture Using a 3D Model: Part 2—Case Studies," *Proc. Unconventional Gas Recovery Symposium*, Pittsburgh, SPE Paper No. 12878.

Advani, S. H., Lee, T. S., and Lee, J. K., 1990, "Three-Dimensional Modeling of Hydraulic Fractures in Layered Media: Part I—Finite Element Formulations," ASME *Journal of Energy Resources Technology*, Vol. 112, pp. 1-9.

Advani, S. H., Torok, J. S., and Lee, J. K., 1986, "Explicit Approximate Solutions Associated with the Mechanics of Hydraulic Fracturing," ASME JOURNAL OF APPLIED MECHANICS, Vol. 53, pp. 462-465.

Advani, S. H., Torok, J. S., Lee, J. K., and Choudhry, S., 1987, "Explicit Time-Dependent Solutions and Numerical Evaluations for Penny-Shaped Hydraulic Fracture Model," *J. Geophysical Research*, Vol. 92, pp. 8047-8055.

Barenblatt, G. I., 1956, "On Some Problems of the Theory of Elasticity Arising in Investigating the Mechanism of Hydraulic Fracture of an Oil-Bearing Stratum," *Prikl. Mat. Mech.*, Vol. 20, pp. 475-486.

Barenblatt, G. I., 1959, "Equilibrium Cracks Forming During Brittle Fracture," *Doklady Akad Nauk USSR*, Vol. 127, pp. 47-50.

Biot, M. A., Masse, L., and Medlin, W. L., 1986, "A Two Dimensional Theory of Fracture Propagation," *SPE Production Engineering*, Vol. 1, pp. 19-30.

Budiansky, B., and Rice, J. R., 1973, "Conservation Laws and Energy Release Rates," ASME JOURNAL OF APPLIED MECHANICS, Vol. 40, pp. 201-203.

Bui, H. D., 1977, "An Integral Equations Method for Solving the Problem of a Plane Crack of Arbitrary Shape," *J. Mech. Phys. Solids*, Vol. 25, pp. 29-39.

Bui, H. D., and Parnes, R., 1982, "A Reexamination of the Pressure at the Tip of Fluid Filled Crack," *Int. J. Engng Sci.*, Vol. 20, No. 11, pp. 1215-1220.

Clifton, R. J., and Abou-Sayed, A. S., 1982, "On the Mechanics of Hydraulic Fracturing," *Proc. Ninth U.S. National Congress of Applied Mechanics*, p. 443.

Clifton, R. J., 1989, "Three-Dimensional Fracture Propagation Models," *Recent Advances in Hydraulic Fracturing*, J. L. Gidley, et al., eds., Society of Petroleum Engineers, Richardson, Texas, Chapter 5.

Lee, J. C., and Keer, L. M., 1986, "Study of a Three-Dimensional Crack Terminating at an Interface," ASME JOURNAL OF APPLIED MECHANICS, Vol. 53, pp. 311-316.

Lee, T. S., Advani, S. H., Avasthi, J. M., and Lee, J. K., 1989, "Characteristic Time Concept Associated with Hydraulic Fracture Configuration Evolution and Optimization," *Proc. Low Permeability Reservoirs Symposium*, Denver, SPE Paper No. 19000, also *SPE Production Engineering*, pp. 323-333 (1991).

Lee, T. S., Advani, S. H., and Lee, J. K., 1988, "Three-Dimensional Analysis of an Arbitrary Shaped Pressurized Crack Traversing a Bi-Material Interface," *Eng. Frac. Mechanics*, Vol. 30, No. 2, pp. 191-209.

Perkins, T. K., and Krech, W. W., 1968, "The Energy Balance Concept of Hydraulic Fracturing," *Soc. Pet. Eng. J.*, Vol. 243, pp. 1-12.

Sack, R. A., 1946, "Extension of Griffith's Theory of Rupture to Three Dimensions," *Proc. Phys. Soc. of London*, Vol. 58, p. 729.

Shah, R. C., and Kobayashi, A. S., 1971, "Stress Intensity Factor for An Elliptical Crack Under Arbitrary Normal Loading," *Engineering Fracture Mechanics*, Vol. 3, pp. 71-96.

Shylyapobersky, J., Wong, G. K., and Walhaug, W. W., 1988, "Overpressure Calibrated Design of Hydraulic Fracture Simulations," SPE Paper No. 18194.

Thiercelin, M., Jeffrey, R. G., and Ben-Naceur, K., 1987, "The Influence of Fracture Toughness on the Geometry of Hydraulic Fractures," *Proc. Low Permeability Reservoirs Symposium*, Denver, SPE Paper No. 16431.

Touboul, E., BenNaceur, K., and Thiercelin, M., 1986, "Variational Methods in the Simulation of Three-Dimensional Fracture Propagation," *Proc. 27th US Symposium on Rock Mechanics*, Tuscaloosa, pp. 659-668.

Veatch, R. W., Jr., Moschovidis, Z. A., and Fast, C. R., 1989, "An Overview of Hydraulic Fracturing," *Recent Advances in Hydraulic Fracturing*, J. L. Gidley et al., eds., Society of Petroleum Engineers, Richardson, Texas, Chapter 1.

Wong, S. K., and Cleary, M. P., 1985, "Numerical Simulation of Unsteady Fluid Flow and Propagation of a Circular Fracture," *Int. J. Num. and Anal. Meth. in Geomech.*, Vol. 9, pp. 1-14.

APPENDIX A

Rate Form of Principle of Virtual Work

To demonstrate the physical relevance of the energy-rate functional (Eq. (1)) and its relationship with the traditional principle of virtual work (PVW), we express the PVW for the hydraulic fracturing process in the form

$$\int_{\Omega_s} \hat{\sigma}_{ij}\delta\dot{\epsilon}_{ij}dVf + \int_{\Omega_f} \tau_{ij}\delta L_{ij}dV - \int_{\Omega_f} f_{gi}\delta v_{fi}dV + 2\int_A (p - n_i\tau_{ij}n_j)\delta v_L dA + \int_{\partial A} (G_{cr} - G)\delta\dot{a}_n\, dS + \int_{\partial A_q} (p - n_i\tau_{ij}n_j)\delta v_{fn}dA + \int_{\Omega_f} \lambda\delta v_{fi,i}dV = 0 \quad \text{(A1)}$$

where $\hat{\sigma}_{ij} = \sigma_{ij} + \sigma^o_{ij}$ is the total formation stress tensor component and τ_{ij} is the deviatoric stress tensor component for the fluid. The variations $\delta\dot{\epsilon}_{ij}$ in Eq. (A1) are restricted to those values of $\delta\dot{\epsilon}_{ij}$ which are compatible with the current fracture configuration. Energy contributions due to a moving fracture front are contained in the energy release rate G. The strain rate and velocity gradient tensor components above are defined by

$$\dot{\epsilon}_{ij} = \frac{1}{2}\left(\frac{\partial v_{si}}{\partial x_j} + \frac{\partial v_{sj}}{\partial x_i}\right) \text{ and } L_{ij} = \frac{1}{2}\left(\frac{\partial v_{fi}}{\partial x_j} + \frac{\partial v_{fj}}{\partial x_i}\right). \quad \text{(A2)}$$

The Lagrange multiplier associated with the last integral in Eq. (A1), for the incompressible fracturing fluid, can be shown to be equal to the fluid pressure, i.e.,

$$\lambda = -p. \quad \text{(A3)}$$

In converting Eq. (A1) to a functional, we retain variations in the variables $\mathbf{v}_s$, $\mathbf{v}_f$, p, and $\dot{a}_n$ only. We do not take variations with respect to $\mathbf{u}_s$ or the physical boundaries.

We now convert Eq. (A1) to a functional form, useful for applications. Since the fluid is incompressible, we require $v_{fi,i} = 0$ in Ω_f and write, after use of the divergence theorem and algebraic manipulations, the identity

$$-\int_{\Omega_f} p\delta v_{fi,i}\, dV = \delta\int_{\Omega_f} p_{,i}v_{fi}dV - 2\delta\int_A v_{fi}n_i pdA - \delta\int_{\partial A_q} pv_{fi}n_i dA$$

to obtain

$$\int_{\Omega_s} \hat{\sigma}_{ij}\delta\dot{\epsilon}_{ij}dV + \int_{\Omega_f} \tau_{ij}\delta L_{ij}dV + \delta\int_{\Omega_f} (p_{,i} - f_{gi})v_{fi}dV - 2\int_A \delta p v_L dA + \int_{\partial A} (G_{cr} - G)\delta\dot{a}_n dS - \int_{\partial A_q} v_{fn}\delta p dA + 2\delta\int_A (v_L - v_{fi}n_i)pdA - 2\int_A n_i\tau_{ij}n_j\delta v_L dA - \int_{\partial A_q} n_i\tau_{ij}n_j\delta v_{fn}dA = 0.$$

Introducing, without loss of generality of the constitutive laws, the relations

Downloaded 03 May 2010 to 171.66.16.247. Redistribution subject to ASME license or copyright; see http://www.asme.org/terms/Terms_Use.cfm

$$\frac{\partial e}{\partial \epsilon_{ij}} = \hat{\sigma}_{ij} \text{ and } \frac{\partial \psi}{\partial L_{ij}} = \tau_{ij} \tag{A5}$$

and the energy release rate expression (Budiansky and Rice, 1974)

$$\delta \frac{d}{dt} \int_{\Omega_s} e dV = \int_{\Omega_s} \hat{\sigma}_{ij} \delta \dot{\epsilon}_{ij} \, dV - \int_{\partial A} G \delta \dot{a}_n \, dS \tag{A6}$$

in Eq. (A4), we obtain the desired functional form

$$\delta F(\mathbf{v}_s, \mathbf{v}_f, p, \dot{a}_n) = \delta \left\{ \frac{d}{dt} \int_{\Omega_s} e dV + \int_{\Omega_f} \psi dV + \int_{\Omega_f} (p_{,i} - f_{gi}) v_{fi} dV - 2 \int_A p v_L dA + \int_{\partial A} G_{cr} \dot{a}_n dS - \int_{\partial A_q} v_{fn} p dA - 2 \int_A v_{si} n_i \, p dA \right\} = 0. \tag{A7}$$

In Eq. (A6), the energy release rate G is expressed as a function of current configuration and displacement (Appendix B). Therefore, its variation with respect to velocity term and loading are neglected. We note here that, in deriving (A7), the velocity constraint expression $v_{fi} n_i = v_{si} n_i + v_L$ is used along with explicitly assumed leakoff and fluid injection velocities ($\delta v_L = \delta v_{fn} = 0$). Also, in considering the variation of the strain energy e above, only the variations with respect to the solid velocity v_{si} and crack propagation velocity $\dot{a}_n$ are considered.

APPENDIX B

Energy Release Rate for a Planar Crack

The principle of virtual work in Appendix A contains the term

$$\int_{\partial A} G \delta \dot{a}_n dS \tag{B1}$$

where G is the energy release rate. Assuming that the crack tip experiences plane strain, mode I loading conditions in a neighborhood near the crack tip, we have

$$w(d) = \frac{4(1-\nu)}{\mu} K_I \sqrt{d/2\pi} \tag{B2}$$

where $w(d)$ is the fracture opening at a small distance d inside the fracture with d measured normal to the leading edge of the fracture.

From Eq. (B2), near the edge of the fracture, we obtain

$$w \nabla w \cdot \mathbf{n} = -\frac{4(1-\nu)^2}{\pi \mu^2} K_I^2 \tag{B3}$$

where $\mathbf{n}$ points in the direction of fracture propagation. Since

$$G = \frac{(1-\nu)}{2\mu} K_I^2 \tag{B4}$$

we can write Eq. (B1) in the form

$$\int_{\partial A} G \delta \dot{a}_n dS = -\int_{\partial A} \left\{ \frac{\pi \mu}{8(1-\nu)} w \nabla w \cdot \mathbf{n} \right\} \delta \dot{a}_n \, dS. \tag{B3}$$

The energy release rate integral above is now expressed as a function of the current crack configuration and displacement.

APPENDIX C

Governing Equations and Solution Procedure for Penny-Shaped Crack

The energy rate components in Eq. (31) are derived using the curtailed two-term crack opening width and fracture fluid profiles given by Eqs. (36) and (37), respectively. The corresponding boundary integral $K_A[w]$ has the form (Shah and Kobayashi, 1971)

$$K_A[w] = \frac{\pi \mu}{4(1-\nu)R} \left(W_1 + \frac{3}{2} W_2 - \frac{9}{4} W_2 \rho^2 \right). \tag{C1}$$

The general series form expression for $K_A[w]$ for a penny-shaped crack corresponding to a polynomial series describing the internal pressure can be obtained from the results of Shah and Kobayashi (1971) by inversion of the appropriate coefficient matrix. The crack opening width rate from Eq. (36) is given by

$$\dot{w} = \dot{W}_1 (1-\rho^2)^{1/2} + \dot{W}_2 (1-\rho^2)^{3/2} + \dot{R}/R \, \rho^2 \{ W_1 (1-\rho^2)^{-1/2} + 3 W_2 (1-\rho^2)^{1/2} \}. \tag{C2}$$

The pertinent energy rate components from Eqs. (C1) and (C2) are

$$\dot{U}_s = \int_A \dot{w} K_A[w] dA = \frac{\pi^2 \mu R}{2(1-\nu)} \left\{ \dot{W}_1 \left(\frac{1}{3} W_1 + \frac{1}{5} W_2 \right) + \dot{W}_2 \left(\frac{1}{5} W_1 + \frac{6}{35} W_2 \right) \right\} + \frac{\pi^2 \mu \dot{R}}{2(1-\nu)} \left(\frac{2}{3} W_1^2 + \frac{1}{5} W_1 W_2 + \frac{3}{35} W_2^2 \right) \tag{C3}$$

$$\dot{U}_p = \int_A \dot{w} (p - \sigma_o) dA = 2\pi R^2 P \left\{ \dot{W}_1 \left(\frac{1}{3} - \frac{2\alpha}{15} \right) + \dot{W}_2 \left(\frac{1}{5} - \frac{2\alpha}{35} \right) \right\} + 2\pi R \dot{R} P \left\{ \frac{2}{3} \left(1 - \frac{4\alpha}{5} \right) W_1 + \frac{2}{5} \left(1 - \frac{4\alpha}{7} \right) W_2 \right\} \tag{C4}$$

$$D_p = \frac{m}{1+m} (\bar{\eta})^{-1/m} \int_A w^{(2+1/m)} \{ (\nabla p - \mathbf{f}_g) \cdot (\nabla p - \mathbf{f}_g) \}^{(1+m)/(2m)} dA = \frac{2\pi m^2}{(1+m)(2m+1)} (\eta_o)^{-1/m} R^{(m-1)/m} (\alpha P)^{(m+1)/m} I(W_1, W_2, m), \tag{C5}$$

where

$$I(W_1, W_2, m) = \int_0^1 [\rho (1-\rho^2)^{1/2} \{ W_1 + W_2 (1-\rho^2) \}]^{(2m+1)/m} d\rho$$

$$\dot{U}_\Gamma = \int_{\partial A} \dot{a}_n \left\{ \frac{\pi \mu}{8(1-\nu)} w \nabla w \cdot \mathbf{n} dS = -\frac{\pi^2 \mu}{4(1-\nu)} \dot{R} W_1^2 \right. \tag{C6}$$

$$\dot{U}_f = \int_{\partial A} G_{cr} \dot{a}_n dS = 2\pi G_{cr} R \dot{R} \tag{C7}$$

$$D_I = \int_{\partial A_q} p Q_n dA = -i_o P \tag{C8}$$

$$D_L = \int_A p q_L dA = 4\pi C_L R^2 P J(\alpha), \tag{C9}$$

where

$$J(\alpha) = \int_0^1 \frac{1 - \alpha \rho^2}{\{ t - \tau(\rho) \}^l} \rho d\rho.$$

Downloaded 03 May 2010 to 171.66.16.247. Redistribution subject to ASME license or copyright; see http://www.asme.org/terms/Terms_Use.cfm

We note that the normal boundary flux Q_n in Eq. (31) corresponds to an outward normal along the boundary ∂A_q, i.e., $Q_n = -i_o$ in Eq. (C8).

We define the functional (Eq. (31)), using Eqs. (C3) through (C9), as

$$F(\dot{W}_1, \dot{W}_2, P, \alpha, \dot{R}) = \dot{U}_s - \dot{U}_p - D_p - D_L - D_I + \dot{U}_\Gamma + \dot{U}_f \tag{C10}$$

and obtain the following governing equations from the first variation:

$$\delta\dot{W}_1: \frac{\pi^2\mu R}{2(1-\nu)}\left(\frac{1}{3}W_1 + \frac{1}{5}W_2\right) = 2\pi R^2 P\left(\frac{1}{3} - \frac{2\alpha}{15}\right) \tag{C11}$$

$$\delta\dot{W}_2: \frac{\pi^2\mu R}{2(1-\nu)}\left(\frac{1}{5}W_1 + \frac{6}{35}W_2\right) = 2\pi R^2 P\left(\frac{1}{5} - \frac{2\alpha}{35}\right) \tag{C12}$$

$$\delta\dot{R}: \frac{\pi^2\mu}{2(1-\nu)}\left(\frac{2}{3}W_1^2 + \frac{1}{5}W_1W_2 + \frac{3}{35}W_2^2\right) - 2\pi RP\left\{\frac{2}{3}\left(1 - \frac{4\alpha}{5}\right)W_1 + \frac{2}{5}\left(1 - \frac{4\alpha}{7}\right)W_2\right\} - \frac{\pi^2\mu}{4(1-\nu)}W_1^2 + 2\pi G_{cr}R = 0 \tag{C13}$$

$$\delta P: -2\pi R^2\left\{\dot{W}_1\left(\frac{1}{3} - \frac{2\alpha}{15}\right) + \dot{W}_2\left(\frac{1}{5} - \frac{2\alpha}{35}\right)\right\} - 2\pi R\dot{R}\left\{\frac{2}{3}\left(1 - \frac{4\alpha}{5}\right)W_1 + \frac{2}{5}\left(1 - \frac{4\alpha}{7}\right)W_2\right\} - \frac{2\pi m}{2m+1}(\eta_o)^{-1/m}R^{(m-1)/m}\alpha^{(m+1)/m}P^{1/m}I(W_1, W_2, m) - 4\pi C_L R^2 J(\alpha) + i_o = 0 \tag{C14}$$

$$\delta\alpha: 2\pi R^2 P\left(\frac{2}{15}\dot{W}_1 + \frac{2}{35}\dot{W}_2\right) + 2\pi R\dot{R}P\left(\frac{8}{15}W_1 + \frac{8}{35}W_2\right) - \frac{2\pi m}{2m+1}(\eta_o)^{-1/m}R^{(m-1)/m}\alpha^{1/m}P^{(m+1)/m}I(W_1, W_2, m) + 4\pi C_L R^2 P J_I = 0 \tag{C15}$$

where

$$J_I = \int_0^1 \frac{\rho^3}{\{t - \tau(\rho)\}^I}\, d\rho.$$

Equations (C10) through (C15) can be rewritten in the form

$$f_1 = \frac{\pi\mu}{4(1-\nu)}W_1 - PR\left(1 - \frac{2}{3}\alpha\right) = 0 \tag{C16}$$

$$f_2 = \frac{9\pi\mu}{16(1-\nu)}W_2 - PR\alpha = 0 \tag{C17}$$

$$f_3 = \frac{\pi\mu}{8(1-\nu)}W_1^2 - G_{cr}R = 0 \tag{C18}$$

$$f_4 = 2\pi\frac{d}{dt}\left\{R^2\left(\frac{1}{3}W_1 + \frac{1}{5}W_2\right)\right\} + 4\pi C_L R^2\int_0^1 \{t - \tau(\rho)\}^{-I}\rho\, d\rho - i_o = 0 \tag{C19}$$

$$f_5 = (\eta_o R^{m+2})^{1/m}\left(\frac{2}{15}\dot{W}_1 + \frac{2}{35}\dot{W}_2\right) + (\eta_o R^2)^{1/m}\dot{R}\left(\frac{8}{15}W_1 + \frac{8}{35}W_2\right) - \frac{m}{2m+1}\left\{\frac{9\pi\mu}{16(1-\nu)}W_2\right\}^{1/m} I(W_1, W_2, m) + 2C_L(\eta_o R^{m+2})^{1/m}J_I = 0. \tag{C20}$$

The developed numerical solution procedure is devised so that Eqs. (C16) through (C20) are simultaneously satisfied, i.e., $f_i^{t+\Delta t} = 0$ at time $t + \Delta t$ using the implicit time marching scheme. We note that Eqs. (C18), (C19), and (C20) can be solved for W_1, W_2, and R using the standard Newton-Raphson iterative method. The iteration is terminated when the convergence, expressed in terms of relative error is achieved within a tolerance of 0.1 percent. The pressure, P, and variable, α, are, obtained from Eqs. (C16) and (C17) using the converged solutions. The solutions are, then, updated for the subsequent time step.

Downloaded 03 May 2010 to 171.66.16.247. Redistribution subject to ASME license or copyright; see http://www.asme.org/terms/Terms_Use.cfm

J. H. Kane
Assoc. Professor,
Mem. ASME.

G. Zhao
Postgraduate Research Associate.

H. Wang
Graduate Research Assistant.

K. Guru Prasad
Graduate Research Assistant.

Mechanical and Aeronautical Engineering,
Clarkson University,
Potsdam, NY 13699

Boundary Formulations for Three-Dimensional Continuum Structural Shape Sensitivity Analysis

The direct, singular, boundary element analysis formulation is shown to provide a basis for a computationally efficient and accurate shape design sensitivity analysis approach for the structural response of three-dimensional solid objects. The theoretical formulation for surface displacement and traction component sensitivities, and all components of the stress tensor is presented along with a formulation for the recovery of displacement and stress components in the interior of the object under consideration. Discussion of computational issues related to the overall efficiency of these formulations is given, along with numerical results to demonstrate the accuracy and efficiency of this approach.

Introduction

Design sensitivity analysis refers to the process of computing the rates of change of an object's response with respect to changes in the design variables that control its shape. These sensitivities are used in shape optimization by numerical optimization procedures to determine effective search directions and move lengths in the space of the design variables and their accurate computation is a pacing item in making larger scale shape optimization tractable. Implicit differentiation of discretized boundary integral equations has been effective for the formulation of design sensitivity analysis relations in two-dimensional linear heat transfer and stress analysis. This approach obviates the requirement to factor perturbed left-hand side matrices, but instead allows for multiple reuse of the $[L][U]$ factorization of the current boundary element analysis system matrix formed during a previous analysis. Kane (1986, 1987) and Kane and Saigal (1988) and Saigal and Kane (1990) have demonstrated implicit differentiation as effective for determination of surface displacement and traction component sensitivities. In subsequent boundary element analysis publications, they have treated axisymmetric solids (Saigal, Borggaard, and Kane, 1989), thermoelastic and other body forces (Kane, Kumar, and Stabinsky, 1990), coupled problems (Kane, 1990), and developed both a semi-analytical (Saigal, Kane, and Aithal, 1989) and a simultaneous (Kane and Stabinsky, 1988) algorithm for design sensitivity analysis, and included boundary element substructuring (Kane, Kumar, and Saigal, 1990), providing significant improvements in computational efficiency. For two-dimensional thermal problems with nonlinear boundary conditions (Kane and Wang, 1991) and temperature-dependent conductivity (Kane and Wang, 1992), an iterative solution of the nonlinear discretized boundary integral equations for sensitivity analysis was accomplished. For these nonlinear problems, multizone analysis and zone condensation strategies were shown to provide substantive computational economies for models with either localized nonlinear boundary conditions or regions of geometric insensitivity to design variables.

In this paper, a theoretical formulation for the matrix sensitivities required in the approach is given that includes sensitivities of three-dimensional fundamental displacement and traction solutions, unit normal vectors, and boundary element Jacobians. This formulation employs quadratic isoparametric boundary elements, and is sufficient for computation of sensitivities of unknown boundary displacement and traction components on the surface of the model. For objects with partial geometric sensitivity, these matrix sensitivities exhibit significant sparsity, and its exploitation is shown to yield considerable savings in computation. A formulation for recovery of sensitivities of stress components on the surface of the model that are *not* surface tractions is presented and it does not require numerical integration. Formulae for recovery of displacement and stress components at interior sample points is also presented. A series of example problems are examined with computed sensitivities compared to analytic sensitivities and CPU timings reported. A problem with considerable stress concentration is used to illustrate a case where sensitivities of global components of the stress tensor can be computed for surface sample points that undergo changes in their local tangential and normal coordinate systems.

Sensitivity Formulation for Surface Displacement and Traction Components

As shown in Kane (1986) and Kane and Saigal (1988), implicit

Contributed by the Applied Mechanics Division of THE AMERICAN SOCIETY OF MECHANICAL ENGINEERS for publication in the ASME JOURNAL OF APPLIED MECHANICS.

Discussion on this paper should be addressed to the Technical Editor, Prof. Leon M. Keer, The Technological Institute, Northwestern University, Evanston, IL 60208, and will be accepted until four months after final publication of the paper itself in the JOURNAL OF APPLIED MECHANICS.

Manuscript received by the ASME Applied Mechanics Division, Oct. 4, 1990; final revision, Apr. 28, 1991. Associate Technical Editor: R. L. Huston.

Copyright © 1992 by ASME
Downloaded 03 May 2010 to 171.66.16.247. Redistribution subject to ASME license or copyright; see http://www.asme.org/terms/Terms_Use.cfm

differentiation of the boundary element analysis algebraic system equations yields

$$\frac{\partial}{\partial X_L}\left([F]\{u\}=[G]\{t\}\right) \tag{1}$$

or

$$[F]\{u\}_{,L}=\left([G]_{,L}\{t\}-[F]_{,L}\{u\}\right) \tag{2}$$

where $[F]$ and $[G]$ are boundary element analysis coefficient matrices corresponding to the column vectors of nodal point unknown response components in $\{u\}$ will contain displacements at nodes with specified tractions and will contain tractions at nodes where displacement components are specified. In the above expression, X_L represents the Lth design variable. Equation (2) reveals a fundamental characteristic of the implicit differentiation approach to design sensitivity analysis. *If the right-hand side vector shown above can be formed, then the unknown nodal response sensitivity vector* $\{u\}_{,L}$ *can be determined by solving Eq. (2), by forward reduction and back substitution, using the* [L][U] *factorization of the left-hand side matrix* [F] *computed in the previous analysis step.*

The entries in the matrix sensitivities shown in Eq. (2) are assembled from contributions associated with pairs of elements and load points as

$$[F]_{,L}^{(E,P)}=\int_0^1\int_0^{1-a_2}\left([T]_{,L}^{T}[H]g+[T]^T[H]g_{,L}\right)da_1da_2 \tag{3}$$

and

$$[G]_{,L}^{(E,P)}=\int_0^1\int_0^{1-a_2}\left([U]_{,L}^{T}[H]g+[U]^T[H]g_{,L}\right)da_1da_2. \tag{4}$$

$[U]_{,L}$ and $[T]_{,L}$ are sensitivities of the 3 × 3 matrix of components of fundamental displacement and traction solutions, respectively, for the elasticity problem for element E due to three unit point loads in each of the coordinate directions at load point P. $g_{,L}$ is the sensitivity of the determinant of the Jacobian matrix for the transformation from intrinsic (isoparametric) coordinates a_i, to real element coordinates x_i, for example, for a 6-noded isoparametric element. $[H]$ is a 3 × 18 matrix of interpolation (shape) functions $h^{(n)}$ for such an element. Sensitivity expressions for these quantities are

$$u^*_{ij,L}=k_1\rho^{-1}\{-\rho^{-1}\rho_{,L}(k_2\delta_{ij}+\rho_{,i}\rho_{,j})+(\rho_{,iL}\rho_{,j}+\rho_{,i}\rho_{,jL})\} \tag{5}$$

and

$$\begin{aligned}t^*_{ij,L}=k_3\rho^{-2}[&-2\rho_{,L}\{\rho_{,k}n_k[k_4\delta_{ij}+3\rho_{,i}\rho_{,j}]\\&-k_4[\rho_{,i}n_j-\rho_{,j}n_i]\}+(\rho_{,kL}n_k+\rho_{,k}n_{k,L})[k_4\delta_{ij}+3\rho_{,i}\rho_{,j}]\\&+3\rho_{,k}n_k(\rho_{,iL}\rho_{,j}+\rho_{,i}\rho_{,jL})-k_4[\rho_{,iL}n_j\\&+\rho_{,i}n_{j,L}-\rho_{,jL}n_i-\rho_{,j}n_{i,L}]]\end{aligned} \tag{6}$$

where

$$k_1=\frac{1}{16\pi\mu(1-\nu)};\quad k_2=3-4\nu;$$

$$k_3=\frac{-1}{8\pi(1-\nu)};\quad k_4=1-2\nu \tag{7}$$

and

$$\rho=(y_ky_k)^{1/2} \tag{8}$$

$$\rho_{,i}=y_i\rho^{-1} \tag{9}$$

$$\rho_{,L}=y_ky_{k,L}\rho^{-1} \tag{10}$$

$$\rho_{,iL}=y_{i,L}\rho^{-1}-\rho^{-3}y_iy_ky_{k,L} \tag{11}$$

$$y_{i,L}=x_{i,L}-d_{i,L} \tag{12}$$

also

$$n_{i,L}=g_{i,L}g^{-1}-g_ig^{-2}g_{,L} \tag{13}$$

where

```
      form k1 k2 k3 & k4
      for each E
            if both E and all P's are geometrically insensitive to XL
                  then go to skip1
c     compute (once) element geometric data at all integration points
            form x,i g,i g & ni
            if E is geometrically insensitive to XL then go to skip2
c     compute (once) element geometric sensitivity data at all integration points
x           form x,iL g,iL gL & niL
skip2:      continue
            for each P
c     compute geometric data at all integration points associated with P
                  form yi ρ ρ,i
                  if both E and this P are geometrically insensitive to XL
                  then go to skip1
                  if P is geometrically insensitive to XL
                  then go to skip3
c     compute geometric sensitivity data at all integration points associated with P
x                 form yi,L ρ,L ρ,iL
skip3:            continue
c     compute fundamental solutions at all integration points
                  form u*ij t*ij
c     compute sensitivities of fundamental solutions at all integration points
x                 form u*ij,L t*ij,L
c     form augmented 3x3 matrices times weigh at all integration points
x                 form [U] <== (u*ij,L * g + u*ij * g,L) * w
x                 form [T] <== (t*ij,L * g + t*ij * g,L) * w
c     perform matrix product & 3x18 sum required for all integration points
                  form [F](E,P) = [F](E,P) + [T] [H]
                  form [G](E,P) = [G](E,P) + [G] [H]
                  next P
            next E
skip1:      continue
      return
      end
```

Fig. 1 Numerical integration algorithm for entries in matrix sensitivities

$$g_{,L}=g^{-1}g_kg_{k,L} \tag{14}$$

$$g_{i,L}=e_{ijk}(x_{j,1L}x_{k,2}+x_{j,1}x_{k,2L}) \tag{15}$$

$$x_{j,1L}=\sum_{n=1}^{6}\frac{\partial h^{(n)}}{\partial a_1}x_jL;\quad x_{j,2L}=\sum_{n=1}^{6}\frac{\partial h^{(n)}}{\partial a_2}x_{j,L}. \tag{16}$$

ρ is the distance from load point **d** to sample point **x**, **n** is the unit outward normal to the surface at **x**, and ν and μ are elastic constants.

Examination of Eqs. (3) through (12) reveals that *the functions involved in the DSA formulation have exactly the same singularity characteristics as those present in the original analysis step.* That is to say, $[U]_{,L}$ and $[T]_{,L}$ contain functions that behave like ρ^{-1} and ρ^{-2}, respectively, as the distance **x** − **d** approaches zero. This fact allows numerical integration techniques (Kane, Gupta, and Saigal, 1989), developed for boundary element analysis, to be employed design sensitivity analysis without modification. This statement is true for both the outside integration (ρ never becomes zero for a particular E, P combination) and inside integration (ρ becomes zero for a particular E, P combination) process.

Figure 1 presents details of the hierarchical algorithm implemented for performance of the above mentioned integrations in design sensitivity analysis. Steps preceded with the symbol **x** indicate steps that are *extra* when compared with an analogous procedure in standard boundary element analysis. Note that only steps associated with computation of sensitivities of the 3 × 3 matrices of fundamental solutions and the sensitivity of the Jacobian and normal are extra. Also, even in these formulae, about half of the quantities present are not sensitivities. Note further that the arithmetic operations associated with formation of the 3 × 18 matrix products remains identical to the operations utilized in standard boundary element analysis. For problems in which a significant portion of the surface is geometrically insensitive to the design variable, considerable savings in computational effort can be accomplished in this design sensitivity analysis integration step, due to the fact that the matrix sensitivities will be sparse. Again,

Downloaded 03 May 2010 to 171.66.16.247. Redistribution subject to ASME license or copyright; see http://www.asme.org/terms/Terms_Use.cfm

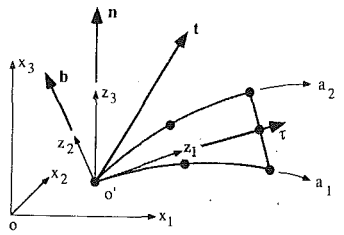


Fig. 2 Coordinate systems involved in membrane stress recovery

Fig. 1 can be used to gain an appreciation of this concept. In several places in this algorithm, tests are made to determine if certain quantities involved in the overall computation are known to be zero, and these operations are appropriately bypassed. In subsequent sections, numerical examples will be presented to demonstrate these assertions regarding computational efficiency.

Sensitivity Formulation for Surface Stress Components

As depicted in Eqs. (1) and (2), the quantities involved in this design sensitivity analysis formulation at the algebraic equation solving level are sensitivities of node-point displacement and boundary traction components. In many practical problems, stress components that are *not* components of the traction vector on the boundary are significant (if not dominant) contributors to the overall stress response. These stresses will be referred to as *membrane* stress components. A sensitivity formulation for these membrane stress components is thus a requirement for use in practical shape optimization systems. The formulae for recovery of membrane stress component information on the surface of a boundary element analysis model can be differentiated with respect to X_L to generate a sensitivity formulation for these stresses. Care must be taken to recognize all of the possible geometric and structural quantities that can be sensitive to the design variable and to include these derivatives in this differentiation process.

Figure 2 can be used to visualize the coordinate systems involved in membrane stress recovery and the subsequent sensitivity recovery process. In the global x_i coordinate system we have u_i, t_i, σ_{ij}, and ϵ_{ij} as components of displacement, traction, stress, and strain tensors, respectively. In the local (tangential and normal) z_i system, located at the node where membrane stresses are to be recovered, v_i, p_i, s_{ij}, and e_{ij} symbolize these components. This local coordinate system is configured so that the z_1 direction is tangent to the boundary element and pointing in the direction of increasing a_1, z_2 is normal to the element and z_3 is perpendicular to z_1 and z_3. Note that τ, **b**, and **n** are unit vectors parallel to the z_1, z_2, and z_3 coordinate directions, respectively. In this local coordinate system, the following relationships exist:

$$\left.\begin{aligned} s_{3i,L} &= p_{i,L} \\ s_{11,L} &= \frac{1}{1-\nu}\left[\nu p_{3,L} + 2\mu(e_{11,L} + \nu e_{22,L})\right] \\ s_{22,L} &= \frac{1}{1-\nu}\left[\nu p_{3,L} + 2\mu(\nu e_{11,L} + e_{22,L})\right] \\ s_{12} &= 2\mu e_{12,L} \end{aligned}\right\} \tag{17}$$

$$e_{11,L} = v_{1,1L}; \quad e_{22,L} = v_{2,2L}; \quad e_{12,L} = \frac{1}{2}(v_{1,2L} + v_{2,1L}) \tag{18}$$

$$v_{i,jL} = \frac{\partial^2 v_i}{\partial X_L \partial z_j}, \text{ and } v_{i,a_jL} = \frac{\partial^2 v_i}{\partial X_L \partial a_j}; \quad i,j,=1,2, \tag{19}$$

letting

$$\left.\begin{aligned} \{v_i\}_{,z} &= \begin{Bmatrix} v_{i,1} \\ y_{i,2} \end{Bmatrix}; \ \{v_i\}_{,aL} = \begin{Bmatrix} v_{i,a_1} \\ v_{i,a_2} \end{Bmatrix} \\ \{v_i\}_{,zL} &= \begin{Bmatrix} v_{i,1L} \\ v_{i,2L} \end{Bmatrix}; \ \{v_i\}_{,aL} = \begin{Bmatrix} v_{i,a_1L} \\ v_{i,a_2L} \end{Bmatrix}; \ [J] = \begin{bmatrix} z_{1,a_1} z_{2,a_1} \\ z_{1,a_2} z_{2,a_2} \end{bmatrix} \end{aligned}\right\} \tag{20}$$

then

$$\{v_i\}_{,zL} = [J]_{,L}^{-1}\{v_i\}_{,a} + [J]\{v_i\}_{,aL} \tag{21}$$

where

$$[J]_{,L}^{-1} = [J]_{,L}^{A}|J|^{-1} - [J]^{A}|J|^{-2}[J]_{,L} \tag{22}$$

and

$$[J] = \begin{bmatrix} j_{11} & j_{12} \\ j_{21} & j_{22} \end{bmatrix}; \ [J]^{A} = \begin{bmatrix} j_{22} & -j_{21} \\ -j_{12} & j_{11} \end{bmatrix}; \ |J| = j_{11}j_{22} - j_{12}j_{21} \tag{23}$$

$$[J]_{,L} = \begin{bmatrix} j_{11,L} & j_{12,L} \\ j_{21,L} & j_{22,L} \end{bmatrix}; \ [J]_{,L}^{A} = \begin{bmatrix} j_{22,L} & -j_{21,L} \\ -j_{12,L} & j_{11,L} \end{bmatrix} \tag{24}$$

$$|J|_{,L} = j_{11,L}j_{22} + j_{11}j_{22,L} - (j_{12,L}j_{21} + j_{12}j_{21,L}) \tag{25}$$

$$j_{km} = z_{m,a_k} = \sum_{n=1}^{6} \frac{\partial h^{(n)}}{\partial a_k} z_m^{(n)}; \ j_{km,L} = (z_{m,a_k})_{,L} = \sum_{n=1}^{6} \frac{\partial h^{(n)}}{\partial a_k} z_{m,L}^{(n)}. \tag{26}$$

The last three lines in Eq. (17) are obtained by manipulating the isotropic stress-strain law to isolate the membrane components and then differentiating with respect to X_L. All vector components shown above are resolved in the local coordinate system. The transformations of the components of these physical entities from the global coordinate system are

$$z_{r,L} = l_{ri,L}x_i + l_{ri}x_{i,L}; \ v_{r,L} = l_{ri,L}u_i + l_{ri}u_{i,L};$$

$$p_{r,L} = l_{ri,L}t_i + l_{ri}t_{i,L} \tag{27}$$

where

$l_{il} = \tau_i$; $l_{i2} = b_i$; $l_{i3} = n_i$;

$$\text{and } l_{i1,L} = \tau_{i,L}; \ l_{i2,L} = b_{i,L}; \ l_{i3,L} = n_{i,L} \tag{28}$$

$$\tau_i = \tau^{-1}x_{i,a_1}; \ \tau_{i,L} = -\tau^{-2}\tau_{,L}x_{i,a_1} + \tau^{-1}x_{i,a_1L} \tag{29}$$

$\tau = (x_{1,a_1}^2 + x_{2,a_1}^2 + x_{3,a_1}^2)^{1/2}$;

$$\tau_{,L} = \tau^{-1}(x_{1,a_1}x_{1,a_1L} + x_{2,a_1}x_{2,a_1L} + x_{3,a_1}x_{3,a_1L}) \tag{30}$$

$$x_{i,a_1} = \sum_{n=1}^{6} \frac{\partial h^{(n)}}{\partial a_1} x_i; \ x_{i,a_1L} = \sum_{n=1}^{6} \frac{\partial h^{(n)}}{\partial a_1} x_{i,L} \tag{31}$$

$$b_i = e_{ijk}n_j\tau_k; \ b_{i,L} = e_{ijk}(n_{j,L}\tau_k + n_j\tau_{k,L}) \tag{32}$$

n_i is the component of the unit surface normal vector used in the original boundary element analysis and $n_{i,L}$ has been defined in Eq. (13).

To obtain sensitivities of the complete stress tensor in the global coordinate system, one needs to differentiate the second rank tensor component transformation law to obtain

$$\sigma_{ij,L} = l_{mi,L}l_{nj}s_{mn} + l_{mi}l_{nj,L}s_{mn} + l_{mi}l_{nj}s_{mn,L} \tag{33}$$

The first two terms on the right-hand side of Eq. (33) determine the sensitivity of σ_{ij} due to a change in orientation of the local coordinate system, with local stresses s_{mn} remaining constant. The last term in Eq. (33) determines the sensitivity of σ_{ij} due to a change in local stresses s_{mn}, with the orientation of the local system remaining constant. Note the considerable involvement of surface differential geometry in this formulation. Later in this paper, an example problem will be presented where both the stress field at a point and the direction of the local coordinate system at that point are simultaneously changing.

Downloaded 03 May 2010 to 171.66.16.247. Redistribution subject to ASME license or copyright; see http://www.asme.org/terms/Terms_Use.cfm

Interior Point Sensitivity Analysis

Integral relations for the recovery of displacement and stress components at sample points in the domain (interior) of a boundary element analysis model can be differentiated to yield new integral equations for the recovery of sensitivities of displacement and stress components. The integral equations that result involve the boundary response (nodal displacement and traction components) and the sensitivity of these response quantities. Thus, recovery of internal point sensitivities can be accomplished via a boundary integration process completely analogous to that performed in the original boundary element analysis process. In this formulation, indical notation is employed in order to conveniently express relations involving the third-rank tensors present in the integral equation for internal point stress recovery.

$$u_{i,L}(\mathbf{d}) = \sum_{E=1}^{NE}\left[\sum_{n=1}^{6}\left(\int_0^1\int_0^{1-a_2}[u^*_{ki,L}h^{(n)}g + u^*_{ki}h^{(n)}g_{,L}da_1da_2\right)t_k^{(n)}\right]^{(E)} - \sum_{E=1}^{NE}\left[\sum_{n=1}^{6}\left(\int_0^1\int_0^{1-a_2}[t^*_{ki,L}h^{(n)}g + t^*_{ki}h^{(n)}g_{,L}]da_1da_2\right)u_k^{(n)}\right]^{(E)} + \sum_{E=1}^{NE}\left[\sum_{n=1}^{6}\left(\int_0^1\int_0^{1-a_2}u^*_{ki}h^{(n)}g\ da_1da_2\right)t_{k,L}^{(n)}\right]^{(E)} - \sum_{E=1}^{NE}\left[\sum_{n=1}^{6}\left(\int_0^1\int_0^{1-a_2}t^*_{ki}h^{(n)}g\ da_1da_2\right)u_{k,L}^{(n)}\right]^{(E)} \quad (34)$$

$$-\sigma_{ij,L}(\mathbf{d}) = \sum_{E=1}^{NE}\left[\sum_{n=1}^{6}\left(\int_0^1\int_0^{1-a_2}[D_{kij,L}h^{(n)}g + D_{kij}h^{(n)}g_{,L}]da_1da_2\right)t_k^{(n)}\right]^{(E)} - \sum_{E=1}^{NE}\left[\sum_{n=1}^{6}\left(\int_0^1\int_0^{1-a_2}[S_{kij,L}h^{(n)}g + S_{kij}h^{(n)}g_{,L}]da_1da_2\right)u_k^{(n)}\right]^{(E)} + \sum_{E=1}^{NE}\left[\sum_{n=1}^{6}\left(\int_0^1\int_0^{1-a_2}D_{kij}h^{(n)}g\ da_1da_2\right)t_{k,L}^{(n)}\right]^{(E)} - \sum_{E=1}^{NE}\left[\sum_{n=1}^{6}\left(\int_0^1\int_0^{1-a_2}S_{kij}h^{(n)}g\ da_1da_2\right)u_{k,L}^{(n)}\right]^{(E)} \quad (35)$$

The sensitivities of all of the quantities in Eqs. (34) and (35) have already been defined except for the third-rank tensors. These new sensitivities are

$$D_{kij,L} = -4k_1\mu\rho^{-3}\rho_{,L}\{(1-2\nu)[\rho_{,k}\delta_{ij} - \rho_{,i}\delta_{kj} - \rho_{,j}\delta_{ki}] - 3\rho_{,i}\rho_{,j}\rho_{,k}] + 2k_1\mu\rho^{-2}\{(1-2\nu)[\rho_{,kL}\delta_{ij} - \rho_{,iL}\delta_{kj} - \rho_{,jL}\delta_{ki}] - 3[\rho_{,iL}\rho_{,j}\rho_{,k} + \rho_{,i}\rho_{,jL}\rho_{,k} + \rho_{,i}\rho_{,j}\rho_{,kL}]\} \quad (36)$$

$$S_{kij,L} = 3k_5\rho^{-4}\rho_{,L}\{3\rho_{,s}n_s[(1-2\nu)\delta_{ij}\rho_{,k} + \nu(\delta_{kj}\rho_{,i} + \delta_{ki}\rho_{,j}) - 5\rho_{,i}\rho_{,j}\rho_{,k}] + 3\nu(\rho_{,i}\rho_{,k}n_j + \rho_{,j}\rho_{,k}n_i) + 3(1-2\nu)\rho_{,i}\rho_{,j}n_k + (1-2\nu)(\delta_{kj}n_i + \delta_{ki}n_j) - (1-4\nu)\delta_{ij}n_k\} - k_5\rho^{-3}\{3(\rho_{,sL}n_s + \rho_{,s}n_{sL})[(1-2\nu)\delta_{ij}\rho_{,k} + \nu(\delta_{kj}\rho_{,i} + \delta_{ki}\rho_{,j}) - 5\rho_{,i}\rho_{,j}\rho_{,k}] + 3\rho_{,s}n_s[(1-2\nu)\delta_{ij}\rho_{,kL} + \nu(\delta_{kj}\rho_{,iL} + \delta_{ki}\rho_{,jL}) - 5(\rho_{,iL}\rho_{,j}\rho_{,k} + \rho_{,i}\rho_{,jL}\rho_{,k} + \rho_{,i}\rho_{,j}\rho_{,kL})] + 3\nu(\rho_{,iL}\rho_{,k}n_j + \rho_{,i}\rho_{,kL}n_j + \rho_{,i}\rho_{,k}n_{j,L} + \rho_{,jL}\rho_{,k}n_i + \rho_{,j}\rho_{,kL}n_i + \rho_{,j}\rho_{,k}n_{i,L}) + 3(1-2\nu)(\rho_{,iL}\rho_{,j}n_k + \rho_{,i}\rho_{,jL}n_k + \rho_{,i}\rho_{,j}n_{k,L}) + (1-2\nu)(\delta_{kj}n_{i,L} + \delta_{ki}n_{j,L}) - (1-4\nu)\delta_{ij}n_{k,L}\} \quad (37)$$

where

$$k_5 = \frac{\mu}{4\pi(1-\nu)}. \quad (38)$$

Careful examination of Eqs. (36), (37), and (8) through (12) again reveals that *the functions involved in this interior point design sensitivity analysis formulation have exactly the same singularity characteristics as those present in the original analysis step.* Thus, numerical integration techniques developed for recovery of interior point response information in standard boundary element analysis can be employed in this design sensitivity analysis step without modification. One might argue that about twice the computational work should be required in the integrations indicated in Eqs. (34) and (35) compared to interior point response recovery in the original boundary element analysis, which is due to the fact that both the surface response and its sensitivity is involved in the computation. Closer examination of the last two terms in these equations, however, reveals that the integrations indicated in *these terms are exactly the same integrations that are required in the original boundary element analysis, internal point response recovery process. Thus, if these coefficients are saved and reused in the design sensitivity analysis step, their recomputation can be avoided.* For problems in which a significant portion of the surface is geometrically insensitive, significant savings in computational effort can be accomplished in the step for interior point response design sensitivity analysis, which is due to the fact that many of the terms in Eqs. (34) and (35) will be zero for a significant number of the elements comprising the overall boundary element analysis model. Note that interior points may or may not be geometrically sensitive to any particular design variable.

First Example Problem

To demonstrate the accuracy and efficiency of this formulation a series of example problems is presented. All problems were run on the same dedicated computer system with a UNIX operating system using the same Fortran 77 compiler and compiler options. In all problems, a modulus of elasticity of $E = 30 \times 10^6$ units and a Poisson's ratio of $u = 0.3$ were employed.

The first physical problem chosen is a thick circular subjected to an internal hydrostatic pressure of 100 units. The plain-strain elasticity solution to this problem is well known (Cook and Young, 1985). Figures 3(*a*) and 3(*b*) show the geometry and boundary conditions imposed on the quarter symmetry boundary element analysis models discussed. u_3 zero-displacement constraints on all nodes located on either the $x_3 = 0$ or $x_3 = -3$ planes were used to impose the condition of plain strain. A series of analyses and design sensitivity analyses were performed based upon this physical problem. In all of these cases, the outer radius b was chosen as the design variable.

The derivatives computed in this implicit differentiation design sensitivity analysis approach are true material derivatives, including the change in the response field and the possible change in the sample point location induced by the change in the design variable. Thus, differentiation of analytical expressions must also be a material differentiation, performed by first parameterizing the sample point location in the exact expression in terms of the design variable and then taking due regard for this derivative in the differentiation process. Figure 3(*c*) shows two different schemes employed to control sets of sample (node) point locations, both based upon the value of

Downloaded 03 May 2010 to 171.66.16.247. Redistribution subject to ASME license or copyright; see http://www.asme.org/terms/Terms_Use.cfm

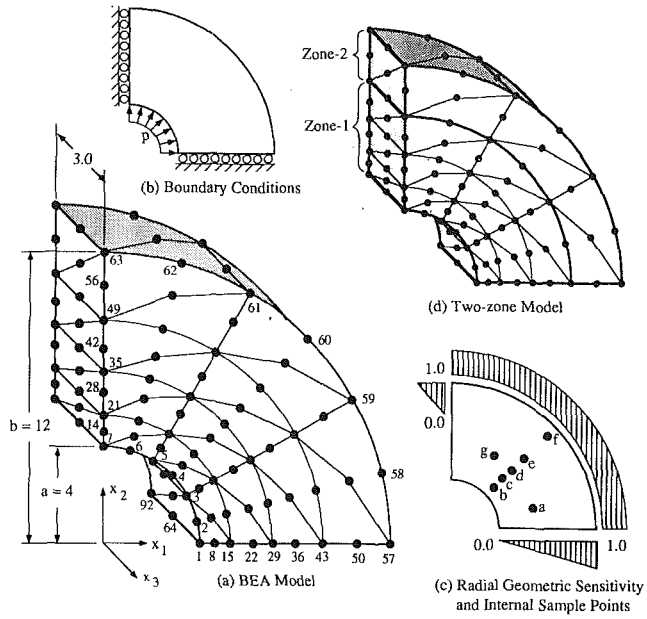


Fig. 3 Pressurized cylinder example problem

the design variable b. The *full* geometric sensitivity scheme has all nodes with radial location greater than a geometrically sensitive to b. This radial geometric sensitivity varies in a linear fashion from zero at $R = a$ to unity at $R = b$. The second scheme, depicted in Fig. 3(c), has only nodes in the radially outward-most row of elements geometrically sensitive to b. Note that a change in b will cause an identical change in the actual stress and displacement fields simulated by either the full or partially sensitive boundary element analysis models. However, because the nodes present in these two boundary element analysis models move to different locations in this response field, the node point sensitivities will be different.

Case 1: One-Zone Model With Full Geometric Sensitivity. Figure 3(a) shows a single-zone boundary element analysis model with 154 nodes and 76 6-node triangular elements and the overall left-hand side matrix requiring 213,444 double precision words of computer memory. Table 1 contains CPU timings for major computational steps involved in both the analysis and design sensitivity analysis process. It is seen that 56.0 CPU seconds spent in the analysis step to factor the boundary element analysis overall system matrix into its $[L]$ $[U]$ decomposition is saved in the design sensitivity analysis process. However, the numerical integrations required in the design sensitivity analysis step take about 170 percent of the integration time required in the analysis, due to the two-term expression for the kernels shown in Eqs. (3) and (4) being about twice as complicated as that integrated in the usual boundary element analysis process. Table 2 contains exact and computed displacement and surface traction sensitivities for the case of full geometric sensitivity illustrated in Fig. 3(c). Table 3 contains exact and computed surface stress sensitivities while Table 4 contains displacement and stress sensitivities for internal points shown in Fig. 3(c). Internal stress recovery points are all located in the $x_3 = -1.5$ plane and have radial geometric sensitivities that are the same as surface nodes located at the same radial locations. *Note the extreme accuracy of the predictions appearing in all these tables with predictions in error less than one percent.*

Case 2: One-Zone Model With Partial Geometric Sensitivity. This boundary element analysis model is identical to the one used in the previous example except that its nodes were only partially sensitive to b. In this example, the numerical

Table 1 CPU timings for major steps in analysis and design sensitivity analysis for various example cases

Step	Case 1	Case 2	Case 3	Case 4	Case 5
Analysis					
Preliminaries	1.9	1.9	1.9	1.9	1.9
Numerical Integration	88.5	88.5	79.4	79.7	79.8
Zone Assembly	30.3	30.3	23.1	23.2	24.7
Zone Condensation	0.0	0.0	0.0	0.0	44.0
Overall Assembly	0.5	0.5	0.5	0.4	0.1
Matrix Factorization	56.0	56.0	45.5	45.6	4.1
Forward Reduction & Back Substitution	1.6	1.6	1.8	1.7	4.6
Surface Stress Recovery	1.9	1.9	1.6	1.7	
Interior Response Recovery	26.8	26.7	18.6	18.7	
Design Sensitivity Analysis					
Preliminaries	0.0	0.0	0.0	0.0	0.0
Numerical Integration	149.9	73.8	137.1	30.0	29.8
Zone Assembly	34.2	34.0	27.0	8.2	7.1
Overall Assembly	0.5	0.4	0.6	0.1	0.3
Forward Reduction & Back Substitution	7.2	7.1	6.9	6.5	5.2
Surface Stress Recovery	0.7	0.7	0.8	0.8	
Interior Response Recovery	82.2	82.2	57.0	56.9	
Total	482.2	405.6	401.7	275.4	

Table 2 Displacement and traction response sensitivities for Case 1

	exact				computed			
Point	$u_1 x10^{-2}$	$u_2 x10^{-2}$	$t_1 x10^{+1}$	$t_2 x10^{+1}$	$u_1 x10^{-2}$	$u_2 x10^{-2}$	$t_1 x10^{+1}$	$t_2 x10^{+1}$
2	-0.63388	-0.16985	0.00000	0.00000	-0.63295	-0.16963	0.00000	0.00000
3	-0.56832	-0.32812	0.00000	0.00000	-0.56766	-0.32838	0.00000	0.00000
4	-0.46403	-0.46403	0.00000	0.00000	-0.46327	-0.46393	0.00000	0.00000
5	-0.32812	-0.56832	0.00000	0.00000	-0.32743	-0.56867	0.00000	0.00000
6	-0.16985	-0.63388	0.00000	0.00000	-0.16939	-0.63376	0.00000	0.00000
8	-0.95074	0.00000	0.00000	-0.70571	-0.94729	0.00000	0.00000	-0.69467
14	0.00000	-0.95074	-0.70571	0.00000	0.00000	-0.94729	-0.69057	0.00000
15	-1.1034	0.00000	0.00000	-0.76371	-1.1009	0.00000	0.00000	-0.79773
21	0.00000	-1.1034	-0.76371	0.00000	0.00000	-1.1006	-0.80113	0.00000
22	-1.1725	0.00000	0.00000	-0.74323	-1.1691	0.00000	0.00000	-0.74328
28	0.00000	-1.1725	-0.74323	0.00000	0.00000	-1.1684	-0.74323	0.00000
29	-1.1924	0.00000	0.00000	-0.69143	-1.1889	0.00000	0.00000	-0.70457
35	0.00000	-1.1924	-0.69143	0.00000	0.00000	-1.1890	-0.70220	0.00000
36	-1.1837	0.00000	0.00000	-0.63051	-1.1806	0.00000	0.00000	-0.62988
42	0.00000	-1.1837	-0.63051	0.00000	0.00000	-1.1804	-0.63182	0.00000
43	-1.1595	0.00000	0.00000	-0.57068	-1.1563	0.00000	0.00000	-0.57265
49	0.00000	-1.1595	-0.57068	0.00000	0.00000	-1.1561	-0.57155	0.00000
50	-1.1277	0.00000	0.00000	-0.51628	-1.1249	0.00000	0.00000	-0.51138
56	0.00000	-1.1277	-0.51628	0.00000	0.00000	-1.1244	-0.51370	0.00000
57	-1.0937	0.00000	0.00000	-0.46875	-1.0943	0.00000	0.00000	-0.47374
58	-1.0564	-0.28398	0.00000	0.00000	-1.0545	-0.28221	0.00000	0.00000
59	-0.94721	-0.54687	0.00000	0.00000	-0.94569	-0.54653	0.00000	0.00000
60	-0.77339	-0.77339	0.00000	0.00000	-0.77174	-0.77139	0.00000	0.00000
61	-0.54687	-0.94721	0.00000	0.00000	-0.54581	-0.94624	0.00000	0.00000
62	-0.28398	-1.0564	0.00000	0.00000	-0.28279	-1.0545	0.00000	0.00000
63	0.00000	-1.0937	-0.46875	0.00000	0.00000	-1.0946	-0.46620	0.00000
92	-0.65625	0.00000	0.00000	-0.46875	-0.65610	0.00000	0.00000	-0.48241
98	0.00000	-0.65625	0.00000	-0.46875	0.00000	-0.65591	0.00000	-0.49128

Table 3 Surface stress response sensitivities for Case 1

	exact			computed		
Point	σ_{11}	σ_{22}	σ_{12}	σ_{11}	σ_{22}	σ_{12}
1	0.0000	-4.6875	0.0000	-0.00008	-4.5893	0.0284
2	-0.3140	-4.3735	1.1719	-0.3123	-4.3497	1.1655
3	-1.1719	-3.5156	2.0297	-1.1510	-3.5230	2.0137
4	-2.3437	-2.3438	2.3437	-2.3472	-2.3472	2.3472
5	-3.5156	-1.1719	2.0297	-3.4722	-1.1807	2.0247
6	-4.3735	-3.1400	1.1719	-4.3330	-.3111	1.1610
7	-4.6675	0.0000	0.0000	-4.5691	-0.00008	0.0198
8	2.3696	-7.0571	0.0000	2.1548	-6.9467	0.0000
14	-7.0571	2.3696	0.0000	-6.9657	2.0588	0.0000
15	2.9496	-7.6371	0.0000	3.4194	-7.9773	0.0000
21	-7.6371	2.9496	0.0000	-8.0113	3.5305	0.0000
22	2.7448	-7.4323	0.0000	2.6726	-7.4328	0.0000
28	-7.4323	2.7448	0.0000	-7.4323	2.6558	0.0000
29	2.2268	-6.9143	0.0000	2.2986	-7.0457	0.0000
35	-6.9143	2.2268	0.0000	-7.0220	2.3501	0.0000
36	1.6176	-6.3051	0.0000	1.5883	-6.2988	0.0000
42	-6.3051	1.6176	0.0000	-6.3182	1.5880	0.0000
43	1.0193	-5.7068	0.0000	1.0489	-5.7265	0.0000
49	-5.7068	1.0193	0.0000	-5.7155	1.0589	0.0000
50	0.4753	-5.1628	0.0000	0.4496	-5.1138	0.0000
56	-5.1628	0.4753	0.0000	-5.1370	0.4714	0.0000
57	0.0000	-4.6875	0.0000	-0.00008	-4.6785	0.0209
58	-3.1400	-4.3735	1.1719	-3.1419	-4.3761	1.1726
59	-1.1719	-3.5156	2.0297	-1.1544	-3.5335	2.0197
60	-2.3437	-2.3438	2.3438	-2.3416	-2.3416	2.3416
61	-3.5156	-1.1719	2.0297	-3.5019	-1.1909	2.0421
62	-4.3735	-3.1400	1.1719	-4.3651	-3.1341	1.1696
63	-4.6875	0.0000	0.0000	-4.6843	-0.00008	0.0203

Downloaded 03 May 2010 to 171.66.16.247. Redistribution subject to ASME license or copyright; see http://www.asme.org/terms/Terms_Use.cfm

Table 4 Internal displacement and stress response sensitivities for Case 1

	exact			computed		
Point	$u_1 \times 10^{-2}$	$u_2 \times 10^{-2}$	u_3	$u_1 \times 10^{-2}$	$u_2 \times 10^{-2}$	$u_3 \times 10^{-6}$
a	-1.1517	-0.3086	0.0000	-1.1973	-0.3093	-0.3962
b	-0.7802	-0.7802	0.0000	-0.8658	-0.8658	-0.3570
c	-0.8291	-0.8291	0.0000	-0.8945	-0.8947	-0.0876
d	-0.8432	-0.8432	0.0000	-0.8844	-0.8846	0.1242
e	-0.8371	-0.8371	0.0000	-0.8545	-0.8574	0.2085
f	-0.7975	-0.7975	0.0000	-0.7679	-0.7676	0.0432
g	-0.5962	-1.0237	0.0000	-0.6231	-1.0806	0.3121
Point	σ_{11}	σ_{22}	σ_{12}	σ_{11}	σ_{22}	σ_{12}
a	1.6144	-6.3019	2.2853	1.6125	-6.2942	2.2838
b	-2.3437	-2.3438	5.2933	-2.3600	-2.3591	5.2649
c	-2.3437	-2.3438	5.0886	-2.3460	-2.3454	5.0848
d	-2.3438	-2.3438	4.5705	-2.3453	-2.3425	4.5658
e	-2.3437	-2.3438	3.9614	-2.3419	-2.3420	3.9550
f	-2.3437	-2.3438	2.8190	-2.3329	-2.3388	2.7343
g	-4.6290	-0.0585	3.9582	-4.6222	-0.0593	3.9493

Table 5 Displacement and traction response sensitivities for Case 2

	exact				computed			
Point	$u_1 \times 10^{-2}$	$u_2 \times 10^{-2}$	$t_1 \times 10^{+1}$	$t_2 \times 10^{+1}$	$u_1 \times 10^{-2}$	$u_2 \times 10^{-2}$	$t_1 \times 10^{+1}$	$t_2 \times 10^{+1}$
1	-0.65625	0.00000	0.00000	-0.46875	-0.65610	0.00000	0.00000	-0.47913
2	-0.63388	-0.16985	0.00000	0.00000	-0.63295	-0.16963	0.00000	0.00000
3	-0.56832	-0.32812	0.00000	0.00000	-0.56766	-0.32838	0.00000	0.00000
4	-0.46403	-0.46403	0.00000	0.00000	-0.46327	-0.46393	0.00000	0.00000
5	-0.32812	-0.56832	0.00000	0.00000	-0.32743	-0.56867	0.00000	0.00000
6	-0.16985	-0.63388	0.00000	0.00000	-0.16939	-0.63376	0.00000	0.00000
7	0.00000	-0.65625	0.46875	0.00000	0.00000	-0.65591	0.47687	0.00000
8	-0.61966	0.00000	0.00000	-0.40492	-0.61866	0.00000	0.00000	-0.40455
14	0.00000	-0.61966	-0.40492	0.00000	0.00000	-0.61941	-0.40426	0.00000
15	-0.599502	0.00000	0.00000	-0.36062	-0.59855	0.00000	0.00000	-0.36226
21	0.00000	-0.599502	-0.36062	0.00000	0.00000	-0.59938	-0.36276	0.00000
22	-0.592936	0.00000	0.00000	-0.32915	-0.59203	0.00000	0.00000	-0.32922
28	0.00000	-0.592936	-0.32915	0.00000	0.00000	-0.59265	-0.32860	0.00000
29	-0.598111	0.00000	0.00000	-0.30635	-0.59709	0.00000	0.00000	-0.30866
35	0.00000	-0.598111	-0.30635	0.00000	0.00000	-0.59792	-0.30705	0.00000
36	-0.613841	0.00000	0.00000	-0.28958	-0.61274	0.00000	0.00000	-0.28433
42	*0.00000*	*-0.613841*	*-0.28958*	*0.00000*	*0.00000*	*-0.61399*	*-0.28655*	*0.00000*
43	-0.639403	0.00000	0.00000	-0.27706	-0.63815	0.00000	0.00000	-0.29583
49	0.00000	-0.639403	-0.27706	0.00000	0.00000	-0.63842	-0.29296	0.00000
50	-0.93474	0.00000	0.00000	-0.41040	-0.93271	0.00000	0.00000	-0.41040
56	0.00000	-0.93474	-0.41040	0.00000	0.00000	-0.93221	-0.40824	0.00000
57	-1.0937	0.00000	0.00000	-0.46875	-1.0939	0.00000	0.00000	-0.47503
58	-1.0564	-0.28398	0.00000	0.00000	-1.0552	-0.28167	0.00000	0.00000
59	-0.94721	-0.54687	0.00000	0.00000	-0.94593	-0.54659	0.00000	0.00000
60	-0.77339	-0.77339	0.00000	0.00000	-0.77294	-0.77189	0.00000	0.00000
61	-0.54687	-0.94721	0.00000	0.00000	-0.54595	-0.94692	0.00000	0.00000
62	-0.28398	-1.0564	0.00000	0.00000	-0.28344	-1.0557	0.00000	0.00000
63	0.00000	-1.0937	-0.46875	0.00000	0.00000	-1.0915	-0.46374	0.00000

Table 6 Displacement and traction response sensitivities for Case 2

	exact				computed			
Point	$u_1 \times 10^{-2}$	$u_2 \times 10^{-2}$	$t_1 \times 10^{+1}$	$t_2 \times 10^{+1}$	$u_1 \times 10^{-2}$	$u_2 \times 10^{-2}$	$t_1 \times 10^{+1}$	$t_2 \times 10^{+1}$
1	-0.65625	0.00000	0.00000	-0.46875	-0.65610	0.00000	0.00000	-0.47913
2	-0.63388	-0.16985	0.00000	0.00000	-0.63295	-0.16963	0.00000	0.00000
3	-0.56832	-0.32812	0.00000	0.00000	-0.56766	-0.32838	0.00000	0.00000
4	-0.46403	-0.46403	0.00000	0.00000	-0.46327	-0.46393	0.00000	0.00000
5	-0.32812	-0.56832	0.00000	0.00000	-0.32743	-0.56867	0.00000	0.00000
6	-0.16985	-0.63388	0.00000	0.00000	-0.16939	-0.63376	0.00000	0.00000
7	0.00000	-0.65625	0.46875	0.00000	0.00000	-0.65591	0.47687	0.00000
8	-0.61966	0.00000	0.00000	-0.40492	-0.61866	0.00000	0.00000	-0.40455
14	0.00000	-0.61966	-0.40492	0.00000	0.00000	-0.61941	-0.40426	0.00000
15	-0.599502	0.00000	0.00000	-0.36062	-0.59855	0.00000	0.00000	-0.36226
21	0.00000	-0.599502	-0.36062	0.00000	0.00000	-0.59938	-0.36276	0.00000
22	-0.592936	0.00000	0.00000	-0.32915	-0.59203	0.00000	0.00000	-0.32922
28	0.00000	-0.592936	-0.32915	0.00000	0.00000	-0.59265	-0.32860	0.00000
29	-0.598111	0.00000	0.00000	-0.30635	-0.59709	0.00000	0.00000	-0.30866
35	0.00000	-0.598111	-0.30635	0.00000	0.00000	-0.59792	-0.30705	0.00000
36	-0.613841	0.00000	0.00000	-0.28958	-0.61274	0.00000	0.00000	-0.28433
42	0.00000	-0.613841	-0.28958	0.00000	0.00000	-0.61399	-0.28655	0.00000
43	-0.639403	0.00000	0.00000	-0.27706	-0.63815	0.00000	0.00000	-0.29583
49	0.00000	-0.639403	-0.27706	0.00000	0.00000	-0.63842	-0.29296	0.00000
50	-0.93474	0.00000	0.00000	-0.41040	-0.93271	0.00000	0.00000	-0.40503
56	0.00000	-0.93474	-0.41040	0.00000	0.00000	-0.93221	-0.40824	0.00000
57	-1.0937	0.00000	0.00000	-0.46875	-1.0939	0.00000	0.00000	-0.47503
58	-1.0564	-0.28398	0.00000	0.00000	-1.0552	-0.28167	0.00000	0.00000
59	-0.94721	-0.54687	0.00000	0.00000	-0.94593	-0.54659	0.00000	0.00000
60	-0.77339	-0.77339	0.00000	0.00000	-0.77294	-0.77189	0.00000	0.00000
61	-0.54687	-0.94721	0.00000	0.00000	-0.54595	-0.94692	0.00000	0.00000
62	-0.28398	-1.0564	0.00000	0.00000	-0.28344	-1.0557	0.00000	0.00000
63	0.00000	-1.0937	-0.46875	0.00000	0.00000	-1.0915	-0.46374	0.00000

integrations required in the design sensitivity analysis step take only 83 percent of the time required in the analysis. Although the two-term expression shown in Eqs. (3) and (4) is again being integrated, this integration is only required for the reduced number of element and load point pairs that produce finite values of $g_{,L}$, $[U]_{,L}$, and $[T]_{,L}$, in this model with partial geometric sensitivity. Tables 5 through 7 contain exact and computed surface and internal response sensitivities for this case. *Note again the extreme accuracy of these predictions.*

Table 7 Internal displacement response sensitivities for Case 2

	exact			computed		
Point	$u_1 \times 10^{-2}$	$u_2 \times 10^{-2}$	u_3	$u_1 \times 10^{-2}$	$u_2 \times 10^{-2}$	$u_3 \times 10^{-6}$
a	-0.5777	-0.1548	0.0000	-0.5399	-0.1432	-0.0293
b	-0.4239	-0.4239	0.0000	-0.4217	-0.4222	-0.0265
c	-0.4193	-0.4193	0.0000	-0.4014	-0.4014	0.0373
d	-0.4229	-0.4229	0.0000	-0.3894	-0.3894	0.0823
e	-0.4341	-0.4341	0.0000	-0.3818	-0.3818	0.1647
f	-0.6609	-0.6609	0.0000	-0.5876	-0.5870	0.0206
g	-0.2991	-0.5180	0.0000	-0.2754	-0.5796	0.0985
Point	σ_{11}	σ_{22}	σ_{12}	σ_{11}	σ_{22}	σ_{12}
a	-1.7204	-2.9671	0.3597	-1.7210	-2.9650	0.3690
b	-2.3437	-2.3438	1.2624	-2.3421	-2.3437	1.2600
c	-2.3438	-2.3438	0.9477	-2.3422	-2.3432	0.9467
d	-2.3438	-2.3438	0.7197	-2.3443	-2.3432	0.7191
e	-2.3438	-2.3438	0.5520	-2.3456	-2.3428	0.5446
f	-2.3437	-2.3438	1.7602	-2.5398	-2.3979	1.7102
g	-2.7036	-1.9839	0.6233	-2.7000	-1.9900	0.6212

Table 8 Displacement and stress response sensitivities for second example problem

		finite difference		DSA formulation	
Point	θ	$u_1 \times 10^{-3}$	$u_2 \times 10^{-4}$	$u_1 \times 10^{-3}$	$u_2 \times 10^{-4}$
1	0.0	.440	0.0	.442	0.0
2	7.5	.440	-.126	.437	-.125
3	22.5	.410	-.340	.406	-.343
4	37.5	.350	-.550	.349	-.548
5	52.5	.269	-.730	.268	-.731
6	67.5	.171	-.860	.171	-.858
7	82.5	.061	-.910	.065	-.938
8	90.0	0.0	-.960	0.0	-.951

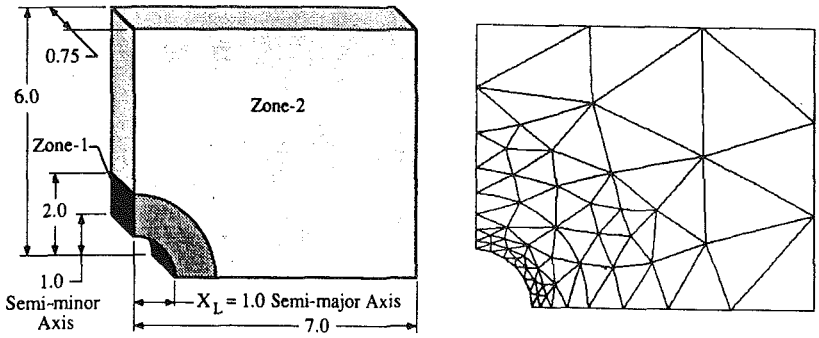
	finite difference				DSA formulation			
Point	σ_{11}	σ_{22}	σ_{33}	σ_{12}	σ_{11}	σ_{22}	σ_{33}	σ_{12}
1	-.00003	-.270	-.079	.00653	-.00003	-.267	-.075	.00615
2	-.043	-.080	-.038	.166	-.043	-.084	-.035	.165
3	-.041	.679	.192	-.096	-.042	.679	.192	-.093
4	.652	.522	.353	-.631	.649	.530	.350	.625
5	1.22	-.445	.237	-.180	1.23	-.442	.242	-.189
6	.178	-.745	-.173	.851	.181	-.753	-.172	.855
7	-1.67	-.141	-.550	.636	-1.68	-.142	-.555	.643
8	-1.91	-.000039	-.571	.0112	-1.92	-.000040	-.577	.0113

Case 3: Two-Zone Model With Full Geometric Sensitivity. Figure 3(*d*) shows a two-zone boundary element analysis model containing 159 nodes and 88 6-node triangular elements and the sparse blocked overall left-hand side matrix requiring 198,252 double precision words of computer memory. From Table 1 it is seen that the 45.5 CPU seconds spent in the analysis step to factor the boundary element analysis overall system matrix is saved in the design sensitivity analysis process. However, the numerical integrations required in the design sensitivity analysis step take about 173 percent of the time required in the analysis. The accuracy of displacement, surface traction, and surface and internal stress sensitivities for this case were similar to the single-zone problem.

Case 4: Two-Zone Model With Partial Geometric Sensitivity. In this two-zone model, only zone-2 is geometrically sensitivity to b, and thus only this zone contributes finite values to $[F]_{,L}$ and $[G]_{,L}$. The numerical integration in this design sesnsitivity analysis step takes only 38 percent of the time required in to perform the numerical integration in the analysis. The accuracy of the response sensitivities for this case were again similar to those obtained in the single zone, partially sensitive problem. This example helps to quantify the significant computer time savings that can be achieved in implicit differentiation for models with partial geometric sensitivity.

Case 5: Two-Zone Model With Partial Geometric Sensitivity and With Zone-1 Condensed. This case is identical to

Downloaded 03 May 2010 to 171.66.16.247. Redistribution subject to ASME license or copyright; see http://www.asme.org/terms/Terms_Use.cfm



(a) Geometry

(b) BEA Mesh

Fig. 4 Tension strip with elliptical hole

the previous one except that zone-2 is condensed in the analysis process as described in Kane, Kumar, and Saigal (1990). All matrices in the design sensitivity analysis process for this case are of reduced size as described in this reference. The accuracies in this case are identical to those occurring in Case 4.

Second Example Problem

A strip with a central elliptical hole is examined because this problem exhibits pronounced stress gradients and also sensitivity of the local coordinate system at surface sample points. The design variable is the size of the semi-major axis of the ellipse, which is aligned with the x_1-axis. This is also the direction of the unit uniaxial tension applied to the strip. Figure 4 shows the geometry and quarter symmetry boundary element mesh used. Note the *circular* shape of the hole present in this model. This is due to the fact that the semi-major and semi-minor axes of the general elliptical hole were taken to be equal. Thus, this sensitivity problem deals with the rate of change of the response of a tension strip with a circular hole as this hole *begins* to turn into an ellipse with semi-minor axis held fixed at the value of the radius of the original circular hole. This two-zone boundary element analysis model contained 541 nodes and 282 elements. The x_1 geometric sensitivity of the nodes in zone-1 of the boundary element analysis model varied linearly with radial position from the circular hole to the zone-1/zone-2 interface. All the nodes in zone-2 were geometrically insensitive. The front and back planes were constrained with $u_3 = 0$ to simulate plane strain. The vertical ($x_1 = 0$) and horizontal ($x_2 = 0$) symmetry planes were also constrained to $u_1 = 0$ and $u_2 = 0$, respectively.

Young (1989) presents stress concentration factors associated with this problem, however, only information at the two points at the major and minor diameters of the ellipse are provided. Timoshenko and Goodier (1970) give relations for the tangential (membrane) stress component distribution on the surface of an elliptical hole in an *infinite* elastic medium. Stress concentration formulae can be differentiated with respect to the semi-major axis size to obtain the sensitivity of the stress at the two points of interest. Finite difference can also be used to obtain rates of change of the entire response distribution. The accuracy of the stress response sensitivity computed using the design sensitivity analysis formulation agreed with differentiated formulae from Roark within 0.05 percent at the two points where the formulae applies. Table 8 contains displacement and stress sensitivity results obtained at a number of sample points on the surface of the elliptical hole by finite difference and from the design sensitivity analysis formulation. Note that the stress sensitivity components shown in Table 8 are components in the global coordinate system, and are computed using Eq. (33). This problem thus exercises of the stress tensor and the direction of the local coordinate system are simultaneously changing. Again in this problem, *this tabulated data indicates that the design sensitivity analysis formulation presented is extremely accurate.*

Summary

A three-dimensional design sensitivity analysis formulation has been presented based upon the boundary element analysis method and implicit differentiation. The theoretical formulation and its implementation has been demonstrated for the accurate and efficient computation of surface displacement and traction components and surface and internal stress component sensitivities, via a series of example problems.

Acknowledgments

Portions of the research discussed herein have been supported by grants from the NASA Lewis Research Center (NAG 3-1089), the U.S. National Science Foundation (DDM-8996171) to Clarkson University. Any opinions, findings, and conclusions or recommendations expressed in this publication are those of the authors and do not reflect the views of these other organizations.

References

Cook, R. D., and Young, W. C., 1985, *Advanced Mechanics of Materials*, Macmillan, New York.

Kane, J. H., 1986, "Shape Optimization Utilizing a Boundary Element Formulation," *BETECH 86: Proceedings*, 1986 Boundary Element Technology Conference, MIT, Cambridge, MA.

Kane, J. H., 1987, "A Second Generation Structural Shape Optimization Capability Employing a Boundary Element Formulation," *Numeta-87: Proceedings*, Vol. 1, G. N. Pande and J. Middleton, eds., Section D43.

Kane, J. H., 1990, "Boundary Element Design Sensitivity Analysis Formulations for Coupled Problems," *Engineering Analysis*, Vol. 7, No. 1, Mar., pp. 21-32.

Kane, J. H., Gupta, A., and Saigal, S., 1989, "Reusable Intrinsic Sample Point (RISP) Algorithm for the Efficient Numerical Integration of Three Dimensional Curved Boundary Elements," *International Journal for Numerical Methods in Engineering*, Vol. 28, No. 7, pp. 1661-1676.

Kane, J. H., Kumar, B. L. K., and Stabinsky, M., 1991, "Transient Thermoelasticity and Other Body Force Effects in Boundary Element Shape Sensitivity Analysis," *International Journal for Numerical Methods in Engineering*, Vol. 31, pp. 1203-1230.

Kane, J. H., and Saigal, S., 1988, "Design Sensitivity Analysis of Solids Using BEM," *Journal of Engineering Mechanics*, ASCE, Vol. 114, No. 10, pp. 1703-1722.

Kane, J. H., and Saigal, S., 1990, "An Arbitrary Multi-zone Condensation Technique for Boundary Element Design Sensitivity," *AIAA Journal*, Vol. 28, No. 7, pp. 1277-1284.

Kane, J. H., and Stabinsky, S., 1988, "Simultaneous Computation of Multiple Sensitivities by a Boundary Element Structural Analysis Formulation," Third International Conference on CAD/CAM Robotics and Factories of the Future.

Downloaded 03 May 2010 to 171.66.16.247. Redistribution subject to ASME license or copyright; see http://www.asme.org/terms/Terms_Use.cfm

Kane, J. H., and Wang, H., 1991, "Boundary Element Shape Sensitivity Analysis Formulations for Thermal Problems with Nonlinear Boundary Conditions," *AIAA Journal*, Vol. 29, pp. 1978–1989.

Kane, J. H., and Wang, H., 1992, "Boundary Formulations for Shape Sensitivity of Temperature Dependent Conductivity Problems," *International Journal for Numerical Methods in Engineering*, Vol. 33, pp. 667–693.

Saigal, S., Borggaard, J. T., and Kane, J. H., 1989, "Boundary Element Implicit Differentiation Equations for Design Sensitivities of Axisymmetric Structures," *International Journal of Solids and Structures*, Vol. 25, No. 5, pp. 527–538.

Saigal, S., and Kane, J. H., 1990, "A Boundary Element Shape Optimization System for Aircraft Components," *AIAA Journal*, Vol. 28, No. 7, pp. 1203–1204.

Saigal, S., Kane, J. H., and Aithal, R., 1989, "Semi-Analytical Structural Sensitivity Formulation using a Boundary Elements," *AIAA Journal*, Vol. 27, No. 11, pp. 1615–1621.

Timoshenko, S. P., and Goodier, J. N., 1970, *Theory of Elasticity*, 3rd ed., McGraw-Hill, New York.

Young, W. C., 1989, *Roark's Formulas for Stress and Strain*, 6th ed., McGraw-Hill, New York, p. 735.

Downloaded 03 May 2010 to 171.66.16.247. Redistribution subject to ASME license or copyright; see http://www.asme.org/terms/Terms_Use.cfm

An Inverse Formulation With Boundary Elements

Xiaogang Zeng

Sunil Saigal
Assoc. Mem. ASME.

Department of Civil Engineering,
Carnegie Mellon University,
Pittsburgh, PA 15213

A mathematical formulation for the solution of inverse problems pertaining to the identification of flaw shapes and the reconstruction of boundary conditions in a continua is described. Integral relationships are derived for the variation of field variables with respect to variation in flaw shape using Taylor series expansions. Similar relationships for the variation of boundary conditions with variation in flaw shape are also obtained. These variations allow the development of an iterative framework to advance an initially assumed flaw shape towards its actual configuration. The iterations are based upon and are driven by the difference in the values of computed response for the assumed flaw shape from their experimentally measured values at specified locations. The resulting equations are cast into the matrix form for solution using the boundary element method.

Introduction

A large class of inverse problems in mechanics falls under two catagories, namely the reconstruction problems and the identification problems (Baumeister, 1987). Reconstruction problems refer to the determination of the boundary conditions or some other input to the system with known geometry that result in an output which is known by experimental measurements. Identification problems deal with the determination of the unknown geometry, such as an internal flaw, of the system for which the boundary conditions are prescribed and for which the measured responses at selected points are given. Inverse problems that include both the reconstruction and the identification problems simultaneously are also of interest. The numerical investigations into inverse problems have largely been done using finite difference methods. A detailed description of such methods may be found in, for example, Beck et al. (1985). The finite element method has also been quite extensively used for the solution of inverse problems. A review of these efforts has been given by, among others, Schnur and Zabaras (1990) and Dorri (1987). Both these methods have been applied to inverse problems in deformation as well as heat transfer analyses.

The boundary integral technique has in the recent years attracted a significant interest as a computational tool. Its unique advantages in the solution of inverse problems have been enumerated in, for example, Dorri (1987). However, not much work concentrating the solution of inverse problems using the boundary integral approach has appeared in the literature thus far. Dorri (1987) presented a boundary integral solution for the determination of the source in heat conduction problems using the least-squares method to determine the unknown coefficients of the Legendre polynomial describing the source; Kojima (1987) provided a formulation for the reconstruction of boundary conditions of a two-dimensional elliptic system; Ohnaka and Uosaki (1985) proposed a method for determining the unknown boundary conditions of a partial differential equation of the parabolic type; Adamiak (1985) described a method for solving inverse problems for the Laplace and Poisson equations in order to determine the system which generates an assumed field; Zabaras et al. (1988) provided a sensitivity formulation for the solution of inverse heat transfer problems with phase changes; Tanaka et al. (1986) determined the geometry of the flaw, described using a set of design variables, through determining sensitivity of the measured quantity and a least-squares solution in an elastostatic analysis; Tanaka et al. (1987) provided an elastodynamic formulation coupled with optimization techniques for the detection of structural flaws; Zabaras et al. (1989) applied spatial regularization to the boundary element solution of an inverse elasticity problem; and Mura (1985) and Mura et al. (1986) employed a boundary integral equation method to find plastic strains from surface displacements.

A mathematical derivation for the unified solution of the reconstruction and identification types of inverse problems is presented in this paper. The variation of the available measured quantity with respect to a variation of an assumed flaw shape towards the actual flaw configuration is expressed in terms of boundary integrals. These integrals involve the known outer boundary and only the boundary of the assumed flaw shape. A distinct advantage of this formulation lies in that it does not require the determination of shape sensitivities. The formulations based on sensitivity calculations are either limited to defining the flaw shape in terms of a small number of design variables or are computationally prohibitive. Flaw shapes of arbitrary shape are thus not easily indentifiable. The present integral expressions are cast into the matrix notation to allow

Contributed by the Applied Mechanics Division of THE AMERICAN SOCIETY OF MECHANICAL ENGINEERS for publication in the ASME JOURNAL OF APPLIED MECHANICS.

Discussion on this paper should be addressed to the Technical Editor, Professor Leon M. Keer, The Technological Institute, Northwestern University, Evanston, IL 60208, and will be accepted until four months after final publication of the paper itself in the JOURNAL OF APPLIED MECHANICS.

Manuscript received by the ASME Applied Mechanics Division, Jan. 25, 1991; final revision, June 17, 1991. Associate Technical Editor: A. K. Noor.

Copyright © 1992 by ASME
Downloaded 03 May 2010 to 171.66.16.247. Redistribution subject to ASME license or copyright; see http://www.asme.org/terms/Terms_Use.cfm

for a solution using boundary elements, and a brief discussion on numerical implementation is given.

Problem Definition

Consider a two-dimensional domain Ω^* bounded by the external boundary Γ_1 and the internal flaw boundary Γ_2^*. The potential (temperature) field is described by the Laplace equation

$$\nabla^2\phi(\mathbf{x})+\psi(\mathbf{x})=0; \quad \mathbf{x}\in\Omega^* \tag{1}$$

$$\phi(\mathbf{x})=\phi^o, \quad \mathbf{x}\in\Gamma_{1\phi} \tag{2}$$

$$q(\mathbf{x})=q^o, \quad \mathbf{x}\in\Gamma_{1q} \tag{3}$$

where ϕ is the potential; $q=\partial\phi/\partial n$; $\mathbf{n}$ is the outward normal; ψ is the specified distribution of source strengths over the domain Ω^*; $\Gamma_{1\phi}$ and Γ_{1q} are the portions of the outer boundary with specified ϕ and q, respectively; $\Gamma_1=\Gamma_{1\phi}+\Gamma_{1q}$; and $\mathbf{x}$ is the position vector. The inverse problems can then be defined as follows.

Identification Problem: Consider that the internal flaw boundary Γ_2^* is not known. A set of experimental measurements are available as

$$\phi(\mathbf{x}_m, \Gamma_2^*)=\phi_e^o(\mathbf{x}_m, \Gamma_2^*), \quad \mathbf{x}_m\in\Gamma_1 \tag{4}$$

$$q(\mathbf{x}_n, \Gamma_2^*)=q_e^o(\mathbf{x}_n, \Gamma_2^*), \quad \mathbf{x}_n\in\Gamma_1 \tag{5}$$

$m=1, 2, \ldots, M$; $n=1, 2, \ldots, N$. A total of $(N+M)$ experimental observations are thus available. The identification problem consists of determining the flaw geometry Γ_2^* based on these given experimental values.

Reconstruction Problem: Consider that the internal flaw boundary is now known (or does not exist) and that the boundaries $\Gamma_{1\phi}$ and Γ_{1q} can be decomposed as

$$\Gamma_{1\phi}=\Gamma_{1\phi^o}+\Gamma_{1\bar{\phi}}$$

$$\Gamma_{1q}=\Gamma_{1q^o}+\Gamma_{1\bar{q}} \tag{6}$$

where the superscript ^{o} denotes that the boundary conditions are specified with the magnitude known, and the superscript $\bar{}$ denotes that the magnitudes of the specified boundary conditions are not known. The boundary conditions depend on the environmental conditions to which the solid is exposed. In some cases, it may not be possible to estimate these conditions due to geometrical or environmental conditions (Dorri, 1987). The superscript $\bar{}$ refers to such boundary conditions. The reconstruction inverse problem consists in determining these boundary conditions based on experimental observations given in Eqs. (4) and (5). In these cases, several temperature measurements at the interior locations of the solid may also be made due to inaccessibility of the exterior boundary for measurements. These observations are expressed as

$$\phi(\mathbf{x}_p, \Gamma_2^*)=\phi_e^o(\mathbf{x}_p, \Gamma_2^*); \quad \mathbf{x}_p\in\Omega^*; \quad p=1, 2, \ldots, P. \tag{7}$$

It is noted that the inverse problem may require the solution of the identification and the reconstruction problems simultaneously.

Theoretical Formulation

The boundary integral relationship (Banerjee and Butterfield, 1980) for potential in the solid corresponding to the actual flaw geometry Γ_2^* is given as

$$\phi(\mathbf{x}, \Gamma_2^*)=\int_{\Gamma_1}\left[\frac{\partial K(\mathbf{x}, \mathbf{y})}{\partial n(\mathbf{y})}\phi(\mathbf{y}, \Gamma_2^*) - K(\mathbf{x}, \mathbf{y})\frac{\partial\phi(\mathbf{y}, \Gamma_2^*)}{\partial n(\mathbf{y})}\right]d\Gamma_1(\mathbf{y}) + \int_{\Gamma_2^*}\left[\frac{\partial K(\mathbf{x}, \mathbf{y}^*)}{\partial n(\mathbf{y}^*)}\phi^*(\mathbf{y}^*, \Gamma_2^*) - K(\mathbf{x}, \mathbf{y}^*)\frac{\partial\phi^*(\mathbf{y}^*, \Gamma_2^*)}{\partial n(\mathbf{y}^*)}\right]d\Gamma_2^*(\mathbf{y}^*) + \int_{\Omega^*}K(\mathbf{x}, \mathbf{z}^*)\psi(\mathbf{z}^*)d\Omega^*(\mathbf{z}^*). \tag{8}$$

The superscript * denotes quantities associated with the actual flaw geometry. To proceed with the solution of the inverse problem, a flaw configuration Γ_2 is assumed. An integral relationship similar to Eq. (8) can be written for the assumed flaw as

$$\phi(\mathbf{x}, \Gamma_2)=\int_{\Gamma_1}\left[\frac{\partial K(\mathbf{x}, \mathbf{y})}{\partial n(\mathbf{y})}\phi(\mathbf{y}, \Gamma_2) - K(\mathbf{x}, \mathbf{y})\frac{\partial\phi(\mathbf{y}, \Gamma_2)}{\partial n(\mathbf{y})}\right]d\Gamma_1(\mathbf{y}) + \int_{\Gamma_2}\left[\frac{\partial K(\mathbf{x}, \mathbf{y})}{\partial n(\mathbf{y})}\phi(\mathbf{y}, \Gamma_2) - K(\mathbf{x}, \mathbf{y})\frac{\partial\phi(\mathbf{y}, \Gamma_2)}{\partial n(\mathbf{y})}\right]d\Gamma_2(\mathbf{y}) + \int_{\Omega}K(\mathbf{x}, \mathbf{z})\psi(\mathbf{z})\,d\Omega(\mathbf{z}). \tag{9}$$

The variation of the potential in the assumed flaw configuration at the field location $\mathbf{x}$ with respect to the actual flaw configuration is defined as

$$\delta\phi(\mathbf{x}, \Gamma_2)=\phi(\mathbf{x}, \Gamma_2^*)-\phi(\mathbf{x}, \Gamma_2). \tag{10}$$

The potential $\phi(\mathbf{x}, \Gamma_2^*)$ is available from experimental measurements at location $\mathbf{x}$. The potential $\phi(\mathbf{x}, \Gamma_2)$ may be computed using the usual boundary element procedure since the assumed boundary Γ_2 is known. Thus, $\delta\phi(\mathbf{x}, \Gamma_2)$ can be obtained at the location $\mathbf{x}$. The right-hand side of Eq. (10) can be expressed in the integral form through substitutions for $\phi(\mathbf{x}, \Gamma_2^*)$ and $\phi(\mathbf{x}, \Gamma_2)$ from Eq. (8) and (9), respectively. The evaluation of the integrals in Eq. (8), however, requires the knowledge of the exact flaw geometry, Γ_2^*, which is not known. It is required to express these integrals in terms of the assumed flaw geometry Γ_2. It is also necessary that the volume integrals in Eqs. (8) and (9) are expressed as surface integrals to obtain a boundary formulation. These two steps are presented as follows.

Consider first the term Γ_2^* in Eq. (8) which is expressed as

$$d\Gamma_2^*=d\Gamma_2+\delta\Gamma_2. \tag{11}$$

From Fig. 1,

$$\mathbf{y}^*=\mathbf{y}+\delta\mathbf{y}. \tag{12}$$

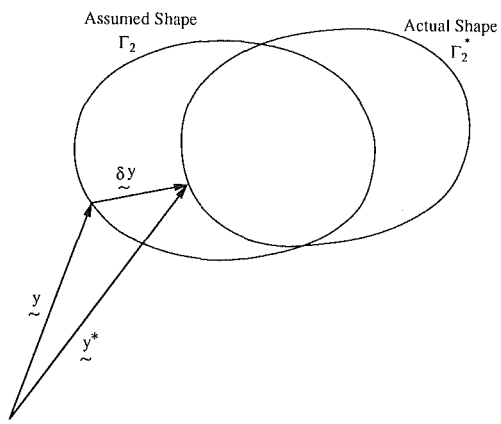


Fig. 1

Downloaded 03 May 2010 to 171.66.16.247. Redistribution subject to ASME license or copyright; see http://www.asme.org/terms/Terms_Use.cfm

Noting that $d\Gamma_2^* = |dy^*|$, $d\Gamma_2 = |dy|$ and taking the differential of Eq. (12) gives

$$d\Gamma_2^* = J_2(\mathbf{y}) d\Gamma_2(\mathbf{y})$$

$$J_2(\mathbf{y}) = \frac{|d\mathbf{y} + d(\delta\mathbf{y})|}{|d\mathbf{y}|}. \tag{13}$$

On expanding $J_2(\mathbf{y})$ and neglecting higher order terms, we obtain

$$J_2(\mathbf{y}) = 1 + \frac{d\mathbf{y} \cdot \delta(d\mathbf{y})}{d\mathbf{y} \cdot d\mathbf{y}}. \tag{14}$$

The fundamental solution terms $K(\mathbf{x}, \mathbf{y}^*)$ and $\partial K(\mathbf{x}, \mathbf{y}^*)/\partial n(\mathbf{y}^*)$ are considered next. Using Eq. (12), followed by a Taylor's expansion, leads to the following relations:

$$K(\mathbf{x}, \mathbf{y}^*) = K(\mathbf{x}, \mathbf{y}) + \frac{dK(\mathbf{x}, \mathbf{y})}{d\mathbf{y}} \cdot \delta\mathbf{y} + o(\|\delta\mathbf{y}\|) \tag{15}$$

and

$$\frac{\partial K(\mathbf{x}, \mathbf{y}^*)}{\partial n(\mathbf{y}^*)} = \frac{\partial K(\mathbf{x}, \mathbf{y})}{\partial n(\mathbf{y})} + \frac{d}{d\mathbf{y}}\left[\frac{\partial K(\mathbf{x}, \mathbf{y})}{\partial n(\mathbf{y})}\right] \cdot \delta\mathbf{y} + o(\|\delta\mathbf{y}\|). \tag{16}$$

Consider now the term $\phi^*(\mathbf{y}^*, \Gamma_2^*)$. Expanding this term about $\mathbf{y}$ using the Taylor's series gives

$$\phi^*(\mathbf{y}^*, \Gamma_2^*) = \phi(\mathbf{y}, \Gamma_2^*) + \frac{d\phi(\mathbf{y}, \Gamma_2^*)}{d\mathbf{y}} \cdot \delta\mathbf{y} + o(\|\delta\mathbf{y}\|). \tag{17}$$

The two terms on the right-hand side involve Γ_2^* and need to be written in terms of Γ_2. Expanding the first term about Γ_2 gives

$$\phi(\mathbf{y}, \Gamma_2^*) = \phi(\mathbf{y}, \Gamma_2) + \frac{d\phi(\mathbf{y}, \Gamma_2)}{d\Gamma_2} \otimes \delta\Gamma_2 + o(\|\delta\Gamma_2\|), \tag{18}$$

or, neglecting higher order terms and using the definition of $\delta\phi$ in Eq. (10), we get

$$\frac{d\phi(\mathbf{y}, \Gamma_2)}{d\Gamma_2} \otimes \delta\Gamma_2 = \delta\phi(\mathbf{y}, \Gamma_2). \tag{19}$$

The second term on the right-hand side of Eq. (17) on expansion yields

$$\frac{d\phi(\mathbf{y}, \Gamma_2^*)}{d\mathbf{y}} \cdot \delta\mathbf{y} = \frac{d\phi(\mathbf{y}, \Gamma_2)}{d\mathbf{y}} \cdot \delta\mathbf{y} + o(\|\delta\Gamma_2\|, \|\delta\mathbf{y}\|). \tag{20}$$

Substituting Eqs. (18)–(20) into Eq. (17), and neglecting higher order terms,

$$\phi^*(\mathbf{y}^*, \Gamma_2^*) = \phi(\mathbf{y}, \Gamma_2) + \frac{d\phi(\mathbf{y}, \Gamma_2)}{d\mathbf{y}} \cdot \delta\mathbf{y} + \delta\phi(\mathbf{y}, \Gamma_2). \tag{21}$$

Similarly,

$$\phi^*{}_{,n}(\mathbf{y}^*, \Gamma_2^*) = \phi_{,n}(\mathbf{y}, \Gamma_2) + \frac{d\phi_{,n}(\mathbf{y}, \Gamma_2)}{d\mathbf{y}} \cdot \delta\mathbf{y} + \delta\phi_{,n}(\mathbf{y}, \Gamma_2) \tag{22}$$

where

$$\delta\phi_{,n}(\mathbf{y}, \Gamma_2) = \phi_{,n}(\mathbf{y}, \Gamma_2^*) - \phi_{,n}(\mathbf{y}, \Gamma_2)$$

$$\phi_{,n}(\mathbf{y}, \Gamma_2) = \frac{d\phi(\mathbf{y}, \Gamma_2)}{dn(\mathbf{y})}. \tag{23}$$

The volume integral in Eq. (8) is finally considered. Consider the flaw shapes Γ_2 and Γ_2^* shown in Fig. 2. These flaw geometries divide the domain into four subregions as shown. From Fig. 2,

$$\int_{\Omega^*} (\cdot) d\Omega^* = \int_{\Omega_4} (\cdot) d\Omega_4 + \int_{\Omega_1} (\cdot) d\Omega_1. \tag{24}$$

Adding and subtracting $\int_{\Omega_3} (\cdot) d\Omega_3$ on the right-hand side and noting that $\Omega = \Omega_4 + \Omega_3$ yields

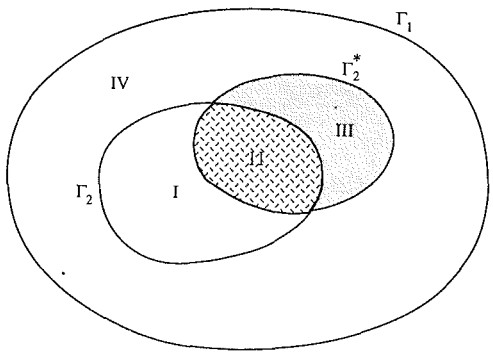


Fig. 2

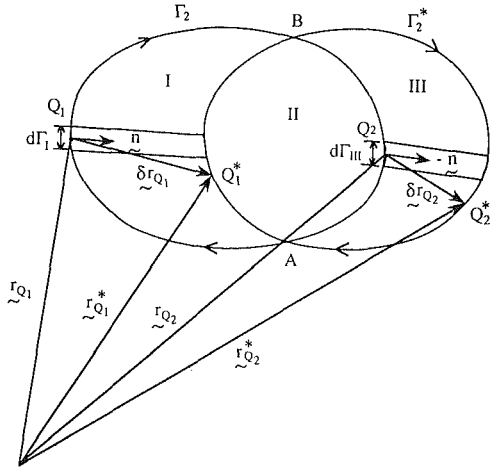


Fig. 3

$$\int_{\Omega^*} (\cdot) d\Omega^* = \int_{\Omega} (\cdot) d\Omega + \int_{\Omega_1} (\cdot) d\Omega_1 - \int_{\Omega_3} (\cdot) d\Omega_3. \tag{25}$$

Now, from Fig. 3, it can be seen that

$$d\Omega_1 = (\delta\mathbf{r}_Q \cdot \mathbf{n}) d\Gamma_1(\mathbf{r}_Q), \quad \mathbf{r}_Q \in \overline{AQ_1B} \tag{26}$$

$$d\Omega_3 = [\delta\mathbf{r}_Q \cdot (-\mathbf{n})] d\Gamma_3(\mathbf{r}_Q), \quad \mathbf{r}_Q \in \overline{BQ_2A}. \tag{27}$$

Substituting Eqs. (26) and (27) into Eq. (25), and noting that the integrand is a function $(\cdot) = F_\Omega(\mathbf{r}_P, \mathbf{r}_Q)$, Eq. (25) can be written as

$$\int_{\Omega^*} F_\Omega(\mathbf{r}_P^*, \mathbf{r}_Q^*) d\Omega^*(\mathbf{r}_Q^*) = \int_{\Omega} F_\Omega(\mathbf{r}_P, \mathbf{r}_Q) d\Omega(\mathbf{r}_Q) + \int_{\Gamma_2} F_\Omega(\mathbf{r}_P, \mathbf{r}_Q) \delta\mathbf{r}_Q \cdot \mathbf{n}(\mathbf{r}_Q) d\Gamma_2(\mathbf{r}_Q) \tag{28}$$

where $\mathbf{r}_P$ and $\mathbf{r}_Q$ are position vectors to points P and Q, respectively.

Substituting Eqs. (13), (15), (16), (21), (22), and (28) into Eq. (10) together with Eqs. (8) and (9) gives the final form of $\delta\phi$ on neglecting higher order terms as

$$\delta\phi(\mathbf{x}, \Gamma_2) = \int_{\Gamma_1} \left[\frac{\partial K(\mathbf{x}, \mathbf{y})}{\partial n(\mathbf{y})} \delta\phi(\mathbf{y}, \Gamma_2) - K(\mathbf{x}, \mathbf{y}) \delta\phi_{,n}(\mathbf{y}, \Gamma_2)\right] d\Gamma_1(\mathbf{y}) + \int_{\Gamma_2} \left\{\frac{\partial K(\mathbf{x}, \mathbf{y})}{\partial n(\mathbf{y})} \delta\phi(\mathbf{y}, \Gamma_2) - K(\mathbf{x}, \mathbf{y}) \delta\phi_{,n}(\mathbf{y}, \Gamma_2) + \phi(\mathbf{y}, \Gamma_2) \frac{d}{d\mathbf{y}}\left[\frac{\partial K(\mathbf{x}, \mathbf{y})}{\partial n(\mathbf{y})}\right] \cdot \delta\mathbf{y} - K(\mathbf{x}, \mathbf{y}) \frac{d\phi_{,n}(\mathbf{y}, \Gamma_2)}{d\mathbf{y}} \cdot \delta\mathbf{y}$$

Downloaded 03 May 2010 to 171.66.16.247. Redistribution subject to ASME license or copyright; see http://www.asme.org/terms/Terms_Use.cfm

$$+\frac{\partial K(\mathbf{x},\mathbf{y})}{\partial n(\mathbf{y})}\frac{d\phi(\mathbf{y},\Gamma_2)}{d\mathbf{y}}\cdot\delta\mathbf{y}-\phi_{,n}(\mathbf{y},\Gamma_2)\frac{dK(\mathbf{x},\mathbf{y})}{d\mathbf{y}}\cdot\delta\mathbf{y}$$
$$+[J_2(\mathbf{y})-1]\left[\frac{\partial K(\mathbf{x},\mathbf{y})}{\partial n(\mathbf{y})}\phi(\mathbf{y},\Gamma_2)-K(\mathbf{x},\mathbf{y})\phi_{,n}(\mathbf{y},\Gamma_2)\right.$$
$$\left.+K(\mathbf{x},\mathbf{y})\psi(\mathbf{y})\mathbf{n}(\mathbf{y})\cdot\delta\mathbf{y}\right\}d\Gamma_2(\mathbf{y}). \quad (29)$$

Equation (29) is the integral equation which provides the relationship between the variations $\delta\phi$ and $\delta\phi_{,n}$ with the variation of coordinates $\delta\mathbf{y}$ of the boundary shape from the assumed flaw geometry. In order to be able to obtain a solution to Eq. (29), it is necessary to obtain the boundary conditions corresponding to $\delta\phi$, $\delta\phi_{,n}$ and $\delta\mathbf{y}$. These boundary conditions are derived in the following section.

Boundary Conditions

Consider first the outer boundary Γ_1 for which the geometry is known. This boundary is composed of three subregions as

$$\Gamma_1=\Gamma_{1\phi^o}+\Gamma_{1\bar{\phi}}+\Gamma_{1q^o}. \quad (30)$$

$\Gamma_{1\phi^o}$ is the portion with prescribed ϕ of known magnitude; $\Gamma_{1\bar{\phi}}$ is the portion with prescribed ϕ whose magnitude is not known; and Γ_{1q^o} is the portion with prescribed $\phi_{,n}$ of known magnitude. The determination of ϕ on $\Gamma_{1\bar{\phi}}$ is part of the solution that we seek for the inverse reconstruction problem.

Portion $\Gamma_{1\phi^o}$: The specified boundary conditions for ϕ on this portion of the boundary are not affected by the location of the flaw inside the body. Thus, $\phi(\mathbf{y},\Gamma_2^*)=\phi(\mathbf{y},\Gamma_2)$, $\mathbf{y}\in\Gamma_{1\phi^o}$ leading to

$$\delta\phi(\mathbf{y},\Gamma_2)=0, \quad \mathbf{y}\in\Gamma_{1\phi^o}. \quad (31)$$

Portion $\Gamma_{1\bar{\phi}}$: Let $\phi^o(\mathbf{y},\Gamma_2^*)$ be the exact, unknown value of the potential on $\Gamma_{1\bar{\phi}}$ corresponding to the exact flaw shape Γ_2^*. Assume a value $\bar{\phi}(\mathbf{y},\Gamma_2)$ on $\Gamma_{1\bar{\phi}}$ corresponding to the assumed flaw configuration Γ_2. Then, using the definition of $\delta\phi$ in Eq. (10),

$$\delta\phi(\mathbf{y},\Gamma_2)=\phi^o(\mathbf{y},\Gamma_2)-\bar{\phi}(\mathbf{y},\Gamma_2). \quad (32)$$

Portion Γ_{1q^o}: Similar to the portion $\Gamma_{1\phi^o}$ of the boundary Γ_1, for this portion, we have $\phi_{,n}(\mathbf{y},\Gamma_2^*)=\phi_{,n}(\mathbf{y},\Gamma_2)$, $\mathbf{y}\in\Gamma_{1q^o}$, leading to

$$\delta\phi_{,n}(\mathbf{y},\Gamma_2^*)=0, \quad \mathbf{y}\in\Gamma_{1q^o}. \quad (33)$$

The flaw boundary Γ_2 is now considered. The boundary Γ_2 is decomposed into three regions analogous to the three subregions of Γ_1 as

$$\Gamma_2=\Gamma_{2\phi^o}+\Gamma_{2\bar{\phi}}+\Gamma_{2q^o}, \quad (34)$$

and similarly for Γ_2^* as

$$\Gamma_2^*=\Gamma_{2\phi^o}^*+\Gamma_{2\bar{\phi}}^*+\Gamma_{2q^o}^*. \quad (35)$$

The three portions of Γ_2 and Γ_2^* are separately considered.

Portion $\Gamma_{2\phi^o}$, $\Gamma_{2\phi^o}^*$: For these portions of Γ_2 and Γ_2^*, the potential ϕ of a known magnitude ϕ^o is prescribed as

$$\phi(\mathbf{y},\Gamma_2)=\phi^o(\mathbf{y},\Gamma_2), \quad \mathbf{y}\in\Gamma_{2\phi^o}$$
$$\phi^*(\mathbf{y}^*,\Gamma_2^*)=\phi^o(\mathbf{y}^*,\Gamma_2^*), \quad \mathbf{y}\in\Gamma_{2\phi^o}^*. \quad (36)$$

Substituting these conditions into Eq. (21) and noting that $\phi^o(\mathbf{y},\Gamma_2)=\phi^o(\mathbf{y}^*,\Gamma_2^*)$ leads to

$$\delta\phi(\mathbf{y},\Gamma_2)=-\frac{d\phi(\mathbf{y},\Gamma_2)}{d\mathbf{y}}\cdot\delta\mathbf{y}. \quad (37)$$

Portion $\Gamma_{2\bar{\phi}}$, $\Gamma_{2\bar{\phi}}^*$: The magnitude of the specified potential, $\phi^o(\mathbf{y}^*,\Gamma_2^*)$, is not known on this portion of the boundary. A value $\bar{\phi}(\mathbf{y},\Gamma_2)$ corresponding to flaw shape Γ_2 is assumed:

$$\phi(\mathbf{y},\Gamma_2)=\bar{\phi}(\mathbf{y},\Gamma_2), \quad \mathbf{y}\in\Gamma_{2\bar{\phi}}$$
$$\phi^*(\mathbf{y}^*,\Gamma_2^*)=\phi^o(\mathbf{y}^*,\Gamma_2^*), \quad \mathbf{y}\in\Gamma_{2\bar{\phi}}^*. \quad (38)$$

Define

$$\delta\phi_2(\mathbf{y},\Gamma_2)=\phi^o(\mathbf{y}^*,\Gamma_2^*)-\bar{\phi}(\mathbf{y},\Gamma_2), \quad \mathbf{y}^*\in\Gamma_{2\bar{\phi}}^*,\ \mathbf{y}\in\Gamma_{2\bar{\phi}}. \quad (39)$$

Then, using Eqs. (38) and (39) in Eq. (21), we get

$$\delta\phi(\mathbf{y},\Gamma_2)=\delta\phi_2(\mathbf{y},\Gamma_2)-\frac{d\phi(\mathbf{y},\Gamma_2)}{d\mathbf{y}}\cdot\delta\mathbf{y}, \quad \mathbf{y}\in\Gamma_{2\bar{\phi}}. \quad (40)$$

Portion Γ_{2q^o}, $\Gamma_{2q^o}^*$: This portion of the boundary is treated similar to portions $\Gamma_{2\phi^o}$, $\Gamma_{2\phi^o}^*$ to give

$$\delta\phi_{,n}(\mathbf{y},\Gamma_2)=-\frac{d\phi_{,n}(\mathbf{y},\Gamma_2)}{d\mathbf{y}}\cdot\delta\mathbf{y}, \quad \mathbf{y}\in\Gamma_{2q^o}. \quad (41)$$

Substituting Eqs. (31), (33), (37), (40), and (41) into Eq. (29) we get the final expression as

$$\delta\phi(\mathbf{x},\Gamma_2)=\int_{\Gamma_{1\phi^o}}[-K(\mathbf{x},\mathbf{y})\delta\phi_{,n}(\mathbf{y},\Gamma_2)]d\Gamma_1(\mathbf{y})$$
$$+\int_{\Gamma_{1\bar{\phi}}}\left[\frac{\partial K(\mathbf{x},\mathbf{y})}{\partial n(\mathbf{y})}\delta\phi(\mathbf{y},\Gamma_2)-K(\mathbf{x},\mathbf{y})\delta\phi_{,n}(\mathbf{y},\Gamma_2)\right]d\Gamma_1(\mathbf{y})$$
$$+\int_{\Gamma_{1q^o}}\left[\frac{\partial K(\mathbf{x},\mathbf{y})}{\partial n(\mathbf{y})}\phi(\mathbf{y},\Gamma_2)\right]d\Gamma_1(\mathbf{y})$$
$$-\int_{\Gamma_{2\phi^o}}[K(\mathbf{x},\mathbf{y})\delta\phi_{,n}(\mathbf{y},\Gamma_2)]d\Gamma_2(\mathbf{y})$$
$$+\int_{\Gamma_{2\bar{\phi}}}\left[\frac{\partial K(\mathbf{x},\mathbf{y})}{\partial n(\mathbf{y})}\delta\phi_2(\mathbf{y},\Gamma_2)-K(\mathbf{x},\mathbf{y})\delta\phi_{,n}(\mathbf{y},\Gamma_2)\right]d\Gamma_2(\mathbf{y})$$
$$+\int_{\Gamma_{2q^o}}\left[\frac{\partial K(\mathbf{x},\mathbf{y})}{\partial n(\mathbf{y})}\delta\phi(\mathbf{y},\Gamma_2)\right]d\Gamma_2(\mathbf{y})$$
$$\int_{\Gamma_{2\phi^o}}\left[-\frac{\partial K(\mathbf{x},\mathbf{y})}{\partial n(\mathbf{y})}\frac{d\phi(\mathbf{y},\Gamma_2)}{d\mathbf{y}}\cdot\delta\mathbf{y}\right]d\Gamma_2(\mathbf{y})$$
$$+\int_{\Gamma_{2\phi}}\left[-\frac{\partial K(\mathbf{x},\mathbf{y})}{\partial n(\mathbf{y})}\frac{d\phi(\mathbf{y},\Gamma_2)}{d\mathbf{y}}\cdot\delta\mathbf{y}\right]d\Gamma_2(\mathbf{y})$$
$$+\int_{\Gamma_{2q^o}}\left[K(\mathbf{x},\mathbf{y})\frac{d\phi_{,n}(\mathbf{y},\Gamma_2)}{d(\mathbf{y})}\cdot\delta\mathbf{y}\right]d\Gamma_2(\mathbf{y})$$
$$+\int_{\Gamma_2}\left\{\phi(\mathbf{y},\Gamma_2)\frac{d}{d\mathbf{y}}\left[\frac{\partial K(\mathbf{x},\mathbf{y})}{\partial n(\mathbf{y})}\right]\cdot\delta\mathbf{y}\right.$$
$$-K(\mathbf{x},\mathbf{y})\frac{d}{d\mathbf{y}}\left[\phi_{,n}(\mathbf{y},\Gamma_2)\right]\cdot\delta\mathbf{y}$$
$$+\frac{\partial K(\mathbf{x},\mathbf{y})}{\partial n(\mathbf{y})}\frac{d}{d\mathbf{y}}[\phi(\mathbf{y},\Gamma_2)]\cdot\delta\mathbf{y}$$
$$\left.-\phi_{,n}(\mathbf{y},\Gamma_2)\frac{d}{d\mathbf{y}}[K(\mathbf{x},\mathbf{y})]\cdot\delta\mathbf{y}\right\}d\Gamma_2(\mathbf{y})$$
$$+\int_{\Gamma_2}[J_2(\mathbf{y})-1]\left\{\frac{\partial K(\mathbf{x},\mathbf{y})}{\partial n(\mathbf{y})}\phi(\mathbf{y},\Gamma_2)\right.$$
$$\left.-K(\mathbf{x},\mathbf{y})\phi_{,n}(\mathbf{y},\Gamma_2)\right\}d\Gamma_2(\mathbf{y})$$
$$+\int_{\Gamma_2}\{K(\mathbf{x},\mathbf{y})\psi(\mathbf{y})\mathbf{n}(\mathbf{y})\cdot\delta\mathbf{y}\}d\Gamma_2(\mathbf{y}). \quad (42)$$

Numerical Discretization

The integral expression in Eq. (42) consists of two types of

Downloaded 03 May 2010 to 171.66.16.247. Redistribution subject to ASME license or copyright; see http://www.asme.org/terms/Terms_Use.cfm

integrals, those containing a dot product with $\delta\mathbf{y}$ and those that do not. The numerical discretization of these integrals is considered separately.

Consider first the terms that do not contain the dot product with $\delta\mathbf{y}$. A term (i) can be written as

$$I^{(i)} = \sum_{e=1}^{N^{(i)}} \int_{\Gamma_e^{(i)}} G^{(i)}(\mathbf{x}, \mathbf{y})\lambda^{(i)}(\mathbf{y}) d\,\Gamma^{(i)}(\mathbf{y}), \tag{43}$$

where e denotes the element number; $N^{(i)}$ is the number of elements used to discretize the boundary over which this term is integrated; and Γ_e^i denotes the surface of element e. For example, for the first term in Eq. (42), $G^{(i)}(\mathbf{x}, \mathbf{y}) = -K(\mathbf{x}, \mathbf{y})$, $\lambda^{(i)}(\mathbf{y}) = \delta\phi_{,n}(\mathbf{y}, \Gamma_2)$, and $\Sigma_{e=1}^{N^{(i)}} \Gamma_e^{(i)} = \Gamma_{1\phi^o}$. The summation sign in Eq. (43) denotes assembly over all the elements.

The variable $\lambda^{(i)}(\mathbf{y})$ is expressed in terms of its nodal values as

$$\lambda^{(i)}(\mathbf{y}) = [h_\lambda(\mathbf{y})]\{\hat{\lambda}_e^{(i)}\} \tag{44}$$

where $h_\lambda(\mathbf{y})$ are the shape functions, and $\hat{\lambda}_e^{(i)}$ are the nodal values. Substituting Eq. (44) into Eq. (43) leads to

$$I_1^{(i)} = \sum_{e=1}^{N^{(i)}} \left[\int_{\Gamma_e^{(i)}} G^{(i)}(\mathbf{x}, \mathbf{y})[h_\lambda(\mathbf{y})] d\,\Gamma_e^{(i)}(\mathbf{y}) \right] \{\hat{\lambda}_e^{(i)}\} \tag{45}$$

which is written in the matrix notation as

$$I_1^{(i)} = [H_\lambda^{(i)}(\mathbf{x})]\{\hat{\lambda}^{(i)}\}. \tag{46}$$

With the contribution of n_μ, such terms to $\delta\phi$ can be written as

$$\delta\phi_\lambda(\mathbf{x}, \Gamma_2) = \sum_{i=1}^{n_\lambda} [H_\lambda^{(i)}(\mathbf{x})]\{\hat{\lambda}^{(i)}\}. \tag{47}$$

The terms containing the dot product with $\delta\mathbf{y}$ are considered next. The variation in nodal coordinates, $\delta\mathbf{y}$, is written as

$$\{\delta\mathbf{y}\} = [\bar{h}(\mathbf{y})]\{\delta\hat{\mathbf{y}}\} \tag{48}$$

where

$$\{\delta\mathbf{y}\} = [\delta x_1, \delta x_2]^T$$

$$\{\delta\hat{\mathbf{y}}\} = [\delta x_1^{(1)}, \delta x_2^{(1)}, \delta x_1^{(2)}, \delta x_2^{(2)}, \ldots, \delta x_1^{(n)}, \delta x_2^{(n)}]^T$$

$$[\bar{h}(\mathbf{y})] = \left[\begin{array}{cc|cc|c|cc} h_1 & 0 & h_2 & 0 & \cdots & h_n & 0 \\ 0 & h_1 & 0 & h_2 & & 0 & h_n \end{array}\right].$$

h_i are the shape functions; superscript $\hat{}$ denotes nodal values; superscript (i) denotes the node number; and δx_1 and δx_2 are the increments in nodal coordinates along the x and y directions, respectively. A term (j) of the terms containing $\delta\mathbf{y}$ can be written as

$$I_2^{(j)} = \sum_{e=1}^{N^{(j)}} \int_{\Gamma_e^{(i)}} f^{(j)}(\mathbf{x}, \mathbf{y})\{a(\mathbf{y})\} \cdot \{\delta\mathbf{y}\}\, d\Gamma_e^{(j)}(\mathbf{y}). \tag{49}$$

Expressing $\{a(\mathbf{y})\} = [a_x, a_y]^T$, and substituting Eq. (48) into Eq. (49) yields

$$I_2^{(j)} = \sum_{e=1}^{N^{(j)}} \left\{ \int_{\Gamma_e^{(j)}} f^{(j)}(\mathbf{x}, \mathbf{y})[a_x, a_y] \times [\bar{h}(\mathbf{y})] d\,\Gamma_e^{(j)}(\mathbf{y}) \right\} \{\delta\hat{\mathbf{y}}_e\}. \tag{50}$$

$\{\delta\hat{\mathbf{y}}_e\}$ is the contribution of element e to the vector $\{\delta\hat{\mathbf{y}}\}$. Equation (50) is written in the matrix notation as

$$I_2^{(j)} = [H_y^{(j)}(\mathbf{x})]\{\delta\hat{\mathbf{y}}\} \tag{51}$$

The contribution of n_y such terms is written as

$$\delta\phi_y(\mathbf{x}, \Gamma_2) = \sum_{j=1}^{n_y} [H_y^{(j)}(\mathbf{x})]\{\delta\hat{\mathbf{y}}\}$$

or as

$$\delta\phi_y(\mathbf{x}, \Gamma_2) = [H_y(\mathbf{x})]\{\delta\hat{\mathbf{y}}\}. \tag{52}$$

Finally,

$$\delta\phi(\mathbf{x}) = \delta\phi_\lambda(\mathbf{x}, \Gamma_2) + \delta\phi_y(\mathbf{x}, \Gamma_2)$$

and using Eqs. (47) and (52), we arrive at the matrix form

$$\delta\phi(\mathbf{x}) = [H(\mathbf{x})]\{\hat{\mathbf{w}}\} \tag{53}$$

where

$$[H(\mathbf{x})] = [H_\lambda^{(1)}(\mathbf{x}), H_\lambda^{(2)}(\mathbf{x}), \ldots, H_\lambda^{(n_\lambda)}(\mathbf{x}), H_y(\mathbf{x})]$$

$$\{\hat{\mathbf{w}}\} = [\{\hat{\lambda}^{(1)}\}, \{\hat{\lambda}^{(2)}\}, \ldots, \{\hat{\lambda}^{(n_\lambda)}\}, \{\delta\hat{\mathbf{y}}\}]^T.$$

Boundary Element Equations: The final boundary element equations are obtained by allowing the field point $\mathbf{x}$ to approach the boundary points ξ on the boundary Γ_1. Additionally, the field point $\mathbf{x}$ is allowed to approach the experimental observation locations which may lie on the boundary Γ_1 or anywhere inside the volume.

(a) Let $\mathbf{x} \to \xi$, $\xi \in \Gamma_1$.

Equation (53) can then be written as

$$[C]\{\delta\phi\} = [H_1]\{\hat{\mathbf{w}}\} \tag{54}$$

where $[C]$ contains the corner tensor terms (Banerjee and Butterfield, 1980). Equation (54) can be expressed as

$$[C_1]\{\hat{\mathbf{w}}\} = [H_1]\{\hat{\mathbf{w}}\}. \tag{55}$$

For the measurement points that lie on the boundary, it is noted that $\{\delta\phi\} = \{\phi^* - \phi\}$ where $\{\phi^*\}$ are the measured values and $\{\phi\}$ are the values computed from the geometry corresponding to Γ_2. Similar to Eq. (54), we then obtain

$$[H_2]\{\hat{\mathbf{w}}\} = [C]\{\phi^* - \phi\}. \tag{56}$$

(b) Let $\mathbf{x} \to \zeta$, $\zeta \in \Omega^*$.

In Ω^*, $\{\delta\phi\} = \{\phi^* - \phi\}$ is known and Eq. (53) reduces to

$$[H_3]\{\hat{\mathbf{w}}\} = \{\phi^* - \phi\}. \tag{57}$$

Combining Eqs. (55), (56), and (57), we obtain

$$\left[\begin{array}{c} [C_1] - [H_1] \\ \hline [H_2] \\ \hline [H_3] \end{array}\right] \{\hat{\mathbf{w}}\} = \left\{\begin{array}{c} \{0\} \\ \hline [C](\{\phi^*\} - \{\phi\}) \\ \hline \{\phi^*\} - \{\phi\} \end{array}\right\}$$

or, in an abbreviated form,

$$[K]\{\hat{\mathbf{w}}\} = \{f\}. \tag{59}$$

The solution of Eq. (59) yields the unknown quantities in $\{\hat{\mathbf{w}}\}$. Out of these $\{\delta\hat{\mathbf{y}}\}$ are used to update the coordinates of the boundary Γ_2. The $\{\delta\phi\}$ corresponding to the boundary $\Gamma_{1\bar{\phi}}$ is used to update the boundary conditions on the portion according to Eq. (32), and the $\{\delta\phi\}$ corresponding to the boundary $\Gamma_{2\bar{\phi}}$ is used to first obtain $\{\delta\phi_2\}$ from Eq. (40) and next update the boundary conditions on this portion using Eq. (39). The update geometry and boundary conditions are then used in the next iteration. This procedure is continued till a suitable convergence criterion is satisfied.

Conclusion

In this paper, an inverse formulation described completely in terms of boundary integrals and boundary quantities is derived. Through the use of Taylor's expansions, estimates for updating the configuration of assumed flaw shape and the assumed boundary conditions are obtained in the terms of potential and potential gradient variations, which are available through physical observations. The final actual flaw shape and boundary conditions are obtained in an iterative procedure through successive determination of such estimates and updating of unknown variables until some preselected convergence criterion are satisfied. An important feature of these derivations is that they do not require the computation of

Downloaded 03 May 2010 to 171.66.16.247. Redistribution subject to ASME license or copyright; see http://www.asme.org/terms/Terms_Use.cfm

sensitivities. Sensitivity-based formulations restrict the definition of any unknown geometry to a small number of design variables and are computationally burdensome. The formulation is applicable to the problems of flaw identification in solids, reconstruction of boundary conditions, and determination of optimal shapes for objects.

Acknowledgment

This material is based upon work supported by the National Science Foundation Presidential Young Investigator Grant No. MSS--9057055 with Dr. L. Anand as the project monitor. The Government has certain rights in this material. Any options, findings, and conclusions or recommendations expressed in this material are those of the author(s) and do not necessarily reflect the views of the National Science Foundation.

References

Adamiak, K., "Application of Integral Equations to Solving Inverse Problems of Stationary Electromagnetic Fields," *Int. J. Num. Meth. Engng.*, Vol. 21, pp. 1447–1458, 1985.

Banerjee, P. K., and Butterfield, R., 1981, *Boundary Element Methods in Engineering Science*, McGraw-Hill, U. K.

Baumeister, J., 1987, *Stable Solution of Inverse Problems*, Friedr. Vieweg, Braunschweig.

Beck, J. V., Blackwell, B., and St. Clair, C. R., Jr., 1985, *Inverse Heat Conduction, Ill-Posed Problems*, John Wiley and Sons, New York.

Dorri, B., 1987, "Solution of Inverse Heat Conduction Problems Using Boundary Integral Method," General Electric CR&D Report.

Kojima, F., 1987, "Shape Identification Technique for a 2-d Elliptic System by Boundary Integral Equation Method," ICASE Report, NASA Langley Research Center.

Mura, T., 1985, "A New NDT: Evaluation of Plastic Strains in Bulk from Displacements on Surfaces," *Mech. Res. Commun.*, Vol. 12, pp. 243–248.

Mura, T., Cox, B., and Gao, Z., 1986, "Computer-aided Nondestructive Measurements of Plastic Strains from Surface Displacements," *Computational Mechanics*, Vol. 1.

Ohnaka, K., and Uosaki, K., 1985, "Boundary Element Approach for Identification of Boundary Conditions of Distributed-Parameter Systems," *Int. J. Control*, Vol. 41, pp. 981-ff.

Schnur, D. S., and Zabaras, N., 1990, "Finite Element Solution of Two-dimensional Inverse Elastic Problems Using Spatial Smoothing," *Int. J. Num. Meth. Engng.*, Vol. 30, pp. 57–75.

Zabaras, N., Mukherjee, S., and Richmond, O., 1988, "An Integral Analysis of Inverse Heat Transfer with Phase Changes," ASME *Journal of Heat Transfer*, Vol. 13, pp. 527–533.

Zabaras, N., Morellas, V., and Schnur, D., 1989, "A Spatially Regularized Solution of Inverse Elasticity Problems Using the Boundary Element Method," *Commun. Appl. Numer. Methods*, Vol. 5, pp. 547–553.

Downloaded 03 May 2010 to 171.66.16.247. Redistribution subject to ASME license or copyright; see http://www.asme.org/terms/Terms_Use.cfm

T. G. Ryall[1]

M. Heller

R. Jones

Defence Science and
Technology Organisation,
Aircraft Structures Division,
Aeronautical Research Laboratory
Fishermens Bend
Port Melbourne 3207, Australia

Determination of Stress Components From Thermoelastic Data Without Boundary Conditions

Recent investigations have shown that the temperature variation caused by sinusoidal loading of a solid consists of two harmonic components. In this paper it is shown that by using an appropriate Airy stress function the separated stress components can be obtained, almost always, with knowledge of these two components. Since the second harmonic response is small compared to the noise level, the question of experimental design is examined. The problem of uniqueness is also studied. The close similarity between the second harmonic response and various energy parameters is also investigated and its role in structural optimization is discussed. The method is demonstrated on a particular example using simulated noisy data.

1 Introduction

In recent years, the thermoelastic stress analysis technique has been shown to be a particularly useful method for experimental stress analysis. The basic principle being that if a body is subjected to an applied dynamic load, then the change in temperature is proportional to the sum of the principal stresses, provided that adiabatic conditions apply (Stanley, 1990; Thomson, 1953). However, a re-examination of the theoretical basis of this technique revealed that for a homogeneous material the temperature response has a small nonlinear term involving a quadratic form of the principal stresses (Wong et al., 1987). This revised formulation showed that the temperature response to an applied sinusoidal loading consists of two harmonic components. The first component is at the loading frequency w, while the second is at $2w$, and their amplitudes depend on the dynamic stress range as well as on the static stresses. These concepts have been verified experimentally (Machin et al., 1987; A. K. Wong et al., 1988) and the results raise the possibility of developing approaches for both residual stress measurement as well for the separation of the principal stresses into the individual stress components.

As far as stress separation is concerned, use of the linear theory plus knowledge of the free boundaries is sufficient, in two-dimensional problems, to determine the stress components. For example, this was shown in Ryall and Wong (1988), which studied a strip of metal loaded in an unknown manner at the two ends with lateral sides remaining free. The uniqueness property for such a completely general problem in two dimensions can be readily shown. In Waldman et al. (1990) and Jones and Paul (1989), the linear formulation was used with boundary conditions to examine the problem of determining the stress components for a three-dimensional stress state. In Waldman et al. (1990), the problem considered was a prism rigidly restrained at one end and subjected to arbitrary loads at the other. The solution to this problem was shown to be unique, provided the cross-section was not circular. On the other hand, in Jones and Paul (1989), uniqueness was only achieved when additional strain gauge data were used. An alternative approach for determining the dominant surface strains/stresses follows from the experimental/numerical work presented in Jones and Paul (1989). This revealed that if a relatively thin, unidirectional boron-epoxy laminate is bonded over a region with a complex three-dimensional stress state, then the observed temperature profile can be correlated reasonably accurately to the surface stresses/strains in the fiber direction. This has implications for the in situ measurement of surface strains in a real structure, which must be sufficiently stiff so that the external laminate does not significantly disturb the local stress field.

The discussion so far has considered only using the linear response; if the nonlinear formulation is used, boundary conditions may or may not be required depending on the problem under consideration. In Ryall et al. (1990) a thin plate with a hole, loaded both dynamically and statically, was examined. Only the response at the fundamental frequency in conjunction with boundary conditions was used to obtain the dynamic and static stress tensors from experimental data. In this case a robust nonlinear least-squares method was applied and the motion of the specimen was modeled.

In the present paper, extensions are made to the work of Wong et al. (1987) and Ryall et al. (1990) and the problem of determining the stress components from both the first and the second harmonic response of an isotropic material without using boundary conditions is studied. The motivation for de-

[1]To whom all correspondence should be addressed.

Contributed by the Applied Mechanics Division of THE AMERICAN SOCIETY OF MECHANICAL ENGINEERS for publication in the ASME JOURNAL OF APPLIED MECHANICS.

Discussion on this paper should be addressed to the Technical Editor, Prof. Leon M. Keer, The Technological Institute, Northwestern University, Evanston, IL 60208, and will be accepted until four months after final publication of the paper itself in the ASME JOURNAL OF APPLIED MECHANICS.

Manuscript received by the ASME Applied Mechanics Division, Nov. 30, 1990; final revision, Aug. 13, 1991. Associate Technical Editor: R. M. Bowen.

Copyright © 1992 by ASME
Downloaded 03 May 2010 to 171.66.16.247. Redistribution subject to ASME license or copyright; see http://www.asme.org/terms/Terms_Use.cfm

termining stress components without using boundary conditions is due to the following reasons; viz:

(i) the parametric shape of the free boundary may not be known;

(ii) the shape of the free boundary is known but special functions are required to satisfy the boundary conditions.

Since the second harmonic response is small compared to the level of noise, particular attention has been paid to the question of experimental design. The problem of uniqueness is also considered. The close similarity between the second harmonic response and various energy parameters is also examined.

2 Thermoelasticity Theory

For a two-dimensional problem the scaled temperature response $T(t)$ resulting from a cyclically applied stress, provided that the frequency is such that adiabatic conditions hold, can be written as (Wong et al. 1987)

$$T(t) = (\Upsilon_1(t) + \Upsilon_2(t)) - \frac{K_2}{K_1}(\Upsilon_1(t) + \Upsilon_2(t))^2 + \frac{K_3}{K_1}(\Upsilon_1(t)\Upsilon_2(t)) \quad (1)$$

where

$$K_1 = \alpha/\rho C$$

$$K_2 = \frac{1}{2\rho C E^2}\frac{\partial E}{\partial T}$$

$$K_3 = \left(\frac{1+\nu}{E^2}\frac{\partial E}{\partial T} - \frac{1}{E}\frac{\partial \nu}{\partial T}\right)\frac{1}{\rho C}.$$

Here, Υ_1 and Υ_2 are principal stresses, E and ν are the Young's modulus and Poisson's ratio, respectively, α is the coefficient of linear expansion, ρ is the density, and C is the specific heat and t is time.

For a sinusoidal loading of

$$\Upsilon_1(t) = \Upsilon_1 \sin(\omega t) \text{ and } \Upsilon_2(t) = \Upsilon_2 \sin(\omega t),$$

substituting into Eq. (1) and neglecting the constant term, it follows that

$$T(t) = (\Upsilon_1 + \Upsilon_2)\sin(\omega t) + \left[\frac{K_2}{2K_1}(\Upsilon_1 + \Upsilon_2)^2 - \frac{K_3}{2K_1}(\Upsilon_1\Upsilon_2)\right]\cos(2\omega t). \quad (2)$$

The amplitudes of the first and second harmonic responses are thus given by

$$Z_1 = (\Upsilon_{rr} + \Upsilon_{\theta\theta})$$

$$Z_2 = \frac{K_2}{2K_1}(\Upsilon_{rr} + \Upsilon_{\theta\theta})^2 - \frac{K_3}{2K_1}(\Upsilon_{rr}\Upsilon_{\theta\theta} - \Upsilon_{r\theta})^2 \quad (3)$$

where Υ_{rr}, $\Upsilon_{\theta\theta}$, and $\Upsilon_{r\theta}$ refer to the amplitudes of the stress components in the polar coordinates.

2.1 Physical Interpretation. The first term on the right-hand side of Eq. (2) (i.e., Z_1) reflects the change in temperature due to a change in volume per unit volume; i.e., dilatation. Infrared thermal cameras which measure this component and give a raster scan are now available commercially; e.g., SPATE 8000. Until recently the temperature fluctuation was thought to be entirely due to this term. Whilst the dilatation is thought to be useful in recognizing the location of possible fracture critical points, it is widely recognized as being inappropriate for use as a measure of the onset of yielding.

The second term on the right-hand side of Eq. (2) (i.e., Z_2) can be written as

$$\frac{Z_2}{K_2/K_1} = Z_1^2 - 2\left((1-\nu) - E\frac{\partial \nu}{\partial T}\Big/\frac{\partial E}{\partial T}\right)\Upsilon_1\Upsilon_2.$$

It is interesting to note that the stress invariants

$$Z_1^2 - 2(1+\nu)\Upsilon_1\Upsilon_2 = 2EW$$

and

$$Z_1^2 - 3\Upsilon_1\Upsilon_2 \equiv \sigma_{eq}^2 \equiv \frac{3ED}{(1+\nu)}$$

where W is the strain energy density, σ_{eq} is the Von Mises equivalent stress, and D is the distortional energy are very similar to the term $\frac{Z_2}{K_2/K_1}$.

This is due to the following reasons:

(i) $E\frac{\partial \nu}{\partial T}\Big/\frac{\partial E}{\partial T}$ is small

and

(ii) $0.3 < \nu < 0.5$,

for most structural materials.

Both the strain energy density and the distortional energy have been used as yield criteria, and a review of their respective merits is given by Lazan (1968). Furthermore, W has also been used to determine the directions of fracture (Sih, 1973). As a result Z_2, which like D and W is an invariant, has the potential to be used for these two purposes. A knowledge of the absolute values of the two quantities; Z_1 and Z_2, would be an advantage in designing against brittle fracture and would aid in ensuring that a component is always kept within the elastic regime. It is interesting to note that more recent studies have indicated that a knowledge of the energy field could also be used to ensure an adequate fatigue life of metallic components (Ellyin and Golos, 1988).

3 Elasticity Theory

For two-dimensional elasticity, the stresses must satisfy $\Upsilon_{ij,j} = 0$ and $\nabla^2\Upsilon_{ii} = 0$, both for plane stress or plane strain. The first equation refers to equilibrium, while the second requirement is the compatibility equation. The equations together imply the existence of an Airy stress function ϕ such that $\nabla^2\phi = 0$. The stress components are related to ϕ by the following equations:

$$\Upsilon_{rr} = \frac{1}{r}\frac{\partial \phi}{\partial r} + \frac{1}{r^2}\frac{\partial^2 \phi}{\partial \theta^2}$$

$$\Upsilon_{\theta\theta} = \frac{\partial^2 \phi}{\partial r^2}$$

$$\Upsilon_{r\theta} = -\frac{\partial}{\partial r}\left(\frac{1}{r}\frac{\partial \phi}{\partial \theta}\right) \quad (4)$$

To illustrate how a knowledge of the temperature T can be used to determine the individual stresses consider a rectangular region (i.e., this represents the scan region) contained within a two-dimensional region of arbitrary loading. The scan region, however, should satisfy two conditions, namely; (i) it is simply connected and (ii) it has no stress discontinuities or singularities (i.e., no step loads or cracks). A stress function appropriate to such a region is given in rectangular coordinates in Timoshenko and Goodier (1982). This can be written in polar coordinates as

Downloaded 03 May 2010 to 171.66.16.247. Redistribution subject to ASME license or copyright; see http://www.asme.org/terms/Terms_Use.cfm

$$\phi = C_0\left(\frac{r}{r_c}\right)^2 + C_1\left(\frac{r}{r_c}\right)^3\cos\theta + D_1\left(\frac{r}{r_c}\right)^3\sin\theta + \sum_{n=2}^{N}\left(A_n\left(\frac{r}{r_c}\right)^n\cos(n\theta) + B_n\left(\frac{r}{r_c}\right)^n\sin(n\theta) + C_n\left(\frac{r}{r_c}\right)^{n+2}\cos(n\theta) + D_n\left(\frac{r}{r_c}\right)^{n+2}\sin(n\theta)\right) \quad (5)$$

where r is the radial distance from the center of the scan region, r_c is an arbitrary characteristic length, and $\{A_n, B_n, C_n, D_n\}$ are arbitrary constants. From Eqs. (4) and (5), the stress components can be written as

$$\Upsilon_{rr} = 2\frac{C_o}{r_c^2} + 2C_1\frac{r}{r_c^3}\cos\theta + 2D_1\frac{r}{r_c^3}\sin\theta + \sum_{n=2}^{N}\left(A_n(n-n^2)\left(\frac{r}{r_c}\right)^n\frac{1}{r^2}\cos(n\theta) + B_n(n-n^2)\left(\frac{r}{r_c}\right)^n\frac{1}{r^2}\sin(n\theta) + C_n(n+2-n^2)\left(\frac{r}{r_c}\right)^n\frac{1}{r_c^2}\cos(n\theta) + D_n(n+2-n^2)\left(\frac{r}{r_c}\right)^n\frac{1}{r_c^2}\sin(n\theta)\right) \quad (6a)$$

$$\Upsilon_{\theta\theta} = \frac{2C_0}{r_c^2} + 6C_1\frac{r}{r_c^3}\cos\theta + 6D_1\frac{r}{r_c^3}\sin\theta + \sum_{n=2}^{N}\left(A_n(n^2-n)\left(\frac{r}{r_c}\right)^n\frac{1}{r^2}\cos(n\theta) + B_n(n^2-n)\left(\frac{r}{r_c}\right)^n\frac{1}{r^2}\sin(n\theta) + C_n(n+2)(n+1)\left(\frac{r}{r_c}\right)^n\cos(n\theta) + D_n(n+2)(n+1)\left(\frac{r}{r_c}\right)^n\frac{1}{r_c^2}\sin(n\theta)\right) \quad (6b)$$

$$\Upsilon_{r\theta} = 2C_1\frac{r}{r_c^3}\sin\theta - 2D_1\frac{r}{r_c^3}\cos\theta + \sum_{n=2}^{N}\left(A_n(n^2-n)\left(\frac{r}{r_c}\right)^n\frac{1}{r^2}\sin(n\theta) - B_n(n^2-n)\left(\frac{r}{r_c}\right)^n\frac{1}{r^2}\cos(n\theta) + C_n(n^2+n)\left(\frac{r}{r_c}\right)^n\frac{1}{r_c^2}\sin(n\theta) - D_n(n^2+n)\left(\frac{r}{r_c}\right)^n\frac{1}{r_c^2}\cos(n\theta)\right). \quad (6c)$$

The stress field is completely described by the parameters $\{A_n, B_n, C_n, D_n\}$. These parameters will now be estimated from a knowledge of Z_1 and Z_2 obtained from the thermoelastic data. Here it should be noted that from Eqs. (3) and (6), Z_1 is a function of only $\{C_n, D_n\}$ while Z_2 is a function of $\{A_n, B_n, C_n, D_n\}$.

4 The Nonlinear Estimation Problem

Let the unknown parameters (i.e., A_n, B_n, C_n, and D_n) be described by the vector β. The least squares problem is to minimize the quantity

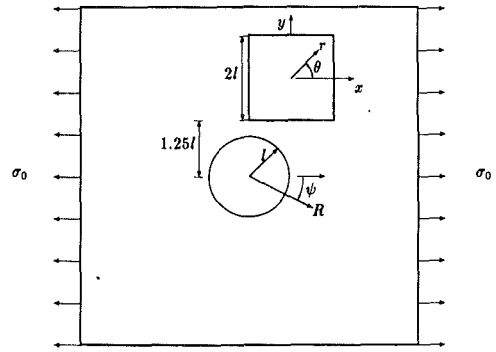


Fig. 1 Geometry for a circular hole in a large uniaxially loaded plate—showing square scan region

$$Y = \frac{1}{2}\sum_D (Z_1 - Z_{1obs})^2 + \frac{1}{2}\sum_D (Z_2 - Z_{2obs})^2 \quad (7)$$

considered as a function of β. Here, D is a rectangular array of discrete data points representing the thermal emission scan, Z_1 and Z_2 are functions of the stress state, as given in Eqs. (3) and (6), and Z_{1obs}, Z_{2obs} are the observed experimental results. In order to solve for β, the following modified Newton-Raphson scheme is used:

$$\beta_j^n = \beta_j^{(n-1)} + \delta\beta_j^{(n-1)} \quad (8)$$

where $\delta\beta_j^{n-1}$ is the solution to

$$\sum_j\left[\sum_D \psi_i\psi_j^T + \lambda_i\lambda_{jD}^T\right]\delta\beta_j = \sum(p_i + q_i)$$

where $p_i = (Z_{1obs} - Z_1)\psi_i$, $\psi_i = \partial Z_1/\partial\beta_i$ and $q_i = (Z_{2obs} - Z_2)\lambda_i$, $\lambda_i = \partial Z_2/\partial\beta_i$.

To be able to perform the matrix inversion associated with the nonlinear least squares problem, it is required that not all C_n's and D_n's are zero. Initial estimates for C_n's and D_n's were obtained by performing a linear least squares analysis on Z_1. Initial estimates of A_n and B_n were taken to be zero. The question of uniqueness is considered in Appendix A.

5 Test Case

To assess the validity of the proposed approach a known problem will be investigated and the direct and inverse solutions compared. The geometry to be considered is shown in Fig. 1 and consists of a large plate containing a circular hole subjected to uniaxial remote stresses of $\sigma_o = 50$ MPa. The scan region is square of size $2l \times 2l$, and also $l = R = 100$ mm. For this problem an analytical solution exists as in Timoshenko and Goodier (1982) where the stresses are given as

$$\Upsilon_{RR} = \frac{1}{2}\sigma_o\left[\left(1-\frac{l^2}{R^2}\right) + \left(1+\frac{3l^4}{R^4}-\frac{4l^2}{R^2}\right)\cos2\psi\right]$$

$$\Upsilon_{\psi\psi} = \frac{1}{2}\sigma_o\left[\left(1+\frac{l^2}{R^2}\right) - \left(1+\frac{3l^4}{R^4}\right)\cos2\psi\right]$$

$$\Upsilon_{R\psi} = -\frac{1}{2}\sigma_o\left(1-\frac{3l^4}{R^4}+\frac{2l^2}{R^2}\right)\sin2\psi. \quad (9)$$

For the inverse problem we take Z_{1obs} and Z_{2obs} to be the values as computed from this stress field corrupted by random noise. Investigation of the experimental data used in Ryall et al. (1990) revealed that for a six-hour scan of $\approx 240 \times 240$ pixels, the random noise on the Z_{1obs} data was of the order 1.5 to 2 MPa. (This corresponds to a sampling time of 0.375 sec per pixel.) As a result the following random noise levels, defined as σ_{Z1} and σ_{Z2}, were used when determining the Z_{1obs}, Z_{2obs} input data.

Downloaded 03 May 2010 to 171.66.16.247. Redistribution subject to ASME license or copyright; see http://www.asme.org/terms/Terms_Use.cfm

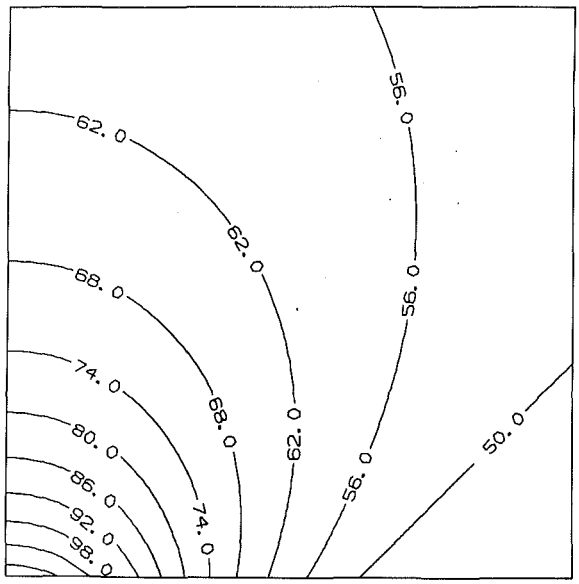


Fig. 2(*a*) First harmonic—Z_1

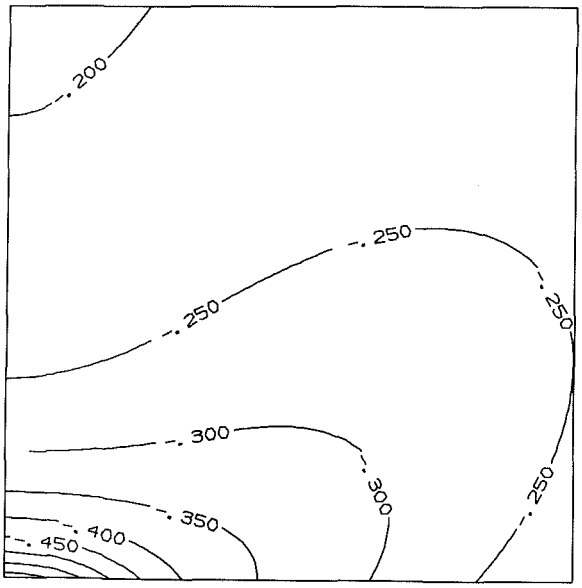


Fig. 2(*b*) Second harmonic—Z_2

Fig. 2 Simulated experimental data obtained from direct solution—shown without noise for illustrative purposes

$\sigma_{Z1} = 2$ MPa per pixel for $T = 0.375$ sec

$\sigma_{Z2} = 2$ MPa per pixel for $T = 0.375$ sec

where T is the sampling time.

The distributions of Z_1 and Z_2 without noise, i.e., the direct solution, are plotted in Figs. 2(*a*) and 2(*b*).

6 Results and Discussion for Test Case

To allow comparisons between the direct and inverse solutions let us define the following statistical parameters:

$$\text{ratio of RMS values} = \sqrt{\frac{\Sigma \hat{X}_i^2}{\Sigma X_i^2}}$$

$$\text{correlation coefficient} = \sqrt{\frac{\Sigma \hat{X}_i X_i}{\Sigma \hat{X}_i^2 \Sigma X_i^2}}$$

Table 1 Comparison of direct and inverse solutions for full scan with σ_{noise} = 2 MPA, N_p = 56,000, scan time = 6 hours, and number of parameters = 15

Quantity	Statistical results		
	Corel. Coeff.	RMS ratio	RMS error
z_1	0.9999	0.9999	0.7880
z_2	0.9986	0.9851	0.0143
τ_1	0.9998	0.9960	1.2030
τ_2	0.9897	1.0067	1.0088
τ_{xx}	0.9999	0.9849	1.3370
τ_{yy}	0.9898	1.0778	1.1700
τ_{xy}	0.5990	2.2666	5.3758

$$\text{RMS error} = \sqrt{\frac{\Sigma (X_i - \hat{X}_i)^2}{N_p}}$$

where $\hat{X}_i$ = point value of quantity of interest from inverse solution.

X_i = point value of quantity of interest from direct solution.

N_p = number of points in region.

To allow a comparison of the various energy fields we will define the following scaled quantities

$$\tilde{W} = W \frac{EK_2}{K_1}$$

and

$$\tilde{D} = D \frac{3EK_2}{2(1+\nu)K_1}.$$

6.1 Full Scan Analysis. An inverse solution was performed using Eq. (8) with Z_{1obs} and Z_{2obs} as computed from the direct solution without noise. In this case a very good correlation between the inverse and direct solutions was obtained. However, in practice we are interested in analyses using noise-corrupted input data to simulate the experimental situation. Consequently, the noise-corrupted values of Z_{1obs} and Z_{1obs} were subsequently used, and typical results are given in Table 1. As expected, Z_1, Z_2, τ_1, and τ_2 are well determined since they are directly observed. Therefore, the least squares formulation in terms of the stress potential serves two roles, viz:

(i) to reduce the effect of noise (particularly on the second harmonic), and

(ii) to determine the principal stress directions (i.e., this is equivalent to determining τ_{xx}, τ_{yy}, and τ_{xy}).

Examination of Table 1 reveals that in general (i) will always be better achieved than (ii), and while τ_{xx} and τ_{yy} are well determined, τ_{xy} is not. (However, it should be noted that τ_{xy} values are small in the region when compared to τ_{xx} and τ_{yy}). It should be mentioned that no improvement in results is obtained for this scan region by increasing the number of parameters. To improve the results further for τ_{xx}, τ_{yy}, and τ_{xy}, consideration is given in the next section to spatial optimization of the scan region while keeping the total scan time constant.

6.2 "Optimized" Scan Analysis. We can now use the spatial variation of the information of the scan region in order to optimize the choice of measurement points, i.e., using only a selected number of points in the scan region. This approach is discussed in detail in Appendix B, and raises the possibility

Downloaded 03 May 2010 to 171.66.16.247. Redistribution subject to ASME license or copyright; see http://www.asme.org/terms/Terms_Use.cfm

Table 2 Comparison of direct and inverse solutions for optimized scan with σ_{noise} = 1.025 MPA, N_p = 15,128, scan time = 6 hours, and number of parameters = 15

Quantity	Statistical results		
	Corel. Coeff.	RMS ratio	RMS error
z_1	0.9999	1.0001	0.8776
z_2	0.9992	0.9915	0.0106
T_1	0.9999	0.9975	0.9396
T_2	0.9931	0.9688	0.8424
T_{xx}	0.9999	0.9963	0.9815
T_{yy}	0.9920	0.9659	0.9010
T_{xy}	0.7293	1.2276	2.4598

Table 3 Comparison of direct and inverse solutions for optimized scan with noise σ_{noise} = 0.7632 MPa, N_p = 8388, scan time = 6 hours, and number of parameters = 23

Quantity	Statistical results		
	Corel. Coeff.	RMS ratio	RMS error
z_1	0.9999	1.0002	0.2589
z_2	0.9985	0.9712	0.0163
T_1	0.9998	0.9893	1.3711
T_2	0.9805	0.9947	1.3821
T_{xx}	0.9998	0.9877	1.4414
T_{yy}	0.9785	0.9919	1.4416
T_{xy}	0.9408	1.2810	1.3954

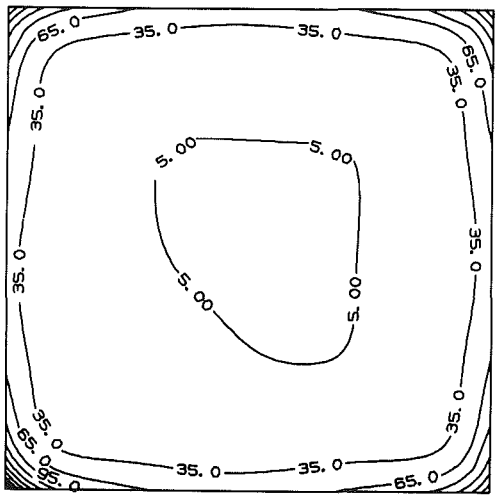


Fig. 3 Variation of information content of data points over a region for full scan analysis with σ_{noise} = 2 MPA, n_p = 56,000, and number of parameters = 15

of determining the information content of each point from an initial "coarse scan" and then subsequently performing a more detailed "optimized scan" in which only the most informative points are sampled. As an example, the information content obtained for the analysis using σ_{noise} = 2 MPa, N_p = 56000, scan time = 6 hours with 15 parameters is plotted in Fig. 3. To illustrate this concept, "optimized" scans based on the grid point information content were analyzed and the results obtained are presented in Tables 2 and 3 for two different numbers of parameters. In this case the total scan time is kept at six

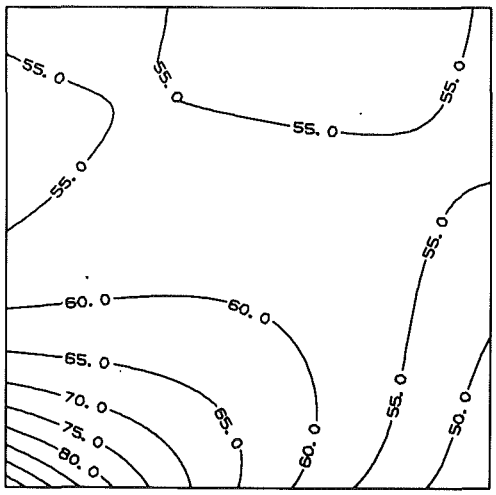


Fig. 4(a) T_{xx}

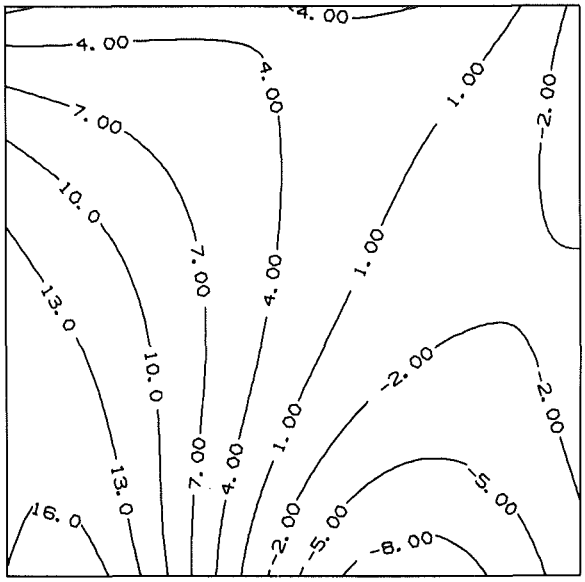


Fig. 4(b) T_{yy}

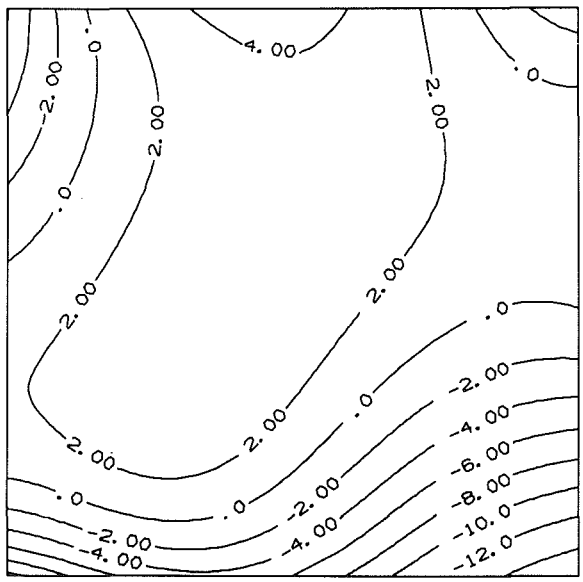

4. 00
2. 00
2. 00
2

Table 4 Comparison of optimization quantities to second harmonic for direct solution over scan region

Quantity	Statistical results		
	Corel. Coeff.	RMS ratio	RMS error
$\tilde{D}$	0.9997	0.9899	0.0069
$\tilde{W}$	0.9997	1.0106	0.0069

Table 5 Comparison of optimization quantities for direct to inverse solutions for optimized scan region with σ_{noise} = 0.7632 MPA, N_p = 8388, scan time = 6 hours, and number of parameters = 23

Quantity	Statistical results		
	Corel. Coeff.	RMS ratio	RMS error
$\tilde{D}$	0.9982	0.9683	0.0174
$\tilde{W}$	0.9987	0.9740	0.0151

hours. Some typical results obtained from such an "optimized" scan are also plotted in Fig. 4. Examination of Tables 2 and 3 shows the significant improvements in the results for Υ_{xy}, and indicates definite advantages of using an optimized scan. It should be noted that infrared thermal array cameras are now available which can reduce the typical six-hour scan time by up to two orders of magnitude.

7 Application to Structural Optimization

One procedure, which is widely used in structural optimization for fatigue or minimum weight considerations, is to design the structure to produce a uniform energy field. An example of this approach is the development of an optimum rework of a stiffener in the wing pivot fitting of the F-111 aircraft (Jones et al., 1990).

Since $\tilde{W}$ closely resembles Z_2, it follows that $\tilde{W}$ is estimated with less error than the individual stress components. (The similarity between the two energy fields $\tilde{W}$, $\tilde{D}$ and the second harmonic response Z_2 is seen in Table 4 for the problem considered in Section 5.) As a result, thermal emission techniques can be readily used to assess the level of optimization achieved by a prototype design. This is important since the mathematical assumptions often inherent in the initial optimum design process are sometimes found to be at odds with the manufactured structure. In this case, regions which are subsequently found to have an excessive energy field can be identified and the structure redesigned prior to a final production run.

To illustrate how this process can be achieved, let us consider the problem discussed in the previous section. The scaled energy field $\tilde{W}$ calculated from the estimated individual stresses is given in Fig. 5(*b*) and can be compared to the exact solution as given in Fig. 5(*a*). Here it can be seen that there is good agreement. Similar agreement is obtained for the scaled distortional energy $\tilde{D}$ as shown in Table 5.

Therefore, it follows that Z_2 can be used as an objective criterion for assessing structural modifications.

8 Conclusions

It has been shown that separated stress components can be obtained from the two harmonic components of the thermoelastic signal. Noise-corrupted values were used with the only

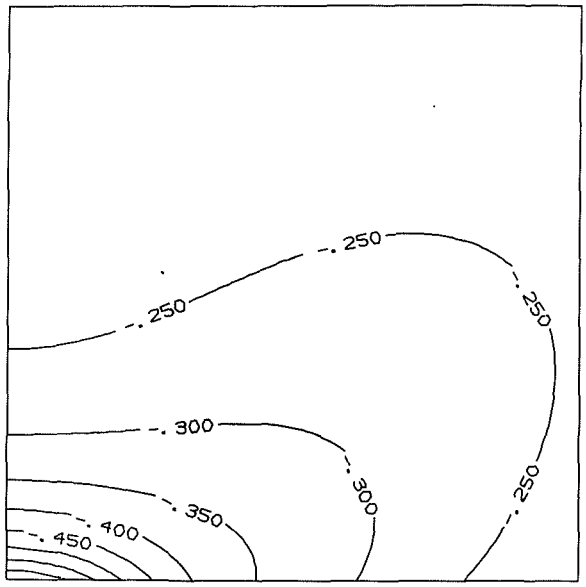


Fig. 5(*a*) Direct

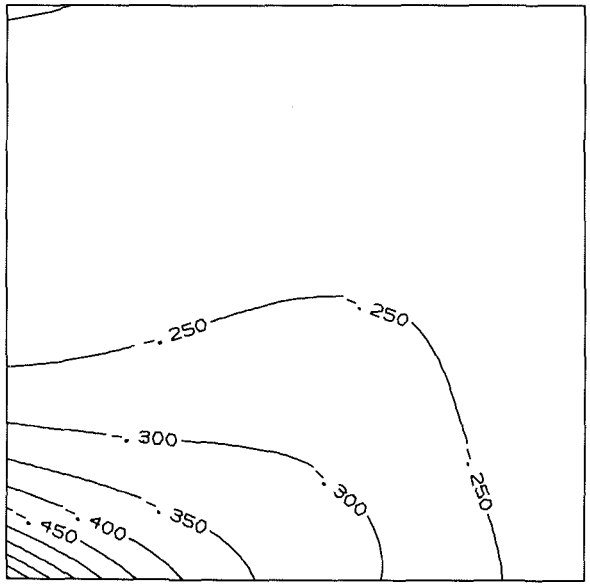


Fig. 5(*b*) Inverse

Fig. 5 Comparison of direct and inverse solutions for optimization quantity *W*. Inverse solution obtaining using σ_{noise} = 0.7632 MPA, N_p = 8388, scan time = 6 hours, and number of parameters = 23.

a priori knowledge being that the equations of two-dimensional elasticity are valid: that is, no free boundary conditions were used. Furthermore, the question of uniqueness and experimental design in terms of scan optimizations was considered.

It is recognised, that in practice, motion effects will need to be accounted for; this can be done by using a Taylor series expansion of Z_1 and Z_2 in terms of the displacements. The close similarity between the second harmonic response and various energy parameters was also highlighted, as was its role in structural optimization.

References

Ellyin, F., and Golos, K., 1988, "Multiaxial Fatigue Damage Criterion," ASME *Journal of Engineering Materials and Technology*, Vol. 110, pp. 63-65.

Jones, R., Heller, M., Sparrow, J. G., and Ryall, T. G., 1990, "A New Approach to Structural Optimisation," *Composite Structures*, Vol. 16, pp. 1-32.

Jones, R., and Paul, J., 1989, "Fibre Composite Repairs to Damaged Struc-

Downloaded 03 May 2010 to 171.66.16.247. Redistribution subject to ASME license or copyright; see http://www.asme.org/terms/Terms_Use.cfm

tural Components, Plenary Lecture," *5th International Conference on Composite Structures, Composite Structures 5*, I. H. Marshall, ed., Elsevier, London, pp. 1–37.

Lazan, B. J., 1968, *Damping of Materials and Members in Structural Mechanics*, Pergamon Press, Oxford, U. K., pp. 183–195.

Machin, A. S., Sparrow, J. G., and Stimson, M. G., 1987, "Mean Stress Dependence of Thermoelastic Constant," *Journal of Strain*, Vol. 23, pp. 27–30.

Ryall, T. G., Cox, P. M., and Enke, N., 1990, "On the Determination of Dynamic and Static Stress Components From Experimental Data," *Journal of Mechanical Systems and Signal Processing*, in press.

Ryall, T. G., and Wong, A. K., 1988, "Determining Stress Components From Thermoelastic Data—A Theoretical Study" *Mechanics of Materials*, Vol. 7, pp. 205–214.

Sih, G. C., 1973, *Methods of Analysis and Solutions of Crack Problems*, Noordhoff Publishers, Leyden, The Netherlands.

Stanley, P., 1990, "Thermoelastic Stress Analysis: Progress and Prospects," *Proceedings of the 9th International Conference on Experimental Mechanics*, Vol. 2, pp. 728–747.

Thomson, W., (Lord Kelvin), 1953, "On the Dynamical Theory of Heat," *Transactions of the Royal Society of Edinburgh*, Vol. 20, pp. 123–136.

Timoshenko, S. P., and Goodier, J. N., 1982, *Theory of Elasticity*, McGraw-Hill, Singapore.

Waldman, W., Ryall, T. G., and Jones, R., 1990, "On the Determination of Stress Components in 3D From Thermoelastic Data," *Computers and Structures*, Vol. 36, No. 3, pp. 553–557.

Wong, A. K., Sparrow, J. G., and Dunn, S. A., 1988, "On the Revised Theory of the Thermoelastic Effect," *Journal of Physics and Chemistry of Solids*, Vol. 49, pp. 395–400.

Wong, A. K., Jones, R., and Sparrow, J. G., 1987, "Thermoelastic Constant or Thermoelastic Parameter," *Journal of the Physics and Chemistry of Solids*, Vol. 48, pp. 749–853.

APPENDIX A

Although the experimental measurements yield information on the sum of the principal stresses and on a known quadratic form of the principal stresses (hence the principal stresses are always uniquely determined), this is not true of the directions of the principal stresses and thus of the stress components. Fortunately, however, the situations where the stress components are not uniquely determined are a set of measure zero and nongeneric. In other words, an arbitrary small perturbation of the applied stresses in a pathological case will guarantee uniqueness of the stress components. The uniqueness problem will not be examined here in its full generality, but the salient points will be examined via a simple example. Consider a stress potential of the following form:

$$\phi = c_0(x^2+y^2) + c_1(x^3+xy^2) + d_1(x^2y+y^3) + a_2(x^2-y^2) + b_2 2xy$$

with corresponding stress components

$$\Upsilon_{xx} = 2c_0 - 2a_2 + 2c_1x + 6d_1y$$
$$\Upsilon_{yy} = 2c_0 + 2a_2 + 6c_1x + 2d_1y$$
$$\Upsilon_{xy} = -2b_2 - 2d_1x - 2c_1y.$$

Since the sum of the principal stresses is experimentally observed via the quantity Z_1, i.e., $(\Upsilon_{xx} + \Upsilon_{yy} = 4c_0 + 8c_1x + 8d_1y)$, this implies that c_0, c_1, and d_1 are uniquely determined. A knowledge of Z_2 is equivalent to observing the product of the principal stresses $\Upsilon_{xx}\Upsilon_{yy} - \Upsilon^2_{xy}$. The constant term in this expression is $4c_0^2 - 4(a_2^2 + b_2^2)$, the coefficient of x is given by $16c_0c_1 - 8a_2c_1 - 8b_2d_1$ and the coefficient of y is given by $16c_0c_1 + 8a_2d_1 - 8b_2c_1$. Higher order powers give no information on the remaining unknown parameters (a_2 and b_2). Since c_0, c_1, and d_1 are determined, then the coefficients of x and y in the product of the principal stresses give a linear set of equations in a_2 and b_2 which may be solved provided that $c_1^2 + d_1^2 \neq 0$. It should be noted that even if $c_1 = 0$ and $d_1 = 0$, a_2 and b_2 are not completely arbitrary since the value of $a_2^2 + b_2^2$ is fixed.

The nonunique cases in this example lie along a "hyper" line in five-dimensional parameter space. A line, of course, has no volume, and hence the pathological cases have no measure.

APPENDIX B

One measure of the information content of a set of grid points in a least squares problem is the "generalized" variance, that is, the determinant of the inverse of the least squares matrix.[2] This Appendix uses results from recursive least squares to calculate the generalized variance with any particular grid point missing, accurately and efficiently, without calculating any determinants. Let P_k be the inverse of the least squares matrix with k pieces of information and Ψ_k is the vector of regressors, then the matrix inversion lemma states that

$$P_k = P_{k-1} - \frac{P_{k-1}\psi_k\psi_k^T P_{k-1}}{1+\psi_k^T P_k \psi_k} \tag{B1}$$

hence, $\det P_k = [\det P_{k-1}].\det[I - (\psi_k\psi_k^T P_{k-1})/(1+\psi_k^T P_{k-1}\psi_k)]$. Now, $\psi_k\psi_k^T P_{k-1}/(1+\psi_k^T P_{k-1}\psi_k)$ is a rank-one matrix having one nonzero eigenvalue $\psi_k^T P_{k-1}\psi_k/(1+\psi_k^T P_{k-1}\psi_k)$.

It follows that

$$\det\left[I - \frac{\psi_k\psi_k^T P_{k-1}}{1+\psi_k^T P_{k-1}\psi_k}\right] = 1 - \frac{\psi_k^T P_{k-1}\psi_k}{1+\psi_k^T P_{k-1}\psi_k} = \frac{1}{1+\psi_k^T P_{k-1}\psi_k}$$

and

$$\det P_{k-1} = \det P_k[1+\psi_k^T P_{k-1}\psi_k].$$

Pre and post multiplying (B1) by ψ_k gives

$$\psi_k^T P_k \psi_k = \frac{\psi_k^T P_{k-1}\psi_k}{1+\psi_k^T P_{k-1}\psi_k}. \tag{B2}$$

(NOTE that $\psi_k^T P_k \psi_k$ lies between 0 and 1.)

So, finally,

$$\frac{\det P_{k-1} - \det P_k}{\det P_k} = \frac{\psi_k^T P_k \psi_k}{1-\psi_k^T P_k \psi_k}. \tag{B3}$$

Since (B3) is a monotonic function of $\psi_k^T P_k \psi_k$, then if this is large, the kth piece of information is very informative.

The particular problem studied in this paper has in effect two pieces of information (i.e., Z_1 and Z_2) associated with each grid point with corresponding vectors of regressors labelled ψ_k and ψ_{k-1}.

Defining $\alpha = \psi_k^T P_k \psi_k$
$\beta = \psi_k^T P_k \psi_{k-1}$
$\gamma = \psi_{k-1}^T P_k \psi_{k-1}$,

then by an extension of the previous argument, details of which are omitted, the information in the kth grid point can be ordered according to the size of

$$\alpha + \gamma + \beta^2 - \alpha\gamma.$$

It should be noted that all results are expressed in terms of P_k which is the inverse of the least squares matrix with all grid points included, and as a result only one inverted matrix is required for the whole scan region.

[2]This determinant measures the "volume" of parameter space the parameters are likely to lie within.

Downloaded 03 May 2010 to 171.66.16.247. Redistribution subject to ASME license or copyright; see http://www.asme.org/terms/Terms_Use.cfm

Three-Dimensional Solutions for the Thermal Buckling and Sensitivity Derivatives of Temperature-Sensitive Multilayered Angle-Ply Plates

A. K. Noor
Professor,
Fellow ASME.

W. Scott Burton
Research Scientist,
Assoc. Mem. ASME.

Center for Computational Structures Technology,
University of Virginia,
Hampton, VA 23681

Analytic three-dimensional thermoelasticity solutions are presented for the thermal buckling of multilayered angle-ply composite plates with temperature-dependent thermoelastic properties. Both the critical temperatures and the sensitivity derivatives are computed. The sensitivity derivatives measure the sensitivity of the buckling response to variations in the different lamination and material parameters of the plate. The plates are assumed to have rectangular geometry and an antisymmetric lamination with respect to the middle plane. The temperature is assumed to be independent of the surface coordinates, but has an arbitrary symmetric variation through the thickness of the plate. The prebuckling deformations are accounted for. Numerical results are presented, for plates subjected to uniform temperature increase, showing the effects of temperature-dependent material properties on the prebuckling stresses, critical temperatures, and their sensitivity derivatives.

Introduction

The unique properties of advanced composite materials have resulted in the expanded use of these materials in aerospace, automotive, shipbuilding, nuclear and other high-tech industries. To date, five major classes of advanced composites are being considered for high-temperature structures, namely, polymer-matrix, metal matrix, ceramic matrix, carbon/carbon, and hybrid composites. Each of these composites is suitable for a particular temperature range. Over certain temperature ranges each of the aforementioned composites may behave elastically, but has variable mechanical properties and thermal expansion characteristics. Therefore, it is desirable to provide a capability for the accurate prediction of the thermal buckling response of temperature-sensitive multilayered composite plates. Because of the uncertainty in material properties, such a capability should include the sensitivity of the buckling response to variations in the material and lamination parameters. To the authors' knowledge, all the studies of temperature-sensitive composite plates reported in the literature have been based on two-dimensional laminated plate theories whose accuracy has not been assessed (see, for example, Chen and Chen (1989), Miller (1981), Kalam (1981), Khalatyan (1978), Khoroshun and Shpakova (1986) and Tauchert (1976) and the two survey papers, Noda (1986) and Noda (1991)).

In this paper, analytic three-dimensional thermoelasticity solutions are presented for the thermal buckling of temperature-sensitive multilayered angle-ply composite plates. Sensitivity derivatives are also evaluated and used to study the sensitivity of the buckling response to variations in different lamination and material parameters of the plate. The plates consist of a number of perfectly bonded layers which have antisymmetric lamination with respect to the middle plane. The loading consists of a temperature change which is independent of the surface coordinates, but can have arbitrary symmetric variation in the thickness direction. The solutions are periodic in the surface coordinates x_1 and x_2. Extensive numerical results are presented to illustrate the effect of the temperature-dependent material properties on the thermal prebuckling and buckling responses of multilayered composite plates.

The present study is an extension of previous work on isothermal free vibrations and thermal buckling of multilayered plates with temperature-independent material properties (see Noor and Burton (1990) and Noor and Burton (1992)).

Mathematical Formulation

Figure 1 shows the geometric characteristics of the plate

Contributed by the Applied Mechanics Division of THE AMERICAN SOCIETY OF MECHANICAL ENGINEERS for presentation at the 1992 ASME Winter Annual Meeting, Anaheim, CA, Nov. 8–13, 1992.

Discussion on this paper should be addressed to Prof. Leon M. Keer, The Technological Institute, Northwestern University, Evanston, IL 60208, and will be accepted until four months after final publication of the paper itself in the ASME JOURNAL OF APPLIED MECHANICS.

Manuscript received by the ASME Applied Mechanics Division, Oct. 29, 1991; final revision, Jan. 9, 1992. Associate Technical Editor: L. M. Keer.

Paper No. 92-WA/APM-2.

Copyright © 1992 by ASME
Downloaded 03 May 2010 to 171.66.16.247. Redistribution subject to ASME license or copyright; see http://www.asme.org/terms/Terms_Use.cfm

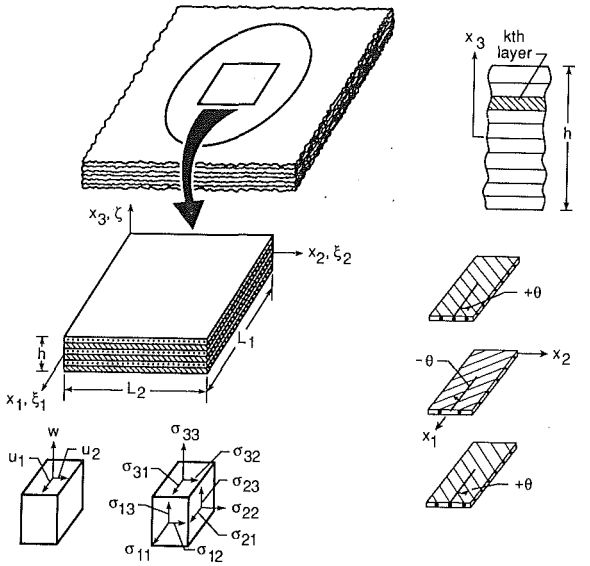


Fig. 1 Laminated anisotropic plates and sign convention for stresses and displacements

segment considered herein, henceforth referred to as the plate, as follows: L_1 and L_2 are the side lengths in the x_1 and x_2 directions, and h is the total thickness of the plate. The dimensionless coordinates ξ_1, ξ_2, and ζ are introduced, where

$$\xi_\beta = \frac{x_\beta}{L_\beta} \quad (\beta = 1,2 \text{ and } \beta \text{ is not summed}) \tag{1}$$

$$\zeta = \frac{x_3}{h} \quad -0.5 \le \zeta \le 0.5. \tag{2}$$

The analytical formulation is based on the geometrically nonlinear three-dimensional theory of anisotropic thermoelasticity (see Hearmon (1961), Lekhnitskii (1981), and Padovan (1986)). The temperature increase (above the room temperature), T, is assumed to be independent of x_1, x_2, i.e.,

$$T = f(\zeta)T^o \tag{3}$$

where $f(\zeta)$ is a normalized (dimensionless) even function of ζ and T^o is a temperature parameter.

The individual layers are assumed to be orthotropic, with the principal material directions not coincident with the coordinate directions, and are antisymmetrically laminated with respect to the middle plane of the plate. At each point a plane of thermoelastic symmetry exists parallel to the middle plane. Initially each layer is assumed to be homogeneous. However, as a consequence of the temperature-dependence of the material properties it may become nonhomogeneous (if $f(\zeta)$ in Eq. (3) is not constant).

Prebuckling State and Buckling Mode. A Lagrangian description of the deformation, which accounts for the large displacements and rotations, is used. The fundamental equations are expressed in terms of the second Piola-Kirchhoff stress tensor and the Green-Lagrange strain tensor. A linear thermoelastic, Duhamel-Neumann type, constitutive model is used which accounts for the temperature dependence of the material properties. A summary of the fundamental equations of three-dimensional thermoelasticity used in the present study is given in Noor and Burton (1992). The sign convention for the different displacement and stress components is shown in Fig. 1.

The prebuckling stresses and displacements generated by the temperature distribution, Eq. (3), are chosen to be independent of x_1 and x_2 and are obtained from the stress displacement relations and the continuity conditions at layer interfaces. They can be written in the following form:

$$\begin{Bmatrix} \sigma^0_{11} \\ \sigma^0_{22} \\ \sigma^0_{12} \end{Bmatrix}^{(k)} = -\left(\begin{bmatrix} a_{11}(T) & a_{12}(T) & a_{16}(T) \\ & a_{22}(T) & a_{26}(T) \\ \text{Symm.} & & a_{66}(T) \end{bmatrix}^{(k)} \right)^{-1} \times \int_{T_r}^{T_r+T} \begin{Bmatrix} \alpha_1(T') \\ \alpha_2(T') \\ 2\alpha_6(T') \end{Bmatrix}^{(k)} dT' \tag{4}$$

$$\begin{Bmatrix} \sigma^0_{13} \\ \sigma^0_{23} \\ \sigma^0_{33} \end{Bmatrix}^{(k)} = 0 \tag{5}$$

$$u^0_1 = u^0_2 = 0 \tag{6}$$

$$w^0 = -h\zeta + \int_0^\zeta [1 + 2k^0]^{1/2} h d\zeta \tag{7}$$

where

$$k^0 = a_{13}(T)\sigma^0_{11} + a_{23}(T)\sigma^0_{22} + a_{36}(T)\sigma^0_{12} + \int_{T_r}^{T_r+T} \alpha_3(T')dT' \tag{8}$$

In Eqs. (4) to (8), the σ^0_{ij} ($i, j = 1$ to 3) are the prebuckling stresses in the kth layer; u^0_1, u^0_2, w^0 are the prebuckling displacements; the a's are compliance coefficients of the material of the kth layer (see Hearmon (1961), Lekhnitskii (1981), and Padovan (1986)); T_r is a base-temperature at which thermal strains are zero; the α's are coefficients of thermal expansion of the layer; and superscript (k) refers to the kth layer. The a's, α's, and σ^0 components are functions of the temperature. Because of the discontinuities of the stresses σ^0_{11}, σ^0_{22}, and σ^0_{12} at layer interfaces, the integration in Eq. (7) is performed piecewise (layer-by-layer).

Equations (4)–(8) satisfy identically the nonlinear equilibrium equations within each layer, and at the interfaces between layers, as well as the stress-free boundary conditions at the top and bottom surfaces of the plate (see Noor and Burton (1992)). Note that when $f(\zeta)$ is an even function of ζ, w^0 is an odd function of ζ, i.e., the distribution of w^0 in the thickness direction is symmetric with respect to the middle plane of the plate.

The buckling mode is assumed to correspond to an adjacent configuration with the following values of displacements and stresses

$$u_\beta = u^0_\beta + \epsilon v_\beta \tag{9}$$

$$w = w^0 + \epsilon\omega \tag{10}$$

where v_β ($\beta = 1, 2$) and ω are perturbation displacements, and ϵ is an infinitesimal. The resulting strains and stresses have the following form:

$$\epsilon_{ij} = \epsilon^0_{ij} + \epsilon\eta_{ij} + \epsilon^2\psi_{ij} \tag{11}$$

$$\sigma_{ij} = \sigma^0_{ij} + \epsilon\tau_{ij} + \epsilon^2 t_{ij} \tag{12}$$

where $i, j = 1$ to 3. The expressions for the strain components ϵ^0_{ij}, η_{ij} and ψ_{ij} in terms of the displacement gradients are given in Noor and Burton (1992) and are summarized in Appendix A. The strain and stress components η_{ij} and τ_{ij} will henceforth be referred to as the perturbation strains and stresses.

Displacement and Stress Expansions. Each of the plate variables is decomposed into symmetric and antisymmetric components in the thickness direction, and is expressed as the sum of products of trigonometric functions in the Cartesian surface coordinates. The trigonometric functions are chosen such that the displacements and stresses are periodic in x_1 and x_2 with periods $2L_1$ and $2L_2$.

Downloaded 03 May 2010 to 171.66.16.247. Redistribution subject to ASME license or copyright; see http://www.asme.org/terms/Terms_Use.cfm

The following expressions are used for the displacement and stress components:

$$\begin{Bmatrix} v_1 \\ v_2 \\ \omega \end{Bmatrix} = \begin{Bmatrix} \hat{v}_{1_{mn}} \sin m\pi\xi_1 \cos n\pi\xi_2 \\ \hat{v}_{2_{mn}} \cos m\pi\xi_1 \sin n\pi\xi_2 \\ \hat{\omega}_{mn} \sin m\pi\xi_1 \sin n\pi\xi_2 \end{Bmatrix} + \begin{Bmatrix} \tilde{v}_{1_{mn}} \cos m\pi\xi_1 \sin n\pi\xi_2 \\ \tilde{v}_{2_{mn}} \sin m\pi\xi_1 \cos n\pi\xi_2 \\ \tilde{\omega}_{mn} \cos m\pi\xi_1 \cos n\pi\xi_2 \end{Bmatrix} \quad (13)$$

$$\begin{Bmatrix} \tau_{11} \\ \tau_{22} \\ \tau_{33} \end{Bmatrix} = \begin{Bmatrix} \hat{\tau}_{11_{mn}} \\ \hat{\tau}_{22_{mn}} \\ \hat{\tau}_{33_{mn}} \end{Bmatrix} \cos m\pi\xi_1 \cos n\pi\xi_2 + \begin{Bmatrix} \tilde{\tau}_{11_{mn}} \\ \tilde{\tau}_{22_{mn}} \\ \tilde{\tau}_{33_{mn}} \end{Bmatrix} \sin m\pi\xi_1 \sin n\pi\xi_2 \quad (14)$$

$$\begin{Bmatrix} \tau_{23} \\ \tau_{13} \\ \tau_{12} \end{Bmatrix} = \begin{Bmatrix} \hat{\tau}_{23_{mn}} \sin m\pi\xi_1 \cos n\pi\xi_2 \\ \hat{\tau}_{13_{mn}} \cos m\pi\xi_1 \sin n\pi\xi_2 \\ \hat{\tau}_{12_{mn}} \sin m\pi\xi_1 \sin n\pi\xi_2 \end{Bmatrix} + \begin{Bmatrix} \tilde{\tau}_{23_{mn}} \cos m\pi\xi_1 \sin n\pi\xi_2 \\ \tilde{\tau}_{13_{mn}} \sin m\pi\xi_1 \cos n\pi\xi_2 \\ \tilde{\tau}_{12_{mn}} \cos m\pi\xi_1 \cos n\pi\xi_2 \end{Bmatrix} \quad (15)$$

In Eqs. (13)–(15), the caret ($\hat{}$) and tilde ($\tilde{}$) refer to the symmetric and antisymmetric quantities with respect to the middle plane. Each of these quantities is a function of the thickness coordinate ζ. The following displacement conditions are satisfied on the middle plane ($\zeta = 0$):

$$\text{At } x_1 = 0, L_1: v_1 = \omega = 0. \quad (16)$$

$$\text{At } x_2 = 0, L_2: v_2 = \omega = 0. \quad (17)$$

The displacement conditions, Eqs. (16) and (17), are satisfied when either m, n, or both, are zero. For $m = n = 0$, only the $\tilde{\omega}$ term in the displacement expressions, Eqs. (13), survives. For $m = 1$, $n = 0$; $\hat{v}_1$, $\tilde{v}_2$, and $\tilde{\omega}$ survive, and for $m = 0$, $n = 1$, $\tilde{v}_1$, $\hat{v}_2$, and $\tilde{\omega}$ survive. Note that the periodicity of the displacement and stress components, Eqs. (13)–(15), is required to obtain exact solutions for the governing equations, as is described in the succeeding subsection.

Governing Equations. A mixed formulation is used with the fundamental unknowns consisting of the symmetric and antisymmetric components of the displacements and stresses. The governing equations of the plate consist of the constitutive relations (strain-stress relations, with the strains expressed in terms of displacements (see Noor and Burton (1992)). For the purpose of simplifying the form of the equations, the material compliance matrix for each layer, $[a]$, which is a function of temperature, is decomposed into the sum of orthotropic and anisotropic (nonorthotropic) parts, $[a_0]$ and $[a_1]$ (see Appendix B). Moreover, the stresses and displacements are each divided into two groups as follows:

$$\{H_1\}_{m,n} = \begin{Bmatrix} \tilde{\tau}_{11_{mn}} \\ \tilde{\tau}_{22_{mn}} \\ \tilde{\tau}_{33_{mn}} \\ \hat{\tau}_{23_{mn}} \\ \hat{\tau}_{13_{mn}} \\ \tilde{\tau}_{12_{mn}} \end{Bmatrix}; \quad \{H_2\}_{m,n} = \begin{Bmatrix} \hat{\tau}_{11_{mn}} \\ \hat{\tau}_{22_{mn}} \\ \hat{\tau}_{33_{mn}} \\ \tilde{\tau}_{23_{mn}} \\ \tilde{\tau}_{13_{mn}} \\ \hat{\tau}_{12_{mn}} \end{Bmatrix} \quad (18)$$

$$\{X_1\}_{m,n} = \begin{Bmatrix} \tilde{v}_{1_{mn}} \\ \tilde{v}_{2_{mn}} \\ \hat{\omega}_{mn} \end{Bmatrix}; \quad \{X_2\}_{m,n} = \begin{Bmatrix} \hat{v}_{1_{mn}} \\ \hat{v}_{2_{mn}} \\ \tilde{\omega}_{mn} \end{Bmatrix}. \quad (19)$$

For each layer and each pair of harmonics, m and n, the governing equations can be partitioned into two coupled sets of equations associated with $\{H_1\}_{m,n}$, $\{X_1\}_{m,n}$ and $\{H_2\}_{m,n}$, $\{X_2\}_{m,n}$ as follows:

$$\left(\begin{bmatrix} 0 & S_0+S_1 \\ S_0^t - S_1^t & 0 \end{bmatrix}_{m,n} \frac{\partial}{\partial x_1} + \begin{bmatrix} -a_0(\lambda) & L_0(\lambda) \\ L_1^t(\lambda) & K_0(\lambda) \end{bmatrix}_{m,n} \right) \begin{Bmatrix} H_1 \\ X_1 \end{Bmatrix}_{m,n} + \begin{bmatrix} -a_1(\lambda) & 0 \\ 0 & K_1(\lambda) \end{bmatrix}_{m,n} \begin{Bmatrix} H_2 \\ X_2 \end{Bmatrix}_{m,n} = 0 \quad (20)$$

and

$$\left(\begin{bmatrix} 0 & -S_0+S_1 \\ -S_0^t - S_1^t & 0 \end{bmatrix}_{m,n} \frac{\partial}{\partial x_1} + \begin{bmatrix} -a_0(\lambda) & -L_1(\lambda) \\ -L_0^t(\lambda) & K_0(\lambda) \end{bmatrix}_{m,n} \right) \times \begin{Bmatrix} H_2 \\ X_2 \end{Bmatrix}_{m,n} + \begin{bmatrix} -a_1(\lambda) & 0 \\ 0 & K_1(\lambda) \end{bmatrix}_{m,n} \begin{Bmatrix} H_1 \\ X_1 \end{Bmatrix}_{m,n} = 0 \quad (21)$$

where $\lambda = \alpha_T^0 T_{cr}$ is the critical temperature parameter; $[S_0]$ is a matrix of coefficients; $[S_1]$ is a matrix of linear first-order ordinary differential operators; $[K_0(\lambda)]$ and $[K_1(\lambda)]$ are matrices of initial stresses which are functions of λ; and $[L_0(\lambda)]$ and $[L_1(\lambda)]$ are matrices of first-order differential operators, which are functions of the initial displacement w^0 (nonlinear functions of the critical temperature parameter). The explicit forms of the arrays appearing in Eqs. (20) and (21) are given in Appendix B.

The complete description of the thermal buckling response of the plate requires: (a) the governing equations, Eqs. (20) and (21), for each layer; (b) the stress equilibrium and the displacement continuity conditions at layer interfaces; and (c) the conditions at the top and bottom surfaces of the plate.

The equilibrium and continuity conditions at the interfaces between the typical layers k and $k + 1$ (top of layer k and bottom of layer $k + 1$) can be written in the following form:

$$\tau_{i3}^{(k)} - \tau_{i3}^{(k+1)} = 0, \quad i = 1 \text{ to } 3 \quad (22)$$

$$v_\beta^{(k)} - v_\beta^{(k+1)} = 0, \quad \beta = 1,2 \quad (23)$$

and

$$\omega^{(k)} - \omega^{(k+1)} = 0 \quad (24)$$

where superscripts k and $k + 1$ refer to the layers k and $k + 1$. Equations (22)–(24) imply perfect bonding between the different layers (i.e., no slip). The stress conditions at the top and bottom surfaces are

$$\tau_{i3} = 0, \quad i = 1 \text{ to } 3. \quad (25)$$

Note that Eqs. (22)–(25) can be replaced by two sets of equations of the same form; one relating the symmetric components (quantities with a caret) and the other relating the antisymmetric components (quantities with a tilde).

The Fourier expansions for the displacements and stresses, Eqs. (13)–(15), provide an *exact representation* for the thermal buckling response of rectangular composite plates. Moreover, the governing equations uncouple in harmonics provided (see Noor and Burton (1992)): (a) the lamination is angle-ply antisymmetric with respect to the middle plane, cross-ply symmetric with respect to the middle plane, or a combination of the two (e.g., antisymmetric quasi-isotropic lamination); (b) the temperature is given by Eq. (3) and the prebuckling displacements, strains and stresses are given by Eqs. (4)–(8); and (c) the perturbation displacements, strains and stresses, Eqs. (9)–(12), are periodic in x_1 and x_2.

Downloaded 03 May 2010 to 171.66.16.247. Redistribution subject to ASME license or copyright; see http://www.asme.org/terms/Terms_Use.cfm

Computational Procedure. The thermal buckling response of the plate is obtained by using a similar procedure to that described in Srinivas and Rao (1970) and Srinivas (1973). The procedure is based on solving the characteristic equation associated with Eqs. (20) and (21) for each layer, and each pair of Fourier harmonics (m, n); finding 12 roots and 12 eigenvectors, then solving a set of simultaneous equations representing the conditions at the top and bottom surfaces, and at the interfaces between the different layers, Eqs. (22)–(24). The procedure was applied to isothermal free vibration problems of angle-ply laminates in Noor and Burton (1990) and to thermal buckling problems of angle-ply laminates with temperature-independent properties in Noor and Burton (1992).

Sensitivity of the Prebuckling and Thermal Buckling Responses to Variations in Lamination and Material Parameters. Sensitivity derivatives can be used to study the sensitivity of the prebuckling and thermal buckling responses of the plate to variations in the different material and lamination parameters. Analytic sensitivity derivatives for the prebuckling stresses are obtained by differentiating Eqs. (4) with respect to d_l, where d_l represents a material or lamination parameter of the plate. To obtain analytic sensitivity derivatives for the critical temperature each of the following equations is differentiated with respect to d_l: (a) the characteristic equation, associated with Eqs. (20) and (21) for each layer and each pair of Fourier harmonics, and (b) Eqs. (22)–(25). Note that the matrices $[S_0]$ and $[S_1]$ are not functions of d_l. On the other hand, the matrices $[a_0]$, $[a_1]$, $[L_0]$, $[L_1]$, $[K_0]$, $[K_1]$ are functions of d_l and λ, which is itself a function of d_l.

Numerical Studies

To study the effect of temperature-dependent material properties on the prebuckling and thermal buckling responses, several thermal buckling problems of multilayered composite plates were solved. For each problem the prebuckling stresses, the critical temperature and their derivatives with respect to the different material and lamination parameters were evaluated, and were compared with the corresponding values for plates with temperature independent properties. These studies are currently being used in assessing the reliability of various two-dimensional theories for predicting the critical temperature and its sensitivity derivatives.

The composite plates considered in this study are square angle-ply laminates with $L_1 = L_2 = 1$. The plates have antisymmetric lamination with respect to the middle plane. The thermal buckling response is assumed to be periodic in x_1 and x_2 with periods $2L_1$ and $2L_2$. The thermoelastic characteristics of each layer are taken to be those typical of advanced composites and are assumed to be linear functions of the temperature as follows:

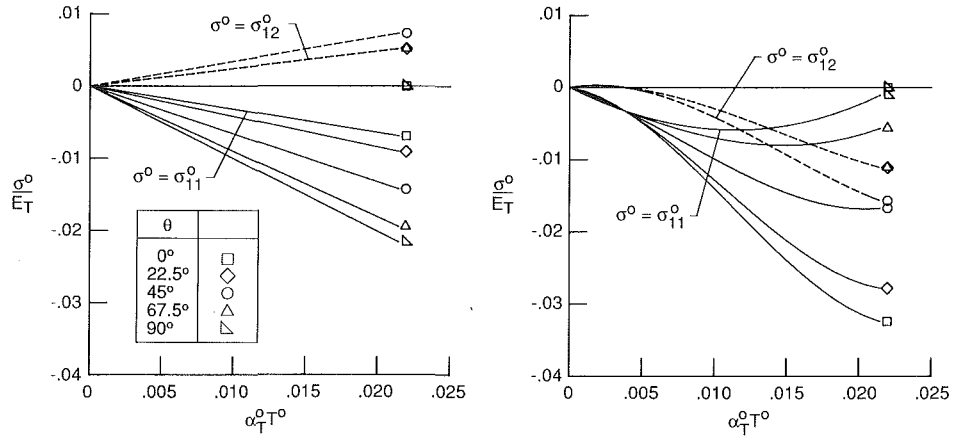
$$\begin{Bmatrix} E_L \\ E_T \\ G_{LT} \\ G_{TT} \\ \nu_{LT} \\ \nu_{TT} \\ \alpha_L \\ \alpha_T \end{Bmatrix} = \begin{Bmatrix} E_L^0 \\ E_T^0 \\ G_{LT}^0 \\ G_{TT}^0 \\ \nu_{LT}^0 \\ \nu_{TT}^0 \\ \alpha_L^0 \\ \alpha_T^0 \end{Bmatrix} - \begin{Bmatrix} \overline{E}_L \\ \overline{E}_T \\ \overline{G}_{LT} \\ \overline{G}_{TT} \\ \cdot \\ \cdot \\ -\overline{\alpha}_L \\ \cdot \end{Bmatrix} T \qquad (26)$$

with

$$E_L^0/E_T^0 = 15, \qquad \overline{E}_L/E_L^0 = 6.4\times10^{-4}$$
$$G_{LT}^0/E_T^0 = 0.52, \qquad \overline{E}_T/E_T^0 = 1.05\times10^{-3}$$
$$G_{TT}^0/E_T^0 = 0.3378, \qquad \overline{G}_{LT}/G_{LT}^0 = 1.1\times10^{-3}$$
$$\alpha_L^0/\alpha_T^0 = 10^{-10}, \qquad \overline{G}_{TT}/G_{TT}^0 = 1.05\times10^{-3}$$
$$\nu_{LT}^0 = 0.32, \qquad \overline{\alpha}_L/\alpha_T^0 = 5.24\times10^{-4}$$
$$\nu_{TT}^0 = 0.48.$$

In Eqs. (26): T is the temperature increase (above the room temperature); subscript L refers to the direction of fibers, and subscript T refers to the transverse direction; ν_{LT} is the major Poisson's ratio; and a dot (.) refers to a zero term. Note that the numerical values selected for the thermoelastic characteristics satisfy all the consistency requirements (e.g., symmetry relations) and the material stiffness matrix is positive definite in the range of the temperature considered. The fiber orientation for the laminates was selected to be $[+\theta/-\theta, \ldots]$, respectively (starting from the top layer). The temperature increase is assumed to be uniform, i.e., $f(\zeta)$ in Eq. (3) is chosen to be 1. Only the lowest critical temperatures and the associated mode shapes and modal stresses are considered herein.

Two parameters were varied, namely, the thickness ratio of the plate, h/L_1; and the fiber orientation angle of the individual layers, θ. In addition, the effect of neglecting the prebuckling displacements w^0 was studied. Typical results are shown in Figs. 2–9, for the two cases of temperature-dependent and temperature-independent material properties. The latter case corresponds to setting all the thermoelastic coefficients with a bar equal to zero; i.e., $\overline{E}_L = \overline{E}_T = \overline{G}_{LT} = \overline{G}_{TT} = \overline{\alpha}_L = 0$. For brevity, the two cases of temperature-dependent and tem-



a) Temperature independent properties (TI)

b) Temperature dependent properties (TD)

Fig. 2 Variation of prebuckling stresses with temperature. Ten-layer angle-ply composite plates. $\sigma_{11}^0|_\theta = \sigma_{22}^0|_{90-\theta}$

Downloaded 03 May 2010 to 171.66.16.247. Redistribution subject to ASME license or copyright; see http://www.asme.org/terms/Terms_Use.cfm

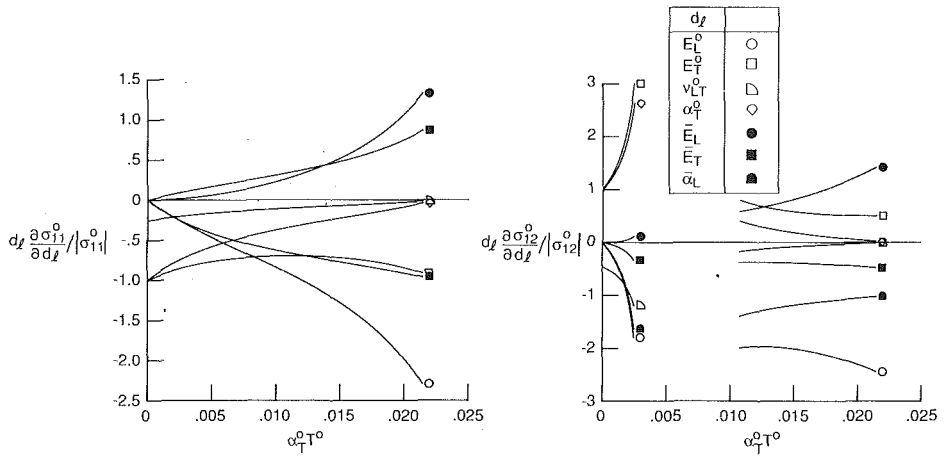


Fig. 3 Variation of the sensitivity derivatives of the prebuckling stresses with temperature. Ten-layer angle-ply composite plates, θ = 45°.

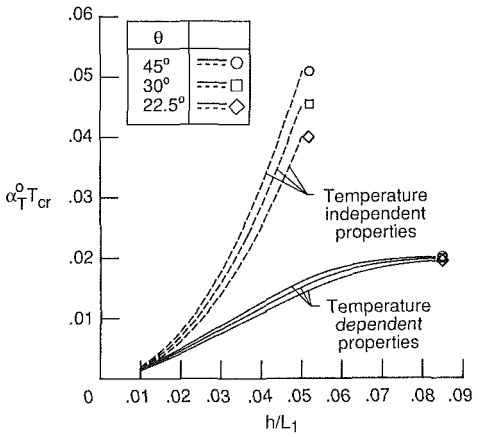


Fig. 4 Effect of thickness ratio and fiber-orientation angle on the critical temperatures obtained by the three-dimensional model. Ten-layer angle-ply composite plates. Solutions are periodic in x_1 and x_2, $m = n = 1$.

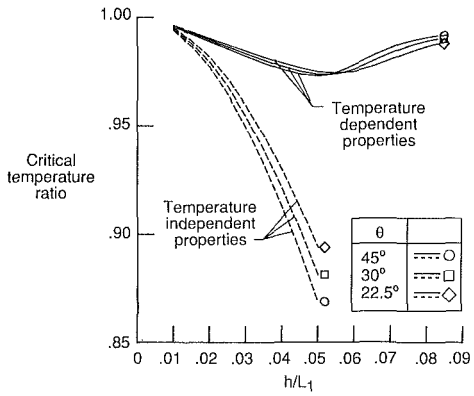


Fig. 6 Effect of prebuckling deformations on the critical temperatures obtained by the three-dimensional models. Critical temperature ratio refers to the ratio of T_{cr} obtained by neglecting w^0 to that obtained by including w^0. Solutions are periodic in x_1 and x_2, $m = n = 1$.

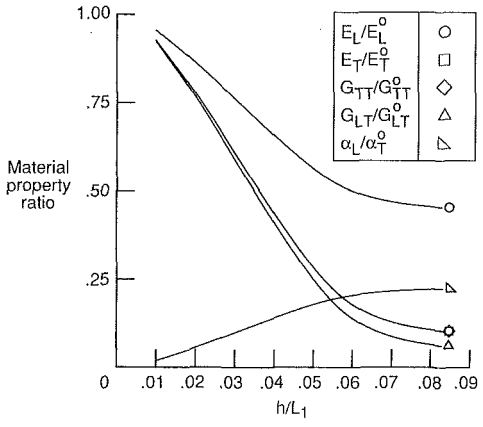


Fig. 5 Values of the material property ratios at the critical temperatures for ten-layer angle-ply composite plates, θ = 45°. Solutions are periodic in x_1 and x_2, $m = n = 1$.

perature-independent properties will henceforth be referred to as TD and TI, respectively.

The variation of the prebuckling stresses with temperature is shown in Fig. 2 for plates with different fiber orientation angles, θ. The range of temperatures considered in Fig. 2 is based on the critical temperatures for plates with thickness ratios, h/L_1, approximately equal to 0.083. For square angle-ply plates $\sigma^0_{22}|_{\theta-90} = \sigma^0_{11}|_\theta$. For the TI case the prebuckling stresses vary linearly with T^0. The stresses σ^0_{11} are compressive and their magnitudes increase with increasing θ from 0° to 90°. The stresses σ^0_{12} are positive and their values increase as θ increases from 0° to 45°. By contrast, for the TD case, the prebuckling stresses are nonlinear functions of T^0, their variations with temperature are significantly different from those of the TI case. For example, for $\alpha^0_T T^0 > 0.02$, the magnitude of the σ^0_{11} decreases with increasing θ from 0° to 90° and the σ^0_{12} stresses are negative.

For the TD case the variations of the sensitivity derivatives, $\partial\sigma^0_{11}/\partial d_l$ and $\partial\sigma^0_{12}/\partial d_l$, with temperature are depicted in Fig. 3, where d_l refers to any of the seven material parameters E^0_L, E^0_T, ν^0_{LT}, α^0_T, $\bar{E}_L$, $\bar{E}_T$ and $\bar{\alpha}_L$. Each of the sensitivity derivatives is normalized through multiplication by $d_l/|\sigma^0|$. The discontinuities in the σ^0_{12} plots are due to the zero (and small) values of σ^0_{12} in the neighborhood of $\alpha^0_T T^0 = 0.0038$. As can be seen from Fig. 3, σ^0_{11} is very sensitive to variations in E^0_L, E^0_T, α^0_T, $\bar{E}_L$, $\bar{E}_T$, $\bar{\alpha}_L$, somewhat sensitive to variations in ν^0_{LT}, and is not sensitive to variations in ν^0_{TT} and α^0_L (results for the latter two are not shown). The magnitudes of the derivatives of σ^0_{11} with respect to E^0_L, $\bar{E}_L$, $\bar{E}_T$, and $\bar{\alpha}_L$ increase with increasing T^0. By contrast, the magnitudes of the derivatives with respect to ν^0_{LT} and α^0_T decrease with increasing T^0, and the derivative of σ^0_{11} with respect to E^0_T does not change monotonically with T^0. At higher temperatures ($\alpha^0_T T^0 > 0.0015$) where σ^0_{12} differs from zero, the magnitude of the derivatives of σ^0_{12} become less insensitive to variations in T^0. The derivatives of σ^0_{12} with respect to E^0_T, $\bar{E}_T$, and $\bar{\alpha}_L$ are nearly constant in this higher temperature

Downloaded 03 May 2010 to 171.66.16.247. Redistribution subject to ASME license or copyright; see http://www.asme.org/terms/Terms_Use.cfm

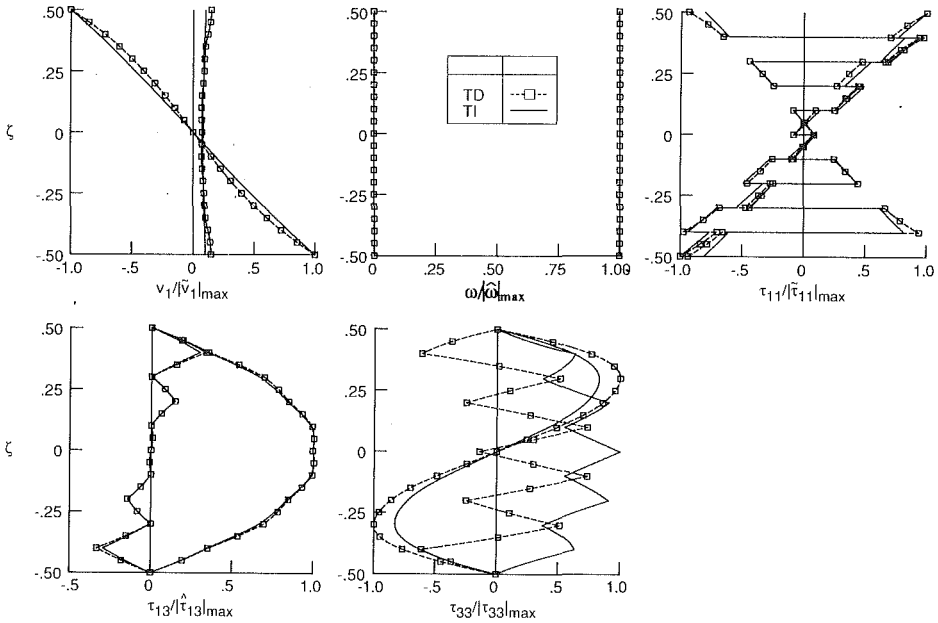


Fig. 7 Thickness variation of the displacements and stresses associated with the minimum critical temperatures. Ten-layer angle-ply composite plates $\theta = 45°$, $h/L_1 = 0.07$. Solutions are periodic in x_1 and x_2, $m = n = 1$ (maximum values are given in Table 2).

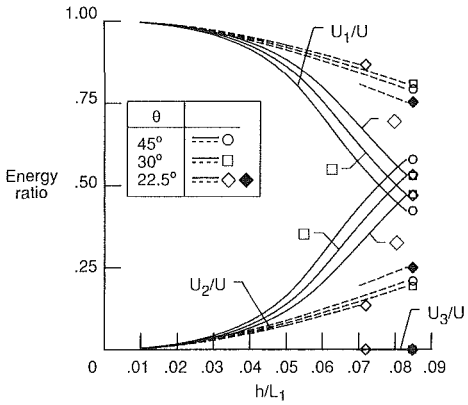


Fig. 8 Effect of thickness ratio and fiber orientation angle on the energy ratios associated with the minimum critical temperatures ten-layer angle-ply composite plates. Solutions are periodic in x_1 and x_2; U_1, U_2, U_3 are energy components associated with $(\tau_{\alpha\beta}, \eta_{\alpha\beta})$, $(\tau_{\alpha 3}, 2\eta_{\alpha 3})$ and (τ_{33}, η_{33}), respectively. $U = U_1 + U_2 + U_3$. Solid lines refer to TD case and dashed lines refer to TI case. Solid symbols refer to buckling modes with $m = 1$, $n = 2$. All other symbols are for $m = n = 1$.

range. The derivatives of σ_{12}^0 with respect to ν_{LT}^0 and α_T^0 tend to zero as $\alpha_T^0 T^0$ approaches 0.022. For the TI case the sensitivity derivatives $\partial\sigma_{11}^0/\partial d_l$ and $\partial\sigma_{12}^0/\partial d_l$ are independent of T^0 and are listed in Table 1. Except for $\partial\sigma_{11}^0/\partial\nu_{LT}^0$ and $\partial\sigma_{11}^0/\partial\alpha_L^0$ all the other derivatives are independent of θ.

The effects of variations in h/L_1 and θ on the minimum critical temperatures are depicted in Fig. 4 for both the TD and TI cases. Note that the values of T_{cr} for the TD case are considerably smaller than the corresponding values for the TI case. This is attributed to the significant changes in the material properties at the critical temperatures of medium thick (and thick) plates as shown in Fig. 5. In Fig. 5 the ratios of the values of the material properties at T_{cr}, to the corresponding values at room temperature ($T = 0$) are plotted versus h/L_1. The curves become nearly flat for $h/L_1 > 0.07$.

The significance of the prebuckling displacements, w^0, is illustrated in Fig. 6 for both the TD and TI cases. The effect of neglecting w^0 on T_{cr} is much more pronounced for the TI case than for the TD case, particularly for medium thick and thick plates ($h/L_1 \geq 0.04$). This is attributed to the significant changes in material properties at the critical temperatures for those plates.

The thickness variations of the displacement components v_1 and ω; and the stress components τ_{11}, τ_{13}, and τ_{33}, for both the TD and TI cases are shown in Fig. 7. Both the symmetric and antisymmetric components of each response quantity are shown. Each displacement and stress component is normalized by dividing by its maximum absolute value. The ratios of the maximum absolute values for the displacements and stresses are listed in Table 2. The thickness distributions of ω, τ_{11}, and τ_{13} for the TD and TI cases are very similar (almost identical for ω). However, for the TD case the nonlinearity of $\tilde{v}_1$ in the thickness direction is more noticeable, and the distribution of $\hat{\tau}_{33}/|\tau_{33}|_{max}$ is considerably different from that for the TI case. However, the magnitude of τ_{33} is considerably smaller than that of other stresses (see Table 2).

As a step towards assessing the significance of transverse stresses associated with thermal buckling of composite plates, the strain energy components of U_1, U_2, and U_3 of the plate were introduced, where

$$U_1 = \frac{1}{2}\int_v \tau_{\beta\gamma} \times \eta_{\beta\gamma} dV \tag{27}$$

$$U_2 = \frac{1}{2}\int_v \tau_{\beta 3} \times 2\eta_{\beta 3} dV \tag{28}$$

$$U_3 = \frac{1}{2}\int_v \tau_{33} \times \eta_{33} dV. \tag{29}$$

In Eqs. (27)–(29), a repeated index β or γ denotes summation over the range 1, 2. The effect of variation of the two parameters h/L_1 and θ on the energy ratios U_1/U, U_2/U, and U_3/U (where $U = U_1 + U_2 + U_3$) was studied. Typical results are shown in Fig. 8 in which the energy ratios U_i/U ($i = 1$ to 3) are plotted versus h/L_1 for the TD and TI cases. The discontinuities in the plots for $\theta = 22.5°$ in the TI case are due to the changes in the buckling modes associated with T_{cr} (from $m = n = 1$ for lower values of h/L_1 to $m = 1$, $n = 2$ for higher values of h/L_1).

The variations of the sensitivity derivatives $\partial T_{cr}/\partial d_l$ with $h/$

Downloaded 03 May 2010 to 171.66.16.247. Redistribution subject to ASME license or copyright; see http://www.asme.org/terms/Terms_Use.cfm

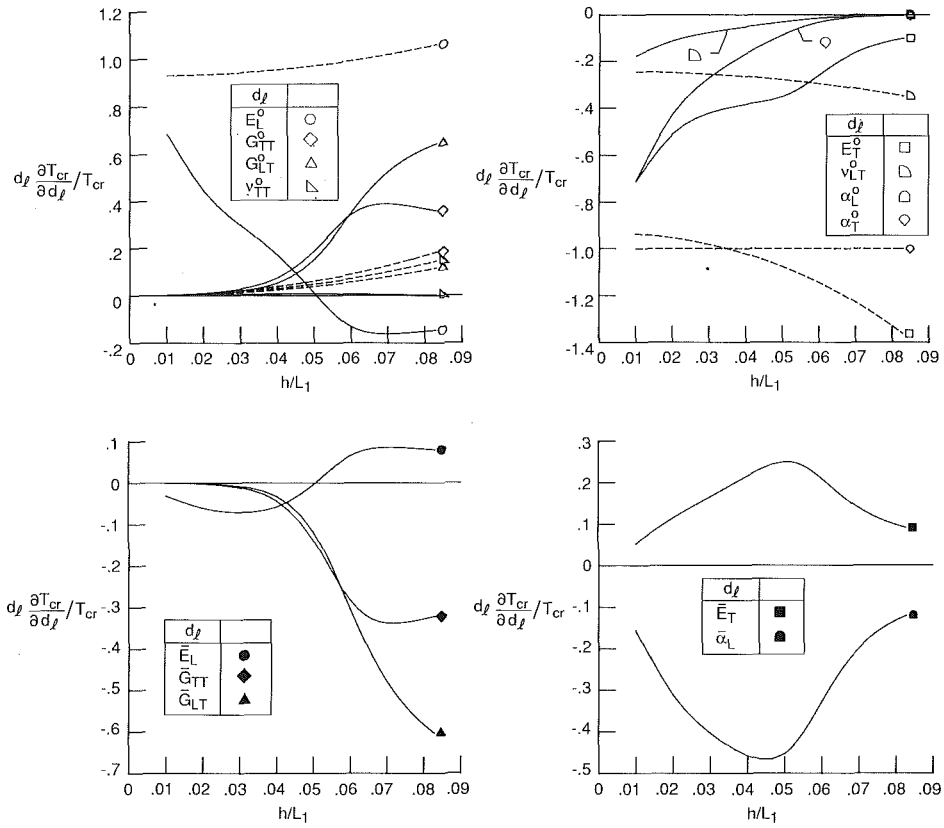


Fig. 9 Effect of thickness ratio on the critical temperature-sensitivity derivatives obtained by the three-dimensional model. Ten-layer angle-ply composite plates, $\theta = 45°$. Solutions are periodic in x_1 and x_2; $m = n = 1$. Solid lines refer to TD case and dashed lines refer to TI case.

Table 1 Values of the sensitivity derivatives of the prebuckling stresses of ten-layer angle-ply composite plate with $\theta = 45°$

d_l	$d_l \frac{\partial \sigma_{11}^0}{\partial d_l}/\lvert\sigma_{11}^0\rvert$	$d_l \frac{\partial \sigma_{12}^0}{\partial d_l}/\lvert\sigma_{12}^0\rvert$
E_L^0	6.874×10^{-3}	-6.874×10^{-3}
E_T^0	-1.007	1.007
ν_{LT}^0	-0.2562	-0.4568
α_L^0	-1.161×10^{-9}	-2.159×10^{-9}
α_T^0	-1	1

Table 2 Maximum absolute values of the displacements and stresses associated with the minimum critical temperature. Ten-layer angle-ply composite plates, $\theta = 45°$, $h/L_1 = 0.07$. Solutions are periodic in x_1 and x_2, $m = n = 1$ (see Fig. 7).

	TI Case	TD Case
$\lvert\tilde{v}_1\rvert_{max}/\lvert\hat{w}\rvert_{max}$	0.1095	0.0733
$\lvert\hat{\tau}_{13}\rvert_{max}/\lvert\tilde{\tau}_{11}\rvert_{max}$	0.1072	0.1041
$\lvert\tau_{33}\rvert_{max}/\lvert\tilde{\tau}_{11}\rvert_{max}$	3.709×10^{-3}	2.966×10^{-3}

Notes: 1) TI and TD refer to temperature-independent and temperature-dependent cases, respectively.
2) For TI, $\lvert\tau_{33}\rvert_{max} = \lvert\hat{\tau}_{33}\rvert_{max}$ and for TD, $\lvert\tau_{33}\rvert_{max} = \lvert\tilde{\tau}_{33}\rvert_{max}$.

L_1 are shown in Fig. 9 where d_l refers to any of the 13 material parameters (E_L^0, G_{LT}^0, G_{TT}^0, ν_{TT}^0), (E_T^0, ν_{LT}^0, α_L^0, α_T^0), ($\bar{E}_L$, $\bar{G}_{TT}$, $\bar{G}_{LT}$), ($\bar{E}_T$, $\bar{\alpha}_L$). For convenience, the material parameters are grouped into four groups (identified by parentheses). Each of the sensitivity derivatives is normalized through multiplication by d_l/T_{cr}. For the first two groups of material parameters, the sensitivity derivatives for the TD and TI cases are compared in Fig. 9. The last two groups of parameters are particular to the TD case. Note that for the TI case, each of the normalized sensitivity derivatives of $d_l \partial T_{cr}/\partial d_l/T_{cr}$ increases (or decreases) monotonically with increasing h/L_1. By contrast, for the TD case the changes of most of the normalized sensitivity derivatives with h/L_1 are nonmonotonic. Moreover, when $d_l = E_L^0$, E_T^0, or ν_{LT}^0, the changes of the normalized derivatives with h/L_1 for the TD case have opposite sense to the corresponding ones for the TI case. Note that if Eq. (26) is written in the compact form $b_l = b_l^0 - \bar{b}_l T$ (where b_l^0 and $\bar{b}_l$ are subsets of d_l), then the following relations hold between the derivatives with respect to b_l^0 and $\bar{b}_l$:

$$\frac{\partial T_{cr}}{\partial b_l^0} = -\frac{1}{T_{cr}} \frac{\partial T_{cr}}{\partial \bar{b}_l}. \tag{30}$$

Concluding Remarks

Analytical three-dimensional thermoelasticity solutions are presented for the thermal buckling of multilayered angle-ply composite plate with temperature-dependent thermoelastic properties. Sensitivity derivatives are also evaluated and used to study the sensitivity of the prebuckling and thermal buckling responses to variations in different lamination and material parameters of the plate. The plates are assumed to have rectangular geometry and an antisymmetric lamination with re-

Downloaded 03 May 2010 to 171.66.16.247. Redistribution subject to ASME license or copyright; see http://www.asme.org/terms/Terms_Use.cfm

spect to the middle plane. The temperature is assumed to be independent of the surface coordinates, but has an arbitrary symmetric variation through the thickness of the plate. A Lagrangian description of the deformation, which accounts for the large displacements and rotations, is used. The fundamental equations are expressed in terms of the second Piola Kirchhoff stress tensor and the Green-Lagrange strain tensor. A linear, Duhamel-Neumann type constitutive model is used and the material properties are assumed to be functions of temperature. A mixed formulation is used with the fundamental unknowns consisting of the six perturbation stress components and the three perturbation displacement components of the plate. Each of the plate variables is decomposed into symmetric and antisymmetric components in the thickness direction, and is expressed in terms of a double Fourier series in the Cartesian surface coordinates.

Extensive numerical results are presented showing the effect of temperature-dependent material properties on the prebuckling stresses, critical temperatures and their sensitivity derivatives. The numerical results show that including the temperature dependence of the material properties in the computational model can result in significant changes in the prebuckling and buckling responses. Specifically, the temperature dependence of the material properties results in:

1 nonlinear dependence of the prebuckling stresses on the temperature and, at higher temperatures, change in the sign of the shear stresses,
2 reduction in the critical temperatures which is amplified with the increase in the thickness ratio of the plate,
3 more noticeable nonlinearities in the thickness distribution of the in-plane displacements for thin plates,
4 less pronounced effect of the prebuckling displacements, w^0, on the critical temperatures; and
5 increase in the transverse shear deformations.

Acknowledgment

The present research is partially supported by an Air Force Office of Scientific Research Grant No. AFOSR-90-0369, and by NASA Grant No. NAG-1-1162. The authors acknowledge useful discussions with Spencer Wu of AFOSR and James H. Starnes, Jr., of NASA.

References

Chen, L. W., and Chen, L. Y., 1989, "Thermal Buckling Behavior of Laminated Composite Plates with Temperature-Dependent Properties," *Composite Structures*, Vol. 13, pp. 275–287.

Hearmon, R. F. S., 1961, *An Introduction to Applied Anisotropic Elasticity*, Oxford University Press, London.

Kalam, M. A., 1981, "Modified Rayleigh-Ritz Method in Non-axisymmetric Thermoelastic Analysis of an Orthotropic Cylinder," *Journal of Thermal Stresses*, Vol. 4, pp. 31–38.

Khalatyan, A. P., 1978, "Axisymmetric Problem of Thermoelasticity for an Orthotropic Heat-Sensitive Shell with a Low Shear Rigidity," *Soviet Applied Mechanics* (a translation of *Prikladnaya Mekhanika*, Vol. 14, No. 5, May 1978, pp. 30–35), pp. 468–472.

Khoroshun, L. P., and Shpakova, S. G., 1986, "Accounting for Thermal Sensitivity in the Equations of Displacement Theory for the Thermoelasticity of Layered Plates and Shells," *Soviet Applied Mechanics* (a translation of *Prikladnaya Mekhanika*, Vol. 22, No. 11, Nov. 1986, pp. 78–85).

Lekhnitski, S. G., 1981, *Theory of Elasticity of an Anisotropic Body*, Mir Publishers, Moscow.

Miller, C. J., Millavec, W. A., and Kicher, T. P., 1981, "Thermal Stress Analysis of Layered Cylindrical Shell," *AIAA Journal*, Vol. 19, pp. 523–530.

Noda, N., 1986, "Thermal Stresses in Materials with Temperature-Dependent Properties," *Thermal Stresses I*, R. B. Hetnarski, ed., North-Holland, Amsterdam, pp. 391–483.

Noda, N., 1991, "Thermal Stresses in Materials with Temperature-Dependent Properties," ASME *Applied Mechanics Reviews*, Vol. 44, No. 9, pp. 383–397.

Noor, A. K., and Burton, W. S., 1990, "Three-Dimensional Solutions for Antisymmetrically Laminated Anisotropic Plates," ASME JOURNAL OF APPLIED MECHANICS, Vol. 57, No. 1, pp. 182–188.

Noor, A. K., and Burton, W. S., 1992, "Three-Dimensional Solutions for the Free Vibrations and Buckling of Thermally Stressed Multilayered Angle-Ply Composite Plates," ASME JOURNAL OF APPLIED MECHANICS (to appear).

Padovan, J., 1986, "Anisotropic Thermal Stress Analysis," *Thermal Stresses I*, R. B. Hetnarski, ed., Elsevier Science Publishers, Amsterdam, pp. 143–262.

Srinivas, S., and Rao, A. K., 1970, "Bending, Vibration and Buckling of Simply-Supported Thick Orthotropic Rectangular Plates and Laminates," *International Journal of Solids and Structures*, Vol. 6, pp. 1464–1481.

Srinivas, S., 1973, "A Refined Analysis of Composite Laminates," *Journal of Sound and Vibration*, Vol. 30, pp. 495–507.

Tauchert, T. R., 1976, "Thermal Stresses in a Spherical Pressure Vessel Having Temperature-Dependent, Transversely Isotropic, Elastic Properties," *Developments in Theoretical and Applied Mechanics*, Proceedings of the Eighth Southeastern Conference on Theoretical and Applied Mechanics, Apr. 29–30, pp. 639–651.

APPENDIX A

Strain-Displacement Relations Used in the Present Study

The expressions of the strain components ϵ^0_{ij}, η_{ij}, and ψ_{ij} in terms of the displacement gradients are given by (see Noor and Burton (1992)).

$$\epsilon^0_{\beta\gamma} = \epsilon^0_{\beta 3} = 0 \tag{A1}$$

$$\epsilon^0_{33} = \partial_3 w^0 + \frac{1}{2}(\partial_3 w^0)^2 \tag{A2}$$

$$\eta_{\beta\gamma} = \frac{1}{2}(\partial_\beta v_\gamma + \partial_\gamma v_\beta) \tag{A3}$$

$$\eta_{\beta 3} = \frac{1}{2}[\partial_3 v_\beta + (1 + \partial_3 w^0)\partial_\beta \omega] \tag{A4}$$

$$\eta_{33} = (1 + \partial_3 w^0)\partial_3 \omega \tag{A5}$$

$$\psi_{\beta\gamma} = \frac{1}{2}(\partial_\beta v_\rho \, \partial_\gamma v_\rho + \partial_\beta \omega \, \partial_\gamma \omega) \tag{A6}$$

$\partial_\beta \equiv \partial/\partial x_\beta$, $\partial_3 \equiv \partial/\partial x_3$, $i, j = 1$ to 3, $\beta, \gamma, \rho = 1, 2$; the repeated index ρ in Eq. (A6) denotes summation over the range 1, 2. Note that the expressions for $\psi_{\beta 3}$ and ψ_{33} in terms of the displacement gradients are not given since they are not needed in the present analysis.

APPENDIX B

Explicit Form of the Arrays in the Governing Equations

The explicit form of the arrays $[a_0]$, $[a_1]$, $[S_0]_{m,n}$, $[S_1]$, $[K_0]_{m,n}$, $[K_1]_{m,n}$, $[L_0]_{m,n}$, and $[L_1]_{m,n}$ in Eqs. (20) and (21) associated with the pair of harmonics (m, n) are given by

$$[a_0(\lambda)] = \begin{bmatrix} a_{11} & a_{12} & a_{13} & . & . & . \\ & a_{22} & a_{23} & . & . & . \\ & & a_{33} & . & . & . \\ & & & a_{44} & . & . \\ & & & & a_{55} & . \\ & & & & & a_{66} \end{bmatrix} \tag{B1}$$

$$[a_1(\lambda)] = \begin{bmatrix} . & . & . & . & . & a_{16} \\ & . & . & . & . & a_{26} \\ & & . & . & . & a_{36} \\ & & & . & a_{45} & . \\ & & & & . & . \\ & & & & & . \end{bmatrix} \tag{B2}$$

Downloaded 03 May 2010 to 171.66.16.247. Redistribution subject to ASME license or copyright; see http://www.asme.org/terms/Terms_Use.cfm

$$[S_0]_{m,n} = \begin{bmatrix} -\frac{m\pi}{L_1} & \cdot & \cdot \\ \cdot & -\frac{n\pi}{L_2} & \cdot \\ \cdot & \cdot & \cdot \\ \cdot & \cdot & \frac{n\pi}{L_2} \\ \cdot & \cdot & \frac{m\pi}{L_1} \\ \frac{n\pi}{L_2} & \frac{m\pi}{L_1} & \cdot \end{bmatrix};$$

$$[S_1] = \begin{bmatrix} \cdot & \cdot & \cdot \\ \cdot & \cdot & \cdot \\ \cdot & \cdot & 1 \\ \cdot & 1 & \cdot \\ 1 & \cdot & \cdot \\ \cdot & \cdot & \cdot \end{bmatrix} \frac{d}{dx_3} \quad \text{(B3)}$$

$$[K_0(\lambda)]_{m,n} = \begin{bmatrix} 1 & \cdot & \cdot \\ \cdot & 1 & \cdot \\ \cdot & \cdot & 1 \end{bmatrix} \left(\frac{m^2\pi^2}{L_1^2} \sigma_{11}^0 + \frac{n^2\pi^2}{L_2^2} \sigma_{22}^0 \right) \quad \text{(B4)}$$

$$[K_1(\lambda)]_{m,n} = \begin{bmatrix} 1 & \cdot & \cdot \\ \cdot & 1 & \cdot \\ \cdot & \cdot & -1 \end{bmatrix} \frac{2mn\pi^2}{L_1 L_2} \sigma_{12}^0 \quad \text{(B5)}$$

$$[L_0(\lambda)]_{m,n} = \frac{dw^0}{dx_3} \begin{bmatrix} \cdot & \cdot & \cdot \\ \cdot & \cdot & \cdot \\ \cdot & \cdot & \frac{d}{dx_3} \\ \cdot & \cdot & \frac{n\pi}{L_2} \\ \cdot & \cdot & \frac{m\pi}{L_1} \\ \cdot & \cdot & \cdot \end{bmatrix} \quad \text{(B6)}$$

$$[L_1(\lambda)]_{m,n} = \frac{dw^0}{dx_3} \begin{bmatrix} \cdot & \cdot & \cdot \\ \cdot & \cdot & \cdot \\ \cdot & \cdot & \frac{-d}{dx_3} \\ \cdot & \cdot & \frac{n\pi}{L_2} \\ \cdot & \cdot & \frac{m\pi}{L_1} \\ \cdot & \cdot & \cdot \end{bmatrix}. \quad \text{(B7)}$$

In Eqs. (B1) and (B2), a_{IJ} ($I, J = 1$ to 6) are the compliance coefficients of the material (see Hearmon (1961) and Lekhnitski (1981)); w^0 is the prebuckling displacement; σ_{11}^0, σ_{22}^0, σ_{12}^0 are the prebuckling stresses; and a dot (.) refers to a zero term. Note that the compliance coefficients $[a_0]$, $[a_1]$, and the prebuckling displacements and stresses w^0, σ_{11}^0, σ_{22}^0, σ_{12}^0 are functions of the critical temperature parameter λ.

Downloaded 03 May 2010 to 171.66.16.247. Redistribution subject to ASME license or copyright; see http://www.asme.org/terms/Terms_Use.cfm

D. Munz

Y. Y. Yang

Institute for Reliability
and Failure Analysis,
University of Karlshuhe,
W-7500 Karlsruhe,
Federal Republic of Germany

Stress Singularities at the Interface in Bonded Dissimilar Materials Under Mechanical and Thermal Loading

Stress singularities occur at the free edge of the interface of bonded dissimilar materials. General relations for a compound with 90-degree angles of the two materials are given for the parameters which describe the stress field. Differences between mechanical and thermal loadings are discussed.

1 Introduction

If two materials with different elastic properties are joined, stress singularities occur at the free edge of the interface under mechanical or thermal loading. A general configuration is shown in Fig. 1, which is characterized by the two angles θ_1 and θ_2. The stress state near the free edge of the interface is given by

$$\sigma_{ij}(r, \theta) = \frac{K}{(r/L)^{\omega}} \cdot f_{ij}(\theta) + \sigma_{ij0}(\theta) \tag{1}$$

where r and θ are the polar coordinates and L is a characteristic length of the configuration. It was shown by Bogy (1971) that ω is the solution of a transcendental equation and is dependenton the elastic constants of the two materials and the angles θ_1 and θ_2. f_{ij}, K, and σ_{ijo} are also dependent on the elastic constants and θ_1 and θ_2. In addition, the stress intensity factor K and σ_{ijo} are dependent on the loading conditions.

In this paper, a rectangular plate with $\theta_1 = \theta_2 = 90$ deg is treated (Fig. 2). The width of the plate is 2 L and the heights of the two components are H_1 and H_2. Two loading conditions are considered:

(*i*) The component is cooled down from a stress-free state. The resulting temperature difference is ΔT. Such a situation occurs during soldering of a ceramic-metal joint.

(ii) The component is loaded by a tensile load σ_∞ perpendicular to the interface.

2 The Stress Singularity ω

The stress singularity parameter ω can be obtained (Bogy, 1971; Suga et al., 1989) by solving the equation

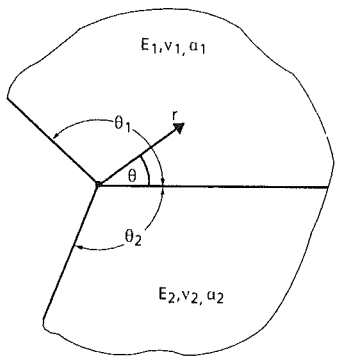


Fig. 1 General configuration at the free edge of a joint between dissimilar materials

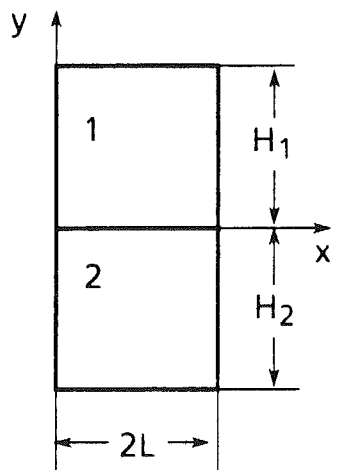


Fig. 2 Investigated compound

Contributed by the Applied Mechanics Division of THE AMERICAN SOCIETY OF MECHANICAL ENGINEERS for publication in the ASME JOURNAL OF APPLIED MECHANICS.

Discussion on this paper should be addressed to the Technical Editor, Prof. Leon M. Keer, The Technological Institute, Northwestern University, Evanston, IL 60208, and will be accepted until four months after final publication of the paper itself in the ASME JOURNAL OF APPLIED MECHANICS.

Manuscript received by the ASME Applied Mechanics Division, Feb. 20, 1991; final revision, Dec. 11, 1991. Associate Technical Editor: C. F. Shih.

Copyright © 1992 by ASME
Downloaded 03 May 2010 to 171.66.16.247. Redistribution subject to ASME license or copyright; see http://www.asme.org/terms/Terms_Use.cfm

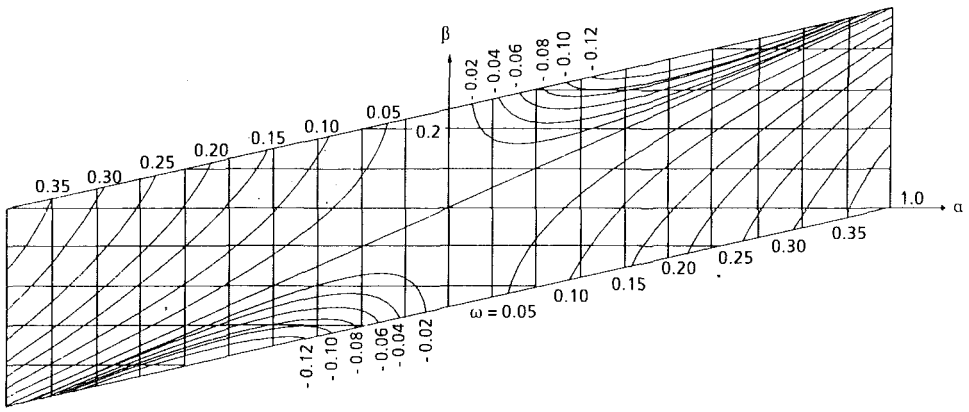


Fig. 3 Curves of constant ω for the possible α and β

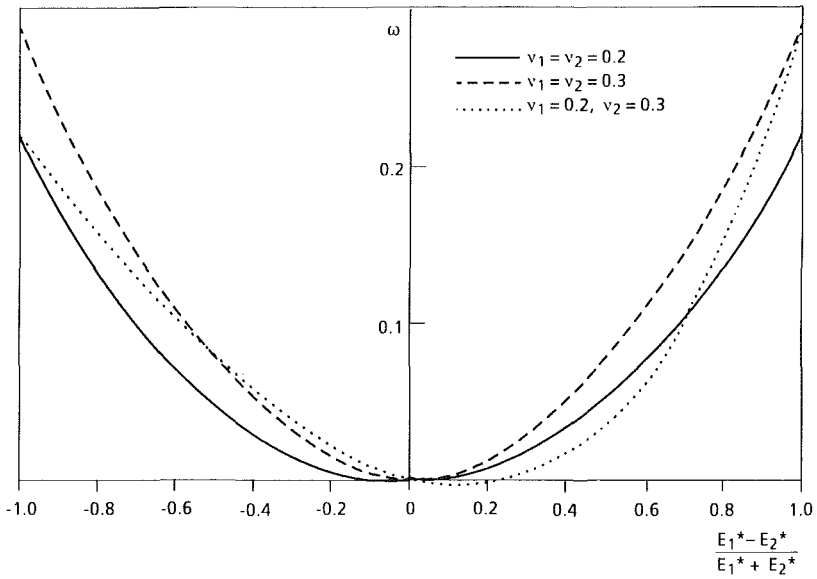


Fig. 4 ω versus difference in effective moduli

$$\lambda^2(\lambda^2-1)\alpha^2+2\lambda^2[\sin^2(\pi\lambda/2)-\lambda^2]\alpha\beta+[\sin^2(\pi\lambda/2)-\lambda^2]^2\beta^2+\sin^2(\pi\lambda/2)\cos^2(\pi\lambda/2)=0 \quad (2)$$

with

$$\lambda=1-\omega. \quad (3)$$

α and β are the Dundurs parameters, which are defined as

$$\alpha=[\mu_2/\mu_1(\kappa_1+1)-(\kappa_2+1)]/[\mu_2/\mu_1(\kappa_1+1)+(\kappa_2+1)] \quad (4a)$$

$$\beta=[\mu_2/\mu_1(\kappa_1-1)-(\kappa_2-1)]/[\mu_2/\mu_1(\kappa_1+1)+(\kappa_2+1)] \quad (4b)$$

with

$$\kappa_i=\begin{cases}(3-\nu_i)/(1+\nu_i) & \text{for plane stress}\\ 3-4\nu_i & \text{for plane strain.}\end{cases} \quad (5)$$

μ is the shear modulus related to the Young's modulus E and the Poisson ratio ν by

$$\mu=\frac{E}{2(1+\nu)}. \quad (6)$$

For $0 < \nu < 0.5$ and all possible variations of E_1 and E_2, the possible values of α and β for plane strain are shown in Fig. 3, which also shows curves for constant ω.

For plane strain condition, the stress singularity vanishes ($\omega = 0$) if $\beta = \alpha/2$ or $\alpha = 0$. $\beta = \alpha/2$ and Eq. (4) then leads to

$$\frac{E_1}{\nu_1(1+\nu_1)}=\frac{E_2}{\nu_2(1+\nu_2)}. \quad (7)$$

An "effective modulus"

$$E^*=\frac{E}{\nu(1+\nu)} \quad (8)$$

will be used in the following considerations and plane strain will be considered.

In Fig. 4, ω is plotted versus $(E_1^* - E_2^*)/(E_1^* + E_2^*)$. For given $\nu_1 = \nu_2$, the singularity parameter ω increases with increasing difference in the effective moduli. For $\nu_1 \neq \nu_2$, there exists a small range with $\omega < 0$, i.e., no singularity.

3 The Constant Stress Term σ_{jio}

It can be shown (Suga et al. 1989; Iancu, 1989) that for the loading condition (i) (thermal stresses)

$$\sigma_{r0}=\frac{\sigma_0}{2}(1-\cos2\theta),$$

$$\sigma_{\theta0}=\frac{\sigma_0}{2}(1+\cos2\theta),$$

$$\tau_{r\theta0}=\frac{\sigma_0}{2}\sin2\theta, \quad (9)$$

Downloaded 03 May 2010 to 171.66.16.247. Redistribution subject to ASME license or copyright; see http://www.asme.org/terms/Terms_Use.cfm

where σ_0 is given by

$$\sigma_0 = \Delta\alpha \cdot \Delta E \cdot \Delta T, \tag{10}$$

with

$$\Delta\alpha = \alpha_1(1+\nu_1) - \alpha_2(1+\nu_2), \tag{11}$$

$$\Delta E = \left[\frac{1}{E_1^*} - \frac{1}{E_2^*}\right]^{-1}. \tag{12}$$

ΔT is defined as negative for cooling conditions. From Eq. (12) it can be seen that σ_0 approaches infinity for $E_1^* \to E_2^*$.

For the loading condition (ii) (mechanical loading perpendicular to the interface), there is $\sigma_0 = 0$.

4 The Angular Term f_{ij}

The angular term f_{ij} depends on ω and can be obtained by analysis (Iancu, 1989). We use the following notations:

$$\sigma_r(r, \theta) = \frac{K_I}{(r/L)^\omega} f_r(\theta) + \sigma_{r0}(\theta) \tag{13}$$

$$\sigma_\theta(r, \theta) = \frac{K_I}{(r/L)^\omega} f_\theta(\theta) + \sigma_{\theta 0}(\theta) \tag{14}$$

$$\tau_{r\theta}(r, \theta) = \frac{K_I}{(r/L)^\omega} f_{r\theta}(\theta) + \tau_{r\theta 0}(\theta). \tag{15a}$$

$f_\theta(\theta)$ is defined in such a way that $f_\theta\ (\theta = 0) = 1$. Equation (15*a*) can alternatively be written as

$$\tau_{r\theta}(r, \theta) = \frac{K_{II}}{(r/L)^\omega} f_{r\theta}^*(\theta) + \tau_{r\theta 0}(\theta) \tag{15b}$$

with $f_{r\theta}^*(\theta = 0) = 1$. Then

$$K_{II} = K_I f_{r\theta}(\theta = 0). \tag{16}$$

5 The Stress Intensity Factor K_I

The stress intensity factor K_I depends on the elastic properties of both materials and the loading conditions. For the loading condition (i), the stress intensity factor K_I is proportional to the temperature difference ΔT and also dependent on α_1 and α_2. For the loading condition (ii), the stress intensity factor K_I is proportional to the external stress σ_∞. K_I is independent of the size of the component however dependent on the shape of the component. It was shown by Mizuno et al. (1988) that K_I is independent of H/L for $H/L \geq 2$.

To find the relationship between K_I and E_I, E_2, ν_1, ν_2, α_1, α_2 stresses were calculated by the finite element method. The geometry was $H_1/L = H_2/L = 2$.

The stress intensity factor and the exponent ω can be obtained from the following plots:

$$lg\,(\sigma_\theta^{FE}(r, \theta) - \sigma_{\theta 0}(\theta))\,|_{\theta=0} \text{ versus } lg\,(r/L)$$

or

$$lg\,\frac{(\sigma_r^{FE}(r, \theta) - \sigma_{r0}(\theta))\,|_{\theta=90\text{ deg}}}{f_\theta(90\text{ deg})} \text{ versus } lg\,(r/L)$$

and

$$lg\,(\tau_{r\theta}^{FE}(r, \theta) - \tau_{r\theta 0}(\theta))\,|_{\theta=0} \text{ versus } lg\,(r/L).$$

Figure 5 shows an example of these plots. It was found that the slopes of the straight line through the data points in the range $0.0004 < r/L < 0.004$ ($-3.4 < lg(r/L) < -2.4$) were in good agreement with the analytically calculated ω. From the location of the straight line, K_I and K_{II}, respectively, were obtained.

Figure 6 shows the effect of α_2 on $K_I/\Delta T$ for thermal loading. From Fig. 7 it can be seen that the ratio K_I/σ_0 is independent of α_2.

Figure 8 shows $K_I/\Delta T$ versus $(E_1^* - E_2^*)/(E_1^* + E_2^*)$. It can be seen that $K_I \to \infty$ for $E_1^* \to E_2^*$. In Fig. 9, $K_I/\Delta T$ is plotted versus ν_2. K_I always has the opposite sign as σ_0.

In Fig. 10, all results are plotted as $-K_I/\sigma_0$ versus the exponent ω of the stress singularity. It can be seen that for all variations in α_2, E_2, and ν_2 there is a unique relationship between K_I/σ_0 and ω. This relationship between K_I/σ_0 and ω can be described by

$$-K_I/\sigma_0 = 1 - 2.89\omega + 11.4\omega^2 - 51.9\omega^3 + 135.7\omega^4 - 135.8\omega^5. \tag{17}$$

For mechanical loading, the same relation holds if $-K_I/\sigma_0$ is replaced by K_I/σ_∞. Results are shown in Fig. 11. Therefore, it can be concluded that a unique relationship exists between K_I/σ_∞ or $-K_I/\sigma_0$ and ω for thermal loading and mechanical loading perpendicular to the interface.

6 Discussion

Four parameters in Eq. (1) are responsible for the stress distribution near the free edge of a joint interface: ω, $\tilde{\sigma}_{fij}$, σ_{ijo}, and K. The exponent ω increases with increasing difference in the effective modulus. For mechanical loading, the stress distribution is influenced by the decreasing value of K/σ_∞ with increasing ω. This decrease, however, is overcome by the singularity term. Therefore, the stress increases with increasing

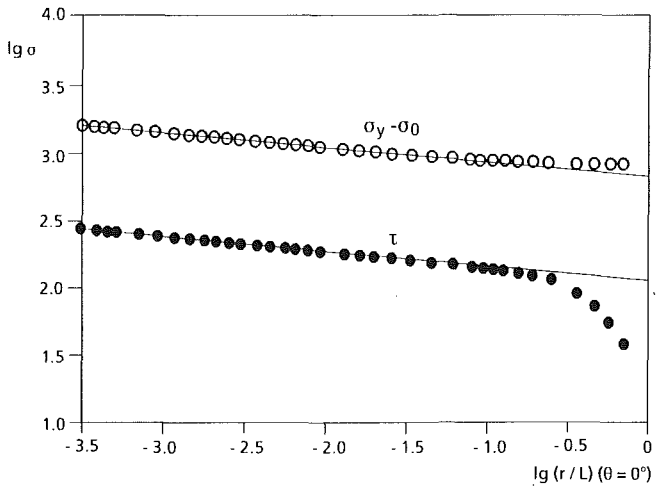


Fig. 5 *FE* plot of $lg\,(\sigma_y - \sigma_0)$ and of $lg\,\tau$ versus $lg\,(r/L)$

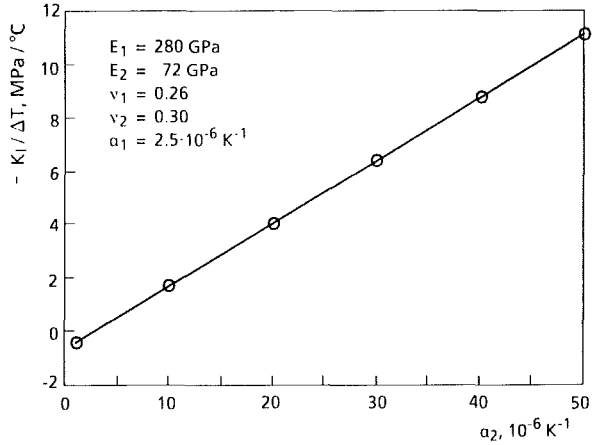


Fig. 6 Effect of α_2 on $K_I/\Delta T$

Downloaded 03 May 2010 to 171.66.16.247. Redistribution subject to ASME license or copyright; see http://www.asme.org/terms/Terms_Use.cfm

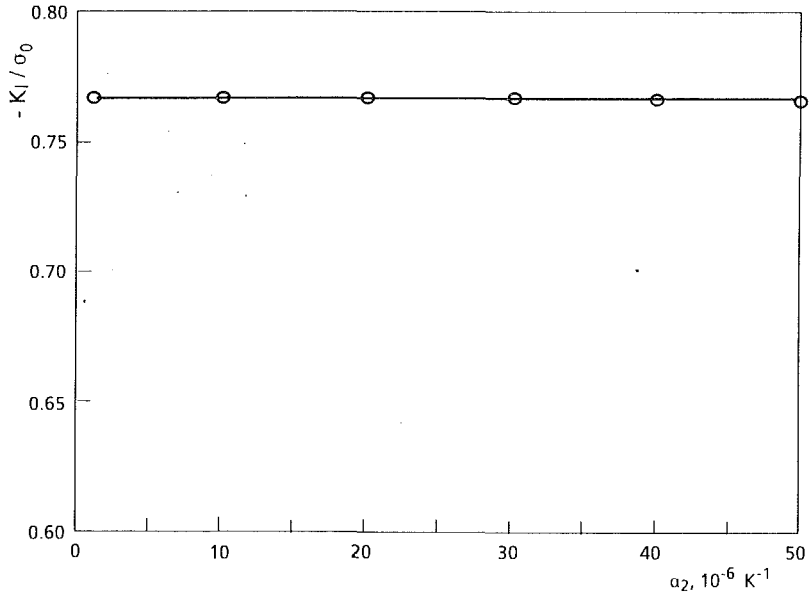


Fig. 7 K_I/σ_0 versus α_2

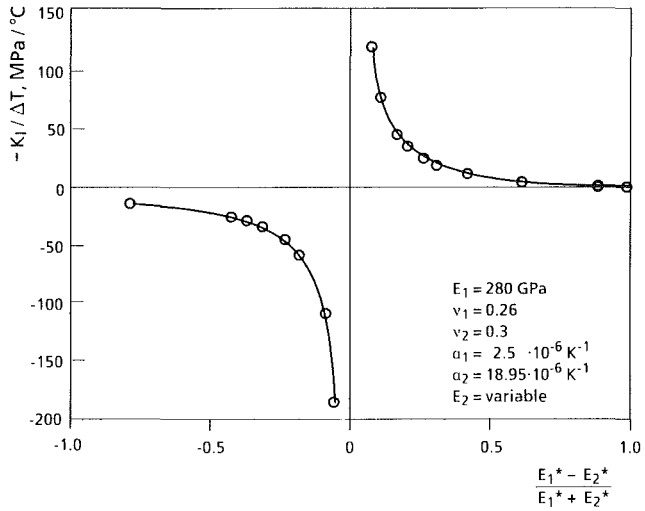


Fig. 8 Effect of difference in effective moduli on $K_I/\Delta T$

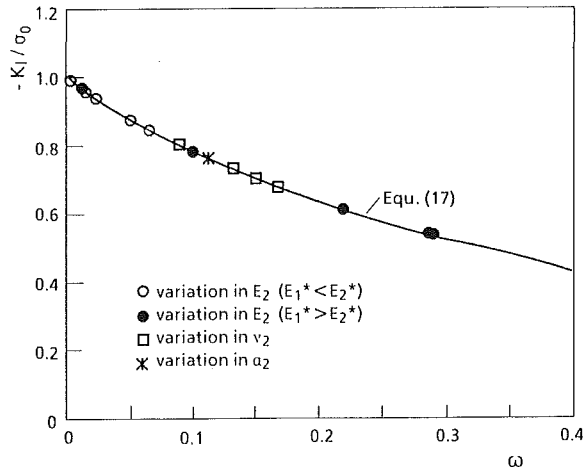


Fig. 10 K_I/σ_0 versus ω for thermal loading

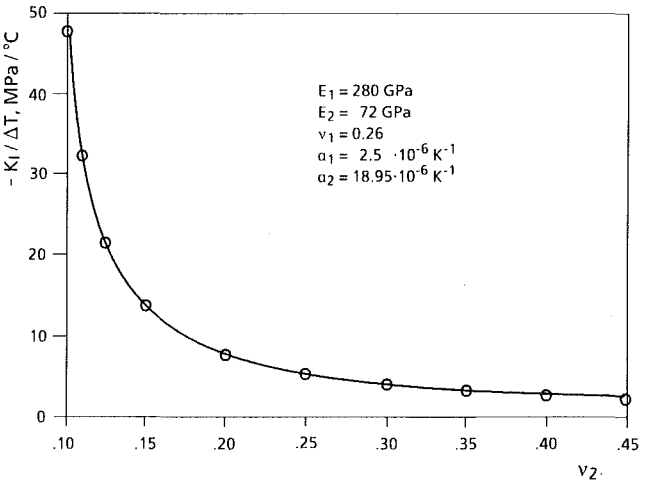


Fig. 9 Effect of ν_2 on $K_I/\Delta T$

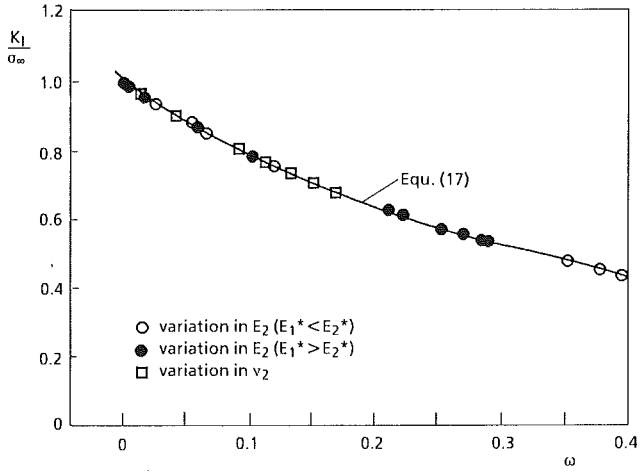


Fig. 11 K_I/σ_∞ versus ω for mechanical loading

Downloaded 03 May 2010 to 171.66.16.247. Redistribution subject to ASME license or copyright; see http://www.asme.org/terms/Terms_Use.cfm

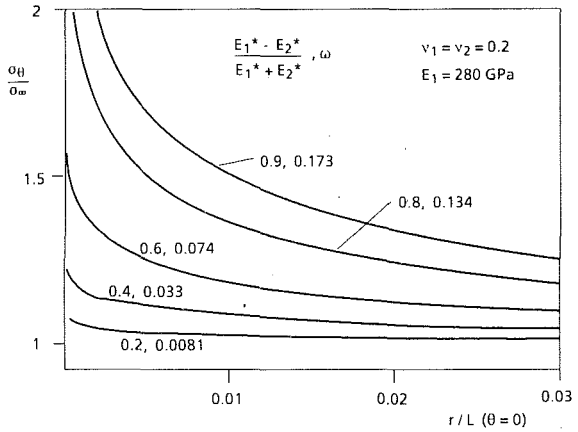


Fig. 12 $\sigma_\theta/\sigma_\infty$ for $\theta = 0$ deg versus r/L for different $E_1^* - E_2^*$

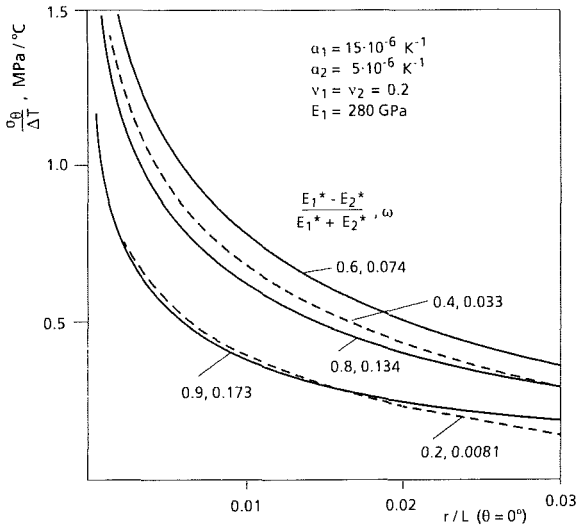


Fig. 13 $\sigma_\theta/\Delta T$ for $\theta = 0$ deg versus r/L for different $E_1^* - E_2^*$

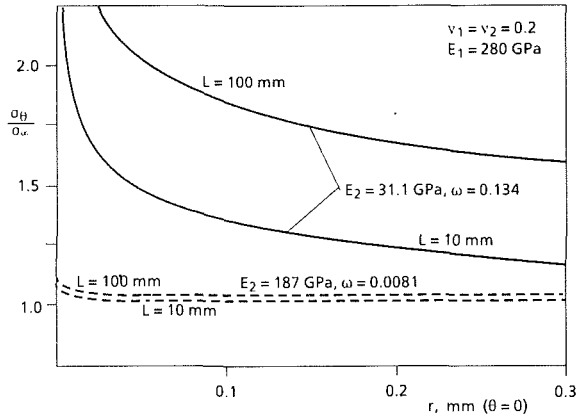


Fig. 14 Effect of component size on $\sigma_\theta/\sigma_\infty$ for mechanical loading

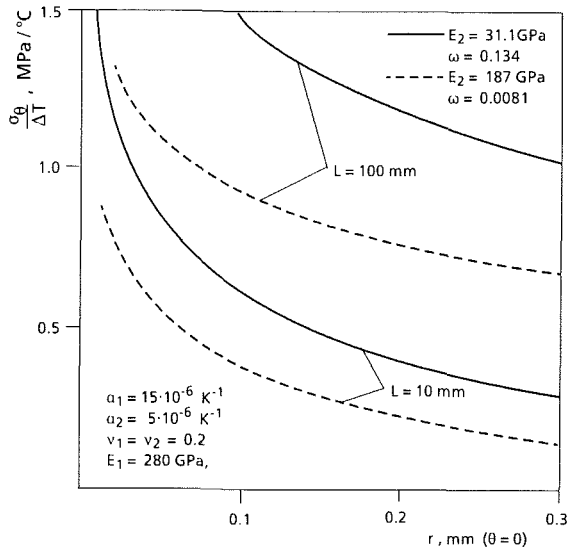


Fig. 15 Effect of component size on $\sigma_\theta/\Delta T$ for thermal loading

difference in the effective moduli, as can be seen from Fig. 12.

For the loading condition (i)—cooling stresses—the situation is more complex. Whereas ω increases with increasing difference in the effective moduli, the stress intensity factor $|K|$ and $|\sigma_0|$ decrease. For $E_1^* \to E_2^*$ the stress intensity factor K and σ_0 approach infinity, however, with different signs. This leads to the effect shown in Fig. 13, that the stress near the free edge of a joint interface do not increase monotonically with increasing singularity exponent ω. Only very close to the free edge of the interface, which cannot be shown in Fig. 13, the stresses monotonically increase with increasing ω.

In many cases, for instance in the evaluation of ceramic-metal joints, the stress distribution near the free edge of the interface is of interest. Though K_I is independent of the size of the component, the stress distribution is dependent on the size. From Eq. (1), a size effect in the stress distribution follows:

$$\sigma_{ij}(r, \theta) = \frac{K}{r^\omega} L^\omega f_{ij}(\theta) + \sigma_{ij0}(\theta). \tag{18}$$

This effect is shown in Figs. 14 and 15, where σ_θ ($\theta = 0$) is plotted versus r, and not versus r/L as in the previous diagrams. For the mechanical loading, the size effect increases with increasing ω. For $\omega = 0.0081$, there is nearly no effect. For the loading situation (i), the size effect is also large for small ω. This is due to the fact that the term σ_0 does not vanish.

Conclusions

Finite element calculations for a compound with 90 deg angles of the two materials have led to the following results:

- A unique relationship exists between K_I/σ_0 for thermal loading or K_I/σ_∞ for mechanical loading (σ_∞ perpendicular to the interface) and the singularity exponent ω.
- For thermal loading, the stresses near the free edge of the interface do not increase with increasing ω.
- A large effect of the component size on the stress at the free edge of the interface exists, especially for thermal loading.

References

Bogy, D. B., 1971, "Two Edge-Bonded Elastic Wedges of Different Materials and Wedge Angles Under Surface Tractions," ASME Journal of Applied Mechanics, Vol. 38, pp. 377–386.

Iancu, O. T., 1989, "Berechnung von thermischen Eigenspannungsfeldern in Keramik/Metall-Verbunden," Ph.D. Thesis, University of Karlsruhe, Karlsruhe, Germany.

Mizuno, K., Miyazawa, K., and Suga, T., 1988, "Characterization of Thermal Stresses in Ceramic/Metal-Joints," *Journal of the Faculty of Engineering*, The University of Tokyo (B), Vol. 39, pp. 401–412.

Suga, T., Mizuno, K., and Miyazawa, K., 1989, "Thermal Stresses in Ceramic-to-Metal-Joints," *Proc. of the MRS International Meeting on Advanced Materials*, Vol. 8, Materials Research Society, pp. 137–142.

Downloaded 03 May 2010 to 171.66.16.247. Redistribution subject to ASME license or copyright; see http://www.asme.org/terms/Terms_Use.cfm

Damping and Resonance Characteristics of Thermal Waves

Da Yu Tzou
Assoc. Professor,
Department of Mechanical Engineering,
University of New Mexico,
Albuquerque, NM 87131
Mem. ASME

Amplification of thermal waves in response to high-frequency excitations is studied in this work. The resonance behavior is explored along with the underdamped behavior in thermal wave oscillations. In transition from an overdamped to an underdamped wave behavior, the relaxation distance is found to dominate the process. A relationship between the resonance frequency and the thermal wave speed is derived. The emphasis is placed on the frequency approach determining the thermal wave speed in engineering materials.

Introduction

In the transient stage of heat transfer in solids, the thermal wave model assumes a *time lag* between the temperature gradient and the heat flux vector. For a material volume at a position $\mathbf{r}$, the temperature gradient established at time $t(\nabla T(\mathbf{r}, t))$ is assumed proportional to the heat flux vector occurred at a *later* time $t + \tau$ ($\mathbf{q}(\mathbf{r}, t + \tau)$) due to the finite speed of heat propagation:

$$\mathbf{q}(\mathbf{r},t+\tau) = -k\nabla T(\mathbf{r},t), \tag{1}$$

where k is the thermal conductivity. In combining with the energy equation

$$-\nabla\cdot\mathbf{q}(\mathbf{r},t) + S(\mathbf{r},t) = \rho C_p T_t(\mathbf{r},t), \tag{2}$$

with subscript t denoting the differentiation with respect to time, all the physical quantities must be at the same instant. For this purpose, the Taylor's series expansion can be applied to $\mathbf{q}(\mathbf{r}, t + \tau)$ around $\tau = 0$. For τ being small, the higher order terms in τ can be neglected and Eq. (1) is approximated by

$$\mathbf{q}(\mathbf{r},t) + \tau\mathbf{q}_t(\mathbf{r},t) \simeq -k\nabla T(\mathbf{r},t). \tag{3}$$

Equation (3) is the constitutive equation in the linear theory of thermal wave propagation (Baumeister and Hamill, 1969; Vick and Özisik, 1983; Özisik and Vick, 1984; Tzou, 1989a,b) which was proposed by considering the kinetic theory of molecules (Chester, 1963). The time lag τ is also called the relaxation time. In relation to the thermal diffusivity (α) and the thermal wave speed (C), $\tau = \alpha/C^2$ (Chester, 1963; Weymann, 1967; Frankel et al., 1985, 1987; Tzou, 1990a,b). In the classical diffusion model assuming C approaching infinity, the value of τ reduces to zero and no phase lag exists. Equation (3) in this case reduces to the Fourier's law in heat conduction.

The energy equation including the wave effect is obtained by combining (2) and (3). By eliminating the heat flux vector, the T-representation results:

$$\alpha\nabla^2 T = (\alpha/C^2)T_{tt} + T_t + (1/\rho C_p)[S + (\alpha/C^2)S_t]. \tag{4}$$

By eliminating temperature, on the other hand, the q-representation is obtained:

$$\alpha\{\nabla[\nabla\cdot\mathbf{q} - \nabla S]\} = (\alpha/C^2)\mathbf{q}_{tt} + \mathbf{q}_t, \tag{5}$$

where all the physical quantities are at the same instant of time. Due to the complicated relationship between the heat flux vector and the temperature gradient, the q-representation has been shown more convenient to use for problems involving flux-specified boundary conditions (Frankel et al., 1985; Tzou, 1989b). Special features in thermal wave propagation have been studied from various physical points of view. In addition to the wave effect in heat transfer, the associated thermoelastic response was pioneered by Lord and Shulman (1967) and Popov (1967). The second-order time derivative of dilatation was found to dominate the thermomechanical coupling. Achenbach (1968) showed that two wavefronts exist in the physical domain when subjecting to thermal excitations. In the presence of thermoelastic coupling, the speed of the fast wavefront is greater than the larger of the speed of the normal stress wave and the thermal wave speed. The speed of the slow wavefront, on the other hand, is less than the smaller of the two. For multidimensional problems, Tzou (1989a,b) extended the research to the thermal shock formation around a fast-moving heat source. The swinging phenomenon of temperature in transition of the thermal Mach number is parallel to that in the high-speed aerodynamics which cannot be depicted by the classical diffusion theory. Due to the wave effect, the singularity of temperature beneath a point heat source transits from a $\ln(r)$-type to a $1/r$-type. The wedge-shaped thermal shock surface further evolves into a quasi-hyperboloidal surface when additional geometrical constraints present (Tzou, 1990c). In predicting the thermoelastic fracture emanating from the heat source, also, a significant difference between the wave and the diffusion models results (Tzou, 1989c). A detailed review on the development of the thermal wave theory is included in a recent annual review article by Tzou (1991a). The research has

Contributed by the Applied Mechanics Division of THE AMERICAN SOCIETY OF MECHANICAL ENGINEERS for presentation at the 1992 ASME Winter Annual Meeting, Anaheim, CA, Nov. 8–13, 1992.

Discussion on this paper should be addressed to Prof. Leon M. Keer, The Technological Institute, Northwestern University, Evanston, IL 60208, and will be accepted until four months after final publication of the paper itself in the ASME JOURNAL OF APPLIED MECHANICS.

Manuscript received by the ASME Applied Mechanics Division, July 22, 1991; final revision, Jan. 6, 1992. Associate Technical Editor: R. M. Bowen.

Paper No. 92-WA/APM-4.

Copyright © 1992 by ASME
Downloaded 03 May 2010 to 171.66.16.247. Redistribution subject to ASME license or copyright; see http://www.asme.org/terms/Terms_Use.cfm

been systematically classified according to their individual emphases.

The recent experiment by Zehnder and Rosakis (1991) sheds light on the wave behavior of heat conduction in the vicinity of a rapidly propagating crack tip. For a crack speed being 900 m/s in 4340 steel, several important features in the experimental observations are preserved in the transonic and supersonic solutions obtained by Tzou (1990a,b). The well-known $1/\sqrt{r}$-singularity of the temperature gradient in the diffusion theory (Tzou, 1991b,c), for example, disappears. It implies diminution of thermal energy accumulation at the crack tip at such a high speed. When the crack speed further increases to 980 m/s, the isotherm pattern parallel to the crack surfaces evolves into hyperbola-like curves. These are salient features pertinent to the wave theory.

When the wave behavior is pronounced in a high-rate environment, it is expected that the process of heat conduction possesses some general features in wave propagation. The resonance of temperature waves, for example, may be a special behavior contributing to the heating technologies. Due to the presence of intrinsic damping from the diffusion effect, however, it will be shown that the temperature resonance is a *high-mode* phenomenon which occurs only if the modal frequency exceeds a critical value. This phenomenon will be analyzed in detail by extracting the underdamped wave modes from the overdamped modes. Special effort will also be made to derive a relationship between the resonance frequency and the thermal wave speed. The purpose is to develop a frequency approach determining the thermal wave speed from the resonance frequency.

Damping Characteristics

Since damping and resonance are responses in time, consideration of a one-dimensional system is sufficient. Moreover, because T- and q-representations have the same time structure, the temperature representation will be used for illustrations. In this case, Eq. (4) becomes

$$T_{xx} = (1/C^2)T_{tt} + (1/\alpha)T_t, \tag{6}$$

where the heat source term is temporarily omitted in studying the damping effects. In the case of C approaching infinity, the time lag τ between the heat flux vector and the temperature gradient vanishes and Eq. (6) reduces to the diffusion equation. In the presence of a finite wave speed, obviously, the thermal diffusivity $(1/\alpha)$ plays a role of damping in the oscillation of temperature waves. Equation (6) is to be solved for temperature T subjecting to appropriate boundary conditions. For simplicity, let us consider isothermal conditions at both ends of $x = 0$ and L:

$$T(0,t) = T(L,t) = 0. \tag{7}$$

By direct substitutions, it can be shown that the temperature wave satisfying (6) and (7) is represented by

$$T(x,t) = \exp(-\gamma t) \sum_{n=1}^{\infty} [A_n \cos(\omega_d t) + B_n \sin(\omega_d t)]\sin(n\pi x/L), \quad \text{with } \gamma = 1/2\tau. \tag{8}$$

Clearly, the time lag τ dictates the damping rate. The damped frequencies ω_d relate to the undamped wave frequencies ω_n by

$$\omega_d^2 = \omega_n^2 - (f/2)^2, \quad \text{with } \omega_n = n\pi C/L \quad \text{for } n = 1,2,3, \ldots, \text{etc.} \tag{9}$$

The critical frequency f, reciprocal of the time lag $\tau (f = 1/\tau)$, has been introduced here for a better physical interpretation. Introducing the following dimensionless quantities,

$$\omega_d^* = \omega_d/f, \quad \omega_n^* = \omega_n/f, \quad t^* = tf, \tag{10}$$

Eq. (8) can be expressed as

$$T(x,t) = \sum_{n=1}^{\infty} [A_n F(t^*) + B_n G(t^*)]\sin(n\pi x/L), \tag{11}$$

while the relationship (9) becomes

$$\omega_d^* = \frac{\sqrt{4(\omega_n^*)^2 - 1}}{2}. \tag{12}$$

The amplitude functions $F(t^*)$ and $G(t^*)$ in (11) depend on the damped frequencies ω_d^*. For ω_d^* being real or, refer to (12), $\omega_n^* > 1/2$,

$$F(t^*) = \exp(-t^*/2)\cos\left[\frac{\sqrt{4(\omega_n^*)^2 - 1}}{2} t^*\right], \tag{13}$$

$$G(t^*) = \exp(-t^*/2)\sin\left[\frac{\sqrt{4(\omega_n^*)^2 - 1}}{2} t^*\right], \quad \text{for } \omega_n^* > \frac{1}{2}. \tag{14}$$

With the magnitude decayed exponentially, $F(t^*)$ and $G(t^*)$ functions oscillate in the time history. For ω_d^* being imaginary or $\omega_n^* < 1/2$, on the other hand,

$$F(t^*) = \exp(-t^*/2)\cosh\left[\frac{\sqrt{1 - 4(\omega_n^*)^2}}{2} t^*\right], \tag{15}$$

$$G(t^*) = \exp(-t^*/2)\sinh\left[\frac{\sqrt{1 - 4(\omega_n^*)^2}}{2} t^*\right], \quad \text{for } \omega_n^* < \frac{1}{2}. \tag{16}$$

No oscillation occurs in this case and the amplitudes are monotonic functions of time. Clearly, Eqs. (13) and (14) represent underdamped modes while (15) and (16) represent overdamped modes of thermal waves. Their occurrence in the time history depends on the modal frequencies ω_n which, in turn, depends on the boundary conditions imposed at $x = 0$ and L. The critical value being half (1/2) for ω_n^* varies if different boundary conditions from those specified in (7) are considered.

Graphical illustrations are provided in Figs. 1 to 3. Figure 1 shows the frequency domains for the under and the overdamped wave modes. They are separated by the evolution equation (12). The damped frequency ω_d^* is always smaller than the undamped frequencies ω_n^*, but the value of ω_d^* approaches that of ω_n^* in the high-frequency domain with ω_n^* being large. For $\omega_n^* = 1$, a typical value in the domain of $\omega_n^* > 1/2$, Fig. 2 displays the oscillatory patterns of the amplitude functions represented by Eqs. (13) and (14). The wave behavior in heat conduction still exists but the amplitudes of $F(t^*)$ and $G(t^*)$ functions decay exponentially due to the damping effect from thermal diffusion. In the frequency domain with $\omega_n^* < 1/2$, Fig. 3 shows the monotonic variations of $F(t^*)$ and $G(t^*)$ functions in the time history. The oscillatory behavior of the amplitude functions disappear due to the strong effects of damping and the temperature waves transit to overdamped modes.

The critical condition of $\omega_n^* = 1/2$ separating the underdamped modes from the overdamped modes can be expressed in terms of the modal number n. From the wave frequencies ω_n shown in Eq. (9), underdamped waves activate when

$$n > \frac{1}{2\pi}\frac{L}{C\tau} \equiv 0.5\frac{R}{\pi} \quad \text{with} \quad R = \frac{L}{C\tau}. \tag{17}$$

The critical mode number (n) depends on the ratio of the characteristic dimension of the solid medium (L) to the distance-like quantity $C\tau$. In parallel to the concept of relaxation time, the quantity $C\tau$ can be defined as the *relaxation distance*. It relates to the thermal wave speed and diffusivity by $C\tau = \alpha/C$ and is another intrinsic thermal property of the medium.

Downloaded 03 May 2010 to 171.66.16.247. Redistribution subject to ASME license or copyright; see http://www.asme.org/terms/Terms_Use.cfm

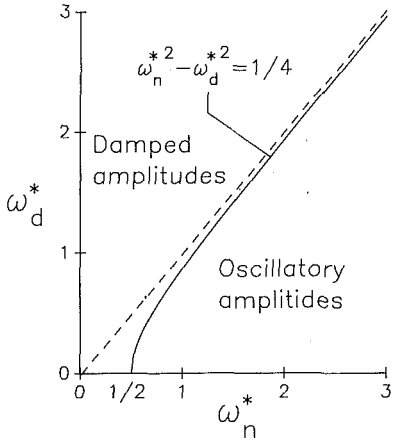


Fig. 1 The relationship between the damped frequency (ω_d^*) and the modal frequency (ω_n^*) for temperature waves

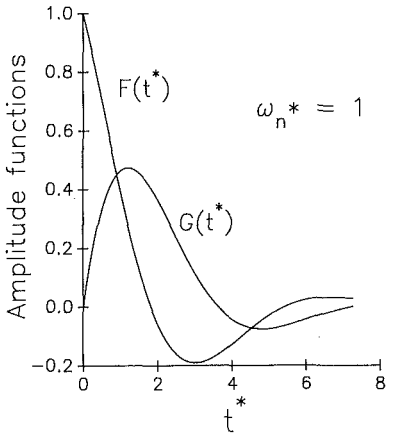


Fig. 2 The oscillatory amplitude functions for the underdamped waves. ω_n^* = 1 (>0.5).

Resonance Phenomenon

As revealed by mechanical oscillations with damping, the amplitude of the temperature wave may become exaggerated if the oscillating frequency of an externally applied heat source reaches a certain value. Subjecting to the excitation of a body heat source, the energy Eq. (4) becomes

$$T_{xx}=(1/C^2)T_{tt}+(1/\alpha)T_t+(1/\rho\alpha C_p)[S+(\alpha/C^2)S_t]. \quad (18)$$

In addition to the wave term in temperature, an *apparent* heat source proportional to the time derivative of the heat source function S exists (Frankel et al., 1985; Tzou, 1989a–d). Due to the apparent heat source term resulting from the finite wave speed, the resonance frequency of temperature waves may deviate from the damped frequency.

For a more detailed understanding, let us consider a heat source oscillating at a frequency Ω:

$$S(x,t)=Q\exp(i\Omega t)g(x), \quad \text{consequently,}$$

$$S_t(x,t)=Q(i\Omega)\exp(i\Omega t)g(x), \quad (19)$$

where Q is the strength of the heat source and $g(x)$ addresses its distribution along the span. Equation (18) then becomes

$$T_{xx}=(1/C^2)T_{tt}+(1/\alpha)T_t+(Q/\rho\alpha C_p)[1+(i\Omega\alpha/C^2)]\exp(i\Omega t)g(x). \quad (20)$$

This equation supports a modal representation

$$T(x,t)=\sum_{n=1}^{\infty}\Gamma_n(t)\phi_n(x) \quad (21)$$

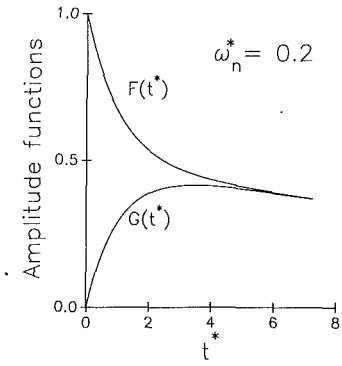


Fig. 3 The monotonic amplitude functions for the overdamped waves. ω_n^* = 0.2 (<0.5).

for the temperature wave. In principle, any complete set of $\phi_n(x)$ can be used for the purpose of expansion. By considering the same boundary conditions in (7), however, the eigenfunctions

$$\phi_n(x)=\sin(\omega_n x) \quad \text{with} \quad \omega_n=n\pi C/L, \quad n=1,2, \ldots \text{ etc.} \quad (22)$$

for the undamped wave will be used. Combination of (20) to (22) then yields

$$(1/C^2)\frac{d^2\Gamma_n}{dt^2}+(1/\alpha)\frac{d\Gamma_n}{dt}+(\omega_n/C)^2\Gamma_n=-(Q/\rho\alpha C_p)(1+i\Omega\alpha/C^2)D_n\exp(i\Omega t) \quad (23)$$

which governs the amplitude function $\Gamma_n(t)$. D_n here is simply the Fourier coefficients of the distribution function $g(x)$,

$$D_n=(2/L)\int_0^L g(x)\sin(n\pi x/L)dx \quad \text{for} \quad n=1,2, \ldots, \text{ etc.} \quad (24)$$

In response to the harmonic excitation $\exp(i\Omega t)$, an admissible form for $\Gamma_n(t)$ is $A_n\exp(i\Omega t)$. Substituting into (23) gives the expression for the complex amplitude A_n:

$$A_n=-\frac{QC^2D_n}{\rho\alpha C_p f^2}A_\Omega \quad \text{with} \quad A_\Omega=\frac{1+i\Omega^*}{[(\omega_n^*)^2-(\Omega^*)^2]+i\Omega^*}, \quad \omega_n^*=\omega_n/f, \quad \Omega^*=\Omega/f. \quad (25)$$

For the resonance to occur at a given value of ω_n^*, the magnitude of A_Ω,

$$|A_\Omega|=\sqrt{A_\Omega\overline{A}_\Omega}=\frac{\sqrt{\omega_n^{*2}(\Omega^{*2}+1)(\omega_n^{*2}-2\Omega^{*2})+\Omega^{*6}+2\Omega^{*4}+\Omega^{*2}}}{\omega_n^{*4}+\Omega^{*2}(1-2\omega_n^{*2})+\Omega^{*4}}, \quad (26)$$

reaches a maximum value. By careful inspections, the stationary condition of $d|A_\Omega|/d\Omega^* = 0$ can be arranged into an eighth-order polynomial:

$$[\Omega^{*2}-\omega_n^*\sqrt{\omega_n^{*2}+2}+1]\cdot[\Omega^{*2}+\omega_n^*\sqrt{\omega_n^{*2}+2}-1]\times\left[\Omega^{*2}-\frac{\sqrt{1-4\omega_n^{*2}}+2\omega_n^{*2}-1}{2}\right]\times\left[\Omega^{*2}-\frac{-\sqrt{1-4\omega_n^{*2}}+2\omega_n^{*2}-1}{2}\right]=0, \quad (27)$$

which facilitates analytical solutions for Ω^*:

Downloaded 03 May 2010 to 171.66.16.247. Redistribution subject to ASME license or copyright; see http://www.asme.org/terms/Terms_Use.cfm

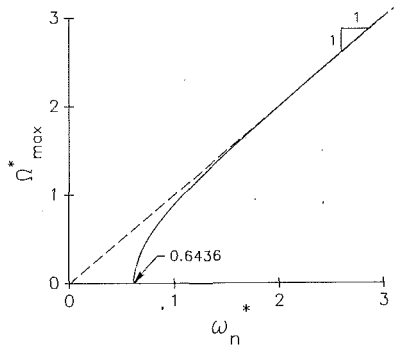


Fig. 4 The relationship between the resonance frequency (Ω^*_{max}) and the modal frequency (ω_n^*).

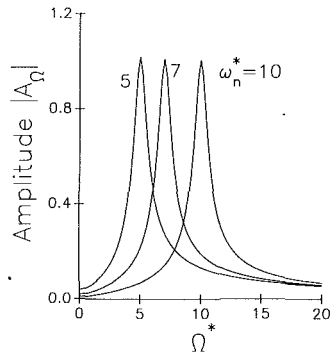


Fig. 6 Amplitudes of temperature waves ($|A_\Omega|$) varying with the applied frequency (Ω^*). ω_n^* = 5, 7, and 10.

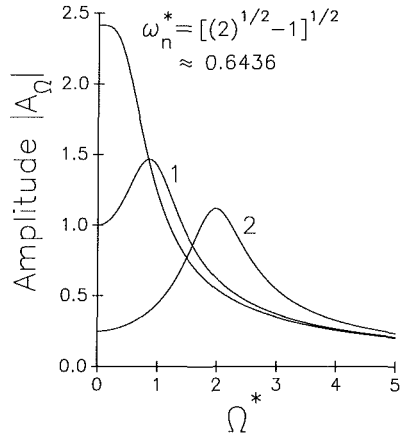


Fig. 5 Amplitudes of temperature waves ($|A_\Omega|$) varying with the applied frequency (Ω^*). ω_n^* = 0.6436, 1 and 2.

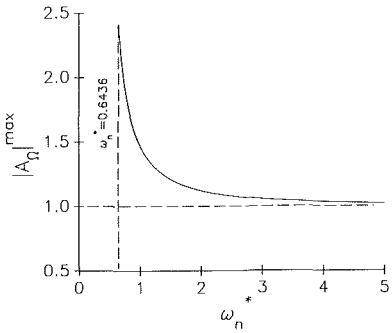


Fig. 7 Asymptotic behavior of the maximum amplitude ($|A_\Omega|^{max}$) in the high-frequency domain

$$\Omega^* = \pm\sqrt{\omega_n^*\sqrt{\omega_n^{*2}+2}-1}, \quad \Omega^* = \pm i\sqrt{\omega_n^*\sqrt{\omega_n^{*2}+2}-1}, \tag{28}$$

$$\Omega^* = \pm\sqrt{(\sqrt{1-4\omega_n^{*2}}+2\omega_n^{*2}-1)/2},$$

$$\Omega^* = \pm\sqrt{(-\sqrt{1-4\omega_n^{*2}}+2\omega_n^{*2}-1)/2}. \tag{29}$$

Physical considerations are needed to remove the auxiliary roots. The frequency of the applied heat source Ω^* and the modal frequency ω_n^*, first of all, must be real. For the first Ω^* shown in (29), this requires

$$\omega_n^* < \frac{1}{2} \tag{30}$$

for the inner square root and

$$\sqrt{1-4\omega_n^{*2}}+2\omega_n^{*2}-1>0 \tag{31}$$

for the outer square root. Combination of (30) and (31), however, requires $4\omega_n^{*4} < 0$ which is not possible for ω_n^* being real. Similarly, the second possibility in (30) requires

$$2\omega_n^{*2}-1>\sqrt{1-4\omega_n^{*2}} \tag{32}$$

Under the same constraint of (30), $2\omega_n^{*2}-1$ on the left-hand side is negative and Eq. (32) is not possible for real values of ω_n^*. The two roots of Ω^* shown in (29) are therefore dropped.

Turning to the first Ω^* in Eq. (28), a real value requires that

$$\omega_n^*\sqrt{\omega_n^{*2}+2}-1>0 \tag{33}$$

which is equivalent to

$$\omega_n^* > \sqrt{\sqrt{2}-1} \approx 0.6436. \tag{34}$$

Refer to Eqs. (13) and (14), ω_n^* in this range renders an underdamped wave behavior. By taking the positive root for frequency, then, we conclude that

$$\Omega^*_{max} = \sqrt{\omega_n^*\sqrt{\omega_n^{*2}+2}-1} \tag{35}$$

is the resonance frequency at which the amplitude of the temperature wave amplifies and reaches a maximum. The modal frequency ω_n^*, however, must satisfy the constraint in Eq. (34). In order for the thermal resonance to occur, clearly, the excited wave mode must have a modal frequency greater than 0.6436 *f*. The thermal resonance is thus a *high-mode* phenomenon. It only occurs for underdamped wave modes with higher frequencies.

The second possibility in (28) also allows real roots for Ω^* under certain conditions. For example, $\Omega^* = [1 - \omega_n^*(\omega_n^{*2} + 2)^{1/2}]^{1/2}$ for $0 < \omega_n^* < 0.6436$. As evident by $\Omega^* = 1$ for $\omega_n^* = 0$, however, some values of Ω^* in this domain are larger than those of ω_n^* which violates the general feature in damped oscillations (Meirovitch, 1967). Besides, no asymptotic behavior for Ω^* exists when the wave behavior dominates over the diffusion behavior. The second root in (28) is thus excluded.

Based on these observations, it is concluded that only the root shown by Eq. (35) is physically acceptable. Figure 4 shows the variation of Ω^* versus ω_n^* under the constraint of $\omega_n^* > 0.6436$. The value of Ω^* is always smaller than that of ω_n^*. In the high-frequency domain with ω_n^* being large, the value of Ω^* asymptotically approaches that of ω_n^*. This important feature becomes explicit if Eq. (35) is rearranged in the following form:

$$(\omega_n^* + \Omega^*_{max})(\omega_n^* - \Omega^*_{max})(\omega_n^{*2} + \Omega^{*2}_{max} + 2) = 1. \tag{36}$$

Downloaded 03 May 2010 to 171.66.16.247. Redistribution subject to ASME license or copyright; see http://www.asme.org/terms/Terms_Use.cfm

For both ω_n^* and $\Omega_{\max}^*$ being positive, $\omega_n^* = \Omega_{\max}^*$ is the asymptote when ω_n^* approaches infinity. By substituting Eq. (35) into (26), the exaggerated amplitude of temperature wave is obtained:

$$|A_\Omega|^{\max} = \frac{\sqrt{2\omega_n^*(\omega_n^{*2}+2)\sqrt{\omega_n^{*2}+2} - (2\omega_n^{*4}+5\omega_n^{*2}+2)}}{2\omega_n^*(\omega_n^{*2}+2) - (2\omega_n^{*2}+1)\sqrt{\omega_n^{*2}+2}}. \quad (37)$$

For $\omega_n^* = 0.6436$, 1, and 2, Fig. 5 shows the amplitude function, $|A_\Omega|$, in response to the frequency excitations. For the temperature wave with a modal frequency ω_n^*, the peak value is depicted by Eq. (37). The value of the resonance frequency (Ω^* at which the amplitude possesses a maximum) approaches the modal frequency for $\omega_n^* \simeq 2$ and thereafter. This situation becomes more clear in Fig. 6 where results for $\omega_n^* = 5$, 7, and 10 are presented. The maximum amplitude of the temperature wave seems to approach a constant value when ω_n^* increases. Such an asymptotic behavior is displayed in Fig. 7 where Eq. (37) is used. The value of $|A_\Omega|^{\max}$ approaches one (1) when the modal frequency ω_n exceeds $5f(\omega_n^* > 5)$. For producing the temperature resonance, it is desirable that the resonance frequency be low while the resonance amplitude be as high as possible. From Fig. 7, it seems not necessary to excite the high-frequency modes since no more pronounced amplitude results in the high-frequency domain.

The Thermal Wave Speed

The resonance frequency of thermal waves is explicitly related to the thermal wave speed. By using (22) for ω_n^*, Eq. (35) becomes

$$\Omega_{\max}^* = \sqrt{\frac{n\pi}{C^*}\sqrt{\left(\frac{n\pi}{C^*}\right)^2 + 2} - 1} \quad \text{with} \quad C^* = \frac{C}{\alpha/L}. \quad (38)$$

Solving C^* explicitly, then,

$$C^* = \frac{n\pi}{\sqrt{-1+\sqrt{1+(\Omega_{\max}^{*2}+1)^2}}} \quad \text{for} \quad n > 0.6436\frac{R}{\pi}. \quad (39)$$

In correspondence with the critical mode number for the activation of underdamped waves, Eq. (17), the critical mode number n in (39) governs the occurrence of thermal resonance. It results from the constraint of (34). Based on a selected mode under excitations, the resonance frequency can thus be used in (39) to determine the dimensionless thermal wave speed C^*. Since the thermal diffusivity α for engineering materials is well tabulated, the thermal wave speed is then calculated by $C = C^*\alpha/L$.

Conclusion

From an analytical point of view, the resonance phenomenon of thermal waves has been proven in this work. The excitable modes are in the high-frequency domain and the thermal resonance is indeed a high-mode phenomenon. The underdamped wave activates when the mode number (n) exceeds $0.5\ R/\pi$. The wave modes become excitable to resonate, however, only when the mode number exceeds $0.6436\ R/\pi$. The quantity R is the ratio between the length of the rod and the relaxation distance $C\tau$. It governs the transition of temperature waves from an overdamped to an underdamped behavior. The difference between the critical mode numbers, $0.5\ R/\pi$ and $0.6436\ R/\pi$, results from the apparent heat source in Eq. (18). It is induced by the finite speed of heat propagation in solids. The wave modes with a modal number between these two critical values, though underdamped, cannot be excited to resonate due to strong effects of damping from thermal diffusion. The damping rate (refer to Eqs. (13) to (16)) is governed by the time lag between the heat flux vector and the temperature gradient. Due to the exponential factor of $\exp(-t/2\tau)$ in the amplitude functions, the stage of critical damping does not exist in oscillations of thermal waves.

The thermal wave speed is the central quantity in the wave theory. At this point, unfortunately, a rigorous table for engineering materials is not available. For geological materials carrying the thermal energy with a relatively low speed, such as sand considered by Kaminski (1990), the thermal wave speed can be measured by traditional thermocouples. The values of 0.143 mm/s for the thermal wave speed (C) and 20 s for the relaxation time (τ) were recorded for sand. Based on these values and assuming 1 m for the length (L) of the sand specimen, the underdamped wave behavior activates from the 56th mode while it becomes excitable (to resonate) from the 72nd mode and thereafter. The resonance frequency for the 72nd mode is approximately 0.07781 hertz which is sufficiently low to be produced by mechanical means. For this type of medium, due to relatively low speed of heat propagation, thermocouples can be used to detect arrival of thermal signals. For multicrystalline materials such as 4340 steel, however, the thermal wave speed is on the order of 10^3 m/s. The thermocouples may not be sufficiently fast to respond when the wavefront passes by. For this type of material, the frequency approach proposed in this work may be feasible to determine the thermal wave speed. Some technical difficulties, however, may exist due to the required excitations oscillating in the high-frequency domain. For 4340 steel with C being approximately 900 m/s, for example, an external heat source oscillating at a frequency of mega- to giga-hertz may be needed to drive the temperature wave to resonate. Microwaves, infrared irradiations, or even optical means may be necessary for reaching such a high frequency. Feasibility of the frequency approach, as a result, needs an experimental support in the future.

Acknowledgment

This work is accomplished in the course of research supported by the National Science Foundation under grant No. CTS-8922494 with the University of New Mexico.

References

Achenbach, J. D., 1968, "The Influence of Heat Conduction on Propagating Stress Jumps," *Journal of the Mechanics and Physics of Solids*, Vol. 16, pp. 273–282.

Baumeister, K. J., and Hamill, T. D., 1969, "Hyperbolic Heat Conduction Equation: A Solution for the Semi-Infinite Body Problem," ASME *Journal of Heat Transfer*, Vol. 91, pp. 543–548.

Chester, M., 1963, "Second Sound in Solids," *Physical Review*, Vol. 131, pp. 2013–2015.

Frankel, J. I., Vick, B., and Özisik, M. N., 1985, "Flux Formulation of Hyperbolic Heat Conduction," *Journal of Applied Physics*, Vol. 58, pp. 3340–3345.

Frankel, J. I., Vick, B., and Özisik, M. N., 1987, "General Formulation and Analysis of Hyperbolic Heat Conduction in Composite Media," *International Journal of Heat and Mass Transfer*, Vol. 3, pp. 467–477.

Kaminski, W., 1990, "Hyperbolic Heat Conduction Equation for Materials with a Nonhomogeneous Inner Structure," ASME *Journal of Heat Transfer*, Vol. 112, pp. 555–560.

Lord, H. W., and Shulman, Y., 1967, "A Generalized Dynamic Theory of Thermoelasticity," *Journal of the Mechanics and Physics of Solids*, Vol. 15, pp. 299–309.

Meirovitch, L., 1967, *Analytical Methods in Vibrations*, Macmillian, New York, Chapters 1 and 9.

Özisik, M. N., and Vick, B., 1984, "Propagation and Reflection of Thermal Waves in a Finite Medium," *International Journal of Heat and Mass Transfer*, Vol. 27, pp. 1845–1854.

Popov, E. B., 1967, "Dynamic Coupled Problem of Thermoelasticity for a Half-Space Taking Into Account of the Finiteness of the Heat Propagation Velocity," *Journal of Applied Mathematics and Mechanics* (PMM), Vol. 31, pp. 349–356.

Tzou, D. Y., 1989a, "On the Thermal Shock Wave Induced by a Moving Heat Source," ASME *Journal of Heat Transfer*, Vol. 111, pp. 232–238.

Tzou, D. Y., 1989b, "Shock Wave Formation Around a Moving Heat Source in a Solid with Finite Speed of Heat Propagation," *International Journal of Heat and Mass Transfer*, Vol. 32, pp. 1979–1987.

Downloaded 03 May 2010 to 171.66.16.247. Redistribution subject to ASME license or copyright; see http://www.asme.org/terms/Terms_Use.cfm

Tzou, D. Y., 1989c, "The Effects of Thermal Shock Waves on the Crack Initiation Around a Moving Heat Source," *Journal of Engineering Fracture Mechanics*, Vol. 34, pp. 1109–1118.

Tzou, D. Y., 1990a, "Thermal Shock Waves Induced by a Moving Crack," ASME *Journal of Heat Transfer*, Vol. 112, pp.21–27.

Tzou, D. Y., 1990b, "Thermal Shock Wave Induced by a Moving Crack A Heat Flux Formulation," *International Journal of Heat and Mass Transfer*, Vol. 33, pp. 877–885.

Tzou, D. Y., 1990c, "Three Dimensional Structures of the Thermal Shock Waves Around a Rapidly Moving Heat Source," *International Journal of Engineering Science*, Vol. 28, pp. 1003–1017.

Tzou, D. Y., 1991a, "Thermal Shock Phenomena under High Rate Response in Solids," *Annual Review of Heat Transfer*, Vol. IV, Chang-Lin Tien, ed., Hemisphere, Washington, DC, Chapter 3.

Tzou, D. Y., 1991b, "A Universal Model for the Overall Thermal Conductivity of Porous Media," *Journal of Composite Materials*, Vol. 25, pp. 1064–1084.

Tzou, D. Y., 1991c, "The Singular Behavior of the Temperature Gradient in the Vicinity of a Macrocrack Tip," *International Journal of Heat and Mass Transfer*, Vol. 33, pp. 2625–2630.

Vick, B., and Ozisik, M. N., 1983, "Growth and Decay of a Thermal Pulse Predicted by the Hyperbolic Heat Conduction Equation," ASME *Journal of Heat Transfer*, Vol. 105, pp. 902–907.

Weymann, H. D., 1967, "Finite Speed of Heat Propagation in Conduction, Diffusion, and Viscous Shear Motion," *American Journal of Physics*, Vol. 35, pp. 488–496.

Zehnder, A. T., and Rosakis, A. J., 1991, "On the Temperature Distribution at the Vicinity of Dynamically Propagating Cracks in 4340 Steel," *Journal of the Mechanics and Physics of Solids*, Vol. 39, pp. 385–415.

Downloaded 03 May 2010 to 171.66.16.247. Redistribution subject to ASME license or copyright; see http://www.asme.org/terms/Terms_Use.cfm

Three-Dimensional Solutions for the Free Vibrations and Buckling of Thermally Stressed Multilayered Angle-Ply Composite Plates

Ahmed K. Noor
Professor,
Fellow ASME.

W. Scott Burton
Research Scientist,
Assoc. Mem. ASME.

Center for Computational Structures Technology,
University of Virginia,
NASA Langley Research Center,
Hampton, VA 23681

Analytic three-dimensional elasticity solutions are presented for the free vibration and buckling of thermally stressed, multilayered, angle-ply composite plates. Sensitivity derivatives are also evaluated and used to study the sensitivity of the vibration and buckling responses to variations in the different lamination and material parameters of the plate. The plates are assumed to have rectangular geometry and an antisymmetric lamination with respect to the middle plane. The temperature is assumed to be independent of the surface coordinates, but has an arbitrary symmetric variation through the thickness of the plate. A linear, Duhamel-Neumann type constitutive model is used, and the material properties are assumed to be independent of temperature. The thermal plate response is subjected to time-varying perturbation displacements, strains, and stresses. A mixed formulation is used with the fundamental unknowns consisting of the six perturbation stress components and the three perturbation displacement components of the plate. The initial thermal deformations are accounted for. Each of the plate variables is decomposed into symmetric and antisymmetric components in the thickness direction, and is expressed in terms of a double Fourier series in the Cartesian surface coordinates. Numerical results are presented showing the effects of variations in material characteristics and fiber orientation of different layers, as well as the effects of initial thermal deformations on the vibrational and buckling responses of the plate, as well as their sensitivity derivatives.

1 Introduction

Although analytic three-dimensional elasticity solutions have been presented for the isothermal stress, free vibration, and buckling problems of laminated plates (see, for example, Pagano (1970), Pagano and Hatfield (1972), Srinivas and Rao (1970), Srinivas (1973), and Noor and Burton (1990)), no three-dimensional solutions exist for the free vibrations of thermally stressed plates. Only one publication exists in which analytic three-dimensional solutions are presented for the thermal buckling of angle-ply composite plates (Noor and Burton, 1992). To the authors' knowledge, all the thermal buckling and vibration studies of composite plates presented in the literature, other than the cited reference of Noor and Burton (1992), are based on two-dimensional laminated plate theories (see, for example, Stavsky (1975), Tauchert (1987), Tauchert and Huang (1987), Chen and Chen (1987), Thangaratnam, Palaninathan, and Ramachandran (1989), Chen and Chen (1989a, 1989b), and Sun and Hsu (1990)). Because of the increasing use of fibrous composites in flight-vehicle structures subjected to high temperatures it is desirable to provide a capability for the accurate prediction of the free vibration and buckling responses of thermally stressed multilayered composite plates, as well as the sensitivity of the responses to variations in the material and lamination parameters.

This paper presents analytic three-dimensional elasticity solutions for the free vibration and buckling of thermally stressed, rectangular multilayered, angle-ply anisotropic plates. Sensitivity derivatives are also evaluated and used to study the sensitivity of the free vibration and thermal buckling responses to variations in different lamination and material parameters of the plate. The temperature change, causing the initial heating, is assumed to be independent of the surface coordinates (but can have arbitrary symmetric variation in the thickness direction). The plates consist of a number of perfectly bonded layers which have antisymmetric lamination with respect to the middle plane. The solutions are periodic in the surface coordinates x_1 and x_2. Numerical results are presented showing the sensitivity of the vibrational and buckling responses to: (a) variations in the material characteristics and fiber orientation of individual layers; (b) temperature change; and (c) initial thermal deformation.

Contributed by the Applied Mechanics Division of THE AMERICAN SOCIETY OF MECHANICAL ENGINEERS for publication in the ASME JOURNAL OF APPLIED MECHANICS.

Discussion on this paper should be addressed to the Technical Editor, Prof. Leon M. Keer, The Technological Institute, Northwestern University, Evanston, IL 60208, and will be accepted until four months after final publication of the paper itself in the JOURNAL OF APPLIED MECHANICS.

Manuscript received by the ASME Applied Mechanics Division, Jan. 16, 1991; final revision, June 26, 1991. Associate Technical Editor: L. M. Keer.

Copyright © 1992 by ASME
Downloaded 03 May 2010 to 171.66.16.247. Redistribution subject to ASME license or copyright; see http://www.asme.org/terms/Terms_Use.cfm

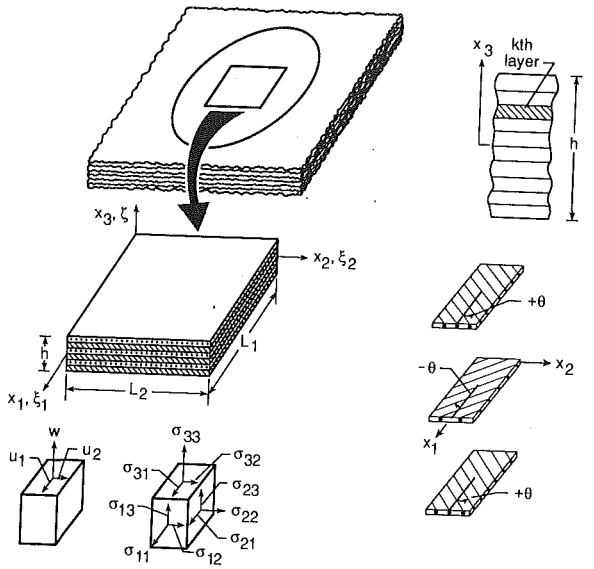


Fig. 1 Laminated anisotropic plates and sign convention for stresses and displacements

2 Mathematical Formulation

Figure 1 shows the geometric characteristics of the plate segment considered herein, henceforth referred to as the plate, as follows: L_1 and L_2 are the side lengths in the x_1 and x_2 directions, and h is the total thickness of the plate. The dimensionless coordinates ξ_1, ξ_2 and ζ are introduced where

$$\xi_\beta = \frac{x_\beta}{L_\beta} \quad (\beta = 1, 2 \text{ and } \beta \text{ is not summed}) \tag{1}$$

$$\zeta = \frac{x_3}{h} \quad -0.5 \le \zeta \le 0.5. \tag{2}$$

The analytical formulation is based on the three-dimensional theory of anisotropic thermoelasticity (see Padovan, 1986). The temperature is assumed to be independent of x_1, x_2, i.e.,

$$T = f(\zeta) T^o \tag{3}$$

where $f(\zeta)$ is a normalized (dimensionless) even function of ζ and T^o is a temperature parameter.

The individual layers are assumed to be homogeneous, anisotropic, and are antisymmetrically laminated with respect to the middle plane of the plate. At each point a plane of thermoelastic symmetry exists parallel to the middle plane.

2.1 Initial and Perturbation Stresses and Deformations. A Lagrangian description of the deformation, which accounts for the large displacements and rotations, is used. The fundamental equations are expressed in terms of the second Piola-Kirchhoff stress tensor and the Green-Lagrange strain tensor. A linear thermoelastic, Duhamel-Neumann type, constitutive model is used and the material properties are assumed to be independent of temperature. A summary of the fundamental equations used in the present study is given in Appendix A. The sign convention for the different displacement and stress components is shown in Fig. 1.

The thermal displacements, strains, and stresses generated by the temperature distribution, Eq. (3), are chosen to be independent of x_1 and x_2 and can be written in the following form:

$$u_\beta^o = 0 \tag{4}$$

$$w^o = w^o(\zeta) \tag{5}$$

$$\epsilon_{\beta\gamma}^o = \epsilon_{\beta 3}^o = 0 \tag{6}$$

$$\epsilon_{33}^o = \epsilon_{33}^o(\zeta) \tag{7}$$

$$\sigma_{\beta\gamma}^o = \sigma_{\beta\gamma}^o(\zeta) \tag{8}$$

$$\sigma_{i3}^o = 0 \tag{9}$$

where superscript o refers to initial (thermally stressed) state; $w^o(\zeta)$ is an odd function of ζ; β, γ = 1, 2; and i = 1 to 3.

The thermal displacements, strains, and stresses given by Eqs. (4) to (9) satisfy all the fundamental equations of the three-dimensional nonlinear theory of thermoelasticity within each layer; the equilibrium and continuity conditions at the interfaces between layers; as well as the stress-free boundary conditions at the top and bottom surfaces of the plate (see Appendix A). All the initial (nonzero) strains and stresses are linear functions of T^o. The displacement component w^o and stress components $\sigma_{\beta\gamma}^o$ are obtained from the stress-displacement relations and the continuity conditions at layer interfaces (see Appendix A). Note that Eqs. (4) to (9) are the three-dimensional counterpart of the two-dimensional initial (thermal prebuckling) state described in Tauchert (1987).

The plate response is subjected to time-varying incremental displacements of the form:

$$u_\beta = u_\beta^o + \epsilon v_\beta \tag{10}$$

$$w = w^o + \epsilon \omega \tag{11}$$

where v_β and ω are perturbation displacements and ϵ is an infinitesimal. The resulting strains and stresses have the following form (see Appendix A):

$$\epsilon_{ij} = \epsilon_{ij}^o + \epsilon \eta_{ij} + \epsilon^2 \psi_{ij} \tag{12}$$

$$\sigma_{ij} = \sigma_{ij}^o + \epsilon \tau_{ij} + \epsilon^2 t_{ij} \tag{13}$$

where

$$\epsilon_{\beta\gamma}^o = \epsilon_{\beta 3}^o = 0 \tag{14}$$

$$\epsilon_{33}^o = \partial_3 w^o + \frac{1}{2}(\partial_3 w^o)^2 \tag{15}$$

$$\eta_{\beta\gamma} = \frac{1}{2}(\partial_\beta v_\gamma + \partial_\gamma v_\beta) \tag{16}$$

$$\eta_{\beta 3} = \frac{1}{2}\left[\partial_3 v_\beta + \left(1 + \partial_3 w^o\right) \partial_\beta \omega \right] \tag{17}$$

$$\eta_{33} = (1 + \partial_3 w^o)\partial_3 \omega \tag{18}$$

$$\psi_{\beta\gamma} = \frac{1}{2}\left(\partial_\beta v_\rho \partial_\gamma v_\rho + \partial_\beta \omega \; \partial_\gamma \omega\right) \tag{19}$$

$\partial_\beta \equiv \dfrac{\partial}{\partial x_\beta}$, $\partial_3 = \dfrac{\partial}{\partial x_3}$; i, j = 1 to 3; β, γ, ρ = 1, 2; the repeated index ρ in Eq. (19) denotes summation over the range 1, 2. Note that the expressions for $\psi_{\beta 3}$, ψ_{33} are not given since they are not needed in the present study. The same applies to the stress components t_{ij}. The strain and stress components, η_{ij} and τ_{ij}, will henceforth be referred to as the perturbation strains and stresses.

2.2 Displacement and Stress Expansions. The incremental (perturbation) displacements, strains, and stresses are assumed to be harmonic in time. Each of the perturbation variables is decomposed into symmetric and antisymmetric components in the thickness direction and is expressed as the sum of products of trigonometric functions in the Cartesian surface coordinates. The trigonometric functions are chosen such that the displacements and stresses are periodic in x_1 and x_2 with periods $2L_1$ and $2L_2$.

The following expressions are used for the displacement and stress components:

Downloaded 03 May 2010 to 171.66.16.247. Redistribution subject to ASME license or copyright; see http://www.asme.org/terms/Terms_Use.cfm

$$\begin{Bmatrix} v_1 \\ v_2 \\ \omega \end{Bmatrix} = \left(\begin{Bmatrix} \hat{v}_{1_{mn}} \sin m\pi\xi_1 \cos n\pi\xi_2 \\ \hat{v}_{2_{mn}} \cos m\pi\xi_1 \sin n\pi\xi_2 \\ \hat{\omega}_{mn} \sin m\pi\xi_1 \sin n\pi\xi_2 \end{Bmatrix} + \begin{Bmatrix} \tilde{v}_{1_{mn}} \cos m\pi\xi_1 \sin n\pi\xi_2 \\ \tilde{v}_{2_{mn}} \sin m\pi\xi_1 \cos n\pi\xi_2 \\ \tilde{\omega}_{mn} \cos m\pi\xi_1 \cos n\pi\xi_2 \end{Bmatrix} \right) e^{i\Omega t} \quad (20)$$

$$\begin{Bmatrix} \tau_{11} \\ \tau_{22} \\ \tau_{33} \end{Bmatrix} = \left(\begin{Bmatrix} \hat{\tau}_{11_{mn}} \\ \hat{\tau}_{22_{mn}} \\ \hat{\tau}_{33_{mn}} \end{Bmatrix} \cos m\pi\xi_1 \cos n\pi\xi_2 + \begin{Bmatrix} \tilde{\tau}_{11_{mn}} \\ \tilde{\tau}_{22_{mn}} \\ \tilde{\tau}_{33_{mn}} \end{Bmatrix} \sin m\pi\xi_1 \sin n\pi\xi_2 \right) e^{i\Omega t} \quad (21)$$

$$\begin{Bmatrix} \tau_{23} \\ \tau_{13} \\ \tau_{12} \end{Bmatrix} = \left(\begin{Bmatrix} \hat{\tau}_{23_{mn}} \sin m\pi\xi_1 \cos n\pi\xi_2 \\ \hat{\tau}_{13_{mn}} \cos m\pi\xi_1 \sin n\pi\xi_2 \\ \hat{\tau}_{12_{mn}} \sin m\pi\xi_1 \sin n\pi\xi_2 \end{Bmatrix} + \begin{Bmatrix} \tilde{\tau}_{23_{mn}} \cos m\pi\xi_1 \sin n\pi\xi_2 \\ \tilde{\tau}_{13_{mn}} \sin m\pi\xi_1 \cos n\pi\xi_2 \\ \tilde{\tau}_{12_{mn}} \cos m\pi\xi_1 \cos n\pi\xi_2 \end{Bmatrix} \right) e^{i\Omega t}. \quad (22)$$

In Eqs. (20), (21), and (22), Ω is the frequency of vibration of the plate, the caret (^) and tilde (~) refer to the symmetric and antisymmetric quantities, with respect to the middle plane. Each of these quantities is a function of the thickness coordinate ζ only. Note that the displacement and stress expressions, Eqs. (20), (21), and (22) are periodic in x_1 and x_2 with periods $2L_1$ and $2L_2$. The following displacement conditions are satisfied on the middle plane ($\zeta = 0$):

$$\text{At } x_1 = 0, L_1 : v_1 = \omega = 0 \quad (23)$$

$$\text{At } x_2 = 0, L_2 : v_2 = \omega = 0. \quad (24)$$

The displacement conditions, Eqs. (23) and (24), are satisfied when either m, n, or both are zero. For $m = n = 0$, only the $\tilde{\omega}$ term in the displacement expressions, Eqs. (20), survives. For $m = 1$, $n = 0$, $\hat{v}_1$, $\tilde{v}_2$ and $\tilde{\omega}$ survive, and for $m = 0$, $n = 1$, $\tilde{v}_1$, $\hat{v}_2$ and $\tilde{\omega}$ survive.

2.3 Governing Equations. A mixed formulation is used with the fundamental unknowns consisting of the symmetric and antisymmetric components of the displacements and stresses. The governing equations for the free vibrational response of the plate consist of:

- the constitutive relations (strain-stress relations, Eqs. (A26), Appendix A) with the strains expressed in terms of displacements, see Eqs. (16), (17), and (18); and
- the linearized equations of motion (Eqs. (A18), Appendix A).

For the purpose of simplifying the form of the equations, the material compliance matrix for each layer, $[a]$, is decomposed into the sum of orthotropic and anisotropic (nonorthotropic) parts, $[a_o]$ and $[a_1]$ (see Appendix A). Moreover, the stresses and displacements are each divided into two groups as follows:

$$\{H_1\}_{m,n} = \begin{Bmatrix} \tilde{\tau}_{11_{mn}} \\ \tilde{\tau}_{22_{mn}} \\ \tilde{\tau}_{33_{mn}} \\ \hat{\tau}_{23_{mn}} \\ \hat{\tau}_{13_{mn}} \\ \tilde{\tau}_{12_{mn}} \end{Bmatrix}; \quad \{H_2\}_{m,n} = \begin{Bmatrix} \hat{\tau}_{11_{mn}} \\ \hat{\tau}_{22_{mn}} \\ \hat{\tau}_{33_{mn}} \\ \tilde{\tau}_{23_{mn}} \\ \tilde{\tau}_{13_{mn}} \\ \hat{\tau}_{12_{mn}} \end{Bmatrix} \quad (25)$$

$$\{X_1\}_{m,n} = \begin{Bmatrix} \tilde{v}_{1_{mn}} \\ \tilde{v}_{2_{mn}} \\ \hat{\omega}_{mn} \end{Bmatrix}; \{X_2\}_{m,n} = \begin{Bmatrix} \hat{v}_{1_{mn}} \\ \hat{v}_{2_{mn}} \\ \tilde{\omega}_{mn} \end{Bmatrix}. \quad (26)$$

For each layer and each pair of harmonics, m and n, the governing equations can be partitioned into two coupled sets of equations associated with $\{H_1\}_{mn}, \{X_1\}_{mn}$ and $\{H_2\}_{mn}, \{X_2\}_{mn}$ as follows:

$$\left(\begin{bmatrix} -a_o & S_o + S_1 \\ S_o^t - S_1^t & 0 \end{bmatrix}_{m,n} + \lambda \begin{bmatrix} 0 & 0 \\ 0 & K_o \end{bmatrix}_{m,n} + \begin{bmatrix} 0 & L_o(w^o) \\ L_1^t(w^o) & 0 \end{bmatrix}_{m,n} - \rho\Omega_{m,n}^2 \begin{bmatrix} 0 & 0 \\ 0 & I \end{bmatrix} \right) \begin{Bmatrix} H_1 \\ X_1 \end{Bmatrix}_{m,n} + \left(\begin{bmatrix} -a_1 & 0 \\ 0 & 0 \end{bmatrix} + \lambda \begin{bmatrix} 0 & 0 \\ 0 & K_1 \end{bmatrix}_{m,n} \right) \begin{Bmatrix} H_2 \\ X_2 \end{Bmatrix}_{m,n} = 0 \quad (27)$$

and

$$\left(\begin{bmatrix} -a_o & -S_o + S_1 \\ -S_o^t - S_1^t & 0 \end{bmatrix}_{m,n} + \lambda \begin{bmatrix} 0 & 0 \\ 0 & K_o \end{bmatrix}_{m,n} + \begin{bmatrix} 0 & -L_o(w^o) \\ -L_1^t(w^o) & 0 \end{bmatrix}_{m,n} - \rho\Omega_{m,n}^2 \begin{bmatrix} 0 & 0 \\ 0 & I \end{bmatrix} \right) \begin{Bmatrix} H_2 \\ X_2 \end{Bmatrix}_{m,n} + \left(\begin{bmatrix} -a_1 & 0 \\ 0 & 0 \end{bmatrix} + \lambda \begin{bmatrix} 0 & 0 \\ 0 & K_1 \end{bmatrix}_{m,n} \right) \begin{Bmatrix} H_1 \\ X_1 \end{Bmatrix}_{m,n} = 0 \quad (28)$$

where λ is a temperature parameter; ρ is the mass density of the material of the plate; $[I]$ is the identity matrix; $[S_o]$ is a matrix of coefficients; $[S_1]$ is a matrix of linear first-order ordinary differential operators; $[K_o]$ and $[K_1]$ are matrices of initial stresses which are independent of the temperature parameter, λ; $[L_o(w^o)]$ and $[L_1(w^o)]$ are matrices of first-order ordinary differential operators, which are functions of the initial displacement w^o (nonlinear functions of the temperature parameter λ); and superscript t denotes matrix transposition. The explicit forms of the arrays appearing in Eqs. (27) and (28) are summarized in Appendix B.

The complete description of the free vibrational response of the plate requires: (a) the governing equations, Eqs. (27) and (28) for each layer; (b) the stress equilibrium and the displacement continuity conditions at layer interfaces; and (c) the conditions at the top and bottom surfaces of the plate.

The equilibrium and continuity conditions at the interfaces between the typical layers k and $k + 1$ (top of layer k and bottom of layer $k + 1$) can be written in the following form:

$$\tau_{i3}^{(k)} - \tau_{i3}^{(k+1)} = 0 \quad i = 1 \text{ to } 3 \quad (29)$$

$$v_\beta^{(k)} - v_\beta^{(k+1)} = 0 \quad \beta = 1,2 \quad (30)$$

and

$$\omega^{(k)} - \omega^{(k+1)} = 0 \quad (31)$$

where superscripts k and $k + 1$ refer to the layers k and $k + 1$. Equations (29), (30), and (31) imply perfect bonding between the different layers (i.e., no slip). The stress conditions at the top and bottom surfaces are:

Downloaded 03 May 2010 to 171.66.16.247. Redistribution subject to ASME license or copyright; see http://www.asme.org/terms/Terms_Use.cfm

$$\tau_{i3}=0 \quad i=1 \text{ to } 3. \tag{32}$$

Equations (29) to (32) can be replaced by two sets of equations of the same form; one relating the symmetric components (quantitities with a caret) and the other relating the antisymmetric components (quantities with a tilde).

The Fourier expansions for the displacements and stresses, Eqs. (20) to (22) provide an exact representation for the free vibration response of rectangular composite plates. Moreover, the governing equations uncouple in harmonics provided (see Noor and Burton, 1990): (a) the lamination is angle-ply antisymmetric with respect to the middle plane, cross-ply symmetric with respect to the middle plane, or a combination of the two (e.g., antisymmetric quasi-isotropic lamination); (b) the temperature is given by Eq. (3) and the initial displacements, strains, and stresses are given by Eqs. (4) to (9); and (c) the perturbation displacements, strains and stresses, Eqs. (10) to (13), are periodic in x_1 and x_2. Note that Eqs. (27) through (32) can be used to describe the thermal buckling response of the plate, provided:

- The initial stresses and deformations, Eqs. (4) through (9), represent the prebuckling state.
- The perturbation displacements, strains, and stresses associated with an adjacent configuration, correspond to the buckling mode.
- λ is considered to be the critical temperature parameter, $\lambda_{m,n}$, associated with the pair of harmonics m, n.
- $\Omega_{m,n}$ is set equal to zero.

2.4 Computational Procedure. The free vibration response of the plate is obtained by using the procedure described in Srinivas and Rao (1970) and Srinivas (1973). The procedure is based on solving the characteristic equation associated with Eqs. (27) and (28) for each layer, and each pair of Fourier harmonics (m, n); finding 12 roots and 12 eigenvectors, then solving a set of simultaneous equations representing the conditions at the top and bottom surfaces, and the conditions at the interfaces between the different layers, Eqs. (29) to (32).

2.5 Sensitivity of the Free Vibration and Thermal Buckling Responses to Variations in Lamination and Material Parameters. Sensitivity derivatives can be used to study the sensitivity of the free vibration and thermal buckling responses of the plate to variations in the different material and lamination parameters. Analytic sensitivity derivatives are obtained by differentiating the characteristic equation associated with Eqs. (27) and (28), for each layer and each pair of Fourier harmonics, as well as Eqs. (29) through (32) with respect to d_l, where d_l represents a material or lamination parameter of the plate. Note that both $\Omega_{m,n}$ and λ are functions of d_l, and the matrices $[S_o]$ and $[S_1]$ are not functions of d_l. For thermal buckling problems $\Omega_{m,n} = 0$.

3 Numerical Studies

To study the effects of variations in the material characteristics and fiber orientation of individual layers on the free vibration and buckling responses of thermally stressed plates, several free vibration and thermal buckling problems were solved. For each problem the derivatives of the various response quantities with respect to the different material and lamination parameters were evaluated. These studies can help in assessing the reliability of various two-dimensional theories for predicting the sensitivity of the free vibration and thermal buckling responses of multilayered composite plates to variations in their material and lamination parameters.

The composite plates considered in this study are square angle-ply laminates with $L_1 = L_2 = 1$. The plates have antisymmetric lamination with respect to the middle plane. The thermal buckling and vibrational responses are assumed to be periodic in x_1 and x_2 with periods $2L_1$ and $2L_2$. The material characteristics of the individual layers are taken to be those typical of high-modulus fibrous composites, namely:

$$E_L/E_T=15,\ G_{LT}/E_T=0.5,\ G_{TT}/E_T=0.3356,$$

$$\nu_{LT}=0.3,\ \nu_{TT}=0.49,\ \alpha_L/\alpha_o=0.015,\ \alpha_T/\alpha_o=1.0$$

where L refers to the direction of fibers and T refers to the transverse direction; ν_{LT} is the major Poisson's ratio; and α_o is a normalization factor for the coefficients of thermal expansion. The fiber orientation for the laminates is selected to be $[+\theta/-\theta/\ldots]$, respectively (starting from the top layer). The temperature is assumed to be uniform, i.e., $f(\zeta)$ in Eq. (3) is chosen to be 1. The composite plates considered cover a wide range of geometric and lamination parameters: thickness ratio, h/L_1, varying between 0.01 and 0.15; number of layers, NL, ranging from 2 to 20; and fiber orientation angle, θ, ranging from 0 to 45 deg. Only the lowest vibration frequencies, lowest critical temperatures and associated mode shapes and modal stresses, for the range $1 \le m, n \le 10$, are considered. Typical results are presented in Figs. 2 through 6, for the two cases of including and neglecting the initial thermal (prebuckling) displacement w^o.

The effect of variations in h/L_1, NL, and θ on the minimum vibration frequencies of thermally stressed plates is shown in Fig. 2. In all the problems considered the frequency of the thermally stressed plate, Ω, is related to that of the unheated plate ($T^o = 0$), Ω_o, by the simple approximate formula:

$$\left(\frac{\Omega}{\Omega_o}\right)^2 = 1-\frac{T^o}{T_{cr.}} \tag{33}$$

where T^o is the temperature rise and $T_{cr.}$ is the critical temperature (corresponding to $\Omega = 0$). A similar formula was discovered by Lurie in 1952, using classical plate theory, for isothermal problems of simply-supported, initially stressed polygonal plates, whose vibrational and buckling modes are identical. As seen from Fig. 2, the effect of w^o on Ω increases as T^o approaches $T_{cr.}$. This effect is amplified with the increase in h/L_1, NL, and θ.

The effects of variations in h/L_1 and θ on the derivatives of the critical temperature and vibration frequency, $\frac{\partial T_{cr}}{\partial d_l}$ and $\frac{\partial \Omega^2}{\partial d_l}$, with respect to the material properties $d_l = E_L$, E_T, G_{LT}, G_{TT}, ν_{LT}, ν_{TT}, α_L, α_T; and the fiber orientation angle, θ, for the case $T^o = 0.5\ T_{cr.}$ are shown in Figs. 3 and 4. An examination of Figs. 3 and 4 reveals:

1 The critical temperature, $T_{cr.}$, is very sensitive to variations in E_L, E_T and α_T. As h/L_1 increases, the sensitivity of $T_{cr.}$ to variations in G_{TT}, ν_{TT}, and G_{LT} increases.

2 The frequency of the thermally stressed plate, Ω, is very sensitive to variations in E_L. It is somewhat sensitive to variations in G_{TT} and G_{LT}, and is insensitive to variations in E_T, ν_{LT}, ν_{TT}, α_L, and α_T.

3 The thermal displacement w^o has a more pronounced effect on $\frac{\partial T_{cr.}}{\partial d_l}/T_{cr.}$ than on $\frac{\partial \Omega^2}{\partial d_l}/\Omega^2$ (compare Figs. 3 and 4). The effect of w^o is amplified with the increase in h/L_1 and θ (in the range $0 \le \theta \le 20$).

4 When w^o is included, the relative magnitudes of $\left|\frac{\partial T_{cr.}}{\partial d_l}\right|/T_{cr.}$ increase with increasing h/L_1, for $d_l = E_L$, E_T, G_{LT}, G_{TT}, ν_{LT}, ν_{TT}, and α_L. This trend is reversed for $d_l = \alpha_T$, as well as for $d_l = E_L$, when w^o is neglected.

5 The discontinuities in the plots for $\frac{\partial T_{cr.}}{\partial d_l}/T_{cr.}$ versus θ, in Fig. 3, occur at the values of θ associated with mode changes.

Downloaded 03 May 2010 to 171.66.16.247. Redistribution subject to ASME license or copyright; see http://www.asme.org/terms/Terms_Use.cfm

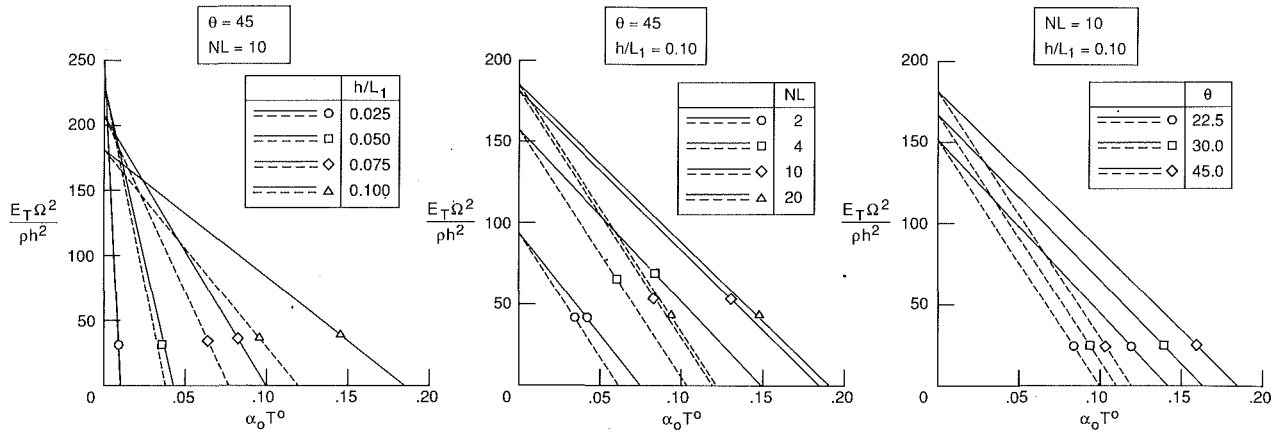


Fig. 2 Effect of lamination, geometric parameters, initial temperature, and thermal displacements on the minimum vibration frequencies of thermally stressed plates, obtained by the three-dimensional model. Angle-ply composite plates with $E_L/E_T = 15$, $G_{LT}/E_T = 0.5$, $G_{TT}/E_T = 0.3356$, $\nu_{LT} = 0.3$, $\nu_{TT} = 0.49$, $\alpha_L/\alpha_o = 0.015$, $\alpha_T/\alpha_o = 1.0$, $m = n = 1$. Solutions are periodic in x_1 and x_2 (see Eqs. (20), (21), and (22)). Full lines refer to the case of including w^o and dashed lines for neglecting w^o.

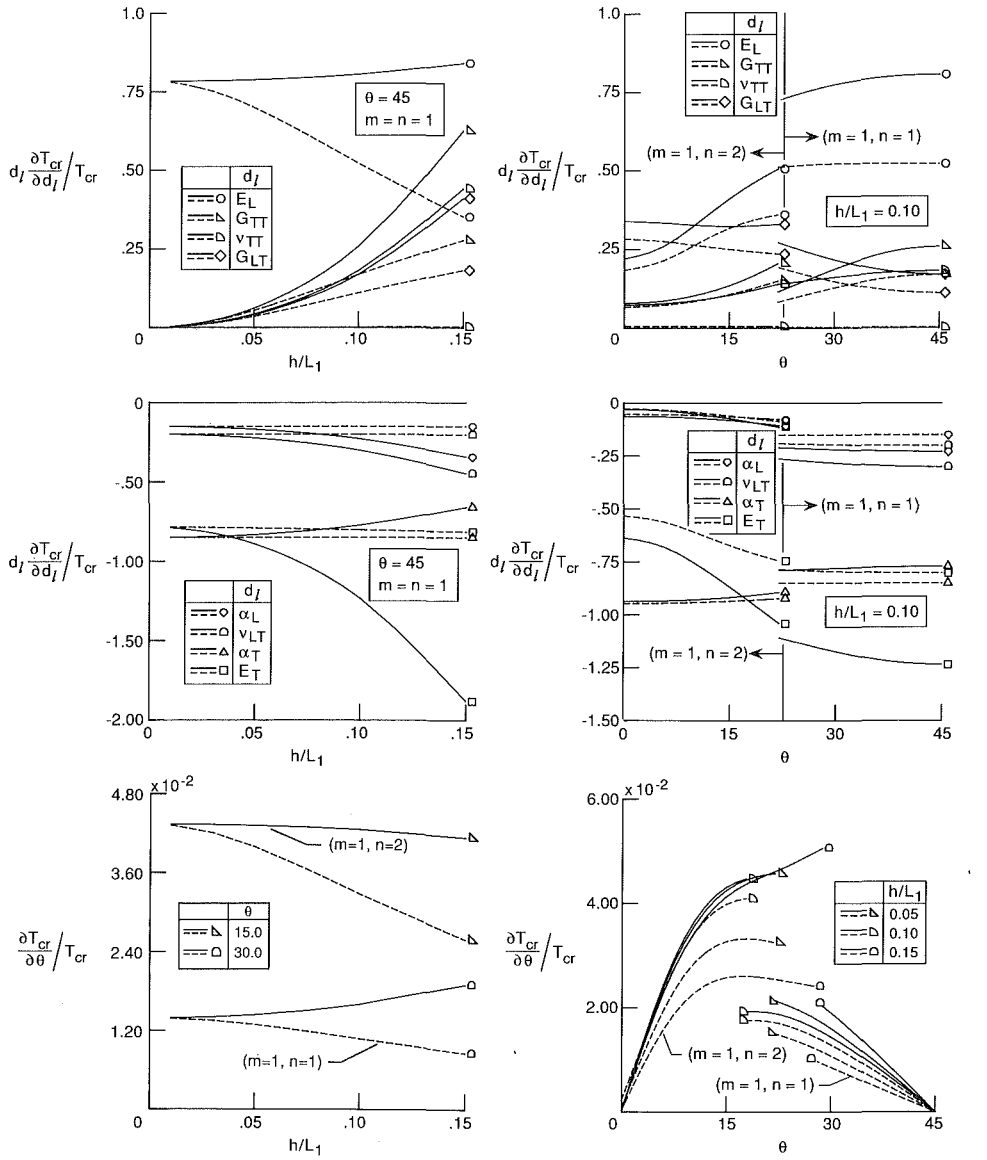


Fig. 3 Effect of lamination, geometric parameters, and prebuckling displacements on the sensitivity derivatives of the critical temperatures for laminated anisotropic plates obtained by the three-dimensional model. Ten-layered angle-ply composite plates with $E_L/E_T = 15$, $G_{LT}/E_T = 0.5$, $G_{TT}/E_T = 0.3356$, $\nu_{LT} = 0.3$, $\nu_{TT} = 0.49$, $\alpha_L/\alpha_o = 0.015$, $\alpha_T/\alpha_o = 1.0$. Solutions are periodic in x_1 and x_2 (see Eqs. (20), (21), and (22)). Full lines refer to the case of including w^o and dashed lines for neglecting w^o.

Downloaded 03 May 2010 to 171.66.16.247. Redistribution subject to ASME license or copyright; see http://www.asme.org/terms/Terms_Use.cfm

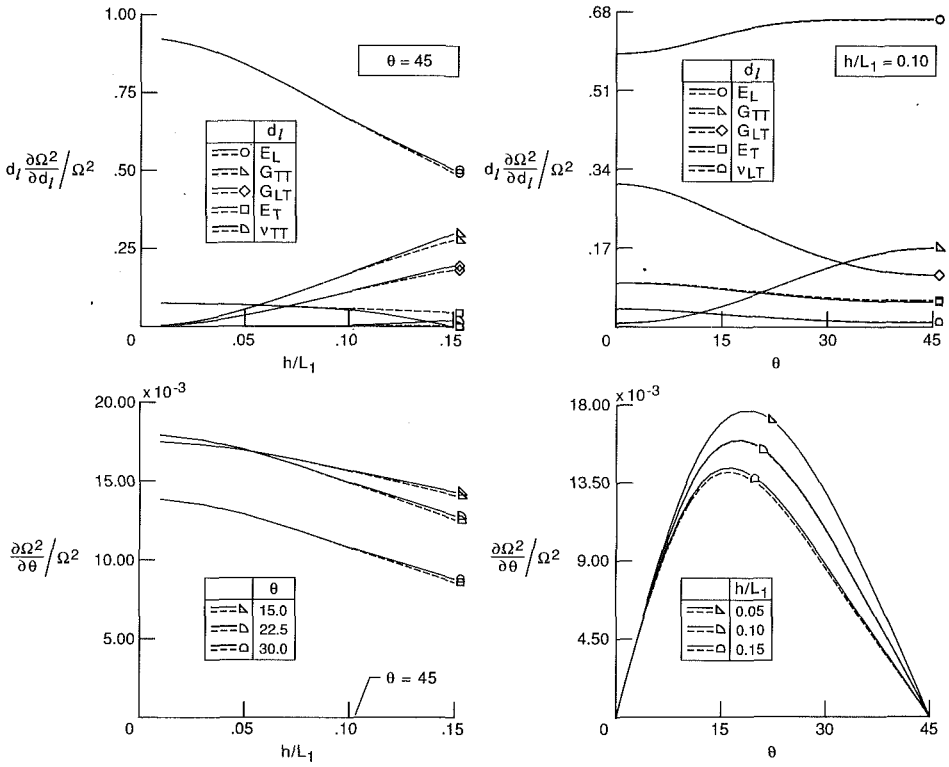


Fig. 4 Effect of lamination, geometric parameters, and initial displacements on the sensitivity derivatives of the minimum vibration frequencies for laminated anisotropic plates obtained by the three-dimensional model. Ten-layered angle-ply composite plates with $E_L/E_T = 15$, $G_{LT}/E_T = 0.5$, $G_{TT}/E_T = 0.3356$, $\nu_{LT} = 0.3$, $\nu_{TT} = 0.49$, $\alpha_L/\alpha_o = 0.015$, $\alpha_T/\alpha_o = 1.0$, $T^o/T_{cr.} = 0.5$, $m = n = 1$. Solutions are periodic in x_1 and x_2 (see Eqs. (20), (21), and (22)). Full lines refer to the case of including w^o and dashed lines for neglecting w^o.

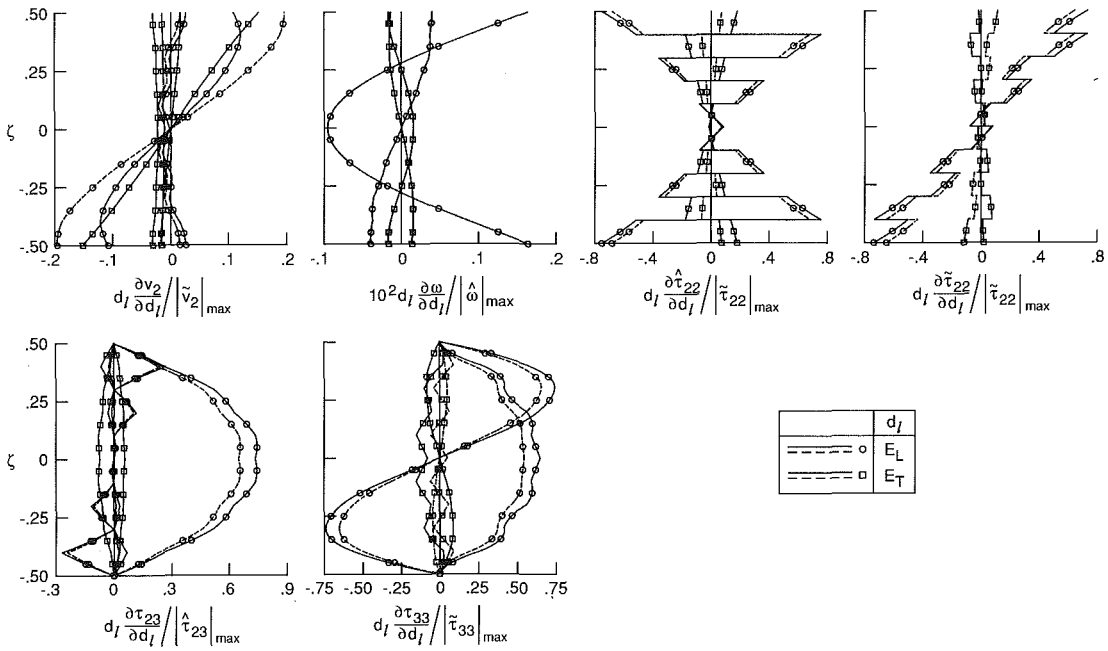


Fig. 5 Thickness distribution of the sensitivity derivatives of the modal displacements and stresses with respect to E_L and E_T, associated with the minimum vibration frequency. Ten-layered angle-ply composite plates with $E_L/E_T = 15$, $G_{LT}/E_T = 0.5$, $G_{TT}/E_T = 0.3356$, $\nu_{LT} = 0.3$, $\nu_{TT} = 0.49$, $\alpha_L/\alpha_o = 0.015$, $\alpha_T/\alpha_o = 1.0$, $T^o/T_{cr.} = 0.5$, $\theta = 45$, $h/L_1 = 0.1$. Solutions are periodic in x_1 and x_2 (see Eqs. (20), (21), and (22)). Full lines refer to the case of including w^o and dashed lines for neglecting w^o.

Downloaded 03 May 2010 to 171.66.16.247. Redistribution subject to ASME license or copyright; see http://www.asme.org/terms/Terms_Use.cfm

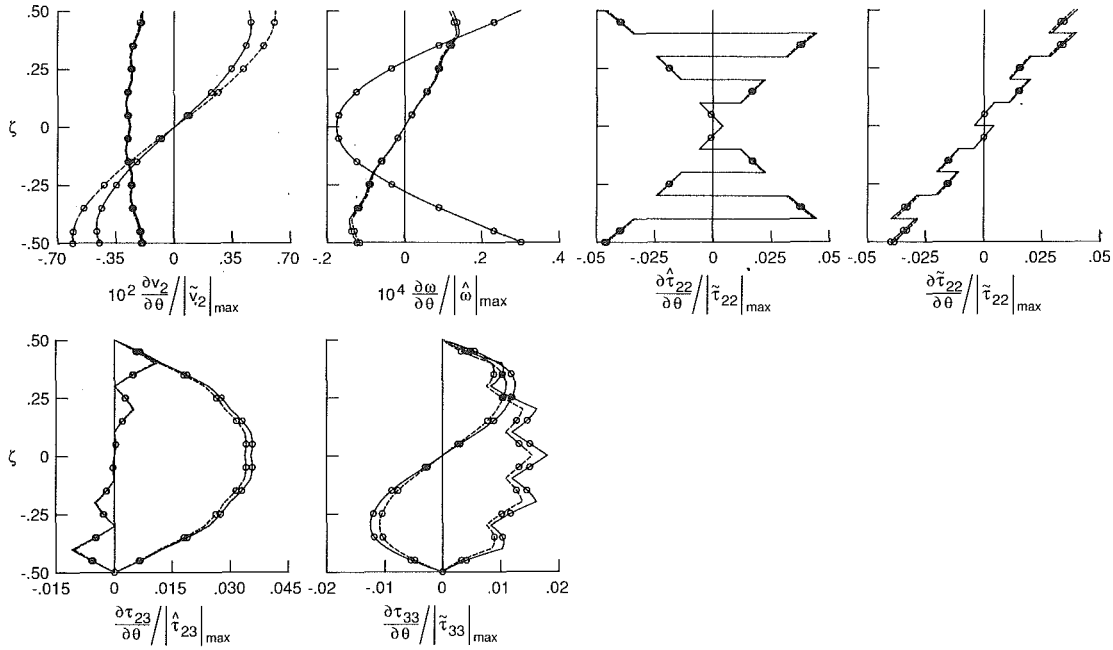


Fig. 6 Thickness distribution of the sensitivity derivatives with respect to θ of the modal displacements and stresses, associated with the minimum vibration frequency. Ten-layered angle-ply composite plates with $E_L/E_T = 15$, $G_{LT}/E_T = 0.5$, $G_{TT}/E_T = 0.3356$, $h/L_1 = 0.10$, $\nu_{LT} = 0.3$, $\nu_{TT} = 0.49$, $\alpha_L/\alpha_o = 0.015$, $\alpha_T/\alpha_o = 1.0$, $T^o/T_{cr.} = 0.5$, $\theta = 30$ deg, $h/L_1 = 0.1$. Solutions are periodic in x_1 and x_2 (see Eqs. (20), (21), and (22)). Full lines refer to the case of including w^o and dashed lines for neglecting w^o.

6 The changes in the relative values of $\frac{\partial T_{cr.}}{\partial d_t}/T_{cr.}$ depend on the values of the two parameters θ and h/L_1. For certain ranges of one parameter, $\frac{\partial T_{cr.}}{\partial \theta}/T_{cr.}$ increases with one or the other parameter (e.g., for $\theta = 30$, it increases with h/L_1), and for other ranges, the trend is reversed (e.g., for $\theta = 15$, it decreases with h/L_1).

7 The relative values of $\frac{\partial \Omega^2}{\partial E_L}/\Omega^2$ decrease with increasing h/L_1, and increase with increasing θ. An opposite trend is observed for $\frac{\partial \Omega^2}{\partial G_{LT}}/\Omega^2$. The relative values of $\frac{\partial \Omega^2}{\partial G_{TT}}/\Omega^2$ increase with the increase in both h/L_1 and θ.

8 The relative values of $\frac{\partial \Omega^2}{\partial \theta}/\Omega^2$ decrease with increasing h/L_1. They have zero values at $\theta = 0$ and $\theta = 45$.

The thickness distributions of sensitivity derivatives of the modal displacements and stresses associated with the minimum frequency, Ω with respect to E_L, E_T and θ, for the case $T^o = 0.5\, T_{cr.}$ are shown in Figs. 5 and 6. The derivatives with respect to E_L are considerably larger than those with respect to the other material parameters. This is particularly true for the stress derivatives. Note that the initial thermal displacement w^o has more pronounced effect on the derivatives of $\tilde{v}_2$, τ_{23}, and τ_{33} with respect to E_L and θ, than on the other displacement and stress derivatives.

4 Concluding Remarks

Analytic three-dimensional elasticity solutions are presented for the free vibrations and buckling of thermally stressed plates. Sensitivity derivatives are also evaluated and used to study the sensitivity of the vibrational and buckling responses to variations in different lamination and material parameters of the plate. The plates are assumed to have rectangular geometry and an antisymmetric lamination with respect to the middle plane. The temperature is assumed to be independent of the surface coordinates, but has an arbitrary symmetric variation through the thickness of the plate. A Lagrangian description of the deformation, which accounts for the large displacements and rotations, is used. The fundamental equations are expressed in terms of the second Piola-Kirchhoff stress tensor and the Green-Lagrange strain tensor. A linear, Duhamel-Neumann type, constitutive model is used and the material properties are assumed to be independent of temperature. The thermal response of the plate is subjected to time-varying perturbation displacements, strains, and stresses. A mixed formulation is used with the fundamental unknowns consisting of the six perturbation stress components and the three perturbation displacement components of the plate. The initial thermal deformations are accounted for. Each of the plate variables is decomposed into symmetric and antisymmetric components in the thickness direction, and is expressed in terms of a double Fourier series in the Cartesian surface coordinates. Numerical results are presented showing the effects of variations in the material characteristics and fiber orientation of different layers, as well as the effects of initial thermal deformations on the vibrational and buckling responses of the plate.

5 Acknowledgment

The present research is partially supported by NASA Cooperative Agreement NCCW-0011 and by an Air Force Office of Scientific Research Grant No. AFOSR-90-0369. The authors

Downloaded 03 May 2010 to 171.66.16.247. Redistribution subject to ASME license or copyright; see http://www.asme.org/terms/Terms_Use.cfm

appreciate the encouragement of Samuel L. Venneri of NASA Headquarters and Spencer Wu of AFOSR and acknowledge useful discussions with James H. Starnes, Jr. of NASA Langley.

References

Chen, L. W., and Chen, L. Y., 1987, "Thermal Buckling of Laminated Composite Plates," *Journal of Thermal Stresses*, Vol. 10, pp. 345–356.

Chen, L. W., and Chen, L. Y., 1989a, "Thermal Buckling Analysis of Composite Laminated Plates by the Finite Element Method," *Journal of Thermal Stresses*, Vol. 12, pp. 41–56.

Chen, L. W., and Chen, L. Y., 1989b, "Thermal Buckling Behavior of Laminated Composite Plates with Temperature-Dependent Properties," *Composite Structures*, Vol. 13, pp. 275–287.

Guz, A. N., 1971, *Stability of Three-Dimensional Deformable Bodies*, Naukova Dumka, Kiev (in Russian).

Hearmon, R. F. S., 1961, *An Introduction to Applied Anisotropic Elasticity*, Oxford University Press, London.

Lekhnitskii, S. G., 1981, *Theory of Elasticity of an Anisotropic Body*, Mir Publishers, Moscow.

Lurie, H., 1952, "Lateral Vibrations as Related to Structural Stability," ASME JOURNAL OF APPLIED MECHANICS, Vol. 19, No. 2, pp. 195–204.

Noor, A. K., and Burton, W. S., 1990, "Three-Dimensional Solutions for Antisymmetrically Laminated Anisotropic Plates," ASME JOURNAL OF APPLIED MECHANICS, Vol. 57, No. 1, pp. 182–188.

Noor, A. K., and Burton, W. S., 1992, "Three-Dimensional Solutions for Thermal Buckling of Multilayered Anisotropic Plates," *Journal of Engineering Mechanics*, Vol. 118, No. 4, April 1992, pp. 683–701.

Novozhilov, V. V., 1958, *Theory of Elasticity*, Sudpromgiz, Leningrad (translated into English and published by the Israel Program for Scientific Translations, 1961).

Padovan, J., 1986, "Anisotropic Thermal Stress Analysis, *Thermal Stresses 1*, R. B. Hetnarski, ed., Elsevier, Amsterdam, pp. 143–262.

Pagano, N. J., 1970, "Exact Solutions for Rectangular Bidirectional Composites and Sandwich Plates," *Journal of Composite Materials*, Vol. 4, pp. 20–34.

Pagano, N. J., and Hatfield, S. J., 1972, "Elastic Behavior of Multilayered Bidirectional Composites," *AIAA Journal*, Vol. 10, pp. 931–933.

Srinivas, S., and Rao, A. K., 1970, "Bending, Vibration and Buckling of Simply Supported Thick Orthotropic Rectangular Plates and Laminates," *Int. J. Solids Struct.*, Vol. 6, pp. 1464–1481.

Srinivas, S., 1973, "A Refined Analysis of Composite Laminates," *Journal of Sound and Vibration*, Vol. 30, pp. 495–507.

Stavsky, Y., 1975, "Thermoelastic Stability of Laminated Orthotropic Circular Plates," *Acta Mechanica*, Vol. 33, pp. 31–51.

Sun, L. X., and Hsu, T. R., 1990, "Thermal Buckling of Laminated Composite Plates with Transverse Shear Deformation," *Computers and Structures*, Vol. 36, No. 5, pp. 883–889.

Tauchert, T. R., 1987, "Thermal Buckling of Thick Antisymmetic Angle-Ply Laminates," *Journal of Thermal Stresses*, Vol. 10, pp. 113–124.

Tauchert, T. R., and Haung, N. N., 1987, "Thermal Buckling of Symmetric Angle-Ply Laminated Plates," *Composite Structures 4*, I. N. Marshall, ed., Proceedings of the Fourth International Conference on Composite Structures, Paisley, Elsevier, U.K., pp. 1.424–1.435.

Thangaratnam, R. K., Palaninathan, R., and Ramachandran, J., 1989, "Thermal Buckling of Composite Laminated Plates," *Computers and Structures*, Vol. 32, No. 5, pp. 1117–1124.

APPENDIX A

Fundamental Equations of the Nonlinear Three-Dimensional Theory of Thermoelasticity Used in the Present Study

The fundamental equations of the three-dimensional theory of thermoelasticity used in the present study are summarized in this Appendix (see Novozhilov, 1961; Guz, 1971; Padovan, 1986).

Strain-Displacement Relations. The strain-displacement relations can be separated into the linear and nonlinear parts and written in the following compact form:

$$\{\epsilon\} = [\bar{L}_o]\{u\} + [\bar{L}(\phi)]\{\phi\} \tag{A1}$$

where

$$\{\epsilon\}^t = [\epsilon_{11}\ \epsilon_{22}\ \epsilon_{33}\ 2\epsilon_{23}\ 2\epsilon_{13}\ 2\epsilon_{12}] \tag{A2}$$

$$\{u\}^t = [u_1\ u_2\ w] \tag{A3}$$

$$\{\phi\}^t = [\{\phi_1\}^t\{\phi_2\}^t\{\phi_3\}^t] \tag{A4}$$

$$\{\phi_1\}^t = [\partial_1 u_1\ \partial_1 u_2\ \partial_1 w] \tag{A5}$$

$$\{\phi_2\}^t = [\partial_2 u_1\ \partial_2 u_2\ \partial_2 w] \tag{A6}$$

$$\{\phi_3\}^t = [\partial_3 u_1\ \partial_3 u_2\ \partial_3 w] \tag{A7}$$

$$[\bar{L}_o] = \begin{bmatrix} \partial_1 & \cdot & \cdot \\ \cdot & \partial_2 & \cdot \\ \cdot & \cdot & \partial_3 \\ \cdot & \partial_3 & \partial_2 \\ \partial_3 & \cdot & \partial_1 \\ \partial_2 & \partial_1 & \cdot \end{bmatrix} \tag{A8}$$

$$[\bar{L}(\phi)] = \frac{1}{2}\begin{bmatrix} \{\phi_1\}^t & 0 & 0 \\ 0 & \{\phi_2\}^t & 0 \\ 0 & 0 & \{\phi_3\}^t \\ 0 & \{\phi_3\}^t & \{\phi_2\}^t \\ \{\phi_3\}^t & 0 & \{\phi_1\}^t \\ \{\phi_2\}^t & \{\phi_1\}^t & 0 \end{bmatrix} \tag{A9}$$

A dot $(\cdot)$ in Eqs. (A8) and (A9) refers to a zero element, and an 0 in Eqs. (A9) refers to a zero vector (3×1 matrix). The initial thermal displacements generated by the temperature distribution, Eq. (3), are given by:

$$u_1^o = u_2^o = 0 \tag{A10}$$

$$w^o = w^o(x_3). \tag{A11}$$

The only nonzero strain component is ϵ_{33}^o. The expression for ϵ_{33}^o in terms of w^o is given by Eq. (15). The expressions of the perturbation strains, η_{ij}, in terms of the perturbation and initial displacements are given in Eqs. (16) to (18). The expression for the strain components $\psi_{\beta\gamma}$ in terms of the perturbation displacements is given by Eqs. (19).

Equations of Motion. The equations of motion for each layer of the plate can be written in the following compact form:

$$\left(\{\partial\}^t\left(\left[[I] + [D]\right][\sigma]\right)\right)^t - \rho\frac{\partial^2}{\partial t^2}\{u\} = 0 \tag{A12}$$

where

$$\{\partial\}^t = [\partial_1\ \partial_2\ \partial_3] \tag{A13}$$

$$[D] = \begin{bmatrix} \partial_1 u_1 & \partial_2 u_1 & \partial_3 u_1 \\ \partial_1 u_2 & \partial_2 u_2 & \partial_3 u_2 \\ \partial_1 w & \partial_2 w & \partial_3 w \end{bmatrix} \tag{A14}$$

$$[\sigma] = \begin{bmatrix} \sigma_{11} & \sigma_{12} & \sigma_{13} \\ \sigma_{12} & \sigma_{22} & \sigma_{23} \\ \sigma_{13} & \sigma_{23} & \sigma_{33} \end{bmatrix} \tag{A15}$$

and $[I]$ is the 3×3 identity matrix.

The equilibrium equations for the heated plate are identically satisfied. This can be verified by setting the inertia terms equal to zero and making the following substitutions in Eqs. (A12):

$$\sigma_{13}^o = \sigma_{23}^o = \sigma_{33}^o = 0 \tag{A16}$$

$$\sigma_{11}^o = \sigma_{11}^o(x_3),\ \sigma_{22}^o = \sigma_{22}^o(x_3),\ \sigma_{12}^o = \sigma_{12}^o(x_3). \tag{A17}$$

The linearized equations of motion for the plate in the perturbed (adjacent) configuration can be written in the following compact form:

$$\left(\{\partial\}^t\left(\left[[I] + [D^o]\right][\tau] + [D][\sigma^o]\right)\right)^t - \rho\frac{\partial^2}{\partial t^2}\{v\} = 0 \tag{A18}$$

Downloaded 03 May 2010 to 171.66.16.247. Redistribution subject to ASME license or copyright; see http://www.asme.org/terms/Terms_Use.cfm

where

$$\{v\}^t = [v_1\ v_2\ \omega] \tag{A19}$$

$$[D^o] = \begin{bmatrix} \cdot & \cdot & \cdot \\ \cdot & \cdot & \cdot \\ \cdot & \cdot & \dfrac{dw^o}{dx_3} \end{bmatrix} \tag{A20}$$

$$[\tau] = \begin{bmatrix} \tau_{11} & \tau_{12} & \tau_{13} \\ \tau_{12} & \tau_{22} & \tau_{23} \\ \tau_{13} & \tau_{23} & \tau_{33} \end{bmatrix} \tag{A21}$$

$$[\sigma^o] = \begin{bmatrix} \sigma^o_{11} & \sigma^o_{12} & \cdot \\ \sigma^o_{12} & \sigma^o_{22} & \cdot \\ \cdot & \cdot & \cdot \end{bmatrix}. \tag{A22}$$

Constitutive Relations. The relations between the strain and stress components in the kth layer of the plate are given by the following Duhamel-Neumann form of Hooke's law:

$$\{\epsilon\} = [a]\{\sigma\} + \{\alpha\}T \tag{A23}$$

where

$$\{\sigma\}^t = [\sigma_{11}\ \sigma_{22}\ \sigma_{33}\ \sigma_{23}\ \sigma_{13}\ \sigma_{12}] \tag{A24}$$

and $\{\alpha\}$ is the vector of coefficients of thermal expansion given by:

$$\{\alpha\}^t = [\alpha_1\ \alpha_2\ \alpha_3\ \cdot\ \cdot\ 2\alpha_6] \tag{A25}$$

The relations between the perturbation strain and stress components can be written in the following compact form:

$$\{\eta\} = [a]\{\tau\} \tag{A26}$$

where

$$\{\eta\}^t = [\eta_{11}\ \eta_{22}\ \eta_{33}\ 2\eta_{23}\ 2\eta_{13}\ 2\eta_{12}] \tag{A27}$$

$$\{\tau\}^t = [\tau_{11}\ \tau_{22}\ \tau_{33}\ \tau_{23}\ \tau_{13}\ \tau_{12}]. \tag{A28}$$

It is convenient to decompose the material compliance matrix $[a]$ into an orthotropic part $[a_o]$ and anisotropic (nonorthotropic) part $[a_1]$, i.e.,

$$[a] = [a_o] + [a_1] \tag{A29}$$

where

$$[a_o] = \begin{bmatrix} a_{11} & a_{12} & a_{13} & \cdot & \cdot & \cdot \\ & a_{22} & a_{23} & \cdot & \cdot & \cdot \\ & & a_{33} & \cdot & \cdot & \cdot \\ & & & a_{44} & \cdot & \cdot \\ & \text{Symm.} & & & a_{55} & \cdot \\ & & & & & a_{66} \end{bmatrix} \tag{A30}$$

$$[a_1] = \begin{bmatrix} \cdot & \cdot & \cdot & \cdot & \cdot & a_{16} \\ & \cdot & \cdot & \cdot & \cdot & a_{26} \\ & & \cdot & \cdot & \cdot & a_{36} \\ & & & \cdot & a_{45} & \cdot \\ & \text{Symm.} & & & \cdot & \cdot \\ & & & & & \cdot \end{bmatrix}. \tag{A31}$$

In Eqs. (A30) and (A31), $a_{IJ}(I, J = 1$ to 6) are the compliance coefficients of the material (see Hearmon (1961) and Lekhnitskii (1981)), and a dot $(\cdot)$ refers to a zero term.

Conditions at the Outer Surfaces and Interfaces Between Layers. The stress-free boundary conditions at the top and bottom surfaces of the plate can be expressed as:

$$\sigma_{i3} = 0 \quad i = 1 \text{ to } 3. \tag{A32}$$

The equilibrium and continuity between the typical layers k and $k + 1$ (top of layer k and bottom of layer $k + 1$) can be written in the following form:

$$\sigma^{(k)}_{i3} - \sigma^{(k+1)}_{i3} = 0 \quad i = 1 \text{ to } 3 \tag{A33}$$

$$u^{(k)}_\beta - u^{(k+1)}_\beta = 0 \quad \beta = 1, 2 \tag{A34}$$

and

$$w^{(k)} - w^{(k+1)} = 0 \tag{A35}$$

where superscripts k and $k + 1$ refer to layers k and $k + 1$. Equations (A33) to (A35) imply perfect bonding between the different layers (i.e., no slip). The initial thermal stresses and displacements, Eqs. (4) through (9), satisfy Eqs. (A32) to (A35) identically.

Initial Thermal Stresses and Displacements. For the case when the temperature is an even function of x_3, the expressions for the thermal stresses and displacements are:

$$\begin{Bmatrix} \sigma^o_{11} \\ \sigma^o_{22} \\ \sigma^o_{12} \end{Bmatrix} = -\begin{bmatrix} a_{11} & a_{12} & a_{16} \\ & a_{22} & a_{26} \\ \text{Symm.} & & a_{66} \end{bmatrix}^{-1} \begin{Bmatrix} \alpha_1 \\ \alpha_2 \\ 2\alpha_6 \end{Bmatrix} T^o \tag{A36}$$

and

$$w^o = -h\zeta + \int_0^\zeta [1 + 2\kappa^o f(\zeta)]^{1/2} h d\zeta \tag{A37}$$

where

$$\kappa^o = (a_{13}\sigma^o_{11} + a_{23}\sigma^o_{22} + a_{36}\sigma^o_{12} + \alpha_3 T^o). \tag{A38}$$

Note that the thermal stresses are linear functions of the temperature parameter T^o and w^o is a nonlinear function of T^o.

APPENDIX B

Explicit Form of the Arrays in the Governing Equations

The explicit form of the arrays $[S_o]_{m,n}$, $[S_1]$, $[K_o]_{m,n}$, $[K_1]_{m,n}$, $[L_o(w^o)]_{m,n}$ and $[L_1(w^o)]_{m,n}$ in Eqs. (27) and (28), associated with the pair of harmonics (m,n), are given by:

$$[S_o]_{m,n} = \begin{bmatrix} -\dfrac{m\pi}{L_1} & \cdot & \cdot \\ \cdot & -\dfrac{n\pi}{L_2} & \cdot \\ \cdot & \cdot & \cdot \\ \cdot & \cdot & \dfrac{n\pi}{L_2} \\ \cdot & \cdot & \dfrac{m\pi}{L_1} \\ \dfrac{n\pi}{L_2} & \dfrac{m\pi}{L_1} & \cdot \end{bmatrix}; \qquad [S_1] = \begin{bmatrix} \cdot & \cdot & \cdot \\ \cdot & \cdot & \cdot \\ \cdot & \cdot & 1 \\ \cdot & 1 & \cdot \\ 1 & \cdot & \cdot \\ \cdot & \cdot & \cdot \end{bmatrix} \frac{d}{dx_3} \tag{B1}$$

$$[K_o]_{m,n} = \begin{bmatrix} 1 & \cdot & \cdot \\ \cdot & 1 & \cdot \\ \cdot & \cdot & 1 \end{bmatrix} \left(\frac{m^2\pi^2}{L_1^2}\sigma^o_{11} + \frac{n^2\pi^2}{L_2^2}\sigma^o_{22} \right) \tag{B2}$$

Downloaded 03 May 2010 to 171.66.16.247. Redistribution subject to ASME license or copyright; see http://www.asme.org/terms/Terms_Use.cfm

$$[K_1]_{m,n} = \begin{bmatrix} 1 & \cdot & \cdot \\ \cdot & 1 & \cdot \\ \cdot & \cdot & -1 \end{bmatrix} \frac{2mn\pi^2}{L_1 L_2} \sigma_{12}^o \tag{B3}$$

$$[L_o(w^o)]_{m,n} = \frac{dw^o}{dx_3} \begin{bmatrix} \cdot & \cdot & \cdot \\ \cdot & \cdot & \cdot \\ \cdot & \cdot & \frac{d}{dx_3} \\ \cdot & \cdot & \frac{n\pi}{L_2} \\ \cdot & \cdot & \frac{m\pi}{L_1} \\ \cdot & \cdot & \cdot \end{bmatrix} \tag{B4}$$

$$[L_1(w^o)]_{m,n} = \frac{dw^o}{dx_3} \begin{bmatrix} \cdot & \cdot & \cdot \\ \cdot & \cdot & \cdot \\ \cdot & \cdot & \frac{-d}{dx_3} \\ \cdot & \cdot & \frac{n\pi}{L_2} \\ \cdot & \cdot & \frac{m\pi}{L_1} \\ \cdot & \cdot & \cdot \end{bmatrix} \tag{B5}$$

where w^o is the thermal displacement; σ_{11}^o, σ_{22}^o, σ_{12}^o are the thermal stresses; and a dot ($\cdot$) refers to a zero term.

Downloaded 03 May 2010 to 171.66.16.247. Redistribution subject to ASME license or copyright; see http://www.asme.org/terms/Terms_Use.cfm

Elastodynamic Response of a Unidirectional Composite Laminate to Concentrated Surface Loads: Part I

Ajit K. Mal
Mem. ASME

Shyh-shiuh Lih
Assoc. Mem. ASME

Department of Mechanical, Aerospace, and Nuclear Engineering, University of California, Los Angeles, CA 90024

The quantitative features of the elastodynamic field produced in a unidirectional graphite/epoxy composite laminate by surface loads are studied. The material of the composite is modeled as a transversely isotropic dissipative medium with its symmetry axis parallel to the laminate surface. The surface displacement produced by a transient concentrated point load on the surface of a uniform half-space and a plate of finite thickness is calculated by means of a multiple transform technique followed by inversion through numerical integration. The two-dimensional (plane-strain) line load problems for the plate are also solved as special cases. In addition, an approximate solution based on the classical plate bending theory which includes transverse shear and rotary inertia is obtained and the range of validity of the approximate solution is determined through comparison with the exact results. The multiple transform technique is shown to be a viable alternative to finite element and other numerically intensive computational schemes for wave field calculations in composite laminates. Part I of the paper contains the formulation, and a discussion of the general features of the response, the numerical treatment and results are given in Part II.

1 Introduction

With the increasing use of advanced composites in a variety of modern applications, it has become necessary to employ reliable and effective nondestructive evaluation (NDE) methods to determine the integrity and serviceability of structural composites. Conventional ultrasonic NDE methods, e.g., through transmission and pulse echo, based on longitudinal waves, have been effective in detecting relatively large isolated flaws that are parallel to the surfaces of the laminate, but these methods are less useful in detecting and characterizing other common defects, e.g., transverse cracks, partial delaminations, etc. (Bar-Cohen and Mal, 1990). The use of ultrasonic setups consisting of guided waves and contact-type transducers have the potential to provide more powerful ultrasonic characterization methods for composites. However, the wave phenomena associated with these methods are, in general, far more complex and less well understood than those associated with the conventional techniques. Realization of the full potential of these newer techniques will require a better understanding of the quantitative features of the wave phenomena than is available at present.

Localized dynamic surface loads are known to cause substantial internal damage to composite laminates and the prediction of the nature and degree of these damages based on modeling and laboratory experiments has been the subject of much research (see, e.g., Mal and Rajapakse, 1990). If the thickness of the laminate is small and the rate of loading is low (as in low-velocity impact) sufficiently accurate estimates of the stress components needed for structural design can often be obtained through approximate quasi-static and thin plate theories (see, e.g., Medick, 1961; Chow, 1971; Sun and Jih, 1990; Lal, 1984; Wu and Springer, 1988). However, in ultrasonic nondestructive inspection of structural components, the loading rate is several orders of magnitude higher than that for low-velocity impact and the quasi-static approximation is clearly not valid. Moreover, there is increasing interest in the use of thicker laminates in a variety of structural applications where the thin plate assumption may not be justified, even for low-velocity impact, and where contact-type transducers may be needed to increase penetration depth of the waves. A full elastodynamic theory needs to be employed in the solution of the problem in order to obtain meaningful results.

To the authors' knowledge, the theoretical solution to the point load problem has not appeared in the literature to date, although the corresponding problems for the isotropic and quasi-isotropic (i.e., transversely isotropic with symmetry axis normal to the plate surface) cases have been solved (e.g., Cer-

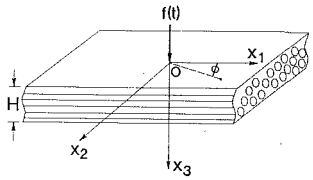
Contributed by the Applied Mechanics Division of THE AMERICAN SOCIETY OF MECHANICAL ENGINEERS for presentation at the 1992 ASME Winter Annual Meeting, Anaheim, CA, Nov. 8-13, 1992.

Discussion on this paper should be addressed to Prof. Leon M. Keer, The Technological Institute, Northwestern University, Evanston, IL 60208, and will be accepted until four months after final publication of the paper itself in the ASME JOURNAL OF APPLIED MECHANICS.

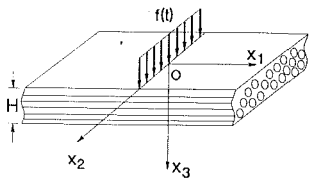
Manuscript received by the ASME Applied Mechanics Division, Feb. 13, 1990; final revision, July 11, 1991. Associate Technical Editor: S. K. Datta.

Paper No. 92-WA/APM-6.

Copyright © 1992 by ASME
Downloaded 03 May 2010 to 171.66.16.247. Redistribution subject to ASME license or copyright; see http://www.asme.org/terms/Terms_Use.cfm



(a) Point load.



(b) Line load.

Fig. 1 Geometry of the point load problem

anoglu and Pao, 1981; Weaver and Pao, 1982; Vasudevan and Mal, 1985; Xu and Mal, 1987). The response of a transversely isotropic half-space with its symmetry axis parallel to the free surface to concentrated time-harmonic or transient-surface loads have been considered by Buchwald (1961), Ricketts and Goldsmith (1972) and Suh et al. (1974). Two-dimensional models involving line loads on half-spaces or plates have been solved by Burridge (1972) and Green and Baylis (1988). The formal solution of the three-dimensional problem consisting of multilayered, angle-ply laminates subjected to *spatially periodic distributed* surface loads has been given by Mal (1988). None of these studies provides a detailed picture of the elastodynamic field. We use a classical integral transform technique coupled with a matrix method to derive a formal solution of the point and line load problems sketched in Fig. 1 in terms of wave number integrals in the frequency domain. Numerical results will be presented in Part II of the paper.

2 Material Modeling: The Complex Moduli

Composite materials are known to be strongly dissipative. For fiber-reinforced composites, dissipation of the waves is caused by the viscoelastic nature of the resin and by scattering from the fibers and other inhomogeneities. Both effects can be modeled in the frequency domain by assuming that the stiffness constants, C_{ij}, are complex and frequency dependent. A possible form of C_{ij} that can model the essential features of the dissipation caused by these factors has been given in Mal and Bar-Cohen (1991) and will be used here. A brief description of the model is presented; the details can be found in the cited paper.

We recall that the linear constitutive equation for a transversely isotropic elastic solid with its symmetry axis along the x_1-axis (Fig. 1) can be expressed in the form (Mal and Singh, 1991)

$$\begin{Bmatrix} \sigma_{11} \\ \sigma_{22} \\ \sigma_{33} \\ \sigma_{23} \\ \sigma_{31} \\ \sigma_{12} \end{Bmatrix} = \begin{bmatrix} c_{11} & c_{12} & c_{12} & 0 & 0 & 0 \\ c_{12} & c_{22} & c_{23} & 0 & 0 & 0 \\ c_{12} & c_{23} & c_{22} & 0 & 0 & 0 \\ 0 & 0 & 0 & c_{44} & 0 & 0 \\ 0 & 0 & 0 & 0 & c_{55} & 0 \\ 0 & 0 & 0 & 0 & 0 & c_{55} \end{bmatrix} \begin{Bmatrix} u_{1,1} \\ u_{2,2} \\ u_{3,3} \\ u_{2,3}+u_{3,2} \\ u_{1,3}+u_{3,1} \\ u_{1,2}+u_{2,1} \end{Bmatrix} \tag{1}$$

where $c_{44}=(c_{22}-c_{23})/2$, σ_{ij} is the Cauchy's stress tensor, u_i is the displacement vector and c_{11}, c_{12}, c_{22}, c_{23}, c_{55} are the five independent real stiffness constants of the material. We introduce five additional constants a_1, a_2, a_3, a_4, and a_5 related to c_{ij} and the density of the material, ρ through (Buchwald, 1961)

$$a_1=c_{22}/\rho,\ a_2=c_{11}/\rho,\ a_3=(c_{12}+c_{55})/\rho,$$
$$a_4=(c_{22}-c_{23})/2\rho=c_{44}/\rho,\ a_5=c_{55}/\rho. \tag{2}$$

It is well known that the quantities $\sqrt{a_1}$, $\sqrt{a_2}$, $\sqrt{a_3}$, $\sqrt{a_4}$, and $\sqrt{a_5}$ represent the velocities of five independent bulk waves that can be transmitted along certain specific directions in the transversely isotropic solid.

Let C_{11}, C_{12}, C_{22}, C_{44}, C_{55} denote the complex and frequency dependent stiffness constants of the fiber-reinforced composite. The complex constants A_1, A_2, A_3, A_4, and A_5 are defined through the relations

$$A_1=C_{22}/\rho,\ A_2=C_{11}/\rho,\ A_3=(C_{12}+C_{55})/\rho,$$
$$A_4=C_{44}/\rho,\ A_5=C_{55}/\rho. \tag{3}$$

Finally, we assume that the two sets of constants A_i and a_i are related through the equations

$$A_1=a_1/(1+ip\sqrt{a_5/a_1}),\ A_2=a_2/(1+ip\sqrt{a_5/a_2}),$$
$$A_3=a_3/(1+ip\sqrt{a_5/a_3}),$$
$$A_4=a_4/(1+ip\sqrt{a_5/a_4}),\ A_5=a_5/(1+ip) \tag{4}$$

where p is the damping factor (Mal, and Bar-Cohen, and Lin 1992).

For many isotropic solids, p is independent of frequency in a broad frequency range (see, e.g., Aki and Richards, 1980). This is generally true if the wavelengths are long compared to the microstructural dimensions (e.g., grain size) of the solid. At higher frequencies the damping factor increases with frequency due to wave scattering. In the case of the fiber-reinforced composite, the effect of wave scattering by the fibers is likely to be significant at higher frequencies. We assume that p is constant below a certain frequency ω_0, beyond which it becomes frequency dependent and that it can be expressed in the form

$$p=p_0\left[1+a_0\left(\frac{f}{f_0}-1\right)^2 H(f-f_0)\right] \tag{5}$$

where $f=\omega/2\pi$ is the frequency in cycles, $f_0=\omega_0/2\pi$, $H(f)$ is the Heaviside step function, and p_0, a_0, f_0 are constants which determine the degree of decay in the amplitude of the waves with propagation distance.

The first term in the right-hand side of (5) represents dissipation due to internal friction and other thermodynamic effects, while the second term represents the attenuation caused by wave scattering by the fibers and other inhomogeneities in the material. Moreover, wave attenuation due to scattering becomes more and more prominent as $f-f_0$ increases. It should be noted that the assumed form of wave attenuation gives rise to noncausal arrival in the response which can be removed through the use of certain causality constraints (see, e.g., Aki and Richards, 1980). In all of the cases considered here the noncausal parts of the time histories were found to be below the numerical noise present in the calculations, and no special efforts were made to remove these.

The material model has been used to calculate the reflected field from several graphite/epoxy plates of different thicknesses immersed in water and the results have been compared with measured data in pulse echo and pitch-catch type arrangements in an ultrasonic test bed. The material properties used in the calculation are listed in Table 1.

Table 1 Material constants of the graphite/epoxy composite used in the calculations

Mass density (g/cm^3)	C_{11}	C_{12}	C_{22}	C_{23}	C_{55} (Gpa)	P_0	F_0	A_0
1.578	160.73	6.44	13.92	6.92	7.07	.005	.3	.1

Downloaded 03 May 2010 to 171.66.16.247. Redistribution subject to ASME license or copyright; see http://www.asme.org/terms/Terms_Use.cfm

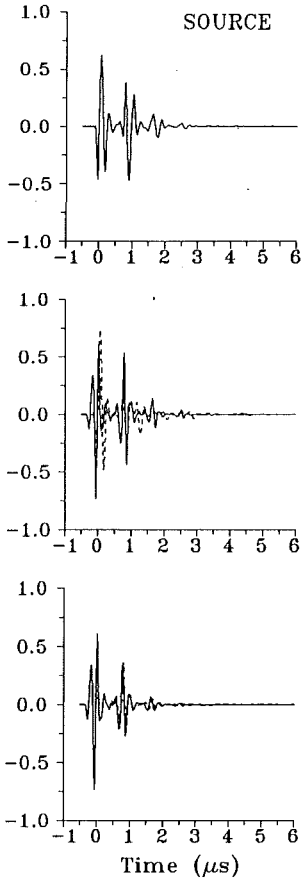


Fig. 2 Comparison between measured (solid curves) and calculated (dashed) reflected signals from a unidirectional graphite/epoxy plate of 1.3-mm thickness immersed in water and excited by an acoustic beam at normal incidence. The calculation in figure at center is for a perfectly elastic model, and at bottom for a model with dissipation.

Typical results of the comparison are shown in Figs. 2 and 3 for a unidirectional specimen of (approximate) thickness 1.3 mm. It can be seen that in general, the reflected pulses calculated in perfectly elastic material model have significantly higher amplitudes than those for the measured signals. Calculations using the complex moduli defined through Eqs. (3)–(5) yield excellent agreement with the measurements. Results for several other specimens ranging in thickness from 1–25 mm have been presented in (Mal and Bar-Cohen and Lih, 1992) where the predicted results have also been found to be in excellent agreement with the measured data. Thus, the model of dissipation proposed here appears to be quite accurate for graphite/epoxy materials in the frequency range .1 – 10 MHz. We now use this model to calculate the elastodynamic field produced by a concentrated surface load on a graphite/epoxy laminate.

3 The Surface Point Load Problem

We introduce Fourier time transforms of all time-dependent variables f through

$$f(x_1, x_2, t) = \mathrm{Re}\,\frac{1}{\pi}\int_0^\infty \hat{f}(x_1, x_2, \omega)e^{-i\omega t}d\omega \tag{6a}$$

$$\hat{f}(x_1, x_2, \omega) = \int_0^\infty f(x_1, x_2, t)e^{i\omega t}dt \tag{6b}$$

and denote the Fourier time transform of the displacement and stress components $u_i(x,t)$, $\sigma_{ij}(x,t)$ by $\hat{u}_i(x,\omega)$, $\hat{\sigma}_{ij}(x,\omega)$. Then, under the assumption of initial rest, $\hat{u}_i(x,\omega)$, $\hat{\sigma}_{ij}(x,\omega)$ are solutions of the system

$$\hat{\sigma}_{ij,j} + \rho\omega^2\hat{u}_i = 0 \tag{7}$$

$$\hat{\sigma}_{\alpha 3}(x_1, x_2, 0, \omega) = 0, \ (\alpha = 1, 2) \tag{8a}$$

$$\hat{\sigma}_{33}(x_1, x_2, 0, \omega) = -\hat{f}(\omega)\delta(x_1)\delta(x_2) \tag{8b}$$

$$\hat{\sigma}_{i3}(x_1, x_2, H, \omega) = 0 \tag{8c}$$

where the applied load $f(t)$ is assumed to be concentrated at the origin on the top surface of the plate and $\hat{f}(\omega)$ is its Fourier time transform. The Cauchy's equations of motion (7) must be supplemented by the constitutive Eq. (1) and the solution must satisfy the outgoing wave (or radiation) condition at large lateral distances from the load. In order to obtain a formal solution of the boundary value problem in the frequency domain, we introduce double spatial Fourier transforms of $\hat{u}_i(x,\omega)$ and $\hat{\sigma}_{ij}(x,\omega)$ through

$$\hat{u}_i(x_1, x_2, x_3, \omega) = \frac{1}{4\pi^2}\int_{-\infty}^{\infty}\int_{-\infty}^{\infty} U_i(\xi_1, \xi_2, x_3, \omega)e^{i(\xi_1 x_1 + \xi_2 x_2)}d\xi_1 d\xi_2 \tag{9a}$$

$$\hat{\sigma}_{ij}(x_1, x_2, x_3, \omega) = \frac{1}{4\pi^2}\int_{-\infty}^{\infty}\int_{-\infty}^{\infty} \Sigma_{ij}(\xi_1, \xi_2, x_3, \omega)e^{i(\xi_1 x_1 + \xi_2 x_2)}d\xi_1 d\xi_2 \tag{9b}$$

Substitution from equations (9a,b) into (7) and (8) leads to a two-point boundary value problem of a system of ordinary differential equations for $U_i(x_3)$ which can in principle be solved. To this end, it is convenient to introduce the six-dimensional "stress-displacement vector" $\{S\}$ in the transformed domain, defined by

$$\{S(x_3)\} = \{U_i(x_3)\ \Sigma_{i3}(x_3)\}. \tag{10}$$

Then, $\{S\}$ can be expressed in a partitioned matrix product form as (Mal, 1988)

$$\{S(x_3)\} = \begin{bmatrix} Q_{11} & Q_{12} \\ Q_{21} & Q_{22} \end{bmatrix}\begin{bmatrix} E^+(x_3) & 0 \\ 0 & E^-(x_3) \end{bmatrix}\begin{Bmatrix} C^+ \\ C^- \end{Bmatrix} \tag{11}$$

where

$$E^+(x_3) = \mathrm{diag}[e^{i\zeta_1 x_3}e^{i\zeta_2 x_3}e^{i\zeta_3 x_3}] \tag{12a}$$

$$E^-(x_3) = \mathrm{diag}[e^{i\zeta_1(H-x_3)}e^{i\zeta_2(H-x_3)}e^{i\zeta_3(H-x_3)}] \tag{12b}$$

$$\{C^\pm\} = \{c_i^\pm\}. \tag{12c}$$

In the above, $c_i^\pm$ are complex constants related to downgoing and upgoing waves within the laminate, $[Q_{ij}]$ are 3×3 matrices, and ζ_i are the "vertical" wave numbers of the three possible waves in the composite with "horizontal" wave numbers ξ_1, ξ_2. The expressions for $[Q_{ij}]$ and ζ_i are given in the Appendix in a slightly different form from those given in Mal (1988). The six constants must be determined from the boundary conditions (8b,c), which can be restated in the spatial transform domain as

$$\{S(0)\} = \{U_i(0) \quad \Sigma_{i3}(0)\} \tag{13a}$$

$$\{S(H)\} = \{U_i(H) \quad \Sigma_{i3}(H)\}, \tag{13b}$$

where

$$\{\Sigma_{i3}(0) = \{0,\ 0,\ -\hat{f}(\omega)\} \tag{14a}$$

$$\{\Sigma_{i3}(H)\} = \{0,\ 0,\ 0\} \tag{14b}$$

The use of (11) in (13a,b) leads to the following system of equations for the 12 unknowns, $\{c_i^\pm\}$, $\{U_i(0)\}$, and $\{U_i(H)\}$,

$$\begin{bmatrix} Q_{11} & Q_{12} \\ Q_{21} & Q_{22} \end{bmatrix}\begin{bmatrix} I & 0 \\ 0 & E(H) \end{bmatrix}\begin{Bmatrix} C^+ \\ C^- \end{Bmatrix} = \begin{Bmatrix} U(0) \\ \Sigma(0) \end{Bmatrix} \tag{15a}$$

$$\begin{bmatrix} Q_{11} & Q_{12} \\ Q_{21} & Q_{22} \end{bmatrix}\begin{bmatrix} E(H) & 0 \\ 0 & I \end{bmatrix}\begin{Bmatrix} C^+ \\ C^- \end{Bmatrix} = \begin{Bmatrix} U(H) \\ \Sigma(H) \end{Bmatrix} \tag{15b}$$

where $[I]$ is the 3×3 identify matrix,

$$E(H) = \mathrm{diag}\ [e^{i\zeta_1 H}e^{i\zeta_2 H}e^{i\zeta_3 H}], \tag{16}$$

and we have used the notations

Downloaded 03 May 2010 to 171.66.16.247. Redistribution subject to ASME license or copyright; see http://www.asme.org/terms/Terms_Use.cfm

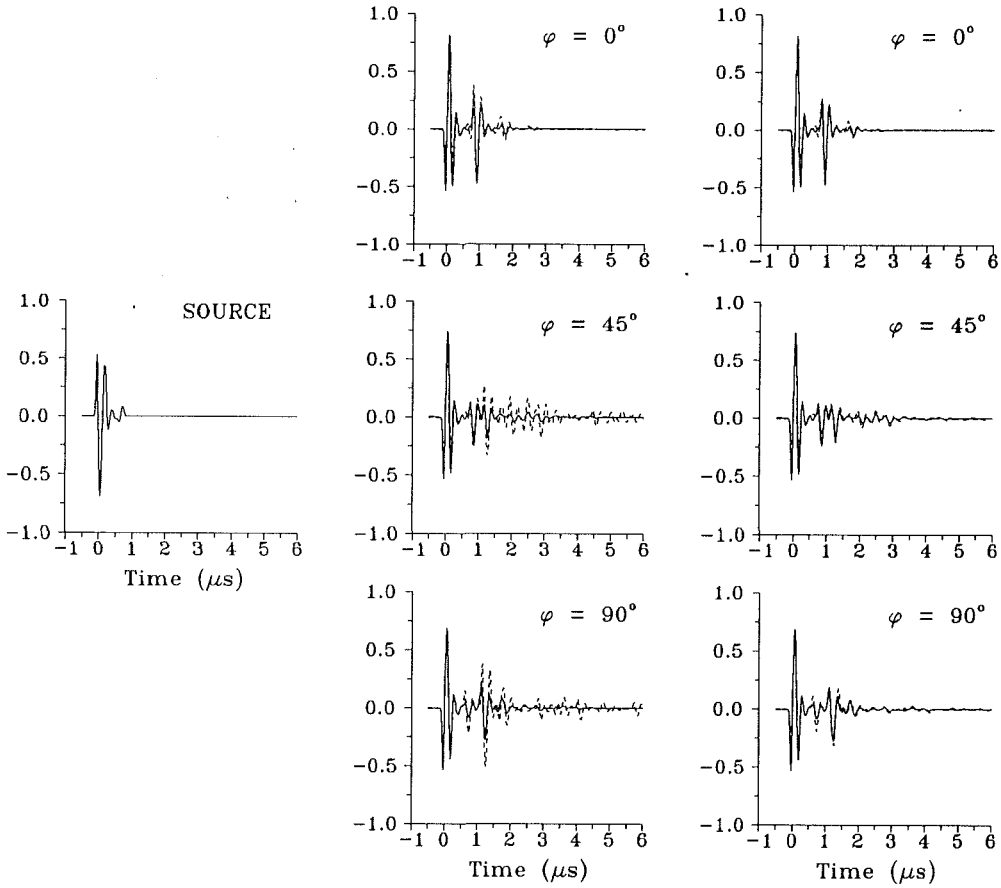


Fig. 3 Same as in Fig. 2 for 20 deg incidence and for three orientations of the laminate relative to the vertical plane containing the axis of the incident beam. Dashed curves at left are for perfectly elastic model while those at right are for the dissipative model.

$$\{U\} = \{U_i\}, \quad \{\Sigma\} = \{\Sigma_i\}. \tag{17}$$

Equations (15*a*,*b*) can be solved to yield

$$\{C^+\} = [Q_{21} - Q_{22}EQ_{22}^{-1}EQ_{21}E]^{-1}\{\Sigma(0) - [Q_{22}EQ_{22}^{-1}]\Sigma(H)\} \tag{18a}$$

$$\{C^-\} = [Q_{22}^{-1}]\{\Sigma(H)\} - [Q_{22}^{-1}Q_{21}E]\{C^+\} \tag{18b}$$

$$\{U(0)\} = [Q_{11}]\{C^+\} + [Q_{12}E]\{C^-\} \tag{18c}$$

$$\{U(H)\} = [Q_{11}E]\{C^+\} + [Q_{12}]\{C^-\} \tag{18d}$$

In view of (14*b*), we have

$$\{U(0)\} = [Q_{11} - Q_{12}EQ_{22}^{-1}Q_{21}E][Q_{21} - Q_{22}EQ_{22}^{-1}Q_{21}E]^{-1}\{\Sigma(0)\} \tag{19a}$$

$$\{U(H)\} = [Q_{11} - Q_{12}EQ_{22}^{-1}Q_{21}]\,[E][Q_{21} - Q_{22}EQ_{22}^{-1}Q_{22}E]^{-1}\{\Sigma(0)\} \tag{19b}$$

where

$$\{\Sigma(0)\} = -\hat{f}(\omega)\{0,\ 0,\ 1\}. \tag{20}$$

In the case of a uniform half-space, $H \to \infty$, $[E] = [0]$ and from (19*a*),

$$\{U(0)\} = [Q_{11}Q_{21}^{-1}]\{\Sigma(0)\}. \tag{21}$$

Equations (19*a*,*b*) give the transformed surface displacements and (11) can then be used to obtain the transformed displacement and stress components in the interior of the plate. The Fourier time-transformed displacements and stresses are given by the double integral expressions (9*a*,*b*).

3.1 Approximate Solution. If the plate is of small thickness H compared to the dominant wavelength, then it may be possible to use one of the several approximate formulations. The accuracy of the approximate results can be examined through comparison with the exact results obtained in the previous section. We apply the shear deformation-type theory retaining transverse shear and rotary inertia of the plate elements (see, e.g., Mindlin, 1951). For convenience we use the notation (x, y, z) for the coordinate and (u, v, w) for the corresponding displacement components. The displacement components are assumed to be of the form

$$\begin{aligned} u(x, y, z) &= u_0(x, y) + z\psi_x(x, y) \\ v(x, y, z) &= v_0(x, y) + z\psi_y(x, y) \\ w(x, y, z) &= w_0(x, y) \end{aligned} \tag{22}$$

where the $x-y$ plane is the midplane of the plate, (u_0, v_0, w_0) are the displacement components of a point in the midplane, and ψ_x and ψ_y denote the rotations of a line element, originally perpendicular to the longitudinal plane, about the y and x-axes, respectively. The governing equations for the out-of-plane displacement for the point load problem can be expressed in the form:

$$A_{55}\frac{\partial}{\partial x}\left(\psi_x + \frac{\partial w_0}{\partial x}\right) + A_{44}\frac{\partial}{\partial x}\left(\psi_y + \frac{\partial w_0}{\partial y}\right) - \rho H\frac{\partial^2 w_0}{\partial t^2} = -f(t)\delta(x)\delta(y)$$

$$\frac{\partial}{\partial x}\left(D_{11}\frac{\partial \psi_x}{\partial x} + D_{12}\frac{\partial \psi_y}{\partial y}\right) + D_{55}\frac{\partial}{\partial y}\left(\frac{\partial \psi_x}{\partial y} + \frac{\partial \psi_y}{\partial x}\right) - A_{55}\frac{\partial}{\partial x}\left(\psi_x + \frac{\partial w_0}{\partial x}\right) - \frac{\rho H^3}{12}\frac{\partial^2 \psi_x}{\partial t^2} = 0$$

Downloaded 03 May 2010 to 171.66.16.247. Redistribution subject to ASME license or copyright; see http://www.asme.org/terms/Terms_Use.cfm

$$D_{55}\frac{\partial}{\partial x}\left(\frac{\partial \psi_x}{\partial_y}+\frac{\partial \psi_y}{\partial x}\right)+\frac{\partial}{\partial y}\left(D_{12}\frac{\partial \psi_x}{\partial x}+D_{22}\frac{\partial \psi_y}{\partial y}\right)$$
$$-A_{44}\frac{\partial}{\partial x}\left(\psi_y+\frac{\partial w_0}{\partial y}\right)-\frac{\rho H^3}{12}\frac{\partial^2 \psi_y}{\partial t^2}=0$$

where

$$A_{ij}=P_{ij}H,\ D_{ij}=P_{ij}H^3/12$$
$$P_{11}=C_{11}-C_{12}^2/C_{22},\ P_{12}=C_{12}(1-C_{23}/C_{22})$$
$$P_{22}=C_{22}-C_{23}^2/C_{22},\ P_{55}=C_{55}.$$

The solution of these equations can be obtained by the transform technique in the form

$$\hat{\psi}_x(x, y, \omega)=\frac{1}{4\pi^2}\int_{-\infty}^{\infty}\int_{-\infty}^{\infty}\Psi_x(\xi_1, \xi_2, \omega)e^{i(\xi_1 x+\xi_2 y)}d\xi_1 d\xi_2$$
$$\hat{\psi}_y(x, y, \omega)=\frac{1}{4\pi^2}\int_{-\infty}^{\infty}\int_{-\infty}^{\infty}\Psi_y(\xi_1, \xi_2, \omega)e^{i(\xi_1 x+\xi_2 y)}d\xi_1 d\xi_2$$
$$\hat{w}_0(x, y, \omega)=\frac{1}{4\pi^2}\int_{-\infty}^{\infty}\int_{-\infty}^{\infty}W_0(\xi_1, \xi_2, \omega)e^{i(\xi_1 x+\xi_2 y)}d\xi_1 d\xi_2 \tag{23}$$

where $\hat{\psi}_x(x, y, w)$, $\hat{\psi}_y(x, y, w)$, $\hat{w}_0(x, y, w)$ are the Fourier time transforms of $\psi_x(x, y, t)$, $\psi_y(x, y, t)$, $w_0(x, y, t)$, respectively. The unknown functions Ψ_x, Ψ_y, W_0 satisfy the system of linear equations

$$[\mathbf{M}]\ \{\mathbf{V}\}=\{\mathbf{F}\} \tag{24}$$

where $\{\mathbf{V}\}=\{W_0, \Psi_x, \Psi_y\}$, $\{\mathbf{F}\}=\{-1, 0, 0\}$ and the matrix **[M]** is given in the Appendix.

The formal solutions of the two-dimensional (in-plane) line load problems in which the load is uniformly distributed along the x_1-axis (the quasi-isotropic case) or along the x_2-axis can be obtained as special cases of the above. We consider the latter of the above two cases, the quasi-isotropic problem can be solved in a similar manner.

3.2 Uniform Line Load Along the x_2-Axis. In this two-dimensional case, the elastic field is independent of x_2 and the displacement component u_2 as well as the stress components σ_{12}, σ_{22}, and σ_{32} are zero. The stress-displacement law (1) reduces to

$$\begin{Bmatrix}\sigma_{11}\\ \sigma_{33}\\ \sigma_{13}\end{Bmatrix}=\begin{bmatrix}c_{11} & c_{13} & 0\\ c_{13} & c_{33} & 0\\ 0 & 0 & c_{55}\end{bmatrix}\begin{Bmatrix}u_{1,1}\\ u_{3,3}\\ u_{1,3}+u_{3,1}\end{Bmatrix}. \tag{25}$$

We introduce Fourier time transforms as in (6) and spatial Fourier transforms through

$$\hat{u}_i(x_1, x_3, \omega)=\frac{1}{2\pi}\int_{-\infty}^{\infty}U_i(\xi, x_3, \omega)e^{i\xi x_1}d\xi \tag{26a}$$

$$\hat{\sigma}_{ij}(x_1, x_3, \omega)=\frac{1}{2\pi}\int_{-\infty}^{\infty}\Sigma_{ij}(\xi, x_3, \omega)e^{i\xi x_1}d\xi. \tag{26b}$$

The boundary conditions are

$$\hat{\sigma}_{13}(x_1, 0, \omega)=0,\ \hat{\sigma}_{i3}(x_1, H, \omega)=0 \tag{27a}$$

$$\hat{\sigma}_{33}(x_1, 0, \omega)=-\hat{f}(\omega)\delta(x_1). \tag{27b}$$

Then the stress-displacement vector, defined by

$$\{S(x_3)\}=\{U_i(x_3)\},\ \Sigma_{i3}(x_3)\}\ (i=1, 3), \tag{28}$$

can be expressed in the matrix form

$$\{S(x_3)\}=\begin{bmatrix}Q_{11} & Q_{12}\\ Q_{21} & Q_{22}\end{bmatrix}\begin{bmatrix}E^+(x_3) & 0\\ 0 & E^-(x_3)\end{bmatrix}\begin{Bmatrix}C^+\\ C^-\end{Bmatrix} \tag{29}$$

where

$$E^+(x_3)=\mathrm{diag}[e^{i\zeta_1 x_3}e^{i\zeta_2 x_3}],$$
$$E^-(x_3)=\mathrm{diag}[e^{i\zeta_1(H-x_3)}e^{i\zeta_2(H-x_3)}]. \tag{30}$$

The matrices $[Q_{ij}]$ and the other quantities which appear in (29) and (30) are defined in the Appendix. The formal solution of the boundary value problem in the transformed domain is still given by Eqs. (19*a*,*b*) and in the case of uniform half space, by (21).

If the plate thickness H is small compared to the dominant wavelength, then the governing equation for u_3 is

$$D_{11}\frac{\partial^4 u_3}{\partial x_1^4}+\rho H\frac{\partial^2 u_3}{\partial t^2}=f(t)\delta(x_1). \tag{31}$$

The solution of this equation can be obtained by the transform technique in the form

$$\hat{u}_3(x_1, \omega)=\frac{\hat{f}}{2\pi}\int_{-\infty}^{\infty}U_3(\xi, \omega)e^{i(\xi x_1)}d\xi \tag{32}$$

where

$$U_3(\xi, \omega)=\frac{1}{D_{11}\xi^4-\rho\omega^2 H} \tag{33}$$

and $\hat{u}_3(x_1, \omega)$ is the Fourier time transform of $u_3(x_1, t)$.

There are two remaining tasks in the calculation of the elastodynamic field. One is the evaluation of the double integrals for a suite of values of ω to obtain the frequency spectra of the field variables of interest, and the other is Fourier inversion to calculate their time histories. Of these, the first task is the most difficult, since the integrand has a number of undesirable features which introduce a variety of problems in the evaluation of the integrals. Once the integral is evaluated, the resulting spectra can be inverted by the highly efficient FFT in a straightforward manner, for realistic forms of the force-time history, $f(t)$. The wave number integral representations of the solutions given by (9) and (26) cannot, in general, be evaluated analytically and a number of difficulties are encountered in their numerical evaluation due to the special properties of their integrands. Thus, before the integral can be evaluated, it is necessary to investigate these special properties.

4 Properties of the Integrands

We assume, for this discussion that $\hat{f}(\omega)=1$ and note that the integrands have the denominator Δ where

$$\Delta=\det[Q_{21}-Q_{22}EQ_{22}^{-1}Q_{21}E] \tag{34}$$

for a plate, and

$$\Delta=\det[Q_{21}] \tag{35}$$

for a half-space. In absence of material dissipation, Δ would vanish at certain points on the $\xi_1\xi_2$-plane that correspond to guided wave modes for a plate and Rayleigh wave modes for a half-space.

In the case of the half-space, the Rayleigh wave speed, v_R, can be determined by setting $\Delta=0$ and using the relation $\xi_1=(\omega/v_R)n_1$, $\xi_2=(\omega/v_R)n_2$, where $n\equiv(n_1, n_2, 0)=(\cos\phi, \sin\phi, 0)$ is the propagation direction. In the special case of propagation parallel to the fibers, $\phi=0$ deg, $\xi_2=0$, $v_R=\omega/\xi_1$ and the Rayleigh wave equation becomes

$$-\zeta_1(q_{11}+q_{21})\delta_2+\zeta_2(q_{12}+q_{22})\delta_1=0$$

where q_{11}, q_{21}, q_{12}, q_{22}, δ_1, δ_2 are given in the Appendix. In the special case of propagation at right angles to the fibers, $\phi=90$ deg, $\xi_1=0$, $v_R=\omega/\xi_2$, and the Rayleigh wave equation takes the simpler form

$$16(v_R^2/a_1-1)\ (v_R^2/a_4-1)-(2-v_R^2/a_4)^4=0.$$

For other directions of propagation, the general equation $\Delta=0$ given in (35) needs to be solved for v_R.

In the case of the plate with perfectly elastic properties, the

Downloaded 03 May 2010 to 171.66.16.247. Redistribution subject to ASME license or copyright; see http://www.asme.org/terms/Terms_Use.cfm

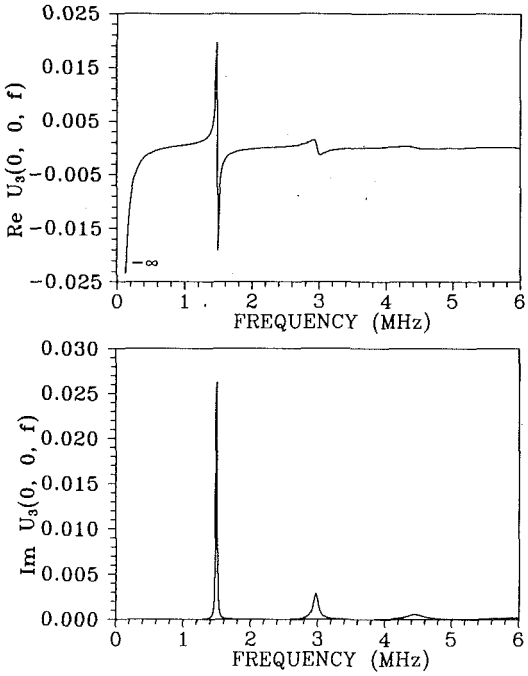


Fig. 4 Behavior of the kernel $U_3(0, 0, f)$ for a 1-mm thick plate

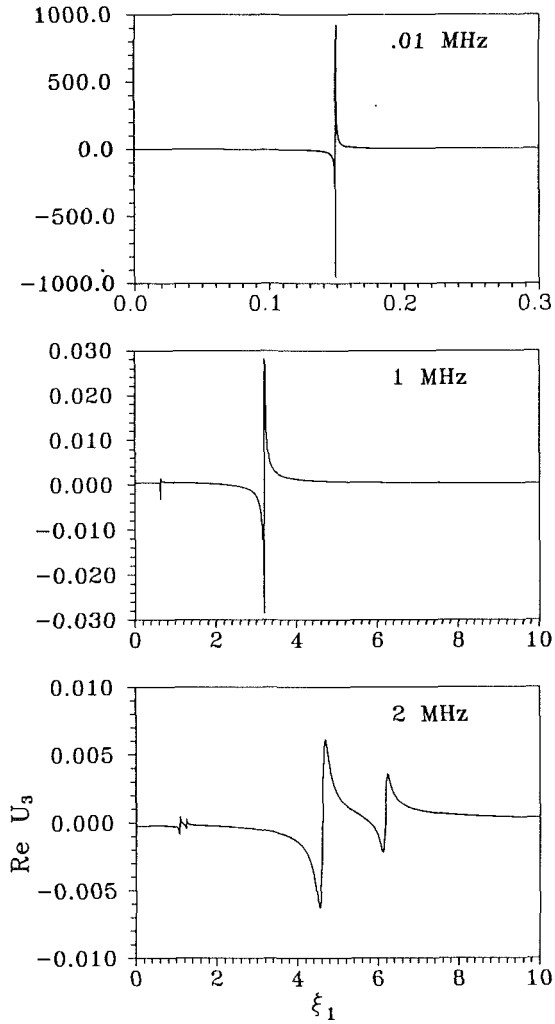


Fig. 5 Behavior of the Kernel $U_3(\xi_1, 0, f)$ for a 1-mm thick plate for $f = .01$, 1 and 2 MHz

denominator Δ is the dispersion function for Lamb waves. As is well known, this equation has a finite number of real roots at a fixed frequency, giving rise to multimode guided waves. The dispersion curves can be found in several earlier publications (see, e.g., Karim, Mal, and Bar-Cohen, 1990; Ju, Datta, and Shah, 1990). The specific frequencies at which the higher modes first appear are called the cutoff frequencies and are of special significance in these calculations as will be seen later.

In the absence of dissipation, the wave number integrals are singular due to the existence of the guided wave modes. Although the singularities can be removed by contour integration or other special techniques, this introduces other difficulties in their numerical evaluation (see, e.g., Kundu and Mal, 1985). In the presence of dissipation, $\Delta \neq 0$, for all real values of ξ_1 and ξ_2; however, the denominators have small values near the points where the poles would be located in the perfectly elastic case.

It should also be noted that for $\xi_1 = 0$, $q_{22} = 0$, and the first row and the second column of $[Q_{ij}]$ vanish; i.e., the matrices become singular. This is due to the fact that the plane $\xi_1 = 0$ is the quasi-isotropic plane of the composite, where there are only two possible waves with their speeds independent of the direction of propagation on this plane. Thus, the expressions in the right-hand sides of (18)–(19) break down, and Eqs. (15) need to be modified before they can be solved. This is accomplished simply by deleting the zero rows and columns from the matrices $[Q_{ij}]$ and recognizing that the unknown vectors $\{c^{\pm}\}$ are two-dimensional. A similar procedure is required for $\xi_2 = 0$ as well.

If both ξ_1 and ξ_2 vanish, then

$$U_1(0, 0, \omega) = U_2(0, 0, \omega) = 0$$

and

$$U_3(0, 0, \omega) = \frac{i(1 + E_1^2)}{\zeta_1 (1 - E_1^2)}$$

where $E_1 = \exp(i\zeta_1 H)$ and $\zeta_1 = \omega\sqrt{a_1}$. It can be seen that for a perfectly elastic material, U_3 tends to infinity when the denominator $1 - E_1^2$ becomes zero, i.e., when

$$\omega = \frac{n\pi\sqrt{a_1}}{H}, \qquad f = \frac{n\sqrt{a_1}}{2H} \quad (n = 0, 1, 2, \ldots). \tag{36}$$

Furthermore, when $\omega \to 0$,

$$U_3(0, 0, \omega) \simeq -1/(\rho H \omega^2). \tag{37}$$

Thus, $U_3(0, 0, \omega)$ has a singularity of $O(\omega^{-2})$ at $\omega = 0$ as in the isotropic plate problem (see, e.g., Vasudevan and Mal, 1985). If the material has dissipation, spikes will be located at the frequencies specified by (36). This can be seen in Fig. 4, where we have plotted the function $U_3(0, 0, f)$ for a 1-mm thick plate using the dissipative material properties given in Table 1. The spikes are located at $f \approx 1.485\ n$ ($n = 0, 1, 2, 3 \ldots$), the cutoff for the symmetric modes. The size of the spike becomes infinite when $f \to 0$ and is finite for $f \neq 0$.

Typical values of the kernel Re $U_3(\xi_1, 0, f)$ for a homogeneous plate of 1-mm thickness are plotted against ξ_1 in Fig. 5 at frequencies .01, 1, and 2 MHz. The spikes are located at specific values of ξ_1 and their size becomes smaller as ξ_1 increases. Furthermore, at higher frequencies the number of spikes increases and moves away from the origin. The modulus of a typical kernel together with their contour plots as functions of ξ_1 and ξ_2 are presented in Fig. 6 for three values of the frequency. It can be seen that the integrands have an extremely irregular behavior which gets worse at higher frequencies and causes considerable difficulty in the numerical evaluation of

Downloaded 03 May 2010 to 171.66.16.247. Redistribution subject to ASME license or copyright; see http://www.asme.org/terms/Terms_Use.cfm

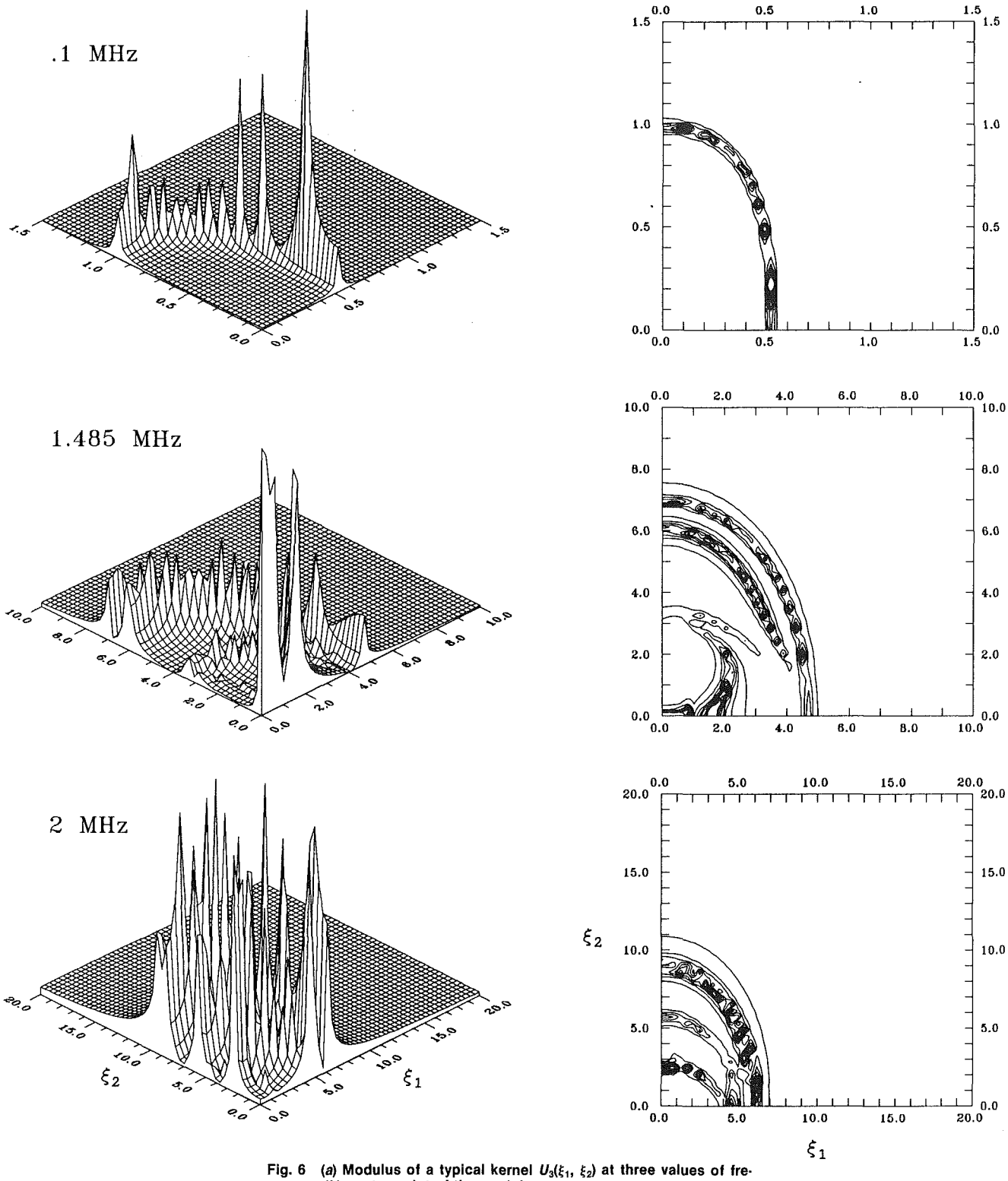


Fig. 6 (*a*) **Modulus of a typical kernel** $U_3(\xi_1, \xi_2)$ **at three values of frequency; (*b*) contour plot of the modulus**

the integrals. The kernel for the two-dimensional case has similar undesirable properties.

An adaptive numerical integration scheme has been developed to evaluate the wave number integrals, and will be described in Part II of the paper. The calculated surface displacement produced by concentrated dynamic loads on the surface of a unidirectional laminate will also be presented in Part II.

Acknowledgments

This research was supported by the Mechanics Division of the Office of Naval Research under Grant N00014-90-J-1857, monitored by Dr. Yapa D. S. Rajapakse. Support was also provided by the Scientific and Environmental Affairs Division of NATO under Grant CRG.890243.

Downloaded 03 May 2010 to 171.66.16.247. Redistribution subject to ASME license or copyright; see http://www.asme.org/terms/Terms_Use.cfm

References

Aki, K., and Richards, P. G., 1980, *Quantitative Seismology: Theory and Methods*, Vol. 1, W. H. Freeman, San Francisco.

Bar-Cohen, Y., and Mal, A. K., 1990, "End Product NDE of Adhesive Bonded Composite Joints," *ASM International Engineering Materials Handbook*, Vol. 3, Adhesives and Sealants, pp. 777–784.

Bose, S. K., and Mal, A. K., 1973, "Longitudinal Shear Waves in a Fiber-Reinforced Composite," *Int. J. Solids Structures*, Vol. 9, pp. 1075–1085.

Bose, S. K., and Mal, A. K., 1974, "Elastic Waves in a Fiber-Reinforced Composite," *J. Mech. Phys. Solids*, Vol. 22, pp. 217–229.

Buchwald, V. T., 1961, "Rayleigh Waves in Transversely Isotropic Media," *Quart. J. Mech. and Appl. Math.*, Vol. 14, pp. 293–317.

Burridge, R., 1971, "Lamb's Problem for an Anisotropic Half-Space," *Quart. J. Mech. and Appl. Math.*, Vol. 24, pp. 81–98.

Ceranoglu, A. N., and Pao, Y. H., 1981, "Propagation of Elastic Pulses and Acoustic Emission in a Plate," ASME JOURNAL OF APPLIED MECHANICS, Vol. 48, pp. 125–147.

Chow, T. S., 1971, "On the Propagation of Flexural Waves on an Orthotropic Laminated Plate and Its Response to an Impulse Load," *J. Composite Materials*, Vol. 5, pp. 306–319.

Christensen, R. M., 1981, *Mechanics of Composite Materials*, John Wiley and Sons, New York.

Datta, S. K., and Ledbetter, H. M., 1983, "Elastic Constants of Fiber-Reinforced Boron-Aluminum: Observation and Theory," *Int. J. Solids and Struct.*, Vol. 19, pp. 885–894.

Dravinski, M., and Mossessian, T. K., 1988, "On the Evaluation of the Green's Functions for Harmonic Line Loads in a Viscoelastic Half-Space," *Int. J. Numerical Methods in Engineering*, Vol. 26, pp. 823–841.

Green, W. A., and Baylis, E. R., 1988, "The Propagation of Impact Stress Waves in Anisotropic Fiber Reinforced Laminates," *Wave Propagation in Structural Composites*, A. K. Mal and T. C. T. Ting, eds., Proceedings of the Joint ASME/SES Applied Mechanics and Engineering Sciences Conference, Berkeley, CA, June 20–22, AMD-Vol. 90, pp. 53–68.

Ju, T. H., Datta, S. K., and Shah, A. H., 1990, "Scattering of Impact Wave by a Crack in Composite Plate," *Impact Response and Elastodynamics of Composites*, A. K. Mal and Y. D. S. Rajapakse, eds., Proceedings of ASME Symposium, Winter Annual Meeting, Dallas, TX, Nov. 25–30, AMD-Vol. 116, pp. 153–171.

Karim, M. R., Mal, A. K., and Bar-Cohen, Y., 1990, "Inversion of Leaky Lamb Wave Data by Simplex Algorithm," *J. Acoust. Soc. Am.*, Vol. 88, pp. 482–491.

Knopoff, L., 1964, "Q," *Review of Geophysics*, Vol. 2, pp. 625–660.

Kundu, T., and Mal, A. K., 1985, "Elastic Waves in a Multilayered Solid Due to a Dislocation Source," *Wave Motion*, Vol. 7, pp. 459–471.

Lal, K. M., 1984, "Coefficients of Restitution for Low Velocity Transverse Impact on Thin Graphite-Epoxy Laminates," *Composite Technology Review*, Vol. 6, pp. 112–117.

Mal, A. K., 1988, "Wave Propagation in Layered Composite Laminates Under Periodic Surface Loads," *Wave Motion*, Vol. 10, pp. 257–266.

Mal, A. K., Bar-Cohen, Y., and Lin, S.-S., 1992, "Wave Attenuation in Fiber-Reinforced Composites," International Symposium on M^{3}D: Mechanics and Mechanisms of Material Damping, (ASTM-STP 1169), in press.

Mal, A. K., and Singh, S. J., 1991, *Deformation of Elastic Solids*, Prentice-Hall, Englewood Cliffs, NJ.

Mal, A. K., Yin, C.-C., and Bar-Cohen, Y., 1991, "Analysis of Acoustic Pulses Reflected from the Fiber-Reinforced Composite Laminates," ASME JOURNAL OF APPLIED MECHANICS, Vol. 59, pp. 5136–5144.

Medick, M. A., 1961, "On Classical Plate Theory and Wave Propagation," ASME JOURNAL OF APPLIED MECHANICS, Vol. 28, pp. 223–228.

Mindlin, R. D., 1951, "Influence of Rotary Inertia and Shear on Flexural Motions of Isotropic, Elastic Plates," ASME JOURNAL OF APPLIED MECHANICS, Vol. 18, pp. 31–38.

Press, W. H., Flannery, B. P., Teukolsky, S. A., and Vetterling, W. T., 1986, *Numerical Recipes*, Cambridge University Press, Cambridge, U.K.

Ricketts, T. E., and Goldsmith, W., 1972, "Wave Propagation in an Anisotropic Half-Space," *Int. J. Rock Mech. and Min. Sci.*, Vol. 9, pp. 493–512.

Suh, S.-L., Goldsmith, W., Sackman, J. L., and Taylor, R. L., 1974, "Impact on a Transversely Anisotropic Half-Space," *Int. J. of Rock Mech., Min. Sci. and Geomech. Abstr.*, Vol. 11, pp. 413–421.

Sun, C. T., and Tan, T. M., 1984, "Wave Propagation in a Graphite/Epoxy Laminate," *J. Astro. Sci.*, Vol. 32, pp. 269–284.

Vasudevan, N., and Mal, A. K., 1985, "Response of an Elastic Plate to Localized Transient Sources," ASME JOURNAL OF APPLIED MECHANICS, Vol. 52, pp. 356–362.

Weaver, R. L., and Pao, Y. H., 1982, "Axisymmetric Elastic Waves Excited by a Point Source in a Plate," ASME JOURNAL OF APPLIED MECHANICS, Vol. 49, pp. 821–836.

Wu, H.-Y. T., and Springer, G. S., 1988, "Measurements of Matrix Cracking and Delamination Caused by Impact on Composite Plates," *J. Composite Materials*, Vol. 22, pp. 518–532.

Xu, P.-C., and Mal, A. K., 1985, "An Adaptive Integration Scheme for Irregularly Oscillating Functions," *Wave Motion*, Vol. 7, pp. 235–243.

Xu, P.-C., and Mal, A. K., 1987, "Calculation of the Green's Functions for a Layered Viscoelastic Solid," *Bull. Seism. Soc. Am.*, Vol. 77, pp. 1823–1837.

APPENDIX

The matrices $[Q_{ij}]$ and the vertical wave numbers ζ_j are defined in this Appendix.

(a) Three-Dimensional Case

$$[Q_{11}] = \begin{bmatrix} i\xi_1 q_{11} & i\xi_1 q_{12} & 0 \\ i\xi_2 q_{21} & i\xi_2 q_{22} & i\zeta_3 \\ i\zeta_1 q_{21} & i\zeta_2 q_{22} & -i\xi_2 \end{bmatrix}$$

$$[Q_{12}] = \begin{bmatrix} i\xi_1 q_{11} & i\xi_1 q_{12} & 0 \\ i\xi_2 q_{21} & i\xi_2 q_{22} & -i\zeta_3 \\ -i\zeta_1 q_{21} & -i\zeta_2 q_{22} & -i\xi_2 \end{bmatrix}$$

$$[Q_{21}] = \begin{bmatrix} -\rho A_5 \xi_1 \zeta_1 (q_{11}+q_{21}) & -\rho A_5 \xi_1 \zeta_2 (q_{11}+q_{22}) & \rho A_5 \xi_1 \xi_2 \\ -2\rho A_4 \xi_2 \zeta_1 q_{21} & -2\rho A_4 \xi_2 \zeta_2 q_{22} & \rho A_4 (\xi_2^2 - \zeta_3^2) \\ \delta_1 & \delta_2 & 2\rho A_4 \xi_2 \zeta_3 \end{bmatrix}$$

$$[Q_{22}] = \begin{bmatrix} \rho A_5 \xi_1 \zeta_1 (q_{11}+q_{21}) & \rho A_5 \xi_1 \zeta_2 (q_{12}+q_{22}) & \rho A_5 \xi_1 \xi_2 \\ 2\rho A_4 \xi_2 \zeta_1 q_{21} & 2\rho A_4 \xi_2 \zeta_2 q_{22} & \rho A_4 (\xi_2^2 - \zeta_3^2) \\ \delta_1 & \delta_2 & -2\rho A_4 \xi_2 \zeta_3 \end{bmatrix}$$

$$\delta_1 = \rho[(A_5 - A_3)\xi_1^2 q_{11} - (A_1 - 2A_4)\xi_2^2 q_{21} - A_1 \zeta_1^2 q_{21}]$$

$$\delta_2 = \rho[(A_5 - A_3)\xi_1^2 q_{12} - (A_1 - 2A_4)\xi_2^2 q_{22} - A_1 \zeta_2^2 q_{22}]$$

$$b_1 = -\left(\frac{\beta}{2\alpha}\right) - \sqrt{\left(\frac{\beta}{2\alpha}\right)^2 - \frac{\gamma}{\alpha}}$$

$$b_2 = -\left(\frac{\beta}{2\alpha}\right) + \sqrt{\left(\frac{\beta}{2\alpha}\right)^2 - \frac{\gamma}{\alpha}}$$

$$q_{11} = A_3 b_1, \quad q_{21} = \omega^2 - A_2 \xi_1^2 - A_5 b_1$$

$$q_{12} = A_3 b_2, \quad q_{22} = \omega^2 - A_2 \xi_1^2 - A_5 b_2$$

$$\alpha = A_1 A_5, \quad \beta = (A_1 A_2 + A_5^2 - A_3^2)\xi_1^2 - \omega^2 (A_1 + A_5)$$

$$\gamma = (A_2 \xi_1^2 - \omega^2)\ (A_5 \xi_1^2 - \omega^2)$$

$$\zeta_1^2 = -\xi_2^2 + b_1, \quad \zeta_2^2 = -\xi_2^2 + b_2,$$

$$\zeta_3^2 = -\xi_2^2 + (\omega^2 - A_5 \xi_1^2)/A_4$$

subject to $\mathrm{Im}(\zeta_j) \geq 0$, $j = 1, 2, 3$.

(b) Two-Dimensional Case

$$[Q_{11}] = \begin{bmatrix} i\xi q_{11} & i\xi q_{12} \\ i\zeta_1 q_{21} & i\zeta_2 q_{22} \end{bmatrix}$$

$$[Q_{12}] = \begin{bmatrix} i\xi q_{11} & i\xi q_{12} \\ -i\zeta_1 q_{21} & -i\zeta_2 q_{22} \end{bmatrix}$$

$$[Q_{21}] = \begin{bmatrix} -C_{55}\xi\zeta_1 (q_{11}+q_{21}) & -C_{55}\xi\zeta_2 (q_{12}+q_{22}) \\ -C_{13} q_{11}\xi^2 - C_{33} q_{21}\zeta_1^2 & -C_{13} q_{12}\xi^2 - C_{33} q_{22}\zeta_2^2 \end{bmatrix}$$

$$[Q_{22}] = \begin{bmatrix} C_{55}\xi\zeta_1 (q_{11}+q_{21}) & C_{55}\xi\zeta_2 (q_{12}+q_{22}) \\ -C_{13} q_{11}\xi^2 - C_{33} q_{21}\zeta_1^2 & -C_{13} q_{12}\xi^2 - C_{33} q_{22}\zeta_2^2 \end{bmatrix}$$

Downloaded 03 May 2010 to 171.66.16.247. Redistribution subject to ASME license or copyright; see http://www.asme.org/terms/Terms_Use.cfm

$$\zeta_1^2 = b_1 = -\left(\frac{\beta}{2\alpha}\right) - \sqrt{\left(\frac{\beta}{2\alpha}\right)^2 - \frac{\gamma}{\alpha}}$$

$$\zeta_2^2 = b_2 = -\left(\frac{\beta}{2\alpha}\right) + \sqrt{\left(\frac{\beta}{2\alpha}\right)^2 - \frac{\gamma}{\alpha}}$$

subject to $\mathrm{Im}(\zeta_j) \geq 0$, $j = 1, 2$.

$$q_{11} = A_3 b_1, \quad q_{21} = \omega^2 - A_2\xi^2 - A_5 b_1$$

$$q_{12} = A_3 b_2, \quad q_{22} = \omega^2 - A_2\xi^2 - A_5 b_2$$

$$\alpha = A_1 A_5, \quad \beta = (A_1 A_2 + A_5^2 - A_3^2)\xi^2 - \omega^2(A_1 + A_5)$$

$$\gamma = (A_2\xi^2 - \omega^2)\ (A_5\xi^2 - \omega^2)$$

The matrix [**M**] for the approximate plate theory is defined as

$$\begin{bmatrix} -(A_{55}\xi_1^2 + A_{44}\xi_2^2 - \rho H\omega^2) & A_{55}\xi_1 i & A_{44}\xi_2 i \\ A_{55}\xi_1 i & D_{11}\xi_1^2 + D_{55}\xi_2^2 + A_{55} - \dfrac{\rho H^3}{12}\omega^2 & (D_{12} + D_{55})\xi_1\xi_2 \\ A_{44}\xi_2 i & (D_{12} + D_{55})\xi_1\xi_2 & D_{22}\xi_2^2 + D_{55}\xi_1^2 + A_{44} - \dfrac{\rho H^3}{12}\omega^2 \end{bmatrix}.$$

Downloaded 03 May 2010 to 171.66.16.247. Redistribution subject to ASME license or copyright; see http://www.asme.org/terms/Terms_Use.cfm

Elastodynamic Response of a Unidirectional Composite Laminate to Concentrated Surface Loads: Part II

Shyh-shiuh Lih
Assoc. Mem. ASME

Ajit K. Mal
Mem. ASME

Department of Mechanical, Aerospace and Nuclear Engineering, University of California, Los Angeles, CA 90024

The quantitative features of the elastodynamic field produced in a unidirectional graphite/epoxy composite laminate by surface loads are studied. The material of the composite is modeled as a transversely isotropic dissipative medium with its symmetry axis parallel to the laminate surface. The surface displacement produced by a transient concentrated point load on the surface of a uniform half-space and a plate of finite thickness is calculated by means of a multiple transform technique followed by inversion through numerical integration. The two-dimensional (plane-strain) line load problems for the plate are also solved as special cases. In addition, an approximate solution based on the classical plate bending theory which includes transverse shear and rotary inertia is obtained and the range of validity of the approximate solution is determined through comparison with the exact results. The multiple transform technique is shown to be a viable alternative to finite element and other numerically intensive computational schemes for wavefield calculations in composite laminates. The mathematical formulation of the problem was described in Part I of the paper, numerical treatment and results are presented in this part.

1 Introduction

We used a classical integral transform technique coupled with a matrix method to derive a formal solution of the point and line load problems for a composite laminate sketched in Fig. 1 in terms of wave number integrals in the frequency domain in Part I of this paper. In this paper, the integrals involved in the spatial inverse transform are evaluated by means of an adaptive integration scheme and the resulting spectra are inverted by FFT. Numerical results for the surface displacements are presented for several locations and for different time histories of the source.

2 Evaluation of the Wave Number Integrals

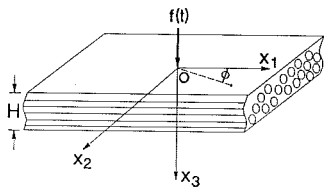
The typical wave number integral representation of the surface displacements derived in Part I is of the form

$$\int_{-\infty}^{\infty} h(\xi,\omega)e^{i\xi x_1}d\xi \tag{1}$$

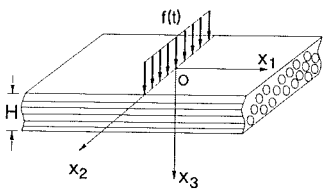
for two-dimensional problems and

$$\int_{-\infty}^{\infty}\int_{-\infty}^{\infty} g(\xi_1,\xi_2,\omega)e^{i(\xi_1 x_1+\xi_2 x_2)}d\xi_1 d\xi_2 \tag{2}$$

for three-dimensional problems. The functions g and h are obtained from complicated matrix computations as described in Part I and, in general, have oscillations and spikes inside the integration domain. These integrals cannot be evaluated



(a) Point load.



(b) Line load.

Fig. 1 Geometry of the problem

Contributed by the Applied Mechanics Division of THE AMERICAN SOCIETY OF MECHANICAL ENGINEERS for presentation at the 1992 ASME Winter Annual Meeting, Anaheim, CA, Nov. 8–13, 1992.

Discussion of this paper should be addressed to the Technical Editor, Prof. Leon M. Keer, The Technological Institute, Northwestern University, Evanston, IL 60208, and will be accepted until four months after final publication of the paper itself in the ASME JOURNAL OF APPLIED MECHANICS.

Manuscript received by the ASME Applied Mechanics Division, Feb. 12, 1990; final revision, July 11, 1991. Associate Technical Editor: S. K. Datta.

Paper No. 92-WA/APM-15.

Copyright © 1992 by ASME
Downloaded 03 May 2010 to 171.66.16.247. Redistribution subject to ASME license or copyright; see http://www.asme.org/terms/Terms_Use.cfm

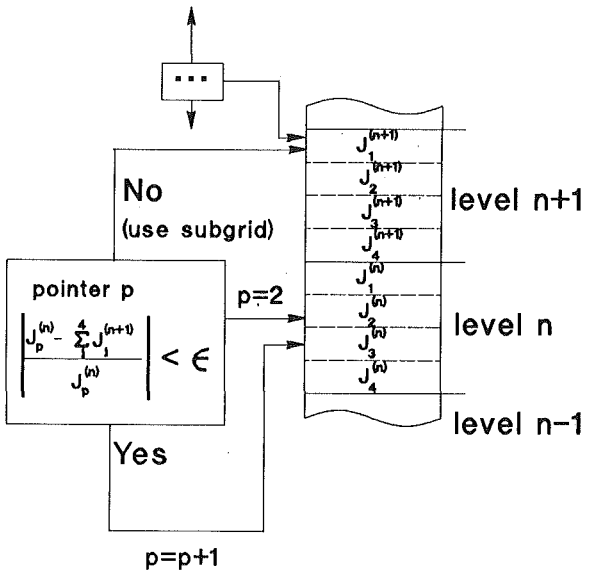


Fig. 2 Algorithm and data structure for adaptive surface-fitting integration

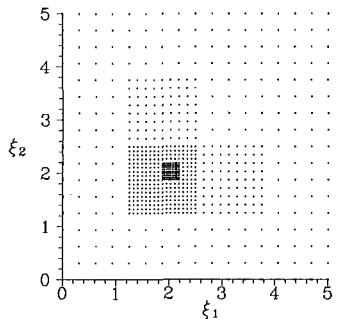


Fig. 3 Typical mesh for adaptive surface-fitting scheme

alytically and a number of difficulties are encountered in their numerical evaluation due to the special properties of their integrands. As pointed out in Part I, the integrands have an extremely irregular behavior which gets worse at higher frequencies and causes considerable difficulty in the numerical evaluation of the integrals.

2.1 The Adaptive Surface-Fitting Scheme. Several methods are available to evaluate the one-dimensional wave number integral (e.g., Davis andRobinnowich, 1975; Longman, 1960). The so-called modified Clenshaw-Curtis quadrature scheme suggested by Xu and Mal (1985, 1987) has been found to work quite well (see Dravinski and Mossesian (1987) for a comparative study) for single integrals due to its adaptive nature. To the authors' knowledge, no efficient integration schemes are available to evaluate wave number integrals involved in the solution of the three-dimensional problem.

In order to carry out the integration efficiently, we introduce an "adaptive surface-fitting" method here. To illustrate the general features of the method consider the double integral

$$I_s=\int_{\beta_1}^{\beta_2}\int_{\alpha_1}^{\alpha_2} g_s(\xi_1,\xi_2)e^{i(\xi_1X_1+\xi_2X_2)}d\xi_1 d\xi_2 \tag{3}$$

where g_s is a bi-quadratic function of the form

$$g_s=C_1+C_2\xi_1+C_3\xi_2+C_4\xi_1^2+C_5\xi_1\xi_2 + C_6\xi_2^2+C_7\xi_1^2\xi_2+C_8\xi_1\xi_2^2+C_9\xi_1^2\xi_2^2 \tag{4}$$

and C_i (i = 1,9), are constants. If we change variables by letting

$$\xi_1=(\alpha_1+\alpha_2)/2+[(\alpha_2-\alpha_1)/2]\zeta_1\equiv A_1+A_2\zeta_1 \tag{5a}$$

$$\xi_2=(\beta_1+\beta_2)/2+[(\beta_2-\beta_1)/2]\zeta_2\equiv B_1+B_2\zeta_2 \tag{5b}$$

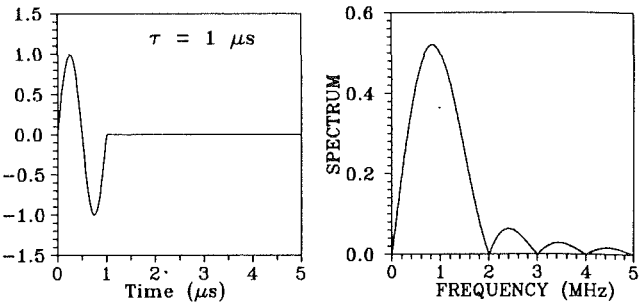


Fig. 4 Time history and spectrum of source function for τ = 1 μs

Table 1 Material constants of the graphite/epoxy composite used in the calculations

Mass density (g/cm^3)	C_{11}	C_{12}	C_{22}	C_{23}	C_{55}(Gpa)	p_0	f_0	a_0
1.578	160.73	6.44	13.92	6.92	7.07	.005	.3	.1

then I_s becomes

$$I_s=k\int_{-1}^{1}\int_{-1}^{1} g_o(\zeta_1,\zeta_2)e^{i(\zeta_1x_1+\zeta_2x_2)}d\zeta_1 d\zeta_2 \tag{6}$$

where

$$k=A_2B_2e^{i(A_1+B_1)},\ x_1=A_2X_1,\ x_2=B_2X_2 \tag{7}$$

and

$$g_0=c_1+c_2\zeta_1+c_3\zeta_2+c_4\zeta_1^2+c_5\zeta_1\zeta_2+c_6\zeta_2^2+c_7\zeta_1^2\zeta_2 + c_8\zeta_1\zeta_2^2+c_9\zeta_1^2\zeta_2^2. \tag{8}$$

Hence, I_s can be integrated analytically as

$$I_s=\sum_{i=1}^{9}c_iS_i \tag{9}$$

where

$S_1=I_0(x_1)I_0(x_2),\ S_2=I_1(x_1)I_0(x_2),\ S_3=I_0(x_1)I_1(x_2),$
$S_4=I_2(x_1)I_0(x_2),\ S_5=I_1(x_1)I_1(x_2),\ S_6=I_0(x_1)I_2(x_2),$
$S_7=I_2(x_1)I_1(x_2),\ S_8=I_1(x_1)I_2(x_2),\ S_9=I_2(x_1)I_2(x_2)$

and

$$I_0(x)=\int_{-1}^{1}e^{ix\zeta}d\zeta=\frac{2\sin(x)}{x}$$

$$I_1(x)=\int_{-1}^{1}\zeta e^{ix\zeta}d\zeta=[I_0-2\cos(x)]\frac{i}{x}$$

$$I_2(x)=\int_{-1}^{1}\zeta^2e^{ix\zeta}d\zeta=I_0+2I_1\frac{i}{x}.$$

Thus, if a function $g(\xi_1, \xi_2)$ in a region $-\alpha_1 \le \xi_1 \le \alpha_2$, $-\beta_1 \le \xi_2 \le \beta_2$ can be fitted as $g_s(\xi_1, \xi_2)$ through node points $p_1 - p_9$ with function values $g_1 - g_9$, then the integration can be carried out as in (9). The coefficients c_i can be evaluated as

$$c_1=g_5,\ c_2=(-g_4+g_6)/2,$$
$$c_3=(-g_2+g_8)/2,\ c_4=(g_4-2g_5+g_6)/2$$
$$c_5=(g_1-g_3-g_7+g_9)/4,\ c_6=(g_2-2g_5+g_8)/2$$
$$c_7=(-g_1+2g_2-g_3+g_7-2g_8+g_9)/4$$
$$c_8=(-g_1+g_3+2g_4-2g_6-g_7+g_9)/4$$
$$c_9=(g_1-2g_2+g_3-2g_4+4g_5-2g_6+g_7-2g_8+g_9)/4. \tag{10}$$

The integration scheme can also be made adaptive as follows. If we divide the integration domain into four grids, the integral over each grid can be evaluated as $J_1^{(1)}$, $J_2^{(1)}$, $J_3^{(1)}$, $J_4^{(1)}$. Next we subdivide this grid into four grids again, and evaluate the

Downloaded 03 May 2010 to 171.66.16.247. Redistribution subject to ASME license or copyright; see http://www.asme.org/terms/Terms_Use.cfm

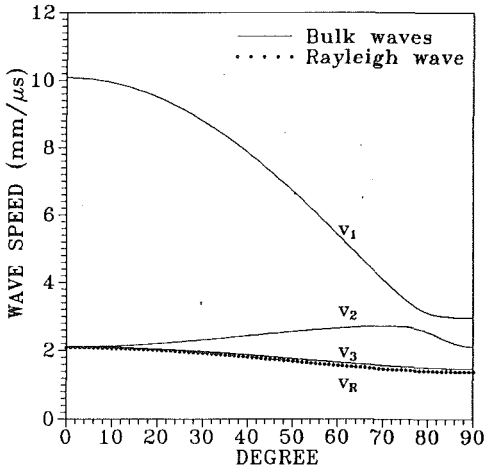


Fig. 5 Velocities of the bulk and Rayleigh waves on the x_1x_2-plane

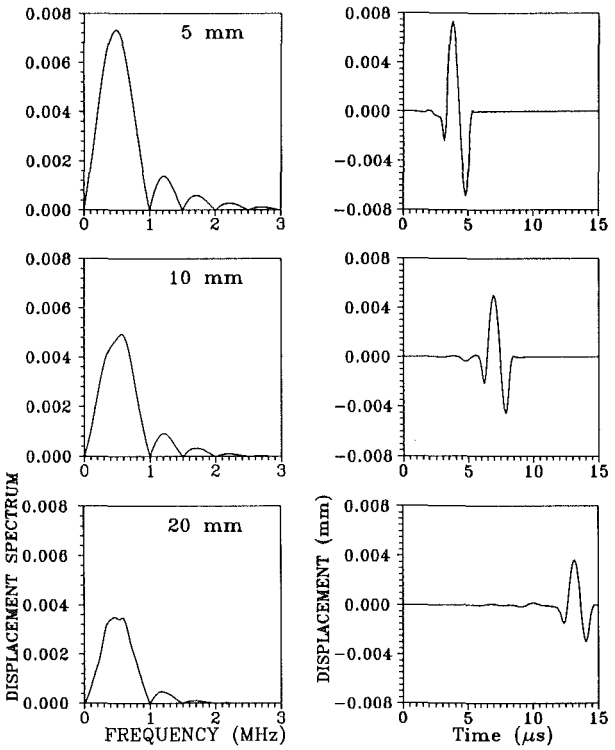


Fig. 6 Spectra and time histories of normal displacement u_3 on a half-space at three locations: 5, 10, and 20 mm from source along at 45 deg to the fibers for $\tau = 2$ μs

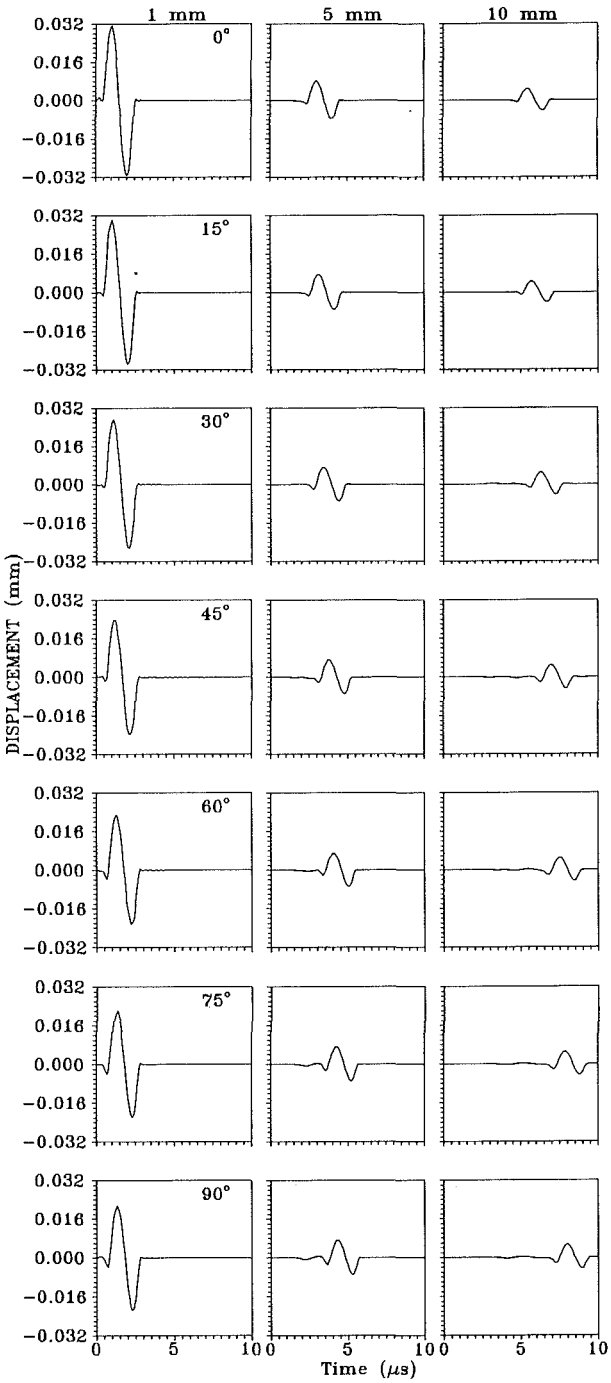


Fig. 7 Time histories of the normal surface displacement on the half-space for $\tau = 2$ μs

integral over the subgrids as $J_1^{(2)}$, $J_2^{(2)}$, $J_3^{(2)}$, $J_4^{(2)}$ and check whether the following criterion is satisfied or not:

$$|[J_1^{(1)} - (J_1^{(2)} + J_2^{(2)} + J_3^{(92)} + J_4^{(2)})]/J_1^{(1)}| \leq \epsilon \qquad (11)$$

where ϵ is a specified tolerance. If (11) is not satisfied, we continue to subdivide each subgrid into four grids until this criterion is satisfied. The associated algorithm is shown in Fig. 2. An additional advantage of this algorithm is that the function values $g(\xi_1, \xi_2)$ can be saved by using limited memories with a stack data structure as shown in Fig. 2. In the algorithm, the parts of the function $g(\xi_1, \xi_2)$ that are evaluated are popped into the stack and popped out when needed. A typical mesh of the integration domain for this method is shown in Fig. 3; it can be seen that a dense mesh is used only near the region where the function changes rapidly.

It should be noted that a repeated one-dimensional integration approach may be used for the double integration, but it is less efficient than the adaptive surface-fitting method described above, since it wastes many calculated function values at points away from the spikes.

3 Numerical Results

In all of the calculations presented here, the source function is assumed to be the delayed sine pulse of time duration τ,

$$f(t) = \sin(2\pi t/\tau),\ 0 < t < \tau. \qquad (12)$$

In order to examine the nature and extent of numerically generated noise before the arrival of the source-generated disturbances at the receiver, a delay of 5 μs was temporarily introduced in the source function. Unacceptable levels of noise are eliminated by refinement of one or more of the various meshes involved in the calculations; the delay was removed

Downloaded 03 May 2010 to 171.66.16.247. Redistribution subject to ASME license or copyright; see http://www.asme.org/terms/Terms_Use.cfm

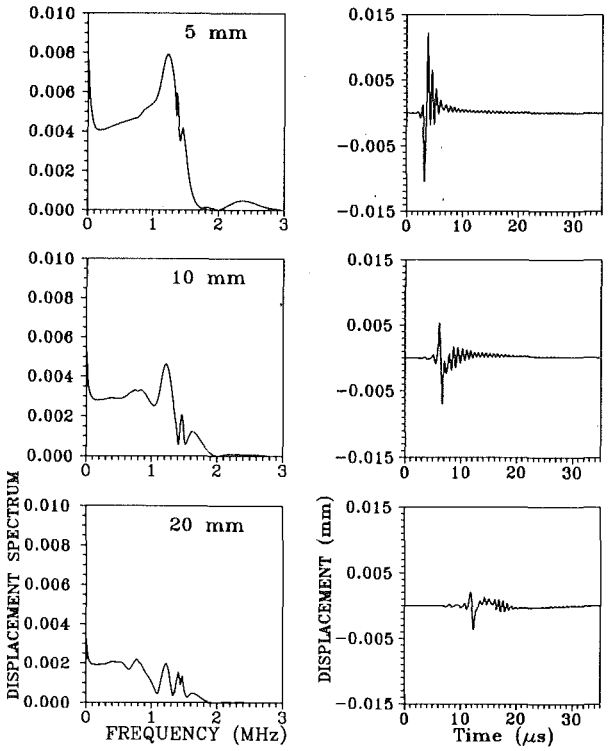


Fig. 8 Spectra and time histories of normal displacement u_3 on a 1-mm thick plate at three locations: 5, 10, 20 mm from source at 45 deg to the fibers for $\tau = 1$ μs

before the time histories were plotted. The values of τ are assumed to be in the range 1 to 10 μs. The source function and its spectra are plotted in Fig. 4 for $\tau = 1$ μs. It can be seen that the source spectrum is maximum at 1 MHz and becomes negligibly small beyond about 5 MHz. Thus, the numerical evaluation of the integrals is restricted to the range $0 < f < 5$ MHz.

The calculations are carried out for the normal component of the surface displacement at different distances from the source and for different orientation angles, ϕ. In order to discuss the nature of the various waves involved in producing the surface motion, it is necessary to determine the velocity of the waves along these directions and also their arrival times at the three locations. In the case of the half-space, the possible waves are the bulk waves and the Rayleigh wave propagating parallel to its surface. The velocities of these waves are denoted by v_1, v_2, v_3, and v_R, respectively, in descending order of magnitude, and assuming perfectly elastic material properties given in Table 1 are plotted in Fig. 5.

The calculated displacements for the half-space with loading time $\tau = 2$ μs are shown in Figs. 6 and 7. In Fig. 6, the amplitude spectra and time histories of the normal surface displacement at three field points on a line inclined at 45 degrees to the fibers are plotted. It can be seen that the spectra becomes quite small beyond about 2.5 MHz and that their general shape is similar to that of the source spectrum. The velocities of the bulk waves and the Rayleigh wave along this direction are given by (Fig. 5) $v_1 = 7.31$ mm/μs, $v_2 = 2.5$ mm/μs, $v_3 = 1.83$ mm/μs, $v_R = 1.75$ mm/μs. Their arrival times at 10-mm distance are, 1.37 μs, 4 μs, 5.47 μs, and 5.71 μs, respectively. It can be seen that the motion at these field points are produced primarily by a bulk wave of speed v_2 which arrives first with a small amplitude, and the Rayleigh wave which follows carrying a large amplitude; the other two waves have very small amplitudes. The time histories of the normal surface displacement at distances 1 mm, 5 mm, and 10 mm, from the source along different directions relative to the fibers are plotted in

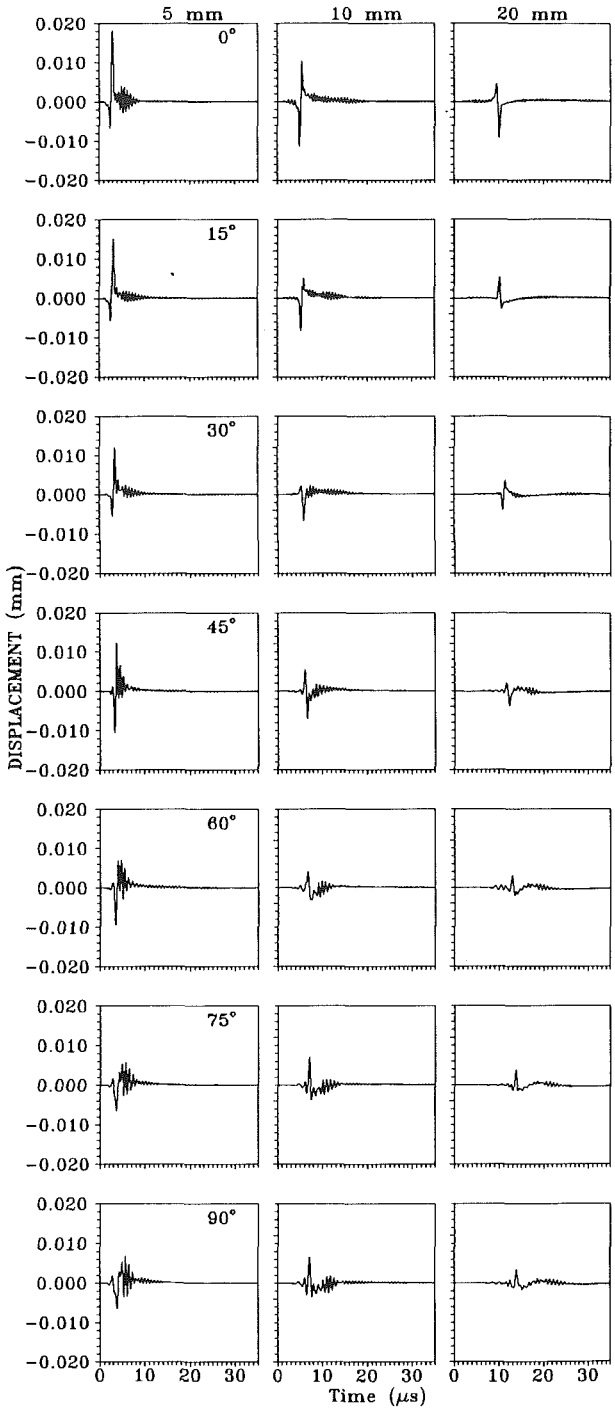


Fig. 9 Time histories of the normal surface displacement on the 1-mm thick plate for $\tau = 1$ μs

Fig. 7. It can be seen that the normal component of the motion is relatively simple and is not as strongly influenced by the anisotropy as one would expect; the most significant effect is on the arrival time of the Rayleigh pulse due to the variation in its propagation speed as specified in Fig. 5. For propagation along 0 deg, the P-wave cannot be seen since its amplitude is quite small, while in the case of propagation at 90 deg, the P-wave with a small amplitude arrives first followed by the transverse and Rayleigh waves, which arrive almost together.

The frequency spectra and time histories of the normal surface displacement for a 1-mm thick plate are shown in Fig. 8 for $\tau = 1$ μs. It can be seen that the spectra become very small beyond 3 MHz and the major contribution to the surface

Downloaded 03 May 2010 to 171.66.16.247. Redistribution subject to ASME license or copyright; see http://www.asme.org/terms/Terms_Use.cfm

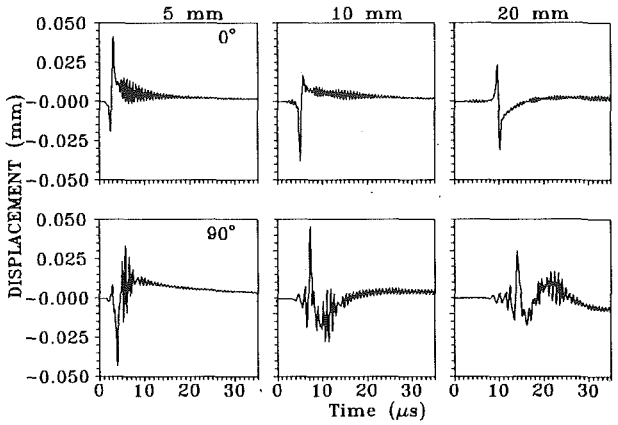


Fig. 10 Time histories of the normal displacement u_3 on a 1-mm thick plate at three locations: 5, 10, 20 mm from source for uniform line load along x_1 (0 deg) and along x_2 (90 deg) for $\tau = 1$ μs

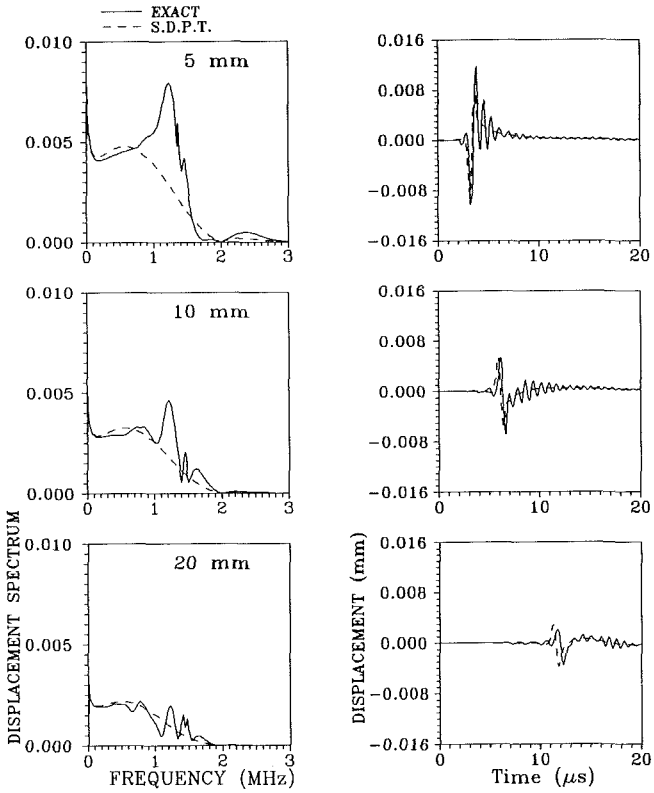


Fig. 11 Comparison between results obtained from exact and shear deformation plate theories: spectra and time histories of normal displacement at three locations: 5, 10, 20 mm from source along 45 deg on a 1-mm thick plate for $\tau = 1$ μs

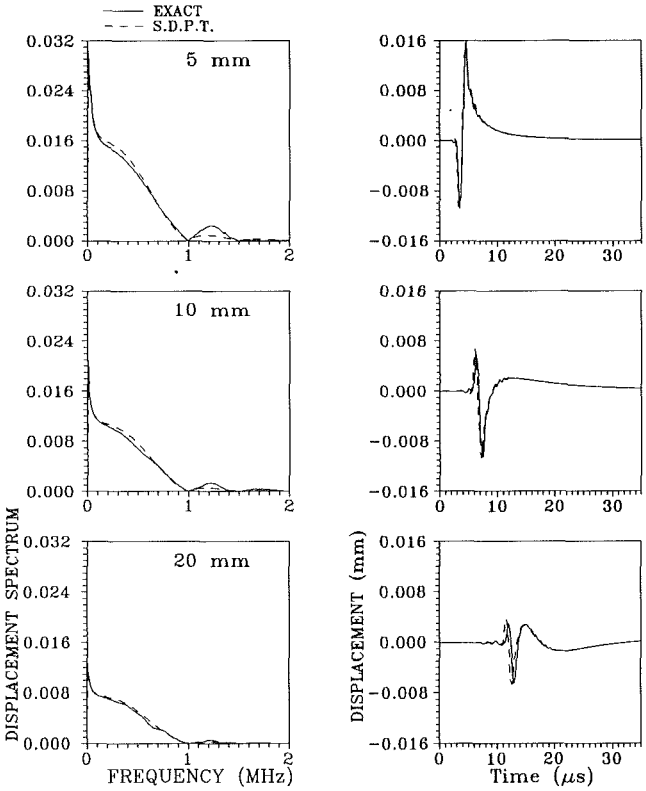


Fig. 12 Same as Fig. 11 for $\tau = 2$ μs

displacement comes from the antisymmetric guided waves which have different propagation speeds along different directions. The spectra contain local peaks around $f = 1.485$ MHz, associated with the first cutoff frequency and this introduces the high-frequency components in the time histories. The pulse shape is significantly distorted due to the interaction of the waves with the free surfaces of the plate and the surface material comes to rest gradually after the passage of the main pulse. The time histories at different field points on the surface of the 1-mm thick plate for $\tau = 1$ μs are plotted in Fig. 9. The figure again shows the strong contribution of the plate-guided waves to the surface motion at all the field points. The high-frequency motion associated with the cutoff frequency can be seen to be present everywhere, its influence is stronger for propagation away from the fiber direction.

The results for the two-dimensional (in-plane) case of a uniform line load along x_2-axis and along the x_1-axis, are presented in Fig. 10 for $\tau = 1$ μs. It can be seen that the two-dimensional results are qualitatively similar to those for the three-dimensional case. However, the amplitudes of the displacements in the three-dimensional case are smaller since the geometrical decay is stronger.

Finally, the results obtained from approximate shear deformation plate theory are compared with the exact results in Figs. 11-13 for propagation at 45 deg to the fibers and for different values of τ. The results by plate theory consist of dispersive flexural waves; the approximate and exact dispersion curves for the phase and group velocities are compared with the exact curves in Fig. 14. The flexural wave speed from plate theory diverges from the exact theory when the frequency increases. Thus, the approximate curves always overestimate the group velocity. As an example, in Fig. 11, where $\tau = 1$ μs, the flexural wave can be seen to arrive much earlier than the first wave arrival predicted from the exact theory. For $\tau = 5$ μs (Fig. 13), the time histories are closer as expected since lower frequencies dominate the response in this case. When the loading time is longer ($\tau > 2$ μs), the spectra calculated by the two methods are almost identical at frequencies less than .1 MHz. The pulse shapes calculated from the two approaches are quite close for larger values of τ, but the pulses gradually separate as the distance from the source increases due to the overestimation of the flexural wave speed in the approximate theory.

4 Concluding Remarks

The proposed multiple transform technique appears to work well and yields accurate surface displacements for the simple three-dimensional point load problem of the homogeneous

Downloaded 03 May 2010 to 171.66.16.247. Redistribution subject to ASME license or copyright; see http://www.asme.org/terms/Terms_Use.cfm

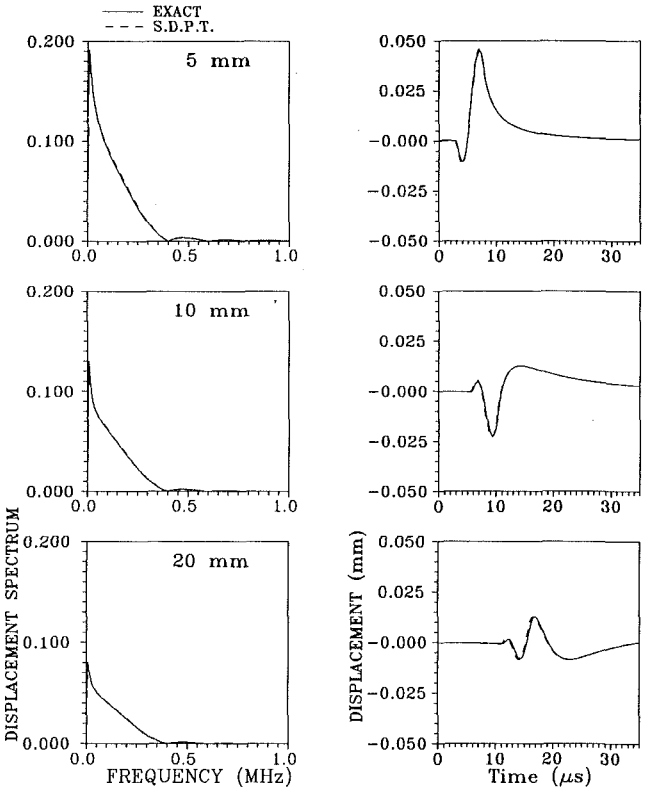


Fig. 13 Same as Fig. 11 for $\tau = 5$ μs

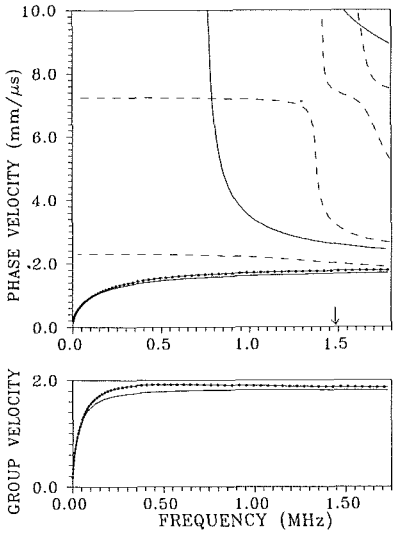


Fig. 14 Dispersion curves for a 1-mm thick graphite/epoxy plate using exact theory (dashed curves for anti-symmetric modes, solid curves for symmetric modes) and shear deformation plate theory (solid circles) for propagation at 45 deg to fibers. Location of the first cutoff frequency for the symmetric mode is indicated by the arrow.

half-space and plate composed of graphite/epoxy. The technique can be applied to more realistic multilayered models of the half-space and plate in a straightforward manner. Although the associated numerical codes are CPU-intensive, they should be much more efficient than other available codes for the analysis of three-dimensional models. The codes are currently being extended to deal with problems involving angle-ply laminates subjected to a variety of surface and subsurface loads.

5 Acknowledgments

This research was supported by the Mechanics Division of the Office of Naval Research under Grant N00014-90-J-1857, monitored by Dr. Yapa D. S. Rajapakse. Support was also provided by the Scientific and Environmental Affairs Division of NATO under Grant CRG.890243. Computer time was provided by the Office of Academic Computing of UCLA.

6 References

Dravinski, M., and Mossessian, T. K., 1988, "On the Evaluation of the Green's Functions for Harmonic Line Loads in a Viscoelastic Half-Space," *Int. J. Numerical Methods in Engineering*, Vol. 26, pp. 823-841.

Kundu, T., and Mal, A. K., 1985, "Elastic Waves in a Multilayered Solid due to a Dislocation Source," *Wave Motion*, Vol. 7, pp. 459-471.

Mal, A. K., and Lih, S. -S., "Elastodynamic Response of a Unidirectional Composite Laminate to Concentrated Surface Loads: Part I," ASME Journal of Applied Mechanics, Vol. 59.

Vasudevan, N., and Mal., A. K., 1985, "Response of an Elastic Plate to Localized Transient Sources," ASME Journal of Applied Mechanics, Vol. 52, pp. 356-362.

Xu, P.-C., and Mal, A. K., 1985, "An Adaptive Integration Scheme for Irregularly Oscillating Functions," *Wave Motion*, Vol. 7, pp. 235-243.

Xu, P.-C., and Mal, A. K., 1987, "Calculation of the Green's Functions for a Layered Viscoelastic Solid," *Bull. Seism. Soc. Am.*, Vol. 77, pp. 1823-1837.

Downloaded 03 May 2010 to 171.66.16.247. Redistribution subject to ASME license or copyright; see http://www.asme.org/terms/Terms_Use.cfm

Nonlinear Dynamics of In-Plane Loaded Imperfect Rectangular Plates

Alavandi Bhimaraddi[1]
Department of Mechanical and Aerospace Engineering and Engineering Mechanics, University of Missouri-Rolla, Rolla, MO 65401-0249
Mem. ASME

This paper deals with the nonlinear vibrations of composite laminated plates using the generalized formulation of which the von Karman-type formulation is a special case. The two-dimensional plate theory used is that of a parabolic shear theory in which the transverse shear strain distribution is parabolic across the plate thickness. The resulting governing equations of this formulation are nonlinear is all the plate displacement parameters unlike the von Karman model in which they are nonlinear in the lateral displacement only. Because of this complex nature of the equations the usual approach for nonlinear plate analysis cannot be used, and hence a regular perturbation technique has been adopted to obtain the solution of these equations. All the complexities like the initial imperfections and in-plane applied edge loads have also been included in the analysis. Numerical examples for simply-supported plates indicate that for in-plane loaded imperfect plates, the von Karman formulation differs slightly when compared with the present more general formulation.

Introduction

Structural applications of laminated composite plates are ever on the increase due to their desirable material characteristics. As a result, analysis of such structures is gaining considerable importance over the years. It is now well known that the analysis of composite plates requires the use of shear deformation theories. Especially for composite laminated plates, one requires the use of parabolic shear theory (see, e.g., Bhimaraddi, 1987a). Many authors have treated the problem of nonlinear response of plates in the presence (or absence) of the applied in-plane edge forces. Discussion on the nature of the complexities involved in the nonlinear analysis of composite plates can be obtained in the excellent summary papers by Bert (1982) and Leissa (1981). Most recent works dealing with the nonlinear plate problems have also been summarized in a book by Chia (1980) and in a very recent article by Sathyamoorthy (1987).

The influence of in-plane loading, initial imperfections, in-plane inertia, and the geometric nonlinearities (taken individually) on the dynamic response of structures has been considered extensively by Bolotin (1964) for isotropic plates. For the first time, Pasic and Herrmann (1984) gave a general formulation for the nonlinear isotropic plate problem treating all these parameters simultaneously. Bhimaraddi (1989b) extended the work of Pasic and Herrmann (1984) to composite orthotropic plates incorporating the shear deformation effects according to the parabolic shear theory (Bhimaraddi and Stevens, 1984; Bhimaraddi, 1987a). In these works the regular perturbation theory was applied to obtain the solution. Using the parabolic shear theory, Bhimaraddi (1987b, 1989a) has also studied the nonlinear vibrations of imperfect laminated plates in the presence of in-plane loads. Some discussion on the available literature on the vibration of plates with in plane edge loads may be found in Bhimaraddi (1987b).

It is clear from the summary papers mentioned that most of the work on nonlinear plate problems is related to the analysis of plates by using the nonlinear plate theory within the domain of von Karman-type large displacement model. In this model, nonlinearity arises due to the retention of the product of rotations $(\partial w/\partial x)$ and $(\partial w/\partial y)$ in the in-plane strain expressions, and thus the products of in-plane displacement gradients are neglected. This results in a much simpler formulation (compared to that which considers full nonlinearity) in which the governing equations are nonlinear in lateral displacement (w) only.

It is difficult to take into account the effects of in-plane inertia in the nonlinear plate analysis if one performs a straightforward analysis such as those by Bhimaraddi (1987b, 1989a). Also, such analyses are restricted to von Karman-type nonlinear plate problems which are basically nonlinear in (w) only. If one formulates a fully nonlinear plate problem, it would involve nonlinearities in other displacements of the plate. In such cases it becomes impossible to apply the straightforward methods mentioned to obtain the solution to the governing nonlinear differential equations. That is the reason why the von Karman-type analysis has been used successfully and has been the favorite nonlinear model all these years.

[1]Currently at DCED, Clawson, MI 48017.

Contributed by the Applied Mechanics Division of THE AMERICAN SOCIETY OF MECHANICAL ENGINEERS for publication in the ASME JOURNAL OF APPLIED MECHANICS.

Discussion on this paper should be addressed to the Technical Editor, Professor Leon M. Keer, The Technological Institute, Northwestern University, Evanston, IL 60208, and will be accepted until four months after final publication of the paper itself in the JOURNAL OF APPLIED MECHANICS.

Manuscript received by the ASME Applied Mechanics Division, Apr. 12, 1991; final revision, July 5, 1991. Associate Technical Editor: S. K. Datta.

Copyright © 1992 by ASME
Downloaded 03 May 2010 to 171.66.16.247. Redistribution subject to ASME license or copyright; see http://www.asme.org/terms/Terms_Use.cfm

It has been indicated by Bhimaraddi (1989b) that the regular perturbation method enables one to consider the inclusion of in-plane inertias. The power and usefulness of this perturbation method has been extended here to obtain the solution of the fully nonlinear plate problem. To keep the formulation fairly general, the problem addressed in this paper simultaneously includes: the initial imperfections, symmetrically laminated cross-ply orientation, the presence of in-plane edge loads, effects of shear deformation according to the parabolic shear theory, and the in-plane inertia. In what follows next we present the background equations relevant to the present paper.

Derivation of Basic Equations

Consider a cartesian coordinate system (x,y,z) and let (x,y) be the in-plane coordinates of the middle surface of the plate and z be the transverse coordinate, normal to the plate middle surface. The Green-Lagrange strain-displacement relations are written as (Saada, 1974),

$$\epsilon_x=\frac{\partial \hat{u}}{\partial x}+\frac{1}{2}\left(\frac{\partial \hat{u}}{\partial x}\right)^2+\frac{1}{2}\left(\frac{\partial \hat{v}}{\partial x}\right)^2+\frac{1}{2}\left(\frac{\partial \hat{w}}{\partial x}\right)^2$$

$$\epsilon_y=\frac{\partial \hat{v}}{\partial y}+\frac{1}{2}\left(\frac{\partial \hat{u}}{\partial y}\right)^2+\frac{1}{2}\left(\frac{\partial \hat{v}}{\partial y}\right)^2+\frac{1}{2}\left(\frac{\partial \hat{w}}{\partial y}\right)^2$$

$$\epsilon_z=\frac{\partial \hat{w}}{\partial z}+\frac{1}{2}\left(\frac{\partial \hat{u}}{\partial z}\right)^2+\frac{1}{2}\left(\frac{\partial \hat{v}}{\partial z}\right)^2+\frac{1}{2}\left(\frac{\partial \hat{w}}{\partial z}\right)^2$$

$$\gamma_{xy}=\frac{\partial \hat{u}}{\partial y}+\frac{\partial \hat{v}}{\partial x}+\left(\frac{\partial \hat{u}}{\partial x}\right)\left(\frac{\partial \hat{u}}{\partial y}\right)+\left(\frac{\partial \hat{v}}{\partial x}\right)\left(\frac{\partial \hat{v}}{\partial y}\right)+\left(\frac{\partial \hat{w}}{\partial x}\right)\left(\frac{\partial \hat{w}}{\partial y}\right)$$

$$\gamma_{xz}=\frac{\partial \hat{u}}{\partial z}+\frac{\partial \hat{w}}{\partial x}+\left(\frac{\partial \hat{u}}{\partial x}\right)\left(\frac{\partial \hat{u}}{\partial z}\right)+\left(\frac{\partial \hat{v}}{\partial x}\right)\left(\frac{\partial \hat{v}}{\partial z}\right)+\left(\frac{\partial \hat{w}}{\partial x}\right)\left(\frac{\partial \hat{w}}{\partial z}\right)$$

$$\gamma_{yz}=\frac{\partial \hat{v}}{\partial z}+\frac{\partial \hat{w}}{\partial y}+\left(\frac{\partial \hat{u}}{\partial y}\right)\left(\frac{\partial \hat{u}}{\partial z}\right)+\left(\frac{\partial \hat{v}}{\partial y}\right)\left(\frac{\partial \hat{v}}{\partial z}\right)+\left(\frac{\partial \hat{w}}{\partial y}\right)\left(\frac{\partial \hat{w}}{\partial z}\right). \tag{1}$$

Here, $\hat{u}$, $\hat{v}$, and $\hat{w}$ are the displacements at any point (x,y,z) in the x-, y-, and z-direction, respectively. It is customary while formulating the two-dimensional plate theory to neglect the influence of transverse normal strain (ϵ_z) and stress (σ_z). Hence, one can write the following stress and strain relations for an orthotropic material:

$$\sigma_x=C_{11}\epsilon_x+C_{12}\epsilon_y;\quad \sigma_y=C_{12}\epsilon_x+C_{22}\epsilon_y$$
$$\tau_{xy}=C_{66}\gamma_{xy};\quad \tau_{xz}=C_{44}\gamma_{xz};\quad \tau_{yz}=C_{55}\gamma_{yz}. \tag{2}$$

As is normally done in the displacement-based plate theories, we start with the assumed displacement forms of the following type:

$$\hat{u}=u+\xi\phi-z\partial w/\partial x;\quad \hat{v}=v+\xi\psi-z\partial w/\partial y;\quad \hat{w}=w$$
$$\xi=z(1-4z^2/3h^2);\quad d\xi/dz=\xi^*=(1-4z^2/h^2). \tag{3}$$

In these equations u, v, and w are the middle-surface displacement components in the x-, y-, and z-direction, respectively; ϕ and ψ are the shear rotations in addition to the usual flexural rotations $\partial w/\partial x$ and $\partial w/\partial y$; and h is the total plate thickness ($h_1,h_2,\ldots$ being the individual layer thicknesses in the case of laminated plates). The detailed discussion on the selection of these displacement forms may be found in other publications of Bhimaraddi (1984, 1987a). It may be noted here that u, v, w, ϕ, and ψ are functions of (x,y) only and they are independent of the coordinate z; ξ is a cubic polynomial in z.

The definitions for the stress resultants (forces and moments) and the integrated stiffness values for the plate, appropriate to the displacement forms of Eqs. (3), can be written as

$$\begin{bmatrix} n_x & n_y & n_{xy} \\ m_x & m_y & m_{xy} \\ \overline{m}_x & \overline{m}_y & \overline{m}_{xy} \end{bmatrix}=\int_{-h/2}^{h/2}\begin{bmatrix} 1 \\ -z \\ \xi \end{bmatrix}\{\sigma_x\ \sigma_y\ \tau_{xy}\}dz;$$

$$\{\overline{q}_x\ \overline{q}_y\}=\int_{-h/2}^{h/2}\xi^*\{\tau_{xz}\ \tau_{yz}\}dz \tag{4}$$

$$(a_{ij}\ d_{ij}\ \overline{d}_{ij}\ \overline{\overline{d}}_{ij})=\int_{-h/2}^{h/2}C_{ij}(1\ z^2\ z\xi\ \xi^2)dz$$

$$(e\ g\ \overline{g}\ \overline{\overline{g}})=\int_{-h/2}^{h/2}\rho(1\ z^2\ z\xi\ \xi^2)dz;\quad \overline{a}_{ij}=\int_{-h/2}^{h/2}C_{ij}\xi^{*2}dz. \tag{5}$$

In the case of a composite laminated plate problem, the integration in the above equations has to be performed, keeping in mind the heterogeneous nature of the plate thickness. Before proceeding further, it is advantageous to non-dimensionalize all the quantities as follows:

$$(X,Y,\delta,U,V,W)=\frac{1}{a}\ (x,y,h,u,v,w);\quad Z=\frac{z}{h};\quad r=\frac{a}{b};$$

$$W_i=\frac{w_i}{\delta a};\quad (A_{ij},\overline{A}_{ij},\overline{Q}_x,\overline{Q}_y)=\frac{1}{K}\ (a_{ij},\overline{a}_{ij},\overline{q}_x,\overline{q}_y);\quad \tau=t\,\frac{\delta}{a}\sqrt{\frac{K}{\rho h}};$$

$$K=\frac{E_y h}{1-\nu_1\nu_2};\quad (D_{ij},\overline{D}_{ij},\overline{\overline{D}}_{ij})=\frac{1}{Kh^2}\ (d_{ij},\overline{d}_{ij},\overline{\overline{d}}_{ij});$$

$$(G,\overline{G},\overline{\overline{G}})=\frac{1}{\rho h^3}\ (g,\overline{g},\overline{\overline{g}});\quad Q=\frac{aq_0}{K\delta^2};\quad E=\frac{e}{\rho h};$$

$$(N_x,N_y,N_{xy})=\frac{1}{K}\ (n_x,n_y,n_{xy});\quad (N_x^*,N_y^*)=\frac{1}{K\delta^2}\ (n_x^*,n_y^*);$$

$$(M_x,M_y,M_{xy},\overline{M}_x,\overline{M}_y,\overline{M}_{xy})=\frac{1}{Kh}\ (m_x,m_y,m_{xy},\overline{m}_x,\overline{m}_y,\overline{m}_{xy});\quad \lambda=\frac{n_x^*}{n_y^*} \tag{6}$$

Here, a and b are the length and width of plate, t is the time coordinate; E_y is the elastic modulus in the y-direction; ν_1 and ν_2 are the Poisson's ratios; w_i is the initial imperfection of the plate; ρ is the mass density of the plate material; q_o is the intensity of the lateral loading (in the z-direction) on the plate surface; and n_x and n_y are the applied in-plane loads on the edges of the plate in the x- and y-direction, respectively. Inserting the assumed displacements (3) in the strain-displacement relations (1) we obtain the following set of strain-displacement relations relevant to the current study:

$$\epsilon_x=U'+\frac{1}{2}\underline{(U'^2+V'^2+W'^2)}$$
$$-\delta Z(W''+\underline{W''U'+W'^oV'})+\delta\Xi(\phi'+\underline{\phi'U'+\psi'V'})$$

$$\epsilon_y=V^o+\frac{1}{2}\underline{(U^{o2}+V^{o2}+W^{o2})}$$
$$-\delta Z(W^{oo}+\underline{W^{oo}V^o+W'^oU^o})+\delta\Xi(\psi^o+\underline{\psi^oV^o+\phi^oU^o})$$

$$\gamma_{xy}=U^o+V'+\underline{U'U^o+V'V^o}+W'W^o$$
$$-\delta Z(2W'^o+\underline{W'^oU'+W''U^o+W'^oV^o+W^{oo}V'})$$
$$+\delta\Xi(\phi^o+\psi'+\underline{\phi^oU'+\phi'U^o+\psi^oV'+\psi'V^o})$$

$$\gamma_{xz}=\Xi^*\phi;\quad \gamma_{yz}=\Xi^*\psi;\quad \Xi=Z\left(1-\frac{4}{3}Z^2\right);\quad \Xi^*=(1-4Z^2) \tag{7}$$

Here, $(\ )'$ and $(\ )^o$ indicate differentiation with respect to X and Y, respectively. In arriving at the above strain relations we have neglected all coefficients of Z^2, $Z\Xi$, Ξ^2 and the nonlinear terms in transverse shear strains. It may be noted here that the underlined terms are the extra terms that appear when the generalization of the von Karman-type model is made.

Downloaded 03 May 2010 to 171.66.16.247. Redistribution subject to ASME license or copyright; see http://www.asme.org/terms/Terms_Use.cfm

Substituting the strain-displacement relations (7) in the stress resultant definitions and performing the indicated integration, one can obtain the following relations for stress resultants:

$$\begin{bmatrix} N_x \\ N_y \\ N_{xy} \end{bmatrix} = \begin{bmatrix} A_{11} & A_{12} & 0 \\ A_{12} & A_{22} & 0 \\ 0 & 0 & A_{66} \end{bmatrix} \begin{bmatrix} U' + \frac{1}{2}(U'^2 + V'^2 + W'^2) \\ V^o + \frac{1}{2}(U^{o2} + V^{o2} + W^{o2}) \\ U^o + V' + U'U^o + V'V^o + W'W^o \end{bmatrix} \tag{8}$$

$$\begin{bmatrix} M_x \\ M_y \\ M_{xy} \\ \overline{M}_x \\ \overline{M}_y \\ \overline{M}_{xy} \end{bmatrix} = \begin{bmatrix} D_{11} & D_{12} & 0 & -D_{11} & -\overline{D}_{12} & 0 \\ D_{12} & D_{22} & 0 & -\overline{D}_{12} & -\overline{D}_{22} & 0 \\ 0 & 0 & D_{66} & 0 & 0 & -\overline{D}_{66} \\ -\overline{D}_{11} & -\overline{D}_{12} & 0 & \overline{\overline{D}}_{11} & \overline{\overline{D}}_{12} & 0 \\ -\overline{D}_{12} & -\overline{D}_{22} & 0 & \overline{\overline{D}}_{12} & \overline{\overline{D}}_{22} & 0 \\ 0 & 0 & -\overline{D}_{66} & 0 & 0 & \overline{\overline{D}}_{66} \end{bmatrix} \times \begin{bmatrix} W'' + W''U' + W'^oV' \\ W^{oo} + W'^oU^o + W^{oo}V^o \\ 2W'^o + W'^oU' + W''U^o + W'^oV^o + W^{oo}V' \\ \phi' + \phi'U' + \psi'V' \\ \psi^o + \psi^oV^o + \phi^oU^o \\ \phi^o + \psi' + \phi^oU' + \phi'U^o + \psi^oV' + \psi'V^o \end{bmatrix} \tag{9}$$

$$\overline{Q}_x = \overline{A}_{44}\phi; \quad \overline{Q}_y = \overline{A}_{55}\psi. \tag{10}$$

Using the Hamilton's principle (Magrab, 1979), the following equilibrium equations in terms of the stress resultants may be obtained:

$$(N_x + N_xU' + N_{xy}U^o + \delta M_xW'' + \delta M_{xy}W'^o + \delta\overline{M}_x\phi' + \delta\overline{M}_{xy}\phi^o)' + (N_{xy} + N_yU^o + N_{xy}U' + \delta M_yW'^o + \delta M_{xy}W'' + \delta\overline{M}_y\phi^o + \delta\overline{M}_{xy}\phi')^o = \delta^2 E\ddot{U}$$

$$(N_{xy} + N_xV' + N_{xy}V^o + \delta M_xW'^o + \delta M_{xy}W^{oo} + \delta\overline{M}_x\psi' + \delta\overline{M}_{xy}\psi^o)' + (N_y + N_yV^o + N_{xy}V' + \delta M_yW^{oo} + \delta M_{xy}W'^o + \delta\overline{M}_y\psi^o + \delta\overline{M}_{xy}\psi')^o = \delta^2 E\ddot{V}$$

$$(\overline{M}_x + \overline{M}_xU' + \overline{M}_{xy}U^o)' + (\overline{M}_{xy} + \overline{M}_yU^o + \overline{M}_{xy}U')^o - \frac{1}{\delta}\overline{Q}_x = \delta^3\overline{\overline{G}}\ddot{\phi} - \delta^3\overline{G}\ddot{W}'$$

$$(\overline{M}_{xy} + \overline{M}_xV' + \overline{M}_{xy}V^o)' + (\overline{M}_y + \overline{M}_yV^o + \overline{M}_{xy}V')^o - \frac{1}{\delta}\overline{Q}_y = \delta^3\overline{\overline{G}}\ddot{\psi} - \delta^3\overline{G}\ddot{W}^o$$

$$(M_x + M_xU' + M_{xy}U^o)'' + (M_y + M_yV^o + M_{xy}V')^{oo} + (2M_{xy} + M_yU^o + M_{xy}U' + M_xV' + M_{xy}V^o)'^o - \frac{1}{\delta}(N_xW' + N_{xy}W^o)' - \frac{1}{\delta}(N_yW^o + N_{xy}W')^o = \delta^2 Q + \delta^3\overline{G}(\ddot{\phi}' + \ddot{\psi}^o) + \delta E\ddot{W} - \delta^3 G(\ddot{W}'' + \ddot{W}^{oo}) \ldots. \tag{11}$$

The associated boundary conditions along the line X-constant read as

$$(N_x + N_xU' + N_{xy}U^o + \delta M_xW'' + \delta M_{xy}W'^o + \delta\overline{M}_x\phi' + \delta\overline{M}_{xy}\phi^o) \text{ or } U$$

$$(N_{xy} + N_yU^o + N_{xy}U' + \delta M_yW'^o + \delta M_{xy}W'' + \delta\overline{M}_y\phi^o + \delta\overline{M}_{xy}\phi') \text{ or } V$$

$$(\overline{M}_x + \overline{M}_xU' + \overline{M}_{xy}U^o) \text{ or } \phi$$

$$(\overline{M}_{xy} + \overline{M}_yU^o + \overline{M}_{xy}U') \text{ or } \psi$$

$$[(M_x + M_xU' + M_{xy}U^o)' + (2M_{xy} + M_yU^o + M_{xy}U' + M_xV' + M_{xy}V^o)^o - \frac{1}{\delta}(N_xW' + N_{xy}W^o) + \delta^3 G\ddot{W}' - \delta^3\overline{G}\ddot{\phi}] \text{ or } W$$

$$(M_x + M_xU' + M_{xy}U^o) \text{ or } W'. \tag{12}$$

Along the line Y-constant, the boundary conditions are

$$(N_{xy} + N_xV' + N_{xy}V^o + \delta M_xW'^o + \delta M_{xy}W^{oo} + \delta\overline{M}_x\psi' + \delta\overline{M}_{xy}\psi^o) \text{ or } U$$

$$(N_y + N_yV^o + N_{xy}V' + \delta M_yW^{oo} + \delta M_{xy}W'^o + \delta\overline{M}_y\psi^o + \delta\overline{M}_{xy}\psi') \text{ or } V$$

$$(\overline{M}_{xy} + \overline{M}_xV' + \overline{M}_{xy}V^o) \text{ or } \phi$$

$$(\overline{M}_y + \overline{M}_yV^o + \overline{M}_{xy}V') \text{ or } \psi$$

$$[(M_y + M_yV^o + M_{xy}V')^o + (2M_{xy} + M_yU^o + M_{xy}U' + M_xV' + M_{xy}V^o)' - \frac{1}{\delta}(N_yW^o + N_{xy}W') + \delta^3 G\ddot{W}^o - \delta^3\overline{G}\ddot{\psi}] \text{ or } W$$

$$(M_y + M_yV^o + M_{xy}V') \text{ or } W^o. \tag{13}$$

In Eqs. (11) to (13), superposed dots indicate differentiation with respect to the normalized time coordinate (τ). One can express Eqs. (11), (12), and (13) in terms of the displacement parameters of the problem (viz. U, V, W, ϕ, and ψ). However, owing to their length and for the sake of brevity, we keep them as they are. It may be noted that the exact solution of these equations to any specified boundary conditions is out of question. However, one can obtain the approximate solution to these equations by using the regular perturbation technique as described in Pasic and Herrmann (1984) and Bhimaraddi (1989b). Following this technique, one can express the displacements in the form of a series with thickness to length ratio (δ) as the perturbation parameter. For the problem under consideration the following series can be written (Bhimaraddi, 1989b):

$$U = \delta^2 U_o + \delta^4 U_1 + \ldots; \quad V = \delta^2 V_o + \delta^4 V_1 + \ldots; \quad W = \delta W_o + \ldots$$
$$\phi = \delta^3\phi_o + \delta^5\phi_1 + \ldots; \quad \psi = \delta^3\psi_o + \delta^5\psi_1 + \ldots. \tag{14}$$

The stress resultants can also be expressed in power series as follows:

$$N_x = \delta^2 N_{xo} + \delta^4 N_{x1} + \ldots; \quad N_y = \delta^2 N_{yo} + \delta^4 N_{y1} + \ldots; \quad N_{xy} = \delta^2 N_{xyo} + \delta^4 N_{xy1} + \ldots$$
$$M_x = \delta^2 M_{xo} + \delta^4 M_{x1} + \ldots; \quad M_y = \delta^2 M_{yo} + \delta^4 M_{y1} + \ldots; \quad M_{xy} = \delta^2 M_{xyo} + \delta^4 M_{xy1} + \ldots$$
$$\overline{M}_x = \delta^2\overline{M}_{xo} + \delta^4\overline{M}_{x1} + \ldots; \quad \overline{M}_y = \delta^2\overline{M}_{yo} + \delta^4\overline{M}_{y1} + \ldots; \quad \overline{M}_{xy} = \delta^2\overline{M}_{xyo} + \delta^4\overline{M}_{xy1} + \ldots$$
$$\overline{Q}_x = \delta^3\overline{Q}_{xo} + \delta^5\overline{Q}_{x1} + \ldots; \quad \overline{Q}_y = \delta^3\overline{Q}_{yo} + \delta^5\overline{Q}_{y1} + \ldots. \tag{15}$$

Substituting the series (14) in the expressions for stress resultants (8) to (10), one can obtain the expressions for various coefficients of series Eqs. (15) as

$$\begin{bmatrix} N_{xo} \\ N_{yo} \\ N_{xyo} \end{bmatrix} = \begin{bmatrix} A_{11} & A_{12} & 0 \\ A_{12} & A_{22} & 0 \\ 0 & 0 & A_{66} \end{bmatrix} \begin{bmatrix} U_o' + \frac{1}{2}W_o'^2 \\ V_o^o + \frac{1}{2}W_o^{o2} \\ U_o^o + V_o' + W_o'W_o^o \end{bmatrix} \tag{16}$$

Downloaded 03 May 2010 to 171.66.16.247. Redistribution subject to ASME license or copyright; see http://www.asme.org/terms/Terms_Use.cfm

$$\begin{bmatrix} M_{xo} \\ M_{yo} \\ M_{xyo} \end{bmatrix} = \begin{bmatrix} D_{11} & D_{12} & 0 \\ D_{12} & D_{22} & 0 \\ 0 & 0 & D_{66} \end{bmatrix} \begin{bmatrix} W_o'' \\ W_o^{oo} \\ 2W_o'^{o} \end{bmatrix};$$

$$\begin{bmatrix} \overline{M}_{xo} \\ \overline{M}_{yo} \\ \overline{M}_{xyo} \end{bmatrix} = \begin{bmatrix} -\overline{D}_{11} & -\overline{D}_{12} & 0 \\ -\overline{D}_{12} & -\overline{D}_{22} & 0 \\ 0 & 0 & -\overline{D}_{66} \end{bmatrix} \begin{bmatrix} W_o'' \\ W_o^{oo} \\ 2W_o'^{o} \end{bmatrix}; \quad (17)\text{-}(18)$$

$$\overline{Q}_{xo} = \overline{A}_{44}\phi_o; \quad \overline{Q}_{yo} = \overline{A}_{55}\psi_o \quad (19)$$

$$\begin{bmatrix} N_{x1} \\ N_{y1} \\ N_{xy1} \end{bmatrix} = \begin{bmatrix} A_{11} & A_{12} & 0 \\ A_{12} & A_{22} & 0 \\ 0 & 0 & A_{66} \end{bmatrix} \begin{bmatrix} U_1' + \frac{1}{2}(U_o'^2 + V_o'^2) \\ V_1^o + \frac{1}{2}(U_o^{o2} + V_o^{o2}) \\ U_1^o + V_1' + U_o' U_o^o + V_o' V_o^o \end{bmatrix} \quad (20)$$

$$\begin{bmatrix} M_{x1} \\ M_{y1} \\ M_{xy1} \\ \overline{M}_{x1} \\ \overline{M}_{y1} \\ \overline{M}_{xy1} \end{bmatrix} = \begin{bmatrix} D_{11} & D_{12} & 0 & -\overline{D}_{11} & -\overline{D}_{12} & 0 \\ D_{12} & D_{22} & 0 & -\overline{D}_{12} & -\overline{D}_{22} & 0 \\ 0 & 0 & D_{66} & 0 & 0 & -\overline{D}_{66} \\ -\overline{D}_{11} & -\overline{D}_{12} & 0 & \overline{\overline{D}}_{11} & \overline{\overline{D}}_{12} & 0 \\ -\overline{D}_{12} & -\overline{D}_{22} & 0 & \overline{\overline{D}}_{12} & \overline{\overline{D}}_{22} & 0 \\ 0 & 0 & -\overline{D}_{66} & 0 & 0 & \overline{\overline{D}}_{66} \end{bmatrix}$$

$$\times \begin{bmatrix} W_o'' U_o' + W_o'^{o} V_o' \\ W_o^{oo} V_o^o + W_o'^{o} U_o^o \\ W_o'^{o} U_o' + W_o'' U_o^o + W_o'^{o} V_o^o + W_o^{oo} V_o' \\ \phi_o' \\ \psi_o^o \\ \phi_o^o + \psi_o' \end{bmatrix} \quad (21)$$

$$\overline{Q}_{x1} = \overline{A}_{44}\phi_1; \quad \overline{Q}_{y1} = \overline{A}_{55}\psi_1. \quad (22)$$

Substituting Eqs. (14) and (15) in the first four force equilibrium Eqs. (11) and in the associated boundary conditions (12) and (13), and equating the like powers of δ^2, δ^4, etc., we obtain sets of equations and the associated boundary conditions. For example, for like powers of δ^2 we have the following set:

$$\begin{aligned} N_{xo}' + N_{xyo}^o &= 0 \\ N_{xyo}' + N_{yo}^o &= 0 \\ \overline{M}_{xo}' + \overline{M}_{xyo}^o - \overline{Q}_{xo} &= 0 \\ \overline{M}_{xyo}' + \overline{M}_{yo}^o - \overline{Q}_{yo} &= 0. \end{aligned} \quad (23)$$

The boundary conditions along X-constant are

$$N_{xo} \text{ or } U_o; \; N_{xyo} \text{ or } V_o; \; \overline{M}_{xo} \text{ or } \phi_o; \; \overline{M}_{xyo} \text{ or } \psi_o, \quad (24)$$

and along Y-constant are

$$N_{xyo} \text{ or } U_o; \; N_{yo} \text{ or } V_o; \; \overline{M}_{xyo} \text{ or } \phi_o; \; \overline{M}_{yo} \text{ or } \psi_o. \quad (25)$$

The next set of equations correspond to the like powers of δ^4 and they are as follows:

Equilibrium Equations:

$$\begin{aligned} &(N_{x1} + N_{xo}U_o' + N_{xyo}U_o^o + M_{xo}W_o'' + M_{xyo}W_o'^{o})' \\ &\quad + (N_{xy1} + N_{yo}U_o^o + N_{xyo}U_o' + M_{yo}W_o'^{o} + M_{xyo}W_o'')^o = E\ddot{U}_o \\ &(N_{xy1} + N_{xo}V_o' + N_{xyo}V_o^o + M_{xo}W_o'^{o} + M_{xyo}W_o^{oo})' \\ &\quad + (N_{y1} + N_{yo}V_o^o + N_{xyo}V_o' + M_{yo}W_o^{oo} + M_{xyo}W_o'^{o})^o = E\ddot{V}_o \\ &(\overline{M}_{x1} + \overline{M}_{xo}U_o' + \overline{M}_{xyo}U_o^o)' \\ &\quad + (\overline{M}_{xy1} + \overline{M}_{yo}U_o^o + \overline{M}_{xyo}U_o')^o - \overline{Q}_{x1} = -\overline{G}\ddot{W}_o' \\ &(\overline{M}_{xy1} + \overline{M}_{xo}V_o' + \overline{M}_{xyo}V_o^o)' \\ &\quad + (\overline{M}_{y1} + \overline{M}_{yo}V_o^o + \overline{M}_{xyo}V_o')^o - \overline{Q}_{y1} = -\overline{G}\ddot{W}_o^o \end{aligned} \quad (26)$$

Boundary Conditions: Along the X-constant:

$$\begin{aligned} &(N_{x1} + N_{xo}U_o' + N_{xyo}U_o^o + M_{xo}W_o'' + M_{xyo}W_o'^{o}) \text{ or } U_1 \\ &(N_{xy1} + N_{yo}U_o^o + N_{xyo}U_o' + M_{yo}W_o'^{o} + M_{xyo}W_o'') \text{ or } V_1 \\ &(\overline{M}_{x1} + \overline{M}_{xo}U_o' + \overline{M}_{xyo}U_o^o) \text{ or } \phi_1; \\ &\quad (\overline{M}_{xy1} + \overline{M}_{yo}U_o^o + \overline{M}_{xyo}U_o') \text{ or } \psi_1 \end{aligned} \quad (27)$$

Along the Y-constant:

$$\begin{aligned} &(N_{xy1} + N_{xo}V_o' + N_{xyo}V_o^o + M_{xo}W_o'^{o} + M_{xyo}W_o^{oo}) \text{ or } U_1 \\ &(N_{y1} + N_{yo}V_o^o + N_{xyo}V_o' + M_{yo}W_o^{oo} + M_{xyo}W_o'^{o}) \text{ or } V_1 \\ &(\overline{M}_{xy1} + \overline{M}_{xo}V_o' + \overline{M}_{xyo}V_o^o) \text{ or } \phi_1; \\ &\quad (\overline{M}_{y1} + \overline{M}_{yo}V_o^o + \overline{M}_{xyo}V_o') \text{ or } \psi_1 \end{aligned} \quad (28)$$

It should be noted here that the set of Eqs. (23) to (25) correspond to the von Karman plate problem and the set of Eqs. (26) to (28) describe the influence of higher order nonlinear effects. Further, it should be noted here that the series (14) have been truncated to the terms shown there. As it will be seen later, consideration of an additional term in these series will require an enormous amount of algebraic manipulations, and it is seen in an earlier study by Bhimaraddi (1989b) that it is quite adequate to truncate these series as indicated above.

Solution of the Equilibrium Equations

As noted earlier, it is difficult to obtain the exact solution to the equilibrium Eqs. (23) and (26) for any given boundary conditions. However, in this paper a simply-supported plate has been considered and the single-mode solution to these equations is sought. The following equilibrium equations in terms of displacements may be obtained by substituting the stress resultant expressions (16) to (19) in the equilibrium Eqs. (23),

$$\begin{aligned} &A_{11}U_o'' + A_{66}U_o^{oo} + (A_{12} + A_{66})V_o'^{o} \\ &\quad = -A_{11}W_o'W_o'' - (A_{12} + A_{66})W_o^oW_o'^{o} - A_{66}W_o'W_o^{oo} \\ &(A_{12} + A_{66})U_o''^{o} + A_{66}V_o'' + A_{22}V_o^{oo} \\ &\quad = -A_{22}W_o^oW_o^{oo} - (A_{12} + A_{66})W_o'W_o'^{o} - A_{66}W_o^oW_o'' \\ &\overline{A}_{44}\phi_o = -\overline{D}_{11}W_o''' - (\overline{D}_{12} + 2\overline{D}_{66})W_o'^{oo} \\ &\overline{A}_{55}\psi_o = -\overline{D}_{22}W_o^{ooo} - (\overline{D}_{12} + 2\overline{D}_{66})W_o''^{o} \end{aligned} \quad (29)$$

and the following simply-supported boundary conditions are assumed:

$$\begin{aligned} &U_o = 0 \text{ at } X = 0; \; V_o = 0 \text{ at } Y = 0; \; W_o = W_o'' = 0 \text{ at } X = 0,1; \\ &\qquad W_o = W_o^{oo} = 0 \text{ at } Y = 0, 1/r \\ &r\int_o^{1/r} N_{xo}dY = N_x^* \text{ at } X = 1 \text{ and } \int_o^1 N_{yo}dX = N_y^* \text{ at } Y = 1/r \\ &\int_o^{1/r} N_{xyo}dY = 0 \text{ at } X = 0,1 \text{ and } \int_o^1 N_{xyo}dX = 0 \text{ at } Y = 0,1/r. \end{aligned} \quad (30)$$

It may be mentioned here that the average in-plane edge force conditions are used and the plate is free from any applied in-plane shear forces along its four edges. The following solution satisfies the aforementioned boundary conditions and the equilibrium equations.

$$\begin{aligned} W_o &= p\sin MX\sin NY \quad (M = \pi, \; N = \pi r) \\ U_o &= p^2 s_1 \sin 2MX + p^2 s_2 \sin 2MX\cos 2NY \\ &\quad + p^2 s_3 X + (r_1 N_x^* + r_2 N_y^*)X \\ V_o &= p^2 s_4 \sin 2NY + p^2 s_5 \cos 2MX \sin 2NY \\ &\quad + p^2 s_6 Y + (r_2 N_x^* + r_3 N_y^*)Y \\ N_{xo} &= p^2 s_7 \cos 2NY + N_x^*; \; N_{yo} = p^2 s_8 \cos 2MX + N_y^*; \; N_{xyo} = 0 \end{aligned}$$

Downloaded 03 May 2010 to 171.66.16.247. Redistribution subject to ASME license or copyright; see http://www.asme.org/terms/Terms_Use.cfm

$$M_{xo}=ps_9\sin MX\sin NY;\quad M_{yo}=ps_{10}\sin MX\sin NY;$$
$$M_{xyo}=ps_{11}\cos MX\cos NY$$
$$\overline{M}_{xo}=ps_{12}\sin MX\sin NY;\quad \overline{M}_{yo}=ps_{13}\sin MX\sin NY;$$
$$\overline{M}_{xyo}=ps_{14}\cos MX\cos NY$$
$$\phi_o=ps_{15}\cos MX\sin NY;\quad \psi_o=ps_{16}\sin MX\cos NY \qquad (31)$$

More details on how one can obtain the solution (31) may be found in the publications of Bhimaraddi (1987b, 1989b). The expressions for constants s_i and r_i have not been given here for the sake of brevity. Having obtained the solution for the first terms of the perturbation series, we move on to obtain the solution for the second terms, as the determination of these terms requires the knowledge of the previous terms. Further, we notice from the last two equations of (26) that ϕ_1 and ψ_1 can be obtained directly, since they are just algebraic equations and the rest of the terms depend only on U_o, V_o, ϕ_o, and ψ_o. We can write the first two equations by partly expressing them in terms of displacements as

$$A_{11}U_1'' + A_{66}U_1^{oo} + (A_{12}+A_{66})V_1'^{o} = E\ddot{U}_o - \frac{1}{2}A_{11}(U_o'^2 + V_o'^2)'$$
$$-\frac{1}{2}A_{12}(U_o^{o2}+V_o^{o2})' - A_{66}(U_o'U_o^o + V_o'V_o^o)^o$$
$$-(N_{xo}U_o' + N_{xyo}U_o^o + M_{xo}W_o'' + M_{xyo}W_o'^o)'$$
$$-(N_{yo}U_o^o + N_{xyo}U_o' + M_{yo}W_o'^o + M_{xyo}W_o'')^o$$
$$(A_{12}+A_{66})U_1'^o + A_{66}V_1'' + A_{22}V_1^{oo} = E\ddot{V}_o - \frac{1}{2}A_{12}(U_o'^2 + V_o'^2)^o$$
$$-\frac{1}{2}A_{22}(U_o^{o2}+V_o^{o2})^o - A_{66}(U_o'U_o^o + V_o'V_o^o)'$$
$$-(N_{xo}V_o' + N_{xyo}V_o^o + M_{xo}W_o''^o + M_{xyo}W_o^{oo})'$$
$$-(N_{xyo}V_o' + N_{yo}V_o^o + M_{xyo}W_o'^o + M_{yo}W_o^{oo})^o \ldots. \qquad (32)$$

In the above equations, the right-hand sides have already been calculated. These equations are to be solved using the following boundary conditions:

$$U_1=0 \text{ at } X=0;\quad V_1=0 \text{ at } Y=0$$
$$\int_o^{1/r}(N_{xy1}+N_{yo}U_o^o+N_{xyo}U_o'+M_{yo}W_o'^o+M_{xyo}W_o'')dY=0$$
$$\text{at } X=0,1$$
$$\int_o^1(N_{xy1}+N_{xo}V_o'+N_{xyo}V_o^o+M_{xo}W_o'^o+M_{xyo}W_o^{oo})dX=0$$
$$\text{at } Y=0,1/r$$
$$\int_o^{1/r}(N_{x1}+N_{xo}U_o'+N_{xyo}U_o^o+M_{xo}W_o''+M_{xyo}W_o'^o)dY=0$$
$$\text{at } X=1$$
$$\int_o^1(N_{y1}+N_{xyo}V_o'+N_{yo}V_o^o+M_{xyo}W_o'^o+M_{yo}W_o^{oo})dX=0$$
$$\text{at } Y=0,1/r. \qquad (33)$$

Again, it should be mentioned here that we have made use of the average edge force conditions in Eqs. (33). One can write the solution of these equations as

$$U_1=p^2(s_{17}X+s_{18}\sin 2MX+s_{19}\sin 2MX\cos 2NY)$$
$$+p^4(s_{20}X+s_{21}\sin 2MX+s_{22}\sin 2MX\cos 2NY$$
$$+s_{23}\sin 2MX\cos 4NY+s_{24}\sin 4MX+s_{25}\sin 4MX\cos 2NY$$
$$+s_{26}\sin 4MX\cos 4NY)+p^2N_x^*(r_4X+r_5\sin 2MX$$
$$+r_6\sin 2MX\cos 2NY)+p^2N_y^*(r_7X+r_8\sin 2MX$$
$$+r_9\sin 2MX\cos 2NY)+N_x^{*2}r_{10}X+N_x^*N_y^*r_{11}X+N_y^{*2}r_{12}X$$
$$+2(p\ddot{p}+\dot{p}^2)(g_1\sin 2MX+g_2\sin 2MX\cos 2NY+g_3X+g_4X^3)$$
$$+\ddot{N}_x^*(g_5X+g_6X^3)+\ddot{N}_y^*(g_7X+g_8X^3)$$
$$V_1=p^2(s_{27}Y+s_{28}\sin 2NY+s_{29}\cos 2MX\cos 2NY)$$
$$+p^4(s_{30}Y+s_{31}\sin 2NY+s_{32}\cos 2MX\sin 2NY$$
$$+s_{33}\cos 2MX\sin 4NY+s_{34}\sin 4NY+s_{35}\cos 4MX\sin 2NY$$
$$+s_{36}\cos 4MX\sin 4NY)+p^2N_x^*(r_{13}Y+r_{14}\sin 2NY$$
$$+r_{15}\cos 2MX\sin 2NY)+p^2N_y^*(r_{16}Y+r_{17}\sin 2NY$$
$$+r_{18}\cos 2MX\sin 2NY)+N_x^{*2}r_{19}Y+N_x^*N_y^*r_{20}Y+N_y^{*2}r_{21}Y$$
$$+2(p\ddot{p}+p\dot{p}^2)(g_9\sin 2NY+g_{10}\cos 2MX\sin 2NY+g_{11}Y+g_{12}Y^3)$$
$$+\ddot{N}_x^*(g_{13}Y+g_{14}Y^3)+\ddot{N}_y^*(g_{15}Y+g_{16}Y^3) \qquad (34)$$

Once U_1, V_1, ϕ_1, and ψ_1 are known we can calculate the forces using the relations given above in Eqs. (16) to (22). These relations are not added here for the sake of brevity. Thus far, we were able to compute the in-plane and transverse shear response of the plate in terms of the lateral deflection (p), which is yet to be computed. To do this let us examine the last equation of (11) which governs the lateral motion of the plate. Substituting the series (14) and (15) in this equation one can obtain the following equation:

$$M_{xo}'' + M_{yo}^{oo} + 2M_{xyo}'^o - (N_{xo}W_o' + N_{xyo}W_o^o)'$$
$$-(N_{yo}W_o^o + N_{xyo}W_o')^o + \delta^2[(M_{x1}+M_{xo}U_o'+M_{xyo}U_o^o)''$$
$$+(M_{y1}+M_{yo}V_o^o+M_{xyo}V_o')^{oo} + (2M_{xy1}+M_{xo}V_o'+M_{yo}U_o^o$$
$$+M_{xyo}U_o'+M_{xyo}V_o^o)'^o - (N_{x1}W_o'+N_{xy1}W_o^o)'$$
$$-(N_{y1}W_o^o+N_{xy1}W_o')^o] = E\ddot{W}_o - \delta^2(G\ddot{W}_o'' + G\ddot{W}_o^{oo}) + Q. \qquad (35)$$

It may be said here that we have neglected all the inertia terms associated with the shear rotations as the contribution due to these inertias has been shown (in an earlier paper by Bhimaraddi (1989b)) to be of insignificant nature. It may also be observed here that we have computed all the quantities of Eq. (35) in terms of the lateral deflection (p). Substituting for these quantities and using the Galerkin's method one obtains the following time differential equation from which the unknown (p) can be determined:

$$\alpha\ddot{p} + p\alpha_1\left[\left(1-\delta^2\frac{\alpha_2}{\alpha_1}\right) + N^*\left(1+\delta^2\frac{\alpha_8+\lambda\alpha_9}{\alpha_6+\lambda\alpha_7}\right)\right.$$
$$\left.+\ddot{N}^*\delta^2\left(\frac{\alpha_{13}+\lambda\alpha_{14}}{\alpha_6+\lambda\alpha_7}\right)\right] + p^3\left[\alpha_3+\delta^2\alpha_4+N^*\delta^2\alpha_1\left(\frac{\alpha_{10}+\lambda\alpha_{11}}{\alpha_6+\lambda\alpha_7}\right)\right]$$
$$+p^5\delta^2\alpha_5+2\delta^2\alpha_{12}(p^2\ddot{p}+p\dot{p}^2) = \bar{\kappa} \qquad (36)$$

In the above equation, $N^*=N_x^*/N_o$, $\bar{\kappa}=Q/4r$, and $N_o=\alpha_1/(\alpha_6+\lambda\alpha_7)$. It may also be noted here that N_o is the bifurcation buckling load of a perfect plate corresponding to the Kirchhoff plate theory. It should be mentioned here that the terms underlined with a single line are the additional terms due to the generalization of the von Karman-type theory, whereas those underlined with a double line are the terms due to the inclusion of the nonlinear in-plane inertia. The shear deformation effects are contained in the α_2 term. To include the initial imperfection of the plate in the present analysis all one needs to do is to augment the strain displacement relations (7) by the strain terms due to such imperfections. Thus, the following terms are to be added to the first three strain-displacement relations (7):

$$\epsilon_x^i = \delta W'W_i' - Z\delta^2(W_i''U' + W_i'^oV')$$
$$\epsilon_y^i = \delta W^oW_i^o - Z\delta^2(W_i^{oo}U^o + W_i'^oV^o)$$
$$\gamma_{xy}^i = \delta(W_i^oW' + W_i'W^o) - Z\delta^2(W_i''U^o$$
$$+W_i'^oU' + W_i'^oV^o + W_i^{oo}V'). \qquad (37)$$

Downloaded 03 May 2010 to 171.66.16.247. Redistribution subject to ASME license or copyright; see http://www.asme.org/terms/Terms_Use.cfm

Following exactly all the steps described above for perfect plates, and assuming that the initial imperfections are of the type $W_i = p_i \sin MX \sin NY$, one can obtain the governing equation for (p) as

$$p(\beta_1 + N^*\beta_2 + \ddot{N}^*\beta_7) + p^2(\beta_3 + N^*\beta_4) + p^3(\beta_5 + N^*\beta_6) + 5p_i\delta^2\alpha_5 p^4 + \delta^2\alpha_5 p^5 + (\alpha + 2\delta^2 p_i^2\alpha_{12})\ddot{p} + 2\delta^2 p_i\alpha_{12}(2p\dot{p} + \dot{p}^2) + 2\delta^2\alpha_{12}(p^2\dot{p} + p\dot{p}^2) = -\dot{N}^* p_i\alpha_1 - \ddot{N}^*\beta_7 p_i + \bar{\kappa}\ldots \quad (38)$$

where β_1 to β_7 have the following definitions:

$$\beta_1 = \alpha_1 - \delta^2\alpha_2 + 2p_i^2\alpha_3 + 2\delta^2 p_i^2(\alpha_4 - \alpha_{15})$$

$$\beta_2 = \alpha_1\left(1 + \delta^2\frac{\alpha_8 + \lambda\alpha_9}{\alpha_6 + \lambda\alpha_7}\right) + 2\delta^2 p_i^2\alpha_1\left(1 + \delta^2\frac{\alpha_{10} + \lambda\alpha_{11}}{\alpha_6 + \lambda\alpha_7}\right)$$

$$\beta_3 = 3p_i(\alpha_3 + \delta^2\alpha_4) + \delta^2 p_i\alpha_{15} + 4\delta^2 p_i^3\alpha_5;$$

$$\beta_4 = 3\delta^2 p_i\alpha_1\left(\frac{\alpha_{10} + \lambda\alpha_{11}}{\alpha_6 + \lambda\alpha_7}\right)$$

$$\beta_5 = \alpha_3 + \delta^2\alpha_4 + 8\delta^2 p_i^2\alpha_5; \quad \beta_6 = \delta^2\alpha_1\left(\frac{\alpha_{10} + \lambda\alpha_{11}}{\alpha_6 + \lambda\alpha_7}\right);$$

$$\beta_7 = \delta^2\alpha_1\left(\frac{\alpha_{12} + \lambda\alpha_{11}}{\alpha_6 + \lambda\alpha_7}\right)\ldots. \quad (39)$$

It may be stated here that for the von Karman-type of analysis, one may substitute $\alpha_4 = \alpha_5 = \alpha_8 = \alpha_9 = \alpha_{10} = \alpha_{11} = \alpha_{15} = 0$ in Eqs. (38) and (39). In the next section an application of the above analysis is given for the case of free vibration of a plate in the presence of applied in-plane forces.

Nonlinear Free Vibration of an In-Plane Loaded Plate

Let us consider the case of a plate vibrating in the presence of the applied in-plane edge forces assumed to be independent of time. For this case on puts $(\ddot{N}^* = \bar{\kappa} = 0)$ in Eq. (38). Changing the independent variable (τ) to $(\bar{\tau} = \Omega_L\tau)$, Eq. (38) can be written as

$$\ddot{p} + p + \epsilon_1 p^2 + \epsilon_2 p^3 + \epsilon_3 p^4 + \epsilon_4 p^5 + \gamma_1(2p\ddot{p} + \dot{p}^2) + \gamma_2(p^2\ddot{p} + p\dot{p}^2) = \mu. \quad (40)$$

Superposed dots indicate the differentiation with respect to $\bar{\tau}$ and the various coefficients in the above equation have the following definitions:

$$\Omega_L^2 = \left(\frac{\beta_1 + N^*\beta_2}{\alpha + 2\delta^2 p_i^2\alpha_{12}}\right); \quad \mu = -\frac{N^* p_i\alpha_1}{\beta_1 + N^*\beta_2}; \quad \gamma_2 = \frac{2\delta^2\alpha_{12}}{\alpha + 2\delta^2 p_i^2\alpha_{12}};$$

$$\gamma_1 = p_i\gamma_2; \quad \epsilon_1 = \frac{\beta_3 + N^*\beta_4}{\beta_1 + N^*\beta_2}; \quad \epsilon_2 = \frac{\beta_5 + N^*\beta_6}{\beta_1 + N^*\beta_2};$$

$$\epsilon_3 = \frac{5\delta^2 p_i\alpha_5}{\beta_1 + N^*\beta_2}; \quad \epsilon_4 = \frac{\delta^2\alpha_5}{\beta_1 + N^*\beta_2}. \quad (41)$$

Using the method of multiple scales (Nayfeh and Mook, 1979) one can obtain the solution to Eq. (40) and the expression for nonlinear frequency, which is dependent on the amplitude (A), as

$$\Omega_{NL} = (1 + b_1 + b_2A^2 + b_3A^4 + b_4A^6)\Omega_L \quad (42)$$

and b_1 to b_4 have the following definition:

Table 1 Nonlinear-to-linear (Ω_{NL}/Ω_L) frequency ratios for various amplitude (A) values for orthotropic homogeneous plates using the approximate (Eq. (42)) and the exact (Eq. (44)) methods ($\delta = 0.1$, $\lambda = 1$, $r = 1$, $N^* = 0$)

	$A = 0.25$		$A = 0.50$		$A = 0.75$		$A = 1.0$		
p_i	$E42$	$E44$	$E42$	$E44$	$E42$	$E44$	$E42$	$E44$	Ω_L
0.0	1.019	1.019	1.075	1.071	1.169	1.150	1.302	1.247	13.192
0.1	1.017	1.043	1.070	1.115	1.150	1.208	1.268	1.313	13.300
0.2	1.012	1.063	1.045	1.149	1.102	1.251	1.179	1.361	13.618
0.3	1.004	1.078	1.017	1.173	1.037	1.279	1.065	1.388	14.125
0.4	0.998	1.089	0.990	1.187	0.976	1.292	0.955	1.399	14.796
0.5	0.992	1.093	0.968	1.193	0.926	1.295	0.867	1.397	15.597

$$b_1 = \mu(\gamma_1 - \epsilon_1 - 2\mu^2\epsilon_3) + \frac{1}{2}\mu^2(-5\gamma_1^2 - 3\epsilon_1^2 - 16\mu^4\epsilon_3^2 + 8\gamma_1\epsilon_1 + 14\mu^2\gamma_1\epsilon_3 - 18\mu^2\epsilon_1\epsilon_3 + 3\epsilon_2 + 5\mu^2\epsilon_1 - \gamma_2)$$

$$b_2 = -2\mu\epsilon_3 + \frac{1}{4}\mu^2(36\gamma_1\epsilon_3 - 34\epsilon_1\epsilon_3 - 82\mu^2\epsilon_3^2 + 15\epsilon_4) + \frac{1}{24}(12\gamma_1\epsilon_1 + 6\gamma_1^2 - 10\epsilon_1^2 + 9\epsilon_2 - 6\gamma_2)$$

$$b_3 = \frac{1}{48}(-360\mu^2\epsilon_3^2 - 44\epsilon_1\epsilon_3 + 32\gamma_1\epsilon_3 + 15\epsilon_4); \quad b_4 = -\frac{209}{480}\epsilon_3^2\ldots. \quad (43)$$

It is well known that the application of the method of multiple scales is limited to weakly nonlinear problems (i.e., the modulus values of ϵ_1, ϵ_2, etc. are less than unity). It was recently observed by Bhimaraddi (1993), in the context of the von Karman-type analysis, that for imperfect plates, the method of multiple scales fails to give any meaningful results even when the coefficient were less than unity. In view of these observations, the nonlinear to linear frequency ratio must be obtained by the exact method as outlined in Chapter 2 of Nayfeh and Mook (1979). Here, only the final result is recorded for the sake of brevity and one can obtain the details from Nayfeh and Mook (1979). Thus, the exact relation for the frequency ratio can be written as

$$\frac{\Omega_L}{\Omega_{NL}} = \frac{2}{\pi}\int_0^{\theta_{\max}} \frac{\cos\theta\sqrt{1 + 2\sqrt{2H}\gamma_1\sin\theta + 2H\gamma_2\sin^2\theta}\,d\theta}{\sqrt{1 + \frac{2\mu}{\sqrt{2H}}\sin\theta - \sin^2\theta - \frac{2}{3}\epsilon_1\sqrt{2H}\sin^3\theta - \epsilon_2 H\sin^4\theta - \frac{4}{5}\epsilon_3 H\sqrt{2H}\sin^5\theta - \frac{4}{3}\epsilon_4 H^2\sin^6\theta}}\ldots. \quad (44)$$

where H and $\theta_{\max}$ are given by the following expressions:

$$\theta_{\max} = \sin^{-1}\left(\frac{A}{\sqrt{2H}}\right);$$

$$H = \frac{1}{2}A^2 + \frac{1}{3}\epsilon_1 A^3 + \frac{1}{4}\epsilon_2 A^4 + \frac{1}{5}\epsilon_3 A^5 + \frac{1}{6}\epsilon_4 A^6 - \mu A. \quad (45)$$

The integration in Eq. (44) is carried out numerically. In all the numerical examples considered here we have used $r = 1$, $\lambda = 1$, and the orthotropic material properties correspond to $E_x = 25E_y$, $G_{xy} = G_{xz} = (1/2)E_y$, $G_{yz} = (1/2)E_y$, $\nu_1 = (1/4)$. Here E_x and E_y are the elastic moduli; G_{xy}, G_{xz}, and G_{yz} are the shear moduli; ν_1 is the Poisson's ratio. Since the von Karmon analysis is the special case of the present formulation, the numerical results were compared with those available in the literature for isotropic plates (Bolotin, 1964) and for orthotropic plates (Bhimaraddi, 1989b) to ensure the correctness of the algebra and the computer implementation of the same.

Table 1 shows numerical results for nonlinear to linear (Ω_{NL}/Ω_L) frequency ratios for different amplitude and imperfection values. It may be seen from this table that the method of multiple scales ($E42$) predicts the softening behavior for

Downloaded 03 May 2010 to 171.66.16.247. Redistribution subject to ASME license or copyright; see http://www.asme.org/terms/Terms_Use.cfm

Table 2 Nonlinear to linear (Ω_{NL}/Ω_L) frequency ratios for various amplitude (A) values for orthotropic homogeneous plates ($\delta = 0.1$, $\lambda = 1$, $r = 1$)

	$A = 0.25$		$A = 0.5$		$A = 0.75$		$A = 1.0$		Ω_L	
p_i	PGF	VKF	PGF	VKF	PGF	VKF	PGF	VKF	PGF	VKF
					$N^* = 0.00$					
0.0	1.019	1.018	1.071	1.071	1.150	1.149	1.247	1.246	13.192	13.192
0.1	1.043	1.043	1.115	1.114	1.208	1.207	1.313	1.312	13.300	13.299
0.2	1.063	1.063	1.149	1.149	1.251	1.250	1.361	1.358	13.618	13.617
0.3	1.078	1.078	1.173	1.173	1.279	1.277	1.388	1.385	14.125	14.124
0.4	1.089	1.088	1.187	1.186	1.292	1.290	1.399	1.395	14.796	14.794
0.5	1.093	1.093	1.193	1.192	1.295	1.293	1.397	1.392	15.597	15.595
					$N^* = -0.25$					
0.0	1.029	1.028	1.108	1.107	1.225	1.223	1.365	1.361	10.761	10.809
0.1	1.086	1.085	1.194	1.192	1.330	1.326	1.480	1.474	10.897	10.945
0.2	1.173	1.170	1.277	1.273	1.416	1.411	1.565	1.557	11.294	11.339
0.3	1.338	1.327	1.342	1.338	1.472	1.466	1.613	1.604	11.919	11.961
0.4	1.378	1.366	1.382	1.377	1.497	1.491	1.625	1.616	12.729	12.767
0.5	1.392	1.380	1.396	1.391	1.497	1.490	1.612	1.603	13.678	13.713

PGF: Present Generalized Formulation; VKF: von Karman Formulation

Table 3 Nonlinear to linear (Ω_{NL}/Ω_L) frequency ratios for various amplitude (A) values for 0/90/0 laminated plates ($\delta = 0.1$, $\lambda = 1$, $r = 1$)

	$A = 0.25$		$A = 0.5$		$A = 0.75$		$A = 1.0$		Ω_L	
p_i	PGF	VKF	PGF	VKF	PGF	VKF	PGF	VKF	PGF	VKF
					$N^* = 0.00$					
0.0	1.017	1.017	1.065	1.065	1.137	1.137	1.227	1.226	13.713	13.713
0.1	1.039	1.039	1.105	1.105	1.191	1.190	1.288	1.287	13.817	13.816
0.2	1.058	1.058	1.138	1.137	1.231	1.230	1.333	1.331	14.120	14.119
0.3	1.072	1.072	1.161	1.160	1.258	1.257	1.360	1.357	14.605	14.604
0.4	1.082	1.082	1.174	1.174	1.272	1.271	1.372	1.368	15.247	15.245
0.5	1.087	1.087	1.180	1.179	1.276	1.274	1.372	1.367	16.016	16.014
					$N^* = -0.25$					
0.0	1.025	1.025	1.096	1.095	1.200	1.199	1.325	1.323	11.422	11.436
0.1	1.074	1.073	1.171	1.170	1.293	1.291	1.428	1.425	11.550	11.563
0.2	1.142	1.142	1.242	1.241	1.369	1.367	1.505	1.501	11.922	11.934
0.3	1.243	1.241	1.300	1.298	1.422	1.419	1.551	1.546	12.510	12.521
0.4	1.279	1.277	1.338	1.336	1.448	1.445	1.568	1.562	13.277	13.286
0.5	1.294	1.292	1.354	1.351	1.452	1.448	1.561	1.554	14.180	14.188

Table 4 Nonlinear to linear (Ω_{NL}/Ω_L) frequency ratios for various amplitude (A) values for orthotropic homogeneous plates ($N^* = -0.25$, $\lambda = 1$, $r = 1$)

	$A = 0.25$		$A = 0.5$		$A = 0.75$		$A = 1.0$		Ω_L	
p_i	PGF	VKF	PGF	VKF	PGF	VKF	PGF	VKF	PGF	VKF
					$\delta = 0.025$					
0.0	1.022	1.022	1.084	1.084	1.179	1.179	1.300	1.300	12.900	12.903
0.1	1.059	1.059	1.147	1.147	1.261	1.261	1.396	1.395	13.021	13.024
0.2	1.107	1.107	1.207	1.207	1.332	1.332	1.474	1.473	13.378	13.381
0.3	1.165	1.164	1.258	1.258	1.387	1.387	1.530	1.529	13.951	13.954
0.4	1.231	1.231	1.297	1.297	1.423	1.423	1.562	1.562	14.716	14.719
0.5	1.309	1.308	1.320	1.320	1.441	1.441	1.575	1.575	15.643	15.646
					$\delta = 0.05$					
0.0	1.024	1.024	1.092	1.092	1.195	1.194	1.323	1.322	12.165	12.179
0.1	1.067	1.067	1.162	1.161	1.284	1.283	1.426	1.425	12.292	12.304
0.2	1.124	1.124	1.228	1.228	1.361	1.360	1.508	1.506	12.663	12.676
0.3	1.198	1.197	1.285	1.284	1.417	1.416	1.563	1.561	13.256	13.267
0.4	1.298	1.296	1.324	1.323	1.451	1.450	0.591	1.589	14.042	14.054
0.5	1.320	1.312	1.346	1.345	1.465	1.463	0.597	1.595	14.987	14.997

imperfections >0.3 and the hardening behavior for imperfections ≤ 0.3. However, the exact method ($E44$) continues to predict the hardening behavior for all imperfections. More detailed discussion on this may be found in a recent paper by Bhimaraddi (1993), in which the nonlinear vibration of plates using the von Karman model has been presented. In view of this, the remaining results have been obtained using the exact method.

Tables 2 to 4 show nonlinear to linear frequency ratios for imperfect plates with in-plane loading for various values of A, p_i, N^*, and δ using the present (PGF) and the von Karman (VKF) formulations. In these tables a negative sign for in-plane loads indicates that they are of compressive nature. Comparing the present formulation and the von Karman-type formulation, one may note from these tables that there is hardly any noticeable difference between these two formulations as far as the linear frequency values are concerned. Also, the von Karman model gives almost identical results for all plates with lower values of p_i, N^*, δ, and A. But for thicker plates with higher imperfections subjected to larger in-plane loads and vibrating at higher amplitudes, the difference between the von Karman-type model and the present model is slightly noticeable. For example, (for $\delta = 0.1$, $\lambda = 1$, $N^* = -0.25$, $p_i = 0.5$ and $A = 1$) the difference is about 0.9 percent as may be seen from Table 2; whereas for the same plate with $N^* = 0$, it is only about 0.3 percent. One would expect higher differences for

Downloaded 03 May 2010 to 171.66.16.247. Redistribution subject to ASME license or copyright; see http://www.asme.org/terms/Terms_Use.cfm

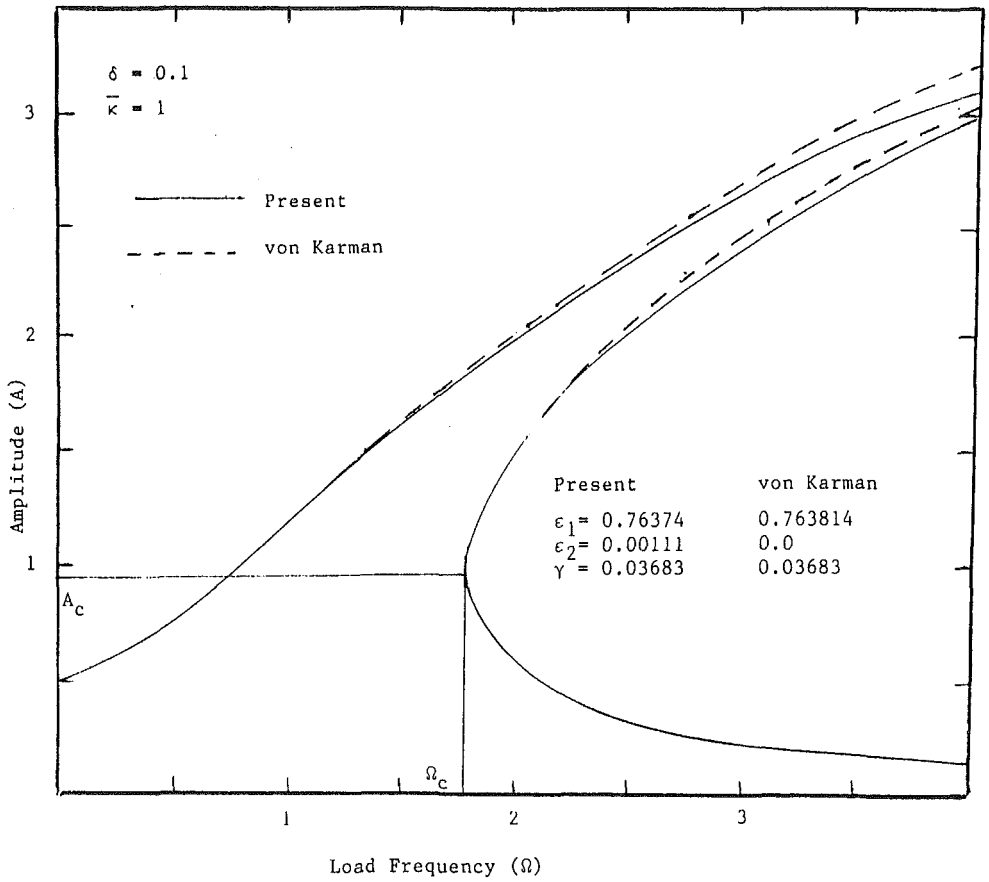


Fig. 1 Nonlinear response curve for an orthotropic square plate

higher values of N^* and δ. As a second example we consider the forced response of perfect plate subjected to harmonically varying lateral pressure on the surface in the absence of any applied in-plane loads.

Forced Response of Perfect Plates Subjected to Harmonic Lateral Pressure

In this section let us consider the nonlinear response of a plate subjected to harmonically varying (with time) pressure on its surface only. For this case we make use of the fact that $N^* = N^* = p_i = 0$ and further assume, for simplicity's sake, that the lateral pressure is varying sinusoidally in the x and y-directions ($q = q_o \sin MX \sin NY \cos\Omega\bar{\tau}$). Thus, Eq. (38) can be written as

$$p + p + \epsilon_1 p^3 + \epsilon_2 p^5 + \gamma(p^2\ddot{p} + p\dot{p}^2) = \kappa\cos\Omega\bar{\tau}. \tag{46}$$

Here the superposed dots indicate the differentiation with respect to $\bar{\tau}$, and Ω is the frequency of the applied lateral pressure. We have used the following definitions in the above equation:

$$\Omega_L^2 = \frac{\alpha_1 - \delta^2\alpha_2}{\alpha};\ \bar{\tau} = \Omega_L\tau;\ \kappa = \frac{aq_0}{4rK\delta^3(\alpha_1 - \delta^2\alpha_2)};$$

$$\epsilon_1 = \frac{\alpha_3 + \delta^2\alpha_4}{\alpha_1 - \delta^2\alpha_2};\ \epsilon_2 = \frac{\delta^2\alpha_5}{\alpha_1 - \delta^2\alpha_2};\ \gamma = \frac{2\delta^2\alpha_{12}}{\alpha}. \tag{47}$$

The solution of Eq. (46) to the first approximation can be written as

$$p = A\cos\Omega\bar{\tau}. \tag{48}$$

Here A is the steady-state amplitude of the vibration of the plate. The relation between amplitude A and the applied load parameters (κ and Ω) can be obtained using the method of multiple scales as

Table 5 Critical frequency (Ω_C) values for orthotropic homogeneous plates for different load intensities (see Eq. (51))

	$\delta = 0.1$		$\delta = 0.05$	
κ	PGF	VKF	PGF	VKF
1.	1.8003	1.7969	1.7759	1.7763
2.	2.2723	2.2650	2.2334	2.2323
3.	2.6691	2.6577	2.6155	2.6148
4.	3.0212	3.0081	2.9587	2.9561
5.	3.3484	3.3302	3.2713	3.2698
6.	3.6534	3.6313	3.5660	3.5632

$$\Omega = 1 + \frac{3}{8}\epsilon_1 A^2 + \frac{5}{16}\epsilon_2 A^4 - \frac{1}{4}\gamma A^2 - \frac{\kappa}{2A}. \tag{49}$$

At the critical point where the "jump" phenomenon takes place we have $d\Omega/dA = 0$ and hence one can obtain the coordinates of the critical point as (see Fig. 1)

$$A_C^5 + \frac{3\epsilon_1 - 2\gamma}{5\epsilon_2} A_C^3 + \frac{2\kappa}{5\epsilon_2} = 0 \tag{50}$$

$$\Omega_C = 1 + \frac{3}{8}(3\epsilon_1 - 2\gamma)A_C^2 + \frac{25}{16}\epsilon_2 A_C^4. \tag{51}$$

Figure 1 shows the plot of Eq. (49) for $\delta = 0.1$, $\kappa = 1$, and the plate material properties correspond to the aforementioned orthotropic elastic constants. Though Eq. (49) is of degree five, it has been observed for various numerical examples that only three roots are real and rest of the roots are complex. Similarly in the case of Eq. (50) only one root is real, and after obtaining it one can compute the critical frequency at which the jump phenomenon takes place from Eq. (51).

One may observe from Fig. 1 that there is not much difference

Downloaded 03 May 2010 to 171.66.16.247. Redistribution subject to ASME license or copyright; see http://www.asme.org/terms/Terms_Use.cfm

in the response curves of the von Karman model and the present formulation. Table 5 shows the critical frequency values at various load (κ) values. It may be seen from this table that the difference between the von Karman model and the present one is insignificant for a thinner plate ($\delta = 0.05$) and is less than one percent for a thicker ($\delta = 0.1$) plate. And hence, for perfect plates subjected to the lateral pressure, only the von Karman model is quite adequate and gives satisfactory results.

Conclusions

In this paper the nonlinear dynamics of composite symmetrically laminated plates has been considered using the generalized formulation. Thus, the in-plane strain and curvature expressions are nonlinear in all the displacement parameters of the plate, unlike the von Karman-type formulation in which only the in-plane strains are nonlinear in the lateral displacement only. Owing to this generalization, the governing equations of equilibrium are the nonlinear differential equations in all the displacement parameters of the plate. This precludes any effort to solve these equations using the usual solution techniques followed in the von Karman formulation. To circumvent this problem a regular perturbation technique has been used. From the numerical examples it has been shown that for plates with initial imperfections subjected to in-plane loads, the von Karman model differs slightly from the present formulation. Also, it has been shown that for perfect plates the von Karman model gives almost identical results.

References

Bert, C. W., 1982, "Research on Dynamics of Composite Sandwich Plates, 1979–1981," *Shock and Vibration Digest*, Vol. 14, pp. 17–34.

Bhimaraddi, A., and Stevens, L. K., 1984, "A Higher-Order Theory for Free Vibration of Orthotropic, Homogeneous, and Laminated Rectangular Plates," ASME JOURNAL OF APPLIED MECHANICS, Vol. 51, pp. 195–198.

Bhimaraddi, A., 1987a, "Static and Transient Response of Rectangular Plates," *Thin-Walled Structures*, Vol. 5, pp. 125–143.

Bhimaraddi, A., 1987b, "Nonlinear Flexural Vibrations of Rectangular Plates Subjected In-Plane Forces Using a New Shear Deformation Theory," *Thin-Walled Structures*, Vol. 5, pp. 309–328.

Bhimaraddi, A., 1989a, "Nonlinear Free Vibration Analysis of Composite Plates With Initial Imperfections and In-Plane Loading," *International Journal of Solids and Structures*, Vol. 25, pp. 33–43.

Bhimaraddi, A., 1989b, "Nonlinear Vibrations of In-Plane Loaded, Imperfect, Orthotropic Plates Using the Perturbation Technique," *International Journal of Solids and Structures*, Vol. 25, pp. 563–575.

Bhimaraddi, A., 1993, "Large Amplitude Vibrations of Imperfect Antisymmetric Angle-Ply Laminated Plates," *Journal of Sound and Vibration*, to be published, Vol. 160, No. 2.

Bolotin, V. V., 1964, *The Dynamic Stability of Elastic Systems*, Holden-Day, San Francisco.

Chia, C. Y., 1980, *Nonlinear Analysis of Plates*, McGraw-Hill, New York.

Leissa, A. W., 1981, "Advances in Vibration, Buckling and Postbuckling Studies on Composite Plates," *Composite Structures: Proceedings of the First Interational Conference*, I. H. Marshell, ed., pp. 312–334.

Magrab, E., 1979, *Vibrations of Elastic Structural Members*, Sijthoff and Noordhoff, Amsterdam.

Nayfeh, A. H., and Mook, D. T., 1979, *Nonlinear Oscillations*, John Wiley and Sons, New York.

Pasic, H., and Herrman, G., 1984, "Effect of In-Plane Inertia on Buckling of Imperfect Plates With Large Deformations," *Journal of Sound and Vibration*, Vol. 95, pp. 469–478.

Saada, A. S., 1974, *Elasticity: Theory and Applications*, Pergamon Press, New York.

Sathyamoorthy, M., 1987, "Nonlinear Vibration Analysis of Plates: A Review and Survey of Current Developments," *Applied Mechanics Reviews*, Vol. 40, pp. 1553–1561.

Downloaded 03 May 2010 to 171.66.16.247. Redistribution subject to ASME license or copyright; see http://www.asme.org/terms/Terms_Use.cfm

Yeh-Hung Lai
Graduate Student.

D. A. Dillard
Assoc. Professor.

Engineering Science and Mechanics Department, Virginia Polytechnic Institute, Blacksburg, VA 24061

J. S. Thornton
Principal Scientist, Texas Research Institute, Austin, TX 78746

The Effect of Compressibility on the Stress Distributions in Thin Elastomeric Blocks and Annular Bushings

The effect of the bulk compressibility of elastomers on the response of rubber blocks and bushings bonded to platens is investigated. Closed-form solutions for the stresses and deformations within the elastomer are presented for the case of rigid adherends. It is shown that even with relatively small shape factors, the compressibility can significantly affect the apparent stiffness. A finite element analysis shows that the closed-form solution accurately predicts the stress distribution for rigid adherends, but also reveals that platen deformations in realistic systems may significantly alter the distributions.

Introduction

Elastomeric blocks and bushings are often used as axial, torsional, shear, or bending springs to give desired flexibility and damping characteristics between machine or structural elements. In many of these applications, the elastomer is bonded to the components, although blocks in compression may be left unbonded. These elastomeric springs can be tailored to give a variety of performance characteristics. For example, in highway bridge supports, interleaving thin metallic plates between elastomeric blocks yields nearly the same stiffness as that of the monolithic elastomer, and yet the axial or bending stiffness is significantly increased.

A system of design concepts has emerged for estimating the stiffness of various sizes and shapes of elastomeric blocks. Much of this work has centered around the idea of a shape factor, S, which is the ratio of the area of one loaded surface divided by the total exposed free area. Solutions for infinite strips of finite width and circular disks may be found in Freakley and Payne (1978). Although this approach can give rough approximations for the stiffness of arbitrary shapes, the actual dependence on S changes with geometry, making the approach of limited usefulness for arbitrary shapes.

The deformations resulting from the compression (or extension) of a rubber box bonded between rigid adherends may be treated as the superposition of the deformation of an unbonded rubber block between frictionless adherends and the subsequent deformation required to restore the points along the interfaces to their original positions. Denoting the total pressure at any point $p(x, y)$ as the sum of these two contributions, we have

$$p(x, y) = [f_1 + f_2(x, y)]E\epsilon \tag{1}$$

where f_1 and f_2 represent the contributions from the first and second deformation modes, respectively. E is the Young's modulus, and ϵ is the strain defined as $\epsilon = \delta/h$ where δ is the relative displacement between the platens, and h is the height of the elastomer. By assuming that the material is incompressible and considering small deflections, Gent and Meinecke (1970) have shown that $f_1(x, y)$ obeys the same different equation (Poisson) as the torsion of prismatic shafts or the pressurized membrane problems. Thus existing solutions to these problems may be applied directly. Although f_1 does not vary across the area, its determination is not obvious. When compressed between lubricated platens and allowed to expand freely in both directions, $f_1 = 1$. On the other hand, for infinitely long strips in which the elastomers are constrained from expanding in one direction, the deformation is known as pure shear (Treloar, 1975) and $f_1 = 4/3$. For intermediate shapes, f_1 takes on values between 1 and 4/3. Gent and Meinecke (1970) have assumed approximate forms for f_1 for rectangular blocks of arbitrary dimensions. For moderate shape factors, f_1 is much smaller than f_2, so any error in the assumed value of f_1 has a negligible effect on the prediction.

Gent et al. (1974) obtained experimental data supporting their predictions for bonded blocks. Thornton et al. (1988) carried the analysis a step further to include the case of an unbonded rubber disk between rough surfaces. Dillard (1989) used the incompressible deformation field to predict the deformations of a flexible plate bonded to an elastomeric foundation. In all of these analysis techniques, however, it was assumed that the elastomer is incompressible. While this assumption is valid for rubber blocks with rather small shape

Contributed by the Applied Mechanics Division of THE AMERICAN SOCIETY OF MECHANICAL ENGINEERS for publication in the ASME JOURNAL OF APPLIED MECHANICS.

Discussion on this paper should be addressed to the Technical Editor, Professor Leon M. Keer, The Technological Institute, Northwestern University, Evanston, IL 60208, and will be accepted until four months after final publication of the paper itself in the JOURNAL OF APPLIED MECHANICS.

Manuscript received by the ASME Applied Mechanics Division, Sept. 22, 1987; final revision, Sept. 25, 1991. Associate Technical Editor: W. Knauss.

Copyright © 1992 by ASME
Downloaded 03 May 2010 to 171.66.16.247. Redistribution subject to ASME license or copyright; see http://www.asme.org/terms/Terms_Use.cfm

factors, it is not appropriate as the shape factor increases for the case of rigid adherends.

Although the determination of f_2 by the membrane analogy is exact for incompressible media, this solution breaks down when the polymer compressibility is not negligible. One may add the compliance of the compressible rubber block to the bulk compliance of the block to obtain the total solution as has been reported in Freakley and Payne (1978). Nonetheless, this does not provide information about the stress distributions within the block.

This paper will outline a simple, closed-form solution corrected for the bulk compressibility for an infinite strip of finite width, and a series solution for a rectangular block of arbitrary dimensions. The procedure is based on the assumption that the platens remain perfectly rigid. This assumption is certainly appropriate for small shape factors, but becomes questionable for larger shape factor configurations. A comparison of the closed-form solutions with a finite element analysis reveals that the closed-form solutions are very accurate for the case of rigid adherends. If flexibility is present in the adherends, however, the closed-form solutions overpredict the stresses within the elastomeric layer. The analysis further assumes that there is perfect bonding between the elastomer and the platens. In addition, it must be assumed that the total deflection of the platens is small compared to the height of the elastomeric block, since there is a stiffening geometric nonlinearity for large deflections. These latter assumptions are very reasonable for typical elastomeric mounting blocks and bushings.

Infinite Strip of Finite Width

Consider the cross-section of an infinitely long strip of width $2a$ shown in Fig. 1. The elastomer has a shear modulus of G and an initial thickness of h. The top platen is displaced a distance of δ resulting in a strain of ϵ, where $\epsilon = \delta/h$. Looking at the differential element, one can write that the volume displaced by the moving platen must be accounted for by the different displacements of the bounding sides and by the dilation of the element due to the bulk compressibility. For the present purposes, it is assumed that the pressure does not vary through the thickness of the elastomer (Gent and Meinecke, 1970). We have accurately confirmed this assumption by finite element analyses, as will be shown later. This leads to the conclusion that the profile of the deformed elements must be parabolic (Gent and Meinecke, 1970). The displacement of the parabola vertex at an arbitrary position is given by $u(x)$. The following equation can then be written:

$$\frac{du(x)}{dx} = (3/2)[\epsilon - p_2(x)/K] \tag{2}$$

where p_2 is the pressure distribution due to the restoring shear stresses, and K is the bulk modulus of the elastomer. From geometry, we may write that the shear strain at the interface is (Gent et al., 1974)

$$\gamma(x) = \frac{4u(x)}{h}. \tag{3}$$

From the equilibrium of an infinitesimal element

$$\frac{dp_2}{dx} = -\frac{2\tau(x)}{h}, \tag{4}$$

where τ is the shear stress at the lower interface.

Combining Eqs. (3) and (4) and utilizing the relation that $\tau(x) = \gamma(x)G$, we may write this equilibrium expression as

$$\frac{dp_2}{dx} = -\frac{8G}{h^2}u(x). \tag{5}$$

Differentiating Eq. (2) and substituting in Eq. (5) yields the governing differential equation

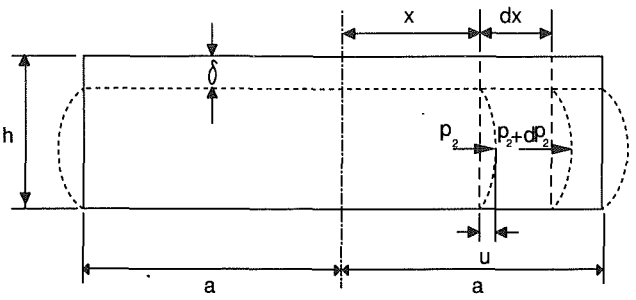


Fig. 1 Cross-section of a compressed elastomeric block

$$\frac{d^2u(x)}{dx^2} = \frac{3}{2K}\left[\frac{8G}{h^2}u(x)\right]. \tag{6}$$

The relevant boundary conditions are

(1) $\tau(0) = 0$ by symmetry

(2) $p_2(a) = 0$ because it is a free edge.

This may be placed in the standard form

$$u'' - \lambda^2 u = 0 \tag{7}$$

where

$$\lambda^2 = \frac{12G}{Kh^2}. \tag{8}$$

The solution is given by

$$u(x) = A \sinh \lambda x + B \cosh \lambda x. \tag{9}$$

By symmetry, $u(0) = 0$ forcing $B \equiv 0$. Substituting Eq. (9) into Eq. (4) yields

$$dp_2(x) = -\frac{8G}{h^2}(A \sinh \lambda x)dx. \tag{10}$$

Integrating between 0 and x gives us

$$p_2(x) = -\frac{8GA}{\lambda h^2}[\cosh \lambda x - 1] + p_2(0). \tag{11}$$

Substitution of $p_2(a) = 0$ allows us to find

$$A = \frac{\lambda h^2}{8G[\cosh \lambda a - 1]}p_2(0). \tag{12}$$

A is still in terms of $p_2(0)$ and since we lost information when we originally differentiated Eq. (2), we may now substitute this value of A back into Eq. (2). This provides

$$p_2(0) = \frac{3\epsilon[8G(\cosh \lambda a - 1)]}{2\lambda^2 h^2 \cosh \lambda a}. \tag{13}$$

We may write the solution in the form

$$p_2(x) = p_2(0)\left[1 - \frac{\cosh \lambda x - 1}{\cosh \lambda a - 1}\right] \tag{14}$$

where

$$p_2(0) = \frac{12G\epsilon}{\lambda^2 h^2}\left[\frac{\cosh \lambda a - 1}{\cosh \lambda a}\right]. \tag{15}$$

From Eqs. (3), (9), (12), and (15), one may also write that the shear stress along the interface is given by

$$\tau(x) = \frac{6G\epsilon}{h\lambda}\frac{\sinh \lambda x}{\cosh \lambda a}. \tag{16}$$

For our purpose, it is convenient to nondimensionalize the above expressions by setting

$$\xi = \frac{x}{a} \quad \eta = \frac{h}{a}$$

and

Downloaded 03 May 2010 to 171.66.16.247. Redistribution subject to ASME license or copyright; see http://www.asme.org/terms/Terms_Use.cfm

$$\beta = a\lambda = \frac{3}{\eta}\sqrt{\frac{2(1-2\nu)}{1+\nu}}$$

where ν is Poisson's ratio of the material. For an infinite strip, η is equal to the inverse of the classical shape factor.

The nondimensionalized expressions are

$$p_2(\xi) = \epsilon K\left[1 - \frac{\cosh \beta\xi}{\cosh \beta}\right] \tag{17a}$$

or

$$p_2(\xi) = \frac{12G\epsilon}{\beta^2\eta^2}\left[1 - \frac{\cosh \beta\xi}{\cosh \beta}\right] \tag{17b}$$

and

$$\tau(\xi) = \frac{\epsilon\beta K\eta}{2}\frac{\sinh \beta\xi}{\cosh \beta} \tag{18a}$$

or

$$\tau(\xi) = \frac{6G\epsilon}{\beta\eta}\frac{\sinh \beta\xi}{\cosh \beta}. \tag{18b}$$

The total pressure is actually equal to the sum of the pressures exerted by the compression of the lubricated block and that generated when the expanded disk is returned to its original interfacial position. Since p_1 is negligible in comparison to p_2, we can neglect it in computing total pressure exerted on the platens. The accuracy of this assumption has been widely accepted (e.g., Gent and Meinecke, 1970) and is further established by the numerical results presented herein.

To find the average pressure over the surface of the platen for calculating the effective stiffness, we integrate the pressure distribution over the width. This yields an expression for the average pressure

$$\bar{p} = \epsilon K\left[1 - \frac{\tanh \beta}{\beta}\right] \tag{19a}$$

$$\bar{p} = \frac{12\epsilon G}{\beta^2\eta^2}\left[1 - \frac{\tanh \beta}{\beta}\right]. \tag{19b}$$

The effective modulus of the elastomer block is simply

$$E_{\text{eff}} = \frac{\bar{p}}{\epsilon} = K\left[1 - \frac{\tanh \beta}{\beta}\right] \tag{20a}$$

or

$$E_{\text{eff}} = \frac{12G}{\beta^2\eta^2}\left[1 - \frac{\tanh \beta}{\beta}\right]. \tag{20b}$$

The following figures illustrate typical stress distributions and give information useful for design purposes. Poisson's ratio and the thickness-to-half-width ratio are used as parameters in these figures. Except as noted, the contribution from f_1 has been neglected, a valid assumption for thin elastomeric strips considered herein.

Figure 2 illustrates the effect of compressibility on pressure distributions for a typical h/a ratio of 0.1. As Poisson's ratio decreases slightly from 0.5, the pressure becomes bounded by a value equal to ϵK. It should be noted that after this work was completed we found that Williams et al. (1963) had obtained similar results from a somewhat different approach. However, numerical analysis discussed in the next section suggests that both William's and our work could be in error if the compliance of adherends is accounted for. In Fig. 3, the pressure distribution normalized with respect to the average pressure $\bar{p}$ is presented for various h/a ratios for a typical elastomer with Poisson's ratio equal to 0.4995. Again we note the gradual transition from a parabolic distribution to a uniform pressure distribution as η decreases.

Figure 4 illustrates the effect of Poisson's ratio on the shear stress distribution along the interface for $\eta = 0.1$. For incompressible materials, τ varies linearly from the center, whereas these stresses decrease significantly and become more concentrated toward the free edge as the compressibility increases.

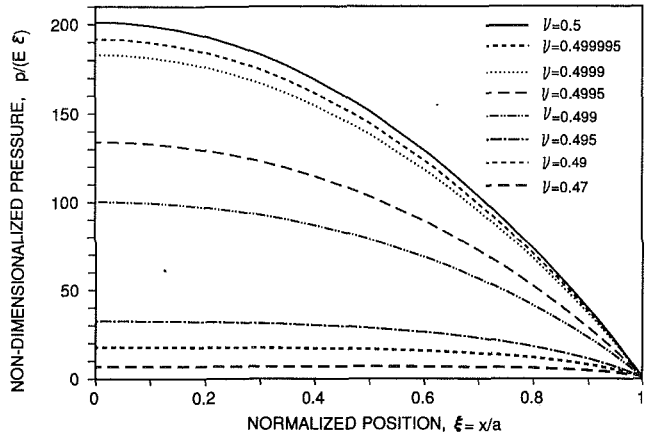


Fig. 2 Nondimensional pressure distributions for several Poisson's ratios for the case of $h/a = 0.1$

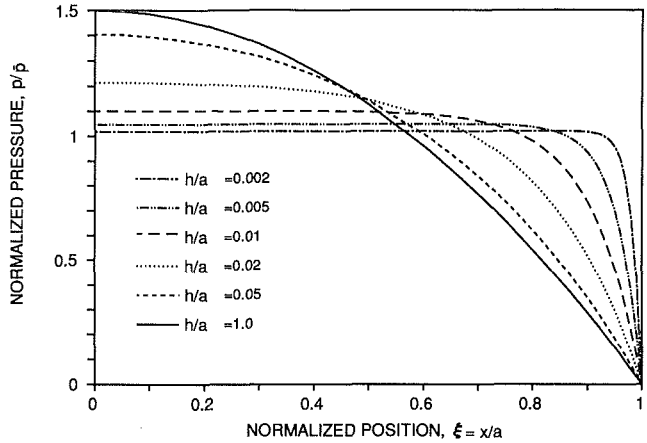


Fig. 3 Normalized pressure distributions for several thicknesses to half-width ratios for the case of $\nu = 0.4995$

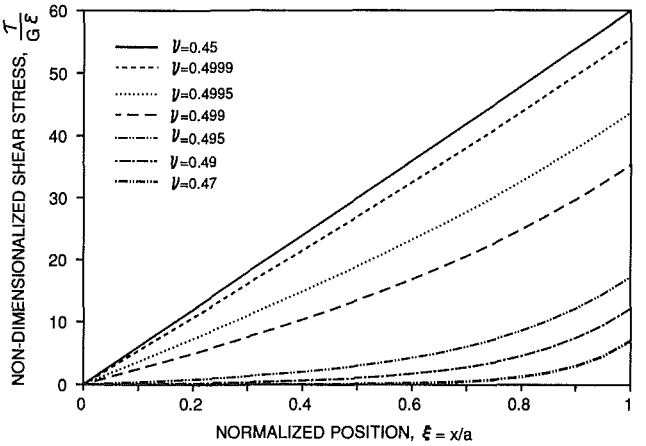


Fig. 4 Nondimensional shear stresses for several Poisson's ratios for the case of $h/a = 0.1$

For design purposes, it is useful to have information about the effective stiffness of the elastomeric strip. Figure 5 shows the average pressure normalized with respect to the average pressure for the incompressible case for a given displacement. For a typical value of $\nu = 0.4995$, it is seen that for $\eta < 0.2$, there is more than a ten percent deviation from the incom-

Downloaded 03 May 2010 to 171.66.16.247. Redistribution subject to ASME license or copyright; see http://www.asme.org/terms/Terms_Use.cfm

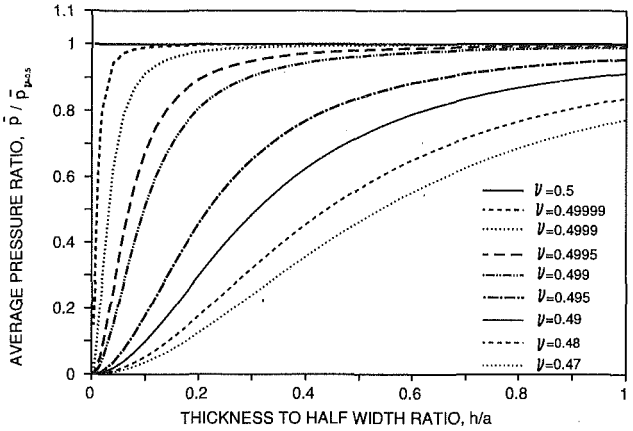


Fig. 5 Average pressure normalized to incompressible case for several Poisson's ratios

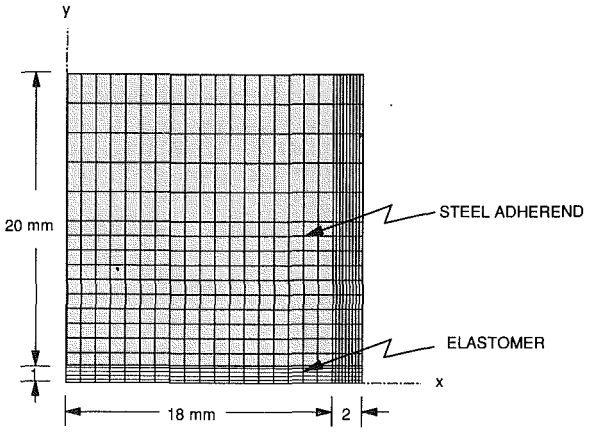


Fig. 7 Typical finite element grid for plane-strain analysis of a quarter of the specimen

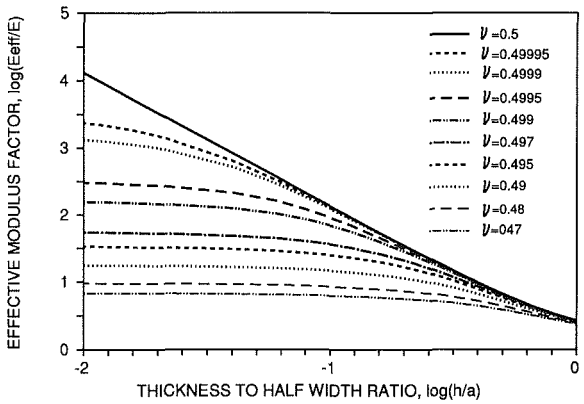


Fig. 6 Effective modulus factors for several Poisson's ratios

pressible case. As the shape factor increases beyond 5, significant reductions in stiffness occur with respect to the incompressible case.

Figure 6 provides a convenient chart for estimating the effective modulus of elastomeric strips of various Poisson's ratio. The chart has been corrected to include the f_1 contribution.

This solution applies to an infinitely long strip of finite width. Perhaps one of the most practical applications for this solution is the case of a thin annular elastomeric bushing between two cylinders which have been shrink fitted together. As long as the thickness of the bushing is small compared to the radius, the solution is expected to be applicable.

For the compression or extension of circular geometries between rigid adherends, a similar differential equation is obtained and the solution is in the form of hyperbolic Bessel functions. These solutions are given by Anderson et al. (1985) and have been attributed to Williams et al. (1963) and Lindsay (1967). Anderson et al. (1985) have also given finite difference solutions obtained by Messner (1963) for materials with different values of Poisson's ratio. These numerical solutions do reveal a more accurate approximation for the stresses within a region 1 1/2 to 2 thicknesses from the edge of the specimens.

It should be noted that all the solutions presented herein are based on the assumption that shear stress varies linearly throughout the layer, giving rise to the parabolic displacements across the thickness and requires the assumption that the pressure is uniform through the thickness. By examining the equilibrium equation

$$\frac{\partial \sigma_{zz}}{\partial z} + \frac{\partial \tau_{xz}}{\partial x} = 0,$$

and considering the incompressible case in which $\partial \tau_{xz}/\partial x$ is greatest, we see that the total variation in σ_{zz} is only $3\epsilon G/4$ which is negligible compared to the pressures in the interior regions. Errors introduced by the uniform pressure assumption become significant only very near the free edges of the material. The validity of the assumption of constant stresses throughout the thickness is demonstrated in the following numerical analysis and the details of stress distributions are also observed.

Numerical Analysis

To check the closed-form solutions and examine the effects of adherend compliance, ABAQUS, a commerically available finite element program, was used. Plane-strain analysis was used for the case of infinite length elastomeric strips. Cases of rigid and compliant adherents have been investigated.

Although ABAQUS allows the use of other material models, the relatively small deformations typical of highly constrained elastomeric blocks allowed us to use Young's modulus and Poisson's ratio for the standard constitutive model. The hybrid element option was used to accommodate the nearly incompressible behavior of our elastomeric material (Zienciewicz, 1977). For our purposes, a modulus of $E = 700$ MPa and cases of Poisson's ratio of 0.5, 0.4995, 0.495, and 0.47 were used. Because of symmetry, a quarter of the cross-section was used for analysis. A typical grid is shown in Fig. 7. For cases in which a rigid adherend was considered, only the elements in the elastomer were used, and the bonded surface was displaced downward by a constant amount in order to model compression of the elastomer by a rigid constraint. The bonded surface nodes were prevented from motion in the x-direction (rigid adherend case only), and nodes along the symmetry axes were prevented from moving perpendicular to the respective axis of symmetry.

We first examine the case of rigid adherends for direct comparison with the closed-form solution. In order to demonstrate the validity of the assumption that stresses remain constant through the thickness, stresses were examined at several lateral positions for each of the Poisson ratios studied. In each case stress remained essentially constant except very near the free edge. Typical results are indicated for the case of $\nu = 0.4995$ in Fig. 8. Excellent agreement was seen between the closed-form solution and the finite element results, as seen in Fig. 9. It is noted that in the analytical solution all pressures have the same sign; however, in the finite element analysis at the ends of elastomer layer the pressures are negative, which suggests the existence of a tensile state. From both analytical and numerical results, it is seen that the bulk compressibility of the elastomer has a tremendous effect on the stress distribution in the elastomer. We further conclude that the closed-form so-

Downloaded 03 May 2010 to 171.66.16.247. Redistribution subject to ASME license or copyright; see http://www.asme.org/terms/Terms_Use.cfm

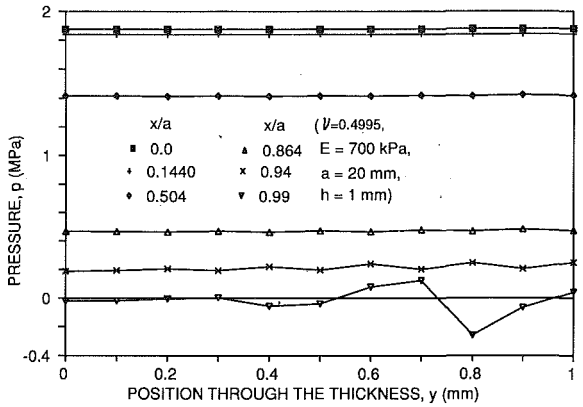


Fig. 8 Pressure variations across the thickness of an elastomeric strip at several lateral positions

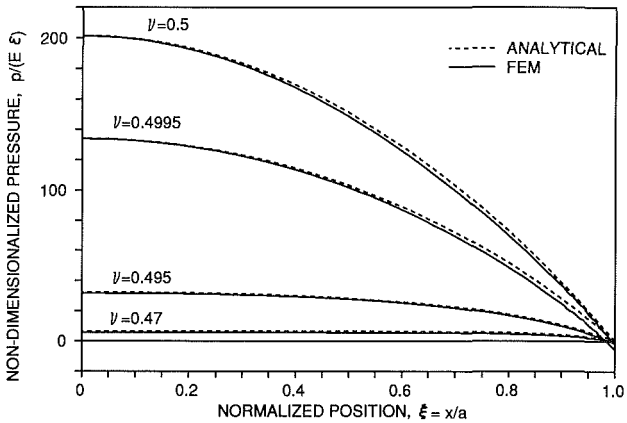


Fig. 9 A comparison of closed-form and finite element method results for pressure distributions for several Poisson's ratios

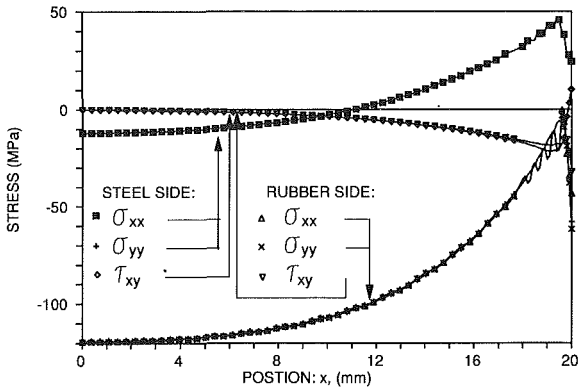


Fig. 10 Distribution of stress components at the steel/elastomer interface

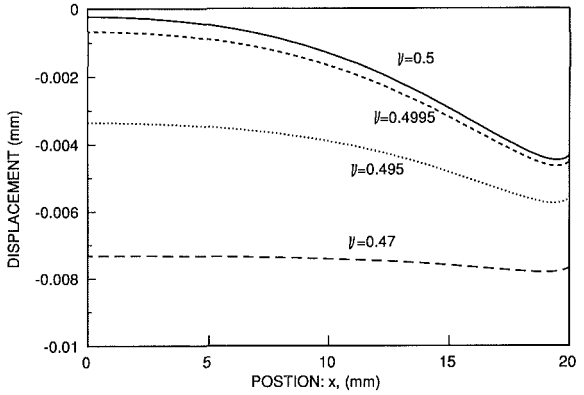


Fig. 11 Displacement of the steel/elastomer interface for several Poisson's ratios

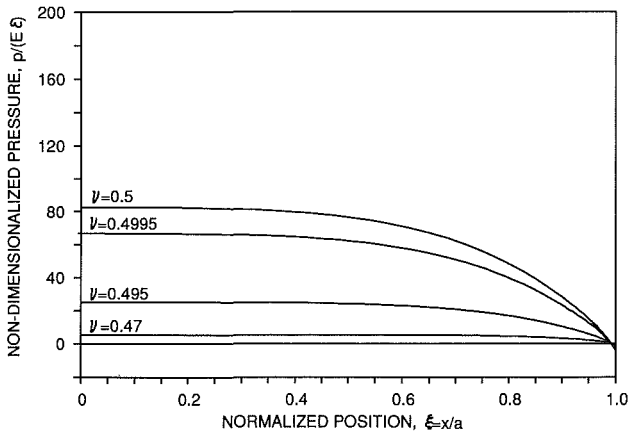


Fig. 12 Pressure distributions for a steel/elastomer sandwich

lution accurately predicts stresses when the adherends may be considered rigid.

Unfortunately, when the shape factor of the elastomer becomes large, compliance of even massive steel adherends may not be negligible when compared to the compressibility of the elastomer. The following finite element results illustrate this effect for a typical case of $h/a = 0.1$. The thickness of the steel adherends was arbitrarily chosen to be 20 mm which is ten times the thickness of the elastomer. Figure 10 shows various stress components along the interface in both the steel and rubber ($\nu = 0.4995$) elements. Note that σ_x and σ_y in the elastomer and σ_y in the steel are all identical except in the vicinity of the free edge. The fact that σ_x and σ_y in the elastomer are indistinguishable validates the assumption used by Gent and Meinecke (1970) and in our analytical solution that $\sigma_x = \sigma_z = \sigma_y - f_1 E\epsilon$, even at a Poisson's ratio slightly less than 0.5. Deviations do become larger as Poisson's ratio decreases to 0.47, but even then there is only a 15 percent difference between σ_x and σ_y over most of the width.

Figure 11 illustrates the effect of compressibility on the displacement along the steel/elastomer interface. The imposed displacement at the top of steel substrate was 0.01 mm. It is seen that the larger the Poisson's ratio, the more significant the change of displacement distribution. It is also found that for large Poisson's ratios, the deformation in the steel is much larger than it is in the elastomeric layer. The results suggest that for the case of large Poisson's ratio, relatively large deformations occur in the steel position due to the high pressure built up at the elastomer layer. Figure 12 illustrates the normalized pressure versus position. Since the displacement is not uniform along the interface, the strain used in the figure has been averaged by the following procedure. First, the total average strain in the steel was calculated by multiplying the average σ_y in the interface and the compliance of steel for the plane-strain case, $(1-\nu^2)/E$. Then the average displacement in the interface and average strain in the elastomer can be easily determined. By comparing with the case of rigid substrate (Fig. 9) it is seen that for $\nu = 0.47$ the deviation is less than six percent, while for $\nu = 0.5$ the deviation is as large as 60 percent. The deviation decreases as ν decreases. These differences could change if different boundary conditions were imposed or if different geometries were used. In estimating compressibility effects it is essential to include the average strains induced in the adherends. This can often be done by knowing the di-

Downloaded 03 May 2010 to 171.66.16.247. Redistribution subject to ASME license or copyright; see http://www.asme.org/terms/Terms_Use.cfm

mensions and constitutive properties of the platens. Local variations in displacements of the platen surfaces can cause further perturbations to the analytical solution. This perturbation becomes more pronounced as the elastomer becomes less compressible, and as the shape factor increases.

Finite Rectangular Geometry

The finite element analysis has shown that the analytical solution is accurate as long as the platens may be considered to be rigid. The analytical approach may easily be extended to the case of a rectangular elastomeric block bonded to rigid adherends. The dimensions are illustrated in Fig. 13.

$$\frac{\partial u}{\partial x}+\frac{\partial v}{\partial y}=\frac{3}{2}\left[\epsilon-\frac{p(x,y)}{K}\right] \tag{21}$$

where u is the displacement of the vertex of the parabola in the x-direction and v is the displacement in the y-direction. The stress equilibrium relations are

$$\frac{\partial p}{\partial x}=\frac{-2\tau_{xz}(x,y)}{h}=-\frac{8G}{h^2}u(x,y) \tag{22}$$

$$\frac{\partial p}{\partial y}=\frac{-2\tau_{yz}(x,y)}{h}=-\frac{8G}{h^2}v(x,y). \tag{23}$$

Again, u and v are measured at the midplane, whereas τ_{xz} and τ_{yz} are the values at the interface. Differentiating Eqs. (22) and (23) substituting into Eq. (21), we obtain the governing differential equation

$$p_{,xx}+p_{,yy}-\lambda^2 p=-q. \tag{24}$$

Subject to

$$p(-a,y)=p(a,y)=p(x,-b)=p(x,b)=0$$

and where

$$\lambda^2=\frac{12G}{Kh^2} \text{ and } q=\frac{12G}{h^2}\epsilon,$$

the solution takes the form

$$p(x,y)=\sum_{n=1.3.5\ldots}^{\infty}\sum_{m=1,3,5\ldots}^{\infty}C_{mn}\cos\frac{n\pi x}{2a}\cos\frac{m\pi y}{2b} \tag{25}$$

where

$$C_{mn}=\frac{\dfrac{192G\epsilon}{nm\pi^2h^2}(-1)^{[(m+n)/2-1]}}{\dfrac{n^2\pi^2}{4a^2}+\dfrac{m^2\pi^2}{4b^2}+\lambda^2}. \tag{26}$$

By integrating over the rectangle, we obtain the average pressure

$$\bar{p}=\sum_{n=1,3,5\ldots}^{\infty}\sum_{m=1,3,5\ldots}^{\infty}\frac{\dfrac{768G\epsilon}{n^2m^2\pi^2h^2}}{\dfrac{n^2\pi^2}{4a^2}+\dfrac{m^2\pi^2}{4b^2}+\lambda^2} \tag{27}$$

The maximum displacement along the edge $x=a$ is obtained from Eq. (22).

$$u(a,y)=\frac{h^2\pi}{16Ga}\sum_{n=1,3,5\ldots}^{\infty}\sum_{m=1,3,5\ldots}^{\infty}nc_{mn}\sin\frac{m\pi y}{2b}. \tag{28}$$

The above expressions can also be placed in nondimensional form by letting

$$\xi=\frac{x}{a},\quad \zeta=\frac{y}{b},\quad \eta=\frac{h}{a},$$

$$\phi=\frac{b}{a},\quad \text{and } \beta=a\lambda.$$

This allows us to write that

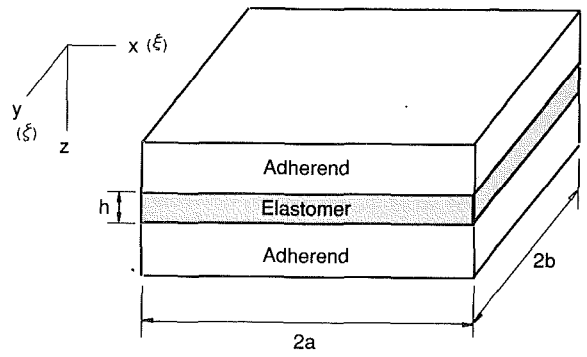


Fig. 13 Configuration of finite rectangular block between two rigid adherends

$$p(\xi,\zeta)=\sum_{n=1,3,5\ldots}^{\infty}\sum_{m=1,3,5\ldots}^{\infty}\frac{768G\epsilon}{mn\pi^4\eta^2}\times(-1)^{\dfrac{[(m+n)/2-1]\cos\frac{n\pi}{2}\xi\cos\frac{m\pi}{2}\zeta}{n^2+m^2/\phi^2+4\beta^2/\pi^2}} \tag{29}$$

and

$$\bar{p}=\sum_{n=1,3,5\ldots}^{\infty}\sum_{m=1,3,5\ldots}^{\infty}\frac{\dfrac{3072G\epsilon}{n^2m^2\pi^6\eta^2}}{n^2+m^2/\phi^2+4\beta^2/\pi^2}. \tag{30}$$

Graphs of these solutions have not been given, although they show similar trends to the infinite strip case. Limiting cases agree with the elementary solution by Freakley and Payne (1978).

$$\frac{E_{\text{eff}}}{E}=\frac{4}{3}\left[1+\left[\frac{1}{\eta}\right]^2\right]$$

Discussion

Solutions have been presented for the stiffness of thin elastomeric layers bonded between rigid platens. By considering the bulk compressibility of the elastomer, the stress redistribution and effective stiffness are substantially different than predicted by an incompressible analysis. When the shape factor of an elastomeric block with $\nu=0.4995$ has a value of 5, effective stiffness is off by ten percent. Shape factors of 10 and 20 result in effective stiffness errors of 47 percent and 187 percent, respectively, unless the rubber compressibility is accounted for. The solution technique has been applied to infinitely long strips with a finite width and rectangular blocks and may be extended to the very practical problem of a thin elastomeric annular bushing. The solutions are based on the assumption that the platen displacement is small compared to the elastomer thickness, but this assumption is well justified for large shape factors in which the stiffnesses become very high. This assumption does not imply that shear strains are small, and in fact they can be quite large at the free edges. Assumptions that the shear modulus of elastomers remains linear up to fairly large strain levels is also physically reasonable.

A numerical analysis has been conducted, and verifies that the assumptions and solutions from the analytical investigation are very accurate if the adherends may be considered rigid. The numerical solutions, however, have revealed that even steel adherends may deform significantly if Poisson's ratio is near 0.5 and if the aspect ratio is large. This renders the closed-form solutions of questionable accuracy for certain problems. Nonetheless, the paper does provide useful insights into the effect of bulk compressibility on the stress distributions and stiffness of large aspect ratio elastomeric blocks and bushings.

Downloaded 03 May 2010 to 171.66.16.247. Redistribution subject to ASME license or copyright; see http://www.asme.org/terms/Terms_Use.cfm

It should be noted that these solutions can be applied directly to the case of thermal expansion or contraction. If a bonded rubber annulus is cooled from vulcanization temperature, rather large shrinkage stresses can occur. Alternatively, cryomating of parts with a rubber annulus can generate compressive stresses which are significantly overestimated by the elementary solution. The results herein are able to estimate these values. At large aspect ratios, however, numerical analysis may be needed to determine the effect of platen compressibility and flexure.

Acknowledgments

The authors would like to acknowledge the support of the Office of Naval Research and the Naval Research Laboratory–Underwater Sound Reference Detachment.

References

Anderson, G. P., Bennett, S. J., and DeVries, K. L., 1977, *Analysis and Testing of Adhesive Bonds*, Academic Press, New York.

Anderson, G. P., DeVries, K. L., and Sharon, G., 1985, "Evaluation of Tensile Tests for Adhesive Bonds," Delamination and Debonding of Material, ASTM STP 876, W. S. Johnson, ed., ASTM, Philadelphia, pp. 115–134.

Dillard, D. A., 1989, "Deformation of Plates on Elastomeric Foundations," ASME JOURNAL OF APPLIED MECHANICS, Vol. 56, pp. 382–386.

Freakley, P. K., and Payne, A. R., 1978, *Theory and Practice of Engineering With Rubber*, Allied Science Publishers, London.

Gent, A. N., Henry, R. L., and Roxbury, M. L., 1974, "Interfacial Stresses for Bonded Rubber Blocks in Compression and Shear," ASME JOURNAL OF APPLIED MECHANICS, pp. 855–859.

Gent, A. N., and Meinecke, E. A., 1970, "Compression, Bending, and Shear of Bonded Rubber Blocks," *Polymer Engineering and Science*, Vol. 10, No. 1, pp. 48–53.

Hibbitt, Carlsson, and Sorensen, Inc., *ABAQUS User Manual*, Version 4-7-1, Providence, RI.

Lindsay, G. H., 1967, "Triaxial Fracture Studies," *Journal of Applied Physics*, Vol. 38, pp. 4843–4852.

Messner, A. M., 1963, "Stress Distributions in Poker Chip Tensile Specimens," Bulletin of Working Group on Mechanical Behavior, CPIA Publ., No. 27, p. 109.

Thornton, J. S., Montgomery, R. E., Thompson, C. M., and Dillard, D. A., 1988, "Analysis of Interfacial Stresses for Elastomeric Gaskets in Compression," *Polymer Science and Engineering*, Vol. 28, No. 10, pp. 655–659.

Treloar, L. R. G., 1975, *The Physics of Rubber Elasticity*, 3rd ed., Clarendon Press, Oxford.

Williams, M. L., Schapery, R. A., Zak, A., and Lindsay, G. H., 1963, "The Triaxial Tensile Behavior of Viscoelastic Materials," California Technological Institute, GALCIT Report No. SM63-6.

Zienciewicz, 1977, *The Finite Element Method*, McGraw-Hill, New York.

Downloaded 03 May 2010 to 171.66.16.247. Redistribution subject to ASME license or copyright; see http://www.asme.org/terms/Terms_Use.cfm

Per C. Hemmer
Professor of Physics,
Institutt for Fysikk,
Norges Tekniske Høgskole,
N-7034 Trondheim, Norway

Alex Hansen
CNRS Staff Scientist,
Group Matière Condensée et Matériaux,
Université de Rennes 1,
F-35042 Rennes Cedex, France

The Distribution of Simultaneous Fiber Failures in Fiber Bundles

A bundle of many parallel fibers, with stochastically distributed thresholds for individual fibers, is loaded until complete failure. Equal load sharing is assumed. During the breakdown process, bursts of several fibers breaking simultaneously at a given load occur. We determine the expected number of such bursts before complete failure, as well as the frequency of bursts in which Δ fibers break simultaneously. This distribution follows asymptotically a universal power-law $\Delta^{-5/2}$, for any statistical distribution of the individual fiber strengths.

1 Introduction

Consider N parallel fibers of equal length l_0 and clamped at both ends. The fibers are stretched until they fail. As each individual fiber breaks, the load distributes itself equally among the surviving fibers, while the failed fibers carry no load. Such a situation is encountered when testing the strength of, say, long flexible cables or low-twist yarns. In order to simplify the problem, each fiber is assumed to obey Hookean elasticity right up to the breaking point. Also, the fibers are assumed to have identical elastic properties, while their strength—i.e., the maximum load they are able to carry before failure—varies from fiber to fiber according to some probability distribution. This may be justified by noting that the distribution of elastic properties of individual fibers narrows down much faster with the length of the fibers than does the distribution of strength of single fibers since the elastic property is an average along the fiber, while its strength is determined by its weakest point (Daniels, 1945).

If fiber i is stretched to a length $l = l_0 + x$, its force response is

$$f_i = \begin{cases} \kappa x & \text{, if } x < t_i; \\ 0 & \text{, if } x \geq t_i. \end{cases} \tag{1}$$

Here, t_i is the failure threshold of this fiber, and κ is the elastic modulus. The threshold value t_i is picked from a continuous cumulative distribution $P(t)$ with corresponding probability density $p(t)$:

$$\text{Prob}(t_i < t) = P(t) = \int_0^t p(u)du. \tag{2}$$

Let x_k be the *ordered* sequence of failure thresholds t_i: $x_1 \leq x_2 \leq \ldots \leq x_N$. The external load F on the bundle at the point where the kth fiber is about to fail can then be expressed as

$$F_k = \kappa(N + 1 - k)x_k, \tag{3}$$

and the maximum strength of the whole bundle, S, is therefore

$$S = \max_k F_k. \tag{4}$$

The average strength $\bar{F}(x)$ at elongation x is easy to assess for large N by noting that $P(x_k) \simeq k/(N + 1)$. Hence, Eq. (3) yields for large N

$$\bar{F}(x)/N \simeq \kappa x[1 - P(x)]. \tag{5}$$

For the average bundle strength, $\bar{S}$, one therefore has asymptotically

$$\bar{S}/N \simeq \max_x \kappa x[1 - P(x)]. \tag{6}$$

The statistical properties of the strength of bundles of such fibers is a classical problem which has been studied over a number of years apparently beginning with the work by Peirce (1926). A major step forward was taken by Daniels (1945), who showed that for a wide class of threshold distributions, $P(t)$, for the individual fibers, the distribution of bundle strengths approaches asymptotically for large N a Gaussian distribution around the value $\bar{S}$ given by Eq. (6).

Further properties of the distribution of the bundle strength have been discussed by Suh et al. (1970), Sen (1973a, 1973b), Phoenix and Taylor (1973), and Sornette (1989). Moreover, this simple model has been generalized in several ways during the last years, by invoking nonlinear elastic properties (Phoenix and Taylor, 1973), and by connecting bundles of parallel fibers in *series* (Smith and Phoenix, 1981; Sornette and Redner, 1989).

In the present paper we study in more detail the rupture process under a steadily increasing external load F on the fiber bundle.

We note first that the sequence $\{F_k\}$ of external loads at which the fibers would fail do *not* form a monotonically increasing sequence. This is easily understood from Eq. (3), since, with increasing k, F_k is a product of a monotonically increasing *fluctuating* factor x_k and a monotonically decreasing factor $(N + 1 - k)$. Since the sequence $\{F_k\}$ is not monotonically increasing, all values F_k will not be realized in the rupture process. Assume that the external load F has reached a value F_k, and that the subsequent values satisfy $F_{k+j} \leq F_k$ for $j =$

Contributed by the Applied Mechanics Division of THE AMERICAN SOCIETY OF MECHANICAL ENGINEERS for publication in the ASME JOURNAL OF APPLIED MECHANICS.

Discussion on this paper should be addressed to the Technical Editor, Professor Leon M. Keer, The Technological Institute, Northwestern University, Evanston, IL 60208, and will be accepted until four months after final publication of the paper itself in the ASME JOURNAL OF APPLIED MECHANICS.

Manuscript received by the ASME Applied Mechanics Division, May 14, 1991; final revision, Nov. 18, 1991. Associate Technical Editor: G. J. Dvorak.

Copyright © 1992 by ASME
Downloaded 03 May 2010 to 171.66.16.247. Redistribution subject to ASME license or copyright; see http://www.asme.org/terms/Terms_Use.cfm

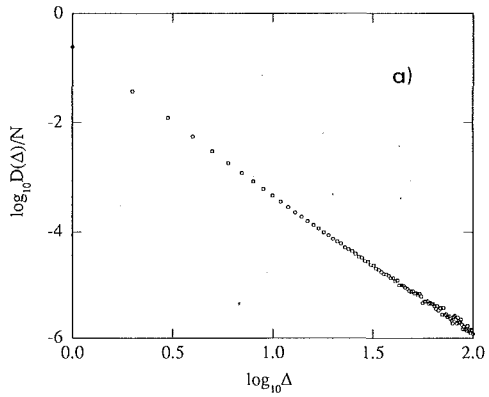


Fig. 1(*a*)

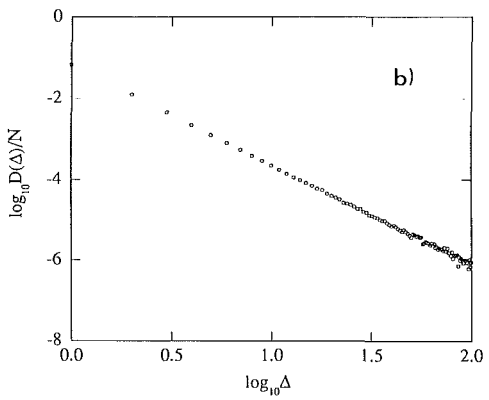


Fig. 1(*b*)

Fig. 1 The distribution of bursts, $D(\Delta)/N$ for (*a*) the uniform threshold distribution, $P(t) = t$, where $0 \le t \le 1$, and (*b*) the Weibull distribution $P(t) = 1 - \exp(-t^5)$, where $0 \le t < \infty$. Both figures are based on 1000 samples of bundles with $N = 50{,}000$ fibers.

1, 2, ..., $\Delta - 1$ while $F_{k+\Delta} > F_k$. In this case all fibers corresponding to F_k, F_{k+1}, ..., $F_{k+\Delta-1}$ fail, without changing the external load, before the bundle again reaches equilibrium. We call this "simultaneous" failure a *burst* of size Δ, and the aim of the present paper is to determine the expected number, $D(\Delta)$, of bursts of size Δ.

In Fig. 1 we show results for $D(\Delta)$ in two simulation experiments on fiber bundles. The cumulative threshold distributions in the two simulations were the uniform distribution on the unit interval, $P(t) = t$, for $0 \le t \le 1$, and the Weibull distribution $P(t) = 1 - \exp(-t^5)$ for $0 \le t < \infty$ (arbitrary units). In both cases the histograms indicate an asymptotic power-law behavior,

$$D(\Delta) \simeq C\Delta^{-\xi}. \tag{7}$$

The exponent ξ is, in both cases, close to the value 2.5, and we will in fact prove that it takes the *universal* value

$$\xi = \frac{5}{2}, \tag{8}$$

independent of the underlying threshold distribution. The prefactor C is nonuniversal.

In Section 2 we derive the burst distribution, $D(\Delta)$, for large N, and in Section 3, the asymptotics and other consequences are extracted from the expression for the burst distribution. We discuss in Section 4 the distribution of *inclusive* bursts, i.e., also counting bursts occurring inside larger bursts. This distribution also shows a universal power law, but with a *different* exponent. Section 5 contains our conclusions and a few remarks on the more complicated models alluded to above.

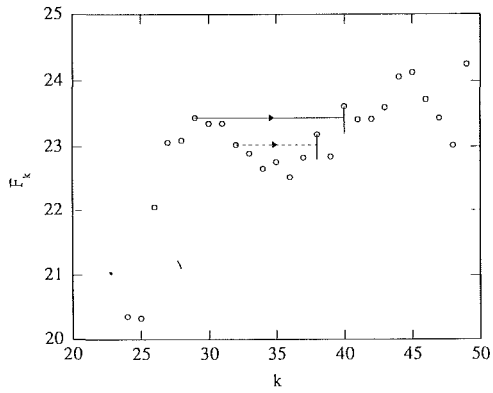


Fig. 2 The figure shows how F_k *versus* k develops for $24 \le k < 50$ for a bundle containing $N = 100$ fibers. The solid line marks a burst of size $\Delta = 11$, while the dashed line exemplifies an *inclusive* burst of size $\Delta = 6$.

2 The Burst Distribution

For a burst of size Δ to start when the kth fiber is about to fail, two conditions must be fulfilled.

The first condition is the forward condition

$$F_{k+j} < F_k \quad \text{for } j = 1,2,\ldots,\Delta-1, \tag{9}$$

and

$$F_{k+\Delta} > F_k. \tag{10}$$

This is not sufficient, however. We must also secure that F_k exceeds all previous values,

$$F_j < F_k \quad \text{for all } j < k, \tag{11}$$

which may be called the backward condition. Otherwise the burst may occur *inside* a larger burst (see Fig. 2), and consequently will not be recorded in experiments with increasing external load.

We note in passing that, although not of direct experimental relevance, the distribution of events in which the backward condition (11) is relaxed, can also be determined (Section 4). This *inclusive* burst distribution will also follow an asymptotic power law of the form (7), but—as we shall see—with an exponent $\xi = 2$ rather than 5/2.

Both the forward and the backward conditions can be phrased as conditions on the threshold values x_k. One sees from Eq. (3) that

$$F_{k+j} \gtrless F_k \tag{12}$$

is equivalent to

$$x_{k+j} \gtrless x_k \frac{N+1-k}{N+1-k-j} = x_k\left[1+\frac{j}{N+1-k-j}\right]. \tag{13}$$

With

$$\delta_k = \frac{x_k}{N+1-k-j} \simeq \frac{x_k}{N-k} \tag{14}$$

assuming $j \ll N - k$, this means that Eq. (12) and Eq. (13) may be simplified to read

$$F_{k+j} \gtrless F_k \Leftrightarrow x_{k+j} \gtrless x_k + j\delta_k. \tag{15}$$

We thus see that for a given Δ and N, $k \to \infty$, the original problem reduces to determining probabilities for threshold values to occur in certain intervals very close to x_k. This simplifying feature arises because all bursts (beyond $\Delta = 1$) are due to *fluctuations* of the $\{F_k\}$ sequence from the average (limiting) characteristics $\bar{F} = F(x)$, Eq. (5), and these fluctuations are very small for large N, of relative order $1/\sqrt{N}$.

2.1 The Forward Condition. We first determine the probability $\phi(\Delta, x_k, k)$ that the forward condition for a burst

Downloaded 03 May 2010 to 171.66.16.247. Redistribution subject to ASME license or copyright; see http://www.asme.org/terms/Terms_Use.cfm

of length Δ starting with the kth fiber at threshold value x_k, is fulfilled.

By Eq. (15) we see that the $\Delta - 1$ threshold values x_{k+1}, ..., $x_{k+\Delta-1}$ must lie in the interval $(x_k, x_k + (\Delta - 1)\delta_k)$, and $x_{k+\Delta}$ must be larger than $x_k + \Delta\delta_k$. The probability for this is

$$\tilde{\phi}(\Delta,x_k,k) = \binom{N-k}{\Delta-1}\left[\frac{P(x_k+(\Delta-1)\delta_k)-P(x_k)}{1-P(x_k)}\right]^{\Delta-1} \times \left[\frac{1-P(x_k+\Delta\delta_k)}{1-P(x_k)}\right]^{N-k-\Delta+1}. \quad (16)$$

Since $\Delta \ll N - k$ is assumed, we may expand in $\Delta\delta_k$. To first order we obtain

$$\tilde{\phi}(\Delta,x_k,k) = \binom{N-k}{\Delta-1}\left[\frac{p(x_k)(\Delta-1)\delta_k}{1-P(x_k)}\right]^{\Delta-1} \times \left[1-\frac{p(x_k)\Delta\delta_k}{1-P(x_k)}\right]^{N-k-\Delta+1}. \quad (17)$$

The last factor on the right-hand side of this expression is, for large $N - k$, essentially

$$\exp\left[-\Delta\frac{x_k p(x_k)}{1-P(x_k)}\right], \quad (18)$$

using $\delta_k = x_k/(N - k)$. The binomial coefficient in Eq. (17) may for $N - k \gg \Delta$ be approximated by

$$\binom{N-k}{\Delta-1} \simeq \frac{(N-k)^{\Delta-1}}{(\Delta-1)!}. \quad (19)$$

Thus,

$$\tilde{\phi}(\Delta,x_k,k) = \frac{1}{(\Delta-1)!}\left[\frac{(\Delta-1)x_k p(x_k)}{1-P(x_k)}\right]^{\Delta-1} \times \exp\left[-\Delta\frac{x_k p(x_k)}{1-P(x_k)}\right]. \quad (20)$$

It remains to secure that all the $\Delta - 1$ inequalities (9) are fulfilled, i.e., that $x_{k+1} < x_k + \delta_k$, $x_{k+2} < x_k + 2\delta_k$, etc., given that all the $\Delta - 1$ threshold values lie in the interval $(x_k, x_k + (\Delta - 1)\delta_k)$. Since the probability density can be considered constant in the small interval $(\Delta - 1)\delta_k$, this is equivalent to the following combinatorial problem: $\Delta - 1$ elements are to be randomly distributed among $\Delta - 1$ numbered slots, and we require the probability $\epsilon_{\Delta-1}$ that the first slot contains at least one element, the two first slots contain at least two elements, and so on. In the Appendix we show that

$$\epsilon_{\Delta-1} = \frac{\Delta^{\Delta-2}}{(\Delta-1)^{\Delta-1}}. \quad (21)$$

The desired probability for the forward condition to be fulfilled is then

$$\phi(\Delta,x_k,k) = \tilde{\phi}(\Delta,x_k,k)\epsilon_{\Delta-1} = \frac{\Delta^{\Delta-1}}{\Delta!}\left[\frac{x_k p(x_k)}{1-P(x_k)}\right]^{\Delta-1} \times \exp\left[-\Delta\frac{x_k p(x_k)}{1-P(x_k)}\right]. \quad (22)$$

2.2 The Backward Condition. The backward condition is simply that F_k should be the largest breaking force that has appeared until the kth fiber (threshold value x_k) fails. For an *average* force $\bar{F}(x)$ which is an increasing function of the elongation x, it is clear that in general it is the first few *neighboring* force values, F_{k-1}, F_{k-2}, ..., that are most likely to exceed F_k due to fluctuations. Let us therefore determine $\chi(d, x_k, k)$, the probability that none of the values F_{k-1}, F_{k-2}, ..., F_{k-d} exceed F_k, for $d \ll N$.

For the simplest case $d = 1$ we have, by Eq. (22),

$$\chi(1,x_k,k) = \exp\left[-\frac{x_k p(x_k)}{1-P(x_k)}\right], \quad (23)$$

since the probability that F_{k-1} does not exceed F_k equals the probability that the forward condition for a burst of size $\Delta = 1$ to occur, is fulfilled.

To determine $\chi(d, x_k, k)$ for $d \neq 1$ we need, according to Eq. (15), the probability that

$$\begin{aligned} x_{k-1} &< x_k - \delta_k \\ x_{k-2} &< x_k - 2\delta_k \\ &\vdots \\ x_{k-d} &< x_k - d\delta_k. \end{aligned} \quad (24)$$

This implies that a number h, not exceeding $d - 1$, of threshold values may be in the small interval $(x_k - d\delta_k, x_k - \delta_k)$, while all the $k - 1 - h$ remaining threshold values (below x_k) must be smaller than $x_k - d\delta_k$. The probability for this is

$$\binom{k-1}{h}\left[\frac{(d-1)\delta_k p(x_k)}{P(x_k)}\right]^h\left[1-\frac{d\delta_k p(x_k)}{P(x_k)}\right]^{k-1-h}. \quad (25)$$

Since k is of order N and $\delta_k = x_k/(N - k)$ of order $1/N$, the last factor on the right-hand side is essentially

$$\exp\left[-\frac{d\delta_k p(x_k)k}{P(x_k)}\right], \quad (26)$$

and the factorial may for $k \gg h$ be approximated by

$$\binom{k-1}{h} \simeq \frac{k^h}{h!}. \quad (27)$$

It remains to secure that the h values in the interval fulfill Eq. (24). This is again a combinatorial problem with $d - 1$ slots, so that at most one value should be found in the slot to the right, at most two values in the two rightmost slots, etc. This problem is also solved in the Appendix, and the probability for all conditions to be fulfilled is

$$\epsilon_{h,d-1} = (d-h)\frac{d^{h-1}}{(d-1)^h}. \quad (28)$$

Multiplying together Eq. (25) and Eq. (28), introducing the simplifications (26) and (27), and summing over the allowed values of h we have

$$\chi(d,x_k,k) = e^{-yd}\sum_{h=0}^{d-1}\frac{(d-h)}{h!d}(yd)^h, \quad (29)$$

with

$$y(x_k) = \frac{\delta_k p(x_k)k}{P(x_k)}. \quad (30)$$

Inserting the expression Eq. (14) for δ_k and again using that $k/N \simeq P(x_k)$ for large N and k, Eq. (30) simplifies to

$$y(x_k) = \frac{x_k p(x_k)}{1-P(x_k)}. \quad (31)$$

The expression (29) may be rewritten as

$$\chi(d,x_k,k) = (1-y)e^{-yd}\sum_{h=0}^{d-1}\frac{(yd)^h}{h!} + e^{-yd}\frac{(yd)^d}{d!}. \quad (32)$$

Note that Eq. (23) is recovered for $d = 1$.

Using $y^d e^{-yd} \leq e^{-d}$, the last term on the right-hand side of Eq. (32) is seen to vanish when d increases. Furthermore, the first term approaches the value it would have had if the sum had continued to ∞, viz. $(1 - y)$. In conclusion,

$$\chi(d,x_k,k) \to m(x_k) \equiv 1 - \frac{x_k p(x_k)}{1-P(x_k)} \quad (33)$$

when d increases. This is therefore the probability that the backward condition is fulfilled when the kth fiber fails.

Downloaded 03 May 2010 to 171.66.16.247. Redistribution subject to ASME license or copyright; see http://www.asme.org/terms/Terms_Use.cfm

Table 1 A comparison between a simulation of 1000 samples of bundles with $N = 50{,}000$ fibers, and numerical integration of Eq. (36). The threshold distribution is $P(t) = t$, where $0 \le t \le 1$.

Δ	Simulation	Eq. (36)
1	0.241897	0.241855
2	0.036876	0.036822
3	0.012173	0.012117
4	0.005548	0.005514
5	0.003018	0.003001
6	0.001842	0.001829
7	0.001206	0.001295
8	0.000853	0.000841
9	0.000620	0.000613
10	0.000469	0.000462

Since we may write

$$m(x) = \frac{1}{1-P(x)} \frac{d}{dx}\left[x(1-P(x))\right], \tag{34}$$

we see that $m(x)$ vanishes at the maximum of the characteristics (5), where the whole bundle fails. This is of course as it should be.

2.3 The Burst Distribution. The probability of a burst of size Δ starting at fiber k with tolerance value x_k is given by the product of the forward and the backward probabilities Eq. (22) and Eq. (33),

$$\frac{\Delta^{\Delta-1}}{\Delta!}\left[1-\frac{x_k p(x_k)}{1-P(x_k)}\right]\left[\frac{x_k p(x_k)}{1-P(x_k)}\right]^{\Delta-1} \times \exp\left[-\Delta \frac{x_k p(x_k)}{1-P(x_k)}\right]. \tag{35}$$

Finally, we must sum over k, since a burst of size Δ may occur at any point before complete failure of the whole bundle. Since Eq. (35) depends only on x_k, we may instead integrate over the threshold values that there are using $Np(x_k)dx_k$ k-values in a small threshold interval dx_k. Thus,

$$\frac{D(\Delta)}{N} = \frac{\Delta^{\Delta-1}}{\Delta!}\int_0^{x_0} dx p(x)\left[1-\frac{xp(x)}{1-P(x)}\right] \times \left[\frac{xp(x)}{1-P(x)}\right]^{\Delta-1} \exp\left[-\Delta \frac{xp(x)}{1-P(x)}\right], \tag{36}$$

where x_0 yields the maximum of the characteristics (5).

This explicit expression for the burst distribution is the main result of our study. We emphasize that it is a large-bundle result, the right-hand side is to be understood as the result for $D(\Delta)/N$ in the limit $N \to \infty$.

In Table 1 we evaluated $D(\Delta)$, Eq. (36), for $\Delta \le 10$ for the uniform distribution $P(t) = t$, $0 \le t \le 1$, and compared it with the simulation data on which Fig. 1(a) is based. The agreement is very good.

3 Properties of the Burst Distribution

We now turn to some consequences of the burst distribution (36).

3.1 Asymptotics. We saw in Fig. 1 that the burst distribution followed the power-law (7) to a good approximation, and we therefore proceed to evaluate $D(\Delta)$ for large Δ. Rewriting Eq. (36) as

$$\frac{D(\Delta)}{N} = \frac{\Delta^{\Delta-1}}{\Delta!}\int_0^{x_0} \frac{dx}{x}\left[1-P(x)-xp(x)\right] \times \left[\frac{xp(x)}{1-P(x)} e^{-\frac{xp(x)}{1-P(x)}}\right]^{\Delta}, \tag{37}$$

we may employ a saddle-point approximation to perform this integration. The function inside the large brackets has a maximum of $1/e$ for the value x_0, satisfying

$$\frac{x_0 p(x_0)}{1-P(x_0)} = 1. \tag{38}$$

Expanding around the maximum to second order in $x - x_0$, integrating and using the Stirling approximation $\Delta! \simeq \Delta^{\Delta} e^{-\Delta}\sqrt{2\pi\Delta}$, we obtain the asymptotic result

$$\frac{D(\Delta)}{N} \simeq C\Delta^{-5/2}, \tag{39}$$

with

$$C = \frac{x_0 p(x_0)^2}{\sqrt{2\pi}\left[x_0 p'(x_0) + 2p(x_0)\right]}. \tag{40}$$

We have thus succeeded in showing that the power-law (39) is *universal*, independent of the threshold distribution. There are only mild restrictions on the cumulative threshold distribution $P(t)$ for the saddle-point evaluation to work. The restrictions are that $x(1 - P(x))$ should have a unique maximum at a finite value x_0, and that $p(x)$ is continuous at x_0.

Since the correction to Eq. (39) is of $O(\Delta^{-3})$, the true asymptotic behavior (39) dominates only when Δ is fairly large.

For a Weibull distribution (in dimensionless form),

$$P(t) = 1 - e^{-t^m}, \quad \text{for } 0 \le t < \infty, \tag{41}$$

say, the amplitude C has the value

$$C = \frac{1}{\sqrt{2\pi}} \frac{1}{me^{1/m}}. \tag{42}$$

It is no surprise that the large bursts mainly appear just before complete failure of the whole bundle, because the fluctuations most effectively introduce nonmonotonicities in the $\{F_k\}$-sequence near the horizontal part of the characteristics. Small bursts occur before that, predominantly at those x-values where the integrand in Eq. (36) is largest.

3.2 The Number of Bursts. The total number of bursts per fiber, B, is obtained by summing the burst distribution over all Δ:

$$B = \sum_{\Delta=1}^{\infty} \frac{D(\Delta)}{N}. \tag{43}$$

We need the sum (with $u \equiv ye^{-y}$)

$$s = \sum_{\Delta=1}^{\infty} \frac{\Delta^{\Delta-1}}{\Delta!} u^{\Delta} = \sum_{\Delta=1}^{\infty} \frac{u^{\Delta}}{\Delta!}\left[\frac{d^{\Delta-1}}{dz^{\Delta-1}} e^{z\Delta}\right]_{z=0}. \tag{44}$$

The theorem of Lagrange (Whittaker and Watson, 1958) allows us to conclude that s satisfies the equation

$$s = ue^{s}. \tag{45}$$

Using the definition $u \equiv ye^{-y}$, we reach the simple conclusion that $s = y$. This yields

$$B = \int_0^{x_0} m(x)p(x)dx = \int_0^{x_0} dx p(x)\left[1-\frac{xp(x)}{1-P(x)}\right]. \tag{46}$$

Downloaded 03 May 2010 to 171.66.16.247. Redistribution subject to ASME license or copyright; see http://www.asme.org/terms/Terms_Use.cfm

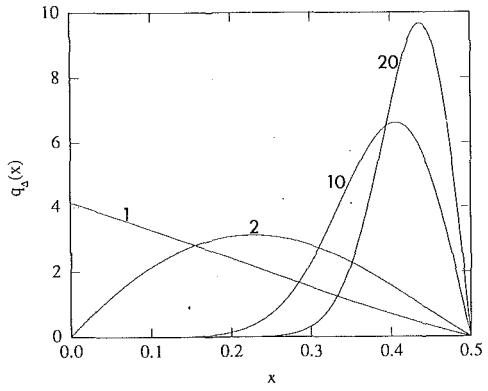


Fig. 3 The probability density $q_\Delta(x)$ for bursts of size $\Delta = 1, 2, 10$, and 20, as function of the elongation x of the fiber bundle. A uniform threshold distribution, $P(t) = t$ for $0 \le t \le 1$, is used. The value of Δ is indicated on the graphs.

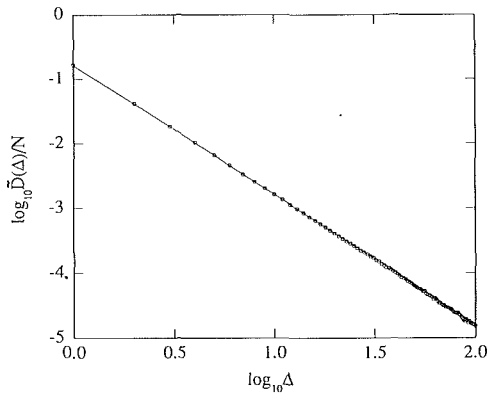


Fig. 4 The distribution of inclusive bursts, $\tilde{D}(\Delta)/N$ for the threshold distribution $P(t) = 1 - \exp(-t^5)$, $0 \le t < \infty$. The straight line is a plot of Eq. (49). The simulation results are based on 1000 samples of bundles with $N = 50{,}000$ fibers.

The physical interpretation is straightforward. Since one always obtains a burst of *some* size in the forward direction, the crucial condition is the backward condition. And Eq. (46) just sums the probabilities for the backward condition to be fulfilled over all fibers.

For a uniform threshold distribution, for instance, one finds $B = 1 - \ln 2 \simeq 0.304$.

3.3 The Failure Process. One may illustrate the development of the failure process by determining the fraction $q_\Delta(x)dx$ of Δ-bursts that occur in the elongation interval $(x, x + dx)$. This is simply the normalized integrand of Eq. (36),

$$q_\Delta(x) = \frac{N}{D(\Delta)} \frac{\Delta^{\Delta-1}}{\Delta!} p(x)m(x)[1 - m(x)]^{\Delta-1} \exp[-\Delta(1-m(x))], \quad (47)$$

where $m(x)$ is given in Eq. (33). As shown in Fig. 3 for the uniform distribution, the single fiber failures become steadily less frequent when the load increases, while bursts of greater length Δ occur most frequently at an elongation that approaches the critical value x_0 when the burst size increases.

4 Inclusive Bursts

If one counts also inclusive bursts, i.e., those bursts occurring *inside* larger bursts as shown in Fig. 2, then the corresponding burst distribution $\tilde{D}(\Delta)$ is identical to Eq. (36), except that the backward condition factor $m(x) = 1 - xp(x)/[1 - P(x)]$ is absent,

$$\frac{\tilde{D}(\Delta)}{N} = \frac{\Delta^{\Delta-1}}{\Delta!} \int_0^{x_0} dx p(x) \left[\frac{xp(x)}{1-P(x)}\right]^{\Delta-1} \times \exp\left[-\Delta \frac{xp(x)}{1-P(x)}\right]. \quad (48)$$

It is noteworthy that the asymptotic behavior of $\tilde{D}(\Delta)$ is again universal, but now with a *different* power law,

$$\frac{\tilde{D}(\Delta)}{N} \simeq \sqrt{2\pi} C \Delta^{-2}. \quad (49)$$

We compare in Fig. 4 this result to simulation results for the Weibull distribution $P(t) = 1 - e^{-t^5}$, where $0 \le t < \infty$. The agreement is excellent.

5 Concluding Remarks

We have obtained the complete analytic distribution law for simultaneous fiber failures in large fiber bundles. A main result is that the power-law exponent $\xi = 5/2$ of the asymptotic burst distribution is *universal*, i.e., independent of the distribution of breaking strengths of the individual fibers.

It is interesting to note that seemingly universal power laws are found empirically for phenomena which have at least a superficial resemblance with the present problem. The phenomenological Gutenberg-Richter law for earthquakes is an example (Knopoff, 1990). In this case the breakdown of elastic forces when the crust ruptures due to buildup of shear stress leads to a power-law dependence of the frequency of earthquakes upon their release of energy. The value of the exponent describing this power law varies little from one earthquake region to another.

If one is interested in fracture processes in real *bulk* materials, the present model must be generalized considerably. More realistic models consisting of networks of elastic elements with a distribution in the individual strengths have recently been studied. As the complete force distribution is redistributed each time an element fails under an increasing load, this results in local areas of intense stress competing with the local strength of the network. These models come close to presenting a realistic picture of fracture processes in real inhomogeneous materials. Herrmann and Roux (1990) present a coherent overview of this active field of research.

One of the simplest generalizations of the fiber bundle model is a model in which a number of bundles of parallel fibers are connected in series. Smith and Phoenix (1981) as well as Sornette and Redner (1989) determine the expected failure strengths for large systems of this type, and find fundamentally different behavior depending upon the relative number of series connections. We are presently working on the distribution of simultaneous fiber failures in these systems.

Acknowledgments

We thank J. Feder, E. L. Hinrichsen, J. S. Høye, T. Jøssang, and S. Roux for their discussions. A. H. thanks the German-Norwegian Research Cooperation for financial support.

References

Daniels, H. E., 1945, "The Statistical Theory of the Strength of Bundles of Threads," *Proceedings of the Royal Society, London*, Vol. A183, pp. 405–35.

Herrmann, H. J., and Roux, S., eds., 1990, *Statistical Models for the Fracture of Disordered Media*, Elsevier Science Publishers, Amsterdam.

Knopoff, L., 1990, "The Phenomenology of Earthquake Occurrence," *Disorder and Fracture*, J. C. Charmet, S. Roux, and E. Guyon, eds., Plenum Press, New York.

Peirce, F. T., 1926, "Theorems on the Strength of Long and of Composite Specimens," *Journal of the Textile Industry*, Vol. 17, pp. 355–368.

Phoenix, S. L., and Taylor, H. M., 1973, "The Asymptotic Strength Distribution of a General Fiber Bundle," *Advances in Applied Probability*, Vol. 5, pp. 200–216.

Sen, P. K., 1973a, "An Asymptotically Efficient Test for the Bundle Strength of Filaments," *Journal of Applied Probability*, Vol. 10, pp. 586–596.

Sen, P. K., 1973b, "On Fixed Size Confidence Bands for the Bundle Strength of Filaments," *The Annals of Statistics*, Vol. 1, pp. 526–537.

Downloaded 03 May 2010 to 171.66.16.247. Redistribution subject to ASME license or copyright; see http://www.asme.org/terms/Terms_Use.cfm

Smith, R. L., and Phoenix, S. L., 1981, "Asymptotic Distributions for the Failure of Fibrious Materials under Series-Parallel Structure and Equal Load-Sharing," ASME JOURNAL OF APPLIED MECHANICS, Vol. 48, pp. 75–82.

Sornette, D., 1989a, "Elasticity and Failure of a Set of Elements Loaded in Parallel," *Journal of Physics A: Mathematical and General*, Vol. 22, pp. L243–L250.

Sornette, D., and Redner, S., 1989b, "Rupture in the Bubble Model," *Journal of Physics A: Mathematical and General*, Vol. 22, pp. L619–L625.

Suh, M. W., Battacharyya, B. B., and Grandage, A., 1970, "On the Distribution and Moments of the Strength of a Bundle of Filaments," *Journal of Applied Probability*, Vol. 7, pp. 712–720.

Whittaker, E. T., and Watson, G. N., 1958, *A Course of Modern Analysis*, 4th ed., Cambridge University Press, Cambridge, U. K., p. 133.

APPENDIX

In this Appendix we prove, by induction, Eq. (21) and Eq. (28). Let $\epsilon_{h,n}$ be the probability that after distributing randomly h nonidentical particles among n boxes numbered from one to n, box number n will contain at most one particle, boxes n and $n-1$ will at most contain two particles, boxes n, $n-1$, and $n-2$ at most three particles, and so on. We make the induction hypothesis that

$$\epsilon_{h,n} = (n-h+1)\frac{(n+1)^{h-1}}{n^h}. \tag{A1}$$

The probability that there are $h-k$ particles in box number one, where $0 \le k \le h$, is

$$\binom{h}{h-k}\left[\frac{1}{n}\right]^{h-k}\left[\frac{n-1}{n}\right]^{k}.$$

Thus, we must have that

$$\epsilon_{h,n} = \sum_{k=0}^{h}\binom{h}{h-k}\left[\frac{1}{n}\right]^{h-k}\left[\frac{n-1}{n}\right]^{k}\epsilon_{k,n-1}. \tag{A2}$$

Using the expression (A1) for $\epsilon_{k,n-1}$, we get

$$\epsilon_{h,n} = \frac{1}{n^h}\sum_{k=0}^{h}\binom{h}{k}(n-k)n^{k-1}$$

$$= \frac{1}{n^h}\left[1-\frac{d}{dn}\right]\sum_{k=0}^{h}\binom{h}{k}n^k$$

$$= (n-h+1)\frac{(n+1)^{h-1}}{n^h}, \tag{A3}$$

which is identical to Eq. (A1). As Eq. (A1) is correct for $n = 2$, the induction hypothesis is proven.

Setting $h = n$ in Eq. (A1) leads to

$$\epsilon_n \equiv \epsilon_{n,n} = \frac{(n+1)^{n-1}}{n^n}, \tag{A4}$$

which is identical to Eq. (21) for $n = \Delta - 1$.

Downloaded 03 May 2010 to 171.66.16.247. Redistribution subject to ASME license or copyright; see http://www.asme.org/terms/Terms_Use.cfm

H. Fan[1]
Assoc. Mem. ASME

G. E. O. Widera[2]
Fellow ASME.

Department of Mechanical Engineering,
University of Illinois at Chicago,
Chicago, IL 60680

On the Proper Boundary Conditions for a Beam

Employing the asymptotic expansion approach, the boundary conditions of a beam are reconsidered in the present paper. Gregory and Wan's (1984) decay analysis technique is extended here to formulate the boundary conditions for the outer expansion. Among the various prescribed boundary data, most of the attention is focused on the displacement case because engineering beam theories employ incorrect conditions for these data. Numerical calculations are carried out for the displacement prescribed beam having a circular cross-section.

1 Introduction

Simplifying three-dimensional elasticity problems into lower dimensional ones (beams, plates, and shells) has been a topic of research since the beginning of the history of elasticity theory. Recently developed refined theories have become more and more elaborate and contain more and more terms in order to describe the behavior of modern materials, such as anisotropic and nonhomogeneous composites. The accuracy of those theories is expected to be much greater than that of the classical ones. Discussion on the accuracy of those refined formulations have been given by many active researchers in this field (such as Horgan and Knowles, 1983; Nicholson and Simmonds, 1977). Studies by Gregory and Wan (1984, 1985) showed that the boundary conditions for refined plate theories are incorrect for displacement prescribed data. A decay analysis was proposed to take care of this type of boundary condition. Some additional studies employing decay analysis can be found in Wan (1989, 1990), Fan (1989), and Widera et al. (1989).

In the present paper an effort is made to extend Gregory and Wan's (1984) formulation to a beam with a symmetrical but otherwise arbitrary cross-section. Starting from the asymptotic expansions, we formulate a beam theory by employing the dimensionless form of the linear elasticity equations. Decay analysis is then employed to obtain the boundary conditions for the outer expansion rather than the conventional matching approach. There are four kinds of boundary data considered in the paper; however, displacement data receive most of the attention. In Section 4, a numerical example is solved illustrating how the complete formulation can be obtained through the solution of an auxiliary problem. The latter is needed so that the correct boundary conditions for the outer expansion can be determined.

2 Asymptotic Expansion for a Beam

Asymptotic expansions are developed after introducing a small geometric parameter, ϵ, which is defined as the ratio of a cross-sectional length scale of the beam to the axial one. An expansion which is valid in the interior of the beam is called an outer expansion, while one which is valid in the boundary layers (beam end zones) is called an inner expansion.

In our formulation, the Latin letters i, j, k, l take on the values 1, 2, and 3; while Greek letters α and β take on values of 1 and 2. The coordinates and geometry of a beam are shown in Fig. 1(*a*). Its boundary consists of two end planes S_0 and S_L and a lateral surface Σ. Dimensionless coordinates and variables are introduced in the following manner:

$$x_\alpha = \frac{y_\alpha}{R}, \quad x_3 = \frac{y_3}{L} \tag{1}$$

and

$$\tau_{ij} = \frac{\sigma_{ij}}{\sigma}, \quad v_i = \frac{u_i}{L}\frac{E}{\sigma}, \tag{2}$$

where σ is typical level of stress. A small parameter is selected as

$$\epsilon = \frac{R}{L}, \tag{3}$$

where R and L are the characteristic length scales (Fig. 1(*a*)). The dimensionless equations of linear elasticity can now be expressed as follows:

$$\tau_{i\alpha,\alpha} + \epsilon\tau_{i3,3} = 0 \tag{4a}$$

$$(1+\nu)\tau_{\alpha\beta} - \nu\tau_{kk}\delta_{\alpha\beta} = \frac{1}{2\epsilon}(v_{\alpha,\beta} + v_{\beta,\alpha})$$

$$(1+\nu)\tau_{3\alpha} = \frac{1}{2}\left(v_{\alpha,3} + \frac{v_{3,\alpha}}{\epsilon}\right) \tag{4b}$$

$$\tau_{33} - \nu\tau_{\alpha\alpha} = v_{3,3}$$

where $(\,)_{,i} = \partial(\,)/\partial x_i$.

[1]Presently at the Department of Mechanical Engineering, Northwestern University, Evanston, IL 60208.

[2]Presently at the Department of Mechanical and Industrial Engineering, Marquette University, Milwaukee, WI 53233.

Contributed by the Applied Mechanics Division of The American Society of Mechanical Engineers for publication in the ASME Journal of Applied Mechanics.

Discussion on this paper should be addressed to the Technical Editor, Professor Leon M. Keer, The Technological Institute, Northwestern University, Evanston, IL 60208, and will be accepted until four months after final publication of the paper itself in the Journal of Applied Mechanics.

Manuscript received by the ASME Applied Mechanics Division, Jan. 25, 1991; final revision, June 17, 1991. Associate Technical Editor: J. G. Simmonds.

Copyright © 1992 by ASME
Downloaded 03 May 2010 to 171.66.16.247. Redistribution subject to ASME license or copyright; see http://www.asme.org/terms/Terms_Use.cfm

The boundary conditions for this elasticity problem are stated as follows: the lateral surface Σ of the beam is taken to be traction-free, i.e.,

$$\sigma_{i\alpha}n_\alpha = 0 \quad \text{on } \Sigma \tag{5}$$

where $\mathbf{n}$ is the normal vector to Σ. The conditions at the ends will be specified as needed in subsequent sections.

2.1 Outer Expansion. It is straightforward to admit representations of the form

$$f(x_1, x_2, x_3; \epsilon) \sim \epsilon^p \sum_{n=0} \epsilon^n f^{(n)}(x_1, x_2, x_3) \tag{6}$$

where f is a generic function which stands for each of the stress and displacement components and p is to be determined according to the type of deformation. Boundary condition (5) leads to

$$\tau_{\alpha\beta}^{(n)} = 0. \tag{7}$$

The coordinate center in the $x_1 - x_2$ plane is selected by taking

$$\int_S x_\alpha dA = 0, \quad \int_S x_1 x_2 dA = 0.$$

A further simplification regarding the shape of the beam is made by assuming that the x_1-axis is a symmetry axis of the cross-section.

We now restrict our attention to a beam subjected to bending and flexure only. The outer expansions in this case are then given by

$$\begin{aligned}
\tau_{3\alpha} &\sim \epsilon^2 \sum_{n=0} \epsilon^n \tau_{3\alpha}^{(n)} \\
\tau_{33} &\sim \epsilon \sum_{n=0} \epsilon^n \tau_{33}^{(n)} \\
v_\alpha &\sim \sum_{n=0} \epsilon^n v_\alpha^{(n)} \\
v_3 &\sim \epsilon \sum_{n=0} \epsilon^n v_3^{(n)}.
\end{aligned} \tag{8}$$

The relative order among the stresses and displacements as given by (8) rests on arguments which have as their basis the results of elementary beam theory. Upon substitution of expansions (8) into Eq. (4), integration over the cross-section and application of the boundary conditions on Σ yields the following expressions:

$$\begin{aligned}
v_1^{(n)} &= \frac{\nu}{2}(x_1^2 - x_2^2) d_{,33}^{(n-2)}(x_3) + d^{(n)}(x_3) \\
v_2^{(n)} &= \nu x_1 x_2 d_{,33}^{(n-2)}(x_3) \\
v_3^{(n)} &= \chi(x_1, x_2) d_{,333}^{(n-2)}(x_3) - x_1 d_{,3}^{(n)}(x_3)
\end{aligned} \tag{9}$$

where

$$d_{,3333}^{(n)}(x_3) = 0 \tag{10}$$

$$\chi_{,\alpha\alpha} = 2x_1 \quad \text{in } S \tag{11}$$

$$\chi_{,\alpha} n_\alpha = -\frac{\nu}{2}(x_1^2 - x_2^2) n_1 - \nu x_1 x_2 n_2 \quad \text{on } \partial S.$$

Equation (10) is simply the equation of classical beam theory, and as such $d^{(n)}$ represents the deflection of the x_3-axis passing through $x_1 = x_2 = 0$. It is to be determined with aid of the boundary conditions discussed in Section 3. The solution of (11) for $\chi(x_1, x_2)$ can be found in standard textbooks on elasticity theory (say, Sokolnikoff, 1956). With these displacement components, the stress components are obtained through use of Hooke's law, Eq. (4*b*):

$$\begin{aligned}
\tau_{31}^{(n)} &= \frac{1}{2(1+\nu)} \left(\frac{\nu}{2}(x_1^2 - x_2^2) + \chi_{,1} \right) d_{,333}^{(n)}(x_3) \\
\tau_{32}^{(n)} &= \frac{1}{2(1+\nu)} (\nu x_1 x_2 + \chi_{,2}) d_{,333}^{(n)}(x_3) \\
\tau_{33}^{(n)} &= -x_1 d_{,33}^{(n)}(x_3).
\end{aligned} \tag{12}$$

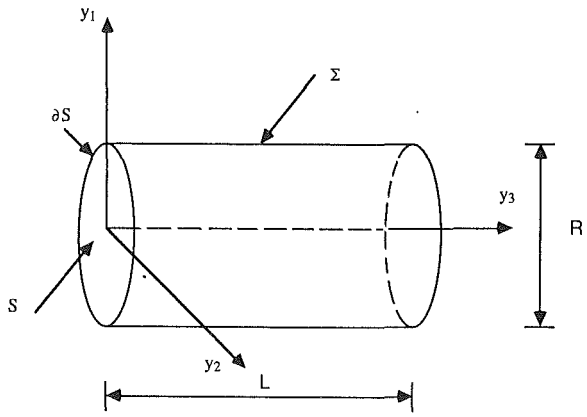


Fig. 1(*a*) Coordinates of beam

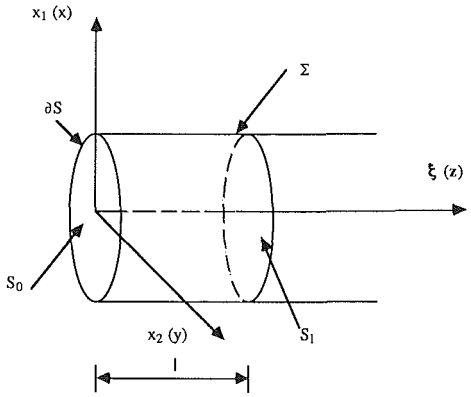


Fig. 1(*b*) Semi-infinite beam

The stress components (12) and displacement components (9) are called the outer expansion and cannot be fully determined until the appropriate boundary conditions for each particular sequence of this expansion are obtained. It is well known that this outer expansion generally can not satisfy the prescribed boundary data at the ends of the beam. Another different type of expansion, one which couples the outer expansions and the prescribed boundary data, is needed.

2.2 Eigenexpansion. With reference to the concept of uniform asymptotic expansion in perturbation theory (see Nayfeh (1973), Section 4.2), one may write the solution for an elastic beam as

$$f(x_1, x_1, x_3, \epsilon) = f^0(x_1, x_2, x_3, \epsilon) + \hat{f}(x_1, x_2, \xi, \epsilon) \tag{13}$$

where

$$\xi = \frac{x_3}{\epsilon}.$$

The first part of (13), $f^0(x_1, x_2, x_3, \epsilon)$, is actually the outer expansion discussed in the previous subsection. The second part, $\hat{f}(x_1, x_2, \xi, \epsilon)$, contains the features of the inner solution which satisfy the boundary conditions on the end planes. Thus, the expression is uniformly valid in the whole domain.

The detailed structure of function $\hat{f}(x_1, x_2, \xi, \epsilon)$ is assumed based upon a consideration of the semi-infinite beam as shown in Fig. 1(*b*). The equilibrium equations and Hooke's law become

$$\hat{\tau}_{i,j} = 0 \tag{14a}$$

$$(1+\nu)\hat{\tau}_{ij} - \nu\hat{\tau}_{kk}\delta_{ij} = \frac{1}{2\epsilon}(\hat{v}_{i,j} + \hat{v}_{j,i}) \tag{14b}$$

where $(\,)_{,3} = \partial(\,)/\partial\xi$, which will be used throughout the eigenexpansion formulation. Note that the domain of this problem is a semi-infinite cylinder, with

Downloaded 03 May 2010 to 171.66.16.247. Redistribution subject to ASME license or copyright; see http://www.asme.org/terms/Terms_Use.cfm

$$\hat{\tau}_{i\alpha}n_\alpha = \bar{t}_i(x_1, x_2, \epsilon\xi) = \bar{t}_i^0(x_1, x_2) + \epsilon\xi\ \bar{t}_i^1(x_1, x_2) + \cdots \text{ on } \Sigma \quad (15a)$$

$$\hat{v}_i = \bar{v}_i \text{ or } \hat{\tau}_{3i} = \bar{\tau}_{3i} \text{ on } S_0 \quad (15b)$$

where $x_1, x_2 \in S$, $\xi \in [0, \infty)$. Another restriction on the solution of the above boundary value problem (BVP) is that both stress and displacement fields do not increase exponentially as $\xi \to \infty$.

We assume that we can expand all the field variables in an ϵ series as follows:

$$\hat{f}(x_1, x_2, \xi; \epsilon) \sim \sum_{n=0} \epsilon^n \hat{f}^{(n)}(x_1, x_2, \xi). \quad (16)$$

Without loss of generality, (14b) can be written as

$$(1+\nu)\hat{\tau}_{ij} - \nu\hat{\tau}_{kk}\delta_{ij} = \frac{1}{2}(\hat{v}_{i,j} + \hat{v}_{j,i}) \quad (17)$$

which is equivalent to neglecting the rigid-body displacements. Furthermore, the traction-free condition

$$\hat{\tau}_{i\alpha}n_\alpha = 0 \quad \text{on } \Sigma$$

allows us to take

$$\hat{f} = \hat{f}(x_1, x_2, \xi). \quad (18)$$

Now, (14a), (16), and (15) form a three-dimensional BVP for a semi-infinite beam. We may expect the solution of this problem to take the following form:

$$\hat{f}(x_1, x_2, \xi) = \sum_{\lambda_k \neq 0} a_k f^k(x_1, x_2) e^{-\lambda_k \xi} \quad (19)$$

where λ_k are eigenvalues to be defined later, and are complex in general. The sum is a group of exponentially decaying terms as $\xi \to \infty$.

With the Navier equations (equilibrium equations in terms of displacement components), we have

$$\hat{v}_{i,jj} + \Lambda\hat{v}_{j,ji} = 0$$

where $\Lambda = 1/1 - 2\nu$. Substituting (13) and (14) into the above equation, we obtain an eigenvalue problem for $\lambda_k \neq 0$ as follows:

$$\begin{cases} v^k_{\alpha,\beta\beta} + \Lambda v^k_{\beta,\beta\alpha} - \Lambda\lambda_k v^k_{3,\alpha} + \lambda_k^2 v^k_\alpha = 0 \\ v^k_{3,\beta\beta} - \Lambda\lambda_k v^k_{\beta,\beta} + \lambda_k^2(1+\Lambda)v^k_3 = 0. \end{cases} \quad (20)$$

The corresponding boundary conditions are a traction-free Σ:

$$\hat{\tau}_{i\alpha}n_\alpha = 0.$$

In view of the above discussion, we may rewrite solution (13) as

$$f(x_1, x_2, x_3, \epsilon) = \sum_{\lambda_k \neq 0} a_k f^k(x_1, x_2) e^{-\lambda_k \xi} + f^0(x_1, x_2, x_3, \epsilon). \quad (13a)$$

The second term in (13a) can generally be written as

$$\tau^0 = T\tau^{VT} + T_m\tau^{VTm} + M\tau^{VB} + Q\tau^{VF}$$

$$\mathbf{v}^0 = T\mathbf{v}^{VT} + T_m\mathbf{v}^{VTm} + M\mathbf{v}^{VB} + Q\mathbf{v}^{VF} + \mathbf{v}_R.$$

The stress and displacement fields are decomposed into four St. Venant solutions. They are tension (T), torsion (T_m), bending (B), and flexure (F). The quantity $\mathbf{v}_R$ represents the rigid-body displacements.

Equation (13a) represents not only the preliminary result for the decay analysis of the next section, but also the starting point of Section 4. By use of this equation, we will show how one can obtain the boundary conditions for the outer expansion without considering explicitly the inner solution.

3 Boundary Conditions for Outer Expansion

Let us start by defining two equilibrium states which will be used throughout this section.

Definition 1. An equilibrium state $\{\tau, \mathbf{v}\}$ in a semi-infinite beam, which satisfies zero surface traction on Σ, is called a *regular state*, if as $\xi \to \infty$, the stress and displacement fields have at worst an algebraic growth.

Definition 2. An equilibrium state $\{\tau, \mathbf{v}\}$ in a semi-infinite beam, which satisfies zero surface traction on Σ, is called a *decay state*, if as $\xi \to \infty$, $\{\tau, \mathbf{v}\} \to \{\mathbf{0}, \mathbf{0}\}$.

The asymptotic expansions in the previous section allow us to write a state $\{\tau, \mathbf{v}\}$ as

$$\tau = M\tau^{\mathbf{VB}} + Q\tau^{\mathbf{VF}} + O(e^{-\lambda\xi}) \quad (21)$$

$$\mathbf{v} = M\mathbf{v}^{\mathbf{VB}} + Q\mathbf{v}^{\mathbf{VF}} + \begin{pmatrix} U - \Theta\xi \\ 0 \\ \Theta x_1 \end{pmatrix} + O(e^{-\lambda\xi}) \quad (22)$$

where

$$\lambda = \text{Min. in } (\lambda_k)$$

$$\tau = \begin{pmatrix} \tau_{\alpha\beta} & \tau_{3\beta} \\ \tau_{\alpha 3} & \tau_{33} \end{pmatrix}, \quad \mathbf{v} = \begin{pmatrix} v_1 \\ v_2 \\ v_3 \end{pmatrix}.$$

Equations (21) and (22) are a mathematical form of St. Venant's principle. Adopting this principle does not mean that we have obtained the correct boundary conditions for the outer expansions. In this paper we will not use the matching technique to obtain the boundary conditions for the outer expansion. Rather a technique, which was proposed by Gregory and Wan (1984) for plate analysis, is used here to obtain the boundary conditions *without* considering the inner expansion solutions.

We take $\{\tau^e_{ij}, v^e_i\}$ as the fields which are obtained from the outer expansion equations, and $\{\tau^p_{ij}, v^p_i\}$ as the exact fields which satisfy all the equations in D and all the prescribed boundary condition data (pointwise) at the ends of the beam. We further take

$$\{\tau_{ij}, v_i\} = \{\tau^e_{ij}, v^e_i\} - \{\tau^p_{ij}, v^p_i\} \quad (23)$$

where $\{\tau_{ij}, v_i\}$ are different from zero only in the boundary layers, i.e.;

$$\{\tau_{ij}, v_i\} = O(e^{-\lambda\xi})$$

holds in the interior of the beam while

$$\{\tau_{ij}, v_i\} = O(1)$$

holds in the boundary layers. From definitions 1 and 2, it is seen that $\{\tau^e_{ij}, v^e_i\}$ and $\{\tau^p_{ij}, v^k_i\}$ are regular states, while $\{\tau_{ij}, v_i\}$ are decay states.

We now employ the technique of Gregory and Wan (1984) to connect the prescribed boundary data at $\xi = 0$ and the interior solutions. This method invokes Betti's Theorem (reciprocity theorem), which is written as

$$\int_{\partial D} (\tau^I_{ij}v^{II}_i - \tau^{II}_{ij}v^I_i)n_j dA = 0 \quad (24)$$

where $\partial D = S_0 + S_l + \Sigma$ (Fig. 1(b)). Because surface Σ is traction-free, the above integral can be written as

$$\int_{S_0} (\tau^I_{ij}v^{II}_i - \tau^{II}_{ij}v^I_i)n_j dA + \int_{S_l} (\tau^I_{ij}v^{II}_i - \tau^{II}_{ij}v^I_i)n_j dA = 0. \quad (25)$$

We select state I as follows:

$$\{\tau^I_{ij}, v^I_i\} = \{\tau^e_{ij}, v^e_i\} - \{\tau^p_{ij}, v^k_i\} = \{\tau_{ij}, v_i\}, \quad (26)$$

while state II is some regular state selected according to the given boundary data at $\xi = 0$.

Recall that

$$\{\tau_{ij}, v_i\}_{\xi=l} = O(e^{-\lambda l}) \to 0 \quad \text{as } l \to \infty. \quad (27)$$

Then, if state II is any regular state, we have

$$\int_{S_0} (\tau_{ij}v^{II}_i - \tau^{II}_{ij}v_i)n_j dA \to 0 \text{ as } l \to \infty. \quad (28)$$

Downloaded 03 May 2010 to 171.66.16.247. Redistribution subject to ASME license or copyright; see http://www.asme.org/terms/Terms_Use.cfm

Apparently, the outer solutions determined by the above technique differ from the exact solutions by just an exponentially small error $e^{-\lambda/}$. One may also note that there are an infinite number of states which can be chosen as states *II*. From this point of view, (28) is a necessary condition for a decay state.

We restrict the prescribed boundary data at $\xi = 0$ to the following four kinds:

Case (A) Stress Data

$$\tau_{3i}^{p}(x_1, x_2, 0) = \bar{\tau}_{3i}(x_1, x_2) \tag{29}$$

Case (B) Mixed Data

$$\tau_{3\alpha}^{p}(x_1, x_2, 0) = \bar{\tau}_{3\alpha}(x_1, x_2) \tag{30a}$$

$$v_3^{p}(x_1, x_2, 0) = \bar{v}_3(x_1, x_2) \tag{30b}$$

Case (C) Mixed Data

$$\tau_{33}^{p}(x_1, x_2, 0) = \bar{\tau}_{33}(x_1, x_2) \tag{31a}$$

$$v_\alpha^{p}(x_1, x_2, 0) = \bar{v}_\alpha(x_1, x_2) \tag{31b}$$

Case (D) Displacement Data

$$v_i^{p}(x_1, x_2, 0) = \bar{v}_i(x_1, x_2) \tag{32}$$

Although the above four cases do not cover all the possibilities of prescribed data, other kinds of boundary data can be worked out in a similar fashion.

The prescribed data are now converted to the boundary conditions for the outer expansion such that the difference between the parameter expansion solution and exact solution is exponentially small. The fundamental solutions listed in the Appendix are used to complete this conversion.

Case (A)

Equation (28) is written as

$$\int_{S_0} \{ (\tau_{3i}^{e} - \tau_{3i}^{p}) v_i^{II} - \tau_{3i}^{II}(v_i^{e} - v_i^{p}) \} dA = 0. \tag{28a}$$

Because the τ_{3i}^{I} are prescribed at $\xi = 0$, a state *II* is needed such that $\tau_{3i}^{II} = 0$ at $\xi = 0$. Among our fundamental solutions, the rigid-body displacements correspond to a zero stress field. Thus, the first condition for this stress data case is

$$\tau_{3i}^{II} = 0, \quad v_i^{II} = (U, 0, 0)^T. \tag{33}$$

Substituting (33) into (28*a*), we obtain

$$\int_{S_0} \tau_{13}^{e} dA = \int_{S_0} \bar{\tau}_{13} dA. \tag{34}$$

A similar choice of rigid-body translation yields

$$\int_{S_0} \tau_{23}^{e} dA = 0. \tag{35}$$

The second rigid-body displacement, which corresponds to a rotation, is selected so as to obtain a condition for τ_{33},

$$\tau_{i3}^{II} = 0, \quad v_i^{II} = (-\Theta\xi, 0, \Theta x_1)^T \tag{36}$$

Then we obtain from (28*a*)

$$\int_{S_0} x_1 \tau_{33}^{e} dA = \int_{S_0} x_1 \bar{\tau}_{33} dA. \tag{37}$$

Equations (34), (35), and (37) are well-known forms, although they are generally obtained by use of variational principles.

Case (B)

This case is called the mixed data case, because $\tau_{3\alpha}$ and v_3 are prescribed at $\xi = 0$. The first state *II* is selected as

$$\tau_{3i}^{II} = 0, \quad v_i^{II} = (U, 0, 0)^T. \tag{38}$$

Thus, we have

$$\int_{S_0} \tau_{31}^{e} dA = \int_{S_0} \bar{\tau}_{31} dA \tag{39a}$$

and

$$\int_{S_0} \tau_{32}^{e} dA = 0. \tag{39b}$$

These conditions are equivalent to Case (A) for $\tau_{3\alpha}$, but the condition to follow is one which has not been discussed in the literature. The second state *II* is selected as the St. Venant bending solution (see Appendix). Note that

$$\tau_{3\alpha}^{VB} = 0, \; v_3^{VB} = 0 \text{ at } \xi = 0. \tag{40}$$

With these features, we have

$$\int_{S_0} ((v_3^{e} - \bar{v}_3)\tau_{33}^{VB} + v_1^{VB}(\tau_{31}^{e} - \bar{\tau}_{31}) + v_2^{VB}(\tau_{32}^{e} - \bar{\tau}_{32}))dA = 0. \tag{41a}$$

That is,

$$\int_{S_0} ((v_3^{e} - \bar{v}_3)x_1 + \epsilon \frac{\nu}{2}(x_1^2 - x_2^2)(\tau_{31}^{e} - \bar{\tau}_{31}) + \epsilon\nu x_1 x_2(\tau_{32}^{e} - \bar{\tau}_{32}))dA = 0. \tag{41b}$$

Case (C)

This case is similar to Case (B), and as such involves mixed data. We take the first state *II* as a rigid-body rotation

$$\tau_{3i}^{II} = 0, \quad v_i^{II} = (-\Theta\xi, 0, \Theta x_1). \tag{42}$$

We then obtain

$$\int_{S_0} x_1 \tau_{33}^{e} dA = \int_{S_0} x_1 \bar{\tau}_{33} dA. \tag{43}$$

Next, the St. Venant flexure solution (see Appendix) is taken as the second state *II*. By noting that

$$\tau_{33}^{VF} = 0, \quad v_\alpha^{VF} = 0 \quad \text{at } x_3 = 0, \tag{44}$$

we have

$$\int_{S_0} \{(v_\alpha^{e} - \bar{v}_\alpha)\tau_{3\alpha}^{VF} + v_3^{VF}(\tau_{33}^{e} - \bar{\tau}_{33})\} dA = 0. \tag{45a}$$

Substituting the St. Venant flexure solution into (45*a*) yields

$$\int_{S_0} ((v_1^{e} - \bar{v}_1)\left(\frac{\nu}{2}(x_1^2 - x_2^2) + \chi_{,1}\right) + (v_2^{e} - \bar{v}_2)(\nu x_1 x_2 + \chi_{,2}) - 2(1+\nu)\epsilon\chi(\tau_{33}^{e} - \bar{\tau}_{33}))dA = 0. \tag{45b}$$

Case (D)

The states *II* for these data are the fundamental solutions for the cantilevered beam (fixed at $\xi = 0$),

(i)

$$\tau_{3i}^{II} = \tau_{3i}^{BB}, \; v_i^{II} = 0 \text{ at } \xi = 0. \tag{46}$$

Thus, the condition for the outer expansion is

$$\int_{S_0} (v_i^{e} - \bar{v}_i)\tau_{3i}^{BB} dA = 0. \tag{47}$$

(ii)

$$\tau_{3i}^{II} = \tau_{3i}^{BF}, \quad v_i^{II} = 0 \text{ at } \xi = 0 \tag{48}$$

$$\int_{S_0} (v_i^{e} - \bar{v}_i)\tau_{3i}^{BF} dA = 0 \tag{49}$$

where $(\,)^{BB}$ represents the fields of bending, and $(\,)^{BF}$ the fields of flexure. Both solutions have no analytical form in general. In order to show how to obtain the cantilever solution and so to complete our formulation we select a numerical example, the solid circular cross-section beam, which has been extensively studied. Our purpose will not be to demonstrate the complexity of this problem, rather the procedure to obtain $(\,)^{BB}$ and $(\,)^{BF}$ is our aim.

Downloaded 03 May 2010 to 171.66.16.247. Redistribution subject to ASME license or copyright; see http://www.asme.org/terms/Terms_Use.cfm

It is clear that these solutions are needed for the first-order approximation of the asymptotic expansion. Because they are not available for most cross-sections, all engineering beam theories, including the Bernoulli-Euler and Timoshenko theories, do not qualify as being first-order beam theories.

4 Stress Distribution at Fixed End of a Beam

In Section 3, for the displacement data case (Case (D)), the boundary conditions for the outer expansion are obtained by using solutions of some auxiliary problems. It is the purpose of the present section to complete the formulation of case (D) by solving for the stress field of a clamped beam. For bending and flexure deformations, τ_{3i}^{BB} and τ_{3i}^{BF} at the fixed end are needed to determine the boundary conditions. In this section, we take one of the simplest cross-section shapes, the circular one, to illustrate how to obtain the τ_{3i}^{BB} and τ_{3i}^{BF}.

From a linear elasticity point of view, the stress distribution at the fixed end of a circular cylinder has been an active research subject for a long period of time. We quote here only relatively recent papers as reference. A more extensive historical review on this subject may be found there. The problem may be divided into two parts. The first part of the work is concerned with eigenexpansions, which can be used for all kinds of prescribed data at the end (Cases (A), (B), (C), and (D)). Major contributions to these expansions were made by Power and Childs (1971), Fama (1972), and, more recently, Robert and Keer (1987). Some of their formulations, such as the orthogonality relations among eigenfunctions, are used in the following without detailed proof and derivation. Other approaches, such as those of Gregory and Gladwell (1982) and Gupta (1973), are also recommended for use in obtaining the solution of the present problem.

Cylindrical coordinates are selected for this problem as follows:

$$x_1 = r\cos\theta,\ x_2 = r\sin\theta,\ \xi = z.$$

As discussed in Section 2, Eq. (13a), the solution of the elasticity problem is taken in the following form:

$$\Phi = \sum_{m=0}^{\infty} \cos m\theta \left(\sum_{\lambda_{mk}} a_{mk} e^{-\lambda_{mk} z} \Phi_{mk}(r) + \Phi_{m0}(r, z) \right) + \sum_{m=1}^{\infty} \sin m\theta \left(\sum_{\lambda_{mk}} b_{mk} e^{-\lambda_{mk} z} \Phi_{mk}(r) + \Phi_{m0}(r, z) \right) \quad (50a)$$

$$\Psi = \sum_{m=0}^{\infty} \sin m\theta \left(\sum_{\lambda_{mk}} a_{mk} e^{-\lambda_{mk} z} \Psi_{mk}(r) + \Psi_{m0}(r, z) \right) - \sum_{m=1}^{\infty} \cos m\theta \left(\sum_{\lambda_{mk}} b_{mk} e^{-\lambda_{mk} z} \Psi_{mk}(r) + \Psi_{m0}(r, z) \right) \quad (50b)$$

where

$$\Phi = \begin{pmatrix} u \\ w \\ \sigma_{zz} \\ \sigma_{rz} \end{pmatrix}, \quad \Psi = \begin{pmatrix} v \\ \sigma_{\theta z} \end{pmatrix}$$

and u, v, and w are the displacements in the r, θ, and z-directions, respectively. In order to use some existing results, we normalize the stresses by dividing them by $2G$ (shear modulus), and the displacements by R (outer radius of the circle). We continue to assume

$$\sigma_{i\alpha} n_\alpha = 0 \quad \text{on } \Sigma.$$

The eigenvalues are restricted by taking $\mathrm{Re}(\lambda_{mk}) > 0$, because we expect that all fields do not approach infinity exponentially as $z \to \infty$.

The bending and flexure deformations correspond to $m = 1$ in the above expansions, i.e.,

$$\Phi = \cos\theta \left(\sum_{\lambda_k \neq 0} a_k e^{-\lambda_k z} \Phi_k(r) + \Phi_0(r, z) \right) \quad (51a)$$

$$\Psi = \sin\theta \left(\sum_{\lambda_k \neq 0} a_k e^{-\lambda_k z} \Psi_k(r) + \Psi_0(r, z) \right). \quad (51b)$$

Readers are referred to Robert and Keer's work (1987) on a finite solid circular cylinder with prescribed displacements at both ends for the detailed formulation. However, their numerical results are not suitable for our application because we need two independent solutions, namely, bending and flexure of the semi-infinite cylinder, to complete the determination of the boundary conditions for Case (D) in Section 3. The calculations in the present paper were carried out by using Mathematica (a symbolic derivation software).

It is well known that the stress distributions at the fixed end ($z = 0$) expanded as series of the above eigenfunctions can not be expected to have a rapid convergence because of the singularity at the corner. A special expansion is used here for these stress distributions. Following Benthem and Minderhoud (1972) and Robert and Keer (1987), the stresses at $z = 0$ are expanded as

$$\sigma_{zz} = k_1 \left((1-r)^{-\alpha} - (1-r) + \frac{\alpha}{2}(\alpha+1)(r-r^2) \right) + \sum_{n=1}^{N} a_n J_1(j_{1n} r) \quad (52a)$$

$$(\sigma_{rz} + \sigma_{\theta z}) = k_2((1-r)^{-\alpha} - (1-r) - (\alpha+1)(r-r^2)) + k_3 r^2 + \sum_{n=1}^{N} b_n J_2(j_{2n} r) \quad (52b)$$

$$(\sigma_{rz} - \sigma_{\theta z}) = k_2((1-r)^{-\alpha} + \alpha(1-r)) - k_3 + \sum_{n=1}^{N} c_n J_0(j_{0n} r), \quad (52c)$$

where k_1, k_2, k_3, a_n, b_n, and c_n are to be determined; and j_{0n}, j_{1n}, and j_{2n} are the zero points of $J_0(x)$, $J_1(x)$, and $J_2(x)$, respectively. As $r \to 1$ (see Robert and Keer (1987) or Fan (1989)),

$$k_2 = -\frac{\alpha + 1 - 2\nu}{-\alpha + 2 - 2\nu} \tan\left(\frac{\alpha}{2}\pi\right) k_1. \quad (53)$$

Because all stresses are assumed to be finite as $z \to \infty$, the participation factors in (51a, b) corresponding to $\mathrm{Re}(\lambda_k) < 0$ are taken as zero. The orthogonality relation is written as

$$\int_0^1 (2\sigma_{zz} w_k - (\sigma_{rz} - \sigma_{\theta z})(u+v)_k - (\sigma_{rz} - \sigma_{\theta z})(u-v)_k) r dr = 0 \quad (54)$$

for all eigenvalues $\mathrm{Re}(\lambda_k) > 0$.

For each k, there are three eigenvalues $\mathrm{Re}(\lambda_k) < 0$ (Table 1). These $3N$ equations can not determine all of the unknown coefficients a_N, b_N, c_N, and k_1 and k_3 (k_2 is related to k_1 by (53)). Overall equilibrium of the beam provides the remaining two conditions which complete our formulation. They are moment and shear force equilibrium, i.e.,

$$\int_0^1 (\sigma_{zz})_{z=0} r^2 dr = \begin{cases} 1, & \text{bending} \\ 0, & \text{flexure} \end{cases} \quad (55a)$$

$$\int_0^1 (\sigma_{rz} - \sigma_{\theta z})_{z=0} r dr = \begin{cases} 0, & \text{bending} \\ 1, & \text{flexure} \end{cases}. \quad (55b)$$

As discussed by Benthem and Minderhoud (1972), expansion (52) is an over-completed series, since the Fourier-Bessel expansion (summation terms in (52)) has been shown to be a complete series. The information contained in the first term in (52) should be expressed by this complete series although

Downloaded 03 May 2010 to 171.66.16.247. Redistribution subject to ASME license or copyright; see http://www.asme.org/terms/Terms_Use.cfm

Table 1 Eigenvalues for $\nu = 1/3$

k=1	2.83260	4.30834+i1.49749
k=2	6.69212	7.60681+i1.73931
k=3	9.96625	10.8133+i1.90197
k=4	13.1692	13.9915+i2.02467
k=5	16.3469	17.1569+i2.12324
k=6	19.5125	20.3153+i2.20560
k=7	22.6714	23.4694+i2.27635
k=8	25.8259	26.6207+i2.33835

Table 2 σ_{zz} for bending

r	N=4	N=5	FEM
0.2	0.6691	0.6956	0.6971
0.4	1.4173	1.3968	1.3664
0.6	2.0547	2.0669	2.0669
0.8	2.8794	2.8779	2.8054
0.9		3.3590	3.3509
$r \to 1$	$1.4752(1-r)^{-0.31}$	$1.4658(1-r)^{-0.31}$	

the convergence is very poor. This poor convergence has made it impossible to carry out practical numerical calculations. A term with a singularity feature at $r = 1$ in the expansion helps us to get a rapid convergence for N being a small number. But the expression will not be stable as N gets larger because of the overcompleteness.

Numerical calculations are carried out for $\nu = 1/3$ for which one can obtain $\alpha = 0.310016$ from a singularity study. Comparisons are made for $N = 4$ and $N = 5$, and with a FEM result which is obtained by using the ANSYS (1987) FEM program. The σ_{zz} for the bending load is listed in Table 2 for comparison.

All the stresses for bending and flexure have been calculated for $N = 5$ and are shown in Figs. 2(*a*) through 3(*c*). The constants are given by

$$k_1 = \begin{cases} 1.4658, & \text{bending} \\ -0.43485, & \text{flexure} \end{cases} \tag{56}$$

$$k_3 = \begin{cases} -0.60394, & \text{bending} \\ -1.2286, & \text{flexure} \end{cases} \tag{57}$$

and Tables 3 and 4.

The above stress distributions are needed in Section 3, where they are noted as τ_{3i}^{BB} for bending and τ_{3i}^{BF} for flexure. With these six stress distributions, one can now derive the correct boundary conditions for the outer expansion of a circular cylinder under bending and flexure deformations. Recall that the states τ_{3i}^{BB} and τ_{3i}^{BF} in Betti's theorem are of homogeneous form, thus all the six figures (2(*a*) through 3(*c*)) can be drawn using any normalized coordinate without influencing the final results.

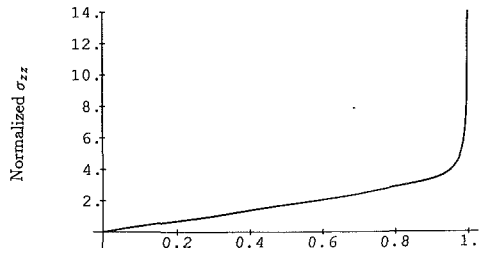


Fig. 2(*a*) σ_{zz} for bending

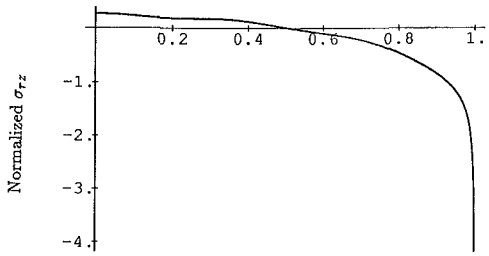


Fig. 2(*b*) σ_{rz} for bending

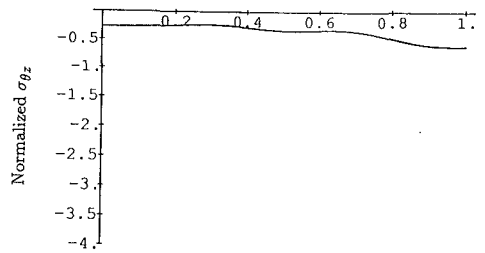


Fig. 2(*c*) $\sigma_{\theta z}$ for bending

Table 3 Constants for bending ($N = 5$)

n	a_n	b_n	c_n
1	1.2601	0.1879	0.5974
2	-0.6097	-0.01401	-0.1250
3	0.3527	-0.06415	0.07073
4	-0.2285	0.1683	-0.06704
5	0.1487	-0.1898	0.1042

Table 4 Constants for flexure ($N = 5$)

n	a_n	b_n	c_n
1	1.8997	-0.06379	1.1422
2	-0.7322	0.08736	-0.1306
3	0.3829	-0.09668	0.01637
4	-0.2233	0.1117	0.01703
5	0.1155	-0.2087	-0.05202

5 Conclusion and Discussion

The present study presents a rigorous formulation of the boundary conditions for a beam structure. The asymptotic expansion technique produces the outer and inner expansion in a consistent manner, and no prior assumptions regarding the displacement and stress distributions need to be made. It was seen that the matching of the outer and inner expansions to obtain a solution is not the aim of this paper; rather Gregory and Wan's scheme (1984) for plane strain is extended to the beam. By using decay analysis, one can expect to obtain the boundary condition for the outer expansion without having to consider the inner expansion.

From the equations in Section 3, it is easy to see that existing refined beam theories contain an error of the first order for displacement prescribed boundary conditions. Variational principles, such as the Reissner variational principle (Reissner 1963), are extensively used for deriving control equations and boundary conditions of these theories. An extension of the present analysis show that those variational principles cannot provide the correct boundary conditions for refined beam theories in general. This subject will be discussed in a separate paper (Fan and Widera (1992)).

The calculations in Section 4 provide the auxiliary solutions which are needed to complete the decay analysis for Case (D).

Downloaded 03 May 2010 to 171.66.16.247. Redistribution subject to ASME license or copyright; see http://www.asme.org/terms/Terms_Use.cfm

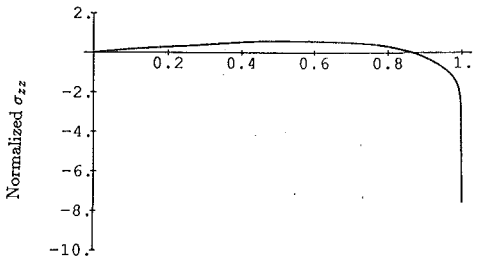


Fig. 3(*a*) σ_{zz} for flexure

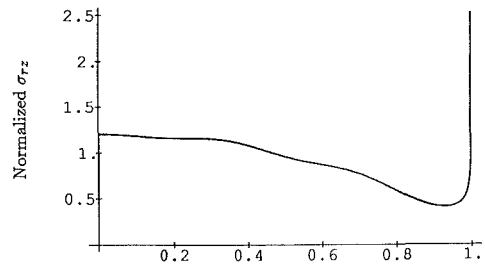


Fig. 3(*b*) σ_{rz} for flexure

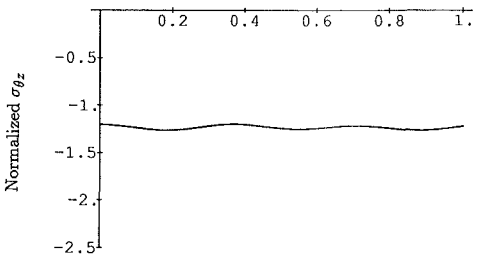


Fig. 3(*c*) $\sigma_{\theta z}$ for flexure

The usefulness of the present analytical result rests in the fact that it provides a benchmark solution which can be used to verify the accuracy of any engineering beam theory, say the Euler-Bernoulli theory (as Gregory and Wan did (1985)) or any variational principle based one. It is seen from Section 4 that although decay analysis provides the correct boundary conditions for a displacement prescribed beam, $(\ )^{BB}$ and $(\ )^{BF}$ are too difficult to obtain for use in an engineering applicable beam theory. As a matter of fact, the formulation and calculations in Section 4 represent the general procedure for the determination of an inner solution. But decay analysis requires only one of these solutions in order to obtain all the boundary conditions for a circular cross-section beam. In other words, the decay analysis reduced the number of inner solutions needed to obtain the boundary conditions for the outer expansions from infinity to one. It seems to the present authors that therein lies the crowning achievement of decay analysis.

Acknowledgment

The authors wish to thank the reviewers for their comments and suggestions on the original version of this paper.

References

ANSYS User's Manual, 1987, Swanson Analysis System Inc., Houston, PA.

Benthem, J. P., and Minderhoud, P., 1972, "The Problem of Solid Cylinder Compressed between Rough Rigid Stamps," *Int. J. Solids and Structures*, Vol. 8, pp. 1027–1042.

Fama, M. E. D., 1972, "Radial Eigenfunctions for the Elastic Circular Cylinders," *Quart. J. Mech. and Applied Math.*, Vol. 25, Pt. 4, pp. 479–495.

Fan, H, 1989, "On the Foundations of Beam Theory," Ph.D. dissertation, University of Illinois at Chicago, Chicago.

Fan, H,. and Widera, G. E. O., 1992, "On the Use of Variational Principles to Derive Beam Boundary Conditions," submitted for publication.

Gregory, R. D., and Gladwell, I. G., 1982, "The Cantilever Beam Under Tension, Bending or Flexure at Infinity," *J. Elasticity*, Vol. 12, No. 4, pp. 317–343.

Gregory, R. D., and Wan, F. Y. M., 1984, "Decaying States of Plane Strain in a Semi-Infinite Strip and Boundary Conditions for Plate Theory," *J. Elasticity*, Vol. 14, pp. 27–64.

Gregory, R. D., and Wan, F. Y. M., 1985, "On Plate Theories and Saint-Venant's Principle," *Int. J. Solids and Structures*, Vol. 21, No. 10, pp. 1005–1024.

Gupta, G. D., 1973, "An Integral Equation Approach to the Semi-Infinite Strip Problem," ASME JOURNAL OF APPLIED MECHANICS, Vol. 40, pp. 948–954.

Horgan, C. O., and Knowles, J. K., 1983, "Recent Developments Concerning Saint-Venant Principle," *Advances in Applied Mechanics*, Vol. 23, pp. 180–271.

Mathematica, 1991, Wolfram Research, Inc., Champaign, IL.

Nayfeh, A. H., 1973, *Perturbation Methods*, John Wiley and Sons, New York.

Nicholson, J. W., and Simmonds, J. G., 1977, "Timoshenko Beam Theory is Not Always More Accurate Than Elementary Beam Theory," ASME JOURNAL OF APPLIED MECHANICS, Vol. 44, pp. 337–338.

Power, L. D., and Childs, S. B., 1971, "Axisymmetric Stresses and Displacements in a Fixed Circular Bar," *Int. J. Eng. Sci.*, Vol. 9, pp. 241–255.

Reissner, E., 1963, "On the Derivation of Boundary Conditions for Plate Theory," *Proc. Royal Society*, London, Vol. A276, pp. 178–186.

Robert, M., and Keer, L. M., 1987, "An Elastic Circular Cylinder with Displacement Prescribed at the Ends-Axially Symmetric Case," *Quart. J. Mech. Applied Math.*, Vol. 40, Pt. 3, pp. 339–363.

Robert, M., and Keer, L. M., 1987, "An Elastic Circular Cylinder with Displacement Prescribed at the Ends-Asymmetric Case," *Quart. J. Mech. Applied Math.*, Vol. 40, Pt. 3, pp. 363–381.

Sokolnikoff, I. S., 1956, *Mathematical Theory of Elasticity*, 2nd ed., McGraw-Hill, New York.

Wan, F. Y. M., 1989, "Interior Solutions for Slender and Thin Elastic Bodies," *Analytical and Computational Models of Shells*, A. K. Noor et al., eds., ASME Press, New York, pp. 55–70.

Wan, F. Y. M., 1990, "Boundary Layers and St. Venant's Principle for Slender and Thin Elastic Bodies," *Advances in the Theories of Plates and Shells*, G. Z. Voyiadjis and D. Karamanlidis, eds., Elsevier, Amsterdam, pp. 153–173.

Widera, G. E. O., Fan, H., and Afshari, P., 1989, "Applicability of Asymptotic Beam Theory to Thin (Thick) Walled Pipes," *Analytical and Computational Models of Shells*, A. K. Noor et al., eds., ASME Press, New York, pp. 33–54.

APPENDIX

St. Venant and Fundamental Solutions

(I) St. Venant Bending Solution. This solution is obtained for a beam loaded by moments at both ends. This solution can be found in any standard elasticity textbook (Sokolnikoff (1956)).

$$v_1^{VB} = \frac{1}{2}\left(\xi^2 + \epsilon^2 \nu (x_1^2 - x_2^2)\right)$$
$$v_2^{VB} = \nu \epsilon^2 x_1 x_2, \quad v_3^{VB} = -\epsilon x_1 \xi \tag{A1}$$
$$\tau_{\alpha i}^{VB} = 0, \quad \tau_{33}^{VB} = -\epsilon x_1$$

Note that this solution has the feature

$$\tau_{3\alpha}^{VB} = 0, \quad v_3^{VB} = 0 \text{ at } \xi = 0.$$

They are used for a certain type of prescribed boundary data (see Section 3, Case (C)).

(II) St. Venant Flexure Solution. This solution represents a semi-infinite beam loaded by a unit shear force at $\xi = 0$, with another unit force acting at the other end along with a moment to balance the beam.

$$v_1^{VF} = -\left(\frac{\xi^3}{6} - k_1 \xi\right) - \epsilon^2 \frac{\nu}{2}(x_1^2 - x_2^2)\xi$$
$$v_2^{VF} = -\epsilon \nu x_1 x_2 \xi$$
$$v_3^{VF} = (\epsilon x_1(\xi^2 - k_1) - \epsilon^3 \chi(x_1, x_2)$$
$$\tau_{\alpha\beta}^{VF} = 0, \quad \tau_{33}^{VF} = \epsilon x_1 \xi$$
$$\tau_{31}^{VF} = -\frac{\epsilon^2}{2(1+\nu)}\left(\frac{\nu}{2}(x_1^2 - x_2^2) + \chi_{,1}\right)$$
$$\tau_{32}^{VF} = -\frac{\epsilon^2}{2(1+\nu)}(\nu x_1 x_2 + \chi_{,2}) \tag{A2}$$

where $\chi(x_1, x_2)$ has been defined in Section 2.

Downloaded 03 May 2010 to 171.66.16.247. Redistribution subject to ASME license or copyright; see http://www.asme.org/terms/Terms_Use.cfm

(III) Rigid Body Displacement. For bending and flexure deformations in the $x_1 - x_3$ plane, we only need a translation in the x_1-direction and rotation in the $x_1 - x_3$ plane, i.e.,

$$\tau_{ij} = 0 \tag{A3a}$$

$$\mathbf{v} = (U, 0, 0)^T \tag{A3b}$$

and

$$\mathbf{v} = (-\Theta\xi, 0, \Theta x_1)^T. \tag{A3c}$$

(IV) Cantilever Beam Solution. This solution is obtained for a beam fixed at $\xi = 0$, and loaded at the other end with a moment or shear force. We write the solution as

$$\tau = \tau^{BB}, \quad \mathbf{v} = \mathbf{v}^{BB} \tag{A4a}$$

and

$$\tau = \tau^{BF}, \quad \mathbf{v} = \mathbf{v}^{BF} \tag{A4b}$$

where $(\,)^{BB}$ represents the fields of bending, and $(\,)^{BF}$ the fields of flexure.

Downloaded 03 May 2010 to 171.66.16.247. Redistribution subject to ASME license or copyright; see http://www.asme.org/terms/Terms_Use.cfm

Closed-Form Vibration Analysis of Sagged Cable/Mass Suspensions

S.-P. Cheng
Research Assistant.

N. C. Perkins
Assistant Professor.
Member ASME.

Mechanical Engineering and
Applied Mechanics,
The University of Michigan,
Ann Arbor, MI 48109-2125

A theoretical model is presented which describes the three-dimensional nonlinear motion of a sagged cable that supports an array of discrete masses. An asymptotic form of this general model is derived for the linear response of a cable/mass suspension having small equilibrium curvature and horizontal supports. While the asymptotic model remains rich enough to capture dominant sagged cable effects, it is simple enough to permit closed-form analysis. A free vibration analysis is pursued that leads to closed-form solutions for problems which, heretofore, were analyzed using purely numerical methods. Among the advantages of the present method is its ability to provide results for: (1) complex mass arrays, (2) high-order modes, and (3) dynamic cable tension. Examples highlight the key role played by mass array symmetry and lead to new conclusions regarding free vibration.

Introduction

Cables are commonly employed in applications that require long, flexible and/or readily deployable structural elements. For example, in ocean engineering applications, cables are used in the mooring and towing of vessels, platforms, and underwater instruments, as tethers and umbilicals, and as electrical and optical signal transmission lines. In such applications, the submerged cable may experience vortex-induced oscillations commonly referred to as *strumming* (Griffin, 1985). In addition to magnifying cable drag forces, strumming accelerates cable fatigue and may also degrade the performance and positioning of attached instruments (e.g., hydrophones). An understanding of cable dynamics is prerequisite to the prediction of strumming.

The history of cable dynamics is detailed in (Irvine and Caughey, 1974) and current developments are reviewed in (Triantafyllou, 1991). The earliest cable models, which consider the linear response of an *inextensible* cable, are deficient in that they cannot reduce to that of a simple taut string in the limit of vanishing sag. As clearly demonstrated by Irvine and Caughey (1974), cable elasticity must be included in order to affect this transition. The transition from a taut string to an inextensible cable is captured in models of "small-sag" elastic cables (Shea, 1955; Simpson, 1966; Soler, 1970) which can be described by the single cable parameter λ^2 introduced by Irvine and Caughey (1974). For cables with horizontal supports, the in-plane modes are either symmetric or antisymmetric with respect to the midspan. The (antisymmetric) symmetric modes (do not) induce dynamic cable stretching[1] and the associated natural frequencies (do not) depend on λ^2. Plotted versus λ^2, the frequencies for a pair of symmetric and antisymmetric modes *crossover* at the particular parameter values $\lambda^2 = 4j^2\pi^2$, $j = 1,2,...$ which mark the transition of each symmetric mode from that of a taut string ($\lambda^2 \to 0$) to that of an inextensible cable ($\lambda^2 \to \infty$). Extensions of small-sag cable theory have considered cables with inclined supports (Triantafyllou, 1984), translation speed (Simpson, 1972a; Triantafyllou, 1985; Perkins 1989), and frictional boundary conditions (Irvine, 1990).

The present study provides an important extension to cables that support an array of attached masses (e.g., weights, instruments, buoyancy elements). The addition of many (perhaps hundreds of) attached masses greatly complicates the description of cable motion and has prompted previous investigators to use purely numerical methods for determining relatively simple solutions for free, linear response. In (Irvine, 1981), a lumped-mass representation of a small-sag cable is developed. Rosenthal (1981) employs Stodola's method to numerically compute eigensolutions of generally sagged cables with attached masses. Convergence limitations, however, restrict reported solutions to the lower-order modes of cables that support few attached masses. Higher-mode solutions for large mass arrays are approximated using a closed-form analysis of a *taut string/mass* system (Sergev and Iwan, 1981). The model employed, however, cannot capture important sagged cable effects such as frequency crossover and dynamic cable stretching. The current study presents a theory for *sagged cable/mass* suspensions that permits the efficient and closed-form evaluation of vibration characteristics. The theory, which is valid for complex multimass arrays, builds upon that recently developed for a suspended cable supporting a single mass (Cheng and Perkins, 1992).

Contributed by the Applied Mechanics Division of THE AMERICAN SOCIETY OF MECHANICAL ENGINEERS for presentation at the 1992 ASME Winter Annual Meeting, Anaheim, CA, Nov. 8-13, 1992.

Discussion on this paper should be addressed to Prof. Leon M. Keer, The Technological Institute, Northwestern University, Evanston, IL 60208, and will be accepted until four months after final publication of the paper itself in the ASME JOURNAL OF APPLIED MECHANICS.

Manuscript received by the ASME Applied Mechanics Division, Sept. 25, 1991; final revision, Feb. 7, 1992. Associate Technical Editor: D. J. Inman.

Paper No. 92-WA/APM-7.

[1]When the quasi-static stretching assumption in (Irvine and Caughey, 1974) is relaxed, the antisymmetric modes may also induce (small) dynamic cable stretching (Irvine, 1981).

Copyright © 1992 by ASME
Downloaded 03 May 2010 to 171.66.16.247. Redistribution subject to ASME license or copyright; see http://www.asme.org/terms/Terms_Use.cfm

General Theory

Figure 1 depicts a sagged elastic cable of length L supporting an arbitrary number of discrete masses and suspended between two horizontal supports. Under gravity, the cable/mass suspension forms the planar equilibrium curve having arc length coordinate S and maximum sag D. The masses M_i, $i=1,2,\ldots,n$, are attached to the cable at positions $S=S_i$, $i=1,2,\ldots,n$, respectively. The two end supports are located at $S_0=0$ and $S_{n+1}=L$. The three-dimensional displacement of the cable about equilibrium $\mathbf{U}(S,T)$ is decomposed into the components $U_1(S,T)$, $U_2(S,T)$ and $U_3(S,T)$, resolved along the local tangential $\mathbf{l}_1$, normal $\mathbf{l}_2$, and bi-normal $\mathbf{l}_3$ directions of the equilibrium curve. The discrete masses lead to a *piecewise smooth* equilibrium curve and the unit vectors $\mathbf{l}_1$ and $\mathbf{l}_2$ exist on the open subintervals defined by the mass locations.

The equations of motion for an elastic cable supporting an array of discrete masses are derived from Hamilton's principle following (Cheng and Perkins, 1991). The cable is modeled as a one-dimensional, flexible, elastic continuum obeying a linear stress-strain law for cable extension. Adopting the Lagrangian strain of the cable centerline as the strain measure, the strain energy is

$$\Pi_S=\Pi_S^i+\sum_{i=1}^{n+1}\int_{S_{i-1}}^{S_i}\left[P(S)e_d+\frac{1}{2}EAe_d^2\right]dS, \tag{1}$$

where Π_S^i is the strain energy of the equilibrium cable, $P(S)$ is the equilibrium cable tension and EA is the cable section stiffness. The quantity e_d denotes the dynamic component of the Lagrangian strain of the final cable centerline given by

$$e_d=U_{1,S}-KU_2+\frac{1}{2}\left[(U_{1,S}-KU_2)^2+(U_{2,S}+KU_1)^2+U_{3,S}^2\right], \tag{2}$$

where $K(S)$ is the equilibrium curvature. The kinetic energy of the cable/mass system is

$$\Pi_T=\frac{1}{2}\sum_{i=1}^{n+1}\int_{S_{i-1}}^{S_i}\rho[(U_{1,T})^2+(U_{2,T})^2+(U_{3,T})^2]dS+\frac{1}{2}\sum_{i=1}^{n}M_i[\dot{U}_1^2+\dot{U}_2^2+\dot{U}_3^2]_{S=S_i^-} \tag{3}$$

where ρ is the cable mass/length, $(\dot{\ })=d(\ )/dT$, and $S_i^{\pm}=S_i\pm\epsilon$ in the limit $\epsilon\to 0$. The work done by gravity is

$$\Pi_W=\Pi_W^i-\sum_{i=1}^{n+1}\int_{S_{i-1}}^{S_i}\rho g[U_1\sin\theta+U_2\cos\theta]dS-\sum_{i=1}^{n}M_ig[U_1\sin\theta+U_2\cos\theta]_{S=S_i^-} \tag{4}$$

where Π_W^i is the gravitational potential energy of the equilibrium cable and $\theta(S)$ denotes the angle of inclination of the unit tangent vector $\mathbf{l}_1$ above the horizontal.

Free, Linear Response. Substitution of (1)–(4) into Hamilton's principle yields the equations of motion for three-dimensional, nonlinear response. Subsequent linearization and satisfaction of equilibrium (Appendix A), leads to the following equations governing free, linear cable response:
tangential direction,

$$[(P+EA)(U_{1,S}-KU_2)]_{,S}-KP(U_{2,S}+KU_1)=\rho U_{1,TT}, \tag{5}$$

normal direction,

$$[P(U_{2,S}+KU_1)]_{,S}+K(P+EA)(U_{1,S}-KU_2)=\rho U_{2,TT}, \tag{5}$$

bi-normal direction,

$$[PU_{3,S}]_{,S}=\rho U_{3,TT}, \tag{7}$$

where $S_{i-1}<S<S_i$, $i=1,2,\ldots,n+1$. The boundary conditions are

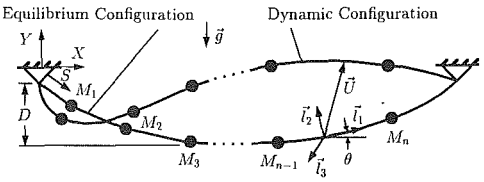


Fig. 1 Definition diagram for horizontally suspended sagged cable supporting an array of n attached masses (M_i, $i=1,2,\ldots,n$). S denotes arc length coordinate measured along the planar equilibrium curve, and the displacement U from equilibrium is decomposed into components aligned with the Frenet triad ($\mathbf{l}_1,\mathbf{l}_2,\mathbf{l}_3$). M_i located at $S=S_i$, $i=1,2,\ldots,n$.

$$U_j(0,T)=0,\ U_j(L,T)=0,\ j=1,2,3. \tag{8}$$

The free, linear response of the attached mass array is governing by

$$(P+EA)(U_{1,S}-KU_2)\delta U_1\Big|_{S_i^-}^{S_i^+}+P(U_{2,S}+KU_1)\delta U_2\Big|_{S_i^-}^{S_i^+}=M_i[\ddot{U}_1\delta U_1+\ddot{U}_2\delta U_2]_{S=S_i^-},\ i=1,2,\ldots,n, \tag{9}$$

for in-plane motion, and

$$PU_{3,S}\delta U_3\Big|_{S_i^-}^{S_i^+}=M_i[\ddot{U}_3\delta U_3]_{S=S_i^-},\ i=1,2,\ldots,n, \tag{10}$$

for out-of-plane motion. In (9) and (10), $\delta U_j, j=1,2,3$, denote virtual cable displacements from equilibrium. Continuity of the displacement field across each attached mass is guaranteed through satisfaction of

$$\begin{bmatrix}\delta U_1\\ \delta U_2\\ \delta U_3\end{bmatrix}_{S=S_i^+}=\begin{bmatrix}\cos(\Delta\theta_i) & \sin(\Delta\theta_i) & 0\\ -\sin(\Delta\theta_i) & \cos(\Delta\theta_i) & 0\\ 0 & 0 & 1\end{bmatrix}\times\begin{bmatrix}\delta U_1\\ \delta U_2\\ \delta U_3\end{bmatrix}_{S=S_i^-}\quad i=1,2,\ldots,n, \tag{11}$$

where

$$\Delta\theta_i=\theta(S_i^+)-\theta(S_i^-),\ i=1,2,\ldots,n, \tag{12}$$

denotes the discontinuous change in the angle of inclination at the location of the ith attached mass.

Asymptotic Model

The linear response model above is valid for cable/mass suspensions with arbitrarily large equilibrium curvature (sag) and nonuniform equilibrium tension. As stated in the Appendix, the general solution to the equations of equilibrium describes a piecewise smooth catenary. In engineering applications requiring positional control (e.g., hydrophone arrays), the cable sag may be reduced by applying large static tension. For small sag-to-length ratios ($D/L<1/8$), a significant simplification of the general theory follows from using a parabolic approximation to the catenary; refer to (Irvine and Caughey, 1974) for analogous approximation for small-sag bare cables.

For cable/mass suspensions, a *piecewise smooth* parabolic equilibrium follows from the boundary value problem below which is obtained from (A3)–(A5) of the Appendix using small angle approximations ($\cos\theta\approx 1$, $\sin\theta\approx\tan\theta=dY/dX$, and $K\approx d^2Y/dX^2$):

$$P(S)=P_o, \tag{13}$$

$$\frac{d^2Y}{dX^2}=\frac{\rho g}{P_o}+\sum_{i=1}^{n}\frac{M_ig}{P_o}\delta(X-X_i),\ 0<X<H, \tag{14}$$

$$Y(0)=0,\ Y(H)=0. \tag{15}$$

Here, X and Y are Cartesian coordinates describing the equi-

Downloaded 03 May 2010 to 171.66.16.247. Redistribution subject to ASME license or copyright; see http://www.asme.org/terms/Terms_Use.cfm

librium profile, P_o is the horizontal component of the equilibrium cable tension, H is distance (span) between the supports, and δ denotes the Dirac delta distribution.

From (14), the nondimensional (subdomain) curvature $k=\rho gL/P_o$ is identified as a small parameter and is used to order the terms in (5)–(12) in obtaining an asymptotic approximation valid in the limit of small curvature. The nondimensional parameters

$$s=\frac{S}{L},\ t=\frac{T}{\sqrt{L/g}},\ u_j=\frac{U_j}{L},\ j=1,2,3,$$

$$v_t^2=\frac{1}{k}=\frac{P_o}{\rho gL},\ v_l^2=\frac{EA}{\rho gL},\ s_i=\frac{S_i}{L},\ m_i=\frac{M_i}{\rho L},\ i=1,2,\ldots,n, \quad (16)$$

are introduced to facilitate this approximation. The parameters v_t and v_l denote the (nondimensional) speed of propagation of transverse and longitudinal waves, respectively. The orderings $Oh(v_t^2)=k^{-1}$ and $Oh(\Delta\theta_i)=k$ follow from the definition (16) and the parabolic approximation (14), assuming $Oh(m_i)\le 1$. Remaining quantities are ordered as $Oh(u_1)=k$, $Oh(u_2)=1$, and $Oh(v_l^2)=k^{-2}$. As with bare suspensions (Irvine and Caughey, 1974), the tangential displacement u_1 is of the order of the equilibrium curvature for suspensions with small curvature (sag); refer to (25) and (26). Furthermore, v_l^2 is (at least) an order of magnitude greater than v_t^2, since for cables of engineering interest, $EA \gg P_o$; refer to (16).

Retaining terms of order k and larger in (5)–(12) leads to the asymptotic model governing the linear response of cable/mass suspensions with small equilibrium curvature:
tangential direction,

$$(u_{1,s}-ku_2)_{,s}=0,\ s_{i-1}<s<s_i,\ i=1,2,\ldots,n+1, \quad (17)$$

$$u_{1,s}-ku_2\Big|_{s_i^-}^{s_i^+}=0,\ i=1,2,\ldots,n, \quad (18)$$

normal direction,

$$v_t^2u_{2,ss}+kv_l^2(u_{1,s}-ku_2)=u_{2,tt},\ s_{i-1}<s<s_i,\ i=1,2,\ldots,n+1, \quad (19)$$

$$v_t^2u_{2,s}\Big|_{s_i^-}^{s_i^+}+m_ikv_l^2(u_{1,s}-ku_2)_{s=s_i}=m_i\ddot{u}_2(s_i^-,t),\ i=1,2,\ldots,n, \quad (20)$$

bi-normal direction,

$$v_t^2u_{3,ss}=u_{3,tt},\ s_{i-1}<s<s_i,\ i=1,2,\ldots,n+1, \quad (21)$$

$$v_t^2u_{3,s}\Big|_{s_i^-}^{s_i^+}=m_i\ddot{u}_3(s_i^-,t),\ i=1,2,\ldots,n, \quad (22)$$

with boundary conditions

$$u_j(0,t)=u_j(1,t)=0,\ j=1,2,3. \quad (23)$$

The two equations of in-plane motion for the attached mass array, (18) and (20), follow from (9) using the continuity conditions (11). To order k, the continuity conditions provide

$$\begin{bmatrix}u_1\\u_2\\u_3\end{bmatrix}_{s=s_i^+}=\begin{bmatrix}1 & km_i & 0\\0 & 1 & 0\\0 & 0 & 1\end{bmatrix}\begin{bmatrix}u_1\\u_2\\u_3\end{bmatrix}_{s=s_i^-},\quad i=1,2,\ldots,n. \quad (24)$$

Note that the equations of out-of-plane response, (21) and (22), are identical to those of a taut string/mass system (Sergev and Iwan, 1981) and are a special case of those for normal response, (19) and (20), obtained in the limit of vanishing curvature ($k\to 0$). The equations of tangential response, (17) and (18), demonstrate that, to order k, the cable/mass suspension stretches in a *quasi-static* manner. This quasi-static stretching is in keeping with the (bare) cable theory (Irvine and Caughey, 1974), which follows from (17)–(22) for vanishing mass array ($m_i=0$). The quasi-static stretching is valid for any cable mode having natural frequency less than that of the fundamental elastic mode, as discussed in (Cheng and Perkins, 1992).

The tangential displacement u_1 can be formally eliminated as an unknown as follows. Integrating (17) twice and using (18), (23), and (24) leads to

$$u_1(s,t)=g(t)s+k\int_0^s u_2(\eta,t)d\eta+k\sum_{i=1}^n m_iu_2(s_i,t)\mu(s-s_i), \quad (25)$$

where μ is the Heaviside function and

$$g(t)=u_{1,s}-ku_2=-k\int_0^1 u_2(\eta,t)d\eta-k\sum_{i=1}^n m_iu_2(s_i,t), \quad (26)$$

is the (linear) dynamic strain.

Free Vibration. Using the separable solution

$$u_2(s,t)=v(s)e^{i\omega t}, \quad (27)$$

and (26) in (19), (20), (23), and (24) yields the eigenvalue problem governing free, in-plane vibration:

$$v''+\Omega^2v=c,\ s_{i-1}<s<s_i,\ i=1,2,\ldots,n+1, \quad (28)$$

$$v'\Big|_{s_i^-}^{s_i^+}+\Omega^2m_iv(s_i^-)=m_ic,\ i=1,2,\ldots,n, \quad (29)$$

$$v(s_i^+)=v(s_i^-),\ i=1,2,\ldots,n, \quad (30)$$

$$v(0)=0,\ v(1)=0, \quad (31)$$

where

$$(\,)'=\frac{d(\,)}{ds},\ \Omega^2=\frac{\omega^2}{v_t^2},\ \lambda^2=\frac{v_l^2}{(v_t^2)^3},\quad c=\lambda^2\left[\int_0^1 v(\eta)d\eta+\sum_{i=1}^n m_iv(s_i)\right]. \quad (32)$$

The quantity λ^2 represents the cable parameter introduced by Irvine and Caughey (1974) and the quantity c captures the change in tension induced by quasi-static cable stretching; refer to (26). Note that c vanishes for any eigenfunction $v(s)$ that is antisymmetric with respect to the midspan ($s=1/2$). Furthermore, note that the eigenvalue problem for out-of-plane vibration is recovered from (28)–(31) for the special case $\lambda^2\to 0$ ($c\to 0$).

The above eigenvalue problem is solved using a transfer matrix method similar to that employed in (Sergev and Iwan, 1981). The general solution to (28) is

$$v(s)=A_i\sin[\Omega(s-s_{i-1})]+B_i\cos[\Omega(s-s_{i-1})]+\frac{c}{\Omega^2},\ s_{i-1}<s<s_i,\ i=1,2,\ldots,n+1, \quad (33)$$

where A_i and B_i are constants of integration for the ith subdomain, $s_{i-1}<s<s_i$. For the arbitrary choice $A_1=1$, the first boundary condition (31) provides $B_1=-c/\Omega^2$. The remaining coefficients are determined from (29) and (30) in the transfer matrix form

$$\begin{bmatrix}A_{i+1}\\B_{i+1}\end{bmatrix}=\begin{bmatrix}\cos\Omega l_i-m_i\Omega\sin\Omega l_i & -\sin\Omega l_i-m_i\Omega\cos\Omega l_i\\ \sin\Omega l_i & \cos\Omega l_i\end{bmatrix}\times\begin{bmatrix}A_i\\B_i\end{bmatrix},\ i=1,2,\ldots,n, \quad (34)$$

where $l_i=s_i-s_{i-1}$ is the (nondimensional) length of the ith subdomain. Thus, upon repeated application of (34), the remaining coefficients (A_i and B_i, $i=2,3,\ldots,n+1$) depend solely

Downloaded 03 May 2010 to 171.66.16.247. Redistribution subject to ASME license or copyright; see http://www.asme.org/terms/Terms_Use.cfm

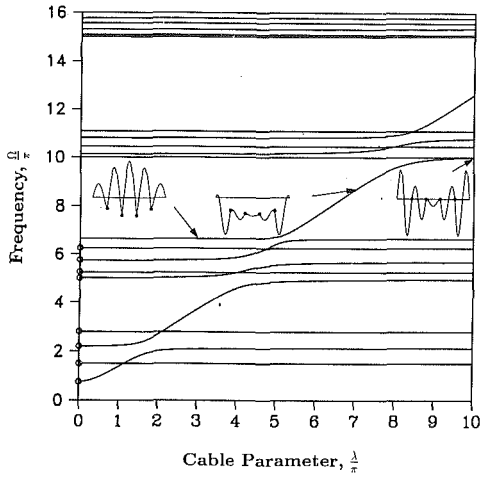


Fig. 2 Frequency spectrum for sagged cable with uniform four-mass array ($m_i = 0.1462$, $l_i = 1/5$). Frequencies of sagged cable ($\lambda/\pi \neq 0$) converge to those (circles) reported in (Sergev and Iwan, 1981) for string/mass system ($\lambda/\pi = 0$). Mode shape of fifth symmetric mode illustrated for $\lambda/\pi = 3,7,10$.

on the two undetermined constants Ω and c. These two constants are chosen to satisfy the second boundary condition $v(1) = 0$ (31), and the definition for c, (32). Simultaneous solution of these two equations for Ω and c are determined herein using standard Newton-Raphson iteration. The corresponding eigenfunction $v(s)$ is then found upon back substitution into (33) and (34).

Results

The first two examples re-examine published results for the natural frequencies of cable/mass suspensions for comparison with the present formulation.

Sergev and Iwan (1981) consider a taut string supporting four equally spaced, equal masses. The first 19 in-plane natural frequencies of the analogous sagged cable/mass suspension are shown in Fig. 2 over a wide range of the cable parameter λ/π. For a perfectly taut cable ($\lambda/\pi \to 0$), the results of the asymptotic model converge to those reported in (Sergev and Iwan, 1981); see circles. Furthermore, the natural frequencies of the perfectly taut cable ($\lambda/\pi \to 0$) are clustered into (four) *pass bands* separated by large *stop bands*. At $\lambda/\pi = 0$, the even-order frequencies are associated with antisymmetric vibration modes and are independent of λ/π; $c = 0$ (32). Only the symmetric modes of this cable/mass suspension induce dynamic stretching ($c \neq 0$) and the associated natural frequencies are strong functions of λ/π. At particular values of λ/π, the natural frequencies of a pair of antisymmetric and symmetric modes are equivalent and the *frequency crossover phenomenon* noted for bare cables exists; refer to Introduction. For the sagged cable/mass suspension ($\lambda/\pi \neq 0$), the crossover phenomenon disrupts the stop band/pass band eigenstructure as the natural frequency associated with the highest-order symmetric mode in each pass band migrates through the adjacent stop band to the next pass band. During this transition, the symmetric mode undergoes substantial changes and ultimately gains two nodes; refer to example mode illustrated in Fig. 2.

Both Rosenthal (1981) and Sergev and Iwan (1981) consider a cable supporting six equal masses of unequal spacing as indicated in Fig. 3. The natural frequencies of in-plane modes (solid curves) and out-of-plane modes (dotted curves) are computed over the entire range of cable sag to length ratio in order to facilitate the comparison with (Rosenthal, 1981). The results of the asymptotic model, Fig. 3(*a*), and the numerical model (Rosenthal, 1981), Fig. 3(*b*), reproduce values reported in (Sergev and Iwan, 1981) for small cable sag. In the limit of vanishing sag, the distinction between in-plane and out-of-plane modes is lost. The distinction between the fundamental in-plane and out-of-plane natural frequencies, however, becomes apparent even at seemingly negligible sag to length ratios ($D/L \cong 0.002$).

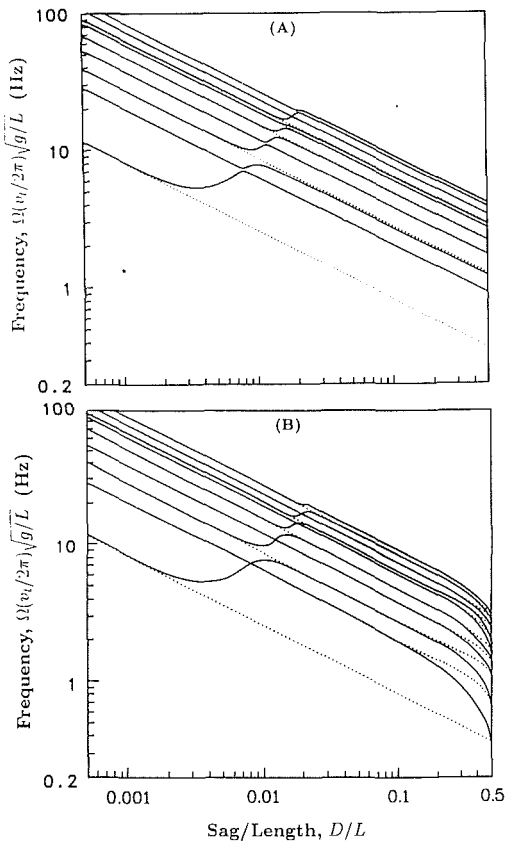


Fig. 3 Comparison of (*a*) asymptotic and (*b*) numerical results for asymmetric six-mass array: $L = 14.376$ ft, $EA = 25{,}000$ lb, $\rho = 8.71 \times 10^{-5}$ slug/ft, $M_i = 12.9 \times 10^{-5}$ slug, $S_i = 3.167, 5.834, 6.667, 7.188, 7.501, 8.501$ ft, $i = 1,2,...,6$ (Rosenthal, 1981). First nine in-plane (solid) and out-of-plane (dotted) natural frequencies plotted versus sag to length ratio, D/L. Figure 3(*b*) reproduced from (Rosenthal, 1981).

In Fig. 3, the frequency spectra of the asymptotic and numerical models are virtually indistinguishable, with two exceptions. The discrepancy observable at large sag levels ($D/L > 0.125$) is expected as the fidelity of the asymptotic (small curvature) model is lost. In the range of small sag (curvature), however, an important qualitative difference persists. While the numerical solution displays the frequency crossover phenomenon (repeated in-plane frequencies) the asymptotic solution does not. Instead, the approaching in-plane frequency loci suddenly turn away in a manner often referred to as *curve veering* (Leissa, 1974). Note that while a bare cable and the suspension of Fig. 2 are both symmetric about the midspan, the current suspension is not due to the asymmetric arrangement of the mass array.[2] As demonstrated in the context of a general eigenvalue problem (Perkins and Mote, 1986), such asymmetry may split the repeated frequencies of the symmetric system and lead to curve veering. The degree of curve veering is mode dependent as observed in Fig. 3. The crossings noted in the numerical solution may have resulted from insufficient computational resolution in the veering regions.

The significance of curve veering for cable/mass suspensions is twofold. First, the mode shapes in the veering region are extremely sensitive to small changes in the sag level. Conse-

[2]Asymmetry in suspended cables is also induced by support inclination (Triantafyllou, 1984), cable translation speed (Perkins and Mote, 1987), or by a single (eccentric) mass (Cheng and Perkins, 1992) and, in all cases, leads to curve veering behavior.

Downloaded 03 May 2010 to 171.66.16.247. Redistribution subject to ASME license or copyright; see http://www.asme.org/terms/Terms_Use.cfm

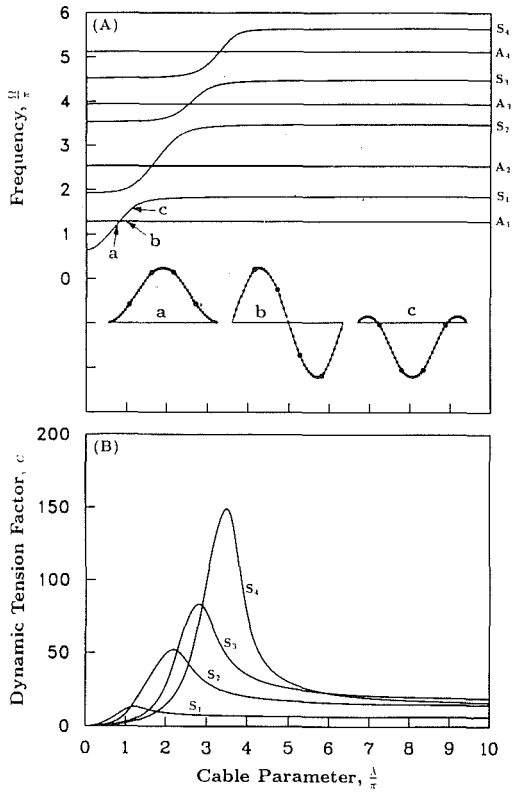


Fig. 4 (*a*) In-plane natural frequencies and mode shapes for large symmetric array. Array composed of $n = 49$ equally spaced ($l_i = 1/50$) attached masses of two sizes ($m_{10} = m_{20} = m_{30} = m_{40} = 0.1$, all other $m_i = 0.02$). First two modes are illustrated in region near fundamental crossover. $S_i(A_i)$ denotes ith symmetric (antisymmetric) in-plane mode. (*b*) Dynamic tension factor c (32) for first four symmetric modes.

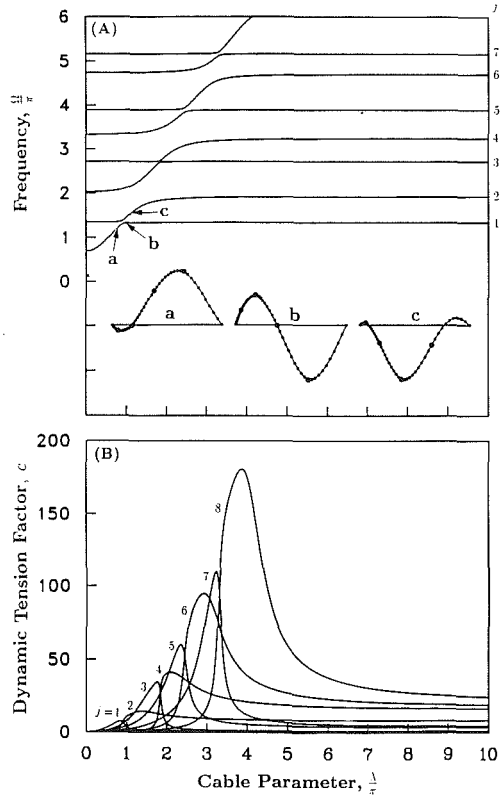


Fig. 5 (*a*) In-plane natural frequencies and mode shapes for large asymmetric mass array. The $n = 49$ masses of Fig. 4 are now spaced according to $l_i = [1 + 0.4(i - 1)]/540$, $i = 1,2,...,50$. First two modes are illustrated near fundamental region of curve veering. (*b*) Dynamic tension factor c (32) for first $j = 1,2,..,8$ in-plane modes.

quently, this sensitivity would be reflected in any subsequent analysis of strumming and resulting drag force distribution; see, for example, (Griffin, 1985). Second, these mode shapes are, in general, highly *asymmetric* and they all induce dynamic cable tension to some degree ($c \neq 0$). The following examples highlight these new characteristics.

A distinct advantage of the current closed-form analysis is the relative ease with which solutions can be obtained for complex arrays of numerous masses. In the example of Fig. 4, a sagged cable supports a symmetric array of (unequal) masses. Figure 4(*a*) confirms the existence of frequency crossovers for this symmetric system. In this (degenerate) case, the vibration mode shapes are either symmetric or antisymmetric and, except for possessing small slope discontinuities, they are nearly identical in appearance to those of a bare cable (Irvine and Caughey, 1974). The cable parameter λ/π influences only symmetric in-plane modes which gain two additional nodes after crossover. Furthermore, only the symmetric modes induce dynamic tension ($c \neq 0$) and to a degree determined by λ/π; refer to Fig. 4(*b*). Note that, for a particular symmetric mode, the maximum dynamic tension occurs in the neighborhood of the crossover.

Arranging the same masses in an asymmetric array leads to nondegenerate eigensolutions and the (former) regions of frequency crossover, Fig. 4(*a*), become regions of curve veering, Fig. 5(*a*). Moreover, all the modes are asymmetric and, therefore, they may *all* induce dynamic cable tension. The dynamic tension factors for the example asymmetric array are shown in Fig. 5(*b*) for comparison with those of the symmetric array, Fig. 4(*b*).

For a *symmetric* array composed of an extremely large number (n) of evenly spaced ($l_i = 1/n + 1$) masses ($m_i = m$), the present model converges to that of a bare cable with uniform (nondimensional) mass density $1 + nm$. This observation is in

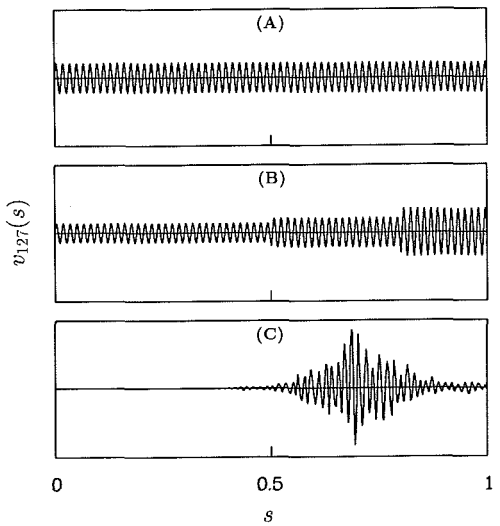


Fig. 6 Sensitivity of high-order mode (#127) for very large array ($n = 500$, $m_i = 0.02$). (*a*) uniform spacing ($l_i = 1/501$); (*b*) near uniform spacing ($l_{250} = l_{400} = 1.9/501$, $l_{251} = l_{401} = 0.1/501$, all other $l_i = 1/501$); (*c*) random spacing (average = 1/501, standard deviation = 0.00118). In all cases, $\lambda/\pi = 8$.

agreement with (Irvine, 1981) for the discretized model of a small-sag cable. While the natural frequencies remain relatively insensitive to changes away from system symmetry (crossings become close veerings), such changes alter *qualitatively* the vibration mode shapes; compare Fig. 4(*a*) and Fig. 5(*a*). This effect becomes more pronounced as the array size and mode number increases. Figure 6(*a*) depicts mode number 127 for a symmetric array composed of $n = 500$ equally spaced, equal masses. The same mode is illustrated in Fig. 6(*b*) after only

Downloaded 03 May 2010 to 171.66.16.247. Redistribution subject to ASME license or copyright; see http://www.asme.org/terms/Terms_Use.cfm

two of the masses are displaced from their nominal positions. This "slight" asymmetry leads to the marked changes in the modal amplitude exactly at the positions of the two displaced masses (m_{250} and m_{400}). The same mode is qualitatively different when a larger degree of asymmetry is introduced as shown in Fig. 6(*c*). In this case, the mass spacings (l_i) are randomly distributed with a standard deviation of approximately 60 percent of the nominal (mean) spacing. The mode shape now becomes largely *localized* to a small subdomain of the cable in a manner commonly observed in disordered repetitive structures (Pierre, 1988). The correction due to cable bending rigidity scales as the square of the mode number (Simpson, 1972b), and the present model provides lower bound estimates for the natural frequencies of these high-order modes.

Summary and Conclusions

An asymptotic model is derived that governs the free, linear response of an elastic cable supporting an array of attached masses. The model is applicable to horizontal cable/mass suspensions having small equilibrium curvature. The model remains rich enough to capture dominant sagged cable effects yet is amenable to closed-form analysis of both in-plane and out-of-plane vibration. The closed-form analysis is distinguished by the relative ease with which solutions for low and high-order modes can be obtained for complex arrays of numerous masses. Example solutions illustrate the following major conclusions:

1 Comparison with numerical solutions (Rosenthal, 1981) reveals that the asymptotic model is valid for cable/mass suspensions having sag/span ratios $D/L < 1/8$ in accordance with the bare cable theory (Irvine and Caughey, 1974).

2 The frequency crossover phenomenon (repeated in-plane frequencies) arises only for *symmetric* mass arrays. In general, *any* degree of array asymmetry may split the degenerate frequencies and regions of frequency crossover may evolve to regions of curve veering (close, but distinct, frequencies). This is in contrast to reported numerical solutions (Rosenthal, 1981) in which frequency crossovers were always observed.

3 In the regions of curve veering, the associated vibration mode shapes are extremely sensitive to small changes in the cable parameter. Moreover, the in-plane modes of asymmetric suspensions are themselves asymmetric and they may *all* induce dynamic tension.

4 Higher-order modes are strongly influenced by system asymmetry and can exhibit mode localization.

Acknowledgment

The authors gratefully acknowledge the support of the U.S.N. Office of Naval Research Young Investigator Program under grant number N00014-89-J-3159.

References

Cheng, S.-P., and Perkins, N. C., 1992, "Free Vibration of a Sagged Cable Supporting a Discrete Mass," *Journal of the Acoustical Society of America*, Vol. 91, No. 5, pp. 2654–2662.

Griffen, O. M., 1985, "Vortex-Induced Vibrations of Marine Cables and Structures," Naval Research Laboratory, Memorandum Report No. 5600.

Irvine, H. M., and Caughey, T. K., 1974, "The Linear Theory of Free Vibrations of a Suspended Cable," *Proc. Royal Soc. London*, Vol. A341, pp. 299–315.

Irvine, H. M., 1981, *Cable Structures*, MIT Press.

Irvine, H. M., 1990, "On the Free Vibrations of Suspended Cables with Frictional End Restraint," ASME JOURNAL OF APPLIED MECHANICS, Vol. 57, pp. 419–422.

Leissa, A. W., 1974, "On a Curve Veering Aberration," *J. Applied Mathematics and Physics (ZAMP)*, Vol. 25, pp. 99–111.

Perkins, N. C., and Mote, C. D., Jr., 1986, "Comments on Curve Veering in Eigenvalue Problems," *J. Sound and Vibration*, Vol. 106, No. 3, pp. 451–463.

Perkins, N. C., and Mote, C. D., Jr., 1987, "Three Dimensional Vibration of Travelling Elastic Cables," *J. Sound and Vibration*, Vol. 114, No. 2, pp. 325–340.

Perkins, N. C., 1989, "Asymptotic Analysis of a Translating Cable Arch," *J. Sound and Vibration*, Vol. 135, No. 3, pp. 375–383.

Pierre, C., 1988, "Mode Localization and Eigenvalue Loci Veering Phenomena in Disordered Structures," *J. Sound and Vibration*, Vol. 126, No. 3, pp. 485–502.

Rosenthal, F., 1981, "Vibrations of Slack Cables with Discrete Masses," *J. Sound and Vibration*, Vol. 78, No. 4, pp. 573–583.

Sergev, S. S., and Iwan, W. D., 1981, "The Natural Frequencies and Mode Shapes of Cables with Attached Masses," ASME *Journal of Energy Resources Technology*, Vol. 103, pp. 237–242.

Shea, J. F., 1955, "A Study of Wind Forces on Suspended Cables and Related Structures," Ph.D. Dissertation, University of Michigan, Chapter 7.

Simpson, A., 1966, "Determination of In-plane Natural Frequencies of Multispan Transmission Lines by a Transfer Matrix Method," *IEE Proceedings*, Vol. 113, No. 5, pp. 870–878.

Simpson, A., 1972a, "On the Oscillatory Motions of Translating Elastic Cables," *J. Sound and Vibration*, Vol. 20, No. 2, pp. 177–189.

Simpson, A., 1972b, "Determination of the Natural Frequencies of Multiconductor Overhead Transmission Lines," *J. Sound and Vibration*, Vol. 20, No. 4, pp. 417–449.

Soler, A. I., 1970, "Dynamic Response of Single Cables with Initial Sag," *J. Franklin Institute*, Vol. 290, No. 4, pp. 377–387.

Triantafyllou, M. S., 1984, "The Dynamics of Taut Inclined Cables," *Quart. J. Mechanics and Applied Mathematics*, Vol. 37, pp. 421–440.

Triantafyllou, M. S., 1985, "The Dynamics of Translating Cables," *J. Sound and Vibration*, Vol. 103, No. 2, pp. 171–182.

Triantafyllou, M. S., 1991, "Dynamics of Cables, Towing Cables and Mooring Systems," *Shock and Vibration Digest*, Vol. 23, No. 7, pp. 3–8.

APPENDIX

Equations of Equilibrium

Substitution of (1)–(4) into Hamilton's principle yields the equations of motion governing three-dimensional, nonlinear response of the cable/mass suspension. The equations of equilibrium are extracted from the equations of motion for vanishing dynamic displacement $U_j \equiv 0$, $j = 1,2,3$. Resolved along the horizontal and vertical directions, the equations of cable and attached mass equilibrium are:

$$P'\cos\theta - PK\sin\theta = 0,\ S_{i-1} < S < S_i,\ i = 1,2,\ldots,n+1, \quad \text{(A1)}$$

$$P\cos\theta \Big|_{S_i^-}^{S_i^+} = 0,\ i = 1,2,\ldots,n, \quad \text{(A2)}$$

$$P'\sin\theta + PK\cos\theta = \rho g,\ S_{i-1} < S < S_i,\ i = 1,2,\ldots,n+1. \quad \text{(A3)}$$

$$P\sin\theta \Big|_{S_i^-}^{S_i^+} = M_i g,\ i = 1,2,\ldots,n. \quad \text{(A4)}$$

Integrating (A1) using $K = d\theta/dS$ and (A2) leads to

$$P(S)\cos\theta = P_o,\ S_0 < S < S_{n+1}, \quad \text{(A5)}$$

where P_o denotes the (constant) horizontal component of cable tension. The general solution to (A3)–(A5) provides the equilibrium tension $P(S)$ and curvature $K(S)$ describing a piecewise smooth catenary (Irvine, 1981).

Downloaded 03 May 2010 to 171.66.16.247. Redistribution subject to ASME license or copyright; see http://www.asme.org/terms/Terms_Use.cfm

An Evaluation of Convex Modeling for Multimode Dynamic Buckling

Herbert E. Lindberg
APTEK, Inc.
San Jose, CA 95129

Convex and probabilistic model solutions are obtained for multimode dynamic buckling of cylindrical shells with uncertain imperfections under symmetric radial impulsive loads. It is found that the maximum possible buckling deformations for any imperfection within uniform bounds $\pm\hat{\delta}$ can be made comparable to the buckling deformations from the probabilistic models at a reliability of about 99.5 percent. Numerical evaluation and interpretation of the convex model is much simpler than for the probabilistic models, and the convex model solution provides means for quality control of each and every shell by simply recording $\hat{\delta}$ from appropriately filtered imperfection measurements. The power and simplicity of convex modeling for multimode buckling shows promise for more complex problems than require finite element modal analysis.

Models of Uncertainty

Probabilistic models are the most widely used method of analyzing uncertainty in engineering systems. When the probability density functions are known for the quantities under investigation, either from a fundamental understanding of the sources of uncertainty or from extensive statistical measurements, this approach is very powerful and gives well-defined results for specified levels of reliability. However, in many problems, the sources of uncertainty are too complex to allow analytical determination of density functions, while in the same instances, it is impractical to obtain enough data to determine the density functions empirically. In these situations, density functions are often simply assumed by analogy to similar problems for which probability densities are known. This leads to questionable reliability estimates, particularly for high levels of reliability associated with the tails of the density functions, which are most questionable for assumed functions.

Also, in application of probabilistic models each member of a probabilistically described population is treated like any other, with no distinction made on the basis of knowledge that may be available for a particular member. For example, in buckling problems of the type analyzed in the following sections, it is difficult to determine with probabilistic methods the increase in buckling load for a shell that by simple inspection has a more nearly perfect shape than others. Conceptually, one could use different density functions for "good quality" and "poor quality" shells, but it is typically prohibitively expensive to obtain the data required to specify such functions.

Recently, Ben-Haim and Elishakoff (1990) proposed a convex model approach to uncertainty analysis to address these limitations of probabilistic models. In this approach the uncertain deviation from the perfect shape of a shell, for example, is represented in terms of a convex set, R, of allowed functions. In order to maximize linear functions on this set of allowed functions (for example, to maximize buckling response), one uses an extreme-point set, E, whose convex hull is R. The pair of sets, E and R, is called a *convex model*. In essence, rather than calculating the response at a specified reliability for probabilistically defined imperfections, one calculates the maximum possible response for any imperfection shape constrained within a known bound.

An advantage of this approach is that less information is needed to define such a bound that to define a probability density function. This removes the need to assume density functions, whose tails may or may not be those of the true density function. Furthermore, the information needed to define the bound may be simple enough that measurements can be made for every item whose reliability is to be assessed. Thus, convex modeling can be used to maintain *uncertainty control* in addition to performing uncertainty analyses. Ben-Haim and Elishakoff (1989; also 1990) found the minimum axial buckling load for a cylindrical shell with any imperfection shape within uniform bounds $\pm\hat{\delta}$. This allows simple quality control inspection to distinguish between "good quality" and "poor quality" shells. One simply monitors the shape of each shell and records the maximum and minimum departures from the perfect shape.

In the following sections a similar analysis is performed for dynamic buckling of cylindrical shells under symmetric radial impulse. The problem is simple enough that extensive probabilistic analyses are also done for comparison to determine the conservatism of using the maximum possible response for the worst possible imperfection shape within uniform bounds, compared with using the probabilistic buckling response from random imperfections of comparable measure. The approach and conservatism estimates may be useful in more complex multimode problems, as discussed when the comparisons are made.

Contributed by the Applied Mechanics Division of THE AMERICAN SOCIETY OF MECHANICAL ENGINEERS for publication in the ASME JOURNAL OF APPLIED MECHANICS.

Discussion on this paper should be addressed to the Technical Editor, Professor Leon M. Keer, The Technological Institute, Northwestern University, Evanston, IL 60208, and will be accepted until four months after final publication of the paper itself in the JOURNAL OF APPLIED MECHANICS.

Manuscript received by the ASME Applied Mechanics Division, Mar. 1, 1991; final revision, Aug. 6, 1991. Associate Technical Editor: A. K. Noor.

Copyright © 1992 by ASME
Downloaded 03 May 2010 to 171.66.16.247. Redistribution subject to ASME license or copyright; see http://www.asme.org/terms/Terms_Use.cfm

Multimode Buckling Response

The problem analyzed in dynamic plastic flow buckling of a long cylindrical shell following symmetric radial impulse. The shell absorbs the kinetic energy imparted by the impulse through plastic hoop strain nominally uniform around the circumference as the shell wall moves to a smaller diameter. This motion is instable; flexural motion is resisted by the bending stresses associated with the material plastic hardening modulus, but the hoop thrust is large enough that imperfections in the initial circular shape of the shell are amplified with time. The duration of inward motion is proportional to the applied impulse, and hence the amount of amplification can be related to the impulsive load. The criterion for acceptable buckling response is a maximum allowable flexural deformation, generally some fraction of the wall thickness.

As discussed in Lindberg (1991), this is a more appropriate criterion for pulse buckling than the more conventional dynamic buckling criterion of threshold divergence of flexure. In fact, in the present rigid-plastic idealization, flexure is divergent for any impulse; the above criterion places a limit on the magnitude of divergent growth. Also, complications such as from strain-rate reversal caused by flexural tensile strains overtaking the uniform compressive plastic strain as the nominally uniform wall velocity decreases, and energy transfer to flexure, are neglected. The purpose is to study methods of imperfection modeling in the simplest idealization by using a buckling theory in the spirit of the original work by Abrahamson and Goodier (1962), without complications that divert attention from this issue. The results are appropriate for conservative design, since the neglected complications all reduce the amplitude of buckling. Perturbation methods have been used for convex modeling of nonlinear buckling (Ben-Haim and Elishakoff, 1989) and can be explored for more precise analysis of the present problem.

At any time, t, the Fourier sine and cosine coefficients (amplitudes) of each flexural node n are equal to the corresponding imperfection coefficients times an "amplification function" $G_n(t)$. Thus, the flexural deformation is a linear function of the imperfection coefficients, i.e., the flexure superposes linearly on the uniform plastic flow. For a given description of imperfections one calculates response to the maximum allowable flexural deformation and, with the time at this maximum response, determines the critical impulse. Since as shown below the variation with n of $G_n(t)/G_{\max}(t)$ does not change markedly as t increases for times of concern, it is useful to compare convex and probabilistic model results at a fixed time near the critical time for acceptable deformation. Conversion of these results into changes in critical impulsive load can be done to reasonably accuracy by using the variation of $G_{\max}$ (the maximum with respect to n) with t and hence with impulse.

This problem is chosen because it is similar to pulse buckling problems that have been explored by probabilistic methods (Lindberg, 1965; Elishakoff, 1978a, 1978b), by finite element methods for measured and assumed random imperfections (Kirkpatrick and Holmes, 1989), and for which forms of random imperfections have been explored for use in finite element calculations (Lindberg, 1988). Also, data reported by Arbocz (1982) and Kirkpatrick and Holmes (1989, 1991) are available on which to base bounding estimates of the forms of random imperfections.

Equations of motion and solutions were derived by Abrahamson and Goodier (1962) and are also given in Lindberg and Florence (1987, pp. 76–85). Here we simply write down the Fourier series for the imperfections and flexural deformation response solution. The imperfections (deviations from a perfect cylindrical shape) are given by

$$\delta(\theta)=\sum_{n=2}^{N}(a_n\cos n\theta+b_n\sin n\theta)\equiv A^T\varphi_c+B^T\varphi_s \qquad (1)$$

where the notation $A^T=\{a_2, a_3, \ldots a_N\}$, and similarly for B^T, is introduced for imperfections, and $\varphi_c^T=\{\cos 2\theta, \cos 3\theta, \ldots \cos N\theta\}$, and similarly for φ_s, for mode shapes. The flexural deformation is given by

$$u(\theta,\tau)=\sum_{n=2}^{N}[a_nG_n(\tau)\cos n\theta+b_nG_n(\tau)\sin n\theta]=A^T\phi_c+B^T\phi_s \qquad (2)$$

where $\phi_c=G\varphi_c$ and $\phi_s=G\varphi_s$, in which G is a diagonal matrix with elements $G_n(\tau)$. The $n=0$ mode is the symmetric motion that gives rise to the hoop thrust, and the $n=1$ mode is a rigid-body translation. The amplification function is

$$G_n(\tau)=\frac{1}{1-\eta^2}\begin{bmatrix}\cosh\\ \cos\end{bmatrix}p_n\tau-1\quad\begin{matrix}\eta<1\\ \eta>1\end{matrix} \qquad (3)$$

where

$$\eta=n/s,\ p_n=[|(\eta^2-1/s^2)(1-\eta^2)|]^{1/2} \qquad (4)$$

a dimensionless time has been defined by

$$\tau=\frac{s^2c_p\alpha}{a}t \qquad (5)$$

and $G_n(\tau)=\tau^2/2$ for $\eta=1$. Typically, $s^2\gg1$, so to a good approximation $G_n(\tau)$ is a function of η and τ, with s simply defining the mode number scale. The dimensionless parameters are defined by

$$\alpha=\frac{h}{a\sqrt{12}},\quad s^2=\frac{\sigma_y}{E_h\alpha^2},\quad c_p=\sqrt{\frac{E_h}{\rho}}. \qquad (6)$$

Physical parameters are: h = wall thickness, a = radius, σ_y = yield stress, E_h = strain hardening modulus, and ρ = density.

The maximum value of τ, and hence the final amplification for a given impulse intensity I per unit area, is found from the symmetric ($n=0$) motion with material behavior simplified to rigid-perfectly plastic (i.e., neglecting the small increase in stress from strain hardening). Thus, the time to bring a unit axial length of wall element, with section are $ha\,d\theta$, to rest from velocity $v=I/\rho h$ at constant deceleration $\sigma_y h\,d\theta/\rho ha\,d\theta=\sigma_y/\rho a$ is $t_f=aI/h\sigma_y$. With (5) and (6) the dimensionless final time is

$$\tau_f=\frac{I}{\rho a\alpha^2c_p}. \qquad (7)$$

The essential result for the purpose here is that τ_f is proportional to I, so τ_f can be used as a measure of I. Having found an allowable amplification $G_{\max}(\tau_f)$ for specified imperfections, one knows τ_f and then finds the allowable impulse intensity from (7).

In Fig. 1, the amplification function is plotted against n for $\tau=4$, 6, and 8, which span the range of values for conservative allowable peak deformation, depending on the imperfections. Figure 2 is a similar plot for the larger times $\tau=6$ and 8, plus $\tau=10$, but with each curve normalized by its maximum $G_{\max}(\tau)$. These curves demonstrate that the shape of $G_n(\tau)/G_{\max}(\tau)$ does not change substantially with τ, particularly for the larger values. In the following sections several alternative representations of uncertain imperfections are used to obtain estimates of the peak flexural deformation resulting from amplification by this function.

Convex Model Solution

Imperfections are first treated as quantities to be determined by quality control inspection. This inspection can be done by measuring radius as a function of angle with a high accuracy, linear variable differential transformer (LVDT) probe riding on the shell as it is turned in a lathe. The simplest measure of

Downloaded 03 May 2010 to 171.66.16.247. Redistribution subject to ASME license or copyright; see http://www.asme.org/terms/Terms_Use.cfm

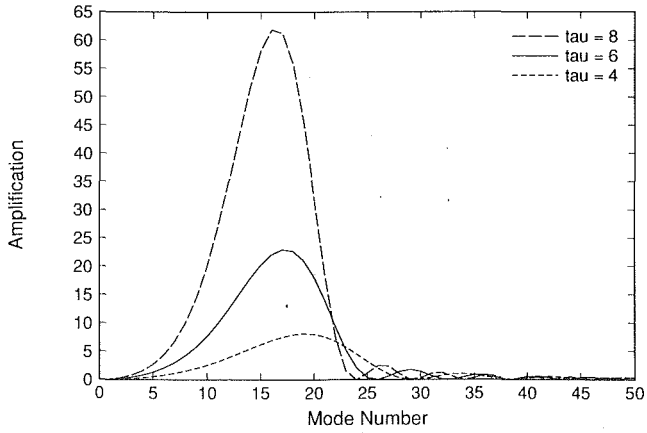


Fig. 1 Amplification function for $\tau = 4, 6, 8$ with $s = 20$

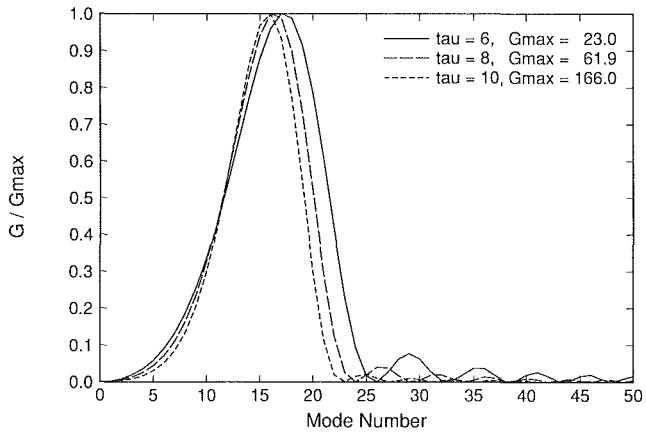


Fig. 2 Normalized amplification function for $\tau = 6, 8, 10$ with $s = 20$

the imperfections is the difference between the minimum and maximum recordings from the probe over the angle θ domain D: $0 \le \theta \le 2\pi$. With this difference, $2\hat{\delta}$, a conservative estimate of amplified deformations is the maximum possible deformation for any imperfection $\delta(\theta)$ within the uniform bounds $\pm\hat{\delta}$, where $\hat{\delta}$ is a positive constant.

Worst-Case Imperfections and Resulting Maximum Response. The set of all possible imperfections within this bound is denoted by $R(\hat{\delta})$:

$$R(\hat{\delta}) = \{\delta: |\delta(\theta)| \le \hat{\delta}\}. \tag{8}$$

The extreme-point functions of set $R(\hat{\delta})$ are

$$E(\hat{\delta}) = \{\delta: \delta(\theta) = \hat{\delta}[K_P(\theta) - K_Q(\theta)],\ P \cap Q = \emptyset,\ P \cup Q = D\} \tag{9}$$

where D is the domain $0 \le \theta \le 2\pi$ and, as indicated, P and Q are disjoint sets that just cover D. The characteristic function $K_V(\theta)$ is defined for any set V such that $K_V(\theta) = 1$ if θ is in V, and $K_V = 0$ otherwise. Thus, the extreme points of R are functions E that assume only the values $+\hat{\delta}$ and $-\hat{\delta}$ and that switch back and forth between $+\hat{\delta}$ and $-\hat{\delta}$ at arbitrary points in D. The solution examples that follow will clarify this nature of E.

Because $u(\,)\theta, t)$ is a linear function of the Fourier coefficients A, B, and the set $R(\hat{\delta})$ is convex, the maximum possible response for any imperfection in set $R(\hat{\delta})$ is

$$u_{\max}(\hat{\delta};\ \theta,\ \tau) \equiv \mu(\hat{\delta};\ \theta,\ \tau) = [A^T\phi_c + B^T\phi_s]_{\max} \text{ for } \delta \in E(\hat{\delta}). \tag{10}$$

The Fourier coefficients A, B are found from

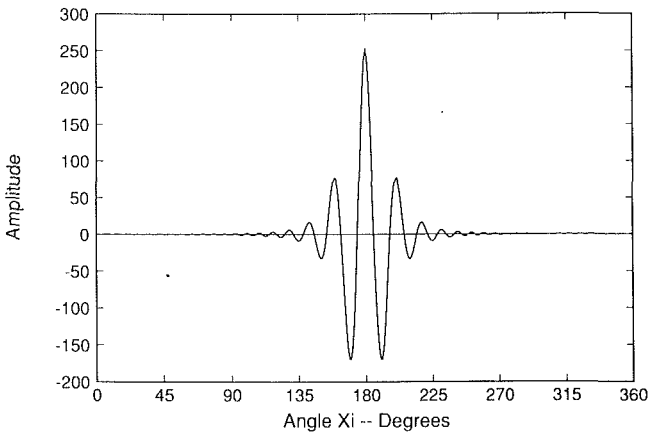


Fig. 3 Bounded imperfection integrand function $S(\xi;\ \theta,\ \tau)$ for $s = 20$, $\tau = 6$ and $\theta = 180$ deg ($G_{\max} = 23.0$, $\mu\hat{\delta} = 31.8$)

$$a_n = \frac{1}{\pi}\int_0^{2\pi} \delta(\xi)\cos n\xi\, d\xi,\quad b_n = \frac{1}{\pi}\int_0^{2\pi} \delta(\xi)\sin n\xi\, d\xi \tag{11}$$

in which ξ has been used as the dummy variable to avoid confusion with θ in expressions that follow. With these expressions for a_n and b_n, the response function in (2) is given by

$$u(\theta,\ \tau) = \frac{1}{\pi}\sum_{n=2}^{N} G_n(\tau)\left[\cos n\theta \int_0^{2\pi} \delta(\xi)\cos n\xi\, d\xi + \sin n\theta \int_0^{2\pi} d(\xi)\sin n\xi\, d\xi\right]. \tag{12}$$

By inspection of this equation we define

$$S(\xi;\ \theta,\ \tau) = \frac{1}{\pi}\sum_{n=2}^{N} G_n(\tau)[\cos n\theta\cos n\xi + \sin n\theta \sin n\xi] = \frac{1}{\pi}\sum_{n=2}^{N} G_n(\tau)\cos n(\xi - \theta). \tag{13}$$

Then (12) becomes

$$u(\theta,\ \tau) = \int_0^{2\pi} \delta(\xi)S(\xi;\ \theta,\ \tau)d\xi. \tag{14}$$

The maximum possible $u(\theta, \tau)$ for δ in $R(\hat{\delta})$ occurs by switching between $+\hat{\delta}$ and $-\hat{\delta}$ such that the integrand is always positive. Thus,

$$\mu(\hat{\delta};\ \tau) \equiv u_{\max}(\hat{\delta};\ \tau) = \hat{\delta}\int_0^{2\pi} |S(\xi;\ \theta,\ \tau)|\, d\xi \tag{15}$$

in which the notation for dependence on θ has been dropped because, from (13), θ simply shifts S along the ξ-axis. This results from the loading symmetry.

Numerical Examples. The integrand function $S(\xi;\ \theta,\ \tau)$ is plotted against ξ in Fig. 3 for $\theta = \pi$ and $\tau = 6$ with the buckling parameter $s = 20$ used in Fig. 1. The function has its largest maximum at the value $\xi = \theta$ for which the deformation is to be maximized, and then oscillates with decreasing amplitude and wavelength on either side of this maximum. The imperfection $\delta(\xi)$ that produces a maximum deformation at θ is a series of rectangles of amplitude $\pm\hat{\delta}$ oscillating in phase with this function. Because the loading is symmetric in θ, the function S is identical for any other value of θ except for a translation along the ξ-axis. For example, $S(\xi;\ \pi/2,\ \tau)$ to produce a maximum deformation at $\theta = \pi/2$ is shifted such that its largest maximum is at $\xi = \pi/2$ (denoted by 90 deg in Fig. 3)

Downloaded 03 May 2010 to 171.66.16.247. Redistribution subject to ASME license or copyright; see http://www.asme.org/terms/Terms_Use.cfm

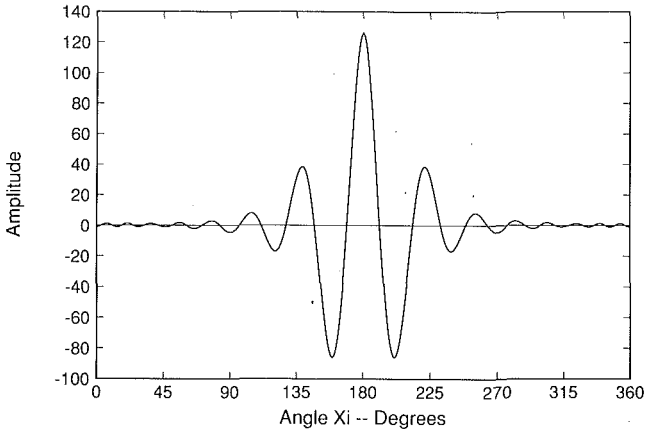


Fig. 4 Bounded imperfection integrand function $S(\xi; \theta, \tau)$ for $s = 10$, $\tau = 6$ and $\tau = 180$ deg ($G_{max} = 23.0$; $\mu/\hat{\delta} = 31.8$)

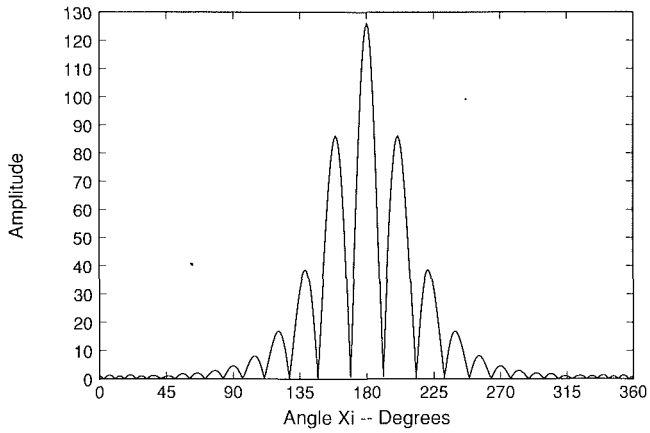


Fig. 5 Bounded imperfection integrand function $|S(\xi; \theta, \tau)|$ for $s = 10$, $\tau = 6$ and $\tau = 180$ deg ($G_{max} = 23.0$; $\mu/\hat{\delta} = 31.8$)

and is otherwise identical with the curve in the figure. For unsymmetric loading or in problems with a spatial boundary (e.g., a pinned column under sudden load (Lindberg, 1965)), an analogous function would be different for each position on the structure. In these cases one would have to also maximize with respect to spatial coordinates.

Thus, S is an influence function that determines the range over which imperfections influence the deformation at θ. Because the most amplified modes have large mode numbers and hence short wavelengths for this $s = 20$ example (see Fig. 1), S in Fig. 3 decays rapidly with ξ and the contribution to the integral in (15) for imperfections some distance from θ is negligible. Therefore, while the "worst-case" imperfection oscillates with uniform amplitude $\pm\hat{\delta}$ over all ξ, the contribution to deformation at θ is small except for imperfections near θ.

For an amplification function with its maximum at a lower mode number, the range of influence is larger. A graph of S is given in Fig. 4 for $s = 10$. The change from Fig. 3 can be explained by first observing from Eq. (3) that the amplification function scales in n with s (for $s^2 \gg 1$). Thus, for other values of s, the function simply shrinks or expands along the n-axis, with no change in amplification magnitudes. As G_n shrinks in mode numbers when s is reduced to 10, S expands in wavelengths by the same factor, and reduces in magnitude by this factor because of the smaller number of terms in the sum; the integral for μ is unchanged. With S more spread out as in Fig. 4, the angular range of influence of imperfections is larger. In this figure the amplitudes are large enough throughout the domain D that the zeros of S can be seen and hence the complete shape of the diabolical worst-case imperfection visualized.

The absolute value $|S|$ for $s = 10$ is plotted in Fig. 5 to show the function that is to be integrated to obtain the maximum deformation. Here it is apparent by visual integration under the humps[1] that about 90 percent of the deformation is from imperfections ranging from 130 to 230 deg, an arc of 100 deg. For $s = 20$, this range is 50. Thus, one can reduce the conservatism in measuring $2\hat{\delta}$ by retaining only minimum and maximum deviations from a perfect shape that are within this range from each other. This reduces the unnecessary contributions to $\hat{\delta}$ from low-order modes. More complete reduction of low-order mode contributions will be discussed when the convex model results are compared with probabilistic model results from random imperfections.

Since μ depends only on $\hat{\delta}$ and τ, and is linearly proportional to $\hat{\delta}$, general results are given in Table 1 as $\mu/\hat{\delta}$ for τ ranging from 4 to 12. Also tabulated are the maximum values G_{max} of the amplification function, and the ratio of $\mu/\hat{\delta}$ to these maximums. The ratio is very nearly constant, particularly for the larger values of τ, reflecting the nearly constant shape of the normalized amplification function. Plots of $S(\xi; \theta, \tau)$ over this range of τ have essentially the same shape over the ξ range of primary influence. The main differences are in the wavelengths of oscillation on either side of this range; wavelengths are shorter at smaller τ because of the larger relative contribution of high mode numbers, as can be seen by comparing the amplification function for $\tau = 4$ and $\tau = 6$ in Fig. 1.

Table 1 Maximum amplifications and convex bounds

τ	G_{max}	$\mu/\hat{\delta}$	Ratio
4	8.00	11.53	1.441
6	22.97	31.77	1.383
8	61.87	84.11	1.359
10	166.00	220.98	1.331
12	437.90	585.60	1.337

The close correspondence between G_{max} and $\mu/\hat{\delta}$ is to be expected, as is the result that the ratios are larger than unity. This demonstrates that the worst-case imperfection gives larger deformations than if the imperfections were a simple sine wave in the most amplified mode, but not much larger.

Probabilistic Model Solutions

Use of the maximum possible deformation μ as a measure of the effect of imperfections on response is obviously conservative. In this example problem, measurements on a wide range of shells (Arbocz, 1982; Kirkpatrick and Holmes, 1989, 1991) show that imperfection bounds $\pm\hat{\delta}$ are dominated by low-order modes. These are not amplified appreciably but nevertheless large dictate the amplitude of the worst-case imperfection shape, which was shown to be an oscillation of rectangular waves with *short* wavelengths.

To test the magnitude of this conservatism, probabilistic model solutions were obtained for two "vertical realities" of random imperfections. That is, two shell populations were hypothesized to have imperfections that can be modeled by random distributions. Although purely hypothetical, the populations appear to bound measurements that have been made on real shells. Thus, in this sense comparisons of deformations for these imperfections with the maximum deformation from

[1] The wave form and ξ span of the dominant humps are about the same from one to another so the integral is approximately proportional to the sum of the ordinate peaks.

Downloaded 03 May 2010 to 171.66.16.247. Redistribution subject to ASME license or copyright; see http://www.asme.org/terms/Terms_Use.cfm

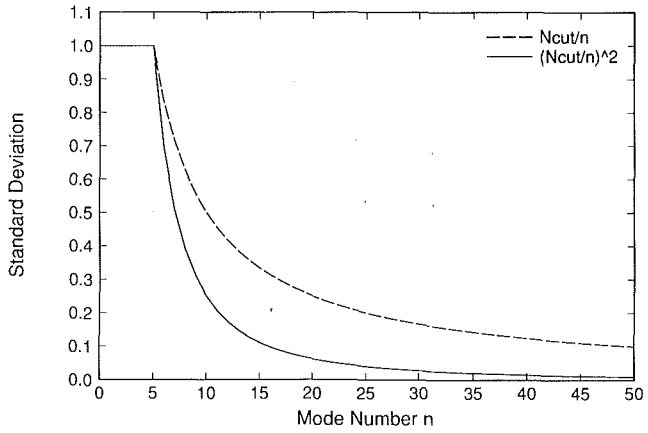


Fig. 6 Decay with mode number of Fourier coefficient standard deviation σ_n for two hypothetical shell populations

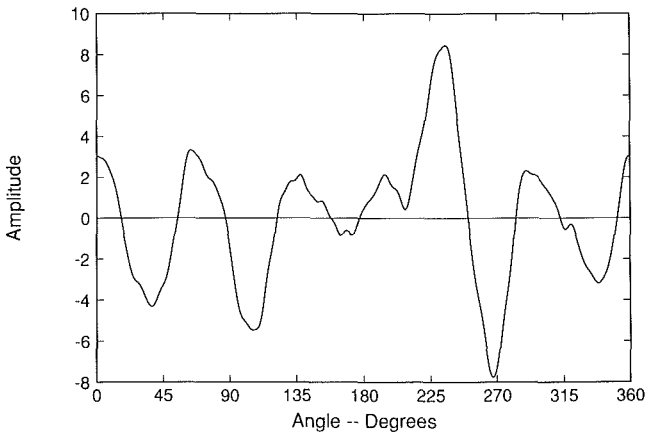


Fig. 7(*a*)

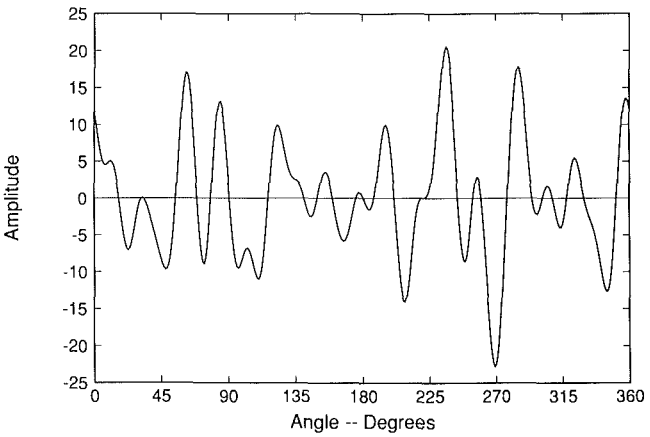


Fig. 7(*b*)

Fig. 7 Example imperfection shape (top) and buckle shape at $\tau = 6$ (bottom) for the $(n_c/n)^2$ imperfection population

the convex model solution give estimates of the range of conservatism of the convex model.

Both populations are assumed to have Fourier coefficients a_n and b_n that are random and uncorrelated, with a Gaussian distribution, zero mean values, and standard deviations σ_n that vary with n. The two variations in Fig. 6 describe the two populations. Both are constant to a "cutoff" mode number $n_c = 5$ and then decay with n, the first as n_c/n and the second as $(n_c/n)^2$. The constant is taken as unity with no loss in generality since the buckle shape is linear in a_n and b_n.

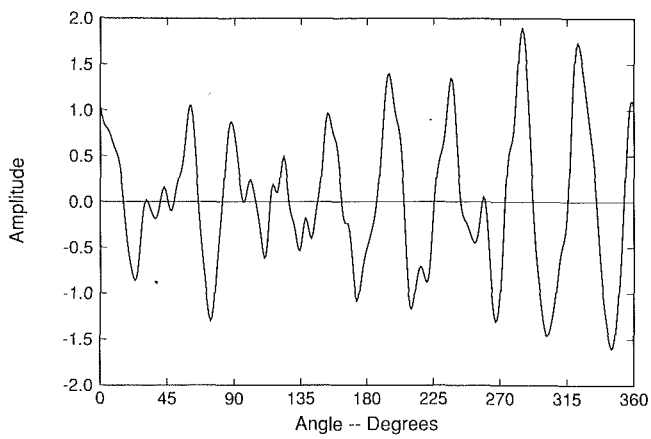


Fig. 8(*a*)

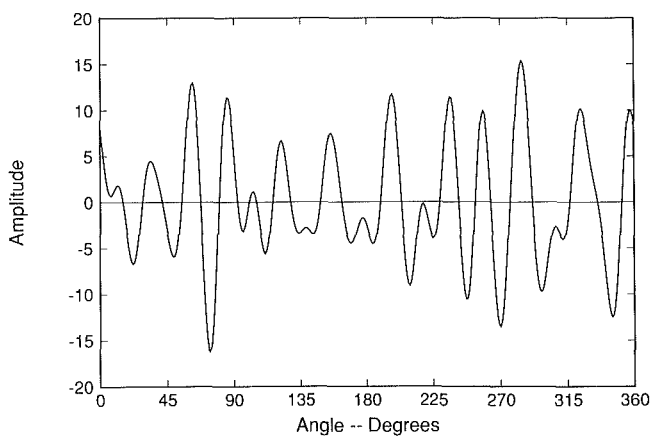


Fig. 8(*b*)

Fig. 8 Imperfection shape (top) and buckle shape (bottom) for same Fourier coefficients as in Fig. 7 but with $a_n = b_n = 0$ for $n \leq 7$

The constant σ_n for low mode numbers represents the observed cutoff in modal amplitudes found in measurements reported by Arbocz (1982). The decay as $(p_c/n)^2$ is the good approximation reported by Kirkpatrick and Holmes (1989) to measurements made to mode numbers as high as 160. This form for high mode numbers agrees with an intuitive notion that these imperfections are the result of "white noise" locked-in stresses that bend the shell wall. Thus, the peak curvatures $n^2 a_n$ have nearly constant σ_c to high mode numbers as long as the wavelength is long compared with the wall thickness. At the other extreme, none of the imperfections reported by Arbocz decayed less rapidly than n_c/n. Thus, the two hypothetical shell populations have imperfection distributions that are reasonable bounds on the form of imperfections for actual shells, motivating use of the expression "virtual reality" popularized by computer simulation technologists.

As will be described shortly, probability density functions for imperfections, and for buckled shapes formed through amplification by the $\tau = 6$ function in Fig. 1, were calculated by the Monte Carlo method for both populations. A typical imperfection shape and corresponding buckled shape are given in Fig. 7 for the $(n_c/n)^2$ population. It is apparent that the buckled form is dominated by high-number modes, although the largest peaks do occur in this case near the largest peaks of the imperfection, which are dominated by low-number modes.

For evaluation of a less conservative method of applying the convex model solution, imperfections filtered to $n = n_f = 7$

Downloaded 03 May 2010 to 171.66.16.247. Redistribution subject to ASME license or copyright; see http://www.asme.org/terms/Terms_Use.cfm

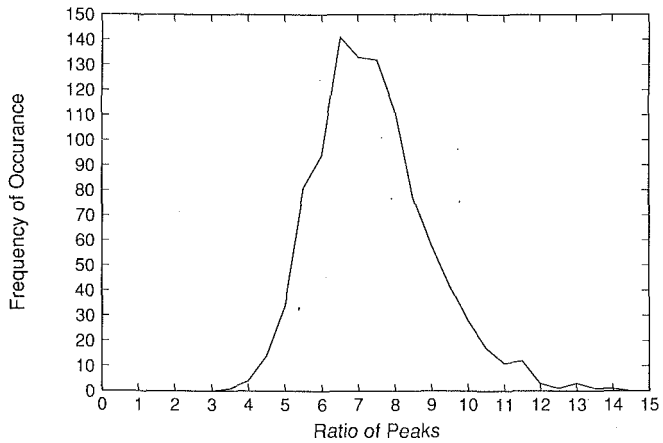


Fig. 9 Probability density of the ratio of the buckle peak to the imperfection peak for the n_c/n imperfection population

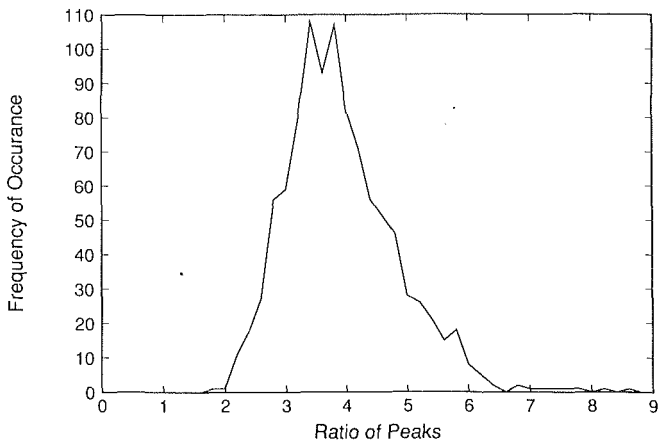


Fig. 11 Probability density of the ratio of the buckle peak to the imperfection peak for the $(n_c/n)^2$ imperfection population

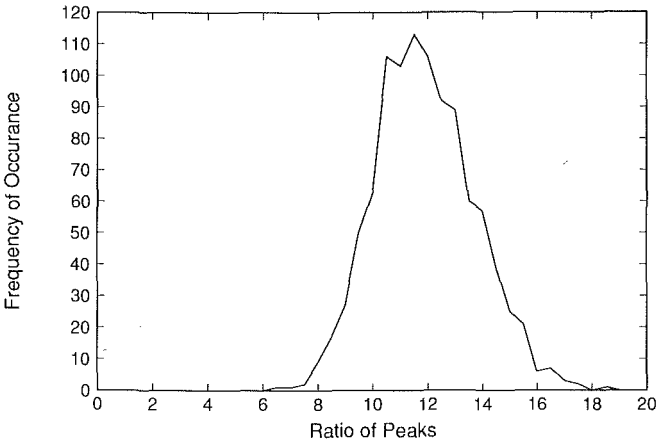


Fig. 10 Probability density of the ratio of the buckle peak to the imperfection peak for the n_c/n imperfection population with filtered Fourier coefficients

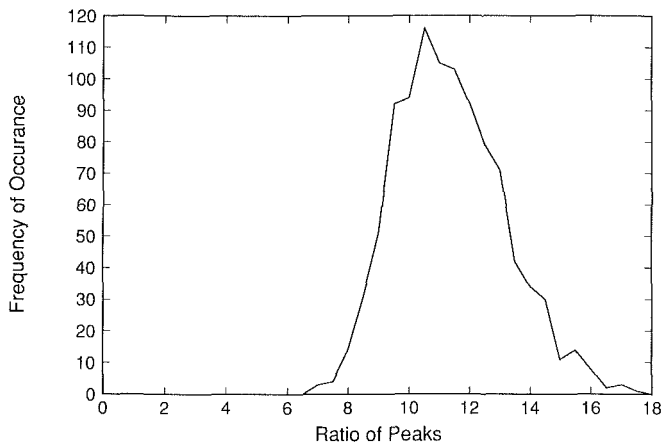


Fig. 12 Probability density of the ratio of the buckle peak to the imperfection peak for the $(n_c/n)^2$ imperfection population with filtered Fourier coefficients

and their resulting buckled shapes were also analyzed. Thus, the same decay with n as in Fig. 6 was used but with $\sigma_n = 0$ for $n \leq 7$. The motivation for and implications of these filtered shapes is discussed in the next section. An example filtered imperfection and buckled shape for the same set of Fourier coefficients as in Fig. 7 is given in Fig. 8.

Probability density functions were calculated for three quantities for each of the populations in both the unfiltered and filtered state, using a Monte Carlo sample size of 1000:

1 *Imperfection peak*: half the span between the largest maximum and most negative minimum imperfection in domain D.
2 *Buckle peak*: the absolute maximum of the buckled shape in D.
3 *Ratio of peaks*: the *buckled peak* divided by the *imperfection peak* for each member of the population.

The 1000 sample size was chosen as a reasonable compromise between accuracy for estimates at a 99.5 percent probability level and time required for the computations. This probability level was chosen rather arbitrarily as representative of the upper range of interest for reliability of military structures and the lower range for civil structures. Readers can use the resulting probability density functions for estimates of response at lower reliabilities. Extension to higher reliabilities would require more sophisticated probabilistic computations but are unwarranted without demonstration that the Gaussian model is appropriate at these high probabilities.

The calculations were done as follows. Each of the 1000 shells from a hypothetical population was defined by choosing 98 random, uncorrelated Fourier coefficients ($2 \leq n \leq 50$ for a_n and b_n) having population statistics as just described. Then the imperfection shape was calculated with Eq. (1) at one-degree increments and the *imperfection peak* stored according to definition 1 above. These same values of a_n and b_n were used to calculate the buckle shape at $\tau = 6$ by using Eq. (2), and the *buckle peak* stored according to definition 2. Then the *ratio of peaks* was stored according to definition 3. Histograms were prepared with the 1000 values for each of these quantities for both n_c/n and $(n_c/n)^2$ populations in both the filtered and unfiltered calculations. Filtered quantities were calculated first, and then the filtered modes were added to obtain unfiltered results. The trigonometric functions were calculated only once, and only for $n = 1$. These were stored in indexed arrays accessed by $n\theta$ modulo 360 for $n > 1$, with θ in degrees (a small step toward fast Fourier techniques).

The density function of most interest for comparison with the convex model results is the ratio of peaks, because this corresponds directly to $\mu/\hat{\delta}$. This density function is given in Figs. 9 through 12 for both imperfection populations in both the filtered and unfiltered state. Density functions for the other quantities have the same basic features as these, namely a skewed distribution with larger deviations on the large side of

Downloaded 03 May 2010 to 171.66.16.247. Redistribution subject to ASME license or copyright; see http://www.asme.org/terms/Terms_Use.cfm

Table 2 Summary and comparison of probabilistic and convex model results (for $s=20$ and $\tau=6$; convex model $\mu/\hat{\delta}=31.8$ unfiltered and $\mu/\hat{\delta}=33.5$ for $\hat{\delta}$ from filtered measurements).

$\sigma_n(n)$	Statistic	Imperf. Peak	Buckle Peak	Ratio R of Peaks	R_{bp} is $\mu/\hat{\delta}R$	$\frac{2R_{bp}}{\pi}$
	$\bar{x}$	7.335	53.416	7.404	4.29	
n_c/n	σ_x	1.093	9.492	1.541		
	$\bar{x}+3\sigma_x$	10.614	81.892	12.027	2.64	1.68
n_c/n	$\bar{x}$	4.390	52.061	11.916	2.81	
filtered	σ_x	0.615	9.460	1.792		
$n_f=7$	$\bar{x}+3\sigma_x$	6.235	80.441	17.292	1.94	1.24
	$\bar{x}$	5.333	20.245	3.907	8.13	
$(n_c/n)^2$	σ_x	0.980	3.408	0.908		
	$\bar{x}+3\sigma_x$	8.273	30.469	6.631	4.80	3.06
$(n_c/n)^2$	$\bar{x}$	1.665	18.634	11.365	2.95	
filtered	σ_x	0.317	3.260	1.788		
$n_f=7$	$\bar{x}+3\sigma_x$	2.606	28.414	16.729	2.00	1.27

the mean than on the small, because the quantities are never negative (the distributions for the filtered imperfections, in Figs. 10 and 12, are only slightly skewed because of their larger mean values relative to their deviations).

Comparison of Convex and Probabilistic Model Results

The principal results of the probabilistic model are summarized in Table 2, along with comparisons to the maximum deformation from the convex model. The first three columns of numerical data are statistical quantities for the three peak quantities defined in the previous section. The values were calculated from the 1000-sample-size Monte Carlo results that were used to plot probability density functions for each of the 12 quantities (three peak types for four imperfections types). For each imperfection type the table gives mean value $\bar{x}$, standard deviation σ_x, and $\bar{x}+3\sigma_x$, for the three peak quantities.

The next column gives comparisons of the *ratio of peaks* with the comparable quantity $\mu/\hat{\delta}$ from the convex model, expressed as $\mu/\hat{\delta}$ divided by a statistic for the ratio of peaks. The first entry, 4.29, shows that the maximum deformation ratio $\mu/\hat{\delta}$ from the convex model is 4.29 times the mean value of the comparable quantity (ratio of peaks) for the n_c/n population of random imperfections. A more consistent comparison is the next entry, 2.64, for the statistic $\bar{x}+3\sigma_x$. From Fig. 9 (and the other density functions for the other imperfection populations) it can be determined that this statistic gives a reliability of about 99.5 percent for all the probability distributions. Thus, for this imperfection population, the maximum possible response from the convex model solution is conservative by a factor of 2.64 compared with a 99.5 percent reliability from a probabilistic solution.

This large conservatism is caused by the substantial contribution of low-order modes to $\hat{\delta}$, but which are not amplified by the buckling motion, as mentioned earlier. Examination of the amplification function in Fig. 1 suggests that imperfection Fourier coefficients for $n\leq 7$ could be filtered out for the determination of $\hat{\delta}$ without introducing substantial error in the calculation of buckle deformation. For comparison with the convex model, S and $\mu/\hat{\delta}$ were also calculated with these lower modes filtered out. There was no essential change in the character of S and $\mu/\hat{\delta}$ increased only slightly, from 31.8 to 33.5, as compared to the more substantial increase in the ratio of peaks for the probabilistic models, from 12.027 to 17.292 for the n_c/n population and from 6.631 to 16.729 for the $(n_c/n)^2$ population.

Table 2 shows that the net result of filtering the imperfections before one measures $\hat{\delta}$ for quality control, with use of the corresponding convex model, is a reduction in conservatism from the factor 2.64 to a factor 1.94 for the n_c/n population. This conservatism is fairly reasonable, considering that the convex model removes all questions concerning the nature of a probabilistic model for the imperfections and the shape of its probability density function. (The factor 1.94, of course, depends on the assumed imperfection population; this is discussed in following paragraphs.) Table 2 shows that neglect of the low modes reduced the $\bar{x}+3\sigma_x$ buckle peak deformation only slightly, from 81.89 to 80.44. A similar small reduction resulted for $\bar{x}$, from 53.42 to 52.06.

The last column in Table 2 shows that this conservatism can be reduced to a more completely reasonable factor 1.24 if the diabolical worst-case imperfection is replaced by a more realistic series of half sine waves rather than rectangular waves. (This ad hoc procedure is unnecessary if one uses a convex model defined by an ellipsoidal bound on the Fourier coefficients of the imperfections (companion paper, Lindberg, 1992).) In essence, this filters out the effects of very high-order modes, which have an effect of response via the amplification function but are unlikely to the present in the imperfection to form rectangular waves. The constant $2/\pi$ is the ratio between the area under a half sine wave (the essential shape of $|S|$ of each hump in Fig. 5) and a sine squared wave (the shape of the μ integral function when S is multiplied by a constant amplitude, varying period sine wave in phase with S).

Similar results are given in Table 2 for the $(n_c/n)^2$ imperfection population. For this population the conservatism factors for unfiltered imperfections are very large: 8.13 for $\bar{x}$ and 4.80 for $\bar{x}+3\sigma_x$. The effect of filtering the imperfection is much more dramatic for this population because the imperfections are so dominated by low-order terms (see Fig. 6). With filtering, the above conservatism factors are reduced to 2.95 and 2.00, respectively, which are about the same as for the filtered n_c/n population. With $\mu/\hat{\delta}$ reduced by the factor $2/\pi$, the conservatism compared with $\bar{x}+2\sigma_x$ is further reduced to 1.27.

Therefore, although these estimates of conservatism depend on the hypothetical imperfections posed, one can conclude, in the sense that these virtual realities bound real imperfections, that tempered application of the convex model solution can give results that are comparable to results from probabilistic methods at a reliability of about 99.5 percent. Since response from the Gaussian probabilistic model is unbounded, at very high reliabilities the convex model results are less conservative than the probabilistic results. Furthermore, the convex model solution removes all uncertainty introduced by an assumed probabilistic description of imperfections, and also allows use of simple methods for quality control.

If the imperfection filtering needed for reasonable conservatism is done digitally by means of Fourier coefficients, these coefficients could be used instead to calculate the exact response for every shell. Similarly, even in more general problems with more complex shell geometry and loading, which must be solved by finite element codes, linear response of the type considered here could be calculated for every shell by using stored modal coefficients from the finite element solution. Thus, one must weigh the complexity of such imperfection data manipulation against the conservatism but simplicity of calculating $\mu/\hat{\delta}$ once and for all. However, the need for measuring Fourier coefficients for every shell, and filtering low-order modes, is eliminated by use of a convex model defined by an ellipsoid bound on the Fourier coefficients, coupled with use of $\hat{\delta}$ as a measure of the size of the ellipsoid. These convex models are presented in a companion paper (Lindberg, 1992).

Conclusions

Comparisons of estimates of maximum buckling response from convex and probabilistic models for multimode buckling

Downloaded 03 May 2010 to 171.66.16.247. Redistribution subject to ASME license or copyright; see http://www.asme.org/terms/Terms_Use.cfm

have shown that the convex model gives a much simpler solution that can be applied with greater confidence and flexibility, and with little increase in conservatism, than for estimates from the probabilistic models. An important flexibility is that the convex model solution can be used to maintain quality control by much simpler means than with probabilistic models. However, with this simple uniform bound model, to obtain conservatism comparable to a 99.5 percent reliability from the probabilistic models, the imperfections must be filtered before the bound is measured. Also, the worst-case rectangular imperfections were replaced by a reasonable but nevertheless ad hoc smooth counterpart. This filtering and ad hoc replacement can be avoided by rigorous application of a convex model defined by an ellipsoidal bound on the imperfection Fourier coefficients, coupled with use of $\hat{\delta}$ as a measure of the ellipsoid size. The present paper provides insight into the physical interpretation of the ellipsoid bound model and probabilistic results that are compared with both convex models.

In the example problem, the convex model solution was obtained with a few minutes of computer time, while the probabilistic model solutions required about ten hours for each of the assumed imperfection populations, and a great deal more manipulation to interpret the numerical results (all on a 12 MHz PC 286/287 desk top computer). It is expected that similar advantages of convex modeling over probabilistic modeling will be obtained in more complex problems that require finite element modal solutions. Development of perturbation methods for convex modeling of nonlinear buckling is a fertile field for further research and applications.

References

Abrahamson, G. R., and Goodier, J. N., 1962, "Dynamic Plastic Flow Buckling of a Cylindrical Shell from Uniform Radial Impulse," *Proceedings of Fourth U.S. National Congress of Applied Mechanics*, Berkeley, CA, pp. 939–950.

Arbocz, J., 1982, "The Imperfection Data Bank: A Means to Obtain Realistic Buckling Loads," *Buckling of Shells: Proceedings of a State-of-the-Art Colloquium*, New York.

Ben-Haim, Y., and Elishakoff, I., 1989, "Non-Probabilistic Methods of Uncertainty in the Non-Linear Buckling of Shells with General Imperfections: Theoretical Estimates of the Knockdown Factor," ASME JOURNAL OF APPLIED MECHANICS, Vol. 56, pp. 403–410.

Ben-Haim, Y., and Elishakoff, I., 1990, *Convex Models of Uncertainty in Applied Mechanics*, Elsevier, New York.

Elishakoff, I., 1978a, "Axial Impact Buckling of a Column With Random Initial Imperfections," ASME JOURNAL OF APPLIED MECHANICS, Vol. 45, pp. 361–365.

Elishakoff, I., 1978b, "Impact Buckling of a Thin Bar Via Monte Carlo Method," ASME JOURNAL OF APPLIED MECHANICS, Vol. 45, pp. 586–590.

Kirkpatrick, S. W., and Holmes, B. S., 1989, "Effect of Initial Imperfections on Dynamic Buckling of Shells," *ASCE Journal of Engineering Mechanics*, Vol. 115, No. 5, pp. 1075–1093.

Kirkpatrick, S. W., and Holmes, B. S., 1991, "Static and Dynamic Buckling of Thin Cylindrical Shells," *Computational Aspects of Contact, Impact and Penetration*, R. F. Kulak and L. E Schwer, eds., Elmepress International, Annandale, VA.

Lindberg, H. E., 1965, "Impact Buckling of a Thin Bar," ASME JOURNAL OF APPLIED MECHANICS, Vol. 32, pp. 315–322.

Lindberg, H. E., and Florence, A. L., 1987, *Dynamic Pulse Buckling*, Martinus Nijhoff Publishers, Dordrecht, The Netherlands; Kluwer, Hingham, MA.

Lindberg, H. E., 1988, "Random Imperfections for Dynamic Pulse Buckling," *ASCE Journal of Engineering Mechanics*, Vol. 114, pp. 1144–1165.

Lindberg, H. E., 1991, "Dynamic Pulse Buckling of Imperfection Sensitive Shells," ASME JOURNAL OF APPLIED MECHANICS, Vol. 58, pp. 743–748.

Lindberg, H. E., 1992, "Convex Models for Uncertain Imperfection Control in Multimode Dynamic Buckling," ASME JOURNAL OF APPLIED MECHANICS, Vol. 59, pp. 937–945.

Downloaded 03 May 2010 to 171.66.16.247. Redistribution subject to ASME license or copyright; see http://www.asme.org/terms/Terms_Use.cfm

Convex Models for Uncertain Imperfection Control in Multimode Dynamic Buckling

H. E. Lindberg
APTEK, Inc.
San Jose, CA 95129

Control of uncertain imperfections by means of convex bounds on finite Fourier transforms is shown to be more direct and not as overly conservative as control based on uniform bounds, i.e., bounding maximum and minimum imperfections. With either method, conservatism in bounds on buckling response is reduced by filtering the imperfection measurements. Extraction of the needed filtered information by operating directly on the Fourier coefficients is straightforward and allows use of additional information on the variation of the coefficients with mode number. Use of this information in example multimode buckling problems gives a bound on maximum possible buckling response that is a factor of 1.6 larger than the response at a reliability of 99.5 percent for hypothetical (but reasonably representative) probabilistic imperfections. The bounding response itself, of course, does not depend on any assumptions concerning the probabilistic distribution of imperfections. Two additional combined uniform and Fourier ellipsoid bound models further reduce this factor to 1.1 and 0.5, and require only a simple, unfiltered imperfection bound measurement during quality control inspection.

1 Probabilistic and Convex Models of Uncertainty

Ben-Haim and Elishakoff (1990) give several examples of the application of probabilistic models of uncertainty which demonstrate the extreme sensitivity of reliable response estimates at high reliability (low probability of failure). To circumvent this difficulty, they advocate use of convex models of uncertainty. In this method, one determines the maximum possible response when the uncertain quantities are confined within specified bounds. This avoids questions concerning the tails of poorly known probability distributions and the high sensitivity of response at high reliabilities, but can introduce inordinate conservatism.

In Lindberg (1992), the degree of conservatism compared with probabilistic methods was explored for hypothetically known distributions of random imperfections in multimode buckling. It was found that, with a convex model for imperfection shapes within uniform bounds (that is, any shape within upper and lower bounds $+\delta$ and $-\delta$), the maximum possible multimode buckling response from the convex model solution was from about three to five times the response from a probabilistic model at a reliability of 99.5 percent, depending on the hypothetical probabilistic imperfections.

At very high reliabilities, of course, the convex model solution eventually becomes less conservative then the probabilistic model solution, since one uses a direct, even though simple, measure of the imperfections. Nevertheless, it is useful to explore methods to reduce the conservatism of convex models. For the uniform bound model used in Lindberg (1992), it was found that if one filters the measured imperfections before measuring the bound, the conservatism is reduced to a factor of about 2 for either type of hypothetical probabilistic imperfections.

If this filtering is done by digital methods, enough information is available to use another convex model based on Fourier coefficients rather than simply the maximum and minimum imperfection amplitudes that define uniform bounds. This model provides a more direct and convenient method of imperfection control than use of uniform bounds on the filtered imperfection shape. In the following sections a convex model solution is derived for a wide class of systematic variations of the Fourier coefficients with mode number. Numerical results are given in generalized dimensionless form. Then several means of applying these results are evaluated by comparisons with probabilistic models for the same forms of hypothetical random imperfections as in Lindberg (1992). By combining ideas from both the uniform and Fourier ellipsoid bound models, improved (lower) estimates of maximum response are obtained that require only simple, unfiltered imperfection bound measurements during quality control inspection.

2 Multimode Buckling Response

The problem analyzed here and in Lindberg (1992) is dynamic plastic flow buckling of a long cylindrical shell following symmetric radial impulse. This problem was chosen because it is similar to pulse buckling problems that have been explored

Contributed by the Applied Mechanics Division of THE AMERICAN SOCIETY OF MECHANICAL ENGINEERS for publication in the ASME JOURNAL OF APPLIED MECHANICS.

Discussion on this paper should be addressed to the Technical Editor, Professor Leon M. Keer, The Technological Institute, Northwestern University, Evanston, IL 60208, and will be accepted until four months after final publication of the paper itself in the JOURNAL OF APPLIED MECHANICS.

Manuscript received by the ASME Applied Mechanics Division, Apr. 10, 1991; final revision, July 9, 1991. Associate Technical Editor: A. K. Noor.

Copyright © 1992 by ASME
Downloaded 03 May 2010 to 171.66.16.247. Redistribution subject to ASME license or copyright; see http://www.asme.org/terms/Terms_Use.cfm

by probabilistic methods (Lindberg, 1964; Elishakoff, 1978a,b), by finite element methods for measured and assumed random imperfections (Kirkpatrick and Holmes, 1989, 1991), and for which forms of random imperfections have been explored for use in finite element calculations (Lindberg, 1988). Also, data reported by Arbocz (1982) and Kirkpatrick and Holmes (1989, 1991) are available on which to base bounding estimates for the forms of random imperfections.

At any time, t, the Fourier sine and cosine coefficients (amplitudes) of each flexural mode n are equal to the corresponding imperfection coefficients times an amplification function $G_n(t)$. Thus, the flexural deformation is a linear function of the imperfection coefficients. The nonlinearity of plastic flow enters only into the nominally uniform inward motion. Buckling is a linear perturbation of this response. For a given description of imperfections, one calculates response to the maximum allowable flexural deformation and, with the time at this maximum response, determines the critical impulse. Since, as shown below, the variation with n of $G_n(t)/G_{\max}(t)$ does not change markedly as t increases for times of concern, it is useful to compare convex and probabilistic model results at a fixed time near the critical time for acceptable deformation. Conversion of these results into changes in critical impulsive load can be done to reasonable accuracy by using the variation of $G_{\max}$ (the maximum with respect to n) with t and hence with impulse.

Equations of motion and solutions were derived by Abrahamson and Goodier (1962) and are also given in Lindberg and Florence (1987, pp. 76–85). Here the Fourier series for the imperfections and flexural deformation response solution are simply written down in forms needed for derivation of the convex model solution. The imperfections (deviations from perfect circularity) are given by

$$\delta(\theta)=\sum_{n=2}^{N}(a_n\cos n\theta+b_n\sin n\theta)=\mathbf{D}^T\varphi \tag{1}$$

where

$$\mathbf{D}^T=\{a_2,\ a_3,\ \cdots\ a_N,\ b_2,\ b_3,\ \cdots\ b_N\}$$

is a vector representation of the Fourier coefficients and

$$\varphi^T=\{\cos 2\theta,\ \cos 3\theta,\ \cdots\ \cos N\theta,\ \sin 2\theta,\ \sin 3\theta,\ \sin N\theta\}.$$

The flexural deformation is given by

$$u(\theta,\ \tau)=\sum_{n=2}^{N}[a_nG_n(\tau)\cos n\theta+b_nG_n(\tau)\sin n\theta]=\mathbf{D}^T\phi \tag{2}$$

where $\phi(\theta,\ \tau)=\mathbf{G}(\tau)\varphi(\theta)$ and $\mathbf{G}$ is the $M\times M$ diagonal matrix

$$\mathbf{G}=\text{diag}\{G_2(\tau),\ G_3(\tau),\ \cdots\ G_N(\tau),\ G_2(\tau),\ G_3(\tau),\ \cdots\ G_n(\tau)\}$$

with $M=2(N-1)$. The $n=0$ mode is the symmetric motion that gives rise to hoop thrust, and the $n=1$ mode is a rigid-body translation. The amplification function is

$$G_n(\tau)=\frac{1}{1-\eta^2}\begin{bmatrix}\cosh\\ \cos\end{bmatrix}\begin{matrix}p_n\tau-1\end{matrix}\quad\begin{matrix}\eta<1\\ \eta>1\end{matrix} \tag{3}$$

where

$$\eta=n/s,\ p_n=[|(\eta^2-1/s^2)(1-\eta^2)|]^{1/2}. \tag{4}$$

A dimensionless time has been defined by

$$\tau=\frac{s^2c_p\alpha}{a}t \tag{5}$$

and $G_n(\tau)=\tau^2/2$ for $\eta=1$. The dimensionless parameters are defined by

$$\alpha=\frac{h}{a\sqrt{12}},\quad s^2=\frac{\sigma_y}{E_h\alpha^2},\quad c_p=\sqrt{\frac{E_h}{\rho}} \tag{6}$$

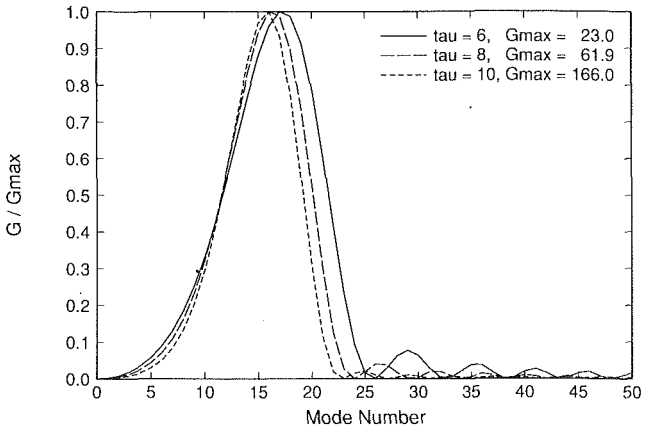


Fig. 1 Normalized amplification function for $\tau=6$, 8, 10 with $s=20$

Physical parameters are: h = wall thickness, a = radius, σ_y = yield stress, E_h = strain-hardening modulus, and ρ = density. The duration of buckling is the time τ_f to bring the symmetric motion to rest from the velocity imparted by symmetric impulse I:

$$\tau_f=\frac{I}{\rho a\alpha^2c_p}. \tag{7}$$

In Fig. 1 the amplification function is plotted in normalized form against n for $\tau=6$, 8, and 10, which span the range of values typically found to produce an allowable peak deformation, depending on the imperfections. The curves demonstrate the observation that the shape of this function does not change substantially with τ, particularly for the larger values.

3 Forms of Imperfections

3.1 Finite Fourier Transforms. Measurements of imperfections in cylindrical shells are typically reported and interpreted in terms of finite Fourier transforms on the interval 0, 2π around the shell circumference. Thus, the coefficients a_n and b_n in (1) are found from

$$a_n=\frac{1}{\pi}\int_0^{2\pi}\delta(\theta)\cos n\theta\,d\theta,\quad b_n=\frac{1}{\pi}\int_0^{2\pi}\delta(\theta)\sin n\theta\,d\theta. \tag{8}$$

These integrations are performed with the trapezoidal rule by using P data points on the interval. Thus, for a_n,

$$a_n=\frac{1}{\pi}\sum_{i=1}^{P}\delta_i\cos\frac{n\,2\pi i}{P}\cdot\frac{2\pi}{P}=\frac{2}{P}\sum_{i=1}^{P}\delta_i\cos\frac{2\pi ni}{P}. \tag{9}$$

Since $\delta(0)=\delta(2\pi)$, the term at $i=P$ gives $[\delta(0)+\delta(2\pi)]/2$ in accordance with the trapezoidal rule. A similar equation results for b_n. The quantity normally plotted as a function of n is the modulus $c_n=\sqrt{a_n^2+b_n^2}$.

3.2 Idealized Representations of Measured Imperfections. It has been found that nominal values of c_n are nearly constant for a small range of low-mode numbers and then decrease markedly with increasing n (Arbocz, 1982; Kirkpatrick and Holmes, 1989, 1991). Plots of idealized functional forms for the variation of a_n, b_n, and c_n with n are given in Fig. 2. These forms are given by

$$f_p(n)=\begin{cases}1 & \text{for } n<n_c\\ (n_c/n)^p & \text{for } n\geq n_c\end{cases} \tag{10}$$

where n_c is a cutoff below which the function is constant.

Measurements by Kirkpatrick and Holmes suggested use of the $(n_c/n)^2$ curve ($p=2$, with $n_c=5$ in the representative ideal-

Downloaded 03 May 2010 to 171.66.16.247. Redistribution subject to ASME license or copyright; see http://www.asme.org/terms/Terms_Use.cfm

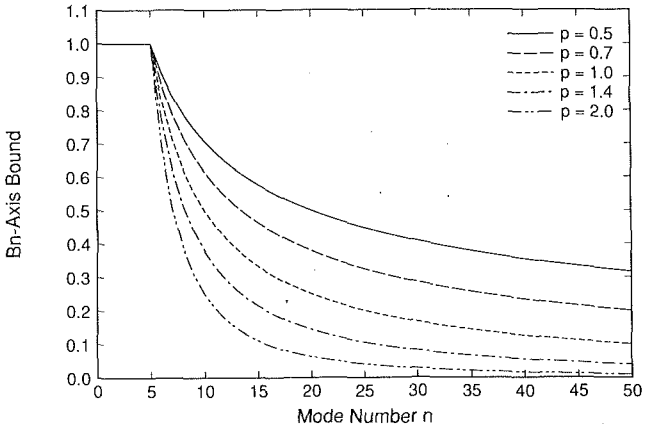


Fig. 2 Idealized variations of imperfection coefficients with n

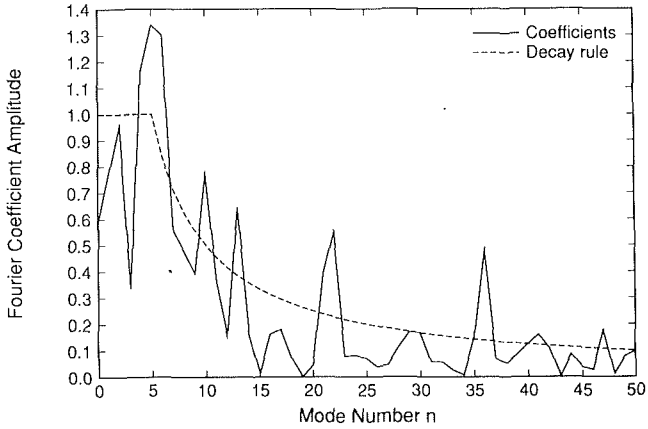


Fig. 3 Random variation of c_n with n for $p=1$, $n_c=5$

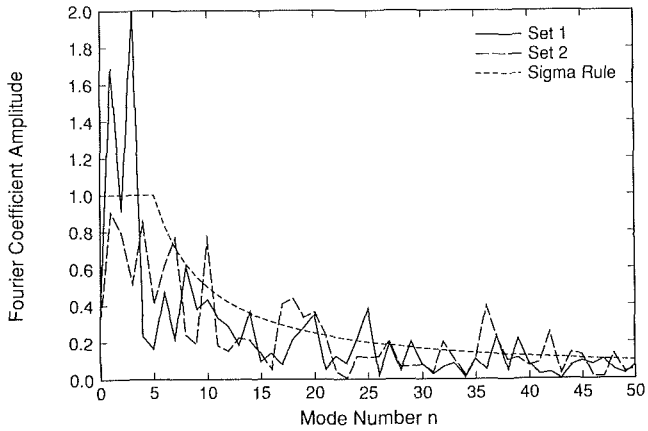


Fig. 4 Further examples from the same population as in Fig. 3

izations in the figure) for simple rolled and welded shells with a single seam, and for spin-formed shells. Measurements reported by Arbocz for much larger and more complex shells, with several seams and many stiffeners, gave coefficients dominated by the seam separations and overall decreases with n generally less rapidly than $(n_c/n)^2$. It is reasonable to assume that imperfections for simple shells can be represented by functional forms between $p=1$ and $p=2$. Curves for still lower values of p are included in the figure to help in visualizing the results of the convex model solution, which is evaluated for p varying continuously from 0 to 2.

Figure 3 gives a plot of c_n versus n generated by taking a_n and b_n as random variables with a Gaussian distribution having zero mean value and standard deviation varying as the $p=1$ curve (divided by $\sqrt{2}$) in Fig. 2. Figure 4 gives two more examples from the same population of c_n, to give a feel for the sets of random imperfections used in the later comparisons of the convex model solution with Monte Carlo calculations for a probabilistic model. The general character of the variation of these coefficients is strikingly similar to those reported by Kirkpatrick and Holmes (1991), except that here $p=1$ was taken to clearly display the amplitudes at large mode numbers.

4 Convex Model Based on Fourier Coefficients

Following the method developed by Ben-Haim and Elishakoff (1989), uncertainty in the initial imperfection profile is represented by allowing the imperfection vector $\mathbf{D}$ in (1) to vary on a convex set of values bounded within an ellipsoid:

$$R(\kappa, \mathbf{W}) = \{\mathbf{D}: \mathbf{D}^T\mathbf{W}\mathbf{D} \le \kappa^2\} \tag{11}$$

where $\mathbf{W}$ is an $M \times M$ positive definite real symmetric matrix that specifies the shape of an ellipsoid in M-dimensional space, and κ^2 is positive number that specifies its size. The set of extreme points of the set $R(\kappa, \mathbf{W})$ is the ellipsoidal shell:

$$E(\kappa, \mathbf{W}) = \{\mathbf{D}: \mathbf{D}^T\mathbf{W}\mathbf{D} = \kappa^2\}. \tag{12}$$

The sets R and E form a convex model in which R (range) is the set allowed coefficients and E is the set of extreme points of R. Because the buckling of displacement $u(\theta, \tau)$ is a linear function of the Fourier coefficients, and because $R(\kappa, \mathbf{W})$ is a convex set (all linear, convex combinations of its extreme points E are members of R, and these combinations completely map R), the maximum response $u_{\max}(\theta, \tau)$ occurs on the set of extreme points $E(\kappa, \mathbf{W})$.

For the Fourier coefficients described in the previous section, $\mathbf{W}$ is taken as

$$\begin{aligned}\mathbf{W} &= \text{diag}\{f_p^{-2}(n), f_p^{-2}(n)\} \\ &= \text{diag}\{1, 1, \cdots (n/n_c)^{2p}, \cdots (N/n_c)^{2p}, 1, 1, \\ &\qquad \cdots (n/n_c)^{2p}, \cdots (N/n_c)^{2p}\}.\end{aligned} \tag{13}$$

The ellipsoid for the set $R(\kappa, \mathbf{W})$ is then (with $n_c=1$ for simplicity)

$$2^{2p}a_2^2 + 3^{2p}a_3^2 + \cdots + n^{2p}a_n^2 + \cdots N^{2p}a_N^2 + 2^{2p}b_2^2 + \cdots + N^{2p}b_N^2 \le \kappa^2. \tag{14}$$

The range for each a_n and b_n is form $-R_n$ to $+R_n$, where

$$R_n = \kappa n^{-p} \tag{15}$$

found by setting all the other coefficients to their nominal zero value. For the more general coefficient variations in (10), $n_c > 1$ and $R_n = \kappa f_p(n)$.

4.1 Maximum Possible Response. Following Ben-Haim and Elishakoff (1989), the maximum deflection $u_{\max}(\theta, \tau)$ that can occur for any imperfection vector $\mathbf{D}$ in set $R(\kappa, \mathbf{W})$ is obtained by maximizing $\mathbf{D}^T\phi$ subject to the constraint that $\mathbf{D}$ is in the extreme-point set E, that is $\mathbf{D}^T\mathbf{W}\mathbf{D} = \kappa^2$. The desired maximum is found with the Hamiltonian

$$H = \mathbf{D}^T\phi + \lambda(\mathbf{D}^T\mathbf{W}\mathbf{D} - \kappa^2) \tag{16}$$

in which $u(\theta, \tau) = \mathbf{D}^T\phi$ is the function to be maximized and λ is a Lagrangian multiplier for the constraint. The extreme condition is

$$0 = \frac{\partial H}{\partial \mathbf{D}} = \phi + 2\lambda\mathbf{W}\mathbf{D}. \tag{17}$$

To express λ in terms of ϕ and κ, the symmetry of $\mathbf{W}$ is first used to transpose the extremum condition

$$\phi^T = -2\lambda\mathbf{D}^T\mathbf{W}. \tag{18}$$

This expression is then post multiplied by $\mathbf{W}^{-1}$ to obtain

Downloaded 03 May 2010 to 171.66.16.247. Redistribution subject to ASME license or copyright; see http://www.asme.org/terms/Terms_Use.cfm

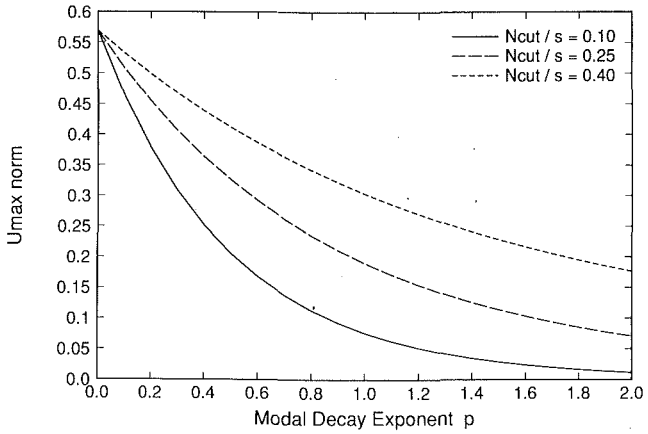


Fig. 5 Normalized maximum buckling response $\hat{u}_{max}$ for bounded imperfections

$$\phi^T \mathbf{W}^{-1} = -2\lambda \mathbf{D}^T. \tag{19}$$

Each side of this equation is post multiplied by the corresponding sides of the untransposed extremum condition (17) to give

$$\phi^T \mathbf{W}^{-1} \phi = 4\lambda^2 \mathbf{D}^T \mathbf{W} \mathbf{D} = 4\lambda^2 \kappa^2. \tag{20}$$

The desired expression for the Lagrange multiplier is then

$$\lambda = \pm \frac{1}{2\kappa} \sqrt{\phi^T \mathbf{W}^{-1} \phi}. \tag{21}$$

The extremum condition is now premultiplied by $\mathbf{D}^T$ to obtain

$$\mathbf{D}^T \phi = -2\lambda \mathbf{D}^T \mathbf{W} \mathbf{D} = \mp \kappa \sqrt{\phi^T \mathbf{W}^{-1} \phi} \tag{22}$$

and hence

$$u_{max}(\theta, \tau) = \kappa \sqrt{\phi(\theta, \tau)^T \mathbf{W}^{-1} \phi(\theta, \tau)} \tag{23}$$

in which the signs have been dropped. The imperfection that gives this maximum response, from (17) and (21), is

$$\mathbf{D}_{mr} = \frac{\kappa \mathbf{W}^{-1} \phi}{[\phi^T \mathbf{W}^{-1} \phi]^{1/2}}. \tag{24}$$

With $\mathbf{W}$ from (13), the maximum response from (23) in expanded form is then

$$u_{max}(\theta, \tau) = \kappa \left\{ \sum_{n=2}^{N} [f_p^2(n) G_n^2(\tau) \cos^2 n\theta + f_p^2(n) G_n^2(\tau) \sin^2 n\theta] \right\}^{1/2}$$
$$= \kappa \left\{ \sum_{n=2}^{N} f_n^2(n) G_n^2(\tau) \right\}^{1/2}. \tag{25}$$

Observe that u_{max} depends only on τ, which reflects the symmetry of the impulsive loading.

4.2 Numerical Results. Numerical evaluation of (25) is most usefully done in a normalized form that allows use of a single set of calculations for a range of values of s and τ. Observe first that for $s \gg 1$, typical of pulse buckling, the sum in (25) can be replaced by an integral in normalized mode number form:

$$u_{max} = \kappa s^{1/2} \left[\int_0^{\eta_m} f_p^2(\eta) G^2(\eta, \tau) d\eta \right]^{1/2} \tag{26}$$

where $\eta = n/s$, $\eta_m = N/s$, $d\eta = \Delta n/s = 1/s$, $G_n(\tau)$ has been denoted by $G(\eta, \tau)$, and similarly for $f_p(n)$. This emphasizes that s is the scale factor for n. Because the shape of the normalized amplification function $G(\eta,\tau)/G_{max}(\tau)$ does not change markedly with τ for time $\tau \geq 6$ of significant amplification (see Fig. 1), a useful normalized maximum response is

Table 1 Normalized maximum buckling response $\hat{u}_{max}$ for bounded imperfections (calculated with $s = 20$, $\tau = 8$, and $N = 50$, but very nearly independent of these values for $s \gg 1$ and $\tau > 5$ with $N > 2s$)

	$\hat{u}_{max}$		
p	$n_c/s = 0.10$	$n_c/s = 0.25$	$n_c/s = 0.40$
0.00	0.56910	0.56910	0.56910
0.10	0.46377	0.50827	0.53269
0.20	0.37819	0.45425	0.49893
0.30	0:30862	0.40625	0.46761
0.40	0.25203	0.36359	0.43857
0.50	0.20598	0.32565	0.41162
0.60	0.16848	0.29191	0.38661
0.70	0.13792	0.26188	0.36339
0.80	0.11301	0.23515	0.34184
0.90	0.09269	0.21134	0.32182
1.00	0.07610	0.19013	0.30323
1.10	0.06254	0.17122	0.28597
1.20	0.05147	0.15437	0.26992
1.30	0.04241	0.13933	0.25502
1.40	0.03499	0.12592	0.24116
1.50	0.02892	0.11394	0.22828
1.60	0.02394	0.10325	0.21631
1.70	0.01986	0.09370	0.20518
1.80	0.01651	0.08517	0.19483
1.90	0.01376	0.07755	0.18521
2.00	0.01150	0.07074	0.17626

$$\hat{u}_{max} = \frac{u_{max}}{\kappa s^{1/2} G_{max}(\tau)} = \frac{1}{G_{max}(\tau)} \left[\int_0^{\eta_m} f_p^2(\eta) G^2(\eta,\tau) d\eta \right]^{1/2}. \tag{27}$$

The integral in (27) was evaluated by means of the sum in (25), with $s = 20$, $\tau = 8$ and $N = 50$. The results, in normalized form for p ranging from 0 to 2 with $n_c = 2$, 5 and 8, are given in Table 1. In Lindberg (1988) it is shown that for $p = 0$, the expression for $\hat{u}_{max}$ ranges only from 0.64 to 0.52 for τ ranging from 5 to 11. Thus, to this accuracy the results in Table 1 can be used for any values of $s \gg 1$ and $\tau > 5$. The data in Table 1 are given in graphical form in Fig. 5. In the present work, N was changed from 50 to 80 with essentially no change in these curves.

4.3 Use of the Maximum Response Bounds. To use the results in Table 1 and Fig. 5 one must know or have some estimate of κ. This is analogous to knowing the standard deviation magnitudes in probabilistic analyses. The most straightforward use is to assume that one will measure κ for every shell to be used, i.e., the convex model solution is viewed as a method for quality control. However, one could argue that if the Fourier coefficients a_n and b_n have been measured, one could use them to calculate the actual response rather than a bound.

Calculating response obviously requires more effort than using a bound that is calculated once and for all for a given structure and loading. Nevertheless, for the linear systems required for this convex model, even if the problem is complex enough to require finite element methods, the primary requirement for calculating actual response is simply storage of the modal response functions for use with a_n and b_n. This tradeoff between complexity in calculating actual response and conservatism is using the bounding response is a matter to be

Downloaded 03 May 2010 to 171.66.16.247. Redistribution subject to ASME license or copyright; see http://www.asme.org/terms/Terms_Use.cfm

settled by those responsible for quality control. Later in the paper, maximum response estimates are given based on measurement of only the uniform bounds on imperfections in each production shell, with knowledge of n_c and p established by more extensive measurement interpretation on shells from the same manufacturing process.

Here it is assumed that a_n and b_n will be measured for every shell. This allows specific discussion of the use of the results from (27) and comparison in the next section with solutions from probabilistic models. The most conservative procedure is to assume no knowledge of the systematic variation of a_n and b_n with n, i.e., no knowledge of $f_p(n)$. In this case, $\mathbf{W}$ is taken as the identity matrix $\mathbf{I}$ and the measure κ of the imperfection bound is simply

$$\kappa_b = [\mathbf{D}^T\mathbf{I}\mathbf{D}]^{1/2} = \left[\sum_{n=N_1}^{n=N_2} (a_n^2 + b_n^2)\right]^{1/2} \tag{28}$$

where the subscript b denotes "band," and is associated with the limits N_1 and N_2 used in forming the sum. These limits are chosen to encompass the range of most amplified modes in Fig. 1. Values of κ_b are used with the convex model bound for $p=0$ in Table 1, namely $\hat{u}_{\max}=0.5691$, i.e., no systematic dependence of a_n and b_n on n.

If one has knowledge of $f_p(n)$, then less conservative bounds can be used. Each coefficient a_n and b_n is then multiplied by $f_p^{-1}(n)$ in accordance with calculating κ with matrix $\mathbf{W}$:

$$\kappa_{bf} = [\mathbf{D}^T\mathbf{W}\mathbf{D}]^{1/2} = \left[\sum_{n=N_1}^{n=N_2} f_p^{-2}(n)\,(a_n^2 + b_n^2)\right]^{1/2} \tag{29}$$

in which f is added to the subscript to denote the use of $f_p(n)$ in calculation. Values of κ_{bf} can be substantially larger than κ_b and are used with the convex model bounds in Table 1 and Fig. 5 evaluated with the corresponding value of p and n_c in $f_p(n)$.

Bounds calculated with κ_{bf} need not be firm bounds because of the $f_p(n)$ constraint on a_n and b_n. That is, the larger κ_{bf} compared with κ_b is compensated by the reduced value of the normalized bound $\hat{u}_{\max}$, but there is no assurance that for a particular shell a_n and b_n near the most amplified mode will not be larger than imposed by the constraint. By contrast, when κ and the associated bound are calculated with the identity matrix $\mathbf{I}$, the imperfection vector $\mathbf{D}$ is free in the convex model maximization to take on the value that gives the absolute maximum possible response.

Values of p and n_c to be used in (27) and (29) can be determined from log-log plots of c_n versus n. Conservatively shallow slopes (small p) can be selected to envelope the data so that use of κ_{bf} gives a firm bound. It is expected that p and n_c depend on manufacturing processes and hence need not to be determined for every shell from a given process.

5 Comparisons With Probabilistic Solutions

The conservatism of using $\hat{u}_{\max}$ from Table 1 and Fig. 5 in reliability analyses was tested by comparisons with maximum responses calculated for imperfections generated with random Fourier coefficients. Monte Carlo calculations were made with uncorrelated a_n and b_n having a Gaussian distribution with zero mean value and standard deviation equal to $f_p(n)$. As in the convex model calculations, shell buckling parameters $s=20$ and $\tau=8$ were used. All of the calculations were made with $n_c=5$ and $N=50$. For each set of 98 random coefficients, the buckle shape was calculated with (2) and the absolute maximum buckle peak recorded in dimensionless forms analogous to that in (27). Approximate probability density functions were prepared with results from 1000 such calculations with $p=1$ and 1000 calculations with $p=2$.

Table 2 Comparison of buckle peak amplitude $\hat{u}_{\text{peak}}$ from the probabilistic model and bound $\hat{u}_{\max}$ from the convex model

Ellipse Matrix	n Band for κ	Mean $\bar{x}$	Dev. σ_x	99.5% $\bar{x}+3\sigma_x$	Convex Bound	Bound/ $\bar{x}+3\sigma_x$
Imperfection type: $p=1$, $n_c/s=0.25$						
$\boldsymbol{I}$	2 to 50	0.1262	0.0253	0.2020	0.5691	2.817
$\boldsymbol{I}$	5 to 23	0.1692	0.0349	0.2738	0.5691	2.078
$\boldsymbol{I}$	8 to 23	0.2358	0.0385	0.3513	0.5691	1.620
$\boldsymbol{W}_1$	5 to 23	0.0801	0.0116	0.1150	0.1901	1.653
$\boldsymbol{W}_1$	8 to 23	0.0875	0.0121	0.1239	0.1901	1.534
Imperfection Type: $p=2$, $n_c/s=0.25$						
$\boldsymbol{I}$	2 to 50	0.0607	0.0160	0.1087	0.5691	5.237
$\boldsymbol{I}$	5 to 23	0.0960	0.0268	0.1763	0.5691	3.228
$\boldsymbol{I}$	8 to 23	0.2021	0.0427	0.3302	0.5691	1.724
$\boldsymbol{W}_2$	5 to 23	0.0304	0.0042	0.0430	0.0704	1.645
$\boldsymbol{W}_2$	8 to 23	0.0332	0.0047	0.0473	0.0704	1.496

Comparisons with the convex model results were made under the assumption that $\hat{u}_{\max}$ is to be used to maintain quality control as described in the preceding section. Thus, for each shell in the Monte Carlo calculations, κ was calculated with (28) or (29) to give normalized $\hat{u}_{\text{peak}}$ values analogous to $\hat{u}_{\max}$ in (27). The normalized buckle peak amplitude with no assumed dependence on a_n and b_n on n is

$$\hat{u}_{\text{peak}-b} = \frac{u_{\text{peak}}}{\kappa_b s^{1/2} G_{\max}(\tau)} \tag{30}$$

The normalized peak response when $f_p(n)$ is taken to be known is

$$\hat{u}_{\text{peak}-bf} = \frac{u_{\text{peak}}}{\kappa_{bf} s^{1/2} G_{\max}(\tau)}. \tag{31}$$

Probability density functions for these normalized peak values are given in Figs. 6 and 7 for the Monte Carlo calculations with $p=1$, and in Figs. 8 and 9 for $p=2$. Statistics from these same data are given in Table 2, where mean value is denoted by $\bar{x}$ and standard deviation is denoted by σ_x. To a suitable approximation for the purpose here, the values tabulated for $\bar{x}+3\sigma_x$ correspond to reliabilities of 99.5 percent, i.e., about 99.5 percent of the calculated maximum normalized peak responses are less than this value for each distribution. No attempt was made to refine these values because considerably more than 1000 calculations would be required for accurate values at this reliability. The 3-sigma response measure was chosen somewhat arbitrarily. Readers can use Figs. 6 through 9 to extend the corresponding entries in Table 2 to lower reliabilities.

In Table 2, five methods of using the convex model bounding responses are evaluated for each of the two imperfection populations. The most straightforward, and conservative, comparison is made by using $\mathbf{I}$ to calculate κ_b with all of the modes from $n=2$ to 50 that were used in the buckling response calculation. As can be anticipated from Fig. 2, this results in a conservatively large value of κ_b because a_n and b_n for low-mode numbers are large compared with values in the range n of most amplified modes that dominate buckling, and a_n and b_n for $n>23$ are included in the sum even though from Fig. 1 they have virtually no influence on buckling response.

Downloaded 03 May 2010 to 171.66.16.247. Redistribution subject to ASME license or copyright; see http://www.asme.org/terms/Terms_Use.cfm

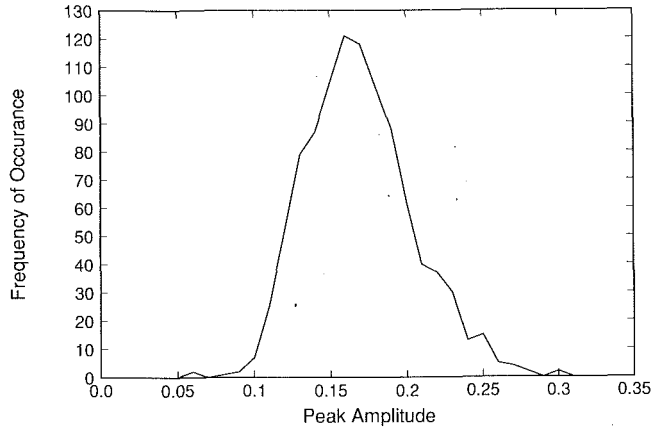


Fig. 6 Probability density of buckle peaks $\hat{u}_{peak\text{-}b}$ for $p=1$ hypothetical imperfections normalized with Fourier coefficient band $5 \le n \le 23$

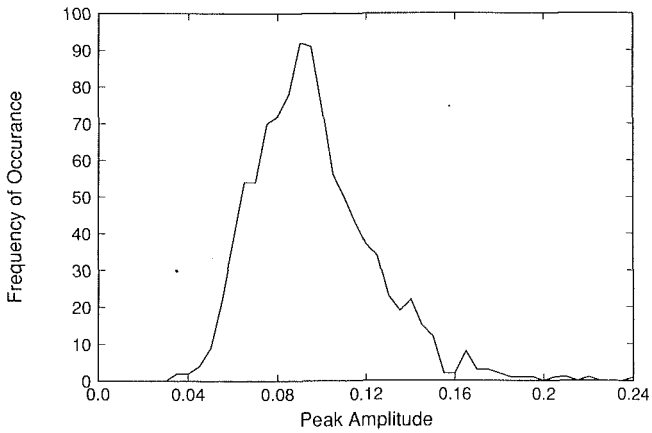


Fig. 8 Probability density of buckle peaks $\hat{u}_{peak\text{-}b}$ for $p=2$ hypothetical imperfections normalized with Fourier coefficient band $5 \le n \le 23$

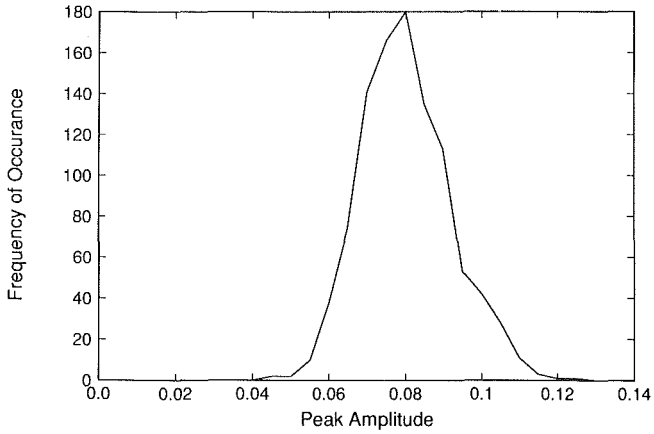


Fig. 7 Probability density of buckle peaks $\hat{u}_{peak\text{-}bf}$ for $p=1$ hypothetical imperfections normalized with Fourier coefficient band $5 \le n \le 23$

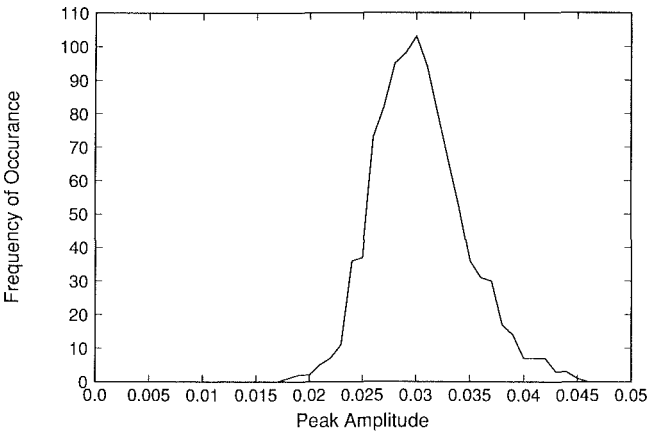


Fig. 9 Probability density of buckle peaks $\hat{u}_{peak\text{-}bf}$ for $p=2$ hypothetical imperfections normalized with Fourier coefficient band $5 \le n \le 23$

The value κ_b for each shell in the Monte Carlo calculations was used to normalize its buckle peak as indicated in (30). The normalized buckle peaks are therefore consistent with the maximum response from the convex model with the same normalization. The entries for the convex bound are taken from Table 1 for appropriate values of p and n_c. The first entry in the last column of Table 2 is a ratio 2.817 of the convex bound to the buckle peak at a 99.5 percent reliability for the $p=1$ population. The corresponding ratio for the $p=2$ population is 5.237, which is larger than for $p=1$ because of the very small values of a_n and b_n in the amplified range compared with values at low-mode numbers. These large ratios of conservatism are unacceptable, which motivated evaluation of other measures for κ.

With essentially no loss in firmness of the bound, the ratios can be reduced by using the same formula (30) to calculate κ_b but with the band for n narrowed to $5 \le n \le 23$, which from Fig. 1 includes all modes with significant amplification. From Table 2 the resulting conservatism ratios are reduced to 2.078 and 3.228, respectively. The ratios are further reduced to 1.620 and 1.724 by narrowing the mode band to $8 \le n \le 23$, but with some loss in firmness of the bound because the additional neglected low modes have small but nevertheless finite amplification.

When knowledge of the systematic variation of a_n and b_n with n is used by calculating κ_{bf} with (31), the conservatism ratios are 1.653 for $p=1$ and 1.645 for $p=2$ even with all the amplified modes $5 \le n \le 23$ included. Because this use of $f_p(n)$ takes account of the much smaller a_n and b_n for large n, further narrowing of the calculation band to $8 \le n \le 23$ reduces these ratios only to 1.534 and 1.496, respectively.

Thus, by taking full advantage of measured Fourier transforms of the imperfections, the convex model gives response bounds that are only factor of about 1.6 conservative compared with probabilistic response at a reliability of about 99.5 percent. However, from the probability densities in Figs. 7 and 9 it is apparent that even these bounds can be several times the amplitude of the buckle peak calculated for a particular shell. It is for such shells that one must consider the tradeoff between the analytical complexity of calculating the actual response for every shell against the conservatism of using the bounding response from the convex model.

6 Combined Uniform and Fourier Ellipsoid Bound

Results in the preceding sections demonstrate that use of a convex model with an ellipsoid bound on the imperfection Fourier coefficients gives maximum response estimates superior to those from the uniform bound convex model developed in Lindberg (1992), because the ellipsoid bound uses (and requires) more knowledge of the imperfection characteristics. Conservatism factors compared with 3-sigma probabilistic estimates are for 1.6 for the Fourier bound compared with 2.0 for a uniform bound on filtered imperfections. However, in Lindberg (1992) it was also shown that the conservatism of the uniform bound results can be further reduced to a factor

Downloaded 03 May 2010 to 171.66.16.247. Redistribution subject to ASME license or copyright; see http://www.asme.org/terms/Terms_Use.cfm

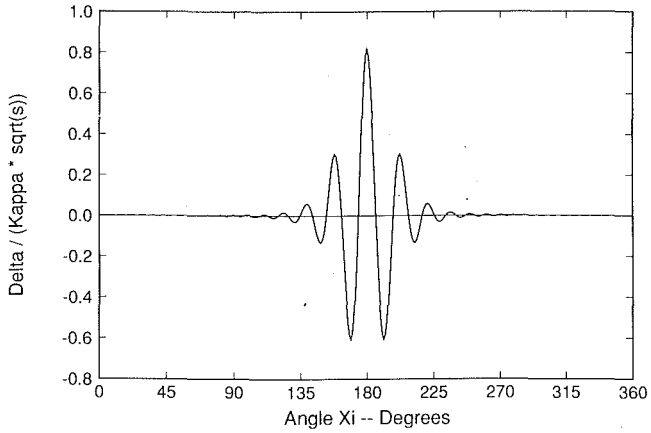


Fig. 10 Worst-case imperfection shape for $p=0$ with $s=20$

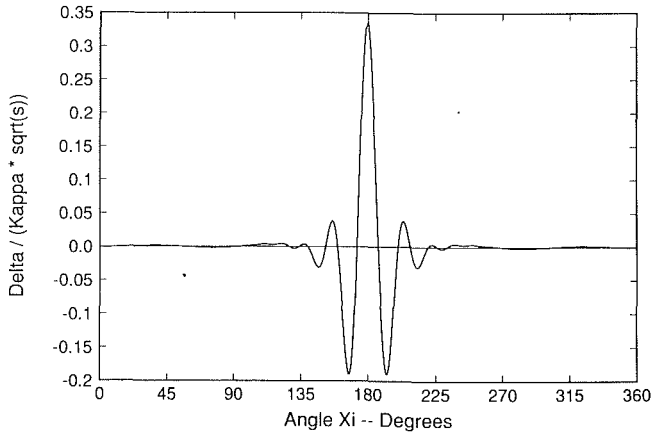


Fig. 11 Worst-case imperfection shape for $p=1$ with $s=20$

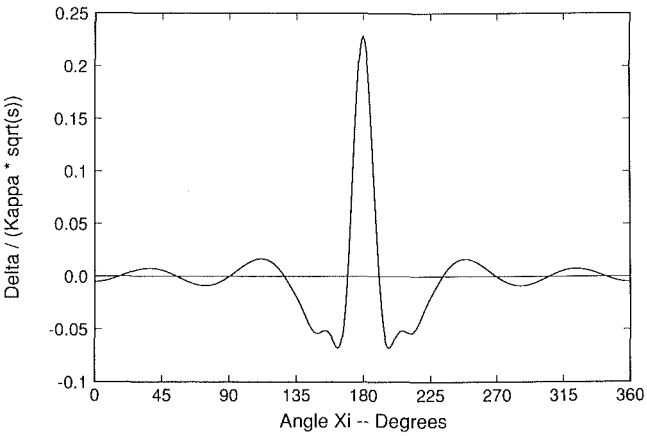


Fig. 12 Worst-case imperfection shape for $p=2$ with $s=20$

1.3 by the ad hoc but reasonable replacement of the worst-case, rectangular-wave imperfection from that model by a smooth function with the same $\pm\hat{\delta}$ amplitude and the same zeros. However, this still requires costly filtering of the imperfections before measurement of the imperfection uniform bound.

An even greater reduction in conservatism is made here by combining ideas from the uniform and ellipsoid bound models. Furthermore, these ideas lead to shell inspection methods that require determination of Fourier transforms only to establish the characteristics of shells produced by a particular manufacturing process, as described in the preceding sections. This information is then used with simple inspection of each production shell to measure a uniform bound $\hat{\delta}$ on its imperfections (defined as half the difference between the maximum and minimum readings of a displacement probe as the shell in turned through one revolution). No further manipulation of the probe data is required to estimate the maximum possible buckling response.

Begin by observing the shapes of the worst-case imperfections defined by the Fourier coefficients in Eq. (24). The imperfection shape (function of ξ at fixed θ and τ for which response is maximized) is

$$\phi(\xi;\,\theta,\,\tau)=\mathbf{D}_{\mathrm{mr}}^{T}\varphi(\xi)=\frac{\kappa\phi^{T}(\theta,\,\tau)\mathbf{W}^{-1}\varphi(\xi)}{[\phi^{T}(\theta,\,\tau)\mathbf{W}^{-1}\phi(\theta,\,\tau)]^{1/2}}. \tag{32}$$

In expanded form this becomes

$$\delta(\xi;\,\theta,\,\tau)=\frac{\kappa\sum_{n=2}^{N}f_p^2(n)G_n(\tau)\cos n(\xi-\theta)}{\left[\sum_{n=2}^{N}f_p^2(n)G_n^2(\tau)\right]^{1/2}} \tag{33}$$

As in the definition of $\hat{u}_{\max}$, it is useful to express this function in the following analogous normalized form:

$$\frac{\delta(\xi;\,\theta,\,\tau)}{\kappa s^{1/2}}=\frac{\int_0^{\eta m}f_p^2(\eta)G(\eta,\,\tau)\cos s\eta(\xi-\theta)d\eta}{\left[\int_0^{\eta m}f_p^2(\eta)G^2(\eta,\,\tau)d\eta\right]^{1/2}}. \tag{34}$$

Figure 10 is a plot of (34)[1] for $\theta=180$ deg with $p=0$, that is, for $\mathbf{W}=\mathbf{I}$. This is the same shape as the function $S(\xi)$ found for the uniform bound model developed in Lindberg (1991). In that paper it is shown that the maximum response when only $\hat{\delta}$ is known is obtained for a worst-case imperfection shape that is a series of rectangles of amplitude $\pm\hat{\delta}$ with the same signs and zeros as S. Thus, imposition of a spheroid bound changes the worst-case imperfection shape from these rectangles to a smooth function with the shape of S. This is reminiscent of the ad hoc replacement that was proposed in Lindberg (1991) to obtain a less diabolical worst-case imperfection shape. The difference here is that the imperfection in Fig. 10 has the varying amplitude shown and is associated with a fixed spheroid size κ, while the worst-case imperfection for a uniform bound has a fixed amplitude $\pm\hat{\delta}$.

Figures 11 and 12 are plots of the worst-case imperfections for $p=1$ and $p=2$, respectively. They show that with increasing p the normalized amplitudes decrease and the wavelengths increase. The central maximum also becomes larger compared with the negative peaks. These changes reflect the increasing relative amplitudes of low-order modes in the imperfection characteristics as p is increased.

These worst-case imperfection shapes can be used to obtain an estimate for κ by setting the maximum imperfection equal to the imperfection peak $\hat{\delta}$ measured by the procedure described above. The maximum occurs at $\xi=\theta$ and the resulting expression for κ is

$$\kappa=\hat{\delta}\frac{\left[\int_0^{\eta\max}f_p^2(\eta)G^2(\eta,\,\tau)d\eta\right]^{1/2}}{\int_0^{\eta m}f_p^2(\eta)G(\eta,\,\tau)d\eta} \tag{35}$$

Substitution of this value into the maximum response formula (25) gives finally

[1] As for the other results in this paper, the integrals were found with finite sums for $s=20$, $N=50$ and $\tau=8$, but the results are essentially the same for any $s\gg1$ and $\tau>6$. It is clear that s affects only the wavelength scale of (34).

Downloaded 03 May 2010 to 171.66.16.247. Redistribution subject to ASME license or copyright; see http://www.asme.org/terms/Terms_Use.cfm

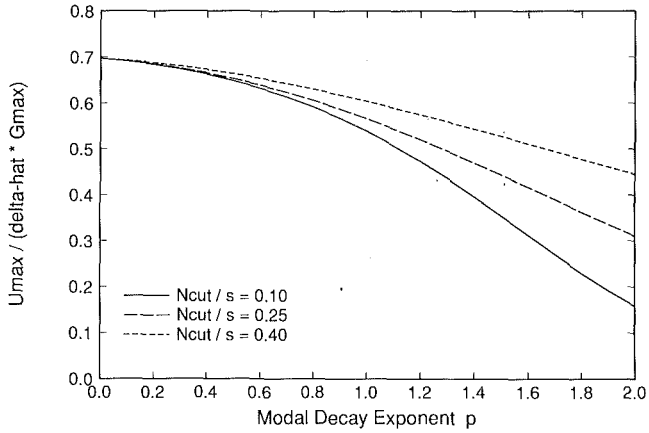


Fig. 13 Normalized ratio-of-peaks $\tilde{u}_{max}$ for known Fourier coefficient ellipsoid bound shapes and measured $\hat{\delta}$

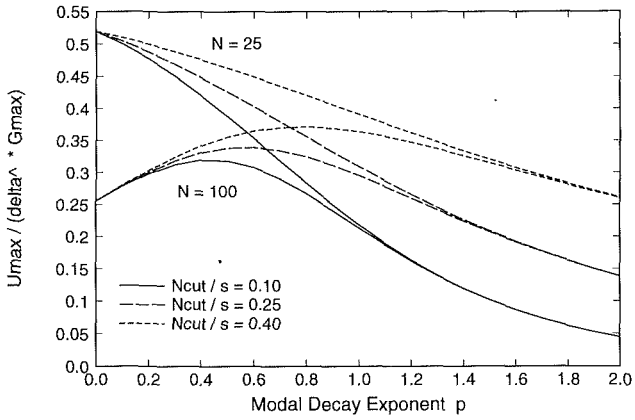


Fig. 14 Normalized ratio-of-peaks $\breve{u}_{max}$ from the Ben-Haim ellipsoidal model

$$\tilde{u}_{\max} \equiv \frac{u_{\max}}{\hat{\delta} G_{\max}} = \frac{\int_0^{\eta_{\max}} f_p^2(\eta) G^2(\eta, \tau) d\eta}{G_{\max} \int_0^{\eta_m} f_p^2(\eta) G(\eta, \tau) d\eta}. \tag{36}$$

A plot of this normalized maximum response (ratio of the peak response to the peak imperfection) as a function of p for three values of n_c/s is given in Fig. 13. Observe first that at $p=0$, $\tilde{u}_{\max}=0.70$, which is smaller than the value $\tilde{u}_{\max}=1$ that would result if the imperfection were a simple sine wave with amplitude $\pm\hat{\delta}$ in the most amplified mode. Such an imperfection is on the spheroid bound by simply taking $c_m=\kappa=\hat{\delta}$, and $a_n=b_n=0$ for all the other modes, where m is the mode number of the most amplified mode. Thus, using the spheroid bound model to find the worst-case imperfection shape and then specifying that the imperfection amplitude with this shape is equal to a measured bound reduces the resulting response compared with response when one knows only κ. This is because the worst-case imperfection given only κ has no restriction on its amplitude; it must merely have Fourier coefficients on the sphere of radius κ.

One further consideration is that $\hat{\delta}$ is based on measurement of peak-to-peak imperfections whereas (36) uses the one-way peak of the worst-case imperfection. This is a reasonable procedure because it has been assumed that $s \gg 1$, so the worst case imperfection shape has significant amplitude only local to θ for which response is maximized, as shown in the examples in Figs. 10 through 12 for $s=20$. In a typical imperfect shell it is very likely that the peak imperfection of opposite sign will occur some distance from θ with about the same magnitude, so using half the magnitude of the two peaks is reasonable (this can be confirmed during the $\hat{\delta}$ measurement). If instead of (36) one uses the peak-to-peak value of the worst-case shapes in Fig. 10 as the more strictly comparable measure, $\tilde{u}_{max}$ increases from 0.70 to 0.81 for $p=0$. Similarly, by using peak-to-peak amplitudes from Figs. 11 and 12, values on the $n_c/s=0.25$ curve in Fig. 13 would increase from 0.57 to 0.72 for $p=1$ and from 0.31 to 0.46 for $p=2$.

Use of such increased values is unnecessarily conservative. In fact, Ben-Haim (personal communication, May 1991; the combined model above is also based on his idea of using $\hat{\delta}$ as a measure for κ) suggests imposition of the $\hat{\delta}$ knowledge of the imperfections *prior* to the response maximization, which results in maximum responses smaller than in Fig. 13. He considers the set of all imperfections within an ellipsoid bound such that $\hat{\delta}$ is simply not exceeded, rather than imposing the condition that the worst-case imperfection have magnitude $\hat{\delta}$. Thus, with the same procedure used to deduce (25), he finds the maximum of $\mathbf{D}^T\varphi(\theta)$ with $\mathbf{D}$ in the ellipsoidal set and equates it $\hat{\delta}$ to determine κ:

$$\kappa = \hat{\delta}[\varphi^T(\theta)\mathbf{W}^{-1}\varphi(\theta)]^{-1/2}. \tag{37}$$

With (25) and κ from (37), the normalized ratio-of-peaks from this model is

$$\breve{u}_{\max} \equiv \left[\frac{\int_0^{\eta_m} f_p^2(\eta) G^2(\eta, \tau) d\eta}{\int_0^{\eta_m} f_p^2(\eta) d\eta} \right]^{1/2}. \tag{38}$$

Results from this model are given in Figure 14. Values of $\breve{u}_{\max}$ are roughly half those of $\tilde{u}_{\max}$ in Fig. 13. However, it is apparent that the results depend on the number of modes N included in the model, whereas the results in Fig. 13 were found to be virtually independent of N for $N>1.5s$. The dependence occurs because the sum in (37) to find κ, given $\hat{\delta}$ and the shape of the ellipsoid, does not include G in its terms, so for small p the corresponding integral in the denominator of (38) increases with increasing N. Thus, while knowledge of the response is not explicitly used in (37), in applying the ratio-of-peaks formula (38) one must have knowledge of the modes of concern when specifying N. As in the preceding section, use of $N=25$ for $s=20$ includes the amplified modes without unduly limiting the amplitudes of the imperfection coefficients from (37). This writer feels that use of the results in Fig. 13 is more straightforward and more reasonably conservative.

The results in both figures can be compared with the ratio-of-peaks found in Lindberg (1991) for a probabilistic model applied at $p=1$ and $p=2$ with $n_c/s=0.25$. From Table 2 in that paper (which uses $\tau=6$, but normalized results are essentially the same as for $\tau=8$), the normalized ratio-of-peaks at 3-sigma responses (a probability of about 99.5 percent) is $(u/\hat{\delta})/G_{\max}=12.027/23.0=0.52$ for $p=1$ and $6.631/23=0.29$ for $p=2$. These are to be compared with values from Fig. 13 of 0.57 and 0.31. In both cases the ratio-of-peaks from the present convex model are about 1.1 times the corresponding probabilistic results for 3-sigma response. If one accepts the Ben-Haim model, results from Fig. 14 reduce this factor to about 0.5, a marked *reduction* compared with the conservatism of the 3-sigma probabilistic result.

7 Conclusions

Application of a convex model based on Fourier coefficients of shell imperfections allows full use of measured coefficients in calculating bounding maximum responses. The convex model solution is more easily evaluated numerically than a Monte

Downloaded 03 May 2010 to 171.66.16.247. Redistribution subject to ASME license or copyright; see http://www.asme.org/terms/Terms_Use.cfm

Carlo method with a probabilistic model, and gives bounding responses that are not overly conservative. At very high reliabilities the bounding responses are more realistic than probabilistic responses.

A convex model based on combined use of uniform and Fourier ellipsoid bounds gives even better (lower) estimates of maximum response, with a simpler method for quality control. One determined the shape of the ellipsoid by complete finite Fourier transform interpretation of measurements on representative shells from a particular manufacturing process, and then for quality control records only the uniform bound on each production shell as a measure of the size of its ellipsoid.

8 References

Abrahamson, G. R., and Goodier, J. N., 1962, "Dynamic Plastic Flow Buckling of a Cylindrical Shell from Uniform Radial Impulse," *Proceedings of Fourth U.S. National Congress of Applied Mechanics*, Berkeley, CA, pp. 939–950.

Arbocz, J., 1982, "The Imperfection Data Bank: A Means to Obtain Realistic Buckling Loads," *Buckling of Shells: Proceedings of a State-of-the-Art Colloquium*, New York.

Ben-Haim, Y., and Elishakoff, I., 1989, "Dynamics and Failure of Structures Based on the Unknown-but-Bounded Imperfection Model," *Recent Advances in Impact Dynamics of Engineering Structures—1989*, AMD-Vol. 105, AD-Vol. 17, ASME, New York, pp. 89–95.

Ben-Haim, Y., and Elishakoff, I., 1990, *Convex Models of Uncertainty in Applied Mechanics*, Elsevier, New York.

Elishakoff, I., 1978a, "Axial Impact Buckling of a Column With Random Initial Imperfections," ASME JOURNAL OF APPLIED MECHANICS, Vol. 45, pp. 361–365.

Elishakoff, I., 1978b, "Impact Buckling of a Thin Bar Via Monte Carlo Method," ASME JOURNAL OF APPLIED MECHANICS, Vol. 45, pp. 586–590.

Kirkpatrick, S. W., and Holmes, B. S., 1989, "Effect of Initial Imperfections on Dynamic Buckling of Shells," *ASCE Journal of Engineering Mechanics*, Vol. 115, No. 5, pp. 1075–1093.

Kirkpatrick, S. W., and Holmes, B. S., 1991, "Static and Dynamic Buckling of Thin Cylindrical Shells," *Computational Aspects of Contact, Impact and Penetration*, R. F. Kulak and L. E Schwer, eds., Elmepress International, Annandale, VA.

Lindberg, H. E., 1965, "Impact Buckling of a Thin Bar," ASME JOURNAL OF APPLIED MECHANICS, Vol. 32, pp. 315–322.

Lindberg, H. E., and Florence, A. L., 1987, *Dynamic Pulse Buckling*, Martinus Nijhoff Publishers, Dordrecht, The Netherlands; Kluwer, Hingham, MA.

Lindberg, H. E., 1988, "Random Imperfections for Dynamic Pulse Buckling," *ASCE Journal of Engineering Mechanics*, Vol. 114, pp. 1144–1165.

Lindberg, H. E., 1992, "An Evaluation of Convex Modelling for Multimode Dynamic Buckling," ASME JOURNAL OF APPLIED MECHANICS, Vol. 59, pp. 929–936.

Downloaded 03 May 2010 to 171.66.16.247. Redistribution subject to ASME license or copyright; see http://www.asme.org/terms/Terms_Use.cfm

Liapunov Stability Analysis of Elastic Shaft-Rigid Disk-Bearing Systems

H.-Y. Huang
Graduate Student.

A. L. Schlack, Jr.
Professor.

Department of Engineering Mechanics,
University of Wisconsin-Madison,
Madison, WI 53706

A general method of analysis based on Liapunov's direct method is presented for studying the dynamic stability of elastic shaft-rigid disk-bearing systems. A model comprised of a rigid disk rigidly attached at an arbitrary location along a flexible, rotating shaft which is mounted on two eight-component end bearings is used to develop stability criteria involving system stiffness and damping parameters. It is quantitatively shown by means of graphs for typical cases how the instability regions are reduced by (a) *increasing the shaft dimensionless stiffness parameters,* (b) *increasing the bearing direct stiffness and damping parameters,* (c) *decreasing the bearing cross-coupling stiffness and damping parameters,* (d) *decreasing the mass ratio of the disk, and* (e) *increasing the disk's radius ratio. These graphs present typical examples of the types of design information available to engineers through the equations provided in this paper. These graphs also verify that a two-modal term* (N = 2) *expansion is normally adequate to model the system deformations since the curves are not significantly altered by adding another term* (N = 3) *to the expansion. The critical value of the shaft dimensionless stiffness parameters is also studied.*

Introduction

Most research papers on the dynamics and stability of rotating flexible shaft-appendage systems, such as Chivens and Nelson (1975), Klompas (1974), Kuo (1975), Masoom (1980), and Wilgen and Schlack (1977, 1979) either ignore the bearing support flexibility or oversimplify the bearing model. Even modeling the bearing support as a single spring and dashpot is not adequate since in many cases the anisotropy of the bearing supports must also be considered, as demonstrated by such authors as Gunter (1966), Klompas (1974), Moore (1972), Nelson and McVaugh (1976), and Parkinson (1965).

The asymmetric bearing model such as the one used by Vance (1988) is still not a completely satisfactory model, especially for large flexible rotors which are usually supported by journal bearings. The journal bearing actually acts as a nonisotropic spring and dashpot system with cross-coupling between the vertical and horizontal directions. The vast majority of investigations found in the literature neglect the cross-coupling stiffness and damping coefficients of the bearing support to simplify the mathematical model. Among the few authors who used an appropriate bearing support model (i.e., taking into account the anisotropic and cross-coupling coefficients by using an eight-coefficient bearing model) are Adams (1980, 1983), Doyle (1971), Gunter (1966), Rao (1985), Stanway and Burrows (1981), Lalanne and Ferraris (1990), and El-Marhomy and Schlack (1991). However, due to the complexity of the problem when an eight-coefficient bearing model is adopted, these studies do not treat the rotating shaft as a continuous elastic model, except for the last two references cited.

Although Liapunov's direct method is a powerful tool for analyzing stability of linear and nonlinear dynamical systems and has frequently been applied successfully in examining attitude stability of satellites, very few investigations (Grolov and Kantemir (1978), and Wilgen and Schlack (1977, 1978) and El-Marhomy and Schlack (1991)) are found in the literature that adapt this technique to the study of rotor dynamics. Moreover, the first two focus mainly on the effect of appendage flexibility on shaft whirl stability, ignoring completely the flexibility of the two end bearing supports. The third discusses only the elastic shaft without an attached disk on eight-coefficient bearings.

The main objective of this paper is to gain a comprehensive insight into the effects of the various end-support parameters coupled with the shaft flexibility parameters, the disk's mass ratio and its location on the whirling stability of rotor-bearing systems. This is done by modeling the system as a rigid disk rigidly attached at an arbitrary location along a flexible, continuous elastic shaft which is mounted on two dissimilar eight-coefficient bearings. Series expansions are used for describing the elastic shaft deflections. Sufficient conditions for the system's whirl stability based on Liapunov's direct method are presented in graphical form.

Contributed by the Applied Mechanics Division of THE AMERICAN SOCIETY OF MECHANICAL ENGINEERS for publication in the ASME JOURNAL OF APPLIED MECHANICS.

Discussion on this paper should be addressed to the Technical Editor, Prof. Leon M. Keer, The Technological Institute, Northwestern University, Evanston, IL 60208, and will be accepted until four months after final publication of the paper itself in the ASME JOURNAL OF APPLIED MECHANICS.

Manuscript received by the ASME Applied Mechanics Division, Apr. 10, 1991; final revision, Sept. 11, 1991. Associate Technical Editor: A. K. Noor.

Copyright © 1992 by ASME
Downloaded 03 May 2010 to 171.66.16.247. Redistribution subject to ASME license or copyright; see http://www.asme.org/terms/Terms_Use.cfm

Problem Formulation

The model consists of a rigid disk of mass m_D rigidly attached at an arbitrary location d along a rotating elastic shaft of length L and mass m_S which is supported at its ends by two dissimilar eight-coefficient bearings shown schematically in Fig. 1. The shaft is initially straight, balanced, uniform, and with a slenderness ratio sufficiently small that the Euler-Bernoulli theory of bending may be used for small displacements. It is assumed that extensional and torsional deformations are negligible, aerodynamic effects are not included, and that the static deflections are negligible compared to the dynamic effects.

Consider that in the dynamic equilibrium configuration of the rotor-bearing system, the undeformed shaft is along the x direction of a rotating x, y, z coordinate system described by unit vectors $\hat{i}$, $\hat{j}$, $\hat{k}$. Denoting the deflection of the center of the left bearing by $\mathbf{r}_1 = y_1\hat{j} + z_1\hat{k}$ and that of the right bearing by $\mathbf{r}_2 = y_2\hat{j} + z_2\hat{k}$ we can describe the displacement of an arbitrary element of the undeformed shaft axis at a distance x from the left bearing as

$$\mathbf{r}_S(x, t) = y(x, t)\hat{j} + z(x, t)\hat{k} = (y_1 + x\theta)\hat{j} + (z_1 + x\phi)\hat{k}, \quad (1)$$

where for small angles and small displacements, we have approximately

$$\theta = \frac{y_2 - y_1}{L} \text{ and } \phi = \frac{z_2 - z_1}{L}. \quad (2)$$

Also, the displacement of the mass center of rigid disk at a distance d from the left bearing is given by

$$\mathbf{r}_D(d, t) = y(d, t)\hat{j} + z(d, t)\hat{k} = (y_1 + \theta d)\hat{j} + (z_1 + \phi d)\hat{k}. \quad (1')$$

Defining the shaft's angular velocity Ω to be directed along the centerline of the bearings in their deflected positions, we may write the system's angular velocity $\omega = \Omega + \dot{\theta} + \dot{\phi}$ as

$$\omega = (\Omega + \dot{\phi}\theta)\hat{i} + (\theta\Omega - \dot{\phi})\hat{j} + (\phi\Omega + \dot{\theta})\hat{k}. \quad (3)$$

Defining the unit vectors $\mathbf{i}_D$, $\mathbf{j}_D$, $\mathbf{k}_D$ to be aligned with the disk's principal axes x_D, y_D, z_D, we may write the disk's angular velocity as

$$\omega_D = \left[\Omega\left(1 - \frac{\phi_D^2}{2} - \frac{\theta_D^2}{2}\right) + \dot{\theta}(\phi + \phi_D) - \theta_D\dot{\phi} + \dot{\theta}\phi_D\right]\mathbf{i}_D + [-\Omega\theta_D - (\dot{\phi} + \dot{\phi}_D)]\mathbf{j}_D + [-\Omega\phi_D + (\dot{\theta} + \dot{\theta}_D)]\mathbf{k}_D \quad (4)$$

where θ_D and ϕ_D are defined, respectively, as the slopes of the elastic shaft at $x = d$:

$$\theta_D = \left.\frac{\partial v}{\partial x}\right|_d \text{ and } \phi_D = \left.\frac{\partial w}{\partial x}\right|_d.$$

Adopting the assumed mode approach the elastic shaft deflections can be expressed as

$$v(x, t) = \sum_{n=1}^{N} a_n(t)\sin\frac{n\pi x}{L}$$

$$w(x, t) = \sum_{n=1}^{N} b_n(t)\sin\frac{n\pi x}{L} \quad (5)$$

where $a_n(t)$ and $b_n(t)$ are time-dependent generalized coordinates and N denotes the number of terms in the truncated series expansion. Therefore, the position vector $\mathbf{r}_S(x, t)$ of a typical differential element at a distance x along the shaft and the position vector $\mathbf{r}_D(d, t)$ of the mass center of rigid disk are

$$\mathbf{r}_S(x, t) = [y(x, t) + v(x, t)]\hat{j} + [z(x, t) + w(x, t)]\hat{k} \quad (6)$$

$$\mathbf{r}_D(d, t) = [y(d, t) + v(d, y)]\hat{j} + [z(d, t) + w(d, t)]\hat{k} \quad (7)$$

where $y(x, t)$, $z(x, t)$ are the rigid body displacements and $v(x, t)$ and $w(x, t)$ are the elastic displacements of the differential element.

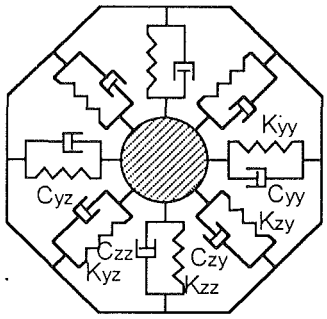


Fig. 1 Eight-coefficient bearing model

Differentiating $\mathbf{r}(x, t)$ with respect to time, the velocity vector of the differential element of shaft ($\dot{\mathbf{r}}_S$) and the velocity vector of the center of the rigid disk ($\dot{\mathbf{r}}_D$) are

$$\dot{\mathbf{r}}_S(x, t) = [(z + w)(-\dot{\phi} + \theta\Omega) - (y + v)(\dot{\theta} + \phi\Omega)]\hat{i} + [(\dot{y} + \dot{v}) - (\Omega + \dot{\phi}\theta)(z + w)]\hat{j} + [(\dot{z} + \dot{w}) + (\Omega + \dot{\phi}\theta)(y + v)]\hat{k} \quad (8)$$

$$\dot{\mathbf{r}}_D(d, t) = [(z + w)(-\dot{\phi} + \theta\Omega) - (y + v)(\dot{\theta} + \phi\Omega)]|_{x=d}\hat{i} + [(\dot{y} + \dot{v}) - (\Omega + \dot{\phi}\theta)(z + w)]|_{x=d}\hat{j} + [(\dot{z} + \dot{w}) + (\Omega + \dot{\phi}\theta)(y + v)]|_{x=d}\hat{k}. \quad (9)$$

The kinetic energy of the shaft (T_S) and rigid disk (T_D), respectively, are

$$T_S = \frac{1}{2}\rho_S\int_0^L \dot{\mathbf{r}}_S \cdot \dot{\mathbf{r}}_S dx = \frac{1}{2}\rho_S\int_0^L \{[(z + w)(-\dot{\phi} + \theta\Omega) - (y + v)(\dot{\theta} + \phi\Omega)]^2 + [(\dot{y} + \dot{v}) - (\Omega + \dot{\phi}\theta)(z + w)]^2 + [(\dot{z} + \dot{w}) + (\Omega + \dot{\phi}\theta)(y + v)]^2\} dx \quad (10)$$

$$T_D = \frac{1}{2}m_D\dot{\mathbf{r}}_D \cdot \dot{\mathbf{r}}_D + \frac{1}{2}\omega_D^T[I_D]_p\omega_D = \frac{1}{2}m_D\{[(z + w) + (-\dot{\phi} + \theta\Omega) - (y + v)(\dot{\theta} + \phi\Omega)]^2 + [(\dot{y} + \dot{v}) - (\Omega + \dot{\phi}\theta)(z + w)]^2 + [(\dot{z} + \dot{w}) + (\Omega + \dot{\phi}\theta)(y + v)]^2\}|_{x=d} + \frac{1}{2}I_D\left[\Omega\left(1 - \frac{\phi_D^2}{2} - \frac{\theta_D^2}{2}\right) + \dot{\theta}(\phi + \phi_D) - \theta_D\dot{\phi} + \dot{\theta}_D\right]^2 + \frac{1}{4}I_D\{[-\theta_D\Omega - (\dot{\phi} + \dot{\phi}_D)]^2 + [\phi_D\Omega + (\dot{\theta} + \dot{\theta}_D)]^2\} \quad (11)$$

where m_D is the mass of the disk, $[I_D]_p$ is the matrix form of the principal moment of inertia of rigid disk along x_D, y_D, z_D axes, ω_D^T is the transpose of vector ω_D, and I_D is the polar moment of inertia about the x_D-axis. The kinetic energy of this system is thus given by

$$T = T_S + T_D. \quad (12)$$

Note that in general, the kinetic energy T can be rewritten as $T = T_2 + T_1 + T_0$ where the subscript refers to the algebraic degree in the generalized velocity variables.

The strain energy expression for the bearing system under consideration is

$$V_b = \frac{1}{2}\sum_i\sum_j k_{ij}q_iq_j = \frac{1}{2}(k_{y_1y_1}y_1^2 + k_{y_1z_1}y_1z_1 + k_{z_1y_1}z_1y_1 + k_{z_1z_1}z_1^2 + k_{y_2y_2}y_2^2 + k_{y_2z_2}y_2z_2 + k_{z_2z_2}z_2^2 + k_{z_2y_2}z_2y_2) \quad (13)$$

Downloaded 03 May 2010 to 171.66.16.247. Redistribution subject to ASME license or copyright; see http://www.asme.org/terms/Terms_Use.cfm

where the subscript 1 refers to the left bearing and 2 to the right bearing. The strain energy expression for the shaft is

$$V_S=\frac{1}{2}EI_S\int_0^L\left[\left(\frac{\partial^2 v(x,t)}{\partial x^2}\right)^2+\left(\frac{\partial^2 w(x,t)}{\partial x^2}\right)^2\right]dx. \quad (14)$$

The strain energy of the system is thus given by

$$V=V_b+V_S. \quad (15)$$

The energy dissipation function of the system is

$$D=\frac{1}{2}\sum_i\sum_j C_{ij}\dot{q}_i\dot{q}_j=\frac{1}{2}(C_{y_1y_1}\dot{y}_1^2+C_{y_1z_1}\dot{y}_1\dot{z}_1+C_{z_1z_1}\dot{z}_1^2$$

$$+C_{z_1y_1}\dot{z}_1\dot{y}_1+C_{y_2y_2}\dot{y}_2^2+C_{y_2z_2}\dot{y}_2\dot{z}_2+C_{z_2z_2}\dot{z}_2^2+C_{z_2y_2}\dot{z}_2\dot{y}_2). \quad (16)$$

The state of motion of the mechanical system under consideration is thus completely defined by the functions $v(x, t)$ and $w(x, t)$ plus the four state variables y_1, z_1, y_2, and z_2 which can be alternatively taken as y_1, z_1, θ, and ϕ. Thus, this mechanical system can be completely defined $2N + 4$ generalized coordinates given by y_1, z_1, θ, ϕ and a_n, b_n for $n = 1, 2, \ldots N$.

Stability Analysis: General Case

The nature of stability in the neighborhood of the equilibrium configuration, identified by $q_i = \dot{q}_i = 0$, is determined using Liapunov's direct method. If damping is neglected, the Hamiltonian H is constant and is a suitable Liapunov function. In the presence of damping, the total time derivative of H can be shown to be

$$\dot{H}=\sum_{i=1}^{n}Q_i\dot{q}_i \quad (17)$$

which indicates that the sign definiteness of $\dot{H}$ depends on the nature of the nonconservative force Q_i. Since Q_i comprises damping forces representing either complete damping or pervasive damping, it does not alter the nature of equilibrium in a meaningful way. That is to say, a stable system becomes asymptotically stable, whereas an unstable one remains unstable.

The system Hamiltonian function can be written as

$$H=T_2-T_0+V. \quad (18)$$

Since the term T_2 is automatically positive definite, the positive definiteness of a function U called the dynamic potential given by

$$U=V-T_0 \quad (19)$$

ensures the positiveness of H. Therefore, introducing expressions for V and T_0 into Eq. (19), the dynamic potential U after algebraic manipulations and integration of Eqs. (10)–(15) can be written as

$$U=\frac{1}{2}\Bigg\{k_{y_1y_1}y_1^2+k_{z_1z_1}z_1^2+(k_{y_1z_1}+k_{z_1y_1})y_1z_1+k_{y_2y_2}(y_1+L\theta)^2$$
$$+k_{z_2z_2}(z_1+L\phi)^2+(k_{y_2z_2}+k_{z_2y_2})(y_1+L\theta)(z_1+L\phi)\Bigg\}$$
$$+\frac{1}{4}k_S\sum_{n=1}^{N}n^4(a_n^2+b_n^2)-\frac{1}{2}m_S\Omega^2\{y_1^2(1+\phi^2)$$
$$+z_1^2(1+\theta^2)-2y_1z_1\theta\phi\}$$
$$+L[y_1\theta(1+\phi^2)+z_1\phi(1+\theta^2)-(y_1\phi+z_1\theta)\theta\phi]+\frac{1}{3}L^2(\theta^2+\phi^2)$$
$$+\sum_{n=1}^{N}\Bigg\{\frac{1}{2}[a_n^2(1+\phi^2)+b_n^2(1+\theta^2)-2a_nb_n\theta\phi]$$
$$-2\frac{((-1)^n-1)}{n\pi}[y_1a_n(1+\phi^2)+z_1b_n(1+\theta^2)-(y_1b_n+z_1a_n)\theta\phi]$$
$$-2\frac{(-1)^n}{n\pi}L[a_n\theta(1+\phi^2)+b_n\phi(1+\theta^2)-(a_n\phi+b_n\theta)\theta\phi]\Bigg\}\Bigg\}$$
$$-\frac{1}{2}m_D\Omega^2\Bigg\{y_1^2(1+\phi^2)+z_1^2(1+\theta^2)-2y_1z_1\theta\phi$$
$$+2d[y_1\theta(1+\phi^2)+z_1\phi(1+\theta^2)$$
$$-(y_1\phi+z_1\theta)\theta\phi]+d^2(\theta^2+\phi^2)+\sum_{n=1}^{N}\Bigg\{\sum_{m=1}^{N}[(1+\phi^2)a_na_m$$
$$+(1+\theta^2)b_nb_m-2\theta\phi a_nb_m]\sin\left(\frac{m\pi}{L}d\right)$$
$$+2(y_1+\theta d)[a_n(1+\phi^2)-b_n\theta\phi]$$
$$+2(z_1+\phi d)[b_n(1+\theta^2)-a_n\theta\phi]\Bigg\}\sin\left(\frac{n\pi}{L}d\right)\Bigg\}$$
$$-\frac{1}{2}I_D\Omega^2+\frac{1}{4}I_D\Omega^2(\theta_D^2+\phi_D^2) \quad (20)$$

where m_S is the mass of the shaft and k_S = shaft stiffness parameter = $EI_SL(\pi/L)^4$.

Using Euler's theorem on homogeneous functions, it can be shown that Eq. (17) becomes

$$\dot{H}=-2D. \quad (21)$$

Thus, a positive definite D leads to a negative definite $\dot{H}$. Therefore, due to Liapunov stability theory if for such a system H is positive definite (which can be guaranteed by the positive definiteness of U), then the system is asymptotically stable; and if H can assume negative values in the neighborhood of the equilibrium point, then the system is unstable. Thus, the problem simplifies to testing for (a) the positive definiteness of U to achieve stability in the undamped case and (b) the positive definiteness of both U and D in order to achieve asymptotic stability of the damped system. Testing for the positive definiteness of U and D can be accomplished by applying Sylvester's theorem to the Hessian matrices of U and D (evaluated at the equilibrium position) given by

$$U_{ij}=\left.\frac{\partial^2 U}{\partial q_i\partial q_j}\right|_E$$

and (22)

$$D_{ij}=\left.\frac{\partial^2 D}{\partial\dot{q}_i\partial\dot{q}_j}\right|_E.$$

Similar Anisotropic Bearings

To demonstrate the general method of analysis similar bearings are adopted to simplify the complexity of the stability calculations and resulting conditions. Dividing U by $m_S\Omega^2$, evaluating the second partial derivatives at the equilibrium position, letting $k_{i_1j_1} = k_{i_2j_2} = 1/2\ k_{ij}$ for similar bearings and making appropriate algebraic manipulations the Hessian matrix, denoted by $U_{ij}^{(N)}$, can be written in the form given by Eq. (23). The shaft stiffness parameter $\alpha = EI_S/\rho_S\Omega^2\ (\pi/L)^4$ and the bearing cross-coupling stiffness parameter $\beta = 1/2\Omega^2\ (\omega_{yz}^2 + \omega_{zy}^2)$ where $\omega_{ij}^2 = k_{ij}/m_S$.

Equation (23) is the Hessian matrix of the system with N modal terms included in the series expressing the shaft elastic deflections. It is a square matrix of order $2N + 4$. The first four rows and columns represent the Hessian matrix for the rigid-body case (rigid shaft-disk on elastic similar bearings) for which the generalized coordinates are y_1, z_1, θ, and ϕ.

According to Sylvester's theorem the positive definiteness of $U_{ij}^{(N)}$ requires the positive definiteness of all its principal minors. It has been shown numerically for the complete range of parameters considered herein that the greatest principal

Downloaded 03 May 2010 to 171.66.16.247. Redistribution subject to ASME license or copyright; see http://www.asme.org/terms/Terms_Use.cfm

minor $\Delta_{2N+4} = |U_{ij}^{(N)}|$ is the relevant principal minor that makes the other principal minors trivially positive provided that it is positive. The special case of the shaft alone was algebraically proved in general by El-Marhomy (1987). In other words, it is only the $|U_{ij}^{(N)}|$ that must be tested each time a term is added to the series expansion in order to understand the pattern of stability conditions as one successively increases the value of N. Each additional term in the pair of series expansions describing the system's deflections corresponds to an additional pair of rows and columns in the system's Hessian matrix leading to two new stability conditions.

Closed-form algebraic stability conditions can be obtained for any given value of N with the degree of algebraic complexity increasing significantly as N increases. These general stability conditions have been determined by the authors for $N = 1$, 2, and 3. Fortunately, as shown in Figs. (3) through (8) for the range of values considered, the graphs for $N = 3$ are nearly identical to those for $N = 2$. Consequently, because of space constraints, only the results for

$$U_{ij}^{(N)} = \begin{bmatrix}
\left[\frac{\omega_{yy}^2}{\Omega^2} - m_1\right] & \beta & \frac{L}{2}\left[\frac{\omega_{yy}^2}{\Omega^2} - 2m_2\right] & \frac{1}{2}L\beta & F_1 & 0 & F_2 & 0 & F_3 & 0 & \cdots & F_N & 0 \\
 & \left[\frac{\omega_{zz}^2}{\Omega^2} - m_1\right] & \frac{1}{2}L\beta & \frac{L}{2}\left[\frac{\omega_{zz}^2}{\Omega^2} - 2m_2\right] & 0 & F_1 & 0 & F_2 & 0 & F_3 & \cdots & 0 & F_N \\
 & & \frac{L^2}{2}\left[\frac{\omega_{yy}^2}{\Omega^2} - 2m_3\right] & \frac{1}{2}L^2\beta & \frac{L}{2}E_1 & 0 & \frac{L}{2}E_2 & 0 & \frac{L}{2}E_3 & 0 & \cdots & \frac{L}{2}E_N & 0 \\
 & & & \frac{L^2}{2}\left[\frac{\omega_{zz}^2}{\Omega^2} - 2m_3\right] & 0 & \frac{L}{2}E_1 & 0 & \frac{L}{2}E_2 & 0 & \frac{L}{2}E_3 & \cdots & 0 & \frac{L}{2}E_N \\
 & & & \text{symmetry} & G_1 & 0 & A_{12} & 0 & A_{13} & 0 & \cdots & A_{1N} & 0 \\
 & & & & G_1 & 0 & A_{12} & 0 & A_{13} & 0 & \cdots & 0 & A_{1N} \\
 & & & & & G_2 & 0 & A_{23} & 0 & \cdots & A_{2N} & 0 & \\
 & & & & & & G_2 & 0 & A_{23} & \cdots & 0 & A_{2N} & \\
 & & & & & & & G_3 & 0 & \cdots & A_{3N} & 0 & \\
 & & & & & & & & G_3 & \cdots & 0 & A_{3N} & \\
 & & & & & & & & & \ddots & \vdots & 0 & \\
 & & & & & & & & & & G_N & \vdots & \\
 & & & & & & & & & & & G_N &
\end{bmatrix}$$

$$m_n = \frac{1}{n} + \frac{m_D}{m_s}\left(\frac{d}{L}\right)^{n-1}$$

$$F_n = \left[\frac{(-1)^n - 1}{n\pi}\right] - \frac{m_D}{m_s}\sin\left(\frac{n\pi d}{L}\right)$$

$$E_n = 2\left[\frac{(-1)^n}{n\pi} - \frac{d}{L}\frac{m_D}{m_s}\sin\left(\frac{n\pi}{L}d\right)\right]$$

$$G_n = \frac{1}{2}\left\{n^4\alpha - \left(1 + \frac{2m_D}{m_s}\sin^2\left(\frac{n\pi}{L}d\right) - \frac{1}{2}\frac{m_D}{m_s}\left[\frac{b_D}{L}\pi n\cos\left(n\pi\frac{d}{L}\right)\right]^2\right)\right\}$$

$$A_{\substack{nm \\ (n\neq m)}} = -\frac{m_D}{m_s}\left[\sin\left(\frac{n\pi}{L}d\right)\sin\left(\frac{m\pi}{L}d\right) - \frac{1}{4}\left(\frac{b_D}{L}\pi\right)^2 nm\cos\left(n\pi\frac{d}{L}\right)\cos\left(m\pi\frac{d}{L}\right)\right]$$

$n, m = 1, 2, \ldots, N$ — b: the outside radius of disk

$b_D = \sqrt{b^2 + a^2}$ — a: the inner radius of disk

(23)

$N = 2$ are presented herein in complete form to serve as an example.

It can be shown by performing the similar row operations as in El-Marhomy and Schlack (1991) that for two modal terms ($N = 2$) the determinant $|U_{ij}^{(2)}|$ can be written in the following form after various algebraic manipulations:

$$|U_{ij}^{(2)}| = \frac{L^4}{16}G_{12}^2 G_2^2 B_2 \tag{24}$$

where

$$B_2 = \beta^2(\beta^2 - S_{22}^2 - S_{32}^2) + S_{22}^2 S_{32}^2 + 4S_{12}S_{42}(\beta^2 - S_{22}S_{32} + S_{12}S_{42}) + [\beta^2(S_{22} - S_{32}) + S_{22}S_{32}(S_{22} - S_{32}) + 2S_{12}S_{42}(S_{32} - S_{22})]\left(\frac{\omega_{yy}^2}{\Omega^2} + \frac{\omega_{zz}^2}{\Omega^2}\right) + (-S_{22}S_{32} + 2S_{12}S_{42})\left[\left(\frac{\omega_{yy}^2}{\Omega^2}\right)^2 + \left(\frac{\omega_{zz}^2}{\Omega^2}\right)^2\right] + \left[-2\beta^2 + (S_{22} - S_{32})^2 - (S_{22} - S_{32})\left(\frac{\omega_{yy}^2}{\Omega^2} + \frac{\omega_{zz}^2}{\Omega^2}\right)\right]\frac{\omega_{yy}^2}{\Omega^2}\frac{\omega_{zz}^2}{\Omega^2} + \left(\frac{\omega_{yy}^2}{\Omega^2}\right)^2\left(\frac{\omega_{zz}^2}{\Omega^2}\right)^2. \tag{24'}$$

The coefficients S_{12}, S_{22}, S_{32}, and S_{42} used in Eq. (24′) are defined by

$$\begin{aligned}
S_{12} &= P_2 - F_2P_{52}/G_2 - P_{51}P_{72}/G_{12} + A_{12}P_{52}P_{72}/(G_{12}G_2) \\
S_{22} &= P_4 - E_2P_{52}/G_2 - 2P_{51}P_{82}/G_{12} + 2A_{12}P_{52}P_{82}/(G_{12}G_2) \\
S_{32} &= -P_1 - F_2P_{62}/G_2 - P_{61}P_{72}/G_{12} + A_{12}P_{62}P_{72}/(G_{12}G_2) \\
S_{42} &= P_3 - E_2P_{62}/(2G_2) - P_{61}P_{82}/G_{12} + A_{12}P_{62}P_{82}/(G_{12}G_2)
\end{aligned} \tag{25}$$

where

Downloaded 03 May 2010 to 171.66.16.247. Redistribution subject to ASME license or copyright; see http://www.asme.org/terms/Terms_Use.cfm

$$P_1 = 2m_1 - 2m_2; \quad P_{51} = -E_1 + F_1; \quad P_{72} = F_1 - A_{12}F_2/G_2$$

$$P_2 = -m_1 + 2m_2; \quad P_{52} = -E_2 + F_2; \quad P_{82} = E_1/2 - A_{12}E_2/(2G_2)$$

$$P_3 = -2m_2 + 2m_3; \quad P_{61} = -E_1 + 2F_1; \quad G_{12} = G_1 - A_{12}^2/G_2$$

$$P_4 = 2(-m_2 + 2m_3); \quad P_{62} = -E_2 + 2F_2. \tag{26}$$

For positive definiteness of $U_{ij}^{(2)}$, $|U_{ij}^{(2)}|$ must be positive definite, i.e., $|U_{ij}^{(2)}| > 0$ which results in the following nontrivial sufficient conditions for system stability:

$$\alpha > C$$

$$\frac{\omega_{yy}^2}{\Omega^2} > \frac{1}{2}\left[(S_{22} - S_{32}) + \sqrt{(S_{32} + S_{22})^2 - 8S_{12}S_{42}}\right] \quad (\beta = 0),$$

and

$$B_2 > 0 \tag{27}$$

where

$$C = \frac{1}{32}\left[(16mds1 + mds2) + \sqrt{(16mds1 - mds2)^2 + 256A_{12}^2}\right]$$

and

$$mds1 = 1 + 2\frac{m_D}{m_S}\sin^2\left(\pi\frac{d}{L}\right) - \frac{1}{2}\frac{m_D}{m_S}\left[\pi\frac{b_D}{L}\cos\left(\pi\frac{d}{L}\right)\right]^2$$

$$mds2 = 1 + 2\frac{m_D}{m_S}\sin^2\left(\pi\frac{d}{L}\right) - 2\frac{m_D}{m_S}\left[\pi\frac{b_D}{L}\cos\left(2\pi\frac{d}{L}\right)\right]^2 \tag{27'}$$

Discussion of Results

Examining the foregoing conditions, the following observations are made:

(1) Equations (27) represent sufficient conditions for whirling stability for a two modal term ($N = 2$) approximation of an elastic shaft with an arbitrarily located rigid disk mounted on eight-coefficient elastic similar bearings possessing both anisotropic and cross coupling stiffnesses.

(2) In the limiting case $\alpha = \infty$ (rigid shaft case), Eq. (27) reduce to

$$\frac{\omega_{yy}^2}{\Omega^2} > (m_1 - 2m_2 + 2m_3) + \sqrt{(m_1 - 2m_2)^2 + 4(m_2 - m_3)^2} \quad (\beta = 0),$$

and

$$[\beta^2(\beta^2 - P_4^2 - P_1^2) + P_4^2P_1^2 + 4P_2P_3(\beta^2 + P_4P_1 + P_2P_3)]$$
$$+ [\beta^2(P_4 + P_1) - P_4P_1(P_4 + P_1) - 2P_2P_3(P_1 + P_4)]\left(\frac{\omega_{yy}^2}{\Omega^2} + \frac{\omega_{zz}^2}{\Omega^2}\right)$$
$$+ (P_4P_1 + 2P_2P_3)\left[\left(\frac{\omega_{yy}^2}{\Omega^2}\right)^2 + \left(\frac{\omega_{zz}^2}{\Omega^2}\right)^2\right]$$
$$+ \left[-2\beta^2 + (P_4 + P_1)^2 - (P_4 + P_1)\left(\frac{\omega_{yy}^2}{\Omega^2} + \frac{\omega_{zz}^2}{\Omega^2}\right)\right]\frac{\omega_{yy}^2}{\Omega^2}\frac{\omega_{zz}^2}{\Omega^2}$$
$$+ \left(\frac{\omega_{yy}^2}{\Omega^2}\right)^2\left(\frac{\omega_{zz}^2}{\Omega^2}\right)^2 > 0 \tag{28}$$

When the shaft acts alone (i.e., $m_D = 0$), we have the same result as El-Marhomy and Schlack (1991).

(3) In the other limiting case $\omega_{yy}^2/\Omega^2 = \omega_{zz}^2/\Omega^2 = \infty$ (rigid bearing case), the second and third parts of Eqs. (27) are trivially satisfied. Therefore, conditions for whirl stability of an elastic rotating shaft with an arbitrarily located rigid disk on rigid bearings simplifies to

$$\alpha > C. \tag{29}$$

For $m_D = 0$ (i.e., shaft alone), then $\alpha > 1$, which is the same result reached by El-Marhomy and Schlack (1991) and others. It is worthwhile noting here that if the inequality sign in condition (29) is changed into an equality sign, we get the critical value α_{cr} where

$$\alpha_{cr} = C. \tag{30}$$

The root of Eq. (30) gives the critical speed of the system (elastic rotating shaft ($N = 2$) with an arbitrarily located rigid disk on rigid bearings) as

$$\Omega_{cr} = \frac{\omega_S}{\sqrt{C}}; \text{ for } \omega_S = \sqrt{\frac{k_S}{m_S}} \tag{31}$$

Figure 2 shows the critical value α_{cr} versus disk location for different disk radii ratios, (b_D/L), which is consistent with the results of Wilgen and Schlack (1977). It is physically impossible for α_{cr} to be negative. However, the complete curves for α_{cr} are presented to help the reader understand how there tends to be a crossover from one family of the numerically generated curves to the other.

(4) In the special case of similar isotropic bearings where the bearing elasticity can be represented by a single spring of constant k_b by letting $\omega_{yy}^2 = \omega_{zz}^2 = \omega_b^2 = k_b/m_S$ and $\beta = 0$ in conditions (27), we get the following sufficient conditions for stability:

$$\alpha > C$$

and

$$\frac{\omega_b^2}{\Omega^2} > \frac{1}{2}\left[(S_{22} - S_{32}) + \sqrt{(S_{32} + S_{22})^2 - 8S_{12}S_{42}}\right]. \tag{32}$$

(5) Figures 3 through 12 are presented to demonstrate the type of information available to the designer through the equations presented herein. Figures 3 through 8 graphically show the effect of modal truncation on the stability boundaries. From Figs. 3, 4, 5, and 6 (similar principal stiffness), we can see that the stability boundaries are not significantly altered between $N = 2$ and $N = 3$. Figures 7 and 8 show the effect of modal truncation for dissimilar principal bearing stiffnesses for two different disk radius ratios. Therefore, Eq. (27) for $N = 2$ is adequate to represent sufficient conditions for whirling stability of the system for the range of parameters presented herein.

(6) The stability criteria in Eq. (27) functionally show the effects of the system's nondimensionalized parameters m_D/m_S, d/L, b_D/L, α, β, ω_{yy}^2/Ω^2, and ω_{zz}^2/Ω^2 and the two modal terms on the whirling stability of the elastic shaft-rigid disk-bearing system under investigation. The effects of these factors on the stability regions of the system based on Eq. (27) are presented graphically in Figs. 3 through 12.

Figures 3, 4, 5, and 6 show the influence of shaft elasticity on the system stability ($\omega_{yy}^2 = \omega_{zz}^2 = \omega_b^2$) for various disk radius ratios and its variation due to disk location. It is easy to see that the curves with higher values of $\alpha = EI_s/\rho_s\Omega^2\ (\pi/L)^4$, smaller values of m_D/m_S, greater b_D/L, and disk locations far

Downloaded 03 May 2010 to 171.66.16.247. Redistribution subject to ASME license or copyright; see http://www.asme.org/terms/Terms_Use.cfm

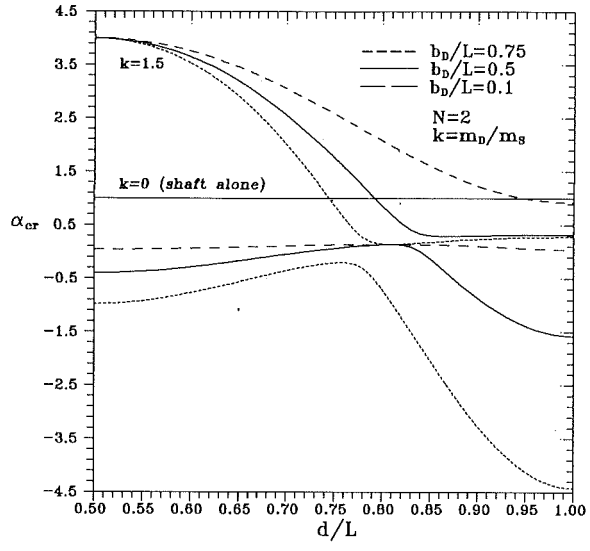


Fig. 2(*a*)

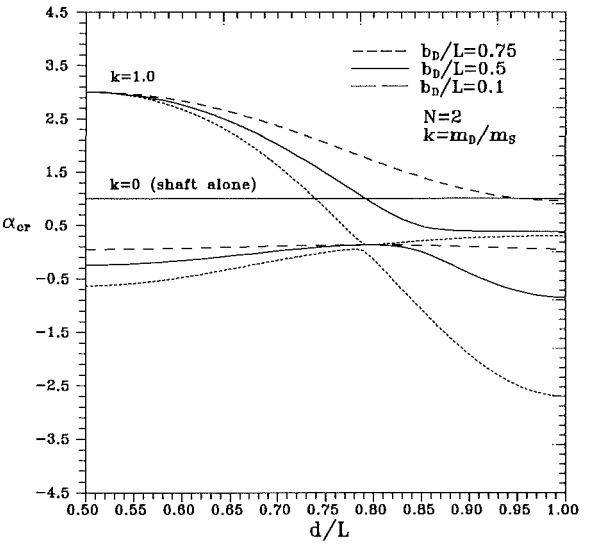


Fig. 2(*b*)

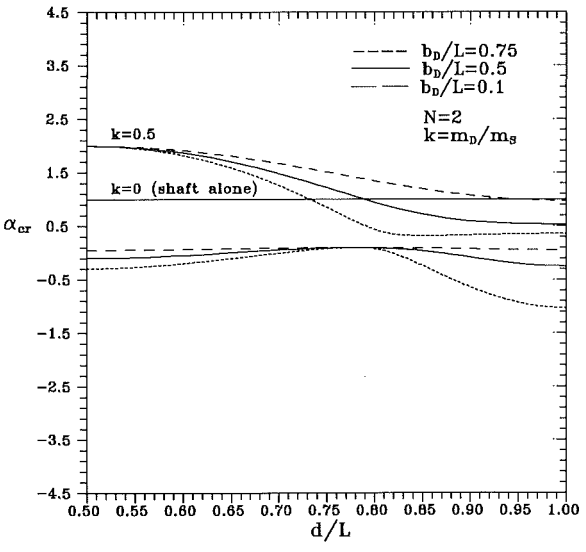


Fig. 2(*c*)

Fig. 2 Critical value α_{cr} versus disk locations

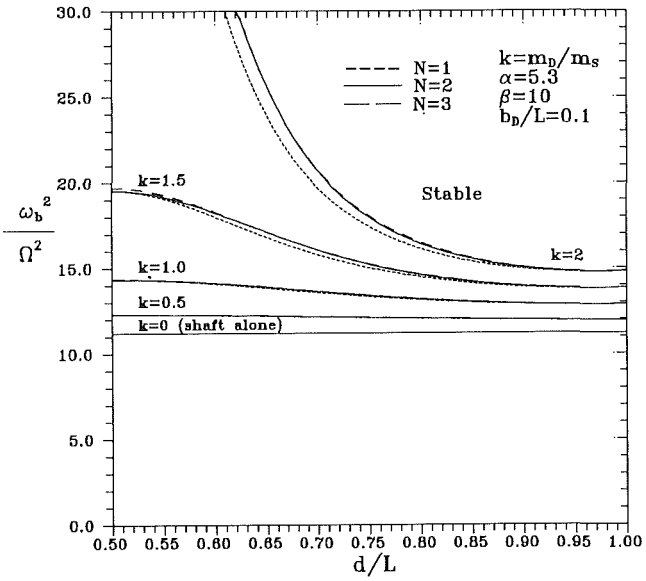


Fig. 3 Effect of modal truncation on stability boundaries for $\omega_{yy}^2 = \omega_{zz}^2$, $\beta = 10$, $\alpha = 5.3$, $b_D/L = 0.1$, and various disk locations

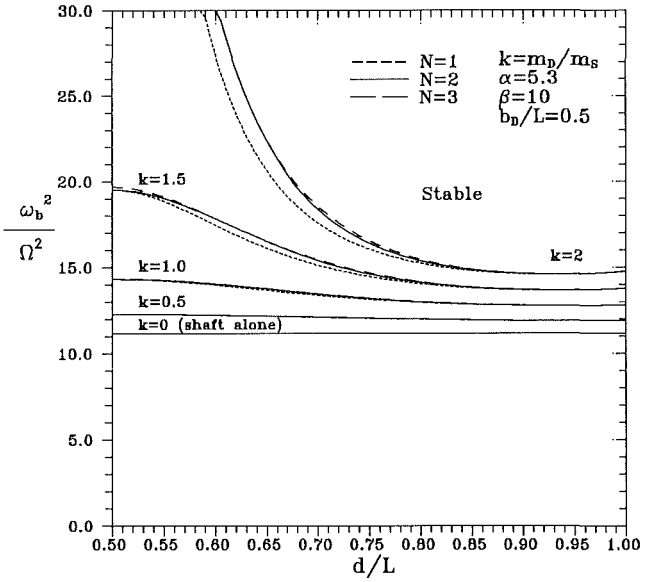


Fig. 4 Effect of modal truncation on stability boundaries for $\omega_{yy}^2 = \omega_{zz}^2$, $\beta = 10$, $\alpha = 5.3$, $b_D/L = 0.5$ and various disk locations

away from the center of shaft contain larger stable regions. It is also obvious that the stability boundaries change dramatically as α approaches the critical value α_{cr} for various disk locations, b_D/L and mass ratios. The stability curves drawn in Figs. 3 and 5 in comparison with Figs. 4 and 6 respectively show the effect of b_D/L on the stability of the system, where greater values of b_D/L lead to larger regions. The stability curves drawn in Figs. 9 and 10 in comparison with Figs. 3 and 4 demonstrate the effect of the bearing cross-coupling parameters β on the stability of the system, where greater values of β lead to smaller stability regions. This points out the important role played by the bearing cross-coupling stiffness coefficients which can be a significant source of instability. Figures 11 and 12 illustrate a typical case of dissimilar bearing stiffnesses, $m_D/L = 1.5$, $d/L = 0.6$ for various b_D/L and the combined effect of α and β on the stability boundaries. It is clear that

Downloaded 03 May 2010 to 171.66.16.247. Redistribution subject to ASME license or copyright; see http://www.asme.org/terms/Terms_Use.cfm

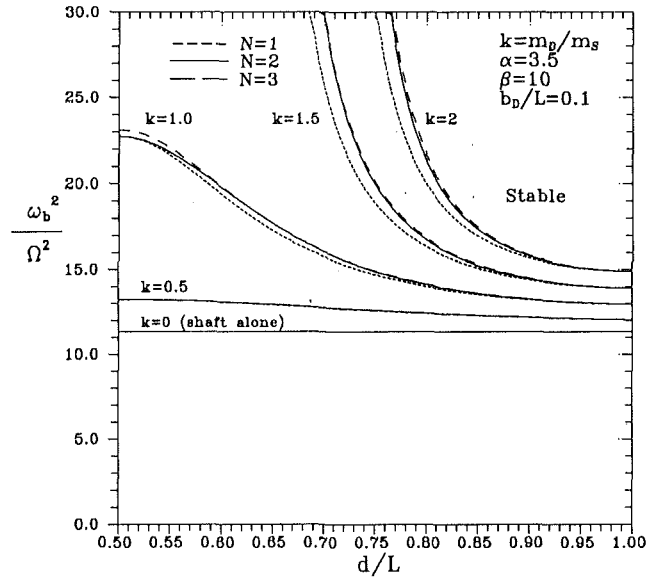


Fig. 5 Effect of modal truncation on stability boundaries for $\omega_{yy}^2 = \omega_{zz}^2$, $\beta = 10$, $\alpha = 3.5$, $b_D/L = 0.1$ and various disk locations

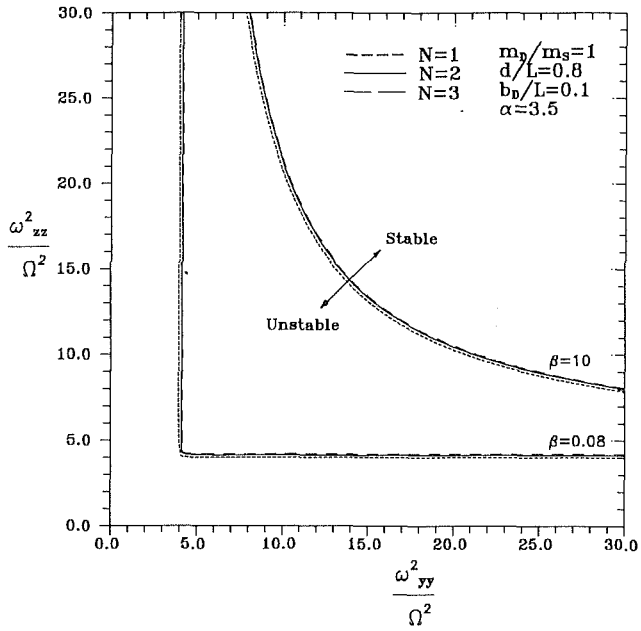


Fig. 7 Effect of modal truncation on stability boundaries for $m_D/m_S = 1$, $d/L = 0.8$, $\alpha = 3.5$, $b_D/L = 0.1$

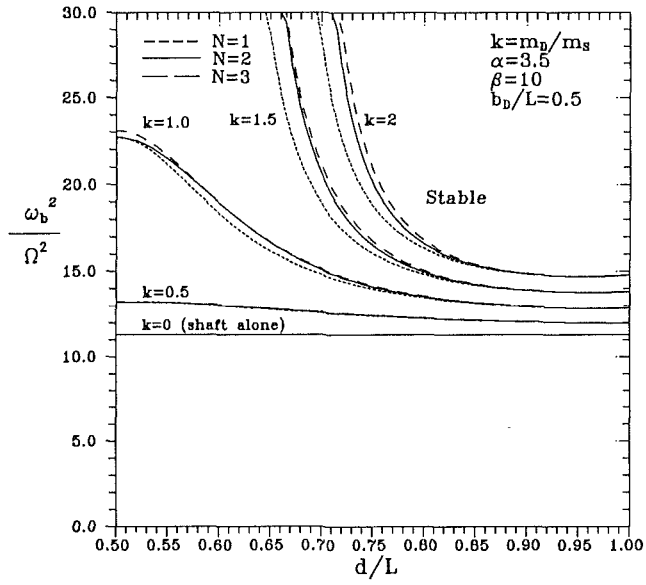


Fig. 6 Effect of modal truncation on stability boundaries for $\omega_{yy}^2 = \omega_{zz}^2$, $\beta = 10$, $\alpha = 3.5$, $b_D/L = 0.5$ and various disk locations

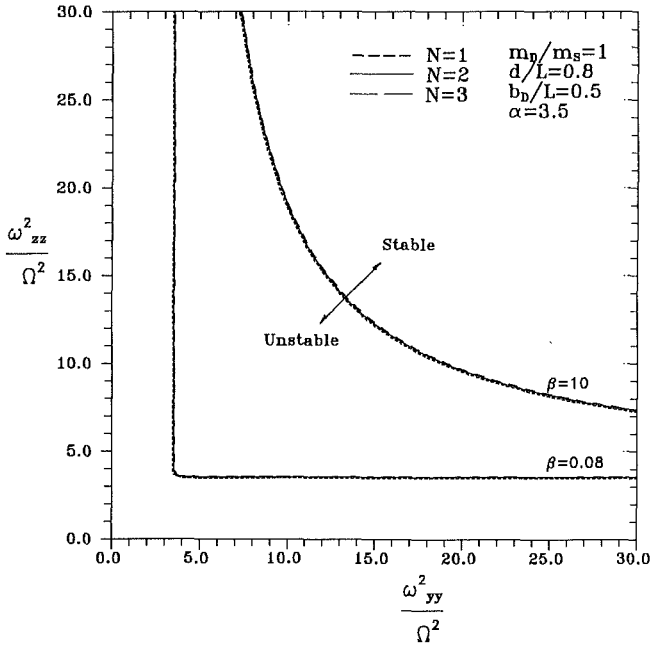


Fig. 8 Effect of modal truncation on stability boundaries for $m_D/m_S = 1$, $d/L = 0.8$, $\alpha = 3.5$, $b_D/L = 0.5$

the stability regions grow with increasing α and b_D/L, and decreasing β. Note also that for larger α, the influence of b_D/L decreases.

(7) In the special case of an elastic rotating shaft on bearings of similar principal stiffness (i.e., $m_D = 0$, shaft alone), we have the same result as El-Marhomy and Schlack (1991).

Effect of Damping

Concerning the damped system, it is necessary to test for the positive definiteness of D in order to study asymptotic stability in the sense of Liapunov. Therefore, letting $C_{i_1j_1} = C_{i_2j_2} = 1/2\ C_{ij}$ in Eq. (16) for similar bearings and evaluating the second partial derivatives of D at the equilibrium position, the Hessian matrix D_{ij} takes the form

$$D_{ij} = \begin{bmatrix} C_{yy} & \gamma & \frac{1}{2}LC_{yy} & L\gamma \\ & C_{zz} & L\gamma & \frac{1}{2}LC_{zz} \\ & & \frac{1}{2}L^2C_{yy} & L^2\gamma \\ \text{symmetry} & & & \frac{1}{2}L^2C_{zz} \end{bmatrix} \tag{33}$$

where the bearing cross-coupling damping parameter $\gamma = 1/2(C_{yz} + C_{zy})$.

Applying Sylvester's theorem to test the positive definiteness of D_{ij} yields the following nontrivial conditions for an asymptotically stable rotating system:

Downloaded 03 May 2010 to 171.66.16.247. Redistribution subject to ASME license or copyright; see http://www.asme.org/terms/Terms_Use.cfm

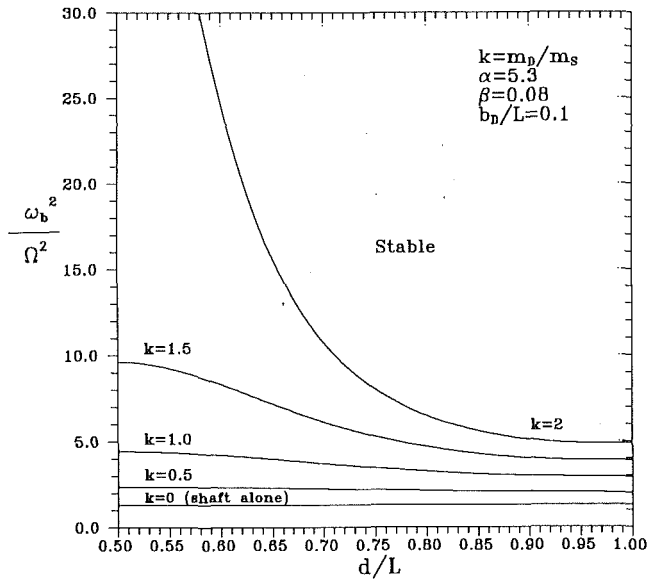


Fig. 9 Stability boundary variation ($N = 2$) due to disk location for $\alpha = 5.3$, $\beta = 0.08$, $b_D/L = 0.1$, $\omega_{yy}^2 = \omega_{zz}^2$

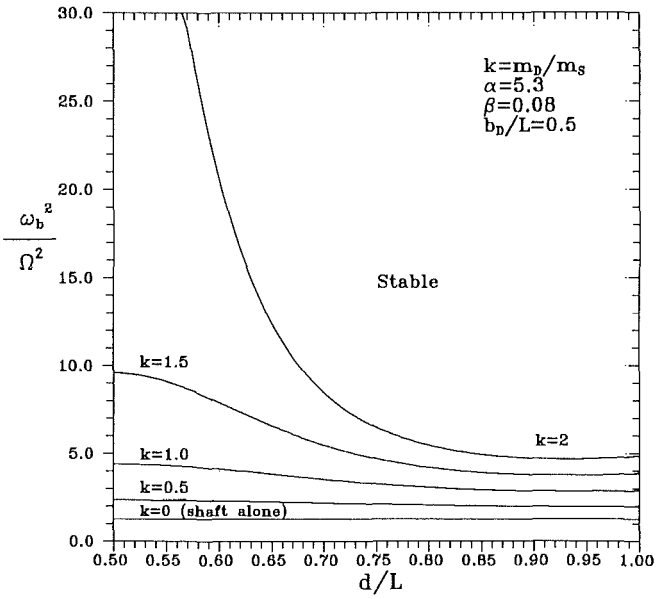


Fig. 10 Stability boundary variation ($N = 2$) due to disk location for $\alpha = 5.3$, $\beta = 0.08$, $b_D/L = 0.5$, $\omega_{yy}^2 = \omega_{zz}^2$

$$C_{yy} > 0$$

and (34)

$$C_{yy}C_{zz} > \gamma^2.$$

These conditions can be geometrically visualized by constructing a three-dimensional space for the bearing damping coefficients with C_{yy}, C_{zz}, and γ as a basis for this space. Accordingly, the subspace of asymptotically stable bearing damping coefficients based on Eqs. (34) is the spatial region inside the hyperboloid of two sheets. This indicates that all possible values of bearing damping coefficients that result in asymptotically stable motion are located inside this stability surface. The cross-sections of the stability surface of the hyperboloid formed by planes perpendicular to either C_{yy} or C_{zz} is a family of parabolas. Thus, the stability regions grow with

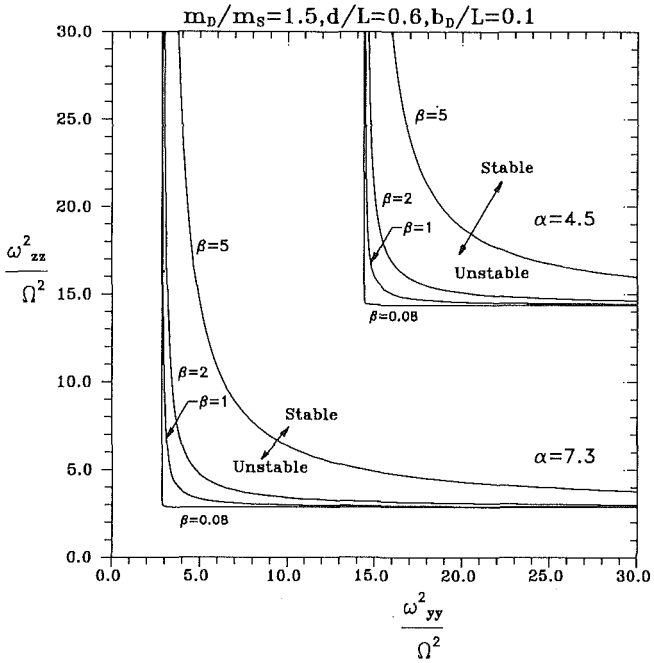


Fig. 11 Combined effect of α and β on stability regions ($N = 2$) for $m_D/m_S = 1.5$, $d/L = 0.6$, $b_D/L = 0.1$

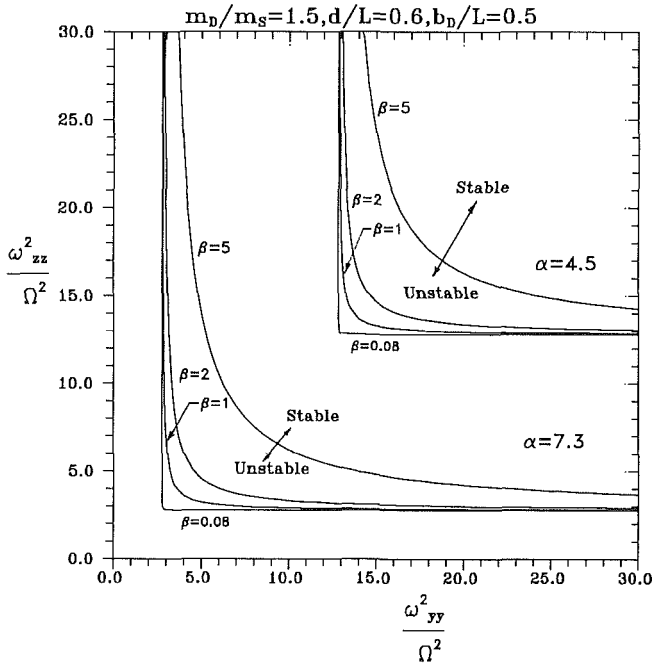


Fig. 12 Combined effect of α and β on stability regions ($N = 2$) for $m_D/m_S = 1.5$, $d/L = 0.6$, $b_D/L = 0.5$

the increase of the principal damping coefficients C_{yy} and C_{zz}. It can also be shown that if the stability surface is cut by planes perpendicular to the γ-axis, then the cross-sections are rectangular hyperbolas representing the stability boundaries in terms of γ as shown in Fig. 13. The area inside each hyperbola decreases with the increase of γ which indicates that the stability regions decrease with the increase of γ. This clearly demonstrates the fact that the bearing damping cross-coupling parameter γ can have a significant influence on the nature of the system's stability.

Downloaded 03 May 2010 to 171.66.16.247. Redistribution subject to ASME license or copyright; see http://www.asme.org/terms/Terms_Use.cfm

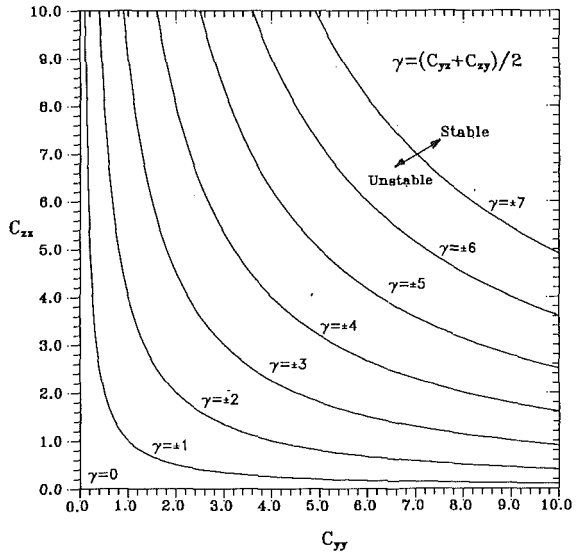


Fig. 13 Effect of damping cross-coupling parameter γ on stability regions

References

Adams, M. L., 1980, "Nonlinear Dynamics of Flexible Multibearing Rotors," *J. Sound and Vib.*, Vol. 71, pp. 129–144.

Adams, M. L., 1983, "A Note on Rotor-Bearing Stability," *J. Sound Vib.*, Vol. 86, pp. 435–438.

Chivens, D. R., and Nelson, H. D., 1975, "The Natural Frequencies and Critical Speeds of a Rotating Flexible Shaft-disk System," ASME *Journal of Engineering for Industry*, Vol. 97, pp. 881–885.

Doyle, R. E., 1971, "A Generalized Matrix Solution for Elliptic Whirling of Elastic Rotors," Ph.D. Thesis, Department of Engineering Mechanics, University of Wisconsin, Madison, WI.

El-Marhomy, A. M., 1987, "Dynamic Stability of Elastic Rotor-Bearing Systems via Liapunov's Direct Method," Ph.D. Thesis, Department of Engineering Mechanics, University of Wisconsin, Madison, WI.

El-Marhomy, A. M., and Schlack, Jr., A. L., 1991, "Dynamic Stability of Elastic Rotor-bearing Systems via Liapunov's Direct Method," ASME JOURNAL OF APPLIED MECHANICS, Vol. 58, No. 4, pp. 1056–1063.

Grobov, A. A., and Kantemir, I. I., 1978, "Stability of the Steady Motions of a Free Solid Body with a Rotor Mounted on an Elastic Shaft," *Prikladnaia Mekhanika*, Vol. 14, pp. 85–93.

Gunter, G. J., Jr., 1966, "Dynamic Stability of Rotor-Bearing Systems," NASA SP-113, 1966.

Klompas, N., 1974, "Theory of Rotor Dynamics with Coupling of Disk and Blade Flexibility and Support Structure Asymmetry," ASME Paper No. 74-GT-159, ASME Gas Turbine Conf., Zurich, Switzerland, Mar.

Kuo, P. S., 1975, "Finite Element Approach to the Vibration Analysis of Plastic Disks on a Flexible Shaft," ASME Paper 75-G7-57.

Lalanne, M., and Ferraris, G., 1990, *Rotor Dynamics Prediction in Engineering*, John Wiley and Sons, New York.

Masoom, A. K. M., 1980, "Effect of Disk Flexibility on the Whirling Frequencies of a Shaft-disc System," M.Sc. Thesis, Carlton University, Ontario.

Moore, L. S., 1972, "The Significance of Anisotropy of Support Conditions Balancing Very Large Flexible Rotors," The Inst. of Mech. Engr. Conf. on Vib. with in Rotating Systems, London, pp. 86–95.

Nelson, H. D., and McVaugh, J. M., 1976, "The Dynamics of Rotor-Bearing Systems Using Finite Elements," ASME *Journal of Engineering for Industry*, Vol. 98, pp. 593–600.

Parkinson, A. G., 1965, "The Vibration and Balancing of Shafts Rotating in Asymmetric Bearings," *J. Sound Vib.*, Vol. 2, p. 477.

Rao, J. S., 1985, "Instability of Rotors in Fluid Film Bearings with a Negative Cross-Coupled Stiffness Coefficient," *Mechanism and Machine Theory*, Vol. 20, pp. 181–187.

Rao, J. S., 1991, *Rotor Dynamics*, 2nd ed., Halsted Press, New York, (printed in India).

Stanway, R., and Burrows, C. R., 1981, "Active Vibration Control of a Flexible Rotor on Flexibly-mounted Journal Bearings," ASME *Journal of Dynamic Systems, Measurement, and Control*, Vol. 103, pp. 383–388.

Vance, J. M., 1988, *Rotordynamics of Turbomachinery*, John Wiley and Sons, New York.

Wilgen, F. J., and Schlack, Jr., A. L., 1977, "Effect of Radial Appendage Flexibility on Shaft Whirl Stability," *AIAA Journal*, Vol. 15, pp. 1531–1533.

Wilgen, F. J., and Schlack, Jr., A. L., 1979, "Effect of Disk Flexibility on Shaft Whirl Stability," ASME *Journal of Mechanical Design*, Vol. 101, pp. 298–303.

Downloaded 03 May 2010 to 171.66.16.247. Redistribution subject to ASME license or copyright; see http://www.asme.org/terms/Terms_Use.cfm

On the Transitivity Equations of Rigid-Body Dynamics

John G. Papastavridis
Assoc. Professor of Mechanics,
School of Mechanical Engineering,
Georgia Institute of Technology,
Atlanta, GA 30332

This paper presents direct derivations of the various forms of the famous transitivity equations of rigid-body kinematics from a simple and unified viewpoint. These forms are indispensable in the derivation of the Eulerian (gyro) equations of motion via the Lagrangean (analytical mechanics) method. Both true (holonomic) and quasi (nonholonomic) coordinate forms are presented. A vectorial derivation of the Eulerian equations from the Central Equation and from Hamilton's Principle is also included in the Appendix.

1 Introduction

One of the important issues in the history and also the contemporary teaching of rigid-body dynamics, since the time of Lagrange (late 18th - early 19th century), has been the derivation of the well-known Eulerian equations of rotational rigid-body motion ("gyro equations") of a free rigid-body via Lagrange's equally well-known equations

$$\frac{d}{dt}\left(\frac{\partial T}{\partial \dot{q}_k}\right)-\frac{\partial T}{\partial q_k}=Q_k, \tag{1}$$

where (using standard notations)

T = kinetic energy of rigid body B relative to an inertial frame F, $\{q_k=q_k(t);\ \dot{q}_k=\dot{q}_k(t)-k=1,2,\ldots,6\}$ = holonomic (or Lagrangian) generalized unconstrained (or independent) system coordinates and velocities, respectively, defining the position of a "base" point P, of B (k = 4,5,6, and its angular orientation (k = 1,2,3), all relative to some inertial, or space-fixed, axes; e.g., $q_{4,5,6}=x_P,y_P,z_P$ (cartesian coordinates of P relative to inertial axes O-XYZ, O: an "origin" fixed in F), $q_{1,2,3}=\phi,\theta,\psi$ (Eulerian angles: $3\rightarrow1\rightarrow3$, or: precession$\rightarrow$nutation$\rightarrow$proper spin), Q_k = holonomic components of generalized system impressed force on B, corresponding to the virtual (system) displacement δq_k; and, finally, overdots denote total time derivatives: $(\bullet\bullet\bullet)^{\cdot}\equiv d(\bullet\bullet\bullet)/dt$ (their frame dependence will be discussed below). From now on we shall consider, with no loss of generality, the special case of (unconstrained) rotation of B about a fixed point, i.e., when points O and P coincide; then k = 1,2,3.

As is well known (see, e.g., McCuskey, 1959; Junkins and Turner, 1986), only the third Eulerian equation can be derived directly from the Lagrangean Eqs. (1) applied for $q_k\rightarrow\psi$ (proper spin). For the other two one must, in addition, relate the Lagrangean components of the angular system acceleration (left side of (1)) and moment (right side of (1)) along the nonorthogonal (semi-mobile, or intermediate) axes $\phi-\theta-\dot{\psi}$, with the corresponding Eulerian components along the orthogonal (principal/body-fixed) ones, at the fixed rotation point; and this involves considerable algebra/trigonometry—see, e.g., Besant (1914), and Hamel (1949). Other authors avoid these algebraic complexities by invoking the following symmetry argument: the labeling of the principal (body) axes directions, at the fixed point O, is arbitrary, as long as we use a cyclic permutation of 1-2-3. Therefore, after having established the third Eulerian equation by Lagrange's method (1), we can say that the other two equations follow by cyclic permutation of the indices: "Having obtained (the third equation) we might at once have written down the other two Euler's equations from considerations of symmetry." (Besant, 1914, p. 424). Another drawback of all these popular derivations (initiated by Lagrange himself in the first edition of his *Mécanique Analytique* of 1788, and, as we shall see, corrected by him just before his death), is that they give the impression that the derivation of Euler's equations from (1) depends on the precise knowledge of the $(\dot{\phi},\dot{\theta},\dot{\psi})\leftrightarrow(\omega_1,\omega_2,\omega_3)$ relationship where $\omega_{1,2,3}$ are the components of the (inertial) angular velocity of B, ω, along the principal body axes $O-1,2,3$, i.e., on the particular choice of Euler-type angles—and, as we know, this is not the case.

Overcoming these theoretical and conceptual drawbacks, and providing a direct and natural (or "trick-free") passage, or transition, from Lagrange's Eqs. (1) (that involve the holonomic variables $q,\dot{q}$), to the Eulerian equations (that involve the nonholonomic variables $\omega_{1,2,3}$ and $\dot{\omega}_{1,2,3}$ (quasi-velocities and quasi-accelerations)), requires the introduction of the nonholonomic equivalent of angle. And this leads us directly to (some form of) the famous transitivity relations in these nonholonomic variables. Schematically we have

LAGRANGE'S Method $\xrightarrow{\text{Transitivity Equation(s)}}$ EULER'S Method (Rotation).

These nontrivial kinematical results are due to the fact that rotation and angular velocity, along either space or body axes, involves quasi-velocities, i.e., time rates of change of infinitesimal angular/rotational displacements, and not Lagrangean

Contributed by the Applied Mechanics Division of THE AMERICAN SOCIETY OF MECHANICAL ENGINEERS for publication in the ASME JOURNAL OF APPLIED MECHANICS.

Discussion on this paper should be addressed to the Technical Editor, Professor Leon M. Keer, The Technological Institute, Northwestern University, Evanston, IL 60208, and will be accepted until four months after final publication of the paper itself in the JOURNAL OF APPLIED MECHANICS.

Manuscript received by the ASME Applied Mechanics Division, June 1, 1990; final revision, Dec. 19, 1990.

Copyright © 1992 by ASME
Downloaded 03 May 2010 to 171.66.16.247. Redistribution subject to ASME license or copyright; see http://www.asme.org/terms/Terms_Use.cfm

(holonomic) velocities. In turn, these quasi-velocities, due to their nonintegrable nature, satisfy noncommutative relations—the transitivity equations (the term seems to have been introduced by Heun around 1901).

Now, these equations come in many special forms. One such form that has been utilized in recent times (see, e.g., Kane (1973) and Kuipers/van de Ven (1982) for ad hoc derivations) is

$$\left.\begin{aligned} &E_k(\omega)\equiv\frac{d}{dt}\left(\frac{\partial\omega}{\partial\dot{q}_k}\right)-\frac{\partial\omega}{\partial q_k}=\omega\times\frac{\partial\omega}{\partial\dot{q}_k},\\ &\text{where}\\ &\qquad\omega=\text{inertial angular velocity of } B,\\ &E_k(\bullet\bullet\bullet)\equiv\frac{d}{dt}\left(\frac{\partial\bullet\bullet\bullet}{\partial\dot{q}_k}\right)-\frac{\partial\bullet\bullet\bullet}{\partial q_k}\text{: Euler/Lagrange operator } [k=1,\ldots,n(\text{here } n=3)] \end{aligned}\right\}\quad(2)$$

In the following, we shall show that Eq. (2) is a special case of the general transitivity equation (see Hamel (1949)):

$$d(\delta\theta)-\delta(d\theta)=d\theta\times\delta\theta, \tag{3}$$

and (dividing by dt both sides)

$$\frac{d}{dt}(\delta\theta)-\delta\omega=\omega\times\delta\theta, \tag{3a}$$

where

$d\theta$ = inertial, kinematically possible, infinitesimal rotation vector of B,

$\delta\theta$ = inertial, virtual infinitesimal rotation vector of B,

$\omega\equiv d\theta/dt$ = inertial (instantaneous) angular velocity vector of B; or $d\theta=\omega dt$ (but $\delta\theta=\omega\delta t$ would be incorrect, since, in general, $\delta\theta\neq 0$, whereas always $\delta t=0$);

i.e., in general, no finite θ exists; θ is a quasi-vector.

To make the exposition as self-contained as possible, we begin, in Section 2, with a derivation of (3) and related results for both inertial and body axes. In Section 3 we derive Eq. (2) from Eq. (3), whereas in Section 4 we extend (2) to quasi-variables. Finally, in the Appendix we present the direct derivation of Euler's equations by utilizing the body axes version of (3) in (i) Lagrange's Central Equation and (ii) in Hamilton's principle.

2 The General Transitivity Equations

As stated earlier we shall consider, with no loss of generality, a rigid-body B rotating about a (space and body) fixed point O. Then, as is well known, and since this system is scleronomic,

$$\left.\begin{aligned} &\mathbf{v}=\frac{d\mathbf{r}}{dt}=\omega\times\mathbf{r},\\ &d\mathbf{r}=\mathbf{v}dt=(\omega\times\mathbf{r})dt=d\theta\times\mathbf{r}, \end{aligned}\right\}\quad(4)$$

$$\delta\mathbf{r}=\delta\theta\times\mathbf{r}, \tag{5}$$

where

$\mathbf{r}$, $\mathbf{v}$: inertial position and velocity vectors, respectively, of a typical particle P, of B

and

$d(\bullet\bullet\bullet)$, $\delta(\bullet\bullet\bullet)$: kinematically possible, and virtual variation operators, respectively, with respect to the inertial/space axes.

Now, d-varying (5) and δ-varying (4) yields

$$\begin{aligned} d(\delta\mathbf{r})&=d(\delta\theta)\times\mathbf{r}+\delta\theta\times d\mathbf{r}\\ &=d(\delta\theta)\times\mathbf{r}+\delta\theta\times(d\theta\times\mathbf{r}), \end{aligned}\tag{6}$$

$$\begin{aligned} \delta(d\mathbf{r})&=\delta(d\theta)\times\mathbf{r}+d\theta\times\delta\mathbf{r}\\ &=\delta(d\theta)\times\mathbf{r}+d\theta\times(\delta\theta\times\mathbf{r}), \end{aligned}\tag{7}$$

and therefore, subtracting (6), (7) side by side, while invoking the possible and "obvious"

$$d(\delta\mathbf{r})-\delta(d\mathbf{r})=0,$$

we find

$$\mathbf{0}=\{d(\delta\theta)-\delta(d\theta)\}\times\mathbf{r}+\delta\theta\times(d\theta\times\mathbf{r})-d\theta\times(\delta\theta\times\mathbf{r}), \tag{8}$$

and applying to the last two terms the (Jacobi-like cyclic) vector identity, for any three vectors $\mathbf{a}$, $\mathbf{b}$, $\mathbf{c}$:

$$\mathbf{a}\times(\mathbf{b}\times\mathbf{c})+\mathbf{b}\times(\mathbf{c}\times\mathbf{a})+\mathbf{c}\times(\mathbf{a}\times\mathbf{b})=\mathbf{0},$$

with the identifications $\mathbf{a}\rightarrow\delta\theta$, $\mathbf{b}\rightarrow d\theta$, $\mathbf{c}\rightarrow\mathbf{r}$, we transform (8) to

$$\mathbf{0}=\{d(\delta\theta)-\delta(d\theta)\}\times\mathbf{r}+(\delta\theta\times d\theta)\times\mathbf{r},$$

from which, since $\mathbf{r}$ is arbitrary, we finally find the fundamental and general transitivity equation

$$d(\delta\theta)-\delta(d\theta)=d\theta\times\delta\theta; \tag{9}$$

and also, dividing it by dt [which does not interact with $\delta(\bullet\bullet\bullet)$], the associated "velocity transitivity equation"

$$(\delta\theta)^{\cdot}-\delta\omega=\omega\times\delta\theta. \tag{10}$$

Here, in addition to (9), (10), we shall need the transitivity equations for differentials/variations relative to body-fixed frame (or axes); these will be denoted as $\tilde{d}(\bullet\bullet\bullet)$, and $\tilde{\delta}(\bullet\bullet\bullet)$, respectively. As is well known (see any dynamics text), the operators, $d(\bullet\bullet\bullet)$and $\tilde{d}(\bullet\bullet\bullet)$, and $\delta(\bullet\bullet\bullet)$ and $\tilde{\delta}$ are related by ($(\bullet\bullet\bullet)$: any vector):

$$d(\bullet\bullet\bullet)=\tilde{d}(\bullet\bullet\bullet)+d\theta\times(\bullet\bullet\bullet), \tag{11}$$

$$\delta(\bullet\bullet\bullet)=\tilde{\delta}(\bullet\bullet\bullet)+\delta\theta\times(\bullet\bullet\bullet); \tag{12}$$

which also yields

$$\tilde{d}\mathbf{r}=\mathbf{0},\ \text{and}\ \tilde{\delta}\mathbf{r}=\mathbf{0}$$

as expected. Let's apply (11), (12) to $\delta\theta$ and $d\theta$, respectively, we find

$$d(\delta\theta)=\tilde{d}(\delta\theta)+d\theta\times\delta\theta, \tag{13}$$

$$\delta(d\theta)=\tilde{\delta}(d\theta)+\delta\theta\times d\theta, \tag{14}$$

and dividing by $dt=\tilde{d}t$ (Newtonian "time relativity"),

$$(\delta\theta)^{\cdot}=\frac{\tilde{d}}{dt}(\delta\theta)+\omega\times\delta\theta, \tag{13a}$$

$$\delta\omega=\tilde{\delta}\omega+\delta\theta\times\omega. \tag{14a}$$

Subtracting (13), (14) side by side, we obtain

$$d(\delta\theta)-\delta(d\theta)=\tilde{d}(\delta\theta)-\tilde{\delta}(d\theta)+2d\theta\times\delta\theta$$

from which, rearranging and invoking (9),

$$\begin{aligned} \tilde{d}(\delta\theta)-\tilde{\delta}(d\theta)&=d(\delta\theta)-\delta(d\theta)-2(d\theta\times\delta\theta)\\ &=d\theta\times\delta\theta-2(d\theta\times\delta\theta), \end{aligned}$$

or finally

$$\tilde{d}(\delta\theta)-\tilde{\delta}(d\theta)=\delta\theta\times d\theta; \tag{15}$$

and dividing by $dt=\tilde{d}t$,

$$\frac{\tilde{d}}{dt}(\delta\theta)-\tilde{\delta}\omega=\delta\theta\times\omega. \tag{15a}$$

The above procedure produces the following additional useful special results:

(i) From (10), (14a), solving for $\delta\omega$, and equating we find

$$(\delta\theta)^{\cdot}-\omega\times\delta\theta=\tilde{\delta}\omega+\delta\theta\times\omega,$$

or

$$\frac{d}{dt}(\delta\theta)=\tilde{\delta}\omega; \tag{15b}$$

Downloaded 03 May 2010 to 171.66.16.247. Redistribution subject to ASME license or copyright; see http://www.asme.org/terms/Terms_Use.cfm

and also, multiplying both sides by dt,

$$d(\delta\theta) = \tilde{\delta}(d\theta). \tag{15c}$$

(ii) A "symmetrical" to it expression follows from (10): we find successively

$$\delta\omega = (\delta\theta)^{\cdot} - \omega \times \delta\theta \qquad \text{(and invoking (13}a\text{))}$$

$$= \left(\frac{\tilde{d}}{dt}(\delta\theta) + \omega \times \delta\theta\right) - \omega \times \delta\theta$$

$$= \frac{\tilde{d}}{dt}(\delta\theta) \qquad (= \tilde{\delta}\omega + \delta\theta \times \omega, \text{ by (15}a\text{))},$$

i.e.,

$$\delta\omega = \frac{\tilde{d}}{dt}(\delta\theta), \tag{15d}$$

or, multiplying by dt,

$$\delta(d\theta) = \tilde{d}(\delta\theta). \tag{15e}$$

(iii) Applying (11) for ω yields

$$d\omega = \tilde{d}\omega, \tag{15f}$$

and multiplying by dt,

$$d(d\theta) = \tilde{d}(d\theta).$$

However, as (12) shows,

$$\delta\omega \neq \tilde{\delta}\omega, \text{ and } \delta(d\theta) \neq \tilde{\delta}(d\theta). \tag{15g}$$

The subtle but important differences between (9) and (15) often go unnoticed. It is worth writing them out in extenso/in components. Only the first, i.e., X and x, equations will be shown; the rest follows cyclically:

(i) Along space/inertial axes O-XYZ

$$d(\delta\theta_X) - \delta(d\theta_X) = d\theta_Y \delta\theta_Z - d\theta_Z \delta\theta_Y, \ \ldots \tag{16}$$

and dividing by dt,

$$(\delta\theta_X)^{\cdot} - \delta\omega_X = \omega_Y \delta\theta_Z - \omega_Z \delta\theta_Y, \ \ldots \tag{16a}$$

(ii) Along body/moving axes O-xyz

$$d(\delta\theta_x) - \delta(d\theta_x) = d\theta_z \delta\theta_y - d\theta_y \delta\theta_z, \ \ldots \tag{17}$$

and dividing by dt

$$(\delta\theta_x)^{\cdot} - \delta\omega_x = \omega_z \delta\theta_y - \omega_y \delta\theta_z, \ \ldots. \tag{17a}$$

Solving (16a) and (17b) for the $\delta\omega\ldots$ we find

$$\begin{cases} \delta\omega_X = (\delta\theta_X)^{\cdot} + \omega_Z \delta\theta_Y - \omega_Y \delta\theta_Z, & \text{(inertial axes)} \\ \delta\omega_x = (\delta\theta_x)^{\cdot} + \omega_y \delta\theta_z - \omega_z \delta\theta_y, & \text{(moving axes).} \end{cases}$$

In these component representations we use d, δ, and $(\bullet\bullet\bullet)^{\cdot}$ for both space and body axes, since there is no danger of misunderstanding when dealing with components.

Equations (17), (17a), for body axes, were given for the first time by a less simple (nonvectorial) method by Lagrange himself (1811–1815; 2nd ed. of his *Mécanique Analytique*). (See also Lur'e (1968, pp. 61–63) for a derivation of (16)–(17a) based on the most general transitivity equations of analytical dynamics.)

Remark: It should be noted that the fundamental relation

$$d(\delta\mathbf{r}) - \delta(d\mathbf{r}) = \mathbf{0} \tag{17b}$$

is not frame invariant, i.e., in general,

$$\tilde{d}(\delta\mathbf{r}) - \tilde{\delta}(d\mathbf{r}) \neq \mathbf{0}. \tag{17c}$$

Proof: Applying (11), (12) we readily find

$$d(\delta\mathbf{r}) = \tilde{d}(\delta\mathbf{r}) + d\theta \times (\delta\mathbf{r})$$

$$= \tilde{d}(\delta\mathbf{r}) + \mathbf{d}\theta \times (\delta\theta \times \mathbf{r})$$

$$= \tilde{d}(\delta\mathbf{r}) + \{(\mathbf{r} \bullet d\theta)\delta\theta - (d\theta \bullet \delta\theta)\mathbf{r}\}, \tag{17d}$$

and

$$\delta(d\mathbf{r}) = \tilde{\delta}(d\mathbf{r}) + \delta\theta \times (d\mathbf{r})$$

$$= \bullet\ \bullet\ \bullet\ \bullet\ \bullet\ \bullet\ \bullet\ \bullet$$

$$= \tilde{\delta}(d\mathbf{r}) + \{(\mathbf{r} \bullet \delta\theta)d\theta - (d\theta \bullet \delta\theta)\mathbf{r}\}, \tag{17e}$$

and therefore

$$\mathbf{0} = d(\delta\mathbf{r}) - \delta(d\mathbf{r})$$

$$= \tilde{d}(\delta\mathbf{r}) - \tilde{\delta}(d\mathbf{r}) + (\mathbf{r} \bullet d\theta)\delta\theta - (\mathbf{r} \bullet \delta\theta)d\theta,$$

or

$$\tilde{d}(\delta\mathbf{r}) - \tilde{\delta}(d\mathbf{r}) = (\mathbf{r} \bullet \delta\theta)d\theta - (\mathbf{r} \bullet d\theta)\delta\theta$$

$$= \mathbf{r} \times (d\theta \times \delta\theta)$$

$$= (\delta\theta \times d\theta) \times \mathbf{r}$$

or

$$\tilde{d}(\delta\mathbf{r}) - \tilde{\delta}(d\mathbf{r}) = d^*\theta \times \mathbf{r} \text{ where } d^*\theta \equiv \delta\theta \times d\theta,$$

or

$$\tilde{d}^*\mathbf{r} = d^*\theta \times \mathbf{r}, \quad \tilde{d}^* \bullet\bullet\bullet \equiv \tilde{d}(\delta \bullet\bullet\bullet) - \tilde{\delta}(d \bullet\bullet\bullet).$$

Similarly, dividing by $dt = \tilde{d}t$,

$$\frac{\tilde{d}}{dt}(\delta\mathbf{r}) - \tilde{\delta}\mathbf{v} = (\delta\theta \times \omega) \times \mathbf{r} \quad (\equiv d^*\omega \times \mathbf{r}).$$

This formalism clearly can be extended to arbitrarily rotating axes, i.e., neither body nor space fixed.

3 The Special Transitivity Eqs. (2)

In general, ω has the following representation

$$\omega = \omega(q_k, \dot{q}_k, t) \equiv \omega(q, \dot{q}, t), \tag{18}$$

where $k = 1,\ldots, n$ (# positional system coordinates). Here, however (body rotating about a fixed point), Eq. (18) specializes to

$$\omega = \omega(q_k, \dot{q}_k) \equiv \omega(q, \dot{q}), \tag{18a}$$

with $k = 1, 2, 3$, (three angular coordinates; say, Euler's angles). Since

$$\delta q \to \delta\theta = \sum_k (\bullet\bullet\bullet)\delta q_k \ \{\to \delta\mathbf{r} = \delta\theta \times \mathbf{r} = \sum_k (\bullet\bullet\bullet)\delta q_k\},$$

we have, successively,

$$\delta\theta = \sum_k \mathbf{a}_k \delta q_k \text{ (definition of the } \mathbf{a}_k) \equiv \sum_k \left(\frac{\partial\theta}{\partial q_k}\right) \delta q_k$$

$$= \sum_k \frac{\partial(d\theta)}{\partial(dq_k)} \delta q_k = \sum_k \left(\frac{\partial\omega}{\partial\dot{q}_k}\right) \delta q_k, \tag{19}$$

where, symbolically,

$$\mathbf{a}_k \equiv \frac{\partial\theta}{\partial q_k} = \frac{\partial(d\theta)}{\partial(dq_k)} = \frac{\partial(\delta\theta)}{\partial(\delta q_k)} = \frac{\partial\omega}{\partial\dot{q}_k}. \tag{20}$$

Also: (i) since the system at hand is scleronomic

$$d\theta = \sum_k \mathbf{a}_k dq_k \equiv \omega dt, \tag{21}$$

and therefore

$$\omega = \frac{d\theta}{dt} = \sum_k \mathbf{a}_k \dot{q}_k = \sum_k \left(\frac{\partial\omega}{\partial\dot{q}_k}\right) \dot{q}_k; \tag{22}$$

and (ii) since ω is a linear function of the $\dot{q}$'s (and, for our system, also homogeneous) $\mathbf{a}_k \equiv \partial\omega/\partial\dot{q}_k$ does not depend on the $\dot{q}$; Eq. (22) is also an application of Euler's homogeneous

Downloaded 03 May 2010 to 171.66.16.247. Redistribution subject to ASME license or copyright; see http://www.asme.org/terms/Terms_Use.cfm

function theorem. Let us now substitute the foregoing into the fundamental Eq. (10):

Left Side:

$$(\delta\theta)^{\cdot} - \delta\omega = \frac{d}{dt}\left(\sum_k \frac{\partial\omega}{\partial\dot{q}_k}\,\delta q_k\right) - \delta\omega$$

$$= \sum_k \frac{d}{dt}\left(\frac{\partial\omega}{\partial\dot{q}_k}\right)\delta q_k + \sum_k \frac{\partial\omega}{\partial\dot{q}_k}\,(\delta q_k)^{\cdot} - \left\{\sum_k \frac{\partial\omega}{\partial q_k}\,\delta q_k + \sum_k \frac{\partial\omega}{\partial\dot{q}_k}\,\delta\dot{q}_k\right\}$$

(and since for holonomic coordinates we can always take $\delta(d\bullet\bullet\bullet) = d(\delta\bullet\bullet\bullet)$)

$$= \sum_k \left\{\frac{d}{dt}\left(\frac{\partial\omega}{\partial\dot{q}_k}\right) - \frac{\partial\omega}{\partial q_k}\right\}\delta q_k, \tag{23}$$

$$\equiv \sum_k E_k(\omega)\delta q_k. \tag{24}$$

Right Side:

$$\omega\times\delta\theta = \omega\times\left\{\sum_k \frac{\partial\omega}{\partial\dot{q}_k}\,\delta q_k\right\} = \sum_k \left(\omega\times\frac{\partial\omega}{\partial\dot{q}_k}\right)\delta q_k. \tag{25}$$

Therefore, and since the δq_k are here independent (but even if the δq were mutually constrained, that would affect the kinetic equations of motion and not these kinematic results), we finally find

$$\underbrace{\frac{d}{dt}\left(\frac{\partial\omega}{\partial\dot{q}_k}\right) - \frac{\partial\omega}{\partial q_k}}_{E_k(\omega)} = \omega\times\frac{\partial\omega}{\partial\dot{q}_k}, \quad \text{q.e.d.;} \tag{2}$$

or in terms of the $\{\mathbf{a}_k\}$ vectors,

$$\frac{d}{dt}\,\mathbf{a}_k = \omega\times\mathbf{a}_k + \frac{\partial\omega}{\partial q_k}. \tag{2a}$$

If ω was a true (holonomic) vector total derivative, and not a (vectorial) quasi-velocity, then $E_k(\omega) = \mathbf{0}$ (integrability condition). Further, recalling (11), (13), we obtain

$$\frac{d}{dt}\left(\frac{\partial\omega}{\partial\dot{q}_k}\right) = \frac{\tilde{d}}{dt}\left(\frac{\partial\omega}{\partial\dot{q}_k}\right) + \omega\times\left(\frac{\partial\omega}{\partial\dot{q}_k}\right), \tag{26}$$

and inserting it into (2), (2a) produces the interesting results:

$$\tilde{E}_k(\omega) \equiv \frac{\tilde{d}}{dt}\left(\frac{\partial\omega}{\partial\dot{q}_k}\right) - \frac{\partial\omega}{\partial q_k} = \mathbf{0}, \text{ or } \frac{\tilde{d}}{dt}\,\mathbf{a}_k = \frac{\partial\omega}{\partial q_k}; \tag{27}$$

or, alternatively,

$$\frac{\tilde{d}}{dt}\left(\frac{\partial\theta}{\partial q_k}\right) = \frac{\partial}{\partial q_k}\left(\frac{d\theta}{dt}\right).$$

or

$$\tilde{d}\left(\frac{\partial\theta}{\partial q_k}\right) = \frac{\partial}{\partial q_k}\,(d\theta),$$

although

$$d\left(\frac{\partial\theta}{\partial q_k}\right) \neq \frac{\partial}{\partial q_k}\,(d\theta).$$

4 Extension of Eq. (2) to Quasi-Variables

Here the starting representation, instead of (19), is

$$\delta\theta \equiv \sum_k \mathbf{A}_k\delta\theta_k \qquad (\theta_k\text{: quasi-coordinates})$$

$$\equiv \sum_k \frac{\partial\theta}{\partial\theta_k}\,\delta\theta_k \equiv \sum_k \frac{\partial(\delta\theta)}{\partial(\delta\theta_k)}\,\delta\theta_k = \sum_k \left(\frac{\partial\omega}{\partial\omega_k}\right)\delta\theta_k \tag{28}$$

where $\omega_k \equiv \dot{\theta}_k$ (along any set of axes)

and

$$d\theta = \sum_k \mathbf{A}_k d\theta_k \equiv \omega dt,$$

from which

$$\omega \equiv \frac{d\theta}{dt} = \sum_k \mathbf{A}_k\dot{\theta}_k = \sum_k \frac{\partial\omega}{\partial\omega_k}\,\omega_k = \omega(q,\,\omega). \tag{29}$$

Therefore, the left side of (10) becomes

$$(\delta\theta)^{\cdot} - \delta\omega = \left\{\sum_k \left(\frac{\partial\omega}{\partial\omega_k}\right)^{\cdot}\delta\theta_k + \sum_k \frac{\partial\omega}{\partial\omega_k}\,(\delta\theta_k)^{\cdot}\right\} - \left\{\sum_k \frac{\partial\omega}{\partial q_k}\,\delta q_k + \sum_k \frac{\partial\omega}{\partial\omega_k}\,\delta\omega_k\right\}$$

$$\left(\text{and setting } \delta q_k = \sum_l \underbrace{A_{kl}}_{\partial\dot{q}_k/\partial\omega_l}\,\delta\theta_l \quad \text{(definition of } A_{kl}\text{)}\right)$$

$$= \sum_k \left\{\frac{d}{dt}\left(\frac{\partial\omega}{\partial\omega_k}\right) - \underbrace{\sum_l A_{lk}\,\frac{\partial\omega}{\partial q_l}}_{\equiv\frac{\partial\omega}{\partial\theta_k}}\right\}\delta\theta_k + \sum_l \frac{\partial\omega}{\partial\omega_l}\underbrace{\{(\delta\theta_l)^{\cdot} - \delta\omega_l\}}_{\equiv\sum_k\Theta_{lk}\delta\theta_k}, \tag{30}$$

while the right side yields

$$\omega\times\delta\theta = \omega\times\left\{\sum_k \frac{\partial\omega}{\partial\omega_k}\,\delta\theta_k\right\} = \sum_k \left(\omega\times\frac{\partial\omega}{\partial\omega_k}\right)\delta\theta_k, \tag{31}$$

and since the $\{\delta\theta_k\}$ are independent, equating right and left sides finally gives (compare with (2)):

$$\underbrace{\frac{d}{dt}\left(\frac{\partial\omega}{\partial\omega_k}\right) - \frac{\partial\omega}{\partial\theta_k} + \sum_l \Theta_{lk}\,\frac{\partial\omega}{\partial\omega_l}}_{E_k^*(\omega)} = \omega\times\frac{\partial\omega}{\partial\omega_k}, \tag{32}$$

where, again, the Θ_{lk} are defined by the (Hamel-type) transitivity equations

$$(\delta\theta_l)^{\cdot} - \delta\omega_l = \sum_k \Theta_{lk}\delta\theta_k. \tag{33}$$

In terms of the $\mathbf{A}_k$ $\left\{\equiv\dfrac{\partial\omega}{\partial\omega_k};\ \omega = \omega\,(q,\,\omega_k)\right\}$ vectors the above read

$$\frac{d}{dt}\,\mathbf{A}_k = \omega\times\mathbf{A}_k + \frac{\partial\omega}{\partial\theta_k} - \sum_l \Theta_{lk}\mathbf{A}_l \quad \text{(compare with (2}a\text{))}; \tag{32a}$$

while for body-fixed variations (for the same vectors $\mathbf{A}_k$),

$$\frac{\tilde{d}}{dt}\,\mathbf{A}_k = \frac{\partial\omega}{\partial\theta_k} - \sum_l \Theta_{lk}\mathbf{A}_l \quad \text{(compare with (27))}. \tag{32b}$$

Downloaded 03 May 2010 to 171.66.16.247. Redistribution subject to ASME license or copyright; see http://www.asme.org/terms/Terms_Use.cfm

Also applying the chain rule yields

$$\frac{\partial \omega(q,\omega)}{\partial \omega_l} = \sum_k \frac{\partial \omega(q,\dot{q})}{\partial \dot{q}_k} \frac{\partial \dot{q}_k(q,\omega)}{\partial \omega_l}$$

or

$$\mathbf{A}_l = \sum_k A_{kl}\mathbf{a}_k; \quad A_{kl} \equiv \frac{\partial \dot{q}_k}{\partial \omega_l} \quad \text{(vector transformation)}. \tag{32c}$$

It should be noted that in this case both ω and $\omega_k \equiv \dot{\theta}_k$ ($\equiv \omega$, collectively) are quasi-variables. Also, Eq. (32*c*) should not be confused with the earlier introduced notation

$$\frac{\partial \omega(q,\omega)}{\partial \theta_l} \equiv \sum_k \frac{\partial \omega(q,\omega)}{\partial q_k} \frac{\partial \dot{q}_k(q,\omega)}{\partial \omega_l}.$$

Equations (32) bear a remarkable formal similarity to the well-known kinetic Boltzmann-Hamel (or, as Hamel called them, Euler-Lagrange) equations—see e.g., Hamel (1949).

Let us now verify (33) for space-fixed axes. In this case as shown earlier

$$(\delta\theta_X)^{\cdot} - \delta\omega_X = (0)\delta\theta_X + (-\omega_Z)\delta\theta_Y + (\omega_Y)\delta\theta_Z,$$
$$(\delta\theta_Y)^{\cdot} - \delta\omega_Y = (\omega_Z)\delta\theta_X + (0)\delta\theta_Y + (-\omega_X)\delta\theta_Z,$$
$$(\delta\theta_Z)^{\cdot} - \delta\omega_Z = (-\omega_Y)\delta\theta_X + (\omega_X)\delta\theta_Y + (0)\delta\theta_Z,$$

i.e.,

$$(\Theta_{lk}) = \left(\begin{array}{c|c|c} 0 & -\omega_Z & \omega_Y \\ \hline \omega_Z & 0 & -\omega_X \\ \hline -\omega_Y & \omega_X & 0 \end{array}\right).$$

Therefore, the first of (32), i.e., $k \to X$, becomes

$$E_X^*(\omega) + \frac{\partial \omega}{\partial \omega_X}\Theta_{XX} + \frac{\partial \omega}{\partial \omega_Y}\Theta_{YX} + \frac{\partial \omega}{\partial \omega_Z}\Theta_{ZX} = \omega \times \frac{\partial \omega}{\partial \omega_X},$$

or

$$E_X^*(\omega) + (\hat{E}_X)(0) + (\hat{E}_Y)(\omega_Z) + (\hat{E}_Z)(-\omega_Y)$$
$$= \omega_Z\hat{E}_Y - \omega_Y\hat{E}_Z = \begin{vmatrix} \hat{E}_X & \hat{E}_Y & \hat{E}_Z \\ \omega_X & \omega_Y & \omega_Z \\ 1 & 0 & 0 \end{vmatrix},$$

where

$\omega = \omega_X\hat{E}_X + \omega_Y\hat{E}_y + \omega_Z\hat{E}_Z$, $\hat{E}_{X,Y,Z}$: unit inertial vectors

or

$$\frac{d}{dt}\left(\frac{\partial \omega}{\partial \omega_X}\right) - \frac{\partial \omega}{\partial \theta_X} = \mathbf{0},$$

or

$$\frac{d}{dt}\hat{E}_X - \sum_l A_{lX}\frac{\partial \omega}{\partial q_l} = \mathbf{0}, \quad \text{i.e., } \mathbf{0} - \mathbf{0} = \mathbf{0},$$

as expected: similarly for Y, Z.

Likewise, in terms of body axes-derivatives, (32)–(32*b*) gives

$$\frac{\tilde{d}}{dt}\left(\frac{\partial \omega}{\partial \omega_X}\right) - \frac{\partial \omega}{\partial \theta_X} + \sum_l \Theta_{lX}\frac{\partial \omega}{\partial \omega_l} = \mathbf{0},$$

or

$$\frac{\tilde{d}}{dt}(\hat{E}_X) - \mathbf{0} + \omega \times \frac{\partial \omega}{\partial \omega_X} = \mathbf{0}$$

$$\frac{\tilde{d}}{dt}\hat{E}_X = (-\omega) \times \hat{E}_X$$

($-\omega$: angular velocity of space relative to body: $\omega \to -\omega$); space unit vector; body derivative

similarly for $k \to Y,Z$.

References

Besant, W. H., 1914, *A Treatise on Dynamics*, 5th ed., revised and enlarged by A. S. Ramsey, Bell, London, pp. 423–425.

Bremer, H., 1988a, "Ueber eine Zentralgleichung in der Dynamik," *Zeitschrift fuer Angewandte Mathematik und Mechanik*, Vol. 68, pp. 307–311.

Bremer, H., 1988b, *Dynamik und Regelung Mechanischer Systeme*, Teubner, Stuttgart, pp. 46–47, 67–71.

Föppl, A., 1909, *Vorlesungen ueber Technische Mechanik*, Vol. 4, (*Dynamik*, 3rd ed.), Teubner, Leipzig, pp. 177–178.

Hamel, G., 1949, *Theoretische Mechanik*, Springer, Berlin, pp. 235, 480–482, 488–489, 523, 733–735.

Junkins, J. L., and Turner, J. D., 1986, *Optimal Spacecraft Rotational Maneuvers*, Elsevier, Amsterdam, pp. 64–67.

Kane, T. R., 1973, "Lagrange's Equations for a Rigid Body," ASME JOURNAL OF APPLIED MECHANICS, Vol. 40, pp. 1118–1119.

Kuipers, M., and van de Ven, A. A. F., 1982, "The Lagrangian Formalism and the Balance Law of Angular Momentum for a Rigid Body," *Journal of Engineering Mathematics*, Vol. 16, pp. 77–90 (pp. 78–83, eq. 228, 229).

Lagrange, J. L., 1811–1815, *Mécanique Analytique*, 2nd ed., Paris (3rd ed., 1853–1855; 4th Ed., 1888–1889); Second Part (La Dynamique), Section 9, Chapter 1, pp. 199–200.

Lur'e, A. I., 1968, *Mécanique Analytique*, (2 volumes), Librairie Universitaire, Louvain, Belgium, (Soviet original: Moscow, 1961, pp. 452–453, eq. (9.6.35)).

McCuskey, S. W., 1959, *An Introduction to Advanced Dynamics*, Addison-Wesley, Reading, Mass., pp. 127–129.

Rosenberg, R. M., 1977, *Analytical Dynamics of Discrete Systems*, Plenum, New York, pp. 167–169.

Wang, C.-C., 1979, *Mathematical Principles of Mechanics and Electromagnetism, Part A: Analytical and Continuum Mechanics*, Plenum, New York, pp. 27–40.

APPENDIX

Independent Derivations of Euler's Equations (EE) from: (i) Lagrange's Central Equation (LCE), and (ii) Hamilton's Principle (HP)

As mentioned earlier, EE have been derived from Eqs. (1) with the help of the special transitivity Eqs. (2); another recent proof based on the general Boltzmann/Hamel equations has appeared in Wang (1979). We think that these derivations represent either too synthetical or too analytical extremes. In the following, we shall present what we think is a simple and natural derivation of EE based on the general principles of dynamics: LCE, and HP; and on the simpler and general transitivity equations (9), (10) and (15), (15*a*). Such proofs were initiated, in scalar component forms, by Lagrange (1811–1815), were reproduced in the 19th century by some of the best mechanicists (e.g., Kirchhoff, C. Neumann, and Mathieu), and were finally vectorized in this century by Heun and Hamel (see Hamel (1949), and Bremer (1988a,b)). However, since no easily available derivations exist, we present two as follows (one via the Central Equation (CE), and one via Hamilton's Principle (HP)):

1 Here the starting point is Lagrange's CE

$$\delta T + \delta' W = \frac{d}{dt}(S(dm\mathbf{v}\cdot\delta\mathbf{r})), \tag{A1}$$

where $\delta' W$ = first-order virtual work of all impressed forces on B; dm = element, or particle, mass; $S(\cdots)$ = material summation over the body B (as in Stieltjes' integral); see e.g., Rosenberg (1977). For a rigid body B rotating about a fixed point O, we have, successively,

Downloaded 03 May 2010 to 171.66.16.247. Redistribution subject to ASME license or copyright; see http://www.asme.org/terms/Terms_Use.cfm

(a)

$$T \equiv S\left(\frac{1}{2}\, dm\mathbf{v}\cdot\mathbf{v}\right)$$

$$= \frac{1}{2}\, S[dm\mathbf{v}\cdot(\omega\times\mathbf{r})]$$

$$= \frac{1}{2}\, S[dm\omega\cdot(\mathbf{r}\times\mathbf{v})]$$

$$= \frac{1}{2}\, \mathbf{H}\cdot\omega, \tag{A2}$$

$\mathbf{H} = S[\mathbf{r}\times(dm\mathbf{v})]$: angular momentum of B about O. (A3)

Therefore,

$$\delta T = \frac{1}{2}\,(\delta\mathbf{H}\cdot\omega + \mathbf{H}\cdot\delta\omega) \quad \text{[and applying (12)]}$$

$$= \frac{1}{2}\,\{(\tilde{\delta}\mathbf{H} + \delta\theta\times\mathbf{H})\cdot\omega + \mathbf{H}\cdot(\tilde{\delta}\omega + \delta\theta\times\omega)\}$$

$$= \frac{1}{2}\,\{(\tilde{\delta}\mathbf{H}\cdot\omega + \mathbf{H}\cdot\tilde{\delta}\omega) + \underbrace{[\delta\theta\cdot(\mathbf{H}\times\omega) + \delta\theta\cdot(\omega\times\mathbf{H})]}_{0}\}$$

$$\left\{\begin{array}{l}\text{and since for body-fixed, not necessarily}\\ \text{principal, axes: } \tilde{\delta}\mathbf{H}\cdot\omega = \mathbf{H}\cdot\tilde{\delta}\omega - \text{see below}\end{array}\right\};$$

finally,

$$\delta T = \mathbf{H}\cdot\tilde{\delta}\omega, \quad \mathbf{H} \equiv \frac{\partial T}{\partial\omega}. \tag{A3}$$

It is well known that

$$\mathbf{H} = \mathbf{I}\cdot\omega, \text{ where } \mathbf{I} = \text{inertia tensor at } O, \tag{A3a}$$

and therefore $\tilde{\delta}$-varying the above (while using body-fixed axes),

$$\tilde{\delta}\mathbf{H} = \tilde{\delta}\mathbf{I}\cdot\omega + \mathbf{I}\cdot\tilde{\delta}\omega = \mathbf{I}\cdot\tilde{\delta}\omega, \ (\tilde{\delta}\mathbf{I} = \mathbf{0} \text{ for body-fixed axes})$$

from which, since $\mathbf{I}$ is symmetric,

$$\tilde{\delta}\mathbf{H}\cdot\omega = (\mathbf{I}\cdot\tilde{\delta}\omega)\cdot\omega = (\mathbf{I}\cdot\omega)\cdot\tilde{\delta}\omega = \mathbf{H}\cdot\tilde{\delta}\omega. \tag{A3b}$$

The result $\tilde{\delta}\mathbf{H}\cdot\omega = \mathbf{H}\cdot\tilde{\delta}\omega$ is reminiscent of the similar "reciprocity" result in linear elasticity:

$$\sigma\cdot d\mathbf{e} = d\sigma\cdot\mathbf{e} \quad (\sigma, \mathbf{e}\text{: stress and strain tensors}).$$

Equation (A3) can also be derived as follows: since $T = T(\omega_x, \omega_y, \omega_z)$, we have

$$\delta T = \frac{\partial T}{\partial\omega_x}\,\delta\omega_x + \frac{\partial T}{\partial\omega_y}\,\delta\omega_y + \frac{\partial T}{\partial\omega_z}\,\delta\omega_z = H_x\delta\omega_x + H_y\delta\omega_y + H_z\delta\omega_z$$

$$= \mathbf{H}\cdot\tilde{\delta}\omega. \tag{A3c}$$

However, despite (A3b), it should be noted that

$$\delta\mathbf{H}\cdot\omega \neq \mathbf{H}\cdot\delta\omega; \tag{A3d}$$

this is a rather treacherous situation (see, e.g., Föppl (1909)) that has claimed many victims in the past. In fact, due to

$$\tilde{\delta}\mathbf{H}\cdot\omega = (\delta\mathbf{H} - \delta\theta\times\mathbf{H})\cdot\omega = \delta\mathbf{H}\cdot\omega + (\omega\times\mathbf{H})\cdot\delta\theta,$$

$$\mathbf{H}\cdot\tilde{\delta}\omega = \mathbf{H}\cdot(\delta\omega - \delta\theta\times\omega) = \mathbf{H}\cdot\delta\omega - (\omega\times\mathbf{H})\cdot\delta\theta,$$

equating their right sides produces

$$\mathbf{H}\cdot\delta\omega - \delta\mathbf{H}\cdot\omega = 2(\omega\times\mathbf{H})\cdot\delta\theta \neq \mathbf{0}. \tag{A3e}$$

By repeating the process using $d(\cdots)$ differentiation, or by applying (A3e) for $\delta(\cdots)\to d(\cdots)$ (since no explicit time dependence occurs here) yields

$$\mathbf{H}\cdot d\omega - d\mathbf{H}\cdot\omega = 2(\omega\times\mathbf{H})\cdot d\theta = 0, \quad \text{since } d\theta = \omega dt,$$

i.e.,

$$d\mathbf{H}\cdot\omega = \mathbf{H}\cdot d\omega. \tag{A3f}$$

An additional related result follows from (A3f): we have

$$\mathbf{H}\cdot d\omega = \mathbf{H}\cdot(\tilde{d}\omega + d\theta\times\omega) = \mathbf{H}\cdot\tilde{d}\omega,$$

$$d\mathbf{H}\cdot\omega = (\tilde{d}\mathbf{H} + d\theta\times\mathbf{H})\cdot\omega = \tilde{d}\mathbf{H}\cdot\omega + \underbrace{(\mathbf{H}\times\omega)\cdot d\theta}_{=0},$$

i.e.,

$$\mathbf{H}\cdot d\omega = \mathbf{H}\cdot\tilde{d}\omega = \tilde{d}\mathbf{H}\cdot\omega. \tag{A3g}$$

All these show us the "obvious" result

$$\left.\begin{array}{l} d(\mathbf{H}\cdot\omega) = \tilde{d}(\mathbf{H}\cdot\omega),\\ \delta(\mathbf{H}\cdot\omega) = \tilde{\delta}(\mathbf{H}\cdot\omega),\end{array}\right\} \tag{A3h}$$

(A3i)

and also

$$\delta T = \tilde{\delta}T, \tag{A3j}$$

since $\mathbf{H}\cdot\omega$, T are scalar invariants.

An independent derivation of

$$\frac{dT}{dt} = \mathbf{H}\cdot\frac{d\omega}{dt} = \mathbf{H}\cdot\frac{\tilde{d}\omega}{dt}\text{: (change comma to a colon)}$$

we have, successively,

$$\frac{dT}{dt} = \frac{d}{dt}\left\{\frac{1}{2}\,\mathbf{H}\cdot\omega\right\} = \frac{d}{dt}\left\{\frac{1}{2}\,\omega\cdot\mathbf{I}\cdot\omega\right\}$$

$$= \frac{1}{2}\left\{\frac{d\omega}{dt}\cdot\mathbf{I}\cdot\omega + \omega\cdot\mathbf{I}\cdot\frac{d\omega}{dt}\right\} + \frac{1}{2}\left\{\omega\cdot\frac{d\mathbf{I}}{dt}\cdot\omega\right\}.$$

But:

(i) $\dfrac{d\omega}{dt}\cdot\mathbf{I}\cdot\omega = \omega\cdot\mathbf{I}\cdot\dfrac{d\omega}{dt}$, due to the $\mathbf{I}$ symmetry,

and

(ii) $$\frac{1}{2}\,\omega\cdot\frac{d\mathbf{I}}{dt}\cdot\omega = \frac{1}{2}\,\omega\cdot\left\{\frac{\tilde{d}\mathbf{I}}{dt} + \omega\times\mathbf{I} - \mathbf{I}\times\omega\right\}\cdot\omega$$

$$= \frac{1}{2}\,\omega\cdot\frac{\tilde{d}\mathbf{I}}{dt}\cdot\omega + \frac{1}{2}\,\omega\cdot(\omega\times\mathbf{I})\cdot\omega - \frac{1}{2}\,\omega\cdot(\mathbf{I}\times\omega)\cdot\omega$$

$$= \frac{1}{2}\,\omega\cdot[\omega\times(\mathbf{I}\cdot\omega)] - \frac{1}{2}\,\omega\cdot[\mathbf{I}\cdot(\omega\times\omega)]$$

$$= \frac{1}{2}\,\omega\cdot[\omega\times\mathbf{H}] = 0 \quad ,$$

i.e.,

$$\omega\cdot\frac{d\mathbf{I}}{dt}\cdot\omega = 0.$$

Here we have used the identities for any two vectors $\mathbf{a}$, $\mathbf{b}$ and a second-order tensor $\mathbf{A}$:

$$(\mathbf{a}\times A)\cdot\mathbf{b} = \mathbf{a}\times(A\cdot\mathbf{b}), \quad (\mathbf{A}\times\mathbf{a})\cdot\mathbf{b} = \mathbf{A}\cdot(\mathbf{a}\times\mathbf{b}),$$

and

Downloaded 03 May 2010 to 171.66.16.247. Redistribution subject to ASME license or copyright; see http://www.asme.org/terms/Terms_Use.cfm

$$\frac{d\mathbf{A}}{dt}=\frac{\tilde{d}\mathbf{A}}{dt}+\omega\times\mathbf{A}-\mathbf{A}\times\omega;$$

see e.g., Lur'e (1968).

From the above $T = \mathbf{H}\cdot\dot{\omega}\equiv\mathbf{H}\cdot\alpha$ follows. All these results are most easily and safely derived using indicial notation (e.g., cartesian tensors)—the latter also makes fewer demands on memory and notation.

(b)

$$\begin{aligned}\delta' W &\equiv S(d\mathbf{f}\cdot\delta\mathbf{r})\\ &= S[d\mathbf{f}\cdot(\delta\theta\times\mathbf{r})]\\ &= [S(\mathbf{r}\times d\mathbf{f})]\cdot\delta\theta\\ &= \mathbf{M}\cdot\delta\theta,\end{aligned}\tag{A4}$$

where

$d\mathbf{f}$ = total impressed force on particle of mass dm and position vector $\mathbf{r}$,

$\mathbf{M}$ = $S(\mathbf{r}\times d\mathbf{f})$

= total impressed moment about O.

(A4*a*)

(c)

$$\begin{aligned}\delta' P &\equiv S(dm\mathbf{v}\cdot\delta\mathbf{r})\\ &= \text{total virtual work of momenta}\\ &= S[dm\mathbf{v}\cdot(\delta\theta\times\mathbf{r})]\\ &= S[dm\delta\theta\cdot(\mathbf{r}\times\mathbf{v})],\end{aligned}$$

or finally

$$\delta' P=\mathbf{H}\cdot\delta\theta,\tag{A5}$$

where

$$\mathbf{H}\equiv S[\mathbf{r}\times(dm\mathbf{v})]=\text{angular momentum } B \text{ about } O.$$

Therefore,

$$\begin{aligned}\frac{d}{dt}\delta' P &= \frac{d}{dt}(\mathbf{H}\cdot\delta\theta)\\ &= \frac{d\mathbf{H}}{dt}\cdot\delta\theta+\mathbf{H}\cdot\frac{d(\delta\theta)}{dt}\\ &= \left(\frac{\tilde{d}\mathbf{H}}{dt}+\omega\times\mathbf{H}\right)\cdot\delta\theta+\mathbf{H}\cdot\left(\frac{\tilde{d}}{dt}(\delta\theta)+\omega\times\delta\theta\right)\\ &= \frac{\tilde{d}\mathbf{H}}{dt}\cdot\delta\theta+\mathbf{H}\cdot\frac{\tilde{d}}{dt}(\delta\theta)+\underbrace{\{(\omega\times\mathbf{H})\cdot\delta\theta+\mathbf{H}\cdot(\omega\times\delta\theta)\}}_{=0}\end{aligned}$$

or

$$\frac{d}{dt}[S(dm\mathbf{v}\cdot\delta\mathbf{r})]=\frac{d\mathbf{H}}{dt}\cdot\delta\theta+\mathbf{H}\cdot\frac{d(\delta\theta)}{dt}=\frac{\tilde{d}\mathbf{H}}{dt}\cdot\delta\theta+\mathbf{H}\cdot\frac{\tilde{d}(\delta\theta)}{dt}.\tag{A6}$$

Again, as pointed out earlier, this is a general result: for any two general vectors $\mathbf{a}$, $\mathbf{b}$, we have

$$\left.\begin{aligned}&\frac{d}{dt}(\mathbf{a}\cdot\mathbf{b})=\frac{d\mathbf{a}}{dt}\cdot\mathbf{b}+\mathbf{a}\cdot\frac{d\mathbf{b}}{dt}=\frac{\tilde{d}\mathbf{a}}{dt}\cdot\mathbf{b}+\mathbf{a}\cdot\frac{\tilde{d}\mathbf{b}}{dt}=\frac{\tilde{d}}{dt}(\mathbf{a}\cdot\mathbf{b});\\ &\text{and}\\ &\delta(\mathbf{a}\cdot\mathbf{b})=\tilde{\delta}(\mathbf{a}\cdot\mathbf{b}),\quad d(\mathbf{a}\cdot\mathbf{b})=\tilde{d}(\mathbf{a}\cdot\mathbf{b}).\end{aligned}\right\}\tag{A7}$$

Similar identities can be found for other "higher" (mixed) invariant products.

Now inserting all these results into the LCE (A1) we find

$$\mathbf{H}\cdot\tilde{\delta}\omega+\mathbf{M}\cdot\delta\theta=\frac{\tilde{d}\mathbf{H}}{dt}\cdot\delta\theta+\mathbf{H}\cdot\frac{\tilde{d}(\delta\theta)}{dt},$$

and rearranging

$$\frac{\tilde{d}\mathbf{H}}{dt}\cdot\delta\theta+\mathbf{H}\cdot\left\{\frac{\tilde{d}(\delta\theta)}{dt}-\tilde{\delta}\omega\right\}=\mathbf{M}\cdot\delta\theta$$

and invoking the transitivity Eq. (15*a*) for the second left-side term, we find

$$\frac{\tilde{d}\mathbf{H}}{dt}\cdot\delta\theta+\mathbf{H}\cdot(\delta\theta\times\omega)=\mathbf{M}\cdot\delta\theta,$$

or

$$\underbrace{\left(\frac{\tilde{d}\mathbf{H}}{dt}+\omega\times\mathbf{H}\right)}_{\frac{d\mathbf{H}}{dt}}\cdot\delta\theta=\mathbf{M}\cdot\delta\theta,\tag{A8}$$

from which if the $\delta\theta$ is independent (unconstrained), we find the familiar Eulerian equations

$$\frac{d\mathbf{H}}{dt}\equiv\frac{\tilde{d}\mathbf{H}}{dt}+\omega\times\mathbf{H}=\mathbf{M}.\tag{A9}$$

Actually, this form is slightly more general than the original Eulerian forms (of 1758/1765, 1760/1767). The proof given here has been sketched by Hamel (1949); the present treatment, however, achieves a hitherto missing clarity. Extensions to the most general rigid-body motion can be easily obtained. Finally, if $\delta\theta$ is constrained, by say

$$\mathbf{l}\cdot\delta\theta=0,\quad \mathbf{l}=\mathbf{l}(t,q)\text{: known vector (in form)},\tag{A10}$$

then (A8) and (A10) combine via the technique of Lagrange's multipliers to yield the equation

$$\begin{aligned}\frac{d\mathbf{H}}{dt} &= \mathbf{M}+\Lambda\mathbf{l}\\ &= \text{total external moment (impressed + constraint)}\end{aligned}\tag{A11}$$

where

$\Lambda=\Lambda(t)$ = Lagrangean multiplier

(so that $\Lambda\mathbf{l}$ = constraint reaction moment).

2 The HP (of varying, or varied, action) derivation: here the starting point is the (time) integral variational equation:

$$\begin{aligned}\delta' A &\equiv \int_{t_1}^{t_2}(\delta T+\delta' W)dt\\ &= \{S(dm\mathbf{v}\cdot\delta\mathbf{r})\}_{t_1}^{t_2},\ (t_{1,2}\text{: two arbitrary times});\end{aligned}\tag{A12}$$

see, e.g., Hamel (1949).

Inserting into it the previously found (15*a*)

$$\begin{aligned}\delta T=\mathbf{H}\cdot\tilde{\delta}\omega &= \mathbf{H}\cdot\left\{\frac{\tilde{d}}{dt}\delta\theta+\omega\times\delta\theta\right\}\\ &= \left(\frac{\tilde{d}}{dt}(\mathbf{H}\cdot\delta\theta)-\frac{\tilde{d}\mathbf{H}}{dt}\cdot\delta\theta\right)-(\omega\times\mathbf{H})\cdot\delta\theta,\end{aligned}$$

$$\delta' W=\mathbf{M}\cdot\delta\theta,$$

Downloaded 03 May 2010 to 171.66.16.247. Redistribution subject to ASME license or copyright; see http://www.asme.org/terms/Terms_Use.cfm

we obtain (invoking (A6),(A7))

$$\delta' A = -\int_{t_1}^{t_2} dt \left\{ \frac{\tilde{d}\mathbf{H}}{dt} + \omega \times \mathbf{H}) - \mathbf{M} \right\} \cdot \delta\theta + \{\mathbf{H} \cdot \delta\theta\}_{t_1}^{t_2} = \{\mathbf{H} \cdot \delta\theta\}_1^{t_2},$$

or

$$-\int_{t_2}^{t_1} \left[\underbrace{\left(\frac{\tilde{d}\mathbf{H}}{dt} + \omega \times \mathbf{H} \right)}_{d\mathbf{H}/dt} - \mathbf{M} \right] \cdot \delta\theta dt = 0,$$

from which, for arbitrary $\delta\theta$, between t_1, t_2, Eq. (A9) follows again.

It is to be noticed that in this derivation no assumptions need be made about $\delta\theta(t_1)$, $\delta\theta(t_2)$, (such as the customary $\delta\theta(t_1) = \delta\theta(t_2) = \mathbf{0}$).

Downloaded 03 May 2010 to 171.66.16.247. Redistribution subject to ASME license or copyright; see http://www.asme.org/terms/Terms_Use.cfm

Charles E. Smith
Professor,
Mem. ASME.

Pao-Pao Liu
Graduate Assistant.

Department of Mechanical Engineering,
Oregon State University,
Corvallis, OR 97331

Coefficients of Restitution

Simplified procedures for predicting post-collision motion in a mechanical system usually incorporate a "coefficient of restitution," a ratio that must be estimated before the prediction can be completed. Two such ratios have been widely used for some time and a third has been introduced recently by W. J. Stronge. The dependence of these ratios on parameters that characterize various collisions is examined here, using simplifying assumptions about the contact mechanism and with a finite element code. For some collisions all three coefficients of restitution are identical, while significant distinctions can result from other combinations of system configuration, direction of approach velocity, and coefficient of friction.

Introduction

Coefficients of restitution have been defined in two ways, in terms of the normal component of impulse during compression and that during restitution, and in terms of the normal components of approach and separation velocities. The ratios so defined have often been regarded as "material constants," with the implication that they are independent of such things as system configuration, direction of approach velocity, and friction. It is sometimes stated that they bear a simple, direct relationship to the loss of kinetic energy during collision, but this is true only under special circumstances.

A third quantity, the ratio of work of the normal force during compression to that during restitution, has been suggested by W. J. Stronge (1990) to be a better candidate for a "material constant" than the above-mentioned coefficients of restitution. In the following, this is incorporated into analysis of planar collisions and the results examined to indicate how the system parameters affect the distinctions among these coefficients.

Impulse, Velocity Change, and Work of Contact Forces

Consider a mechanical system, within which rigid bodies B and B' collide as the points P and P' on their respective surfaces move into coincidence. The difference between the velocities of P and P' will be denoted as

$$\bar{\mathbf{v}} = \mathbf{v}^P - \mathbf{v}^{P'}$$

and the impulse of the force exerted on B by B' denoted as $\mathbf{g}$. Then, if the duration of contact is sufficiently short that changes in configuration during contact and impulses of other forces are negligible, the change in the velocity difference will be related to the impulse by[1]

$$\bar{\mathbf{v}} - \mathbf{v} = \mathbf{N} \cdot \mathbf{g} \tag{1}$$

in which $\mathbf{v}$ is the value of $\bar{\mathbf{v}}$ at initial contact, and the symmetric dyadic $\mathbf{N}$ may be evaluated as follows: First, introduce a set of generalized speeds u_r and corresponding partial velocities $\mathbf{v}_r$ such that

$$\bar{\mathbf{v}} = \sum_{r=1}^{n} \mathbf{v}_r u_r.$$

Next, write the kinetic energy of the system in terms of these generalized speeds[2]

$$K = \frac{1}{2} \sum_r \sum_s m_{rs} u_r u_s$$

and invert the symmetric matrix of the coefficients

$$[n_{rs}] \triangleq [m_{rs}]^{-1}.$$

Next, introduce a set of mutually perpendicular unit vectors $\mathbf{e}_i$ ($i = 1, 2, 3$) and evaluate the quantities

$$l_{ir} = \mathbf{e}_i \cdot \mathbf{v}_r.$$

The components of $\mathbf{N}$ may then be evaluated from

$$\mathbf{e}_i \cdot \mathbf{N} \cdot \mathbf{e}_j = \sum_r \sum_s l_{ir} l_{js} n_{rs}. \tag{2}$$

The impulse-momentum relationships for the system, focused on the point of contact, are embodied in Eq. (1). The dyadic $\mathbf{N}$ provides complete inertial information necessary for relating the reaction at the contact point to local change in motion. It depends on the distribution of mass and the constraints, if any.

The inertia operator $\mathbf{N}$ also plays an important role in the work done by the contact forces at P and P'. In the definition

Contributed by the Applied Mechanics Division of THE AMERICAN SOCIETY OF MECHANICAL ENGINEERS for presentation at the 1992 ASME Winter Annual Meeting, Anaheim, CA, Nov. 8–13, 1992.

Discussion on this paper should be addressed to Prof. Leon M. Keer, The Technological Institute, Northwestern University, Evanston, IL 60208, and will be accepted until four months after final publication of the paper itself in the ASME JOURNAL OF APPLIED MECHANICS.

Manuscript received by the ASME Applied Mechanics Division, Sept. 18, 1991. Associate Technical Editor: R. L. Huston.

Paper No. 92-WA/APM-5.

[1] A derivation and two examples are presented in Smith (1991). The inverse of $\mathbf{N}$ is denoted there as $\mathbf{M}$.

[2] Situations in which K contains terms that are linear in generalized speeds will not be considered here.

Copyright © 1992 by ASME
Downloaded 03 May 2010 to 171.66.16.247. Redistribution subject to ASME license or copyright; see http://www.asme.org/terms/Terms_Use.cfm

of this work, the displacements of P and P' are understood to be consistent with their belonging to *rigid* bodies B and B', even though it is recognized that deformation is necessary to preclude penetration in the real system. With this in mind and the force exerted on B by B' at P denoted as $\mathbf{f}$, the sum of the works of this force and that of the force exerted on B' by B at P' may be expressed as

$$W = \int \mathbf{f} \cdot \mathbf{v}^P dt + \int -\mathbf{f} \cdot \mathbf{v}^{P'} dt$$

$$= \int \mathbf{f} \cdot \bar{\mathbf{v}} dt$$

$$= \int \bar{\mathbf{v}} \cdot d\mathbf{g}$$

$$= \int (\mathbf{v} + \mathbf{g} \cdot \mathbf{N}) \cdot d\mathbf{g}$$

$$= \mathbf{v} \cdot \mathbf{g} + \frac{1}{2} \mathbf{g} \cdot \mathbf{N} \cdot \mathbf{g}$$

$$= \left[\mathbf{v} + \frac{1}{2} (\bar{\mathbf{v}} - \mathbf{v}) \right] \cdot \mathbf{g}$$

$$= \frac{\mathbf{v} + \bar{\mathbf{v}}}{2} \cdot \mathbf{g} \tag{3}$$

As it must, this agrees with the expression for change in kinetic energy, Eq. (11*b*), of Smith (1991). In the real system, this "work" represents a transformation of rigid-body kinetic energy to forms associated with deformation and dissipation.

Combining Eqs. (1) and (3) leads to the following alternative expression for the change in kinetic energy:

$$\Delta K = \frac{1}{2} (\bar{\mathbf{v}} \cdot \mathbf{N}^{-1} \cdot \bar{\mathbf{v}} - \mathbf{v} \cdot \mathbf{N}^{-1} \cdot \mathbf{v}). \tag{4}$$

Because $\mathbf{x} \cdot \mathbf{N}^{-1} \cdot \mathbf{x}$ is a positive definite function of $\mathbf{x}$, this indicates that the greatest possible loss of kinetic energy during contact would occur if $\bar{\mathbf{v}} = \mathbf{0}$ (i.e., if the points P and P' have the same velocity) at the instant the reaction $\dot{\mathbf{g}} = \mathbf{0}$.

For evaluation of the impulse and changes in velocities, additional relationships between force and relative motion in the region of contact are required. If the complexity of the interactions among deformations, surface tractions, and sliding with friction renders a careful analysis impracticable for the purpose at hand, an acceptably accurate prediction may still be obtainable using suitable simplifying assumptions. Some such assumptions are discussed in Smith (1991).

To express contact relationships, it is convenient to choose one of the basis vectors to be perpendicular to the surfaces at contact; specifically, let $\mathbf{n}$ be a unit vector perpendicular to the common tangent to the surfaces at P and P' and directed from B' into B, and let $\mathbf{t}_1$ and $\mathbf{t}_2$ be unit vectors parallel to this tangent plane. Normal and tangential components of impulse will then be denoted as

$$\mathbf{g}_n = \mathbf{n} \cdot \mathbf{g}\mathbf{n}$$

$$\mathbf{g}_t = \mathbf{n} \times (\mathbf{g} \times \mathbf{n}) = g_1 \mathbf{t}_1 + g_2 \mathbf{t}_2$$

and those of velocities denoted similarly.

Contact Assumptions

To simplify the analysis, it is common to assume that one of two ratios, each called the *coefficient of restitution*, can be estimated with acceptable accuracy. The definitions of these and of a third, related ratio are given in the following. Two of the three definitions incorporate the notion of two phases of the contact. The duration between initial contact and the instant at which the normal component of the velocity difference $\bar{\mathbf{v}} = \mathbf{v}^P - \mathbf{v}^{P'}$ reaches zero is called the "compression phase" and the remainder of the period of contact is called the "restitution phase." In this definition, the motions of P and P' are understood to be consistent with their belonging to *rigid* bodies B and B', as stated previously in conjunction with the definition of work. Thus, the instant that separates the compression and restitution phases is that at which maximum penetration (in the rigid-body idealization) is reached, i.e., when $\mathbf{n} \cdot (\mathbf{N} \cdot \mathbf{g} + \mathbf{v}) = 0$.

One of the quantities commonly called the coefficient of restitution is the ratio

$$c \triangleq \frac{g_{nR}}{g_{nC}} \tag{5}$$

in which g_{nC} is the normal component of impulse $\mathbf{g}$ accumulated during the compression phase and g_{nR} is that accumulated during the restitution phase.

Another ratio, also known as the coefficient of restitution, is defined by

$$e \triangleq \frac{\mathbf{n} \cdot \mathbf{w}}{-\mathbf{n} \cdot \mathbf{v}} \tag{6}$$

in which $\mathbf{w}$ denotes the value of the velocity difference $\mathbf{v}^P - \mathbf{v}^{P'}$ at the instant contact ends. In some circumstances, the foregoing two coefficients of restitution are equal, but in general they may differ.

A third quantity, which may be equal to the two ratios above under some circumstances, is defined by

$$d \triangleq \sqrt{\frac{W_{nR}}{-W_{nC}}} \tag{7}$$

in which W_{nC} is the work of the normal components of the reaction forces at the contact point during the compression phase, and W_{nR} is the work for the restitution phase. As in the definition leading to Eq. (3), the work of the normal forces incorporates displacements of P and P' as points of *rigid* bodies (which would imply an artificial penetration, as mentioned above). In the real system, deformation must be such that the normal component of relative displacement remains zero during contact. $-W_{nC}$ then represents a transformation of kinetic energy to forms associated with deformation during the compression phase, and W_{nR} represents the return of deformation-associated energy to rigid-body kinetic energy during the restitution phase.

The work of the normal components of reaction forces at any time during contact may be expressed as

$$W_n = \int \bar{v}_n dg_n.$$

Now, if there is no inertia coupling between the normal and tangential directions (i.e., $\mathbf{n}$ is parallel to a principal direction of $\mathbf{N}$) or if the tangential component of the contact force is zero (as when the surfaces are smooth), the variation of $\bar{v}_n$ with g_n is linear:

$$\bar{v}_n = v_n + N_{nn} g_n.$$

In either of these cases, then,

$$W_n = \int (v_n + N_{nn} g_n) dg_n = \frac{v_n + \bar{v}_n}{2} g_n$$

and, as can be seen from Fig. 1,

$$c = d = e.$$

However, the presence of **t-n** inertia coupling permits tangential impulse to affect normal velocity, so that the $\bar{v}_n - g_n$ curve may be nonlinear. In general, then, the sum of the works of

Downloaded 03 May 2010 to 171.66.16.247. Redistribution subject to ASME license or copyright; see http://www.asme.org/terms/Terms_Use.cfm

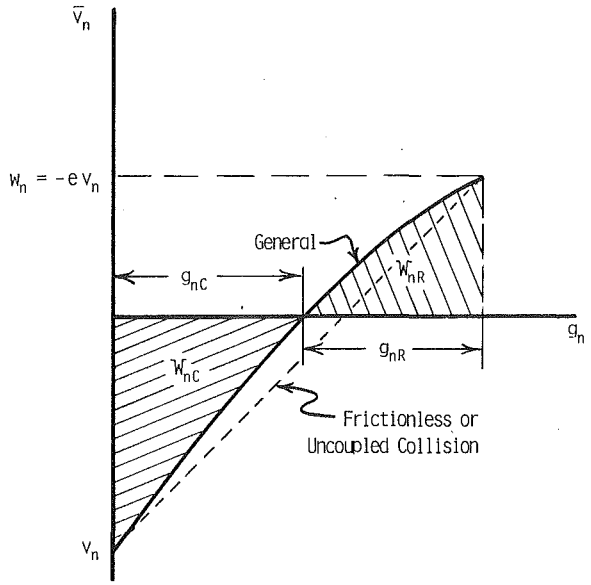


Fig. 1 Variation of normal velocity with normal impulse during contact

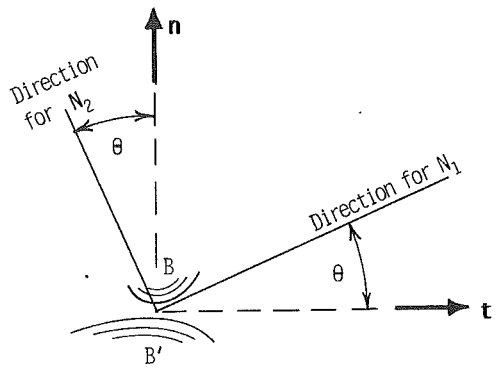


Fig. 2 Alignment of principal directions of inertia dyadic with contact surface

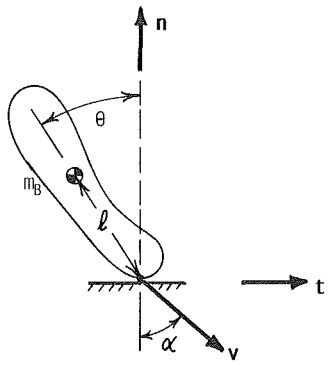


Fig. 3 Unconstrained body impinging on an immobile plane

the normal components of the contact forces is *not* equal to $g_n(v_n + \bar{v}_n)/2$ and the values of c, d, and e may be expected to differ.

The extent to which these values may differ depends on several parameters in addition to the inertia coupling expressed in **N**, such as the coefficient of friction, the compliance characteristics of the contacting bodies, and the approach velocity. Evaluation of these effects requires examination of the contact process in some detail. Results of two such analyses are presented in the following; the first is of planar collisions under the simplifying assumption that the tangential compliance is zero, and the second is of four collisions analyzed by means of a computer code based on a finite element model.

Simplified Prediction of Planar Collisions

If one of the principal directions of **N** is parallel to the plane tangent to the bodies at the point of contact, if **v** (the velocity difference at initiation of contact) is perpendicular to this direction, and if the contact mechanism does not contain coupling between this and other directions, then the impulse **g** and velocity change $\bar{\mathbf{v}} - \mathbf{v}$ can be expected to be perpendicular to this direction. It is then natural to define one of the unit tangent vectors to be perpendicular to this direction and drop its subscript, the other unit tangent vector being of no use to the analysis. In this basis, Eq. (1) can then be written as

$$\begin{Bmatrix} \bar{v}_t - v_t \\ \bar{v}_n - v_n \end{Bmatrix} = \begin{bmatrix} N_{tt} & N_{tn} \\ N_{nt} & N_{nn} \end{bmatrix} \begin{Bmatrix} g_t \\ g_n \end{Bmatrix}. \tag{8}$$

The components of **N** in the above array are the a, b, and a' introduced in the procedure described in Routh (1905), which deals with the special case of the collision of two, unconstrained bodies. The procedure described there will be used to examine possible distinctions among the ratios c, d, and e defined above. Assumptions inherent in this procedure are that the tangential force obeys Coulomb's law of friction, and that there is no tangential compliance of the bodies in contact. This latter assumption can lead to inaccuracies in the prediction, especially where there is a tendency to reverse the direction of sliding during contact; nevertheless, the predictions give an indication of the effects of parameters on the disctinctions among c, d, and e. These assumptions are precisely those inherent in the analyses of Keller (1986) and Stronge (1990), so that relationshps among c, d, and e predicted by each should be identical.

Any **N** for a planar collision can be characterized completely by its two eigenvalues and the angle between the normal direction and a selected one of the two principal directions of **N**. With this and simplicity of expressions for **N** in mind, the following definitions are made. The larger eigenvalue of **N** will be denoted as N_1, the smaller as N_2, and corresponding principal directions oriented as shown in Fig. 2. The array of components of **N** can then be expressed as

$$\begin{bmatrix} N_{tt} & N_{tn} \\ N_{nt} & N_{nn} \end{bmatrix} = \frac{1}{m} \begin{bmatrix} 1+\lambda\cos 2\theta & \lambda\sin 2\theta \\ \lambda\sin 2\theta & 1-\lambda\cos 2\theta \end{bmatrix}$$

in which

$$m \triangleq \frac{2}{N_1+N_2} \quad \lambda \triangleq \frac{N_1-N_2}{N_1+N_2}.$$

λ can be seen to lie between zero and one, larger values reflecting more pronounced inertia coupling. For contact between an end of an unconstrained, slender rod and an immobile body, $\lambda = 0.6$, while the value of λ for the double pendulum discussed in Smith (1991) is 0.964 in the configuration considered here.

An example that may help to promote a physical sense of the meanings of these parameters is the collision of an unconstrained body with an immobile body, as depicted in Fig. 3. In this case the principal directions of **N** are evident without calculation, and the eigenvalues can be readily determined from simple application of linear and angular impulse-momentum relationships. In terms of the mass m_B, the central radius of gyration k, and the distance l from the contact point to the center of mass, the principal values of **N** are

$$N_1 = \frac{1+l^2/k^2}{m_B}, \quad N_2 = \frac{1}{m_B}$$

Downloaded 03 May 2010 to 171.66.16.247. Redistribution subject to ASME license or copyright; see http://www.asme.org/terms/Terms_Use.cfm

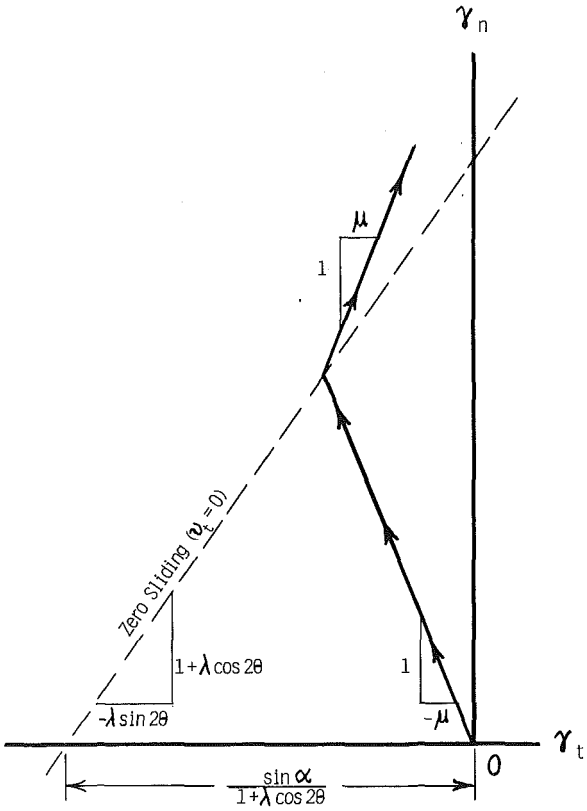


Fig. 4 Variation of normal impulse with tangential impulse during contact, with no tangential compliance

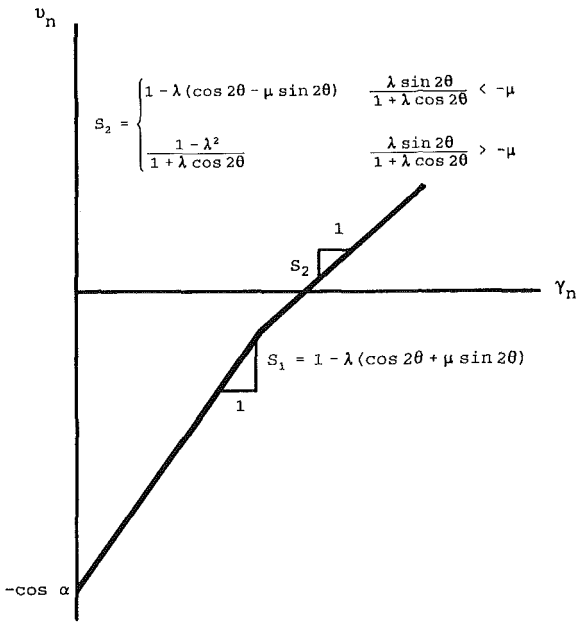


Fig. 5 Variation of normal velocity with normal impulse during contact, with no tangential compliance

and the mass and coupling parameters become

$$m=\frac{m_B}{1+l^2/2k^2},\ \lambda=\frac{1}{1+2k^2/l^2}.$$

Another parameter that affects the collision is the angle α between $-\mathbf{n}$ and $\mathbf{v}$. (See Fig. 3.) Observe that a redundancy in results would occur if the sign of both the angles θ and α were reversed; in the following, this redundancy is avoided by restricting α to the range $(0, \pi/2)$ and considering values of θ throughout the range $(-\pi/2, \pi/2)$.

The values of velocity difference and impulse during contact will be designated in terms of dimensionless quantities v and γ, according to the definitions

$$\bar{\mathbf{v}}=v(v_t\mathbf{t}+v_n\mathbf{n})$$

$$\mathbf{g}=mv(\gamma_t\mathbf{t}+\gamma_n\mathbf{n})$$

wherein v designates the magnitude of the velocity difference at initial contact. In terms of these quantities, Eq. (8) becomes

$$\begin{Bmatrix} v_t-\sin\alpha \\ v_n+\cos\alpha \end{Bmatrix}=\begin{bmatrix} 1+\lambda\cos2\theta & \lambda\sin2\theta \\ \lambda\sin2\theta & 1-\lambda\cos2\theta \end{bmatrix}\begin{Bmatrix} \gamma_t \\ \gamma_n \end{Bmatrix}. \tag{9}$$

The maximum possible loss in kinetic energy can be determined by setting $\mathbf{v} = \mathbf{0}$ in Eq. (4) and expressed in terms of the parameters introduced for planar collisions as

$$|\Delta K|_{\max}=\frac{1}{2}\,\mathbf{v}\cdot\mathbf{N}^{-1}\cdot\mathbf{v}=\frac{[1+\lambda\cos2(\alpha-\theta)]mv^2}{2(1-\lambda^2)} \tag{10}$$

This will be used to normalize the loss of kinetic energy as predicted by the following simplified analysis and by a finite element code.

Following the procedure described in Routh (1905), a plot of tangential impulse versus normal impulse is constructed, with the line of zero sliding, expressed by

$$v_t=(1+\lambda\cos2\theta)\gamma_t+(\lambda\sin2\theta)\gamma_n+\sin\alpha=0$$

included. A typical such diagram is shown in Fig. 4. A point representing the value of impulse at any stage of the contact begins at point 0 and generates a path with increasing γ_n throughout contact. Now, the assumption of zero tangential compliance and Coulomb's law of friction imply that, whenever $v_t \neq 0$,

$$\frac{d\gamma_t}{d\gamma_n}=-\mu\,\frac{v_t}{|v_t|}.$$

This means that any portion of the path to the right of the zero-sliding line (where $v_t > 0$) will be linear with $d\gamma_t/d\gamma_n = -\mu$, and any portion to the left of this line (where $v_t < 0$) will be linear with $d\gamma_t/d\gamma_n = \mu$. Coulomb's law further requires that whenever $|d\gamma_t/d\gamma_n| < \mu$, $v_t = 0$. Thus, upon reaching the zero-sliding line, the representative point will either follow that line or pass into the region of reverse sliding, depending on the slope of the zero-sliding line; specifically, during the remainder of contact, reverse sliding will occur if

$$\mu<\frac{-\lambda\sin2\theta}{1+\lambda\cos2\theta}$$

and no sliding will occur if this condition is not met. It is also possible for contact to end before the representative point reaches the line of zero sliding, in which case unidirectional sliding takes place throughout contact. This will necessarily occur if

$$\frac{-\lambda\sin2\theta}{1+\lambda\cos2\theta}<-\mu$$

but can also occur without this condition.

Previously, a value of c (Eq. (5)) has been selected as the criterion to estimate where separation occurs. W. J. Stronge (1990) has suggested that the quantity d (Eq. (7)) would be a better selection as "the" coefficient of restitution, i.e., a quantity that would be primarily dependent on materials. To incorporate this into the present graphical analysis, it is helpful to map the path of the representative point onto the $v_n - \gamma_n$ plane, since work of the normal components of the reactions at $P - P'$ can be expressed by

$$W_n=\int \bar{v}_n dg_n=mv^2\int v_n d\gamma_n.$$

Downloaded 03 May 2010 to 171.66.16.247. Redistribution subject to ASME license or copyright; see http://www.asme.org/terms/Terms_Use.cfm

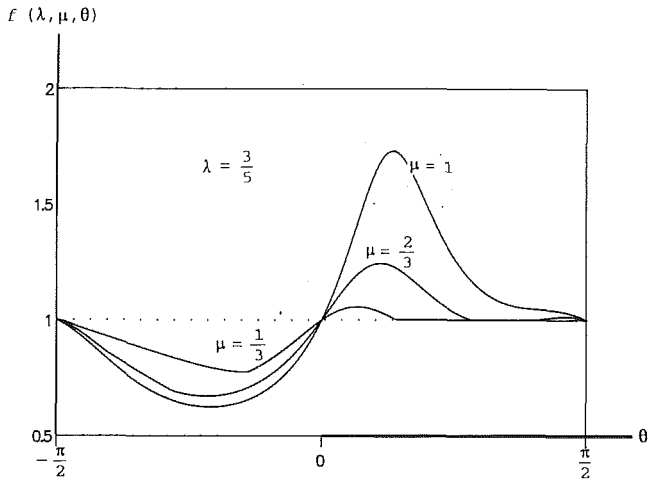


Fig. 6 Ratios *e/d* = d/c, extreme with respect to α, with no tangential compliance

A typical such map, obtained using the second line of Eq. (9), is shown in Fig. 5. If the path in this figure happens to have a single slope throughout, $c = d = e$. More generally, however, there will be two segments with different slopes, these slopes depending on λ, θ, and μ. The approach angle α affects the positions of the segments, but not the slopes. With this in mind it can be shown that, for fixed λ, θ, and μ, the value of α that yields the greatest distinctions among c, d, and e is that that places the discontinuity in slope on the γ_n-axis, and which satisfies

$$\tan\alpha = \frac{\mu(1+\lambda\cos2\theta) - \lambda\sin2\theta}{1-\lambda(\cos2\theta+\mu\sin2\theta)}. \tag{11}$$

The dependence of c/d and e/d (extreme with respect to α) on the remaining parameters may be expressed with the help of the expressions for slopes shown in Fig. 5, and are

$$\left(\frac{e}{d}\right)_{\text{extr}} = \left(\frac{d}{c}\right)_{\text{extr}} = f(\lambda,\mu,\theta)$$

in which

$$f = \begin{cases} \sqrt{\dfrac{1-\lambda(\cos2\theta-\mu\sin2\theta)}{1-\lambda(\cos2\theta+\mu\sin2\theta)}} & \dfrac{\lambda\sin2\theta}{1+\lambda\cos2\theta} \le -\mu \\ \sqrt{\dfrac{1-\lambda^2}{(1+\lambda\cos2\theta)[1-\lambda(\cos2\theta+\mu\sin2\theta)]}} & -\mu \le \dfrac{\lambda\sin2\theta}{1+\lambda\cos2\theta} \le \mu \\ 1 & \mu \le \dfrac{\lambda\sin2\theta}{1+\lambda\cos2\theta}. \end{cases} \tag{12}$$

For the lower values of $\lambda \sin 2\theta/(1 + \lambda\cos2\theta)$, reverse sliding takes place; for the intermediate values, sliding does not occur once it is halted; and for the higher values, unidirectional sliding takes place throughout contact.

The effects of μ and θ on the distinctions among c, d, and e are indicated in Fig. 6. The value of λ used there is 3/5, which is that for the end of a slender rod colliding with an immobile body.

Predictions From a Finite Element Code

To reveal how much error might result from the assumptions underlying the above-described prediction, four collisions were analyzed by means of the ANSYS finite element code. Each collision was between a circular cylindrical rod with hemispherical ends and an infinitely stiff, immobile plane. In each case the overall length of the rod was 3.5 diameters and the normal component of the approach velocity was $3.95 \times 10^{-6}\sqrt{E/\rho}$, wherein E is Young's modulus and ρ is the density. The rod was treated as perfectly elastic, with Poisson's ratio equal to 0.28. For each of two coefficients of friction, 0.5 and 1.0, two collisions were analyzed; one was with the axis of the cylinder oriented such that the simplified prediction described above would yield a maximum value of f and the other with the axis oriented to yield a minimum value of f. The direction of the approach velocity was chosen to satisfy Eq. (11) in each case.

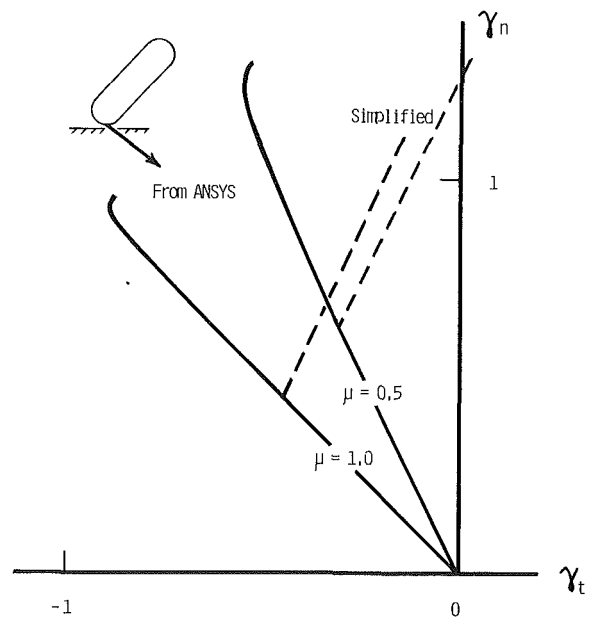


Fig. 7 Variation of normal impulse with tangential impulse, for two cases in which $\theta < 0$

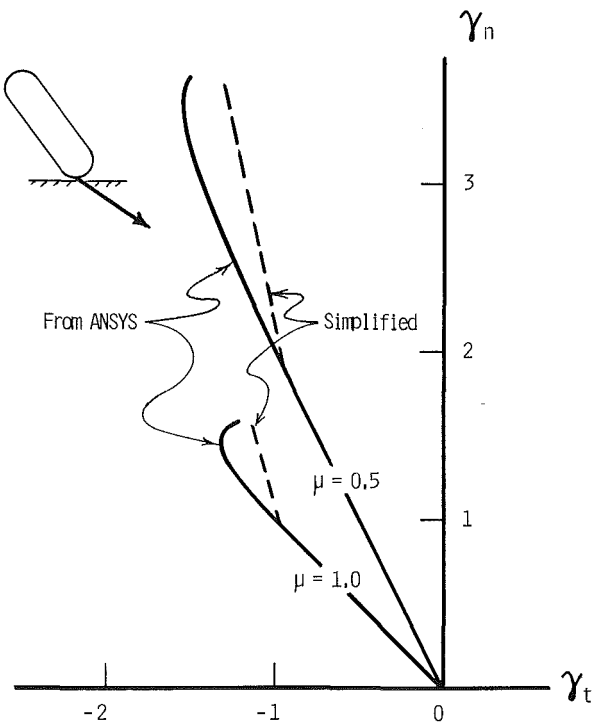


Fig. 8 Variation of normal impulse with tangential impulse, for two cases in which $\theta > 0$

Downloaded 03 May 2010 to 171.66.16.247. Redistribution subject to ASME license or copyright; see http://www.asme.org/terms/Terms_Use.cfm

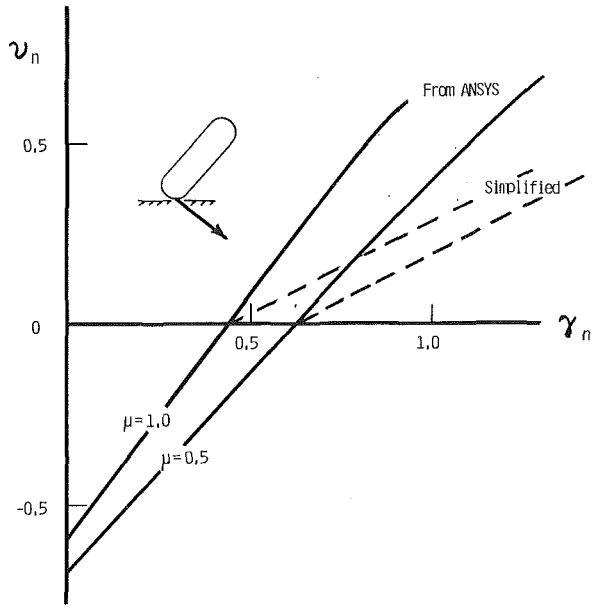


Fig. 9 Variation of normal velocity with normal impulse, corresponding to Fig. 7

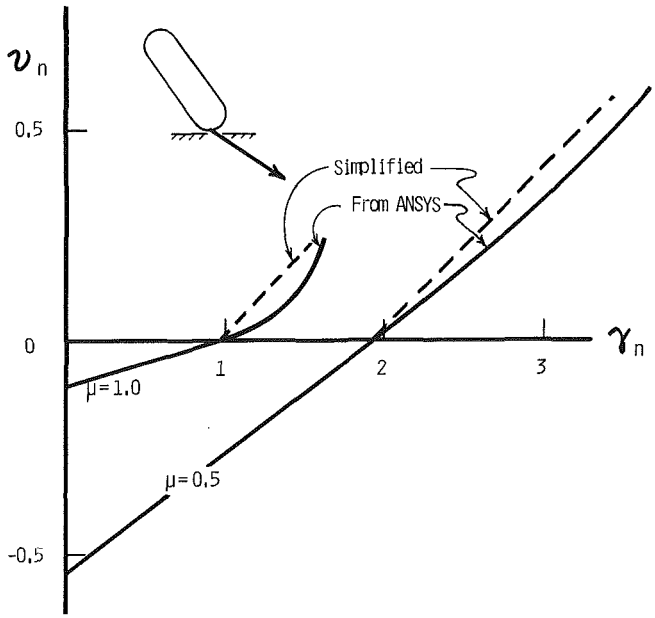
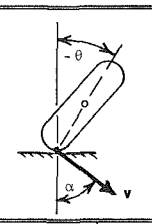
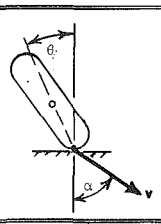


Fig. 10 Variation of normal velocity with normal impulse, corresponding to Fig. 8

For each case, a node was located at the point of initial contact, and this surrounded by 96 nodes throughout the region of the surface extending from the first-contact node to about 0.02 of the radius of the rod. Inward from this surface region, the mesh was correspondingly fine to a depth of about 0.0002 of the radius. The mesh was coarser throughout the remainder of the rod. "Gap" elements were used to deal with the formation and release of contact throughout a neighborhood of the initial contact point, each element sticking or sliding according to Coulomb's law of friction.

Of course, deformation will be a major contributor to the velocity of the node at the point of initial contact. To make meaningful comparisons between the results from the code and those from the analysis based on rigid-body mechanics, the following procedure was used to filter out the contribution from deformation: Components of stress were integrated throughout the region of contact to determine components of force, and these then integrated with respect to time to determine the impulse. This impulse was then used in Eq. (8) to evaluate the "rigid-body velocity," to be compared hereinafter with the values of $\bar{\mathbf{v}}$ predicted by the simplified analysis.

Table 1

				
μ	0.5	1.0	0.5	1.0
θ	$-0.198\ \pi$	$-0.188\ \pi$	$0.086\ \pi$	$0.124\ \pi$
α	$0.2619\ \pi$	$0.2971\ \pi$	$0.3175\ \pi$	$0.4667\ \pi$
λ	0.6124	0.6157	0.6392	0.6325
$\lambda\sin2\theta/(1+\lambda\cos2\theta)$	-0.4847	-0.4616	0.2124	0.3065
f	0.69	0.61	1.15	1.98
e/d	0.93	0.97	1.2	2.3
c/d	1.01	1.00	0.96	0.7
$(\Delta K)_{SIMP}/\lvert\Delta K\rvert_{max}$	-0.35	-0.57	-0.44	-0.91
$(\Delta K)_{ANSYS}/\lvert\Delta K\rvert_{max}$	-0.06	-0.01	-0.28	-0.84

Figures 7 and 8 show the variation of the direction of impulse during contact, as predicted by the simplified theory and by the ANSYS code. As these figures show, the assumption of negligible tangential compliance has a striking effect on the predicted tangential reaction, particularly where the inertia coupling is such that the normal reaction tends to reverse the direction of tangential velocity (i.e., $\theta < 0$). Figures 9 and 10 show the corresponding variations of the normal component of velocity with the normal component of impulse, permitting visual estimates of W_{nC} and W_{nR}.

Table 1 summarizes results from the ANSYS code and corresponding predictions of the simplified analysis for the same four collisions. The code yielded values of d that differ from 1 by less than error we believe may accumulate through the computation. The loss of rigid-body kinetic energy predicted by the ANSYS code were computed using Eq. (3) with computed values of $\mathbf{g}$ and $\bar{\mathbf{v}}$ at the time the reaction $\dot{\mathbf{g}} = \mathbf{0}$. For the simplified analysis, Stronge's suggestion (assuming $d = 1$) was used to determine the implied loss of kinetic energy. Kinetic energy losses for both predictions are given as ratios of that predicted to the maximum possible, which is given by Eq. (10). The values of e/d and c/d from the code are to be compared with f and $1/f$, the values predicted by the simplified analysis.

Conclusions

The simplified analysis of the contact presented in Routh (1905) and used by Keller (1986) and Stronge (1990) indicates that the three coefficients of restitution can differ significantly, depending on the amount of friction, the direction of the approach velocity, and the inertial characteristics of the system. For planar collisions in which inertia coupling tends to reverse the direction of tangential velocity, the normal velocity ratio may be expected to be lower than the other two coefficients, whereas for cases in which α and θ have the same sign, the normal velocity ratio may be expected to be larger than the other two coefficients. When applied to the perfectly elastic body we modeled with the ANSYS program, the simplified analysis (which neglects tangential compliance) appears to overestimate the distinction considerably in the first case and to underestimate slightly the distinction in the latter case.

Downloaded 03 May 2010 to 171.66.16.247. Redistribution subject to ASME license or copyright; see http://www.asme.org/terms/Terms_Use.cfm

If the suggestion by Stronge (1990) is valid, that the normal work ratio d is essentially a material-dependent constant, then normal velocity ratios would be expected to vary considerably with α and θ if significant inertia coupling and friction are present. Some simple experiments with a "superball" bonded to the end of a rod support this expectation, this body exhibiting values of e ranging from 0.7 to 1.4 when colliding with a rigid surface with orientations and approach velocities corresponding to the minimum and maximum values of f (Eqs. (11) and (12) and Fig. 6).

Where there is significant internal dissipation, the tangential compliance neglected by Stronge and others may well play an important part in the dissipation mechanism, since stiffnesses are typically of the same order of magnitude in the tangential and normal directions. Thus, if there is to be a constant that rationally predicts internal dissipation, it will need to be incorporated in a model capable of separating dissipation through sliding from that associated with normal *and* tangential deformation.

Acknowledgments

We are indebted to George P. Laird of the U.S. Bureau of Mines for his substantial guidance in the use of the ANSYS code.

The experiments mentioned above were carried out by Ronald W. Buckingham, David R. Morris, and Carl T. Soderquist, senior students in Mechanical Engineering.

References

Keller, J. B., 1986, "Impact with Friction," ASME JOURNAL OF APPLIED MECHANICS, Vol. 53, pp. 1–4.

Routh, E. J., 1905, *Dynamics of a System of Rigid Bodies*, Vol. 1, Macmillan and Co., London.

Smith, C. E., 1991, "Predicting Rebounds Using Rigid-Body Dynamics," ASME JOURNAL OF APPLIED MECHANICS, Vol. 58, pp. 754–758.

Stronge, W. J., 1990, "Rigid Body Collisions with Friction," *Proc. R. Soc. Lond.*, Vol. A431, pp. 169–181.

Downloaded 03 May 2010 to 171.66.16.247. Redistribution subject to ASME license or copyright; see http://www.asme.org/terms/Terms_Use.cfm

A Second-Order Approximate Analytical Solution of a Simple Pendulum by the Process Analysis Method

S. J. Liao[1]

Institute of Shipbuilding,
University of Hamburg,
Laemmerseith 90,
D-2000 Hamburg 60,
Federal Republic of Germany

In this paper, a new kind of analytical method of nonlinear problem called the process analysis method (PAM) is described and used to give a second-order approximate solution of a simple pendulum. The PAM does not depend on the small parameter supposition and therefore can overcome the disadvantages and limitations of the perturbation expansion method. The analytical approximate results at the second-order of approximation are in good agreement with the numerical results. They are compared with perturbation solutions, and it appears that even the first-order solutions are more accurate than the perturbation solutions at second-order of approximation.

1 Introduction

It is difficult to solve nonlinear problems, either numerically or theoretically. Traditionally, iterative techniques were used to find numerical solutions of nonlinear problems, but nearly all iterative methods are sensitive to initial solutions. Thus, it is not easy to obtain converged results in cases of strong nonlinearity. On the other side, as mentioned by Nayfeh (1980) and O'Malley (1974), the perturbation expansion method is widely used to analyze simple nonlinear problems. It is well known that the perturbation method is based on *small* or *great* parameters. But, unfortunately, not every nonlinear problem has such *small* or *great* parameters. And it also seems difficult to decide whether or not a parameter is *small* or *great enough*.

For example, it is well known that the motion of a simple pendulum is periodical, which can be described mathematically as follows:

$$\begin{cases} \dfrac{d^2\theta}{dt^2}+\omega_0^2 \sin\theta=0 \\ \theta(t)=\beta \quad \text{for} \quad t=0 \\ \theta'(t)=0 \quad \text{for} \quad t=0 \end{cases} \tag{1}$$

where θ is the angle of swing, t is the time, β is the initial angle of swing, $\omega_0 = \sqrt{\dfrac{g}{l}}$; here, g is the gravity acceleration and l is the length of the simple pendulum.

It is easy to know that $|\theta(t)| \le \beta$. If the initial angle β is small enough, then θ is a small quantity and $\sin(\theta) \approx \theta$ is a good approximation; thus, the above equation has the solution

$$\theta(t)=\beta \cos(\omega_0 t) \tag{2}$$

with the period

$$T_0=\frac{2\pi}{\omega_0}. \tag{3}$$

But, if β is not small, the above solutions are not accurate. For example, when $\beta = 5\pi/9$, the numerical result of the period is $1.232T_0$. Therefore, higher-order approximate solutions should be given in this case. However, this is not easy, because Eq. (1) is nonlinear and has *no* small parameters. It seems doubtful to be able to give a good perturbation approximation of $\theta(t)$ and its corresponding period, especially in the case of the great initial angle β.

As mentioned by Ortega and Rheinboldt (1970), the continuous mapping technique, or so-called homotopy method, has been generally used to widen the domain of convergence of a given method or as a procedure to obtain sufficiently close starting points. The continuous mapping technique embeds a parameter that typically ranges from zero to one. When the embedding parameter is zero, the equation is one of the linear system. When it is one, the equation is the same as the original. Then, one can *iterate*, numerically along the solution path, by incrementing the imbedding parameter from zero to one; this continuously maps the initial linear solutions into the solutions of the original equation. Note that iterative techniques are used at each step along the solution path if the equation is nonlinear.

[1]Present address: Institute of Underwater Engineering, Department of Naval Architecture and Ocean Engineering, Shanghai Jiao Tong University, Shanghai 200030, P. R. China.

Contributed by the Applied Mechanics Division of THE AMERICAN SOCIETY OF MECHANICAL ENGINEERS for publication in the ASME JOURNAL OF APPLIED MECHANICS.

Discussion on this paper should be addressed to the Technical Editor, Prof. Leon M. Keer, The Technological Institute, Northwestern University, Evanston, IL 60208, and will be accepted until four months after final publication of the paper itself in the JOURNAL OF APPLIED MECHANICS.

Manuscript received by the ASME Applied Mechanics Division, May 5, 1990; final revision, Sept. 30, 1991. Associate Technical Editor: D. J. Inman.

Copyright © 1992 by ASME
Downloaded 03 May 2010 to 171.66.16.247. Redistribution subject to ASME license or copyright; see http://www.asme.org/terms/Terms_Use.cfm

If we derive the continuous mapping with respect to the imbedding parameter we will obtain the corresponding *linear* equations of this kind of derivatives. This is an interesting property of continuous mapping and a pure mathematical proof can be given. By means of this property of continuous mapping, a kind of general numerical method for nonlinear problems, called the finite process method (FPM), has been described by Liao (1991a, 1991b). The finite process method can avoid the use of iterative techniques to solve numerically nonlinear problems and it is insensitive to the initial solutions. Therefore, it can overcome the disadvantages and limitations of iterative techniques.

Based on the same property of continuous mapping, an analytical method for nonlinear problems, called the process analysis method (PAM), has been derived. It is interesting that this kind of analytical method *does not* depend on *small* or *great* parameters and therefore can overcome the limitations of perturbation techniques.

In this paper, the basic idea of the process analysis method is described and examined by using a simple pendulum as an example. The main purpose of this paper is to give a kind of general analytical method for nonlinear problems, which is *independent* on *small* or *great* parameters.

2 Basic Ideas of the Process Analysis Method

Let

$$\omega=\frac{2\pi}{T} \tag{4}$$

and

$$z=\omega t \tag{5}$$

where T is the period and ω is the frequence of a simple pendulum, respectively.

Then Eq. (1) is transformed into

$$\begin{cases} \dfrac{d^2\theta}{dz^2}+\lambda^2\sin\theta=0 \\ \theta(z)=\beta \quad \text{for } z=0 \\ \theta'(z)=0 \quad \text{for } z=0. \end{cases} \tag{6}$$

Here,

$$\lambda=\frac{\omega_0}{\omega}=\frac{T}{T_0} \tag{7}$$

denotes the non-dimensional frequence or period of a simple pendulum.

A kind of continuous mapping, $\theta(z)\to\theta(z;p),\lambda\to\lambda(p)$ can be constructed as follows:

$$\begin{cases} \dfrac{\partial^2\theta(z;p)}{\partial z^2}+\lambda^2(p)\theta(z;p) \\ \quad +p\lambda^2(p)\{\sin[\theta(z;p)]-\theta(z;p)\}=0 \\ \theta(z;p)=\beta \quad \text{for } z=0 \\ \dfrac{\partial\theta(z;p)}{\partial z}=0 \quad \text{for } z=0 \end{cases} \tag{8}$$

where $p\in[0,1]$, called the process-independent variable or imbedding variable.

For simplicity, call the continuous mapping $\theta(z;p)$ and $\lambda(p)$ *process*, or more precisely, *zero-order process*. Then, Eq. (8) could be called the *zero-order process equation*.

When $p=0$, from zero-order process Eq. (8), one has the *initial equation*:

$$\begin{cases} \dfrac{\partial^2\theta(z;0)}{\partial z^2}+\lambda^2(0)\theta(z;0)=0 \\ \theta(z;0)=\beta \quad \text{for } z=0 \\ \dfrac{\partial\theta(z;0)}{\partial z}=0 \quad \text{for } z=0. \end{cases} \tag{9}$$

Denote $\lambda_0=\lambda(0)$ and $\theta_0(z)=\theta(z;\theta)$. For simplicity, select $\lambda_0=1.0$, called the *initial solution* of $\lambda(p)$. It is easy to know that the above *linear* Eq. (9) has the solution

$$\theta_0(z)=\beta\cos(z). \tag{10}$$

When $p=1.0$, from the zero-order process Eq. (8), one has the *final equation*

$$\begin{cases} \dfrac{\partial^2\theta(z;1.0)}{\partial z^2}+\lambda^2(1.0)\sin\theta(z;1.0)=0 \\ \theta(z;1.0)=\beta \quad \text{for} \quad z=0 \\ \dfrac{\partial\theta(z;1.0)}{\partial z}=0 \quad \text{for} \quad z=0. \end{cases} \tag{11}$$

Equations (11) are the same as (6). Denote that $\theta_f(z)=\theta(z;1.0)$ and $\lambda_f=\lambda(1.0)$, called the *final solution*. It is easy to understand that $\theta_f(z)$ and λ_f are just what we want to know.

From the above analysis, we can see that the zero-order process Eq. (8) gives a kind of relation between the initial solutions $\theta_0=\beta\cos(z)$, $\lambda_0=1.0$ and the final solutions θ_f, λ_f. But this kind of relation is nonlinear, because the zero-order process Eq. (8) is generally a nonlinear one. In the following part of this section, a linear relation between θ_0, λ_0, and θ_f, λ_f will be introduced and used to give a kind of solution at the second-order approximation.

Define

$$\theta^{[k]}(z;p)=\frac{\partial^k\theta(z;p)}{\partial p^k} \tag{12}$$

$$\lambda^{[k]}(p)=\frac{\partial^k\lambda(p)}{\partial p^k} \tag{13}$$

as the kth-order *process derivative* of $\theta(z;p)$ and $\lambda(p)$, respectively.

Suppose:

1 $\theta(z;p)$, $\lambda(p)$ have definition in $p\in[0,1]$, $0\le z<\infty$ and
2 there exist $\theta^{[k]}(z;p)$ and $\lambda^{[k]}(p)$ in $p\in[0,1]$, $0\le z<\infty$ for $k\ge 1$

then, according to Taylor's theory, $\theta_0(z)$, λ_0 and $\theta_f(z)$, λ_f have the following relations:

$$\theta_f(z)=\theta_0(z)+\sum_{k=1}^{\infty}\frac{\theta^{[k]}(z;p)}{k!}\bigg|_{p=0} \tag{14}$$

$$\lambda_f=\lambda_0+\sum_{k=1}^{\infty}\frac{\lambda^{[k]}(p)}{k!}\bigg|_{p=0} \tag{15}$$

where $k!=1\times2\times\cdots\times(k-1)\times k$ is the factorial of k. $\theta^{[k]}(z;p)$,$\lambda^{[k]}(p)$ at $p=0$ can be obtained in the following way.

Deriving the zero-order process Eq. (8) with respect to p, one can obtain the *first-order process equation* as follows:

Downloaded 03 May 2010 to 171.66.16.247. Redistribution subject to ASME license or copyright; see http://www.asme.org/terms/Terms_Use.cfm

$$\begin{cases} \dfrac{\partial^2\theta^{[1]}(z;p)}{\partial z^2}+\lambda^2(p)\theta^{[1]}(z;p)+2\lambda(p)\lambda^{[1]}(p)\theta(z;p) \\ +\lambda^2(p)\{\sin[\theta(z;p)]-\theta(z;p)\} \\ +2p\lambda(p)\lambda^{[1]}(p)\{\sin[\theta(z;p)]-\theta(z;p)\} \\ +p\lambda^2(p)\{\cos\theta(z;p)-1\}\theta^{[1]}(z;p)=0 \\ \theta^{[1]}(z;p)=0 \quad \text{for } z=0 \\ \dfrac{\partial\theta^{[1]}(z;p)}{\partial z}=0 \quad \text{for } z=0. \end{cases} \tag{16}$$

When $p = 0.0$, from first-order process Eq. (16), one has

$$\begin{cases} \dfrac{\partial^2\theta^{[1]}(z;0)}{\partial z^2}+\lambda_0^2\theta^{[1]}(z;0) \\ =\lambda_0^2\{\theta_0(z)-\sin\theta_0\}-2\lambda_0\lambda^{[1]}(0)\theta_0 \\ \theta^{[1]}(z;0)=0 \quad \text{for } z=0 \\ \dfrac{\partial\theta^{[1]}(z;0)}{\partial z}=0 \quad \text{for } z=0. \end{cases} \tag{17}$$

It can be derived that

$$\sin(\theta_0)=2\sum_{m=0}^{\infty}(-1)^m J_{2m+1}(\beta)\cos(2m+1)z \tag{18}$$

and

$$\cos(\theta_0)=J_0(\beta)+2\sum_{m=1}^{\infty}(-1)^m J_{2m}(\beta)\cos(2mz) \tag{19}$$

where, $J_n(\beta)$ is first-sort of Bessel function denoted as

$$J_n(\beta)=\sum_{k=0}^{\infty}\frac{(-1)^k(\beta/2)^{2k+n}}{k!(k+n)!}. \tag{20}$$

Substituting (18) in (17), one has the first-order process equation at $p = 0$ as follows:

$$\begin{cases} \dfrac{\partial^2\theta^{[1]}(z;0)}{\partial z^2}+\theta^{[1]}(z;0)=\{\beta-2J_1(\beta)-2\beta\lambda_0^{[1]}\}\cos(z) \\ \qquad -2\displaystyle\sum_{m=1}^{\infty}(-1)^m J_{2m+1}(\beta)\cos(2m+1)z \\ \theta^{[1]}(z;0)=0, \quad \text{for } z=0 \\ \dfrac{\partial\theta^{[1]}(z;0)}{\partial z}=0, \quad \text{for } z=0. \end{cases} \tag{21}$$

In order to let the above Eq. (21) have finite solution (i.e., the secular terms should be eliminated), it must be satisfied that

$$\begin{aligned} \lambda^{[1]}(0)&=\frac{1}{2}-\frac{J_1(\beta)}{\beta} \\ &=\frac{1}{2}\sum_{k=1}^{\infty}(-1)^{k+1}\left(\frac{\beta}{2}\right)^{2k}\frac{1}{k!(k+1)!} \\ &=\frac{\beta^2}{16}-\frac{1}{24}\left(\frac{\beta}{2}\right)^4+\cdots. \end{aligned} \tag{22}$$

Thus, the *linear* differential Eq. (21) has solution

$$\theta^{[1]}(z;0)=\sum_{m=0}^{\infty}a_m\cos(2m+1)z, \tag{23}$$

where

$$a_0=-\sum_{m=1}^{\infty}a_m \tag{24}$$

$$a_m=\frac{(-1)^m J_{2m+1}(\beta)}{2m(m+1)} \quad (m\geq 1). \tag{25}$$

Deriving the first-order process Eq. (16) with respect to p and then let $p = 0$, one can obtain the *second-order process equation* at $p = 0$ as follows:

$$\begin{cases} \dfrac{\partial^2\theta^{[2]}(z;0)}{\partial z^2}+\theta^{[2]}(z;0) \\ =4\lambda^{[1]}(0)\{\theta_0-\sin\theta_0\}+2\{1-\cos\theta_0)\theta^{[1]}(z;0) \\ \quad -4\lambda^{[1]}(0)\theta^{[1]}(z;0)-2\{(\lambda^{[1]})^2+\lambda^{[2]}(0)\}\theta_0 \\ \theta^{[2]}(z;0)=0 \quad \text{for } z=0 \\ \dfrac{\partial\theta^{[2]}(z;0)}{\partial z}=0 \quad \text{for } z=0. \end{cases} \tag{26}$$

The above equation is linear with respect to $\theta^{[2]}(z;0)$. Substituting (18), (19), (22), (23) in (26) and eliminating the secular terms, we have

$$\begin{aligned} \lambda_0^{[2]}=3&\left[\frac{1}{2}-\frac{J_1(\beta)}{\beta}\right]^2-\frac{J_2(\beta)J_3(\beta)}{4\beta} \\ &-\frac{1}{\beta}\left[\frac{J_1(\beta)}{\beta}+\frac{J_2(\beta)-J_0(\beta)}{2}\right]\sum_{m=1}^{\infty}\frac{(-1)^m J_{2m+1}(\beta)}{m(m+1)} \\ &-\sum_{m=2}^{\infty}\frac{J_{2m}(\beta)}{2m\beta}\left[\frac{J_{2m+1}(\beta)}{m-1}-\frac{J_{2m-1}(\beta)}{m-1}\right] \end{aligned} \tag{27}$$

and

$$\begin{aligned} \theta^{[2]}(z;0)=&\sum_{m=0}^{\infty}b_m\cos(2m+1)z \\ &+\sum_{m=1}^{\infty}\sum_{n=1}^{\infty}c_{mn}\cos[2(n+m)+1]z \\ &+\sum_{m=1}^{\infty}\left(\sum_{\substack{n=1\\ n\neq m\\ n\neq m-1}}^{\infty}\right)d_{mn}\cos[2(n-m)+1]z \end{aligned} \tag{28}$$

where

$$b_0=-\sum_{m=1}^{\infty}b_m-\sum_{m=1}^{\infty}\sum_{n=1}^{\infty}c_{mn}-\sum_{m=1}^{\infty}\left(\sum_{\substack{n=1\\ n\neq m\\ n\neq m-1}}^{\infty}\right)d_{mn} \tag{29}$$

$$b_m=\frac{(-1)^m J_{2m+1}(\beta)}{2m(m+1)}\left\{2-\frac{4J_1(\beta)}{\beta}-\frac{1}{m(m+1)}\left[\frac{J_1(\beta)}{\beta}-\frac{J_0(\beta)}{2}\right]\right\} +\frac{(-1)^m a_0[J_{2m}(\beta)-J_{2m+2}(\beta)]}{2m(m+1)} \quad (m\geq 1) \tag{30}$$

$$c_{mn}=\frac{(-1)^{m+n}J_{2m}(\beta)J_{2n+1}(\beta)}{4n(n+1)(n+m)(n+m+1)} \quad (m\geq 1, n\geq 1) \tag{31}$$

$$d_{mn}=\frac{(-1)^{m+n}J_{2m}(\beta)J_{2n+1}(\beta)}{4n(n+1)(n-m)(n-m+1)} \quad (m\geq 1; n\geq 1,\ n\neq m,\ n\neq m-1). \tag{32}$$

2.1 Approximation of Frequence ω. According to

$$\omega(p)=\frac{\omega_0}{\lambda(p)} \tag{33}$$

and Taylor's theory, one has the first-order approximation of frequence ω as

Downloaded 03 May 2010 to 171.66.16.247. Redistribution subject to ASME license or copyright; see http://www.asme.org/terms/Terms_Use.cfm

$$\omega_1 = \omega_0 \left\{ \frac{1}{\lambda(p)} - \frac{\lambda^{[1]}(p)}{\lambda^2(p)} \right\} \Bigg|_{p=0}$$

$$= \omega_0 (1 - \lambda_0^{[1]}) \tag{34}$$

and second-order approximation of frequence as

$$\omega_2 = \omega_0 \left\{ \frac{1}{\lambda(p)} - \frac{\lambda^{[1]}(p)}{\lambda^2(p)} + \frac{[\lambda^{[1]}(p)]^2}{\lambda^3(p)} - \frac{\lambda^{[2]}(p)}{2\lambda^2(p)} \right\} \Bigg|_{p=0}$$

$$= \omega_0 \left\{ 1 - \lambda_0^{[1]} - \frac{1}{2} \lambda_0^{[2]} + (\lambda_0^{[1]})^2 \right\}. \tag{35}$$

2.2 Approximation of Period T. According to $T/T_0 = \omega_0/\omega$, one has the first-order approximation of period T as

$$\frac{T_1}{T_0} = \frac{1}{1 - \lambda_0^{[1]}}$$

$$= 1 + \frac{\beta^2}{16} + \frac{1}{48} \left(\frac{\beta}{2} \right)^4 + \cdots \tag{36}$$

and the second-order approximation of period as

$$\frac{T_2}{T_0} = \frac{1}{1 - \lambda_0^{[1]} - \frac{1}{2}\lambda_0^{[2]} + (\lambda_0^{[1]})^2}. \tag{37}$$

2.3 Approximation of $\theta(t)$. $\theta(t)$ at first-order of approximation is

$$\theta_1(t) = (\beta + a_0) \cos z + \sum_{m=1}^{\infty} a_m \cos(2m+1)z$$

$$= (\beta + a_0) \cos z - \frac{J_3(\beta)}{4} \cos(3z) + \frac{J_5(\beta)}{12} \cos(5z)$$

$$- \frac{J_7(\beta)}{24} \cos(7z) + \cdots = \left\{ \beta + \frac{\beta^3}{192} - \frac{1}{90} \left(\frac{\beta}{2} \right)^5 + \cdots \right\} \cos(\omega_1 t)$$

$$- \left\{ \frac{\beta^3}{192} - \frac{1}{96} \left(\frac{\beta}{2} \right)^5 + \cdots \right\} \cos(3\omega_1 t)$$

$$+ \left\{ \frac{1}{1440} \left(\frac{\beta}{2} \right)^5 + \cdots \right\} \cos(5\omega_1 t) + \cdots \tag{38}$$

and $\theta(t)$ at second-order of approximation is

$$\theta_2(t) = \left(\beta + a_0 + \frac{b_0}{2} \right) \cos(\omega_2 t) + \sum_{m=1}^{\infty} \left(a_m + \frac{b_m}{2} \right)$$

$$\times \cos[(2m+1)\omega_2 t] + \sum_{m=1}^{\infty} \sum_{n=1}^{\infty} \frac{c_{mn}}{2} \cos[2(n+m)+1](\omega_2 t)$$

$$+ \sum_{m=1}^{\infty} \left(\sum_{\substack{n=1 \\ n \neq m \\ n \neq m-1}}^{\infty} \right) \frac{d_{mn}}{2} \cos[2(n-m)+1](\omega_2 t). \tag{39}$$

As the last part of this section, let us discuss simply the expressions (14), and (15). The expressions (14), (15) describe a kind of relation between the initial solution $\theta_0 = \beta \cos(z)$, $\lambda_0 = 1.0$ and the final solution θ_f, λ_f by means of kth-order process derivatives $\theta^{[k]}(z;p)$ and $\lambda^{[k]}(p)$ at $p = 0$. The first-order process Eq. (17) and the second-order process Eq. (26) are *linear* with respect to $\theta^{[1]}(z;0)$ and $\theta^{[2]}(z;0)$, respectively. One can prove easily that the kth-order process equation ($k = 1, 2, 3, \cdots$) is *alway* linear with respect to $\theta^{[k]}(z;0)$. Therefore, $\theta^{[1]}(z;0)$, $\theta^{[2]}(z;0), \cdots, \theta^{[k]}(z;0), \cdots$, can be obtained without great difficulties. It means that the expressions (14), (15) give a kind of linear relation between the initial solution and final solution, although the zero-order process Eq. (8) is generally nonlinear. Using process derivatives, a nonlinear problem with respect to $\theta(z)$ can be transformed into an infinite number of linear problems with respect to $\theta^{[k]}(z;p)$ ($k = 1, 2, 3, \cdots, \infty$) at $p = 0$. But, only a finite number of linear problems with respect to $\theta^{[k]}(z;p)$($k = 1, 2, \cdots, n_p$) at $p = 0$ can be solved. It means that a nonlinear problem can be approximated by a finite number of linear problems. One would say that a nonlinear problem could be discretized into n_p linear problems with respect to kth-order process derivatives ($k = 1, 2, \cdots, n_p$). The greater n_p is, the more exact this approximation is. These are the basic ideas of the Process Analysis Method.

3 Comparisons to the Numerical and Perturbation Results

In order to examine the solutions given by PAM, it is valuable to compare them to the numerical results and perturbation solutions at the same order of approximation.

The original Eq. (1) can be solved numerically by means of Runge-Kutta's method. In numerical computation we select $\Delta t = 0.0001$ second and use double precision variables in the computer program.

On the other side, substitute

$$\sin(\theta) = \theta - \frac{\theta^3}{3!} + \frac{\theta^5}{5!} + \cdots \tag{40}$$

in (6) and *suppose* that β be *small enough* and θ and λ could be described, respectively, as

$$\theta = \beta \{ \Theta^{(0)} + \beta \Theta^{(1)} + \beta^2 \Theta^{(2)} + \cdots \}, \tag{41}$$

$$\lambda = 1 + \beta \Lambda^{(1)} + \beta^2 \Lambda^{(2)} + \cdots, \tag{42}$$

then, we can obtain

(a) perturbation solutions at first-order of approximation:

$$\theta(t) = \beta \cos(\omega_0 t) \tag{43}$$

$$\frac{T_1}{T_0} = 1, \tag{44}$$

(b) perturbation solutions at second-order of approximation:

$$\theta(t) = \left(\beta + \frac{\beta^3}{192} \right) \cos \left(\frac{\omega_0 t}{1 + \frac{\beta^2}{16}} \right) - \frac{\beta^3}{193} \cos \left(\frac{3\omega_0 t}{1 + \frac{\beta^2}{16}} \right) \tag{25}$$

$$\frac{T_2}{T_0} = 1 + \frac{\beta^2}{16}. \tag{46}$$

3.1 Comparison of Nondimensional Period T/T_0. The numerical and analytical results show that the nondimensional period T/T_0 of a simple pendulum is only dependent on the initial angle β. The detailed comparison of numerical and analytical results of T/T_0 obtained, respectively, by PAM and the perturbation method is given in Table 1. It seems that PAM solutions, even at first-order of approximation, generally agree

Table 1 Comparison of theoretical and numerical results of T/T_0

β	numerical method	PAM first-order	PAM second-order	perturbation method (second-order)
20°	1.008	1.008	1.008	1.008
30°	1.017	1.017	1.017	1.017
40°	1.031	1.031	1.031	1.030
50°	1.050	1.048	1.050	1.048
60°	1.073	1.070	1.073	1.069
70°	1.102	1.096	1.101	1.093
80°	1.138	1.127	1.136	1.122
90°	1.180	1.162	1.177	1.154
100°	1.232	1.201	1.225	1.190
110°	1.295	1.246	1.282	1.230
120°	1.373	1.296	1.347	1.274
130°	1.471	1.351	1.424	1.322

Downloaded 03 May 2010 to 171.66.16.247. Redistribution subject to ASME license or copyright; see http://www.asme.org/terms/Terms_Use.cfm

better with the numerical results than perturbation solutions at second-order of approximation. Even in the case of a great initial angle $\beta = 130$ deg, the second-order PAM solution can also give a good enough approximate value of a period, but the perturbation solution at the same-order of approximation has about a ten percent relative error.

3.2 Spectrum Analysis. It is well known that the solution $\theta(t)$ of the original Eq. (1) is a periodical function. So, $\theta(t)$ can be expressed in the form of a Fourier series.

Table 2 Spectrum analysis: Numerical result

β	30°	60°	90°	120°
$\bar{A}_1/\beta$	1.001	1.006	1.015	1.030
$\bar{A}_2/\beta$	3.29E-6	-2.21E-7	4.77E-8	3.38E-6
$\bar{A}_3/\beta$	-1.45E-3	-6.14E-3	-1.53E-2	-3.20E-2
$\bar{A}_4/\beta$	5.90E-7	-8.39E-8	-4.24E-8	1.43E-7
$\bar{A}_5/\beta$	3.43E-6	6.62E-5	3.96E-4	1.65E-3
$\bar{A}_6/\beta$	2.25E-7	-6.85E-8	-4.86E-8	1.41E-7
$\bar{A}_7/\beta$	-1.61E-7	-7.84E-7	-1.22E-5	-1.01E-4

Table 3 Spectrum analysis: First-order PAM solutions

β	30°	60°	90°	120°
A_1/β	1.001	1.005	1.011	1.017
A_3/β	-1.40E-3	-5.33E-3	-1.10E-2	-1.72E-2
A_5/β	1.61E-6	2.49E-5	1.19E-4	3.47E-4
A_7/β	-1.32E-9	-8.23E-8	-8.95E-7	-4.70E-6

Table 4 Spectrum analysis: Second-order PAM solutions

β	30°	60°	90°	120°
A_1/β	1.001	1.006	1.014	1.025
A_3/β	-1.45E-3	-6.03E-3	-1.41E-2	-2.60E-2
A_5/β	1.96E-6	4.57E-5	3.29E-4	1.34E-3
A_7/β	-1.88E-9	-2.22E-7	-4.27E-6	-3.57E-5

According to (38) and (39), the PAM solutions, at both first and second-order of approximation, can be written in the form of

$$\theta(t) = \sum_{k=1}^{\infty} A_{2k-1} \cos\,[(2k-1)\omega t] \qquad (k = 1, 2, \cdots). \quad (47)$$

Numerically, we have

$$\bar{A}_n = \frac{4}{T} \int_0^{T/2} \theta(t)\, \cos(n\omega t) dt \qquad (n = 1, 2, \cdots) \quad (48)$$

where the numerical solution of $\theta(t)$ is used, and thus a numerical integral over $[0, T/2]$ is needed.

The numerical values $\bar{A}_k (k = 1, 2, \cdots)$ and their corresponding analytical values at first and second-order of approximation given by PAM are shown as Table 2, Table 3, and Table 4, respectively. These results show that the second-order PAM solutions are in better agreement with the numerical solutions than the first-order PAM results. Note that the analytical values of $A_{2k} (k = 1, 2, \cdots)$ are zero and the corresponding numerical values of $\bar{A}_2$, $\bar{A}_4$, and $\bar{A}_6$ given in Table 2 are so small that they can be as the numerical errors in the integral. It appears that PAM captures the leading nonlinear harmonics found in the numerical solutions.

The numerical results and analytical solutions at second-order of approximation given, respectively, by the perturbation method and PAM, in case of $\beta = 5\pi/9$, are shown Fig. 1.

The analytical and numerical values of $A_k (k > 1)$ are so much smaller than A_1 that

$$\theta(t) = \beta \cos(\omega_2 t) \quad (49)$$

can give a good enough approximation of the original Eq. (1). This simplified expression gives essentially the same results as the second-order PAM solutions (39).

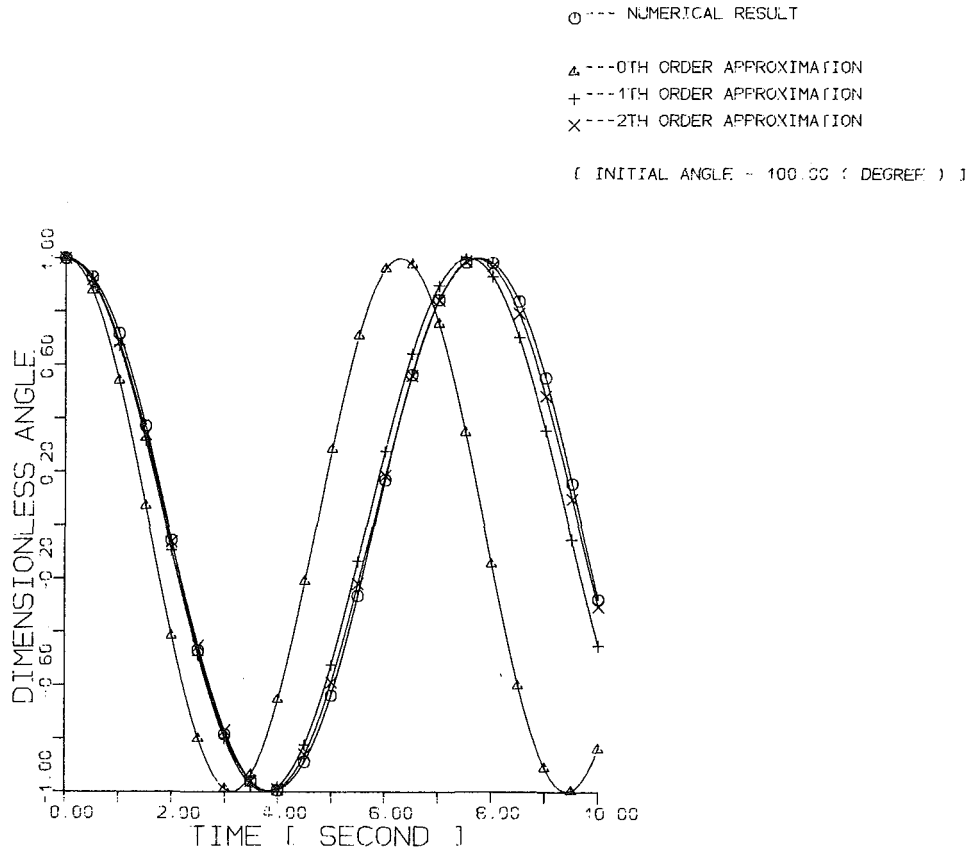


Fig. 1 Comparison of the analytical solutions at second-order of approximation to the numerical results

Downloaded 03 May 2010 to 171.66.16.247. Redistribution subject to ASME license or copyright; see http://www.asme.org/terms/Terms_Use.cfm

With comparison of expressions (36), (38), to expressions (46) and (45), it appears that the first-order PAM solutions include the terms of the perturbation solutions at second-order of approximation.

4 Conclusion and Discussion

In this paper, the basic idea of a new kind of analytical method for nonlinear problems, called PAM, is described and used to give a second-order approximate solutions of a simple pendulum. These solutions are compared to the numerical and perturbation solutions. The comparison shows that even the first-order PAM solutions agree better with the numerical solutions than the second-order perturbation solutions. So, we have reason to believe that PAM can indeed give more accurate analytical results than the perturbation method. Note that small or great parameter supposition is *not* needed for PAM. This is an advantage of PAM.

The perturbation method seems like a kind of art. Especially in the case of singular perturbation problems one must use different techniques, for example, the methods of multiple-scale expansions, the method of matched asymptotic expansions and so on, to solve different problems. Therefore, experiences seem important for the perturbation method. But, contrary to perturbation techniques, PAM has the simplicity in logic. This is another advantage of PAM.

The process analysis method is based on the two concepts of *process* and *process derivatives*. Process is a kind of continuous mapping which connects the initial solutions with the solutions of the original nonlinear problem. But this continuous mapping described by the zero-order process equation is generally nonlinear for a nonlinear problem. It is interesting and important that the kth-order process equations are linear with respect to the kth-order process derivatives. Then, according to Taylor's theory, the final solution and initial solution can be connected by the kth-order process derivatives ($k = 1, 2, \cdots$). That is why the process derivatives should be used.

The process analysis method is also based on suppositions, i.e., there should exist zero-order process and kth-order process derivatives, and the corresponding Taylor's series should converge to the solution of the original equations. Therefore, PAM is also dependent on suppositions, but these suppositions are *not* small-parameter suppositions. Owing to this reason, one can use it to solve more nonlinear problems, especially those without small or great parameters.

However, it should be pointed out that Taylor's series has generally a *finite* radius of convergence. (Only few functions have converged Taylor's series with infinite radius of convergence; for example, $\sin(x)$, $\cos(x)$, and so on.) PAM requires the kth-order process derivatives ($k = 1, 2, \cdots$) to exist, and to be well behaved and be bounded (i.e., they must not have turning points or diverge to infinity in $p \in [0, 1]$), and converge. Up to now, it is unknown whether or not the corresponding Taylor's series, given by PAM, have *always* a larger radius of convergence than an asymptotic series based on the perturbation method. These are the limitations of PAM.

Acknowledgments

Professors W. H. Isay and H. Soeding are acknowledged for their suggestions. Thanks to the DAAD for the financial support.

References

Liao, S. J., 1991a, "A General Numerical Method for The Solution of Gravity Wave Problems. Part 1: 2D Steep Gravity Waves in Shallow Water," *International Journal for Numerical Methods in Fluids*, Vol. 12, pp. 727–745.

Liao, S. J., 1991b, "The numerical limiting form of 2D nonlinear gravity waves past a submerged vortex by Finite Process Method (FPM)," *The Sixth International Workshop on Water Waves and Floating Bodies*, Woods Hole, Mass., pp. 139–143.

Nayfeh, A. H., 1980, *International to Perturbation Techniques*, John Wiley and Sons, New York.

Ortega, J. M., and Rheinboldt, W. C., 1970, *Iterative Solution of Nonlinear Equations in Several Variables*, New York, Academic Press, pp. 230–235.

O'Malley, R. E., 1974, *Introduction to Singular Perturbations*, Academic, New York.

Downloaded 03 May 2010 to 171.66.16.247. Redistribution subject to ASME license or copyright; see http://www.asme.org/terms/Terms_Use.cfm

Dynamic Analysis of Flexible Gear Trains/Transmissions: An Automated Approach

F. M. L. Amirouche
Professor,
Mem. ASME.

N. H. Shareef
Research Assistant.

M. Xie
Research Assistant.

Department of Mechanical Engineering,
University of Illinois at Chicago,
Chicago, IL 60680

In this paper an automated algorithmic method is presented for the dynamic analysis of geared trains/transmissions. These are treated as a system of interconnected flexible bodies. The procedure developed explains the switching of constraints with time as a result of the change in the contacting areas at the gear teeth. The elastic behavior of the system is studied through the employment of three-dimensional isoparametric elements having six degrees-of-freedom at each node. The contact between the bodies is assumed at the various nodes, which could be either a line or a plane. The kinematical expressions, together with the equations of motion using Kane's method, strain energy concepts, are presented in a matrix form suitable for computer implementation. The constraint Jacobian matrices are generated automatically based on the contact information between the bodies. The concepts of the relative velocity at the contacting points at the tooth pairs and the subsequent use of the transmission ratios in the analysis is presented.

1 Introduction

Geared transmissions are very common in a variety of mechanical engineering applications, which include machine tools, rotor craft systems, and automobiles, with the objective of torque multiplication/reduction and change of rotational speeds/directions. Two important aspects of these transmissions are the high speeds of rotation and the subsequent vibrations associated with them. The later is the result of the elastic deformation of the flexible bodies in the system, causing noise and transmission errors, the criticality of which is based on the type of application. A better understanding of the dynamic interaction between the various bodies, with the special emphasis on the contact problem, becomes more crucial. This would provide a means of improving the reliability of performance and to ultimately achieve an optimized design.

In the recent years, increased interest and attention is being paid to advance the state of art in the simulation of geared systems. Integration of the concepts of dynamic modeling and the finite element analysis is being done by the researchers to understand the phenomenon in more depth. Finite element analysis using Chebyshev polynomials has been studied with the application to gears, treating them as quasi-prismatic bodies (Vijayakar et al., 1987). Imposition of contact constraints by using the penalty methods has been carried out (Endo et al., 1984; Simo et al., 1986). Frictional contact problems associated with the gears has been undertaken at Gear Dynamics and Gear Noise research laboratory at Ohio State University (Vijayakar, 1988). The method of Lagrange multipliers to solve the two and three-dimensional dynamic frictional contact problem has been used (Bathe et al., 1985; Chaudhury et al., 1986).

In the recent past, procedures involving relative coordinates based on the partial velocity arrays in the study of rigid-body dynamics has been developed (Huston et al., 1979). The relative coordinate systems are convenient in terms of lesser number of equations and easier handling of the constraints. A recursive formulation of multibody dynamics carried out by a number of researchers (Schwertassek, 1985; Bae et al., 1988; Ider and Amirouche, 1989a) proves to be promising in terms of computational aspects.

With the advent of computers having large memory capacities and high speeds of execution, there is a possibility of revolution in the field of multibody dynamics. Comparison of performance of a recursive algorithm in a parallel processing environment and the symbolic manipulation techniques (Nielan, 1988) are worth mentioning in this regard. The handling of the constraint equations resulting from closed loops, prescribed motions, and other kinematical and geometric conditions have been studied by a number of researchers (Ider and Amirouche, 1988). The equations of motion that are applicable at the neighborhood of the singular configuration have been derived based on the modification of the constraint equations (Ider and Amirouche, 1989b).

In this paper a new technique has been presented for handling of the time variant constraints in the geared transmissions,

Contributed by the Applied Mechanics Division of THE AMERICAN SOCIETY OF MECHANICAL ENGINEERS for publication in the ASME JOURNAL OF APPLIED MECHANICS.

Discussion on this paper should be addressed to the Technical Editor, Prof. Leon M. Keer, The Technological Institute, Northwestern University, Evanston, IL 60208, and will be accepted until four months after final publication of the paper itself in the JOURNAL OF APPLIED MECHANICS.

Manuscript received by the ASME Applied Mechanics Division, Aug. 23, 1990; final revision, May 28, 1991. Associate Technical Editor: R. L. Huston.

Copyright © 1992 by ASME
Downloaded 03 May 2010 to 171.66.16.247. Redistribution subject to ASME license or copyright; see http://www.asme.org/terms/Terms_Use.cfm

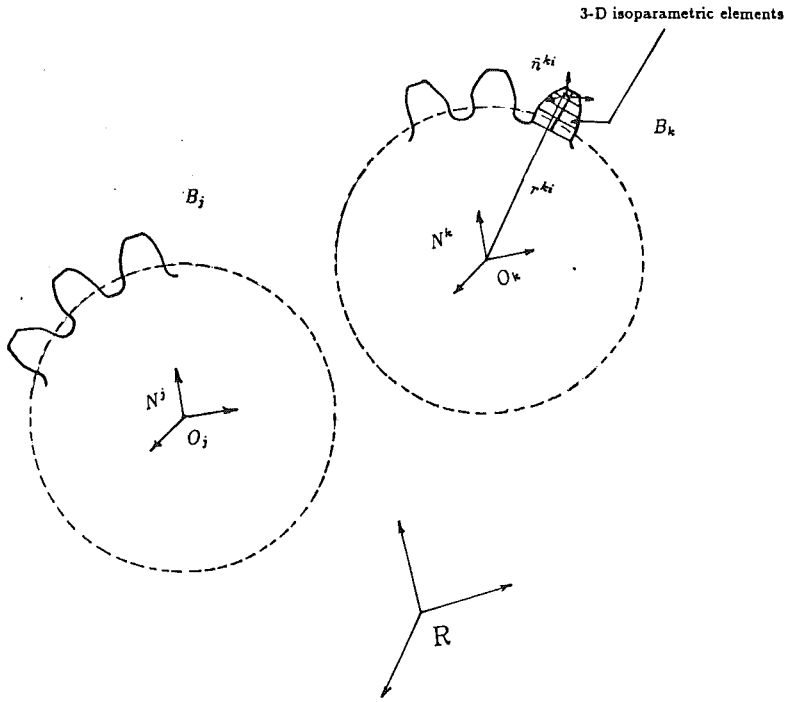


Fig. 1 Various reference frames in flexible gears

assuming the contacting regions have one or more points of contact during the cycle of a particular revolution. The constraints have been classified based on their contact between a shaft and a gear or a gear and a gear. Mathematical equations are developed for the constraints, and a generalized procedure described for automatic generation of the constraint Jacobian matrices in time, keeping track of the new contacting points between the gear teeth, is presented. The dynamical equations of motion presented in this paper are based on the method developed by Amirouche and Shareef (1991) and include the complete interaction between the rigid and flexible motions. The associated modes of vibration are selected a priori (preprocessor) and are integrated in the equations through the single relationship between nodal coordinates of the elements and the modal coordinates.

This research is intended to get a better understanding of the transmission gear/shaft and rotor craft dynamics with an emphasis on the vibrational aspects as a result of elastic deformations due flexibility features of the bodies in the system. The ultimate objective is to increase the reliability of performance of such systems minimizing the associated vibration, noise, and transmission loss problems and arrive at an optimized design. The algorithmic procedure developed will be hopefully implemented in the computer which will serve as a tool for computations and for predicting the dynamic behavior of the system.

Recursive formulation of the Kane's equations, concepts of strain energy, component mode synthesis, and finite element form the basis of dynamical equations of motion (Amirouche and Shareef, 1991). These automatically generated Jacobian matrices associated with the constraints will be used for reducing the number of equations to minimum dimension (Amirouche and Jia, 1987). The new concepts of the use of the indices of reference arrays have been utilized by Amirouche and Shareef (1991) for the kinematical derivations, which have improved the computational efficiency enormously.

A geared transmission with fairly complex multigears/shafts is presented, as an example, to demonstrate the procedure developed.

2 Topology and Kinematical Description of the System

2.1 Kinematical Description of the Rigid/Flexible Bodies. The interconnection between two flexible bodies B_k and B_j is shown in Fig. 2 (Ider and Amirouche, 1989a). N^k and N_j are the floating reference frames for B_k and B_j located outside the bodies, with respect to which the associated elastic deformations are evaluated. These are transformed to the inertial reference frame R through the local reference frames n^k and n^j for the two bodies located at Q_k and Q_j. The rigid-body rotations/translations of the bodies are with reference to n^{k*}. The bodies could be discretized using suitable finite elements based on their geometric configurations. Each element i has its local reference frame denoted by n^{ki}. Further details of the relative and floating reference frames and the different associated vectors are found in Ider and Amirouche (1989a). Concepts of the indices of reference arrays have been incorporated in the kinematical equations which were shown to improve the computational efficiency enormously (Amirouche and Shareef, 1991).

The mathematical equations describing the vectors q, d and the angular velocity $\bar{\Omega}$ could be written in terms of the shape function matrices denoted as $\mathfrak{N}$ and $\mathfrak{M}$ (for the linear and rotational elastic deformation), which include the necessary transformations

$$q^{ki} = \mathfrak{N}^{ki}\bar{u}_e^{ki} + \mathfrak{N}^k\bar{u}_e^k \tag{1}$$

$$d^k = \mathfrak{N}^{k*}\bar{u}_e^{k*} - \mathfrak{N}^j\bar{u}_e^j \tag{2}$$

$${}^{n^j}\bar{\Omega}^{n^{k*}} = \mathfrak{M}^{k*}\dot{\bar{u}}_e^j - \mathfrak{M}^j\dot{\bar{u}}_e^j \tag{3}$$

$${}^{n^k}\dot{\bar{\Omega}}^{N^k} = -\mathfrak{M}^k\dot{\bar{u}}_e^k \tag{4}$$

where $\bar{u}_e$ represents the identified and extracted vector containing the exact kinematical quantities associated with either the element or the flexible body.

The generalized speeds $\mathcal{Y}$ are chosen to be

$$\mathcal{Y} = [\Omega^T, \dot{\Upsilon}^T, \dot{\eta}^T]^3 \tag{5}$$

where Ω, $\dot{\gamma}$, $\dot{\eta}$ are the vectors of the components of the angular velocity of the bodies in the system, derivatives of the com-

Downloaded 03 May 2010 to 171.66.16.247. Redistribution subject to ASME license or copyright; see http://www.asme.org/terms/Terms_Use.cfm

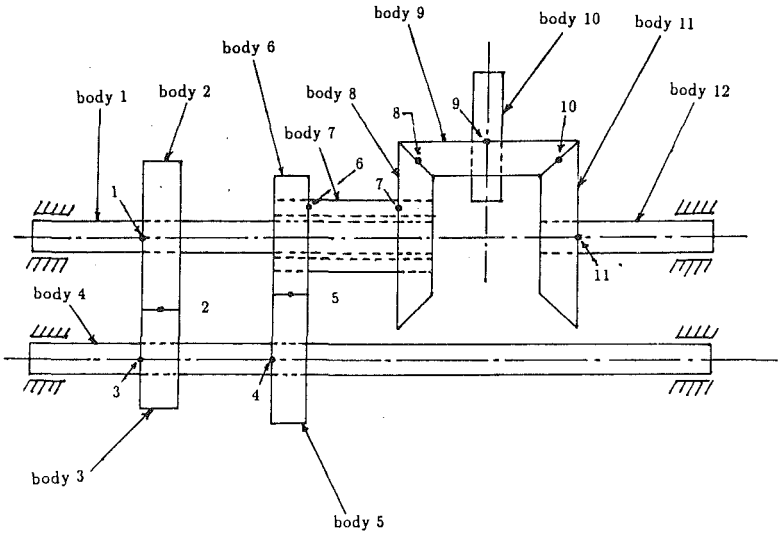


Fig. 2 Gear trains with many shafts/gears

ponents of translational velocities, and the derivatives of the components of modal coordinates of the flexible bodies in the system, respectively. The relationship between the derivatives of Euler angles $\dot{\theta}_i$ or the Euler parameters $\dot{\Theta}_i$ are given by

$$\dot{\theta}_i^k = \overline{D}\Omega_i^k \tag{6}$$

$$\dot{\Theta}_i^k = \overline{E}\Omega_i^k \tag{7}$$

where $\overline{D}$ and $\overline{E}$ are the related transformation matrices.

The use of component mode synthesis lies in expressing rotational elastic deformation $\overline{\varphi}$ and translational elastic deformation $\overline{\tau}$ in terms of nodal-modal-transformation matrix $\overline{\chi}$ and the modal coordinate vectors η associated with the selected mode shapes as:

$$\overline{\varphi}^{ki} = \mathfrak{M}^{ki}\overline{\chi}_e^{ki}\eta_e^{ki} \tag{8}$$

$$\overline{\tau}^{ki} = \mathfrak{N}^{ki}\overline{\chi}_e^{ki}\eta_e^{ki} \tag{9}$$

where the subscript e refers to the index of reference array *edof* (Amirouche and Shareef, 1991).

2.2 Velocity and Acceleration of an Arbitrary Point. A more detailed explanation of the kinematical matrix representation could be seen in the reference of Amirouche and Shareef (1992). Let us now, for the sake of completion, discuss in brief the kinematical equations involved here.

The partial velocity vectors $\overline{\zeta}$ and $\overline{\xi}$ associated with the rigid and flexible motions, respectively, could be utilized to express the angular velocities of any body k of the multibody system in R as:

$$\overline{\Omega}^k = \overline{\zeta}^k\Omega + \overline{\xi}^k\dot{\eta} \tag{10}$$

$$\overline{\Omega}^{k^*} = \overline{\zeta}^j\Omega + \overline{\xi}^{k^*}\dot{\eta} \tag{11}$$

each of which is given by

$$\overline{\zeta}^k = \overline{\zeta}^j + \overline{\mathbb{S}}^{k^*}a^k \tag{12}$$

where $\overline{\mathbb{S}}^{k^*}$ is the (3*3) coordinate transformation matrix between n^{k^*} and R, obtained by multiplying successive transformation matrices, which are expressed in terms of the Euler angles or Euler parameters. Similarly, $\overline{\mathbb{S}}^k$ is the transformation matrix between n^k and R. a^k is the incidence matrix, used for the sake of convenience, and is defined by $\overline{\Omega}^k = a^k\Omega^k$.

$$\overline{\xi}^k = \overline{\xi}^j + \overline{\mathbb{S}}^j\mathfrak{M}^{k^*}\overline{\chi}_{eb} - \overline{\mathbb{S}}^k\mathfrak{M}^k\overline{\chi}_{eb} \tag{13}$$

Once more, k and k^* refer to the unit vectors, fixed at the interconnected elements of the adjacent bodies B_k and B_j (see Fig. 2, Ider and Amirouche, 1989). The subscripts *eb* refer to the indices connected with both the reference arrays *edof* and *bdof* (Amirouche and Shareef, 1991). The velocity and acceleration of an arbitrary point, in a similar fashion, could be written as

$$V^{ki} = \gamma^{ki}\Omega + \nu^k\dot{\Upsilon} + \beta^{ki}\dot{\eta} \tag{14}$$

$$A^{ki} = \gamma^{ki}\dot{\overline{\Omega}} + \nu^k\ddot{\overline{\Upsilon}} + \beta^{ki}\ddot{\eta} + \dot{\gamma}^{ki}\overline{\Omega} + \dot{\nu}^k\dot{\overline{\Upsilon}} + \dot{\beta}^{ki}\dot{\eta} \tag{15}$$

where γ, ν, and β are again the partial velocity arrays associated with Ω, $\dot{\Upsilon}$, and $\dot{\eta}$, respectively. ν is the same as the partial angular velocity matrix. γ and β could be written in a recursively computed form as

$$\gamma^{ki} = \gamma^k + \overline{q}^{ki}\nu^k \tag{16}$$

$$\beta^{ki} = \beta^k + [\overline{\mathbb{S}}^k[\mathfrak{M}^{ki}\overline{\chi}_{eb}^{ki} - \mathfrak{N}^k\overline{\chi}_{eb}^k] + \overline{q}^{ki}\overline{\xi}^k\overline{\chi} \tag{17}$$

where

$$\gamma^k = \gamma^j + \Upsilon^k\nu^j + \overline{d}^k\nu^j \tag{18}$$

and

$$\beta^k = \beta^j + [\overline{\Upsilon}^k\overline{\xi}^j + \overline{d}^k\overline{\xi}^j]\overline{\chi} + \mathbb{S}^j\mathfrak{N}^{k^*}\overline{\chi}_{eb}^{k^*} - \overline{\mathbb{S}}^j\mathfrak{N}^j\overline{\chi}_{eb}^j. \tag{19}$$

3 Equations of Motion Based on Recursive Formulation

The details of the equations of motion in a matrix representation form based on Kane's equations is given in reference Amirouche and Shareef (1991), which, after simplification, could be written as

$$\mathfrak{M}\dot{\mathcal{Y}} + \mathcal{P} + \mathcal{Q} + \lambda^{\mathcal{J}} = \mathcal{F}, \tag{20}$$

where $\mathfrak{M}$, $\mathcal{Q}$, λ, $\mathcal{J}$, $\mathcal{F}$, and $\mathcal{P}$ represent the coefficient matrices for the generalized coordinate accelerations, quadratic velocity vector, c-dimensional vector of undetermined multipliers, constraint Jacobian matrix, generalized external forces, and stiffness due to strain energy of the flexible bodies in the system, respectively. These matrices are given by $\mathfrak{M}$ = :

$$\begin{bmatrix} \Sigma\Sigma\int\rho\gamma^{ki^T}\gamma^{ki}\partial V/\partial\mathcal{Y}dV & \Sigma\Sigma\int\rho\gamma^{ki^T}\nu^{ki}\partial V/\partial\mathcal{Y}dV & \Sigma\Sigma\int\rho\gamma^{ki^T}\beta^{ki}\partial V/\partial\mathcal{Y}dV \\ \Sigma\Sigma\int\rho\gamma^{ki^T}\nu^{ki}\partial V/\partial\mathcal{Y}dV & \Sigma\Sigma\int\rho\nu^{ki^T}\nu^{ki}\partial V/\partial\mathcal{Y}dV & \Sigma\Sigma\int\rho\nu^{ki^T}\beta^{ki}\partial V/\partial\mathcal{Y}dV \\ \Sigma\Sigma\int\rho\gamma^{ki^T}\beta^{ki}\partial V/\partial\mathcal{Y}dV & \Sigma\Sigma\int\rho\nu^{ki^T}\beta^{ki}\partial V/\partial\mathcal{Y}dV & \Sigma\Sigma\int\rho\beta^{ki^T}\beta^{ki}\partial V/\partial\mathcal{Y}dV \end{bmatrix} \tag{21}$$

Downloaded 03 May 2010 to 171.66.16.247. Redistribution subject to ASME license or copyright; see http://www.asme.org/terms/Terms_Use.cfm

where ρ is the mass density of the material used and $\Sigma\Sigma$ is the summation of the volume of the element V over all the elements of a body and all the bodies in the system.

$$\mathcal{Q} = \begin{bmatrix} \Sigma\Sigma\int_V^{ki} \rho \gamma^{ki^T} [\dot{\gamma}^{ki}\Omega + \dot{\nu}^{k}\dot{\Upsilon} + \dot{\beta}^{ki}\dot{\eta}] \\ \Sigma\Sigma\int_V^{ki} \rho \nu^{ki^T} [\dot{\gamma}^{ki}\Omega + \dot{\nu}^{k}\dot{\Upsilon} + \dot{\beta}^{ki}\dot{\eta}] \\ \Sigma\Sigma\int_V^{ki} \rho \beta^{ki^T} [\dot{\gamma}^{ki}\Omega + \dot{\nu}^{k}\dot{\Upsilon} + \dot{\beta}^{ki}\dot{\eta}] \end{bmatrix} \tag{22}$$

$$\mathcal{F} = \begin{bmatrix} \Sigma\Sigma\int_{S_{ki}} \gamma^{ki^T} f^{ki} dS + \int \gamma^{ki^T} b^{ki} dV \\ \Sigma\Sigma\int_{S_{ki}} \nu^{ki^T} f^{ki} dS + \int \nu^{ki^T} b^{ki} dV \\ \Sigma\Sigma\int_{S_{ki}} \beta^{ki^T} f^{ki} dS + \int \beta^{ki^T} b^{ki} dV \end{bmatrix} \tag{23}$$

where f^{ki} and b^{ki} are the surface traction and body forces associated with the global boundary of the finite elements and their weights, respectively, and

$$\mathcal{P} = \begin{bmatrix} 0 \\ 0 \\ \chi^T [K + G] \chi \eta \end{bmatrix} \tag{24}$$

where K and G are the block diagonal matrices, whose diagonal submatrices are K^k and G^k, being referred to as the structural stiffness and geometric stiffness for body K.

4 Derivation of the Constrained Equations

Use of partial velocity arrays in the recursive formulation of the dynamical equations of motion renders a noteworthy benefit of the automatic generation of the constraint equations. Basically, the various constraints could be broadly classified as:

1 contact between interconnected bodies
2 prescribed motions, and
3 closed loops.

The first type of constraint, mentioned above, is by virtue of the contacts between the interconnected bodies, and could be identified in the geared transmissions. This contact could be between a shaft and a gear, or a gear and a gear, as shown in Figs. 1 and 2. The contact could be assumed as a line contact or a planar contact as shown by points 1, 2, 3, . . . in Fig. 2. It will be shown, in the following sections of the paper, that the Jacobian matrices associated with the generalized coordinate derivatives could be generated automatically for the cases of flexible gears/shafts.

The end-effector motion, if specified for a particular robot, could be the example of a constraint of the second type. Based on the linear and angular velocity being specified as a function of time, say, $G(t)$ and $h(t)$, the constraint equation could be written as (Ider and Amirouche, 1988):

$$[\gamma^{ri} \quad \nu^{r} \quad \beta^{ri}] \begin{bmatrix} \Omega \\ \dot{\Upsilon} \\ \dot{\eta} \end{bmatrix} = G(t) \tag{25}$$

$$[\bar{\xi}^{r} \quad \bar{\xi}^{r}] \begin{bmatrix} \Omega \\ \dot{\eta} \end{bmatrix} = h(t) \tag{26}$$

where r refers to the position vector C^r of a point A which has the specified velocity in the local reference frame of body K.

The third type of constraint, the closed loops, are a common type of constraint found in various mechanisms. The joining point where the closed loop occurs could be reached in two ways from the fixed inertial reference frame. Denoting these two ways by p and q, the constraint equation could be written in a compact form as (Ider and Amirouche, 1988):

$$[[\gamma_i^p - \gamma_i^q] \quad [\nu_i^p - \nu_i^q] \quad [\beta_i^p - \beta_i^q]] \begin{bmatrix} \Omega \\ \dot{\Upsilon} \\ \dot{\eta} \end{bmatrix} = 0. \tag{27}$$

Thus, the holonomic and nonholonomic constraints at the velocity level could be written in a compact form as:

$$\mathcal{J}\mathcal{Y} = G(t) \tag{28}$$

where $\mathcal{J}$ is the Jacobian matrix of the order of c by n—c being the number of the constraints in the system and n the number of generalized coordinates.

Differentiating the above equation once more and combining, we get the equations of motion in the final form as

$$\mathcal{L}\dot{\mathcal{Y}} = \mathcal{R} \tag{29}$$

where

$$\mathcal{L} = [\mathcal{C}^T \mathfrak{M} / \mathcal{J}] \tag{30}$$

and

$$\mathcal{R} = [\mathcal{C}^T [\mathcal{F} - \mathcal{P} - \mathcal{Q}] / \dot{G} - \dot{\mathcal{J}}\mathcal{Y}]. \tag{31}$$

$\mathcal{C}$ in the above equation is the orthogonal-complement to the Jacobian matrix $\mathcal{J}$ and is obtained by the pseudo-uptriangular decomposition method. Subsequent numerical integration could give the time history of the generalized speeds or generalized coordinates after simple mathematical manipulations.

4.1 Constraints in Flexible Geared Transmissions. Figure 3 shows a set of two gears with the contacting teeth. The teeth of the gears has been discretized using eight-noded three-dimensional isoparametric elements. The contact between the teeth is shown through the nodal points located on the surface of contact. Based on the refinement of the discretization the number of contacting nodes could vary. This would depend on the assumption one would make and the type of gears involved.

In the following sections the constraint equations based on the velocity of the contacting nodal points are developed. These constraints vary with time, depending on the nodal points being in contact.

Let us assume the number of teeth in gear i and gear j to be z_1 and z_2, respectively. For the sake of simplicity and convenience, let the number of elements on the boundaries of the mating teeth and the corresponding contacting nodes be the same as shown in the Fig. 3. At time $t = 0$, node 1 of tooth 1 of gear i is in contact with the node 1 of tooth 1 of gear j. At time $t = N.dt$ (where N and dt represent the number of increments and time intervals, respectively), the position with

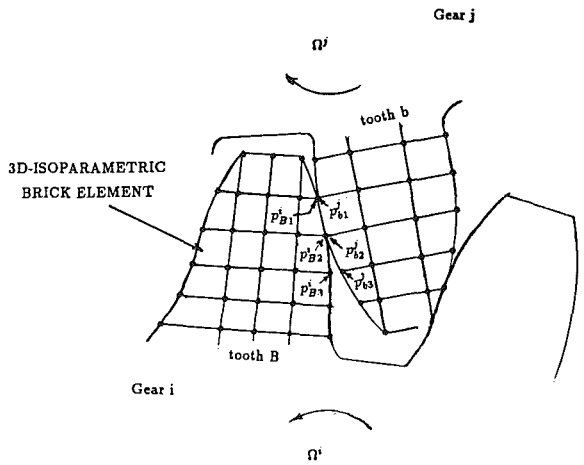


Fig. 3 Interaction between flexible gear teeth

Downloaded 03 May 2010 to 171.66.16.247. Redistribution subject to ASME license or copyright; see http://www.asme.org/terms/Terms_Use.cfm

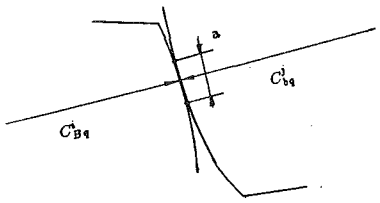


Fig. 4 Length of the contact plane

respect to the inertia frame R for the contacting node q between the tooth B and b of the gears i and j could be written as

$$P^i_{Bq} = P^j_{bq} \tag{32}$$

where

$$B = \text{Rem}[1/z_1[\text{Int}[N/n]]] + 1 \tag{33}$$

$$b = \text{Rem}[1/z_2[\text{Int}[N/n]]] + 1 \tag{34}$$

$$q = \text{Rem}[N/n] + 1. \tag{35}$$

n is the number of nodal points on the contacting surface and N is the number of time intervals. Int and Rem denote the integer and the remainder of the fraction following them in the brackets.

Example 1. If $z_1 = 17$, $z_2 = 20$, $n = 5$, $N = 100$, then

$$B = \text{Rem}[1/17[\text{Int}[100/5]]] + 1 = 4 \tag{36}$$

$$b = \text{Rem}[1/20[\text{Int}[100/5]]] + 1 = 1 \tag{37}$$

$$q = \text{Rem}[100/5] + 1 = 1 \tag{38}$$

which means that after $t = 100.dt$, the first node of the fourth tooth in gear 1 is in contact with the first node of the first tooth of the gear 2. The assumption in this case is that there is a line contact between the teeth, with any number of nodes across the width of the teeth. For the case with the surface contact, more than one node on the surface will be in contact at the same instant.

Example 2. Let us assume that the two gears have three nodes in contact. Let $z_1 = 20$, $z_2 = 50$, $n = 6$, and $N = 150$. Let, at $t = 0$, the contact pairs be p^1_{11} with p^2_{11}, and p^1_{12} with p^2_{12}, and p^1_{13} with p^2_{13}. Then

$$B = \text{Rem}[1/20[\text{Int}[150/6]]] + 1 = 6 \tag{39}$$

$$b = \text{Rem}[1/50[\text{Int}[150/6]]] + 1 = 26 \tag{40}$$

$$q = \text{Rem}[150/6] + 1 = 1. \tag{41}$$

Hence, the contact pairs are: p^1_{61} with $p^2_{26,1}$, p^1_{62} with $p^2_{26,2}$, $p^1_{26,3}$ with $p^2_{26,3}$. A value of $q = 5$ in the above example indicates that the fifth and sixth are the two nodes in contact. Similarly, for $q = 6$, only the sixth node is in contact.

4.2 Kinematical Expressions for the Contacting Nodes on Gear Teeth. The length of the contact plane a between the gear teeth as shown in Fig. 4 is given by

$$a = [16F[K_1 + K_2]C^i_{Bq}C^j_{bq}/\overline{B}(C^i_{Bq} + C^i_{bq})]^{1/2} \tag{42}$$

where

a = length of the contact plane,
F = normal force, and
$\overline{B}$ = width of the gears.

C^i_{Bq}, C^j_{bq} are the radii of curvatures for tooth B and b at the node q on gears i and j, respectively, given by

$$C^i_{Bq} = r_{qi}\sin v_i \tag{43}$$

$$C^j_{bq} = r_{qj}\sin v_j \tag{44}$$

where r_{qi} and y_{qj} are the radii of the contact point q on the gears i and j, v_i is the pressure angle for this point on the two gears, and K_1 and K_2 are the coefficients of the materials of the gears given by

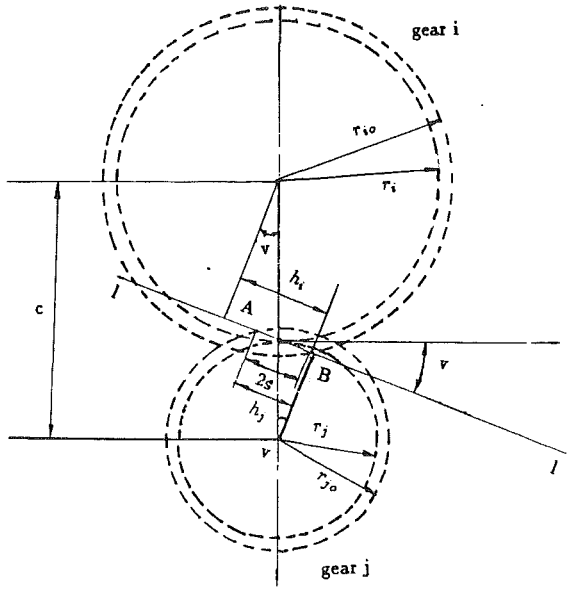


Fig. 5 Details of geometry of meshing gears

$$K_1 = [1 - u_1^2]/\Pi E_1 \tag{45}$$

$$K_2 = [1 - u_2^2]/\Pi E_2 \tag{46}$$

where u_i, $E_i i = 1, 2$ are the Poisson's ratio and Young's Modulus of elasticity, respectively, for the materials of the gears. The average length of the contact plane at the pitch circle is given by

$$a_{av} = [16F[K_1 + K_2]r_i r_j \sin v/\overline{B}[r_i + r_j]]^{1/2} \tag{47}$$

where r_i and r_j are the pitch circle radii of the gears i and j and v is the corresponding pressure angle.

4.3 Constraint Equations for the Contacting Nodes on Gear Teeth. As shown in Fig. 5, the line 1-1 represents the line of action along which the contacting point moves with time. Points A and B are the points of intersection between the line 1-1 and the addendum circles of gears i and j, respectively. The length of the line of action l_{ab} is thus given by

$$2s = h_i + h_g - c.\sin v \tag{48}$$

where c denotes the center distance between the gears i and j and h_i and h_j represent the normal line lengths of the base circles of two gears, which are expressed as:

$$h_i = [r_i^2 - r_{io}^2\cos^2 v]^{1/2} \tag{49}$$

$$h_j = [r_j^2 - r_{jo}^2\cos^2 v]^{1/2} \tag{50}$$

where r_{io} is the addendum circle radius of the gear i and r_{jo} is the addendum circle radius of the gear j. Also we have

$$c = r_i + r_j. \tag{51}$$

The relative velocity V^{ij}_{Bbq} between the velocity of the contact nodal point q on tooth B of gear i and tooth b of gear j is given by

$$V^{ij}_{Bbq} = V^i_{Bq} - V^j_{bq}. \tag{52}$$

The components of the velocities V^i_{Bq} and V^j_{bq} in the x and y-direction, denoted by V^i_{Bqx} and V^j_{bqx}, can be written as

$$V^i_{Bqx} = \Omega^i[r_i + s_t \sin v] \tag{53}$$

$$V^i_{Bqy} = \Omega^i s_t \cos v \tag{54}$$

$$V^j_{bqx} = \Omega^j[r_j - s_t \sin v] \tag{55}$$

$$V^j_{bqy} = \Omega^j s_t \cos v \tag{56}$$

Downloaded 03 May 2010 to 171.66.16.247. Redistribution subject to ASME license or copyright; see http://www.asme.org/terms/Terms_Use.cfm

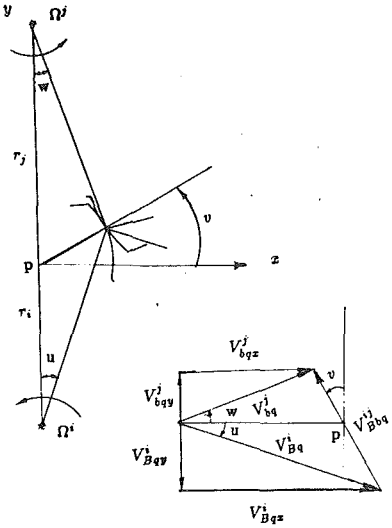


Fig. 6 Components of velocities at meshing gear teeth

where s_t is the distance between pitch point and the contact point and is a function of time.

Using the above equations, the transmission ratio in the x-direction can be written as

$$i_x = |V^i_{Bqx}/V^j_{bqx}| = |\Omega^i[r_i + s_t \sin v]/\Omega^j[r_j - s_t \sin v]|, \quad (57)$$

since

$$|\Omega^i/\Omega^j| = r_j/r_i. \quad (58)$$

We get, by substituting in the above equations,

$$i_x = (1 + s_t \sin v/r_i r_j)/(1 - s_t \sin v/r_i r_j). \quad (59)$$

Now,

$$|(s_{\max}| \cong 1/2[h_i + h_j - c \sin v]. \quad (60)$$

Substituting the values of the h_i and h_j and simplifying we get

$$|s_{\max}| \cong 1/2[\sqrt{r_i^2 - r_{io}^2 \cos^2 v} + \sqrt{r_j^2 - r_{jo}^2 \cos^2 v} - (r_i + r_j)\sin v]. \quad (61)$$

The value of i_x varies for the points between A and B and is given by

$$i_x \geq (1 - |s_{\max}| \sin v/r_i r_j)/(1 + |s_{\max}| \sin v/r_i r_j) \quad (62)$$

$$i_x \leq (1 + |s_{\max}| \sin v/r_i r_j)/(1 - |s_{\max}| \sin v/r_i r_j). \quad (63)$$

In a similar fashion, the transmission ratio in the y-direction is given by

$$i_y = -|V^i_{Bqy}/V^j_{bqy}| = -|\Omega^i s_t \cos v/\Omega^j s_t \cos v| = -|\Omega^i/\Omega^j|. \quad (64)$$

The velocity of the contacting node is governed by the following relationship:

$$V^i_{Bq} = V^{ijr}_{Bbq} V^j_{bq} \quad (65)$$

where V^{ijr}_{Bbq} could be written in terms of the transmission ratios as

$$V^{ijr}_{Bbq} = \begin{bmatrix} i_x & 0 & 0 \\ 0 & i_y & 0 \\ 0 & 0 & 1 \end{bmatrix}. \quad (66)$$

Thus, from the above discussions, the constraint equation could be written as

$$V^i_{Bq} - V^{ijr}_{Bbq} V^j_{bq} = 0. \quad (67)$$

Using Eq. (15) for the velocity of a point and substituting in the above equation, we get the constraint equation as

$$\gamma^i_{Bq}\Omega + \nu^i_{Bq}\dot{\Upsilon} + \beta^i_{Bq}\dot{\eta} - V^{ijr}_{Bbq}[\gamma^j_{bq}\Omega + \nu^j_{bq}\dot{\Upsilon} + \beta^j_{bq}\dot{\eta}] = 0. \quad (68)$$

Writing the above equation in the matrix form we get

$$[(\gamma^i_{Bq} - \gamma^j_{bq})\, V^{ijr}_{Bbq}\, (\nu^i_{Bq} - \nu^j_{bq})\, V^{ijr}_{Bbq}\, (\beta^i_{Bq} - \beta^j_{bq})\, V^{ijr}_{Bbq}] \begin{bmatrix} \Omega \\ \dot{\Upsilon} \\ \dot{\eta} \end{bmatrix} = 0. \quad (69)$$

As discussed earlier, the switching of the constraints could be achieved by changing the node numbers of the contacting nodes between the teeth with time and using the right coefficients matrices in the constraint Eq. (68). Thus, in this fashion, the dynamic analysis of the complete gear train/transmission, as shown in Fig. 2, could be carried out by extending the discussions in this paper for more than two bodies. The governing equations of motion given by Eq. (29) will make use of the gear teeth contact constraint equation given by Eq. (69) and no other kinematical or geometrical constraints is needed.

Conclusion

In this paper, a comprehensive method for the dynamic analysis of multibody flexible geared transmission system is presented. The strain energy concepts, Kane's method, and finite element technique are integrated to arrive at the dynamical equations of motion, which are presented in a compact matrix form suitable for computer implementation. Special emphasis is placed on the handling of the constraints subsequent to the contact between the flexible bodies. The nature of the contact could be a line/planar contact through the nodal points of three-dimensional isoparametric brick elements. An automated procedure for getting the node numbers for the contacting areas developed, which explains the switching of the constraint with time. The generation of the constraint Jacobian matrices, through proper evaluation of the coefficient matrices using the relative velocity at the contacting node between the gear teeth, is clearly explained.

Acknowledgments

The support of this work by the U.S. Army Aviation Research and Technology Activity—AVSCOM under grant number NASA/LEWIS NAG3-1092 is gratefully acknowledged. The authors wish to thank Mr. Mark Valco and Mr. Albert Kasack for their keen interest and encouragement during the course of the present work.

References

Amirouche, F. M. L., and Tongyi, J., 1987, "Automatic Elimination of Undetermined Multipliers in Kanes Equations using a Pseudo-uptriangular Decomposition Method," *Computers and Structures*, Vol. 27, No. 2, pp. 203-210.

Amirouche, F. M. L., and Shareef, N. H., 1991, "Implementation of 3D-Isoparametric Finite Elements on Supercomputer for the Formulation of Recursive Dynamical Equations of Multi-body Systems," *Non-linear Dynamics*, in press.

Amirouche, F. M. L., and Shareef, N. H., 1991, "Gain in Computational Efficiency by Vectorization in the Dynamic Simulation of Multi-Body Systems," *Computers and Structures*, in press.

Bae, D.S., Hwang, R. S., and Haug, E. J., 1988, "A Recursive Formulation for Real Time Dynamic Simulations," *ASME Proceedings Advances in Design Automation DE*, Vol. 14, S. S. Rao, ed., pp. 499-508.

Bathe, K., and Choudhury, A., 1985, "A Solution Method for Planar and Axisymmetric Contact Problem," *International Journal for Numerical Methods in Engineering*, Vol. 21, pp. 65-88.

Chaudhury, A., and Bathe, K. J., 1986, "A Solution Method for Static and Dynamic Analysis of Three Dimensional Contact Problems with Friction," *Computers and Structures*, Vol. 24, No. 6, pp. 855-873.

Dudley, D. W., 1954, *Practical Gear Design*, 1st ed., McGraw-Hill, New York.

Endo, T., Oden, J. T., Becker, E. B., and Miller, T., 1984, "A Numerical Analysis of Contact and Limit Point Behavior in a Class of Problems of Finite Elastic Deformation," *Computers and Structures*, Vol. 18, pp. 899-910.

Huston, R. L., and Passarello, C. E., 1979, "On Multi-rigid-body System Dynamics," *Computers and Structures*, Vol. 10, pp. 439-446.

Downloaded 03 May 2010 to 171.66.16.247. Redistribution subject to ASME license or copyright; see http://www.asme.org/terms/Terms_Use.cfm

Ider, S. K., and Amirouche, F. M. L., 1989, "Non-linear Modelling of Flexible Multi-body Systems Dynamics Subjected to Variable Constraints, *Journal of Applied Mechanism*, Vol. 56, No. 2, pp. 444–450.

Ider, S. K., and Amirouche, F. M. L., 1988, "A Recursive Formulation of Equations of Motion for Articulated Structures with Closed Loops—An Automated Approach," *Computers and Structures*, Vol. 30, No. 5, pp. 1135–1145.

Ider, S. K., and Amirouche, F. M. L., 1989, "Numerical Stability of Constraints Near Singular Positions in the Dynamic of Multi-body Systems," *Computers and Structures*, Vol. 33, No. 1, pp. 129–138.

Meirovitch, L., 1986, *Elements of Vibration Analysis*, 2nd ed., McGraw-Hill, New York.

Merritt, H. E., 1954, *Gears*, 3rd ed., Sir Isaac Pitman and Sons, London.

Nielan, P. E., 1988, "Symbolic Manipulation Techniques," *Proceedings of the Workshop on Multibody Simulation*, National Aeronautics and Space Administration, Jet Propulsion Laboratory, California Institute of Technology, Pasadena, Calif.

Schwertassek, R., 1988, "Recursive Generation of Multi-body System Equations," *Proceedings of the Workshop on Multibody Simulation*, National Aeronautics and Space Administration, Jet Propulsion Laboratory, California Institute of Technology, Pasadena, Calif.

Simo, J C., Wriggers, P., Schweizerhof, K. H., and Taylor, R. L., 1986, "Finite Deformation Post-buckling Analysis Involving Inelasticity and Contact Constraints," *International Journal of Numerical Methods in Engineering*, Vol. 23, pp. 779–800.

Vijayakar, S. M., Busby, H. R., and Houser, D. R., 1988, "Linearization of Multi-body Frictional Contact Problem," *Computers and Structures*, Vol. 29, No. 4, pp. 569–576.

Vijayakar, S. M., Busby, H. R., and Houser, D. R., 1987, "Finite Element Analysis of Quasi-prismatic Bodies Using Chebyshev Polynomials," *International Journal for Numerical Methods in Engineering*, Vol. 24, pp. 1461–1477.

Zienkiewicz, O. C., 1977, *The Finite Element Method*, 3rd ed., McGraw-Hill, New York.

Downloaded 03 May 2010 to 171.66.16.247. Redistribution subject to ASME license or copyright; see http://www.asme.org/terms/Terms_Use.cfm

Node Control of Uniform Beams Subject to Various Boundary Conditions

L. Weaver, Jr.
Graduate Research Assistant.

L. Silverberg
Associate Professor,
Mem. ASME.

Mars Mission Research Center,
North Carolina State University,
Raleigh, NC 27695-7910

This paper introduces node control, whereby discrete direct feedback control forces are placed at the nodes of the N+1th mode (the lowest N modes participate in the response). Node control is motivated by the node control theorem which states, under certain conditions, that node control preserves the natural frequencies and natural modes of vibration of the controlled system while achieving uniform damping. The node control theorem is verified for uniform beams with pinned-pinned, cantilevered, and free-free boundary conditions, and two cases of beams with springs on the boundaries. A general proof of the node control theorem remains elusive.

Introduction

Nodal points and nodal lines of resonating structures have been a curiosity as far back as ancient times. During this period, nodal patterns were modified to produce pure tones in ancient Chinese bells. Today we know that the distance between adjacent nodes, that is the wavelength, strongly determines the spatial behavior of the associated radiated sound intensity. This paper introduces another property associated with nodes, stated in the form of a theorem. The theorem, which pertains to the area of structural control and which is called the *node control theorem*, is both curious and easy to apply.

As just mentioned, the node control theorem pertains to the area of structural control, which deals predominantly with the application of linear control theory to structures. More specifically, structural control is concerned with the relationships between structural dynamic parameters and control parameters. Structural dynamic parameters include natural frequencies of oscillation, natural modes of vibration, settling times, peek overshoots, modal decay rates, nodes, antinodes, etc. Control parameters include feedback control gains, control points, power and fuel requirements, etc. A structural control theory that provides desirable relationships between structural dynamic parameters and control parameters is given by Meirovitch and Silverberg (1983). That paper shows, for undamped structures, that power requirements increase as the closed-loop frequencies increasingly differ from the natural frequencies, as the closed-loop modes increasingly differ from the open-loop modes, and as the modal decay rates increase. These results give rise to the concepts of *natural control* (Silverberg and Morton, 1989) and *uniform damping control* (Silverberg, 1986). As shown by Silverberg (1986), an approximation of uniform damping control is achieved by applying control forces at discrete points that directly feed back the state measurements. The associated feedback control gains are determined by the mass distribution. The method is approximate in that the modal decay rates are only approximately uniform, depending on the placement of the control forces.

The Node Control Theorem states for certain types of structures with the lowest N modes participating in the system response that if N direct state feedback control forces are placed at the N nodes of the $N+1$th mode, then the control gains can be selected such that (1) the closed-loop frequencies are identical to the open-loop frequencies, (2) the closed-loop modes are identical to the open-loop modes, and (3) the decay rates can be set identically equal to an arbitrary decay rate. The computation of the associated control gains is directly carried out by use of a generalized inverse of a pseudo-mode participation matrix. This paper verifies the theorem for beams under a variety of boundary conditions. However, note that a general proof of the node control theorem remains elusive.

2 Beam Equations and Notation

This section introduces the beam equations and the notation to be used throughout the paper. The differential equation of motion for a uniform beam is (Meirovitch, 1986)

$$m\frac{\partial^2 u(x,\,t)}{\partial t^2}+EI\frac{\partial^4 u(x,\,t)}{\partial x^4}=f(x,\,t) \tag{1}$$

where u represents displacement, m represents mass per unit length, f represents force per unit length, and EI represents beam flexural rigidity.

The force per unit length f is composed of M discrete control forces located at x_1 to x_M, as follows:

$$f(x,\,t)=\sum_{i=1}^{M} f_i(t)\delta(x-x_i) \tag{2}$$

where $\delta(x-x_i)$ represents a spatial impulse at x_i. The discrete

Contributed by the Applied Mechanics Division of THE AMERICAN SOCIETY OF MECHANICAL ENGINEERS for publication in the ASME JOURNAL OF APPLIED MECHANICS.

Discussion on this paper should be addressed to the Technical Editor, Prof. Leon M. Keer, The Technological Institute, Northwestern University, Evanston, IL 60208, and will be accepted until four months after publication of the paper itself in the ASME JOURNAL OF APPLIED MECHANICS.

Manuscript received by the ASME Applied Mechanics Division, Mar. 7, 1991; final revision, July 21, 1991. Associate Technical Editor: D. J. Inman.

Copyright © 1992 by ASME
Downloaded 03 May 2010 to 171.66.16.247. Redistribution subject to ASME license or copyright; see http://www.asme.org/terms/Terms_Use.cfm

control forces directly feed back the state and are governed by

$$f_i(t) = h_i \frac{\partial u(x_i, t)}{\partial t} + g_i u(x_i, t), \quad i = 1, M \tag{3}$$

in which h_i and g_i denote the ith velocity gain and displacement gain, respectively.

The displacement u is now approximated by a truncated infinite sum of open-loop mode shapes multiplied by time-varying coefficients

$$u(x, t) = \sum_{r=1}^{N} \phi_r(x) q_r(t) \tag{4}$$

where the mode shapes satisfy the orthonormality conditions $\int_0^L m\phi_r(x)\phi_s(x)dx = \delta_{rs}$ $(r, s = 1, N)$ where δ_{rs} is the Kronecker delta function.

Substituting Eq. (4) into Eq. (1) and applying the orthonormality conditions yields the modal equations, expressed in vector form:

$$\ddot{\mathbf{q}}(t) + \Lambda \mathbf{q}(t) = G\mathbf{q}(t) + H\dot{\mathbf{q}}(t) \tag{5}$$

in which $\mathbf{q}(t) = [q_1(t)q_2(t)\ldots q_N(t)]^T$ and $\Lambda = \text{diag}(\omega_1^2, \ldots, \omega_N^2)$, where G and H are gain matrices with elements

$$g_{rs} = \sum_{i=1}^{M} g_i \phi_r(x_i)\phi_s(x_i), \quad h_{rs} = \sum_{i=1}^{M} h_i \phi_r(x_i)\phi_s(x_i). \tag{6}$$

The stability of Eq. (5) is governed by the closed-loop eigenvalue problem

$$(\lambda_r^2 I + \Lambda)\phi_r = (G + \lambda_r H)\phi_r \tag{7}$$

in which λ_r and ϕ_r denote the rth closed-loop eigenvalue and vector of modal coupling coefficients, respectively.

The system with feedback control is called the closed-loop or controlled system, while the system with no control is called the open-loop or uncontrolled system. The open-loop modes $\phi_r(x)$ are the natural mode shapes and the open-loop eigenvalues are pure imaginary natural frequencies ω_r. The closed-loop modes can now be described in terms of the modal coupling coefficients and open-loop modes as

$$\phi_{CL,r}(x) = \sum_{s=1}^{N} \phi_{sr}\phi_s(x), \; r = 1, N \tag{8}$$

where $\phi_r = [\phi_{1r}\phi_{2r}\ldots\phi_{Nr}]^T$.

The negative of the real part of the rth closed-loop eigenvalue is a decay rate and the imaginary part is the associated closed-loop frequency, given by

$$\lambda_r = \begin{cases} -\alpha_r + i\beta_r & r = 1, N \\ -\alpha_r - i\beta_r & r = N+1, 2N. \end{cases} \tag{9}$$

Several sets of boundary conditions are used as examples in this paper as shown in Fig. 1. They include cantilever, free-free, pinned-pinned boundary conditions, and two sets of boundary conditions associated with linear and torsional

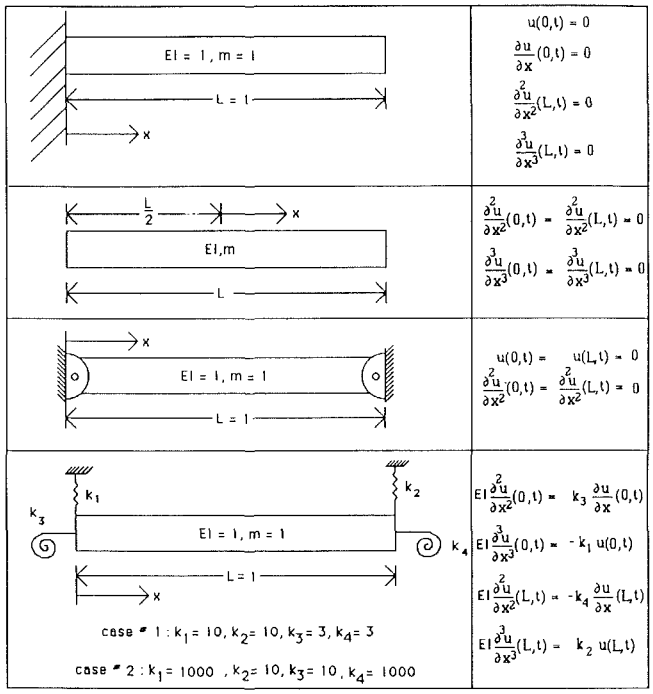


Fig. 1 Various beams and boundary conditions

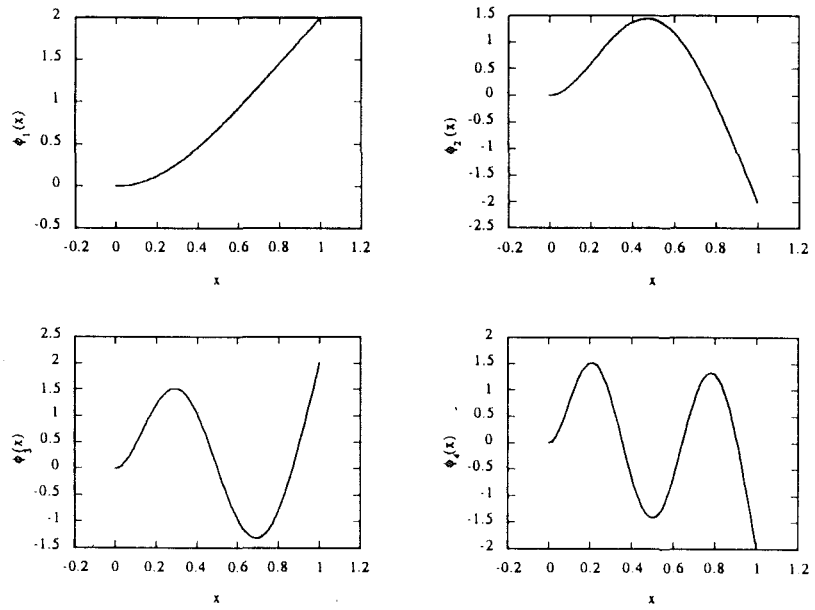


Fig. 2 Cantilevered beam

Downloaded 03 May 2010 to 171.66.16.247. Redistribution subject to ASME license or copyright; see http://www.asme.org/terms/Terms_Use.cfm

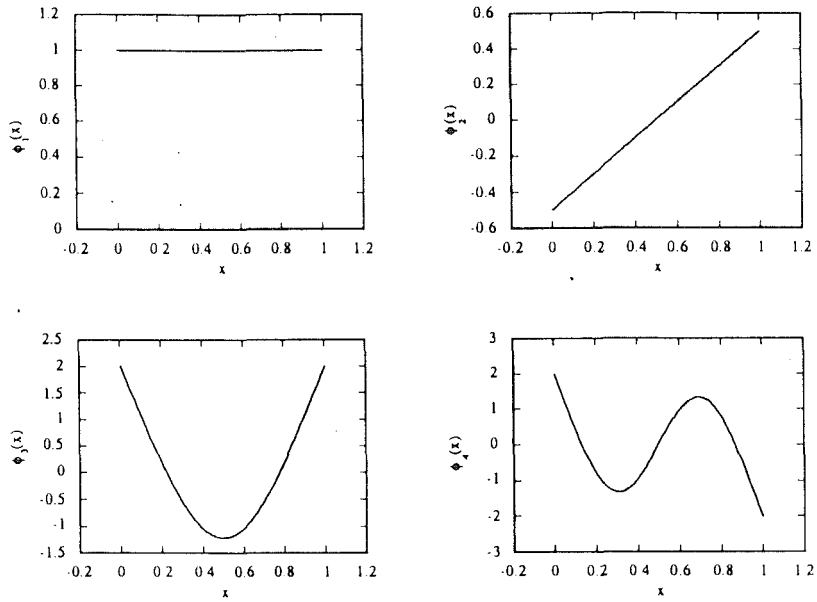


Fig. 3 Free-free beam

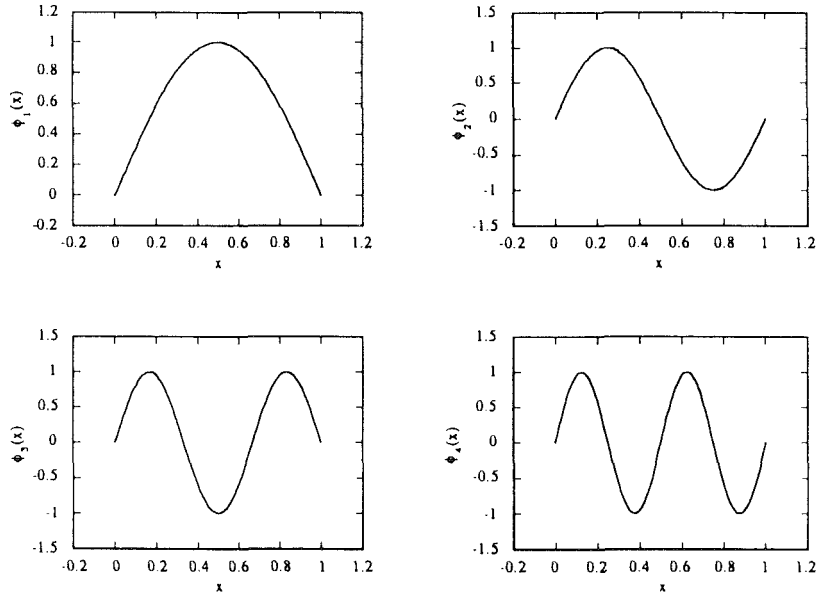


Fig. 4 Pinned-pinned beam

springs on the ends. Figures 2-6 show the first four natural mode shapes for each set of boundary conditions.

3 Node Control of a Free-Free Beam

The method of node control consists of selecting the number of modes N to be controlled and placing N forces at the N nodes of the $N+1$th mode. The control gains h_i and $g_i (i = 1, N)$ are then selected to uniformly dampen the closed-loop modes.

This form of control is motivated in part by examining beams constrained by various sets of boundary conditions. First, let us consider free-free beams. For simplicity, polynomial functions approximate the natural mode shapes. The origin of the coordinate system for the beam is located at the center of the beam as shown in Fig. 1. The first five polynomial mode shapes are given by

$$\phi_1(x)=\frac{1}{\sqrt{mL}},\ \phi_2(x)=\frac{2\sqrt{3}}{\sqrt{mL}}\frac{x}{L},\ \phi_3(x)=\frac{6\sqrt{5}}{\sqrt{mL}}\left[\left(\frac{x}{L}\right)^2-\frac{1}{12}\right],$$
$$\phi_4(x)=\frac{20\sqrt{7}}{\sqrt{mL}}\frac{x}{L}\left[\left(\frac{x}{L}\right)^2-\frac{3}{20}\right],$$
$$\phi_5(x)=\frac{210}{\sqrt{mL}}\left[\left(\frac{x}{L}\right)^4-\frac{3}{14}\left(\frac{x}{L}\right)^2+\frac{3}{560}\right]. \quad (10)$$

The approximate natural mode shapes satisfy the orthonormality conditions

$$\int_{\frac{-L}{2}}^{\frac{L}{2}} m\phi_r(x)\phi_s(x)dx=\delta_{rs}(r, s=1, N).$$

Two Control Forces and Two Modes ($N = M = 2$). Let

Downloaded 03 May 2010 to 171.66.16.247. Redistribution subject to ASME license or copyright; see http://www.asme.org/terms/Terms_Use.cfm

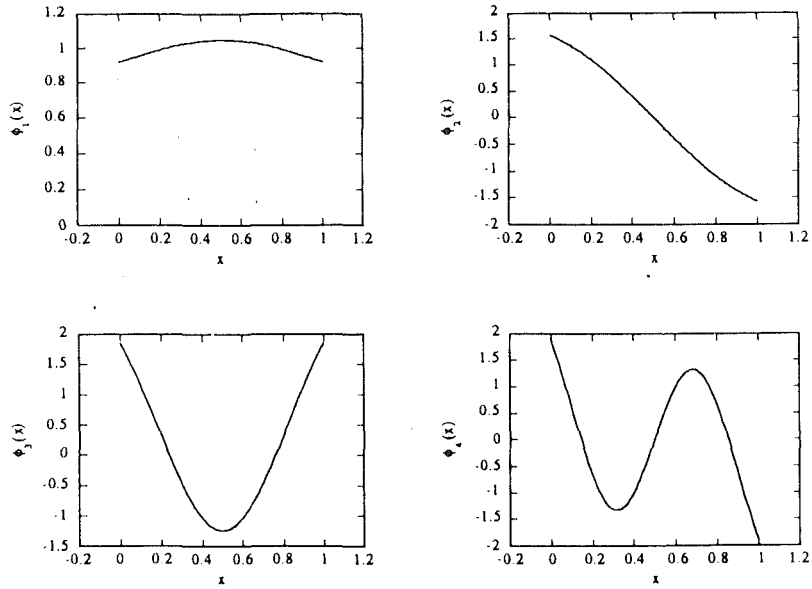


Fig. 5 Spring-beam case 1

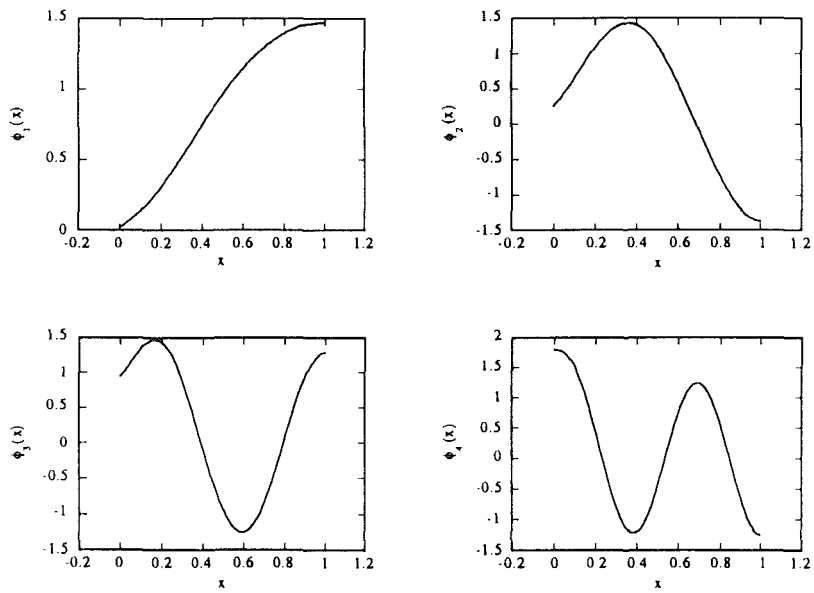


Fig. 6 Spring-beam case 2

the displacement be expressed as a linear combination of the first two mode shapes (Eq. (4)) and we consider two symmetrically placed control forces ($x_1 = -a$, $x_2 = a$). Uniform damping while uncoupling the two closed-loop mode shapes is achieved by diagonalizing the H and G matrices by letting $H = -2\alpha I$ and $G = -\alpha^2 I$. Indeed, by letting $H = -2\alpha I$ and by letting each control gain $g_i = \alpha/2\, h_i$ ($i = 1, N$), we obtain $G = -\alpha^2 I$. The H matrix in Eq. (6) is of the form

$$H = \begin{bmatrix} \dfrac{h_1+h_2}{mL} & a\sqrt{12}\,\dfrac{h_2-h_1}{mL^2} \\ a\sqrt{12}\,\dfrac{h_2-h_1}{mL^2} & 12a^2\,\dfrac{h_1+h_2}{mL^3} \end{bmatrix}, \quad G = \frac{\alpha}{2} H. \tag{11}$$

Letting $h_1 = h_2 = h$,

$$H = \begin{bmatrix} \dfrac{2h}{mL} & 0 \\ 0 & 12a^2\,\dfrac{2h}{mL^3} \end{bmatrix}. \tag{12}$$

Uniform damping is achieved when $12a^2/L^2 = 1$ or $a = L/\sqrt{12}$. This results in control force locations $x_1 = -L/\sqrt{12}$ and $x_2 = L/\sqrt{12}$, which are, identically, the two nodes of the third orthonormal polynomial

$$\phi_3(x) = \frac{6\sqrt{5}}{\sqrt{mL}}\left[\left(\frac{x}{L}\right)^2 - \frac{1}{12}\right].$$

Three Control Forces and Three Modes ($N = M = 3$). Let the displacement be expressed as a linear combination of the first three mode shapes (Eq. (4)) and we consider three sy-

Downloaded 03 May 2010 to 171.66.16.247. Redistribution subject to ASME license or copyright; see http://www.asme.org/terms/Terms_Use.cfm

metrically placed control forces ($x_1 = -a$, $x_2 = 0$, $x_3 = a$). The H matrix in Eq. (6) is

$$H = \begin{bmatrix} \frac{h_1+h_2+h_3}{mL} & a\sqrt{12}\,\frac{h_3-h_1}{mL^2} & \frac{6\sqrt{5}}{mL^3}\left[(h_1+h_3)\left(a^2-\frac{L^2}{12}\right)-h_2\frac{L^2}{12}\right] \\ & 12a^2\,\frac{h_1+h_3}{mL^3} & \frac{12a\sqrt{15}}{mL^4}(h_3-h_1)\left(a^2-\frac{L^2}{12}\right) \\ \text{symm.} & & \frac{180}{mL^5}\left[(h_1+h_3)\left(a^2-\frac{L^2}{12}\right)^2+h_2\frac{L^4}{144}\right] \end{bmatrix} \quad (13)$$

which is diagonalized by letting $h_1 = h_3$ and $h_2 = 2h_1(12a^2/L^2 - 1)$. Uniform damping is now achieved when $a = \sqrt{3/20}L$ which results in control force locations $x_1 = -\sqrt{3/20}L$, $x_2 = 0$, $x_3 = \sqrt{3/20}L$ which are identically the nodes of the fourth polynomial mode shape.

Four Control Forces and Four Modes ($N = M = 4$). Let the displacement be expressed as a linear combination of the first four mode shapes (Eq. (4)) and we consider four symmetrically placed control forces ($x_1 = -a$, $x_2 = a$, $x_3 = -b$, $x_4 = b$). This results in the following equations for the H matrix:

$$H_{11} = \frac{h_1+h_2+h_3+h_4}{mL}$$

$$H_{12} = H_{21} = \frac{\sqrt{12}}{mL^2}[a(h_2-h_1)+b(h_4-h_3)]$$

$$H_{13} = H_{31} = \frac{6\sqrt{5}}{mL^3}\left[(h_1+h_2)\left(a^2-\frac{L^2}{12}\right)+(h_3+h_4)\left(b^2-\frac{L^2}{12}\right)\right]$$

$$H_{14} = H_{41} = \frac{20\sqrt{7}}{mL^4}\left[a(h_2-h_1)\left(a^2-\frac{3L^2}{20}\right)+b(h_4-h_3)\left(b^2-\frac{3L^2}{20}\right)\right]$$

$$H_{22} = \frac{12}{mL^3}[a^2(h_1+h_2)+b^2(h_3+h_4)]$$

$$H_{23} = H_{32} = \frac{12\sqrt{15}}{mL^4}\left[a(h_2-h_1)\left(a^2-\frac{L^2}{12}\right)+b(h_4-h_3)\left(b^2-\frac{L^2}{12}\right)\right]$$

$$H_{24} = H_{42} = \frac{40\sqrt{21}}{mL^5}\left[a^2(h_1+h_2)\left(a^2-\frac{3L^2}{20}\right)+b^2(h_3+h_4)\left(b^2-\frac{3L^2}{20}\right)\right]$$

$$H_{33} = \frac{180}{mL^5}\left[(h_1+h_2)\left(a^2-\frac{L^2}{12}\right)^2+(h_3+h_4)\left(b^2-\frac{L^2}{12}\right)^2\right]$$

$$H_{34} = H_{43} = \frac{120\sqrt{35}}{mL^6}\left[a(h_2-h_1)\left(a^2-\frac{L^2}{12}\right)\left(a^2-\frac{3L^2}{20}\right)+b(h_4-h_3)\left(b^2-\frac{L^2}{12}\right)\left(b^2-\frac{3L^2}{20}\right)\right]$$

$$H_{44} = \frac{2800}{mL^7}\left[a^2(h_1+h_2)\left(a^2-\frac{3L^2}{20}\right)^2+b^2(h_3+h_4)\left(b^2-\frac{3L^2}{20}\right)^2\right]. \quad (14)$$

The H matrix is diagonalized by setting $h_1 = h_2$, $h_3 = h_4$, and solving $H_{13} = H_{24} = 0$. The remaining diagonal elements are then set equal to -2α and the four resulting equations are solved for a and b yielding the four control force locations. Once again, these control force locations are identical to the nodes of the fifth polynomial.

4 Node Control of a Pinned-Pinned Beam

The analysis carried out in the previous section can similarly be carried out for a pinned-pinned beam. The actual mode shapes of the pinned-pinned beam are shown in Fig. 1 (with the origin now at the left end of the beam).

$$\phi_r(x) = \sqrt{\frac{2}{mL}}\sin\frac{r\pi x}{L} \quad (15)$$

Two Control Forces and Two Modes ($N = M = 2$). Let the displacement be expressed as a linear combination of the first two mode shapes (Eq. (4)) and we consider two symmetrically placed control forces ($x_1 = L/2 - a$, $x_2 = L/2 + a$). The H matrix is

$$H = \frac{2}{mL}\begin{bmatrix} (h_1+h_2)\cos^2\left(\frac{\pi a}{L}\right) & (h_1-h_2)\cos\left(\frac{\pi a}{L}\right)\sin\left(\frac{2\pi a}{L}\right) \\ (h_1-h_2)\cos\left(\frac{\pi a}{L}\right)\sin\left(\frac{2\pi a}{L}\right) & (h_1+h_2)\sin^2\left(\frac{2\pi a}{L}\right) \end{bmatrix}. \quad (16)$$

The off-diagonal terms are set to zero by letting $h_1 = h_2$, and uniform damping occurs when $a = L/6$, which corresponds to control force locations of $x_1 = L/3$, $x_2 = 2L/3$. These are the nodes of the third mode $\phi_3(x) = \sqrt{2/mL}\sin 3\pi x/L$.

Three Control Forces and Three Modes ($N = M = 3$). Let the displacement be expressed as a linear combination of the first three mode shapes (Eq. (4)) and we consider three symmetrically placed control forces ($x_1 = L/2 - a$, $x_2 = L/2$, and $x_3 = L/2 + a$). The H matrix is

Downloaded 03 May 2010 to 171.66.16.247. Redistribution subject to ASME license or copyright; see http://www.asme.org/terms/Terms_Use.cfm

$$H=\frac{2}{mL}\begin{bmatrix}(h_1+h_3)\cos^2\left(\frac{\pi a}{L}\right)+h_2\ (h_1-h_3)\cos\left(\frac{\pi a}{L}\right)\sin\left(\frac{2\pi a}{L}\right) & -(h_1+h_3)\cos\left(\frac{\pi a}{L}\right)\cos\left(\frac{3\pi a}{L}\right)-h_2\\ (h_1+h_3)\sin^2\left(\frac{2\pi a}{L}\right) & (h_3-h_1)\sin\left(\frac{2\pi a}{L}\right)\cos\left(\frac{3\pi a}{L}\right)\\ \text{symm.} & (h_1+h_3)\cos^2\left(\frac{3\pi a}{L}\right)+h_2\end{bmatrix}. \tag{17}$$

The H matrix is diagonalized by setting $h_1 = h_3$ and $H_{13} = 0$. Requiring uniform damping yields $a = L/4$ and control force locations $x_1 = L/4$, $x_2 = L/2$, $x_3 = 3L/4$, which are the nodes of the fourth mode shape $\phi_4(x) = \sqrt{2/mL}\sin 4\pi x/L$.

Four Control Forces and Four Modes ($N = M = 4$). Let the displacement be expressed as a linear combination of the first four mode shapes (Eq. (4)) and we consider four symmetrically placed control forces ($x_1 = L/2 - b$, $x_2 = L/2 - a$, $x_3 = L/2 + a$, $x_4 = L/2 + b$). The H matrix is

$$H_{11}=\frac{2}{mL}\left[(h_1+h_4)\cos^2\left(\frac{\pi b}{L}\right)+(h_2+h_3)\cos^2\left(\frac{\pi a}{L}\right)\right]$$

$$H_{12}=H_{21}=\frac{2}{mL}\left[(h_1-h_4)\cos\left(\frac{\pi b}{L}\right)\sin\left(\frac{2\pi b}{L}\right)+(h_2-h_3)\cos\left(\frac{\pi a}{L}\right)\sin\left(\frac{2\pi a}{L}\right)\right]$$

$$H_{13}=H_{31}=\frac{-2}{mL}\left[(h_1+h_4)\cos\left(\frac{\pi b}{L}\right)\cos\left(\frac{3\pi b}{L}\right)+(h_2+h_3)\cos\left(\frac{\pi a}{L}\right)\cos\left(\frac{3\pi a}{L}\right)\right]$$

$$H_{14}=H_{41}=\frac{2}{mL}\left[(h_4-h_1)\cos\left(\frac{\pi b}{L}\right)\sin\left(\frac{4\pi b}{L}\right)+(h_3-h_2)\cos\left(\frac{\pi a}{L}\right)\sin\left(\frac{4\pi a}{L}\right)\right]$$

$$H_{22}=\frac{2}{mL}\left[(h_1+h_4)\sin^2\left(\frac{2\pi b}{L}\right)+(h_2+h_3)\sin^2\left(\frac{2\pi a}{L}\right)\right]$$

$$H_{23}=H_{32}=\frac{2}{mL}\left[(h_4-h_1)\sin\left(\frac{2\pi b}{L}\right)\cos\left(\frac{3\pi b}{L}\right)+(h_3-h_2)\sin\left(\frac{2\pi a}{L}\right)\cos\left(\frac{3\pi a}{L}\right)\right]$$

Table 1 Node control for a pinned-pinned beam

i	location x	gain g	gain h	decay rate	frequency (rad/s)
1	.3333333	.0133333	.1333333	.2000000	9.8690
2	.6666667	.0133333	.1333333	.1999999	39.47842
	Coupling Index		0.000000045582088		
1	.250	0.01000	.10000	.2000001	9.8690
2	.500	0.01000	.10000	.2000000	30.4784
3	.750	0.01000	.10000	.1999999	88.8264
	Coupling Index		0.00000002162307993		
1	.200	0.00800	0.08000	.2000001	9.8696
2	.400	0.00800	0.08000	.2000001	39.4784
3	.600	0.00800	0.08000	.2000000	88.8264
4	.800	0.00800	0.08000	.1999995	157.9137
	Coupling Index		0.00000005947994476		
1	.1666667	0.006667	0.066667	.2000000	9.8696
2	.3333333	0.006667	0.066667	.2000000	39.4784
3	.5000000	0.006667	0.066667	.2000000	88.8264
4	.6666667	0.006667	0.066667	.1999999	157.9137
5	.8333333	0.006667	0.066667	.1999999	246.7401
	Coupling Index		0.000000057474115995		
1	.0909091	.0036364	.0363636	.2000000	9.8696
2	.1818182	.0036364	.0363636	.2000000	39.4784
3	.2727273	.0036364	.0363636	.2000000	88.8264
4	.3636364	.0036364	.0363636	.2000000	157.9137
5	.4545454	.0036364	.0363636	.2000000	246.7401
6	.5454545	.0036364	.0363636	.2000000	355.3057
7	.6363636	.0036364	.0363636	.2000000	483.6106
8	.7272727	.0036364	.0363636	.1999999	631.6547
9	.8181818	.0036364	.0363636	.1999999	799.4380
10	.9090909	.0036364	.0363636	.1999999	986.9604
	Coupling Index		0.0000000638727273021		

Table 2 Node control for a cantilevered beam

i	location x	gain g	gain h	decay rate	frequency (rad/s)
1	0.503548	.0164254	0.164254	.2000040	03.51608
2	0.867678	.0120456	0.120456	.1999960	22.03405
	Coupling Index		0.0037391237733		
1	0.358338	0.011938	0.119333	.2000000	3.51602
2	0.644088	0.011027	0.110271	.2000011	22.03461
3	0.905564	0.008747	0.087467	.1999989	61.69687
	Coupling Index		0.0018924787476		
1	0.278752	.0091758	0.091758	.2000000	3.51602
2	0.499915	.0088966	0.088966	.2000004	22.03453
3	0.723224	.0087160	0.087160	.1999997	61.69713
4	0.926547	.0067754	0.067754	.1999999	120.9019
	Coupling Index		0.001270943899764		
1	0.228068	.0075234	0.075234	.2000000	3.51602
2	0.409058	.0071794	0.071794	.2000001	22.03450
3	0.590876	.0073729	0.073729	.2000001	61.69725
4	0.773545	.0071102	0.071102	.1999998	120.9018
5	0.939903	.0055470	0.055470	.1999999	199.8595
	Coupling Index		0.00091507500759		
1	0.119464	.0039380	0.039380	.2000000	3.51602
2	0.214268	.0037691	0.037691	.2000000	22.03449
3	0.309525	.0038160	0.038160	.2000000	61.69722
4	0.404762	.0038150	0.038150	.2000000	120.9019
5	0.500000	.0038096	0.038096	.2000000	199.8595
6	0.595238	.0038043	0.038043	.2000000	298.5555
7	0.690477	.0038037	0.038037	.2000000	416.9908
8	0.785696	.0038526	0.038526	.2000000	555.1652
9	0.881381	.0037267	0.037267	.2000000	713.0789
10	0.968534	.0029047	0.029047	.2000000	890.7318
	Coupling Index		0.000314892620428		

Downloaded 03 May 2010 to 171.66.16.247. Redistribution subject to ASME license or copyright; see http://www.asme.org/terms/Terms_Use.cfm

Table 3 Node control for spring beam (case #1)

i	location x	gain g	gain h	decay rate	frequency (rad/s)
1	.2386933	.0204113	.204113	.2055905	4.29314
2	.7613066	.0204113	.204113	.1940779	9.58627
	Coupling Index		2.6595395 *	10^{-9}	
1	.1442347	.0126558	0.126558	.2036451	4.29319
2	.5	.0153298	0.153298	.1988212	9.58622
3	.8557654	.0126558	0.126558	.1974272	30.3069
	Coupling Index		9.4328082 *	10^{-5}	
1	.1024072	.0090944	.090944	.2027340	4.29321
2	.3616265	.0111632	.111632	.2009101	9.58620
3	.6383735	.0111632	.111632	.1968352	30.3069
4	.8945928	.0090944	.090944	.1994274	70.5656
	Coupling Index		6.08028736 *	10^{-5}	
1	.0789942	.0070528	.070528	.2022326	4.29322
2	.2824228	.0088018	.088018	.2014944	9.58620
3	.5	.0087245	.087245	.1980562	30.3069
4	.7175772	.0088018	.088018	.1978658	70.5656
5	.9210052	.0070527	.070527	.2002931	130.389
	Coupling Index		4.88428365 *	10^{-5}	
1	.0408328	.0037451	.037451	.2001792	4.29327
2	.1492711	.0047195	.047195	.2018846	9.58619
3	.2664817	.0045801	.045801	.2016587	30.3069
4	.3832310	.0046395	.046395	.1983051	70.5656
5	.5	.0046996	.046996	.1978004	130.389
6	.6167690	.0046395	.046395	.1979804	209.770
7	.7335183	.0045801	.045801	.1987382	308.775
8	.8507288	.0047195	.047195	.2013394	427.442
9	.9591667	.0037450	.037450	.2019867	565.797
	Coupling Index		3.900864294 *	10^{-5}	

Table 4 Node control for spring beam (case #2)

i	location x	gain g	gain h	decay rate	frequency (rad/s)
1	.3934881	.0159785	.159785	.2000000	6.705107
2	.7953705	.0162112	.162112	.2000000	25.81324
	Coupling Index		6.60909188 *	10^{-5}	
1	.2336100	.0112950	.112950	.2000001	6.705111
2	.5359964	.0139968	.139968	.1999999	25.81323
3	.8452560	.0115332	.115332	.2000000	59.79727
	Coupling Index		8.693521094 *	10^{-4}	
1	.1438878	.0087644	.087644	.2000002	6.705113
2	.3825860	.0105592	.105592	.1999998	25.81322
3	.6299214	.0113054	.113054	.2000000	59.79727
4	.8766910	.0087306	.087306	.2000000	103.2628
	Coupling Index		8.2710022564 *	10^{-4}	
1	.0994375	.0070270	.070270	.2000000	6.705108
2	.2934444	.0091215	.091215	.2000000	25.81324
3	.4957115	.0073493	.073493	.2000000	59.79727
4	.6975859	.0091712	.091712	.2000000	103.2628
5	8993453	.0073780	.073780	.2000000	161.8567
	Coupling Index		6.61713385 *	10^{-4}	
1	.0517192	.0044529	.044529	.2000000	6.705107
2	.1728019	.0050976	.050976	.2000000	25.81324
3	.3004007	.0051614	.051614	.2000000	59.79728
4	.4276769	.0050672	.050672	.2000000	103.2628
5	.5549670	.0051088	.051088	.2000000	161.8567
6	.6822562	.0050209	.050209	.2000000	242.1531
7	.8095505	.0053132	.053132	.2000000	344.0245
8	.9367289	.0049107	.049107	.2000000	466.5098
	Coupling Index		9.22682943905 *	10^{-5}	

$$H_{24}=H_{42}=\frac{-2}{mL}\left[(h_1+h_4)\sin\left(\frac{2\pi b}{L}\right)\sin\left(\frac{4\pi b}{L}\right)+(h_2+h_3)\sin\left(\frac{2\pi a}{L}\right)\sin\left(\frac{4\pi a}{L}\right)\right]$$

$$H_{33}=\frac{2}{mL}\left[(h_1+h_4)\cos^2\left(\frac{3\pi b}{L}\right)+(h_2+h_3)\cos^2\left(\frac{3\pi a}{L}\right)\right]$$

$$H_{34}=H_{43}=\frac{2}{mL}\left[(h_1-h_4)\cos\left(\frac{3\pi b}{L}\right)\sin\left(\frac{4\pi b}{L}\right)+(h_2-h_3)\cos\left(\frac{3\pi a}{L}\right)\sin\left(\frac{4\pi a}{L}\right)\right]$$

$$H_{44}=\frac{2}{mL}\left[(h_1+h_4)\sin^2\left(\frac{4\pi b}{L}\right)+(h_2+h_3)\sin^2\left(\frac{4\pi a}{L}\right)\right]. \tag{18}$$

This matrix reduces to $H = -2\alpha I$ when $h_1 = h_2 = h_3 = h_4 = -2/5\ \alpha mL$ and the control force locations are $x_1 = L/5$, $x_2 = 2L/5, x_3 = 3L/5, x_4 = 4L/5$, which are the node locations for the fifth mode shape $\phi_5(x) = \sqrt{2/mL}\sin 5\pi x/L$.

In each of the previous cases, the modal equations were decoupled and natural control was achieved. That is, the open-loop frequencies and mode shapes were preserved. These simple studies suggest certain properties of node control for beams in general. These properties are described in the following theorem.

Node Control Theorem. If a uniform beam with homogeneous boundary conditions and with the lowest N modes participating in the system response is subject to N direct state feedback control forces placed at the N nodes of the $N+1$th mode, then the control gains can be selected such that the following properties apply to the controlled system:

(1) frequency invariance $\beta_r = \omega_r$ $(r = 1, N)$,
(2) mode invariance $\phi_{CL,r}(x) = \phi_r(x)$ $(r = 1, N)$, and
(3) uniform damping $\alpha_r = \alpha$ $(r = 1, N)$.

The node control theorem is further tested in the next section by considering beams with various homogeneous boundary conditions.

Table 5 Ten lowest natural frequencies (rad/s)

Mode Number	Cantilever Beam	Pinned - Pinned Beam	Spring Beam (case #1)	Spring Beam (case # 2)
1	3.51602	9.8696	4.293275	6.705107
2	22.03449	39.4784	9.586212	25.81324
3	61.69721	88.8264	30.30686	59.79728
4	120.9019	157.9137	70.56564	103.2628
5	199.8595	246.7401	130.3891	161.8567
6	298.5555	355.3058	209.7703	242.1531
7	416.9908	483.6106	308.7749	344.0246
8	555.1652	631.6547	427.4421	466.5098
9	713.0789	799.4380	565.7965	609.1368
10	890.7318	986.9604	723.8534	771.6943

5 Node Control of Beams With Varying Boundary Conditions

It has been shown from a perturbation analysis that the first-order approximation of the decay rates for $\alpha/\omega < .4$ in matrix form is (Weaver, 1990)

$$\boldsymbol{\alpha} = -\frac{1}{2}\Phi\mathbf{h}, \tag{19}$$

where $\mathbf{h} = [h_1 h_2 \ldots h_M]^T$, $\boldsymbol{\alpha} = [\alpha_1\alpha_2 \ldots \alpha_N]^T$, and the matrix Φ is given by

$$\Phi_{ij} = \phi_i^2(x_j) \quad (i = 1, N;\ j = 1, M). \tag{20}$$

Downloaded 03 May 2010 to 171.66.16.247. Redistribution subject to ASME license or copyright; see http://www.asme.org/terms/Terms_Use.cfm

The perturbation analysis yields accurate decay rates when $\alpha_r/\omega_r < 0.4$. Clearly, from Eq. (19), if $N = M$ and the matrix Φ is nonsingular, the control gain vectors $\mathbf{h}$ and $\mathbf{g}$ can be found directly from

$$\mathbf{h} = -2\Phi^{-1}\alpha, \quad \mathbf{g} = \frac{\alpha}{2}\mathbf{h}. \tag{21}$$

Otherwise, if the Φ matrix is not invertible, a generalized inverse can be used to obtain the control gains. Eq. (21) is extremely useful for node control cases.

So far, two beams with symmetric boundary conditions have been studied to motivate node control. Now, beams with nonsymmetric boundary conditions are examined. In particular we consider a cantilevered beam and two spring beam cases (see Fig. 1). These cases further test the node control method and the properties predicted by the node control theorem of the previous section. In the following cases we chose the number N of modes and forces, then the N forces are placed at the N nodes of the next uncontrolled mode (based on the natural modes computed for each beam). Next the control gains are determined from Eq. (21) using the generalized inverse.

Several cases of node control of a pinned-pinned beam are summarized in Table 1, along with the mode coupling index. The mode coupling index is calculated by adding the magnitude of the off diagonal terms of the coupling coefficients matrix $[\phi_1\phi_2 \ldots \phi_N]$ and dividing the result by the total sum of magnitudes. The mode coupling index indicates the degree to which the closed-loop modes differ from the open-loop modes. A mode coupling index of zero indicates that the closed-loop modes are identical to the open-loop modes in which case the coupling coefficients matrix is the identity matrix.

Table 2 shows node control for several cases of a cantilevered beam, while Tables 3 and 4 show the spring beam cases. Clearly in all of the cases, uniform damping is achieved. The low modal coupling achieved with node control in all of the cases is on the order of numerical round-off error. Furthermore as expected, the closed-loop frequencies closely approximate the open-loop frequencies (which are shown in Table 5). Thus the tables confirm the three properties predicted by the node control theorem.

6 Conclusions

This paper introduced a method of control called node control whereby control forces are placed at the nodes of the first uncontrolled mode. Node control was motivated by the node control theorem introduced in this paper. The node control theorem was verified for specific boundary conditions. The theorem states, under certain conditions, that node control preserves the natural frequencies and natural modes of vibration of the controlled system while achieving uniform damping. In the cases considered, the open-loop and closed-loop modes and frequencies were indistinguishable. The systems considered were pinned-pinned, cantilevered, free-free beams, and two cases of beams with springs on the boundaries. The node control theorem was not proven in general, but only verified for the cases considered. It is conceivable that some or all of the properties of the node control theorem apply to other types of structures.

7 References

Meirovitch, L., 1986, *Elements of Vibrational Analysis*, 2nd ed., McGraw-Hill, New York.

Meirovitch, L., and Silverberg, L., 1983, "Globally Optimal Control of Self-Adjoint Distributed Systems," *Journal of Optimal Control, Applications and Methods*, Vol. 4, pp. 365–386.

Silverberg, L., 1986, "Uniform Damping Control of Spacecraft," *Journal of Guidance, Control and Dynamics*, Vol. 9, No. 2, pp. 221–227.

Silverberg, L., and Morton, M., 1989, "On the Nature Of Natural Control," ASME *Journal of Vibration, Stress, and Reliability in Design*, Vol. 111, pp. 412–422.

Weaver, Jr., L., 1990, "Two Methods That Uniformly Dampen Beam Motion Using Discrete Control Forces," Master's Thesis, North Carolina State University, Raleigh, NC.

Downloaded 03 May 2010 to 171.66.16.247. Redistribution subject to ASME license or copyright; see http://www.asme.org/terms/Terms_Use.cfm

Z. E. Boutaghou
Staff Development Member,
Prototype and File Technology,
IBM Corporation,
Rochester, MN 55901

Arthur G. Erdman
Professor,
Mechanical Engineering Department,
University of Minnesota,
Minneapolis, MN 55455
Fellow ASME

Henryk K. Stolarski
Associate Professor,
Civil and Mineral Engineering Department,
University Minnesota,
Minneapolis, MN 55455

Dynamics of Flexible Beams and Plates in Large Overall Motions

The dynamic response of flexible beams, plates, and solids undergoing arbitrary spatial motions are systematically derived via a proposed approach. This formulation is capable of incorporating arbitrary representation of the kinematics of deformation, phenomenon of dynamic stiffening, and complete nonlinear interaction between elastic and rigid-body dynamics encountered in constrained multibody systems. It is shown that the present theory captures the phenomenon of dynamic stiffening due to the transfer of the axial and membrane forces to the bending equations of beams and plates, respectively. Examples are presented to illustrate the proposed formulations.

Introduction

A wealth of formulations have been presented enabling the assertions of dynamic stiffening effects (Kane, Ryan, and Banerjee, 1986; Simo and Vu-Quoc, 1987; Wu and Haug, 1988; Ider and Amirouche, 1989; Padilla and von Flotow, 1989; Peterson, 1989; Boutaghou and Erdman, 1990), initial curvature (Bartelone and Shabana, 1989), rotary inertia (Gau and Shabana, 1990), and others on the response of beams undergoing large overall motions. Further, the formulation of multibody systems involves satisfaction of various kinematic and geometric constraints (Gear, 1971; Walton and Steenes, 1984; Kane and Levinson, 1980; Wehage and Haug, 1982; Ider and Amirouche, 1989; Singh et al., 1984; Yoo and Haug, 1985; Agrawal and Shabana, 1985; Park et al., 1988). As a consequence, a diversity of approaches for studying deformable beamlike multibody components have been formulated as illustrated by the works of Sunada and Dubowsky (1981), Thompson and Sung (1984), Shabana (1985), Nagathan and Soni (1986), Kim and Haug (1988), and Ider and Amirouche (1989).

On the other hand, the formulation of plates undergoing arbitrary spatial motion have been limited to a few investigations (Banerjee and Kane, 1989; Chang and Shabana, 1989, 1990) even though plate-like multibody components are of interest to a wide variety of multibody systems and in particular spacecrafts. Spacecrafts consist of a rigid main body and several flexible appendages, such as antenna, solar panel, robot manipulators, etc. Light-weight design, minimum energy consumption, and vibration suppression are the major concerns for spacecraft design.

Recently, Banerjee and Kane (1989) proposed the dynamics of a thin plate with inextensible middle surface undergoing large rigid-body motion. Their formulations are capable of capturing the dynamic stiffening effects by retaining the appropriate nonlinearities. However, the extension of this approach to general multibody situations is extremely cumbersome. The theory assumes a given rigid-body motion. A spin-up maneuver problem of a thin plate was considered.

Chang and Shabana (1990) utilized the Love-Kirchhoff hypothesis to model the large rigid-body motion and small elastic deformation of a thin plate in large overall motion. Their formulation are suitable for multibody situations since the kinematic constraints between connected bodies are accounted for. A spatial RSSR mechanism comprising a flexible coupler plate and two rigid input and follower links was investigated via their formulations. However, the rotational speed of the RSSR mechanism was maintained small such that the dynamic stiffening effects remain negligible.

In this paper, the derivation of the equations of motion for general systems has been undertaken from a fundamental point of view by the introduction of arbitrary representation of the kinematics of deformation. These formulations are based on Hamilton's principle allowing the introduction of various kinematic and geometric constraints relating the deformation variables. As a consequence, the equations of motion of beams, plates, and solids undergoing arbitrary spatial motion can be derived via the generalized approach by specifying the particular representation of kinematics of deformation which may include shear, initial curvature, initial twist, arbitrary cross-sectional effects, dynamic stiffening effects, rotary inertia, von Karman geometric constraints, and kinematic constraints. This

Contributed by the Applied Mechanics Division of THE AMERICAN SOCIETY OF MECHANICAL ENGINEERS for publication in the ASME JOURNAL OF APPLIED MECHANICS.

Discussion on this paper should be addressed to the Technical Editor, Professor Leon M. Keer, The Technological Institute, Northwestern University, Evanston, IL 60208, and will be accepted until four months after final publication of the paper itself in the ASME JOURNAL OF APPLIED MECHANICS.

Manuscript received by the ASME Applied Mechanics Division, Apr. 19, 1991; final revision, Oct. 17, 1991. Associate Technical Editor: D. J. Inman.

Copyright © 1992 by ASME
Downloaded 03 May 2010 to 171.66.16.247. Redistribution subject to ASME license or copyright; see http://www.asme.org/terms/Terms_Use.cfm

research contributed a step towards the generalization of the existing formulations for flexible multibody systems relative to a moving reference frame. Application examples were carried out for two cases to validate the proposed formulations: (a) the Euler-Bernoulli beam kinematics with the von Karman geometric constraint, and (b) the Love-Kirchhoff hypothesis for plates with the von Karman geometric constraints.

The equations of motion for a thin plate in an arbitrary spatial motion are developed by constraining the displacement of a point off the membrane of the plate to satisfy the von Karman geometric constraints. This practice yields linear equations capable of accounting for the dynamic stiffening effects in multibody systems; thus avoiding the cumbersome numerical difficulties associated with the corresponding nonlinear formulations.

This paper is divided in four sections. The first section gives an introduction to the motivation. Section 2 presents the development of the equations of motion of a generalized system employing Hamilton's principle without prior hypothesis about the kinematic representation of deformation. With emphasis on the Euler-Bernoulli beam model, the theoretical considerations relevant to the dynamic stiffening effects are discussed through a numerical example in the third section. The fourth section applies the proposed formulation to derive the equations of motion for a thin plate in a specified spatial motion. The finite element discretization of the resulting equations of motion is briefly outlined. Conclusions form the last section.

2 Dynamics of a Deformable System

Hamilton's principle is used to formulate the governing equations of an elastic body undergoing three-dimensional motion. We assume here that the external forces are conservative. If this is not the case, the corresponding modification of the generalized external forces due to nonconservative load can be introduced after variation of the least action functional is calculated. In either case the inertia and stiffness terms of the resulting equations are identical. Those are the terms that are responsible for the dynamic stiffening effects which is emphasized in this work.

The variation of the kinetic energy of a deformable body is shown to contain the inertial forces from the rigid-body motion, the coupling between the rigid-body motion and the elastic-body motion, and the coupling between the elastic deformations. The equations of motion describing the uncoupled longitudinal and transverse motions for a typical member of a multibody system are developed in this section using Hamilton's principle.

Hamilton's form of the principle of least action requires that the action (Arnold, 1980)

$$L=\int_{t_1}^{t_2}(T-\Pi+W)dt \tag{1}$$

be stationary for the solution path among arbitrary neighboring paths connecting two points at time t_1 and t_2 in the configuration space. T, Π, and W are the kinetic energy, the strain energy, and the work done by the forces acting on the deformable body, respectively.

This position vector $\mathbf{R}$ of an arbitrary infinitesimal element dm located on a deformable body can be represented by Fig. 1

$$\mathbf{R}=\mathbf{R}_o+\mathbf{r}. \tag{2}$$

Here, $\mathbf{R}_o(\bar{x},\bar{y},\bar{z},t)=\Sigma_{i=1}^{3}R_{oi}(\bar{x},\bar{y},\bar{z},t)\,\mathbf{i}_i$ is the position vector of the joint located on a translating frame $[\mathbf{e}_1(t)\mathbf{e}_2(t)\mathbf{e}_3(t)]$ which is defined with respect to the inertial frame $[\mathbf{i}_1\mathbf{i}_2\mathbf{i}_3]$ and $\mathbf{r}$ is the position vector of an infinitesimal element dm located on the deformable body with respect to the translating frame.

$\mathbf{r}$ may depend on the rigid-body rotation variables, Ω_i ($i=1,3$), and the generalized coordinates of deformation, q_j ($j=1,n$), (see Meirovitch, 1980):

$$\mathbf{r}=\mathbf{r}(q_1,q_2,\ldots,q_n,\Omega_1,\Omega_2,\Omega_3) \tag{3}$$

where $\Omega(t)=\Sigma_{i=1}^{3}\Omega_i(t)\mathbf{e}_i(t)$ contains the rotation variables (such as Rodrigues parameters) monitoring the motion of a rigid frame embedded in the deformable body (floating frame $[\mathbf{a}_1(t)\mathbf{a}_2(t)\mathbf{a}_3(t)]$) with respect to the translating frame and $\mathbf{q}(x,y,z,t)=\Sigma_{j=1}^{n}q_j(x,y,z,t)\,\mathbf{a}_j(t)$ is the vector containing the generalized coordinates of deformation defined with respect to the floating frame.

The time derivative of the position vector $\mathbf{R}$ is (Meirovitch, 1980):

$$\frac{d\mathbf{R}}{dt}=\frac{d\mathbf{R}_o}{dt}+\omega\times\mathbf{r}+\sum_{s=1}^{n}\frac{\partial\mathbf{r}}{\partial q_s}\dot{q}_s \tag{4}$$

where $\dot{(\ )}$ is the first time derivative, $(\times)$ vector product, and $\omega=\Sigma_{i=1}^{3}\omega_i\mathbf{e}_i$ the angular velocity of the floating frame with respect to the translating frame.

The kinetic energy of the entire system is

$$T=\frac{1}{2}\int_m\frac{d\mathbf{R}}{dt}\cdot\frac{d\mathbf{R}}{dt}\,dm, \tag{5}$$

where $(\cdot)$ denotes the dot product.

Substituting the expression for the velocity, Eq. (4), into the expression for the kinetic energy, Eq. (5), yields

$$T=\frac{1}{2}m\mathbf{V}_o\cdot\mathbf{V}_o+m\mathbf{V}_o\cdot(\omega\times\mathbf{r}_c)+\frac{1}{2}(\omega\cdot\mathbf{J}\omega)+\int_m\left\{\mathbf{V}_o\cdot\sum_{r=1}^{n}\frac{\partial\mathbf{r}}{\partial q_r}\dot{q}_r+\omega\times\left(\mathbf{r}\times\sum_{r=1}^{n}\frac{\partial\mathbf{r}}{\partial q_r}\dot{q}_r\right)+\frac{1}{2}\sum_{r=1}^{n}\sum_{t=1}^{n}\frac{\partial\mathbf{r}}{\partial q_r}\cdot\frac{\partial\mathbf{r}}{\partial q_t}\dot{q}_r\dot{q}_t\right\}dm. \tag{6}$$

Here $\mathbf{V}_o(\bar{x},\bar{y},\bar{z},t)=d\mathbf{R}_o(\bar{x},\bar{y},\bar{z},t)/dt=\Sigma_{i=1}^{3}V_{oi}(\bar{x},\bar{y},\bar{z},t)\,\mathbf{i}_i$ is the translation velocity of the joint of the deformable body with respect to the inertial frame. m is the total mass of the body. $\mathbf{r}_c=\int_m\mathbf{r}dm/m$ is the mass center of the deformable body, and $\mathbf{J}$ is the inertia tensor of the deformable body.

The variation of the kinetic energy, Eq. (6), with respect to the generalized coordinates of deformation, the translational variables, and the rotational variables can be derived as follows (Whittaker, 1937):

$$\delta T=\sum_{s=1}^{n}\left(\frac{\partial T}{\partial q_s}\delta q_s+\frac{\partial T}{\partial\dot{q}_s}\delta\dot{q}_s\right)+\sum_{i=1}^{3}\left(\frac{\partial T}{\partial R_{oi}}\delta R_{oi}+\frac{\partial T}{\partial V_{oi}}\delta V_{oi}\right)+\sum_{i=1}^{3}\left(\frac{\partial T}{\partial\Omega_i}\delta\Omega_i+\frac{\partial T}{\partial\omega_i}\delta\omega_i\right). \tag{7}$$

Integrating Eq. (7) by parts yields an expression for the variation of the kinetic energy free of $\delta\dot{q}_s$, $\delta\omega_i$ and δV_{oi}:

$$\delta T=\sum_{s=1}^{n}\left(\frac{\partial T}{\partial q_s}+\frac{d}{dt}\frac{\partial T}{\partial\dot{q}_s}\right)\delta q_s+\sum_{i=1}^{3}\left(\frac{d}{dt}\frac{\partial T}{\partial V_{oi}}+\sum_{(j,k=1)}^{3}e_{ijk}\omega_j\frac{\partial T}{\partial V_{ok}}\right)\delta R_{oi}+\sum_{i=1}^{3}\left(\frac{d}{dt}\frac{\partial T}{\partial\omega_i}+\sum_{(j,k=1)}^{3}e_{ijk}\omega_j\frac{\partial T}{\partial\omega_k}+\sum_{(j,k=1)}^{3}e_{ijk}V_{oj}\frac{\partial T}{\partial V_{ok}}\right)\delta\Omega_i \tag{8}$$

where e_{ijk} is the permutation symbol and assumes the value 0, +1, or −1 as follows:

$$e_{ijk}=\begin{cases}0 \text{ when any two indices are equal}\\ +1 \text{ when } ijk \text{ are in cyclic permutation}\\ -1 \text{ when } ijk \text{ are in anticyclic permutation.}\end{cases} \tag{9}$$

The elementary work done by the generalized forces $\mathbf{F}$, $\mathbf{M}$,

Downloaded 03 May 2010 to 171.66.16.247. Redistribution subject to ASME license or copyright; see http://www.asme.org/terms/Terms_Use.cfm

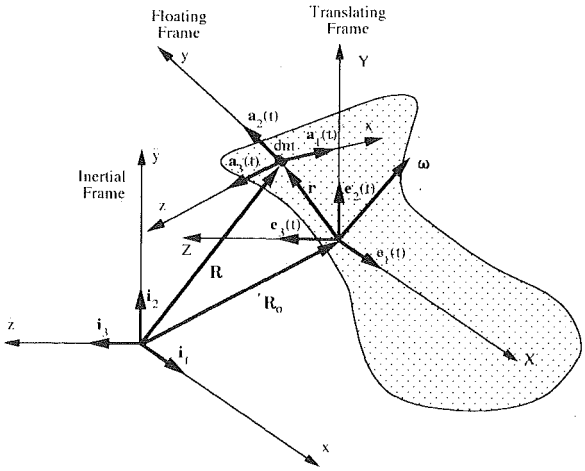


Fig. 1 Deformable body with generalized position vectors

and **Q** acting on the deformable body can be expressed as (Meirovitch, 1980)

$$\delta W = \mathbf{F}\cdot\delta\mathbf{R}_o + \mathbf{M}\cdot\delta\Omega + \mathbf{Q}\cdot\delta\mathbf{q}. \tag{10}$$

Application of Eq. (8) necessitates taking the derivatives of the kinetic energy, Eq. (6), with respect to the generalized coordinates of deformations, the translational variables, and the rotational variables. After performing the necessary differentiations the following equation is derived:

$$\delta L = \int_{t_1}^{t_2} \left\{ \int_m \sum_{s=1}^{n} \left[\sum_{r=1}^{n} \frac{\partial \mathbf{r}}{\partial q_r}\cdot\frac{\partial \mathbf{r}}{\partial q_s}\ddot{q}_r + \sum_{(r,t=1)}^{3} \frac{\partial^2 \mathbf{r}}{\partial q_r \partial q_t}\cdot\frac{\partial \mathbf{r}}{\partial q_s}\dot{q}_r\dot{q}_t \right.\right.$$
$$+ 2\omega\cdot\sum_{r=1}^{n}\frac{\partial \mathbf{r}}{\partial q_r}\times\frac{\partial \mathbf{r}}{\partial q_s}\dot{q}_r + (\dot{\mathbf{V}}_o + \omega\times\mathbf{V}_o)\cdot\frac{\partial \mathbf{r}}{\partial q_s} + \dot{\omega}\cdot\left(\mathbf{r}\times\frac{\partial \mathbf{r}}{\partial q_s}\right)$$
$$\left.\left. - \frac{1}{2m}\left(\omega\cdot\frac{\partial \mathbf{J}}{\partial q_s}\omega\right)\right] \delta q_s dm - \mathbf{Q}\cdot\delta\mathbf{q} - \delta\Pi + \int_m \left[\mathbf{J}\dot{\omega} + \sum_{r=1}^{n}\frac{\partial \mathbf{J}}{\partial q_r}\dot{q}_r\omega \right.\right.$$
$$+ (\omega\times\mathbf{J}\omega) + \sum_{(r,t=1)}^{n}\frac{\partial \mathbf{r}}{\partial q_r}\times\frac{\partial \mathbf{r}}{\partial q_t}\dot{q}_t\dot{q}_r + \mathbf{r}\times\sum_{(r,t=1)}^{n}\frac{\partial^2 \mathbf{r}}{\partial q_r\partial q_t}\dot{q}_r\dot{q}_t$$
$$+ \mathbf{r}\times\sum_{r=1}^{n}\frac{\partial \mathbf{r}}{\partial q_r}\ddot{q}_r + \omega\times\left(\mathbf{r}\times\sum_{r=1}^{n}\frac{\partial \mathbf{r}}{\partial q_r}\dot{q}_r\right)$$
$$\left.\left. + \mathbf{r}\times(\dot{\mathbf{V}}_o + \omega\times\mathbf{V}_o)\right] dm\cdot\delta\Omega - \mathbf{M}\cdot\delta\Omega + \int_m \left[\dot{\mathbf{V}}_o + (\omega\times\mathbf{V}_o) \right.\right.$$
$$+ \omega\times(\omega\times\mathbf{r}) + \dot{\omega}\times\mathbf{r} + 2\omega\times\sum_{r=1}^{n}\frac{\partial \mathbf{r}}{\partial q_r}\dot{q}_r + \sum_{(r,t=1)}^{n}\frac{\partial^2 \mathbf{r}}{\partial q_r\partial q_t}\dot{q}_r\dot{q}_t$$
$$\left.\left. + \sum_{r=1}^{n}\frac{\partial \mathbf{r}}{\partial q_r}\ddot{q}_r\right] dm\cdot\delta\mathbf{R}_o - \mathbf{F}\cdot\delta\mathbf{R}_o \right\} dt = 0 \tag{11}$$

where (¨) denotes the second time derivative.

Note that the above equation is expressed independent of the geometry of the deformable body and the representation of the kinematics of deformations. The expression for the variation of the strain energy depends on the particular beam and plate model selected to describe the work done by the internal forces. In this regard, the following sections confine attention to the development of beam and plate motion equations based on the Euler-Bernoulli and Love-Kirchoff hypothesis with the von Karman geometric constraints, respectively.

3 Thin Beam Formulations

The equations describing the flexural and longitudinal motions for beam-like members encountered in spin-up maneuver problems are developed here. These members are modeled as Euler-Bernoulli beam models.

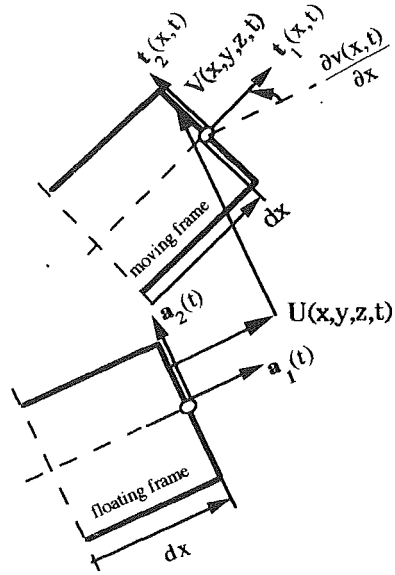


Fig. 2 Kinematics of deformation: Euler-Bernoulli beam

3.1 Basic Representation of Deformation Kinematics. Let us consider an inertial frame denoted by $[\mathbf{i}_1\mathbf{i}_2\mathbf{i}_3]$. The position of a point O located on a translating frame $[\mathbf{e}_1(t)\mathbf{e}_2(t)\mathbf{e}_3(t)]$ positioned on the origin of the center line of the elastic beam before deformation is monitored by the vector position $\mathbf{R}_o(t)$ (Fig. 2). In the stage of rigid-body transformation, the translating frame is carried to the floating frame $[\mathbf{a}_1(t)\mathbf{a}_2(t)\mathbf{a}_3(t)]$, respectively, by the prescribed rigid-body rotation $\Omega(t)$.

The elastic displacement components of every point off the center line of the elastic beam are described by $\mathbf{q}(x,y,z,t) = [U(x,y,z,t) \quad V(x,y,z,t) \quad W(x,y,z,t)]^T$ in the direction $[\mathbf{a}_1(t)\mathbf{a}_2(t)\mathbf{a}_3(t)]$, respectively. A material point initially located off the center line of the beam is given with respect to the floating frame after deformation by

$$\mathbf{r}(x,y,z,t) = \mathbf{R}(x,y,z,t) - \mathbf{R}_o(t) = (x + U(x,y,z,t))\mathbf{a}_1(t) + V(x,y,z,t)\mathbf{a}_2(t) + W(x,y,z,t)\mathbf{a}_3(t). \tag{12}$$

In this approach, $u(x,t)$, $v(x,t)$, and $w(x,t)$ are the components of the deformation vector so that the total displacement of the center line $\overline{U}(x,t)$, $\overline{V}(x,t)$, and $\overline{W}(x,t)$ are

$$\overline{U}(x,t) = u(x,t) + \frac{1}{2}\int_x^L \left(\frac{\partial v(\xi,t)}{\partial \xi}\right)^2 d\xi + \frac{1}{2}\int_x^L \left(\frac{\partial w(\xi,t)}{\partial \xi}\right)^2 d\xi$$
$$\overline{V}(x,t) = v(x,t)$$
$$\overline{W}(x,t) = w(x,t) \tag{13a-c}$$

where the beam is free of any stress at $x = L$, and the integrals represent displacement due to inextensional bending.

The axial strain due to $\overline{U}(x,t)$, $\overline{V}(x,t)$, and $\overline{W}(x,t)$ is

$$\epsilon_x = \frac{\partial \overline{U}}{\partial x} + \frac{1}{2}\left(\frac{\partial \overline{V}}{\partial x}\right)^2 + \frac{1}{2}\left(\frac{\partial \overline{W}}{\partial x}\right)^2. \tag{14}$$

Substituting Eqs. (13*a–c*) into Eq. (14) yields

$$\epsilon_x = \frac{\partial u}{\partial x}. \tag{15}$$

Equivalently, one could use the usual approach in which $\overline{u}(x,t)$, $\overline{v}(x,t)$, and $\overline{w}(x,t)$ represent the total displacement components of the center line (not the components of the deformation vector). In this case, instead of Eq. (15), one could use

Downloaded 03 May 2010 to 171.66.16.247. Redistribution subject to ASME license or copyright; see http://www.asme.org/terms/Terms_Use.cfm

$$\epsilon_x = \frac{\partial \bar{u}}{\partial x} + \frac{1}{2}\left(\frac{\partial \bar{v}}{\partial x}\right)^2 + \frac{1}{2}\left(\frac{\partial \bar{w}}{\partial x}\right)^2. \quad (16)$$

The displacement of a point off the center line $U(x,y,z,t)$, $V(x,y,z,t)$, and $W(x,y,z,t)$ in terms of the components of the deformation vector can be expressed as follows:

$$U(x,y,z,t) = \bar{U}(x,t) - yv(x,t)' - zw(x,t)'$$
$$= u(x,t) - yv(x,t)' - zw(x,t)' + \frac{1}{2}\int_x^L \left(\frac{\partial v(\xi,t)}{\partial \xi}\right)^2 d\xi + \frac{1}{2}\int_x^L \left(\frac{\partial w(\xi,t)}{\partial \xi}\right)^2 d\xi$$

$$V(x,y,z,t) = v(x,t)$$
$$W(x,y,z,t) = w(x,t) \quad (17a\text{–}c)$$

where $(\,)'$ indicates partial differentiation with respect to x.

The development of the equations of motion for a typical member of the multibody system are presented here by first expressing the strain energy of the system using the components of the deformation vector (Eq. (15)):

$$\Pi = \frac{1}{2}\int_0^L EA(u')dx + \frac{1}{2}\int_0^L EI_{zz}(v'')^2 dx + \frac{1}{2}\int_0^L EI_{yy}(w'')^2 dx \quad (18)$$

where E is the modulus of elasticity, I_{zz} and I_{yy} the area moments of inertia, A the cross-sectional area, and L the length of the beam. Throughout, the material is assumed to be homogeneous, isotropic, and linearly elastic.

3.2 Application of Hamilton's Principle. Consistently applying Hamilton's principle of least action (Eq. (9)) using the Euler-Bernoulli beam kinematics (Eq. (12)) and the strain energy (Eq. (18)) yields the following expression:

$$\delta(T-\Pi) = \int_m [\ddot{\mathbf{q}} + 2\tilde{\omega}\dot{\mathbf{q}} + (\dot{\tilde{\omega}} - \omega^2\mathbf{I}_3)\mathbf{q} + \mathbf{f}]\cdot\delta\mathbf{q}\,dm + \int_0^L \begin{bmatrix} EAu'' \\ EI_{zz}v'''' \\ EI_{yy}w'''' \end{bmatrix}\cdot\delta\mathbf{d}\,dx \quad (19)$$

with $\delta\mathbf{q} = \begin{bmatrix} \delta U \\ \delta V \\ \delta W \end{bmatrix}$, $\delta\mathbf{d} = \begin{bmatrix} \delta u \\ \delta v \\ \delta w \end{bmatrix}$,

$$\mathbf{f}(x,y,t) = \begin{bmatrix} f_x(x,t) \\ f_y(x,t) \\ f_z(x,t) \end{bmatrix} = \begin{bmatrix} -x\omega^2 + f_u \\ x\dot{\omega}_3 + f_v \\ -x\dot{\omega}_2 + f_w \end{bmatrix},$$

$$\omega^2 = \omega_1^2 + \omega_2^2 + \omega_3^2, \text{ and } \begin{bmatrix} f_u(t) \\ f_v(t) \\ f_w(t) \end{bmatrix} = [\dot{\mathbf{V}}_o + \omega\times\mathbf{V}_o]\cdot\begin{bmatrix} \mathbf{a}_1(t) \\ \mathbf{a}_2(t) \\ \mathbf{a}_3(t) \end{bmatrix}. \quad (20a\text{–}d)$$

Note that the rigid-body translation $\mathbf{R}_o(t)$ and the rigid-body rotation $\Omega(t)$ are prescribed a priori. The angular velocity of revolution is defined with respect to the floating frame as follows:

$$\omega(t) = \omega_1\mathbf{a}_1(t) + \omega_2\mathbf{a}_2(t) + \omega_3\mathbf{a}_3(t). \quad (21)$$

Note that the expression for the inertia forces in Eq. (19) are developed using the displacement components of a point off the center line (U,V,W) which include the axial displacements due to large deflection represented by $1/2\,(\partial v/\partial x)^2$ and $1/2\,(\partial w/\partial x)^2$. The nonlinear terms do not appear explicitly in the expression for the internal forces and moments, due to a particular kinematic description used in Eq. (13). The presence of the nonlinear terms is implicit since, as stated following Eq. (15), strains described by the latter equation would be equivalent to those defined by Eq. (16) if another kinematic representation were used.

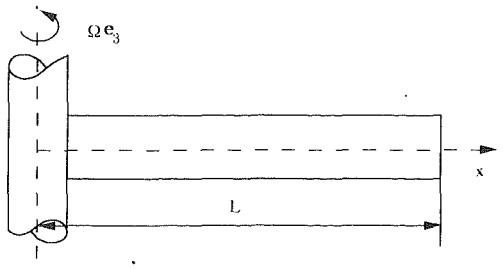


Fig. 3 Beam in spin-up maneuver

3.3 Basic Equations of Motion. The variation of the displacement components of a point off the center line, δU, δV, and δW in terms of the variation of the components of the deformation vector, δu, δv, and δw are obtained by taking the variation of Eqs. (17*a–c*) as follows:

$$\delta U = \delta u - y\delta v' - z\delta w' + v'\delta v + w'\delta w - \int_x^L v(\xi,t)''\delta v\,d\xi - \int_x^L w(\xi,t)''\delta w\,d\xi$$

$$\delta V = \delta v$$
$$\delta W = \delta w. \quad (22a\text{–}c)$$

Substituting the expression for the total displacement components of the center line U, V, and W (Eqs. (17*a–c*)), and their corresponding variations δU, δV, and δW (Eqs. (22*a–c*)) into the expression for Hamilton's principle of least action (Eq.(19)) and applying the condition that the components of the deformation vector $u(x,t)$, $v(x,t)$, and $w(x,t)$ are independent yields the following governing equations of motion for the elastic deformation:

$$A\rho\ddot{\mathbf{d}} + 2A\rho\tilde{\omega}\dot{\mathbf{d}} + A\rho(\dot{\tilde{\omega}} - \omega^2\mathbf{I}_3)\mathbf{d} + \begin{bmatrix} EAu'' \\ EI_{zz}v'''' \\ EI_{yy}w'''' \end{bmatrix} - \begin{bmatrix} 0 \\ -\rho I_{zz}\ddot{v}'' \\ -\rho I_{yy}\ddot{w}'' \end{bmatrix} + \begin{bmatrix} 0 \\ (v'N^{vK1})' \\ (w'N^{vK2})' \end{bmatrix} + A\rho\mathbf{f} = 0 \quad (23)$$

with $N^{vK1} = -A\rho\dfrac{L^2-x^2}{2} - \omega^2 + A\rho(L-x)f_u(t) + \rho I_{zz}\omega^2$,

and $N^{vK2} = -A\rho\dfrac{L^2-x^2}{2}\omega^2 + A\rho(L-x)f_u(t) + \rho I_{yy}\omega^2 \quad (24a\text{–}b)$

where ρ is the constant mass density.

The first four terms of Eq. (23) represent the first-order theory for the transverse vibration of a rotating Euler-Bernoulli beam. The fifth term represents the influence of the rotatory inertia (attributed to Rayleigh). The sixth term is introduced from the transfer of the axial forces N^{vK1} and N^{vK2} along the $\mathbf{a}_1(t)$-direction and contributes to the stability of the bending equations.

3.4 Numerical Application. The spin-up maneuver problem originally suggested by Kane, Ryan, and Banerjee (1986) is used to verify the validity of the proposed formulations. The rotating cantilever beam with rectangular cross-section of Fig.

Downloaded 03 May 2010 to 171.66.16.247. Redistribution subject to ASME license or copyright; see http://www.asme.org/terms/Terms_Use.cfm

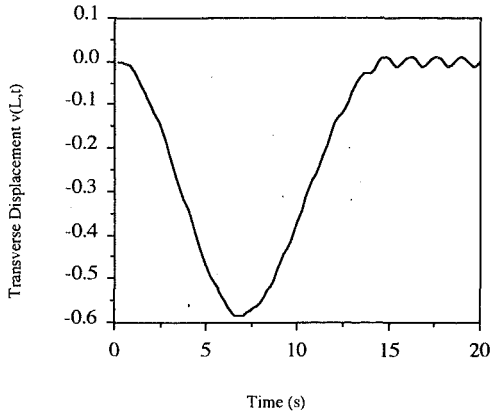


Fig. 4 Tip transverse displacement: Euler-Bernoulli beam model with von Karman constraint

3 is used. The tip deformation in the local beam axis is analyzed using the following data:

$$L=8.0,\ \rho=2766.67,\ E=6.8952\times10^{10},$$
$$I=8.2189\times10^{-9},\ A=7.2986\times10^{-5}\ \text{and}$$
$$\dot{\Omega}=\begin{cases}\dfrac{2\pi n^*}{60t^*}\left(t-\dfrac{t^*}{2\pi}\sin\left(\dfrac{2\pi t}{t^*}\right)\right) & t<t^*\\[2ex] \dfrac{2\pi n^*}{60} & t\geq t^*\end{cases}\qquad(25)$$

The spin-up maneuver problem is characterized by two phases: the acceleration phase and the constant revolution phase. The acceleration phase is achieved by prescribing the rotation law of Eq. (25) the beam is spin up until it reaches an ultimate spin speed $n^* = 60/\pi$ during a spin-up time of $t^* = 15$, then a constant revolution phase is maintained by applying a constant ultimate spin speed $n^* = 60/\pi$. Figure 4 shows the tip transverse displacement using the Euler-Bernoulli beam model with the von Karman geometric constraint (Eq. (23)).

4 Thin Plate Formulations

In this section, the equations describing the deformations of a plate-like multibody component under a given spatial motion are derived.

4.1 Deformation Kinematics. Let $\mathbf{R}_o(t)$ monitor the rigid-body location of the origin O located on a translating frame $[\mathbf{e}_1(t)\mathbf{e}_2(t)\mathbf{e}_3(t)]$ which is attached to the middle plane of the undeformed rectangular thin plate with respect to an inertial frame $[\mathbf{i}_1\mathbf{i}_2\mathbf{i}_3]$ (Fig. 5). In the stage of rigid-body rotation of the thin plate, the translating frame is carried to the floating frame $[\mathbf{a}_1(t)\mathbf{a}_2(t)\mathbf{a}_3(t)]$ by the rigid-body rotation $\Omega(t)$. The vector $\mathbf{a}_3(t)$ is normal to the middle surface. $[x\ y\ z]$ denotes a Cartesian coordinate system along $[\mathbf{a}_1(t)\mathbf{a}_2(t)\mathbf{a}_3(t)]$, respectively. The position of a point on the undeformed middle surface of the plate is given by $\mathbf{r}_o(x,y,t) = x\mathbf{a}_1(t)+y\mathbf{a}_2(t)$. After deformation, the position of a point located on a thin rectangular plate with respect to the floating frame is described in the following form:

$$\mathbf{r}(x,y,z,t)=\mathbf{R}-\mathbf{R}_o=(x+U(x,y,z,t)\mathbf{a}_1(t)+(y+V(x,y,z,t))\mathbf{a}_2(t)+W(x,y,t)\mathbf{a}_3(t).\qquad(26)$$

Note that $\mathbf{q}(x,y,z,t) = [U(x,y,z,t)\ V(x,y,z,t)\ W(x,y,z,t)]^T$ is the displacement vector of a point off the middle surface of a thin rectangular plate under the Love-Kirchhoff hypothesis.

Normally the displacement coordinates of the middle surface $\bar{u}$, $\bar{v}$, and $\bar{w}$ are used to calculate the strains as follows (Mansfield, 1989):

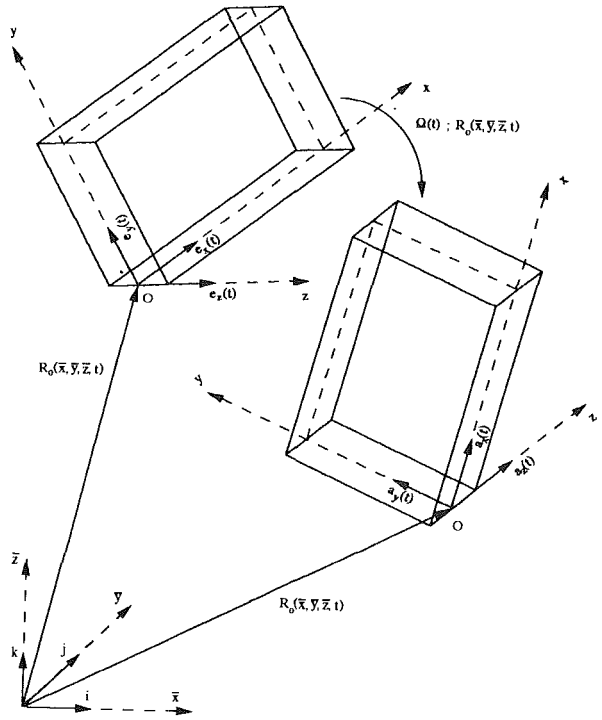


Fig. 5 Rectangular plate in prescribed rigid-body motion

$$\epsilon_x=\frac{\partial\bar{u}}{\partial x}+\frac{1}{2}\left(\frac{\partial\bar{w}}{\partial x}\right)^2$$
$$\epsilon_y=\frac{\partial\bar{v}}{\partial y}+\frac{1}{2}\left(\frac{\partial\bar{w}}{\partial\bar{y}}\right)^2$$
$$\gamma_{xy}=\frac{\partial\bar{u}}{\partial y}+\frac{\partial\bar{v}}{\partial x}+\frac{\partial\bar{w}}{\partial x}\frac{\partial\bar{w}}{\partial y}.\qquad(27a\text{–}c)$$

The geometric stiffness matrix responsible for capturing the dynamic stiffening effects can be deduced from the following form of the strain energy (Mansfield, 1989):

$$\Pi_1=\int_A\begin{bmatrix}\dfrac{\partial\bar{w}}{\partial x}\\[2ex]\dfrac{\partial\bar{w}}{\partial y}\end{bmatrix}^T\begin{bmatrix}N_x & N_{xy}\\ N_{xy} & N_y\end{bmatrix}\begin{bmatrix}\dfrac{\partial\bar{w}}{\partial x}\\[2ex]\dfrac{\partial\bar{w}}{\partial y}\end{bmatrix}dA.\qquad(28)$$

The internal forces N_x, N_y, and N_{xy} acting on an infinitesimal element of the plate are defined in Section 4.2.

If $N_{xy} \approx 0$, then the cross-product $(\partial\bar{w}/\partial w)\ (\partial\bar{w}/\partial_y)$ in Eq. (28) disappears. In this case a procedure similar to the one presented for beams in Section 3 and using the components of the deformation vector $u(x,y,t)$, $v(x,y,t)$, and $w(x,y,t)$ is proposed. When this process is applied to plates, the following expressions for the total displacement of the middle surface are obtained:

$$\bar{U}=u+\frac{1}{2}\int_x^a\left(\frac{\partial w}{\partial x}\right)^2dx$$
$$\bar{U}=v+\frac{1}{2}\int_y^b\left(\frac{\partial w}{\partial y}\right)^2dy$$
$$\bar{W}=w.\qquad(29a\text{–}c)$$

Note that for high angular accelerations of pitch motion of the plate ($N_{xy} \neq 0$), additional terms must be introduced in the expressions for the total displacement components of the

Downloaded 03 May 2010 to 171.66.16.247. Redistribution subject to ASME license or copyright; see http://www.asme.org/terms/Terms_Use.cfm

middle surface. This situation is not considered in this paper. Therefore, the displacement components of a point off the middle surface $U(x,y,t)$, $V(x,y,t)$, and $W(x,y,t)$ in terms of the components of the deformation vector can be expressed as follows (Eqs. (29*a–c*)):

$$U(x,y,z,t)=\overline{U}-z\frac{\partial w(x,y,t)}{\partial x}=u(x,y,t)-z\frac{\partial w(x,y,t)}{\partial x}+\frac{1}{2}\int_x^a\left(\frac{\partial w(\xi,y,t)}{\partial \xi}\right)^2 d\xi$$

$$V(x,y,z,t)=\overline{V}-z\frac{\partial w(x,y,t)}{\partial y}=v(x,y,t)-z\frac{\partial w(x,y,t)}{\partial y}+\frac{1}{2}\int_y^b\left(\frac{\partial w(x,\eta,t)}{\partial \eta}\right)^2 d\eta$$

$$W(x,y,t)=w(x,y,t) \qquad (30a\text{–}c)$$

where $\mathbf{d}(x,t) = [u(x,y,t)\ v(x,y,t)\ w(x,y,t)]^T$ denotes the deformation vector, and $\partial w/\partial x$ and $\partial w/\partial y$ represent the bending slope in the y and x-directions, respectively. The nonlinear terms are compatible with the von Karman assumptions for large deflections of plates.

4.2 Strain Energy: Work of Internal Forces. The Love-Kirchhoff hypothesis is adopted here. The variation of the strain energy throughout the rectangular plate of thickness h due to bending and extension is assumed as follows (Mansfield, 1989):

$$\delta\Pi_2=\int_0^a\int_0^b\left\{\left(\frac{\partial N_x}{\partial x}+\frac{\partial N_{xy}}{\partial y}\right)\delta u+\left(\frac{\partial N_y}{\partial y}+\frac{\partial N_{xy}}{\partial x}\right)\delta v+\left(\frac{\partial^2 M_x}{\partial x^2}+2\frac{\partial^2 M_{xy}}{\partial x\partial y}+\frac{\partial^2 M_y}{\partial y^2}\right)\delta w\right\}dx\,dy. \qquad (31)$$

The internal forces acting on an infinitesimal element of the plate are

$$N_x=\frac{Eh}{1-\nu^2}\left(\frac{\partial u}{\partial x}+\nu\frac{\partial v}{\partial y}\right),\quad N_y=\frac{Eh}{1-\nu^2}\left(\frac{\partial v}{\partial y}+\nu\frac{\partial u}{\partial x}\right)$$

and

$$N_{xy}=\frac{Eh}{2(1+\nu)}\left(\frac{\partial u}{\partial y}+\frac{\partial v}{\partial x}\right). \qquad (32)$$

The internal moments acting on an infinitesimal element of the plate are

$$M_x=-D\left(\frac{\partial^2 w}{\partial x^2}+\nu\frac{\partial^2 w}{\partial y^2}\right),\quad M_y=-D\left(\frac{\partial^2 w}{\partial y^2}+\nu\frac{\partial^2 w}{\partial x^2}\right)$$

and

$$M_{xy}=-D(1-\nu)\frac{\partial^2 w}{\partial x\partial y}, \qquad (33)$$

where E is the modulus of elasticity, ν is the Poisson ratio, and $D = Eh^3/12(1-\nu^2)$ is the flexural rigidity of the plate.

Note that the internal forces and moments are linear in terms of the displacements and that the membrane strains due to large deflection $1/2\ (\partial w/\partial x)^2$, $1/2\ (\partial w/\partial y)^2$, and $(\partial w/\partial x)(\partial w/\partial y)$ are not explicitly included in the expression for the strain-displacement relations. This is analogical to the situation explained in the preceding section related to beams. This introduces, however, some additional inertia coupling, important from the viewpoint of the overall response of the system.

4.3 Application of Hamilton's Principle. The variation of the kinetic energy of the deforming plate is developed via the application of the methodology developed in Section 2. Let the generalized variables of deformation $\mathbf{q} = [q_1\ q_2\ q_3]^T$ be coincident with the displacement coordinates for a point off the middle surface $\mathbf{q} = [U\ V\ W]^T$, respectively. The relations expressed by the von Karman geometrical constraints show that the components of the deformation vector are not independent. Performing the necessary differentiations with respect to the components of the deformation vector and consistently applying Eq. (9) using the simplified Love-Kirchhoff hypothesis yields the following expression for Hamilton's principle of least action:

$$\delta T-\delta\Pi=\int_m\{\ddot{\mathbf{q}}+2\tilde{\omega}\dot{\mathbf{q}}+(\dot{\tilde{\omega}}-\omega^2\mathbf{I}_3)\mathbf{q}+\mathbf{f}\}\cdot\delta\mathbf{q}\,dm-\int_A\begin{bmatrix}\dfrac{\partial N_x}{\partial x}+\dfrac{\partial N_{xy}}{\partial y}\\[2ex]\dfrac{\partial N_y}{\partial y}+\dfrac{\partial N_{xy}}{\partial x}\\[2ex]\dfrac{\partial^2 M_x}{\partial x^2}+2\dfrac{\partial^2 M_{xy}}{\partial x\partial y}+\dfrac{\partial^2 M_y}{\partial y^2}\end{bmatrix}\cdot\delta\mathbf{d}\,dA \qquad (34)$$

with $\delta\mathbf{q}=\begin{bmatrix}\delta U\\ \delta V\\ \delta W\end{bmatrix}$, $\delta\mathbf{d}=\begin{bmatrix}\delta u\\ \delta v\\ \delta w\end{bmatrix}$,

$$\mathbf{f}(x,y,t)=\begin{bmatrix}f_x(x,y,t)\\ f_y(x,y,t)\\ m(x,y,t)\end{bmatrix}=\begin{bmatrix}-y\dot{\omega}_3-x\omega^2+f_u\\ x\dot{\omega}_3-y\omega^2+f_v\\ y\dot{\omega}_1-x\dot{\omega}_2+f_w\end{bmatrix},$$

$$\omega^2=\omega_1^2+\omega_2^2+\omega_3^2 \text{ and } \begin{bmatrix}f_u\\ f_v\\ f_w\end{bmatrix}=[\dot{\mathbf{V}}_o+\boldsymbol{\omega}\times\mathbf{V}_o]\cdot\begin{bmatrix}\mathbf{a}_1(t)\\ \mathbf{a}_2(t)\\ \mathbf{a}_3(t)\end{bmatrix}. \qquad (35a\text{–}e)$$

Note that the rigid-body translation $\mathbf{R}_o(t)$ and rigid-body rotation $\boldsymbol{\Omega}(t)$ are prescribed.

4.4 Basic Equations of Motion. The goal here is to describe the kinetic energy of the deforming plate in terms of the components of the deformation vector. The variation of the kinetic energy, Eq. (34), is expressed in terms of the displacement components of a point off the middle surfaces. Now let us express the variation of the displacement components of a point located off the middle surface, Eqs. (30*a–c*), in terms of the components of the deformation vector as follows:

$$\delta U=\delta u-z\delta\left(\frac{\partial w}{\partial x}\right)+\frac{\partial w}{\partial x}\delta w+\int_x^a\frac{\partial^2 w(\xi,y,t)}{\partial\xi^2}\delta w\,d\xi$$

$$\delta V=\delta v-z\delta\left(\frac{\partial w}{\delta y}\right)+\frac{\partial w}{\partial y}\delta w+\int_y^b\frac{\partial^2 w(x,\eta,t)}{\partial\eta^2}\delta w\,d\eta$$

$$\delta W=\delta w. \qquad (36a\text{–}c)$$

Substituting the coordinates $\mathbf{q}$ (Eqs. (30*a–c*)) and $\delta\mathbf{q}$ (Eqs. (38*a–c*)) into the expression for the variation of the kinetic energy, Eq. (36), yields an expression in terms of the components of the deformation vector $\mathbf{d}^T = [u\ v\ w]$ only:

Downloaded 03 May 2010 to 171.66.16.247. Redistribution subject to ASME license or copyright; see http://www.asme.org/terms/Terms_Use.cfm

$$\rho h\ddot{\mathbf{d}}-\frac{\rho h^3}{12}\begin{bmatrix}0&0&0\\0&0&0\\0&0&L_1\end{bmatrix}\ddot{\mathbf{d}}+2\rho h\tilde{\omega}\dot{\mathbf{d}}\ -\frac{\rho h^3}{6}\omega_3\begin{bmatrix}0&0&0\\0&0&0\\0&0&L_2\end{bmatrix}\dot{\mathbf{d}}+\rho h(\dot{\tilde{\omega}}-\omega^2\mathbf{I}_3)\mathbf{d}$$

$$-\begin{bmatrix}0\\0\\\frac{\partial}{\partial x}\left(\frac{\partial w}{\partial x}N^{ox}\right)+\frac{\partial}{\partial y}\left(\frac{\partial w}{\partial y}N^{oy}\right)\end{bmatrix}-\begin{bmatrix}\frac{\partial N_x}{\partial x}+\frac{\partial N_{xy}}{\partial y}\\\frac{\partial N_y}{\partial y}+\frac{\partial N_{xy}}{\partial x}\\\frac{\partial^2 M_x}{\partial x^2}+2\frac{\partial^2 M_{xy}}{\partial x\partial y}+\frac{\partial^2 M_y}{\partial y^2}\end{bmatrix}+\rho h\mathbf{f}=0 \quad (37)$$

with $L_1=\frac{\partial^2}{\partial x^2}+\frac{\partial^2}{\partial y^2}$, $N^{ox}=-\int_x^a \rho h f_x(\xi,y,t)d\xi-\frac{\partial h^3}{12}(\omega^2-\dot{\omega}_3)$

and $L_2=\frac{\partial^2}{\partial x^2}-\frac{\partial^2}{\partial y^2}$, $N^{oy}=-\int_y^b \rho h\, f_y(x,\eta,t)d\eta-\frac{\rho h^3}{12}(\omega^2+\dot{\omega}_3)$. (38*a–d*)

The first term represents the axial and transverse vibration of the plate. The second term represents the influence of the rotary inertia on the transverse vibration of the plate. The third term represents the contribution of the Coriolis forces to the vibration of the plate. The fourth term has not been reported in existing literature. It represents an additional Coriolis effect due to the coupling between the rotary inertia effects and the pitch motion of the plate introduced in the analysis. The fifth term considers the dynamic coupling between the rigid-body motion and the components of deformation of the middle surface often referred to as the softening term (Simo and Vu-Quoc, 1986). The sixth term is introduced from the transfer of the membrane forces to the bending equation. This term appropriately accounts for the dynamic stiffening effects. The validity of this interpretation is supported in the numerical example section. The seventh term accounts for the work done by the internal forces according to the linear Love-Kirchoff hypothesis. The last term represents the inertia forces acting on the plate. The resulting set of linear partial differential equations can be solved using standard multibody finite element codes. The prematurely linearized theory omits the introduction of the fourth and sixth terms present in the consistent linear theory (Eq. (37)).

4.5 Finite Element Implementation. A 20-degree-of-freedom plate element developed by Greene (1962) is used here to illustrate the solutions. The shape functions completely satisfy the compatibility conditions of slope and deflection along the boundaries of the element. The assumed displacement field of the plate element can be written as

$$[u\ v\ w]^T=\mathbf{N}(x,y)\mathbf{q}(t) \quad (39)$$

in which $\mathbf{N}(x,y)$ is a 3×20 matrix of shape functions, and $\mathbf{q}(t)$ the nodal coordinates of the four-noded rectangular plate such that

$$\mathbf{q}(t)=[\mathbf{q}_1^T(t)\ \mathbf{q}_2^T(t)\ \mathbf{q}_3^T(t)\ \mathbf{q}_4^T(t)]^T \quad (40)$$

where $\mathbf{q}_i=[u_i\ v_i\ w_i\ \theta_{xi}\ \theta_{yi}]^T$ in which u_i, v_i, and w_i are the generalized coordinates of node i located on the middle surface of the rectangular plate, and θ_{xi} and θ_{yi} are the rotation of node i about the x and y-axes, respectively.

The weak form of the governing equations is obtained by interpolating over the surface area of the plate element of this equation by an arbitrary trial function. The resulting equation of motion is

$$\mathbf{M}\ddot{\mathbf{q}}(t)+\mathbf{G}(t)\dot{\mathbf{q}}(t)+[\mathbf{S}+\mathbf{D}(t)]\mathbf{q}(t)=\mathbf{P}(t). \quad (41)$$

Total mass matrix:

$$\mathbf{M}=\int_A \rho h\mathbf{N}^T\mathbf{N}dA+\int_A \frac{\rho h^3}{12}[\mathbf{L}_r\mathbf{N}]^T[\mathbf{L}_r\mathbf{N}]dA. \quad (42)$$

Total gyroscopic matrix:

$$\mathbf{G}(t)=\int_A 2\rho h\mathbf{N}^T\tilde{\omega}\mathbf{N}dA+\int_A \frac{\rho h^3}{6}\omega_z[\mathbf{L}_g\mathbf{N}]^T[\mathbf{L}_g\mathbf{N}]dA. \quad (43)$$

Total material stiffness:

$$\mathbf{S}=\int_A [\mathbf{L}_m\mathbf{N}]^T\mathbf{D}_m[\mathbf{L}_m\mathbf{N}]dA+\int_A [\mathbf{L}_b\mathbf{N}]^T\mathbf{D}_b[\mathbf{L}_b\mathbf{N}]dA. \quad (44)$$

Total dynamic stiffness:

$$\mathbf{D}(t)=\int_A \rho h\mathbf{N}^T(\dot{\tilde{\omega}}-\omega^2\mathbf{I}_3)\mathbf{N}dA+\int_A [\mathbf{L}_r\mathbf{N}]^T[\mathbf{L}_d\mathbf{N}]dA. \quad (45)$$

Inertial load:

$$\mathbf{P}(t)=\int_A \rho h\mathbf{N}^T\mathbf{f}dA. \quad (46)$$

Elastic matrix:

$$\mathbf{D}_m=\frac{Eh}{1-\nu^2}\begin{bmatrix}1&0&0&\nu\\0&\frac{1-\nu}{2}&\frac{1-\nu}{2}&0\\0&\frac{1-\nu}{2}&\frac{1-\nu}{2}&0\\\nu&0&0&1\end{bmatrix}$$

and $\mathbf{D}_b=D\begin{bmatrix}1&\nu&0\\\nu&1&0\\0&0&\frac{1-\nu}{2}\end{bmatrix}$. (47*a–b*)

Spatial differential operators:

$$\mathbf{L}_b=\begin{bmatrix}0&0&\frac{\partial^2}{\partial x^2}\\0&0&\frac{\partial^2}{\partial y^2}\\0&0&2\frac{\partial^2}{\partial x\partial y}\end{bmatrix},\quad \mathbf{L}_g=\begin{bmatrix}0&0&\frac{\partial}{\partial x}\\0&0&-\frac{\partial}{\partial y}\end{bmatrix},$$

$$\mathbf{L}_d=\begin{bmatrix}0&0&N^{ox}\frac{\partial}{\partial x}\\0&0&N^{oy}\frac{\partial}{\partial y}\end{bmatrix},$$

Downloaded 03 May 2010 to 171.66.16.247. Redistribution subject to ASME license or copyright; see http://www.asme.org/terms/Terms_Use.cfm

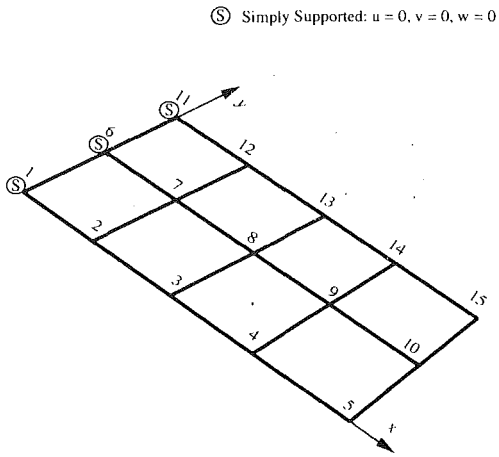


Fig. 6 Finite element mesh of a simply-supported plate at one end

$$\mathbf{L}_m = \begin{bmatrix} \frac{\partial}{\partial x} & 0 & 0 \\ 0 & \frac{\partial}{\partial x} & 0 \\ \frac{\partial}{\partial y} & 0 & 0 \\ 0 & \frac{\partial}{\partial y} & 0 \end{bmatrix} \quad \text{and} \quad \mathbf{L}_r = \begin{bmatrix} 0 & 0 & \frac{\partial}{\partial x} \\ 0 & 0 & \frac{\partial}{\partial y} \end{bmatrix}. \qquad (48a\text{–}e)$$

The discretized equation of motion, Eq. (41), has been implemented on a standard finite element program.

4.6 Numerical Application. In this section a spin-up maneuver problem is studied to show that the present linear theory captures the dynamic stiffening effects. The plate undergoes a rigid-body rotation by imposing $\mathbf{R}_o(t) = \Omega_1(t) = \Omega_3(t) = 0$ and

$$\omega^2(t) = \begin{cases} \dfrac{2\pi n^*}{60t^*}\left(t - \dfrac{t^*}{2\pi}\sin\left(\dfrac{2\pi t}{t^*}\right)\right) & t < t^* \\ \dfrac{2\pi n^*}{60} & t \geq t^* \end{cases} \qquad (49)$$

where $n^* = 40$ is the ultimate spin speed, and $t^* = 15$ is the spin-up time.

We now investigate the local deflection of node #10 ($y = 0.25$ (m) and $x = 2.0$ (m)) located at the tip center of an aluminum plate with one simply-supported end as depicted by Fig. 6. Figure 7 compares the plate tip deflection using a prematurely linearized theory (dashed line) and the present theory (solid line). The prematurely linearized theory omits the contribution of the membrane forces transmitted to the bending equation giving erroneous results. Note that during the acceleration phase, the plate-tip experiences a maximum deflection $w_{10} = 0.182$ (m). During the constant angular speed, the transverse deflection of the plate tip has an oscillatory motion of amplitude $w_{10} = 0.0162$ (m) referred to as "ringing" by Banerjee and Kane (1989).

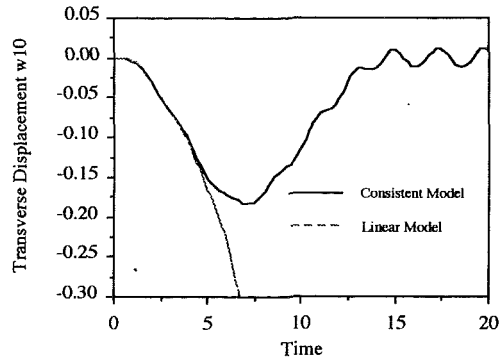


Fig. 7 Transient transverse deformation of node #10 of a cantilevered plate; (solid line) Love-Kirchhoff hypothesis with von Karman constraint; (dashed line) Love-Kirchhoff hypothesis

5 Conclusions

The proposed use of arbitrary representation of deformation kinematics allows for the derivation of the equations of motion governing rigid-body and elastic-body motion for beams, plates, and solids relative to a reference frame undergoing large three-dimensional rotation and translation. As a consequence, the proposed formulations unify a diversity of approaches for studying deformable multibody systems comprising flexible beams and plates.

The equations of motion for a thin beam and a thin plate in a prescribed motion are developed by constraining the generalized coordinates of deformations to satisfy the von Karman geometric constraints. As a result, the dynamic stiffening effects are automatically incorporated in the linear equations of motion through the transfer of the axial and membrane forces to the bending equations.

Acknowledgments

Financial support for Zine-Eddine provided by an IBM doctoral dissertation fellowship is gratefully acknowledged.

References

Arnold, V. I., 1980, *Mathematical Methods of Classical Mechanics*, Springer-Verlag, New York.

Agrawal, O. P., and Shabana, A. A., 1985, "Dynamic Analysis of Multibody Systems Using Large Component Modes," *Computers and Structures*, Vol. 21, No. 6, pp. 1303–1312.

Banerjee, A. K., and Kane, T. R., 1989, "Dynamics of a Plate in Large Overall Motion," ASME JOURNAL OF APPLIED MECHANICS, Vol. 56, pp. 887–892.

Bartelone, D. F., and Shabana, A. A., 1989, "Effect of Beam Initial Curvature on the Dynamics of Deformable Multibody Systems," *Mechanism and Machine Theory*, Vol. 24, No. 5, pp. 411–429.

Boutaghou, Z.-E., and Erdman, A. G., 1990, "On Various Nonlinear Rod Theories for the Dynamic Analysis of Multi-Body Systems: Part I and Part II," *Journal of Sound and Vibrations*, in review.

Chang, B., and Shabana, A. A., 1989, "Total Lagrangian Formulation for the Large Displacement Analysis of Rectangular Plates," *International Journal for Numerical Methods in Engineering*, Vol. 29, pp. 73–103.

Chang, B., and Shabana, A. A., 1990, "Nonlinear Finite Element Formulation for the Large Displacement Analysis of Plates," ASME JOURNAL OF APPLIED MECHANICS, Vol. 57, pp. 707–718.

Gau, S. J., and Shabana, A. A., 1990, "Effects of Shear Deformation and Rotary Inertia on the Nonlinear Dynamics of Rotating Curved Beams," ASME *Journal of Vibration, Acoustics, Stress, and Reliability in Design*, Vol. 122, pp. 183–193.

Gear, C. W., 1971, "Simultaneous Numerical Solutions of Differential/Algebraic Equations," *Circuit Theory*, IEEE Trans., CT-18, pp. 89–95.

Greene, B. E., 1962, "Stiffness Matrix for Bending of a Rectangular Element with Initial Membrane Stresses," *Structural Analysis Research Memorandum*, No. 45, The Boeing Company, Seattle.

Ider, S. K., and Amirouche, F. M. L., 1989, "Nonlinear Modeling of Flexible Multibody Systems Dynamics Subjected to Variable Constraints," ASME JOURNAL OF APPLIED MECHANICS, Vol. 56, pp. 444–450.

Kane, T. R., and Levinson, D., 1980, "Formulation of Equations of Motion for Complex Spacecraft," *Journal of Guidance and Control*, Vol. 3, pp. 99–112.

Kane, T. R., Ryan, R. R., and Banerjee, A. K., 1986, "Dynamics of a Cantilever Beam Attached to a Moving Base," *AIAA Journal*, Vol. 10, No. 2, pp. 139–151.

Kim, S.-S., and Haug, E. J., 1988, "A Recursive Formulation for Flexible Multibody Dynamics. Part I: Open-Loop Systems," *Computer Methods in Applied Mechanics and Engineering*, Vol. 71, pp. 293–314.

Mansfield, E. H., 1989, *The Bending and Stretching of Plates*, 2nd ed., Cambridge Univ. Press, Cambridge, U.K.

Downloaded 03 May 2010 to 171.66.16.247. Redistribution subject to ASME license or copyright; see http://www.asme.org/terms/Terms_Use.cfm

Meirovitch, L., 1980, *Computational Methods in Structural Dynamics*, Sijthoff and Nordhoff, Maryland.

Nagathan, G., and Soni, A. H., 1986, "Nonlinear Modeling of Kinematic and Flexibility Effects in Manipulator Design," ASME Paper No. 86-DET-88.

Padilla, C. E., and von Flotow, A. H., 1989, "Nonlinear Strain-Displacement Relations and Flexible Multibody Dynamics," AIAA Paper No. 89-1202-CP.

Park, K. C., Chiou, J. C., and Downer, J. D., 1988, "Recent Advances in Multi-Body Analysis Procedures," *Comp. Method Bioeng.*, ASME Bioengineering Division, BED Vol. 9, pp. 53-69.

Peterson, L. D., 1989, "Nonlinear Finite Element Simulation of the Large Angle Motion of Flexible Bodies," AIAA Paper No. 89-1201-CP.

Shabana, A. A., 1985, "Transient Analysis of Flexible Multi-Body Systems. Part I: Dynamics of Flexible Bodies," *Computer Methods in Applied Mechanics and Engineering*, Vol. 54, pp. 75-91.

Simo, J. C., and Vu-Quoc, L., 1987, "The Role of Non-Linear Theories in Transient Dynamic Analysis of Flexible Structures," *Journal of Sound and Vibrations*, Vol. 119, No. 3, pp. 487-508.

Sunada, W., and Dubowsky, S., 1981, "The Application of Finite Element Methods to the Dynamic Analysis of Flexible Spatial and Co-Planar Linkage Systems," ASME *Journal of Mechanical Design*, Vol. 103, pp. 643-651.

Singh, R. P., VanderVoort, R. J., and Likins, P. W., 1984, "Dynamics of Flexible Bodies in Tree Topology—A Computer Oriented Approach," AIAA Paper 84-1024.

Thompson, B. S., and Sung, C. K., 1984, "A Variational Formulation for the Nonlinear Finite Element Analysis of Flexible Linkages: Theory, Implementation, and Experimental Results," ASME Paper No. 84-DET-15.

Walton, W. C., Steenes, E. C., 1984, "A New Matrix Theorem and Its Application for Establishing Independent Coordinates for Complex Dynamical Systems with Constraints," NASA TR-R326.

Wehage, R. C., and Haug, E. J., 1982, "Generalized Coordinate Partitioning for Dimension Reduction in Analysis of Constrained Dynamic Systems," ASME *Journal of Mechanical Design*, Vol. 104, pp. 347-355.

Whittaker, E. T., 1937, *A Treatise on the Analytical Dynamics of Particles and Rigid Bodies*, Cambridge Univ. Press, Cambridge, U.K.

Wu, S.-C., and Haug, E. J., 1988, "Geometric Non-Linear Substructuring for Dynamics of Flexible Mechanical Systems," *International Journal for Numerical Methods in Engineering*, Vol. 26, pp. 2211-2226.

Yoo, W. S., and Haug, E. J., 1985, "Dynamics of Flexible Mechanical Systems Using Vibration and Static Correction Modes," ASME Design Engineering Technical Conference, Cincinnati, Ohio.

Downloaded 03 May 2010 to 171.66.16.247. Redistribution subject to ASME license or copyright; see http://www.asme.org/terms/Terms_Use.cfm

Stability of the Vertical Autorotation of a Single-Winged Samara

D. Seter

A. Rosen

Faculty of Aerospace Engineering,
Technion—Israel Institute of Technology,
Haifa 32000, Israel

A numerical model to investigate the stability of the vertical autorotation of a single-winged samara is presented. This model is obtained after the method of small perturbations about an equilibrium state is applied on the nonlinear equations of motion of the samara. The aerodynamic stability derivatives of the wing are obtained by numerical differentiation. The model is used in order to study the influence of different parameters on the stability. Since the stability is highly dependent on the basic equilibrium state, the influence of the different parameters on the basic state is also presented and discussed. The theoretical model is validated by comparing its results with qualitative experimental results.

1 Introduction

The autorotation of a single wing with a concentrated mass at its root, that spins while descending, is a very common phenomenon in nature. It is used to reduce the falling speed of seeds of different trees or bushes, thus increasing the distance that they may be transported by horizontal winds. The principle of the samara has also been adopted by different engineering devices; for example, a decelerator that was described by Crimi (1988).

Recently Rosen and Seter (1991) presented a theoretical model of the vertical autorotation of a single-winged samara. The interested reader may find a detailed literature survey in that paper. Although general equations of motion were presented by Rosen and Seter (1991), the investigation concentrated on a steady-state uniform vertical descent, while stability analysis or transient motions were not considered. The theoretical model was validated by comparing its results with experimental results of a real samara (reported in the literature), and a cardboard model. Quite good agreement between the results was obtained. The differences between the calculated and measured rotational speeds were 0.9 percent and 17.9 percent, for the samara and cardboard model, respectively. The differences in the sinking rate and coning angle were 43.3 percent and 21.4 percent for the samara, and 8.5 percent and 25 percent for the cardboard model. As expected and as had been discussed qualitatively by other investigators, the authors showed that the samara motion presents a very delicate balance between inertia and aerodynamic loads. Thus, the question of the stability of that motion immediately arises.

Contributed by the Applied Mechanics Division of THE AMERICAN SOCIETY OF MECHANICAL ENGINEERS for publication in the ASME JOURNAL OF APPLIED MECHANICS.

Discussion on this paper should be addressed to the Technical Editor, Prof. Leon M. Keer, The Technological Institute, Northwestern University, Evanston, IL 60208, and will be accepted until four months after publication of the paper itself in the ASME JOURNAL OF APPLIED MECHANICS.

Manuscript received by the ASME Applied Mechanics Division, May 14, 1991; final revision, July 31, 1991. Associate Technical Editor: A. K. Noor.

Among the investigations of free autorotation only very few addressed the problem of stability. Stilley (1967) investigated the stability of autorotating glide bomblets. Because of the symmetry and relative simplicity of that problem, the author succeeded in obtaining simple expressions that were analyzed using classical methods. The single-winged samara presents a much more complicated case, and thus its stability problem was previously addressed only qualitatively, using an over simplified model that did not take into account the highly complicated, coupled and delicate nature of the phenomenon. Norberg (1973), by using a simple two-dimensional model, explained that chordwise variations of the center of pressure location, as a result of variations in the angle of attack, form the mechanism that leads to the stability of the samara autorotation.

The present paper will outline a detailed and accurate investigation on the stability of a single-winged samara. The theoretical approach will be based on a perturbation of the nonlinear six-degrees-of-freedom equations of motion, that were presented in the previous paper by the authors (Rosen and Seter, 1991). The aerodynamic stability derivatives will be calculated numerically. An eigenvalue analysis of the resulting linear equations determines the system stability. The influence of different parameters on the stability will be studied and discussed. In order to support the calculations, experiments on the stability of samara models were also carried out. Because of the complexity of any trial to obtain accurate measures of the stability, the experiments yielded only qualitative results, indicating if the model is stable or not. During the experiments, certain characteristics of the experimental model were varied and the influence of these variations on the stability was examined.

2 The Perturbation Equations

In Fig. 1 a single-winged samara in a vertical autorotation is shown. X, Y, Z present an inertial system of coordinates.

Copyright © 1992 by ASME
Downloaded 03 May 2010 to 171.66.16.247. Redistribution subject to ASME license or copyright; see http://www.asme.org/terms/Terms_Use.cfm

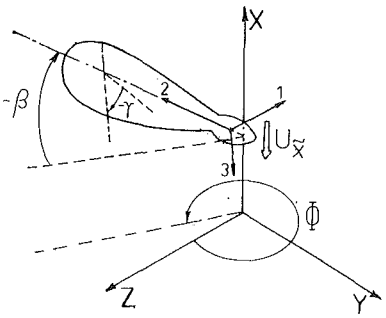


Fig. 1 General description of the systems of coordinates and dynamic variables

X points upwards in the negative gravity direction. For the sake of simplicity and without losing any generality, it is assumed that X coincides with the axis of rotation of the vertical autorotation. The coordinates system (1, 2, 3) is attached to the rotating samara, with its origin located at the wing's center of mass. $\hat{e}_1$, $\hat{e}_2$, and $\hat{e}_3$ are unit vectors in the 1, 2, and 3, directions, respectively. For the sake of convenience the (1, 2, 3) system coincides with the principal axes of inertia. Thus, the only nonzero components of the mass moment or inertia tensor are: I_{11}, I_{22}, I_{33}.

The transformation from the inertial system directions to those of the (1, 2, 3) system is described by three Euler angles (see Fig. 1), the order of which is: ϕ (a rotation about X), γ (the pitch angle about the new Y-axis), and β (a coning angle about the 3 axes).

The absolute velocity of the center of mass of the wing is described by its components u_1, u_2, and u_3, in the 1, 2, and 3 directions, respectively.

The external loads that act on the wing include the weight and aerodynamic loads. The aerodynamic force is described by its components (F_{1A}, F_{2A}, F_{3A}), while the components of the aerodynamic moment about the center of mass are (T_{1A}, T_{2A}, T_{3A}). All the above components are in the directions (1, 2, 3), respectively.

The six equations of motions were derived previously by Rosen and Seter (1991), and are presented here again for the sake of completeness:

$$m[\dot{u}_1 + u_3(\cos\beta\dot{\gamma} - \dot{\Phi}\cos\gamma\sin\beta) - (\dot{\Phi}\sin\gamma + \dot{\beta})u_2] = F_{1A} - mg\cos\beta\cos\gamma \quad (1a)$$

$$m[\dot{u}_2 + u_1(\dot{\Phi}\sin\gamma + \dot{\beta}) - u_3(\dot{\Phi}\cos\gamma\cos\beta + \sin\beta\dot{\gamma})] = F_{2A} + mg\cos\gamma\sin\beta \quad (1b)$$

$$m[\dot{u}_3 + u_2(\dot{\Phi}\cos\gamma\cos\beta + \sin\beta\dot{\gamma}) - u_1(\cos\beta\dot{\gamma} - \dot{\Phi}\cos\gamma\sin\beta)] = F_{3A} - mg\sin\gamma \quad (1c)$$

$$I_{11}[\ddot{\Phi}\cos\gamma\cos\beta - \dot{\Phi}(\sin\gamma\cos\beta\dot{\gamma} + \cos\gamma\sin\beta\dot{\beta}) + \ddot{\gamma}\sin\beta + \dot{\gamma}\cos\beta\dot{\beta}] + (I_{33} - I_{22})(\dot{\beta} + \sin\gamma\dot{\Phi})(\cos\beta\dot{\gamma} - \cos\gamma\sin\beta\dot{\Phi}) = T_{1A} \quad (1d)$$

$$I_{22}[\ddot{\gamma}\cos\beta - \ddot{\Phi}\cos\gamma\sin\beta + \dot{\Phi}(\sin\gamma\sin\beta\dot{\gamma} - \cos\gamma\cos\beta\dot{\beta}) - \dot{\gamma}\dot{\beta}\sin\beta] + (I_{11} - I_{33})(\cos\gamma\cos\beta\dot{\Phi} + \sin\beta\dot{\gamma})(\sin\gamma\dot{\Phi} + \dot{\beta}) = T_{2A} \quad (1e)$$

$$I_{33}[\ddot{\Phi}\sin\gamma + \dot{\Phi}\cos\gamma\dot{\gamma} + \ddot{\beta}] + (I_{22} - I_{11})(\cos\gamma\cos\beta\dot{\Phi} + \sin\beta\dot{\gamma})(\cos\beta\dot{\gamma} - \cos\gamma\sin\beta\dot{\Phi}) = T_{3A}. \quad (1f)$$

m is the mass of the wing, g is the gravity acceleration, and the upper dot indicates differentiation with respect to time.

The calculation of the aerodynamic loads was presented in detail by Rosen and Seter (1991).

For the sake of convenience, the variables that define the wing's motion are grouped into two vectors, $\{Y_1\}$ and $\{Y_2\}$:

$$\{Y_1\}^T = \langle u_1, u_2, u_3, \dot{\Phi}\rangle \quad (2a)$$

$$\{Y_2\}^T = \langle \gamma, \beta\rangle. \quad (2b)$$

As indicated above, the stability of a steady vertical autorotation will be investigated. A steady vertical autorotation is time independent (except for azimuthal variations), therefore all the time derivatives of the variables, except for $\dot{\Phi}$, become zero. $\dot{\Phi}$ is constant. Thus, Eqs. (1*a–f*) result in a nonlinear system of algebraic equations. A solution of these equations define the basic equilibrium state about which stability will be investigated. It should be pointed out that since dynamic terms have been neglected, it is mathematically possible to obtain basic equilibrium states which are unstable and thus physically impossible. The variables of the basic state will be marked by the index o. $\{Y_1\}_o$ and $\{Y_2\}_o$ are constant and are not functions of time.

The small perturbations about the basic state are denoted $\{\Delta Y_1\}$ and $\{\Delta Y_2\}$. At any moment,

$$\{Y_1\} = \{Y_1\}_o + \{\Delta Y_1\} \quad (3a)$$

$$\{Y_2\} = \{Y_2\}_o + \{\Delta Y_2\}. \quad (3b)$$

Aerodynamic force $\{F_A\}$ and moment $\{T_A\}$ vectors are defined as follows:

$$\{F_A\}^T = \langle F_{1A}, F_{2A}, F_{3A}\rangle \quad (4a)$$

$$\{T_A\}^T = \langle T_{1A}, T_{2A}, T_{3A}\rangle. \quad (4b)$$

It is possible to express these loads in a similar manner to Eqs. (3*a–b*):

$$\{F_A\} = \{F_A\}_o + \{\Delta F_A\} \quad (5a)$$

$$\{T_A\} = \{T_A\}_o + \{\Delta T_A\}. \quad (5b)$$

All the perturbation vectors $\{\Delta Y_1\}$, $\{\Delta Y_2\}$, $\{\Delta F_A\}$ and $\{\Delta T_A\}$, are functions of time. Substitution of Eqs. (3*a, b*), (4*a, b*), and (5*a, b*) into Eqs. (1*a–f*), and subtracting the equilibrium equations of the basic state from those equations, lead to the following system of linear perturbation equations:

$$\begin{bmatrix} \begin{bmatrix} 0 \\ 3\times 2 \end{bmatrix} \\ \begin{bmatrix} A1 \\ 3\times 2 \end{bmatrix} \end{bmatrix} \{\Delta\ddot{Y}\}_2 + \begin{bmatrix} A2 \\ 6\times 6 \end{bmatrix} \begin{Bmatrix} \Delta\dot{Y}_1 \\ \Delta\dot{Y}_2 \end{Bmatrix} + \begin{bmatrix} A3 \\ 6\times 6 \end{bmatrix} \begin{Bmatrix} \Delta Y_1 \\ \Delta Y_2 \end{Bmatrix} = \begin{Bmatrix} \Delta F_A \\ \Delta T_A \end{Bmatrix}. \quad (6)$$

The elements of the matrices A_1, A_2, and A_3 are defined in the Appendix.

As it is common in the stability analysis of aircraft, the perturbations of the aerodynamic loads can be described as series about the basic state. In the case of small perturbations, terms including products of perturbations are neglected compared to the perturbations themselves. Thus, the perturbation in the load Q_{iA} is described as follows:

$$\Delta Q_{iA} = \left(\frac{\partial Q_{iA}}{\partial u_1}\right)_o \Delta u_1 + \left(\frac{\partial Q_{iA}}{\partial u_2}\right)_o \Delta u_2 + \left(\frac{\partial Q_{iA}}{\partial u_3}\right)_o \Delta u_3 + \left(\frac{\partial Q_{iA}}{\partial \dot{\Phi}}\right)_o \Delta\dot{\Phi} + \left(\frac{\partial Q_{iA}}{\partial \gamma}\right)_o \Delta\gamma + \left(\frac{\partial Q_{iA}}{\partial \beta}\right)_o \Delta\beta + \left(\frac{\partial Q_{iA}}{\partial \dot{\gamma}}\right)_o \Delta\dot{\gamma} + \left(\frac{\partial Q_{iA}}{\partial \dot{\beta}}\right)_o \Delta\dot{\beta} \quad (7)$$

The index o in Eq. (7) indicates that the partial derivatives are calculated at the basic equilibrium state.

The partial derivatives of the aerodynamic loads are commonly referred to as the stability derivatives.

As mentioned above, the calculations of the aerodynamic loads in the present case are very complicated and thus analytic calculations of the aerodynamic derivatives are practically impossible. Therefore, the derivatives are calculated numerically. Trials have led to the conclusion that a central difference scheme is simple to apply and accurate enough. According to this scheme

Downloaded 03 May 2010 to 171.66.16.247. Redistribution subject to ASME license or copyright; see http://www.asme.org/terms/Terms_Use.cfm

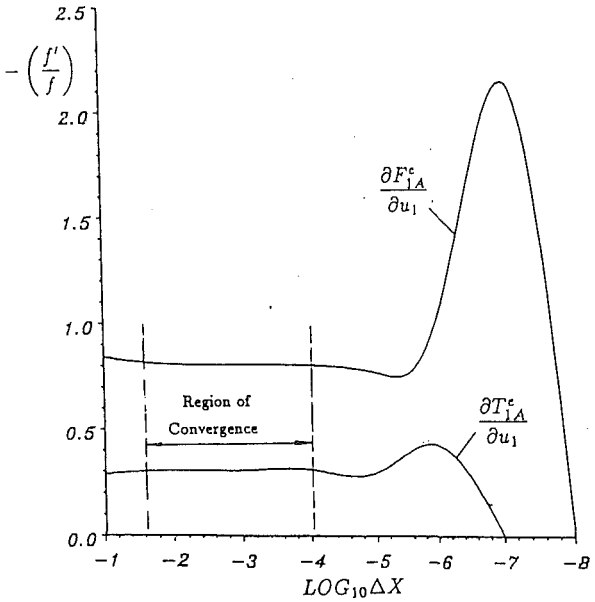


Fig. 2 The variation of representative aerodynamic stability derivatives (normalized by the values of the appropriate loads) as a function of the variable step size, ΔX

$$f_i' = \frac{f_{i+1} - f_{i-1}}{2\Delta X}, \tag{8}$$

where f_i' is the derivative of the function f at point i while f_{i+1} and f_{i-1} are the function values at the points $i+1$ and $i-1$, respectively. ΔX is the step size between points $i-1$ and i, or i and $i+1$. The error associated with Eq. (8) is of the order ΔX^2.

Numerical investigations have shown that there is always a relatively wide region of ΔX magnitude where satisfactory convergence of the derivative value is obtained. Examples of two derivatives (one of a force component and the other of a moment component) are presented in Fig. 2. It is shown that if the values of ΔX are too small, then increasing errors, due to numerical problems, are obtained.

According to Eq. (7), the perturbation vector of the aerodynamic loads may be written as follows:

$$\begin{Bmatrix} \Delta F_A \\ \Delta T_A \end{Bmatrix} = \begin{bmatrix} A4 \\ 6\times 2 \end{bmatrix} \{\Delta \dot{Y}_2\} + \begin{bmatrix} A5 \\ 6\times 6 \end{bmatrix} \begin{Bmatrix} \Delta Y_1 \\ \Delta Y_2 \end{Bmatrix}. \tag{9}$$

The elements of the matrices $[A4]$ and $[A5]$ are defined in the Appendix.

Equation (6) is a system of ordinary differential equations of order two. In order to solve the eigenvalue problem, it is convenient to use a state-space approach. The state vector is defined as follows:

$$\{X\}^T = \langle \{Y_1\}^T, \{Y_2\}^T, \{\dot{Y}_2\}^T \rangle = \langle \Delta u_1, \Delta u_2, \Delta u_3, \Delta\dot{\Phi}, \Delta\gamma, \Delta\beta, \Delta\dot{\gamma}, \Delta\dot{\beta} \rangle. \tag{10}$$

If Eq. (9) is substituted into Eq. (6), and use is made of Eq. (10), then the perturbation equations become:

$$\begin{bmatrix} B1 \\ 8\times 8 \end{bmatrix} \{\dot{X}\} + \begin{bmatrix} B2 \\ 8\times 8 \end{bmatrix} \{X\} = \{0\}. \tag{11}$$

The matrices $[B1]$ and $[B2]$ are defined in the Appendix.

Equation (11) presents a direct eigenvalue problem, and for each basic state the eigenvalues can be calculated. In general, these eigenvalues are complex numbers Z. If the real part of Z is negative, then the mode is stable. The imaginary part defines the angular frequency of an oscillating mode.

3 Experiments

The models that were used in the stability experiments present simple variations of the configuration that was used to validate the theoretical model of the steady vertical autorotation of samara wings, as described by Rosen and Seter (1991). This model is shown in Fig. 3.

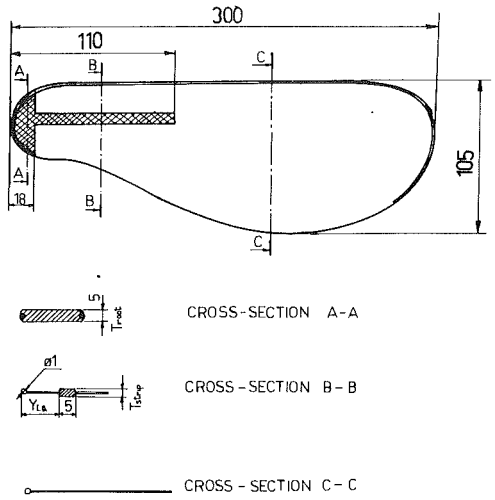


Fig. 3 The experimental samara model (all the dimensions are in mm)

The model is not a scale-up of a certain samara wing from nature. Instead, a trial and error procedure led to this model that exhibited stable and efficient autorotation relative to other designs that were tested.

The model is made of 0.35-mm thick cardboard. An aluminum wire of 1-mm diameter was used to strengthen the leading edge of the entire model and the trailing edge at the tip. This wire also simulates the concentration of ribs along the leading edge of many of the samara wings in nature.

The mass concentration at the wing's inner region, that simulates the seed or fruit in nature, is obtained by placing plasticine (putty) there. This technique is very convenient since it allows easy and simple variations of the mass distribution over this region. It is convenient to divide the mass concentration at the inner region into two subregions: The first one is the root itself (see Fig. 3, cross-section *A-A*). While the geometry of this region will be kept unchanged, its thickness, T_{root}, will be varied. The second subregion includes a strip of plasticine which is placed in the spanwise direction, parallel to the leading edge (see Fig. 3, cross-section *B-B*). The length of this strip will not be changed, but its thickness (T_{strip}), and distance from the leading edge ($Y_{l.e.}$) will be varied in order to check their influence on the stability.

The samara wing was dropped from a height of six meters and its behavior was observed qualitatively. For each configuration ten drops were performed. In cases where the behavior was not obvious and there was some doubt, an additional five drops were performed.

Configurations where clear rotation with small coning angles along a vertical path was observed (in most of the drops) are defined stable. Configurations that were defined as unstable included:

(a) fast spinning with high (greater than 45 deg) coning angles,

(b) falling along a helical path with slow rotation and high coning angles, and

(c) a free fall typical of rectangular wings, which sometimes includes rotation about the wing's longitudinal axis,

There were also intermediate cases that indicated problems of entering a stable autorotation, or cases of a very sensitive stability. These included:

(a) cases where the wing falls a long distance before it enters stable autorotation,

(b) cases where initial rotation (impulse) was necessary in order to obtain stable autorotation,

Downloaded 03 May 2010 to 171.66.16.247. Redistribution subject to ASME license or copyright; see http://www.asme.org/terms/Terms_Use.cfm

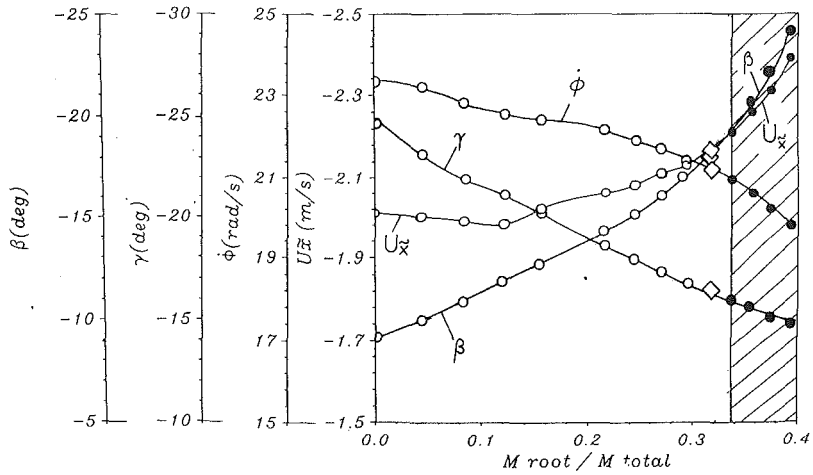


Fig. 4 The influence of variations of the mass at the root on the vertical autorotation

(c) cases where due to small disturbances (gusts for example) the autorotation turned into a free fall, and
(d) cases where small disturbances turned into larger ones, and it took long distances before steady stable autorotation was observed again.

The first two of the above cases indicate problems of entering steady autorotation, while the other two probably indicate configurations with a very small stability margin.

4 Results and Discussion

The investigation that will be presented in this section will consider the experimental model that was described in the previous section. The configuration that was presented by Rosen and Seter (1991) will be referred to as the nominal configuration. As indicated above, this configuration is the result of an experimental "trial and error" procedure that leads to a relatively stable and efficient configuration. The nominal thickness of the mass at the root (T_{root}), thickness of the leading-edge strip (T_{strip}), and strip chordwise location ($Y_{l.e.}$) were: 5 mm, 5 m, and 0 mm, respectively. These parameters will be varied, and the influence of their variations on the stability will be discussed.

As indicated above, all the variations of the nominal configuration have an important influence on the basic state, about which the stability is investigated. The basic state is defined by six variables: u_1, u_2, u_3, Φ, β, and γ. In what follows, the variations of $U_{\tilde{x}}$, $\dot{\Phi}$, β, and γ will be presented. $U_{\tilde{x}}$ is the sinking rate of the wing, which is a function of all the other six variables. In all the basic states that will be considered, the coning angle β and pitch angle γ are negative. For simplicity and clarity, most of the discussions in what follows will refer to the absolute values of these angles. Thus, indicating that the coning (angle) is increased means that the angle obtains larger negative values. In all the plots of the basic state variations, the nominal configuration will be indicated by a diamond. Areas of an unstable basic state, which is possible only theoretically (as indicated above), will be shaded.

The stability level of the configuration will be shown by plotting the real part, $R_e(Z)$, of the eigenvalue with the largest real part (when all the real parts are negative, this means the root having the smallest absolute value of the real part). The angular frequency of modes which are periodic will also be indicated in the figures.

4.1 Variations of the Root Mass. In Fig. 4, the influence on the basic equilibrium state of varying the root thickness, T_{root}, is shown. T_{root} is varied between zero and seven mm. These variations correspond to ratios between the root mass

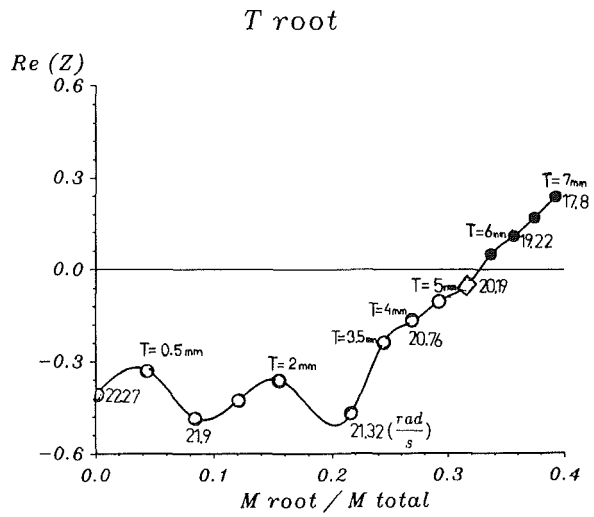


Fig. 5 The influence of variations of the mass at the root on the autorotation stability

(M_{root}) and the total mass of the wing (M_{total}), ranging between 0 and 0.38.

In the region $0 < (M_{root}/M_{total}) < 0.15$ the sinking rate, $U_{\tilde{x}}$, remains practically unchanged. It starts to increase at higher mass ratios, and the rate of increase grows as the mass ratio increases. The angular speed, $\dot{\Phi}$, decreases and the rate of decrease grows as the mass ratio increases.

As the total weight of the wing increases, the aerodynamic vertical force should also increase. This increase results in an additional aerodynamic moment that tends to increase the coning angle. This moment is balanced by the moment of the centrifugal forces that tends to reduce this angle. Since the centrifugal forces are reduced due to the decrease in the angular velocity, the coning angle β increases rapidly. This variation of the coning angle results in an increase of the moment arm of the centrifugal forces that counteracts the aerodynamic flapping moment.

The magnitude of the pitch angle γ decreases as the mass ratio increases. This contributes to the aforementioned increase of the aerodynamic lift force.

As shown in Fig. 4, and more clearly in Fig. 5, stability is lost as the mass ratio increases beyond 0.32. The stability level up to a mass ratio of 0.22 is practically kept at the same level and then drops as the mass ratio is further increased. In the stable region there are only small variations of the frequency of the mode. The value of this frequency drops more rapidly in the unstable region. Examination of the mode shapes them-

Downloaded 03 May 2010 to 171.66.16.247. Redistribution subject to ASME license or copyright; see http://www.asme.org/terms/Terms_Use.cfm

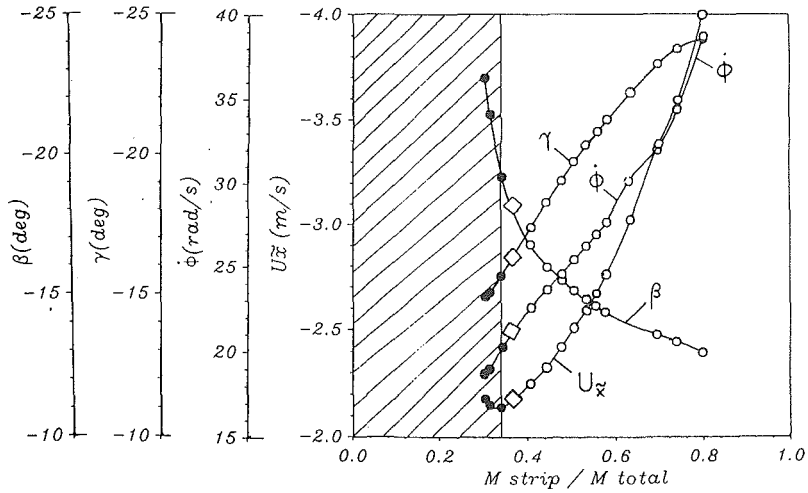


Fig. 6 The influence of variations of the mass of the leading-edge strip on the vertical autorotation

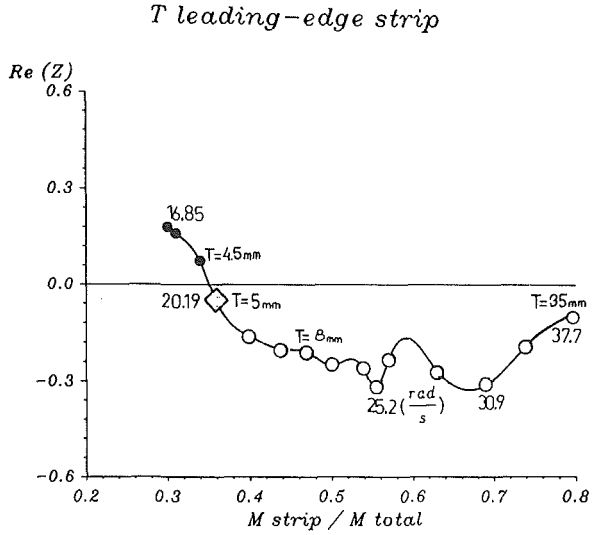


Fig. 7 The influence of variations of the mass of the leading-edge strip on the autorotation stability

selves (eigenvectors) indicates that in the modes of interest there is a high coupling between all the six variables, which are of the same order of magnitude. Nevertheless, it seems that the pitch angle plays a major roll in the unstable modes. This is expected since this variable presents a very delicate balance between inertia effects (which are essential to stabilize this angle) and aerodynamic loads (the magnitude of which is directly related to the pitch angle).

The experiments concentrated on two extreme configurations in addition to the nominal configuration. In the first configuration there was a minimum root mass ($T_{root} = 0$), and in the other case, T_{root} was made equal to 10 mm (a mass ratio of 0.58). In addition, intermediate cases were tested and they indicated the trends which are shown in Fig. 4, namely: as the root mass was increased, the descending velocity and coning angle increased (it was difficult to determine the trend of the rotational speed without performing accurate measurements).

For the case where $T_{root} = 0$, the wing was released from a vertical orientation with its root downward. In four cases out of ten, the wing entered autorotation after descending almost six meters. Later on, five additional drops were performed where an initial spin was given to the wing. In all these cases, stable rotation was observed. The results validate the theoretical predictions of a stable autorotation, but on the other hand, they indicate problems in the transient procedure of entering autorotation.

For the other extreme configuration, $T_{root} = 10$ mm, in all the cases the wing developed a vertical motion that was characterized by a high sinking rate and very high coning angles. As indicated above, this motion does not represent a stable autorotation and again it validates the theoretical results.

4.2 Variations of the Mass of the Leading-Edge Strip (T_{strip}). The results of variations in the thickness of the leading-edge plasticine strip, and thus variations of the ratio between the mass of the strip, M_{strip}, and the total mass of the wing, are shown in Figs. 6 and 7. While in the case of varying the root mass the wing encountered instability when the root mass exceeded 32 percent of the total mass, here the trends are reversed. When the strip mass is smaller than 34 percent of the total mass the autorotation is unstable, whereas increasing the ratio above this value results in a stable autorotation. When the strip mass exceeds 80 percent of the total mass, it is not possible to obtain a steady basic-state solution.

As in the case of varying the root mass (and as expected), increasing the strip mass results in an increase in the descending velocity. This velocity is almost doubled over the investigated range, compared to an increase of 13 percent in the case of varying the root mass. Opposite to the effect of increasing the root mass, increasing the leading-edge strip mass results in an increase of the rotational speed, which is also doubled over the examined range. The large increase in the rotational speed results in a large increase of the aerodynamic vertical force. This increase due to rotation is "more than required" and thus an increase in the absolute value of the pitch angle γ is allowed, opposite to what happens while increasing the root mass. Furthermore, the increase in the rotational speed and the movement of the center of mass towards the tip as a result of increasing the percentage of the leading-edge mass (relative to the total mass), cause a large increase of the inertial moment that tends to reduce the coning angle. Since the increase in this moment is larger than the increase in the aerodynamic moment that tends to increase coning, the coning angle is decreased (thus reducing the inertial coning moment), resulting in equilibrium between these two opposing moments. The coning angle is decreased over the entire range by almost a factor of two.

As indicated above, it was not possible to obtain steady-state solutions for mass ratios smaller than 0.34 and greater than 0.8. There are indications in Fig. 6 (see the behavior of β and γ near a mass ratio of 0.34, and $U_{\tilde{x}}$ and $\dot{\Phi}$ near a mass

Downloaded 03 May 2010 to 171.66.16.247. Redistribution subject to ASME license or copyright; see http://www.asme.org/terms/Terms_Use.cfm

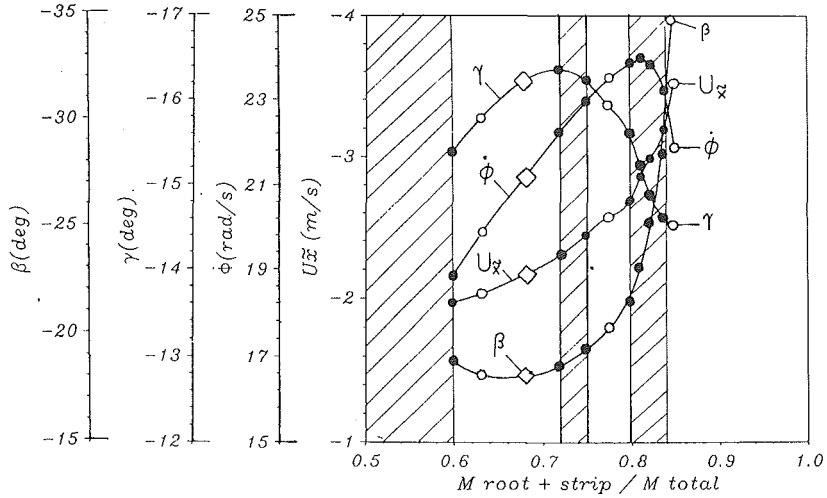


Fig. 8 The influence of mutual variations of the root and leading-edge strip masses, on the vertical rotation

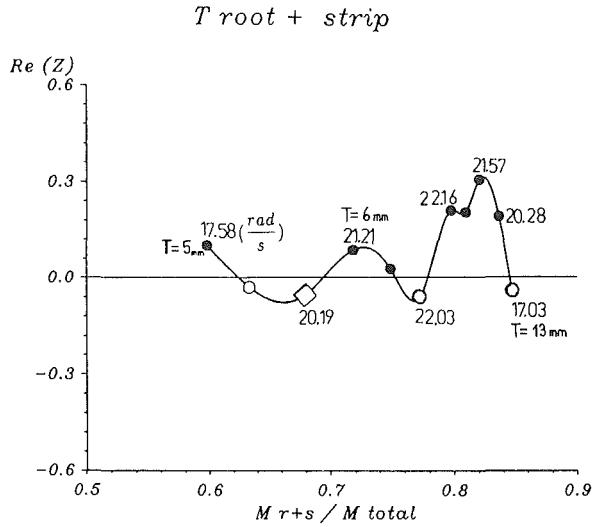


Fig. 9 The influence of mutual variations of the root and leading-edge strip masses, on the autorotation stability

ratio of 0.8) that the system approaches divergence when it gets close to these mass ratios.

Figure 7 indicates that the mode with the largest real part is periodic over the entire range of mass ratios. As the ratio between the mass of the leading-edge strip and the total mass increases, the angular frequency also increases, from a value of 16.85 rad/sec (for a mass ratio of 0.3) to 37.71 rad/sec (at a mass ratio of 0.8). The variations of the magnitude of the real part are moderate throughout the entire stable region.

The experiments in this case, similar to what was done while investigating the influence of the root mass, included two extreme configurations apart from the nominal case. In one configuration, T_{strip} was equal to zero, while in the other one, T_{strip} was equal to 15 mm (representing a mass ratio of 0.63). Any trial to increase T_{strip} further resulted in problems with the strength of the wing.

In the first case ($T_{strip} = 0$), the wing developed a high sinking rate accompanied by a very large coning angle. This steep helical rotation, which indicates a lack of steady autorotation, validates the theoretical results. In the other case a large increase in the sinking rate, as predicted by Fig. 6, was observed. Entry into a stable autorotation was fast and sensitivity to the external disturbances very low. Thus, the stable autorotation predicted by theory is confirmed.

4.3 A Mutual Increase of the Mass at the Root and the Leading-Edge Strip. In Subsection 4.1, influences of varying the root mass by changing its thickness were discussed. In Subsection 4.2, the mass of the spanwise leading-edge strip was varied. In the present subsection, the thickness of both will be varied in the range 5–15 mm, keeping the thickness of both equal. The results are presented in Figs. 8 and 9.

As indicated above, and as was presented in Figs. 4–7, the results of increasing the root or leading-edge masses, exhibit opposite trends. The trends in Fig. 8 are in general more similar to those of Fig. 6, indicating that in the present case variations of the mass of the leading-edge strip are more dominant than variations of the mass of the root. At the same time, it is clear that the parallel increase of the root mass (while increasing the leading-edge mass) reduces the magnitude of the influence. The contradicting influences result in a small decrease and then an increase of the coning angle, and a pitch angle which exhibits very small variations, as the thickness is increased.

The contradicting effects on the stability, of increasing the root or leading-edge strip masses (see Figs. 6–8—in general a decrease of stability with an increase of the root mass, and an opposite behavior while varying the mass of the leading-edge strip), result in an "undecided" behavior when the thicknesses of both masses are equally varied. As shown in Fig. 9, there are oscillations from an unstable to a stable behavior and back. Within the range of variation which is considered here, there are three subregions of stable autorotation accompanied by three other subregions of unstable behavior. As the mass ratio of the sum of the root and leading-edge strip masses (to the total mass) is increased, the angular frequency is increased from 17.58 rad/sec at a ratio of 0.6, to 22.03 rad/sec at a mass ratio of 0.78. Then it drops again to 17.0 rad/sec at a ratio of 0.84. The rate of change of the frequency at the borders of the region is larger than the rate of change at the rest of the region.

Similar to the previous tests, also in this case, experiments of two extreme configurations were performed. One case included a wing without root and strip masses $T_{root} = T_{strip} = 0$, and in the other case $T_{root} = T_{strip} = 8$ mm, which indicates a mass ratio of 0.75.

In the case of a zero mass the wing did not succeed in entering a stable autorotation, even when initial spin was applied. This unstable behavior validates the theoretical predictions. In part of the tests, rotation about the spanwise axis of the wings, similar to the behavior of a free falling rectangular wing, was observed.

In the case of $T_{root} = T_{strip} = 8$ mm, stable autorotation at

Downloaded 03 May 2010 to 171.66.16.247. Redistribution subject to ASME license or copyright; see http://www.asme.org/terms/Terms_Use.cfm

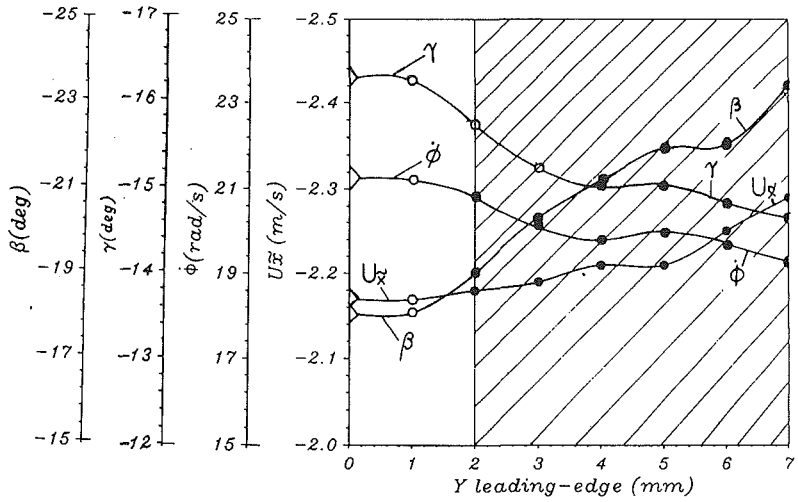


Fig. 10 The influence of variations of the chordwise location of the leading-edge strip, on the vertical autorotation

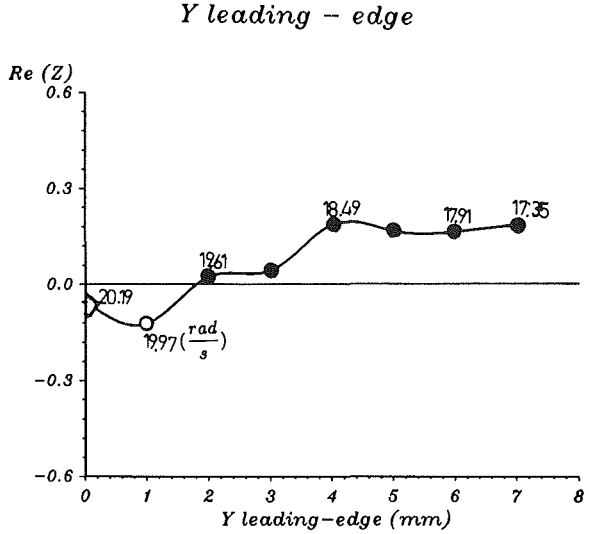


Fig. 11 The influence of variations of the chordwise location of the leading-edge strip, on the autorotation stability

a relatively high rotational speed and a low coning angle, in accordance with the theoretical predictions, was observed. Although this configuration is, according to Fig. 9, on the verge of instability, in all the tests fast entry into a stable autorotation was observed.

4.4 Variations in the Chordwise Location of the Strip. Figure 10 presents the influence of variations in $Y_{l.e.}$ on the vertical autorotation. It can be concluded that $Y_{l.e.}$ has only a small influence on the variables that define the steady basic state. On the other hand, there is a large influence on the stability. When $Y_{l.e.}$ is greater than 2 mm, the autorotation becomes unstable (see Fig. 11). It should be noted that a change in $Y_{l.e.}$ of 2 mm results in only a very small change in the cross-sectional center of mass location, and that this change occurs only along 30 percent of the wing span. This result is an indication of the sensitivity of the phenomenon to chordwise mass variations. At the same time it should also be noted that the instability is relatively weak since the real part of the eigenvalue remains smaller than 0.2 1/sec. As $Y_{l.e.}$ is increased, the frequency of the mode gradually decreases from a value of 20.19 rad/sec at $Y_{l.e.}$ = 0 to 17.35 rad/sec at $Y_{l.e.}$ = 7 mm.

In addition to the nominal stable configuration where $Y_{l.e.}$ = 0, another configuration with $Y_{l.e.}$ = 9 mm was tested. Unlike the calculations that predict instability of this configuration, in all the drops the wing entered autorotation. Yet, it took the wing almost the entire falling distance before it entered a steady autorotation state. The autorotation itself was very sensitive to disturbances and weak gusts caused the wing to lose stability and enter a simple free fall. This behavior indicates that the samara wing is probably close to instability.

4.5 The Influence of the Chordwise Location of Cross-Sectional Center of Pressure. As indicated previously, Norberg (1973) explained that the mechanism of variations in the cross-sectional center of pressure (as a function of the angle of attack) is the main mechanism that leads to the stability of the samara autorotation. It should be pointed out that the oversimplified two-dimensional model that led to this conclusion considers stability with respect to the pitch angle alone.

As explained previously by Rosen and Seter (1991), this effect was introduced into the present model by using the results of Bradford (1954).

Calculations have shown that if the nominal configuration is considered, the absolute value of the real part of the eigenvalue is reduced by 25 percent if this effect is ignored. Thus, while this effect seems to contribute to the stability, it is by no means the sole stabilizing mechanism of the entire phenomena.

5 Conclusions

A theoretical model to investigate the stability of the vertical autorotation of a samara wing was described. The model was obtained by using the method of small perturbations about a basic steady-state. This method was applied to the nonlinear model that was derived previously by the authors. Since the aerodynamic calculations are fairly complicated and obtaining analytical expressions is practically impossible, a numerical approach was used in order to calculate the aerodynamic stability derivatives.

The linear model was used to investigate the influence of different parameters on the stability. A basic nominal stable configuration was chosen and the influences of variations of this configuration were investigated. Since the stability depends on the basic state, the influence of the different parameters on the basic state was also discussed.

In general, increasing the weight of the samara wing results in an increase in the sinking rate.

It is difficult to point out a single parameter that determines the rotational speed of the samara, instead it is probably the

Downloaded 03 May 2010 to 171.66.16.247. Redistribution subject to ASME license or copyright; see http://www.asme.org/terms/Terms_Use.cfm

result of highly nonlinear coupling between the influences of different parameters. On the other hand, there is a consistent relation between the rotational speed and the coning angle, which is decreased as the rotational speed is increased.

There is a very high sensitivity of the phenomenon to the chordwise mass distribution. Small variations of this distribution, like moving the center of mass towards the trailing edge, may cause instability. Concentration of mass at the leading edge is very important for a quick entry into steady autorotation.

A previous investigation explained (qualitatively) the stability as a result of variations in the cross-sectional center of pressure location, as a function of the angle of attack. The present research showed that this effect is relatively small and it usually increases the deviation between the theoretical and experimental results. Instead it was shown that stability is a result of fairly complicated, highly coupled, inertia/aerodynamic and gravity effects. Therefore, in order to investigate this stability, a complete coupled six-degrees-of-freedom model is required—like the model that was described in the paper.

A series of experiments were performed where the autorotation and stability of different configurations of a samara wing were tested. In most of the cases, good qualitative agreement was obtained between the tests' results and the theoretical predictions.

It should be pointed out that the present theoretical investigation is based on a small perturbation analysis. It is well known that in certain cases, while such an analysis predicts instability, a global nonlinear stability may exist.

Acknowledgment

The authors would like to thank Mr. S. Nachmani and Mr. A. Grunwald for their assistance in carrying out the experiments. Thanks are also expressed to Mrs. B. Hirsch for typing the manuscript.

References

Bradford, H. W., 1954, "Study of the Subsonic Forces and Moments on an Inclined Plate of Infinite Span," NACA-TN 3221.

Crimi, P., 1988, "Analysis of Samara-Wing Decelerator Steady State Characteristics," *Journal of Aircraft*, Vol. 25, No. 1, pp. 41–47.

Norberg, R. Ake, 1973, "Autorotation, Self-Stability and Structure of Single-Winged Fruits and Seeds (Samaras) With Comparative Remarks on Animal Flight," *Biol. Rev.*, Vol. 48, pp. 561–596.

Rosen, A., and Seter, D., 1992, "Vertical Autorotation of a Single Winged Samara," ASME JOURNAL OF APPLIED MECHANICS, Vol. 58, pp. 1064–1071.

Stilley, G. D., 1967, "Unified Stability Criteria for Autorotating Glide Bomblets," *Proc. Conf. Dyn. Aerody. Bomblets*, Vol. 1, Tech. Rep. AFATL-TR-67-195, Eglin AFB, Fla., pp. 24–109.

APPENDIX

In Subsections A.1, A.2, and A.3, the elements of the matrices [A1], [A2], and [A3] are defined. Only the nonzero elements are given, while it should be understood that the rest of the elements are equal to zero.

A.1 The Element of the Matrix [$A1$]

$$A1_{1,1} = I_{11}\sin(\beta_o)$$

$$A1_{2,1} = I_{22}\cos(\beta_o)$$

$$A1_{3,2} = I_{33}$$

A.2 The Elements of the Matrix [$A2$]

$$A2_{1,1} = m$$

$$A2_{1,5} = mu_{30}\cos(\beta_o)$$

$$A2_{1,6} = -mu_{20}$$

$$A2_{2,2} = m$$

$$A2_{2,5} = -mu_{30}\sin(\beta_o)$$

$$A2_{2,6} = mu_{10}$$

$$A2_{3,3} = m$$

$$A2_{3,5} = m(-u_{10}\cos(\beta_o) + u_{20}\sin(\beta_o))$$

$$A2_{4,4} = I_{11}\cos(\gamma_o)\cos(\beta_o)$$

$$A2_{4,5} = (I_{33} - I_{22} - I_{11})\dot{\phi}_o\sin(\gamma_o)\cos(\beta_o)$$

$$A2_{4,6} = (I_{22} - I_{33} - I_{11})\dot{\phi}_o\cos(\gamma_o)\sin(\beta_o)$$

$$A2_{5,4} = -I_{22}\cos(\gamma_o)\sin(\beta_o)$$

$$A2_{5,5} = (I_{11} + I_{22} - I_{33})\dot{\phi}_o\sin(\gamma_o)\sin(\beta_0)$$

$$A2_{5,6} = (I_{11} - I_{22} - I_{33})\dot{\phi}_o\cos(\gamma_o)\cos(\beta_o)$$

$$A2_{6,4} = I_{33}\sin(\gamma_o)$$

$$A2_{6,5} = (I_{33} + (I_{22} - I_{11})\cos(2\beta_o))\dot{\phi}_o\cos(\gamma_o)$$

A.3 The Elements of the Matrix [$A3$]

$$A3_{1,2} = -m\dot{\phi}_o\sin(\gamma_o)$$

$$A3_{1,3} = -m\dot{\phi}_o\cos(\gamma_o)\sin(\beta_o)$$

$$A3_{1,4} = -m[u_{20}\sin(\gamma_o) + u_{30}\cos(\gamma_o)\sin(\beta_o)]$$

$$A3_{1,5} = -m[u_{20}\dot{\phi}_o\cos(\gamma_o) - u_{30}\dot{\phi}_o\sin(\gamma_o)\sin(\beta_o) + g\sin(\gamma_o)\cos(\beta_o)]$$

$$A3_{1,6} = -m\cos(\gamma_0)[u_{30}\dot{\phi}_o\cos(\beta_o) + g\sin(\beta_o)]$$

$$A3_{2,1} = m\dot{\phi}_o\sin(\gamma_o)$$

$$A3_{2,3} = -m\dot{\phi}_o\cos(\gamma_o)\cos(\beta_o)$$

$$A3_{2,4} = m[u_{10}\sin(\gamma_o) - u_{30}\cos(\gamma_o)\cos(\beta_o)]$$

$$A3_{2,5} = m(u_{10}\dot{\phi}_o\cos(\gamma_o) + u_{30}\dot{\phi}_o\sin(\gamma_o)\cos(\beta_o) + g\sin(\gamma_o)\sin(\beta_o)]$$

$$A3_{2,6} = m\cos(\gamma_o)(u_{30}\dot{\phi}_o\sin(\beta_o) - g\cos(\beta_o)]$$

$$A3_{3,1} = m\dot{\phi}_o\cos(\gamma_o)\sin(\beta_o)$$

$$A3_{3,2} = m\dot{\phi}_o\cos(\gamma_o)\cos(\beta_o)$$

$$A3_{3,4} = m\cos(\gamma_o)[u_{10}\sin(\beta_o) + u_{20}\cos(\beta_o)]$$

$$A3_{3,5} = m[-u_{10}\dot{\phi}_o\sin(\gamma_o)\sin(\beta_o) - u_{20}\dot{\phi}_o\sin(\gamma_o)\cos(\beta_o) + g\cos(\gamma_o)]$$

$$A3_{3,6} = m\dot{\phi}_o\cos(\gamma_o)[u_{10}\cos(\beta_o) - u_{20}\sin(\beta_o)]$$

$$A3_{4,4} = (I_{22} - I_{33})\dot{\phi}_o\sin(2\gamma_o)\sin(\beta_o)$$

$$A3_{4,5} = (I_{22} - I_{33})\dot{\phi}_o^2\cos(2\gamma_o)\sin(\beta_o)$$

$$A3_{4,6} = \frac{1}{2}(I_{22} - I_{33})\dot{\phi}_o^2\sin(2\gamma_o)\cos(\beta_o)$$

$$A3_{5,4} = (I_{11} - I_{33})\dot{\phi}_o\sin(2\gamma_o)\cos(\beta_o)$$

$$A3_{5,5} = (I_{11} - I_{33})\dot{\phi}_o^2\cos(2\gamma_o)\cos(\beta_o)$$

$$A3_{5,6} = \frac{1}{2}(I_{33} - I_{11})\dot{\phi}_o^2\sin(2\gamma_o)\sin(\beta_o)$$

$$A3_{6,4} = (I_{11} - I_{22})\dot{\phi}_o\cos^2(\gamma_o)\sin(2\beta_o)$$

$$A3_{6,5} = \frac{1}{2}(I_{22} - I_{11})\dot{\phi}_o^2\sin(2\gamma_o)\sin(2\beta_o)$$

$$A3_{6,6} = (I_{11} - I_{22})\dot{\phi}_o^2\cos^2(\gamma_o)\cos(2\beta_o)$$

A.4 The Matrix [$A4$]

$$[A4]^T = \begin{bmatrix} \left(\frac{\partial F_{1A}}{\partial \dot{\gamma}}\right)_0 & \left(\frac{\partial F_{2A}}{\partial \dot{\gamma}}\right)_0 & \left(\frac{\partial F_{3A}}{\partial \dot{\gamma}}\right)_0 & \left(\frac{\partial T_{1A}}{\partial \dot{\gamma}}\right)_0 & \left(\frac{\partial T_{2A}}{\partial \dot{\gamma}}\right)_0 & \left(\frac{\partial T_{3A}}{\partial \dot{\gamma}}\right)_0 \\ \left(\frac{\partial F_{1A}}{\partial \dot{\beta}}\right)_0 & \left(\frac{\partial F_{2A}}{\partial \dot{\beta}}\right)_0 & \left(\frac{\partial F_{3A}}{\partial \dot{\beta}}\right)_0 & \left(\frac{\partial T_{1A}}{\partial \dot{\beta}}\right)_0 & \left(\frac{\partial T_{2A}}{\partial \dot{\beta}}\right)_0 & \left(\frac{\partial T_{3A}}{\partial \dot{\beta}}\right)_0 \end{bmatrix}$$

Downloaded 03 May 2010 to 171.66.16.247. Redistribution subject to ASME license or copyright; see http://www.asme.org/terms/Terms_Use.cfm

A.5 The Matrix [A5]

$$[A5] = \begin{bmatrix} \left(\frac{\partial F_{1A}}{\partial u_1}\right)_0 & \left(\frac{\partial F_{1A}}{\partial u_2}\right)_0 & \left(\frac{\partial F_{1A}}{\partial u_3}\right)_0 & \left(\frac{\partial F_{1A}}{\partial \dot{\phi}}\right)_0 & \left(\frac{\partial F_{1A}}{\partial \gamma}\right)_0 & \left(\frac{\partial F_{1A}}{\partial \beta}\right)_0 \\ \left(\frac{\partial F_{2A}}{\partial u_1}\right)_0 & \cdot & \cdot & \cdot & \cdot & \cdot \\ \left(\frac{\partial F_{3A}}{\partial u_1}\right)_0 & \cdot & \cdot & \cdot & \cdot & \cdot \\ \left(\frac{\partial T_{1A}}{\partial u_1}\right)_0 & \cdot & \cdot & \cdot & \cdot & \cdot \\ \left(\frac{\partial T_{2A}}{\partial u_1}\right)_0 & \cdot & \cdot & \cdot & \cdot & \cdot \\ \left(\frac{\partial T_{3A}}{\partial u_1}\right)_0 & \cdot & \cdot & \cdot & \cdot & \left(\frac{\partial T_{3A}}{\partial \beta}\right)_0 \end{bmatrix}$$

A.6 The Matrix [B1]

$$[B1] = \begin{bmatrix} \begin{bmatrix} A2 \\ 6\times 6 \end{bmatrix} & \begin{bmatrix} 0 \\ 3\times 2 \end{bmatrix} \\ & \begin{bmatrix} A1 \\ 3\times 2 \end{bmatrix} \\ \begin{bmatrix} 0 \\ 2\times 4 \end{bmatrix} \begin{bmatrix} 1 & 0 \\ 0 & 1 \end{bmatrix} & \begin{bmatrix} 0 \\ 2\times 2 \end{bmatrix} \end{bmatrix}$$

A.7 The Matrix [B2]

$$[B2] = \begin{bmatrix} \begin{bmatrix} [A3]-[A5] \\ 6\times 6 \end{bmatrix} & \begin{bmatrix} -A4 \\ 6\times 2 \end{bmatrix} \\ \begin{bmatrix} 0 \\ 6\times 6 \end{bmatrix} & \begin{bmatrix} -1 & 0 \\ 0 & -1 \end{bmatrix} \end{bmatrix}$$

Downloaded 03 May 2010 to 171.66.16.247. Redistribution subject to ASME license or copyright; see http://www.asme.org/terms/Terms_Use.cfm

Transfer Functions of One-Dimensional Distributed Parameter Systems

B. Yang
Asst. Professor,
Department of Mechanical Engineering,
University of Southern California,
Los Angeles, CA 90089-1453
Assoc. Mem. ASME

C. A. Tan
Asst. Professor,
Department of Mechanical Engineering,
Wayne State University,
Detroit, MI 48202
Assoc. Mem. ASME

Distributed parameter systems describe many important physical processes. The transfer function of a distributed parameter system contains all information required to predict the system spectrum, the system response under any initial and external disturbances, and the stability of the system response. This paper presents a new method for evaluating transfer functions for a class of one-dimensional distributed parameter systems. The system equations are cast into a matrix form in the Laplace transform domain. Through determination of a fundamental matrix, the system transfer function is precisely evaluated in closed form. The method proposed is valid for both self-adjoint and non-self-adjoint systems, and is extremely convenient in computer coding. The method is applied to a damped, axially moving beam with different boundary conditions.

1 Introduction

The distributed parameter system in consideration is described by the one-dimensional, nth-order, linear partial differential equation

$$\left(A\frac{\partial^2}{\partial t^2}+B\frac{\partial}{\partial t}+C\right)w(x,t)=f(x,t),\quad x\in(0,1),\quad t>0 \qquad (1)$$

with the inhomogeneous boundary conditions

$$M_j w(x,t)\,|_{x=0}+N_j w(x,t)\,|_{x=1}=\gamma_{Bj}(t),\quad t\geq 0,$$
$$j=1,2,\ldots,n. \qquad (2)$$

Here, $w(x, t)$ is the response of the system; $f(x, t)$ is the external disturbance; A, B, and C are spatial differential operators of the form

$$A=\sum_{k=0}^{n}a_k\frac{\partial^k}{\partial x^k}\quad B=\sum_{k=0}^{n}b_k\frac{\partial^k}{\partial x^k}\quad C=\sum_{k=0}^{n}c_k\frac{\partial^k}{\partial x^k}; \qquad (3)$$

a_k, b_k, and c_k are constants; $|a_n|^2+|b_n|^2+|c_n|^2\neq 0$; M_j and N_j are temporal-spatial, linear differential operators of proper order; and $\gamma_{Bj}(t)$ are known functions. Also, the initial conditions of the distributed parameter system are specified as

$$w(x,t)\,|_{t=0}=u_0(x)\quad \frac{\partial}{\partial t}w(x,t)\,|_{t=0}=v_0(x),\quad x\in(0,1). \qquad (4)$$

In this study, we assume that the boundary value problem (1)–(4) is well posed, and has one and only one solution.

Equation (1), which can be hyperbolic, parabolic, elliptic, and of other types, describes many important physical processes in continua such as diffusion, heat conduction, vibration, wave propagation, and processes in hydrodynamics and aerodynamics. For example, in describing vibration of a continuum, (1) is of hyperbolic type, the operator $A\ \partial^2/\partial t^2$ is associated with the inertia properties of the continuum, the operator $B\ \partial/\partial t$ evolves from damping, Coriolis acceleration, and mass transport, and the operator C is related to stiffness, centrifugal forces, and circulatory effects.

The system response $w(x, t)$ can be expressed in an integral form with the integral kernel being the Green's function of the distributed parameter system. The transfer function of the distributed parameter system, by the terminology of Butkovskiy (1983), is the Laplace transform of the Green's function with respect to time. The transfer function contains all information required to predict the system spectrum, the system response under any initial and external disturbances, and the stability of the system response (Butkovskiy, 1983; Yang and Mote, 1991 a,b). A knowledge of the transfer function is important in the analysis, control, and synthesis of the distributed parameter system.

In determining the transfer function of the distributed parameter system, classical methods lead to an eigenfunction expansion, i.e., the transfer function expressed by an infinite series of the system eigenfunctions. The eigenfunction expansion, while useful in theoretical analysis, has some disadvantages in numerical evaluation. First, the method requires exact eigensolutions, which may be difficult to obtain particularly for some non-self-adjoint systems. Second, the series converges very slowly for second-order systems (such as a vibrating string). Third, truncation of the series has to be made in numerical

Contributed by the Applied Mechanics Division of THE AMERICAN SOCIETY OF MECHANICAL ENGINEERS for presentation at the 1992 ASME Winter Annual Meeting, Anaheim, CA, Nov. 8–13, 1992.

Discussion on this paper should be addressed to Prof. Leon M. Keer, The Technological Institute, Northwestern University, Evanston, IL 60208, and will be accepted until four months after final publication of the paper itself in the ASME JOURNAL OF APPLIED MECHANICS.

Manuscript received by the ASME Applied Mechanics Division, Jan. 3, 1991; final revision, Nov. 18, 1991. Associate Technical Editor: P. D. Spanos.

Paper No. 92-WA/APM-1.

Copyright © 1992 by ASME
Downloaded 03 May 2010 to 171.66.16.247. Redistribution subject to ASME license or copyright; see http://www.asme.org/terms/Terms_Use.cfm

computation. This, along with inaccuracy in estimated eigensolutions, can result in large numerical error, especially when the Laplace transform parameter s approaches the singularities of the system transfer function. Finally, the series truncation reduces the order of the system model, which can lead to loss of information about the system dynamics of high-frequency modes, and cause spillover instability in the active control of distributed parameter systems. Thus, for numerical purposes, instead of the eigenfunction expansion, precise evaluation of the system transfer function in closed form is desired.

While closed-form transfer functions are available for second-order systems and some fourth-order symmetric systems (for example, see Butkovskiy (1982) and Bergman and Hyatt (1989)), no technique has been discussed in the literature for determining closed-form transfer functions of general distributed parameter systems, which can be non-self-adjoint and of any order. In Yang (1989), a special matrix formulation is proposed to evaluate the transfer function of an undamped axially moving beam (a non-self-adjoint system) in closed form. This transfer function is then used to calculate the dynamic response of an axially moving beam coupled to hydrodynamic bearings (Tan et al., 1992). The objective of this paper is to extend the concept presented in Yang (1989) to develop a numerical scheme for closed-form evaluation of the transfer function of the distributed parameter system (1). In Section 2, the system equations are transformed into the s domain in order to determine the system transfer function. In Section 3, the Laplace transformed equations are cast into a first-order matrix differential equation. The fundamental matrix of the matrix equation is calculated leading to the transfer function in closed form. Numerical results on the proposed scheme are shown in Section 4.

2 Laplace Domain Formulation

Laplace transform of (1) leads to

$$(s^2A+sB+C)\bar{w}(x,s)=\bar{f}_{el}(x,s) \equiv \bar{f}(x,s)+(sA+B)u_0(x)+Av_0(x) \quad (5)$$

where $\bar{w}(\cdot, s)$ and $\bar{f}(\cdot, s)$ are the Laplace transforms of $w(\cdot, t)$ and $f(\cdot, t)$, respectively, s is a complex parameter, A, B, and C are the differential operators defined in (3), and $u_0(x)$ and $v_0(x)$ are the initial conditions given in (4). Laplace transform of the boundary conditions (2) gives

$$\bar{M}_j\bar{w}(x,s)\,|_{x=0}+\bar{N}_j\bar{w}(x,s)\,|_{x=1}=\bar{\gamma}_j(s) \equiv \bar{\gamma}_{Bj}(s)+\bar{\gamma}_{Ij}(s), \quad j=1,2,\ \ldots,\ n \quad (6)$$

where $\bar{M}_j$ and $\bar{N}_j$ are the operators M_j and N_j with the time-derivative operators $\partial/\partial t$ and $\partial^2/\partial t^2$ replaced by s and s^2, respectively, $\bar{\gamma}_{Bj}(s)$ is the Laplace transform of $\gamma_{Bj}(t)$, and $\bar{\gamma}_{Ij}(s)$ is a polynomial of s representing the initial conditions at the boundaries $x = 0$ and 1. Symbolically, the solution of (5) and (6) can be written in the form (Roach, 1981)

$$\bar{w}(x,s)=\int_0^1 W_o(x,\xi,s)\bar{f}_{el}(\xi,s)\,d\xi+\sum_{j=1}^{n}\phi_j(x,s)\bar{\gamma}_j(s) \quad (7)$$

where the integral kernel, $W_o(x, \xi, s)$, is the transfer function of the distributed parameter system (1) (Butkovskiy, 1983), and the functions $\phi_j(x, s)$ represent the influence of the inhomogeneity of the boundary conditions (6) on the system response. It is noted that the inverse Laplace transform of $W_o(x, \xi, s)$ is the Green's function of the distributed parameter system (1).

3 Closed-Form Evaluation of System Transfer Functions

Set

$$\eta(x,s)=\left\{\bar{w}(x,s)\ \frac{\partial}{\partial x}\bar{w}(x,s)\ \ldots\ \frac{\partial^{n-1}}{\partial x^{n-1}}\bar{w}(x,s)\right\}^T\in C^n \quad (8a)$$

$$q(x,s)=\left\{0\ \ 0\ \ \ldots\ \ 0\ \ \frac{\bar{f}_{el}(x,s)}{a_ns^2+b_ns+c_n}\right\}^T\in C^n \quad (8b)$$

$$\gamma(s)=\{\bar{\gamma}_1(s)\ \ \bar{\gamma}_2(s)\ \ \ldots\ \ \bar{\gamma}_n(s)\}^T\in C^n \quad (8c)$$

$$F(s)=\begin{bmatrix} 0 & 1 & & & \\ & 0 & 1 & & \\ & & \ddots & \ddots & \\ & & & 0 & 1 \\ -d_0(s) & -d_1(s) & \ldots & \ldots & -d_{n-1}(s) \end{bmatrix}\in C^{n\times n} \quad (8d)$$

where the symbol T denotes transposition, $\bar{\gamma}_j(s)$ are defined in (6), and the coefficients of the matrix $F(s)$

$$d_k(s)=\frac{a_ks^2+b_ks+c_k}{a_ns^2+b_ns+c_n}, \quad k=0,1,\ \ldots,\ n-1 \quad (8e)$$

with a_k, b_k, and c_k given in (3). Note that the matrix $F(s)$ is not a function of x. By (8), Eqs. (5) and (6) are cast into a matrix form

$$\frac{\partial}{\partial x}\eta(x,s)=F(s)\eta(x,s)+q(x,s), \quad x\in(0,1) \quad (9a)$$

$$M(s)\eta(0,s)+N(s)\eta(1,s)=\gamma(s) \quad (9b)$$

where $M(s)$ and $N(s)$ are $n \times n$ complex matrices, consisting of the coefficients of the operators $\bar{M}_j$ and $\bar{N}_j$, $j = 1, 2, \ldots, n$.

In Yang (1989) and Tan et al. (1992), a similar formulation is used for an undamped axially moving beam with homogeneous boundary conditions. Here, more general distributed parameter systems with inhomogeneous boundary conditions are analyzed.

Equations (9a,b) define a one-dimensional boundary value problem. The following theorem, an extension of the result about the matrix Green's function of a set of ordinary differential equations by Coddington and Levinson (1955), gives the structure of the solution for $\eta(x, s)$.

Theorem. Let the problem (9) with $q = 0$ and $\gamma = 0$ have only the null solution. Then there exists the unique solution of (9)

$$\eta(x,s)=\int_0^1 G(x,\xi,s)q(\xi,s)\,d\xi+H(x,s)\gamma(s), \quad x\in(0,1) \quad (10)$$

where the matrix Green's function

$$G(x,\xi,s)=\begin{cases} e^{F(s)x}(M(s)+N(s)e^{F(s)})^{-1}M(s)e^{-F(s)\xi}, & \xi<x \\ -e^{F(s)x}(M(s)+N(s)e^{F(s)})^{-1}N(s)e^{F(s)(1-\xi)}, & \xi>x \end{cases} \quad (11)$$

the transfer matrix between $\gamma(s)$ and $\eta(x, s)$

$$H(x,s)=e^{F(s)x}(M(s)+N(s)e^{F(s)})^{-1}, \quad (12)$$

and $e^{F(s)x}$ is the fundamental matrix of (9a). □

The proof of the theorem is straightforward: simply substitute (10)–(12) into (9) and use the property $\partial/\partial x(e^{F(s)x}) = F(s)e^{F(s)x}$ to see that Eqs. (9a, b) are satisfied by (10).

Now write

Downloaded 03 May 2010 to 171.66.16.247. Redistribution subject to ASME license or copyright; see http://www.asme.org/terms/Terms_Use.cfm

$$G(x,\xi,s)=\begin{bmatrix} g_{11}(x,\xi,s) & \cdots & g_{1n}(x,\xi,s) \\ \vdots & & \vdots \\ g_{n1}(x,\xi,s) & \cdots & g_{nn}(x,\xi,s) \end{bmatrix}$$

$$H(x,s)=\begin{bmatrix} h_{11}(x,s) & \cdots & h_{1n}(x,s) \\ \vdots & & \vdots \\ h_{n1}(x,s) & \cdots & h_{nn}(x,s) \end{bmatrix}. \quad (13)$$

By (8), (10), and (13), it is seen that

$$\bar{w}(x,s)=\int_0^1 \frac{g_{1n}(x,\xi,s)}{a_n s^2+b_n s+c_n}\bar{f}_{el}(\xi,s)d\xi+\sum_{j=1}^{n} h_{1j}(x,s)\bar{\gamma}_j(s). \quad (14)$$

Comparison of (7) and (14) yields

$$W_o(x,\xi,s)=\frac{g_{1n}(x,\xi,s)}{a_n s^2+b_n s+c_n} \quad (15a)$$

$$\phi_j(x,s)=h_{1j}(x,s), \quad j=1,2,\ \ldots,\ n. \quad (15b)$$

Equations (11), (12), and (15) suggest a new method for evaluation of the system transfer function. To determine $W_o(x, \xi, s)$ and $\phi_j(x, s)$, one only needs to calculate the fundamental matrix $e^{F(s)x} \in C^{n\times n}$ and the inverse matrix $(M(s) + N(s)e^{F(s)})^{-1} \in C^{n\times n}$. These two matrices, with low order in general (for example, for vibration and wave propagation in continua, usually $n \leq 4$), can be accurately calculated. Note that $G(x, \xi, s)$ and $H(x, s)$ in (11) are in closed form. Therefore, $W_o(x, \xi, s)$ and $\phi_j(x, s)$ can be precisely evaluated in closed form.

The numerical scheme for evaluation of $W_o(x, \xi, s)$ and $\phi_j(x, s)$ is as follows:

(i) for given the system Eq. (1) and the boundary conditions (2), form the matrices $F(s)$, $M(s)$, and $N(s)$;
(ii) for given x and s, evaluate the matrices $e^{F(s)x}$ and $(M(s) + N(s)e^{F(s)})^{-1}$; and
(iii) calculate $W_o(x, \xi, s)$ and $\phi_j(x, s)$ based on (11), (12), and (15).

A flowchart of the scheme is shown in Fig. 1.

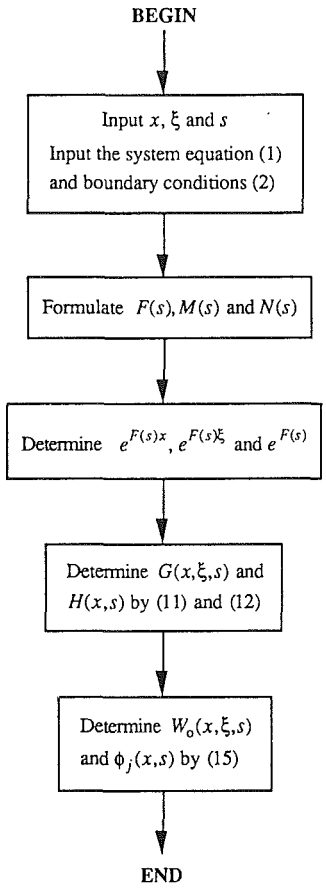


Fig. 1 Flowchart of the numerical scheme

Remarks. (1) There are many methods that give exact presentations of $e^{F(s)x}$ (Moler and Van Loan, 1978). However, because of the special form of $F(s)$ in (8*d*), the matrix diagonalization may be simpler to use (see Appendix A).

(2) The proposed method is exact; no truncation or approximation has been made. It does not require a knowledge of the system eigensolutions. The method is valid for both self-adjoint and non-self-adjoint systems.

(3) The above numerical scheme is extremely convenient in computer coding. The system type, differential operators, and boundary conditions are treated uniformly through easy assignment of the matrices $F(s)$, $M(s)$, and $N(s)$ (see Section 4). Because $F(s)$ is independent of $M(s)$ and $N(s)$, changes in the boundary conditions do not require recalculation of the fundamental matrix $e^{F(s)x}$.

(4) The characteristic equation of the distributed parameter system (1), according to (11) and (12), is

$$\det[M(s)+N(s)e^{F(s)}]=0 \quad (16)$$

whose roots are the eigenvalues of the distributed parameter system (1), or the poles of $W_o(x, \xi, s)$ and $\phi_j(x, s)$.

(5) Although this research is focused on the distributed system with constant parameters, the result obtained can be extended to distributed systems with parameters as functions of the spatial coordinate x, i.e., $a_k = a_k(x)$, $b_k = b_k(x)$ and $c_k = c_k(x)$. In this case the matrix formulation (8), (9) is still valid; $W_o(x, \xi, s)$ and $\phi_j(x, s)$ are determined in terms of a fundamental matrix $\Phi(x, s)$ (see Appendix B). The closed form of $\Phi(x, s)$ for general distributed parameter systems is usually difficult to obtain although approximation methods are available. However, for a nonuniformly distributed parameter system, exact determination of its eigensolutions is also difficult (and may be more difficult). So, the eigenfunction expansion representation of the system transfer function may not be appropriate. The method presented in this paper is potentially useful for nonuniformly distributed parameter systems.

4 Examples

The method is illustrated for an axially moving beam under uniform viscous damping. The nondimensional equation of the transverse displacement $w(x, t)$ of the beam is (Mote, 1972)

$$\left\{\frac{\partial^2}{\partial t^2}+\left(2c\frac{\partial}{\partial x}+d\right)\frac{\partial}{\partial t}+\frac{\partial^4}{\partial x^4}+(c^2-p_0)\frac{\partial^2}{\partial x^2}\right\}w(x,t)$$
$$=f(x,t), \quad x\in(0,1), \quad t>0 \quad (17)$$

where c and p_0 are the dimensionless transport speed and tension of the beam, respectively, d is the dimensionless viscous damping coefficient, and $f(x, t)$ is the transverse external force. It is seen that (17) is a fourth-order, non-self-adjoint, hyperbolic system.

Three sets of the boundary conditions are considered:

Case (a) pinned-pinned (Fig. 2(*a*)):

$$w(0,t)=w(1,t)=0 \quad \frac{\partial^2}{\partial x^2}w(0,t)=\frac{\partial^2}{\partial x^2}w(1,t)=0. \quad (18a)$$

Case (b) pinned-clamped (Fig. 2(*b*)):

$$w(0,t)=w(1,t)=0 \quad \frac{\partial^2}{\partial x^2}w(0,t)=0 \quad \frac{\partial}{\partial x}w(1,t)=0. \quad (18b)$$

Case (c) pinned-pinned with one end subject to a torque and the other to transverse motion (Fig. 2(*c*))

Downloaded 03 May 2010 to 171.66.16.247. Redistribution subject to ASME license or copyright; see http://www.asme.org/terms/Terms_Use.cfm

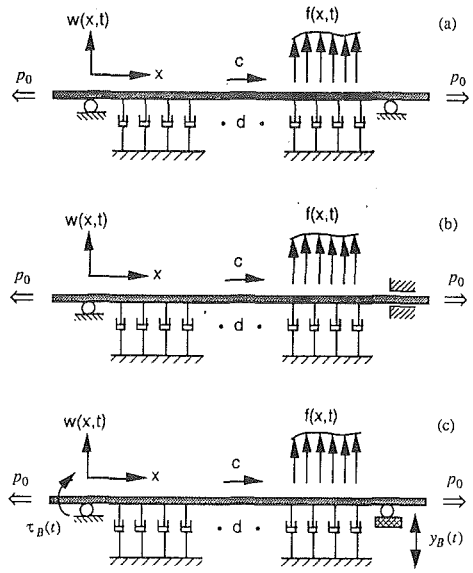


Fig. 2 Schematic of the damped axially moving beam with (*a*) pinned-pinned ends; (*b*) pinned-clamped ends; (*c*) pinned-pinned ends, the left end subject to a torque, the right end subject to transverse motion

$$w(0,t)=0 \quad \frac{\partial^2}{\partial x^2} w(0,t)=\tau_B(t)$$

$$w(1,t)=y_B(t) \quad \frac{\partial^2}{\partial x^2} w(1,t)=0 \quad (18c)$$

where $\tau_B(t)$ is the torque at $x = 0$, and $y_B(t)$ specifies the transverse motion of the support at $x = 1$. Note that (18*c*) presents inhomogeneous boundary conditions.

By (8*d*) and (17), the matrix $F(s)$ is

$$F(s)=\begin{bmatrix} 0 & 1 & 0 & 0 \\ 0 & 0 & 1 & 0 \\ 0 & 0 & 0 & 1 \\ -s^2-ds & -2cs & p_0-c^2 & 0 \end{bmatrix}. \quad (19)$$

The matrices $M(s)$ and $N(s)$ and the vector $\gamma(s)$ in (9*b*) are

Case (a):

$$M(s)=\begin{bmatrix} 1 & 0 & 0 & 0 \\ 0 & 0 & 1 & 0 \\ 0 & 0 & 0 & 0 \\ 0 & 0 & 0 & 0 \end{bmatrix} \quad N(s)=\begin{bmatrix} 0 & 0 & 0 & 0 \\ 0 & 0 & 0 & 0 \\ 1 & 0 & 0 & 0 \\ 0 & 0 & 1 & 0 \end{bmatrix} \quad \gamma(s)=0, \quad (20a)$$

Case (b):

$$M(s)=\begin{bmatrix} 1 & 0 & 0 & 0 \\ 0 & 0 & 1 & 0 \\ 0 & 0 & 0 & 0 \\ 0 & 0 & 0 & 0 \end{bmatrix} \quad N(s)=\begin{bmatrix} 0 & 0 & 0 & 0 \\ 0 & 0 & 0 & 0 \\ 1 & 0 & 0 & 0 \\ 0 & 1 & 0 & 0 \end{bmatrix} \quad \gamma(s)=0, \quad (20b)$$

Case (c):

$$M(s)=\begin{bmatrix} 1 & 0 & 0 & 0 \\ 0 & 0 & 1 & 0 \\ 0 & 0 & 0 & 0 \\ 0 & 0 & 0 & 0 \end{bmatrix} \quad N(s)=\begin{bmatrix} 0 & 0 & 0 & 0 \\ 0 & 0 & 0 & 0 \\ 1 & 0 & 0 & 0 \\ 0 & 0 & 1 & 0 \end{bmatrix} \quad \gamma(s)=\begin{bmatrix} 0 \\ \bar{\tau}_B(s) \\ \bar{y}_B(s) \\ 0 \end{bmatrix}. \quad (20c)$$

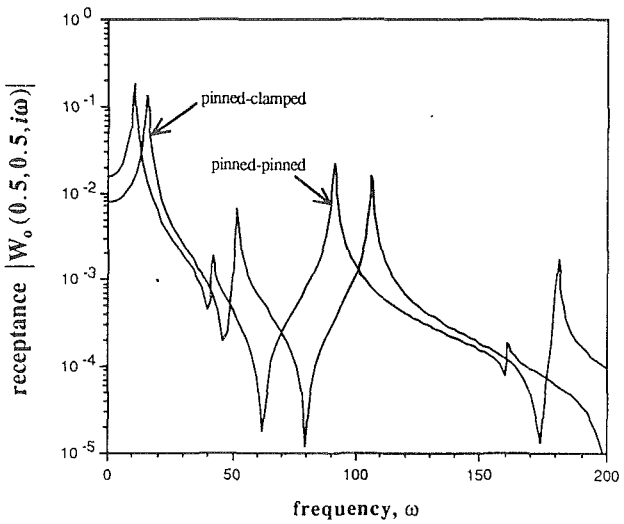


Fig. 3 The receptance $|W_o(0.5, 0.5, i\omega)|$ of the damped axially moving beam; $c = 0.5$, $p_0 = 10$, $d = 1$

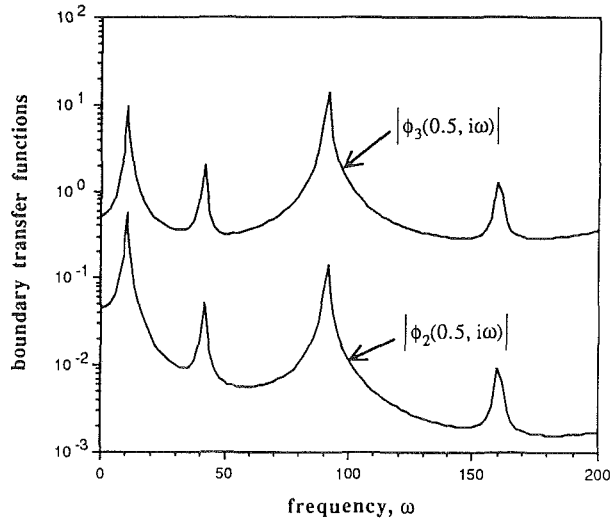


Fig. 4 Effect of the inhomogeneous boundary conditions (Case (c)) on the system response; $c = 0.5$, $p_0 = 10$, $d = 1$

Here, $\bar{\tau}_B(s)$ and $\bar{y}_B(s)$ are the Laplace transforms of $\tau_B(t)$ and $y_B(t)$, respectively. Note that $M(s)$ and $N(s)$ in (20*a*) and (20*c*) are the same. This indicates that the transfer function $W_o(x, \xi, s)$ is the same for both Case (a) and Case (c). In Cases (a) and (b), due to the homogeneous boundary conditions, all $\bar{\gamma}_j(s)$ in (7) vanish. In Case (c), $\bar{\gamma}_1(s) = \bar{\gamma}_4(s) = 0$, $\phi_2(x, s) = \bar{w}(x, s)/\bar{\tau}_B(s)$ defines the transfer function from the torque at the left end of the beam to the beam vibration, and $\phi_3(x, s) = \bar{w}(x, s)/\bar{y}_B(s)$ describes the relationship between the motion of the right end of the beam and the beam vibration. Equations (20*a*)–(20*c*) show that changes in the boundary conditions do not introduce any complexity in the evaluation of the transfer functions.

In Fig. 3 through 6, $c = 2.5$, $p_0 = 10$, $d = 1$; unless otherwise specified. Figure 3 shows the system receptance $|W_o(0.5, 0.5, i\omega)|$, $i = \sqrt{-1}$, $\omega > 0$. Four resonance peaks are shown. The receptance function for Cases (a) and (c) is given by the curve labelled "pinned-pinned," while that for Case (b) is given by the "pinned-clamped" curve. Because of the clamped boundary condition at $x = 1$, the pinned-clamped beam is a more "constrained" continuum than the pinned-pinned beam. Hence

Downloaded 03 May 2010 to 171.66.16.247. Redistribution subject to ASME license or copyright; see http://www.asme.org/terms/Terms_Use.cfm

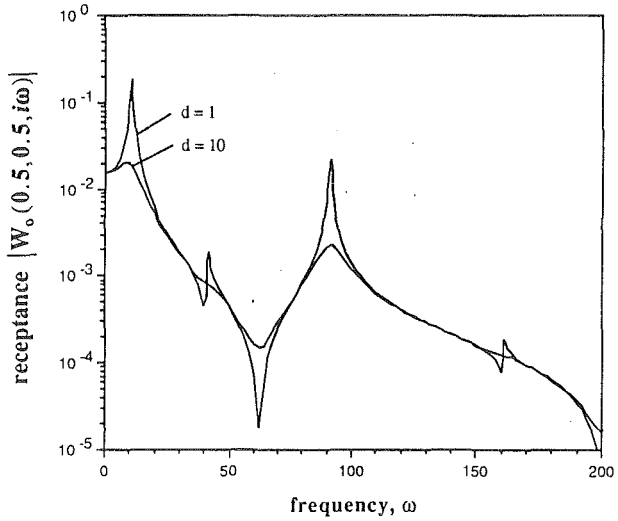


Fig. 5 Effect of the viscous damping on the steady-state response of the axially moving beam with pinned-pinned ends (Cases (a) and (c)); $c = 0.5$, $p_0 = 10$

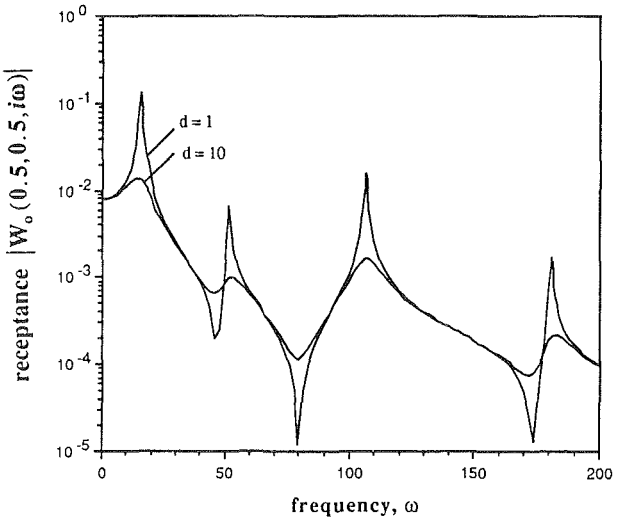


Fig. 6 Effect of the viscous damping on the steady-state response of the axially moving beam with pinned-clamped ends (Case (b)); $c = 0.5$, $p_0 = 10$

the resonant frequencies of Case (b) are higher. It is also seen that the frequency shift becomes larger for higher modes. Note that the pinned-pinned beam has a larger static displacement.

In Fig. 4 the boundary transfer functions $|\phi_j(0.5, i\omega)|$, $j = 2, 3$, for Case (c) show the influence of the inhomogeneity of the boundary conditions on the response of the beam. Note that the resonant frequencies are the same as those of the pinned-pinned beam without boundary disturbances (Case (a)); see Fig. 3. This is expected: the boundary disturbances $\tau_B(t)$ and $y_B(t)$, like the transverse external force $f(x, t)$, do not change the dynamic characteristics of the beam. Mathematically, because $W_o(x, \xi, s)$ and $\phi_j(x, s)$ have the same characteristic equations, the inhomogeneity of the boundary conditions does not alter the system spectrum. It is also seen that the shape of $|\phi_j(0.5, i\omega)|$ between the resonance peaks is different from that of $|W_o(0.5, 0.5, i\omega)|$.

The effect of the viscous damping on the steady state response of the beam is illustrated in Fig. 5 (pinned-pinned) and Fig. 6 (pinned-clamped). In both figures, the damping increase causes a slight decrease in the first resonant frequency, and reduces the response amplitudes of all modes. For $d = 10$, the second and fourth modes of the pinned-pinned beam are overdamped.

5 Conclusion

An exact closed-form evaluation of transfer functions for a class of one-dimensional distributed parameter systems has been presented. This method does not require a knowledge of the system eigensolutions, and is valid for non-self-adjoint systems with inhomogeneous boundary conditions. In the evaluation, the type and order of the distributed parameter system and the boundary conditions are treated in a unified manner, which is convenient for computer coding.

6 Acknowledgment

The first author would like to thank the National Science Foundation, the Charles Lee Powell Foundation, and the USC FRIF for their partial support of this investigation. The second author would like to acknowledge the ANR Faculty Research Award for this work.

7 References

Butkovskiy, A. G., 1982, *Green's Functions and Transfer Functions Handbook*, Halsted Press, John Wiley and Sons, New York.

Butkovskiy, A. G., 1983, *Structural Theory of Distributed Systems*, Halsted Press, John Wiley and Sons, New York.

Bergman, L. A., and Hyatt, J. E., 1989, "Green's Functions for Transversely Vibrating Uniform Euler-Bernoulli Beams Subject to Constant Axial Preload," *Journal of Sound and Vibration*, Vol. 134, No. 1, pp. 175–180.

Coddington, E. A., and Levinson, N., 1955, *Theory of Ordinary Differential Equations*, McGraw-Hill, New York.

Moler, C., and Van Loan, C., 1978, "Nineteen Dubious Ways to Compute the Exponential of a Matrix," *SIAM Review*, Vol. 20, No. 4, Oct., pp. 801–836.

Mote, C. D., Jr., 1972, "Dynamic Stability of Axially Moving Materials," *Shock and Vibration Digest*, Vol. 4, No. 4, Apr., pp. 2–11.

Roach, G. F., 1981, *Green's Functions*, Cambridge University Press, New York.

Tan, C. A., Yang, B., and Mote, C. D., Jr., 1992, "Dynamic Response of an Axially Moving Beam Coupled to Hydrodynamic Bearings," *ASME Journal of Vibration and Acoustics*, in press.

Vidyasagar, M., 1970, "A Novel Method of Evaluating e^{At} in Closed Form," *IEEE Trans. Automatic Control*, Vol. AC-15, No. 5, Oct., pp. 600–601.

Yang, B., 1989, "Active Vibration Control of Axially Moving Materials," Ph.D. Dissertation, University of California, Berkeley, Calif., pp. 38–41.

Yang, B., and Mote, C. D., Jr., 1991a, "Frequency-Domain Vibration Control of Distributed Gyroscopic Systems," ASME *Journal of Dynamic Systems, Measurement and Control*, Vol. 113, Mar., pp. 18–25.

Yang, B., and Mote, C. D., Jr., 1991b, "Active Vibration Control of the Axially Moving String in the s Domain," ASME JOURNAL OF APPLIED MECHANICS, Vol. 58, pp. 189–196.

APPENDIX A

Evaluation of the Fundamental Matrix

The fundamental matrix can be expressed by

$$e^{F(s)x} = Q(s)e^{J(s)x}Q^{-1}(s) \tag{A1}$$

where $Q(s)$ is a nonsingular transformation matrix related to the eigenvectors of $F(s)$, $J(s)$ is the Jordan form of $F(s)$ consisting of the eigenvalues of $F(s)$. For given s, denote the eigenvalues of $F(s)$ by $\lambda_l(s)$, $l = 1, 2, \ldots, n$. According to (8d), $\lambda_l(s)$ satisfy

$$\sum_{k=0}^{n} (a_k s^2 + b_k s + c_k)\lambda^k(s) = 0 \tag{A2}$$

where a_k, b_k, and c_k are given in (3). In many applications, $\lambda_l(s)$ are distinct (Yang, 1989; Tan et al., 1992). In this case $J(s)$ becomes diagonal and $Q(s)$ is a Vandermode matrix:

Downloaded 03 May 2010 to 171.66.16.247. Redistribution subject to ASME license or copyright; see http://www.asme.org/terms/Terms_Use.cfm

$$J(s)=\begin{bmatrix}\lambda_1(s) & & & \\ & \lambda_2(s) & & \\ & & \ddots & \\ & & & \lambda_n(s)\end{bmatrix}$$

$$Q(s)=\begin{bmatrix}1 & 1 & \dots & 1\\ \lambda_1(s) & \lambda_2(s) & \dots & \lambda_n(s)\\ \vdots & & & \vdots\\ \lambda_1^{n-1}(s) & \lambda_2^{n-1}(s) & \dots & \lambda_n^{n-1}(s)\end{bmatrix}. \quad \text{(A3)}$$

The matrix $e^{J(s)x}$ is also diagonal; $e^{J(s)x} = \operatorname{diag}_j(e^{\lambda_j(s)x})$. The inverse matrix $Q^{-1}(s)$ can be given in an explicit form (Vidyasagar, 1970)

$$(Q^{-1}(s))_{jk}=\frac{\sum_{m=k}^{n}(a_m s^2+b_m s+c_m)\lambda_j^{(m-k)}(s)}{(a_n s^2+b_n s+c_n)\prod_{l\neq j}(\lambda_j(s)-\lambda_l(s))}. \quad \text{(A4)}$$

Evaluation of $e^{F(s)x}$ follows three steps: (i) For given s, solve (A2) for $\lambda_l(s)$; (ii) establish the matrices $Q(s)$, $Q^{-1}(s)$, and $e^{J(s)x}$; (iii) calculate $Q(s)e^{J(s)x}Q^{-1}(s)$.

APPENDIX B

Transfer Functions of Nonuniformly Distributed Systems

For the nonuniformly distributed parameter system

$$\sum_{k=0}^{n}\left(a_k(x)\frac{\partial^2}{\partial t^2}+b_k(x)\frac{\partial}{\partial t}+c_k(x)\right)\frac{\partial^k}{\partial x^k}w(x,t) = f(x,t), \quad x\in(0,1), \quad t>0, \quad \text{(B1)}$$

the matrix formulation (8), (9) is also valid except $d_k(s)$ in (8d) are replaced by

$$d_k(x,s)=\frac{a_k(x)s^2+b_k(x)s+c_k(x)}{a_n(x)s^2+b_n(x)s+c_n(x)}, \quad k=0,1,\dots,n-1 \quad \text{(B2)}$$

and $F(s)$ in (9a) is replaced by $F(x, s)$. Let the fundamental matrix of the system be $\Phi(x, s)$, which satisfies $\partial/\partial x\,\Phi(x, s) = F(x, s)\Phi(x, s)$ and $\Phi(0, s) = I$. It is easy to show that the solution of (9) has the same form as (10) with the matrix Green's function

$$G(x,\xi,s)=\begin{cases}\Phi(x,s)\,(M(s)+N(s)\Phi(1,s))^{-1}M(s)\Phi(-\xi,s), & \xi<x\\ -\Phi(x,s)\,(M(s)+N(s)\Phi(1,s))^{-1}N(s)\Phi(1-\xi,s), & \xi>x\end{cases} \quad \text{(B3)}$$

and the transfer matrix between $\gamma(s)$ and $\eta(x, s)$

$$H(x,s)=\Phi(x,s)\,(M(s)+N(s)\Phi(1,s))^{-1}. \quad \text{(B4)}$$

Downloaded 03 May 2010 to 171.66.16.247. Redistribution subject to ASME license or copyright; see http://www.asme.org/terms/Terms_Use.cfm

G. Leng

N. Sri Namachchivaya
Mem. ASME

S. Talwar

Department of Aeronautical and Astronautical Engineering, University of Illinois, Urbana, IL 61801

Robustness of Nonlinear Systems Perturbed by External Random Excitation

The effect of external random excitation on nonlinear continuous time systems is examined using the concept of the Lyapunov exponent. The Lyapunov exponent may be regarded as the nonlinear/stochastic analog of the poles of a linear deterministic system. It is shown that while the stationary probability density function of the response undergoes qualitative changes (bifurcations) as system parameters are varied, these bifurcations are not reflected by changes in the sign of the Lyapunov exponent. This finding does not support recent proposals that the Lyapunov exponent be used as a basis for a rigorous theory of stochastic bifurcation.

Introduction

The design of practical control systems requires that the mathematical model used be sufficiently robust. This implies that qualitative properties should be preserved under the effect of all possible perturbations. Such systems were referred to by Andronov, Vitt, and Chaikin (1965) as "coarse systems" and formed the basis for the concept of structural stability in the mathematical theory of dynamical systems (Arnold, 1983). In the context of single-input single output (SISO) linear control systems, robustness is characterized by the Nyquist plot and the concepts of phase and gain margins. The extension of these ideas to multiple-input multiple-out (MIMO) linear systems is documented by Dorato (1987). Currently, there are two major approaches to robustness analysis. The first assumes unstructured additive or multiplicative perturbations of the plant transfer function. Robustness is then measured by the singular values of the return difference matrix. This is a frequency domain technique which does not make explicit use of the nonlinearities present in the system. The second method is referred to as a structured or parametric approach. The precise values of system parameters are unknown but the uncertainty is assumed to be bounded. The degree of robustness, indicated by the system poles of the linearized system, is then determined in terms of these bounds using Kharitonov-type theorems (Barmish, 1988). These two techniques constitute a deterministic approach to the robustness analysis of linear systems. The possibility of random parametric or external excitation is not considered.

So far the robustness analysis of stochastic systems has received relatively limited attention. Wonham (1967) investigated the problem of a linear continuous time system with linear multiplicative white noise gain in terms of optimal stationary control using a state space formulation. A similar problem was studied by Willems and Blankenship (1971) in the frequency domain (see also Willems and Willems, 1983). In both instances, robustness was measured by a mean-square type criterion. Robustness measures of stable, linear discrete time systems were obtained by Yaz and Yildizbayrak (1985) and Yaz (1988). Their robustness measures are based on the sample stability of the perturbed system. The references mentioned above are mainly concerned with the effect of parametric fluctuations/uncertainties on linear systems. For nonlinear systems, as systems parameters are varied, qualitative changes (bifurcations) in the system response can occur. In this paper, the robustness of such bifurcations under the effect of random external excitation will be examined. In the following section, the problem is formulated in a general context and the idea of the Lyapunov exponent as a quantitative measure of robustness is introduced. Examples of systems undergoing codimension 1 and 2 bifurcations are then studied.

Problem Formulation

Consider the following system:

$$\frac{dX}{dt} = AX + f(X) + \sigma\eta(t) \tag{1}$$

where X is a vector in R^n and without loss of generality it is assumed that A is in canonical form, $f(X)$ are nonlinear terms, and $\eta(t)$ represents independent zero-mean white noise excitation of unit intensity. Since only additive noise is present, it does not matter whether the Itô or Stratonovich interpretation is used. Assuming that a stationary solution X_s exists, the problem of robustness is concerned with the sample stability of this stationary solution. As with deterministic systems, con-

Contributed by the Applied Mechanics Division of THE AMERICAN SOCIETY OF MECHANICAL ENGINEERS for presentation at the 1992 ASME Winter Annual Meeting, Anaheim, CA, Nov. 8-13, 1992.

Discussion on this paper should be addressed to Prof. Leon M. Keer, The Technological Institute, Northwestern University, Evanston, IL 60208, and will be accepted until four months after final publication of the paper itself in the ASME JOURNAL OF APPLIED MECHANICS.

Manuscript received by the ASME Applied Mechanics Division, June 4, 1990; final revision, Feb. 10, 1992. Associate Technical Editor: D. J. Inman.

Paper No. 92-WA/APM-3.

Copyright © 1992 by ASME

Downloaded 03 May 2010 to 171.66.16.247. Redistribution subject to ASME license or copyright; see http://www.asme.org/terms/Terms_Use.cfm

sider a small perturbation x, about this stationary solution. Then to first order in the perturbation, a linear system with stochastic coefficients is obtained:

$$\frac{dx}{dt}=\left[A+\frac{\partial f}{\partial X}\right]x=[A+F(t)]x. \tag{2}$$

Define a norm $\rho = (x^T x)^{1/2}$, the exponential growth rate of the perturbation is then given by

$$\frac{d(\log\rho)}{dt}=\frac{x^T[(A+F(t))+(A+F(t))^T]x}{2\rho^2}. \tag{3}$$

The Lyapunov exponent, Λ, is simply the time-averaged exponential growth rate defined by

$$\Lambda=\lim\frac{1}{t}\left(\log\left(\frac{\rho(t)}{\rho(0)}\right)\right),\ t\to\infty \tag{4}$$

where

$$\log\left(\frac{\rho(t)}{\rho(0)}\right)=\int_0^t\frac{x^T[(A+F(s))+(A+F(s))^T]x}{2\rho^2}\,ds.$$

The stationary solution is sample stable if $\Lambda < 0$, and this is a necessary condition for a robust system. Assuming that the stationary state is also ergodic, the temporal average may be replaced by the ensemble average and a quantitative measure for robustness can then be computed, i.e.,

$$\Lambda=E\left[\frac{x^T[(A+F(t))+(A+F(t))^T]x}{2\rho^2}\right]. \tag{5}$$

One may regard the Lyapunov exponent as the stochastic analog of the poles of a deterministic system. This concept of the Lyapunov exponent (Bylov et al., 1966) has been proposed by L. Arnold (1988) as a basis for a rigorous theory of stochastic bifurcation. A similar approach was also used by Caughey and Gray (1965), Infante (1968), Kozin and Wu (1973), and Ariaratnam and Xie (1988a) in their derivation of sufficient conditions for the sample stability of linear systems with stochastic coefficients.

One-Dimensional Systems

For one-dimensional systems, the computation of the Lyapunov exponent is fairly simple. Consider the general one-dimensional system written as

$$\frac{dX}{dt}=\lambda X+f(X)+\sigma\eta(t), \tag{6}$$

and the perturbed system is

$$\frac{dx}{dt}=\left[\lambda+\frac{df(X_s)}{dX}\right]x. \tag{7}$$

If the stationary state is ergodic, then the Lyapunov exponent is given by

$$\Lambda=\lambda+E\left[\frac{df(X_s)}{dX}\right] \tag{8}$$

and the stationary probability density function can be obtained by solving the Fokker-Planck equation (FPE) for the system

$$0=-\frac{\partial}{\partial X}\left\{[\lambda X+f(X)]p(X)-\frac{\sigma^2}{2}\frac{\partial p}{\partial X}\right\}. \tag{9}$$

The stationary probability density function (pdf) is given by

$$p_s(X)=N\exp\left(\frac{2}{\sigma^2}\left(\lambda\frac{X^2}{2}+\int^X f(z)dz\right)\right) \tag{10}$$

where N is an appropriate normalization constant. It is instructive to consider a simple example:

Example 1 (Simple Bifurcation—Soft Loss of Stability). For a symmetric system undergoing a soft loss of stability (i.e., a loss of stability to a nearby equilibrium, $f(X) = aX^3$ with $a < 0$) and the stationary probability density function is

$$p_s(X)=\exp\left(\frac{2}{\sigma^2}(\lambda X^2/2+aX^4/4)\right)\Bigg/\int_{-\infty}^{\infty}\exp\left(\frac{2}{\sigma^2}(\lambda X^2/2+aX^4/4)\right)dX. \tag{11}$$

Assuming that the stationary solution is ergodic, the Lyapunov exponent is then given by Eq. (8):

$$\Lambda=\lambda+3aE[X^2]. \tag{12}$$

The Lyapunov exponent Λ is plotted against the eigenvalue λ for the deterministic system in Fig. 1 with $\sigma^2 = 0.1$ and $a = -1$. The deterministic system undergoes a bifurcation at $\lambda = 0$ and the probability density function changes from a unimodal density to a bimodal density (Fig. 2(*a*) and 2(*b*)). As evident from Fig. 1, the Lyapunov exponent Λ is negative which indicates that this is a robust feature, but the system is least robust at $\lambda = 0$. Physically, this implies that perturbations will take a much longer time to decay. It should be noted that the Lyapunov exponent does not indicate the qualitative change in the stationary pdf. This point was not adequately emphasized by L. Arnold (1988) in his theory of stochastic bifurcation based on the Lyapunov exponent.

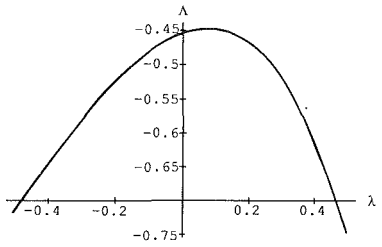


Fig. 1 Lyapunov exponent (soft loss of stability)

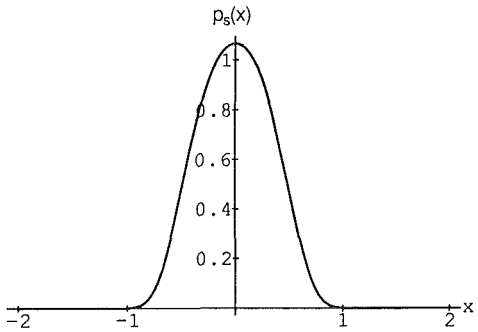


Fig. 2(*a*) Probability density function (soft loss of stability), $\lambda = -0.2$

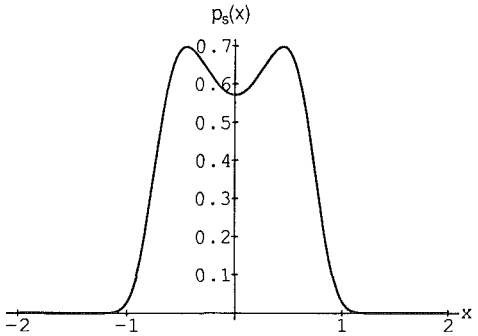


Fig. 2(*b*) Probability density function (soft loss of stability), $\lambda = 0.2$

Downloaded 03 May 2010 to 171.66.16.247. Redistribution subject to ASME license or copyright; see http://www.asme.org/terms/Terms_Use.cfm

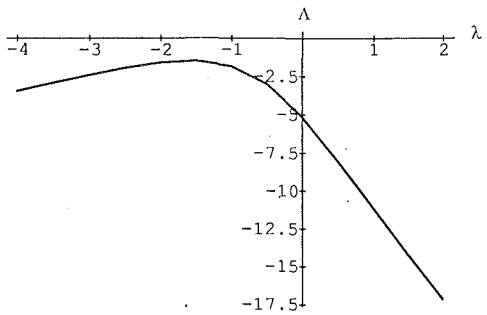


Fig. 3 Lyapunov exponent (hard loss of stability)

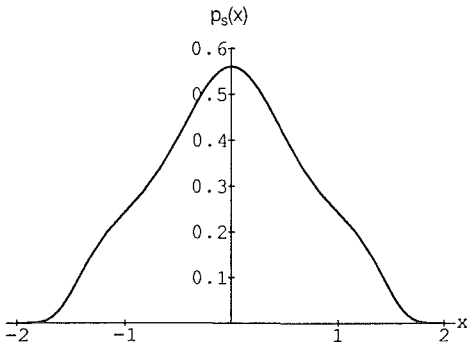


Fig. 4(*a*) Probability density function (hard loss of stability), $\lambda = -1.5$

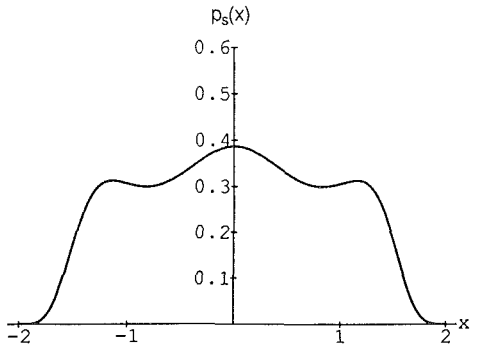


Fig. 4(*b*) Probability density function (hard loss of stability), $\lambda = -0.9$

Example 2 (Simple Bifurcation—Hard Loss of Stability). Now consider the one-dimensional system

$$\frac{dX}{dt} = \lambda X + C_3 X^3 + C_5 X^5 + \sigma\eta(t) \tag{13}$$

where $C_3 > 0$, $C_5 < 0$ for a hard loss of stability. The steady-state pdf is given by

$$p_s(X) = N \exp\left[\frac{2}{\sigma^2}\left(\lambda\frac{X^2}{2} + C_3\frac{X^4}{4} + C_5\frac{X^6}{6}\right)\right] \tag{14}$$

where the normalization constant N is defined by

$$N = \int_{-\infty}^{\infty} \exp\left[\frac{2}{\sigma^2}\left(\lambda\frac{X^2}{2} + C_3\frac{X^4}{4} + C_5\frac{X^6}{6}\right)\right] dX \tag{15}$$

and the Lyapunov exponent is (from Eq. (8))

$$\Lambda = \lambda + 3C_3E[X^2] + 5C_5E[X^4] \tag{16}$$

where the expectation is taken with respect to the steady-state pdf defined by Eq. (14). Numerical results for $C_3 = 2$, $C_5 = -1$ and $\sigma^2 = 1$ are shown as Fig. 3. In this case, the system is least robust just before the deterministic bifurcation point at $\lambda = 0$. It is interesting to compare this result with the qualitative changes in the pdf as λ is varied (Fig. 4). It can be seen that the decrease in robustness coincides with the emergence of two additional peaks in the pdf. Once again, it should be noted that the Lyapunov exponent remains negative and cannot be used as a bifurcation parameter.

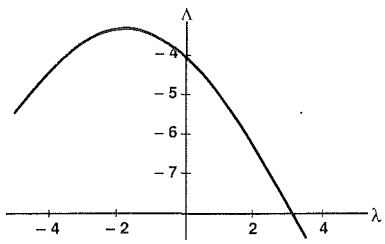


Fig. 5 Lyapunov exponent for $dX = (1 + \lambda X - X^3)dt + \sqrt{2}X \circ dW$

The results derived here for nonlinear systems under external random excitation is by no means typical. In fact, parametically excited systems studied by previous researchers in stochastic bifurcation theory are extremely sensitive to errors in the reference input. Consider the nonlinear system with fluctuating gain:

$$dX = (\lambda X - X^3)dt + \sqrt{2}X \circ dW, \tag{17}$$

where "$\circ$" denotes that the Stratonovich interpretation is used. It is well known that the Lyapunov exponent is simply λ and the trivial solution $X = 0$ loses its stability at $\lambda = 0$ and this coincides with a qualitative change in the probability density function. Suppose now that a nonzero reference input is present, i.e.,

$$dX = (1 + \lambda X - X^3)dt + \sqrt{2}X \circ dW. \tag{18}$$

Since the drift term is not zero at $X = 0$, the system is ergodic and a steady-state solution exists and is defined by the steady-state pdf:

$$p_s(X) = \begin{cases} X^{\lambda-1}\exp[-(1/X + X^2/2)]/C & X > 0 \\ 0 & \text{else} \end{cases} \tag{19}$$

where

$$C = \int_0^{\infty} X^{\lambda-1}\exp[-(1/X + X^2/2)]dx,$$

Perturbing about this stationary (ergodic) solution leads to the following linear system with stochastic coefficients:

$$dx = [\lambda - 3(X_s)^2]xdt + \sqrt{2}xodW. \tag{20}$$

The Lyapunov exponent is then given by

$$\Lambda = \lim_{t\to\infty}\frac{1}{t}\log\frac{|x(t)|}{x(0)|} = \lambda - 3E[X^2] \tag{21}$$

since the Wiener process $W(t) \sim (t \log\log t)^{1/2}$ as $t \to \infty$ with probability one. The Lyapunov exponent Eq. (21) is plotted in Fig. 5 and is negative. The variation of the Lyapunov exponent with λ is not unlike that of a system perturbed by external random excitation. This "quasi-external excitation" effect of a nonzero reference input is apparent if the transformation $X = Y + C$ is made in Eq. (18) so that the nonzero reference input is eliminated. One sees that an additional external excitation term (CdW) is then generated from the multiplicative noise term $XodW$.

Two-Dimensional Systems

Noting that the problem of robustness leads to a linear system with stochastic coefficients, it is convenient to first consider the general two-dimensional linear system with stochastic coefficients:

Downloaded 03 May 2010 to 171.66.16.247. Redistribution subject to ASME license or copyright; see http://www.asme.org/terms/Terms_Use.cfm

$$\frac{dx_1}{dt}=F_{11}(t)x_1+F_{12}(t)x_2$$
$$\frac{dx_2}{dt}=F_{21}(t)x_1+F_{22}(t)x_2 \tag{22}$$

where the $F_{ij}(t)$ are colored noise sources generated from white noise. Making the transformation, $x_1 = r\cos\theta$, $x_2 = r\sin\theta$,

$$\frac{dr}{dt}=\frac{1}{2}[(F_{11}+F_{22})+(F_{12}+F_{21})\sin2\theta+(F_{11}-F_{22})\cos2\theta]r$$
$$\frac{d\theta}{dt}=\frac{1}{2}[(F_{21}-F_{12})+(F_{22}-F_{11})\sin2\theta+(F_{21}+F_{12})\cos2\theta] \tag{23}$$

If the θ process and the $F_{ij}(t)$'s are ergodic then the Lyapunov exponent is given by

$$\Lambda=\frac{1}{2}E[(F_{11}+F_{22})+\sqrt{(F_{12}+F_{21})^2+(F_{11}-F_{22})^2}\sin(2\theta+\phi)] \tag{24}$$

where ϕ is a random phase angle defined by

$$\phi=\arctan\left(\frac{F_{11}-F_{22}}{F_{12}+F_{21}}\right). \tag{25}$$

Noting that $|\sin(2\theta+\phi)| \leq 1$, an upper bound for the Lyapunov exponent can be found and hence a sufficient condition for sample stability is:

$$E[(F_{11}+F_{22})+\sqrt{(F_{12}+F_{21})^2+(F_{11}-F_{22})^2}]<0. \tag{26}$$

A necessary condition for sample stability requires that the joint moment of the stochastic coefficients and the phase process θ be computed. These ideas are applicable to the following system:

Example 3: Hopf Bifurcation (Dynamic Instability). Consider the nonlinear system perturbed by independent external white noise sources:

$$\frac{dX}{dt}=\mu X-\omega Y+(aX-bY)(X^2+Y^2)+\sigma\eta_1(t)$$
$$\frac{dY}{dt}=\omega X+\mu Y+(aY+bX)(X^2+Y^2)+\sigma\eta_2(t) \tag{27}$$

where the deterministic terms correspond to the normal form for the Hopf bifurcation. A stationary state exists for the case $a < 0$, and the pdf is given by

$$p_s(X, Y)=N\exp\left[\frac{2}{\sigma^2}\left(\mu\frac{(X^2+Y^2)}{2}+a\frac{(X^2+Y^2)^2}{4}\right)\right] \tag{28}$$

and

$$N^{-1}=\int_{-\infty}^{\infty}\int_{-\infty}^{\infty}\exp\left[\frac{2}{\sigma^2}\left(\mu\frac{(X^2+Y^2)}{2}+a\frac{(X^2+Y^2)^2}{4}\right)\right]dXdY. \tag{29}$$

Perturbing about this stationary state, the resulting linear system, Eq. (22), is defined by $x_1 = x$, $x_2 = y$ and

$$F_{11}=\mu+a(3X^2+Y^2)-2bXY$$
$$F_{12}=-\omega-b(X^2+3Y^2)+2aXY$$
$$F_{21}=\omega+b(3X^2+Y^2)+2aXY$$
$$F_{22}=\mu+a(X^2+3Y^2)+2bXY \tag{30}$$

which leads to

$$\frac{dr}{dt}=\{\mu+2a(X^2+Y^2)+\sqrt{a^2+b^2}[(X^2-Y^2)\sin\psi-2XY\cos\psi]\}r \tag{31}$$
$$\frac{d\theta}{dt}=\omega+2b(X^2+Y^2)+\sqrt{a^2+b^2}[(X^2-Y^2)\cos\psi+2XY\sin\psi]$$

where $\psi = 2\theta + \arctan(a/b)$. Since ω is nonzero and the X, Y processes are assumed to be ergodic, the Lyapunov exponent is then given by

$$\Lambda=E[\mu+2a(X^2+Y^2)+\sqrt{a^2+b^2}[(X^2-Y^2)\sin\psi-2XY\cos\psi]] \tag{32}$$

where the expectation is taken with respect to the steady-state joint probability density function $p_s(X, Y, \theta)$. A perturbation expansion for this steady-state pdf may be constructed using a separation of time scales technique given in Blankenship and Papanicoloau (1978). Roughly, since the X, Y processes are assumed to be stationary to start with, these processes must have evolved sufficiently fast to reach a stationary state and should be scaled accordingly for consistency. The technique has also been applied by Horsthemke and Lefever (1984) and is explained in Appendix A. Then the Lyapunov exponent can be computed term-wise from such an expansion has been proven by Arnold et al. (1988). For simplicity, the technique will be applied for the case $b = 0$ and the angular frequency ω is large. The system defining the steady-state pdf is scaled as follows:

$$\frac{d\theta}{dt}=\frac{\omega}{\epsilon^2}-\frac{a}{\epsilon}[(X^2-Y^2)\sin2\theta-2XY\cos2\theta]$$
$$\frac{dX}{dt}=\frac{1}{\epsilon^2}[\mu X-\omega Y+aX(X^2+Y^2)]+\frac{\sigma}{\epsilon}\eta_1(t)$$
$$\frac{dY}{dt}=\frac{1}{\epsilon^2}[\omega X-\mu Y+aY(X^2+Y^2)]+\frac{\sigma}{\epsilon}\eta_2(t) \tag{33}$$

Let the steady-state pdf take the following form:

$$p_s(X, Y, \theta)=p_0(X, Y, \theta)+\epsilon p_1(X, Y, \theta)+\ldots. \tag{34}$$

The steady-state Fokker-Planck Equation for Eq. (33) may be written as

$$\frac{1}{\epsilon^2}L_0[p_s]+\frac{1}{\epsilon}L_1[p_s]=0, \tag{35}$$

where the operators L_0 and L_1 are defined as follows:

$$L_0[p]=-\frac{\partial}{\partial X}\left([\mu X-\omega Y+aX(X^2+Y^2)]p-\frac{\sigma^2}{2}\frac{\partial p}{\partial X}\right)$$
$$-\frac{\partial}{\partial Y}\left([\omega X+\mu Y+aY(X^2+Y^2)]p-\frac{\sigma^2}{2}\frac{\partial p}{\partial Y}\right)-\omega\frac{\partial p}{\partial\theta}$$
$$L_1[p]=-a\frac{\partial}{\partial\theta}[[(X^2-Y^2)\sin2\theta-2XY\cos2\theta]p]. \tag{36}$$

Substituting Eq. (34) for the pdf leads to the system of equations:

$$L_0[p_0]=0$$
$$L_0[p_1]=L_1[p_0]$$
$$\ldots.$$
$$L_0[p_n]=L_1[p_{n-1}]. \tag{37}$$

The solution to the lowest order equation is

Downloaded 03 May 2010 to 171.66.16.247. Redistribution subject to ASME license or copyright; see http://www.asme.org/terms/Terms_Use.cfm

$$p_0(X, Y, \theta) = p_s(X, Y)p_s(\theta)$$
$$= N \exp\left[\frac{2}{\sigma^2}\left(\mu\frac{(X^2+Y^2)}{2} + a\frac{(X^2+Y^2)^2}{4}\right)\right]\cdot\frac{1}{2\pi}, \quad (38)$$

and an approximation to the Lyapunov exponent is then obtained from Eq. (32) by taking expectation with respect to Eq. (38),

$$\Lambda = \mu + 2aE[X^2+Y^2]. \quad (39)$$

This is compared in Fig. 6 with the sufficient condition obtained from Eq. (26), which states that the system is robust if

$$\mu + (2a + |a|)E[X^2+Y^2] < 0. \quad (40)$$

For $a = -0.5$ and $\sigma^2 = 1$, the sufficient condition Eq. (40) is satisfied. This indicates that the system is robust but as expected, it provides a more conservative robustness measure compared to Eq. (39).

One may also check if the polar representation of the Hopf bifurcation, Eq. (27), is robust to external excitation. Consider

$$\frac{dR}{dt} = \mu R + aR^3 + \sigma\eta_1(t), \quad a<0,\ R\geq 0$$

$$\frac{d\theta}{dt} = \omega + bR^2 + \sigma\eta_2(t) \quad (41)$$

where the noise terms are included for the robustness analysis and, for purposes of comparison, b will be set to zero. Observing that the amplitude R is decoupled from the phase, the Lyapunov exponent is then given by

$$\Lambda = \mu + 3aE[R^2], \quad (42)$$

where the expectation is taken with respect to the probability density function

$$p_s(R, \theta) = N\exp\left(\frac{2}{\sigma^2}(\mu R^2/2 + aR^4/4)\right)\cdot\frac{1}{2\pi}$$

and

$$N^{-1} = \int_0^\infty \exp\left(\frac{2}{\sigma^2}(\mu R^2/2 + aR^4/4)\right)dR. \quad (43)$$

The Lyapunov exponent, Eq. (42), is also plotted against μ in Fig. 6 for the same parameters, i.e., $\sigma^2 = 1$ and $a = -0.5$. It is evident that the polar representation is less robust to external random excitation. Physically, in Eq. (41), the perturbations are aligned with the radial direction and hence the perturbations should have a greater effect on the amplitude.

Example 4 (Hopf-Pitchfork Interaction—Coupled Dynamic/Static Instability). Consider the deterministic normal form for the Hopf-pitchfork bifurcation perturbed by external independent white noise sources:

$$\frac{dR}{dt} = \mu R + c'R^3 + e'RZ^2 + \sigma_1\eta_1(t)$$

$$\frac{dZ}{dt} = \lambda Z + b'Z^3 + d'R^2Z + \sigma_2\eta_2(t), \quad (44)$$

where R represents the dynamic mode ($R > 0$), and Z, the static mode. Based on Example 3, the polar representation is used since from a robustness viewpoint, this corresponds to a "worst-case" situation. It is convenient to rescale the state variables by

$$R \leftarrow \sqrt{2}R/\sigma_1,\ Z \leftarrow \sqrt{2}Z/\sigma_2,$$

resulting in

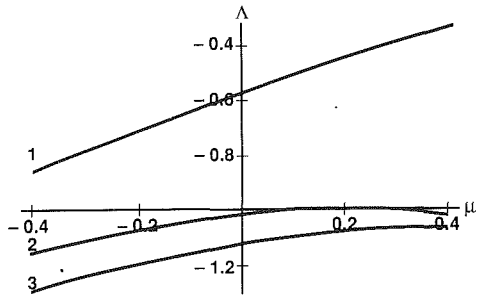


Fig. 6 Lyapunov exponent (Hopf bifurcation) (1) upper bound—nonradial excitation, (2) exact—radial excitation, (3) lowest-order approximation—nonradial excitation

$$\frac{dR}{dt} = \mu R + cR^3 + eRZ^2 + \sqrt{2}\eta_1(t)$$

$$\frac{dZ}{dt} = \lambda Z + bZ^3 + dR^2Z + \sqrt{2}\eta_2(t), \quad (45)$$

where the new system parameters are given by

$$b = b'(\sigma_2)^2/2,\ c = c'(\sigma_1)^2/2,\ d = d'(\sigma_1)^2/2,\ e = e'(\sigma_2)^2/2.$$

An explicit normalizable solution to the steady-state FPE for Eq. (45) can be found for the case $d = e = k$, provided $b, c < 0$ and if $k > 0$, then $bc - k^2 > 0$ must also be satisfied. The steady-state probability density function is then

$$p_s(R, Z) = N\exp\left(\frac{1}{4}(2\mu + cR^2)R^2 + 2kR^2Z^2 + (2\lambda + bZ^2)Z^2\right), \quad (46)$$

with N as a normalization constant. Perturbing about this stationary state and to first order in the perturbation,

$$\frac{dr}{dt} = (\mu + 3cR^2 + kZ^2)r + (2kRZ)z$$

$$\frac{dz}{dt} = (2kRZ)r + (\lambda + 3bZ^2 + kR^2)z. \quad (47)$$

Using the formula derived earlier, Eqs. (22)–(23), and letting $r = \rho\cos\theta$, $z = \rho\sin\theta$, the growth rate of the norm of the perturbation, ρ, is governed by

$$\frac{d\rho}{dt} = \frac{1}{2}[(\lambda+\mu) + (3c+k)R^2 + (3b+k)Z^2 + 4kRZ\sin 2\theta$$
$$+ ((\mu-\lambda) + (3c-k)R^2 + (k-3b)Z^2)\cos 2\theta]\rho. \quad (48)$$

Scaling the θ, R, Z processes as in Appendix A yields

$$\frac{d\theta}{dt} = \frac{1}{2}(\lambda-\mu)\sin 2\theta + \frac{1}{2\epsilon}\{4kRZ\cos 2\theta$$
$$+ [(3b-k)Z^2 + (k-3c)R^2]\sin 2\theta\}$$
$$\frac{dR}{dt} = \frac{1}{\epsilon^2}(\mu R + cR^3 + kRZ^2) + \frac{1}{\epsilon}\sqrt{2}\,\eta_1(t)$$
$$\frac{dZ}{dt} = \frac{1}{\epsilon^2}(\lambda Z + bZ^3 + kR^2Z) + \frac{1}{\epsilon}\sqrt{2}\eta_2(t). \quad (49)$$

For simplicity, let $k = 3b = 3c$. The steady-state FPE is given by

$$\frac{1}{\epsilon^2}L_0[p] - \frac{1}{\epsilon}L_1[p] - L_2[p] = 0, \quad (50)$$

with L_0, L_1, L_2 defined by

Downloaded 03 May 2010 to 171.66.16.247. Redistribution subject to ASME license or copyright; see http://www.asme.org/terms/Terms_Use.cfm

$$L_0[p] = -\frac{\partial}{\partial R}\left\{\left(\mu R + \frac{k}{3}R^3 + kRZ^2\right)p - \frac{\partial p}{\partial R}\right\} - \frac{\partial p}{\partial Z}\left\{\left(\lambda Z + \frac{k}{3}Z^3 + kZR^2\right)p - \frac{\partial p}{\partial Z}\right\}$$

$$L_1[p] = 2kRZ\frac{\partial}{\partial \theta}[p\cos 2\theta]$$

$$L_2[p] = \frac{(\lambda-\mu)}{2}\frac{\partial}{\partial \theta}[p\sin 2\theta].$$

Let the perturbation expansion be of the form

$$p_s(R, Z, \theta) = p_0(R, Z, \theta) + \epsilon p_1(R, Z, \theta) + \epsilon^2 p_2(R, Z, \theta) + \ldots, \quad (51)$$

and the system of perturbation equation is

$$L_0[p_0] = 0$$

$$L_0[p_1] = L_1[p_0]$$

$$L_0[p_2] = L_1[p_1] + L_2[p_0]$$

$$\ldots\ \ldots$$

$$L_0[p_n] = L_1[p_{n-1}] + L_2[p_{n-2}]. \quad (52)$$

It is convenient to let $p_n(R, Z, \theta) = p_s(R, Z)r_n(r, Z, \theta)$, where $p_s(R, Z)$ is defined in Eq. (46), so that the operator $L_0[p_n]$ takes the form

$$L_0[p_n] = L_0[p_s r_n] = \frac{\partial}{\partial R}\left[p_s\frac{\partial r_n}{\partial R}\right] + \frac{\partial}{\partial Z}\left[p_s\frac{\partial r_n}{\partial Z}\right], \quad (53)$$

which is a linear self-adjoint operator. Substituting into the FPE, Eq. (5) and collecting terms, the $O(\epsilon^0)$ equation is trivally satisfied with $p_0(R, Z, \theta) = p_s(R, Z)r_0(\theta)$, but unlike Example 3, $r_0(\theta)$ has yet to be defined. The $O(\epsilon^1)$ equation is

$$L_0[p_s r_1] = L_1[p_s r_0(\theta)] = 2kRZp_s(R, Z)\frac{\partial}{\partial \theta} = r_0(\theta)\cos 2\theta. \quad (54)$$

According to the solvability condition,

$$\int_0^{2\pi}\int_0^{\infty}\int_{-\infty}^{\infty} 2kRZp_s(R, Z)\frac{\partial}{\partial \theta} = r_0(\theta)\cos 2\theta \times p_s(R, Z)N(\theta)dZdRd\theta = 0$$

where the term $p_s(R, Z)N(\theta)$ belongs to the kernel of L_0. Since this has to hold for an arbitrary $N(\theta)$, it is required that

$$\int_0^{\infty}\int_{-\infty}^{\infty} 2kRZp_s^2(R, Z)dZdR = 0. \quad (55)$$

As $p_s(R, Z)$ is symmetric in Z, this implies that Fredholm's alternative is satisfied and that a unique solution for r_1 can be found. Using the fact that L_0 is a linear operator, r_1 can then be expressed as the sum of a homogeneous and particular solution

$$r_1(R, Z, \theta) = H(\theta) + 2k\frac{\partial}{\partial \theta} = r_0(\theta)\cos 2\theta P(R, Z), \quad (56)$$

where $H(\theta)$ is the homogeneous solution of $L_0[p_s H(\theta)] = 0$ and $P(R, Z)$ is a particular solution of $L_0[p_s P(R, Z)] = RZp_s(R, Z)$. It remains now to solve for $P(R, Z)$. Using Galerkin's approximation, let $P = \Sigma C_{mn}R^m Z^n$ and take weight functions of the form $R^p Z^s$. Define

$$M(m, n) = \int_0^{\infty}\int_{-\infty}^{\infty} R^m Z^n p_s(R, Z)dZdR. \quad (57)$$

A simple 3-mode expansion, $P(R, Z) = C_{20}R^2 + C_{11}RZ + C_{02}Z^2$, yields

$$P(R, Z) = -\frac{M(2, 2)}{M(0, 2) + M(2, 0)}RZ. \quad (58)$$

Now, at $O(\epsilon^2)$:

$$L_0[p_s r_s] = 2kRZ\frac{\partial}{\partial \theta}[r_1(R, Z, \theta)\cos 2\theta] + \frac{(\lambda-\mu)}{2}\frac{\partial}{\partial \theta}[r_0(\theta)\sin 2\theta]. \quad (59)$$

Substituting for $r_1(R, Z, \theta)$ and invoking Fredholm's alternative, $r_0(\theta)$ has to satisfy

$$\frac{\partial}{\partial \theta}\left\{2Cr_0(\theta)\sin 2\theta + \cos 2\theta\frac{\partial}{\partial \theta}[r_0(\theta)\cos 2\theta]\right\} = 0, \quad (60)$$

with $C = (\lambda - \mu)/(16k^2E[RZP(R, Z)]$, where the expectation is taken with respect to $p_s(R, Z)$. This equation may be rewritten as

$$-\frac{\partial}{\partial \theta}\left\{-\left[C\sin 2\theta + \frac{1}{2}\sin 4\theta\right]r_0\right\} + \frac{1}{2}\frac{\partial^2}{\partial \theta^2}[r_0\cos^2 2\theta] = 0, \quad (61)$$

which takes the form of a steady-state Fokker-Planck equation with drift and diffusion defined, respectively, by

$$\Phi(\theta) = -\left[C\sin 2\theta + \frac{1}{2}\sin 4\theta\right] \text{ and } \Psi^2(\theta) = \cos^2 2\theta. \quad (62)$$

The process evolves on the half circle $\theta \in [0, \pi]$ with singularities at $\theta = \pi/4$ and $3\pi/4$. As $C \neq 0$, the drift at the singular points is not zero and thus the singular points can be classified as left and right shunts depending on the sign of the drift term. The boundary point classification is performed using the Feller classification scheme (1954). It is shown in Appendix B that the boundary points $\theta = 0, \pi$ are both perfectly reflecting regular points. Therefore, the θ process is ergodic and the Lyapunov exponent can be found using Eq. (24) to be

$$\Lambda = \frac{\lambda+\mu}{2} + \frac{\mu-\lambda}{2}E[\cos 2\theta] + k(E[R^2] + E[Z^2]). \quad (63)$$

Now consider the case $C > 0$, (similar results can be derived for $C < 0$). The singular points are given as left and right shunts for $\theta = \pi/4$ and $3\pi/4$, respectively. That a nontrivial normalizable solution for r_0 exists on the intervals, $(0, \pi/4)$ and $(3\pi/4, \pi)$ is shown in Appendix B. r_0 is given by:

$C > 0.$

$$r_0(\theta) = \begin{cases} \dfrac{N}{\exp(C/\cos 2\theta)\cos 2\theta} & 0 \le \theta \le \pi/4 \text{ or } 3\pi/4 \le \theta \le \pi \\ 0 & \text{else} \end{cases} \quad (64)$$

where N is a normalization constant. The Lyapunov exponent, Eq. (63), is plotted against ν (where $\lambda = \nu$ and $\mu = \nu + 1$) in Fig. 7 for $k = -1$. The deterministic system undergoes primary bifurcations at $\nu = 0$ and -1. A secondary bifurcation occurs at $\nu = 0.5$. It can be seen that these features are robust (i.e., the Lyapunov exponent remains negative) and a decrease in robustness coincides with the occurrence of the first primary

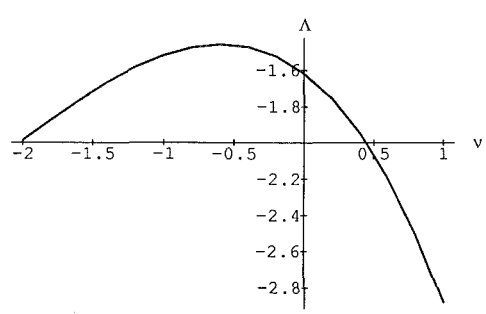


Fig. 7 Lyapunov exponent (Hopf-pitchfork bifurcation)

Downloaded 03 May 2010 to 171.66.16.247. Redistribution subject to ASME license or copyright; see http://www.asme.org/terms/Terms_Use.cfm

bifurcation. Once again, the Lyapunov exponent does not reflect the qualitative changes in the pdf but does indicate when nonlinear effects become significant.

Conclusion

The major conclusions of this investigation are as follows:

1 While the Lyapunov exponent provides a robustness measure for the combined effects of nonlinearities and noise, it is not a suitable bifurcation parameter for nonlinear stochastic systems in the sense that it does not reflect the qualitative changes in the steady-state probability density function. This occurs whenever $X = 0$ *is not a solution* of the nonlinear stochastic system. Examples of nonlinear systems under external (additive) random excitation and systems under parametric random excitation (multiplicative noise) with a nonzero reference input were shown to possess negative Lyapunov exponents.

2 The results of this investigation suggest that the extremum of the Lyapunov exponent (with respect to the bifurcation parameter for the deterministic system) provides an indication of when nonlinear effects become important. For the one and two-dimensional systems perturbed by external random excitation, it was observed that this extremum follows the occurrence of the first bifurcation in the corresponding deterministic system. It is left as a conjecture that this is a general characteristic of nonlinear systems perturbed by external random excitation.

Acknowledgment

This research was partially supported by the NSF through Grant 90-57437 PYI which is monitored by Dr. Devendra Garg and AFOSR through Grant 91-0041 which is monitored by Dr. Spencer Wu.

References

Andronov, A. A., Vitt, A. A., and Khaikin, S. E., 1966, *Theory of Oscillators*, Pergamon Press, London.

Arnold, L., 1988, "Lyapunov Exponent of Nonlinear Stochastic Systems," *Nonlinear Stochastic Dynamic Engineering Systems*, F. Ziegler, and G. I. Schueller, eds., Springer-Verlag, New York.

Arnold, L., Papanicolaou, G., and Wihstutz, V., 1986, "Asymptotic Analysis of the Lyapunov Exponent and Rotation Number of the Random Oscillator and Applications," *SIAM Journal of Applied Mathematics*, Vol. 46, No. 3, pp. 427-450.

Arnold, V., 1983, *Geometrical Methods in the Theory of Ordinary Differential Equations*, Springer-Verlag, New York.

Ariaratnam, S. T., and Xie, W. C., 1988a, "Stochastic Stability of Oscillatory Systems," ASME JOURNAL OF APPLIED MECHANICS, Vol. 55, pp. 458-488.

Ariaratnam, S. T., and Xie, W. C., 1988b, "Dynamic Snap-Buckling of Structures under Stochastic Loads," *Stochastic Structural Dynamics: Progress in Theory and Applications*, S. T. Ariaratnam, G. I. Schueller, and I. Elishakoff, eds., Elsevier, New York.

Barnish, B. R., 1988, "New Tools for Robustness Analysis," *IEEE Proceedings of the 27th Conference on Decision and Control*, pp. 1-6.

Blankenship, G., and Papanicolaou, G. C., 1978, "Stability and Control of Stochastic Systems with Wide-Band Noise Disturbances: I," *SIAM Journal of Applied Mathematics*, Vol. 34, No. 3, pp. 437-476.

Bylov, B. F., Vinograd, R. E., Grobman, D. M., and Nemytski, V. V., 1966, *Theory of Lyapunov Exponents*, NAUKA, Moscow.

Caughey, T. K., and Gray, A. H., Jr., 1965, "On the Almost-Sure Stability of Linear Dynamics Systems with Stochastic Coefficients," ASME JOURNAL OF APPLIED MECHANICS, Vol. 32, pp. 365-372.

Dorato, P., 1987, "A Historical Review of Robust Control," *IEEE Control Systems Magazine*, Apr., pp. 44-47.

Feller, W., 1954, "Diffusion Process in One Dimension," *Trans. of Amer. Math Society*, Vol. 97, pp. 1-31.

Horsthemke, W., and Lefever, R., 1984, *Noise-Induced Transitions*, Springer-Verlag, New York.

Infante, E. F., 1968, "On the Stability of Some Linear Nonautonomous Random Systems," ASME JOURNAL OF APPLIED MECHANICS, Vol. 35, pp. 7-12.

Kozin, F., and Wu, C. M., 1973, "On the Stability of Linear Stochastic Differential Equations," ASME JOURNAL OF APPLIED MECHANICS, Vol. 40, pp. 87-92.

Lin, Y. K., 1986, *Probabilistic Theory of Structural Dynamics*, R. Krieger, FL.

Nishioka, K., 1976, "On the Stability of Two-Dimensional Linear Stochastic Systems," *Kodai Mathematics Seminar Report*, Vol. 27, pp. 211-230.

Willems, J. C., and Blankenship, G. C., 1971, "Frequency Domain Stability Criteria for Stochastic Systems," *IEEE Transactions on Automatic Control*, Vol. 16, pp. 292-299.

Willems, J. L., and Willems, J. C., 1983, "Robust Stabilization of Uncertain Systems," *SIAM Journal of Control and Optimization*, Vol. 21, pp. 352-374.

Wonham, W. H., 1967, "Optimal Stationary Control of a Linear System with State Dependent Noise," *SIAM Journal of Control*, Vol. 5, pp. 486-500.

Yaz, E., 1988, "Deterministic and Stochastic Robustness Measures for Discrete Systems," *IEEE Transactions on Automatic Control*, Vol. 33, pp. 952-955.

Yaz, E., and Yildizbayrak, N., 1985, "Robustness of Feedback-Stabilized Systems in the Prèsence of Non-linear and Random Perturbations," *International Journal of Control*, Vol. 41, pp. 345-353.

APPENDIX A

The scaling employed is adapted from Horsthemke and Lefever (1984) and may be justified as follows:

1 The X and Y processes are assumed from the start to be stationary (ergodic) processes. This stationary state is achieved only in the limit $t \to \infty$. Hence, in the Itô representation of the X and Y processes, time is scaled as $t \leftarrow t/\epsilon^2$ so that the stationary state is reached in the limit $\epsilon \to 0$.

2 Now consider the effect of such a scaled process $Z(t) = X(t/\epsilon^2)$ in the θ equation. For example,

$$d\theta = f(\theta)dt + Z(t)g(\theta)dt. \tag{65}$$

The spectrum of $Z(t) = X(t/\epsilon^2)$ is given by

$$S_Z(\omega) = \frac{1}{2\pi}\int_{-\infty}^{\infty} E[Z(t)Z(t+\tau)]\exp(-j\omega\tau)d\tau$$

$$= \frac{1}{2\pi}\int_{-\infty}^{\infty} E[X(t/\epsilon^2)X(t/\epsilon^2+\tau/\epsilon^2)]\exp(-j\omega\tau)d\tau$$

$$= \frac{\epsilon^2}{2\pi}\int_{-\infty}^{\infty} E[X(t/\epsilon^2)X(t/\epsilon^2+s)] \times \exp(-j\epsilon^2\omega s)ds \,(\text{let } s=\tau/\epsilon^2)$$

$$= \epsilon^2 S_X(\epsilon^2\omega) \tag{66}$$

which tends to zero as $\epsilon \to 0$. This implies that by simply scaling time alone, one will obtain a noiseless limit. Hence, the amplitude of the process $X(t/\epsilon^2)$ should be multiplied by a factor of $1/\epsilon$ to ensure that noise effects are not excluded in the limit.

APPENDIX B

The ergodic assumption is shown to be valid by considering the properties of the sample paths of the θ process on the unit half circle. The drift and diffusion are, respectively,

$$\Phi(\theta) = -\left[C\sin 2\theta + \frac{1}{2}\sin 4\theta\right] \text{ and } \Psi^2(\theta) = \cos^2 2\theta. \tag{67}$$

Take $C > 0$, and by symmetry it is only necessary to study the process on $(0, \pi/4)$. The diffusion is singular at $\theta = \pi/4$ with $\Phi(\pi/4) = -C < 0$, yielding $\theta = \pi/4$ as a left shunt.

In order to complete the proof of ergodicity, the behavior at $\theta = 0$ must be known. To this end, we introduce scale and speed measures defined, respectively, as

$$S(\theta) = \int^{\theta} s(x)dx, \quad M(\theta) = \int^{\theta} m(x)dx \tag{68}$$

where

$$s(x) = \text{Exp}[-B(x)], \quad m(x) = \frac{1}{\psi^2(x)s(x)}$$

$$B(x) = \int^{x} \frac{2\Phi(\eta)}{\psi^2(\eta)}d\eta \tag{69}$$

Downloaded 03 May 2010 to 171.66.16.247. Redistribution subject to ASME license or copyright; see http://www.asme.org/terms/Terms_Use.cfm

$s(x)$ and $m(x)$ are called the scale and speed densities. The scale and speed measures are found to be

$$S(\theta)=\int^{\theta}\frac{\mathrm{Exp}\left[\dfrac{C}{\cos 2\eta}\right]}{|\cos 2\eta|}\,d\eta,\quad M(\theta)=\int^{\theta}\frac{\mathrm{Exp}\left[-\dfrac{C}{\cos 2\eta}\right]}{|\cos 2\eta|}\,d\eta. \tag{70}$$

Again, only consider $C > 0$ and $\theta \in [0, \pi/4)$. Both functions are bounded and continuous on $\theta \in [0, \pi/4)$ and as such the integrals on this region are also bounded. Thus, $\theta = 0$ is a regular point.

The property of pure reflection can be determined from a physical argument. It is clear that unless the coupling coefficients are both zero, it is not possible to have a solution with $z(t) = 0$. Since $\theta = 0$ implies $z = 0$, there can be no accumulation of probability mass at the point.

As $\theta = 0$ is purely reflecting and $\theta = \pi/4$ is a left shunt, the region $(0, \pi/4)$ has the property of recurrence or ergodicity and a unique, normalizable stationary density exists on this interval. Similar conclusions may be made for the interval $(3\pi/4, \pi)$. Should θ start outside the intervals $(0, \pi/4)$ and $(3\pi/4, \pi)$, it can be shown (Nishoka, 1976) that the θ process moves into either one of the two intervals in finite time with probability one. The temporal average can then be replaced by the ensemble average computed with respect to

$$p(\theta)=Nm(\theta)=\frac{N}{\cos 2\theta\,\mathrm{Exp}[C/\cos 2\theta]} \tag{71}$$

where N is a normalization constant. Similar results can be obtained for $C < 0$.

Downloaded 03 May 2010 to 171.66.16.247. Redistribution subject to ASME license or copyright; see http://www.asme.org/terms/Terms_Use.cfm

P. McIver
Department of Mathematical Sciences,
Loughborough University of Technology,
Loughborough, Leicestershire LE11 3TU
England

A. D. Rawlins
Department of Mathematics and Statistics,
Brunel University,
Uxbridge, Middlesex UB8 3PH
England

Scattering of Water Waves by a Pair of Semi-infinite Barriers

A previously published solution by the method of matched asymptotic expansions for scattering of long water waves by a pair of semi-infinite barriers is known to be incorrect. Here the reasons for this are examined and a revised procedure given that recovers the long-wave expansion of the known exact solution.

Introduction

The method of matched asymptotic expansions has found wide application in water-wave scattering problems. In particular, Tuck (1975) has proposed a simple procedure applicable to cases involving flow through small holes. Tuck's method has been applied widely and found to produce results that are often surprisingly accurate when compared with exact solutions. A similar procedure has been applied by a number of authors to scattering problems involving parallel-walled ducts. In particular, an asymptotic theory for the scattering of an incident plane water wave, of wave number k, by a parallel pair of semi-infinite, thin, vertical barriers has been given by Liu (1975). Following Tuck's ideas, his solution is based on a simple application of the method of matched asymptotic expansions and assumes that the wavelength $2\pi/k$ is much greater than the gap, of width $2a$, between the barriers, that is he assumes $ka \ll 1$. In particular, Liu calculates the normalized amplitude $|T|$ of the wave transmitted to infinity in the gap between the barriers. However, in a subsequent paper, Rawlins (1981) pointed out that the exact solution to this problem is known (Noble, 1958, p.100) and that the long-wave expansion of $|T|$ from this solution does not agree with Liu's result. At the time, the reasons for this discrepancy were not clear. It is important to detect the error in order that the matched asymptotic expansions technique can be used with confidence in more complicated problems for which no accurate solution can be obtained.

The present authors have recently re-examined this problem and it is now apparent that the procedure used by Liu contains an inconsistency. Very briefly, Liu's method was as follows. Bearing in mind the assumption that $ka \ll 1$, he argued that in an external outer region many gap widths from their ends the barriers appeared as a single thin wall. The corresponding outer solution would therefore be the well-known Sommerfeld solution for wave scattering by a thin vertical wall together with a Helmholtz source placed at the tip to model the flow through the opening between the barriers. The unknown source strength Q was found by matching with an inner solution valid near the opening and, in turn, matching that with an internal outer, or duct, solution between the barriers. The error in Liu's solution arose from the implicit assumption that the source strength was of the same order in ka as the incident wave. In fact, from his equation (25), it may be seen that Q is of $O(ka)$ relative to the incident wave. A consequence of this is that the inner expansion of the outer solution, his Eq. (10), is not correct. For example, in obtaining Eq. (10), Liu assumes that terms of $O(kr)$, where r is radial distance from the wall tip, are negligible in the inner expansion of the incident wave. With the term containing Q $(=O(ka))$ retained, this is equivalent to assuming that $r \ll a$ violating the fundamental assumption behind the construction of the outer solution, namely that $r \gg a$. A correctly formulated inner expansion will obey $kr \ll 1$ and $r \gg a$, that is the expansion applies in an overlap region between the inner region (defined by $kr \ll 1$) and the outer region (defined by $r \gg a$).

Independent confirmation of the arguments concerning the source strength in the outer solution may be found in the work of Smallman (1986) who considered scattering by a pair of nonparallel barriers. For this problem the leading order outer solution contains a source whose strength is of the same order of magnitude as the incident wave and dependent on the relative inclination of the barriers. If the barriers are allowed to become parallel, the source strength tends to zero indicating that, in these circumstances, that part of the outer solution representing the flow through the opening first appears at some higher order in ka.

In the present work, a modified matching procedure is suggested for the parallel-barriers case, and the solution obtained is found to agree with expansion of the exact solution.

Formulation

The basic formulation and notation are as used by Liu. A plane wave of amplitude A, wave number k and frequency ω is incident at an angle α to a pair of parallel, semi-infinite, thin vertical barriers. The barriers are a distance $2a$ apart and stand in water of uniform depth h. Cartesian axes are chosen with origin in the mean free surface, the z-axis directed ver-

Contributed by the Applied Mechanics Division of THE AMERICAN SOCIETY OF MECHANICAL ENGINEERS for publication in the JOURNAL OF APPLIED MECHANICS.

Discussion on this paper should be addressed to the Technical Editor, Professor Leon M. Keer, The Technological Institute, Northwestern University, Evanston, IL 60208, and will be accepted until four months after final publication of the paper itself in the JOURNAL OF APPLIED MECHANICS.

Manuscript received by the ASME Applied Mechanics Division, June 25, 1991; final revision, Dec. 11, 1991. Associate Technical Editor: T. K. Akylas.

Copyright © 1992 by ASME
Downloaded 03 May 2010 to 171.66.16.247. Redistribution subject to ASME license or copyright; see http://www.asme.org/terms/Terms_Use.cfm

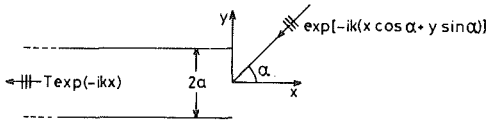


Fig. 1 Plan view of barrier configuration

tically upwards and the x-axis directed parallel to the barriers. A plan view of the geometry is given in Fig. 1.

Under the usual assumptions of the linearized theory of water waves, the flow may be described by a velocity potential

$$\Phi(x,y,z,t)=\Re\left\{-\frac{igA\cosh k(z+h)}{\omega\cosh kh}\phi(x,y)e^{-i\omega t}\right\}. \quad (1)$$

This form of the potential satisfies the boundary conditions on the free surface ($z=0$) and the bed ($z=-h$). The complex-valued function $\phi(x,y)$ satisfies the Helmholtz equation

$$\frac{\partial^2\phi}{\partial x^2}+\frac{\partial^2\phi}{\partial y^2}+k^2\phi=0 \quad (2)$$

in the fluid region, no flow through the solid barriers

$$\frac{\partial\phi}{\partial y}=0 \text{ on } y=\pm a,\ x<0 \quad (3)$$

and appropriate radiation conditions between the barriers and in the open water. The incident wave is described by

$$\phi_I=\exp(-ik(x\cos\alpha+y\sin\alpha)). \quad (4)$$

With the restriction $ka<\pi/2$, only the fundamental mode will be able to propagate between the barriers and for that region the radiation condition is

$$\phi\sim Te^{-ikx} \text{ as } x\to-\infty, \quad (5)$$

where T is the complex transmission coefficient. It may be observed that for head-on incidence, $\alpha=0$, the waves are unaffected by the barriers and so $T=1$ for all frequencies. Liu's solution does not recover this result.

The principal aim is to find T and this is determined entirely by that part of the solution that is symmetric in y. Write

$$\phi=\phi_S+\phi_A \quad (6)$$

where ϕ_S is the symmetric part of the solution defined for $y\geq 0$ by

$$\phi_S(x,y)=\frac{1}{2}(\phi(x,y)+\phi(x,-y)), \quad (7)$$

and ϕ_A is the antisymmetric part of the solution. Solving only for the symmetric part of the potential removes the need to use the Sommerfeld solution for scattering by a thin wall, as the scattered part of that solution contributes only to the antisymmetric part of the potential. Dropping the subscript S, the symmetric potential satisfies the Helmholtz Eq. (2), the barrier condition (3) for $y=a$, the symmetry condition.

$$\frac{\partial\phi}{\partial y}=0 \quad \text{on} \quad y=0,\ x<0, \quad (8)$$

the radiation condition (5), and the open water radiation condition. The symmetric part of the incident wave is

$$\phi_I=\exp(-ikx\cos\alpha)\cos(ky\sin\alpha). \quad (9)$$

A solution is sought under the assumption that the wavelength is much larger than the barrier spacing, that is $ka\ll 1$. The fluid domain is divided into three regions as illustrated in Fig. 2. The outer region is the domain external to the barriers for $r=(x^2+y^2)^{1/2}\gg a$, the inner region is the area around the opening for which $r\ll k^{-1}$ and the duct region lies between the barriers for $|x|\gg a$.

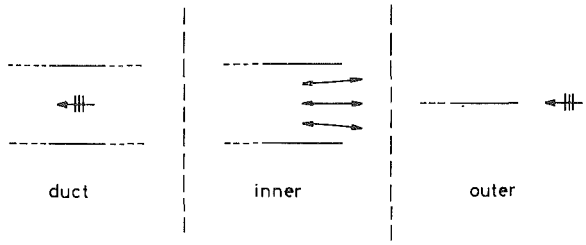


Fig. 2 The three flow regions

Outer and Duct Solutions

In the outer region the boundary condition (3) on the barriers may be transferred onto $y=0$ by Taylor expansion to give

$$\frac{1}{k}\frac{\partial\phi}{\partial y}+ka\frac{1}{k^2}\frac{\partial^2\phi}{\partial y^2}+O((ka)^2)=0 \quad \text{on} \quad y=0,\ x<0. \quad (10)$$

In Eq. (10), extra factors of k^{-1} have been introduced into the derivatives to highlight the ordering of the terms. From Liu's solution it is known that the effects of the flow through the opening appear at $O(ka)$, and so an analysis including $O(1)$ terms is not sufficient. With this in mind write

$$\phi=\phi_0+ka\phi_1+\ldots \quad . \quad (11)$$

Substitute into (10) and equate like powers of ka to get the barrier boundary conditions

$$\frac{\partial\phi_0}{\partial y}=0,\ \frac{\partial\phi_1}{\partial y}=-\frac{1}{k}\frac{\partial^2\phi_0}{\partial y^2} \quad \text{on} \quad y=0,\ x<0. \quad (12)$$

The outer solution is written as

$$\phi=\phi_I+ka(QH_0^{(1)}(kr)+\phi_P)+o(ka), \quad (13)$$

where $H_0^{(1)}$ is the Hankel function of the first kind and order zero. In Eq. (13), the first term on the right-hand side $\phi_I(\equiv\phi_0)$ is the symmetric part of the incident wave, given by (9) and the second is a Helmholtz source of strength kaQ placed at the origin. A factor of ka has been displayed explicitly so that now $Q=O(1)$. The final term, ϕ_P, is a particular solution of the Helmholtz equation satisfying the second part of (12), that is

$$\frac{\partial\phi_1}{\partial y}=-\frac{1}{k}\frac{\partial^2\phi_I}{\partial y^2}=k\sin^2\alpha\exp(-ikx\cos\alpha). \quad (14)$$

There is no term corresponding to this particular solution in Liu's work. An appropriate particular solution is given by Crighton and Leppington (1973, Eq. (3.8)) and, correcting an error of omission, it has an expansion

$$\phi_P=\frac{\alpha\sin\alpha}{\pi i}+O(kr\ln kr). \quad (15)$$

The consistent inner expansion of (13) is

$$\phi=1-ikx\cos\alpha+O((kr)^2)+ka\left\{Q\left(1+\frac{2i}{\pi}(\ln\frac{1}{2}kr+\gamma)\right)+\frac{\alpha\sin\alpha}{\pi i}+O(kr\ln kr)\right\}. \quad (16)$$

There are two points of difference to notice when comparing with Liu's inner expansion of the outer solution; an extra term has been retained in the expansion of the incident wave, and there is an additional constant from the particular solution.

From the radiation condition (5) the duct solution is simply

$$\phi=Te^{-ikx} \quad (17)$$

which has an inner expansion

$$\phi\sim T(1-ikx+O((kr)^2). \quad (18)$$

Downloaded 03 May 2010 to 171.66.16.247. Redistribution subject to ASME license or copyright; see http://www.asme.org/terms/Terms_Use.cfm

Inner Solution

In the inner region the characteristic length scale is a and to a first approximation wave effects are not discernible because of the assumption $ka \ll 1$. Thus, the leading order term in the inner solution is governed by Laplace's equation

$$\frac{\partial^2\phi}{\partial x^2}+\frac{\partial^2\phi}{\partial y^2}=0 \tag{19}$$

and also must have zero normal derivative on the barriers. The inner solution may therefore be found with the aid of the conformal mapping

$$z=x+jy=\frac{a}{\pi}(1-\pi j-\zeta^2+2\ln\zeta) \tag{20}$$

which maps the inner region to the upper half of the complex ζ plane. Here, j is used as the imaginary unit to distinguish it from the i first appearing in Eq. (1). The tips of the barriers map to $\zeta=\pm 1$, as $x\to-\infty$ between the barriers $\zeta\to 0$ and as $r\to\infty$ in the outer region $|\zeta|\to\infty$. Further,

$$\zeta\sim\exp\left\{\frac{1}{2}\left(\frac{\pi z}{a}+\pi j-1\right)\right\} \text{ as } \zeta\to 0 \tag{21}$$

and

$$\zeta\sim j\left(\frac{\pi z}{a}\right)^{1/2} \text{ as } |\zeta|\to\infty. \tag{22}$$

The inner solution is written as

$$\phi=A+B\Re_j\ln\zeta-ikx\cos\alpha. \tag{23}$$

The first two terms correspond with the form taken by Liu but the third term (a solution of (19) satisfying the barrier boundary condition) is new and is needed to match with the inner expansion of the outer solution (16). Using the result (22), the outer expansion of this is

$$\phi\sim A+B\frac{1}{2}\ln\frac{\pi r}{a}-ikx\cos\alpha, \tag{24}$$

and from (21), the duct expansion is

$$\phi\sim A+B\frac{1}{2}\left(\frac{\pi x}{a}-1\right)-ikx\cos\alpha. \tag{25}$$

Matching

Matching term by term the inner expansion of the outer solution (16) with the outer expansion of the inner solution (24) gives

$$1+ka\left\{Q\left(1+\frac{2i}{\pi}\left(\ln\frac{1}{2}k+\gamma\right)\right)+\frac{\alpha\sin\alpha}{\pi i}\right\}=A+B\frac{1}{2}\ln\frac{\pi}{a} \tag{26}$$

and

$$kaQ\frac{2i}{\pi}=\frac{1}{2}B, \tag{27}$$

while matching the inner expansion of the duct solution (18) with the duct expansion of the inner solution (25) gives

$$T=A-\frac{1}{2}B \tag{28}$$

and

$$-ikT=B\frac{\pi}{2a}-ik\cos\alpha. \tag{29}$$

Equations (26)-(29) are four simultaneous equations for the unknowns Q, T, A, and B. Solving for T and expanding as a series in ka gives

$$T=1-ka\ln ka\frac{2i}{\pi}\sin^2\frac{\alpha}{2}+ka\left\{\sin^2\frac{\alpha}{2}\left(\frac{2i}{\pi}(1-\gamma+\ln 2\pi)-1\right)-\frac{i}{\pi}\alpha\sin\alpha\right\}+o(ka) \tag{30}$$

in agreement with the expansion of the exact solution. As a simple check, for $\alpha = 0$, the transmission coefficient is unity as expected. From (30),

$$|T|=1-ka\sin^2\frac{\alpha}{2}+O((ka)^2), \tag{31}$$

which is the result given by Rawlins (1981).

Discussion

In the solution by matched asymptotic expansions of the problem considered here, the source strength modeling the flow through the barrier opening is $O(ka)$ relative to the incident wave. This can be traced back to the matching of uniform flow terms in the duct between the barriers (see Eqs. (18) and (25)) that "feeds" the small parameter ka into the constants in the solution. In problems involving flow through small holes (Tuck, 1975), the flow is source-like (i.e., logarithmic) on both sides of the aperture and the matching can only result in the small parameter appearing within the arguments of logarithms.

Liu implicitly assumed that the source strength was of the same order as the incident wave and this led to inconsistencies in his solution. These inconsistencies are removed by the revised procedure proposed here. An extended form for the outer solution is needed, including a solution to a nonhomogeneous problem (ϕ_P in Eq. (13)), and in the inner expansion of the incident wave a further term is retained (Eq. (16)). This extra term in the expansion of the incident wave in turn requires an extra term in the inner solution (Eq. (23)) for matching to be successful.

Other duct problems have been treated by the method adopted by Liu. Mei (1983, p. 199) found a solution for scattering by a perpendicular indentation in a plane wall and again the source strength is $O(ka)$. However, the leading order term in the symmetric outer solution is the incident wave together with its reflection from a plane wall at $x = 0$, that is the symmetric part of the incident wave is

$$\phi_I=\cos(kx\cos\alpha)\cos(ky\sin\alpha)=1+O(kr)^2), \tag{32}$$

and for this problem, there is no term at $O(kr)$ in the inner expansion of ϕ_I. Further, it turns out that there is no particular solution corresponding to ϕ_P so that, in fact, no modification to the procedure used by Liu is needed.

Newman (1974) used the simple matching procedure to calculate the reflection and transmission properties of two closely spaced vertical plates extending a finite distance down from the free surface. However, Newman was interested in the solution near resonance and then the source modeling the flow from the duct correctly appears at the same order as the incident wave and the simple procedure is valid. Finding a solution away from resonance would require a more careful analysis.

References

Crighton, D. C., and Leppington, F. G., 1973, "Singular Perturbation Methods in Acoustics: Diffraction by a Plate of Finite Thickness," *Proc. Roy. Soc. Lond.*, Vol. A335, pp. 313-339.

Liu, P. L.-F., 1975, "Scattering of Water Waves by a Pair of Semi-Infinite Barriers," ASME JOURNAL OF APPLIED MECHANICS, Vol. 42, pp. 777-779.

Mei, C. C., 1983, *The Applied Dynamics of Ocean Surface Waves*, John Wiley and Sons, New York.

Newman, J. N., 1974, "Interaction of Water Waves With Two Closely-Spaced Vertical Obstacles," *J. Fluid Mech.*, Vol. 66, pp. 97-106.

Noble, B., 1958, *The Wiener-Hopf Technique*, Pergamon, London.

Rawlins, A. D., 1981, "Note on a Paper by Liu on the Scattering of Water Waves by a Pair of Semi-infinite Barriers," ASME JOURNAL OF APPLIED MECHANICS, Vol. 48, p. 656.

Tuck, E. O., 1975, "Matching Problems Involving Flow Through Small Holes," *Adv. Appl. Mech.*, Vol. 15, pp. 90-158.

Downloaded 03 May 2010 to 171.66.16.247. Redistribution subject to ASME license or copyright; see http://www.asme.org/terms/Terms_Use.cfm

Journal of Applied Mechanics

Brief Notes

A Brief Note is a short paper that presents a specific solution of technical interest in mechanics but which does not necessarily contain new general methods or results. A Brief Note should not exceed 1500 words *or equivalent* (a typical one-column figure or table is equivalent to 250 words; a one line equation to 30 words). Brief Notes will be subject to the usual review procedures prior to publication. After approval such Notes will be published as soon as possible. The Notes should be submitted to the Technical Editor of the JOURNAL OF APPLIED MECHANICS. Discussions on the Brief Notes should be addressed to the Editorial Department, ASME, United Engineering Center, 345 East 47th Street, New York, N. Y. 10017, or to the Technical Editor of the JOURNAL OF APPLIED MECHANICS. Discussions on Brief Notes appearing in this issue will be accepted until two months after publication. Readers who need more time to prepare a Discussion should request an extension of the deadline from the Editorial Department.

Alternative Formulation of Elastic Fields due to Inhomogeneous Isotropic Spherical Inclusions Undergoing Shape-Conserving Volume Change

S. Schmauder[1] and W. Mader[1]

In this Note alternative formulae are derived for the elastic fields due to homogeneous initial strains in an isotropic spherical inclusion embedded in an isotropic infinite medium, assuming a shape conserving volume change of the inclusion. The bulk modulus of the inclusion and the shear modulus of the matrix are the only physically relevant elastic constants necessary to describe analytically displacements, strains, and stresses in the inclusion and the matrix.

Introduction

The initial strains ϵ_{ij}^* of a shape-conserving volume change of a sphere may be given by

$$\epsilon_{ij}^* = \frac{r_1 - r_0}{r_0} \ (i = 1, 2, 3), \ \epsilon_{ij}^* = 0 \ (i \neq j), \tag{1}$$

where r_0 is the initial radius and r_1 the radius of the transformed stress-free spherical inclusion. For symmetry reasons it is more convenient to use spherical coordinates, r, φ, ψ. The initial strain components can then be written:

$$\epsilon_{rr}^* = \epsilon_{\varphi\varphi}^* = \epsilon_{\psi\psi}^* = \frac{r_1 - r_0}{r_0}, \ \epsilon_{r\varphi}^* = \epsilon_{\varphi\psi}^* = \epsilon_{r\psi}^* = 0. \tag{2}$$

The solutions of the homogeneous inclusion problem (matrix and inclusion possess the same elastic constants) were given explicitly by Eshelby (1961):

$$u_r^c = \frac{1}{3} \cdot \frac{1+\nu}{1-\nu} \epsilon_{rr}^* \cdot r, \ u_\varphi^c = u_\psi^c = 0, \ r < r_0 \tag{3a}$$

$$u_r^c = \frac{1}{3} \cdot \frac{1+\nu}{1-\nu} \epsilon_{rr}^* \cdot \frac{r_0^3}{r^2}, \ u_\varphi^c = u_\psi^c = 0 \ r > r_0. \tag{3b}$$

Here and in the following, the subscript c denotes the so-called complete displacements, u^c, and complete strains, ϵ^c. It should be noted that the only elastic constant entering the expressions above is Poisson's ratio, ν.

The derivatives of the displacements lead to the strains

$$\epsilon_{rr}^c = \epsilon_{\varphi\varphi}^c = \epsilon_{\psi\psi}^c = \frac{1}{3} \cdot \frac{1+\nu}{1-\nu} \epsilon_{rr}^*, \ \epsilon_{r\varphi}^c = \epsilon_{\varphi\psi}^c = \epsilon_{r\psi}^c = 0, \ r < r_0 \tag{3c}$$

$$\left.\begin{aligned} \epsilon_{rr}^c &= -\frac{2}{3} \cdot \frac{1+\nu}{1-\nu} \epsilon_{rr}^* \cdot \frac{r_0^3}{r^3} \\ \epsilon_{\varphi\varphi}^c = \epsilon_{\psi\psi}^c &= \frac{1}{3} \cdot \frac{1+\nu}{1-\nu} \epsilon_{rr}^* \cdot \frac{r_0^3}{r^3}, \ \epsilon_{r\varphi}^c = \epsilon_{\varphi\psi}^c = \epsilon_{r\psi}^c = 0. \end{aligned}\right\} r > r_0. \tag{3d}$$

The *elastic* strains in the inclusion (subscript I) and in the matrix (subscript M) are given by Eshelby (1961)

$$\epsilon_{ij}^I = \epsilon_{ij}^c - \epsilon_{ij}^* \ (i,j = r, \varphi, \psi) \ r < r_0 \tag{4}$$

$$\epsilon_{ij}^M = \epsilon_{ij}^c \ (i,j = r, \varphi, \psi) \ r > r_0. \tag{5}$$

For elastically isotropic materials, the elastic strains ϵ_{ij} are related to stresses σ_{ij} according to Hooke's law,

$$\sigma_{ij} = (K - \frac{2}{3} G) \ \epsilon_{kk} \delta_{ij} + 2G \ \epsilon_{ij} \ (i,j = 1, 2, 3), \tag{6}$$

where δ_{ij} is the Kronecker delta.

The term $\frac{1}{3} \cdot \frac{1+\nu}{1-\nu}$ in Eqs. (3) may be replaced by $\frac{3K}{3K+4G}$ where K is the bulk modulus and G the shear modulus (cf. Eqs. (18)).

Elastic strains and stresses inside the inclusion are thus homogeneous and can be expressed in their simplest form as

$$\epsilon_{rr}^I = \epsilon_{\varphi\varphi}^I = \epsilon_{\psi\psi}^I = -\frac{2}{3} \cdot \frac{1-2\nu}{1-\nu} \epsilon_{rr}^*, \ \epsilon_{r\varphi}^I = \epsilon_{\varphi\psi}^I = \epsilon_{r\psi}^I = 0, \ r < r_0, \tag{7}$$

$$\sigma_{rr}^I = \sigma_{\varphi\varphi}^I = \sigma_{\psi\psi}^I = \frac{-12 \, GK}{3K+4G} \epsilon_{rr}^*, \ \sigma_{r\varphi}^I = \sigma_{\varphi\psi}^I = \sigma_{r\psi}^I = 0, \ r < r_0. \tag{8}$$

The inclusion suffers from a shape-conserving volume change and is under a hydrostatic pressure p

[1]Max-Planck-Institut für Metallforschung, Institut für Werkstoffwissenschaft, D-7000 Stuttgart 1, Germany.

Manuscript received by the ASME Applied Mechanics Division, Nov. 4, 1988; final revision, Sept. 11, 1990. Associate Technical Editor: R. M. McMeeking.

Copyright © 1992 by ASME
Downloaded 03 May 2010 to 171.66.16.247. Redistribution subject to ASME license or copyright; see http://www.asme.org/terms/Terms_Use.cfm

$$p = -\frac{1}{3}\,\text{Trace}\,(\sigma^I) = -\sigma^I_{rr} \tag{9}$$

because the deviatoric components of the strains and stresses in the inclusion are zero:

$$\text{Dev}\,(\epsilon^I) = 0,\ \text{Dev}\,(\sigma^I) = 0. \tag{10a}$$

On the contrary, the volume elements in the matrix suffer from a volume conserving shape change since

$$\text{Trace}\,(\epsilon^M) = 0,\ \text{Trace}\,(\sigma^M) = 0. \tag{10b}$$

The displacements u_i^c $(i = r, \varphi, \psi)$ as well as the radial elastic stresses are continuous at the inclusion/matrix interface,

$$(\sigma^I_{rr} - \sigma^M_{rr})_{r=r_0} = 0, \tag{10c}$$

whereas the tangential stresses are discontinuous at the interface:

$$\Delta\sigma_{\varphi\varphi} = \Delta\sigma_{\psi\psi} = (\sigma^I_{\varphi\varphi} - \sigma^M_{\varphi\varphi})_{r=r_0} = -\frac{18GK}{3K+4G}\,\epsilon^*_{rr}. \tag{10d}$$

The Elastically Inhomogeneous Inclusion

Because of the spherical symmetry, the form of the above results must also be valid for an isotropic spherical inclusion with elastic constants *different* from those of the isotropic matrix:

$$u^c_r = e\,r,\ u^c_\varphi = u^c_\psi = 0,\ r < r_0 \tag{11a}$$

$$u^c_r = e\,\frac{r_0^3}{r^2},\ u^c_\varphi = u^c_\psi = 0,\ r > r_0 \tag{11b}$$

$$\epsilon^c_{ij} = e\delta_{ij}\ (i,j = r, \varphi, \psi)\ r < r_0 \tag{11c}$$

$$\epsilon^c_{rr} = -2e\,\frac{r_0^3}{r^3},\ \epsilon^c_{\varphi\varphi} = \epsilon^c_{\psi\psi} = e\,\frac{r_0^3}{r^3},\ \epsilon^c_{r\varphi} = \epsilon^c_{\varphi\psi} = \epsilon^c_{r\psi} = 0,\ r > r_0 \tag{11d}$$

$$\epsilon^I_{ij} = \epsilon^c_{ij} - \epsilon^*_{ij},\ (i,j = r, \varphi, \psi)\ r < r_0 \tag{12a}$$

$$\epsilon^M_{ij} = \epsilon^c_{ij},\ (i,j = r, \varphi, \psi)\ r > r_0 \tag{12b}$$

$$\text{Dev}\,(\epsilon^I) = 0,\ \text{Dev}\,(\sigma^I) = 0 \tag{13a}$$

$$\text{Trace}\,(\epsilon^M) = 0,\ \text{Trace}\,(\sigma^M) = 0 \tag{13b}$$

$$(\sigma^I_{rr} - \sigma^M_{rr})_{r=r_0} = 0. \tag{13c}$$

According to Eqs. (13*a*) and (6), a purely hydrostatic pressure p again exists inside the inclusion:

$$-p^I = \sigma^I_{rr} = 3K^I(e - \epsilon^*_{rr}) = K^I \cdot \text{Trace}\,(\epsilon^I). \tag{14}$$

The radial stress in the matrix is given by (cf. Eqs. (6) and (13*b*))

$$\sigma^M_{rr} = 2G^M\epsilon^M_{rr} = -4G^M e \cdot \frac{r_0^3}{r^3}. \tag{15}$$

The unknown strain e can now be obtained from Eqs. (13*c*), (14), and (15):

$$e = \frac{3\,K^I}{3\,K^I + 4G^M}\,\epsilon^*_{rr}. \tag{16a}$$

A slightly different expression using E^M and ν^M instead of G^M was found by Mott and Nabarro (1940).

In a more complex formula, Eshelby (1961) has defined this strain as

$$e = \frac{1}{3}\,\frac{1+\nu^M}{1-\nu^M} \cdot \left(\frac{-3\,K^I\,\epsilon^*_{rr}\,(1-\nu^M)}{(4\nu^M - 2)K^M - (1+\nu^M)K^I}\right), \tag{16b}$$

which can be easily converted to Eq. (16*a*) by making use of the identity

$$K^M = \frac{2G^M\,(1+\nu^M)}{3\,(1-2\nu^M)}.$$

Substituting Eq. (16*a*) into Eqs. (11) leads to the displacements, strains, and stresses in inclusion and matrix. For the special case of a shape-conserving volume change (Eq. (2)), the radial stresses in inclusion and matrix are thus given by Eqs. (14), (15), and (16*a*) as

$$\sigma^I_{rr} = -\frac{12G^M\,K^I}{3K^I + 4G^M}\,\epsilon^*_{rr},\ r < r_0 \tag{17a}$$

$$\sigma^M_{rr} = -\frac{12G^M\,K^I}{3K^I + 4G^M}\,\epsilon^*_{rr}\,\frac{r_0^3}{r^3},\ r > r_0 \tag{17b}$$

Equation (17*a*) is readily identified with Eq. (8) if inclusion and matrix are of the same material. On the other hand, the equivalences

$$G = \frac{E}{2(1+\nu)}, \tag{18a}$$

and

$$K = \frac{E}{3(1-2\nu)} \tag{18b}$$

can be used to reformulate Eq. (17*a*):

$$\sigma^I_{rr} = \frac{-1}{\dfrac{1-2\nu^I}{E^I} + \dfrac{1+\nu^M}{2E^M}}\,\epsilon^*_{rr}. \tag{19}$$

This expression given by Selsing (1961) is frequently used in literature. The different sign of Eq. (7) in this reference is due to a definition of ϵ^*_{ij}, which differs from ours in sign. The description of the elastic fields in terms of e (Eq. (16*a*)) is especially valuable because only the two elastic constants K^I and G^M are necessary: The bulk modulus K^I and the shear modulus G^M are the only physically relevant elastic constants for the shape-conserving volume change of the inclusion and the volume conserving shape change of the matrix, respectively.

The tangential stresses in inclusion and matrix can be obtained from Eqs. (11), (12), and (6) and depend only on K^I and G^M:

$$\sigma^I_{\varphi\varphi} = \sigma^I_{\psi\psi} = \frac{-12G^M\,K^I}{3K^I + 4G^M}\,\epsilon^*_{rr},\ \sigma^I_{r\varphi} = \sigma^I_{\varphi\psi} = \sigma^I_{r\psi} = 0,\ r < r_0, \tag{20a}$$

$$\sigma^M_{\varphi\varphi} = \sigma^M_{\psi\psi} = \frac{6G^M\,K^I}{3K^I + 4G^M}\,\epsilon^*_{rr},\ \frac{r_0^3}{r^3}\,\sigma^M_{r\varphi} = \sigma^M_{\varphi\psi} = \sigma^M_{r\psi} = 0,\ r > r_0. \tag{20b}$$

At the inclusion/matrix interface, these stresses show the same relation as for the homogeneous inclusion problem

$$\sigma^I_{\varphi\varphi} = -2\,\sigma^M_{\varphi\varphi},\ \sigma^I_{\psi\psi} = -2\,\sigma^M_{\psi\psi}, \tag{21}$$

and give rise to a stress jump at the interface of magnitude

$$\Delta\sigma_{\varphi\varphi} = (\sigma^I_{\varphi\varphi} - \sigma^M_{\varphi\varphi})_{r=r_0} = \frac{-18G^M\,K^I}{3K^I + 4G^M}\,\epsilon^*_{rr}, \tag{22}$$

which is identical with Eq. (10*d*) when the elastic constants of inclusion and matrix are the same.

References

Eshelby, J. D., 1961, "Elastic Inclusions and Inhomogeneities," *Progress in Solid Mechanics*, Vol. II, I. N. Sneddon and R. Hill, eds., North-Holland, Amsterdam, pp. 89–140.

Mott, N. F., and Nabarro, F. R. N., 1940, "An Attempt to Estimate the Degree of Precipitation Hardening with a Simple Model," *Proc. Roy. Soc.* Vol. 52, pp. 86–89.

Selsing, J., 1961, "Internal Stresses in Ceramics," *J. Am. Ceram. Soc.*, Vol. 44, p. 419.

Downloaded 03 May 2010 to 171.66.16.247. Redistribution subject to ASME license or copyright; see http://www.asme.org/terms/Terms_Use.cfm

Equations for the Nonlinear Planar Deformation of Beams

Avinoam Libai[2]

Introduction

The purpose of this Note is twofold: (a) present basic equations and approach to nonlinear beam theory in a form which is not readily available to researchers in the field, and (b) utilize the equations to obtain some more specific results for shear-deformable geometrically and materially nonlinear rods.

The material of the first part is based in part on a book and paper by Libai and Simmonds (1988, 1983), and on papers by Antman (1968, 1972, 1974) and Reissner (1972). The substantial increase in the number of papers on the various aspects of the nonlinear behavior of beams in recent years lends additional weight to the availability of formulations of the beam problem which could help to reduce cumbersome analysis or repetitions.

Specific topics discussed in the second part include:

- for extensible, shearable, and materially linear curved beams subjected to normal loading and end loads: a method of reducing the problem to elliptic integrals. A detailed analysis was made by Libai (1984) in a report which was not published in journal form. For end loads only, a short version was included in a book by Libai and Simmonds (1988) and an independent proof was given by Gotto et al. (1990).
- For long, straight cantilevered beams subjected to end pulling forces and couples: (a) a closed-form solution for the case of quadratic strain energy. An interesting point is that, even for these long beams, extensional and shearing deformations have the same effects and (b) an integral form solution of the inextensional case with *arbitrary* moment-curvature relations. Explicit results are given for the power and the cubic relations. The need for caution in the choice of appropriate material models is demonstrated.

Analysis

Let the undeformed reference curve of a beam be a circular arc L in the xy-plane, with curvature k_o, arc length s (taken as the Lagrangian variable), and angles α between its tangents and the x direction. For a straight beam, take $k_o=\alpha=0$. It is assumed that all beam properties and loads are symmetric with respect to the xy-plane, and that the deformed reference line $\bar{L}$ is a planar curve with arc length $\bar{s}$ and angles $\bar{\alpha}$.

During the deformation, planar normal cross-sections rotate[3] through angles β. Let $\tilde{\alpha}=\alpha+\beta$. The shear deformation angle is $\gamma=\bar{\alpha}-\tilde{\alpha}$. The internal stress resultants: normal force N, shearing force Q, and bending moment M, are assumed to act on the rotated cross-sections and in the rotated directions (Fig. 1(*a*)).

Strain measures, which are exact conjugates to the stress measures defined above, are

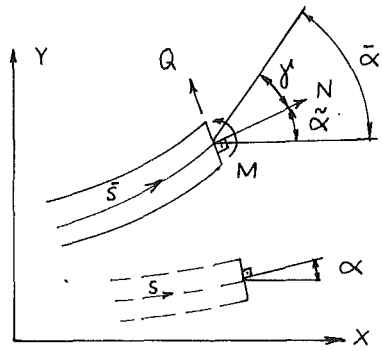


Fig. 1(*a*) Geometry and forces

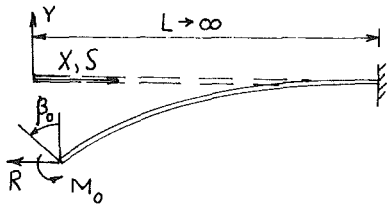


Fig. 1(*b*) Long cantilever beam

$$e=\bar{s}_{,s}\cos\gamma-1=\text{extensional strain} \tag{1}$$

$$g=\bar{s}_{,s}\sin\gamma=\text{shearing strain} \tag{2}$$

$$k=\beta_{,s}=\text{bending strain} \tag{3}$$

where the comma denotes differentiation with respect to the corresponding variable. For small shearing and extensional strains, the common strain measures of beam theory emerge (other strain measures are possible, provided that they form conjugate pairs with appropriately defined stress measures). It is assumed that a strain energy function $U=U(e, g, k)$ per unit length of L exists, such that

$$N=U_{,e};\quad Q=U_{,g};\quad M=U_{,k}. \tag{4a,b,c}$$

The beam may be subjected to end forces, end moments, and to a constant normal loading p (per unit deformed length).

With these definitions and assumptions, the three beam equilibrium equations (Libai and Simmonds, 1988, p. 98) possess the following two exact integrals:

$$(1+e)N+(k_o+k)M+gQ-U=C_1 \quad (\text{"energy integral"}) \tag{5}$$

$$N^2+Q^2+2pM=C_2 \quad (\text{"equilibrium integral"}). \tag{6}$$

The two integrals, the three constitutive equations, and the remaining equilibrium equation (any of the other two may be chosen, instead)

$$N_{,s}=(k_o+k)Q-gp \tag{7}$$

constitute the basic beam equations. The last equation can be reduced to quadrature by utilizing the other five algebraic equations to express all the field variables on its right side in terms of N (this "extraction process" may be difficult for complex forms of U). The equation reduces to

$$N_{,s}=f(N)\quad\text{or}\quad s=\int\frac{dN}{f(N)}+C_3. \tag{8}$$

This determines the six beam quantities (N, Q, M, e, g, k) as functions of s and the three constants C_i. The rotation and the position $\bar{x}$, $\bar{y}$ of $\bar{L}$ can then be found (if needed) from

$$\tilde{\alpha}=\int(k+k_o)ds+C_4 \tag{9}$$

$$\bar{x}=\int[(1+\bar{e})\cos\tilde{\alpha}-g\sin\tilde{\alpha}]ds+C_5 \tag{10}$$

[2] Professor, Faculty of Aerospace Engineering, Technion, Haifa 32000, Israel.

Contributed by the Applied Mechanics Division, of THE AMERICAN SOCIETY OF MECHANICAL ENGINEERS. Manuscript received by the ASME Applied Mechanics Division, Feb. 14, 1991; final revision, June 23, 1991. Associate Technical Editor: J. G. Simmonds.

[3] This is the essence of the first-order shear deformation theory. Actually, β is an average (in some sense) over the cross-section and so are some of the other beam quantities. It is convenient, however, to regard it as the angle of rotation of a plane. (See Libai and Simmonds, 1988, Chapter 4.)

Copyright © 1992 by ASME
Downloaded 03 May 2010 to 171.66.16.247. Redistribution subject to ASME license or copyright; see http://www.asme.org/terms/Terms_Use.cfm

$$\bar{y} = \int [(1+\bar{e})\sin\tilde{\alpha} + g\cos\tilde{\alpha}]ds + C_6. \tag{11}$$

The C_j $(j=1-6)$ should be determined from the six end conditions of beam theory. In many cases the constants enter the integrals and appropriate techniques should be devised for their determination, but these involve only algebra and quadratures.

As a useful example for the extraction process, take the uncoupled quadratic energy $2U = K_M k^2 + K_E e^2 + K_G g^2$. Rearrangement of Eqs. (5)–(7) yields:

$$\left(k_o + k - \frac{P}{K_G}\right)^2 = K_M^{-1}\left[C_8^2 - \left(rN + \frac{1}{r}\right)^2\right] \tag{5a}$$

$$Q^2 = C_7 - N^2 - 2pK_M^{1/2}\left[C_8^2 - \left(rN + \frac{1}{r}\right)^2\right]^{1/2} \tag{6a}$$

$$N_{,s} = \left(k_o + k - \frac{p}{K_G}\right)Q \tag{7a}$$

where $r^2 = (K_E^{-1} - K_G^{-1})$, and C_7, C_8 are new constants. Substitution of (5*a*) and (6*a*) into the right side of (7*a*) produces $f(N)$. The transformation

$$\left(rN + \frac{1}{r}\right) = \frac{1-u^2}{1+u^2}C_8$$

reduces (7*a*) to

$$u_{,s} = \left(\sum_0^4 a_m u^m\right)^{1/2},$$

which is a standard form for the general elliptic integral. The far simpler case of end-loaded curved beams is discussed next.

End-Loaded Curved Beams

Here $p=0$. Let $R=\sqrt{C_2}$ be the constant resultant force acting along the beam, making a constant angle α^* with the positive X direction. Then

$$N = R\cos(\alpha^* - \tilde{\alpha}),\ Q = R\sin(\alpha^* - \tilde{\alpha}). \tag{12a,b}$$

Equations (12) replace (6) and (7) in the beam equations. The unknown variable $\tilde{\alpha}$ is determined as follows: The constitutive relations are used to express (e, g, M) in terms of (N, Q, k). The results are substituted into the energy integral which is put in the form $(k+k_o) = F(N, Q)$. Substitution into Eq. (9) yields the solution

$$s - s_o = \int_{\alpha_o}^{\tilde{\alpha}} \frac{d\tilde{\alpha}}{F(N, Q)} = \int_{\tilde{\alpha}_o}^{\tilde{\alpha}} \frac{d\tilde{\alpha}}{F[R\cos(\alpha^* - \tilde{\alpha}),\ R\sin(\alpha^* - \tilde{\alpha})]}. \tag{13}$$

An example: in the case of quadratic U, Eq. (7*a*) reduces to

$$F(N, Q) = -K_M^{-1/2}\left(C - N - \frac{N^2}{2K_E} - \frac{Q^2}{2K_G}\right)^{1/2} = F(\tilde{\alpha})$$

with (N, Q) expressed in terms of $\tilde{\alpha}$ by (12). The integral (13), with $F(\tilde{\alpha})$ as denominator, reduces by an elementary substitution into an elliptic integral. Extension and shear effects appear in the last two terms of F.

Long Rods

Consider a long, initially straight, cantilever beam. At its end $s=0$, a pulling force R (in the $-x$ direction) and rotation β_0 are applied. At its other end, $s=L\to\infty$, the beam is fully clamped (Fig. 1(*b*)). Here, $\alpha=\alpha^*=0$. The requirements at infinity: $N=R$, $Q=M=\beta=k=g=0$, are sufficient to determine C_1. This fully determines the general solution (13) for given constitutive relations. Two cases are examined in more detail:

(a) extensible, shearable beam with quadratic U. Here,

$$k = F(N, Q) = -\left[\frac{4R}{K_M}\left(1 + \bar{e}\cos^2\beta/2\right)\right]^{1/2}\sin\beta/2$$

with

$$\bar{e} = \left(\frac{R}{K_E} - \frac{R}{K_G}\right).$$

The explicit solution of (13) is

$$\frac{\sin\beta/2}{\sin\beta_0/2} = \frac{(1+\bar{e}\cos^2\beta/2)^{1/2} + (1+\bar{e})^{1/2}\cos\beta/2}{(1+\bar{e}\cos^2\beta_0/2)^{1/2} + (1+\bar{e})^{1/2}\cos\beta_0/2} \times \exp\left\{-\left[\frac{R}{K_M}(1+\bar{e})\right]^{1/2}s\right\}. \tag{14}$$

Two points are of interest: (i) the effects of the shearing and extensional strains are virtually the same. There is no reason to keep one and drop the other and (ii) for unshearable rectangular $(b\times 2h)$ rods, the effective decay rate of a boundary disturbance β_0 is $(\sqrt{3\bar{e}(1+\bar{e})}\ s/h$. A similar form appears in other decay problems. For the classical case, see also Frisch-Fay, Sec 1.4.

(b) inextensible unshearable beam with a *general* nonlinear constitutive relation $M=M(k)$. Let $U^* = G(k) = kM(k) - U(k)$ be the complementary energy, and let $k = G^{-1}(U^*)$ be its inverse. The solution reduces to the integral

$$s = \int_{\beta_0}^{\beta} \frac{d\beta}{G^{-1}(2R\sin^2\beta/2)}. \tag{15}$$

As examples, consider first the power-law $M = Dk^{2n-1}$. Here

$$s = -\int_{\beta_0}^{\beta}\left[\sqrt{\frac{(2n-1)D}{4nR}}\csc\frac{\beta}{2}\right]^{1/n}d\beta. \tag{16}$$

For $n>1$, the requirement of $\lim_{s\to\infty}\beta = 0$ cannot be met, and a solution *does not exist*. The mechanical reason is the accumulation of deformations over large distances in the small moment range (due to the power law)—which leads to divergence. For $n=1$ (only!) an exponential decay rate is obtained—as in (a). As $n\to 1/2$, a hyperbolic decay is approached. As a second example, consider the cubic constitutive relation $M = D(k + mk^3)$ where D and $m \lesseqgtr 0$ are constants. Here the integral becomes

$$\sqrt{\frac{8R}{D}}s = \int_{\beta}^{\beta_0}[1 + (1 + d\sin^2\beta/2)^{1/2}]^{1/2}\csc\beta/2\,d\beta$$

where

$$d = \frac{24mR}{D}.$$

For sufficiently small β_0, the integrand can be expanded as power series in $\sin\beta/2$ which can be integrated term by term:

$$\sqrt{\frac{4R}{D}}s = \int_{\beta}^{\beta_0}\left\{\csc\frac{\beta}{2} + \frac{1}{8}d\sin\frac{\beta}{2}\left[1 - \frac{5}{16}d\sin^2\frac{\beta}{2} + 0\left(\sin^4\frac{\beta}{2}\right)\right]\right\}d\beta.$$

As $\beta\to 0$, the first term (which represents the linear part of the constitutive law) dominates the solution and supplies the required singularity at $s\to\infty$. It follows that a hardening constitutive law *requires a linear component* for a solution to exist. The two examples demonstrate the sensitivity of the solution to the choice of approximate constitutive models.

Downloaded 03 May 2010 to 171.66.16.247. Redistribution subject to ASME license or copyright; see http://www.asme.org/terms/Terms_Use.cfm

References

Antman, S., 1968, "General Solutions of Plane Extensible Elasticae Having Nonlinear Stress-Strain Laws," *Q. J. Applied Math.*, Vol. 26, pp. 35–47.

Antman, S., 1972, "Qualitative Theory for the Ordinary Differential Equations of Nonlinear Elasticity," *Mechanics Today*, Vol. 1, pp. 58–101.

Antman, S., 1974, "Kirchhoff's Problem for Nonlinearly Elastic Rods," *Q. Appl. Math.*, Vol. 32, pp. 221–240.

Frisch-Fay, R., 1962, *Flexible Bars*, Butterworths, London.

Goto, Y., Yoshimitsu, T., and Obata, M., 1990, "Elliptic Integral Solutions of Plane Elastica with Axial and Shear Deformations," *Int. J. Solids Struct.*, Vol. 26, pp. 375–390.

Libai, A., 1984, "Strongly Nonlinear Bending, Extensional and Shearing Deformations of Ringlike Structures," T.A.E. Report 552, Technion, Haifa, Israel.

Libai, A., and Simmonds, J. G., 1983, "Highly Nonlinear Cylindrical Deformations of Rings and Shells," *Int. J. Nonlinear Mech.*, Vol. 18, pp. 181–197.

Libai, A., and Simmonds, J. G., 1988, *The Nonlinear Theory of Elastic Shells*, Academic Press, Boston.

Reissner, E., 1972, "On One Dimensional Finite Strain Beam Theory," *ZAMP*, Vol. 23, pp. 795–804.

Some Remarks on a Class of Uniform Fields in Fibrous Composites

Y. Benveniste[4] and G. J. Dvorak[5]

1 Introduction

In a series of recent papers, Dvorak (1983, 1986) pointed out that a one-parameter uniform strain field can be created in certain fibrous composite media of any transverse geometry by a superposition of a uniform overall stress with a uniform change in temperature. Moreover, under such superimposed loads, Dvorak and Chen (1989) found a uniform strain field in a three-phase fibrous composite, and Benveniste and Dvorak (1990a, 1990b) constructed uniform stress and strain fields in two-phase media of any geometry and phase material symmetry. Finally, Dvorak (1990a) identified uniform strain fields in both fibrous and general two-phase media of any phase material symmetry in the presence of arbitrary but uniform eigenstrains in the phases.

The existence of uniform strain fields is useful in solution of problems which involve phase eigenstrains, e.g., thermal, swelling, or plastic strains. If such eigenstrains are or are taken as uniform, then it is possible to evaluate an auxiliary uniform overall stress state which will change the initial strain field into a uniform strain field in the entire volume. Of course, the auxiliary stress needs to be removed, but that can be accomplished in a purely mechanical loading step. In this way, eigenstrain problems may be converted into much simpler mechanical loading problems. For example, thermoplasticity problems in composite media can be solved as mechanical problems along a modified loading path. Many other applications of the technique can be found in Dvorak (1990a, 1990b).

This Note is concerned with Dvorak's (1986) paper, where a one-parameter family of uniform strain fields was created in a binary fibrous composite through a uniform temperature change and proportional mechanical loading. The parameter can be selected in many different ways, the actual choice in Dvorak (1986) related the longitudinal normal stress and the transverse hydrostatic stress in the matrix through a scalar parameter ρ. The results included a derivation of the instantaneous effective thermal expansion coefficients of two-phase composite aggregates with plastically deforming matrices. Even though the derivation utilized an arbitrary parameter, it was expected that the resulting effective thermal expansion coefficients would be independent of that parameter. This was verified in Dvorak (1986) by numerical examples, but not established analytically. Moreover, since the overall expansion coefficients depend on some overall moduli, the examples had to make recourse to approximate micromechanical models for evaluation of such moduli.

The present Note gives an analytical proof of the independence of Dvorak's (1986) final result for the overall thermal expansion coefficients on the free parameter ρ. Although Dvorak's analysis applies to fibrous systems with transversely isotropic phases, we restrict ourselves to the simpler case of isotropic phases. First, the Note presents a simplified derivation of the relevant results of the (1986) paper. Then, an analytical proof shows that these results are independent of the parameter ρ. The proof is completely general and does not rely on any micromechanical model. Finally, it is shown that the thermal expansion coefficients found with the uniform fields technique coincide with those derived by Levin (1967) from the virtual work theorem. This supplements a similar conclusion reached by a different route in Dvorak (1990a), and confirms that the uniform field technique, while offering a much more extensive scope in applications, gives results in agreement with those that follow from Levin's approach.

2 Analysis

Let us consider a binary composite consisting of an isotropic matrix reinforced by perfectly bonded, aligned, isotropic cylindrical fibers of arbitrary cross-section. A Cartesian coordinate system is chosen with the x_3-axis aligned with the direction of the fibers. As pointed out by Dvorak (1986), a uniform strain field and a piecewise uniform stress field can be created in this binary composite by superposition of a uniform temperature change with certain auxiliary tractions on the external boundary. Let the desired uniform fields be denoted by $\hat{\sigma}_{ij}^s$ and $\hat{\epsilon}_{ij}^s$ with $s = f, m$ for the fiber and matrix, respectively. They must satisfy the traction and displacement continuity at the cylindrical fiber-matrix interfaces. Since the fields are uniform, the continuity requirements are met if the fields conform to the following conditions:

$$\hat{\sigma}_{11}^f = \hat{\sigma}_{11}^m = \hat{\sigma}_{22}^m = \hat{\sigma}_{22}^f = \hat{\sigma} \tag{1}$$

$$\hat{\epsilon}_{33}^f = \hat{\epsilon}_{33}^m, \quad \hat{\epsilon}_{11}^f = \hat{\epsilon}_{11}^m, \quad \hat{\epsilon}_{22}^f = \hat{\epsilon}_{22}^m. \tag{2}$$

The shear strain and stress components of the auxiliary fields vanish in the present situation. The $\hat{\sigma}_{33}^f$ and $\hat{\sigma}_{33}^m$ need not be equal to each other, but are also uniform within each phase. In other words, the $\hat{\sigma}_{33}$ stresses are piecewise constant in the fibrous composite, while all the other strains and stresses are uniform throughout.

We now appeal to the familiar thermoelastic constitutive relations, and express the phase strains in (2) under the constraints indicated by (1). Thus, Eq. $(2)_1$ results in

$$(\hat{\sigma}_{33}^f/E_f) - (2\nu_f/E_f)\hat{\sigma} + \alpha_f\theta_0 = (\hat{\sigma}_{33}^m/E_m) - (2\nu_m/E_m)\hat{\sigma} + \alpha_m\theta_0 \tag{3}$$

where E_s, ν_s, α_s with $s = f, m$ denote, respectively, the Young's modulus, Poisson's ratio, and the thermal expansion coeffi-

[4]Department of Solid Mechanics, Materials and Structures, Faculty of Engineering, Tel-Aviv University, Ramat-Aviv 69978, Israel. Also, Visiting Professor, Rensellaer Polytechnic Institute, Troy, NY 12180.

[5]Institute Center for Composite Materials and Structures, Rensselaer Polytechnic Institute, Troy, NY 12180. Fellow ASME.

Manuscript received by the ASME Applied Mechanics Division, Oct. 3, 1990; final revision, Aug. 6, 1991. Associate Technical Editor: L. M. Keer.

Downloaded 03 May 2010 to 171.66.16.247. Redistribution subject to ASME license or copyright; see http://www.asme.org/terms/Terms_Use.cfm

References

Antman, S., 1968, "General Solutions of Plane Extensible Elasticae Having Nonlinear Stress-Strain Laws," *Q. J. Applied Math.*, Vol. 26, pp. 35–47.

Antman, S., 1972, "Qualitative Theory for the Ordinary Differential Equations of Nonlinear Elasticity," *Mechanics Today*, Vol. 1, pp. 58–101.

Antman, S., 1974, "Kirchhoff's Problem for Nonlinearly Elastic Rods," *Q. Appl. Math.*, Vol. 32, pp. 221–240.

Frisch-Fay, R., 1962, *Flexible Bars*, Butterworths, London.

Goto, Y., Yoshimitsu, T., and Obata, M., 1990, "Elliptic Integral Solutions of Plane Elastica with Axial and Shear Deformations," *Int. J. Solids Struct.*, Vol. 26, pp. 375–390.

Libai, A., 1984, "Strongly Nonlinear Bending, Extensional and Shearing Deformations of Ringlike Structures," T.A.E. Report 552, Technion, Haifa, Israel.

Libai, A., and Simmonds, J. G., 1983, "Highly Nonlinear Cylindrical Deformations of Rings and Shells," *Int. J. Nonlinear Mech.*, Vol. 18, pp. 181–197.

Libai, A., and Simmonds, J. G., 1988, *The Nonlinear Theory of Elastic Shells*, Academic Press, Boston.

Reissner, E., 1972, "On One Dimensional Finite Strain Beam Theory," *ZAMP*, Vol. 23, pp. 795–804.

Some Remarks on a Class of Uniform Fields in Fibrous Composites

Y. Benveniste[4] and G. J. Dvorak[5]

1 Introduction

In a series of recent papers, Dvorak (1983, 1986) pointed out that a one-parameter uniform strain field can be created in certain fibrous composite media of any transverse geometry by a superposition of a uniform overall stress with a uniform change in temperature. Moreover, under such superimposed loads, Dvorak and Chen (1989) found a uniform strain field in a three-phase fibrous composite, and Benveniste and Dvorak (1990a, 1990b) constructed uniform stress and strain fields in two-phase media of any geometry and phase material symmetry. Finally, Dvorak (1990a) identified uniform strain fields in both fibrous and general two-phase media of any phase material symmetry in the presence of arbitrary but uniform eigenstrains in the phases.

The existence of uniform strain fields is useful in solution of problems which involve phase eigenstrains, e.g., thermal, swelling, or plastic strains. If such eigenstrains are or are taken as uniform, then it is possible to evaluate an auxiliary uniform overall stress state which will change the initial strain field into a uniform strain field in the entire volume. Of course, the auxiliary stress needs to be removed, but that can be accomplished in a purely mechanical loading step. In this way, eigenstrain problems may be converted into much simpler mechanical loading problems. For example, thermoplasticity problems in composite media can be solved as mechanical problems along a modified loading path. Many other applications of the technique can be found in Dvorak (1990a, 1990b).

This Note is concerned with Dvorak's (1986) paper, where a one-parameter family of uniform strain fields was created in a binary fibrous composite through a uniform temperature change and proportional mechanical loading. The parameter can be selected in many different ways, the actual choice in Dvorak (1986) related the longitudinal normal stress and the transverse hydrostatic stress in the matrix through a scalar parameter ρ. The results included a derivation of the instantaneous effective thermal expansion coefficients of two-phase composite aggregates with plastically deforming matrices. Even though the derivation utilized an arbitrary parameter, it was expected that the resulting effective thermal expansion coefficients would be independent of that parameter. This was verified in Dvorak (1986) by numerical examples, but not established analytically. Moreover, since the overall expansion coefficients depend on some overall moduli, the examples had to make recourse to approximate micromechanical models for evaluation of such moduli.

The present Note gives an analytical proof of the independence of Dvorak's (1986) final result for the overall thermal expansion coefficients on the free parameter ρ. Although Dvorak's analysis applies to fibrous systems with transversely isotropic phases, we restrict ourselves to the simpler case of isotropic phases. First, the Note presents a simplified derivation of the relevant results of the (1986) paper. Then, an analytical proof shows that these results are independent of the parameter ρ. The proof is completely general and does not rely on any micromechanical model. Finally, it is shown that the thermal expansion coefficients found with the uniform fields technique coincide with those derived by Levin (1967) from the virtual work theorem. This supplements a similar conclusion reached by a different route in Dvorak (1990a), and confirms that the uniform field technique, while offering a much more extensive scope in applications, gives results in agreement with those that follow from Levin's approach.

2 Analysis

Let us consider a binary composite consisting of an isotropic matrix reinforced by perfectly bonded, aligned, isotropic cylindrical fibers of arbitrary cross-section. A Cartesian coordinate system is chosen with the x_3-axis aligned with the direction of the fibers. As pointed out by Dvorak (1986), a uniform strain field and a piecewise uniform stress field can be created in this binary composite by superposition of a uniform temperature change with certain auxiliary tractions on the external boundary. Let the desired uniform fields be denoted by $\hat{\sigma}_{ij}^s$ and $\hat{\epsilon}_{ij}^s$ with $s = f, m$ for the fiber and matrix, respectively. They must satisfy the traction and displacement continuity at the cylindrical fiber-matrix interfaces. Since the fields are uniform, the continuity requirements are met if the fields conform to the following conditions:

$$\hat{\sigma}_{11}^f = \hat{\sigma}_{11}^m = \hat{\sigma}_{22}^m = \hat{\sigma}_{22}^f = \hat{\sigma} \tag{1}$$

$$\hat{\epsilon}_{33}^f = \hat{\epsilon}_{33}^m, \quad \hat{\epsilon}_{11}^f = \hat{\epsilon}_{11}^m, \quad \hat{\epsilon}_{22}^f = \hat{\epsilon}_{22}^m. \tag{2}$$

The shear strain and stress components of the auxiliary fields vanish in the present situation. The $\hat{\sigma}_{33}^f$ and $\hat{\sigma}_{33}^m$ need not be equal to each other, but are also uniform within each phase. In other words, the $\hat{\sigma}_{33}$ stresses are piecewise constant in the fibrous composite, while all the other strains and stresses are uniform throughout.

We now appeal to the familiar thermoelastic constitutive relations, and express the phase strains in (2) under the constraints indicated by (1). Thus, Eq. $(2)_1$ results in

$$(\hat{\sigma}_{33}^f/E_f) - (2\nu_f/E_f)\hat{\sigma} + \alpha_f\theta_0 = (\hat{\sigma}_{33}^m/E_m) - (2\nu_m/E_m)\hat{\sigma} + \alpha_m\theta_0 \tag{3}$$

where E_s, ν_s, α_s with $s = f, m$ denote, respectively, the Young's modulus, Poisson's ratio, and the thermal expansion coeffi-

[4]Department of Solid Mechanics, Materials and Structures, Faculty of Engineering, Tel-Aviv University, Ramat-Aviv 69978, Israel. Also, Visiting Professor, Rensellaer Polytechnic Institute, Troy, NY 12180.

[5]Institute Center for Composite Materials and Structures, Rensselaer Polytechnic Institute, Troy, NY 12180. Fellow ASME.

Manuscript received by the ASME Applied Mechanics Division, Oct. 3, 1990; final revision, Aug. 6, 1991. Associate Technical Editor: L. M. Keer.

Copyright © 1992 by ASME
Downloaded 03 May 2010 to 171.66.16.247. Redistribution subject to ASME license or copyright; see http://www.asme.org/terms/Terms_Use.cfm

cient of the matrix and fiber, respectively; θ_0 is the uniform temperature change. Similarly, under (1), Eqs. $(2)_2$ and $(2)_3$ become

$$\left(\frac{1-\nu_f}{E_f}\right)\hat{\sigma}-\frac{\nu_f}{E_f}\,\hat{\sigma}^f_{33}+\alpha_f\theta_0=\left(\frac{1-\nu_m}{E_m}\right)\hat{\sigma}-\frac{\nu_m}{E_m}\,\hat{\sigma}^m_{33}+\alpha_m\theta_0. \quad (4)$$

For a given temperature change, (3) and (4) provide two equations for the three unknown components $\hat{\sigma}$, $\hat{\sigma}^f_{33}$, $\hat{\sigma}^m_{33}$ of the piecewise uniform stress field. This suggests that an additional relation may be prescribed between these unknowns. In accordance with Dvorak (1986), we chose

$$\hat{\sigma}^m_{33}=\rho\hat{\sigma}, \quad (5)$$

where ρ is an arbitrary parameter. From (3), (4), and (5) one readily obtains

$$\hat{\sigma}^f_{33}=\hat{\sigma}\{1+[(1+\nu_m)E_f(\rho-1)/(1+\nu_f)E_m]\} \quad (6)$$

$$\hat{\sigma}=\frac{(1+\nu_f)(\alpha_f-\alpha_m)\theta_0}{[1-\nu_m-2\nu_m\nu_f+\rho(\nu_f-\nu_m)]/E_m+(1+\nu_f)(2\nu_f-1)/E_f}. \quad (7)$$

Therefore, for any finite value of ρ, uniform fields can be created in the fibrous composite by application of the stresses (5) and (6) on planes x_3 = constant, together with tractions resulting from $\hat{\sigma}$ on the lateral surface, and by a uniform temperature change θ_0 throughout. These uniform fields can be used to derive the effective thermoelastic constants of the composite.

At this stage we focus our attention on a fibrous composite which is transversely isotropic on the macroscale and is subjected to a uniform temperature change, while its external surface is kept traction-free. By definition, the longitudinal and transverse thermal expansion coefficients of the composite are given by

$$\alpha_L\theta_0=c_f\bar{\epsilon}^f_{33}+c_m\bar{\epsilon}^m_{33} \quad (8)$$

$$\alpha_T\theta_0=c_f\bar{\epsilon}^f_{11}+c_m\bar{\epsilon}^m_{11}=c_f\bar{\epsilon}^f_{22}+c_m\bar{\epsilon}^m_{22} \quad (9)$$

where an overbar denotes an average over the volume of respective phases and c_s, $s = f, m$ are the volume fractions.

The thermal strains on the left-hand side of (8) and (9) can be derived from the uniform strain field. This is accomplished by an application of a loading/unloading sequence where the loading consists of θ_0 and $\hat{\sigma}_{ij}$, and the unloading is a subtraction of the average surface tractions, which have been induced by $\hat{\sigma}_{ij}$. Then, (8) and (9) may be rewritten as

$$\alpha_L\theta_0=\hat{\epsilon}_{33}-(c_f\hat{\sigma}^f_{33}+c_m\rho\hat{\sigma})/E_L+(2\nu_L/E_L)\hat{\sigma} \quad (10)$$

$$\alpha_T\theta_0=\hat{\epsilon}_{11}-[(1-\nu_T)/E_T]\hat{\sigma}+(\nu_L/E_L)(c_m\rho\hat{\sigma}+c_f\hat{\sigma}^f_{33}), \quad (11)$$

where E_L, E_T, ν_L, and ν_T are, respectively, the effective longitudinal and transverse Young's moduli and longitudinal and transverse Poisson's ratios of the transversely isotropic fibrous composite.

The expressions for $\hat{\sigma}$, $\hat{\sigma}^f_{33}$ and $\hat{\epsilon}^f_{33}$, $\hat{\epsilon}^f_{11}$ obtained in (6), (7), (3), and (4), render Eqs. (10) and (11) in the form

$$\alpha_L=\alpha_m+(\alpha_f-\alpha_m)(1+\nu_f)(A_L+B_L\rho)/(C_L+D_L\rho) \quad (12)$$

$$\alpha_T=\alpha_m+(\alpha_f-\alpha_m)(1+\nu_f)(A_T+B_T\rho)/(C_T+D_T\rho), \quad (13)$$

where

$$A_L=-\left[\frac{2\nu_m}{E_m}-\frac{2\nu_L}{E_L}\right]-\frac{c_f}{E_L}\left[1-\frac{(1+\nu_m)E_f}{(1+\nu_f)E_m}\right],$$

$$B_L=\frac{1}{E_m}-\frac{1}{E_L}\left[c_m+c_f\frac{(1+\nu_m)E_f}{(1+\nu_f)E_m}\right],$$

$$C_L=\left[\frac{1}{E_m}(1-\nu_m-2\nu_m\nu_f)+\frac{1}{E_f}(1+\nu_f)(2\nu_f-1)\right],$$

$$D_L=(\nu_f-\nu_m)/E_m \quad (14)$$

$$A_T=\frac{1-\nu_m}{E_m}-\frac{1-\nu_T}{E_T}+\frac{\nu_L}{E_L}c_f\left[1-\frac{(1+\nu_m)E_f}{(1+\nu_f)E_m}\right]$$

$$B_T=-\frac{\nu_m}{E_m}+\frac{\nu_L}{E_L}\left[c_m+c_f\frac{(1+\nu_m)E_f}{(1+\nu_f)E_m}\right],$$

$$C_T=C_L,\quad D_T=D_L. \quad (15)$$

At this stage we ask whether the results (12) and (13) are independent of the arbitrary parameter ρ, and whether these expressions can be reduced to the following well-known formulae, originally derived by a different approach by Levin (1967)

$$\alpha_L=\alpha_m+\frac{\alpha_f-\alpha_m}{\left[\frac{1}{K_f}-\frac{1}{K_m}\right]}\left[\frac{3(1-2\nu_L)}{E_L}-\frac{1}{K_m}\right] \quad (16)$$

$$\alpha_T=\alpha_m+\frac{\alpha_f-\alpha_m}{\left[\frac{1}{K_f}-\frac{1}{K_m}\right]}\left[\frac{3}{2k}-\frac{3(1-2\nu_L)\nu_L}{E_L}-\frac{1}{K_m}\right], \quad (17)$$

where

$$K_s=E_s/[3(1-2\nu_s)] \text{ with } s=f,m, \quad (18)$$

and k denotes the effective plane-strain bulk modulus for lateral dilatation without axial extension.

In what follows, the equivalence between (12)–(13) and (16)–(17), respectively, is established by recalling first Hill's (1964) universal relations between the effective moduli of a binary, transversely isotropic fibrous composite with cylindrical, transversely isotropic phases. Two of these relations which will be needed here are (see, for example, Hashin, 1983):

$$E_L=(c_fE_f+c_mE_m)+\left(4(\nu_f-\nu_m)^2\left(\frac{c_f}{k_f}+\frac{c_m}{k_m}-\frac{1}{k}\right)\Big/\left(\frac{1}{k_f}-\frac{1}{k_m}\right)^2\right) \quad (19)$$

$$\nu_L=(c_f\nu_f+c_m\nu_m)-\left((\nu_f-\nu_m)\left(\frac{c_f}{k_f}+\frac{c_m}{k_m}-\frac{1}{k}\right)\Big/\left(\frac{1}{k_f}-\frac{1}{k_m}\right)\right) \quad (20)$$

where

$$k_s^{-1}=2(1+\nu_s)(1-2\nu_s)E_s^{-1} \text{ with } s=f,m, \quad (21)$$

and k is the same effective modulus appearing in (17). Equations (19) and (20) allow one to write

$$E_L=a+b\nu_L,\quad \frac{1}{k}=c+d\nu_L \quad (22)$$

with

$$a=(c_fE_f+c_mE_m)+\left\{[4(\nu_f-\nu_m)(c_f\nu_f+c_m\nu_m)]/\left(\frac{1}{k_f}-\frac{1}{k_m}\right)\right\}$$

$$b=\frac{4(\nu_m-\nu_f)}{\left[\frac{1}{k_f}-\frac{1}{k_m}\right]},\quad c=\left(\frac{\nu_f}{k_m}-\frac{\nu_m}{k_f}\right)/(\nu_f-\nu_m), \quad (23)$$

$$d=-4/b.$$

Let us now show the equivalence of (12) and (16). To this end we first express ν_L in terms of E_L and the constituent properties through $(22)_1$. Then, (18) allows one to cast (16) into the form

Downloaded 03 May 2010 to 171.66.16.247. Redistribution subject to ASME license or copyright; see http://www.asme.org/terms/Terms_Use.cfm

$$\alpha_L = \alpha_m + \left[\frac{1+\nu_f}{\nu_f-\nu_m} - \frac{1}{E_L}\left(\frac{c_f(1+\nu_m)E_f}{\nu_f-\nu_m} + \frac{c_m(1+\nu_f)E_m}{\nu_f-\nu_m} \right) \right] (\alpha_f-\alpha_m) \quad (24)$$

which involves only E_L as the single effective elastic modulus.

Application of the same procedure to (14_1) makes it possible to express the constant A_L in terms of constituents properties and E_L only. It is now clear that for the parameter ρ to disappear altogether from (12), the following relation must hold between A_L, B_L, C_L, and D_L:

$$A_L/C_L = B_L/D_L, \quad (25)$$

which results in

$$(A_L + B_L\rho)/(C_L + D_L\rho) = B_L/D_L. \quad (26)$$

Some algebra shows that (25) is indeed fulfilled, and it becomes then an easy matter to verify that one can use (26), together with $(14)_2$ and $(14)_4$ to reduce Eq. (12) identically to (24).

Establishing the equivalence between (13) and (17) is similar in principle to the procedure described previously. We start by using (22) in conjunction with (18) and (21) and choose this time to cast (17) in terms of the constituent properties and ν_L only. After considerable manipulation, (17) can be written in the form

$$\alpha_T = \alpha_m + (\alpha_f-\alpha_m)(e+f\nu_L)/(a+b\nu_L) \quad (27)$$

where a and b are given by (23) and

$$e = a[-\nu_m(1+\nu_f)/(\nu_f-\nu_m)], \quad f = f_1 + c_f f_2 \quad (28)$$

with

$$f_1 = \frac{2(1+\nu_f)k_m[2k_f\nu_m(\nu_f-\nu_m) - (1+\nu_m)(2\nu_m-1)(k_m-k_f)]}{(k_m-k_f)(\nu_f-\nu_m)} \quad (29)$$

$$f_2 = -(1+\nu_f)(1+\nu_m)[2k_m^2(1+\nu_m)(1-2\nu_m) + 2k_f^2(1+\nu_f)(1-2\nu_f) + k_m k_f(8\nu_m\nu_f - 4 + 2\nu_m + 2\nu_f)] / \{(\nu_f-\nu_m)[(1+\nu_m)k_m - k_f(1+\nu_f)]\}. \quad (30)$$

Next we turn to Eq. (13). In analogy to (25) and (26), what now needs to be established is that

$$A_T/C_T = B_T/D_T \quad \text{or} \quad A_T/B_T = C_T/D_T \quad (31)$$

or

$$(A_T + B_T\rho)/(C_T + D_T\rho) = B_T/D_T \quad (32)$$

so that ρ disappears from (13). Furthermore, it needs to be shown that

$$(1+\nu_f)(B_T/D_T) = (e+f\nu_L)/(a+b\nu_L). \quad (33)$$

The ratio C_T/D_T in $(31)_2$ easily follows from (15_1), (15_2), $(14)_3$, $(14)_4$ as

$$C_T/D_T = [E_m(1+\nu_f)(2\nu_f-1) + E_f(1 - \nu_m - 2\nu_m\nu_f)]/[E_f(\nu_f-\nu_m)] \quad (34)$$

which is seen not to contain any effective moduli. On the other hand, the expression A_T/B_T in $(31)_2$ does contain the effective constants ν_T, E_T, ν_L, and E_L as seen from $(14)_5$ and $(16)_6$.

At this stage, we recall the identity (see, for example, Hashin, 1983, Eq. 3.2.4)

$$(1-\nu_T)/E_T = [E_L + 4k\nu_L^2]/(2kE_L), \quad (35)$$

and make use of $(22)_1$ and (22) to express all the effective moduli in $(15)_1$ and $(15)_2$ in terms of ν_L only. The ratio A_T/B_T can eventually be written as

$$A_T/B_T = [(1+\nu_L h)/(1+\nu_L j)](C_T/D_T) \quad (36)$$

where

$$h = b/a - (E_m d - 2c_f g/a)[2(1-\nu_m) - cE_m]^{-1}$$
$$g = E_m\left[1 - \frac{(1+\nu_m)E_f}{(1+\nu_f)E_m}\right] \quad (37)$$
$$j = -(E_m - \nu_m b - c_f g)/(\nu_m a),$$

and a, b, c, d, are given by (23).

To establish the validity of $(31)_2$, it needs to be shown that $h = j$; this follows after some algebra from (23) and (37).

Finally, to prove the validity of (33), B_T in $(14)_6$ needs to be expressed in terms of ν_L and the constituents properties from $(22)_1$. Then, the expressions for a, b, e, f which were derived in (23) and (28) lead, after considerable manipulation, to Eq. (33). This shows that (33) is indeed valid.

3 Conclusion

In summary, we have shown that Eqs. (12) and (13) derived by the procedure described in Dvorak's (1986) paper are indeed independent of the free parameter ρ, and that they reduce properly to the forms (16) and (17) originally derived by Levin (1967). Of course, the proof has been constructed only for the case of isotropic constituents, whereas Dvorak's results also apply to transversely isotropic phases. Extension of the proof to such systems should be possible, but it if beyond our present scope.

Acknowledgment

This work was supported by the DARPA-HiTASC program at Rensselaer Polytechnic Institute.

References

Benveniste, Y., and Dvorak, G. J., 1990a, "On a Correspondence Between Mechanical and Thermal Effects in Two-Phase Composites," *Micromechanics and Inhomogeneity*, (Toshio Mura Anniversary Volume), G. J. Weng, M. Taya, and H. Abe, eds., Springer-Verlag, New York, pp. 65–81.

Benveniste, Y., and Dvorak, G. J., 1990b, "On a Correspondence Between Mechanical and Thermal Fields in Composites with Slipping Interfaces," *Inelastic Deformation of Composite Materials*, G. J. Dvorak, ed., IUTAM Symposium, Troy, NY, May 29–June 1, 1990, Springer-Verlag, New York, pp. 77–98.

Dvorak, G. J., 1983, "Metal Matrix Composites: Plasticity and Fatigue," *Mechanics of Composite Materials: Recent Advances*, Z. Hashin and C. Herakovich, eds., Pergamon Press, New York, pp. 73–92.

Dvorak, G. J., 1986, "Thermal Expansion of Elastic-Plastic Composite Materials," ASME JOURNAL OF APPLIED MECHANICS, Vol. 53, pp. 737–743.

Dvorak, G. J., 1986, "Thermomechanical Deformation and Coupling in Elastic-Plastic Composite Materials," *Thermomechanical Couplings in Solids*, H. D. Bui and Q.S. Nguyen, North-Holland, Amsterdam, pp. 43–54.

Dvorak, G. J., and Chen, T., 1989, "Thermal Expansion of Three-Phase Composite Materials," ASME JOURNAL OF APPLIED MECHANICS, Vol. 56, pp. 418–422.

Dvorak, G. J., 1990a, "On Uniform Fields in Heterogeneous Media," *Proceedings of the Royal Society, London*, Vol. A431, pp. 89–110.

Dvorak, G. J., 1990b, "Plasticity Theories for Fibrous Composite Materials," *Metal Matrix Composites*, R. J. Arsenault and R. K. Everett, eds., Academic Press, Boston, MA.

Hashin, Z., 1983, "Analysis of Composite Materials," ASME JOURNAL OF APPLIED MECHANICS, Vol. 50, pp. 481–505.

Hill, R., 1964, "Theory of the Mechanical Properties of Fiber-Strengthened Materials—1. Elastic Behavior," *Journal of the Mechanics and Physics of Solids*, Vol. 12, pp. 199–212.

Levin, V. M., 1967, "Thermal Expansion Coefficients of Heterogeneous Materials," *Mekhanika Tverdogo Tela*, Vol. 2, pp. 88–94, (English translation: *Mechanics of Solids*, Vol. 11, pp. 58–61).

Downloaded 03 May 2010 to 171.66.16.247. Redistribution subject to ASME license or copyright; see http://www.asme.org/terms/Terms_Use.cfm

Another Look at Orthogonal Curvilinear Coordinates in Kinematic and Dynamic Analyses

C. Q. Liu[6] and R. L. Huston[7]

Introduction

In dynamic analysis, it is often convenient to use orthogonal curvilinear coordinates for describing complex geometries. In such cases an analyst needs expressions for angular velocity components of the unit vector triad of the curvilinear coordinate system. In computational analyses it is also useful to have expressions for the elements of the transformation matrix between this unit vector triad and a triad of an observer's reference frame.

Recently, Kane and Levinson (1990) presented an efficient and innovative procedure for determining the angular velocity components. In this Note, we present two alternative procedures for determining these components. We then extend the analysis by developing expressions for the elements of the transformation matrix ("direction cosines").

Orthogonal Curvilinear Coordinates

Let A be a reference frame containing three mutually perpendicular unit vectors $\mathbf{a}_i$ (i = 1, 2, 3) and let O be a point fixed in A. Let P be a point moving in A and let the vector $\mathbf{p}$ locating P to O be expressed as:

$$\mathbf{p} = x_1\mathbf{a}_1 + x_2\mathbf{a}_2 + x_3\mathbf{a}_3 \tag{1}$$

where the scalar components x_i (i = 1, 2, 3) are Cartesian coordinates of P in A. Let these x_i be function of three other variables q_j (j = 1, 2, 3), called "curvilinear coordinates" such that $\det(\partial x_i/\partial q_j)$ is nonzero.

Since P moves in A, and since the $\mathbf{a}_i$ are fixed in A, the x_i are functions of time t. Hence, the q_j are also function of time t, and thus $\mathbf{p}$ may be expressed as a function of t as an independent variable, and of x_i or q_j as intermediate, dependent variables.

The partial derivatives in A of $\mathbf{p}$ with respect to q_j, forms a set of vectors tangent to the coordinate curves, called "base vectors." With $\det(\partial x_i/\partial q_j)$ being nonzero, these base vectors are noncoplanar. However, they are not necessarily mutually perpendicular and they generally are not unit vectors. When they are mutually perpendicular, the curvilinear coordinate system is said to be "orthogonal."

Unit Vector Triad

Consider an orthogonal curvilinear coordinate system. Let $\mathbf{g}_j$ (j = 1, 2, 3) be the base vectors and let $\mathbf{b}_j$ (j = 1, 2, 3) be unit vectors, respectively, parallel to the $\mathbf{g}_j$ with the same sense. Let the magnitudes of the vectors, called "scale factors," be designated by h_j (j = 1, 2, 3). Thus we have

$$\mathbf{g}_j = \frac{\partial \mathbf{p}}{\partial q_j} = h_j\mathbf{b}_j \quad (j = 1,2,3) \tag{2}$$

where in the sequel a repeated index does **not** represent a sum.

Let B be a rigid body, or reference frame, in which the $\mathbf{b}_j$ are fixed.

Transformation Matrix

Let S be a transformation matrix relating the $\mathbf{a}_i$ and $\mathbf{b}_j$ whose elements S_{ij} are defined as $\mathbf{a}_i \cdot \mathbf{b}_j$. Then from Eqs. (1) and (2), S may be expressed as

$$S = [\mathbf{a}_i \cdot \mathbf{b}_j] = \begin{bmatrix} \dfrac{\partial x_1}{h_1\partial q_1} & \dfrac{\partial x_1}{h_2\partial q_2} & \dfrac{\partial x_1}{h_3\partial q_3} \\ \dfrac{\partial x_2}{h_1\partial q_1} & \dfrac{\partial x_2}{h_2\partial q_2} & \dfrac{\partial x_2}{h_3\partial q_3} \\ \dfrac{\partial x_3}{h_1\partial q_1} & \dfrac{\partial x_3}{h_2\partial q_2} & \dfrac{\partial x_3}{h_3\partial q_3} \end{bmatrix}. \tag{3}$$

(It is readily seen that S is itself orthogonal. That is, the inverse and transpose of S are identical.)

Angular Velocity

Let ω represent the angular velocity of B in A. Then ω may be expressed in the forms

$$\omega = \omega_1\mathbf{b}_1 + \omega_2\mathbf{b}_2 + \omega_3\mathbf{b}_3 \tag{4}$$

we can obtain expressions for the ω_i by considering the time derivative in A of the base vectors: From Eq. (2) we have

$$\frac{d\mathbf{g}_i}{dt} = \frac{dh_i}{dt}\mathbf{b}_i + h_i\frac{d\mathbf{b}_i}{dt} = \dot{h}_i\mathbf{b}_i + h_i\omega\times\mathbf{b}_i \quad (i = 1,2,3) \tag{5}$$

where the last equality follows from the definition of angular velocity (see, for example, Kane and Levinson, 1985) and the overdot is an abbreviation of d/dt. Thus, the projection along $\mathbf{g}_j$ is

$$\begin{aligned} \frac{d\mathbf{g}_i}{dt}\cdot\mathbf{g}_j &= (\dot{h}_i\mathbf{b}_i + h_i\omega\times\mathbf{b}_i)\cdot\mathbf{g}_j = 0 + h_ih_j(\omega\times\mathbf{b}_i)\cdot\mathbf{b}_j \\ &= h_ih_j\omega\cdot\mathbf{b}_i\times\mathbf{b}_j = h_ih_j\omega\cdot\mathbf{b}_k = h_ih_j\omega_k \end{aligned} \tag{6}$$

or

$$\omega_k = \frac{1}{h_ih_j}\frac{d\mathbf{g}_i}{dt}\cdot\mathbf{g}_j \tag{7}$$

where the indices i, j, k represent a cyclic permutation of 1, 2, 3.

Equation (7) may also be developed directly from Eq. (3): Let the angular velocity matrix W be defined as

$$W = \begin{bmatrix} 0 & -\omega_3 & \omega_2 \\ \omega_3 & 0 & -\omega_1 \\ -\omega_2 & \omega_1 & 0 \end{bmatrix}. \tag{8}$$

The W and the derivation of the transformation matrix S are related by the expressions (Huston, 1990)

$$\dot{S} = SW \quad \text{or} \quad W = S^T\dot{S}. \tag{9}$$

Solving for the ω_i we obtain

$$\begin{aligned} \omega_1 &= \dot{S}_{12}S_{13} + \dot{S}_{22}S_{23} + \dot{S}_{32}S_{33} \\ \omega_2 &= \dot{S}_{13}S_{11} + \dot{S}_{23}S_{21} + \dot{S}_{33}S_{31} \\ \omega_3 &= \dot{S}_{11}S_{12} + \dot{S}_{21}S_{22} + \dot{S}_{31}S_{32} \end{aligned} \tag{10}$$

where the S_{ij} (i, j = 1, 2, 3) are elements of S. By recognizing these expressions as dot products we obtain, using Eq. (3),

[6]Research Associate, University of Cincinnati, Cincinnati, OH.
[7]Professor of Mechanics, University of Cincinnati, Cincinnati, OH. Fellow ASME.

Manuscript received by the ASME Applied Mechanics Division, Jan. 16, 1991; final revision, Apr. 10, 1991. Associate Technical Editor: L. M. Keer.

Copyright © 1992 by ASME
Downloaded 03 May 2010 to 171.66.16.247. Redistribution subject to ASME license or copyright; see http://www.asme.org/terms/Terms_Use.cfm

$$\omega_1 = \left[\frac{d}{dt}\left(\frac{1}{h_2}\frac{\partial \mathbf{p}}{\partial q_2}\right)\right]\cdot\left(\frac{1}{h_3}\frac{\partial \mathbf{p}}{\partial q_3}\right) = \frac{1}{h_2 h_3}\frac{dg_2}{dt}\cdot\mathbf{g}_3$$

$$\omega_2 = \left[\frac{d}{dt}\left(\frac{1}{h_3}\frac{\partial \mathbf{p}}{\partial q_3}\right)\right]\cdot\left(\frac{1}{h_1}\frac{\partial \mathbf{p}}{\partial q_1}\right) = \frac{1}{h_3 h_1}\frac{dg_3}{dt}\cdot\mathbf{g}_1 \qquad (11)$$

$$\omega_3 = \left[\frac{d}{dt}\left(\frac{1}{h_1}\frac{\partial \mathbf{p}}{\partial q_1}\right)\right]\cdot\left(\frac{1}{h_2}\frac{\partial \mathbf{p}}{\partial q_2}\right) = \frac{1}{h_1 h_2}\frac{dg_1}{dt}\cdot\mathbf{g}_2.$$

These expressions are seen to be identical to Eq. (7).

Remark 1

Equations (7) and (11) are consistent with a result obtained earlier by Kane and Levinson (1990). It provides an efficient algorithm for obtaining the desired angular velocity components. Indeed, they have used this result to create tables of components for a number of common orthogonal curvilinear coordinate systems. An extension of this data for the elements of the transformation matrix may be obtained using Eq. (3). Table 1 presents these results.

Example

A solid-right circular cone C of mass m, base radius r, and altitude h, is suspended at its vertex O as depicted in Fig. 1. Suppose the cone can freely rotate about O without spinning. Let G, the mass center of C, be located using spherical coordinates q_1 $(= 3/4\ h)$, q_2, q_3 as shown.

The Cartesian coordinates of G are

$$x_1 = \frac{3}{4}h\ \sin q_2\ \cos q_3$$

$$x_2 = \frac{3}{4}h\ \sin q_2\ \sin q_3 \qquad (12)$$

$$x_3 = \frac{3}{4}h\ \cos q_2.$$

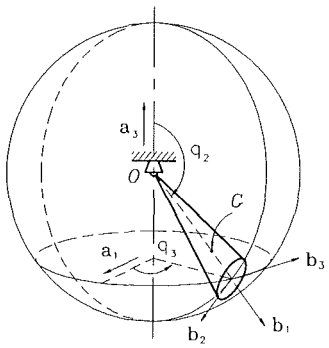


Fig. 1 A suspended circular cone

Table 1 Transformation matrix elements

Common Name for q_1, q_2, q_3	Cartesian Coordinates	Transformation Matrix
Parabolic Coordinates	$x_1 = q_1 q_2 c_3$ $x_2 = q_1 q_2 s_3$ $x_3 = (q_1^2 - q_2^2)/2$	$\begin{bmatrix} \frac{q_2 c_3}{(q_1^2+q_2^2)^{1/2}} & \frac{q_1 c_3}{(q_1^2+q_2^2)^{1/2}} & -s_3 \\ \frac{q_2 s_3}{(q_1^2+q_2^2)^{1/2}} & \frac{q_1 s_3}{(q_1^2+q_2^2)^{1/2}} & c_3 \\ \frac{q_1}{(q_1^2+q_2^2)^{1/2}} & \frac{-q_2}{(q_1^2+q_2^2)^{1/2}} & 0 \end{bmatrix}$
Parabolic Cylindrical Coordinates	$x_1 = (q_1^2 - q_2^2)/2$ $x_2 = q_1 q_2$ $x_3 = q_3$	$\begin{bmatrix} \frac{q_1}{(q_1^2+q_2^2)^{1/2}} & \frac{-q_2}{(q_1^2+q_2^2)^{1/2}} & 0 \\ \frac{q_2}{(q_1^2+q_2^2)^{1/2}} & \frac{q_1}{(q_1^2+q_2^2)^{1/2}} & 0 \\ 0 & 0 & 1 \end{bmatrix}$
Elliptic Cylindrical Coordinates	$x_1 = a\,ch_1 c_2$ $x_2 = a\,sh_1 s_2$ $x_3 = q_3$	$\begin{bmatrix} \frac{sh_1 c_2}{(sh_1^2 c_2^2 + ch_1^2 s_2^2)^{1/2}} & \frac{-ch_1 s_2}{(sh_1^2 c_2^2 + ch_1^2 s_2^2)^{1/2}} & 0 \\ \frac{ch_1 s_2}{(sh_1^2 c_2^2 + ch_1^2 s_2^2)^{1/2}} & \frac{sh_1 c_2}{(sh_1^2 c_2^2 + ch_1^2 s_2^2)^{1/2}} & 0 \\ 0 & 0 & 1 \end{bmatrix}$
Prolate Spheroidal Coordinates	$x_1 = a\,sh_1 s_2 c_3$ $x_2 = a\,sh_1 s_2 s_3$ $x_3 = a\,ch_1 c_2$	$\begin{bmatrix} \frac{ch_1 s_2 c_3}{(sh_1^2 c_2^2 + ch_1^2 s_2^2)^{1/2}} & \frac{sh_1 c_2 c_3}{(sh_1^2 c_2^2 + ch_1^2 s_2^2)^{1/2}} & -s_3 \\ \frac{ch_1 s_2 s_3}{(sh_1^2 c_2^2 + ch_1^2 s_2^2)^{1/2}} & \frac{sh_1 c_2 s_3}{(sh_1^2 c_2^2 + ch_1^2 s_2^2)^{1/2}} & c_3 \\ \frac{sh_1 c_2}{(sh_1^2 c_2^2 + ch_1^2 s_2^2)^{1/2}} & \frac{-ch_1 s_2}{(sh_1^2 c_2^2 + ch_1^2 s_2^2)^{1/2}} & 0 \end{bmatrix}$

Downloaded 03 May 2010 to 171.66.16.247. Redistribution subject to ASME license or copyright; see http://www.asme.org/terms/Terms_Use.cfm

Table 1 Transformation matrix elements (continued)

Common Name for q_1, q_2, q_3	Cartesian Coordinates	Transformation Matrix
Oblate Spheroidal Coordinates	$x_1 = a\,ch_1 s_2 c_3$ $x_2 = a\,ch_1 s_2 s_3$ $x_3 = a\,sh_1 c_2$	$\begin{bmatrix} \frac{sh_1 s_2 c_3}{(sh_1^2 s_2^2 + ch_1^2 c_2^2)^{1/2}} & \frac{ch_1 c_2 c_3}{(sh_1^2 s_2^2 + ch_1^2 c_2^2)^{1/2}} & -s_3 \\ \frac{sh_1 s_3}{(sh_1^2 s_2^2 + ch_1^2 c_2^2)^{1/2}} & \frac{ch_1 c_2 s_3}{(sh_1^2 s_2^2 + ch_1^2 c_2^2)^{1/2}} & c_3 \\ \frac{ch_1 c_2}{(sh_1^2 s_2^2 + ch_1^2 c_2^2)^{1/2}} & \frac{-sh_1 s_2}{(sh_1^2 s_2^2 + ch_1^2 c_2^2)^{1/2}} & 0 \end{bmatrix}$
Spherical Coordinates	$x_1 = q_1 s_2 c_3$ $x_2 = q_1 s_2 s_3$ $x_3 = q_1 c_2$	$\begin{bmatrix} s_2 c_3 & c_2 c_3 & -s_3 \\ s_2 s_3 & c_2 s_3 & c_3 \\ c_2 & -s_2 & 0 \end{bmatrix}$

Let $\mathbf{b}_i$ $(i = 1, 2, 3)$ be mutually perpendicular unit vectors (fixed in C) associated with the spherical coordinate system, and let $\mathbf{a}_i$ $(i = 1, 2, 3)$ be mutually perpendicular unit vectors fixed in a Newtonian reference frame. Then, from Eq. (3) the transformation matrix between $\mathbf{a}_i$ and $\mathbf{b}_i$ is

$$S=\begin{bmatrix} \sin q_2 \cos q_3 & \cos q_2 \cos q_3 & -\sin q_3 \\ \sin q_2 \sin q_3 & \cos q_2 \sin q_3 & \cos q_3 \\ \cos q_2 & -\sin q_2 & 0 \end{bmatrix}. \tag{13}$$

Using Eq. (7), the angular velocity of C (and the triad of $\mathbf{b}_i$) is found to be

$$\omega=\dot{q}_3\cos q_2\mathbf{b}_1-\dot{q}_3\sin q_2\mathbf{b}_2+\dot{q}_2\mathbf{b}_3. \tag{14}$$

The angular acceleration of C is then

$$\alpha=(\ddot{q}_3\cos q_2-\dot{q}_2\dot{q}_3\sin q_2)\mathbf{b}_1 - (\ddot{q}_3\sin q_2+\dot{q}_2\dot{q}_3\cos q_2)\mathbf{b}_2+\ddot{q}_2\mathbf{b}_3. \tag{15}$$

The velocity of G is

$$\mathbf{V}^G=\omega\times\left(\frac{3}{4}h\mathbf{b}_1\right)=\frac{3}{4}h(\dot{q}_2\mathbf{b}_2+\dot{q}_3\sin q_2\mathbf{b}_3). \tag{16}$$

The acceleration of G is then

$$\mathbf{a}^G=-\frac{3}{4}h(\dot{q}_2^2+\dot{q}_3^2\sin^2 q_2)\mathbf{b}_1 +\frac{3}{4}h(\ddot{q}_2-\dot{q}_3^2\sin q_2\cos q_2)\mathbf{b}_2 +\frac{3}{4}h(\ddot{q}_3\sin q_2+2\dot{q}_2\dot{q}_3\cos q_2)\mathbf{b}_3. \tag{17}$$

To find the generalized forces, we can use the transformation matrix (13) and the following equation:

$$K_{q_i}=-mg\mathbf{a}_3\cdot\frac{\partial\mathbf{V}^G}{\partial\dot{q}_i}\ (i=2,3). \tag{18}$$

The generalized inertial forces can be found from the following equation:

$$K^*_{q_i}=\frac{\partial\mathbf{V}^G}{\partial\dot{q}_i}\cdot(-m\mathbf{a}^G)+\frac{\partial\omega}{\partial\dot{q}_i}\cdot(-\mathbf{I}\cdot\alpha-\omega\times\mathbf{I}\cdot\omega)\,(i=2,3) \tag{19}$$

where $\mathbf{I}$ is the central inertia dyadic of C, and its components are

$$I_1=\frac{3}{10}mr^2,\ I_2=I_3=\frac{3}{80}m(4r^2+h^2). \tag{20}$$

Using Kane's equation, we obtain the equation of motion of C as

$$(4h^2+r^2)\ddot{q}_2-(4h^2-r^2)\dot{q}_3^2\sin q_2\cos q_3=5gh\sin q_2 \tag{21}$$

$$[(4h^2+r^2)\sin^2 q_2+2r^2\cos^2 q_2]\ddot{q}_3 +2(4h^2-r^2)\dot{q}_2\dot{q}_3\sin q_2\cos q_2=0. \tag{22}$$

Remark 2

This example is intended to illustrate the use of Eqs. (3) and (7). However, these expressions are likely to be of greatest use with systems having more complex geometry, such as biosystem joints and large multibody systems.

Acknowledgment

A part of the research for this paper was supported by the National Science Foundation under grant MSS 8912521.

References

Huston, R. L., 1990, *Multibody Dynamics*, Butterworth-Heinemann, Boston, p. 46.

Kane, T. R., and Levinson, D. A., 1985, *Dynamics, Theory and Applications*, McGraw-Hill, New York, p. 16.

Kane, T. R., and Levinson, D. A., 1990, "Orthogonal Curvilinear Coordinates and Angular Velocities," ASME JOURNAL OF APPLIED MECHANICS, Vol. 57, pp. 468-470.

Downloaded 03 May 2010 to 171.66.16.247. Redistribution subject to ASME license or copyright; see http://www.asme.org/terms/Terms_Use.cfm

On Finite Twisting and Bending of Nonhomogeneous Anisotropic Elastic Plates

E. Reissner[8]

Introduction

In what follows, we utilize an intrinsic form of the equations for small finite deflections of plates, based on the original Kirchhoff displacement version rather than on the von Karman deflection-stress function version, in order to obtain generalizations of known exact solutions for the problem of twisting and bending of rectangular plates. This problem was first stated and solved, on the basis of von Karman's equations, for isotropic transversely homogeneous plates of constant thickness by Reissner (1957). Subsequently, solutions were obtained for isotropic plates of variable thickness of the symmetrical double-wedge type by Bisplinghoff (1957) and Simmonds (1958), and of the symmetrical lenticular type, independently by Mansfield (1959) and Simmonds (1958). A solution for orthotropic plates of constant thickness has been given by Chen (1974). We now consider anisotropic transversely nonhomogeneous plates with constitutive coupling of stretching and transverse bending and show that for this class of problems, it is again possible to effect a reduction of the problem to a system of two simultaneous linear second-order ordinary differential equations, with the significant nonlinear effects coming from the coefficients as well as from the right-hand sides of these equations.

In the present analysis, the boundary conditions at the loaded ends of the plate are, as before, prescribed in a global rather than in a local sense, so as to make possible a one-dimensional solution procedure. We complement our one-dimensional analysis by the statement of a two-dimensional problem with a suitable system of local boundary conditions, where it remains to establish that the one-dimensional result does in fact represent the interior portion of an asymptotic solution of the two-dimensional problem.

Differential Equations and Boundary Conditions

We begin with a statement of the equilibrium and strain displacement equations for small finite deflections in the form

$$N_{x,x}+N_{t,y}=0, \quad N_{t,x}+N_{y,y}=0 \tag{1}$$

$$M_{x,xx}+2M_{t,xy}+M_{y,yy}=N_x\kappa_x+N_y\kappa_y+N_t\kappa_t \tag{2}$$

$$\kappa_x=-w_{,xx}, \quad \kappa_y=-w_{,yy}, \quad \kappa_t=-2w_{,xy} \tag{3}$$

$$\epsilon_x=u_{,x}+\frac{1}{2}w_{,x}^2, \quad \epsilon_y=v_{,y}+\frac{1}{2}w_{,y}^2, \quad \epsilon_t=u_{,y}+v_{,x}+w_{,x}w_{,y}. \tag{4}$$

In this, x and y are coordinates in the undeflected midplane of the plate; N and M are midsurface parallel stress resultants and couples; u, v, and w are base plane parallel and perpendicular displacement components; and κ and ϵ are bending and stretching strains, respectively.

We here associate these equations with constitutive relations of the form

$$\{N_xN_yN_t\}=\mathbf{B}\{\epsilon_x\epsilon_y\epsilon_t\}+\mathbf{C}\{\kappa_x\kappa_y\kappa_t\} \tag{5}$$

$$\{M_xM_yM_t\}=\mathbf{C}\{\epsilon_x\epsilon_y\epsilon_t\}+\mathbf{D}\{\kappa_x\kappa_y\kappa_t\}. \tag{6}$$

For what follows it is of importance to transform the above system to an intrinsic form by deducing from the strain displacement relations (3) and (4) the three compatibility equations

$$2\kappa_{x,y}-\kappa_{t,x}=0, \quad 2\kappa_{y,x}-\kappa_{t,y}=0 \tag{7}$$

$$\epsilon_{x,yy}-\epsilon_{t,xy}+\epsilon_{x,yy}+\kappa_x\kappa_y-\frac{1}{4}\kappa_t^2=0. \tag{8}$$

The differential equation system (1), (2), and (5) to (8) is to be solved for a rectangular region $|x| \le a$, $|y| \le b$, with the edges $y = \pm b$ being traction-free and with the edges $x = \pm a$ acted upon by twisting moments T and transverse bending moments M.

In the statement of these boundary conditions, account must be taken of the nature of the *effective* transverse edge stress resultants

$$Q_x^e=Q_x+M_{t,y}=M_{x,x}+2M_{t,y} \tag{9a}$$

$$Q_y^e=Q_y+M_{t,x}=M_{y,y}+2M_{t,x} \tag{9b}$$

and of the transverse corner forces $2M_t(\pm a, \pm b)$, in accordance with Kirchhoff. The transverse corner forces are equivalent to base-plane perpendicular forces. The transverse resultants Q^e are distinct from base-plane perpendicular resultants P which are

$$P_x=Q_x^e+N_xw_{,x}+N_tw_{,y}, \quad P_y=Q_y^e+N_tw_{,x}+N_yw_{,y}. \tag{10}$$

The conditions for the traction-free edges are

$$y=\pm b; \quad N_y=N_t=P_y=0, \quad M_y=0 \tag{11}$$

and the conditions for the loaded edges are here stipulated to consist of three integrated moment conditions

$$x=\pm 0; \begin{cases} \int_{-b}^{b} N_x y dy=0, \ \int_{-b}^{b}(M_x+wN_x)dy=M \\ \int_{-b}^{b} P_x y dy-[2yM_t]_{-b}^{b}=T \end{cases} \tag{12}$$

and of three integrated force conditions

$$x=\pm 0; \int_{-b}^{b}(N_x,N_t,P_x)dy=(0,\ 0,\ [2M_t]_{-b}^{b}). \tag{13}$$

Remark. The analysis which follows turns out to be not applicable to the more general problem for which

$$\int_{-b}^{b} N_x dy=F, \quad \int_{-b}^{b} N_x y dy=M_s, \tag{14}$$

in place of the conditions with $F = 0$ and $M_s = 0$ in (12) and (13).

The One-Dimensional Semi-inverse Problem

We restrict attention to plates for which the elements of the constitutive matrices are independent of x and we attempt a solution of the given boundary value problem with stresses and strains also independent of x.

We then have, on the basis of (1) in conjunction with (11), and on the basis of (7),

$$N_y=N_t=0, \quad \kappa_x=k, \quad \kappa_t=2\theta \tag{15}$$

with k and θ as arbitrary constants.

With (15), and with the omission of all x-derivative terms, Eqs. (2) and (8) take on the form

$$M_y''=kN_x, \quad \epsilon_x''+k\kappa_y=\theta^2 \tag{16}$$

[8]Department of Applied Mechanics and Engineering Sciences, University of California-San Diego, La Jolla, CA 92093. Honorary Mem. ASME.

Manuscript received by the ASME Applied Mechanics Division, May 30, 1991; final revision, Oct. 17, 1991. Associate Technical Editor: J. G. Simmonds.

Copyright © 1992 by ASME
Downloaded 03 May 2010 to 171.66.16.247. Redistribution subject to ASME license or copyright; see http://www.asme.org/terms/Terms_Use.cfm

where the primes indicate differentiation with respect to y.

With P_y as in (10), and with (15) and (9b), the solution of (16) has to satisfy the boundary conditions

$$y=\pm b;\quad M_y=0,\quad M_y'=0. \tag{17}$$

Of the six global traction conditions in (12) and (13), the four homogeneous conditions are readily shown to be automatically satisfied on the basis of the contents of (16) and (17). The two remaining conditions may be transformed in a similar way, so as to come out in the intrinsic form

$$M=\int_{-b}^{b}(M_x-k^{-1}\kappa_y M_y)\,dy \tag{18}$$

$$T=-\int_{-b}^{b}(2M_t+2k^{-1}\theta M_y)\,dy. \tag{19}$$

In order to solve (16) and (17), for the purpose of determining M and T as functions of k and θ, use has to be made of a semi-inverted form of the constitutive Eqs. (5) and (6), in conjunction with (15), as follows:

$$\{N_x\kappa_y\}=\mathbf{J}\{\epsilon_x M_y\}+\mathbf{K}\{k\theta\} \tag{20}$$

$$\{M_x M_t\}=\mathbf{J}_M\{\epsilon_x M_y\}+\mathbf{K}_M\{k\theta\} \tag{21}$$

$$\{\epsilon_y\epsilon_t\}=\mathbf{J}_\epsilon\{\epsilon_x M_y\}+\mathbf{K}_\epsilon\{k\theta\}. \tag{22}$$

The last of these relations is needed only for the purpose of an eventual determination of the displacement components u and v in terms of the solution of the intrinsic problem.

Explicit Form of the Semi-inverse Problem Without Constitutive Coupling

With the stipulation of a vanishing **C**-matrix in (5) and (6), and with (15), we now have as constitutive relations

$$N_x=B_{xx}\epsilon_x+B_{xy}\epsilon_y+B_{xt}\epsilon_t \tag{23a}$$

$$0=B_{yx}\epsilon_x+B_{yy}\epsilon_y+B_{yt}\epsilon_t \tag{23b}$$

$$0=B_{tx}\epsilon_x+B_{ty}\epsilon_y+B_{tt}\epsilon_t \tag{23c}$$

where $B_{yx}=B_{xy}$, etc., and

$$M_x=D_{xx}k+D_{xy}\kappa_y+D_{xt}2\theta \tag{24a}$$

$$M_y=D_{yx}k+D_{yy}\kappa_y+D_{yt}2\theta \tag{24b}$$

$$M_t=D_{tx}k+D_{ty}\kappa_y+D_{tt}2\theta \tag{24c}$$

where $D_{yx}=D_{xy}$, etc.

The differential equations in (16) become two simultaneous equations for M_y and ϵ_x upon deducing from (23) that

$$N_x=B_x\epsilon_x,\quad B_x\equiv B_{xx}-\frac{B_{xy}^2B_{tt}+B_{xt}^2B_{yy}-2B_{xy}B_{xt}B_{yt}}{B_{yy}B_{tt}-B_{ty}^2}, \tag{25}$$

and upon writing (24b) in the form

$$\kappa_y=\frac{M_y}{D_{yy}}-\frac{D_{yx}k+D_{yt}2\theta}{D_{yy}}. \tag{26}$$

The elimination of ϵ_x then leaves as a fourth-order differential equation for M_y:

$$\left(\frac{M_y''}{B_x}\right)''+k^2\frac{M_y}{D_{yy}}=k\,\frac{D_{yx}k^2+2D_{yt}k\theta+D_{yy}\theta^2}{D_{yy}}. \tag{27}$$

The introduction of (26) into (24a, c) gives an expressions for M_x and M_t to be used in the determination of $M(k,\theta)$ and $T(k,\theta)$ on the basis of (18) and (19)

$$M_x=\left(D_{xx}-\frac{D_{xy}^2}{D_{yy}}\right)k+\left(D_{xt}-\frac{D_{xy}D_{yt}}{D_{yy}}\right)2\theta+\frac{D_{xy}}{D_{yy}}M_y \tag{28a}$$

$$M_t=\left(D_{xt}-\frac{D_{xy}D_{yt}}{D_{yy}}\right)k+\left(D_{tt}-\frac{D_{yt}^2}{D_{yy}}\right)2\theta+\frac{D_{yt}}{D_{yy}}M_y. \tag{28b}$$

Remark. The same for the orthotropic case, with $B_{xt}=B_{yt}=0$ and $D_{xt}=D_{yt}=0$, we have that (27) is an equation with constant coefficients for plates with constant values of the constitutive coefficients.

The same for the isotropic case in Mansfield (1959) and Simmonds (1958), it is found that for lenticular cross-section plates with

$$B=B_o\left(1-\frac{y^2}{b^2}\right),\ D=D_o\left(1-\frac{y^2}{b^2}\right)^3, \tag{29}$$

Eq. (27) has the particular solution

$$M_{yp}=M_{ypo}\left(1-\frac{y^2}{b^2}\right)^3 \tag{30a}$$

where now

$$M_{ypo}=k\,\frac{B_{xo}b^4}{60D_{yyo}}\,\frac{D_{yxo}k^2+2D_{yto}k\theta+D_{yyo}\theta^2}{1+k^2B_{xo}b^4/60D_{yyo}}. \tag{30b}$$

For this case the solution of the homogeneous Eq. (27) is not needed, inasmuch as M_{yp} by itself satisfies (17).

A Local Boundary Value Problem

The physical significance of the one-dimensional solution of the problem with the global boundary conditions (12) and (13) depends on its being an asymptotic interior solution portion, for sufficiently small values of b/a, of a suitably stated problem with all boundary conditions of the local kind. Inasmuch as this aspect of the problem has not been discussed in the previous literature, we here formulate a system of local boundary conditions for an eventual use in conjunction with an asymptotic analysis of the two-dimensional problem.

We replace the global conditions on N_x and N_t in (12) and (13) by the two local conditions:

$$x=\pm a;\ N_x=N_t=0. \tag{31}$$

Given that the expressions for κ_x and κ_t in (15) imply that $w=W(y)-1/2\,kx^2-\theta xy$, we replace the global conditions on M_x, P_x, and M_t in (12) and (13) by two local conditions:

$$x=\pm a;\ w=-\frac{1}{2}ka^2\mp\theta ay,\ w_{,x}=\mp ka-\theta y. \tag{32}$$

It remains to be established that the boundary value problem with (31) and (32) in place of (12) and (13) does in fact have a solution which asymptotically coincides with the solution of the one-dimensional problem, except in zones of order b adjacent to the edges $x=\pm a$.

Summary

An intrinsic version of Kirchhoff's equations for small finite deflections of elastic plates, together with an appeal to St. Venant's principle, is used to obtain a one-dimensional form of the problem of twisting and bending of transversely nonhomogeneous anisotropic plates. This is complemented by a consideration concerning the analysis which is required to establish this one-dimensional result as the interior portion of an asymptotic solution of the two-dimensional problem, with local instead of global loading conditions.

References

Bisplinghoff, R. L., 1957, "The Finite Twisting and Bending of Heated Elastic Lifting Surfaces," D.Sc. Dissertation, Zurich Institute of Technology.

Chen, C. H. S., 1974, "Finite Twisting and Bending of Thin Rectangular Orthotropic Plates," ASME JOURNAL OF APPLIED MECHANICS, Vol. 41, pp. 315–316.

Downloaded 03 May 2010 to 171.66.16.247. Redistribution subject to ASME license or copyright; see http://www.asme.org/terms/Terms_Use.cfm

Mansfield, E. H., 1959, "The Large-Deflection Behavior of a Thin Strip of Lenticular Section," *Quarterly Journal of Mechanics and Applied Mathematics*, Vol. 12, pp. 421–430.

Reissner, E., 1957, "Finite Twisting and Bending of Thin Rectangular Plates," ASME JOURNAL OF APPLIED MECHANICS, Vol. 24, pp. 391–396.

Simmonds, J. G., 1958, "Finite Bending and Twisting of Thin Wings," B.S. and M.S. Thesis, Massachusetts Institute of Technology, Cambridge, MA.

Small Vibrations of Rotating Ring Segments and Full Rings Under External or Internal Pressure

Christoph Pelchen[9] and Jörg Wauer[9,10]

The combined effect of a radial pressure load and a centrifugal field on the vibrations of an inextensible, circular, slender ring structure is treated. First, the stationary pre-buckling state of the segment or the full ring is specified. Then small oscillations about this configuration are investigated. The variations of vibration frequencies with the pressure load and the speed rate are examined and possible buckling loads are determined.

1 Introduction

The dynamics of inextensible ring or membrane structures under various loading conditions has recently been studied by Wang (1984), Wauer (1987), Plaut and Leeuwrik (1988), and Plaut and Fagan (1988). Since most of these papers need more or less significant corrections, the problem will be discussed once more. The investigation is focussed on circular members under uniform radial pressure so that in the case of an inextensible structure, the cross-sectional "equilibrium" shape remains unchanged, i.e., circular.

In the present paper, linear in-plane vibrations are considered. The governing nonlinear equations of motion are formulated in Section 2. The quasi-static analysis is described in Section 3, and the equations of motion for small oscillations about the stationary configuration are generated in Section 4. Finally, the solution procedure and numerical results are presented in Section 5.

2 Formulation

Consider an inextensible circular ring segment or full ring with radius R, shown in Fig. 1. In the case of the segment with opening angle $\alpha < 2\pi$, the ends are simply supported (see Fig. 1(*a*)), while for the full ring (see Fig. 1(*b*)), a special anchorage is not necessary. The elastica with mass per unit length μ has bending stiffness EI and rotates about the central axis with a constant angular velocity ω. The rotational axis is vertical so that weight influences do not appear if out-of-plane motions are avoided. The gauge pressure p_0 (force/length) is assumed to be positive when it acts externally.

In order to analyze motion of the structure in the horizontal plane, a rotating coordinate system, ξ, η is introduced. The arc length measured from the ξ-axis is s and the angle between a line parallel to the η-axis and the tangent to the ring element lying in its undeformed reference configuration between s and

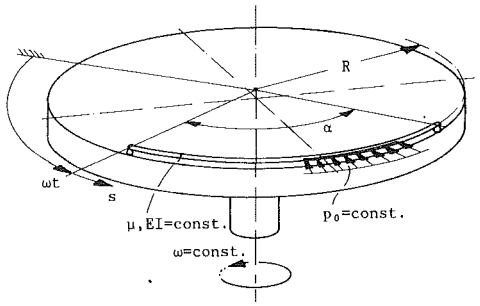


Fig. 1(*a*) Ring segment

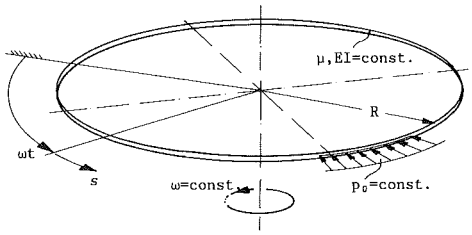


Fig. 1(*b*) Full ring

Fig. 1 Rotating structure

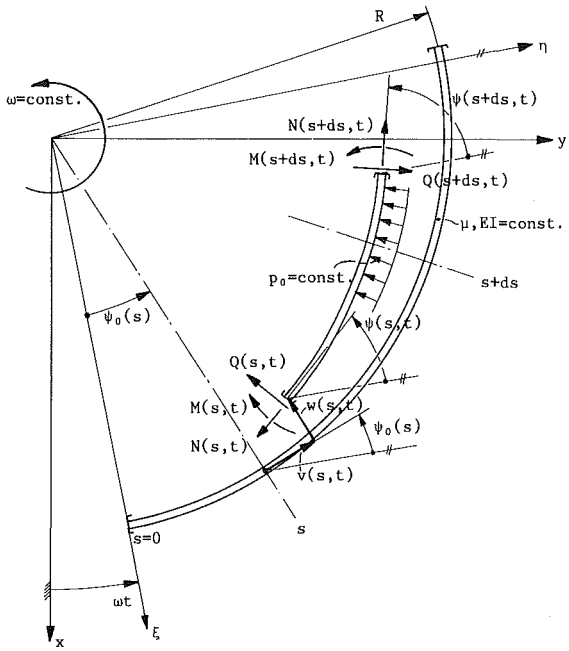


Fig. 2 Element of structure during motion

$s + ds$ is $\psi_0 = s/R$. Consider the deformed element (Fig. 2) with the angle ψ of the ring tangent in its actual position, the reactions (normal force N, shear force Q, bending moment M), and displacements v, w (measured in the tangential and normal direction, respectively, of the circular reference configuration), which are all functions of arc length s and time t. Using the well-known relations between Q, M, and ψ,

$$Q = M_s = EI\psi_{ss},\ M = EI(\psi_s - \psi_{0,s}), \tag{1}$$

a local balance of forces yields the governing equations of motion:

$$EI\psi_{ss}\psi_s\cos(\psi-\psi_0) + EI\psi_{sss}\sin(\psi-\psi_0) + N_s\cos(\psi-\psi_0) - \psi_s N\sin(\psi-\psi_0) - \mu v_{tt} + \mu\omega^2 v + 2\mu\omega w_t - p_0\sin(\psi-\psi_0) = 0, \tag{2a}$$

[9]Institut für Technische Mechanik, Universität Karlsruhe, W-7500 Karlsruhe 1, Federal Republic of Germany.

[10]To whom correspondence should be addressed.

Manuscript received by the ASME Applied Mechanics Division, Feb. 14, 1991; final revision, Nov. 12, 1991. Associate Technical Editor: D. J. Inman.

Downloaded 03 May 2010 to 171.66.16.247. Redistribution subject to ASME license or copyright; see http://www.asme.org/terms/Terms_Use.cfm

Mansfield, E. H., 1959, "The Large-Deflection Behavior of a Thin Strip of Lenticular Section," *Quarterly Journal of Mechanics and Applied Mathematics*, Vol. 12, pp. 421–430.

Reissner, E., 1957, "Finite Twisting and Bending of Thin Rectangular Plates," ASME JOURNAL OF APPLIED MECHANICS, Vol. 24, pp. 391–396.

Simmonds, J. G., 1958, "Finite Bending and Twisting of Thin Wings," B.S. and M.S. Thesis, Massachusetts Institute of Technology, Cambridge, MA.

Small Vibrations of Rotating Ring Segments and Full Rings Under External or Internal Pressure

Christoph Pelchen[9] and Jörg Wauer[9,10]

The combined effect of a radial pressure load and a centrifugal field on the vibrations of an inextensible, circular, slender ring structure is treated. First, the stationary pre-buckling state of the segment or the full ring is specified. Then small oscillations about this configuration are investigated. The variations of vibration frequencies with the pressure load and the speed rate are examined and possible buckling loads are determined.

1 Introduction

The dynamics of inextensible ring or membrane structures under various loading conditions has recently been studied by Wang (1984), Wauer (1987), Plaut and Leeuwrik (1988), and Plaut and Fagan (1988). Since most of these papers need more or less significant corrections, the problem will be discussed once more. The investigation is focussed on circular members under uniform radial pressure so that in the case of an inextensible structure, the cross-sectional "equilibrium" shape remains unchanged, i.e., circular.

In the present paper, linear in-plane vibrations are considered. The governing nonlinear equations of motion are formulated in Section 2. The quasi-static analysis is described in Section 3, and the equations of motion for small oscillations about the stationary configuration are generated in Section 4. Finally, the solution procedure and numerical results are presented in Section 5.

2 Formulation

Consider an inextensible circular ring segment or full ring with radius R, shown in Fig. 1. In the case of the segment with opening angle $\alpha < 2\pi$, the ends are simply supported (see Fig. 1(*a*)), while for the full ring (see Fig. 1(*b*)), a special anchorage is not necessary. The elastica with mass per unit length μ has bending stiffness EI and rotates about the central axis with a constant angular velocity ω. The rotational axis is vertical so that weight influences do not appear if out-of-plane motions are avoided. The gauge pressure p_0 (force/length) is assumed to be positive when it acts externally.

In order to analyze motion of the structure in the horizontal plane, a rotating coordinate system, ξ, η is introduced. The arc length measured from the ξ-axis is s and the angle between a line parallel to the η-axis and the tangent to the ring element lying in its undeformed reference configuration between s and

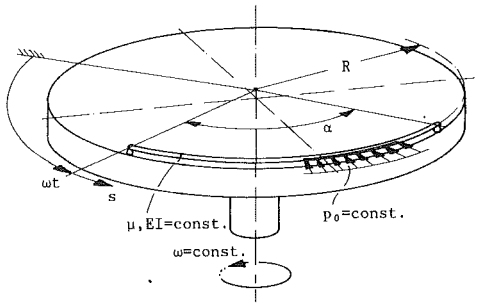


Fig. 1(*a*) Ring segment

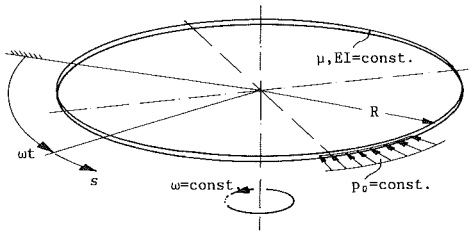


Fig. 1(*b*) Full ring

Fig. 1 Rotating structure

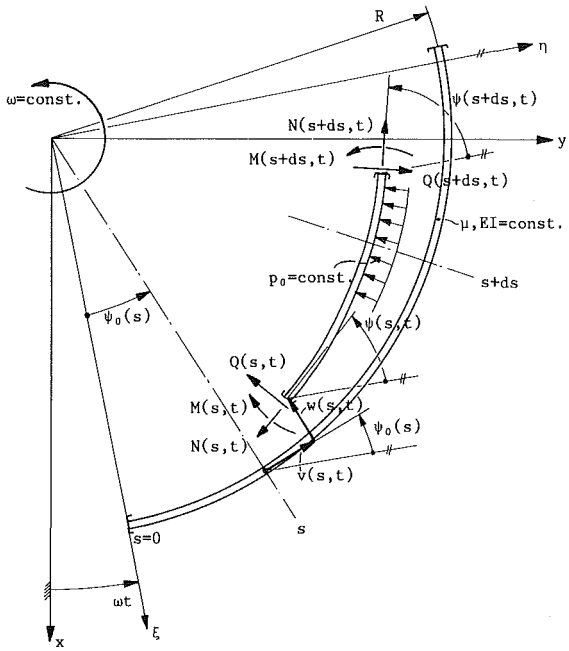


Fig. 2 Element of structure during motion

$s + ds$ is $\psi_0 = s/R$. Consider the deformed element (Fig. 2) with the angle ψ of the ring tangent in its actual position, the reactions (normal force N, shear force Q, bending moment M), and displacements v, w (measured in the tangential and normal direction, respectively, of the circular reference configuration), which are all functions of arc length s and time t. Using the well-known relations between Q, M, and ψ,

$$Q = M_s = EI\psi_{ss},\ M = EI(\psi_s - \psi_{0,s}), \tag{1}$$

a local balance of forces yields the governing equations of motion:

$$EI\psi_{ss}\psi_s\cos(\psi-\psi_0) + EI\psi_{sss}\sin(\psi-\psi_0) + N_s\cos(\psi-\psi_0) - \psi_s N\sin(\psi-\psi_0) - \mu v_{tt} + \mu\omega^2 v + 2\mu\omega w_t - p_0\sin(\psi-\psi_0) = 0, \tag{2a}$$

[9]Institut für Technische Mechanik, Universität Karlsruhe, W-7500 Karlsruhe 1, Federal Republic of Germany.

[10]To whom correspondence should be addressed.

Manuscript received by the ASME Applied Mechanics Division, Feb. 14, 1991; final revision, Nov. 12, 1991. Associate Technical Editor: D. J. Inman.

Copyright © 1992 by ASME
Downloaded 03 May 2010 to 171.66.16.247. Redistribution subject to ASME license or copyright; see http://www.asme.org/terms/Terms_Use.cfm

$$EI\psi_{ss}\psi_s\sin(\psi-\psi_0)-EI\psi_{sss}\cos(\psi-\psi_0)+N_s\sin(\psi-\psi_0)$$
$$+\psi_s N\cos(\psi-\psi_0)-\mu w_{tt}-\mu\omega^2(R-w)$$
$$-2\mu\omega v_t+p_0\cos(\psi-\psi_0)=0. \quad (2b)$$

Subscripts s and t denote derivatives with respect to s and t, respectively. For the ring segment, boundary conditions have to be added, i.e.,

$$v(0,t)=w(0,t)=\psi_s(0,t)=v(R\alpha,t)=w(R\alpha,t)=\psi_s(R\alpha,t)=0, \quad (3)$$

while for the full ring, conditions of periodicity have to be fulfilled:

$$v(0,t)=v(2\pi R,t),\ w(0,t)=w(2\pi R,t),\ \psi(0,t)=\psi(2\pi R,t),$$
$$N(0,t)=N(2\pi R,t),\ \psi_s(0,t)=\psi_s(2\pi R,t),\ \psi_{ss}(0,t)=\psi_{ss}(2\pi R,t). \quad (4)$$

The assumption of inextensibility is formulated by using the so-called Lagrangian strain ϵ to vanish (Pelchen and Wauer, 1991):

$$\epsilon=(v_s-w/R)+(v_s-w/R)^2/2+(v/R+w_s)^2/2=0. \quad (5)$$

Finally, the dynamic curvature, ψ_s, can be calculated in the form (Pelchen and Wauer, 1991)

$$\psi_s=1/R+(w_{ss}+v_s/R)(1+v_s-w/R)$$
$$-(v_{ss}-w_s/R)(w_s+v/R). \quad (6)$$

The system of Eq. (2)–(6) is different from that used in Plaut and Leeuwrik (1988) and Plaut and Fagan (1988), apparently due to an incorrect evaluation with respect to the nonlinear parts in their expressions for dynamic curvature and inextensibility, and in Wang (1984), where Coriolis forces were not included. Obviously, in Plaut and Leeuwrik (1988) it cannot be clearly distinguished between the actual and reference configuration.

3 Quasi-static Analysis

Since the deformation are measured in the body-fixed rotating frame, for the nonvibrating, stationary pre-buckling state of the rotating preloaded structure (p_0, $\omega \neq 0$), all time derivatives in the equations of motion (2) vanish. Due to the condition of inextensibility (5), the deformations $v = v_0$, $w = w_0$ vanish so that the original shape (which is circular) remains unchanged. It follows that the curvature retains its natural value, $\psi_s = \psi_{0,s} = 1/R$ (and bending moments and shear forces do not occur). The first equation of motion, (2*a*), simplifies to

$$N_{0,s}=0, \text{ i.e., } N_0=\text{const.} \quad (7)$$

and then (2*b*) gives

$$N_0=-p_0R+\mu\omega^2R^2. \quad (8)$$

4 Small Vibrations

To generate the governing equations of motion, the dependent variables are perturbed about the stationary state determined in Section 3:

$$v(s,t)=\Delta v(s,t),\ w(s,t)=\Delta w(s,t),$$
$$\psi(s,t)=\psi_0+\Delta\psi(s,t)\rightarrow\psi_s(s,t)=1/R+\Delta\psi_s(s,t),$$
$$\psi_{ss}(s,t)=\Delta\psi_{ss}(s,t),$$
$$N(s,t)=N_0+\Delta N(s,t). \quad (9)$$

After some algebra, Eqs. (2) are linearized to

$$EI\Delta\psi_{ss}/R+\Delta N_s-\mu\omega^2R\Delta\psi-\mu\Delta v_{tt}+\mu\omega^2\Delta v+2\mu\omega\Delta w_t=0, \quad (10a)$$

$$-EI\Delta\psi_{sss}+\Delta N/R+(\mu\omega^2R^2-p_0R)\Delta\psi_s-\mu\Delta w_{tt}$$
$$+\mu\omega^2\Delta w-2\mu\omega\Delta v_t=0. \quad (10b)$$

The boundary conditions (3) or conditions of periodicity (4) remain unchanged if all dependent variables are replaced by Δ-quantities. The linearized assumption of inextensibility reads

$$\Delta v_s-\Delta w/R=0 \quad (11)$$

and the perturbation of the curvature is

$$\Delta\psi_s=\Delta w_{ss}+\Delta v_s/R. \quad (12)$$

To solve the obtained boundary value problem (10), (3) (or (4)), (11), and (12), the most straightforward way is to rewrite it as a single differential equation for Δv and corresponding boundary conditions or conditions of periodicity. For that purpose, differentiate (10*b*) with respect to s and subtract it from (10*a*). In this way, the tension ΔN is eliminated. Then, replace Δw, $\Delta\psi_s$ according to (11) and (12) by Δv-quantities and, finally, introduce the following nondimensional quantities:

$$\tau=\omega_0 t\left(\omega_0^2=\frac{EI_0}{\mu R^4}\right),\ \beta_0=\frac{p_0R^3}{EI_0},\ \gamma=\frac{EI}{EI_0},\ \Omega=\frac{\omega}{\omega_0} \quad (13)$$

where EI_0 is a reference rigidity. This leads to the governing equation of motion in the form

$$\Delta\ddot{v}-\Delta v''-4\Omega\Delta\dot{v}'+3\Omega^2\Delta v''+\Omega^2\Delta v''''-\beta_0(\Delta v''''+\Delta v'')$$
$$-\gamma(\Delta v''''''+2\Delta v''''+\Delta v'')=0 \quad (14)$$

where $\dot{} = \partial/\partial\tau$, $' = \partial/\partial\psi_0$. In the corresponding boundary conditions (3) or conditions or periodicity (4) applied for Δ-quantities, the linearized relations (11) and (12) are also used so that the equation of motion (14) is completed by

$$\Delta v(0,\tau)=\Delta v'(0,\tau)=\Delta v'''(0,\tau)=0,$$
$$\Delta v(\alpha,\tau)=\Delta v'(\alpha,\tau)=\Delta v'''(\alpha,\tau)=0, \quad (15)$$

for a ring segment and

$$\Delta v(0,\tau)=\Delta v(2\pi,\tau),\ \ldots,\ \Delta v''''(0,\tau)=\Delta v''''(2\pi,\tau) \quad (16)$$

for the full ring. By choosing EI_0 appropriately, both a ring (or a shell) with bending stiffness and a chain (or a membrane) without bending stiffness can be discussed. In the first case $\gamma = 1$ can be chosen, while in the second case, $\gamma = 0$. For a membrane structure, the order of the differential Eq. (14) reduces from six to four so that in (15), the conditions for $\Delta v'''$ and in (16) for $\Delta v''''$, $\Delta v''''$ have to be dropped.

The boundary value problem (14), (16)—especially the field equation—is the same as that derived by Wauer (1987) as a limiting case of an extensible ring, except that the dependent variable there is the normal displacement rather than the tangential displacement. In that way, it is verified that in a linear analysis, the elastica theory, and the classical theory of elasticity can generate the same final results. For a nonrotating cylindrical membrane with negligible bending stiffness, the boundary value problem takes the form derived by Plaut and Fagan (1988). It follows that for the study of small vibrations within a linear theory, the distinction between the actual and the reference configuration has no consequences.

5 Results

First, the full ring is considered for which the computation of the eigenfrequencies performed in Wauer (1987) is fairly simple. Assume a solution in the form

$$\Delta v(\psi_0,\tau)=A\,e^{i(n\psi_0+\lambda\tau)},\quad n=2,3,\ldots,\infty \quad (17)$$

satisfying all conditions of periodicity (16), and substitute it into the equation of motion (14). This yields a quadratic characteristic equation which can be solved to give

$$\lambda_{n1},\ \lambda_{n2}=\frac{2n\Omega}{n^2+1}\pm\left\{\frac{n^2(n^2-1)^2}{n^2+1}\left(\gamma+\frac{\Omega^2}{n^2+1}\right)\right.$$
$$\left.-\frac{n^2(n^2-1)}{n^2+1}\beta_0\right\}^{1/2}. \quad (18)$$

Downloaded 03 May 2010 to 171.66.16.247. Redistribution subject to ASME license or copyright; see http://www.asme.org/terms/Terms_Use.cfm

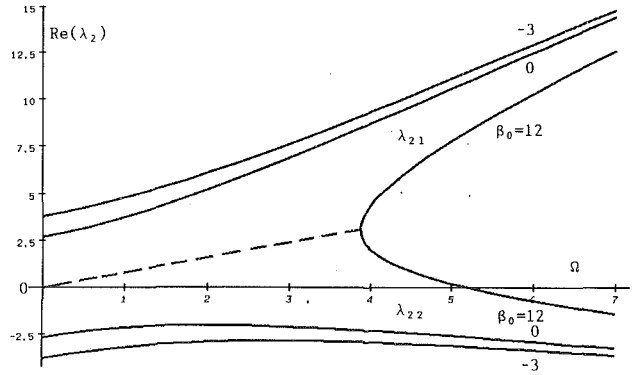


Fig. 3 Eigenvalues of second order versus speed for a full ring

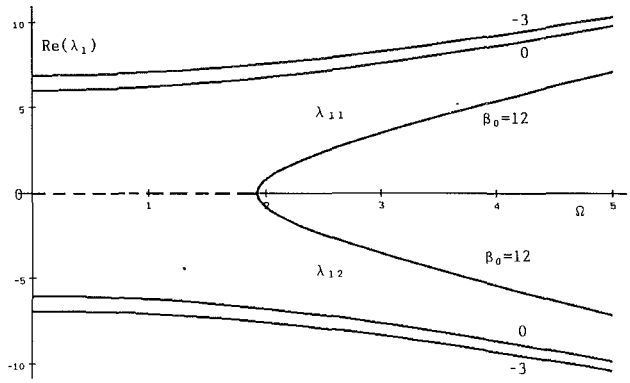


Fig. 4 Lowest eigenvalues versus speed for a semi-circular ring segment

For three different load parameters β_0, Fig. 3 shows the real part of the two eigenvalues (i.e., the nondimensional vibration frequencies) of second order λ_{21}, λ_{22} (most likely) versus speed Ω for a ring where $\gamma = 1$. It documents—in contrast to Wang (1984) omitting the Coriolis forces and also to Wauer (1987) in which the evaluation of (18) is not correct—that for $\Omega \neq 0$, buckling occurs in the form of a flutter instability. The stability boundary is characterized by a point at which the two eigenvalues λ_{n1} and λ_{n2}, originally (for high speed) purely real, coalesce and bifurcate again (in a form that then the real part remains positive and the absolute value of the imaginary part increases if the speed decreases furthermore). The critical (external) pressure can be determined by a vanishing radicand in (18), and this leads to the n-fold buckling load

$$\beta_{0,\text{crit}}^{(n)} = n^2 - 1 + \frac{n^2-1}{n^2+1}\,\Omega^2, \quad n \geq 2. \tag{19}$$

Rotation increases the critical pressure and this increase is not the same as predicted by Wang (1984). For twofold buckling (most likely), the critical pressure increases by three-fifths of the centrifugal force:

$$\beta_{0,\text{crit}}^{(2)} = 3 + \frac{3}{5}\,\Omega^2. \tag{20}$$

For a chain (or a membrane), if the rigidity vanishes ($\gamma = 0$), the criterion for n-fold buckling is

$$\beta_{0,\text{crit}}^{(n)} = \frac{n^2-1}{n^2+1}\,\Omega^2, \; n \geq 2. \tag{21}$$

Also, for a segment, an exact characteristic equation can be derived. Modifying the solution (17) and replacing the integral exponent by a number κ (complex in general) leads (applying (14) and (15)) to the characteristic equation in the form of a vanishing determinant

$$\begin{vmatrix} 1 & 1 & \cdots & 1 \\ \kappa_1 & \kappa_2 & \cdots & \kappa_6 \\ \kappa_1^2 & \kappa_2^2 & \cdots & \kappa_6^2 \\ e^{i\kappa_1\alpha} & e^{i\kappa_2\alpha} & \cdots & e^{i\kappa_6\alpha} \\ \kappa_1 e^{i\kappa_1\alpha} & \kappa_2 e^{i\kappa_2\alpha} & \cdots & \kappa_6 e^{i\kappa_6\alpha} \\ \kappa_1^2 e^{i\kappa_1\alpha} & \kappa_2^2 e^{i\kappa_2\alpha} & \cdots & \kappa_6^2 e^{i\kappa_6\alpha} \end{vmatrix} = 0 \tag{22}$$

where κ_j are the roots κ of the equation

$$\gamma\kappa^6 + (\Omega^2 - \beta_0 - 2\gamma)\kappa^4 + (\beta_0 - \lambda^2 - 3\Omega^2 + \gamma)\kappa^2 + 4\Omega\lambda\kappa - \lambda^2 = 0. \tag{23}$$

For a chain (or a membrane), in (22) the third and the sixth row and column have to be cancelled and, due to $\gamma = 0$ in (23), the polynomial in κ is again of fourth order. To avoid a numerical solution of (23), Galerkin s method is applied. For a one-term approximation, let

$$\Delta v(\psi_0, \tau) = e^{i\lambda_1\tau}\sin^j \pi\psi_0/\alpha, \quad j = 2(\gamma = 0) \text{ or } 4(\gamma = 1) \tag{24}$$

so that all corresponding boundary conditions (15) are satisfied. Equation (24) is substituted into the left side of (14), and the result is multiplied by $\sin^j \pi\psi_0/\alpha$, integrated from $\psi_0 = 0$ to $\psi_0 = \alpha$, and set equal to zero. This yields the algebraic equation

$$\lambda_1^2\left\{\frac{35}{128} + \frac{5}{8}\left(\frac{\pi}{\alpha}\right)^2\right\}\left(\frac{\alpha}{\pi}\right)^2 = \left\{\frac{5}{8} - 8\left(\frac{\pi}{\alpha}\right)^2 + 40\left(\frac{\pi}{\alpha}\right)^4\right\} + \left\{\frac{5}{8} - 4\left(\frac{\pi}{\alpha}\right)^2\right\}\beta_0 + \left\{4\left(\frac{\pi}{\alpha}\right)^2 - \frac{15}{8}\right\}\Omega^2 \tag{25}$$

for a ring and

$$\lambda_1^2\left\{\frac{3}{8} + \frac{1}{2}\left(\frac{\pi}{\alpha}\right)^2\right\}\left(\frac{\alpha}{\pi}\right)^2 = \left\{\frac{1}{2} - 2\left(\frac{\pi}{\alpha}\right)^2\right\}\beta_0 + \left\{2\left(\frac{\pi}{\alpha}\right)^2 - \frac{3}{2}\right\}\Omega^2 \tag{26}$$

for a chain (or a membrane) to compute the lowest eigenvalue λ_1^2. The accuracy seems to be excellent. For a nonrotating membrane ($\gamma = 0$), a quantitative comparison can be drawn. It shows that for an opening angle $0 \leqq \alpha \leqq 3\,\pi/2$, the approximate eigenvalue, λ_1^2 (26), and the numerical solution of the corresponding exact characteristic equation, given by Plaut and Fagan (1988), differ by not more than one percent. For $\alpha = \pi$, for instance, in the work of Plaut and Fagan (1988), the lowest eigenvalue is listed as $\lambda_1^2 = -1.70\beta_0$, while here Galerkin s method yields $\lambda_1^2 = -1.71\beta_0$.

Also, for $\alpha = \pi$ in Fig. 4, the real part of the eigenvalues λ_{11}, λ_{12} versus speed Ω is depicted for a ring segment ($\gamma = 1$). It corresponds to Fig. 3 and shows that in the case of the segment, buckling occurs in the form of a divergence instability. The reason is that the eigenvalues λ_{11} and λ_{12} coalesce at a point where the real part vanishes and remains zero if the eigenvalue branches bifurcate again. The critical load can be found setting $\lambda_1 = 0$ in (25) (or (26)). For $\alpha = \pi$, one obtains

$$\beta_{0,\text{crit}} = (261 + 17\Omega^2)/27. \tag{27}$$

Similar to the case of a full ring, rotation increases the critical pressure.

References

Pelchen, Ch., and Wauer, J., 1990, "On the Dynamics of Rotating Circular Cable Structures," *Non-linear Dynamics*, Vol. 1, pp. 421-432.

Plaut, R. H., and Fagan, T. D., 1988, "Vibrations of an Inextensible, Air-Inflated, Cylindrical Membrane," ASME JOURNAL OF APPLIED MECHANICS, Vol. 55, pp. 672-675.

Plaut, R. H., and Leeuwrik, M. G., 1988, "Non-linear Oscillations of an Inextensible, Air-Inflated, Cylindrical Membrane," *Int. J. Non-linear Mechanics*, Vol. 23, pp. 347-353.

Wang, C. Y., 1984, "Stability of a Rotating Ring Under External Pressure," ASME JOURNAL OF APPLIED MECHANICS, Vol. 51, pp. 439-440.

Wauer, J., 1987, "Stabilität dünner rotierender Kreisringe unter radialem Druck," *ZAMM*, Vol. 67, pp. T159-161.

Downloaded 03 May 2010 to 171.66.16.247. Redistribution subject to ASME license or copyright; see http://www.asme.org/terms/Terms_Use.cfm

Axisymmetric Vibrations of Layered Tapered Plates

P. V. Navaneethakrishnan[11,13], K. Chandrasekaran[12,13], and N. Ravisrinivas[14]

1 Introduction

In a previous paper by Navaneethakrishnan and Chandrasekaran (1989), the axisymmetric free vibrations of layered annular plates were studied using a spline function approach. The thickness of each layer, and hence of the plate, was proportional to the distance of the point considered from the center of the plate. In practice, however, plates with more general linear variation in thickness are also abundantly used. For this reason, this paper extends such a study to the vibrations of annular layered plates whose thickness anywhere varies as the radial distance from an arbitrary concentric circle.

2 Formulation

The section of the plate considered is shown in Fig. 1. Each layer is assumed to behave macroscopically as a homogeneous orthotropic and linearly elastic one. Shear deformation and rotary inertia are neglected. The plate is so thin that the angular shifting of the axes of material symmetry of each layer due to the linear variation in thickness is considered to be negligible. The material axes of symmetry of the layers can therefore be taken to be parallel to the principal coordinate lines of the reference surface. The layers are assumed to be perfectly bonded at the interfaces. The inner and the outer radii of the plate are a and b. The bounding surfaces of all layers when extended are assumed to meet along a concentric circle of radius c. The plane of this circle is the reference surface. In Fig. 1, the section of this reference surface is the line $00'$. The thickness of the kth layer of the plate at any point at distance x from center is given by

$$(h_k)_x = \frac{x-c}{a-c}(h_k)_a, \quad ((h_k)_a \neq 0). \tag{1}$$

Note that (i) when $c = 0$, the thickness is proportional to the distance from center and (ii) when $c \to \infty$, each layer assumes a constant thickness, viz., the thickness at the inner edge. Note also that we must have $c > b$, or $\ll a$, in order to avoid zero and large thicknesses.

Proceeding in the same way as in the paper by Navaneethakrishnan and Chandrasekaran (1989), equations of vibration of the plate in terms of the radial and normal reference surface displacement components $U(x)$ and $W(x)$ are obtained in the form

$$\begin{bmatrix} L_{11} & L_{13} \\ L_{31} & L_{33} \end{bmatrix} \begin{Bmatrix} U \\ W \end{Bmatrix} = \begin{Bmatrix} 0 \\ 0 \end{Bmatrix} \tag{2}$$

in which L_{ij} are differential operators fully described in the Appendix. The $U'''(x)$ term is eliminated as before and the following cubic and quintic spline functions are assumed:

$$U^*(X) = \sum_{i=0}^{2} a_i X^i + \sum_{i=0}^{N-1} b_i (X - X_i)^3 H(X - X_i)$$

$$W^*(X) = \sum_{i=0}^{4} c_i X^i + \sum_{i=0}^{N-1} d_i (X - X_i)^5 H(X - X_i) \tag{3}$$

where $H(X)$ is a Heaviside step function and $X = x/a \in [0, 1]$.

Imposing the condition that $U^*(X)$ and $W^*(X)$ coincide with $U(X)$ and $W(X)$ of Eq. (2), at the points $X = X_s$, $s = 0, 1, 2, \ldots, N$, we have $2N + 2$ field equations in the $2N + 8$ coefficients of the splines assumed in Eqs. (3).

The boundary conditions imposed on the inner and outer edges are: (i) both the edges clamped ($C - C$), (ii) both the edges hinged ($H - H$), and (iii) the inner edge clamped and the outer edge free ($C - F$). Each of these sets gives six more equations, which together with the field equations, give rise to a generalized eigenvalue problem. This is solved for the values of an eigenfrequency parameter λ defined by

$$\lambda = l\omega \sqrt{\frac{R_o}{A_{11}}} \tag{4}$$

where l is the width ($b - a$) of the plate, ω is the circular frequency of vibration, R_o is the inertial coefficient, and A_{11} is the extensional elastic coefficient of a plate of constant thickness, equal to the thickness at the inner edge. The corresponding eigenvectors are also computed from which the mode shapes of vibration are constructed.

The other parameters used are: the radii ratio $\beta = a/b$, the thickness-radius ratio at the inner edge $\gamma = h_a/a$, the relative layer thickness $\delta_k = (h_k)_a/h_a$, and the taper parameter $\tau = h_a/h_b$. When there are only two layers we call $\delta_1 = \delta$, ($\delta_2 = 1 - \delta$).

3 Numerical Results and Discussion

Based on convergence studies, it was found sufficient to take $N = 10$ for numerical computations. Since the influence of coupling between extension and bending is most significant only for two-layered elements, the discussion is confined to vibrations of only two-layered plates.

Tapering of the plate affects the frequency parameter values significantly. Figures 2(a), (b) pertain to Steel-S Glass Epoxy (St-SGE) and High Strength Graphite Epoxy-S Glass Epoxy (HSG-SGE) layered plates. Their inner and outer boundaries are held fixed. All parameters excepting τ have constant values as shown. Each diagram consists of two parts: one in which τ varies from 0.1 to 1; and the other in which $1/\tau$ varies from 1 to 0.1. They have been pieced together so as to offer a wholesome picture of the phenomenon for a continuous variation of τ. It is seen that λ's have high values at $\tau = 0.1$. This is in keeping with the fact that the smaller is the value of τ, larger is the thickness at the outer edge, resulting in higher stiffness. (The thickness at the inner edge can be imagined to be constant, since γ is constant.) As $\tau \to 1$ (constant thickness), the curves are almost straight. The point $\tau = 1$ seems to be a point of inflexion. With further increase in τ, λ's decrease further, attaining minimum values at $1/\tau = 0.1$. This phenomenon is commonly found for all modes of vibration for plates under C-C and H-H conditions. These are in agreement with the observations on homogeneous plates made by Raju et al. (1974).

The behavior of HSG-SGE and St-SGE plates under H-H conditions (Fig. 2(c)) with respect to τ is similar to what was observed under C-C conditions. Figure 2(d) shows that for the same plates, now under C-F conditions, the λ-τ curves exhibit different characteristics. The values of λ_1 for the two plates considered tend to increase as $\tau \to 10$, whereas, near τ

[11]Professor of Mathematics.
[12]Professor of Mechanical Engineering.
[13]College of Engineering, Anna University, Madras 600 025, India.
[14]Department of Mechanical Engineering, The University of Texas at Austin, Austin, TX 78713.

Manuscript received by the ASME Applied Mechanics Division, Aug. 23, 1990; final revision, June 19, 1991. Associate Technical Editor: P. D. Spanos.

Copyright © 1992 by ASME
Downloaded 03 May 2010 to 171.66.16.247. Redistribution subject to ASME license or copyright; see http://www.asme.org/terms/Terms_Use.cfm

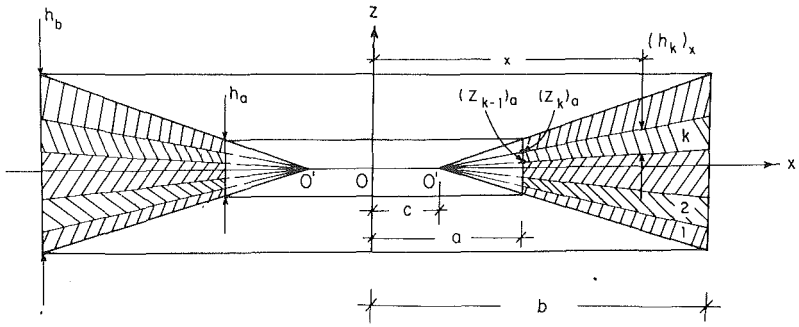


Fig. 1 Geometry of layered plate

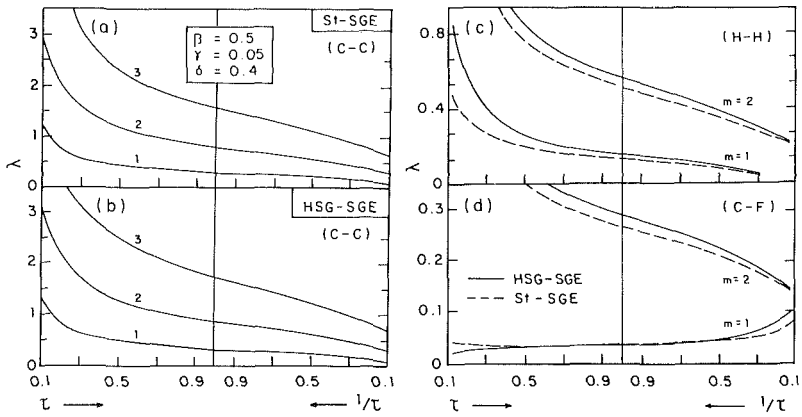


Fig. 2 Influence of taper on frequency parameter

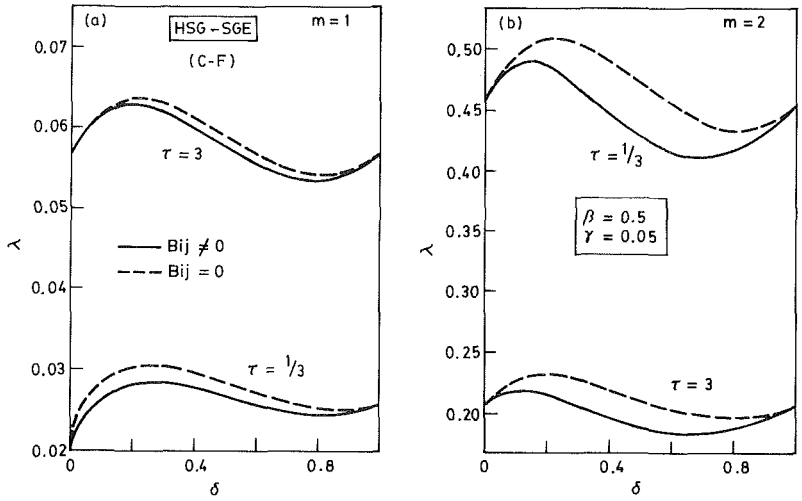


Fig. 3 Effect of relative layer thickness and coupling on frequency parameter

= .1, λ_1 increases with τ for HSG-SGE and decreases for St-SGE. The boundary conditions and the dissimilarity in them combined with the layer properties must be the reasons. Following HSG-SGE plate through different boundary conditions, (Figs. 2(*b*), (*c*), and (*d*)), it is seen that there is the maximum percentage difference in λ due to tapering for *C-C* conditions (1952 percent) and the minimum for *C-F* conditions (435 percent).

The manner of variation of λ with the ratio δ is illustrated in Fig. 3. A HSG-SGE layer combination, with inner edge clamped and the outer edge free, is considered. The plate is of medium width ($\beta = 0.5$). Two representative cases of tapering, thickness increasing in one ($\tau = 1/3$) and decreasing in the other ($\tau = 3$), as the radius increases, are considered. When $\delta = 0$ or 1, the plate is of homogeneous material, SGE or HSG, accordingly. The curves are continuous, with maximum and minimum values, showing that it is often possible to attain frequencies corresponding to homogeneous plates of either of the two materials by making one or more proper choices of the relative layer thickness. The dashed lines in the figure correspond to the cases when the coupling terms B_{ij} are omitted. The relative changes in λ due to neglect of coupling are so small that coupling can be ignored resulting in considerable analytical and computational advantage. The frequencies are found to be higher for plates of smaller width.

Figure 4 exhibits the relation between ω and β for some cases considered. It is seen that all curves, of different modes, have the same characteristic form. The frequencies always increase

Downloaded 03 May 2010 to 171.66.16.247. Redistribution subject to ASME license or copyright; see http://www.asme.org/terms/Terms_Use.cfm

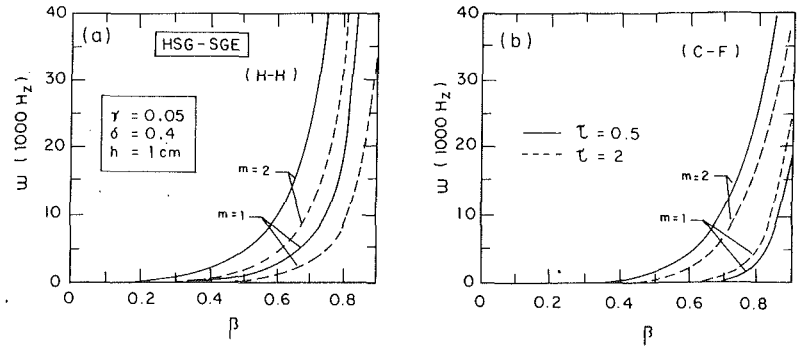


Fig. 4 Effect of plate width on frequencies

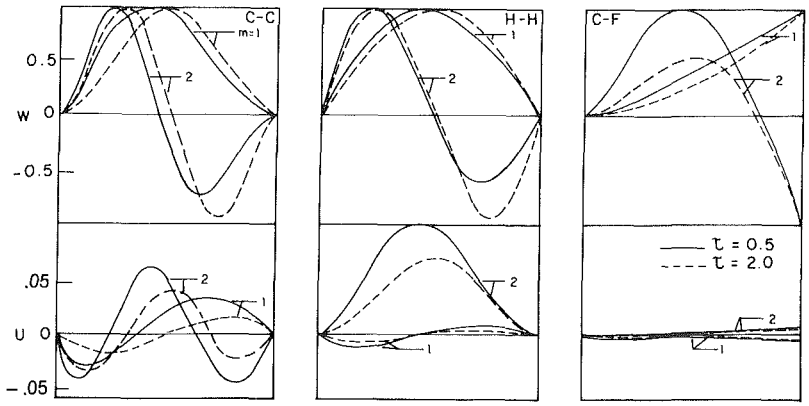


Fig. 5 Mode shapes of vibration of plates

with β; gradually up to some value of β, and then steeply. The steep changes commence at smaller values of β at higher flexural modes; at higher values of β for *C-F* conditions than for *C-C* and *H-H* conditions. The effect of increase in τ is to lower the frequencies in the cases of *C-C* and *H-H* conditions. These results closely follow those observed in the case of homogeneous plates of linearly varying thickness.

Some typical mode shapes of axisymmetric vibrations are shown in Fig. 5. All pertain to HSG-SGE plates with $\beta = 0.5$, $\gamma = 0.05$, and $\delta = 0.4$. It can be seen that the flexural vibrations are more predominant than the extensional ones. For the *C-C* plate, the extensional modes always have one extra node. For the *H-H* plate, the first two extensional modes have reverse correspondence in number of nodes with the respective flexural modes. With the increased value of τ, more symmetry and antisymmetry are introduced in the mode shapes, for plates of symmetric boundary conditions and the amplitudes of extensional mode shapes get reduced for all the boundary conditions considered.

References

Navaneethakrishnan, P. V., and Chandrasekaran, K., 1989, "A Spline Function Analysis of Axisymmetric Free Vibrations of Layered Conical Shells and Plates of Variable Thickness," *Structural Vibration and Acoustics*, ASME, DE-Vol. 18-3, pp. 153-159.

Raju, I. S., Prakasa Rao, I. S., and Venkateswara, Rao, 1974, "Axisymmetric Vibrations of Linearly Tapered Annular Plates," *Journal of Sound and Vibration*, Vol. 32-4, pp. 507-512.

APPENDIX

The following are the differential operators appearing in Eq. (2):

$$L_{11}=\frac{d^2}{dx^2}+\frac{2x-c}{x(x-c)}\frac{d}{dx}+\frac{s_2}{x(x-c)}-\frac{s_3}{x^2}+\frac{\lambda^2}{l^2}$$

$$L_{13}=-\frac{(x-c)s_4}{(a-c)}\frac{d^3}{dx^3}-\frac{(3x-c)s_4}{x(a-c)}\frac{d^2}{dx^2}+\left[\frac{(x-c)s_6}{x}-2s_5\right]\frac{1}{(a-c)x}\frac{d}{dx}$$

$$L_{31}=\frac{(x-c)s_4}{(a-c)}\frac{d^3}{dx^3}+\frac{2(3x-c)s_4}{x(a-c)}\frac{d^2}{dx^2}+\left[\frac{2(3x-2c)s_4}{(x-c)}+2s_5-\frac{(x-c)s_6}{x}\right]\frac{1}{x(a-c)}\frac{d}{dx}+\left[\frac{2s_5}{(x-c)}-\frac{(x+c)s_6}{x^2}\right]\frac{1}{x(a-c)}$$

$$L_{33}=-\frac{(x-c)^2s_7}{(a-c)^2}\frac{d^4}{dx^4}-\frac{2(x-c)(4x-c)s_7}{x(a-c)^2}\frac{d^3}{dx^3}+\left[\frac{2(x-c)^2s_9}{x}-6(2x-c)s_7-3(x-c)s_8\right]\frac{1}{x(a-c)^2}\frac{d^2}{dx^2}+\left[\frac{(x-c)(2x+c)s_9}{x^2}-6s_8\right]\frac{1}{x(a-c)^2}\frac{d}{dx}+\frac{\lambda^2}{l^2}$$

where $s_2 = A_{12}/A_{11}$, $s_3 = A_{22}/A_{11}$, $s_4 = B_{11}/A_{11}$, $s_5 = B_{12}/A_{11}$, $s_6 = B_{22}/A_{11}$, $s_7 = D_{11}/A_{11}$, $s_8 = D_{12}/A_{11}$, $s_9 = D_{22}/A_{11}$, and A_{ij}, B_{ij}, C_{ij} are extensional, extensional-bending, and bending elastic coefficients.

Downloaded 03 May 2010 to 171.66.16.247. Redistribution subject to ASME license or copyright; see http://www.asme.org/terms/Terms_Use.cfm

Journal of Applied Mechanics

Discussion

Circumferential Stresses in Curved Beams[1]

Robert Schmidt.[2] The common formula for the circumferential normal stress σ_θ (author's Eq. (1)) usually is *not* "obtained by superposing bending stress and direct stress," as stated by the author, but is a direct consequence of Winkler's hypothesis. This hypothesis that plane normal cross-sections of the curved beam before deformation remain plane, normal, and inextensible during deformation leads to the following expression for the extensional strain ϵ_θ (Schmidt, 1979; Huddleston, 1968; Schmidt and DaDeppo, 1970):

$$\epsilon_\theta = \frac{1}{r}\left[R\epsilon_c - (R-r)\beta'\right],$$

where ϵ_c and β are the strain and angle of rotation, respectively, of an element $Rd\theta$ of the centroidal curve, and $\beta' = d\beta/d\theta$. With the Hooke law $\sigma_\theta = E\epsilon_\theta$, the first integral in the author's Eq. (3) yields the force

$$N = \frac{EA\,(R\epsilon_c + e\beta')}{R-e}.$$

The bending moment M is given by

$$M = \int (R-r)\sigma_\theta dA = \frac{EARe(\epsilon_c - \beta')}{R-e}.$$

Solving the last two equations for ϵ_c and β', we obtain

$$\epsilon_c = \frac{RN-M}{EAR}, \qquad \beta' = \frac{eN-M}{EAe},$$

two structurally similar expressions. Substituting this result into our expression for ϵ_θ and employing Hooke's law, $\sigma_\theta = E\epsilon_\theta$, we obtain the author's Eq. (1).

Now we may say that the author's numerical examples make it clear that the Winkler hypothesis of rigid normal sections, although very dependable in the case of pure flexure, should be used with great caution in other cases of applied loads. Needless to say, we should appreciate the author's revealing calculations.

That the author's semi-empirically modified formulas have yielded more accurate results at some points is not surprising, since the modification was contrived with that intent. It also should be kept in mind that, in view of the Saint-Venant principle, Winkler's theory was not intended for extremely thick curved beams.

In the case $P > 0$, $M_o = -PR$, $a/b = 2$, for example, at $\theta = 90$ deg and $r = b$, $s_b \equiv (a/P)\sigma_\theta = 25.766$ as calculated by the plane-stress theory (Timoshenko and Goodier, 1970) for $P > 0$, $M_o = 0$; and $\bar{s}_b = -23.265 = -1.5 \times 2 \times 7.755$ from page 74 of Timoshenko and Goodier (1970) for $P = 0$, $M_o = -PR$; so that $s_b + \bar{s}_b = 25.766 - 23.265 = 2.501$, a small difference. Author's formula (1) analogously yields $25.176 - 23.176 = 2.000$, so that the ratio $2.000/2.501 = 0.800$ is the same as in the author's Table 1. At $r = a$, we have $s_a + \bar{s}_a = -12.883 + 14.751 = 1.868$ by the exact theory, and the ratio is $2.000/1.868 = 1.071$. The approximate value of the dimensionless stress at $r = b$, $\theta = 90$ deg can seemingly be improved by employing a stress concentration factor of circa 1¼ found in most elementary textbooks on mechanics of materials in the case of straight rods; thus, $2 \times 1\frac{1}{4} = 2.5$. The calculations in this paragraph demonstrate that small differences result when large stresses are superposed in the author's example, and this fact is a partial explanation of the inaccuracy of the rationally derived Formula (1).

Additional References

Huddleston, J. V., 1968, "Finite Deflections and Snap-Through of High Circular Arches," ASME Journal of Applied Mechanics, Vol. 35, pp. 763–769.

Schmidt, R., 1979, "Initial Postcritical Behavior of Circular Arches with Hinged Ends," *Industrial Mathematics*, Vol. 29, pp. 27–38.

Schmidt, R., and DaDeppo, D. A., 1970, "Large Deflections of Eccentrically Loaded Arches," *Zeitschrift fuer angewandte Mathematik und Physik*, Vol. 21, pp. 991–1004.

Author's Closure[3]

The author would like only to add that all these assessments of accuracy are based on rectangular cross-sections because exact solutions are available only for plane-stress problems. The practical situation typically involves a nonrectangular cross-section and is fully three dimensional. In this case, the standard of comparison must be experimental results or finite elements results, and very few are available.

Quite recently I was able to compare curved-beam formulas with results from a detailed three-dimensional finite element analysis of a crane hook whose cross-section was the typical one, i.e., a slender trapezoid with rounded ends and larger part toward the center of curvature. The hook was loaded by a force directed through its center of curvature so as to create both bending and tension on the cross-section analyzed. At the inside, Eqs. (1) and (4) of the Note gave circumferential stress values that were, respectively, 14 and 8 percent lower than the finite element stress.

I suspect that most of the discrepancy comes from displacements not being independent of coordinate z, as is assumed in the analysis of curved beams. This effect appeared in another finite element study (Cook, 1989) where in one test case of a

[1]By Robert D. Cook and published in the March 1992 issue of the ASME Journal of Applied Mechanics, Vol. 59, pp. 224–225.

[2]Professor of Engineering Mechanics, College of Engineering and Science, University of Detroit and College of Mercy, Detroit, MI 48221. Mem. ASME.

[3]Robert D. Cook, Department of Engineering Mechanics, University of Wisconsin, Madison, WI 53706.

Copyright © 1992 by ASME
Downloaded 03 May 2010 to 171.66.16.247. Redistribution subject to ASME license or copyright; see http://www.asme.org/terms/Terms_Use.cfm

trapezoidal cross-section the neutral axis was found to be curved, even with a zero Poisson ratio, and inside circumferential stresses varied by a factor of 2 in the z direction for $a/b = 3$. (The latter finite element study is mathematically two-dimensional but can deal only with pure bending.)

References

Cook, R. D., 1989, "Axisymmetric Finite Element Analysis for Pure Moment Loading of Curved Beams and Pipe Bends," *Computers and Structures*, Vol. 33, pp. 483–487.

Dynamic Crack Propagation Analysis by Moving Singular Boundary Elements[4]

Robert B. Haber[5]. The authors present a numerical method for solving elastodynamic crack propagation problems based on the boundary element method and moving singular elements. As the authors suggest, the problem of controlling the evolution of the mesh geometry for crack propagation problems is considerably easier in the boundary element method than in the finite element method; so the proposed approach seems attractive. The discussion below addresses a minor graphical error and some omissions in the literature review, and comments on the numerical results and the authors' boundary element formulation.

1 A minor error appears in Fig. 2. According to the authors' discussion, four elements should appear to the right of the crack-tip position in Figs. 2(*b*) and 2(*c*) (rather than three elements), since the effects of the remeshing operation should not appear until Fig. 4(*d*).

2 The authors omitted *remeshing methods*, such as those proposed by Swenson and Ingraffea (1988), in their review of the finite element literature on elastodynamic fracture. Also omitted from the literature survey on moving-grid finite element methods were the papers by Koh and Haber (1986) and Koh, Lee, and Haber (1988) based on the Eulerian-Lagrangian description of motion (ELD).

3 The authors' Fig. 8 compares their boundary element solution for the finite body problem depicted in Fig. 6 with analytic results by Freund (1973) and a moving-grid finite element solution reported by Nishioka and Atluri (1980). There is generally good agreement, except that the two numerical solutions fail to capture the jump in the dynamic stress intensity factor that occurs immediately after the onset of crack propagation in Freund's analytical result. The results obtained for the same problem by Koh, Lee, and Haber (1988) with the ELD finite element method do not suffer this deficiency and compare well with Freund's solution, even in the transient period following the initiation of crack growth. This suggests that solutions obtained with the ELD finite element method would provide a better benchmark for comparing the authors' formulation to existing numerical methods. It would be useful to identify which aspect of the authors' method is responsible for the error in the predicted transient response.

For later times, when reflections from the structure boundaries and interactions between the crack tips affect the near-tip fields, the authors' solution differs somewhat from the two finite element solutions which are in reasonably close agreement (the only significant difference between the finite element results arises from the different signals generated by the two models' representations of the transient crack initiation behavior, as discussed above). It would be useful to identify the reasons for the differences between the boundary element solution and the two finite element solutions and to undertake mesh refinement studies to find an accurate reference solution for times when Freund's analytical results are not valid.

4 The analysis of elastodynamic crack propagation involves a boundary value problem defined on a variable material domain. That is, both the material domain Ω and its boundary Γ vary continuously over time. It is clear that Γ varies as the crack extends, but perhaps less obvious that Ω also varies. Although there is no transport of material across $\partial\Omega$ as the crack extends (for finite body problems), the topology of the material domain is continuously varying. Since there is no time-invariant material domain Ω for this class of problems, function descriptions of the form ψ: $\Omega \times [0, t] \rightarrow \Re$ are ambiguous. For example, consider a position vector r that at time t_1 lies directly in front of the advancing crack tip and at a later time t_2 lies on the newly formed crack surface. At time t_1 there is a continuous, single-valued function that describes displacements in the neighborhood of r in Ω. However, at time t_2, the displacement function is no longer single-valued at r due to the topology change caused by the advancing crack. In fact, a one-to-one mapping cannot be constructed between corresponding material locations in the distinct domains $\Omega(t_1)$ and $\Omega(t_2)$.

In view of the topology changes generated by crack growth, the definition of the time-dependent shape function in Eq. (18) needs clarification. In general, the definition of the admissible function spaces becomes quite complicated if one attempts to develop a variational formulation of the elastodynamic boundary value problem directly on a time-varying material domain. The trouble in evaluating the time integrals in the boundary element formulation analytically is another difficulty associated with time-varying shape functions, as discussed in the paper.

The ELD formulation presented by Koh and Haber (1986) circumvents these problems. The key step is the reformulation of the boundary value problem using a time-invariant *reference domain*, which we denote here as Ω^r. A geometry function, $\mathbf{X}$: $\Omega^r \times [0, t] \rightarrow \Omega(t)$ defines the time-varying material domain. There is an Eulerian component to this kinematic model, since a fixed position in Ω^r maps to different material particles at different times. In isoparametric element formulations based on the ELD, the parent element geometry provides a local definition of the reference domain and we write time-invariant shape functions using the element natural coordinates. These basis functions are used to express both the domain mapping $\mathbf{X}$ and the various response functions. The ELD leads to a modified set of governing equations that define a new boundary value problem on the fixed reference domain Ω^r. This provides a consistent basis for the formulation of moving-grid numerical methods.

The reader should refer to the literature for a complete development of the elastodynamic ELD, but it is worthwhile to note here that the combination of the ELD and moving singular-quarter-point elements automatically introduces the proper $r^{-1/2}$ singular forms in both the strain and velocity fields for elastodynamic crack propagation problems. The singularity in the velocity field vanishes when the geometry mapping is steady, so the ELD velocity field is nonsingular, as expected, in the case of a stationary crack.

It would be interesting to see whether the ELD could be used to formulate a moving singular boundary element method along the lines proposed in this paper. The time dependence of the shape functions would be eliminated, so that it might still be possible to evaluate the time integrals analytically, as in the standard boundary element method. There would be no need to assume constant mesh or crack-tip velocity within each time step as in Eqs. (18) and (19). This would be a significant advantage if the discrepancies that appear in the numerical

[4]By Rafael Gallego and Josè Dominguez and published in the June 1992 issue of the ASME JOURNAL OF APPLIED MECHANICS, Vol. 59, Part 2, pp. S158–S162.

[5]Department of Theoretical and Applied Mechanics, University of Illinois at Urbana-Champaign, Urbana, IL 61801.

Copyright © 1992 by ASME
Downloaded 03 May 2010 to 171.66.16.247. Redistribution subject to ASME license or copyright; see http://www.asme.org/terms/Terms_Use.cfm

results for the transient response following the sudden initiation of crack growth are caused by this approximation.

References

Freund, L. B., 1973, "Crack Propagation in an Elastic Solid Subjected to General Loading-III: Stress-Wave Loading," *J. Mech. Phys. Solids*, Vol. 21, pp. 47-61.

Koh, H. M., and Haber, R. B., 1986, "Elastodynamic Formulation of the Eulerian-Lagrangian Kinematic Description," ASME JOURNAL OF APPLIED MECHANICS, Vol. 53, pp. 839-845.

Koh, H. M., Lee, H. S., and Haber, R. B., 1988, "Dynamic Crack Propagation Analysis Using Eulerian-Lagrangian Kinematic Descriptions," *Computational Mechanics*, Vol. 3, pp. 141-155.

Nishioka, T., and Atluri, S. N., 1980, "Numerical Modelling of Dynamic Crack Propagation in Finite Bodies by Moving Singular Element, Part I: Formulation; Part II: Results," ASME JOURNAL OF APPLIED MECHANICS, Vol. 47, pp. 570-576; pp. 577-582.

Swenson, D. V., and Ingraffea, A., 1988, "Modeling Mixed-Mode Dynamic Crack Propagation Using Finite Elements: Theory and Applications," *Computational Mechanics*, Vol. 3, pp. 381-387.

Authors' Closure[6]

We like to thank Professor Haber for pointing out the error in Fig. 2, and the articles by Swenson and Ingraffea and Koh, Lee, and Haber of which we were not aware.

Regarding the comparison of the boundary element method solution with the analytical one by Freund (1973), it is not very clear in Fig. 8, but the numerical solution does capture the jump in the dynamic stress intensity factor (DSIF) that occurs right after the crack propagation. The scale and quality of the figure may not be good enough to properly exhibit this fact. By the other hand, the time interval used in the calculation (0.34 μs) is too big to *show* a sharp jump in the DSIF, even though the numerical solution agrees fairly closely with the analytical one, before and after the onset of crack propagation. We have obtained better agreement using a finer mesh in time and space, though this issue was not stressed in the paper. For later times, where the analytical solution is no longer valid, further work is needed to determine the origin of the discrepancies between the numerical solutions.

Professor Haber rightly states that a one-to-one mapping cannot be constructed between material locations in $\Omega(t_1)$ and $\Omega(t_2)$ in a general crack propagation problem. However, in the problem under consideration, the domain is reduced to a simply connected one due to the symmetry of loads and geometry. In this simplified problem, neither the material domain nor its boundary actually change with time: only the applied boundary conditions change. Even in a general mixed-mode problem, the subdomain method (Dominguez and Gallego, 1992, for stationary cracks under dynamic mixed mode conditions) will render the changing domain to two coupled simply connected ones where the above argument can be equally applied.

The time integrals are evaluated analytically when a linear time variation of the shape functions is considered. Further terms in the time expansion of the shape functions, if desired or needed, will lead to new time integrals which can be calculated analytically as well.

Nevertheless, it would be very interesting to check the applicability of the Eulerian-Langrangian description formulation to the boundary element method as proposed by Professor Haber.

References

Freund, L. B., 1973, "Crack Propagation in an Elastic Solid Subjected to General Loading—III: Stress-Wave Loading," *J. Mech. Phys. Solids*, Vol. 21, pp. 47-61.

Dominguez, J., and Gallego, R., 1992, "Time Domain Boundary Element Method for Dynamic Stress Intensity Factor Computations," *Int. J. Num. Meth. Engrg.*, Vol. 33, pp. 635-647.

[6]Rafael Gallego, ESII—Depto. Estructuras, c/Reina Mercedes s/n, E-41012 Sevilla, Spain and José Dominguez, Professor, Escuela Tecnica Superior de Ingenieros Industriales, Universidad de Sevilla, 41012 Sevilla, Spain.

Natural Frequencies and Normal Modes of a Spinning Timoshenko Beam With General Boundary Conditions[7]

Charles W. Bert[8]. The authors are to be congratulated for their very interesting analysis of the vibration of a spinning Timoshenko beam. However, some comments are in order.

First, the authors' identification of the forward and backward precession frequencies is exactly opposite to that of all previous investigations known to the present writer: Dimentberg (1961) and Yu (1987) for a spinning Euler-Bernoulli beam and Dimentberg (1961), Eshleman and Eubanks (1969), Porat and Niv (1971), and Pedersen (1972) for a spinning Timoshenko beam.

Secondly, it was shown by Porat and Niv (1971) and Pedersen (1972) that backward-precession critical speeds are impossible for the case of a perfect system (i.e., no imperfections). However, Pedersen (1972) showed that backward-precession critical speeds are possible in the case of a system with anisotropic bearings.

References

Dimentberg, F. M., 1961, *Flexural Vibrations of Rotating Shafts*, Butterworths, London.

Eshleman, R. L., and Eubanks, R. A., 1969, "On the Critical Speeds of a Continuous Rotor," ASME *Journal of Engineering for Industry*, Vol. 91, pp. 1180-1188.

Pedersen, P. T., 1972, "On Forward and Backward Precession of Rotors," *Ingenieur-Archiv*, Vol. 42, pp. 26-41.

Porat, I., and Niv, M., 1971, "Vibration of a Rotating Shaft by the 'Timoshenko Beam' Theory," *Israel Journal of Technology*, Vol. 9, pp. 535-546.

Yu, H., 1987, "The Stability of Rotating Shafts When Distributed Gyroscopic Effects Are Taken into Account," *Rotating Machinery Dynamics*, Vol. 1, A. Muszynska and J. C. Simonis, eds., DE-Vol. 1, ASME, NY, pp. 35-39.

Authors' Closure[9]

The authors would like to express their thanks to Professor Charles Bert for his interest in our work (Zu and Han, 1992). In particular, we would like to convey our appreciation to him for pointing out the typographical error in the identification of the forward and backward precession frequencies. We would also like to further add that the same error was made in the mode shape plots.

Another interesting point mentioned by Professor Bert is that of critical speeds. Although this issue was not discussed in our paper, we would like to confirm that for a system with no imperfections (i.e., unbalanced mass or initial deflections) or other excitations, it is impossible to get *either* forward or backward precession resonance. This is because resonance can only occur when there is a forced vibration. For a system with imperfections, it should be pointed out that, generally, there is no backward precession resonance but there is forward precession resonance, and this was proved theoretically by Porat and Niv (1971) for the case of a simply-supported Timoshenko beam. We would like to extend this proof to handle a spinning Timoshenko beam with any general classical conditions and this is done as follows:

[7]By J. W. Z. Zu and R. P. S. Han and published in the June 1992 issue of the ASME JOURNAL OF APPLIED MECHANICS, Vol. 59, Part 2, pp. S197-S204.

[8]Director and Perkinson Chair, School of Aerospace and Mechanical Engineering, University of Oklahoma, Norman, OK 73019-0601.

[9]Jean Wu-Zheng Zu, Graduate Student, and Ray P. S. Han, Associate Professor, Mem. ASME, Department of Mechanical and Industrial Engineering, University of Manitoba, Winnipeg, Manitoba, Canada, R3T 2N2.

Downloaded 03 May 2010 to 171.66.16.247. Redistribution subject to ASME license or copyright; see http://www.asme.org/terms/Terms_Use.cfm

results for the transient response following the sudden initiation of crack growth are caused by this approximation.

References

Freund, L. B., 1973, "Crack Propagation in an Elastic Solid Subjected to General Loading-III: Stress-Wave Loading," *J. Mech. Phys. Solids*, Vol. 21, pp. 47-61.

Koh, H. M., and Haber, R. B., 1986, "Elastodynamic Formulation of the Eulerian-Lagrangian Kinematic Description," ASME JOURNAL OF APPLIED MECHANICS, Vol. 53, pp. 839-845.

Koh, H. M., Lee, H. S., and Haber, R. B., 1988, "Dynamic Crack Propagation Analysis Using Eulerian-Lagrangian Kinematic Descriptions," *Computational Mechanics*, Vol. 3, pp. 141-155.

Nishioka, T., and Atluri, S. N., 1980, "Numerical Modelling of Dynamic Crack Propagation in Finite Bodies by Moving Singular Element, Part I: Formulation; Part II: Results," ASME JOURNAL OF APPLIED MECHANICS, Vol. 47, pp. 570-576; pp. 577-582.

Swenson, D. V., and Ingraffea, A., 1988, "Modeling Mixed-Mode Dynamic Crack Propagation Using Finite Elements: Theory and Applications," *Computational Mechanics*, Vol. 3, pp. 381-387.

Authors' Closure[6]

We like to thank Professor Haber for pointing out the error in Fig. 2, and the articles by Swenson and Ingraffea and Koh, Lee, and Haber of which we were not aware.

Regarding the comparison of the boundary element method solution with the analytical one by Freund (1973), it is not very clear in Fig. 8, but the numerical solution does capture the jump in the dynamic stress intensity factor (DSIF) that occurs right after the crack propagation. The scale and quality of the figure may not be good enough to properly exhibit this fact. By the other hand, the time interval used in the calculation (0.34 μs) is too big to *show* a sharp jump in the DSIF, even though the numerical solution agrees fairly closely with the analytical one, before and after the onset of crack propagation. We have obtained better agreement using a finer mesh in time and space, though this issue was not stressed in the paper. For later times, where the analytical solution is no longer valid, further work is needed to determine the origin of the discrepancies between the numerical solutions.

Professor Haber rightly states that a one-to-one mapping cannot be constructed between material locations in $\Omega(t_1)$ and $\Omega(t_2)$ in a general crack propagation problem. However, in the problem under consideration, the domain is reduced to a simply connected one due to the symmetry of loads and geometry. In this simplified problem, neither the material domain nor its boundary actually change with time: only the applied boundary conditions change. Even in a general mixed-mode problem, the subdomain method (Dominguez and Gallego, 1992, for stationary cracks under dynamic mixed mode conditions) will render the changing domain to two coupled simply connected ones where the above argument can be equally applied.

The time integrals are evaluated analytically when a linear time variation of the shape functions is considered. Further terms in the time expansion of the shape functions, if desired or needed, will lead to new time integrals which can be calculated analytically as well.

Nevertheless, it would be very interesting to check the applicability of the Eulerian-Langrangian description formulation to the boundary element method as proposed by Professor Haber.

References

Freund, L. B., 1973, "Crack Propagation in an Elastic Solid Subjected to General Loading—III: Stress-Wave Loading," *J. Mech. Phys. Solids*, Vol. 21, pp. 47-61.

Dominguez, J., and Gallego, R., 1992, "Time Domain Boundary Element Method for Dynamic Stress Intensity Factor Computations," *Int. J. Num. Meth. Engrg.*, Vol. 33, pp. 635-647.

[6]Rafael Gallego, ESII—Depto. Estructuras, c/Reina Mercedes s/n, E-41012 Sevilla, Spain and José Dominguez, Professor, Escuela Tecnica Superior de Ingenieros Industriales, Universidad de Sevilla, 41012 Sevilla, Spain.

Natural Frequencies and Normal Modes of a Spinning Timoshenko Beam With General Boundary Conditions[7]

Charles W. Bert[8]. The authors are to be congratulated for their very interesting analysis of the vibration of a spinning Timoshenko beam. However, some comments are in order.

First, the authors' identification of the forward and backward precession frequencies is exactly opposite to that of all previous investigations known to the present writer: Dimentberg (1961) and Yu (1987) for a spinning Euler-Bernoulli beam and Dimentberg (1961), Eshleman and Eubanks (1969), Porat and Niv (1971), and Pedersen (1972) for a spinning Timoshenko beam.

Secondly, it was shown by Porat and Niv (1971) and Pedersen (1972) that backward-precession critical speeds are impossible for the case of a perfect system (i.e., no imperfections). However, Pedersen (1972) showed that backward-precession critical speeds are possible in the case of a system with anisotropic bearings.

References

Dimentberg, F. M., 1961, *Flexural Vibrations of Rotating Shafts*, Butterworths, London.

Eshleman, R. L., and Eubanks, R. A., 1969, "On the Critical Speeds of a Continuous Rotor," ASME *Journal of Engineering for Industry*, Vol. 91, pp. 1180-1188.

Pedersen, P. T., 1972, "On Forward and Backward Precession of Rotors," *Ingenieur-Archiv*, Vol. 42, pp. 26-41.

Porat, I., and Niv, M., 1971, "Vibration of a Rotating Shaft by the 'Timoshenko Beam' Theory," *Israel Journal of Technology*, Vol. 9, pp. 535-546.

Yu, H., 1987, "The Stability of Rotating Shafts When Distributed Gyroscopic Effects Are Taken into Account," *Rotating Machinery Dynamics*, Vol. 1, A. Muszynska and J. C. Simonis, eds., DE-Vol. 1, ASME, NY, pp. 35-39.

Authors' Closure[9]

The authors would like to express their thanks to Professor Charles Bert for his interest in our work (Zu and Han, 1992). In particular, we would like to convey our appreciation to him for pointing out the typographical error in the identification of the forward and backward precession frequencies. We would also like to further add that the same error was made in the mode shape plots.

Another interesting point mentioned by Professor Bert is that of critical speeds. Although this issue was not discussed in our paper, we would like to confirm that for a system with no imperfections (i.e., unbalanced mass or initial deflections) or other excitations, it is impossible to get *either* forward or backward precession resonance. This is because resonance can only occur when there is a forced vibration. For a system with imperfections, it should be pointed out that, generally, there is no backward precession resonance but there is forward precession resonance, and this was proved theoretically by Porat and Niv (1971) for the case of a simply-supported Timoshenko beam. We would like to extend this proof to handle a spinning Timoshenko beam with any general classical conditions and this is done as follows:

[7]By J. W. Z. Zu and R. P. S. Han and published in the June 1992 issue of the ASME JOURNAL OF APPLIED MECHANICS, Vol. 59, Part 2, pp. S197-S204.

[8]Director and Perkinson Chair, School of Aerospace and Mechanical Engineering, University of Oklahoma, Norman, OK 73019-0601.

[9]Jean Wu-Zheng Zu, Graduate Student, and Ray P. S. Han, Associate Professor, Mem. ASME, Department of Mechanical and Industrial Engineering, University of Manitoba, Winnipeg, Manitoba, Canada, R3T 2N2.

Copyright © 1992 by ASME
Downloaded 03 May 2010 to 171.66.16.247. Redistribution subject to ASME license or copyright; see http://www.asme.org/terms/Terms_Use.cfm